

FILE COPY

AD-A223 125

AIR FORCE OFFICE OF
SCIENTIFIC RESEARCH
UNITED STATES AIR FORCE
RESEARCH INITIATION
PROGRAM

CONDUCTED BY
UNIVERSAL ENERGY SYSTEMS
U.E.S.

1988

TECHNICAL REPORT

VOLUME 3 OF 4

RODNEY C. DARRAH
PROGRAM DIRECTOR, UES

SUSAN K. ESPY
PROGRAM ADMINISTRATOR, UES

LT. COL. CLAUDE CAVENDER
PROGRAM MANAGER, AFOSR

DISTRIBUTION STATEMENT A

Approved for public release

REPORT DOCUMENTATION PAGE

Form Approved
OMB No. 0704-0188

[illegible]

1. AGENCY USE ONLY (Leave blank)		2. REPORT DATE		3. REPORT TYPE AND DATES COVERED	
				Technical Report	
4. TITLE AND SUBTITLE				5. FUNDING NUMBERS	
United States Air Force Research Initiation Program				61102F 3484/D5	
6. AUTHOR(S)					
Rodney C. Darrah Lt Col Claude Cavender					
7. PERFORMING ORGANIZATION NAME(S) AND ADDRESS(ES)				8. PERFORMING ORGANIZATION REPORT NUMBER	
Universal Energy Systems				AFOSR-TR- 90 0709	
9. SPONSORING / MONITORING AGENCY NAME(S) AND ADDRESS(ES)				10. SPONSORING / MONITORING AGENCY REPORT NUMBER	
AFOSR/XOT Bld 410 Bolling AFB DC 20332-6448				F49620-88-C-0053	
11. SUPPLEMENTARY NOTES					
12a. DISTRIBUTION / AVAILABILITY STATEMENT				12b. DISTRIBUTION CODE	
Unlimited					
13. ABSTRACT (Maximum 400 words)					
See Attached					
14. SUBJECT TERMS				15. NUMBER OF PAGES	
				16. PRICE CODE	
17. SECURITY CLASSIFICATION OF REPORT	18. SECURITY CLASSIFICATION OF THIS PAGE	19. SECURITY CLASSIFICATION OF ABSTRACT	20. LIMITATION OF ABSTRACT		
Unclassified	Unclassified	Unclassified	N/A		

INTRODUCTION

Research Initiation Program - 1988

AFOSR has provided funding for follow-on research efforts for the participants in the Summer Faculty Research Program. Initially this program was conducted by AFOSR and popularly known as the Mini-Grant Program. Since 1983 the program has been conducted by the Summer Faculty Research Program (SFRP) contractor and is now called the Research Initiation Program (RIP). Funding is provided to establish RIP awards to about half the number of participants in the SFRP.

Participants in the 1988 SFRP competed for funding under the 1988 RIP. Participants submitted cost and technical proposals to the contractor by 1 November 1988, following their participation in the 1988 SFRP.

Evaluation of these proposals was made by the contractor. Evaluation criteria consisted of:

1. Technical Excellence of the proposal
2. Continuation of the SFRP effort
3. Cost sharing by the University

The list of proposals selected for award was forwarded to AFOSR for approval of funding. Those approved by AFOSR were funded for research efforts to be completed by 31 December 1989.

The following summarizes the events for the evaluation of proposals and award of funding under the RIP.

- A. Rip proposals were submitted to the contractor by 1 November 1988. The proposals were limited to \$20,000 plus cost sharing by the universities. The universities were encouraged to cost share since this is an effort to establish a long term effort between the Air Force and the university.
3. Proposals were evaluated on the criteria listed above and the final award approval was given by AFOSR after consultation with the Air Force Laboratories.
- C. Subcontracts were negotiated with the universities. The period of performance of the subcontract was between October 1988 and December 1989.

Copies of the Final Reports are presented in Volumes I through IV of the 1988 Research Initiation Program Report. There were a total of 92 RIP awards made under the 1988 program.

UNITED STATES AIR FORCE
1988 RESEARCH INITIATION PROGRAM

Conducted by
UNIVERSAL ENERGY SYSTEMS, INC.

under
USAF Contract Number F49620-88-C-0053

RESEARCH REPORTS
VOLUME III OF IV

Submitted to
Air Force Office of Scientific Research
Bolling Air Force Base
Washington, DC

By
Universal Energy Systems, Inc.
April 1990



Accession For	
NTIS	CRA&I
DTIC	Exp
Unannounced	
Justification	
By	
Distribution	
Availability	
Dist	
A-1	

TABLE OF CONTENTS

<u>SECTION</u>	<u>PAGE</u>
INTRODUCTION	i
STATISTICS	ii
PARTICIPANT LABORATORY ASSIGNMENT	vii
RESEARCH REPORTS	xvii

INTRODUCTION

Research Initiation Program - 1988

AFOSR has provided funding for follow-on research efforts for the participants in the Summer Faculty Research Program. Initially this program was conducted by AFOSR and popularly known as the Mini-Grant Program. Since 1983 the program has been conducted by the Summer Faculty Research Program (SFRP) contractor and is now called the Research Initiation Program (RIP). Funding is provided to establish RIP awards to about half the number of participants in the SFRP.

Participants in the 1988 SFRP competed for funding under the 1988 RIP. Participants submitted cost and technical proposals to the contractor by 1 November 1988, following their participation in the 1988 SFRP.

Evaluation of these proposals was made by the contractor. Evaluation criteria consisted of:

1. Technical Excellence of the proposal
2. Continuation of the SFRP effort
3. Cost sharing by the University

The list of proposals selected for award was forwarded to AFOSR for approval of funding. Those approved by AFOSR were funded for research efforts to be completed by 31 December 1989.

The following summarizes the events for the evaluation of proposals and award of funding under the RIP.

- A. Rip proposals were submitted to the contractor by 1 November 1988. The proposals were limited to \$20,000 plus cost sharing by the universities. The universities were encouraged to cost share since this is an effort to establish a long term effort between the Air Force and the university.
- B. Proposals were evaluated on the criteria listed above and the final award approval was given by AFOSR after consultation with the Air Force Laboratories.
- C. Subcontracts were negotiated with the universities. The period of performance of the subcontract was between October 1988 and December 1989.

Copies of the Final Reports are presented in Volumes I through IV of the 1988 Research Initiation Program Report. There were a total of 92 RIP awards made under the 1988 program.

STATISTICS

PROGRAM STATISTICS

Total SFRP Participants	153
Total RIP Proposals submitted by SFRP	121
Total RIP Proposals submitted by GSRP	5
Total RIP Proposals submitted	126
Total RIP's funded to SFRP	85
Total RIP's funded to GSRP	3
Total RIP's funded	88
Total RIP's Proposals submitted by HBCU's	8
Total RIP's Proposals funded to HBCU's	4

LABORATORY PARTICIPATION

<u>Laboratory</u>	<u>SFRP Participants</u>	<u>RIP's Submitted</u>	<u>RIP's Funded</u>
AAMRL	10	8 (1 GSRP)	5
AFWAL/APL	8	8	4
ATL	8	9 (1 GSRP)	8 (1 GSRP)
AEDC	5	5 (1 GSRP)	4 (1 GSRP)
AFWAL/AL	8	8	4
ESMC	1	0	0
ESD	2	2	2
ESC	8	7	5
AFWAL/FDL	10	9 (1 GSRP)	6 (1 GSRP)
FJSRL	7	5	4
AFGL	12	7	5
HRL	14	13	9
AFWAL/ML	12	9	6
OEHL	4	3	3
AL	8	7	6
RADC	12	8	8
SAM	16	9	8
WL	6	7 (1 GSRP)	4
WHMC	2	2	1
Total	153	126	88

LIST OF UNIVERSITIES THAT PARTICIPATED

Akron, University of	- 1	Louisiana Tech. University	- 1
Alabama, University of	- 1	Lowell, University of	- 2
Albany College	- 1	Maine, University of	- 1
Arizona State University	- 1	Meharry Medical College	- 1
Arizona, University of	- 1	Miami University	- 1
Arkansas State University	- 1	Miami, University of	- 1
Arkansas, University of	- 2	Michigan State University	- 1
Auburn University	- 1	Michigan Tech. University	- 1
Austin Peay State Univ.	- 1	Michigan, University of	- 2
Ball State University	- 1	Minnesota, University of	- 1
Boston College	- 1	Missouri Western State Coll.	- 1
California State Univ.	- 2	Missouri, University of	- 2
California, Univ. of	- 1	Montana, University of	- 1
Calvin College	- 1	Montclair State College	- 1
Carnegie Mellon University	- 1	Morehouse College	- 1
Central State University	- 3	Muhlenberg College	- 1
Central Wesleyan College	- 1	Murray State University	- 1
Cincinnati, University of	- 3	Nebraska, University of	- 1
Clarkson University	- 2	New Hampshire, Univ. of	- 3
Clemson University	- 1	New Mexico, University of	- 1
Colorado State University	- 2	New York State University	- 2
Columbia Basin College	- 1	New York, City College of	- 1
Dayton, University of	- 5	North Carolina State Univ.	- 1
Delta State University	- 1	North Carolina, Univ. of	- 2
East Texas State University	- 1	Northern Illinois Univ.	- 1
Eastern New Mexico Univ.	- 1	Ohio State University	- 2
Fairleigh Dickinson Univ.	- 1	Oklahoma State University	- 1
Fayetteville State Univ.	- 1	Oral Roberts University	- 1
Florida Inst. of Technology	- 1	Oregon Inst. of Technology	- 2
Florida, University of	- 1	Oregon State University	- 1
Francis Marion University	- 1	Pennsylvania State Univ.	- 1
George Mason University	- 1	Polytechnic University	- 1
Georgia Inst. of Technology	- 2	Prairie View A&M Univ.	- 2
Georgia, University of	- 1	Presbyterian College	- 1
Gonzaga University	- 1	Purdue University	- 1
Hampton University	- 1	Redlands, University of	- 1
Illinois Inst. of Technology	- 1	Rennselaer Polytechnic Inst	- 1
Indiana University	- 1	Rice University	- 1
Iowa State University	- 1	Rochester Inst. of Tech.	- 1
Jackson State University	- 3	Rose-Hulman Inst. of Tech.	- 1
Jacksonville State Univ.	- 1	Saint Paul's College	- 1
Jarvis Christian College	- 1	San Francisco State Univ.	- 1
Kentucky, University of	- 1	Santa Clara University	- 1
LaVerne, University of	- 1	Southeast Oklahoma State U.	- 1
Louisiana State University	- 2	Southern Mississippi, Univ.	- 1

LIST OF UNIVERSITIES THAT PARTICIPATED
Continued

Southern University	- 2	Tuskegee University	- 1
Southwest Missouri State U.	- 1	Virginia Polytechnic Inst.	- 1
St. Norbert College	- 1	Warren Wilson College	- 1
Staten Island, College of	- 1	Wayne State University	- 1
Syracuse University	- 1	Wesleyan College	- 1
Taylor University	- 1	West Florida, University of	- 1
Tennessee Space Inst., Univ.	- 1	West Texas State Univ.	- 1
Tennessee Tech. University	- 2	West Virginia Tech.	- 1
Tennessee, University of	- 1	Western Illinois University	- 1
Texas A&I University	- 1	Western Michigan University	- 1
Texas Lutheran College	- 1	Widener University	- 1
Texas, University of	- 4	Wilberforce University	- 1
Towson State University	- 1	Wisconsin-Madison, Univ. of	- 1
Trinity University	- 1	Wright State University	- 5
Total			153

PARTICIPANTS LABORATORY ASSIGNMENT

PARTICIPANT LABORATORY ASSIGNMENT

AERO PROPULSION LABORATORY

(Wright-Patterson Air Force Base)

Dr. Suresh K. Aggarwal (1987)
University of Illinois at Chicago
Specialty: Aerospace Engineering

Dr. Mingking K. Chyu
Carnegie Mellon University
Specialty: Heat Transfer

Dr. Derek Dunn-Rankin
University of California
Specialty: Laser Diagnostics (combustion)

Dr. Wayne A. Eckerle
Clarkson University
Specialty: Experimental Fluid Mechanics

Dr. Arthur A. Mason (1986)
University of Tennessee Space Institute
Specialty: Physics

Dr. Douglas G. Talley
University of Michigan
Specialty: Combustion

Dr. Richard Tankin (1987)
Northwestern University
Specialty: Mechanical Engineering

Dr. Cheng-Hsiao Wu (1987)
University of Missouri
Specialty: Solid State Physics

ARMAMENT LABORATORY

(Eglin Air Force Base)

Dr. Ibrahim A. Ahmad
Northern Illinois University
Specialty: Statistics and Operations

Dr. Charles Bell (1987)
Arkansas State University
Specialty: Mechanical Engineering

Dr. Stephen J. Dow
Univ. of Alabama in Huntsville
Specialty: Discrete Mathematics

Dr. Joseph J. Feeley (1987)
University of Idaho
Specialty: Electrical Engineering

Dr. Manuel A. Huerta
University of Miami
Specialty: Plasma Physics

Prof. Anastas Lazaridis
Widener University
Specialty: Ablation, Solar Energy

Dr. Kwang S. Min
East Texas State University
Specialty: Signal Processing

Dr. Joseph J. Molitoris
Muhlenberg College
Specialty: Nuclear Physics

Prof. Wafa E. Yazigi
Columbia Basin College
Specialty: Solid Mechanics

Harry G. Armstrong Aerospace Medical Research Laboratory
(Wright-Patterson Air Force Base)

Dr. Charles D. Covington
University of Arkansas
Specialty: Digital Signal Processing

Dr. Barry P. Goettl
Clemson University
Specialty: Engineering Psychology

Dr. David G. Payne
SUNY Binghamton
Specialty: Human Memory

Dr. Donald Robertson (1987)
Indiana University of PA
Specialty: Psychology

Dr. Joseph E. Saliba
University of Dayton
Specialty: Engineering Mechanics

Dr. Sanford S. Singer
University of Dayton
Specialty: Enzymology

ARNOLD ENGINEERING DEVELOPMENT CENTER
(Arnold Air Force Base)

Mr. Ben A. Abbott (GSRP)
Vanderbilt University
Specialty: Electrical Engineering

Dr. Eustace L. Dereniak
University of Arizona
Specialty: Infrared Physics

Prof. William M. Grissom
Morehouse College
Specialty: Combustion Diagnostics

Dr. William Sutton (1985)
University of Oklahoma
Specialty: Heat Transfer

Dr. Ahmad D. Vakili
Univ. of Tennessee Space Inst.
Specialty: Unsteady Flows

ASTRONAUTICS LABORATORY
(Edwards Air Force Base)

Dr. Gurbux S. Alag (1987)
Western Michigan University
Specialty: Systems Engineering

Dr. Clarence Calder
Oregon State University
Specialty: Stress Wave Propagation

Mr. David B. Chenault (GSRP)
University of Alabama
Specialty: Physics

Dr. David W. Jensen
Pennsylvania State University
Specialty: Advanced Composite Materials

Dr. John Kenney (1987)
Eastern New Mexico University
Specialty: Physical Chemistry

Dr. Mark A. Norris
Virginia Polytechnic Inst. & State Univ.
Specialty: Structural Dynamics &
Controls

ASTRONAUTICS LABORATORY

(Edwards Air Force Base)

(continued)

Dr. Phillip A. Christiansen
Clarkson University
Specialty: Physical Chemistry

Dr. Susan T. Collins
California State University
Specialty: Matrix Isolation Spectroscopy

Dr. Rameshwar P. Sharma
Western Michigan University
Specialty: Fluid Mechanics

Dr. Siavash H. Sohrab (1986)
Northwestern University
Specialty: Engineering Physics

AVIONICS LABORATORY

(Wright-Patterson Air Force Base)

Prof. William K. Curry (1987)
Rose-Hulman Inst. of Technology
Specialty: Computer Science

Dr. Gerald W. Grams
Georgia Tech.
Specialty: Atmospheric Physics

Dr. David Hemmendinger
Wright State University
Specialty: Logic Programming

Dr. Periasamy K. Rajan
Tennessee Tech. University
Specialty: Digital Signal Processing

Dr. Mateen M. Rizki
Wright State University
Specialty: Modeling and Simulation

ENGINEERING AND SERVICES CENTER

(Tyndall Air Force Base)

Dr. Wayne A. Charlie
Colorado State University
Specialty: Geotechnical Engineering

Dr. David H. DeHeer
Calvin College
Specialty: Molecular Biology

Dr. Deanna S. Durnford
Colorado State University
Specialty: Groundwater

Dr. Neil J. Hutzler
Michigan Tech. University
Specialty: Environmental Engineering

Dr. Peter Jeffers (1987)
S.U.N.Y.
Specialty: Chemistry

Dr. Richard S. Myers
Delta State University
Specialty: Experimental Physical Chem.

Dr. William Schulz (1987)
Eastern Kentucky University
Specialty: Chemistry

Dr. Dennis Truax (1987)
Mississippi State University
Specialty: Civil Engineering

ELECTRONIC SYSTEMS DIVISION

(Hanscom Air Force Base)

Mr. George N. Bratton
Austin State Peay State Univ.
Specialty: Statistics

Dr. John F. Dalphin
Towson State University
Specialty: Computer Science

Dr. Stephan Kolitz (1986)
University of Massachusetts
Specialty: Operations Reserach

FLIGHT DYNAMICS LABORATORY

(Wright-Patterson Air Force Base)

Dr. Peter J. Disimile (1986)
University of Cincinnati
Specialty: Fluid Mechanics

Dr. James A. Sherwood
University of New Hampshire
Specialty: Solid Mechanics

Mr. Thomas Enneking (GSRP), (1987)
University of Notre Dame
Specialty: Civil Engineering

Dr. Gary Slater (1987)
University of Cincinnati
Specialty: Aerospace Engineering

Dr. Awatef Hamed
University of Cincinnati
Specialty: Engineering

Dr. Kenneth M. Sobel
The City College of New York
Specialty: Eigenstructure

Dr. Yulian B. Kin
Purdue University Calumet
Specialty: Stress Analysis

Dr. Forrest Thomas (1987)
University of Montana
Specialty: Chemistry

Dr. Oliver McGee (1987)
Ohio State University
Specialty: Engineering Mechanics

Mr. David F. Thompson (GSRP)
Purdue University
Specialty: Computer Information

Dr. William E. Wolfe
Ohio State University
Specialty: Geotechnical Engineering

FRANK J. SEILER RESERACH LABORATORY

(United States Air Froce Academy)

Dr. Richard Bertrand (1985)
University of Colorado
Specialty: NMR Spectroscopy, Atomic Spectroscopy

Dr. Tammy J. Melton
St. Norbert College
Specialty: Inorganic Synthesis

FRANK J. SEILER RESERACH LABORATORY

(United States Air Froce Academy)

(continued)

Dr. Dan R. Bruss
Albany College of Pharmacy
Specialty: Physical Organic Chemistry

Dr. Charles M. Bump (1987)
Hampton University
Specialty: Organic Chemistry

Dr. Michael L. McKee
Auburn University
Specialty: Molecular Orbital Theory

Dr. Patricia L. Plummer
Columbia Univ. of Missouri
Specialty: Quantum Chemistry

Dr. Howard Thompson (1987)
Purdue University
Specialty: Mechanical Engineering

Dr. Melvin Zandler (1987)
Wichita State University
Specialty: Physical Chemistry

GEOPHYSICS LABORATORY

(Hanscom Air Force Base)

Dr. Lucia M. Babcock
Louisiana State University
Specialty: Gas Phase Ion-Molecule Chem.

Dr. Pradip M. Bakshi
Boston College
Specialty: Quantum Theory

Dr. Donald F. Collins
Warren Wilson College
Specialty: Optics, Image Processing

Dr. Lee Flippin (1987)
San Francisco State University
Specialty: Organic Chemisty

Dr. Janet U. Kozyra
University of Michigan
Specialty: Space Physics

Dr. Steven Leon (1987)
Southeastern Massachusettes
Specialty: Mathematics

Dr. John P. McHugh
University of New Hampshire
Specialty: Fluid Mechanics

Dr. Timothy Su (1987)
Southeastern Massachusetts Univ.
Specialty: Physical Chemistry

HUMAN RESOURCES LABORATORY

(Brooks, Williams and Wright-Patterson Air Force Base)

Dr. Ronna Dillion (1987)
Southern Illinois University
Specialty: Educational Psychology

Dr. J. Kevin Ford
Michigan State University
Specialty: Industrial/Organ. Psychology

Dr. Jorge L. Mendoza (1986)
Texas A&M University
Specialty: Psychology

Dr. Philip D. Olivier (1986)
University of Texas
Specialty: Electrical Engineering

HUMAN RESOURCES LABORATORY

(Brooks, Williams and Wright-Patterson Air Force Base)

(continued)

Dr. Hugh. P. Garraway, III
Univ. of Southern Mississippi
Specialty: Computer Based Learning

Dr. Douglas E. Jackson
Eastern New Mexico University
Specialty: Math/Statistical Information

Dr. Charles E. Lance
University of Georgia
Specialty: Industrial/Organizational Psy.

Dr. Thomas L. Landers
University of Arkansas
Specialty: Reliability & Maintainability

Dr. Mufit H. Ozden
Miami University
Specialty: Operations Research

Dr. Dharam S. Rana
Jackson State University
Specialty: Quantitative Techniques

Dr. Jonathan M. Spector
Jacksonville State University
Specialty: Logic

Dr. Charles Wells (1987)
University of Dayton
Specialty: Management Science

Dr. Robert K. Young
University of Texas
Specialty: Experimental Psychology

LOGISTICS COMMAND

(Wright-Patterson Air Force Base)

Dr. Ming-Shing Hung (1986)
Kent State University
Specialty: Business Administration & Management Science

MATERIALS LABORATORY

(Wright-Patterson Air Force Base)

Dr. Bruce Craver (1987)
University of Dayton
Specialty: Physics

Dr. Parvis Dadras
Wright State University
Specialty: Mechanics of Materials

Dr. David A. Grossie
Wright State University
Specialty: X-ray Crystallography

Dr. Gordon Johnson (1987)
Walla Walla College
Specialty: Electrical Engineering

Dr. L. James Lee
The Ohio State University
Specialty: Polymer & Composite
Processing

MATERIALS LABORATORY

(Wright-Patterson Air Force Base)

(continued)

Dr. Barry K. Fussell
University of New Hampshire
Specialty: Systems Modeling & Controls

Dr. John W. Gilmer (1987)
Penn State University
Specialty: Physical Chemistry

Dr. Michael Sydor
University of Minnesota
Specialty: Optics, Material Science

Dr. Richard S. Valpey
Wilberforce University
Specialty: Organic Synthesis

OCCUPATIONAL AND ENVIRONMENT HEALTH LABORATORY

(Brooks Air Force Base)

Dr. Steven C. Chiesa
Santa Clara University
Specialty: Biological Waste Treatment

Dr. Larry R. Sherman
University of Akron
Specialty: Organotin Chemistry

Dr. Gary R. Stevens
Oklahoma State University
Specialty: Stochastic Processes

Dr. Shirley A. Williams (1986)
Jackson State University
Specialty: Physiology

ROME AIR DEVELOPMENT CENTER

(Griffiss Air Force Base)

Dr. Keith A. Christianson
University of Maine
Specialty: Electronic Materials

Dr. Hugh K. Donaghy
Rochester Inst. of Technology
Specialty: Natural Language Processing

Dr. Oleg G. Jakubowicz
State University of New York
Specialty: Neural Nets

Dr. Louis Johnson (1987)
Oklahoma State University
Specialty: Electrical Engineering

Dr. Samuel P. Kozaitis
Florida Institute of Tech.
Specialty: Optics, Computer Architecture

Dr. David Sumberg (1987)
Rochester Institute of Tech.
Specialty: Physics

Dr. Donald R. Ucci
Illinois Inst. of Technology
Specialty: Adaptive Arrays

Dr. Peter J. Walsh
Fairleigh Dickinson University
Specialty: Superconductivity

Dr. Kenneth L. Walter
Prairie View A&M University
Specialty: Chemical Engineering Process

Dr. Gwo-Ching Wang
Rensselaer Polytechnic Inst.
Specialty: Surface Sciences

SCHOOL OF AEROSPACE MEDICINE

(Brooks Air Force Base)

Dr. Ronald Bulbulian
University of Kentucky
Specialty: Exercise Physiology

Dr. John A. Burke, Jr.
Trinity University
Specialty: Inorganic Compounds

Dr. Hoffman H. Chen (1986)
Grambling State University
Specialty: Mechanical Engineering

Dr. Frank O. Hadlock (1986)
Florida Atlantic University
Specialty: Mathematics

Dr. Eric R. Johnson
Ball State University
Specialty: Protein Biochemistry

Dr. Harold G. Longbotham
Univ. of Texas - San Antonio
Specialty: Nonlinear Digital Filtering

Dr. Mohammed Maleque (1987)
Meharry Medical College
Specialty: Pharmacology

Dr. Parsottam J. Patel (1986)
Meharry Medical College
Specialty: Microbiology

Dr. William Z. Plachy
San Francisco State University
Specialty: Physical Chemistry

Dr. Ralph Peters (1987)
Wichita State University
Specialty: Zoology

Dr. Thomas R. Rogge
Iowa State University
Specialty: Finite Element Analysis

Prof. Sonia H. Sawtelle-Hart
Univ. of Texas - San Antonio
Specialty: Exercise Physiology

Dr. Wesley Tanaka (1987)
University of Wisconsin
Specialty: Biochemistry

Dr. John R. Wright
Southeast Oklahoma State Univ.
Specialty: Biochemistry

WILFORD HALL MEDICAL CENTER

(Lackland Air Force Base)

Dr. David R. Cecil
Texas A&I University
Specialty: Algebra (Finite Fields)

Dr. Donald Welch (1986)
Texas A&M University
Specialty: Microbiology

WEAPONS LABORATORY

(Kirtland Air Force Base)

Dr. Albert W. Biggs (1986)
University of Alabama
Specialty: Electrical Engineering

Dr. William M. Jordan
Louisiana Tech. University
Specialty: Composite Materials

WEAPONS LABORATORY
(Kirtland Air Force Base)
(continued)

Dr. Lane Clark
University of New Mexico
Specialty: Graph Theory

Dr. David A. Dolson
Murray State University
Specialty: Laser Spectroscopy

Dr. Arkady Kheyfets
North Carolina State Univ.
Specialty: Mathematical Physics

Dr. Barry McConnell (1987)
Florida A&M University
Specialty: Computer Science

Dr. William Wheless (1987)
New Mexico State University
Specialty: Electrical Engineering

RESEARCH REPORTS

MINI-GRANT RESEARCH REPORTS
1988 RESEARCH INITIATION PROGRAM

<u>Technical Report Number</u>	<u>Title and Mini-Grant No.</u>	<u>Professor</u>
Volume I		
Armament Laboratory		
1	Statistical Analysis of Residual Target Performance and for Measures of Target Partial Availability Pending Approval 210-9MG-010	Dr. Ibrahim A. Ahmad
2	Synergistic Effects of Bomb Cratering, Phase II 760-7MG-025	Dr. Charles Bell (1987)
3	Automated Motion Parameter Determi- nation from an Image Sequence 210-9MG-025	Dr. Stephen J. Dow
4	Modeling and Simulation on Micro- computers, 1989 760-7MG-070	Dr. Joseph J. Feeley (1987)
5	Two Dimensional MHD Simulation of Accelerating Arc Plasmas 210-9MG-090	Dr. Manuel A. Huerta
6	Modeling Reactive Fragments 210-9MG-011	Prof. Anastas Lazaridis
7	Target-Aerosol Discrimination for Active Optical Proximity Sensors 210-9MG-016	Dr. Kwang S. Min
8	The Dynamics of Impact 210-9MG-008	Dr. Joseph J. Molitoris
9	Report Not Acceptable at this Time 210-9MG-015	Prof. Wafa E. Yazigi

Arnold Engineering Development Center

- | | | |
|----|--|---------------------------|
| 10 | Multigraph Kernel for Transputer Based Systems
21-9MG-087 | Mr. Ben A. Abbott (GSRP) |
| 11 | MTF Studies of IR Focal Plane Arrays at Low Flux Levels
210-9MG-020 | Dr. Eustace L. Dereniak |
| 12 | Droplet Size Distributions and Combustion Modeling in a Pintle Injector Spray
210-9MG-069 | Prof. William M. Grissom |
| 13 | Multiple Scattering in Solid Fuel Rocket Plumes
760-0MG-091 | Dr. William Sutton (1985) |
| 14 | Influence of Forced Disturbances on the Vortex Core and the Vortex Burst
210-9MG-056 | Dr. Ahmad D. Vakili |

Astronautics Laboratory

- | | | |
|----|--|------------------------------|
| 15 | Large Space Structure Parameter Estimation
760-7MG-042 | Dr. Gurbux S. Alag (1987) |
| 16 | Integrated Strain Measurement in Composite Members Using Embedded Constantan Wire
Pending Approval
210-9MG-076 | Dr. Clarence Calder |
| 17 | Calibration of the Infrared Spectropolarimeter
210-9MG-026 | Mr. David B. Chenault (GSRP) |
| 18 | Computer Code to Include Core Polarization in Effective Potential Basis Set Expansion Studies
210-9MG-092 | Dr. Phillip A. Christiansen |
| 19 | Fluorescence Spectra of Matrix-isolated Lithium
210-9MG-115 | Dr. Susan T. Collins |

20	Calibration of Composite-Embedded Fiber-Optic Strain Sensors Pending Approval 210-9MG-052	Dr. David W. Jensen
21	Energy-And Time-Resolved Photophysics and Photochemistry of High Energy Cryogenic Metal-Containing Rocket Fuels 760-7MG-019	Dr. John Kenney (1987)
22	Experimental Verification and Develop- ment of Structural Identification Techniques on a Grid 210-9MG-045	Dr. Mark A. Norris
23	Report Not Available at this Time 210-9MG-103	Dr. Rameshwar P. Sharma
24	Experimental Investigation of the Stability of Jets Near the Critical Point 760-6MG-110	Dr. Siavash H. Sohrab (1986)
Electronics Systems Division		
25	HF Network Evaluation 210-9MG-012	Mr. George N. Bratton
26	Report Not Available at this Time 210-9MG-023	Dr. John F. Dalphin
27	Reliability in Satellite Communication Networks Pending Approval 760-6MG-094	Dr. Stephan Kolitz (1986)
Engineering and Services Center		
28	High Intensity Compressive Stress Wave Propagation Through Unsaturated Sands 210-9MG-075	Dr. Wayne A. Charlie
29	Decontamination and Elisa Analysis of Blood Group Substances from Human Tissue Pending Approval 210-9MG-112	Dr. David H. DeHeer

- | | | |
|----|---|---------------------------|
| 30 | Estimation of Jet Fuel Contamination
in Soils
210-9MG-074 | Dr. Deanna S. Durnford |
| 31 | Extraction of Volatile Organic Chemicals
from Unsaturated Soil: Experimental
Results and Model Predictions
210-9MG-059 | Dr. Neil J. Hutzler |
| 32 | Homogeneous Hydrolysis Rate Constants
for Selected Chlorinated Methanes,
Ethanes, Ethenes, and Propanes
760-7MG-038 | Dr. Peter Jeffers (1987) |
| 33 | Sorption Kinetics of Volatile Organic
Compounds on Aquifer Materials
210-9MG-047 | Dr. Richard S. Myers |
| 34 | Report will be Submitted Under
Mini-Grant 210-10MG-095 | Dr. William Schulz (1987) |
| 35 | Report Not Available at this Time
760-7MG-105 | Dr. Dennis Truax (1987) |

Volume II

Frank J. Seiler Research Laboratory

- | | | |
|----|---|-----------------------------|
| 36 | NMR Studies of Alkylammonium-Chloro-
oaluminate Room-Temperature Electrolytes
760-0MG-095 | Dr. Richard Bertrand (1985) |
| 37 | Mechanistic Studies on the Thermal
Decomposition of NTO by High
Performance Liquid Chromatography
210-9MG-111 | Dr. Dan R. Bruss |
| 38 | Aromatic Nitrations in Chloroaluminate
Melts
760-7MG-076 | Dr. Charles M. Bump (1987) |
| 39 | Calculated C-NO ₂ Bond Dissociation
Energies (Part I) and A MCSCF Study of
the Rearrangement of Nitromethane to
Methyl Nitrite (Part II)
210-9MG-054 | Dr. Michael L. McKee |
| 40 | Sodium as an Electrode for Chloroaluminate
Melts
210-9MG-098 | Dr. Tammy J. Melton |

41	Report Not Available at this Time 210-9MG-097	Dr. Patricia L. Plummer
42	Transient Shock Waves in a Mach 3 Flow 760-7MG-071	Dr. Howard Thompson (1987)
43	Ab-initio and Semi-Empirical Molecular Orbital Studies of Energetic Materials (Nitrogen Heterocyclics) and Polymers 760-7MG-092	Dr. Melvin Zandler (1987)
Geophysics Laboratory		
44	Radiative Association in Ion-Molecule Reactions: Reactions of Some Carbon Cations 210-9MG-086	Dr. Lucia M. Babcock
45	Impulse Approximation Formalism for Atom Molecule Collisions 210-9MG-109	Dr. Pradip M. Bakshi
46	Stellar Photometry, Vehicle Glow, and Advanced Image Analysis 210-9MG-100	Dr. Donald F. Collins
47	Synthesis of Organometallic Reagents for SIFT Studies of Electron Attachment Reactions 760-7MG-056	Dr. Lee Flippin (1987)
48	Theoretical and Observational Studies of Geomagnetic Storm-Related Ion and Electron Heating in the Subauroral Region 210-9MG-084	Dr. Janet U. Kozyra
49	Algorithms for Generalized Exponential Inversion 760-7MG-036	Dr. Steven Leon (1987)
50	Report Not Available at this Time 210-9MG-125	Dr. John P. McHugh
51	Trajectory Calculations of High Tempera- ture and Kinetic Energy Dependent Ion- Polar Molecule Collision Rate Constants 760-7MG-040	Dr. Timothy Su (1987)

Rome Air Development Center

- | | | |
|----|---|---------------------------|
| 52 | Aging Studies of GaAs Schottky Barriers
210-9MG-073 | Dr. Keith A. Christianson |
| 53 | Report Not Available at this Time
210-9MG-094 | Dr. Hugh K. Donaghy |
| 54 | Neural Network for Aiding Intelligent
Analysis
Pending Approval
210-9MG-124 | Dr. Oleg G. Jakubowicz |
| 55 | Supply Line Testing in CMOS Digital
Circuits
760-7MG-050 | Dr. Louis Johnson (1987) |
| 56 | Characterization of Detectors for
Optical Pattern Recognition
210-9MG-018 | Dr. Samuel P. Kozaitis |
| 57 | Fiber Optic Distribution for Phased
Array Antennas
Pending Approval
760-7MG-113 | Dr. David Sumberg (1987) |
| 58 | Continuation Study of the Effect of
Nonlinearities of High Speed Analog-
to-Digital Converters on Digital
Beamforming Arrays
210-9MG-040 | Dr. Donald R. Ucci |
| 59 | Analysis of Microwave Surface Impedance
of High Temperature Superconductors
210-9MG-072 | Dr. Peter J. Walsh |
| 60 | Report Not Available at this Time
210-9MG-113 | Dr. Kenneth L. Walter |
| 61 | X-Ray Pole-Figure Analysis of $\text{YBa}_2\text{Cu}_3\text{O}_{7-x}$
Thin Film on $\text{SrTiO}_3(100)$ Prepared by RF
Diode Sputtering
210-9MG-077 | Dr. Gwo-Ching Wang |

Weapons Laboratory

- | | | |
|----|--|----------------------------|
| 62 | Slow Wave Transmission Line Transformers | Dr. Albert W. Biggs (1986) |
| | 760-6MG-072 | |

- | | | |
|----|--|----------------------------|
| 63 | Report Not Available at this Time
210-9MG-119 | Dr. Lane Clark |
| 64 | Vibrational Energy Transfer in Sulfur
Monoxide
210-9MG-101 | Dr. David A. Dolson |
| 65 | Development of an Experimental Program
to Evaluate Laser Composite Material
Damage Models
210-9MG-034 | Dr. William M. Jordan |
| 66 | Report Not Available at this Time
210-9MG-114 | Dr. Arkady Kheyfets |
| 67 | Report Not Available at this Time
760-7MG-047 | Dr. Barry McConnell (1987) |
| 68 | Slow to Fast Wave Transition Analysis
760-7MG-068 | Dr. William Wheless (1987) |

Volume III

Air Force Wright Aeronautical Laboratories

Aero Propulsion Laboratory

- | | | |
|----|--|-------------------------------|
| 69 | Vaporization Behavior of Pure and
Multicomponent Fuel Droplets in a
Hot Air Stream
760-7MG-061 | Dr. Suresh K. Aggarwal (1987) |
| 70 | Effects of Injection-To-Mainstream
Density Ratios on Film Cooling Heat
Transfer
Pending Approval
210-9MG-096 | Dr. Mingking K. Chyu |
| 71 | Accurate Temperatures Using Cars in
Droplet Laden Flows
Pending Approval
210-9MG-055 | Dr. Derek Dunn-Rankin |
| 72 | Report Not Available at this Time
210-9MG-019 | Dr. Wayne A. Eckerle |
| 73 | Report Not Available at this Time
760-6MG-099 | Dr. Arthur A. Mason (1986) |
| 74 | Report Not Available at this Time
210-9MG-022 | Dr. Douglas G. Talley |

- | | | |
|-----------------------------------|---|--------------------------------------|
| 75 | Vortical Structures in 2-D Slot
Burner-Cold Flow
760-7MG-051 | Dr. Richard Tankin (1987) |
| 76 | Calculations of Interface-State Occupation
Function and GaAs/Ge Heterostructure Solar
Cell Efficiency
760-7MG-093 | Dr. Cheng-Hsiao Wu (1987) |
| Avionics Laboratory | | |
| 77 | Computer Simulation of Adaptive Resource
Management in Real-Time
760-7MG-081 | Prof. William K. Curry (1987) |
| 78 | Study of Sky Backgrounds and Subvisual
Cirrus
Pending Approval
210-9MG-120 | Dr. Gerald W. Grams |
| 79 | Proving Equivalence of High-and Low-Level
Architectural Descriptions in VHDL
210-9MG-108 | Dr. David Hemmendinger |
| 80 | Report Not Available at this Time
210-9MG-051 | Dr. Periasamy K. Rajan |
| 81 | Applications of Evolutionary Learning
Strategies to Pattern Recognition Tasks
210-9MG-058 | Dr. Mateen M. Rizki |
| Flight Dynamics Laboratory | | |
| 82 | The Effect of a Roughened Surface on
Turbulent Boundary Layer Separation
at Mach 6.0
760-6MG-075 | Dr. Peter J. Disimile (1986) |
| 83 | A Stochastic Model of Fatigue Crack
Growth Due to Random Loading for
Application to Aircraft Wheels
760-7MG-124 | Mr. Thomas Enneking (GSRP)
(1987) |
| 84 | An Investigation of the Flow Field in
Shock Wave/Boundary Layer/Bleed
Interactions
Pending Approval
210-9MG-061 | Dr. Awatef Hamed |

- | | | |
|-----------------------------|--|------------------------------|
| 85 | Fatigue Characteristics of F-16 Composite Transparency Material Determined by Long-Term and Accelerated Methods
210-9MG-038 | Dr. Yulian B. Kin |
| 86 | Convergence of Upper-Bound Optimum Design of Large-Scale Structures with Specified Frequency Bands
760-7MG-115 | Dr. Oliver McGee (1987) |
| 87 | Report Not Available at this Time
210-9MG-088 | Dr. James A. Sherwood |
| 88 | Robustness with Positive Real Controllers for Large Space Structures
760-7MG-088 | Dr. Gary Slater (1987) |
| 89 | Robust Eigenstructure Assignment for Flight Control Design
210-9MG-035 | Dr. Kenneth M. Sobel |
| 90 | Comparative Burning Rates and Duplex Loads of Solid Propellants
760-7MG-080 | Dr. Forrest Thomas (1987) |
| 91 | Optimal and Sub-Optimal Loop Shaping in Quantitative Feedback Theory
Pending Approval
210-9MG-106 | Mr. David F. Thompson (GSRP) |
| 92 | Low Velocity Impact of Composite Materials.
760-7MG-102 and 210-9MG-082 | Dr. William E. Wolfe |
| Logistics Command | | |
| 93 | Aircraft Availabilty Model: Feasibility Study for POM Forecasting
760-6MG-105 | Dr. Ming S. Hung (1986) |
| Materials Laboratory | | |
| 94 | Tunable Absorption in Doping Superlattices
760-7MG-097 | Dr. Bruce Craver (1987) |
| 95 | Joining of Carbon-Carbon Composites
210-9MG-004 | Dr. Parviz Dadras |
| 96 | Report Not Available at this Time
210-9MG-064 | Dr. Barry K. Fussell |

- | | | |
|--|---|-----------------------------|
| 97 | Characterization of the Phase Separation Behavior of Poly(p-phenylene benzobisthiazole)/Amorphous Nylon Molecular Composites by Small Angle Light Scattering
760-7MG-013 | Dr. John W. Gilmer |
| 98 | Structural Analysis of Model Compounds with Potential Second and Third Order Nonlinear Optical Properties
210-9MG-080 | Dr. David A. Grossie |
| 99 | Liquid Crystal Biomolecules for use as Optical Filters
760-7MG-075 | Dr. Gordon Johnson (1987) |
| 100 | Knowledge Development for the Rule Based Process Automation of Resin Transfer Molding
210-9MG-063 | Dr. L. Jmaes Lee |
| 101 | Photorefectance Measurements of the Quality of Undoped GaAs
210-9MG-031 | Dr. Michael Sydor |
| 102 | Synthesis of 2, 6-Diformyl Pyridobisimidazoles
210-9MG-029 | Dr. Richard S. Valpey |
|
Volume IV | | |
| Human Systems Division Laboratories | | |
| Harry G. Armstrong Aerospace Medical Research Laboratory | | |
| 103 | Auditory Modeling
210-9MG-060 | Dr. Charles D. Covington |
| 104 | Assessing the Cognitive Demands of Tracking Strategies
210-9MG-078 | Dr. Barry P. Goettl |
| 105 | Report Not Available at this Time
210-9MG-121 | Dr. David G. Payne |
| 106 | Effect of System Reliability on Probabilistic Inference
Pending Approval
760-7MG-094 | Dr. Donald Robertson (1987) |

- | | | |
|----------------------------|--|------------------------------|
| 107 | Optimization of the Nonlinear Discrete
Parameter Model of the Seated Human
Spine
210-9MG-071 | Dr. Joseph E. Saliba |
| 108 | In Vitro Modeling of Perfluoro-N-Decanoate
Effects on Enzymes of Fatty Acid Metabolism
210-9MG-002 | Dr. Sanford S. Singer |
| Human Resources Laboratory | | |
| 109 | Report Not Acceptable at this Time
760-7MG-100 | Dr. Ronna Dillion (1987) |
| 110 | An Investigation of Training Content
Validity and Training Efficiency in the
Air Force Airmen Basic-In-Residence
Training Course
210-9MG-066 | Dr. J. Kevin Ford |
| 111 | An Intelligent Tool to Facilitate the
Development of Qualitative Process Models
in Novice Programmers
210-9MG-007 | Dr. Hugh P. Garraway, III |
| 112 | On the Effect of Range Restriction on
Correlation Coefficient Estimation
210-9MG-027 | Dr. Douglas E. Jackson |
| 113 | Validation of an Enlisted Air Force
Specialty Task Taxonomy and Cross-AFS
Ease-of-Movement Predictions
210-9MG-017 | Dr. Charles E. Lance |
| 114 | Proportional Intensity Reliability
Analysis for Repairable Items
210-9MG-104 | Dr. Thomas L. Landers |
| 115 | A Monte Carlo Comparison of Validity
Generalization Procedures
760-6MG-136 | Dr. Jorge L. Mendoza (1986) |
| 116 | A Network Tutor Based on the Heuristic
of Polya
760-6MG-032 | Dr. Philip D. Olivier (1986) |
| 117 | Graphical Programming of Simulation
Models in an Object-Oriented Environment
210-9MG-028 | Dr. Mufit H. Ozden |

118	Report Not Available at this Time 210-9MG-043	Dr. Dharam S. Rana
119	Refinement Considerations for an Advanced Instructional Design Advisor 210-9MG-021	Dr. Jonathan M. Spector
120	Engineering Design with Decision Support: An Application of Goal Decomposition 760-7MG-046	Dr. Charles Wells (1987)
121	Report Not Available at this Time 210-9MG-099	Dr. Robert K. Young
Occupational and Environment Health Laboratory		
122	Solvent Extraction of Boron from Industrial Wastewaters 210-9MG-102	Dr. Steven C. Chiesa
123	Comparison of Asbestos Analysis by SEM-EDXA and TEM-SAED 210-9MG-122	Dr. Larry R. Sherman
124	An Examination of Kriging Techniques for Ground Water Monitoring 210-9MG-070	Dr. Gary R. Stevens
125	Cortisol Prevention of Chronic Beryllium Disease in Postpartum Rats: A Pilot Study 760-6MG-078	Dr. Shirley A. Williams (1986)
School of Aerospace Medicine		
126	Blood Flow Distribution in the Non- Working Forearm During Exercise 210-9MG-057	Dr. Ronald Bulbulian
127	Photophysics and Photochemistry of Transition Metal Complexes 210-9MG-091	Dr. John A. Burke, Jr.
128	Serum Squalene and Cholesterol Ratio as Risk Predictor for Coronary Artery Disease 760-6MG-118	Dr. Hoffman H. Chen (1986)
129	A Feasibility Study for a Computerized ECG Database 760-6MG-073	Dr. Frank O. Hadlock (1986)

- | | | |
|---------------------------------|--|---------------------------------|
| 130 | Development of a New Ultrasensitive Cholesterol Assay System for the Determination of Free Cholesterol in Biological Fluids
210-9MG-105 | Dr. Eric R. Johnson |
| 131 | Application of Nonlinear Filters to VEP Data
210-9MG-033 | Dr. Harold G. Longbotham |
| 132 | Effects of Low Dose Soman on CNS Neurotransmitters
760-7MG-078 | Dr. Dr. Mohammed Maleque (1987) |
| 133 | Cleansing of Bone-Marrow by Lymphokine Activated Killer Cells (LAK-Cells)
760-6MG-131 | Dr. Parsottam J. Patel (1986) |
| 134 | Transcutaneous Oxygen Delivery
210-9MG-042 | Dr. William Z. Plachy |
| 135 | Report Not Acceptable at this Time
760-7MG-091 | Dr. Ralph Peters (1987) |
| 136 | A Computer Model of the Human Systemic Arterial Tree
210-9MG-003 | Dr. Thomas R. Rogge |
| 137 | The Effect of Age, Family Status, and Physical Activity on Select Dietary Components of TAC Pilots
210-9MG-095 | Prof. Sonia H. Sawtell-Hart |
| 138 | Comprehensive Lipoprotein Analysis by High-Performance Molecular Exclusion Chromatography
760-7MG-043 | Dr. Wesley Tanaka (1987) |
| 139 | Nmr and Temperature-Dependence Studies of the Metal-Ion Catalyzed Chemiluminescence of Luminol
210-9MG-037 | Dr. John R. Wright |
|
Wilford Hall Medical Center | | |
| 140 | Enhancements to PC-Mainframe Interface for Data Entry
210-9MG-048 | Dr. David R. Cecil |

141

Effect of Hyperoxia on the Permeability
of the Blood-Brain Barrier in Several
Laboratory Species and on Organotypic
Explant Tissue Cultures of Hamster Brain
760-6MG-091

Dr. Donald Welch (1986)

USAF-UES RESEARCH INITIATION PROGRAM

**Sponsored by the
AIR FORCE OFFICE OF SCIENTIFIC RESEARCH**

**Conducted by the
Universal Energy Systems, Inc.**

FINAL REPORT

**VAPORIZATION BEHAVIOR OF PURE
AND MULTICOMPONENT FUEL DROPLETS
IN A HOT AIR STREAM**

Prepared by	Suresh K. Aggarwal
Academic Rank:	Assistant Professor
Department and University:	Department of Mechanical Engineering University of Illinois at Chicago
Research Location:	Fuels Division, Aero-Propulsion Laboratory
USAF Researcher:	Dr. T.A. Jackson and Dr. M. Roquemore
Period:	January 1988 - April 16, 1989.
Contract No.:	F49620-85-C-0013/SB5851-0360

VAPORIZATION BEHAVIOR OF PURE AND MULTICOMPONENT FUEL DROPLETS IN A HOT AIR STREAM

By

S.K. Aggarwal* and G. Chen**

ABSTRACT

The vaporization behavior of a liquid fuel droplet in a laminar hot air flow has been studied theoretically and experimentally. In the experimental study, conducted at the WPAFB, a droplet-on-demand generator facility has been developed and extensive data has been obtained on the dynamics and vaporization of a fuel droplet injected into a well-characterized hot laminar flow. The droplet size and velocity histories have been measured by the Phase-Doppler Particle Analyzer. In the theoretical study, the vaporization behavior has been studied by using three liquid-phase models, namely the thin-skin, diffusion-limit, and infinite-diffusion. Predicted results generally show good agreement with the measured data. It is recommended that, for relatively low-temperature conditions, either the diffusion-limit model or the infinite-diffusion model be used. The comparison also indicates that the thermophysical properties of the gas film surrounding the droplet should be calculated accurately; especially the effect of fuel vapor should be included.

*Assistant professor

**Graduate Assistant

INTRODUCTION

Literature on the behavior of an evaporating/burning droplet is extensive. Starting with the classic d^2 -law model [1], several improved vaporization models [2,3] have been developed. Numerous experimental studies [2] have also been reported. However, not much information is available on the behavior of evaporating droplets in relatively low temperature air streams. Under such conditions, the possibility of an envelope flame is precluded and the droplet gasification rate is low. The droplet heat-up time may not be negligibly small compared to its lifetime, although the latter is relatively large under low-temperature conditions, and the liquid-phase transient processes may still be important.

In the present study, an experimental-theoretical investigation of the vaporization behavior of a fuel droplet in a well-controlled hot laminar flow has been conducted. As indicated above, the past research on droplet vaporization has not considered such conditions. The study is also relevant to the understanding and modeling of the processes in non-dilute sprays, where the gas temperature and vaporization rates are relatively low.

In the following, a brief description of the experimental set-up, development of the theoretical models, and comparison of the theoretical and experimental results are given.

EXPERIMENTAL FACILITY

The experimental part of the research has been conducted by Dr. T.A. Jackson and G.L. Switzer at the Wright-Patterson Air Force Base. The test configuration has been designed for injecting fuel droplets in a well controlled laminar on well-characterized turbulent, heated flow field with only axial gradients of temperature and velocity. It consists of heating elements, inlet flow conditioning equipment, a droplet-on-demand injection system, and a confined test section. The instrumentation used include a Phase Doppler Particle Analyzer (PDPA), a hot wire anemometer, a micro-thermocouple, and a laser sheet lighting system.

Air was filtered, dried to a dew point of 22 K, and metered into a 25.4 cm diameter plenum chamber. This chamber contains, in series, a scintered metal diffusing element, a fine mesh screen, two resistance heating elements, a second fine mesh screen, and a flow straightening honey comb. At the end of this section the flow had been evenly distributed, heated to 400 K, and decelerated to a velocity of 0.16 m/s. This air then enters a circular-to-square transition section leading to the test section. In this transition the flow is accelerated to a mean velocity of 1 m/s. The velocity and velocity rms profiles at the test section inlet are illustrated in Figure 1. Note the very low values of the rms, indicating turbulence intensities of less than 3%. These measurements were made with a hot wire anemometer and confirmed with the PDPA. Figure 2 indicates the inlet air temperature profile (orthogonal to each other and both are through the center of the test section). These measurements were taken with microthermocouple (Chromel-Alumel, 0.13 mm diameter lead joined to form a measurement bead approximately 0.25 mm in diameter) positioned in the test section by a long sting inserted from the exit plane of the section.

The test section is 8.9 x 8.9 cm and 45.0 cm long, constructed of four pyrex panels. the flow is driven vertically upward. Figures 1 and 2 indicate that conditions in the test section were uniform out to a radial position of approximately 1.5 cm. In the center of this section droplets are injected. Figure 3 is an illustration of the test section along with a photo of a stream of droplets illuminated with a sheet of laser light. Optical measurements of droplet diameter and local velocity are made along the flow axis by the PDPA. For this experiment the test chamber assembly is positioned, relative to fixed measurement volumes, by a x-y-z precision traversing table.

The Phase Doppler Particle Analyzer is an interferometric droplet sizing device. It sizes single droplets by measuring the radius of curvature of the droplet. There are several publications [4,5,6,7] describing its features and the accuracy with which it determines droplet size. For this effort a single component system was used. Some velocity limitations were discovered during this effort and are reported in a separate paper [8].

The most critical component of the experimental set-up is the droplet-on-demand generator. The study of the droplet vaporization behavior for various fuels requires a generator which can inject droplets axially into a flow of air heated to 400 K without perturbing the velocity or temperature uniformity of the flow. Single monosized droplets are required having diameters in the range 50-90 μm , each droplet having identical velocity and trajectory. An essential characteristic of the system requires long-term stability. That is, once a droplet of given diameter and velocity is produced, these two parameters must remain stable for a period of up to 0.5 hours, while relative diameter measurements are being performed. Several designs were testing before deciding on the final configuration for the droplet-on-demand generator, as shown in Fig. 4. Its operation is based on a piezoelectric (PZT) cylinder 0.7 mm ID x 1.3 mm OD x 19 mm in length. A voltage pulse applied between the inner and outer surfaces of the PZT causes the cylinder to contract radially. This contraction creates a pressure pulse which forces liquid in the cylinder through a glass nozzle whose aperture diameter is equal to that of the desired droplet. The most critical aspect of this generator design is the shape and quality of the nozzle which is formed by melting and polishing glass capillary tubing. A properly formed nozzle produces clean, single droplets with PZT drive voltage as low as 10 V. One of the most useful features incorporated in the design shown in Fig. 5 is a nozzle-mounting configuration which allows convenient removal of the glass tip for cleaning or replacement. Another important aspect of the generator operation is the thermal isolation required over the 60 cm length of the droplet-generator support, shown in Fig. 4, from the heated air flow to prevent pre-vaporization of the fuel. This isolation is provided by a water-cooled sheath which also serves as a support for the generator. Note that the generator is located at the tip of the generator support.

Several operational parameters have been identified which have a major influence upon successful generator performance, the most sensitive of these being PZT drive-voltage amplitude.

pulse width, pulse-repetition frequency, and liquid pressure. The liquid viscosity, PZT temperature, and rise and fall times of the PZT pulse also impact generator performance but to a lesser extent. Proper generation operation, as shown in Fig. 3, requires a delicate balance among these parameters. When control of these parameters is exerted with sufficient sensitivity and stability, the generator performs very reliably.

Development efforts during this study resulted in a compact, versatile and reliable technique for production of single droplets and introduction of these droplets into a well-controlled hot air flow. The droplet-on-demand has produced droplets using water, hexane, and decane as the working fluids. Through precise control of the operational parameters, several discrete diameters in the range of 40-90 μm can be stably generated from a single 65 μm nozzle aperture. Droplet-generation frequencies range from one droplet up to a stream of droplets at 1 kHz, with adjustable exit velocities varying between 0.2 and 10 m/s.

Several data sets have been obtained by using the above generator facility. The parameter varied in these sets is the fuel type. Fuels considered are hexane, decane, and a bicomponent fuel with equal amounts of hexane and decane. For each set, the droplet size and velocity are measured along its trajectory. The local gas velocity and temperature profiles are also measured. The latter information along with the initial drop size and velocity are used in the predictions. Note that the gas-phase turbulence level has been maintained sufficiently low so that the hot air flow can be considered essentially laminar. The experimental data is used to compare the vaporization models as described next.

THEORETICAL MODEL

The theoretical model involves the calculation of velocity, size, and surface properties of an evaporating droplet along its trajectory in a laminar hot air flow. The time-dependent Lagrangian equations for the droplet position, velocity, and size are solved numerically. The local values of gas velocity and temperature required in the computations are taken from the experiments described

earlier. Three vaporization models studied are the thin-skin, infinite-diffusion, and diffusion-limit. Basically, the models differ in the representation of the transient liquid-phase processes, and, thus, in the calculation of droplet surface properties.

The thin-skin model for the single-component case neglects the liquid-phase transport completely. The droplet surface is assumed to be at a wet-bulb temperature which is determined by the local conditions. The infinite-diffusion model considers the temporal variation of temperature and composition (for the multicomponent case) but assumes that these are uniform spatially.

In the diffusion-limit model, the transient heat and mass transport within the droplet are assumed to be represented by the unsteady heat and mass diffusion equations. The solution of these equations provides the temperature and composition at the droplet surface. These properties are needed in the Lagrangian calculations. Further details can be found elsewhere [3,9]. Also the details of the theoretical model will be provided in a separate publication [10].

RESULTS AND DISCUSSION

The predicted and the experimental results are presented for an evaporating fuel droplet injected into a prescribed hot air flow. The results are obtained for three fuels, namely hexane, decane, and a mixture of hexane and decane. Initial conditions for the Lagrangian calculations and the local gas-phase properties are taken from the measured data.

Preliminary comparison with the experimental data indicated that the predicted results are quite sensitive to the thermophysical properties of gas film outside the droplet. An accurate calculation of these properties requires that not only the properties be considered temperature-dependent, but the effect of changing composition should also be included. Note that in the presented study the gas-phase flow field is laminar and steady. A droplet, however, encounters an unsteady flow field due to the velocity and temperature gradients in the axial direction.

Figure 6 shows the predicted and experimental droplet velocity along its trajectory. Results are given for both hexane and decane fuel droplets. The measured gas velocity is also shown in the figure. The droplet velocity, which is much higher than the gas velocity at the injection point, relaxes rapidly to an equilibrium value and then follows the variation of gas velocity along the trajectory. The important observation is that the calculated values agree very well with the experiment data. This means that the solid sphere drag correlation works well for the present situation. However, as mentioned earlier, the properties of the gas film surrounding the droplet needs to be calculated accurately.

Figure 7 shows the variation of the diameter squared obtained experimentally and predicted by the thin-skin (T.S.), diffusion-limit (D.L.), and infinite-diffusion (I.D.) models as well as the experimental values. The fuel is hexane. Two data sets are shown to assess the repeatability of data. The corresponding plots for decane are given in Fig. 8. For all the cases shown, the overall agreement between predictions and experiment is quite good. For hexane, all three models predict a slightly faster rate of vaporization compared to that obtained experimentally. In addition, the calculated values are not sensitive to the models. However, for the decane case, some sensitivity to the models is indicated. The diffusion-limit and infinite-diffusion models show better agreement with the experimental data compared to the thin-skin model. This can be easily explained by the plots of droplet surface temperature given in Fig. 9. For hexane, the wet-bulb temperature is quite low, the droplet surface temperature does not vary significantly, and all three models predict almost the same surface temperature. Consequently, the droplet size variation is not sensitive to the models. For decane, however, the wet-bulb temperature is relatively high and the droplet transient heating becomes important. As a result, the vaporization behavior is sensitive to the models.

Another interesting observation is that the infinite-diffusion and diffusion-limit models predict almost the identical behavior for the decane case. There is no discernible difference in the droplet surface temperature and size predictions for the two models. The implication is that for

relatively low-temperature environment, one could use either the infinite-diffusion or the diffusion-limit model. The thin-skin model is not recommended, however, especially for relatively non-volatile fuels.

Figure 10 demonstrates the importance of including the effect of composition on fuel vapor in calculating the thermophysical properties of the gas film outside the droplet. For curve M1, these properties are calculated for a mixture of air and fuel vapor based on a weighted average of the surface and environment values. For curve M2, the mass fraction of fuel vapor in the gas film is assumed to be zero. As indicated in the figure, the exclusion of fuel vapor in the calculation of transport properties leads to an overprediction of the vaporization rate. It is also important to note that for the present conditions, the fuel vapor mass fraction at the droplet surface is relatively small since the surface temperature is low. This means that the effect of fuel vapor in calculating properties will be even more important for the high-temperature environment, where the fuel vapor mass fraction will be relatively large.

Results for an evaporating multicomponent fuel droplet are given in Fig. 11. The fuel is a mixture of hexane and decane with initial mass fraction of each being 0.5. The predicted results are shown for the modified d-square law, infinite-diffused, and diffusion-limit models. It is interesting to note that the experimental data indicates a batch-distillation type of behavior, which is better simulated by the infinite-diffusion model. However, the difference between this model and the diffusion-limit model are negligible. The modified d-square law does not show as good an agreement as that by the other two models.

CONCLUSIONS

The vaporization behavior of a fuel droplet in a laminar hot air flow has been studied theoretically and experimentally. Pure as well as multicomponent fuels have been considered. Numerical results predicted by three vaporization models, namely the thin-skin, diffusion-limit, and infinite-diffusion, have been compared with the experimental values. Important conclusions are:

- (1) The predicted droplet velocity variation along the trajectory shows excellent agreement with the measured data, indicating that the solid-sphere drag law is quite adequate for the conditions considered. However, an accurate calculation of the gas-film properties has a strong effect on the predictions.
- (2) The vaporization behavior of hexane fuel droplets is not sensitive to the vaporization models. However, for a less volatile fuel such as decane, the vaporization behavior shows some degree of sensitivity to the models. The implication is that even for low-temperature conditions such as considered here, where the droplet lifetime is relatively large, the transient droplet heating should be represented in the theoretical model.
- (3) The variable property effects are important for an accurate prediction of droplet velocity (and thus droplet trajectory) and size. Not only the effect of temperature but also that of fuel vapor should be considered for calculating the thermophysical properties of the gas film surrounding the droplet.

The present study is by no means complete. Future work should include (i) measurement of droplet surface properties such as temperature and composition (for the multicomponent case), (ii) droplet vaporization in a well-characterized turbulent flow field, and (iii) higher environment temperature.

REFERENCES

1. G.A.E. Godsave, "Studies of the Combustion of Drops in a Fuel Spray: The Burning of Single Droplets of Fuel, Fourth Symposium (International) on Combustion, Baltimore, 1953, pp. 818-830.
2. C.K. Law, "Recent Advances in Droplet-Vaporization and Combustion," Prog. Energy Comb. Sci., 1982, pp. 171-201.

3. S.K. Aggarwal, A. Tong, and W.A. Sirignano, "A Comparison of Vaporization Models for Spray Calculations," AIAA, Vol. 22, 1984, pp. 1448-1457.
4. W.D. Bachalo, "Method for Measuring the Size and Velocity of Spheres by Dual-Beam Light-Scatter Interferometry," Applied Optics, Vol. 19, 1980, pp. 363-370.
5. W.D. Bachalo, and M.J. Houser, "Development of the Phase/Doppler Spray Analyzer Drop Size and Velocity Characterization, AIAA-84-1199, AIAA 20th Joint Propulsion Conference, 1984.
6. T.A. Jackson and G.S. Samuelsen, "Droplet Sizing Interferometry: A Comparison of the Visibility and Phase/Doppler Techniques, Applied Optics, Vol. 26, No. 11, 1987, pp. 2137-2134.
7. L.G. Dodge, D.J. Rhodes, and R.D. Reitz, "Comparison of Drop Sizing Measurement Techniques in Fuel Sprays: Malvern Laser Diffraction and Aerometrics Phase/Doppler," Applied Optics, Vol. 26, No. 11, 1987.
8. G.L. Switzer, and T.A. Jackson, "Investigation of Velocity and Turbulence Intensity Measurement Limitations of the Phase/Doppler Particle Analyzer," Central States Meeting of the Combustion Institute, May, 1988.
9. S.K. Aggarwal, "Modeling of Multicomponent Fuel Spray Vaporization," Int. J. Heat Mass Transfer, Vol. 30, 1987, pp. 2162-2173.
10. S.K. Aggarwal, G. Chen, T.A. Jackson, and G.L. Switzer, "Vaporization Behavior of Pure and Multicomponent Fuel Droplets in a Hot Air Stream," Int. J. Heat Mass Transfer (to be submitted).

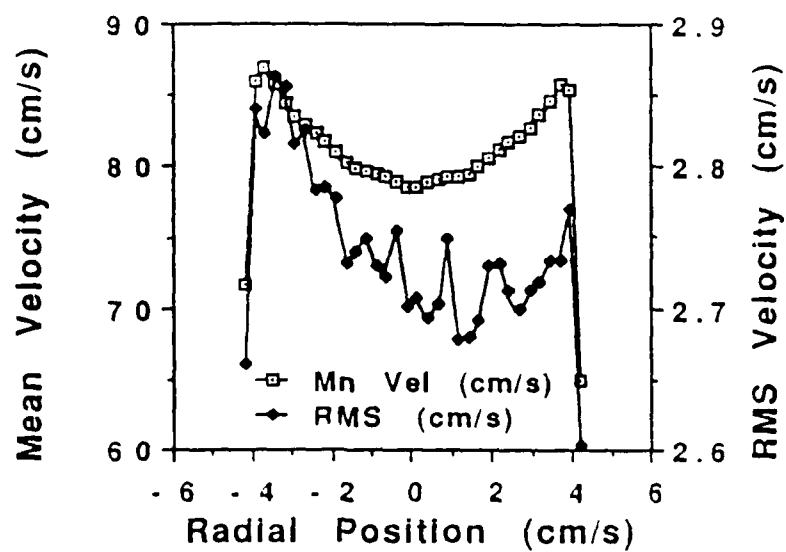


FIGURE 1. Inlet Air Velocity and Velocity RMS Profiles

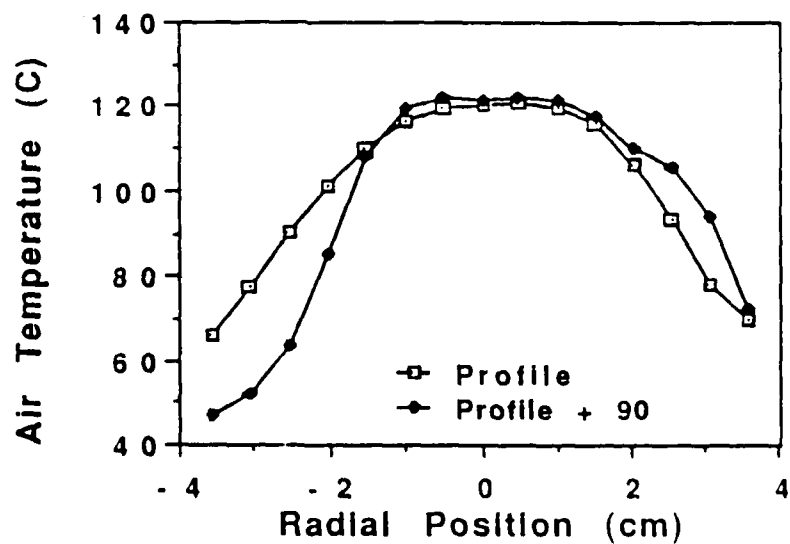


FIGURE 2. Inlet Air Temperature Profiles



Figure 3. Generation of 55- μm Droplets at 10-Hz Rate.

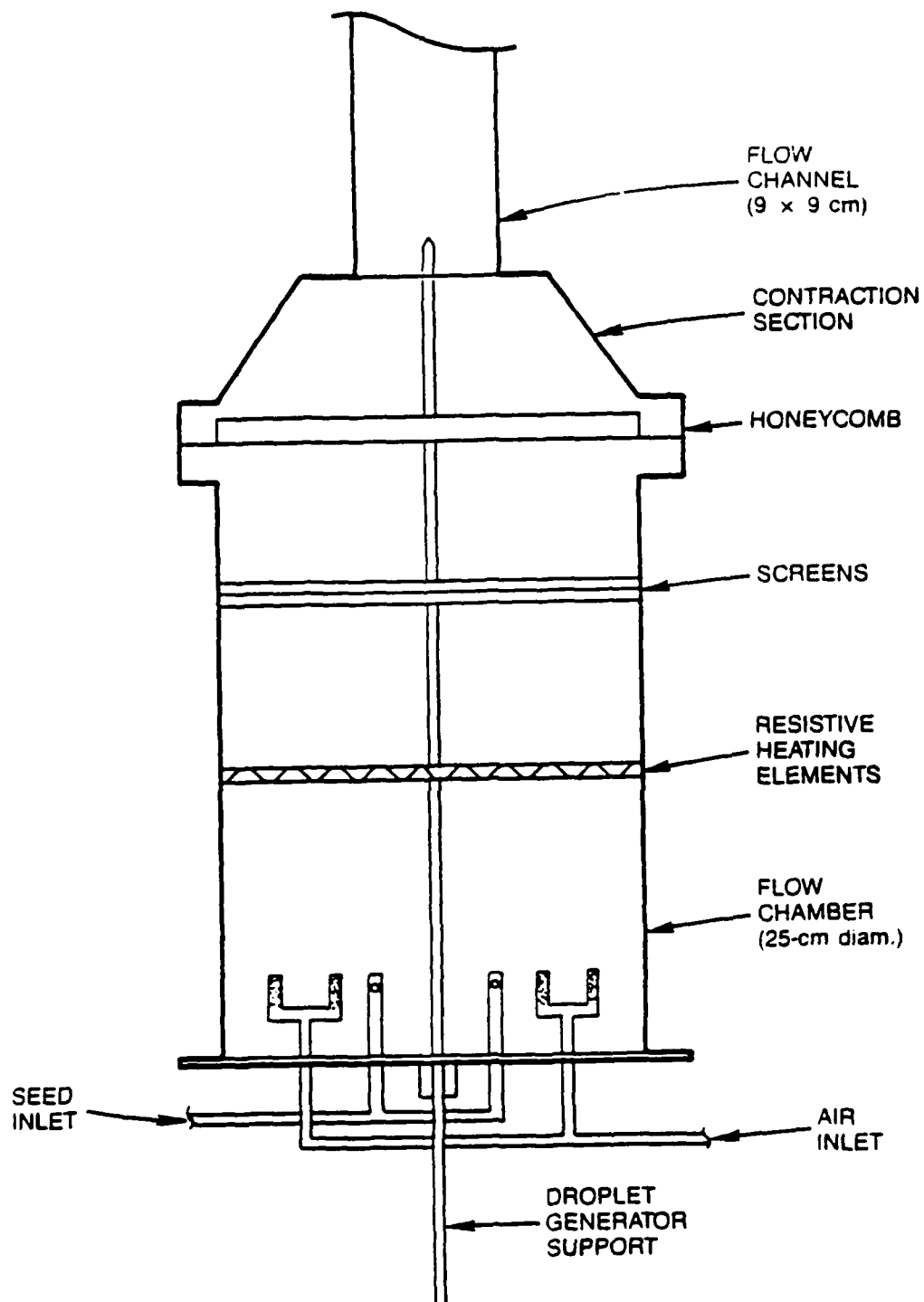


Figure 4. Diagram of Flow Chamber Employed for Droplet-Vaporization Studies.

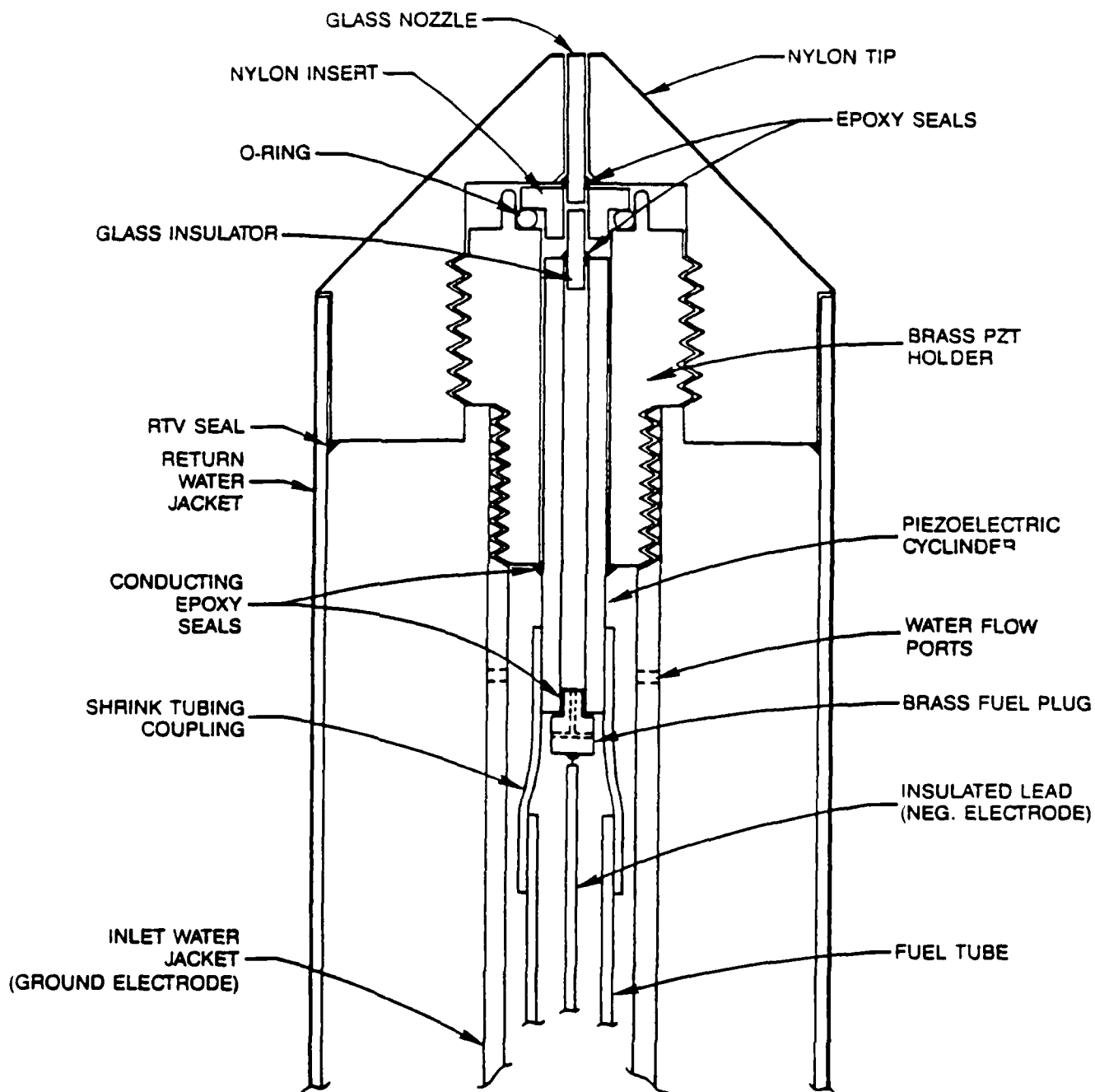


Figure 5. Schematic Diagram of Water-Cooled Droplet-on-Demand Generator.

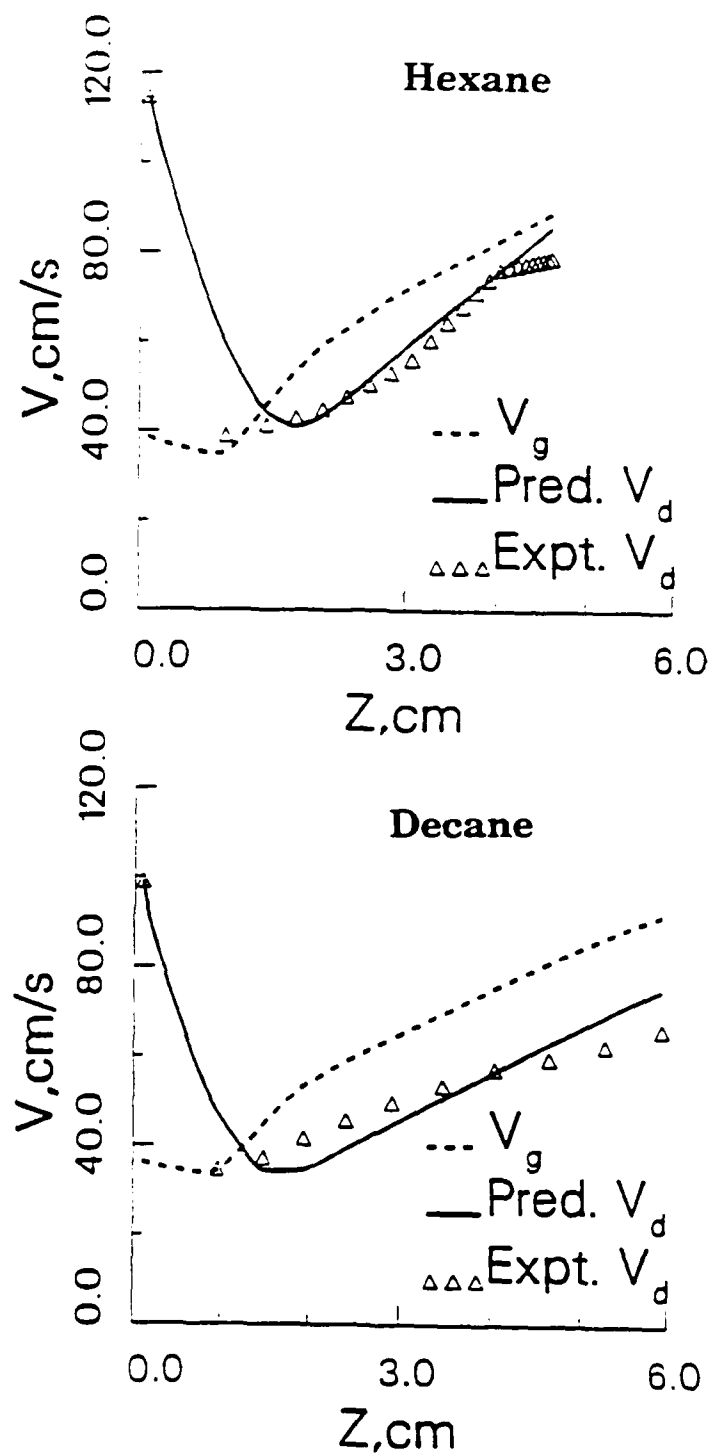


Fig 6. Comparision of predicted and experimental droplet velocity.

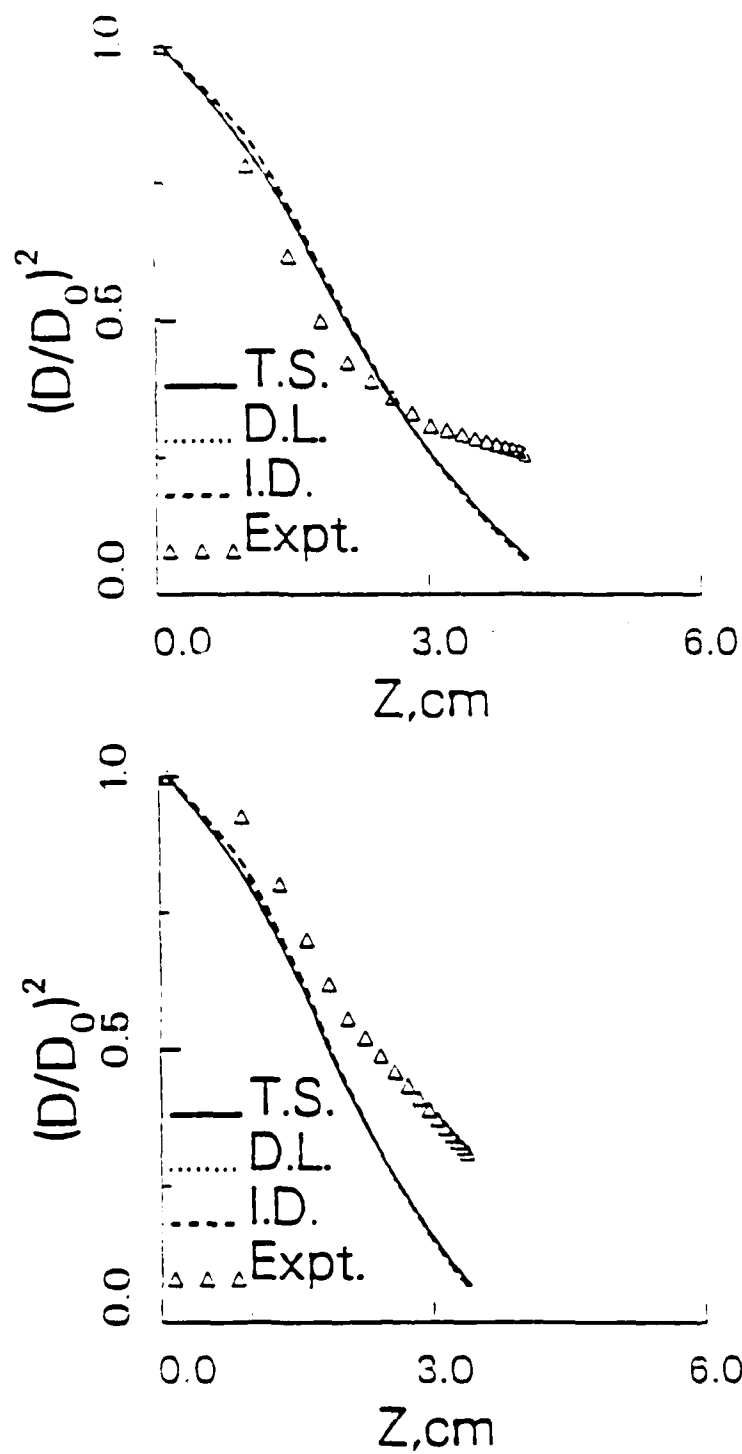


Fig 7. Diameter squared
along the trajectory
for a hexane fuel droplet.

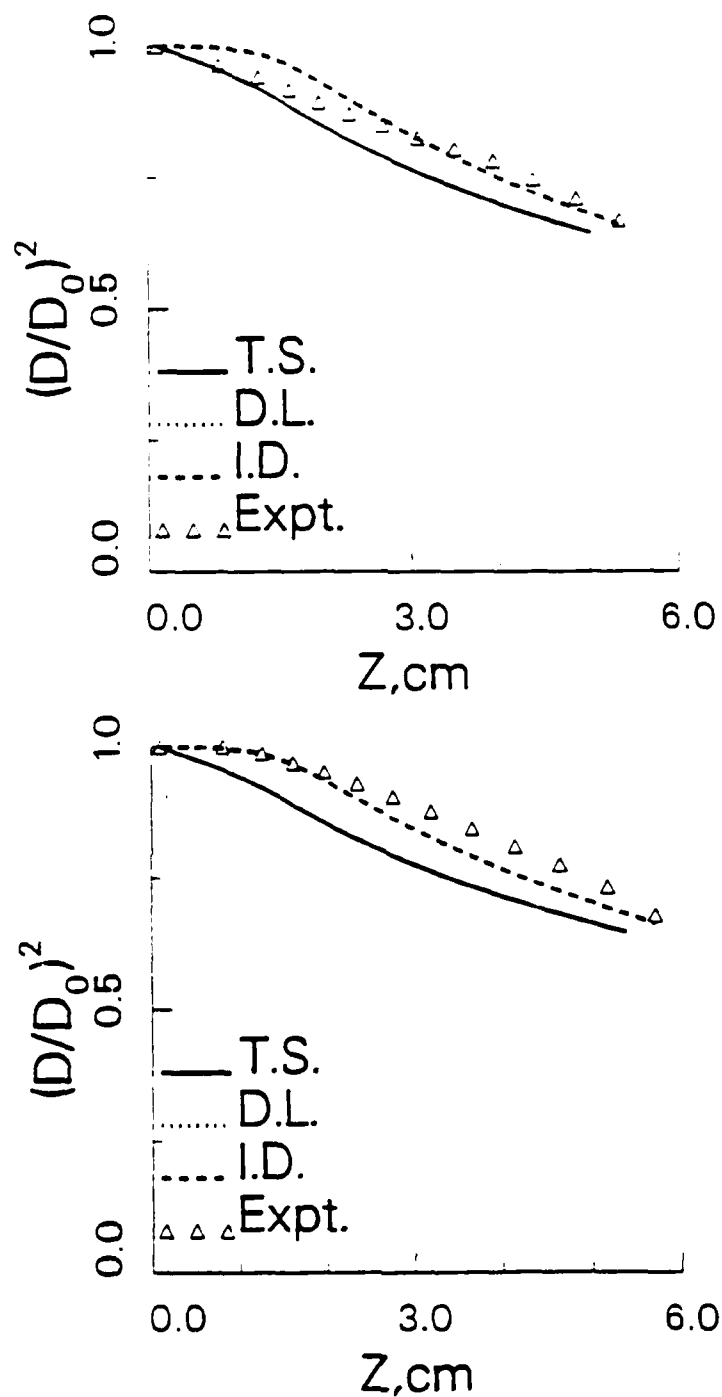


Fig 8. Diameter squared along the trajectory for a decane fuel droplet.

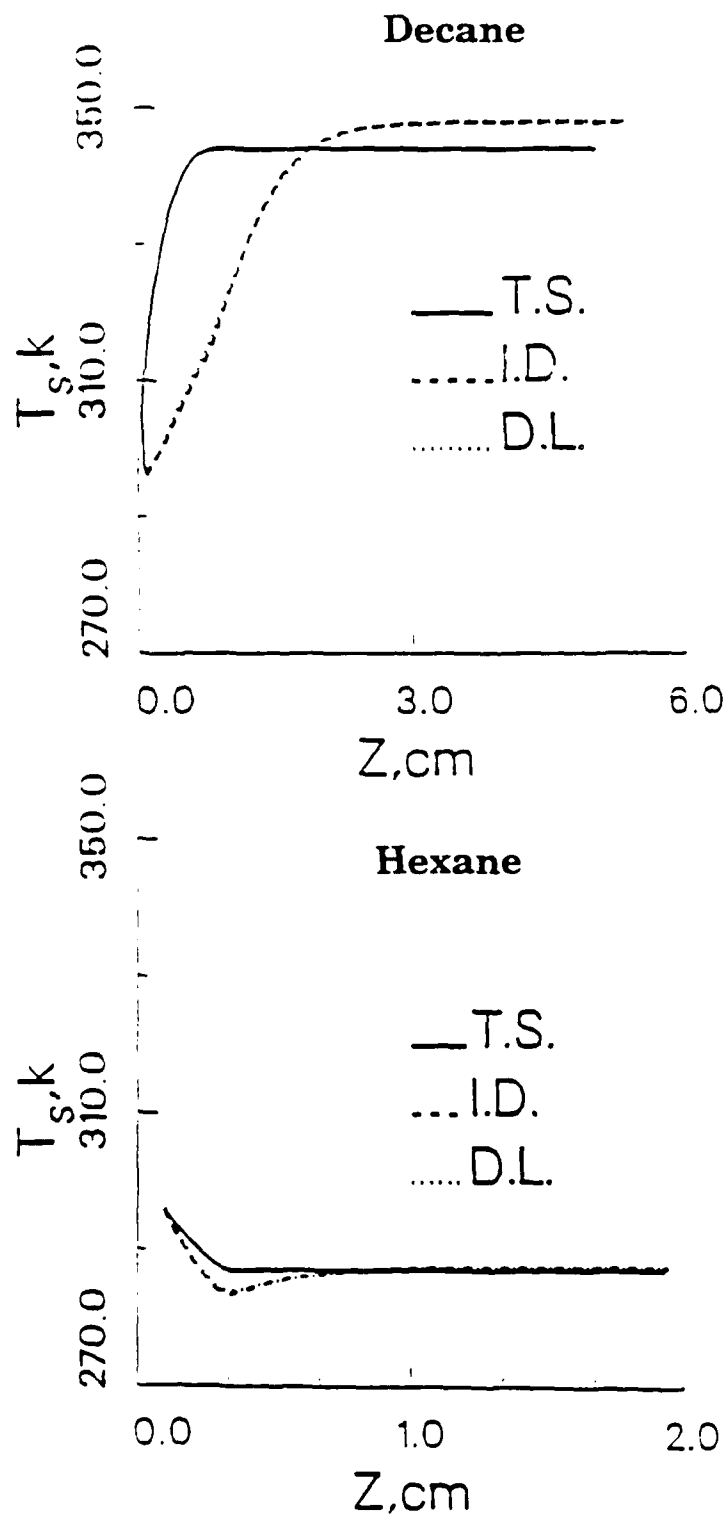


Fig 9. Droplet surface temperature
predicted by three
vaporization models.

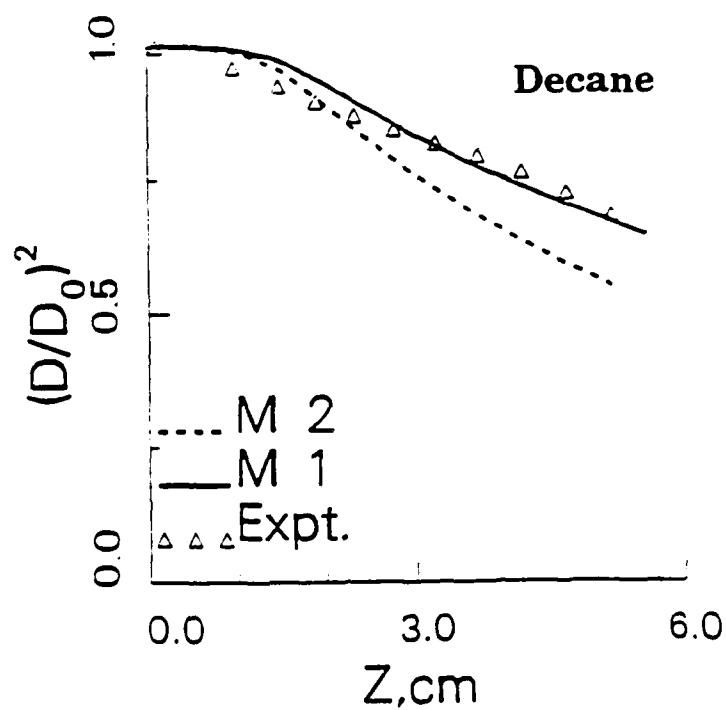
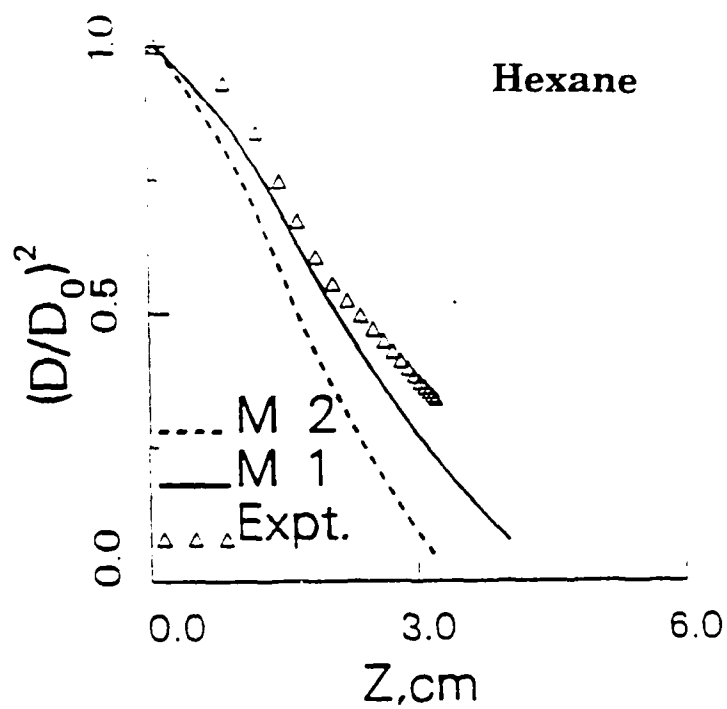


Fig 10. Droplet size squared
along the trajectory
M1-with fuel vapor effect
M2-without fuel vapor effect.

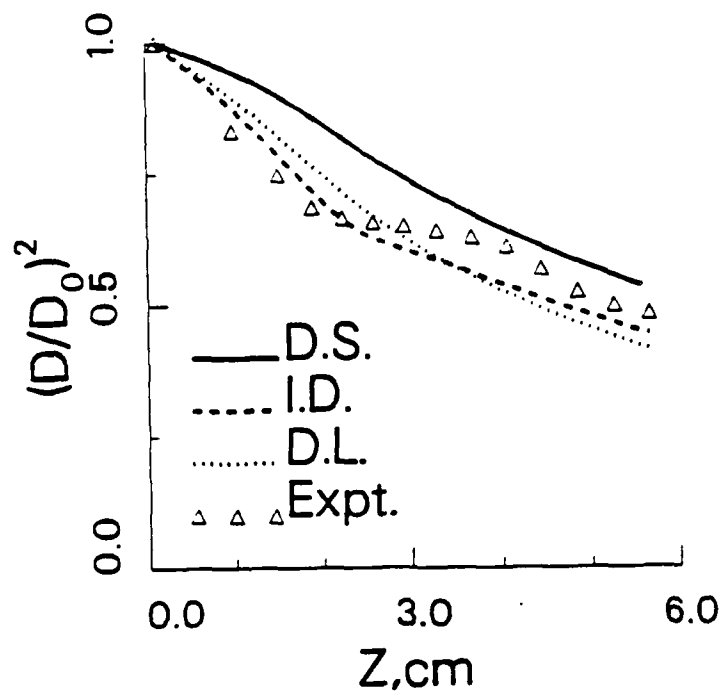


Fig 11. Droplet diameter squared along the trajectory for a multicomponent fuel droplet.

FINAL REPORT NUMBER 70
EFFECTS OF INJECTION-TO-MAINSTREAM DENSITY
RATIOS ON FILM COOLING HEAT TRANSFER
PENDING APPROVAL
Dr. Mingking K. Chyu
210-9MG-096

**FINAL REPORT NUMBER 71
ACCURATE TEMPERATURES USING CARS
IN DROPLET LADEN FLOWS
PENDING APPROVAL
Dr. Derek Dunn-Rankin
210-9MG-055**

FINAL REPORT NUMBER 72
REPORT NOT AVAILABLE AT THIS TIME
Dr. Wayne A. Eckerle
210-9MG-019

FINAL REPORT NUMBER 73
REPORT NOT AVAILABLE AT THIS TIME
Dr. Arthur A. Mason
760-6MG-099

FINAL REPORT NUMBER 74
REPORT NOT AVAILABLE AT THIS TIME
Dr. Douglas G. Talley
210-9MG-022

FINAL REPORT
VORTICAL STRUCTURES IN 2-D SLOT
BURNER - COLD FLOW

Sponsored by
AIR FORCE OFFICE OF SCIENTIFIC RESEARCH

Conducted by the
Universal Energy Systems

Prepared by:	Richard S. Tankin
Academic Rank:	Professor
Department and	Mechanical Engineering Department
University:	Northwestern University
Date:	1 February 89
Contract No:	S 745 007 001

Vortical Structures in 2-D Slot Burner - Cold Flow

Richard S. Tankin
Northwestern University

ABSTRACT

Vortical structures are examined experimentally for cold flow from a 2-D slot burner. The vortical shedding processes are clearly observed using a two-dimensional sheet lighting technique coupled with a chemically reacting system. By varying the flow rates, four different types of vortical structures are observed - separated by regions of stability (transition regions). From sets of data, flow maps were constructed showing the zones occupied by the four types of vortical structures and the regions of stability. The effect of the width of the bluff-body (burner lip) on the flow map and frequency of vortical shedding are presented. Hot wire measurements were used to obtain frequency spectra. For the range of Reynolds numbers in this study, a single vortical shedding frequency appeared except in an isolated region where the spectra are quasi-periodic. Broad-band spectra are characteristic of the transition regions. The Reynolds number of the slot flow varied from 2 to 110; the Reynolds number of the air flow varied from 50 to 400.

INTRODUCTION

Flame stabilization has been, and still is, an important subject in combustion research. Bluff-body nozzles in combustors represent a typical configuration for accomplishing flame stabilization. This configuration of nozzles is widely used in industry; for premixed and diffusion flames, for liquid fuels (sprays) and gaseous fuels. The flow field behind a bluff body nozzle, even without combustion, is very complicated. Small scale mixing (molecular) is accompanied by large scale mixing due to the vortical structures that are created. Since these vortical structures may be very intricate, it was decided to obtain some information about their formation and growth through flow visualization.

In practical applications, the geometrical arrangement for bluff-body nozzles is usually axially symmetric (cylindrical shape). The fuel - liquid in the form of a spray or gaseous - issues from the center of the nozzle; and the air (for diffusion flames) issues from a concentric annular region. Many text books describe the essential

al,1983; Li and Tankin, 1987; Namazian and Kelly, 1985; Kimoto et al, 1981) and numerically (e.g., Scott and Hankey,1983; Boyson et al, 1981). The 2-D bluff-body geometry has not been studied as extensively; partly because of the added difficulty involved in obtaining uniform 2-D flow at the nozzle exit. However when properly designed, this nozzle has the advantage of generating vortices that are simpler to analyze experimentally than axially symmetric nozzles.

For flow past cylinders (2-D bluff-body), vortices that are formed at the points of separation are regularly shed from alternate sides of the cylinder. Recent papers, such as, those by Perry et al, 1982; Perry and Steiner, 1987; Eaton,1987; etc. clearly demonstrate this. 2-D jets have likewise been studied both experimentally and theoretically. For 2-D jets, vortical shedding occurs when a critical Reynolds number is exceeded. The vortical shedding pattern may be symmetric or antisymmetric - depending on the velocity distribution profile at the exit of slot (see Sato, 1960)- and is due to the instability that occurs at the free boundary layer (see Sato and Sakao,1964; Beavers and Wilson,1970; Rockwell and Niccolls, 1972; Thomas and Goldschmidt,1986; etc.). We have mentioned the flow past cylinders (2-D bluff-body) and 2-D jet flows because the flow in this study is, in some respects, a combination of these two flows.

Recently chaotic analysis has been used to describe the transition from laminar to turbulent flow. Fenstermacher et al,1979 have applied chaotic analysis to Taylor vortex flow; Curry et al, 1984 applied it to Benard natural convection flow; Sreenivasan,1985 applied it to wakes behind cylinders; and Dubiri et al,1987 applied it to a two-stream mixing layer. Williamson, 1988, re-examined the discontinuity in the vortex shedding from a circular cylinder. He explained this phenomenon as a change in the mode of oblique shedding, not as a "route to chaos". In the present paper, we have observed different regions of vortical shedding for gas flow from a 2-D slot burner immersed in a co-current 2-D air flow. The results are interesting because as one proceeds from one region of vortical structures to another (by changing the flow rates), one passes through regions of stability (where vortical shedding ceases). The streamwise component of the velocity fluctuations were measured for all the identifiable types of vortical structures and transition regions. From the velocity fluctuation measurements, frequency spectra were obtained; and the relative amplitudes of the peak frequencies were examined.

EXPERIMENTAL SETUP

A schematic diagram of the experimental setup is shown in Figure 1. The details describing the introduction of $TiCl_4$ into the apparatus has been adequately described by Roquemore et al, 1983 and Li and Tankin, 1987.

Figure 2 is a schematic drawing of the slot burner and Figure 3 is a photograph of the burner. Three different inner slot widths were used in this study - 0.25cm, 0.45cm, and 0.60cm. The slot length is 15 cm. Laterally surrounding the inner slot is a bluff-body; the outer dimension of the bluff-body is fixed at 2.5cm. The width of the bluff-body is formed by a quarter-round, circular insert (one on each side) which in addition to forming a bluff-body provides contraction of the slot flow, thus resulting in more uniform flow at the slot exit. The thickness of the boundary layer and the intensity of the turbulence is reduced when the flow is contracted. Depending on the insert used, the contraction ratio was 3.2, 4.2, or 7.6.. Special care was taken in transitioning the flow from a round tube to a rectangular channel before it entered the slot burner. Downstream of this transition region are guide vanes and screens within the burner body, which results in a uniform 2-D flow at the slot outlet.

The slot-bluff body unit was centered in a nearly square test section that measures 26cm by 23cm and through which air flows. Quarter round inserts were mounted on each side (at the exit) of this container, contracting the flow from 23cm to 4cm; thus providing a contraction ratio of 5.75. The air enters this portion of the test section on each side of the slot burner, impinges on deflector plates, passes through screens and exits the nozzle as 2-D flow. To reduce the effects of external disturbances, the test section is fitted with a chimney which is 36cm high - made of aluminum and containing glass windows. A coarse screen (1/2" x 1/2" mesh) was placed on top of the chimney to further reduce the effects of external disturbances.

Since combustng flow is planned in the future, two small channels are located at the ends of the slot (see Figures 2 and 3) through which a non-combustible (N_2) gas will flow. Propane will flow through the slot burner - air will flow outside. The N_2 will suppress the flame from burning inward from the ends; in this manner the two dimensionality of the flow will hopefully be maintained.

To visualize the flow field, laser sheet-lighting in conjunction with TiO_2 particles, which are generated at the nozzle exit, was used. This setup provides a very useful visualization technique. A dry gas, in this case bottled N_2 , passes over a pool of $TiCl_4$ liquid, picking up some $TiCl_4$ vapor which is carried with N_2 through the slot burner. This $TiCl_4$ vapor reacts with water vapor, which is present in the air flow external to the slot exit, to form TiO_2 particles. These particles act as scattering centers for the laser light. The TiO_2 particles, formed in this manner, have been reported to be fairly uniform - ranging in size from 0.2 to 1mm; thus they follow the flow field. The importance of this method of seeding is that the particles are formed external to the nozzle; thus eliminating the problem of clogged screens. To further insure no clogging in the test section, a transparent filter containing

a series of fine mesh screens is installed just upstream of the test section. If there is any water vapor present in the N_2 gas line, TiO_2 particles be detected in the transparent filter unit. Thus, the problem can be addressed before the screens in the test section become clogged. Another important aspect of this method of seeding is that the TiO_2 particles do not appear uniformly distributed throughout the flow but in a thin layer where the two gases - N_2 (containing the $TiCl_4$ vapor) and air (containing water vapor) - come in contact. Thus, allowing one to observe in detail the vortical structures, which are formed at this interface. When we wished to examine the recirculating zones near the slot, the experimental setup was slightly modified. $TiCl_4$ was introduced into the air flow through two small hypodermic tubes as well as in the slot (N_2) flow. A very small flow rate of N_2 , which acted as a carrier gas, trickled through these tubes. This tiny flow of N_2 , which has no observable effects on the flow pattern (recirculating zones or vortical structures downstream), seeds the recirculating zones that are formed on the air side of the bluff body.

Three photographic techniques were used in this study; each having certain advantages and disadvantages. In one case, normal photography was employed. The resolution of the film was excellent but the shutter speed limited the resolution of the fine scale structures that are present in the vortices. Using a 3 watt Argon ion laser as a sheet-light source, Tri X film, and an aperture setting of $f=1.4$; we were limited to shutter speed of 1/500 sec. For the second method, a high speed video camera was used. This unit, with sufficient light, could take video pictures at a rate as high as 6000 frames per second. However because of the limited light intensity, we were not able to exceed 250 frames per second - which was more than adequate for tracking the overall motion of the vortical structures in our experiments. With this camera, we were able to follow the progress of a selected vortex; thus, measure its shedding frequency, position, and translational velocity. The resolution of this camera, which contained 240×192 pixels, was inferior to normal photographic film. In the third method, a digital image processor camera was used. This camera has an intensifier and better resolution (244×388 pixels) than the high speed video camera. Pictures were taken with this image processor at shutter speeds of less than 1 microsecond. This unit, which was capable of 1 to 60 images per second, has supportive software which enhances and extends the measurements to include, for example, intensity distribution. A shutter speed is essential if one wishes to examine the fine structures of a vortex. A comparison of the three photographic techniques is shown in Figure 4 where $Re_{slot} = 45.0$ and $Re_{air} = 328$. This is not really a comparison, because the advantages of the digital image processor (higher shutter speed) is not apparent. Later, one will see typical pictures illustrating the fine vortical structures obtained with this unit.

To examine the two dimensionality of the flow, the flow is sheet lighted horizontally. This was achieved by rotating the glass rod (lens) 90 degrees (vertical) and positioning a plane mirror above the test section. When taking these pictures, the 1/2"x 1/2" mesh screen on top of the chimney was removed.

The shedding frequency of the vortical structures is measured with the high speed video camera. The method used is as follows: A fixed point is chosen in the flow (on the video screen). The framing time for each frame appears on the screen along with the video image. Each time a vortex passes the fixed point on the screen, a shedding period can be determined. The shedding period (shedding frequency) is obtained by averaging over at least 10 vortices. To determine the influence of the selected position, the shedding frequency was measured at different selected points in the flow field. The variation of the measured shedding frequency with selected position was negligible. Also a chopper, driven by an A.C. motor, was used to form a strobe of the laser beam and check the frequency measurements.

A hot-wire, constant temperature anemometer was used to measure the streamwise component of the velocity fluctuations. The hot wire was operated at an overheat ratio of 20%. The probe supporting the hot wire is "L" shaped and was inserted vertically from above. The hot wire was positioned about 7 cm downstream (above) of the slot, mid-plane of the slot length and 0.8 cm laterally from the slot centerline. Frequency spectra were obtained from the measured velocity fluctuations using a R360 real spectrum analysis software and an IBM AT PC.

In these hot wire measurements, for each frequency spectrum, 1024 data points of velocity are collected. The resolution of the spectrum depends on the time interval chosen between data points. In order to reduce the electronic noise in the system, a 225Hz low-pass filter was used, as well as averaging successive spectra (4 to 64 spectra were sometimes averaged). The "Hanning window" was applied to each spectrum to improve the frequency resolution. A linear scale was chosen to display the frequency spectra.

The experiments were conducted at low Reynolds numbers for both the slot and the air flows. The Reynolds number is defined as VD/v , where V (the average exit velocity) is the volumetric flow rate divided by the exit area, and D is the width of the slot or the air channel. In this study, Re_{slot} ranged from 2 to 110 and Re_{air} ranged from 50 to 400. Three slot widths (0.25, 0.45 and 0.60cm) were used to determine the effect of slot width (bluff-body) on the vortical structures. During the experiments, the supply pressures at the rotameters of the air and N_2 were maintained constant.

RESULTS AND DISCUSSION

The results of this study will be presented as follows:

- (1) A series of photographs showing the vortical structures will be presented for typical sets of experiments.
- (2) Plots indicating the flow maps for various types of vortical shedding for a given bluff-body configuration will be presented.
- (3) Measurements of shedding frequency, intensities within a vortical structure, path-lines of individual vortices, etc. will be presented.
- (4) A series of photographs were taken to determine the validity of the assumption that the flow is two-dimensional.
- (5) Measurements of velocity fluctuations obtained with a hot wire anemometer and their frequency spectra will be presented.

Figures 5 and 6 are typical sets of photographs showing the vortical structures. These experiments were performed with a slot width of 0.45 cm and with $Re_{air}=392$ and 222 respectively. The Re_{slot} was varied from 2.0 to 108.2. Before describing the classification of the vortical structures, some general characteristics and nomenclature should be mentioned. The bluff-body, in this case, separates the slot flow (N_2 with $TiCl_4$ vapor) from the air flow; and in the process, usually results in a pair of recirculating zones. One member of the pair is caused by the expansion of the slot flow and is designated the "IRZ" (inner recirculating zone). The other member is caused by the expansion of the air flow and is designated the "ORZ" (outer recirculating zone). The relative size and the dynamic interaction between these recirculating zones determine the shedding characteristics and the type of vortical structures observed. There also is interaction between the vortical structures on each side of the slot.

Type I (Figures 5a, 5b, 7a, 7b)

As can be seen from Figures 5a and particularly 7a, the slot jet (N_2) does not penetrate the ORZ. This condition occurs for relatively high air flow (Re_{air} greater than 335) and low slot flow. The structures of these shedding vortices are similar to the Von Kármán vortical structures (see Perry, 1982, Figure 7). The influence of the slot flow on the shedding vortical structures is negligible because of the low momentum flux of N_2 as compared to the momentum flux of the air. The size of the unstable (shedding) ORZ is much larger than the IRZ. This is evident in Figures 7a and 7b, which are photographs along with schematic drawings showing in greater detail the recirculating zones. These pictures were taken with the digital image processor at shutter speeds of about 1 microsecond. For the photographs shown in Figure 7, the experimental setup, as mentioned earlier, was slightly

shown in Figure 7, the experimental setup, as mentioned earlier, was slightly modified. $TiCl_4$ was introduced into the air flow through two small hypodermic tubes as well as in the slot flow. A tiny flow of N_2 , which acted as a carrier gas, in the hypodermic tubes had no observable effects on the flow pattern (vortical structures downstream or both recirculating zones). The seed particles (TiO_2) are carried by the air that flows near the slot; thus providing visualization of the ORZ (not visible with $TiCl_4$ only in slot flow). The dashed lines in the schematic drawings represent structures that are believed to be present, but not observed. At $Re_{air}=222$ (Figure 6), Type I flow does not exist. $Re_{air}>335$ is required for Type I to exist, as will be seen later on the flow map.

Transition I-II (Figures 5c,6a,7d)

When Re_{slot} is increased to 6.6 in Figure 5, the first transition region occurs. In this region no vortical shedding occurs - both recirculating zones (ORZ and IRZ) are stable. For $Re_{air}=222$, this transition region exists from $0 < Re_{slot} < 3.3$. Figure 6a is a photograph at $Re_{slot} = 2.0$. In Figure 7c, it is seen that the inner recirculating zone has grown in magnitude due to the increased slot flow rate.

Type II (Figures 5d,5e,6b,7d)

When Re_{slot} is increased to 9.2 in Figure 5, vortical shedding is observed again (5d). This is also seen in Figure 6b where $Re_{slot}= 6.6$. By examining the video pictures taken at 125 frames/sec, it was observed that both sets of vortices (from ORZ and IRZ) were unstable and shedding. The downstream roll-up of vortices are not seen. From Figure 6b,7d, it is seen that only a small amount of fluid is split away from the vortices in both the ORZ and IRZ. This fluid is convected downstream. The interaction between the air flow and the slot flow is rather weak. This unstable flow region occurs over a relatively narrow range of Re_{slot} .

Transition II-III (Figures 5f,6c,7e)

When the Re_{slot} is increased to 17.9 in Figure 5 and 9.3 in Figure 6, the vortical shedding again ceases. Both recirculating zones are stable. The vortices in these zones are comparatively equal in size (see Figure 7e). The high speed video records reveal a very smooth flow.

Type III (Figures 5g - 5m,6d - 6k,7f,7g)

When Re_{slot} is increased to 20.5 in Figure 5 and 10.5 in Figure 6, vortical shedding reappears and much more complicated vortical structures appear downstream. In this region, the IRZ, in contrast to Type II, are lifted off the bluff-body and the interaction between the air flow and the slot flow is

much more intense. In Type III, the process involving vortex roll-up dominates the structure; but this roll-up is accompanied by bending, stretching, and irregular deformation of the rolled-up vortices. In Type III a special vortical shedding behavior was observed when Re_{slot} lies between about 23.5 and 31.0 (see Figures 5h,5i). These structures are not seen in Figure 6 because the Re_{air} is not high enough (this will be seen later on flow maps). In this isolated region ($23.5 < Re_{slot} < 31.0$), the two vortices, that are shed within one period, collide with each other; thus generating greatly erratic and deformed vortical structures downstream - not repeating their structures from vortex to vortex. Orderly structures are not observed. With further increase in Re_{slot} (larger than 32 in Figure 5) the vortical structures downstream are ordered again and can be clearly identified (Figures 5j, 5k, 5l, 5m). Thus, at sufficiently high Re_{air} , there exists in Type III an isolated region where there is strong interaction resulting in disorderly vortical structures. Vortical crossover is an interesting phenomenon observed in Type III. This is clearly shown in Figure 8 where the trajectories for a single vortex is plotted for different Re_{slot} values (note: these data were obtained at $Re_{air} = 264$ and is typical of plots at other Re_{air} in Type III - except for the "disordered structures" regime). On this plot (Figure 8) there is a trajectory of a vortex of Type IV which is seen not to crossover. Near the upper and lower boundaries of Type III, (labelled "Borderline Type III" in Figure 8 - upper boundary), the rolled-up vortical structures are not so intense; so crossover doesn't occur.

The static and dynamic structures of vortices in the recirculating zones in Type III are similar to those in Type II (compare Figures 7d and 7f, 7g), except the IRZ has lifted and is located above the ORZ. The IRZ and ORZ are separated by a "cavity" in Type III which is not found in prior types. This "cavity" is located beneath the IRZ at higher values of Re_{slot} (see Figure 7g).

Figure 9 is a schematic drawing showing the typical type III vortical structures similar to those seen in Figures 5k and 6h. The vortex crosses to the opposite side of the slot and is encased in a "pocket" formed by the distorted interface. The two consecutive vortices are connected by a "braid" structure which is produced by the merging of the two interfaces. The "braid" structure has been defined and discussed in research on mixing layers by Corcos and Sherman, 1984.

Transition III-IV (Figures 5n,6l,7h)

When Re_{slot} is increased to 65.2 in Figure 5 and 28.8 in Figure 6, the shedding of vortices ceases and again vortical structures downstream of the recirculating zones are absent. In this region, which exists over a very narrow range of Re_{slot} , the IRZ present in previous types does not appear in this transition state. The "cavity" and the ORZ are stable with no vortical

shedding (see Figure 7h). From the experimental observations, it appears that the "cavity" has replaced the role of the IRZ.

Type IV (Figures 5o,5p,5q,5r,6m,6n,6o,7i)

This is the last type of vortical structure identified in this study. As Re_{slot} is increased from about 67 to 108 in Figure 5 and for values greater than 32 in Figure 6, the influence of the air flow on the formation of vortical shedding structures is very small. The shedding vortices appear to originate in the "cavity" and have the appearance of vortical structures observed for 2-D jet flow. Table I summarizes the classification of vortical structures, and indicates the relations between IRZ and ORZ.

A summary of the data for more than 90 flow conditions, obtained in the manner described, is shown in Figure 10 (slot width is 0.45 cm). The dark circles indicate vortical shedding and empty circles indicate no vortical shedding. The isolated region - designated as "disordered structures" - within Type III is where vortices are being shed - but not orderly. Similar plots were obtained with slot widths of .25 cm and .60 cm. These results are seen in Figures 11 and 12 respectively. Table II gives the critical Reynolds numbers for each of the types of vortical shedding, and the approximate equations that separate the different regimes.

The shedding frequency is an important parameter in hydrodynamic stability theory because it represents the most unstable mode in the flow field. The effects of three independent quantities - Re_{slot} , Re_{air} , and D_{slot} - on shedding frequency are examined in Figure 13. Figure 13a shows the effect of Re_{slot} on shedding frequency for a slot width of .45cm and $Re_{air}=328$. These data (as well as those in Figures 13b and 13c) were obtained from high speed video recordings. As can be seen the shedding frequency increases monotonically with Re_{slot} . There appears to be a discontinuity in the slopes at the Transition II-III and Transition III-IV. Similar results were obtained for other slot widths and other air flow rates. The effect of Re_{air} is shown in Figure 13b in which the shedding frequency is measured for $D_{slot}=0.60$ cm and Type III vortical structures. Likewise Figure 13c shows the effects of D_{slot} for three different slot widths - 0.25cm, 0.45cm, and 0.6 cm.

Another feature which becomes apparent from this study is the interaction of the vortices as they move downstream. The interaction occurs in pairs and each pair consists of vortices of opposite sign (vortex couple). This is seen in Figures 5j, 5k, 5l, 5m, 5p, 5q and 5r; it is believed to occur further downstream for flows seen in Figures 5a, 5b and 5g (the field of view was limited by the windows in our test section). This interaction between vortices (pairing of vortices of opposite sign) has been predicted by

several investigators; such as, Batchelor, 1967; Deem and Zabusky, 1978; Pierrehumbert, 1980; etc.

Three dimensional structures, produced by end effects, will be present in these experiments since the experimental device (slot) is of finite length (15cm). In addition, strong nonlinear interactions are occurring. Since we assumed the flow was two-dimensional (over the measured region), it was necessary to check this assumption. To do this, the laser sheet light was oriented horizontally (by rotating the glass rod 90°-vertically) and a plane mirror was placed above the test section (tilted about 45 degrees from the vertical). In this manner, pictures were obtained looking from above at horizontally, sheet-lighted flow. A series of pictures were taken at three different vertical positions: (1) the laser sheet-light was located just above the nozzle exit, (2) the laser sheet-light was located 2.5 cm above the nozzle exit, and (3) the laser sheet-light was located 7.5 cm above the nozzle exit. These vertical positions are shown in Figure 5a. Pictures were taken over the entire range of flow rates. Figure 14 shows some typical photographs. End effects are seen in all cases, but the flow appears to be two-dimensional - especially at the surface and 2.5 cm elevations. This is apparent, because the TiO_2 particles are clearly aligned - nearly straight lines with curvature only at the ends. At the 2.5cm and 7.5 cm elevations, the pictures as seen in Figures 14 oscillate laterally as a unit (at the shedding frequency). At the 7.5cm location, the three-dimensional effects are more apparent - particularly in Figure 14f, where the illuminated particles are not aligned in straight lines. At other times, at the same flow conditions, these strong three dimensional effects were not so obvious when similar pictures were taken. Thus, we believe some of the three dimensionality was caused by outside disturbances such as the removal (before each photograph was taken) of the screen located on top of the chimney. Normally, we would have claimed the flow to be two-dimensional along the midplane of the slot (7.5cm from each end) where the vortical data were taken. However, in a recent paper by Williamson, 1988, in which he examines the vortical shedding from a cylinder, he found oblique shedding exists. He used oblique shedding to explain the discontinuities in the Strouhal-Reynolds number relationship. Thus, oblique shedding may account for some of the curvatures seen in the horizontally lighted flow; see for example Figure 14f where both "three-dimensional" and "oblique shedding" are labelled. To check this possibility, a sheet of vertical light is aligned along the length of the slot. Oblique shedding, we think, occurs and is more apparent in Type III. A photograph showing what we consider oblique shedding is seen in Figure 15. We don't know whether its cause is the same as in Williamson's experiments.

Figures 16a and 16b are examples of typical photographs taken with the digital image processor having a shutter speed of 1 microsecond. These two photographs were at similar flow conditions as those in Figures 6h and 5j

respectively. One can see in these enlargements the fine structures present in the vortices. Figure 17 is an enlargement of a shed vortical structure similar to the flow conditions in Figure 5k. Superimposed on this vortex is the optical intensity distribution measured along the centrally-located dotted line in the photograph (the two outer dotted lines represent the limits of the intensity amplitude). As a shed-vortex passes a velocity measuring probe (such as a hot wire anemometer), one might expect to see velocity fluctuations which are related to these intensity fluctuations superimposed on the shedding frequency (since slot flow, N_2 , and air flow are rolled up into these vortical structures). These may give the appearance of the onset of turbulent flow. However, the diffusion of vorticity will probably be much more rapid than the diffusion of the TiO_2 particles in the flow; thus the velocity changes, which may be present, would not be as abrupt as the intensity changes shown in Figure 17.

To check this conjecture, hot wire measurements were made. The mean value of the velocity was removed from the signal because we were primarily interested in the frequency spectrum associated with the velocity fluctuations. The scale of the velocity amplitude is not maintained constant from one set of experimental tests to another. In this study, we were interested in the number of independent frequencies and the relative amplitudes between the fundamental frequency (shedding frequency - f_s) and its harmonic modes (for each test). Typical measured results are shown in Figure 18 where $Re_{air}=392$, $D_{slot}=0.45cm$ and Re_{slot} was chosen to include all types of vortical structures. The frequency spectrum for each type of vortical structure is described as follows:

Type I (Figure 18a)

The flow is periodic and only one frequency appears (the shedding frequency - f_s) along with its first and second harmonic frequencies.

Type II (Figure 18c)

The spectrum is similar to that for Type I. The shedding frequency is dominant. The amplitudes of the higher harmonic modes are much smaller than the amplitude of f_s .

Type III (Figures 18e, 18f, 18g, 18h, 18i)

Figure 18e falls within the shaded region of the flow map labelled "Disordered Structures" in Figure 10. Owing to the strong interaction between the vortices, the velocity fluctuation record is more erratic and less periodic than in Types I and II. The accompanying frequency spectrum shows that the flow in this region is not as random as one might expect. Two independent frequencies are found which explain this spectrum (quasi-

periodic flow); the fundamental frequency, f_s , is 4.5Hz., and the second independent frequency is 1.6 Hz. This second independent frequency can be identified as having the second largest amplitude. The other significant peaks are simply linear combinations of f_s and f_2 . When the Reslot is increased to 36 (beyond the "Disordered Structures"), the periodic flow field reappears and only one fundamental frequency is found (Figure 18f; $f_s=5.5\text{Hz}$). Further increase in Reslot (Figures 18g, 18h, 18i) results in more complicated time series records (velocity) which are attributed to the rolling-up processes of the vortices. In Figure 18i, the flow field is dominated by the first harmonic (biharmonic resonance) instead of the shedding frequency- f_s . In this flow - Type III, high Reslot - the vortices from each side line up along the centerline of the slot; thus, producing a signal that is twice f_s . This can be seen in Figure 5m and in the trajectories plotted in Figure 8 - particularly the one labelled "Borderline Type III".

Type IV (Figure 18k)

In Type IV, two peak frequencies are observed in the frequency spectrum - Figure 18 k is typical. The shedding frequency, which is the peak frequency occurs at 30Hz; the second frequency at 18.2Hz, is believed to be due to intermittent pairing or subharmonic resonances. That is, if shedding is precise and uniform, then we would obtain subharmonic frequency (15Hz instead of 18.2 Hz) due to pairing. Petersen and Samet (1988) examined pure jet flow and obtained subharmonic resonances.

Transition Regions I-II (Figure 18b), II-III (Figure 18d) and III-IV (Figure 18j)

In these transition regions a common characteristic is the broad-band spectrum. The velocity fluctuating signal is very weak in these regions as can be seen in Figures 18b,d,and j. The spectra associated with these velocity fluctuations is not caused by electronic noise. If the experimental conditions are extremely well adjusted, without any external disturbances, and carefully maintained (the transition region is very narrow); we believe there would be no vortex shedding (thus, no frequency spectrum). Because of the sensitivity of these transition regions to small disturbances, the flow will tend to oscillate - ever so slightly - between its two neighboring regions. Thus we conclude the broad band spectra is due to vortical structural changes which occurs between Types I and II, II and III, and III and IV.

CONCLUSIONS

For the configuration considered in this study - 2-D slot burner - there are four different regions of vortical shedding observed. These regions are

separated from each other by transitional regions in which there is no vortical shedding.

We ascribe the different regions of vortical shedding (Types I, II, III, and IV) to the interaction between the inner and outer recirculating zones.

We observed a region (a portion of Type III) where the vortical structures were not orderly, but actually quasi-periodic with two independent frequencies.

In Type III the vortices crossed over from one side of the slot to the other side of the slot. This crossover phenomenon is associated with the rolling-up process of the vortices and the interaction between vortices on each side of the slot.

ACKNOWLEDGEMENTS

The authors wish to acknowledge Dr. W. M. Roquemore for suggesting an investigation of the 2-D slot burner. AFOSR supported this research through a grant with UES under contract # S 745 007 001. The authors wish to thank NSF under contract # NSF MSM - 8705062 for providing photographic equipment used in this study.

Thanks is also extended to Prof Richard S.L. Lee, Director of the Applied Mechanics Institute, National Taiwan University for his hospitality.

REFERENCES

Batchelor, G.K., An Introduction to Fluid Dynamics, Cambridge University Press, 1967.

Beavers, G.S. and Wilson, T.A., Vortex Growth in Jets, Journal of Fluid Mechanics, v.44, 1970.

Beer, J.M. and Chigier, N.A. Combustion Aerodynamics, Robert Krieger Publishing Co., 1983.

Boyson, F., Ayers, W.H., Swithenbank, J., and Pan, Z., Three Dimensional Model of Spray Combustion in Gas Turbine Combustors, AIAA, Paper No. 81-0324, 1981.

Corcos, G.M. and Sherman, F.S., The mixing layer : deterministic models of a turbulent flow. Part 1. Introduction and the two-dimensional flow, Journal of flow mechanics, v.139, 1984.

Curry, J.H., Herring, J.R., Loncaric, J. and Orszag, S.A., Order and Disorder in Two and Three- Dimensional Benard Convection, Journal of Fluid Mechanics, v. 147, 1984.

Dabiri, A.D., Daily, J.W., Chaotic Analysis of a Two-Stream Plane Mixing Layer, AIAA, 87-0223, 1987.

Deem, G.S. and Zabusky, N.J. Solitons in Action (ed. Lonngre and Scott), Academic, 1978.

Eaton, B.E., Analysis of Laminar Vortex Shedding Behind a Circular Cylinder by Computer Aided Flow Visualization, Journal of Fluid Mechanics, v.180, 1987.

Fenstermacher, P.R., Swinney, H.L. and Gollub, J.P., Dynamical Instabilities and the Transition to Chaotic Vortex Flow, Journal of Fluid Mechanics, v.94, 1979.

Kimoto, K., Shiraishi, I., and Matsumoto, R., Structure of Turbulent Jet Flames Stabilized in Annular Air Jet, Combustion Science and Technology, vol.25, 1981.

Lefebvre, A.H., Gas Turbine Combustion, Hemisphere Publishing Corp., 1983.

Li, X., and Tankin, R.S., A Study of Cold and Combusting Flow Around Bluff-Body Combustors, Combustion Science and Technology, v. 52, 1987.

Namazian, M., and Kelly, J., Flow and Combustion in Bluff-Body Stabilized Flames, Combustion Institute, San Antonio, Texas, 1987.

Perry, A.E., Chong, M.S. and Lim, T.T., The Vortex-Shedding Process Behind Two Dimensional Bluff-Bodies, Journal of Fluid Mechanics, v.116 1982.

Perry, A.E., and Steiner, T.R. Large Scale Vortex Structures in Turbulent Wakes Behind Bluff-Bodies, Journal of Fluid Mechanics, v. 174, 1987.

Petersen, R.A. and Samet, M.M., On the Preferred Mode of Jet Instability, Journal of Fluid Mechanics, v. 194, 1988.

Pierrehumbert, R.T., A Family of steady translating vortex pairs with distributed vorticity, Journal of Fluid Mechanics, v.99, 1980.

Rockwell, D.O. and Niccolls, W.O., Natural Breakdown of Planar Jets, Trans. ASME, Journal of Basic Engineering, v. 94, 1972.

Roquemore, W.M., Bradley, R.P., Stutrud, J.S., Reeves, C.M. and Britton, R.L., Influence of Vortex Shedding Process on a Bluff-Body Diffusion Flame, AIAA, 83- 0335, 1983.

Roquemore, W.M., Tankin, R.S., Chiu, H.H. and Lottes, S.A., The Role of Vortex Shedding in a Bluff-Body Combustor, Symposium on Experiments and Techniques in Turbulent and Non-Reactive Flows, ASME 105th Winter Annual Meeting, 1984.

Sato, H., The stability and transition of a two-dimensional jet, Journal of Fluid Mechanics, v. 7, 1960.

Sato, H. and Sakao, F., A Two-Dimensional Jet at Low Reynolds Numbers, Journal of Fluid Mechanics, v. 20, 1964.

Scott, J.M. and Hankey, W.K., Numerical Simulation of Cold Flow in an Axisymmetric Centerbody Combustor.

Stambuleanu, A., Flame Combustion Processes in Industry, Abacus Press, 1976.

Sreenivasan, K.R., Transition and Turbulence in Fluid Flows and Low Dimensional Chaos, Frontiers in Fluid Mechanics, 1985.

Tankin, R.S. Visualization, Velocity and Frequency Measurements of a Two-Dimensional Jet, UES Report, 1987.

Thomas, F.O. and Goldschmidt, V.W., Structural Characteristics of a Developing Turbulent Planar Jet, Journal of Fluid Mechanics, v. 163, 1986.

Williamson, C.H.K., Defining a Universal and Continuous Strouhal-Reynolds Number Relationship for the Laminar Vortex Shedding of a Circular Cylinder, Physics of Fluids, vol. 31, 1988.

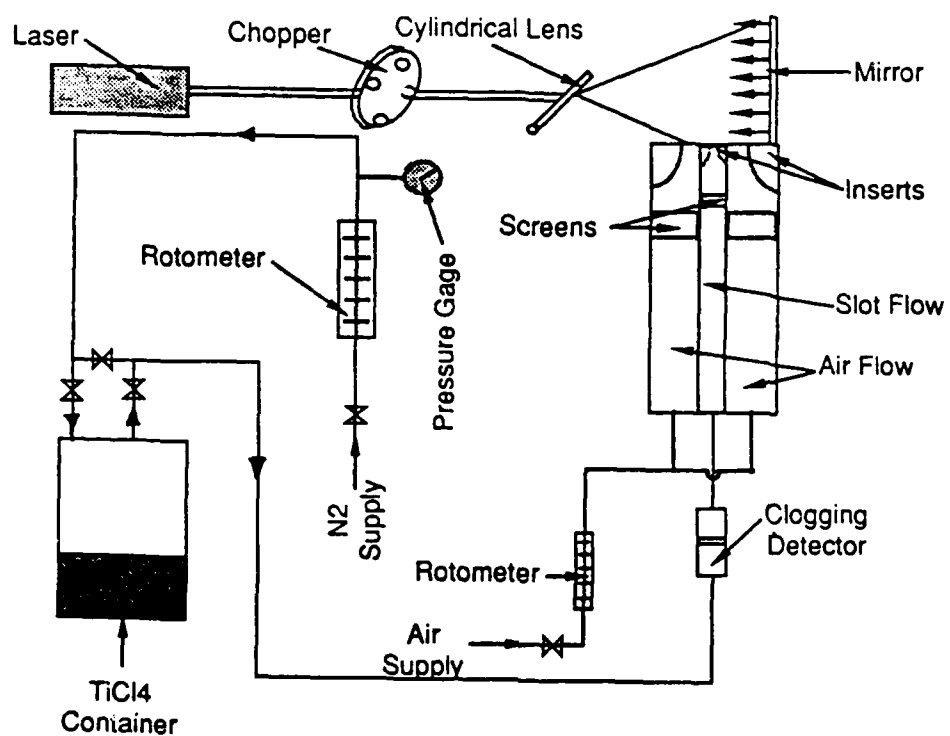


Figure 1 Schematic diagram of the experimental setup.

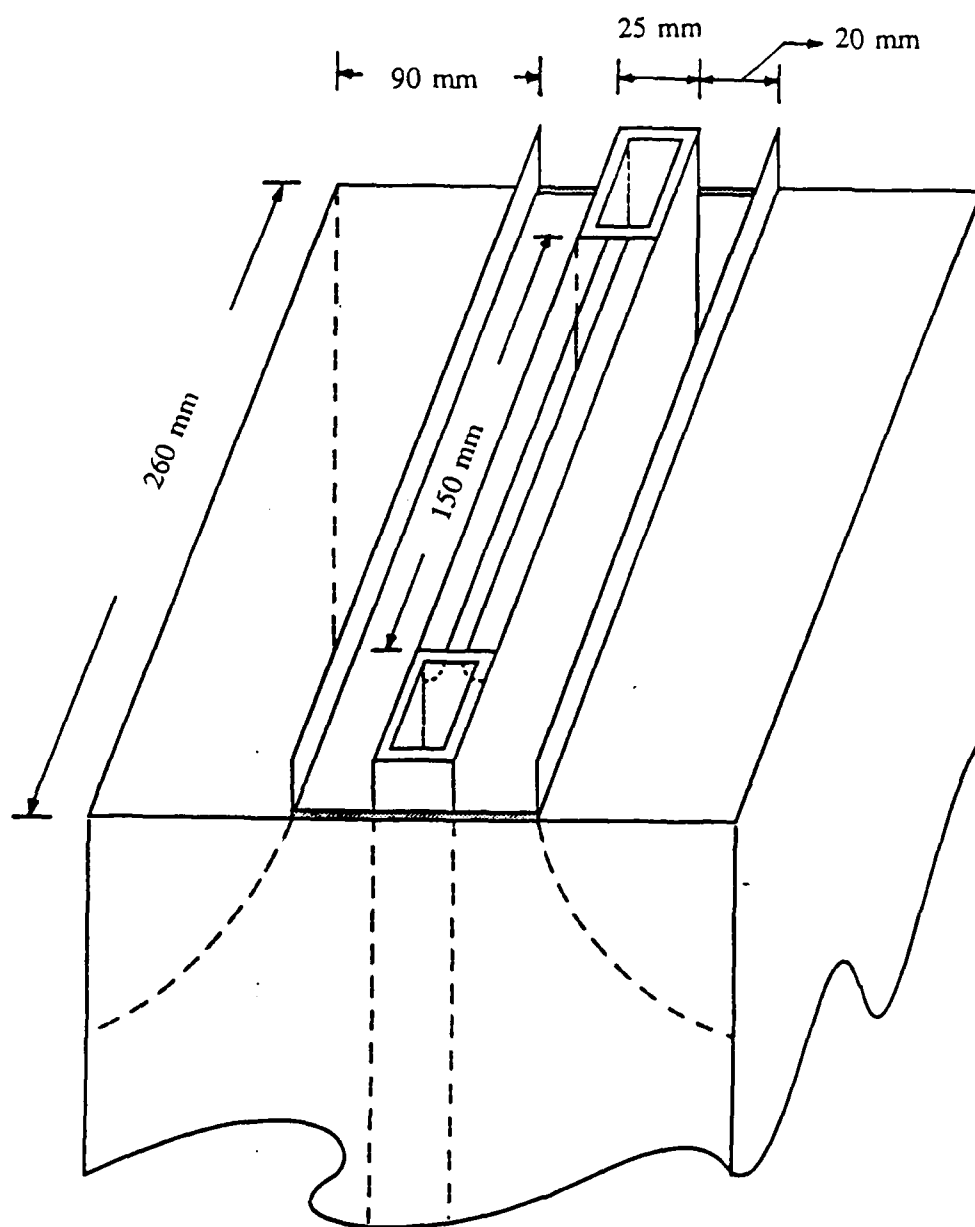


Figure 2 Schematic drawing of the slot burner (top view).

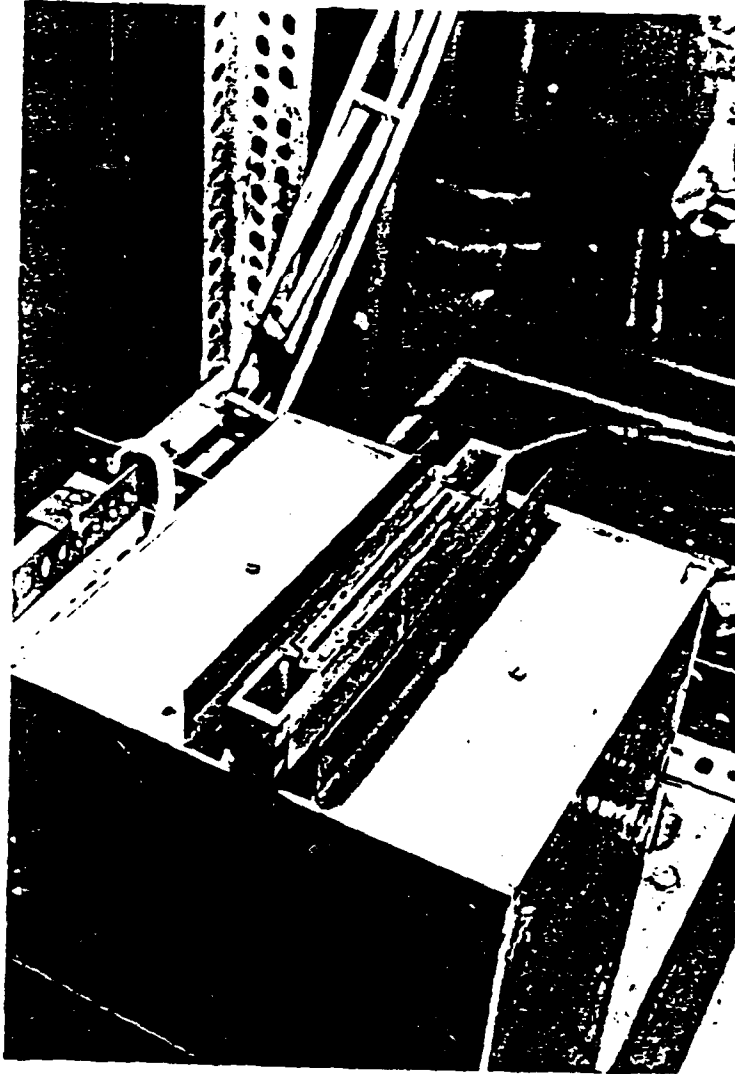
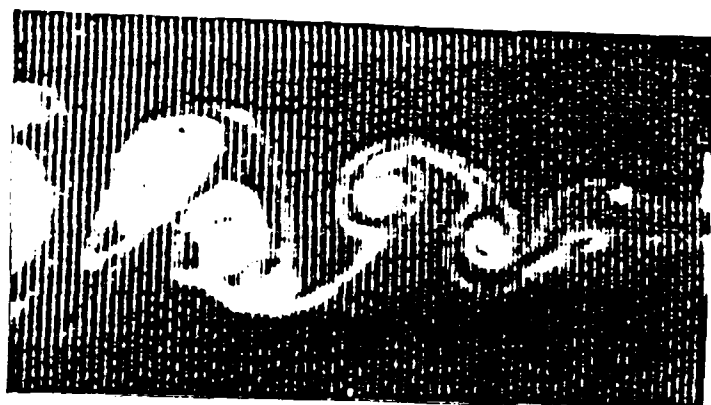
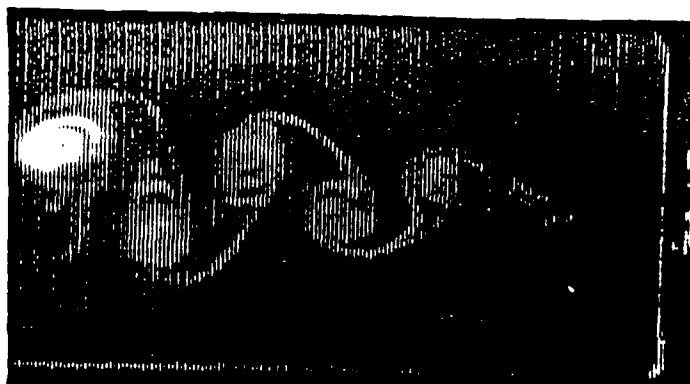


Figure 3 Photograph of the slot burner.



(a) from regular 35 mm camera. (b) from high speed video camera. (c) from digital image processor.

Figure 4 Comparison of pictures taken from different photographic techniques.

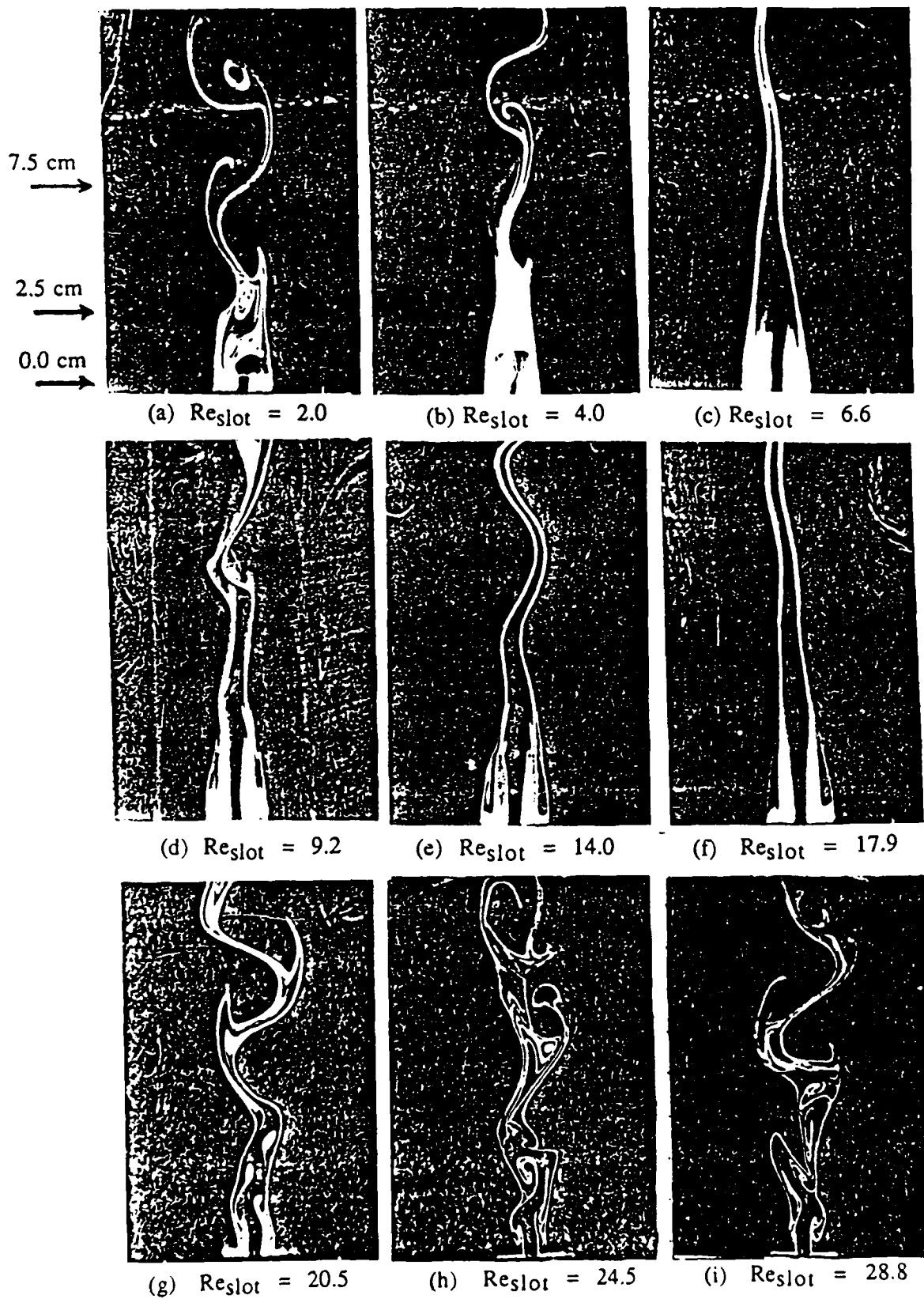


Figure 5 Photographs of vortical shedding structures for $D_{slot} = 0.45$ cm and $Re_{air} = 392$



(j) $Re_{slot} = 37.2$



(k) $Re_{slot} = 45.0$



(l) $Re_{slot} = 49.6$



(m) $Re_{slot} = 54.8$



(n) $Re_{slot} = 65.2$



(o) $Re_{slot} = 70.3$



(p) $Re_{slot} = 82.4$



(q) $Re_{slot} = 93.5$



(r) $Re_{slot} = 108.2$

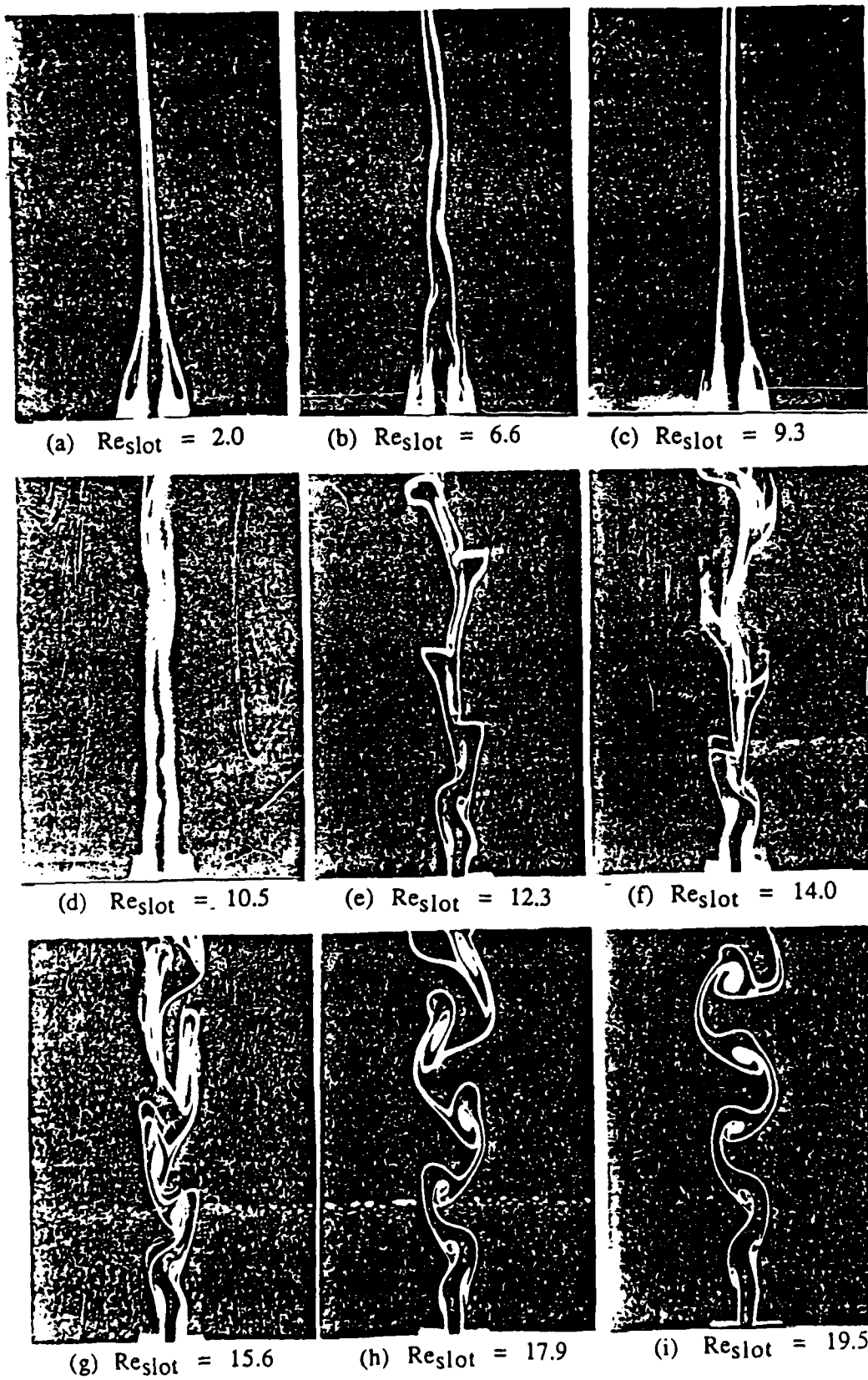


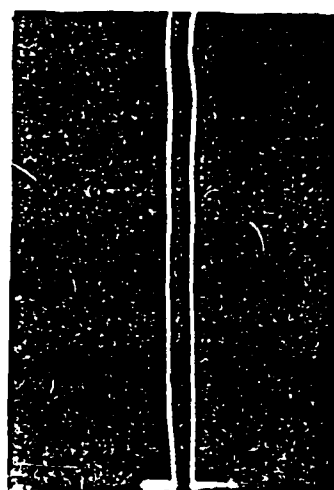
Figure 6 Photographs of vortical shedding structures for $D_{slot} = 0.45$ cm and $Re_{air} = 222$.



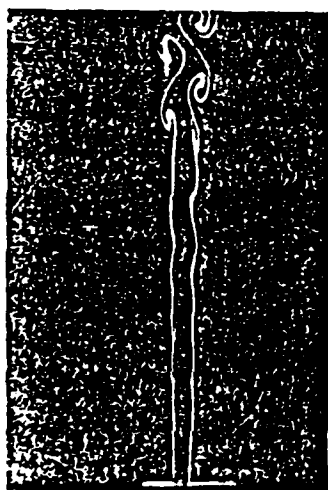
(j) $Re_{slot} = 20.5$



(k) $Re_{slot} = 22.0$



(l) $Re_{slot} = 28.8$



(m) $Re_{slot} = 37.2$



(n) $Re_{slot} = 54.8$



(o) $Re_{slot} = 82.4$

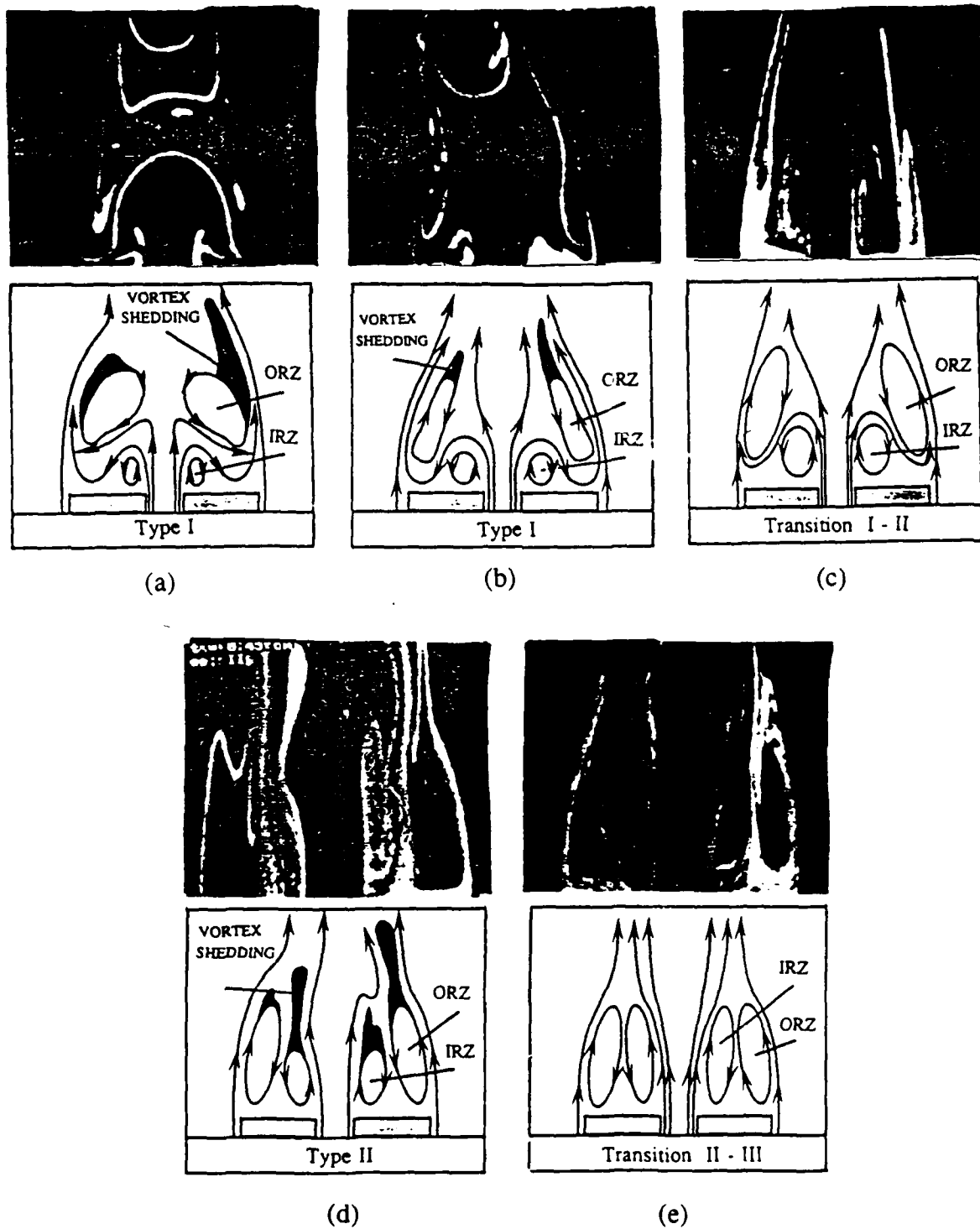
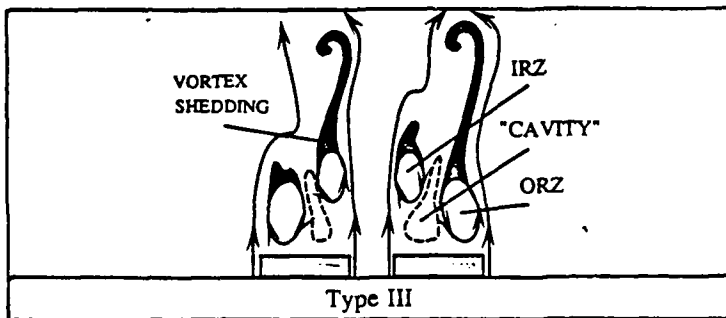
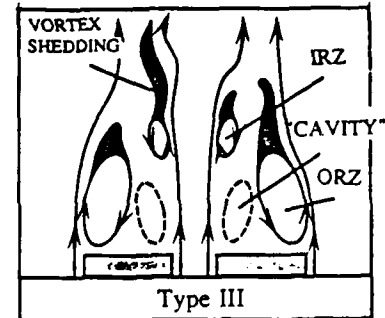


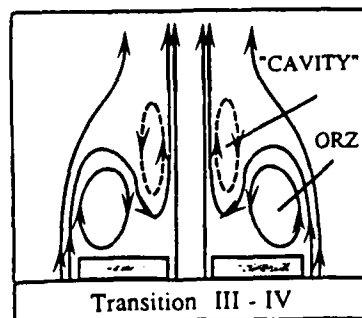
Figure 7 Structures of recirculating zones for various types of vortical shedding (photographs and schematic drawings).



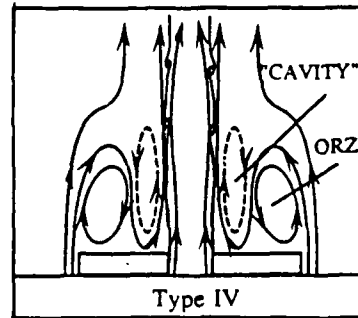
(f)



(g)



(h)



(i)

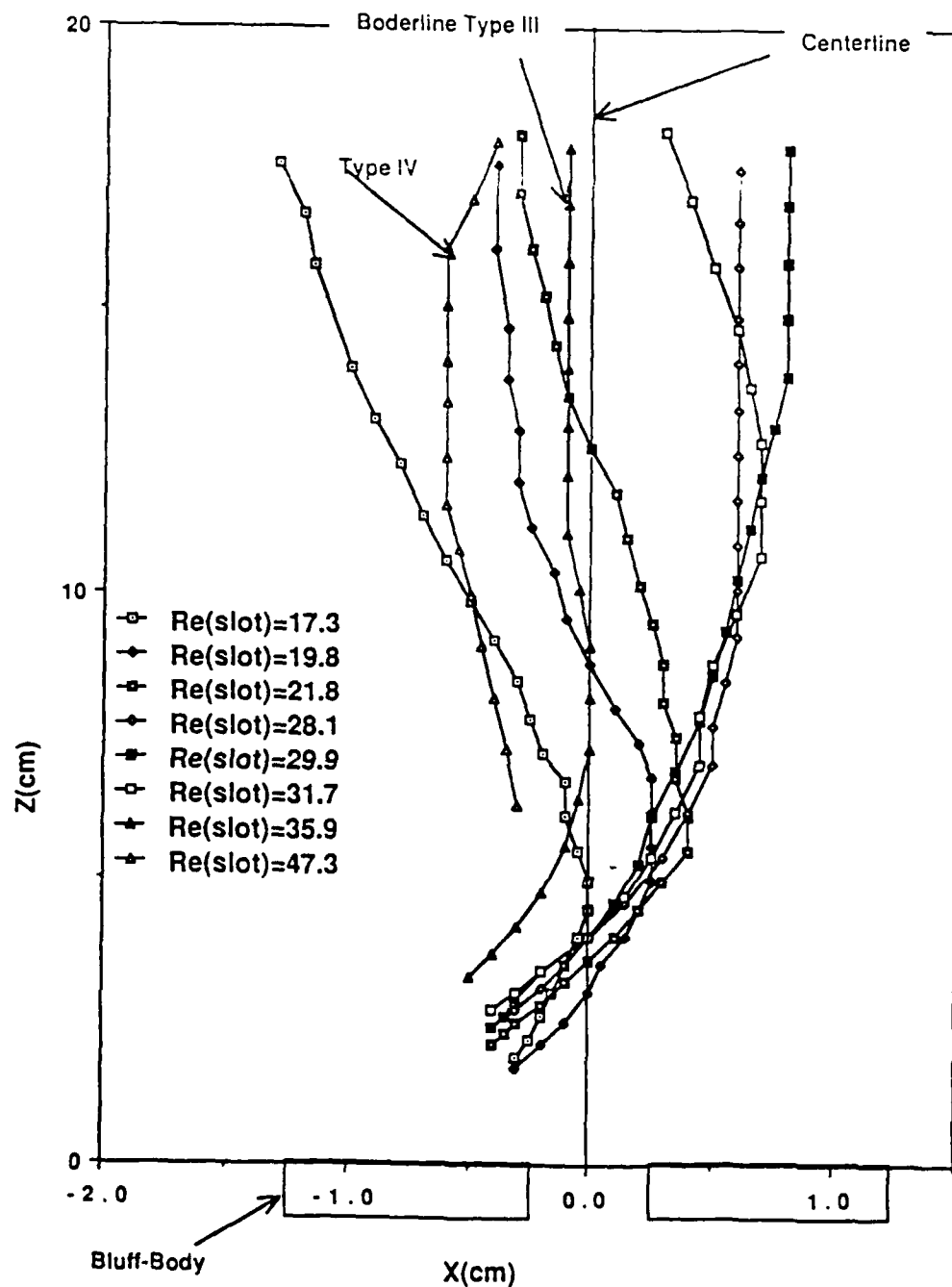


Figure 8 Trajectories of a single vortex for different values of Re_{slot} ($D_{slot} = 0.45 \text{ cm}$ and $Re_{air} = 264$).

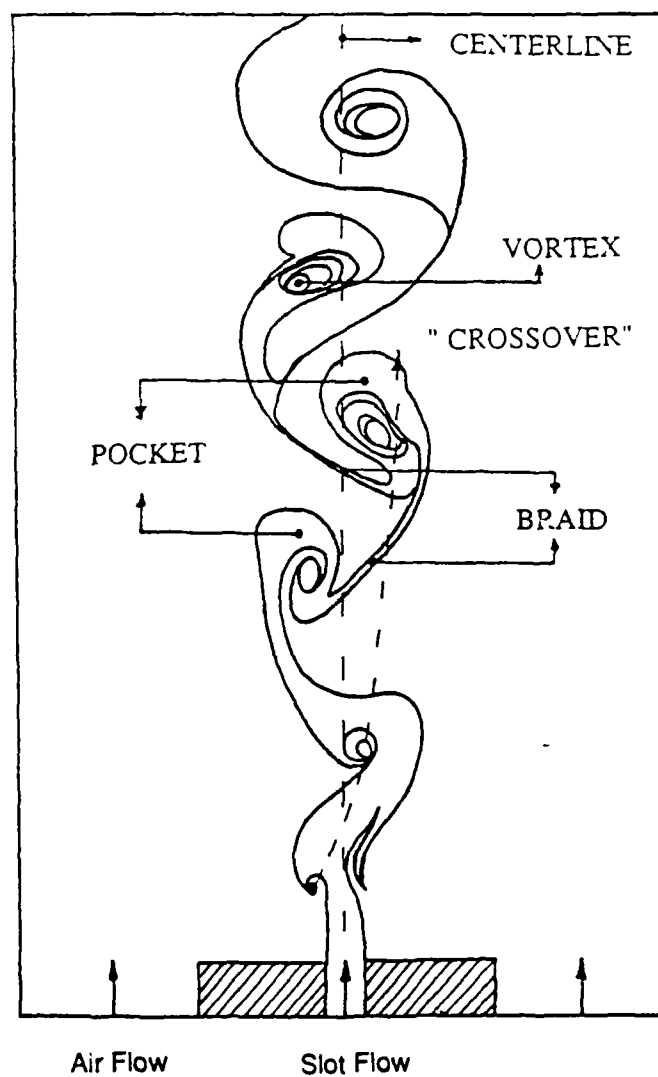


Figure 9 Schematic drawing of vortical shedding structure

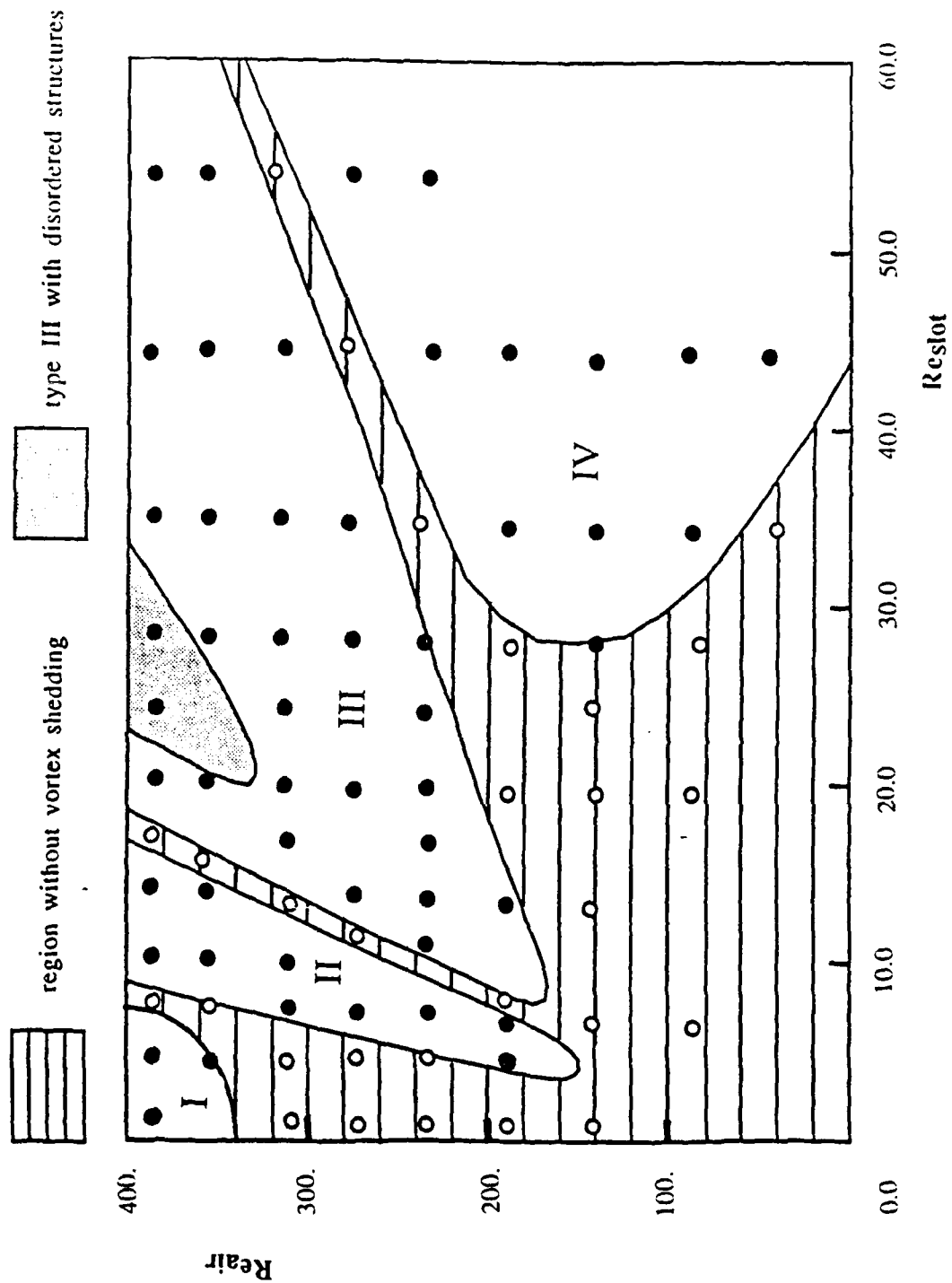


Figure 10 Flow map for $D_{slot} = 0.45$ cm.

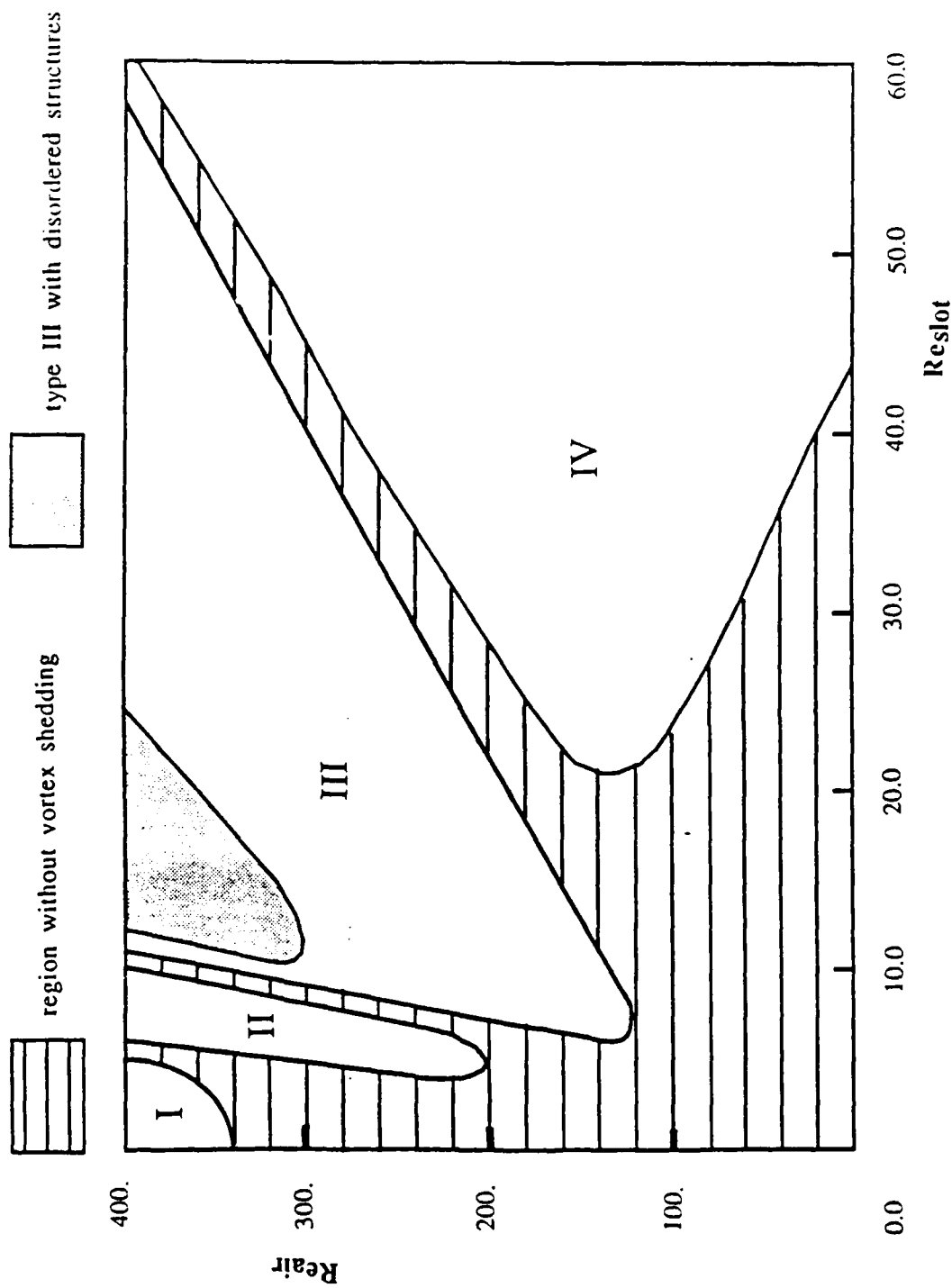


Figure 11 Flow map for $D_{slot} = 0.25$ cm.

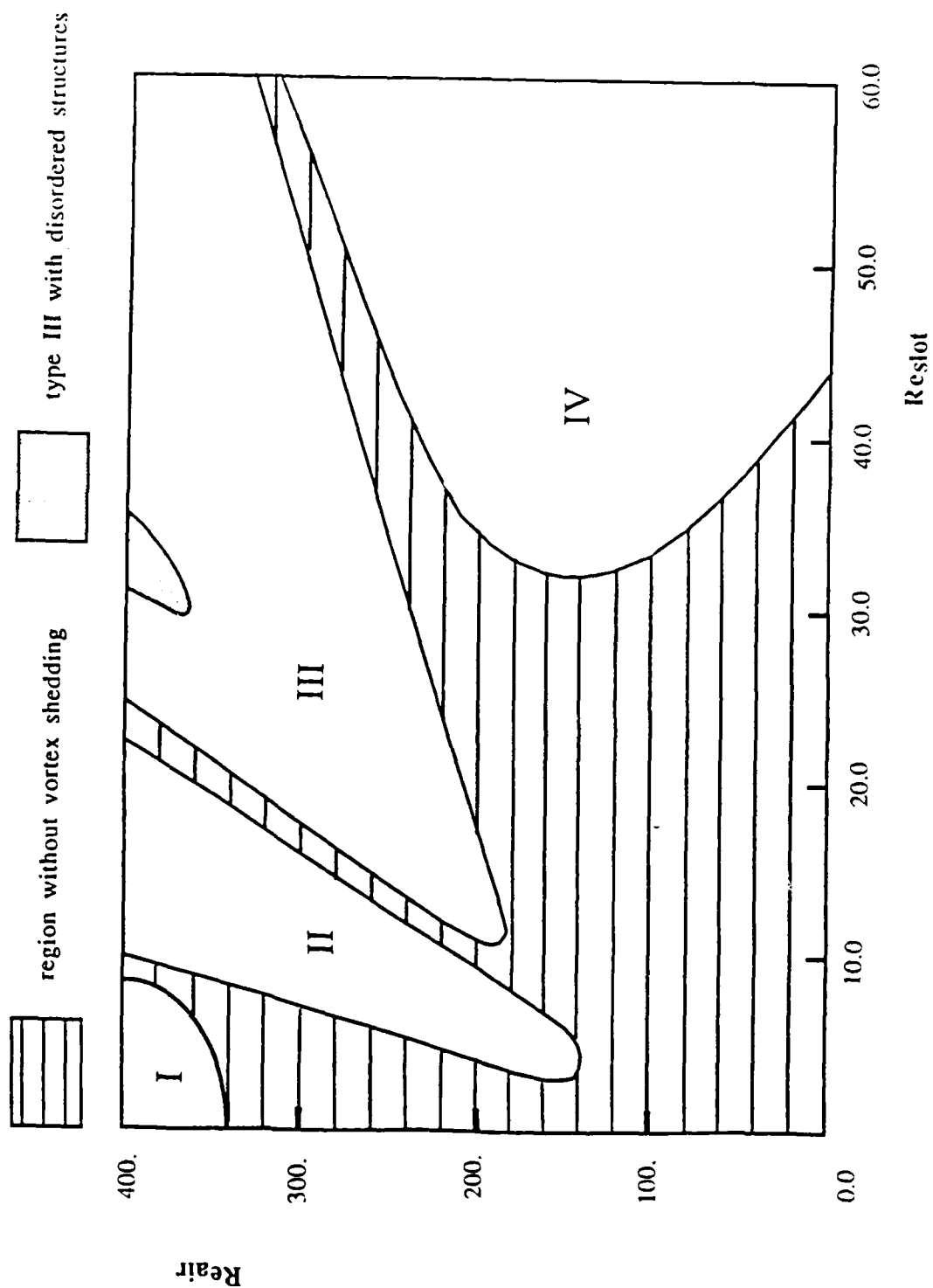


Figure 12 Flow map for $D_{slot} = 0.60$ cm.

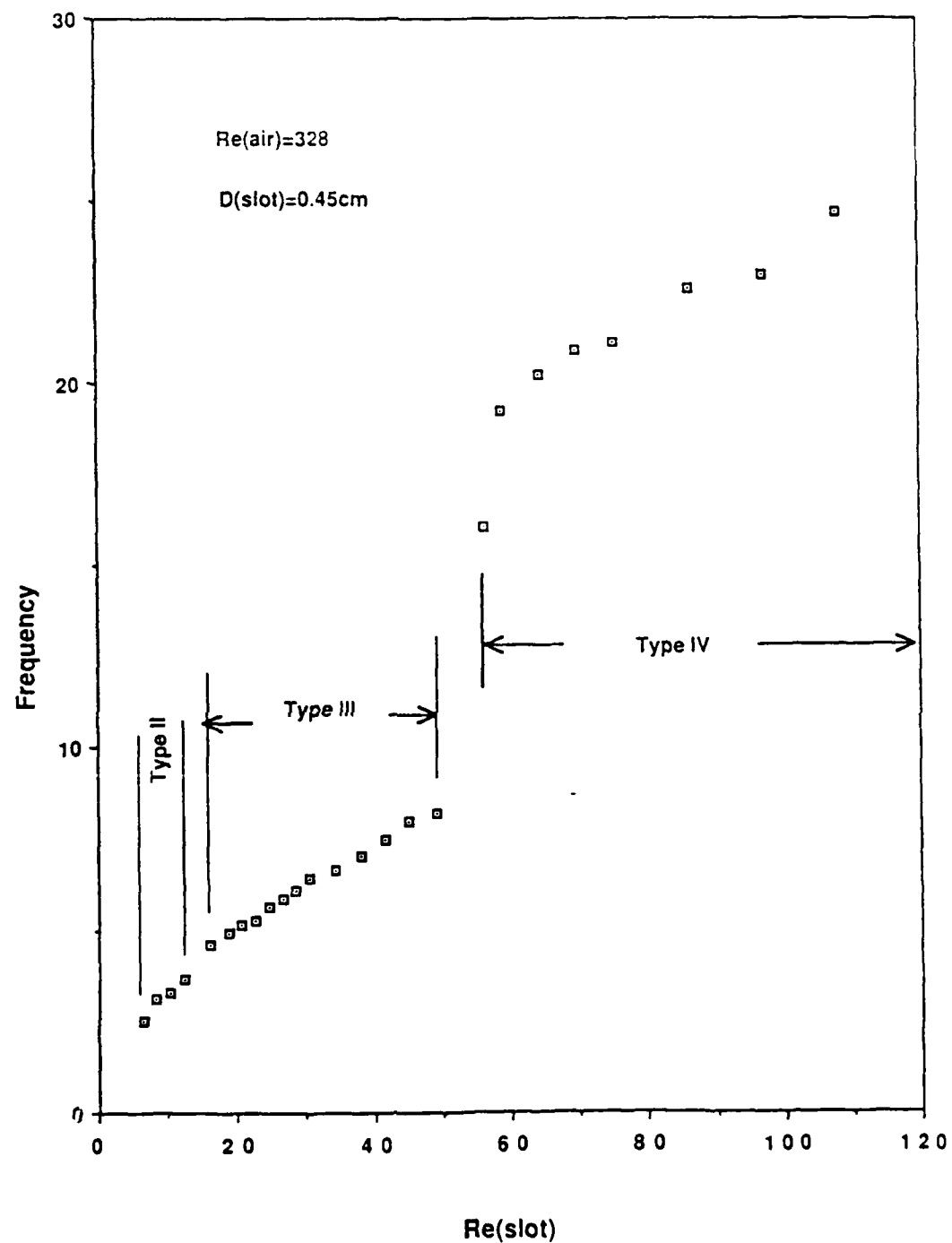


Figure 13(a) Shedding frequency of vortex vs. Re_{slot} ($D_{slot} = 0.45$ cm and $Re_{air} = 328$).

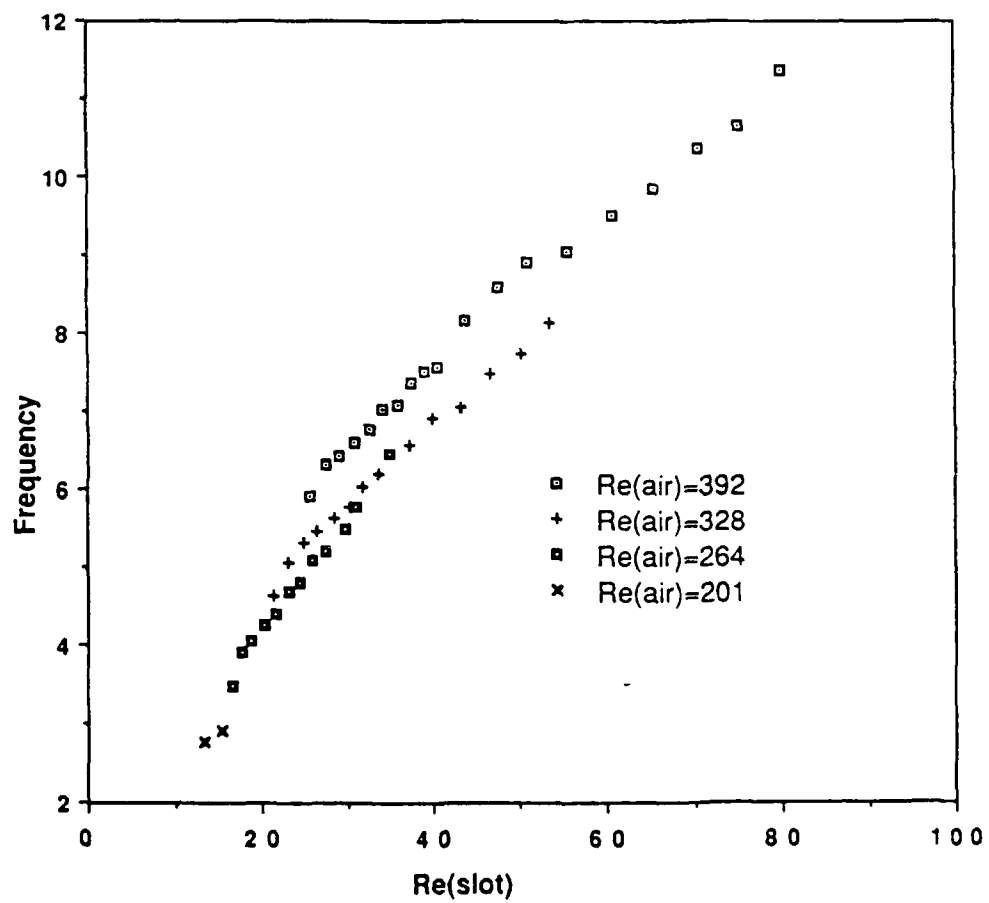


Figure 13(b) The effect of Re_{air} on the shedding frequency
 ($D_{slot} = 0.60$ cm).

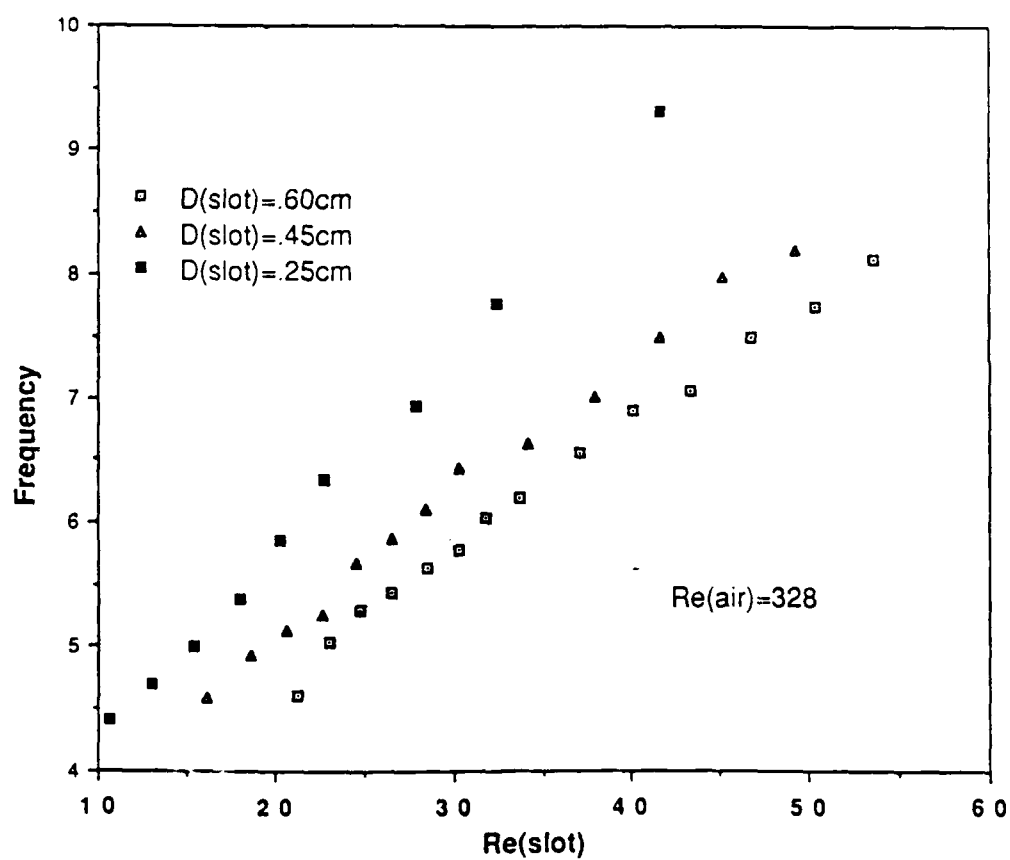


Figure 13(c) The effect of D_{slot} on the shedding frequency
 ($Re_{\text{air}} = 328$).

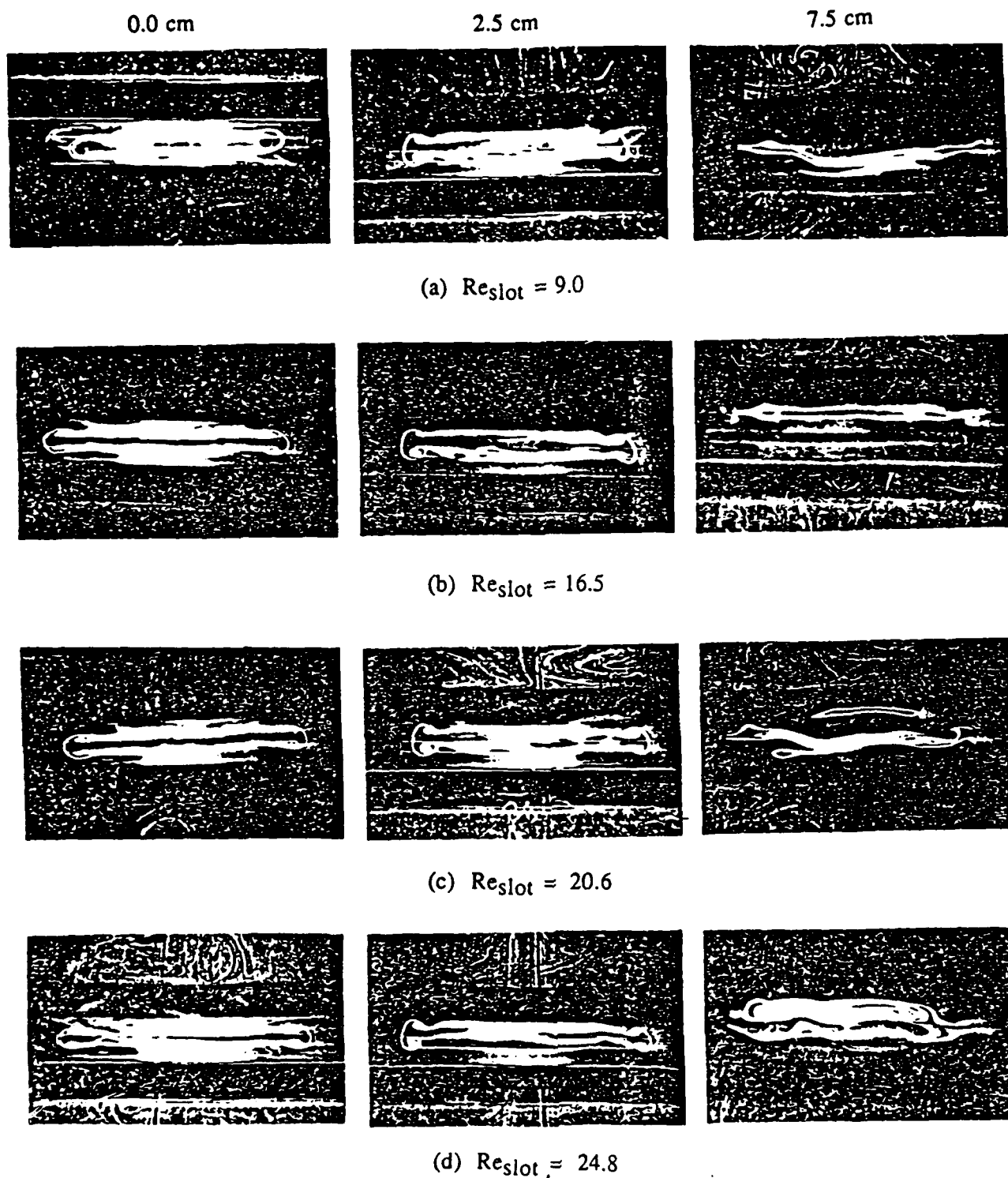
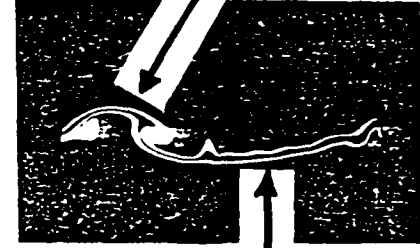
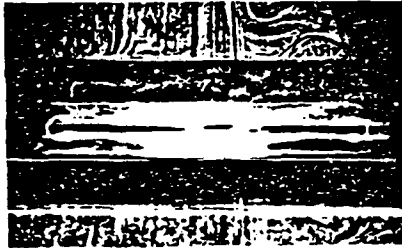


Figure 14. Photographs of horizontally sheet-lighted flow
 ($D_{slot}=0.45$ cm, $Re_{air}=307$).



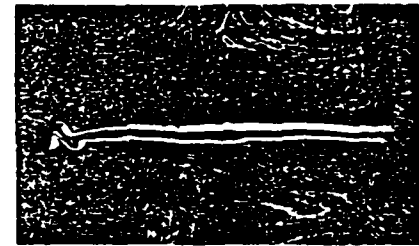
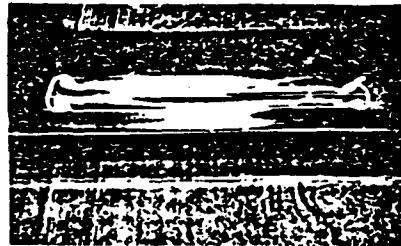
(e) $Re_{slot} = 30$

curvature due to
disturbance from end

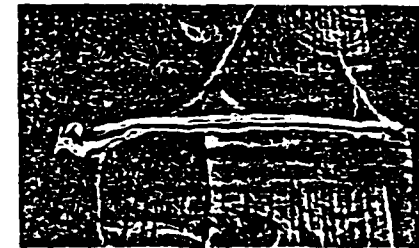
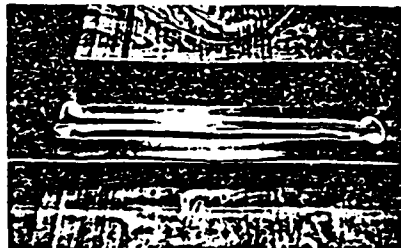
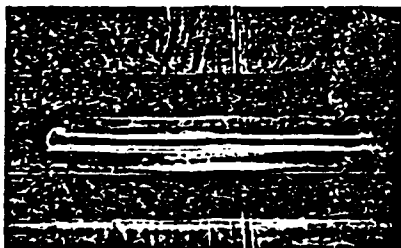


(f) $Re_{slot} = 35.5$

curvature due to
oblique shedding



(g) $Re_{slot} = 40.2$



(h) $Re_{slot} = 45.0$

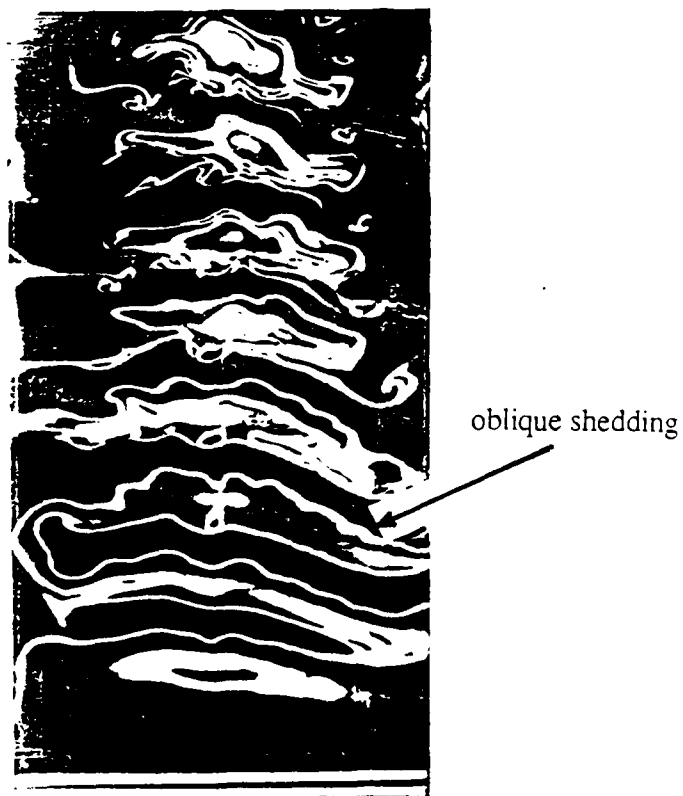
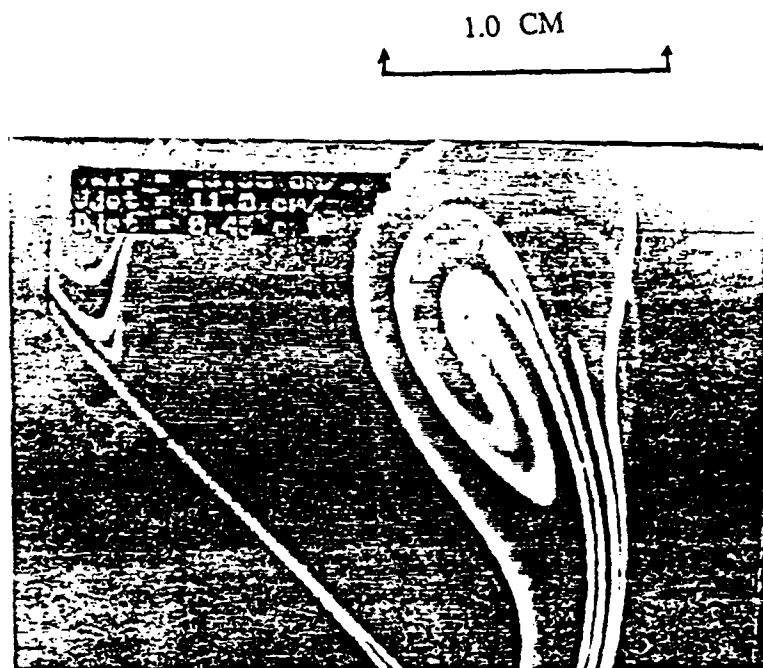
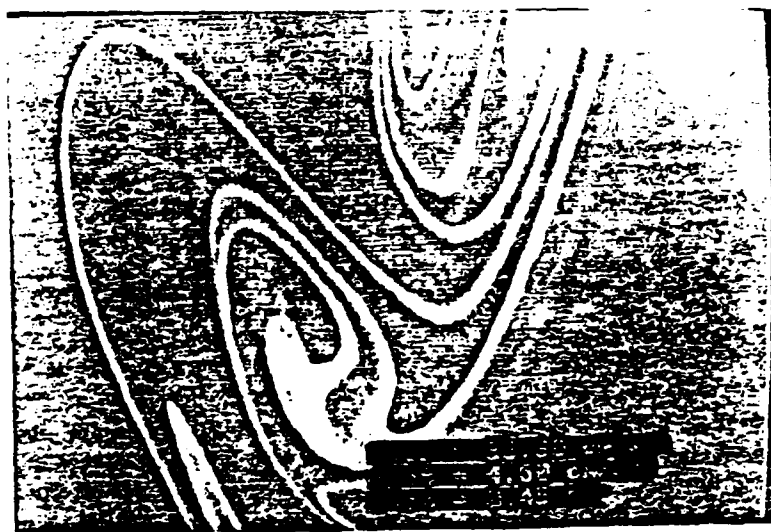


Figure 15 Photograph of vertically sheet-lighted flow. ($D_{\text{slot}} = 0.45$ cm,
 $Re_{\text{air}} = 328$, $Re_{\text{slot}} = 34.0$)



(a)



(b)

Figure 16 Enlarged images of vortical structures taken with Digital Image Processor.

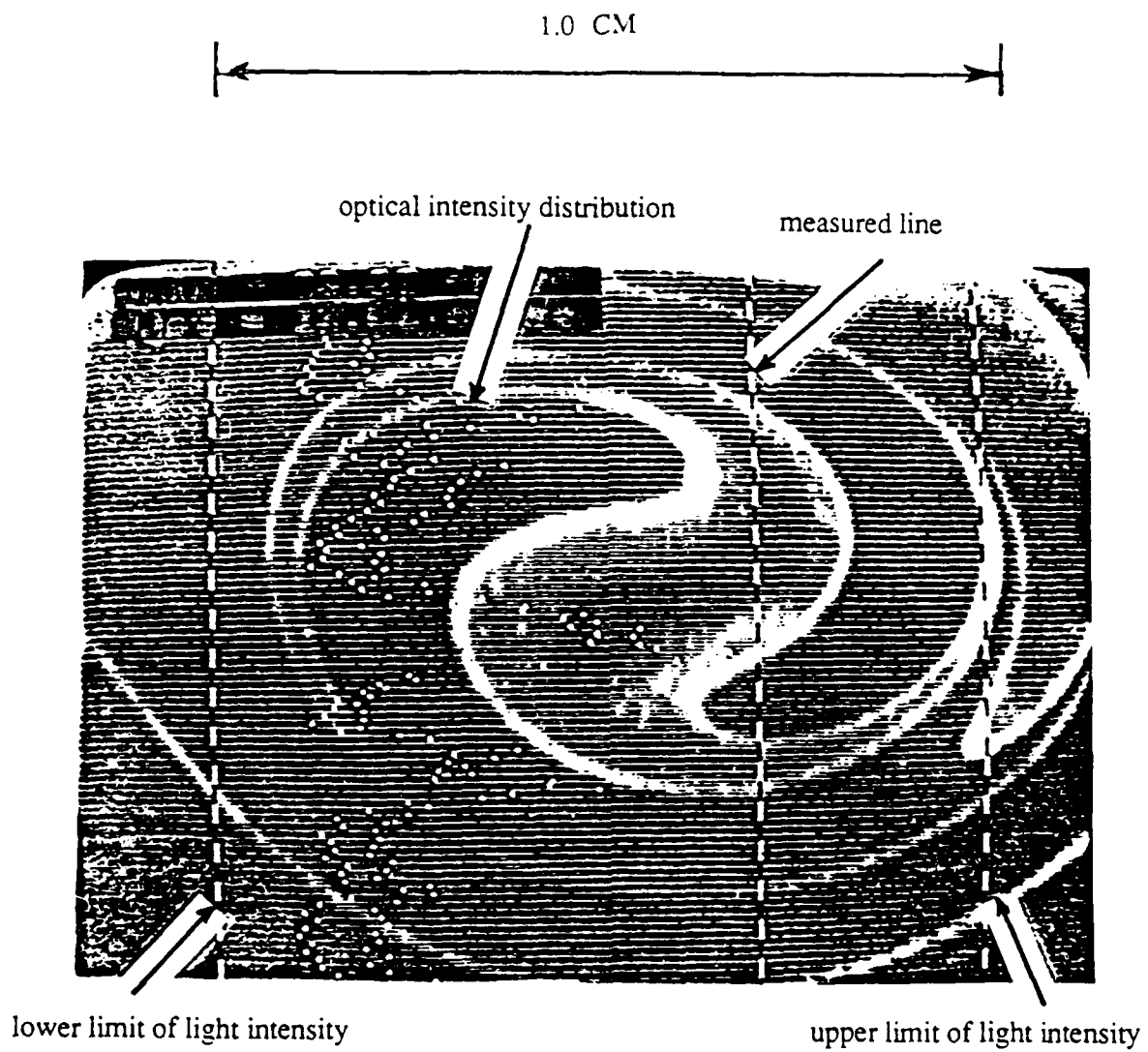
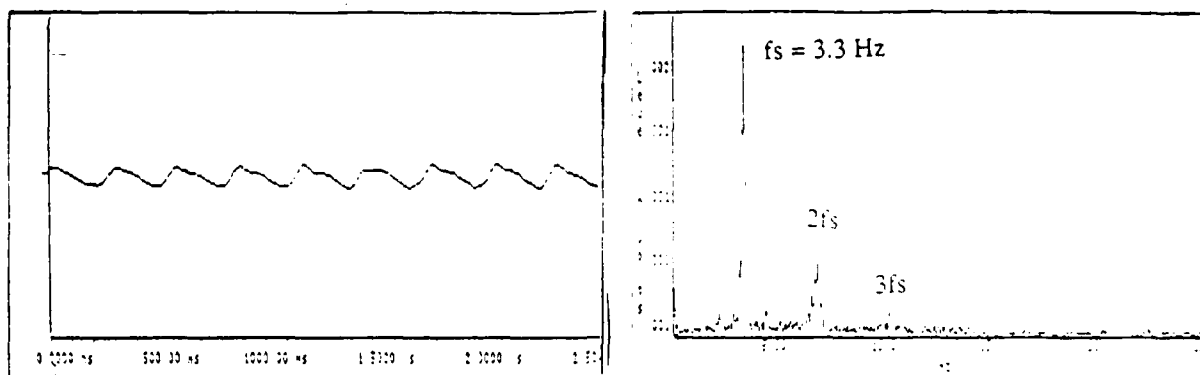
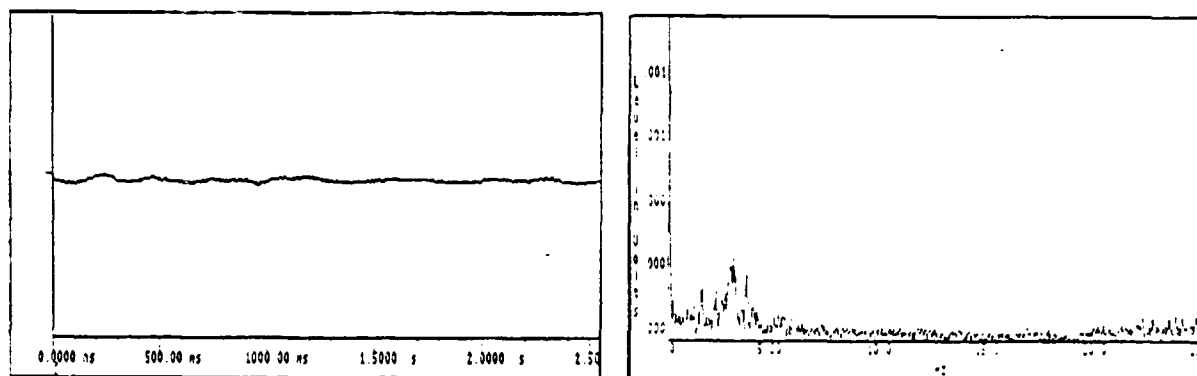


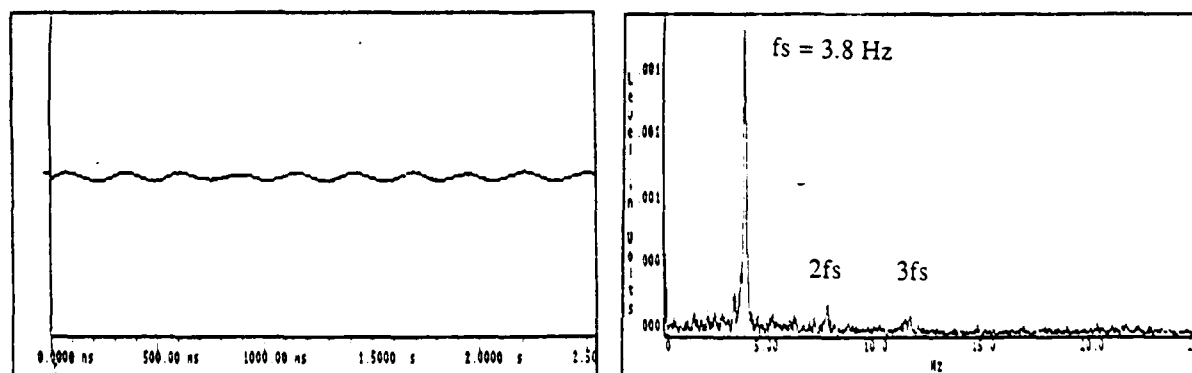
Figure 17 Digital image of vortical structures with vertical distribution of light intensity measured along central dotted line.



(a) $Re_{slot} = 3.6$



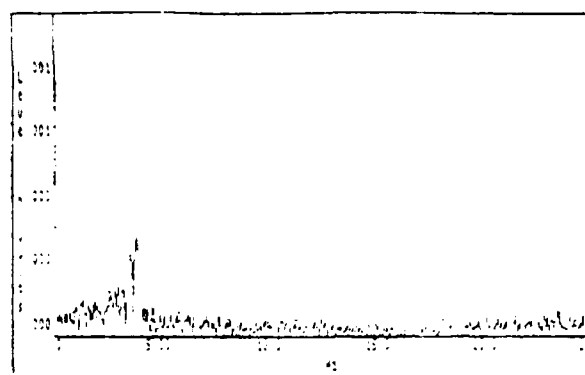
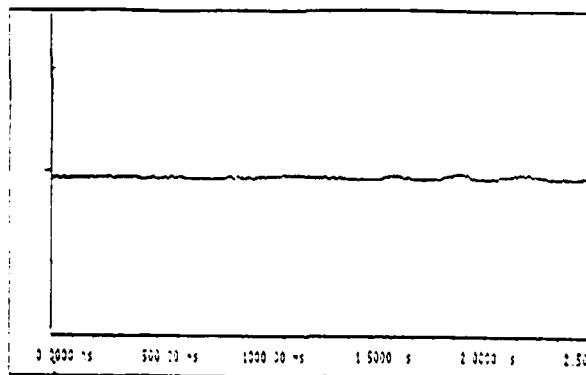
(b) $Re_{slot} = 6.6$



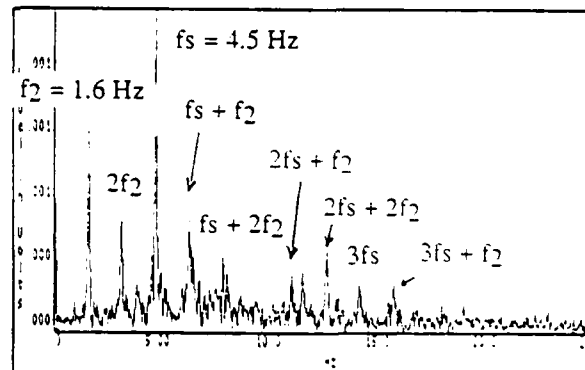
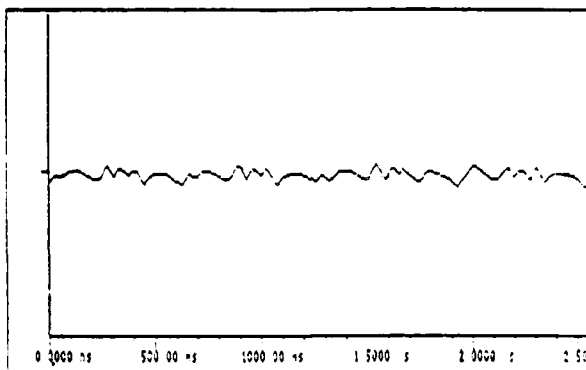
(c) $Re_{slot} = 11.2$

Figure 18 Frequency spectra of streamwise velocity fluctuations.

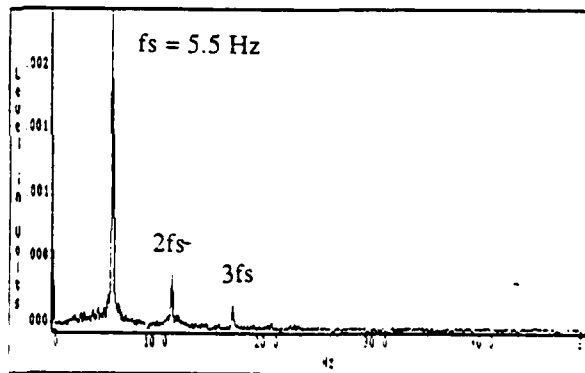
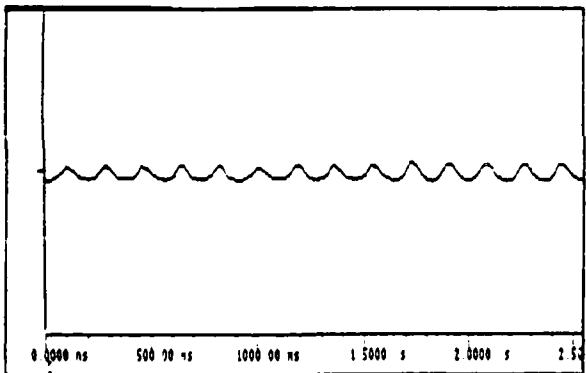
($Re_{air} = 392$ and $D_{slot} = 0.45$ cm)



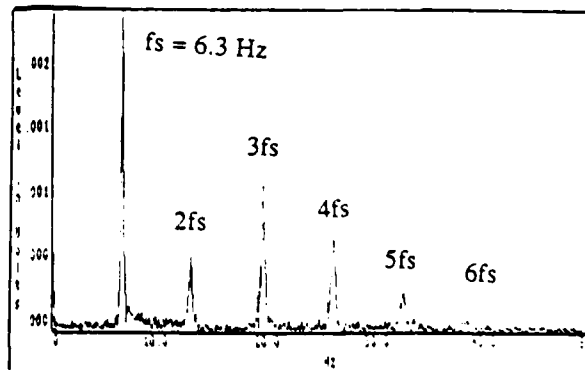
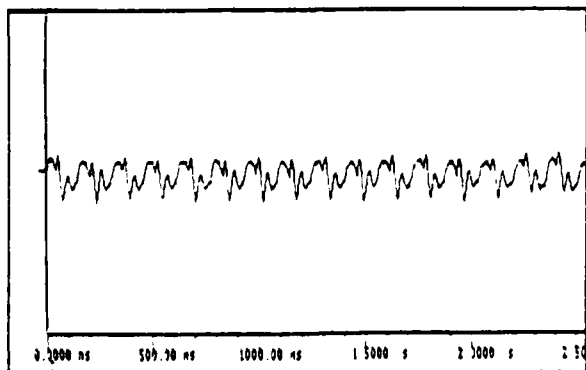
(d) Reslot = 17.9



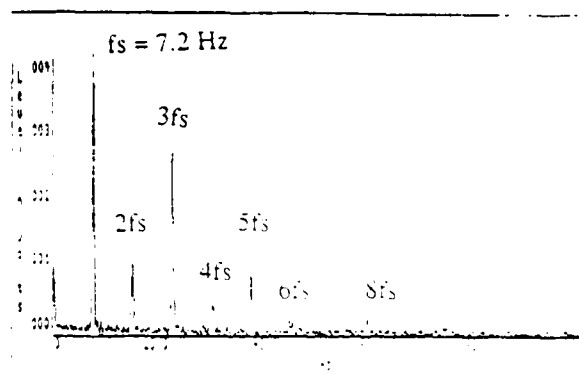
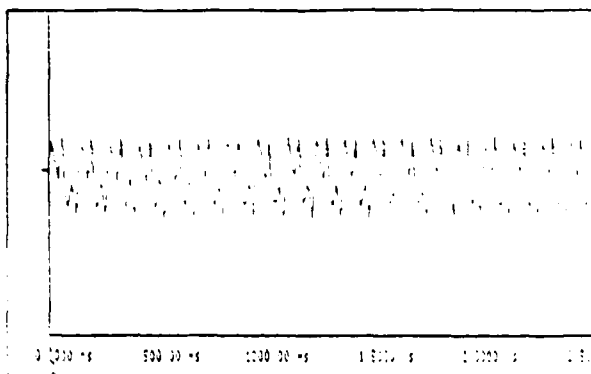
(e) Reslot = 28.8



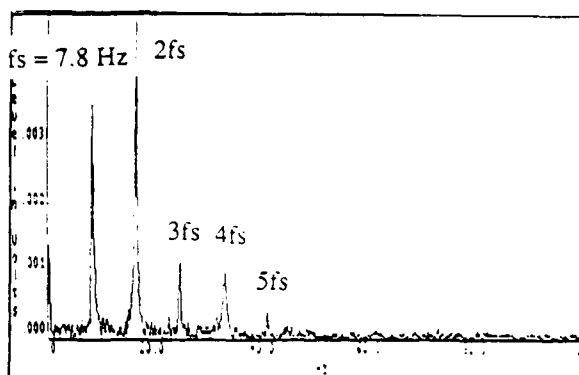
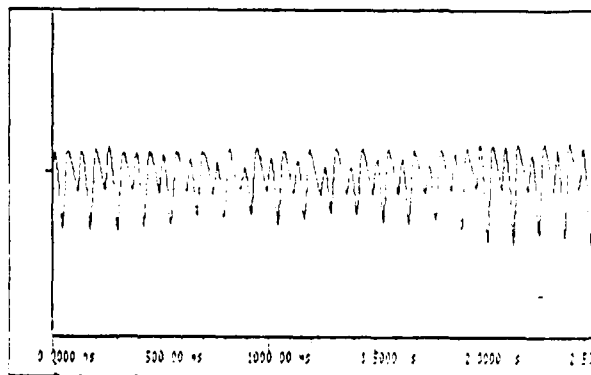
(f) Reslot = 36.0



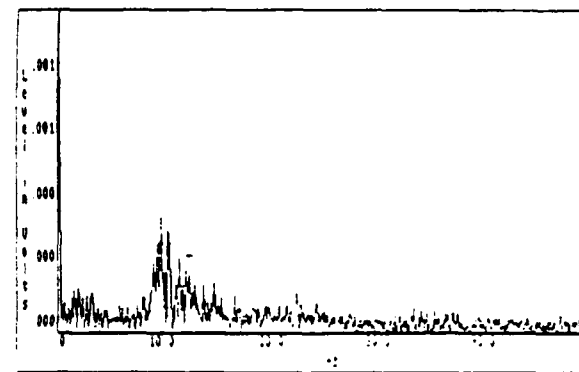
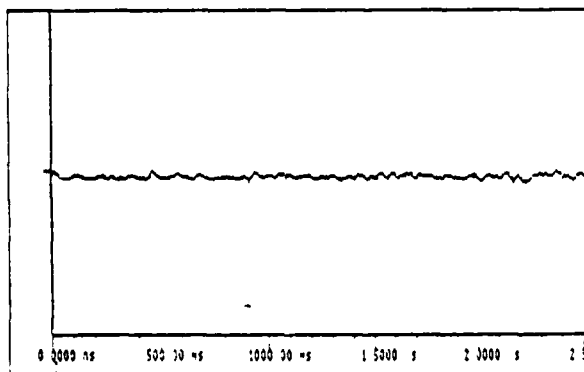
(g) Reslot = 42.2



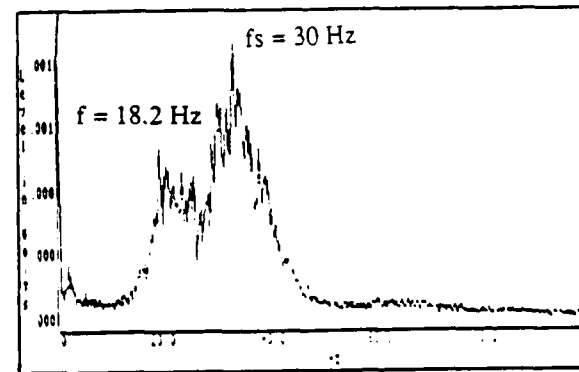
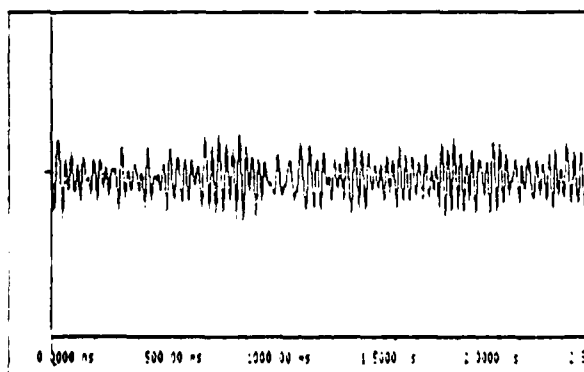
(h) Reslot = 49.6



(i) Reslot = 54.8



(j) Reslot = 65.2



(k) Reslot = 108.2

Table I Summary on the classification of vortical structures.

structure type	I.R.Z.		O.R.Z.		Cavity
	stability	size	stability	size	
type I	stable	small	unstable	large	
transition state I-II	stable	small	stable	large	
type II	unstable	small	unstable	large	
transition state II-III	stable	equal	stable	equal	
type III	unstable (lifted)		unstable		present
transition state III-IV	absent		stable		present
type IV	absent		stable		present

Table II Critical values of Re number for various types of vortical structures.			
D_{slot} type	0.25 cm	0.45 cm	0.60 cm
type I	$R > 82$	$R > 56$	$R > 44$
	$Re_{air} > 330$		
type II	$37.5 < R < 82$	$21.9 < R < 56$	$17.3 < R < 44$
	$Re_{slot} > 2.6$	$Re_{slot} > 3.0$	$Re_{slot} > 3.3$
	$Re_{air} > 190$	$Re_{air} > 153$	$Re_{air} > 136$
type III	$5.6 + 75/Re_{slot} < R < 37.5$	$4 + 117/Re_{slot} < R < 21.9$	$3.6 + 129/Re_{slot} < R < 17.3$
	$Re_{slot} > 6.3$	$Re_{slot} > 8.5$	$Re_{slot} > 11.8$
	$Re_{air} > 128$	$Re_{air} > 161$	$Re_{air} > 186$
type III'	$9 + 166/Re_{slot} < R < 30.5$	$6.8 + 173/Re_{slot} < R < 17.5$	$5.5 + 186/Re_{slot} < R < 12.6$
	$Re_{slot} > 10.6$	$Re_{slot} > 20.8$	$Re_{slot} > 31.0$
	$Re_{air} > 289$	$Re_{air} > 330$	$Re_{air} > 374$
type IV	$R < 5.6 + 75/Re_{slot}$	$R < 4.0 + 117/Re_{slot}$	$R < 3.6 + 129/Re_{slot}$
	$Re_{slot} > 20.8$	$Re_{slot} > 28.0$	$Re_{slot} > 33.0$
Note	$R = Re_{air} / Re_{slot}$		

FINAL REPORT

Submitted to: Universal Energy Systems, Inc.

Principal Investigator: Dr. Cheng-Hsiao Wu *Cheng-Hsiao Wu*
Department of Electrical Engineering
University of Missouri-Rolla
Rolla, MO 65401
Tel 314-341-4677

Title of Research: Calculations of Interface-State Occupation
Function and GaAs/Ge Heterostructure Solar
Cell Efficiency

Period: December 1, 1987 to November 30, 1988

Contract Number 760-7MG-093

FINAL REPORT on

Calculations of Interface-State Occupation Function and GaAs/Ge Heterostructure Solar Cell Efficiency

SUMMARY and ABSTRACT

In the course of performing the research under this grant, we have enlarged our earlier research under the sponsorship of 1987 USAF-UES Summer Faculty Research Program and subsequently published the results (J. N. Bullock, C. H. Wu, J. F. Wise, "Interface Contribution to GaAs/Ge Heterojunction Solar Cell Efficiency," in IEEE Transactions on Electron Devices , 1238-1243, July 1989). We have also made calculations on interface-state occupation function. Part of this result has been presented (C. H. Wu, T. T. Huang and J. N. Bullock, "Theory of Non-equilibrium Heterojunction Interface-State Occupancy in Semiconductors," Bulletin of the American Physical Society, Vol. 34, No. 3, p. 1028, 1989) and the completed result is to be submitted for publication soon.

In our study, we have shown that in certain heterojunction interfaces, such as GaAs/Ge n-n heterojunction, interface states plays an important role in the performance of GaAs/Ge solar cell efficiency. The interface-state occupation function depends not only on local electrons and holes at the heterojunction but also on carriers within the diffusion length of the junction. Simmons-Taylor's theory of trap-state occupation function is modified to include the heterojunction interface and non-local carrier concentration effects. Our calculations of the interface-state occupancy for a n-n GaAs/Ge heterojunction show that equilibrium Fermi level is not shifted by V_1 , where V_1 is the potential across the Ge side when a total voltage of V is applied across the heterojunction. Thus, GaAs side also contributes to the Fermi level shift. Recombination rates for electrons and

holes are not equal at any position across the junction because carriers can tunnel into the interface. As a result, total current is not conserved at either side of the heterojunction.

Introduction:

In our earlier work, under the sponsorship of 1987 USAF-VES Summer Faculty Research Program, we have shown ⁽¹⁾ that the amount of interface charge present at GaAs/Ge heterojunction plays an important role in determining the GaAs/Ge solar cell efficiency. As we have pointed out, the more the interface charge, the better the solar cell efficiency until a limit is reached. However, we have assumed that interface charge is independent of the applied voltage. This points out the importance of studying the occupation function of interface trap-states in order to calculate the interface charges. The occupation function of heterojunction interface states under a non-equilibrium situation has not been investigated. In particular, as applied voltage is increased, an electron at a distance away from one side of the junction can tunnel via, or be captured by, interface states into the other side of the junction. This non-local effect causes the total current from the continuity equation to become non-conservative. Therefore, it is very important to know how the occupation function varies with applied voltage when this non-local effect is also included in the calculations in order to evaluate accurately the overall solar cell efficiency. In this report, we formulate the theory of heterojunction interface state occupation function and present the calculated results.

Theory of Heterojunction Interface-State Occupation Function:

A GaAs/Ge heterojunction under an applied voltage V is shown in Figure 1. The conduction and valence band discontinuities are ΔE_c and ΔE_v respectively. V_{b1} and V_{b2} are built-in voltages and V_1 and V_2 are applied voltages on Ge and GaAs sides respectively.

The interface states are illustrated by the short horizontal bars at the interface. At equilibrium, these interface states are filled up to the Fermi level, E_{f0} . When the heterojunction is under applied voltage V , the Fermi level on the GaAs side is shifted upward by voltage V_2 to E_{f2} and the Fermi level on the Ge side is shifted downward by voltage V_1 to E_{f1} so that $V = V_1 + V_2$. It is obvious from Figure 2 that at the interface the same interface states will be increasingly filled to E_{f2} if one considers only the GaAs side and will be decreasingly filled to E_{f1} if one considers only the Ge side. However, there can be just one interface occupation function that governs the filling of those states. This illustrates the necessity of finding the correct function so that the heterojunction solar cell efficiency can be evaluated accurately. Another problem that cannot be neglected is that when the interface charges increase, the barrier height is also increased. However, the barrier thickness is reduced in such a way that an electron within the distance of the mean free path can be captured by the interface trap and then re-emit to the other side of the junction. Thus, there is a second transport mechanism that is dominated by tunneling via interface states. This mechanism is different from the conventional mechanism of carrier transport by a thermionic mechanism with direct tunneling from one side of the junction to the other. Tunneling transport via interface states is a nonlocal effect and can be taken into consideration when one evaluates the heterojunction interface occupation

function⁽²⁾. In bulk defects at nonequilibrium condition, Simmons and Taylor⁽³⁾ have provided a theory to calculate the occupation probability that can be extended to evaluate the heterojunction interface occupation. There are essentially four rate processes from each side of the junction that interact with the interface states. Denote r_{a1} as the rate of capture per unit area (number of carriers/cm²-sec) from the Ge side to the interface states at energy E and density of states $N_t(E)$. If the capture cross section of the interface trap is σ_{n1} for an electron at the Ge side whose thermal velocity is v and mean free path ℓ_1 , then r_{a1} can be written as

$$r_{a1} = \sigma_{n1} \cdot v \cdot [n_1(0) + \frac{1}{\ell_1} \int_0^{\ell_1} T_{n1}(x) \cdot n_1(x) dx] \cdot (1-f) \cdot N_t \quad (1)$$

Equation (1) expresses that an electron at a distance x away from the interface from the Ge side and within the mean free path to the interface will be captured if there is a tunneling probability $T_{n1}(x)$ to the interface state and $n_1(0)$ is the local electron density. The rate r_{a1} is expressed in terms of a joint probability that is proportional to the number of vacancies available at the traps, $(1-f)N_t$, and the total number of electrons available from the conduction band at position $x=0$, including non-local effect. Here f is the interface occupation function. The integration over variable x gives the total rate from all possible conduction electrons.

An electron that is captured by the interface trap can re-emit to the Ge side with a rate of r_{b1} which is

$$r_{b1} = \int_0^{\ell_1} N_t \cdot f \cdot e_{n1}(x) dx \quad (2)$$

in which $e_{n1}(x)$ is the emission rate for an electron at interface state

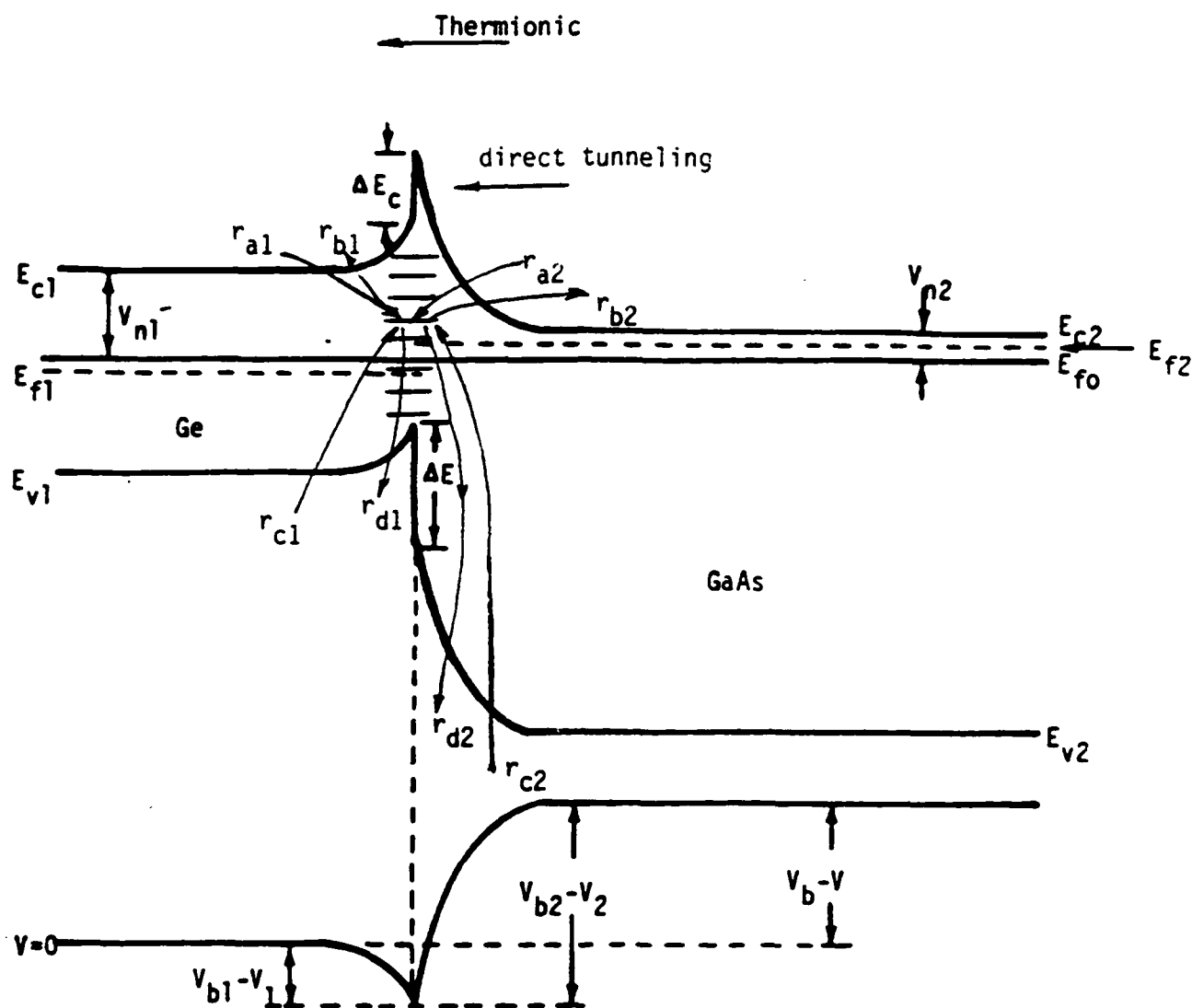


Figure 1: Ge/GaAs Interface Band Diagram. E_{f0} is the Fermi level at equilibrium. E_{f1} (E_{f2}) is the Fermi level on Ge (GaAs) side under applied voltage, V . The lower diagram is the potential profile across the junction. At equilibrium, $V_1 = V_2 = V = 0$, and V_{b1} (V_{b2}) is the built-in voltage in Ge (GaAs) side. The potential profile indicates the existence of interface charges at the junction. Horizontal bars indicated interface states r_{a1} , r_{b1} , r_{c1} and r_{d1} are four rate processes associated with electrons and holes from Ge side. Similarly r_{a2} , r_{b2} , r_{c2} and r_{d2} are those associated with GaAs side.

energy E to emit to the conduction band of Ge at position x . The quantity $(N_t \cdot f)$ is the number of electrons available to make such emission.

Holes at position x can be captured and re-emitted in the same way as electrons. Denote r_{c1} and r_{d1} as those rate processes. We have

$$r_{c1} = \sigma_{p1} \cdot V \cdot [p_1(0) + \frac{1}{\ell_1} \int_0^{\ell_1} T_{p1}(x) \cdot p_1(x) dx] \cdot N_t \cdot f \quad (3)$$

and

$$r_{d1} = \int_0^{\ell_1} (1-f) \cdot e_{p1}(x) dx \quad (4)$$

in which σ_{p1} , and T_{p1} have the same meanings as the corresponding terms in Equations (1) and (2), except they are for holes.

Similarly, there are four corresponding rate processes from the GaAs side. They are denoted by r_{a2} , r_{b2} , r_{c2} , and r_{d2} respectively. At equilibrium we have the conditions that

$$r_{a1} + r_{a2} = r_{b1} + r_{b2} \quad (5)$$

and

$$r_{c1} + r_{c2} = r_{d1} + r_{d2} \quad (6)$$

In this case, the interface occupation function f reduces to the Fermi distribution function f_0 , which can be written as

$$f_0 = \frac{1}{1 + e^{(E - E_{fo})/kT}} \quad (7)$$

Thus Equations (5) and (6) can be used to express e_{n1} and e_{n2} in terms of the parameters used in Equation (1) and the corresponding quantities from the GaAs side.

At nonequilibrium and steady-state conditions, we have a net

recombination rate that can be expressed as

$$r_{a1} - r_{b1} + r_{a2} - r_{b2} = r_{c1} - r_{d1} + r_{c2} - r_{d2} \quad (8)$$

The left hand side of Equation (8) denotes the net electrons coming into the interface trap, while the right hand side denotes the net holes into the trap. Equation (8) is the condition that determines the occupation function $f(E,V)$ as a function of the interface energy E and applied voltage V . The result can be written as

$$f(E,V) = \frac{\bar{n}_1 + \bar{n}_2 + \bar{e}_{p1} + \bar{e}_{p2}}{\bar{n}_1 + \bar{n}_2 + \bar{p}_1 + \bar{p}_2 + \bar{e}_{n1} + \bar{e}_{n2} + \bar{e}_{p1} + \bar{e}_{p2}} \quad (9)$$

where

$$\bar{n}_1 = \sigma_{n1} \cdot v \cdot [n_1(0) + \frac{1}{\ell_1} \int_0^{\ell_1} T_{n1}(x) n_1(x) dx] \quad (10)$$

$$\bar{p}_1 = \sigma_{p1} \cdot v \cdot [p_1(0) + \frac{1}{\ell_1} \int_0^{\ell_1} T_{p1}(x) p_1(x) dx] \quad (11)$$

$$\bar{e}_{n1} = \sigma_{n1} \cdot v \cdot N_{c1} [e^{-(E_{c1}(0)-E)/kT} + \int_0^{\ell_1} T_{n1}(x) e^{-(E_{c1}(x)-E)/kT} dx] \quad (12)$$

$$\bar{e}_{p1} = \sigma_{p1} \cdot v \cdot N_{v1} [e^{-(E_{v1}(0)-E)/kT} + \int_0^{\ell_1} T_{p1}(x) e^{-(E_{v1}(x)-E)/kT} dx] \quad (13)$$

Similarly for \bar{n}_2 , \bar{p}_2 , \bar{e}_{n2} and \bar{e}_{p2} .

We note that in the n-type limit

$$\bar{e}_{p1} = \bar{e}_{p2} = 0$$

and

$$\bar{p}_1 = \bar{p}_2 = 0$$

Thus, equation (9) is reduced to

$$f = \frac{1}{1 + \left(\frac{\bar{e}_{n1} + \bar{e}_{n2}}{\bar{n}_1 + \bar{n}_2} \right)} \quad (14)$$

Where the occupation f may not be written in the form of Fermi distribution with a quasi-Fermi level. Rather, the occupation function depends on properties from both sides of the heterojunction.

The occupation function for GaAs/Ge heterojunction for doping concentration of $10^{17}/\text{cm}^3$ in Ge side and $5 \times 10^{18}/\text{cm}^3$ of GaAs side is shown in Figure 2 when the equilibrium interface charge is $Q_{s0} = 2.8 \times 10^{12}/\text{cm}^2$. It is worth noting that the Fermi-energy shift is not equal to V_1 as indicated in Figure 3 because of the contribution from GaAs side.

Conclusions

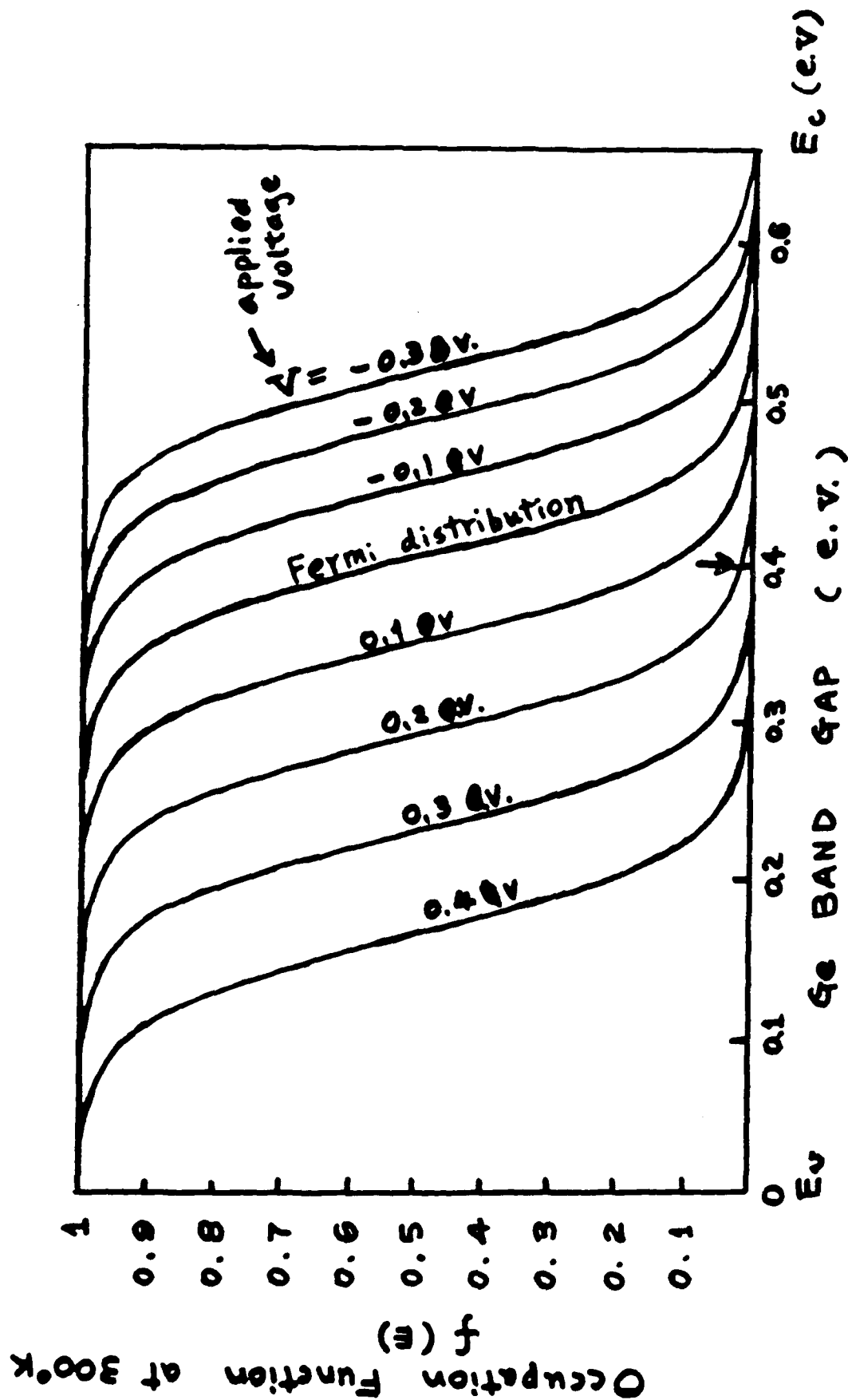
Non-equilibrium steady-state occupation for heterojunction semiconductors is derived for the first time. It can be generalized to include non-local effects of electron-hole captures and emissions.

The distribution function generally depends on free carrier densities on both sides of the heterojunction. In the GaAs/Ge heterojunction example, our calculations show that the occupation function resembles closely the Fermi distribution with a Fermi level shift that is not equal to V_1 or V_2 .

With non-local effects, electrons and holes are not recombined in equal amounts on each side of the heterojunction. Processes such as $r_{a2} \rightarrow r_{b1}$ allow electrons from side 2 be captured at the interface and re-emitted at side 1.

References

1. J. N. Bullock, C. H. Wu and J. F. Wise, "Interface Contribution to GaAs/Ge Heterojunction Solar Cell Efficiency," IEEE Transactions on Electron Devices, 1238-1243, July 1989.
2. C. H. Wu, T. T. Huang and J. N. Bullock, "Theory of Non-Equilibrium Heterojunction Interface-State Occupancy in Semiconductors," Bulletin of the American Physical Society, Vol. 34, No. 3, P. 1028, 1989.
3. J. G. Simmons and G. W. Taylor, "Non-Equilibrium Steady-State Statistics and Associated Effects for Insulators and Semiconductors Containing an Arbitrary Distribution of Traps," Phys. Rev. B, Vol. 4, 502-511, (1971).



Dopings: Ge : $10^{17}/cm^3$
GaAs : $5 \times 10^{18}/cm^3$
at equilibrium $Q_{50} = 2.8 \times 10^{12} \#/cm^2$

Fig. 2

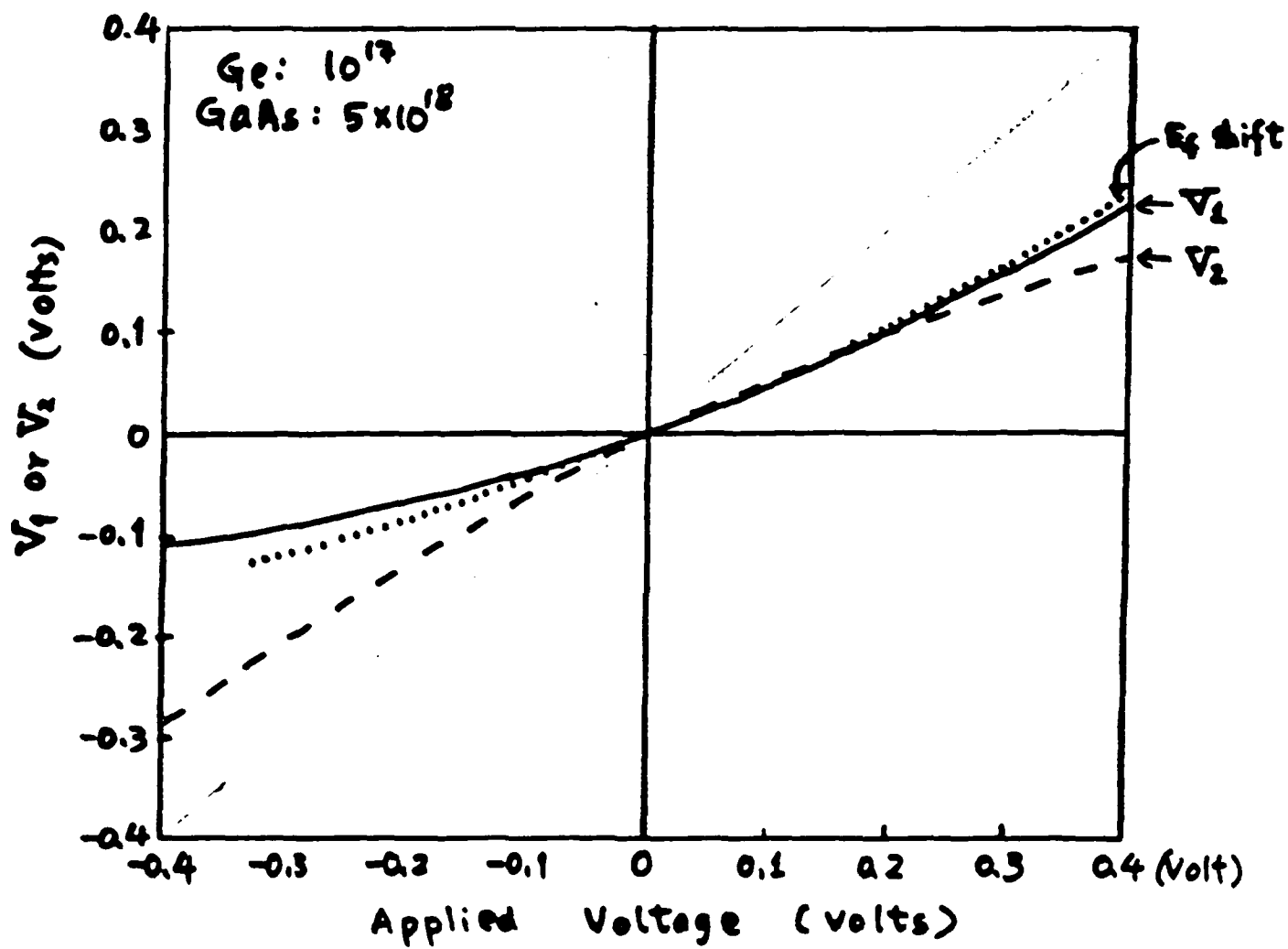


Fig 3.

1987-88 RESEARCH INITIATION PROGRAM

Sponsored by the
AIR FORCE OFFICE OF SCIENTIFIC RESEARCH

Conducted by the
Universal Energy Systems, Inc.

FINAL REPORT

Prepared by:	William K. Curry
Academic Rank:	Assistant Professor
Department and	Computer Science
University:	Rose-Hulman Institute of Technology Terre Haute, Ind
Date:	December 1988
Contract No:	S-760-7MG-081 F49620-85-C-0013

Computer Simulation of Adaptive Resource
Management in Real-Time

William K. Curry

ABSTRACT

An investigation was made into utilizing techniques from the field of artificial intelligence to create adaptable resource management systems. The systems of particular interest in this investigation were aircraft electronic counter measure (ECM) control systems. These systems are tightly constrained to give a reliable, real-time response specifying aircraft counter measure resource allocation. The characteristics of this problem which this research focused on were the representation of resource management knowledge, solutions to the "credit assignment" problem to facilitate learning in the electronic warfare (EW) environment, and the learning techniques best suited for achieving real-time, reliable updating of stored resource management knowledge.

Acknowledgments

This research was performed under contract number F49620-85-C-0013/S-760-7MG-081 and sponsored by the Air Force Office of Scientific Research (AFOSR) through the management of Universal Energy Systems (UES).

I wish to thank the AFOSR for their sponsorship of these efforts. I also wish to thank UES and Rose-Hulman Institute of Technology (RHIT) for their handling of the administrative portion of this research. Credit and thanks are also due to Steve Moak, Mark Monnin and Troy Thomas, the RHIT undergraduate student assistants who worked with me on this project.

I INTRODUCTION

The increasing density of the enemy threat environment in Electronic Warfare (EW), and the increasing sophistication of the threat radars used, have combined to make the field of Electronic Counter Measures (ECM) one in which response time and the effectiveness of resource allocation have become critical factors [1]. When a hostile presence is detected there is a short period of time during which an ECM technique can be expected to succeed. The difficulty is compounded by these ECM resources being specialized, in the sense that a particular technique may or may not be an effective deterrent in a given threat situation. These constraints suggest that as much of the decision process as possible should be automated.

The problem presented by automated control is that computer software has generally relied on static responses to previously anticipated input patterns. Thus systems are, in general, unable to adapt to new types of inputs or unanticipated input combinations within real-time constraints, if at all. In the case of an ECM system, this limitation may force the aircraft crew back into a slow, manual decision making mode and thereby jeopardize the mission and/or the aircraft.

The Software Development Group of the Avionics Lab of AFWAL has been studying the application of new computer system design concepts generated by the fields of Artificial Intelligence (AI) and Software

Engineering, to the solution of complex and highly constrained systems such as these. This research is a continuation of the work I began with this group during the summer of 1987 under the Summer Faculty Research Program sponsored by the Air Force Office of Scientific Research.

Using computer simulation, investigation was made into the management of limited, specialized resources, under real-time response constraints. The primary focus was the automatic control and assignment of Electronic Counter Measure (ECM) resources for an aircraft operating in a hostile electronic environment. Techniques from the fields of AI and object oriented system design were utilized in an attempt to maintain real-time response in a very large space of possible situations while designing a flexible, maintainable system. We also utilized AI techniques to endow our system with adaptive capabilities to allow for simple, unassisted "learning" of acceptable responses to unanticipated situations.

II OBJECTIVES OF THE RESEARCH EFFORT

Several existing AI techniques have potential in enabling software systems to undergo very simple learning processes. If an ECM control system can be developed which, by use of these learning techniques, will adapt to its current environment and "learn" the proper response to an unexpected threat, then the system might be relied upon in new situations to, at worst, degrade gracefully in its performance and at best, generate an effective response. If a generated response was found to be effective it could also store that information for later addition to the pool of knowledge known by all ECM systems.

The learning techniques we were most interested in were characterized by the "connection strength", "goal-seeking adaptive element" approaches which have lately been studied under the classification of neural network applications [6]. Our particular problem seemed to belong to the domain of associative-learning problems and seemed to lend itself most naturally to a linear-mapping approach for mapping threat combinations to responses.

The research goal was to produce a computer simulation of the problem, modeling the mechanisms by which a system such as this could adapt to new inputs correctly while giving a resource allocation recommendation on a real-time basis. Due to the real-time constraints placed on this

system, the capability was needed to produce both a good, quick response when fast response was critical and an optimal response when the processing time was available. Since a system such as this would most likely have a long maintenance period, it was also important to consider simplicity, flexibility and maintainability in our implementation.

III Model Design Constraints

1. Domain

In an attempt to generalize the problem area to a non-militarized, generic, resource management problem, it was decided to map the ECM environment, in as much detail as possible, to the problem of an imaginary creature (we named an EWOK) trying to survive in a hostile world. Whereas the aircraft has threats, the EWOK has predators, the aircraft has ECM tools, the EWOK has various techniques of confusing or evading his enemies, etc. In our EWOK world the number, type, and current activity of the predators combine to produce an overall situation. This situation is evaluated by our EWOK, which then responds with a defensive strategy consisting of one or more techniques. The natural constraints placed on the EWOK's responses were found to have a reasonable correspondence to the constraints placed on the aircraft's ECM system. For example the aircraft may release a flare, while the EWOK may release an odor, but both actions are limited by distance, time, threats against which they may prove effective, and the number of times during a single encounter that they may be used.

2. Knowledge Representation

Our EWOK needed both the capability to quickly evaluate the current environment's threat potential and to perform simple learning functions when needed. We therefore utilized concepts from Fuzzy Cognitive Map (FCM) structures to translate environment situations to EWOK responses and to represent the knowledge the EWOK had accumulated concerning response effectiveness. These structures were chosen because, a) they are fairly simple in concept and provide adequate support for a linear-mapping approach to an associative-learning type problem, b) they provide for fast, efficient querying and updating mechanisms for the current knowledge base via simple matrix operations, and c) their representation lends itself to a formal mathematical analysis [4] with more ease than some of the other representational schemes. This last attribute allows for its capabilities and limitations to be studied and documented with some precision, providing greater confidence in its use in situations where the cost of failure is high.

A FCM structure is a fuzzy signed digraph type of structure used to represent the interrelationships between the entities being modeled. Digraphs are used to represent the causation believed by the current model to be present among the model's entities. Entities in these models may represent objects, concepts, conditions, etc. The causation connections are signed because both positive (positive causal influence) and negative (inhibitive causal influence) relationships may be present, and they are called fuzzy because the strengths of the connections may be allowed to change as the system perceives a stronger or weaker causal

relationship between the nodes. For example an entity representing high interest rates would have a negative influence on an entity representing high consumer spending. High consumer spending would have a positive influence on high economic growth, which in turn might have a positive influence on high inflation. High inflation would tend to have a positive influence on high interest rates, completing the cycle. B. Kosko [4] gives a fuller explanation of the FCM's structure and operation.

3. Learning Technique

This ability to change the represented causal strength between two items during system operation by modifying their connection value in the FCM structure provides a simple learning mechanism which we felt could be utilized in creating an adaptable system. How this connection value should be modified has been the subject of much research in the past [7]. Hebb advanced the formula $\Delta W_{ij} = C X_i Y_j$ where C was a learning rate constant, the X_i s were the input conditions (in our case the environment characteristics) and the Y_j s were the output response vector. This approach however would allow for no decrease in our connection value, a capability that is vital if we need to learn to discard a option that was previously thought to be valid. In our model we needed a function of ΔX_i to influence our connection values since it is the change in status of the threats in the environment as they reacted to our defensive techniques that determined whether those techniques should be used again. Two of the existing equations

utilizing a change in the input vector to adjust the connection values are the Differential Hebbian: $\Delta W_{ij} = -W_{ij} + \Delta X_i \Delta Y_j$, which for our model had the problem of not allowing previously derived connection strengths to change gradually, so as to give preference to historically derived knowledge, and Klopff's formula [6]: $\Delta W_{ij} = \Delta X_i \Delta Y_j$, which also considers any change in the output vector when computing the new connection values. For our model, since the output vector (Y_j s or the set of defensive responses) is held constant over a learning period, we adopted a learning formula of the form $\Delta W_{ij} = f(\Delta X_i) Y_j$ where Y_j was 1 if the j^{th} technique was used and 0 otherwise. Our function, f , returned a delta to apply to the connection values which was based on the change in the environment's danger potential to the EWOK, the extent to which credit for the change could be assigned to individual responses, and the level at which the EWOK was working when it made the response (since general knowledge should change much more slowly than knowledge about a particular threat).

In our model the collection of these connection values were treated as a transformation matrix which transformed an initial vector representing the current environment to a vector representing both the current environment and the EWOK's selected responses to that environment. The transformation was applied repeatedly to the vector until subsequent transformations yielded resultant vectors within a tolerance range of 5% of the previous vector's values. This tolerance range was introduced due the difficulty of achieving exact convergence with some transformation matrices, as is discussed in Kosko [4]. This final

transformed vector yielded the pattern of defense techniques that were nominated for activation within the EWOK.

Each vector element represented either an environment characteristic to be considered or else a EWOK response to be applied. A simple model which allows for only the presence of a bear or a hawk and a response of only run or hide is shown in figure 1. Our model allowed for no self-activation, thus the diagonals of the transformation matrix which do not correspond to input conditions were zero to represent no effect. Matrix diagonal elements which do correspond to input conditions were set to 1.0 because the input conditions needed to be preserved in the input vector. Since the use of one response may have an effect on the use of another response, our model also stored connection values to model the effect of a response choice on the other responses available. In this case, one can't run and hide at the same time so there is a negative connection value between the two. The transformation matrix mapped the input vector to a new vector using the mapping equation

$$V_i = \sum_j T_{ji} V_j$$

To avoid unbounded increase or decrease of the vector elements, each resultant vector element was clipped at the values 1.0 and -1.0 after each transformation. The input vector, as shown in Figure 1, represents only that a bear is present in the environment. After the first transformation via the above equation we have a result vector of (1.0 0.0 0.5 0.3). Feeding this vector back into the transformation equation we get a new result vector of (1.0 0.0 0.2 -0.2). We can continue this

procedure until convergence is achieved at the 11th iteration with both the input and resultant vectors being (1.0 0.0 1.0 -0.7), representing that we have decided to place more confidence in running than in hiding when a bear is present. If the situation grows worse after trying to run, we may attempt to reduce the current connection weight between bear and run in our transformation matrix.

Bear Hawk Run Hide
 Vector = (1.0 0.0 0.0 0.0)

Transformation
 Matrix =

	Bear	Hawk	Run	Hide
Bear	1.0	0.0	0.5	0.3
Hawk	0.0	1.0	0.2	0.6
Run	0.0	0.0	0.0	-1.0
Hide	0.0	0.0	-1.0	0.0

Figure 1

4. Control Mechanisms

Our system objects communicate by passing messages between one another. In order to control the complexity of the system's message passing, it was designed using some of the concepts found in the work of P. Green [5] on Activation Frameworks. The use of these techniques offered us two advantages. First, the number of objects with which any individual object must communicate is reduced, making the system's data flow, and thus future modifications, much simpler. This is accomplished by separating the objects in the model's domain into major object classes and then placing them under the control of a central transaction manager for that class of objects. If a message needs to be sent to a particular object it is first routed through that object's class manager. The second advantage found in this approach is that, if needed, the class manager of an object class can be designed so as to queue incoming messages to objects in its class, rather than immediately sending them on. The messages can then be forwarded only when some type of "process" message is received. This can aid response time in those cases where the processing of these messages may be very time consuming and may subsequently be found unnecessary for the system's next required response. In a system placed under real-time constraints this lower level processing may need to be scheduled for periods of less processing demand or ignored completely when the situation permits.

An example of how our model uses this approach can be found in the communications path between our EWOK creature and the individual threats

around it. When the EWOK has decided what response it wishes to make to its current situation that information is not sent directly to each individual threat currently present. The information is sent only to a class manager object known as the environment where it is placed in a queue. The environment object must be explicitly told to process its queue contents before the information is distributed to each of the individual threats. Since the processing that a threat must go through to determine its counter response may be significant, our system has thus achieved some measure of control over when non-critical processing is actually performed.

IV Model Implementation Details

1. Hardware and Language Base for the Model

The system was originally developed on an LMI (Lisp Machines Inc.) Lisp machine using the ZetaLisp dialect [3] of the LISP programming language. It was later ported to a Digital Equip. Corp. VAX environment running the VMS operating system and using the Common Lisp implementation developed by LUCID. In an attempt to make the system as portable as possible, with the exception of parts of the user interface, only Common Lisp [2] constructs were used. To aid in management of the the system's complexity and to introduce added flexibility, the system was designed with an object oriented approach and implemented using the Flavors object oriented development constructs [3].

2. Model Structure

The system is built around a collection of objects, the five primary objects of the system being the environment object, the EWOK object, the EWOK memory object, the connection weight table object, and the user interface object. All other system objects are subservient to one of these primary objects. A high level diagram of the system is shown in figure 2.

The environment object communicates with a collection of threat objects representing the EWOK's predators. The threat objects contain all of the information needed to uniquely identify their type, what they are currently doing, and how dangerous their current activity is to the EWOK. These threat objects also contain information about which techniques are effective against them and which techniques may actually aid their cause. This information is used in determining the threat response to the EWOK's defenses.

The EWOK object represents the actual creature. It communicates with four types of subservient objects, state objects, mission objects, its internal memory system object, and technique classification objects. The technique classification objects are used to break the EWOK's defenses into major categories, such as expendables which have quantity limitations, territorial techniques which depend on surrounding terrain, etc. Each category may require different preconditions in the EWOK and the environment before its techniques are viewed as applicable. Each technique classification object knows about and communicates with its own group of defense technique objects. These classifications were created so as to have a one-to-one correspondence to the ECM technique classifications used by the Air Force. The EWOK memory system object is where the EWOK's current knowledge of threats and techniques known to be effective against them is stored. It is the heart of the system and is described in more detail in the next section.

Due to time constraints on this research the state objects and mission objects were only partially implemented and there was no analysis made

of their impact on the EWOK's response behavior. The intended purpose of the state objects were to represent the effect of internal EWOK states (i.e. hunger, tired, etc.) on the response given to a threat. For example if the EWOK is healthy he may choose an active defense technique against a threat, such as fighting, whereas if he is not healthy he may simply try to flee from the threat. These objects correspond to conditions that may exist onboard the aircraft, such as low fuel, aircraft damage, etc. The mission objects were intended to keep track of what the EWOK is trying to accomplish and how important it is that it be completed. These objects, when active, would influence the class of responses the EWOK considers first when a threat appears. This is the area in an ECM system where the relative importance of crew safety and mission completion would be accounted for.

When any of the technique, EWOK state, or EWOK mission factor objects fire (i.e. become active, become selected, etc.) they send a message communicating this event to all of the other internal EWOK objects. When an object receives information about another object's firing it checks the weight table object for any effect this event should have on its own tendency to fire. Thus we achieve a representation for the interdependent relationships of technique use on other techniques, EWOK internal states on technique use, and EWOK mission factors on technique use. To avoid a large amount of background processing in the EWOK object these messages are queued by their object class manager as they are created and are actually processed only on direction, as described above in the control mechanisms section.

The weight table object is where the initial connection strengths of the system's entries are kept. It represents the knowledge the EWOK has before any learning takes place. When the system is first invoked the EWOK's memory system is initialized with the weights found in this object. It not only stores initial threat-technique connection values but also stores the weights used to represent the technique-technique, EWOK state-technique and EWOK mission-technique interactions.

3. User Interface

The system is menu driven with top level options of setting environment characteristics or talking to the EWOK. If the user opts to set environment characteristics then a second set of options is presented allowing him to turn on/off threats or modify threat characteristics. When a threat is turned on or a currently active threat has its characteristics changed, update messages are sent to the EWOK via the environment object. When the user opts to communicate with the EWOK he is also given a second menu of options. Capabilities are provided for querying for and/or modifying the EWOK internal state and mission/goal factors which are active, and for asking the EWOK to produce a response to its current environment. The example program runs in appendix C show a complete list of the menu options present.

4. Basic Operations

When the EWOK is asked to respond to its current environment, the EWOK's memory system is used to construct a defense for each of the threats

currently active in the environment. A simple example of this process can be seen in example 1 of appendix C, which is discussed in detail in part 1 of section V of this report. The EWOK memory structure functions only as a knowledge base for the effectiveness of the EWOK's techniques against threats encountered. Whether the technique chosen by the memory structure is currently in use against another threat (which may make it unavailable for use against the current threat being considered), or has been used up in the past (for expendable techniques), or violates the current EWOK mission or state factor constraints, must be determined by examining the current state of the EWOK's technique objects. Although the technique objects have been implemented, the interaction of these objects with the EWOK's memory structure has not been completed. At present the EWOK's techniques are assumed to be unconstrained in these regards and the response returned from the memory structure is taken as the EWOK's final response with no further investigation.

The selection process is a function of how dangerous the current threat is to the EWOK and whether a quick answer is needed or the optimal answer can be found. The threats in the current environment are first ordered by the gravity that their presence lends to the situation, thus the more serious threats get matched with a response first. If the situation poses an immediate, critical danger to the EWOK it may be necessary to formulate a quick response which avoids as much processing as possible. This kind of response could be likened to a creature's reflex actions. However if the EWOK has the time to completely assess the situation it would want to do all of the processing needed to return the response it felt was optimal. If a quick answer is needed, the

number of iterations the EWOK's memory FCM objects are allowed to perform while seeking output vector convergence are reduced. If the FCM cannot converge in this limited amount of time then it will give up and force a higher level default response to the threat. Also, the constraint checking performed by the technique objects would be limited by checking selections on the basis of a high level estimate of which defense groups would be the most effective in dealing with the current threats. The processing needed to recognize and account for all of the technique to technique interactions possible would thus be bypassed. As mentioned above, these constraint checking mechanisms of the model are not fully implemented at this time. If time permits a optimal answer, then the EWOK's memory FCM objects are given more time to converge on a response. Also, when constraint checking is performed, all messages in the EWOK's object input buffers are processed and a steady internal state achieved prior to this checking. This allows for all possible interactions between techniques, mission factors and EWOK internal states to be recognized and provided for.

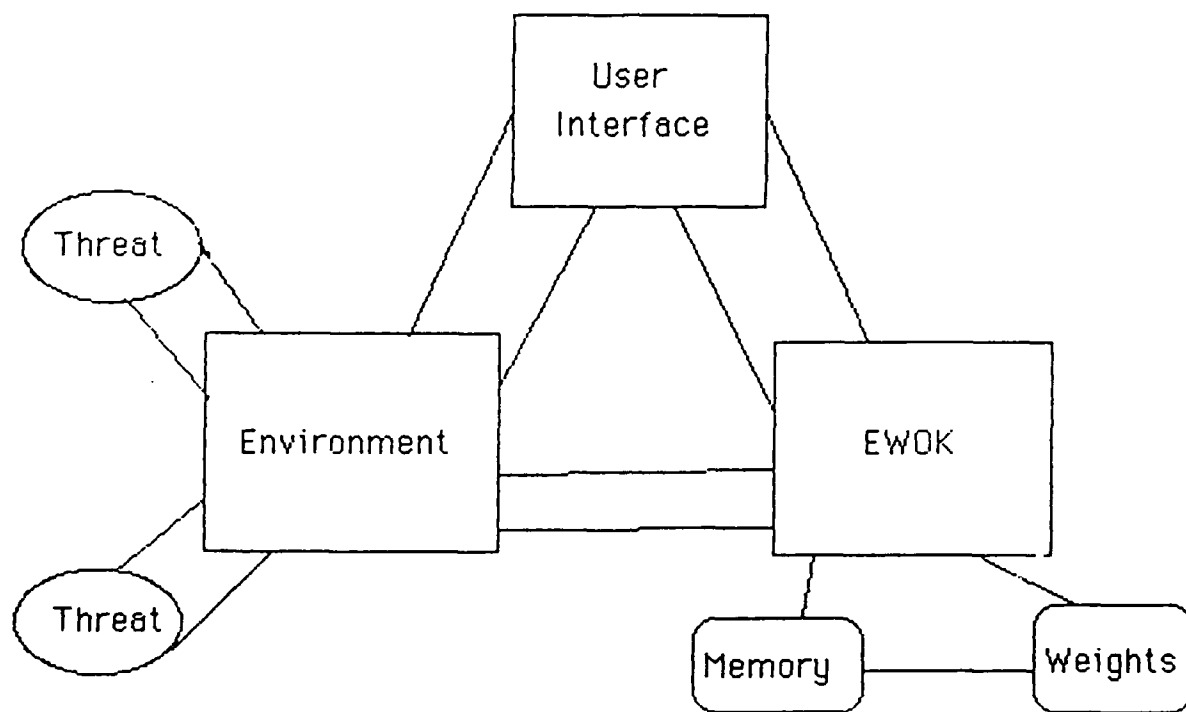


Figure 2

5. Credit Assignment

One of the problems faced by a learning system is how to assign credit for effected changes to the correct factors. These changes may be produced in a complex environment by a complex response, thus making this process a very difficult one. Determining when learning could take place and in what direction that learning should be applied was delegated to a learning critic in our system. During the cycle of environment evaluation, response generation that the EWOK goes through, the learning critic is constantly comparing the previous environment's threat characteristics with those of the current environment. If the two cases are similar enough (for our system this meant that the threat population had not changed in number and type) then learning was attempted. The defensive techniques used in the response to the previous environment are determined and, using the EWOK's memory object, the confidence that the EWOK had in those techniques when it chose them is retrieved. This is accomplished by having the EWOK's memory, upon special request, return the final activation vector for the current situation rather than just the most active technique. For example, the result returned in our previous bear/hawk/run/hide example would be the vector (1.0 0.0 1.0 -0.7) instead of the selection "run". The credit assigned to a technique is then based upon that technique's previous confidence value (the value in the returned activation vector associated with that technique). A normalization process is then performed to assure that no more than 100% total credit is being assigned. This approach to credit assignment allows for the introduction of a weighting

factor on the learning rate so that techniques the EWOK had previously developed a high confidence in, lose that confidence gradually when they prove ineffective in isolated encounters, while techniques whose previous effect were unknown are allowed to gain confidence rapidly when they prove effective.

6. The EWOK's Memory Structure

The EWOK's memory is structured as a type of a discrimination network. Each node in the network has its own FCM object whose connection strength values are tailored to that particular level of detail. At the highest node the EWOK distinguishes between friends and threats. At present the EWOK makes no use of the information that a friend is present. If a threat is sensed then more discrimination is attempted along such lines as land based threats, air based threats, or water based threats. At the bottom of the discrimination network individual threats are identified. The FCM at each node needs to be initialized with the current knowledge of how to deal with threats at that particular level. The EWOK is able to generate a response at any level of the network, but the further down the threat can be discriminated the more confidence can be placed in the response generated because the more individualized the connection strengths become to that threat. If the EWOK memory receives a threat that has characteristics that do not exist in its current network it creates a new memory node for that type of threat at the lowest level in the network to which it can be identified. The FCM at this new node may be initialized to the values of the FCM of the node immediately above it in the discrimination network to obtain a

starting point (this mechanism has not yet been implemented). It can then begin to learn and store proper responses to this new type of threat. An example of this operation is given in example 4 of appendix C, which is discussed in part 4 of section V of this report.

7. FCM Implementation

Each node in the EWOK's memory network has a FCM object associated with it. This FCM contains the current knowledge of the effectiveness of the various responses to threats distinguished to that level. If the EWOK decides to generate a response at a particular level it sends the FCM at that level a vector containing information on the current environment. The FCM uses its transformation matrix to map this input vector to a new vector containing the pattern identifying which responses are valid candidates for the given situation. This transformation is an iterative process with the output vector of the previous mapping being input to the next mapping operation. This iteration continues until either the process reaches a steady state, identified by the transformed vector being within a tolerance distance of the input vector the transform was applied to, or else the maximum number of iterations allowed is reached. This final vector is returned as the EWOK memory's response to the situation.

As is detailed by B. Kosko [4], when working with simple FCMs restricted to binary integer node connection values of 1 or -1, there are only 2^n possible binary states for a FCM representing n nodes. Thus the FCM must converge in at most 2^n iterations. In practice FCMs usually

converge after the first few iterations. In our system the connection values have been relaxed to allow for real number values between 1.0 and -1.0, but by introducing a tolerance distance we are still able to achieve convergence to within that specified tolerance in a small number of iterations.

8. Model Effectiveness

The advantages of this model lie in the run time flexibility of the EWOK's memory system. When unknown threats appear, they are given their own memory space and the EWOK begins the process of learning how to deal with them. Since each memory node has its own FCM, the ability to store and utilize general knowledge is available. The EWOK is therefore never at a loss for some type of reasoned response, even if it must be a very general, default type of response.

One of the disadvantages of the representation chosen is the structure can in some situations lead to a large overhead of processing needed to generate a response. Also it should be noted that the learning critic is still only a first cut, simplistic approach to the decisions that it must make. Its current effectiveness has much room for improvement and there are many degrees of freedom still to be investigated in this area.

9. Operations Implemented in the C Language

A couple of the system's operations were found to be too time consuming when implemented in LISP and an equivalent C implementation was

developed. This inefficiency was associated with large numbers of matrix operations, for which C produces more optimal code. The operations for which this alternate implementation was necessary were the application of the transformation matrix to the environment vector in the FCM objects and the look-up of initial knowledge from the weight table when initializing the EWOK's memory on system start-up processing. The C code for these operations has been included in appendix B.

V Model Results

Several model test runs are shown in appendix C. The following sections give a detailed explanation of the model's actions as observed in these examples. The model is menu driven and thus the test runs shown consist of the sequence of menus presented by the system, the menu option selected and the system's response. In each example the first action is to enter a dialogue with the environment object and define the threats currently present. No threats are present when the system is initially started but there are several threat types whose characteristics are known to the environment object.

1. Example 1 - No Learning

In this example, through an environment object dialogue, a lion is placed 80 units from our creature and a snake is placed 25 units from our creature. Both threats are allowed to take on their default mode of activity which is the search mode. After the threats are defined, a dialogue with the EWOK object is started and the creature is asked to generate its best response to the current situation. The response given is to shriek at the snake and growl at the lion. If, as is shown, the EWOK is asked to respond again to the same situation, two new responses are selected. This is due to a arbitration mechanism built into our EWOK which works to assure that no response will be repeated for that threat until other equally valid responses have their chance to

influence the situation. This arbitration is needed because the learning process requires experience before allowing the EWOK's memory system to indicate a definite preferred response to a particular threat, and therefore the EWOK's memory must eventually try all responses which are equally valid for that threat.

2. Example 2 - Learning for a Single Threat

In the second example, one of the system's trace flags is turned on to show part of the learning process. By way of an environment object dialogue, a lion object is placed 50 units from the EWOK in its default search mode of operation. When the EWOK is asked to respond to this threat it reports that the lion should be shrieked at. As in example 1, the EWOK is asked to respond again to the same situation with no situation changes. The EWOK stores internally the previous situation it encountered. When asked to respond to a situation it compares the last situation with the current situation and if they are similar enough (for our simple approach this simply means the same threat set is present) learning is attempted. The EWOK also stores a measure of the seriousness of the previous situation and if learning is attempted the seriousness of the previous situation is compared with the seriousness of the current situation. In this case, since there were no situation changes the seriousness measure was the same, as shown in the display of the old measure and new measure both being 1.25. Since the situation has not been impacted at all by the previous response, no change is made in the confidence factor for shrieking at lions. The small value

displayed, -0.001, is due to round off error in the calculations and has little effect on the confidence factors.

In the example we then go back into a dialogue with the environment object and make a significant change in the situation. We assume that the last response, which was the use of camouflage, caused the lion to drift 100 units further away from the EWOK. Since the threat set is the same when we return to the EWOK and request a new response, learning is attempted. This time the new situation seriousness measure is down to 1.0 and a significant change in the positive direction is made to the confidence level of using camouflage against lions. We then see that the EWOK memory system returns to camouflage as the current desired response to the lion.

To show learning in the negative direction we then return to the environment and indicate that the previous response, which was our camouflage response, caused the lion to take notice of the EWOK and move from the search mode of operation to the track mode of operation. When we return to the EWOK and request a response this time the seriousness measure has increased to 2.0 and camouflage's confidence rating for lions is moved in the negative direction. The change factor is printed as a positive number but the direction it is applied is negative when the new seriousness measure is higher than the old one. Thus the next response selected is to try mimicry on the lion.

3. Example 3 - Learning With Several Threats

The third example shows the effects of having several threats in the threat set when learning is attempted. First, a crocodile is placed 100 units away in track mode, a tiger is placed 100 units away in search mode, and killer bees are placed 300 units away in chase mode. The EWOK's response to the situation is a preliminary shrieking at the killer bees and the crocodiles and growling at the tiger. We then go to the environment and indicate that the response set helped the situation with the crocodile but hurt the situation with the tiger. Returning to the EWOK and asking for a new response, we find that the impact of the previous response set was so mixed that our learning mechanism does not single out growling as a preferred response for tigers but returns the new response set of camouflaging itself from the killer bees and crocodile and using mimicry on the tiger. If we now go to the environment and indicate that this new response set causes clear improvements in the situation with the tiger and has no impact on the crocodile or killer bees we find that the EWOK's learning process selects camouflage as the response to have confidence in for tigers. This is because camouflage is the dominate response in the previous response set and is therefore given most of the credit for the situation improvement. Much work and research is needed in this area of the model to prevent difficulties such as this.

4. Example 4 - Adding New Memory Nodes for New Threat Types

In the fourth example the FCM trace flag for the system is turned on to show the memory node creation that is performed. A new threat type, a wild boar, is created through an environment object dialogue in which the threat characteristics are specified. The only identifying characteristic we give to our wild boar that the EWOK can recognize is that it is a land based threat. When the EWOK is queried for a response to this new threat the EWOK's memory module looks down its discrimination network and finds it can discriminate no farther than land_based threats. It then creates a new memory node at this level. It may be useful to take the current land_based threat node's FCM as a initial FCM to use with this threat's memory node, although this option has not yet been implemented. A response of shrieking at the wild boar is returned because it currently uses the same default FCM as the other threat memory nodes.

VI REMAINING PROBLEMS AND GAPS IN THE SYSTEM

Some of the areas of the system needing further study and analysis are described below.

1. Rate of Learning

Little investigation had been made into the proper rate of learning that the EWOK's memory should undergo. It is currently designed such that the rate of learning increases as the threat recognition moves down the discrimination network. The observation that the response of shrieking doesn't work well on a lion would have a small negative impact on the shrieking response's confidence factor stored in the FCM object at the threat level, a little greater impact in the FCM object at the land_based threat level, and its greatest impact in the FCM object actually at the lion threat level. Due to time constraints this behavior has not yet been fully implemented. This approach is based on the ideal that the more specific the new information is the more impact it should have and the more general the knowledge, the less likely it should be to change. The overall rate of learning and exactly how closely it should be tied to various aspects of the environment's changed factors is a subject of further investigation.

2. Factors Influencing Learning

There are many characteristics of the environment that may be considered in determining the direction and amount of learning appropriate in any given situation. These characteristics include such factors as overall seriousness of the situation, the seriousness of individual threat potentials, number of threats, number of friends saved or lost, etc. How each of these factors should contribute to the change the EWOK's knowledge base undergoes has yet to be fully investigated.

3. Mission Characteristics and Internal EWOK Conditions

The effect of the immediate high priority goals of the EWOK, such as achieving a specific objective, reaching safety, protecting others, etc. has not been studied for its impact on response desirability. This area is one of importance because in the ECM field these questions would translate into the needs of the mission, which greatly impact the final defensive behavior.

Another area deserving consideration is the effect of internal EWOK conditions on response selection. Factors such as the EWOK being hungry, hurt, strong, etc. may strongly influence which measures are more desirable.

Both of these considerations will produce a competing goal problem for this model since the EWOK may find it has two or more valid goals whose satisfaction interfere with one another. The creature will eventually need methods of setting goal priorities and determining whether all

goals may be satisfied at the same time or some goals will need to be sacrificed in favor of more important ones.

4. Effects of Other EWOK Creatures Present

The EWOK should be able to take advantage of the presence of friends in its defense strategy. This would, however, greatly increase the complexity of the situation and the number of options the EWOK must consider when responding.

5. Good Response And Best Response

More investigation is needed into the criteria and methods to use in generating a good quick response as opposed to a best, more process intensive response. At present this is implemented by controlling when messages sent to selected objects are actually processed and by limiting the number of iterations the FCM structure in the EWOK's memory will go through while seeking a steady state situation. Other options might include generating a response at a higher level in the EWOK's memory discrimination network, implementing reflex actions which are independent of the EWOK's memory system altogether, or having an alternate knowledge representation mechanism whose flexibility isn't as great as that of the FCM approach but which doesn't depend on an iterative process to produce a reasonable response.

6. Arbitration of Equally Confident Responses.

No detailed analysis has been made of the best way to choose between two or more responses which have equal confidence ratings in the current situation. This is current done on a random basis with no real analytic approach. Some of the possibilities include associating priorities with technique classes (e.g. always choose a passive technique over an active one, use last any techniques which are classified as expendables, minimize the use of internal energy, etc.), associating priorities with each individual technique, allowing us to designate some techniques as last resort actions, or using some type of least-recently-used or most-recently-used technique approach.

7. Credit Assignment

The assigning of credit to the active techniques when a situation improves or grows worse is an area which merits more investigation. When multiple techniques are being employed against multiple threats, considering only the overall situation measure and past technique confidence levels leaves large gaps in our learning algorithm where the system may miss significant, previously unknown, cause and effect relationships. The best method of determining the direct effect of a particular technique on a particular threat in the presence of other techniques and threats is not clear at this point but is a question of great importance to the goals of this project.

The additional problem of how to detect, assign credit for, and subsequently represent in our EWOK's memory system, the causative effect of technique combinations on an individual threat also remains in the

current system. For example it may be that hiding and shrieking at the same time may be more effective against bears than either of the two techniques taken individually, but that this combination is not useful, or even harmful in the presence of other threat types. Our system currently has no mechanism for capturing or representing this type of information. This information would need to be incorporated into the technique-technique activation connection strengths but at present there is no provision for making these connection strengths a function of the particular threat.

8. Memory and Technique Object Interaction

The system needs the capability to represent both the current knowledge about the effectiveness of techniques against threats and the constraints placed on technique use, such as limited quantities, technique/technique interference, etc. The FCM structures in the EWOK's memory object provides for a flexible representation of technique effectiveness while creating technique objects to contain all of a technique's current status information and limiting characteristics, provides a flexible method for representing a technique's fixed and dynamic constraints. If both representational forms are to be used in the same system, as was the approach taken in this project, they must have a complete interface between them so as to give a comprehensive assessment of which techniques to activate. At present this interface has not been developed in our system. It is envisioned as being one in which the EWOK memory object's selections are filtered through the technique object's constraint information before they are delivered as a recommended action.

VII CONCLUSIONS AND SUMMARY

The system described in this report shows promise for providing real-time adaptation in a reasonably reliable fashion. There are still a number of aspects that need more detailed study and analysis. The memory structure accounts for the general, default reasoning option which we feel is important in this type of system. The Fuzzy Cognitive Map structure utilized in knowledge representation provides for a relatively simple, straight forward way of modifying a knowledge base gradually in a controlled direction.

The object oriented design utilized in developing this system has proven to be a great aid in complexity management throughout the project. It has allowed for clean interfaces and a natural modularization which other design approaches would have rendered more difficult. It can, however, in some instances lead to more overhead processing if a great deal of information needs to cross object boundaries. This is a liability in a system where real-time response is critical.

**Appendices can be obtained from
Universal Energy Systems, Inc.**

**FINAL REPORT NUMBER 78
STUDY OF SKY BACKGROUNDS AND
SUBVISUAL CIRRUS
PENDING APPROVAL
Dr. Gerald W. Grams
210-9MG-120**

Research Initiation Program, 1988-89

Final Report

to

Universal Energy Systems

and

Air Force Office of Scientific Research

**Proving equivalence of high- and low-level
architectural descriptions in VHDL**

Award P. O. S-210-9MG-108

*David Hemmendinger**

Department of Electrical Engineering and Computer Science

Union College

Schenectady, NY 12309

* The major portion of this work was carried out at Wright State University, Dayton, Ohio 45435, while the principal investigator was a member of the Department of Computer Science and Engineering.

Proving equivalence of high- and low-level architectural descriptions in VHDL

Summary

The purpose of this project has been to conduct preliminary investigations of possible techniques for doing formal verification of hardware designs written in the VHDL hardware description language. VHDL is a new industry standard (IEEE-1076) for hardware specification and its implementation includes a simulator for descriptions written in the language. While simulation is a vital tool, it cannot provide a demonstration that a design meets its specification except in those simple cases where exhaustive simulation is possible and feasible. Formal verification that a design is correct with respect to its specification is currently an active area of research [7, 8, 11, 18], although relatively little has involved the use of VHDL ([22] presents some very preliminary steps).

A proof that a design or implementation is correct must compare a design with its specification. The degree to which the proof can be formal depends on the precision with which a specification and a design can be stated. In certain respects VHDL is an ideal tool for the task, since it combines the ability to give both high-level and low level-descriptions in a single language, accessible to practicing designers. One may give a behavioral description of a component that states how it is to function. One may also give a low-level architectural VHDL description in terms of the simple logic elements that are intended to provide the desired behavior. In addition, VHDL has two features that are useful in approaching formal verifications. One of these is the set of signal attributes that carry a great deal of information about the state of hardware signals, such as their recent history and stability. The other is the capability of embedding assertions in VHDL that specify conditions that should hold at a certain point. When a VHDL specification is 'executed' by the simulator program that is part of the language description, these assertions cause exceptions to be raised if they fail to hold. The hardware designer can thus check that a design meets its specification by making the specification take the form of such assertions. Such checks are a useful preliminary to explicit verification.

The principal work in this project was to continue the exploration of these features that the investigator had started during his UES Summer Faculty Fellowship. This included further development of the translation from VHDL to the language of a proof-assistant, HOL (Higher Order Logic), further study of the semantics of the signal attributes in VHDL, initial steps in using the VAL preprocessor [Vhdl Annotation Language] from Stanford, and explorations with the HOL tool. On the negative side, the author and his graduate-student assistant, Mr. John Van Tassel, found that some of the features we most needed to use in VHDL, such as the signal attributes, remained not fully implemented in the VHDL toolset that they used. More important, however, we also found that we had to shift the focus of the study to some extent, since a crucial issue became the precise specification of VHDL itself. The language reference manual [LRM] that gives the semantics of the language is not itself a formal document, and at times it became difficult to know precisely how to interpret parts of it. As a result, during the final stage of our study we began to look at how to use the apparatus we had developed in order to give a formal specification of parts of VHDL, particularly of its timing model and hence, of the simulation cycle defined in the LRM.

STAGES OF THE PROJECT

1. Automatic generation of VHDL temporal assertions

By using the built-in signal attributes of VHDL, it is possible to write assertions in the language that state the meaning of signal-assignment statements and the contexts, such as guarded blocks, in which they occur. We have focused on assertions that give the temporal properties of these statements, such as the simple example of a statement and the automatically generated assertion that states its meaning:

$$S1 \leq (S2 \text{ and } S3) \text{ after } D$$

```
assert( (not S2'stable(D)) or (not S3'stable(D)) or (S1 = (S2'delayed(D) and S3'delayed(D))))
```

These are a first step toward formal verification since they can then be translated further to the language of theorem provers. We continued the development of the Prolog translation program that generates these assertions automatically as it analyzes a VHDL specification; it was started during the summer, 1988 UES Fellowship. Since the assertions that it generates are those that should always be true during a simulation run, one side-effect of using this program has been enabling us to test our understanding of the VHDL model of time against the implementation of the simulator by checking to see if our translations of such temporal statements ever yield false assertions.

The translation program now handles signal assignment statements with both transport and inertial delay and with guards, standard control structures such as if-then-else and case-statements, processes and guarded blocks. It is based on a Prolog program in the form of an attributed translation grammar, a particularly convenient form in which to develop such source-to-source translations. It can readily be extended to include additional VHDL constructs, since it recognizes even those parts of the language for which it does not generate equivalent assertions.

The implementation in the Internetrics VHDL simulator of the signal attributes such as *'stable* that we use in these assertions is now correct. However, as we developed our program we continued to find further flaws in the implementation of other attributes. Toward the end of the project we needed to use the *'last_event* and *'last_active* attributes, for instance, but found that they were not correctly initialized. This error has since been fixed, but too late for our use in the project.

2. Automatic translation of VHDL temporal assertions into Higher Order Logic

The original plan, to translate from VHDL to Cambridge LCF, a theorem-prover, was superseded by translation to HOL (Higher Order Logic, another mechanization of formal logic. The primary reason for this was that HOL has already been used extensively for studies of formal verification of hardware design, particularly by groups working under Dr. Michael Gordon at Cambridge University and Dr. Graham Birtwistle at the University of Calgary. The use of higher-order predicate logic, rather than just first-order logic, provides a precise way of representing hardware components formally. Briefly, a signal is a function that maps time to a domain of signal values; components are higher-order functions that map functions (input signals) to functions (outputs). HOL itself is a proof-assistant rather than a mechanical theorem-prover; the user has to direct the search for a proof. The translation from VHDL to HOL was also easily automated, using another Prolog translation grammar with a new set of output operations to generate HOL rather than VHDL assertions. At present the same VHDL statements that can automatically be translated into equivalent VHDL assertions can also be translated into HOL by our program.

There is an obvious question, however: how do we know that our translations from VHDL to HOL are correct? In generating VHDL assertions about signal-assignments statements the corresponding question can be partially answered by the VHDL simulator. If the assertions do not generate exceptions, then they are at least consistent with the implementation of VHDL provided by the simulator. The answer to the question is that we do not. Our translations appear reasonable, but in the absence of a formal specification of VHDL, and in particular, of the timing model and simulation cycle, it is impossible to ascertain the correctness of the translation. In fact, we prefer to regard our restatement of VHDL in HOL as a first step toward such a formal specification, and the first conclusion that we have reached in this project is

There is a great need for a formal semantics of VHDL, particularly of its timing model and simulation cycle. HOL is a formal language with the clean semantics of a functional language. It is a good candidate for such a formal specification language for VHDL.

3. Proofs that implementations meet specifications

Our approach here was to take advantage of the fact that VHDL permits — indeed, encourages — the use of descriptions at different levels of detail. One may write a high-level behavioral description of a device and also a gate-level architecture for it. The behavioral description is essentially a specification of the device. It is easy to obtain a VHDL assertion or the equivalent HOL that characterizes this behavior, either explicitly if the designer writes the assertion or by means of our translation programs. This assertion may then be embedded in the entity declaration for the low-level description, where it will apply to any architecture for that entity. A simulation run will then test the specification against the implementation, and if the tests are passed, one may then turn to formal verification methods to prove that the implementation is correct with respect to that specification. Our position is that the ability to use the assertions first at the simulation level and then, by translation to HOL, at the formal level, is a benefit, since it permits initial evaluation by simulation before undertaking the harder task of verification.

There is a rapidly growing body of work on hardware verification with HOL, we looked at how it might be applied to our VHDL translations. We choose a small example from the literature, a parity checker [18].* Writing the behavioral and the gate-level VHDL was straight-forward, and the automatic translation to HOL was virtually identical to the original HOL descriptions. In emulation of the HOL example, the VHDL model used transport delay for simplicity. However, even with this simplification, the VHDL simulation found momentary violations of the assertion derived from the behavioral description, when that assertion was embedded in the gate-level architecture. The reason, of course, was that signal assignments take at least time in VHDL, so that assertions that express outputs as functions of inputs momentarily fail when the inputs change. This is a general problem with VHDL descriptions, and one needs to be able to express the notion of *eventually*: eventually, when all changes in inputs have propagated through a component, then test an assertion. The VAL preprocessor for VHDL [3, 4] provides precisely this capability; it permits the designer to make assertions in a more natural style. Eventually we acquired a preliminary implementation of VAL, thanks to the kindness of its implementors, and were able to experiment briefly with it. However, due to implementation problems, we were able only to get to the point of seeing that what we would eventually need to do would be to express VAL-like assertions in HOL.

* This example is also included in the paper that appears in the appendix of this report.

In comparing the simulation of the VHDL description of the parity-checker with the HOL description, we also observed that one of the assertion violations generated by the simulator represented a race-condition in the device. It did not exist in the simplified unit-delay timing model used in the HOL description, but VHDL does not permit one to simplify to that degree. In fact, one could argue that the HOL model is oversimplified, at least in the absence of an explicit description of the clocking of input signals that would guarantee that internal state of the device has stabilized before the input is clocked. Much of the work with formal verification to date does not spell out the assumptions it makes about details of timing. A tentative conclusion that we have reached in this project is that on the one hand, the timing model of VHDL, particularly its treatment of assertions as true at every -step, is too fine-grained for verification purposes. On the other hand, formal verification techniques need to take into account more of timing details than they have so far, and need to give formal descriptions of these details. In short,

The timing-model of VHDL, or something like that, needs to be incorporated into verification in HOL or in other formalism. In fact, giving a formal specification of the VHDL timing model would be a means of achieving this end as well.

We made some very preliminary investigations into how one might represent that timing model in HOL. These initial steps focused on appropriate data-structures; we intend to carry them further to experiment with their utility.

4. Conclusions and presentation of project results

Mr. Van Tassel and the investigator presented a paper at the IFIP-IMEC International Workshop on Applied Formal Methods for Correct VLSI Design (Belgium, Nov. 13-16, 1989) [30]. This paper, "Toward Formal Verification of VHDL Specifications", summarizes work done in the project, and is included as the Appendix of the present report. It will also appear in the proceedings, to be published by Elsevier. Portions of this work were done by Mr. Van Tassel as part of his M.S. thesis for Wright State University, supervised by the investigator. The thesis, "The Semantics of VHDL with VAL and HOL: Towards Practical Verification Tools" [29], will appear as a technical report.

The present grant provided support for the investigator to attend a workshop, Banff III: Higher Order Logic and Hardware Verification, Sept., 1989. This workshop provided a good review of theoretical tools in mathematics and theorem-proving. It also appears that some of the work in [15, 16] on HOP, a process-oriented hardware model will be applicable to our work, since the translation between this language and HOL can be adapted to the similar translation of VHDL. With other sources of support, I was also able to attend two other conferences on hardware verification, CHDL '89 (Washington, D.C., June, 1989) and a workshop on Hardware Specification, Verification, and Synthesis at Cornell University (July, 1989).

In conclusion, the goal of the Research Initiation Program project was to explore some possible ways of applying formal verification techniques to VHDL descriptions. Such an open-ended goal is subject to change as the project advances, and to some degree that occurred here. We were successful in developing the prototype tools to generate VHDL assertions automatically and to translate them to HOL, and we believe that these can be expanded to be of practical value. Along the way we found that we needed a more formal specification of VHDL itself than has yet been developed, and it appears to us that the most fruitful next step would be to work out such a formal specification using HOL itself. Indeed, we regard some such precise specification of the VHDL simulator as an immediate necessity. Without it, versions of VHDL will multiply as fast as new simulators are implemented. If VHDL is to succeed as the standard it is intended to be, it must be truly standardized as rapidly as possible.

ACKNOWLEDGEMENTS

I wish to thank Dr. John Hines of the Electronics Technology Lab of Wright-Patterson AFB for his support in this project. I am also grateful to him and to Dr. Victor Berman for giving me access to the Intermetrics VHDL Toolset. The present grant provided support for Mr. Van Tassel for only a small portion of the grant period, but the liberal use of 'we' in this report reflects the large part he played in the entire project.

REFERENCES

1. Armstrong, J.R., *Chip-Level Modeling with VHDL* (Prentice-Hall, Englewood Cliffs, 1988).
2. Augustin, L., An Algebra of Waveforms, in *Proc. of the IFIP-IMEC International Workshop on Applied Formal Methods for Correct VLSI Design*, ed. L. Claesen (1989), pp. 159-168.
3. Augustin, L., et al., VAL: An Annotation Language for VHDL, in: *Proceedings of IEEE ICCAD-87*, 1987, pp. 418-421.
4. Augustin, L, et al., An Overview of VAL, Technical Report CSL-TR-88-367 (Computer Systems Lab, Stanford University, Palo Alto, CA, 1988).
5. Barrow, H.G, VERIFY: A Program for Proving Correctness of Digital Hardware Designs, *Artificial Intelligence*, 24 (1984), pp. 437-491.
6. Birtwistle, G, et al., Verifying an SECD Chip in HOL, in *Proc. of the IFIP-IMEC International Workshop on Applied Formal Methods for Correct VLSI Design*, ed. L. Claesen (1989), pp. 149-158.
7. Birtwistle, G. and Subrahmanyam, P.A., eds., *Current Trends in Hardware Verification and Automated Theorem Proving*, (Springer, New York, 1989).
8. Birtwistle, G. and Subrahmanyam, P.A., eds., *VLSI Specification, Verification, and Synthesis* (Academic Press, Boston, 1988).
9. Borriane, D. and Paillet, J.L., An Approach to the Formal Verification of VHDL Descriptions, Technical Report RR 683-I (Institut National Polytechnique de Grenoble, Grenoble, 1987).
10. Camilleri, A., et al., Hardware Verification Using Higher-Order Logic, in: *Proceedings of the IFIP WG 10.2 Working Conference: From HDL Descriptions to Guaranteed Correct Circuit Designs*, ed. D. Borriane and IMAG/ARTEMIS (North-Holland, Amsterdam, 1987), pp. 43-70.
11. Camurati, P. and Prinetto, P. Formal Verification of Hardware Correctness: An Introduction, in *Computer Hardware Description Languages and Their Applications*, ed. M. R. Barbacci and C. J. Koomen (North-Holland: Amsterdam, 1987), pp. 225-247.
12. Clarke, E.M., et al, Automatic Verification of Finite-State Concurrent Systems Using Temporal Logic Specifications, *ACM Transactions on Programming Languages and Systems* 8, no. 2 (1986), pp. 244-263.
13. Davie, B.S. and Milne, G.J., The Role of Behaviour in VLSI Design Languages, in: *Proceedings of the IFIP WG 10.2 Working Conference: From HDL Descriptions to Guaranteed Correct Circuit Designs*, ed. D. Borriane and IMAG/ARTEMIS (North-Holland, Amsterdam, 1987), pp. 3-20.
14. Fujita, M., et al., Verification with Prolog and Temporal Logic, in: *Computer Hardware Description Languages and Their Applications (Proc. of the 6th Int. Symp. on CHDL's)*, ed. T. Uehara and M. Barbacci (North-Holland, Amsterdam, 1983), pp. 103-114.

15. Gopalakrishnan, G., Specification and Verification of Pipelined Hardware in HOP, in *Proc. of the Ninth International Symposium on Computer Hardware Description Languages*, ed. J. A. Darringer and F. J. Rammig, Washington, D. C., June, 1989, pp. 117-131 (to be published by Elsevier).
16. Gopalakrishnan, G., et al., HOP: A Process Model for Synchronous Hardware, Semantics and Experiments in Process Composition, forthcoming, *Integration: The VLSI Journal*.
17. Gordon, M., Why Higher-Order Logic is a Good Formalism for Specifying and Verifying Hardware, in: *Formal Aspects of VLSI Design*, ed. G. Milne and P. A. Subrahmanyam (North-Holland, Amsterdam, 1986), pp. 153-178.
18. Gordon, M., HOL: A Proof Generating System for Higher-Order Logic, in: *VLSI Specification, Verification and Synthesis*, ed. G. Birtwistle and P. A. Subrahmanyam (Academic Press, Boston, 1988), pp. 73-127.
19. Herbert, J., Temporal Abstraction of Digital Design, Technical Report No. 122 (Computer Laboratory, Univ. of Cambridge, Cambridge, England, 1988).
20. Hunt, W.A., Jr., The Mechanical Verification of a Microprocessor Design, in: *Proceedings of the IFIP WG 10.2 Working Conference: From HDL Descriptions to Guaranteed Correct Circuit Designs*, ed. D. Borriane and IMAG/ARTEMIS (North-Holland, Amsterdam, 1987), pp. 89-132.
21. Institute of Electrical and Electronics Engineers, *IEEE Standard VHDL Language Reference Manual* (IEEE Press, New York, 1988).
22. Kelem, S., A Subset of VHDL for Formal Verification, presented at VHDL Users' Group Meeting, Redondo Beach, California, Oct. 1988.
23. Milne, G. and Subrahmanyam, P.A., ed., *Formal Aspects of VLSI Design* (North-Holland, Amsterdam, 1987).
24. Mishra, B. and Clarke, E.M., Automatic and Hierarchical Verification of Asynchronous Circuits Using Temporal Logic, Technical Report CMU-CS-83-155 (Carnegie Mellon University, Pittsburgh, PA, 1983).
25. Moszkowski, B., *Executing Temporal Logic Programs* (Cambridge University Press, New York, 1986).
26. Narendran, P. and Stillman J., Hardware Verification in the Interactive VHDL Workstation, in: *VLSI Specification, Verification and Synthesis*, ed. G. Birtwistle and P. A. Subrahmanyam (Academic Press, Boston, 1988), pp. 235-256.
27. Subrahmanyam, P. A., What's in a Timing Discipline: Considerations in the Specification and Synthesis of Systems with Interacting Asynchronous and Synchronous Components, presented at the Workshop on Hardware Specification, Verification, and Synthesis: Mathematical Aspects, Cornell University, July, 1989 (to be published in Springer LNCS).
28. Uehara, T., et al., DDL Verifier and Temporal Logic, in: *Computer Hardware Description Languages and Their Applications (Proc. of the 6th Int. Symp. on CHDL's)*, ed. T. Uehara and M. Barbacci (North-Holland, Amsterdam, 1983), pp. 91-101.
29. Van Tassel, J., *The Semantics of VHDL with VAL and HOL: Towards Practical Verification Tools*, M. S. thesis, Wright State University, Dayton, Ohio, 1989.
30. Van Tassel, J. and Hemmendinger, D., Toward Formal Verification of VHDL Specifications, in *Proc. of the IFIP-IMEC International Workshop on Applied Formal Methods for Correct VLSI Design*, ed. L. Claesen (1989), pp. 261-270.

Appendices can be obtained from
Universal Energy Systems, Inc.

FINAL REPORT NUMBER 80
REPORT NOT AVAILABLE AT THIS TIME
Dr. Periasamy K. Rajan
210-9MG-051

FINAL REPORT

SUBMITTED TO THE 1988 RESEARCH INITIATION PROGRAM

Sponsored by the

AIR FORCE OFFICE OF SCIENTIFIC RESEARCH

Conducted by

Universal Energy Systems

Contract No:	F49620-88-C-0053/SB5881-0378
Purchase Order No:	S-210-9MG-058
Principal Investigator:	Mateen M. Rizki, Ph.D.
Address:	Computer Science Department Wright State University Dayton, Ohio 45435
Project Title:	Applications Of Evolutionary Learning Strategies To Pattern Recognition Tasks
Submission Date:	December 31, 1989

1. SUMMARY

The major goal of this research program was the development of a learning system capable of automating the tasks of image processing and pattern recognition. This objective was accomplished by using a hybrid learning system consisting of adaptive control mechanisms coupled with evolutionary learning strategies. To test the principles incorporated in this system, a prototype closed-loop learning system was implemented and used to design morphological feature detectors. These detectors were then applied to the task of handwritten character recognition. The prototype system achieved near perfect performance on sets of training images and excellent results on independent test sets.

2. INTRODUCTION

Methods for analysis of raw image data typically utilize statistical processing techniques to extract critical features of images that are then passed to a symbolic information processing system for interpretation. This approach to image processing requires human expertise for the identification of crucial components of the images and organization of a knowledge base. Once implemented, these systems are rigidly structured and their application is restricted to a small class of images. To overcome the limitation of this traditional approach to image processing, alternate systems that are capable of managing non-structured information must be developed.

During the tenure of a UES Summer Fellowship in 1988, I was assigned to the Image Calculus Program of Dr. Louis Tamburino at Wright-Patterson Air Force Base. That summer, we successfully developed a basic software system for binary image processing and the collaborative effort has continued throughout the period of the Initiation Award.

The Image Calculus Program is a hybrid learning system consisting of two major components, a classical pattern recognition module and a learning module. The pattern recognition module is composed of two components, a feature detector subsystem and a classifier subsystem. The feature detector subsystem extracts features from images and passes a feature vector to the classifier subsystem that assigns each image to a class. A set of pre-classified images are processed by the system during a training phase. Whenever an image is placed in an incorrect class during the training period, a system error is recorded. These errors are passed to an evaluation component of the learning subsystem that assesses the performance of different activities of the recognition system. The learning system then adjusts the pattern recognition system to reduce future classification errors.

The feature detector subsystem is based on principles of mathematical morphology that utilize image erosion operations. Image erosion is the systematic removal of points from the input image as it is compared to the structuring element, or second image. For our initial detectors morphological analysis was limited to erosion operations that utilize structuring elements to evaluate

binary images. The structuring element is a collection of points that serves as a template that is translated across the surface of the input image. Each coincidence between the template and the image is marked as a single point in a third, or resultant, image. The marked point is a distinguished point in the structuring element, and the ultimate result of eroding an image by a specific structuring element is the production of a smaller collection of points in a resultant image. If a detector defined by a structuring element produces a non-null resultant image after an erosion, then the input image contains the feature embodied by the detector. When a structuring element is applied to a set of input images, the collection of binary responses forms a feature vector that is fed to the classification system. Our current experiments are limited to two-class identification problems so the classification system is not required. When the system is complete, a single layer neural network classifier will be included to handle multi-class problems.

3. WORK COMPLETED

3.1 Laboratory Setup

The Computer Science and Engineering Department at Wright State University established an Adaptive Vision Laboratory to specifically support this program on image processing and pattern recognition. The Avionics Laboratory at Wright-Patterson Air Force Base provided funds to purchase a Sun 3/260 workstation that was placed in the laboratory. In addition, the University contributed two Sun 3/60 workstations and two Zenith 80386

micro-computers. This equipment is connected to the Ethernet so that all personnel on the project can collaborate on software development. Since the initial studies were performed in the PC-DOS environment, considerable time and effort was devoted to transitional existing software to the new environment.

3.2 Design Formalism and the Model

A formalism was developed to describe the structure of the closed-loop hybrid learning system. In this formalism, two major system components are identified: the pattern recognition module and the learning module. The pattern recognition module is defined using the principles of mathematical morphology, and the learning module is described using learning automata. The closed-loop learning process consists of selection, application, evaluation, and variation. Specifically, the learning module selects a rule and passes it to the recognition module. The recognition module applies the rule to the current processing task and returns the result to the learning module. The learning module evaluates the result and varies the rule. This evolutionary process is then repeated. When a satisfactory level of performance is achieved, the learning module is turned off leaving an adapted rule in the recognition module. Existing research in learning automata was reviewed and our work represents an extension of stochastic learning automata to the area of adaptive control in

image processing. The formalism was presented to Dr. Horst Wittman, Air Force Office of Scientific Research on December 7, 1988.

3.3 Control Strategies

A control strategy was developed for allocating resources to the pattern recognition module. The purpose of this strategy is to achieve an acceptable level of performance in the recognition module using a limited amount of computational resources. The control strategy, termed the envelope strategy, computes the range of parameter settings that produce the highest expected performance by monitoring a series of trajectories through a resource allocation parameter space. To test the control strategy, ideal parameter ranges were established for a sample image processing problem by an extensive series of experiments. The envelope strategy was then applied to the same problem. The parameter settings generated by the envelope control strategy agreed with the ideal ranges at a fraction of the computational cost. A formal mathematical treatment of the envelope strategy was presented at the NAECON Meetings, 1989.

3.4 Image Database

We designed and implemented software to facilitate the generation of an image database. This effort included interfacing a 300dpi scanner to a 80386 workstation. The images scanned using this device were low quality and unsegmented, so we developed a software tool to assist in the conversion from raw scanner input

to segmented 32x32 binary images. This scanner provides images in a TIFF file format and these are converted to an unpacked binary format. An editor program was developed to allow a user to preview the image files, select a 32x32 pixel region of the image, and load the chosen image into an edit buffer. The individual pixels of the buffered image can then be selectively altered. Noise can be added or removed in the border of the images during this process. To further improve the quality of the images, preprocessing algorithms were developed and applied to remove chatter from the edges of the images. This preprocessing consisted of applications of morphological closing and opening operations followed by a thinning process that reduced the images to skeletons of uniform thickness. Using this system, approximately one thousand examples of alpha-numeric characters were prepared and loaded into the database. These images were used to construct training and test sets for subsequent experiments.

3.5 Automated Feature Extraction Experiment

The first long term experiment using the image processing system was initiated on the 80386 PC. The entire experiment consisted of a series of independent two class recognition sub-experiments. Each sub-experiment involved the automatic generation of an erosion template capable of discriminating a set of target images from a set of non-target images. The target set was composed of four samples of a single alpha-numeric character from the set (A-Z,a-z,0-9) while the non-target set

was composed of four samples of each of the remaining alpha-numeric characters. A variety of template sizes was tested. In addition, each sub-experiment was repeated using hit-or-miss and foreground-only templates. With each run requiring approximately one hour, the entire experiment required approximately 1200 machine hours.

On preprocessed training images, an accuracy rate close to 100% was obtained using templates of size 5x5 to 10x10 on images of size 32x32 pixels. Smaller template sizes (3x3 and 4x4) also performed well (%60-%80 accuracy). These results demonstrate that with preprocessed images, discriminating features are extremely local. The generated hit-or-miss templates contained too many background points. In essence the system eliminated non-target images using background points as opposed to recognizing target images using foreground points. We observed a stability property with respect to the location where a template fits into an image. Across a class of images, a good template fits in the same general area in each image. This implies that the template is extracting an invariant feature of the image.

After completing the transition from the PC environment to the Sun environment, a new series of experiments using handwritten characters was initiated. Sixteen samples of the characters A-Z and digits 0-9 were collected from different individuals. Each character was framed in a 32x32 window but not enhanced in anyway. Our previous images were skeletonized, but these new images are thick and highly distorted. We have successfully recognized a

set of training images and are obtaining reasonable performance on sets of test images. We have begun to modify the learning system to incorporate a two-phase genetic learning algorithm which should increase system performance.

4. PUBLICATIONS

- "Automated Feature Detection Using Evolutionary Learning Processes", L.A. Tamburino, M.M.Rizki, and W. VanValkenburgh, NAECON, Dayton, Ohio, pp. 1080-1087, (1989).
- "Computational Resource Management in Supervised Learning Systems", L.A. Tamburino, M.M.Rizki, and M.A. Zmuda, NAECON, Dayton, Ohio, pp. 1074-1079, (1989).
- "Automatic Generation of Binary Feature Detectors", L.A. Tamburino and M.M.Rizki, IEEE Aerospace and Electronic Systems Magazine, September (1989).

FINAL REPORT
SUBMITTED TO
UNIVERSAL ENERGY SYSTEMS, INC
4401 Dayton-Xenia Road
Dayton, Ohio 45432

ENTITLED
"The Effect of a Roughened Surface on
Turbulent Boundary Layer Separation at Mach 6.0"

Prepared by
P.J. Disimile
Bradley Jones Assistant Professor
Department of Aerospace Engineering
and Engineering Mechanics
University of Cincinnati
Cincinnati, OH 45221

Contract No. F49620-85-C-0013/SB 5851-0360

Grant Period: April 1987 to May 1989

Abstract

An experimental investigation into the effects of a roughened surfaces on boundary layer characteristics in an adverse pressure gradient was undertaken. This study was carried out at hypersonic speeds using the High Reynolds Number Facility located at the AF Wright Research and Development Center in Dayton, Ohio. Unit Reynolds numbers between 10 million/ft and 30 million/ft were obtained at a nominal Mach Number of 6. The rough surface topography consisted of machined proturbances 0.020 inches high, 0.040 inches in both length and width, with spacing between the individual elements of 0.040 inches.

Surface pressure distributions indicate that the separation point, x_s , moved approximately 10 percent when the unit Re was increased from 10 million/ft to 30 million/ft, for the 22° case. In the 28 and 34 degree cases the x_s increased by 3 and 5.5 times that of the 22° case, respectively, but appeared insensitive to Reynold's number.

Pitot pressures on the ramp surface were also acquired and found to be several times larger than those recorded upstream on the flat plate segment of the model. Total temperature profiles obtained on the flat portion of the model were found to overshoot the freestream stagnation temperature by approximately 3 to 5 percent. Similarlity on the ramp total temperature profiles were observed to overshoot the freestream stagnation temperature by 10 to 30 percent.

List of Figures

- Figure 1 Wind Tunnel Facility Overview
- Figure 2 Detailed Nozzle/Jet/Collector Configuration
- Figure 3 Model Topography
- Figure 4a Model Instrumentation Locations
- Figure 4b Detail of the Model Instrumentation in the Interaction Zone
- Figure 5 Nondimensionalized Surface Pressures at a Given Ramp Angle and Stagnation Pressure
- Figure 6 Nondimensionalized Surface Pressures at a Given Ramp Angle and Stagnation Pressure
- Figure 7 Nondimensionalized Surface Pressures at a Given Ramp Angle and Stagnation Pressure
- Figure 8 Nondimensionalized Surface Pressures at a Given Ramp Angle and Stagnation Pressure
- Figure 9 Nondimensionalized Surface Pressures at a Given Ramp Angle and Stagnation Pressure
- Figure 10 Nondimensionalized Surface Pressures at a Given Ramp Angle and Stagnation Pressure
- Figure 11 Nondimensionalized Surface Pressures at a Given Ramp Angle and Stagnation Pressure
- Figure 12 Nondimensionalized Surface Pressures at a Given Ramp Angle and Stagnation Pressure
- Figure 13 Nondimensionalized Surface Pressures at a Given Ramp Angle and Stagnation Pressure
- Figure 14 Nondimensionalized Surface Pressures with Side Fences at a Given Ramp Angle
- Figure 15 Combined Nondimensionalized Surface Pressures at a Given Ramp Angle

Figure 16 Combined Nondimensionalized Surface Pressures at a Given Ramp Angle

Figure 17 Combined Nondimensionalized Surface Pressures at a Given Ramp Angle

Figure 18 Combined Nondimensionalized Surface Pressures at a Single Stagnation Pressure

Figure 19 Combined Nondimensionalized Surface Pressures at a Single Stagnation Pressure

Figure 20 Combined Nondimensionalized Surface Pressures at a Single Stagnation Pressure

Figure 21 Comparison of the Nondimensionalized Surface Pressures with and without Side Fences

Figure 22a Nondimensionalized Pitot Pressure Distribution at a Given Location and Stagnation Pressure

Figure 22b Mach Number Distribution at a Single Location

Figure 22c Static Temperature Distribution at a Given Location and Stagnation Pressure

Figure 22d Local Mean Velocity Distribution at a Given Location and Stagnation Pressure

Figure 23a Nondimensionalized Pitot Pressure Distribution at a Given Location and Stagnation Pressure

Figure 23b Mach Number Distribution at a Single Location

Figure 23c Static Temperature Distribution at a Given Location and Stagnation Pressure

Figure 23d Local Mean Velocity Distribution at a Given Location and Stagnation Pressure

Figure 24a Nondimensionalized Pitot Pressure Distribution at a Given Location and Stagnation Pressure

Figure 24b Mach Number Distribution at a Single Location

Figure 24c Static Temperature Distribution at a Given Location and Stagnation Pressure

Figure 24d Local Mean Velocity Distribution at a Given Location and Stagnation Pressure

Figure 25a Nondimensionalized Pitot Pressure Distribution at a Given Location and Stagnation Pressure

Figure 25b Mach Number Distribution at a Single Location

Figure 25c Static Temperature Distribution at a Given Location and Stagnation Pressure

Figure 25d Local Mean Velocity Distribution at a Given Location and Stagnation Pressure

Figure 26a Nondimensionalized Pitot Pressure Distribution at a Given Location and Stagnation Pressure

Figure 26b Mach Number Distribution at a Single Location

Figure 26c Static Temperature Distribution at a Given Location and Stagnation Pressure

Figure 26d Local Mean Velocity Distribution at a Given Location and Stagnation Pressure

Figure 27a Nondimensionalized Pitot Pressure Distribution at a Given Location and Stagnation Pressure

Figure 27b Mach Number Distribution at a Single Location

Figure 27c Static Temperature Distribution at a Given Location and Stagnation Pressure

Figure 27d Local Mean Velocity Distribution at a Given Location and Stagnation Pressure

Figure 28 Nondimensionalized Pitot Pressure Distribution at a Given Location and Stagnation Pressure

- Figure 29 Nondimensionalized Pitot Pressure Distribution at a Given Location and Stagnation Pressure
- Figure 30 Nondimensionalized Pitot Pressure Distribution at a Given Location and Stagnation Pressure
- Figure 31 Combined Nondimensionalized Pitot Pressure Distributions at a Single Location
- Figure 32 Combined Nondimensionalized Pitot Pressure Distributions at a Single Location
- Figure 33 Combined Nondimensionalized Pitot Pressure Distributions at a Single Location
- Figure 34 Combined Nondimensionalized Pitot Pressure Distributions at a Single Stagnation Pressure
- Figure 35 Combined Nondimensionalized Pitot Pressure Distributions at a Single Stagnation Pressure
- Figure 36 Combined Nondimensionalized Pitot Pressure Distributions at a Single Stagnation Pressure
- Figure 37 Combined Mach Number Distributions at a Single Location
- Figure 38 Combined Mach Number Distributions at a Single Location
- Figure 39 Combined Mach Number Distributions at a Single Stagnation Pressure
- Figure 40 Combined Mach Number Distributions at a Single Stagnation Pressure
- Figure 41 Combined Mach Number Distributions at a Single Stagnation Pressure
- Figure 42a Total Temperature Distribution at a Given Location and Stagnation Pressure
- Figure 42b Normalized Total Temperature Distribution at a Given Location and Stagnation Pressure

Figure 43a Total Temperature Distribution at a Given Location and Stagnation Pressure

Figure 43b Normalized Total Temperature Distribution at a Given Location and Stagnation Pressure

Figure 44a Total Temperature Distribution at a Given Location and Stagnation Pressure

Figure 44b Normalized Total Temperature Distribution at a Given Location and Stagnation Pressure

Figure 45a Total Temperature Distribution at a Given Location and Stagnation Pressure

Figure 45b Normalized Total Temperature Distribution at a Given Location and Stagnation Pressure

Figure 46a Total Temperature Distribution at a Given Location and Stagnation Pressure

Figure 46b Normalized Total Temperature Distribution at a Given Location and Stagnation Pressure

Figure 47a Total Temperature Distribution at a Given Location and Stagnation Pressure

Figure 47b Normalized Total Temperature Distribution at a Given Location and Stagnation Pressure

Figure 48a Total Temperature Distribution at a Given Location and Stagnation Pressure

Figure 48b Normalized Total Temperature Distribution at a Given Location and Stagnation Pressure

Figure 49a Total Temperature Distribution at a Given Location and Stagnation Pressure

Figure 49b Normalized Total Temperature Distribution at a Given Location and Stagnation Pressure

- Figure 50a Total Temperature Distribution at a Given Location and Stagnation Pressure
- Figure 50b Normalized Total Temperature Distribution at a Given Location and Stagnation Pressure
- Figure 51 Combined Normalized Total Temperature Distributions at a Given Location
- Figure 52 Combined Normalized Total Temperature Distributions at a Given Location
- Figure 53 Combined Normalized Total Temperature Distributions at a Given Location
- Figure 54 Combined Normalized Total Temperature Distributions at a Given Stagnation Pressure
- Figure 55 Combined Normalized Total Temperature Distributions at a Given Stagnation Pressure
- Figure 56 Combined Normalized Total Temperature Distributions at a Given Stagnation Pressure
- Figure 57 Combined Static Temperature Distributions at a Given Location
- Figure 58 Combined Static Temperature Distributions at a Given Location
- Figure 59 Combined Static Temperature Distributions at a Given Stagnation Pressure
- Figure 60 Combined Static Temperature Distributions at a Given Stagnation Pressure
- Figure 61 Combined Static Temperature Distributions at a Given Stagnation Pressure
- Figure 62 Combined Local Mean Velocity Distributions at a Given Location
- Figure 63 Combined Local Mean Velocity Distributions at a Given Location
- Figure 64 Combined Local Mean Velocity Distributions at a Given Stagnation Pressure

- Figure 65 Combined Local Mean Velocity Distributions at a Given Stagnation Pressure
- Figure 66 Combined Local Mean Velocity Distributions at a Given Stagnation Pressure
- Figure 67 Boundary Layer Velocity Distribution Comparison at a Given Location and Stagnation Pressure
- Figure 68 Boundary Layer Velocity Distribution Comparison at a Given Location and Stagnation Pressure
- Figure 69 Boundary Layer Velocity Distribution Comparison at a Given Location and Stagnation Pressure

List of Tables

- Table 1a Overall Model Instrumentation Coordinates
- Table 1b Interaction Zone Instrumentation Coordinates
- Table 2 Surface Pressure Data at a Given Ramp Angle and Stagnation Pressure
- Table 3 Surface Pressure Data at a Given Ramp Angle and Stagnation Pressure
- Table 4 Surface Pressure Data at a Given Ramp Angle and Stagnation Pressure
- Table 5 Surface Pressure Data at a Given Ramp Angle and Stagnation Pressure
- Table 6 Surface Pressure Data at a Given Ramp Angle and Stagnation Pressure
- Table 7 Surface Pressure Data at a Given Ramp Angle and Stagnation Pressure
- Table 8 Surface Pressure Data at a Given Ramp Angle and Stagnation Pressure
- Table 9 Surface Pressure Data at a Given Ramp Angle and Stagnation Pressure
- Table 10 Surface Pressure Data at a Given Ramp Angle and Stagnation Pressure
- Table 11 Surface Pressure Data at a Given Ramp Angle and Stagnation Pressure with the Side Fences
- Table 12 Pitot Pressure Distribution Data for the 22 Degree Ramp Angle at a Given Location and Stagnation Pressure

- Table 13 Pitot Pressure Distribution Data for the 22 Degree Ramp Angle at a Given Location and Stagnation Presure
- Table 14 Pitot Pressure Distribution Data for the 22 Degree Ramp Angle at a Given Location and Stagnation Presure
- Table 15 Pitot Pressure Distribution Data for the 22 Degree Ramp Angle at a Given Location and Stagnation Presure
- Table 16 Pitot Pressure Distribution Data for the 22 Degree Ramp Angle at a Given Location and Stagnation Presure
- Table 17 Pitot Pressure Distribution Data for the 22 Degree Ramp Angle at a Given Location and Stagnation Presure
- Table 18 Pitot Pressure Distribution Data for the 22 Degree Ramp Angle at a Given Location and Stagnation Presure
- Table 19 Pitot Pressure Distribution Data for the 22 Degree Ramp Angle at a Given Location and Stagnation Presure
- Table 20 Pitot Pressure Distribution Data for the 22 Degree Ramp Angle at a Given Location and Stagnation Presure
- Table 21 Total Temperature Distribution Data for the 22 Degree Ramp Angle at a Given Location and Stagnation Pressure
- Table 22 Total Temperature Distribution Data for the 22 Degree Ramp Angle at a Given Location and Stagnation Pressure
- Table 23 Total Temperature Distribution Data for the 22 Degree Ramp Angle at a Given Location and Stagnation Pressure
- Table 24 Total Temperature Distribution Data for the 22 Degree Ramp Angle at a Given Location and Stagnation Pressure
- Table 25 Total Temperature Distribution Data for the 22 Degree Ramp Angle at a Given Location and Stagnation Pressure
- Table 26 Total Temperature Distribution Data for the 22 Degree Ramp Angle at a Given Location and Stagnation Pressure

Table 27 Total Temperature Distribution Data for the 22 Degree Ramp Angle
at a Given Location and Stagnation Pressure

Table 28 Total Temperature Distribution Data for the 22 Degree Ramp Angle
at a Given Location and Stagnation Pressure

Table 29 Total Temperature Distribution Data for the 22 Degree Ramp Angle
at a Given Location and Stagnation Pressure

Nomenclature

x	→ streamwise distance
y	→ lateral distance along the width of the plate
z	→ distance taken perpendicular to the plate
x_s	→ separation distance measured from flat plate/ramp intersection point
Re	→ unit Reynolds number/ft
P_0	→ stagnation pressure
P_t	→ local pitot pressure
P_s	→ static pressure
P_{14}	→ undisturbed reference surface pressure acquired at $x = -6.727$ inches.
M	→ Mach number
c	→ speed of sound
T_0	→ stagnation temperature
T_t	→ local total temperature
T_s	→ static temperature
U	→ local velocity
U_{inf}	→ free stream velocity

Introduction

Current interest in hypersonic airbreathing propulsion systems and maneuverable re-entry vehicles has brought to the forefront aerothermodynamic problems not previously considered in detail. The advent of a National Aerospace Plane program, concomitant with many new unresolved complex technical issues surrounding the space shuttle, has culminated to demand a more rigorous pursuit in the fundamental understanding of fluid flow phenomena that influence aerodynamic performance. Developing an understanding and prediction capability for fully developed turbulent boundary layer separation in hypersonic flows is one such area relevant to the Air Force mission. Investigating the physical mechanisms of high speed flow separation and developing a modelling capability based on this understanding will promote advanced theoretical techniques and initiate new design concepts pertinent to high speed flight vehicles.

Along with drag and heat transfer, a dominant characteristic of high speed turbulent flow, inherently coupled to vehicle stability, is that of boundary layer separation. Aerodynamic devices, which encounter turbulent boundary layer flow through an adverse pressure gradient, can experience boundary layer separation if the pressure gradient is too severe. Separation will occur with a number of devices, such as deflected flaps, ailerons, supersonic diffusers and high pressure compressor airfoils. It is well documented that surface skin friction and the boundary layer velocity distribution are controlling factors in boundary layer separation. Furthermore, through research it has been shown that surface roughness cause changes in skin friction, heat transfer and boundary layer profiles. These changes are known to result in; (i) inadvertent fluctuation in vehicle control, (ii) range reduction due to increased drag and (iii) increased vehicle mass to ensure thermal protection.

Reference Background

A recent review of aerothermodynamic problems surrounding hypersonic flight and its associated research by Holden² demonstrates our present lack of predictive capability to support the design of such systems. Holden states that the intense research programs of the 1960's and early 70's were superceded by hypersonic flow investigation that was limited to supporting specific and conservatively designed systems such as the space shuttle, the Jovian entry vehicle and ballistic re-entry vehicles. The results of this review vividly point out the scarcity of previous research encompassing the combined effects of surface roughness and turbulent boundary layer separation in hypersonic flows. Although these criteria have escaped an integrated approach for study, much work has emanated in hypersonic flow research considering surface roughness effects or boundary layer separation dependence on Mach number and Reynold's number.

Many earlier studies on turbulent boundary layer separation were performed in supersonic/hypersonic flow regimes. These studies investigated incipient separation using compression corners to simulate flow over aerodynamic flaps or ailerons. The work of Bogdonoff, et. al.³ revealed that separation is a gradual phenomenon and that this separation is without significant Reynold's number dependence. However, in an earlier report by Kuehn^{4 5}, it was observed that in the lower Reynold's number range, a substantial effect on the pressure rise for separation existed in the upper Mach number range of 3 to 5. Namely, the pressure rise required for separation decreased with increasing Reynold's number. For low Mach numbers of 2.0 and high Reynold's numbers there appeared to be no dependence. Roshko et. al.⁶ obtained data at considerably higher Reynold's numbers which showed just the opposite effect of Kuehn's findings. Starrett et. al.⁷, working at Mach 5.6, stated that the pressure ratio necessary for separation

depends on the ramp shape and Reynold's number if the pressure gradient is of the type produced by two-dimensional wedges. To the contrary, again, Todisco and Reeves⁸ observed that for fully turbulent separation, the measured plateau pressure was independent of Reynold's number at speeds of Mach 6.5. Hypersonic flow researchers today, endeavoring to draw conclusive evidence from these studies exploring the question of Reynold's number effect on separation phenomenon, may find their efforts endless.

Investigations, addressing the effects of surface roughness on turbulent boundary layer profiles and skin friction, carried out by Goddard⁹ demonstrated that surface imperfections on a non-smooth plate at a height greater than the viscous sublayer produce increases in the skin friction. Additionally, the inner portion of the boundary layer is shown to decrease under similar conditions. This experimental work has been consistently endorsed by other researchers that followed. Namely, Young¹⁰, Reda et.al.¹¹ and Thompson¹² all were in accord with Goddard's initial findings for Mach numbers up to 5.0. The latest work, on turbulent boundary layer profile/skin friction dependence on the surface roughness in a two-dimensional flow, is that from Fiore and Christoph^{13 14} at a Mach number of 5.75 and a Reynold's number of 3.8×10^7 . They found that "the rough surface velocity is less fuller than the velocity profile for the smooth wall case. The rough surface decrease in the local velocity is believed to be caused by momentum loss resulting from the presence of the individual protuberances pressure drag and particle wakes." Because vehicles in high speed flight exhibit a variety of inherent textured surface conditions and employ various external control devices that can produce large areas of flow separation, the importance of surface roughness effects on boundary layer separation becomes very relevant. If a relationship between surface

roughness and fully turbulent boundary layer separation does exist, the question becomes to what degree does roughness influence separation and what are the physical mechanisms involved that control this effect.

In an effort to determine the current understanding of the effects of surface roughness on the separation of a fully developed turbulent boundary layer in hypersonic flows, a comprehensive literature search and review was performed by the author¹⁵. This was performed during his summer faculty research assignment in the High Speed Aerodynamics Group of the Flight Dynamics Laboratory, Wright Patterson Air Force Base. In total, over 170 documents were reviewed. Only one document was identified that incorporated the combined effects of surface roughness, turbulent boundary layer separation and hypersonic flows. The document, a final report by M.S. Holden¹, although preliminary in nature, demonstrated the effect of surface roughness on a slender cone and its' apparent enhancement of flow separation. The fact that the only applicable document did not provide prediction techniques or insight into the degree of separation enhancement lead to the present investigation. The objective of this research program was to investigate the effect of fixed surface irregularities on the turbulent boundary layer characteristics in an adverse pressure gradient exhibiting flow separation. This program was also repeated on a smooth model and results to be compared. Using a high Reynold's number hypersonic wind tunnel, research on flow over the simple geometry of a flat plate with a compression corner (with and without surface roughness) was conducted. Qualitative evaluation of the flow field was obtained using Schlieren flow visualization techniques. Subsequent quantitative data acquisition, using appropriate pressure, temperature and velocity measurement systems was also carried out.

Facility

This investigation was carried out using the Flight Dynamics Laboratory, High Reynold's Number Mach 6 flow facility located in building 450. This wind tunnel is an open jet type blowdown facility (Figure 1). It is configured with a contoured axisymmetric nozzle having an exit diameter of approximately 12 inches (Figure 2). Side wall boundary layer effects reduce the actual test core to a diameter of approximately 10 inches. Stagnation pressures range from 700 to 2100 psia at a total temperature in the proximity of 1100°R. These conditions correspond to free stream unit Reynold's numbers ranging from 10×10^6 to 30×10^6 per foot. Air storage capability allows for extended run times of up to 25 minutes. For further details of the Mach 6 facility can be obtained, see Fiore and Law¹⁶.

Experiment

The present research program examined the "Effect of Surface Roughness on Turbulent Boundary Layer Separation at Mach 6.0". This work was divided into two phases. The first phase being the rough surface case and the second the smooth surface. Turbulent boundary layer characteristics on both smooth and roughened surfaces in an adverse pressure gradient were documented including the extent of separation. Unfortunately, at the time of this writing, phase II (smooth plate) data was not available for analysis.

Models

Two existing flat plate models simulating smooth and rough surface topography were used in the present study. The smooth flat plate has a number 32 surface finish. The roughened plate surface is configured with milled grooves or protuberances measuring .020" in height and .040" in the lateral and streamwise widths (Figure 3). The machined cavities separating the individual roughness elements in the cross stream and streamwise

directions measure .040". Starting location of the roughness pattern on the models was previously determined by calculations performed by Shang¹⁷. This distance was approximately 1.2" downstream of the plate's leading edge, where laminar-turbulent boundary layer transition was expected. The plates are 18.5 inches long, over 12" wide and feature a sharp 10 degree asymmetric leading edge. The presence of interchangeable spacers mounted at the model's trailing edge, provided the necessary adverse pressure gradient for flow separation near the ramp incidence. These spacers were (6° and 12°) placed under the instrumented ramp and provided ramp angles of 28° and 34° . In addition, the complete removal of the spacers provided for a 22° ramp angle. This allowed the instrumentation to be placed on the ramp only. Both models contain similar surface static pressure tap instrumentation positioned downstream of the leading edge for monitoring longitudinal and lateral pressure variations. Wall temperatures are measured using thermocouples that were embedded in the plate surface adjacent to the pressure taps.

Instrumentation

For the rough surface case, there were 24 static pressure ports on the flat plate portion of the model and 21 pressure ports on the ramp (Figure 4a & 4b, Table 1a & 1b). For the smooth plate phase, there were 32 surface (or static) pressure ports, connected to the transducers, on the flat plate portion of the model and 21 ports on the ramp. In both cases the pressure transducers used had a 15 PSID maximum.

Also, eight type J (iron/constantan) thermocouple junctions were present in the flat plate portion of the model. Note, no thermocouples were attached to the models ramp. Miniature pitot pressure and total temperature probes were mounted on the XYZ probe drive system located in the test chamber. The pitot pressure probe measured 0.020 inch in diameter and was

connected in parallel to two pressure transducers, thereby allowing for high resolution. The range of the transducers were 75 and 250 PSID. A total temperature probe based on the Winkler design was used in all tests. This probe had a outer dimension of 0.060 inches in diameter and a type K (chromel/alumel) thermocouple placed at the centerline of the probe. The probe recovery factor was determined for the present study to be 0.984.

Pneumatic and electrical signals from these devices are transmitted to their respective transducers and amplifier/reference junctions mounted external to the test cavity. The signals were then converted and transmitted to a Prime 650 mini-computer. In addition to test data acquisition, the computer provided for sensor calibration.

The experimental plate models are designed to extend the full width across the wind tunnel's open jet. However, the instrumented portion of the flat plates are only four inches wide and well within the test core of the exiting jet (see, Figures).

Experimental

All tests for the present investigation were performed at a nominal flow speed of Mach 6 over a free stream unit Reynolds number range of 10×10^6 to 30×10^6 per foot, incremented by units of 10×10^6 per foot. These high unit Reynolds numbers were achieved in the AF Wright Research and Development Centers Mach 6 facility, thus ensuring the existence of a turbulent boundary layer several inches downstream of the leading edge. The resulting boundary layer was documented at locations along the model's streamwise centerline upstream of the flat plate/ramp intersection at $x = -6.484$ and -2.172 inches and downstream of the intersection point at $x = +1.563$ inches. Documentation was accomplished by traversing pitot pressure and total temperature probes normal to the models surface in steps of 0.020

inches. Corresponding wall temperature and static pressure were also required for determining the velocity distribution within the shear layer. Both smooth and rough plate models employed the same procedure throughout the investigation.

All boundary layer traverses acquired upstream of the plate/ramp intersection point were taken perpendicular to the plates surface. The one exception that differentiates the probe traverses obtained at $x = + 1.563$ inches (on the ramp) is that the instrumentation location will be displaced, corresponding to the particular angle investigated. The measurement probe was rotated in such a manner to maintain a parallel position to the inclination and ensure that all traverses are normal to the ramp surface.

Schlieren photographs were also acquired to evaluate the interaction (separation) region on both smooth and textured models for all Reynold's number and ramp angle combinations. This optical system uses a standard single pass mirror/lens arrangement and a continuous light source. From these photographs an estimation of the angle of incipient separation was expected. Due to their poor quality, they are not included here.

This systematic experimental program utilized a large test matrix, constructed from a variety of pressure gradients and free stream unit Reynold's numbers, with the intent to demonstrate the effects of surface roughness on the turbulent boundary layer characteristics and flow separation in a hypersonic flow.

Results

In the present work, boundary layer characteristics were determined from the static and local total (pitot) flow conditions acquired at several streamwise measurement locations. Measurements included static pressures at 45 locations, wall temperatures at 8 locations and temperature and pressure probe traverses at 3 streamwise positions. Two of the probe measurement

locations, at $x = -6.484, -2.172$ inches, were upstream of the plate/ramp intersection, and the third located on the ramp at $x = +1.563$ inches downstream of the intersection point. By traversing a pitot pressure probe through the boundary layer, the local total pressure distributions were obtained for each of the three stagnation pressures tested. These reservoir pressures (700, 1400 and 2000 psia) correspond to approximate unit Reynolds numbers of $10 \times 10^6/\text{ft}$, $20 \times 10^6/\text{ft}$, and $30 \times 10^6/\text{ft}$, respectively.

Surface (or static) pressures were recorded for the flat plate-22, 28 and 34 degree ramp combinations. These surface pressures were normalized by the undisturbed static pressure obtained upstream (at $x = -6.727$ inches) of the interaction zone. The following figures also indicate the lateral variation of the surface pressure obtained at nominal locations of 0, ± 0.36 " and ± 2.00 ".

Figure 5, Flat plate 22 degree ramp, stagnation pressure - 700 psia

Figure 6, Flat plate 22 degree ramp, stagnation pressure - 1400 psia

Figure 7, Flat plate 22 degree ramp, stagnation pressure - 2000 psia

Figure 8, Flat plate 28 degree ramp, stagnation pressure - 700 psia

Figure 9, Flat plate 28 degree ramp, stagnation pressure - 1400 psia

Figure 10, Flat plate 28 degree ramp, stagnation pressure - 2000 psia

Figure 11, Flat plate 34 degree ramp, stagnation pressure - 700 psia

Figure 12, Flat plate 34 degree ramp, stagnation pressure - 1400 psia

Figure 13, Flat plate 34 degree ramp, stagnation pressure - 2000 psia

Tables listing the raw data acquired during the experiments are also included. The heading in each table specifies the case run, (i.e. rough flat plate) ramp angle, nominal stagnation pressure and data file number. The identification number and spatial location of the pressure ports are also included. Static pressures (P_s) are listed in millimeters of Mercury

(mmH_g). In addition, the P_s obtained at a given streamwise location has been nondimensionalized by the value obtained at port #6 ($x = -6.727$ ") and listed according to its lateral spatial location.

Table 2 Flat plate 22 degree ramp, stagnation pressure = 700 psia

Table 3 Flat plate 22 degree ramp, stagnation pressure = 1400 psia

Table 4 Flat plate 22 degree ramp, stagnation pressure = 2000 psia

Table 5 Flat plate 28 degree ramp, stagnation pressure = 700 psia

Table 6 Flat plate 28 degree ramp, stagnation pressure = 1400 psia

Table 7 Flat plate 28 degree ramp, stagnation pressure = 2000 psia

Table 8 Flat plate 34 degree ramp, stagnation pressure = 700 psia

Table 9 Flat plate 34 degree ramp, stagnation pressure = 1400 psia

Table 10 Flat plate 34 degree ramp, stagnation pressure = 2000 psia

The above format was repeated for the case of the flat plate 22° ramp combination incorporating side fences, Figure 14 and Table 11.

Figures 15, 16 and 17 compare the surface pressure distributions obtained on the model configured with the 22, 28 and 34 degree ramps respectively, in the absence of side fences for the three stagnation pressures tested. Figures 18, 19 and 20 compare the surface pressure distribution obtained at the three ramp angles for the stagnation pressures of 700, 1400 and 2000 psia, respectively. The final surface pressure distribution plot is a comparison of the 22 degree ramp model configuration with and without side fences for a stagnation pressure of 700 psia (Figure 21).

As previously mentioned, pitot pressure traverses (for the 22 degree ramp case only) were performed at the streamwise positions of $x = -6.484$, -2.172 and $+1.563$ inches along the surface of the model. These values were nondimensionalized by P_0 and plotted against the corrected distance measured

perpendicular to the plate surfaces. Based on the vertical height measure of the pitot probe's center and an estimation of the location of the virtual origin of the rough surface, a correction of 0.020 inches was applied to all raw transverse (z coordinate) locations. The following list of figures indicate the streamwise location and stagnation pressure conditions present during testing.

Figure 22a, x = -6.484 inches and stagnation pressure = 700 psia

Figure 23a, x = -6.484 inches and stagnation pressure = 1400 psia

Figure 24a, x = -6.484 inches and stagnation pressure = 2000 psia

Figure 25a, x = -2.172 inches and stagnation pressure = 700 psia

Figure 26a, x = -2.172 inches and stagnation pressure = 1400 psia

Figure 27a, x = -2.172 inches and stagnation pressure = 2000 psia

Figure 28, x = +1.563 inches and stagnation pressure = 700 psia

Figure 29, x = +1.563 inches and stagnation pressure = 1400 psia

Figure 30, x = +1.563 inches and stagnation pressure = 2000 psia

Similarly, tables were compiled listing tunnel conditions, probe location, local static pressure and wall temperature as well as the momentum thickness (θ). Note that the wall temperature was determined by an interpolation of local wall temperature measurements. Unfortunately, this could only be done upstream of the plate/ramp intersection point due to the absence of temperature instrumentation on the ramp. The main section of the tables are divided into eight columns in which the transverse position of the probe, pitot pressure, both dimensionally and normalized, Mach Number, total temperature, static temperature, speed of sound and velocity are tabulated. Exception to this format are the traverses obtained above the ramp surface, where transverse position of the probe, pitot pressure, both dimensionally and normalized, are included. This change is a result of an

inability to obtain a value for the static pressure over the ramp. The following is a list of the pitot pressure tables.

Table 12 x = -6.484 inches and stagnation pressure = 700 psia

Table 13 x = -6.484 inches and stagnation pressure = 1400 psia

Table 14 x = -6.484 inches and stagnation pressure = 2000 psia

Table 15 x = -2.172 inches and stagnation pressure = 700 psia

Table 16 x = -2.172 inches and stagnation pressure = 1400 psia

Table 17 x = -2.172 inches and stagnation pressure = 2000 psia

Table 18 x = +1.563 inches and stagnation pressure = 700 psia

Table 19 x = +1.563 inches and stagnation pressure = 1400 psia

Table 20 x = +1.563 inches and stagnation pressure = 2000 psia

Nondimensional pitot pressure profile combinations for the three stagnation pressures tested are given in Figures 31, 32 and 33 for x = -6.484, -2.172 and +1.563 inches, respectively. Also, plotted in Figures 34, 35 and 36 is the streamwise variation of pitot pressure for stagnation pressures of 700, 1400 and 2000 psia, respectively.

Utilizing the assumption that the static-pressure through the boundary layer is constant upstream of the interaction region, the Mach number distributions were calculated for all cases except those at x = +1.563 inches, where this assumption is not valid. Using the Fayleigh-pitot equation;

$$\left[\frac{\gamma+1}{2} M^2 \right]^{\gamma/\gamma-1} \left[\frac{\frac{\gamma+1}{2}}{\gamma M^2 - \frac{(\gamma-1)}{2}} \right]^{1/\gamma-1} = \frac{P_t}{P_s}$$

one can determine the Mach number. That is, once the working fluid is known, the ratio of specific heat (γ) can be selected and by iterating the Mach number, M, one can determine its value such that the pressure ratio calculated is equal to the ratio measured in the test, pitot pressure/free

stream static pressure. As previously mentioned, the value of Mach number as a function of position are tabulated in Tables 11 through 16 and plotted in the following figures.

Figure 22b, x = -6.484 inches and stagnation pressure = 700 psia

Figure 23b, x = -6.484 inches and stagnation pressure = 1400 psia

Figure 24b, x = -6.484 inches and stagnation pressure = 2000 psia

Figure 25b, x = -2.172 inches and stagnation pressure = 700 psia

Figure 26b, x = -2.172 inches and stagnation pressure = 1400 psia

Figure 27b, x = -2.172 inches and stagnation pressure = 2000 psia

Mach number combination plots are also included at x = -6.484 and -2.172 inches for the three stagnation pressures tested (Figures 37 and 38). Similarly, at a constant stagnation pressure the streamwise variation in Mach number is also presented (Figures 39, 40 and 41).

Total temperature distributions throughout the boundary layer were also acquired at the three streamwise measurement locations. As with the pitot pressure traverses, the probe position reading was corrected to take into account both the rough surface and effective location of the thermocouple within the probe. An effective correction of 0.040 inches was applied to all raw transverse (z coordinate) locations.

To take into account the various heat losses from the probe, a correction factor was estimated to be

$$K = \frac{T_{ind} - T_{\infty}}{T_t - T_{\infty}} = 0.984$$

Therefore all temperatures indicated by the probe, (column 3) in the data tables, were corrected in column 4 of the total temperature data sheets. Column 5 lists the stagnation temperature and column 6 the nondimensional total temperature. The following are the associated figures and tables.

Figure 42a, T_t at $x = -6.484$ inches and stagnation pressure = 700 psia

Figure 42b, Normalized T_t at $x = -6.484$ inches and $P_0 = 700$ psia

Figure 43a, T_t at $x = -6.484$ inches and $P_0 = 1400$ psia

Figure 43b, Normalized T_t at $x = -6.484$ inches and $P_0 = 1400$ psia

Figure 44a, T_t at $x = -6.484$ inches and $P_0 = 2000$ psia

Figure 44b, Normalized T_t at $x = -6.484$ inches and $P_0 = 2000$ psia

Figure 45a, T_t at $x = -2.172$ inches and $P_0 = 700$ psia

Figure 45b, T_t at $x = -2.172$ inches and $P_0 = 700$ psia

Figure 46a, T_t at $x = -2.172$ inches and $P_0 = 1400$ psia

Figure 46b, Normalized T_t at $x = -2.172$ inches and $P_0 = 1400$ psia

Figure 47a, T_t at $x = -2.172$ inches and $P_0 = 2000$ psia

Figure 47b, Normalized T_t at $x = -2.172$ inches and $P_0 = 2000$ psia

Figure 48a, T_t at $x = +1.563$ inches and $P_0 = 700$ psia

Figure 48b, Normalized T_t at $x = +1.563$ inches and $P_0 = 700$ psia

Figure 49a, T_t at $x = +1.563$ inches and $P_0 = 1400$ psia

Figure 49b, Normalized T_t at $x = +1.563$ inches and $P_0 = 1400$ psia

Figure 50a, T_t at $x = +1.563$ inches and $P_0 = 2000$ psia

Figure 50b, Normalized T_t at $x = +1.563$ inches and $P_0 = 2000$ psia

Table 21 Total temperature at $x = -6.484$ inches, $P_0 = 700$ psia

Table 22 Total temperature at $x = -6.484$ inches, $P_0 = 1400$ psia

Table 23 Total temperature at $x = -6.484$ inches, $P_0 = 2000$ psia

Table 24 Total temperature at $x = -2.172$ inches, $P_0 = 700$ psia

Table 25 Total temperature at $x = -2.172$ inches, $P_0 = 1400$ psia

Table 26 Total temperature at $x = -2.172$ inches, $P_0 = 2000$ psia

Table 27 Total temperature at $x = +1.563$ inches, $P_0 = 700$ psia

Table 28 Total temperature at $x = +1.563$ inches, $P_0 = 1400$ psia

Table 29 Total temperature at $x = +1.563$ inches, $P_0 = 2000$ psia

Similarly, the effect of stagnation pressure (or Reynolds number) on the normalized total temperature at each streamwise measurement location ($x = -6.484$, -2.172 and $+1.563$ inches) are examined in Figures 51, 52 and 53, respectively. Likewise, the streamwise variation of the temperature ratio can be seen Figures 54, 55 and 56 for stagnation pressures of 700, 1400 and 2000 psia, respectively.

Using the adiabatic relation between Mach number and temperature ratio (T_s/T_c) the static temperatures (T_s) throughout the boundary layer at $x = -6.484$ and -2.172 inches were calculated (Figures 22c to 27c). Figures 57 and 58 compare the effect of stagnation pressure variation on the static temperature at $x = -6.484$ and -2.172 inches, respectively. Similarly, Figures 59, 60, and 61 compare the streamwise static temperature variation at a constant stagnation pressure. Once the value of T_s was determined, the local speed of sound (c) and hence the local mean velocity was determined (Figures 22d to 27d). Figures 62 and 63 display the variation in velocity at $x = -6.484$ and -2.172 inches as the stagnation pressure is varied. Rearranging, one can view this velocity variation over the streamwise measurement stations for constant stagnation pressures (Figures 64, 65 and 66).

The present boundary layer velocity distributions at $x = -2.172$ " were then compared (Figures 67, 68 and 69) to both the $1/7$ power law profile and

the profile obtained using the Van Driest¹⁸ velocity transformation. Based on the knowledge of the local P_s and T_s throughout the boundary layer, the magnitude of the local density and the momentum thickness (θ) was determined using;

$$\theta = \int_0^{\infty} \frac{\rho u}{\rho_e u_e} \left(1 - \frac{u}{u_e}\right) dy$$

Discussion

In this investigation, detailed documentation of the boundary layer characteristics and the extent of separation (x_s) were obtained both upstream and downstream of the ramp intersection point. An examination of the surface pressure distributions in Figures 5 to 14 clearly indicate the extent of separation and the two-dimensional nature of the flow. From a comparison of surface pressures obtained at $y = 0$ and $y = \pm 0.36$ inches, it can be concluded that the assumption of two-dimensionality is correct over the center portion of the plate through the interaction zone. To further check the two-dimensionality of the flow, side fences were added to the model. No notable difference in the surface pressure was observed (Figure 21). Assuming the location of the inflection point in the surface pressure distributions (Figures 5 to 14) to be the location of separation point (x_s), then x_s for the 22 degree ramp (Figure 15) can be estimated to be approximately 0.9 inches upstream of the plate/ramp intersection point in the low Re ($P_0 = 700$ psia) case and approximately 1.1 inch upstream for the medium ($P_0 = 1400$ psia) and high Re ($P_0 = 2000$ psia) case. If we estimate the value of x_s in the 28 degree (Figure 16) and 34 degree (Figure 17) ramp cases, it's magnitude increases to approximately 3.0 and 5.5 inches, respectively, but appears not to change as the unit Reynolds number is

increased from 10 to 30 million/ft. This increase in x_s , as the ramp angle increases (i.e., 22, 28 and 34 degrees), can be seen in Figures 18, 19 and 20 for the Reynolds Numbers tested. In addition, these ramp angle combination plots indicate an increase in the plateau pressure ratio as the angle was increased.

As previously stated, Figures 22a to 27a and Figures 28 to 30 indicate the individual pitot pressure distributions obtained at the three streamwise measurement stations for the stagnation pressures tested. To gain insight into the effect of Reynolds number on the normalized pitot pressure profiles (Figures 31, 32 and 33), comparisons were made at each of the streamwise measurement locations. For $x = -6.484$ inches (Figure 31) the profiles were observed to become fuller as the Reynolds number decreased (i.e., the P_0 dropped from 2000 psia to 700 psia). At $x = -2.172$ inches (Figure 32) the same trend with Re was observed, whereas at $x = +1.563$ inches (Figure 33) no significant difference was found between $P_0 = 700$ and 2000 psia, which were found to have a fuller profile than the $P_0 = 1400$ psia case. In addition, the peak values were found to vary by a couple of percent. As one may expect, if a streamwise comparison is made at a constant stagnation pressure, a sizable overshoot or peak in the pitot pressure would be observed. This is a result of the local shock structure in the reattachment region. Specifically, as can be observed in Figure 34, the peak P_t/P_0 is approximately 3.5 times larger than the pressure ratio obtained at the edge of the boundary layer, upstream of the interaction zone. Similarly, for the medium and high Re cases (Figures 35 and 36, respectively) an increase of 300 to 350 percent was noted.

Figures 22b to 27b show the Mach number distribution as a function of corrected distance (z) away from the wall, for the three Re cases tested. From these figures, it appears that the indicated free stream mach number for all three cases is approximately 5.9. Further, Figures 37 and 38 suggest that the boundary layer is slightly thinner at the lower Re# case at $x = -6.484$ inches, but takes on the proper trend at $x = -2.172$ inches and becomes thinner as the unit Re is increased from 10 to 30 million/ft. Although one would expect a greater thinning of the boundary layer as the Re was increased from 10 to 20 million/ft, this short fall was probably due to the forward movement of the separation point. Also, an examination of Figures 39, 40 and 41 indicate a fuller Mach number profile at $x = -6.484$ inches.

The corrected T_t and normalized temperature ratio is plotted in Figures 42a to 50a and 42b to 50b, respectively. To allow for a direct evaluation the affect of Re on the normalized temperature, see Figures 51, 52 and 53. At streamwise locations upstream of the ramp, the Re affect was relatively weak and the normalized total temperature was observed to overshoot the stagnation temperature by 2 to 4 percent. Examining this variable on the ramp at $x = +1.563$ inches, a noticable difference was recorded for the high Re case. Further, to this writer's knowledge, this is the first time a bimodal character was observed in T_t/T_0 . In addition, the occurrence of this double peak in the total temperature produced an overshoot that appeared to be approximately 10 to 30 greater than T_0 .

This increase in T_t is a result of the combined viscous and turbulent shear stresses in the outer portion of the boundary layer doing work on the fluid to increase its internal energy, hence, increasing the temperature of the fluid in the inner region of the boundary layer. This was observed at

Profiles determined for $x = -6.484$ inches show no difference between the $P_0 = 1400$ and 2000 psia cases, but there appears to be a fuller profile for the 700 psia case. In addition, a slightly thinner boundary layer is indicated. The same holds for $x = -2.172$ inches with a small difference evident between the $P_0 = 1400$ and 2000 psia cases. Comparing both x stations (Figures 64, 65 and 66) it is apparent that the profiles become fuller at $x = -2.172$ inches. Although some spread in the velocity is found close to the wall, all tests appear to converge at a freestream velocity of approximately 3200 ft/sec. The momentum thicknesses at $x = -2.172$ inches, were determined to be 0.00999 , 0.0109 and 0.01117 inches for Re of 10 , 20 and 30 million/ft.

Finally, Figures 67, 68 and 69 indicate the deviation of the experimental data from both the $1/7$ power law formulation and the Van Driest velocity transformation. The lack of fullness of the velocity profile near the wall is believed to be a result of the momentum loss in the boundary layer flow. That is, it is felt that this loss is a result of the shocklets and wakes produced by the individual roughness elements.

Summary

An experimental investigation into the effects of a rough surface on turbulent boundary layer characteristics at hypersonic speeds has been undertaken. These experiments were carried out on a rough flat plate/ramp combination at a nominal Mach number of 6 for unit Reynolds numbers of approximately 10 , 20 and 30 million/ft. The roughened surface geometry consisted of machined proturbances 0.020 inches high and 0.040 inches in both length and width, with spacing between the individual elements of 0.040 inches.

The results of the surface pressure distributions indicate a two-dimensional flow on the model. To further assure and verify two-dimensionality, fences were added to the model at the position of the intersection region. Comparison of the surface pressure distributions with and without the fences proved excellent. Using the first inflection point in the surface pressure distribution as an indication of separation, the extent of separation, x_s , was determined. It was estimated that x_s , for the 22 degree ramp case, moved upstream by approximately 10 percent as the unit Re was increased from 10 to 30 million/ft. For the 28 and 30 degree ramps, x_s increased to 3 inches and 5.5 inches, respectively, and appeared to be independent of Reynolds number, although the plateau pressure ratio was sensitive to Re .

Pitot pressure profiles obtained perpendicular to the ramp surface reached levels approximately 3.5 times greater than the freestream pitot pressure at all Reynold's numbers tested. Total temperature profiles acquired perpendicular to the ramp surface indicated a bimodal character. This double maximum was found to exceed the stagnation temperature by 5 to 30 percent. It is felt that this increase in T_t is a result of the combined turbulent/viscous shear stresses in the outer portions of the boundary layer, doing work on the fluid to increase its internal energy, hence, increasing the temperature of the fluid in the linear region of the boundary layer.

A comparison of the experimentally determined velocity to the profiles calculated using both the 1/7th power law form and the Van Driest velocity transformation was performed. These results indicated that the experimentally obtained velocity profile was not as full near the wall, representing a reduction in momentum. This momentum loss is believed to be a result of the viscous/turbulent dissipation resulting from the rough

surface. That is, this loss is a result of the shocklets and wakes produced on and by the individual roughness elements.

Acknowledgements

The writer would like to express his gratitude and thanks to Mr. C. Fox for his computer processing wizardry and Mr. R. DiMicco for his meticulous review and help in the preparation of this report. Also, a special thanks is extended to Mr. N.E. Scaggs of the AF Flight Dynamics Laboratory, for his support and assistance during the research program.

This project was sponsored by the United States Air Force Office of Scientific Services, Bolling A.F.B., Washington, D.C., and the Flight Dynamics Laboratory, Wright-Patterson A.F.B.

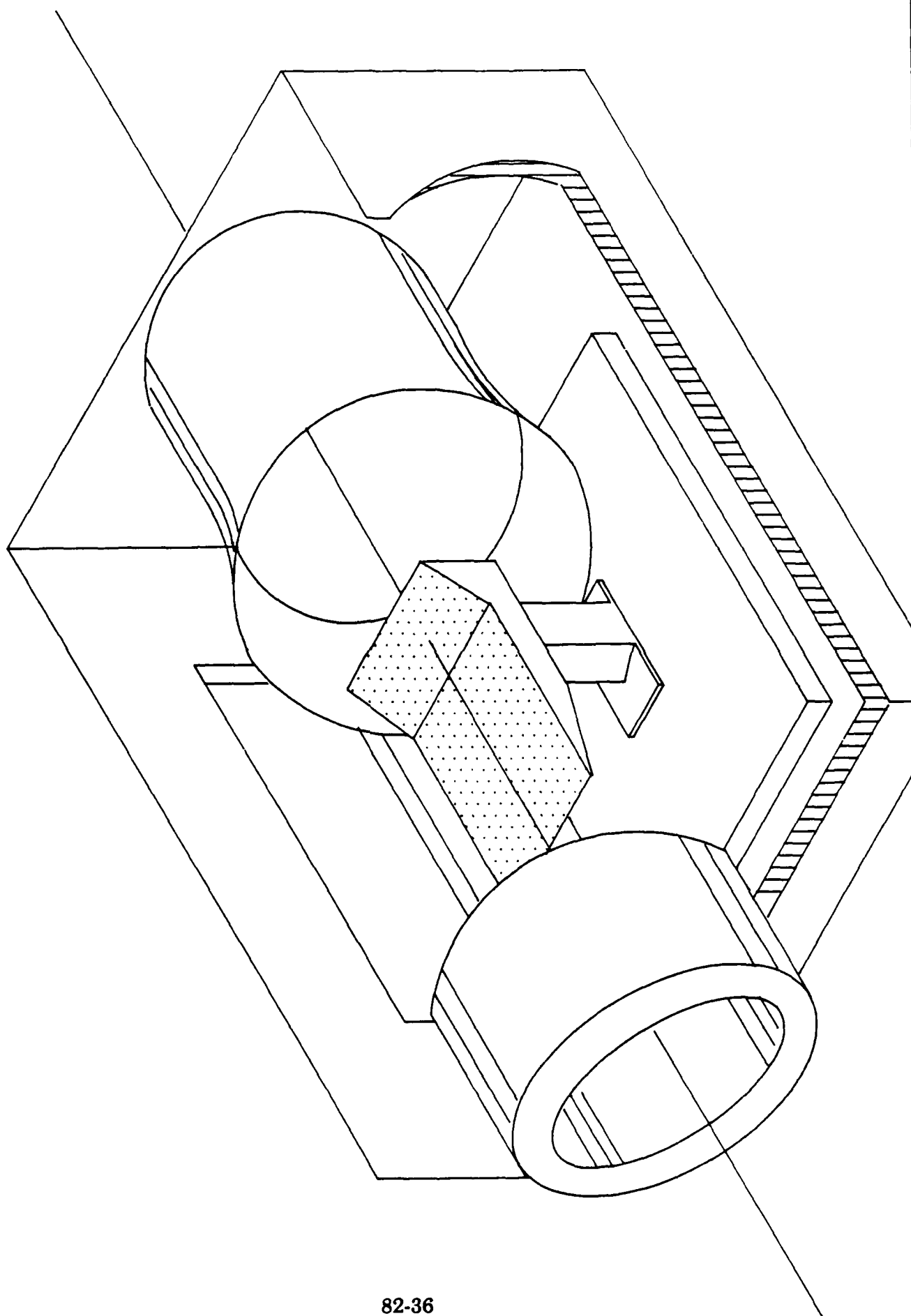
REFERENCES

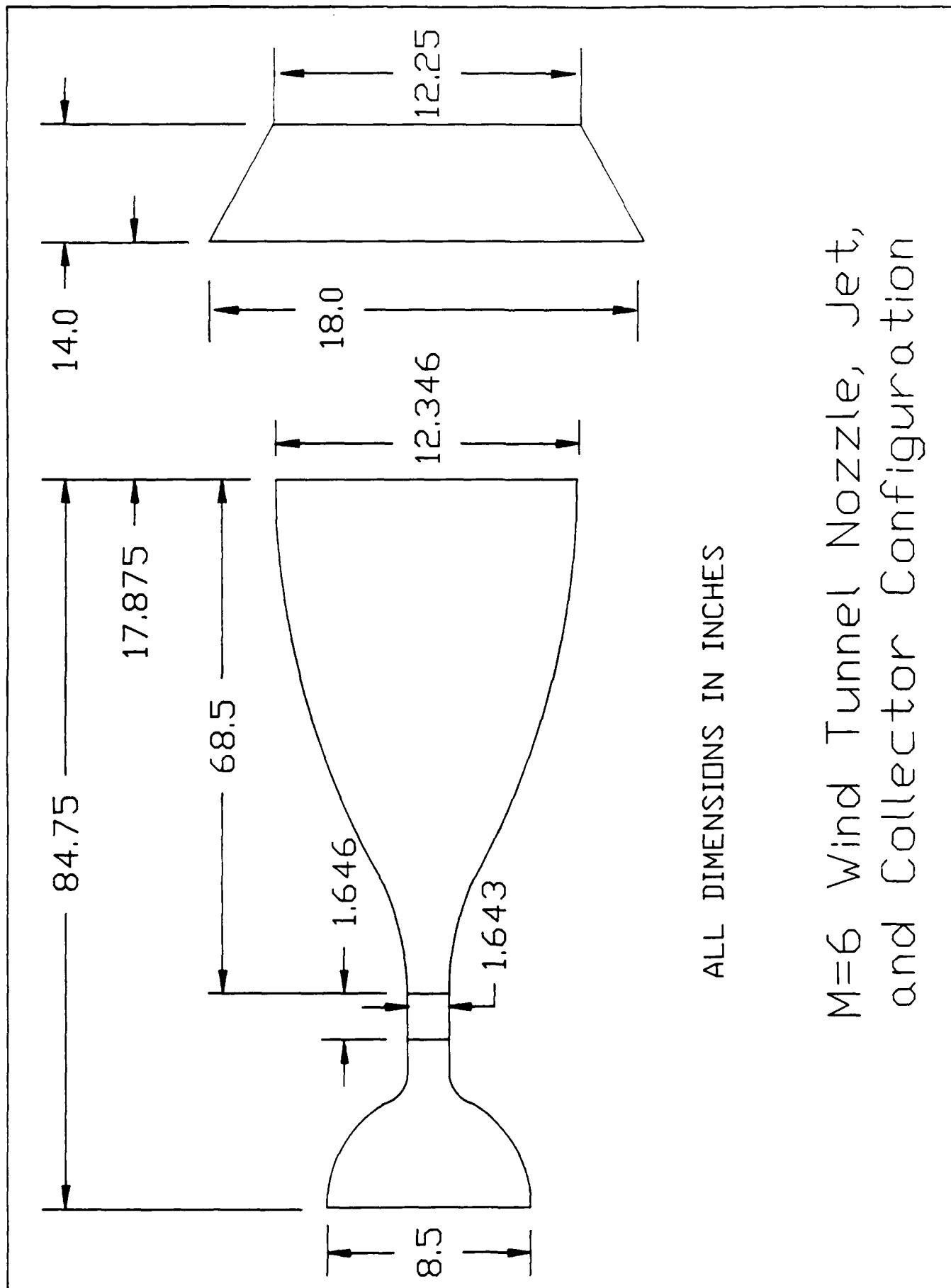
- (1) Holden, M.S., "Studies of Boundary Layer Transition and Surface Roughness Effects in Hypersonic Flow," Final Report #6430-A-5, AFOSR, October 1983.
- (2) Holden, M.S., "A Review of Aerothermal Problems Associated with Hypersonic Flight," presented as paper #86-0267 at the AIAA 24th. Aerospace Sciences Meeting, Reno, Nevada, January 6-9, 1986.
- (3) Bogdonoff, S.M., Vas, I.E., Settles, G.S. and Simper, G., "Research on Supersonic Turbulent Separated and Reattached Flows," Final Report, ARL 75-0220, Aerospace Research Laboratory, Wright-Patterson AFB, Dayton, OH, June 1975.
- (4) Kuehn, D.M., "Turbulent Boundary-Layer Separation Induced by Flares on Cylinders at Zero Angle of Attack," NASA Tech. Report, TR R-117, 1961.
- (5) Kuehn, D.M., "Experimental Investigation of the Pressure Rise Required for the Incipient Separation of Turbulent Boundary Layers in Two-Dimensional Supersonic Flow," NASA MEMO 1-21-59A, February 1959.

- (6) Roshko, A. and Thomke, G.J., "Supersonic, Turbulent Boundary-Layer Interaction with a Compression Corner at Very High Reynolds Number," Viscous Interaction Phenomena in Supersonic and Hypersonic Flow Symposium, May 1969, held at the USAF, Aerospace Research Laboratories, Dayton, p 109.
- (7) Sterrett, J.R. and Emery, J.C., "Experimental Separation Studies for Two-Dimensional Wedges and Curved Surfaces at Mach Numbers of 4.8 to 6.2," NASA Tech. Note, TN D-1014, February 1962.
- (8) Todisco, A. and Reeves, B.L., "Turbulent Boundary Layer Separation and Reattachment at Supersonic and Hypersonic Speeds," Viscous Interaction Phenomena in Supersonic and Hypersonic Flow, Symposium, May 1969, held at the USAF, Aerospace Research Laboratories, Dayton, Ohio, p 139.
- (9) Goddard, F.E., Jr., "Effect of Uniformly Distributed Roughness on Turbulent Skin-Friction Drag at Supersonic Speeds," J. of the Aero/Space Sciences, Vol. 26, #1, pp 1, January 1959.
- (10) Young, F.L., "Experimental Investigation of the Effects of Surface Roughness in Compressible Turbulent Boundary Layer Skin Friction and Heat Transfer," Defense Research Laboratory, Report DRL-532, The University of Texas at Austin, May 1965.
- (11) Reda, D.C., Ketter, F.C., Jr., and Fan, C., "Compressible Turbulent Skin Friction on Rough and Rough/Wavy Walls," J. AIAA, Vol. 13, #5, May 1975.
- (12) Thompson, M.J., "Skin Friction and Heat Transfer in Turbulent Boundary Layers as Influenced by Roughness," Applied Research Laboratory, Report ARL-TR-70-43, December 1970.

- (13) Christoph, G.H. and Fiore, A.W., "Numerical Simulation of Flow Over Rough Surfaces, Including Effects of Shock Waves," USAF, Flight Dynamics Laboratory, Final Report, AFWAL-TR-83-3071, Dayton, OH, August 1983.
- (14) Fiore, A.W. and Christoph, G.H., "Roughness Effects on Turbulent Boundary Layer Profiles at $M = 6$ " presented at the 1983 U.S.A.F.-DVFLR Data Exchange Meeting on Viscous and Interacting Flow Field Effects.
- (15) Disimile, P.J., "The Effects of Surface Roughness on Turbulent Boundary Layer Separation at Hypersonic Speeds," 1986 U.S.A.F.-UES Summer Faculty Research Program Final Report, September 1986.
- (16) Fiore, A.W. and Law, C.H., "Aerodynamic Calibration of the Aerospace Research Laboratories M-6 High Reynolds Number Facility," USAF, Aerospace Research Laboratory Final Report, ARL TR 75-0028, February 1975.
- (17) Shang, J.S., Hankey, W.L., and Dyer, D.L., "Compressible Turbulent Boundary Solutions Employing Eddy Viscosity Models," Aerospace Research Laboratories Report No. ARL-73-0041, Wright-Patterson Air Force Base, Dayton, Ohio, March, 1973.
- (18) Van Driest, E.R., "Turbulent Boundary in Compressible Fluids," J. of Aero. Sci. Vol. 18, No. 3, March 1951, P 145-160.

Figure 1 Wind Tunnel Facility Overview

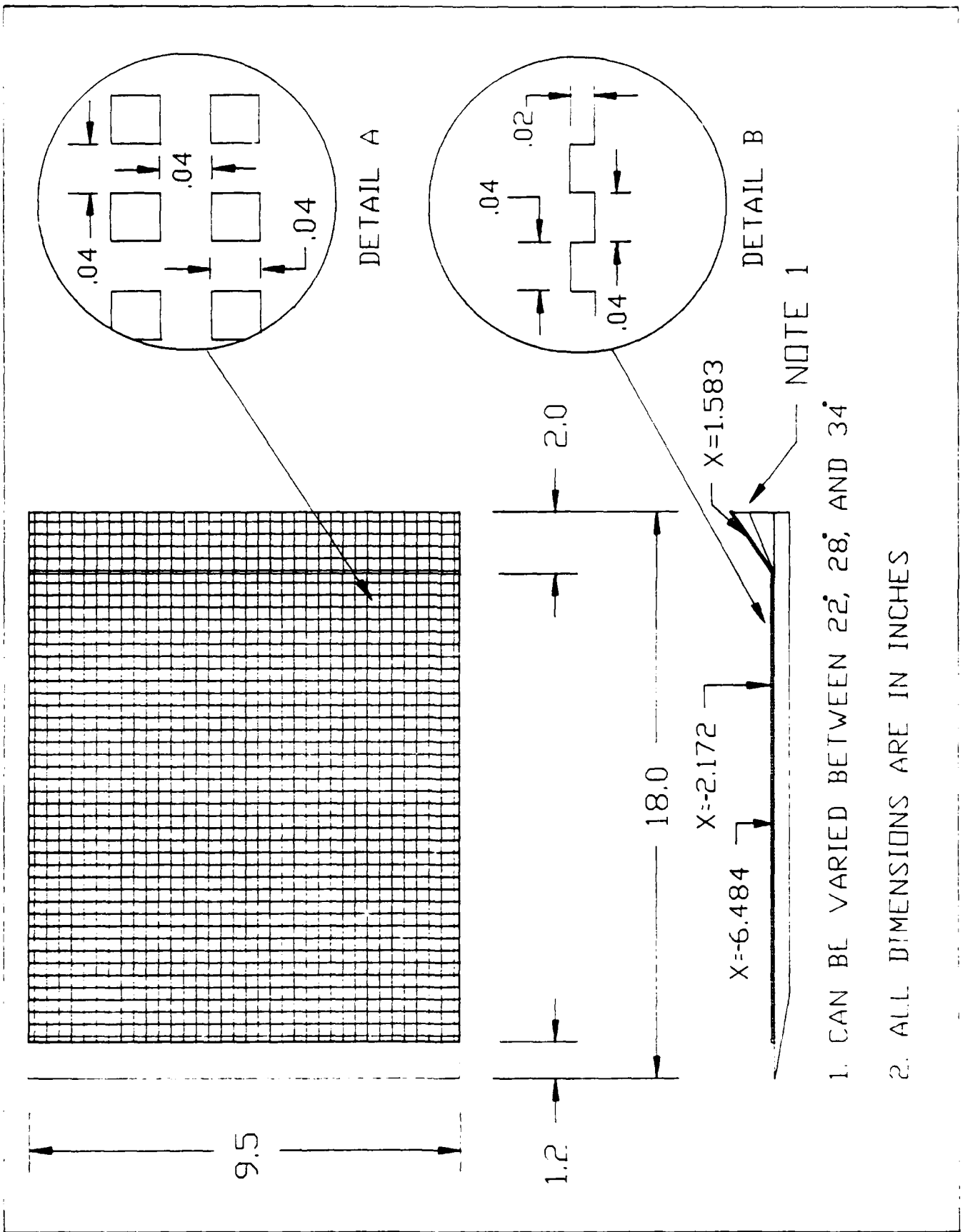




ALL DIMENSIONS IN INCHES

M=6 Wind Tunnel Nozzle, Jet,
and Collector Configuration

Figure 2 Detailed Nozzle/Jet/Collector Configuration



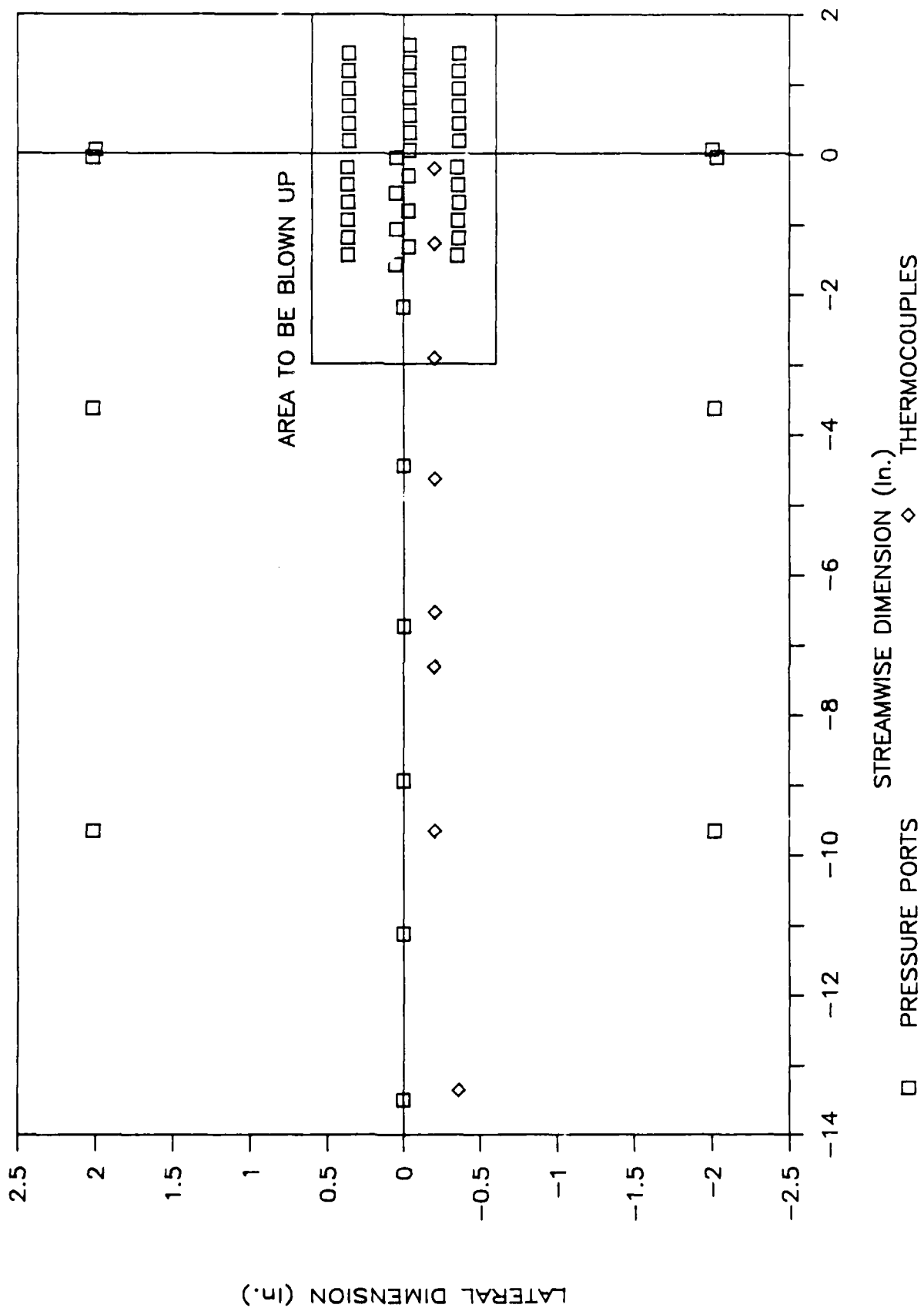
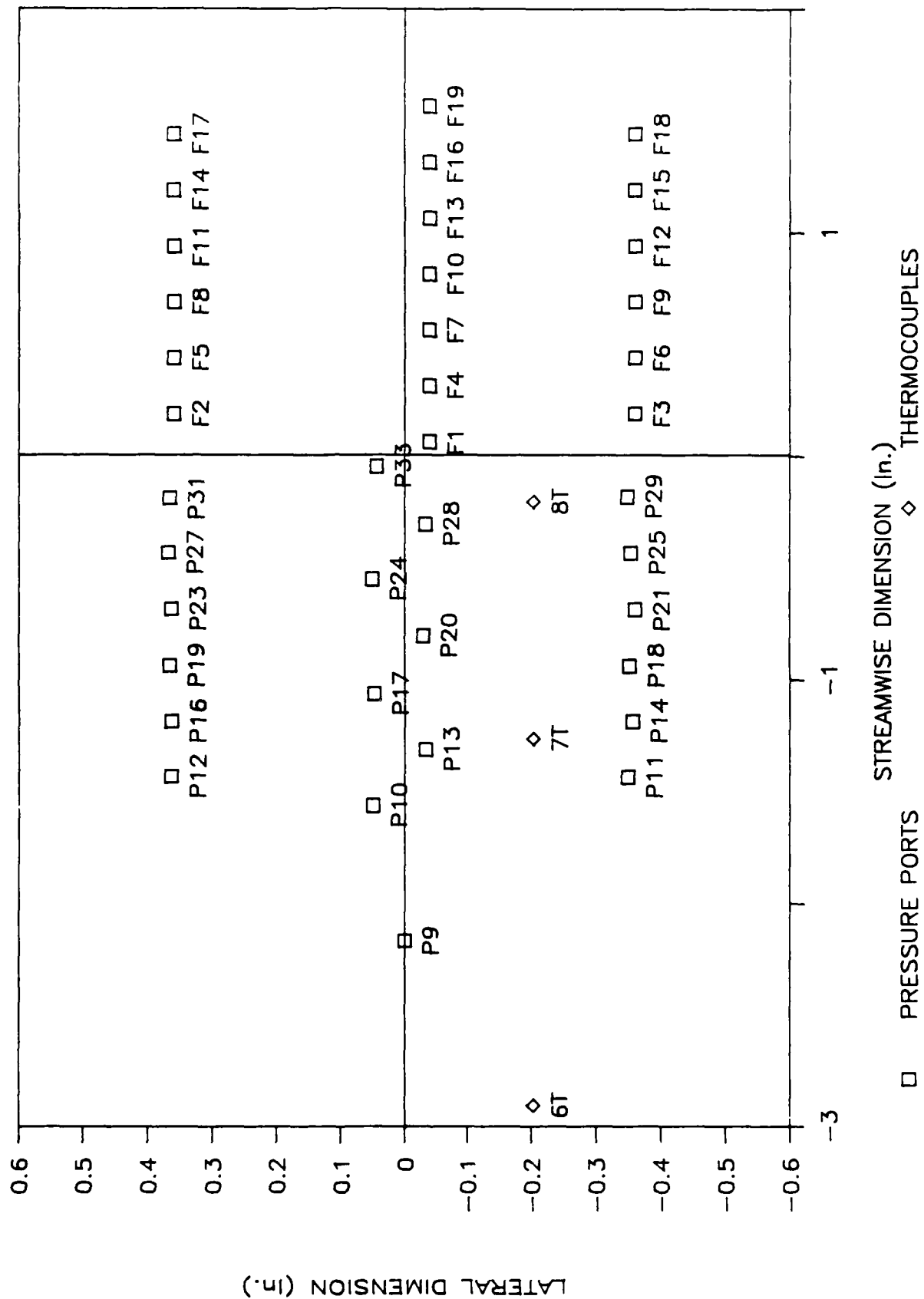


Figure 4a Model Instrumentation Locations



ROUGH PLATE 22 DEG. RAMP

Po=700 Psia, FILE=HPSR2150

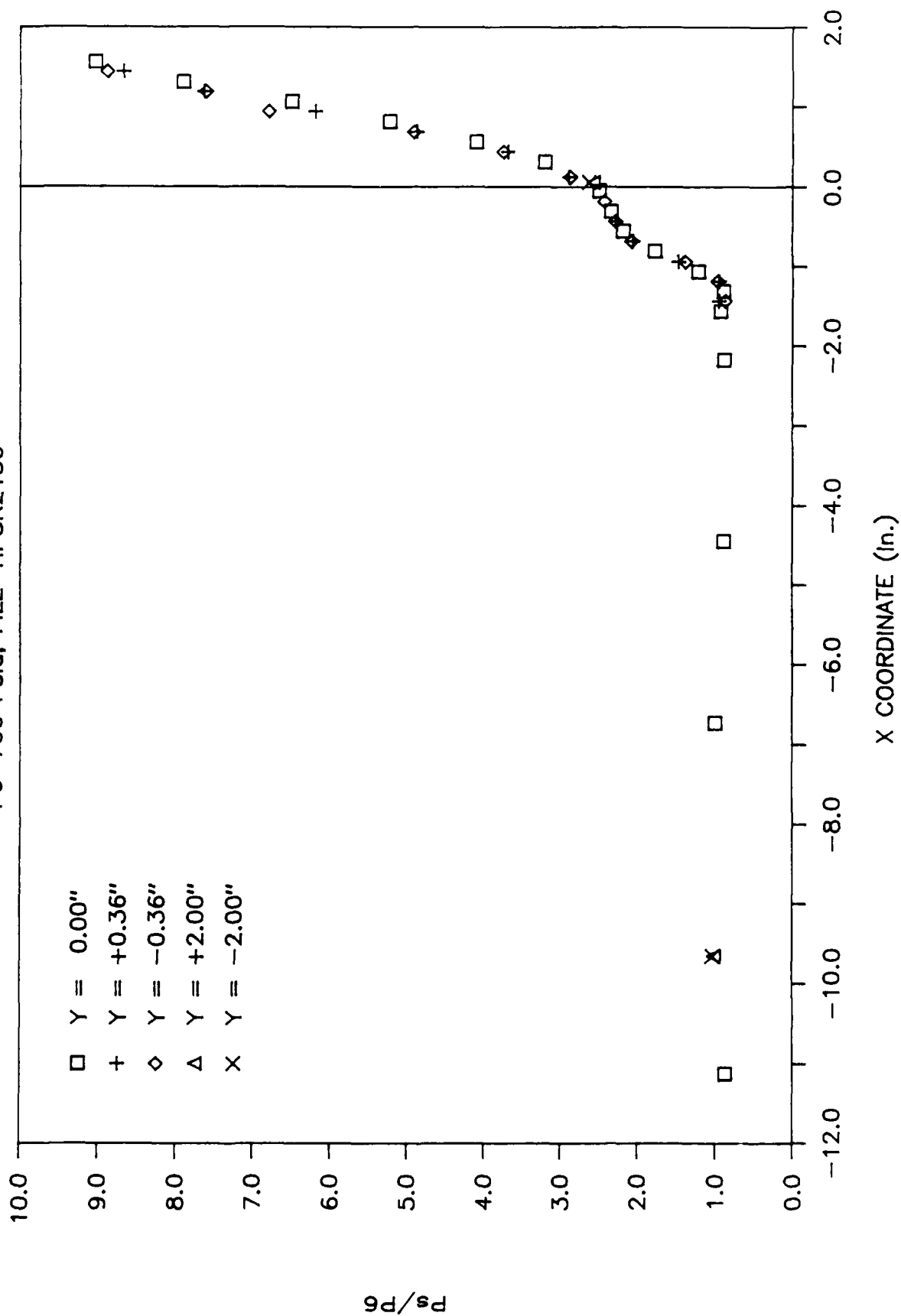


Figure 6 Nondimensionalized Surface Pressures at a Given Ramp Angle and Stagnation Pressure

ROUGH PLATE 22 DEG. RAMP

$P_o = 1400$ Psia, FILE=HPSR2149

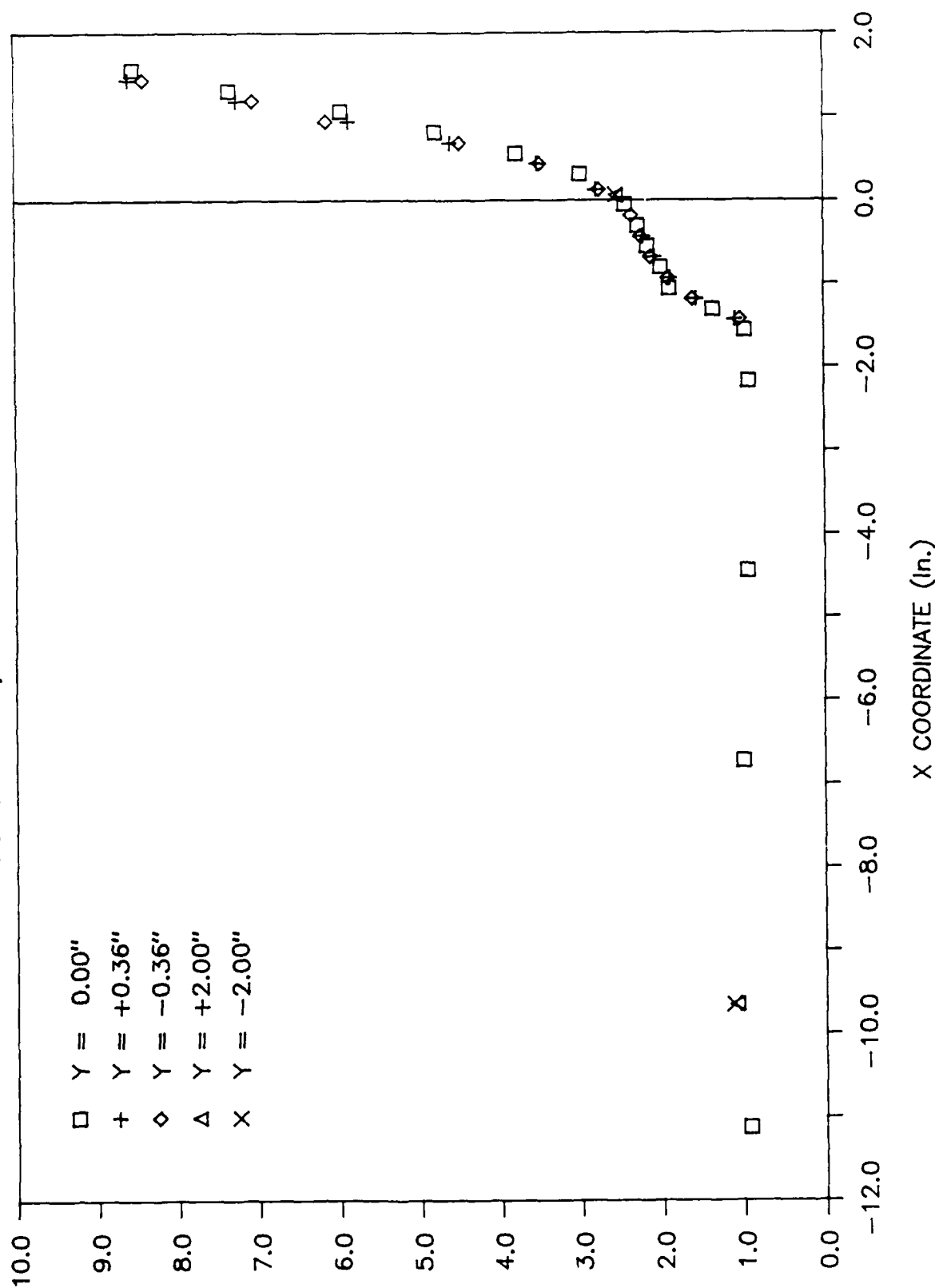


Figure 6 Nondimensionalized Surface Pressures at a Given Ramp Angle and Stagnation Pressure

ROUGH PLATE 22 DEG. RAMP

Po=2000 Psia, FILE=HPSR2148

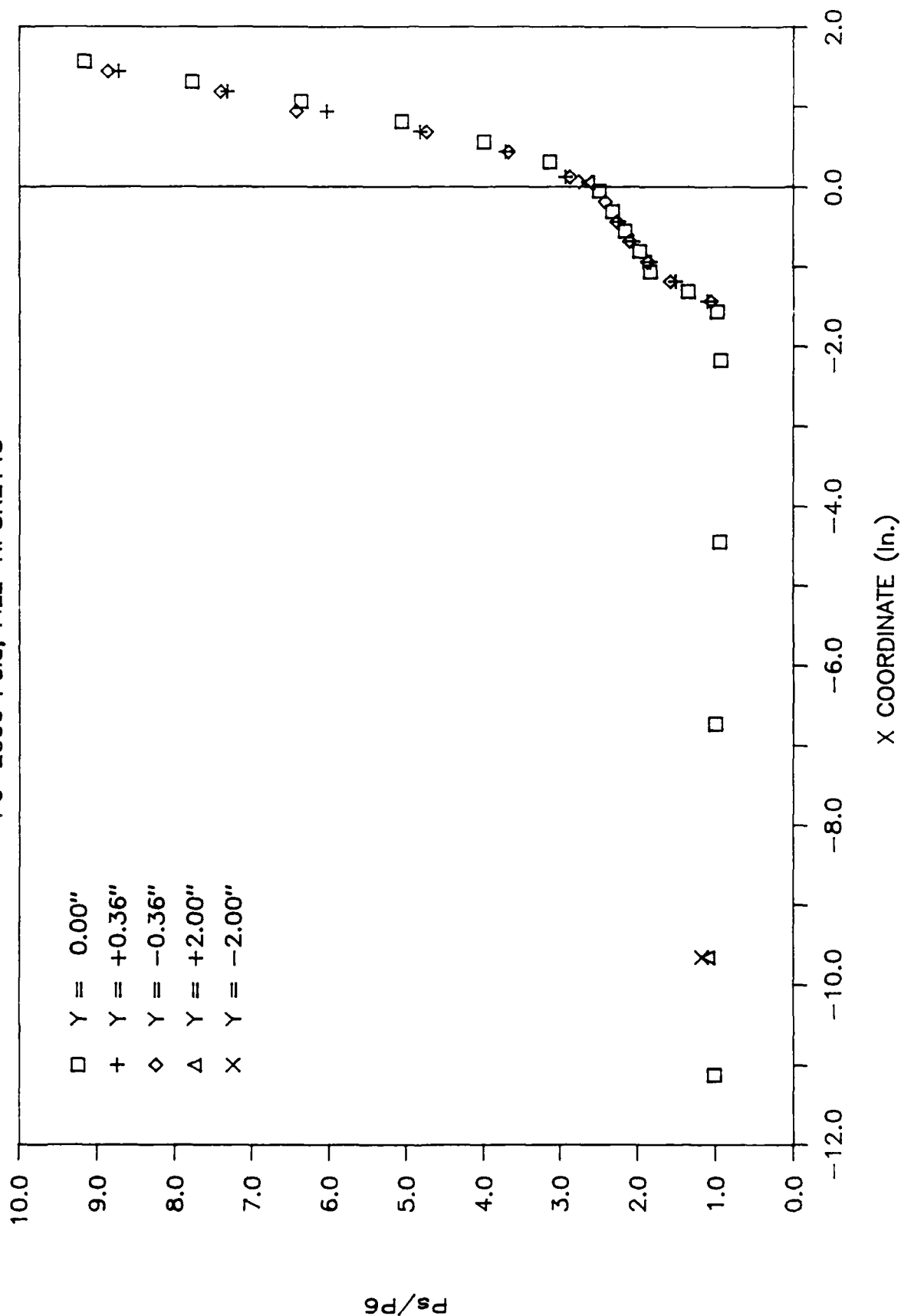


Figure 7 Nondimensionalized Surface Pressures at a Given Ramp Angle and Stagnation Pressure

ROUGH PLATE 28 DEG. RAMP

Po=700 Psia, FILE=HPSR2186

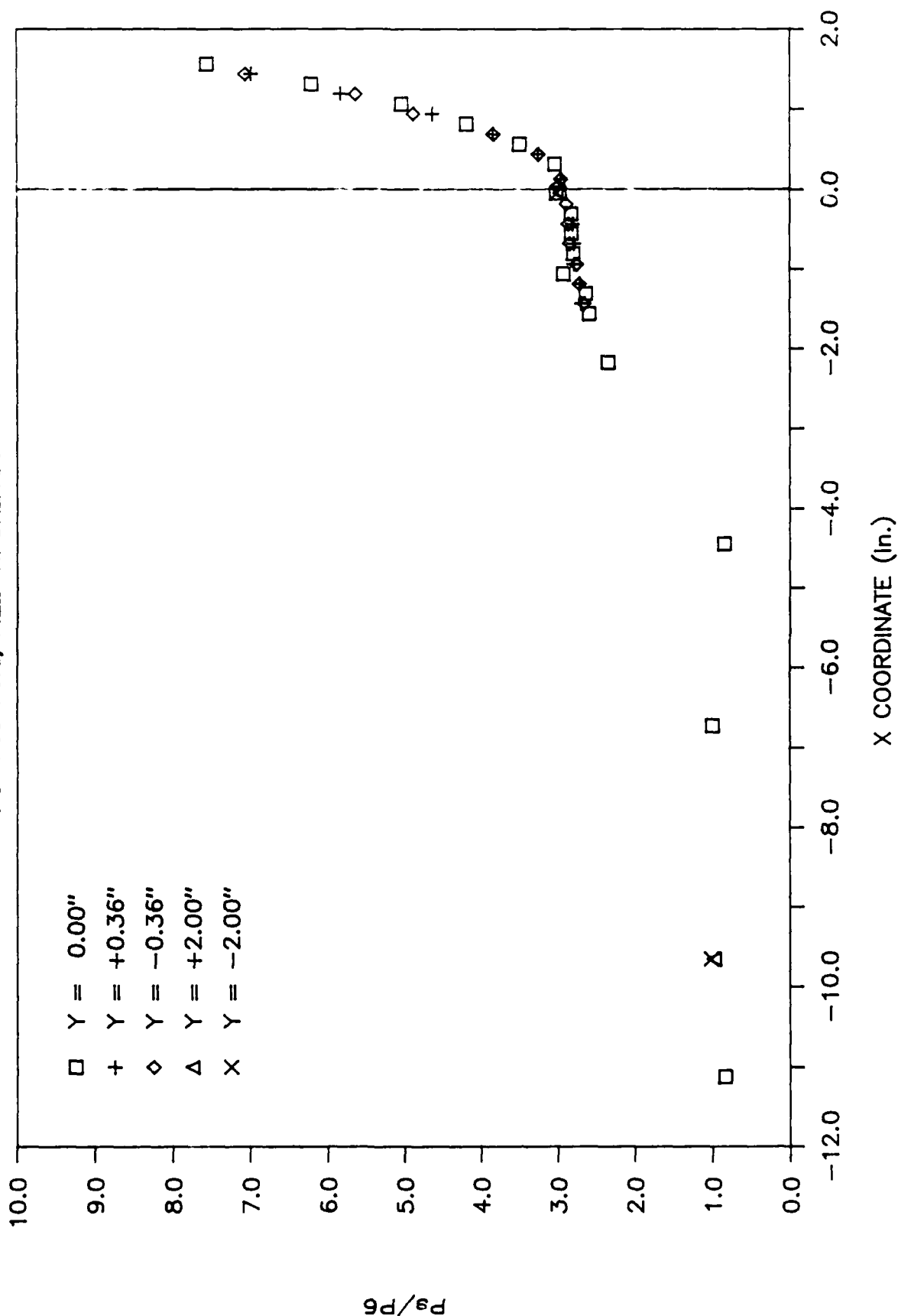


Figure 8 Nondimensionalized Surface Pressures at a Given Ramp Angle and

ROUGH PLATE 28 DEG. RAMP

Po=1400 Psia, FILE=HPSR2185

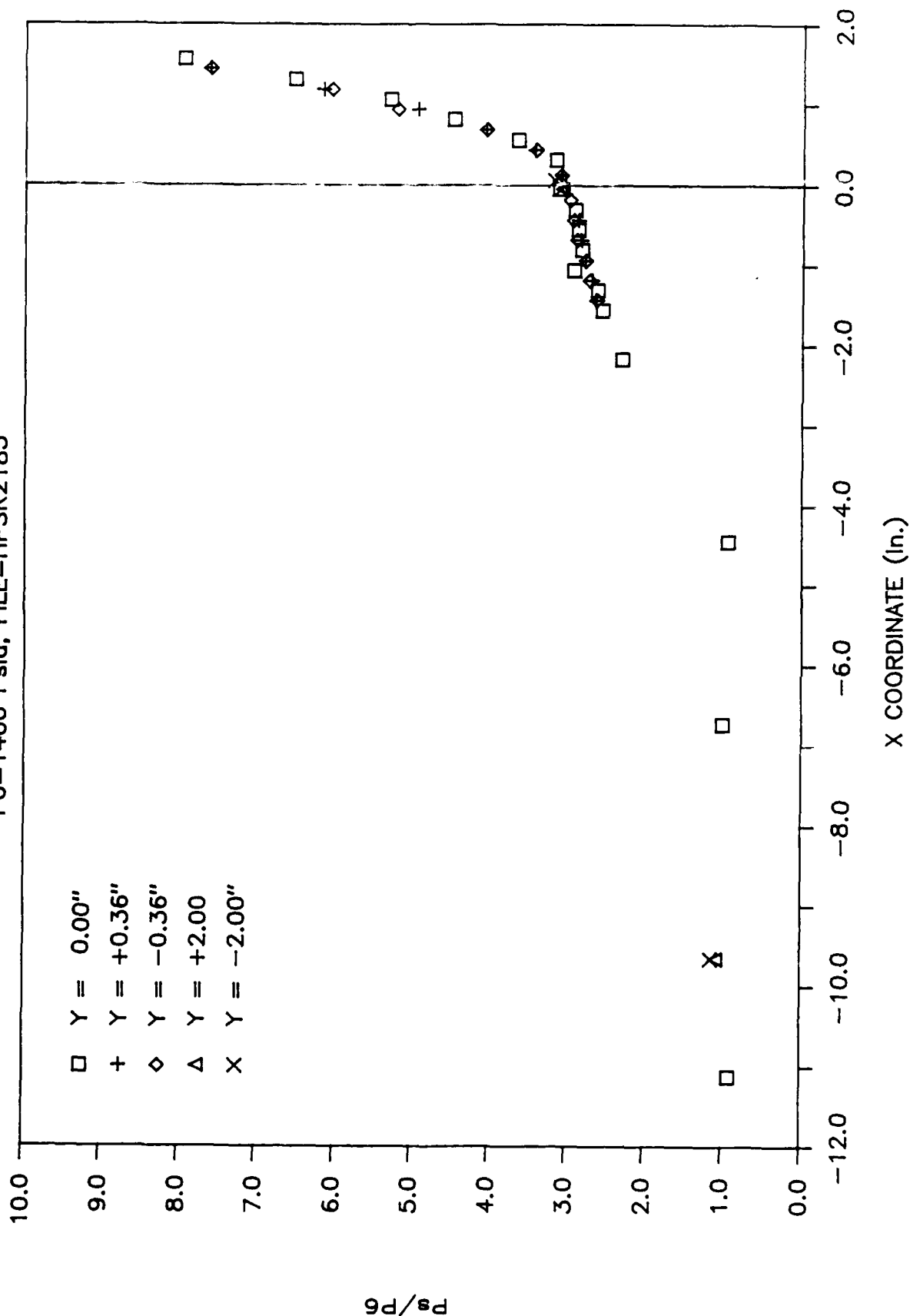


Figure 9 Nondimensionalized Surface Pressures at a Given Ramp Angle and Stagnation Pressure

ROUGH PLATE 28 DEG. RAMP

Po=2000 Psia, FILE=HPSR2184

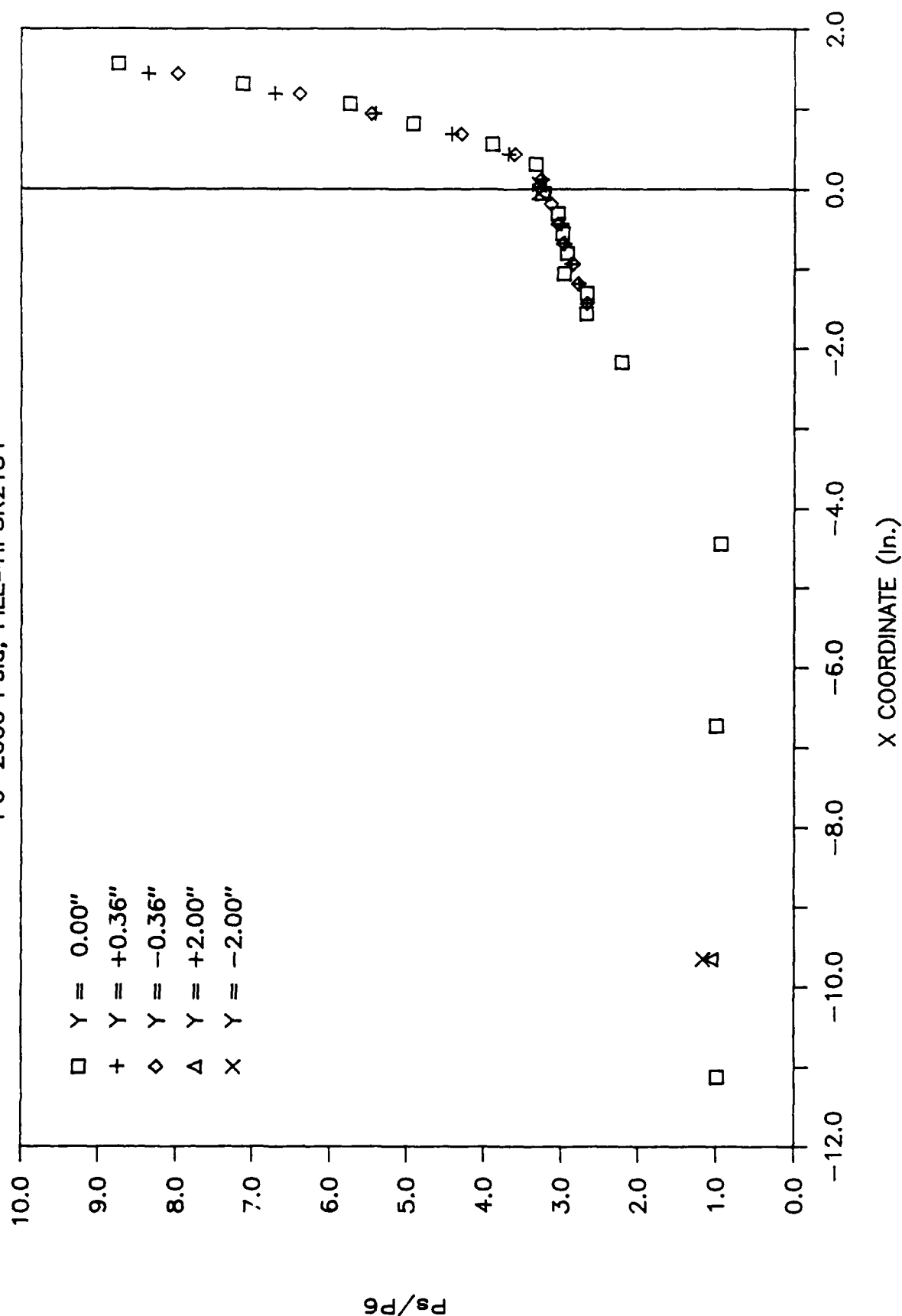


Figure 10 Nondimensionalized Surface Pressures at a Given Ramp Angle and

ROUGH PLATE 34 DEG. RAMP

Po=700 Psia, FILE=HPSR2192

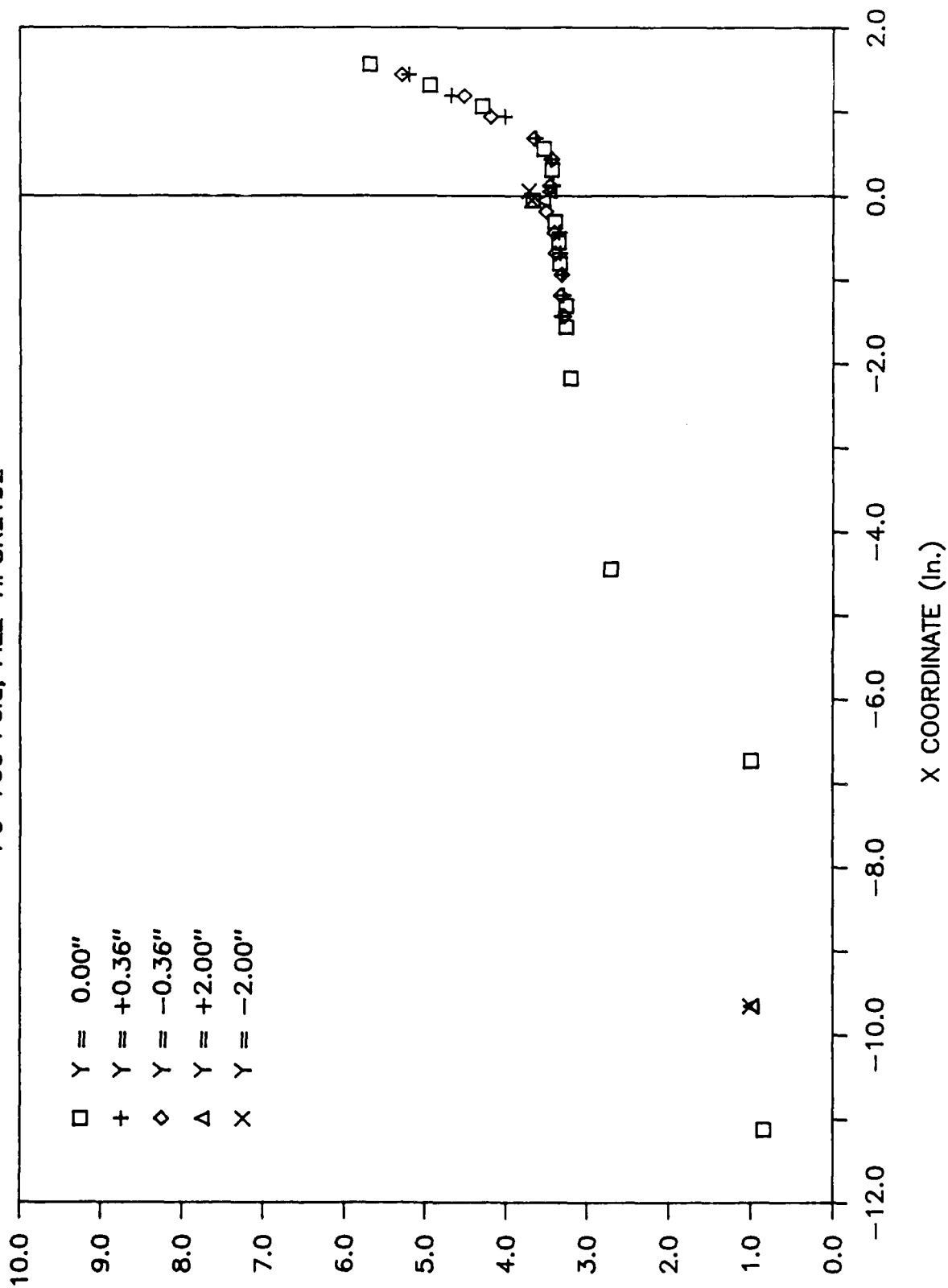


Figure 11 Nondimensionalized Surface Pressures at a Given Ramp Angle and Stagnation Pressure

ROUGH PLATE 34 DEG. RAMP

Po=1400 Psia, FILE=HPSR2191

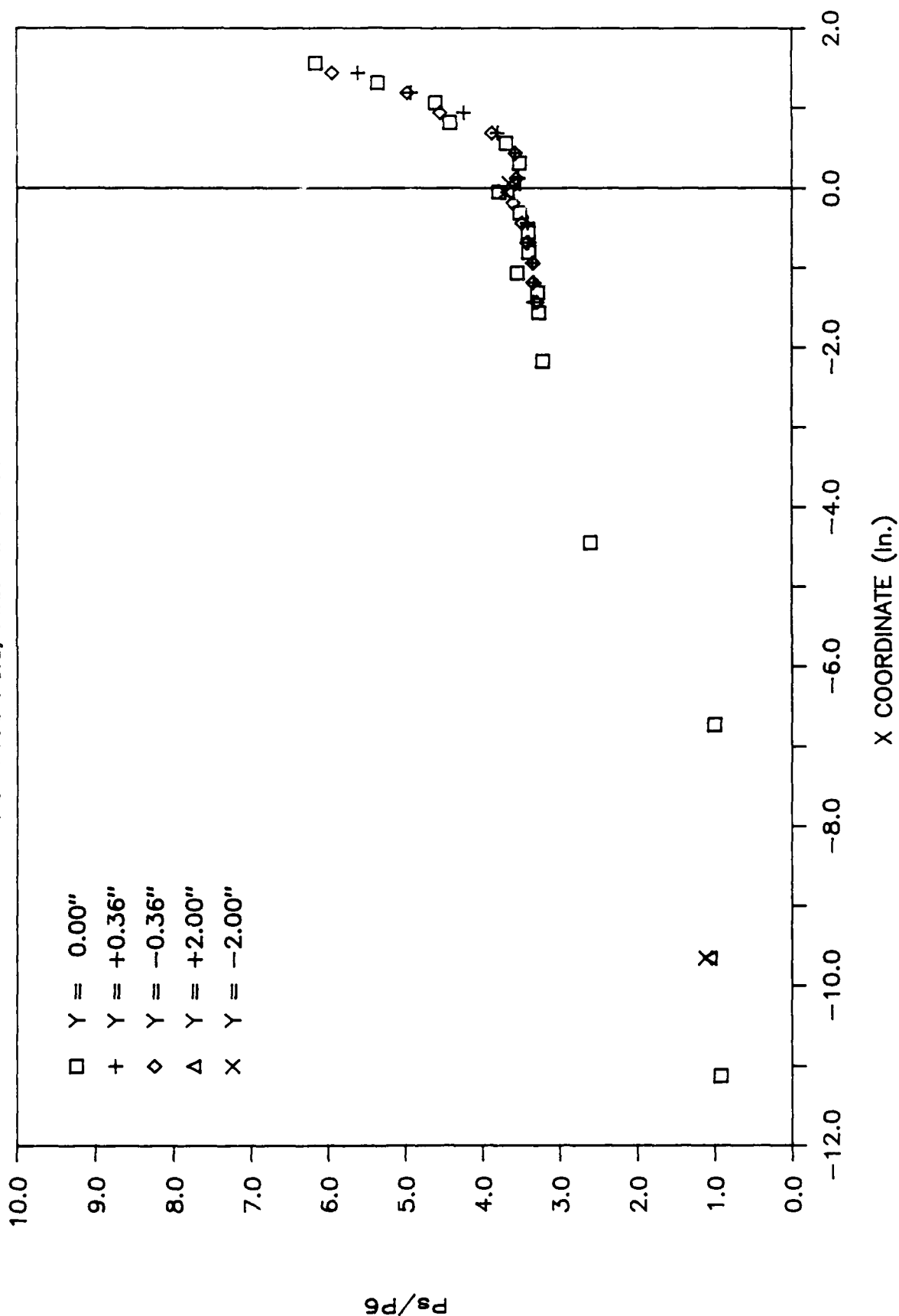


Figure 12 Nondimensionalized Surface Pressures at a Given Ramp Angle and Stagnation Pressure

ROUGH PLATE 34 DEG. RAMP

Po=2000 Psia, FILE=HPSR2188

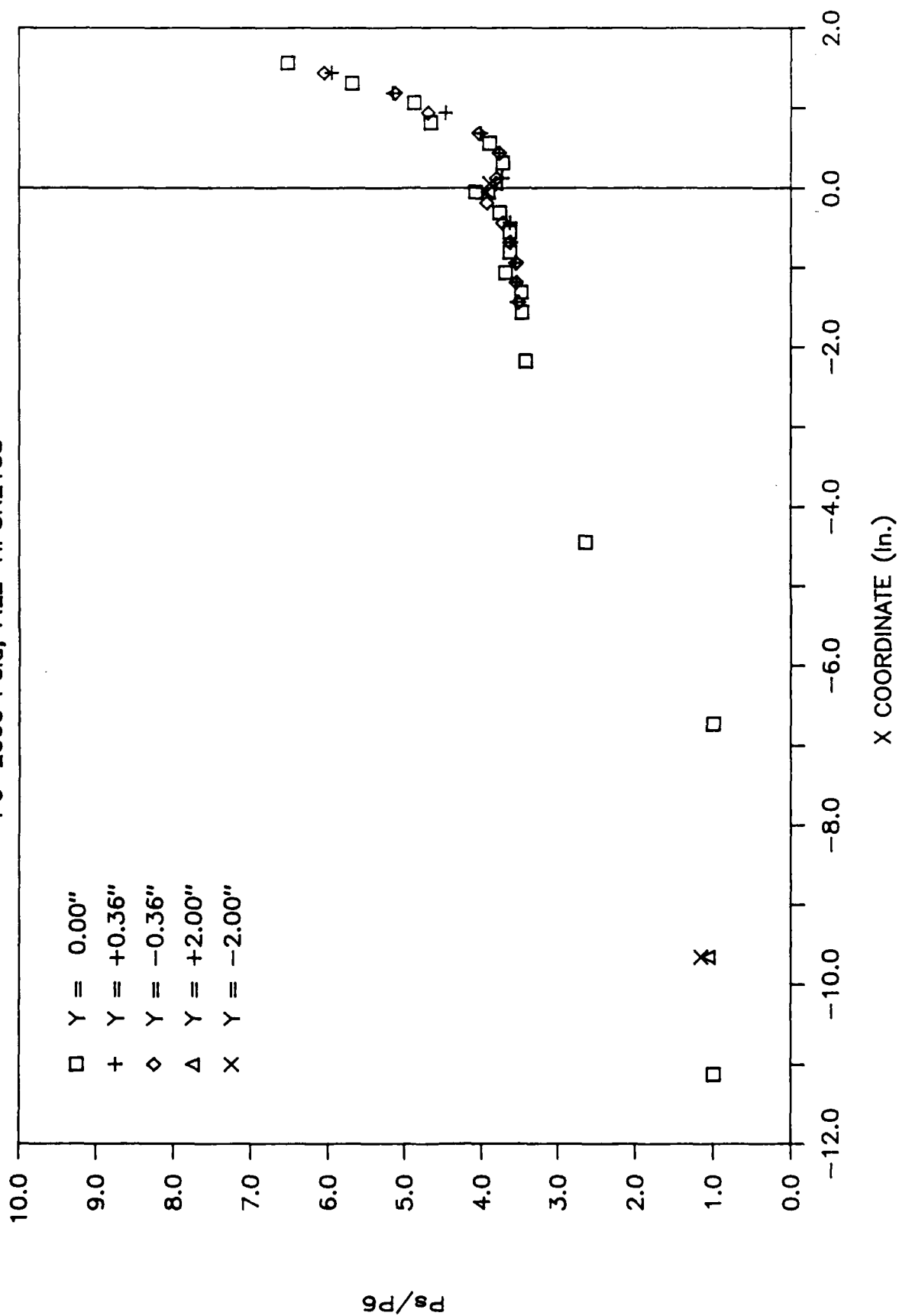


Figure 13 Nondimensionalized Surface Pressures at a Given Ramp Angle and Stagnation Pressure

ROUGH PLATE 22 DEG. RAMP WITH FENCE

Po=700 Psia, FILE=HPSR2166

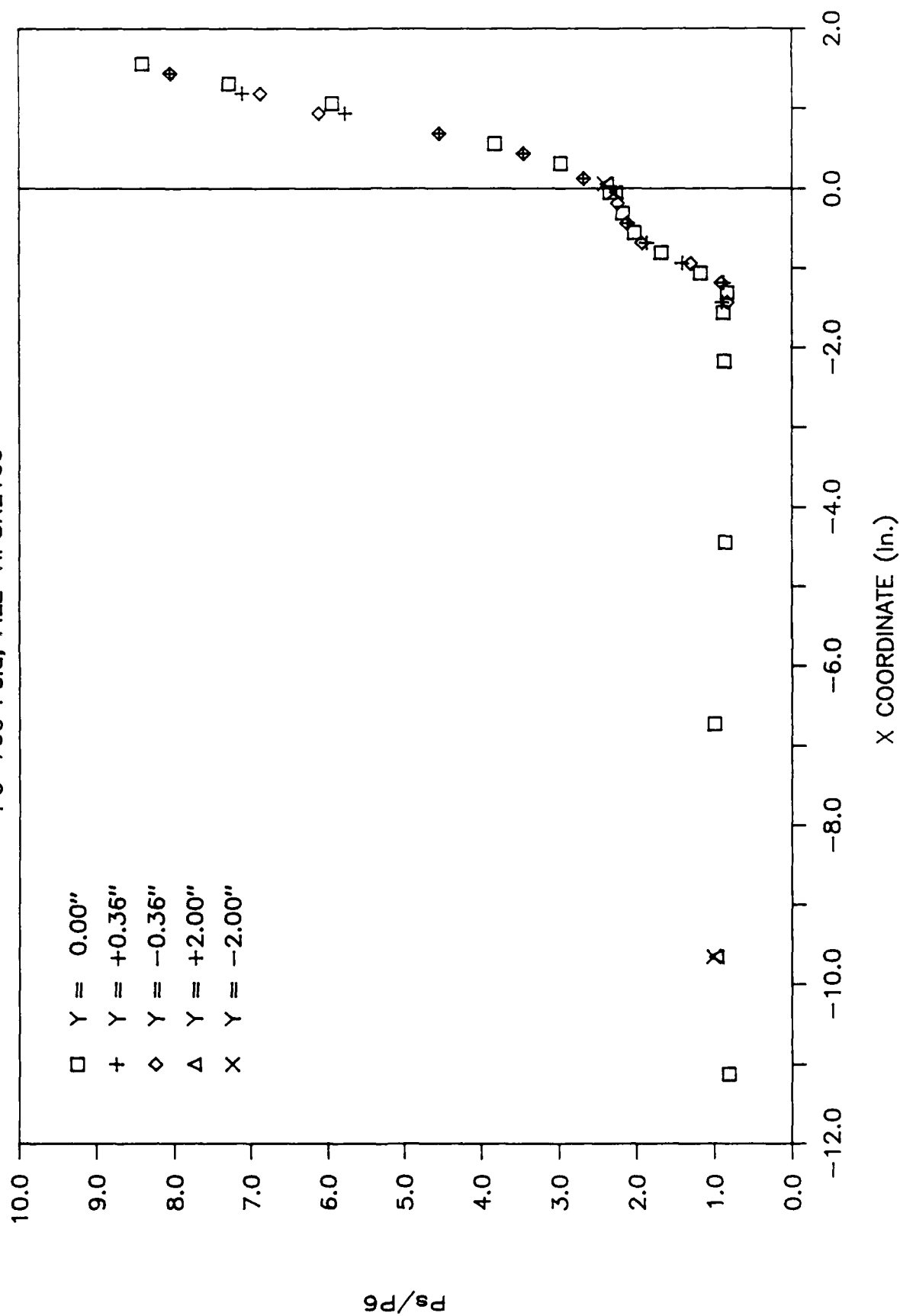


Figure 14 Nondimensionalized Surface Pressures with Side Fences at a Given Ramp Angle

ROUGH PLATE 22 DEG. RAMP

$P_o=700,1400,2000$ Psia, FILE=PSRCOMB2

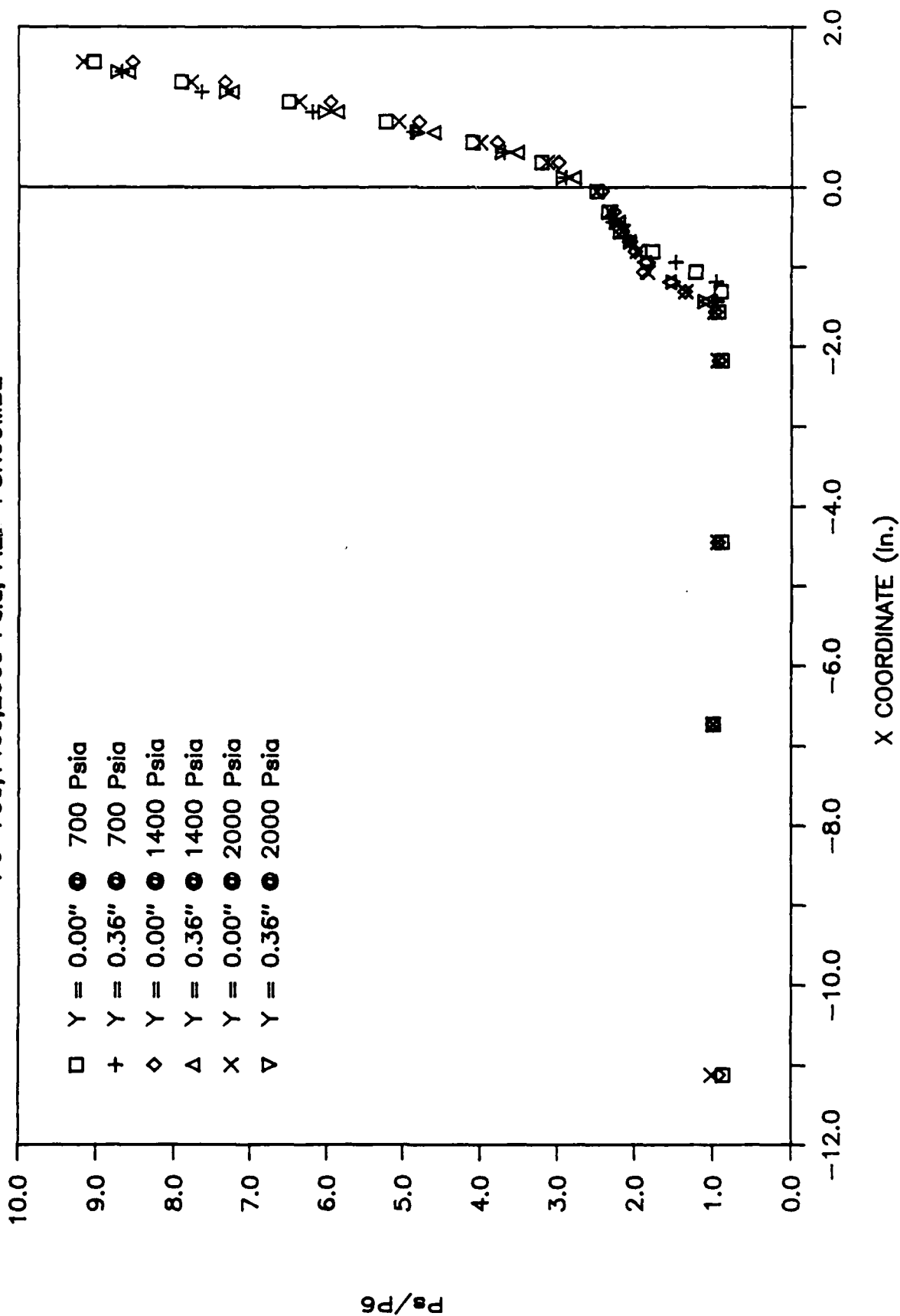


Figure 15 Combined Nondimensionalized Surface Pressures at a Given Ramp Angle

ROUGH PLATE 28 DEG. RAMP

$P_o=700, 1400, 2000$ Psia, FILE=PSRCOMB1

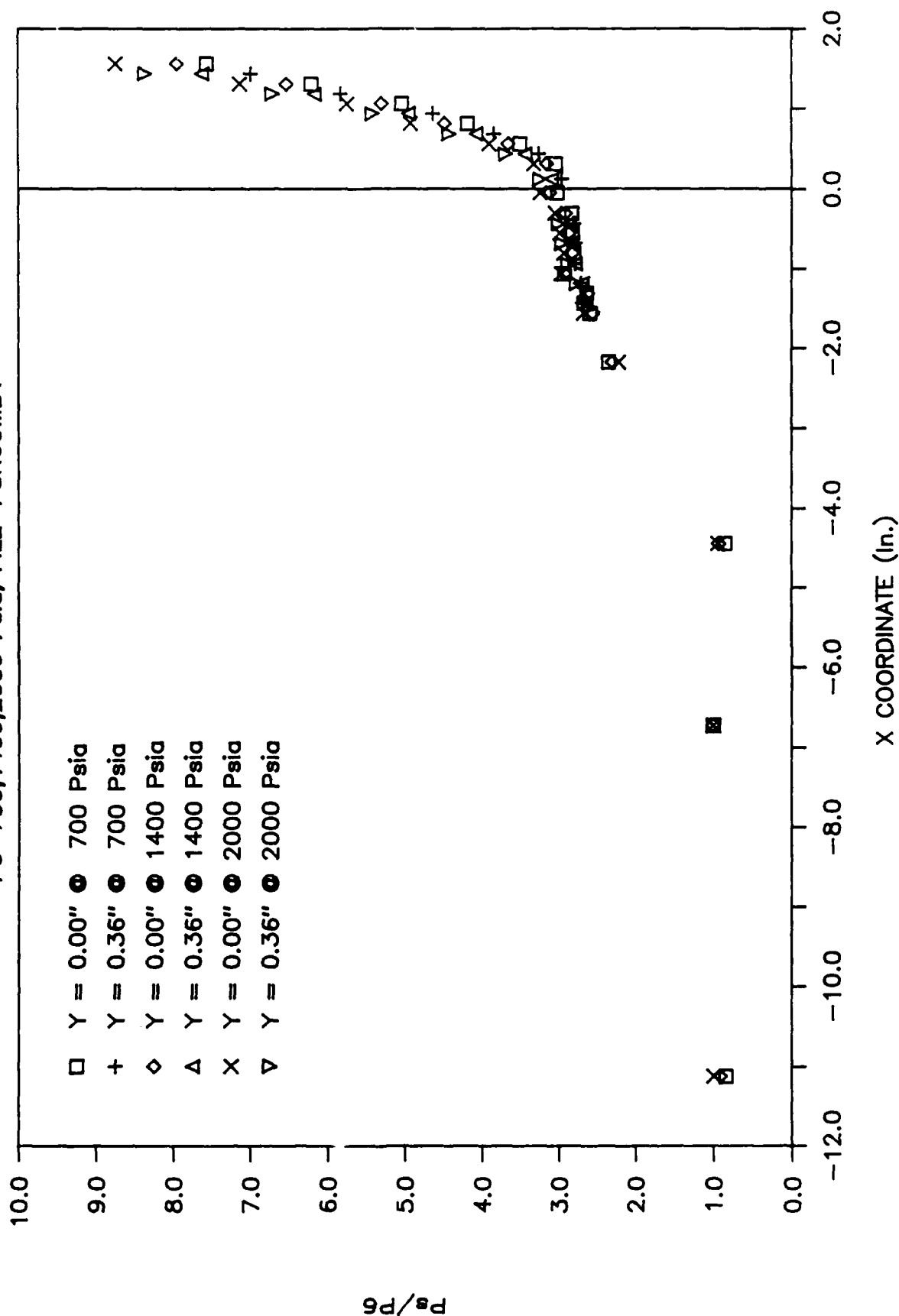


Figure 16 Combined Nondimensionalized Surface Pressures at a Given Ramp Angle

ROUGH PLATE 34 DEG. RAMP

Po=700,1400,2000 Psia, FILE=PSRCOMB3

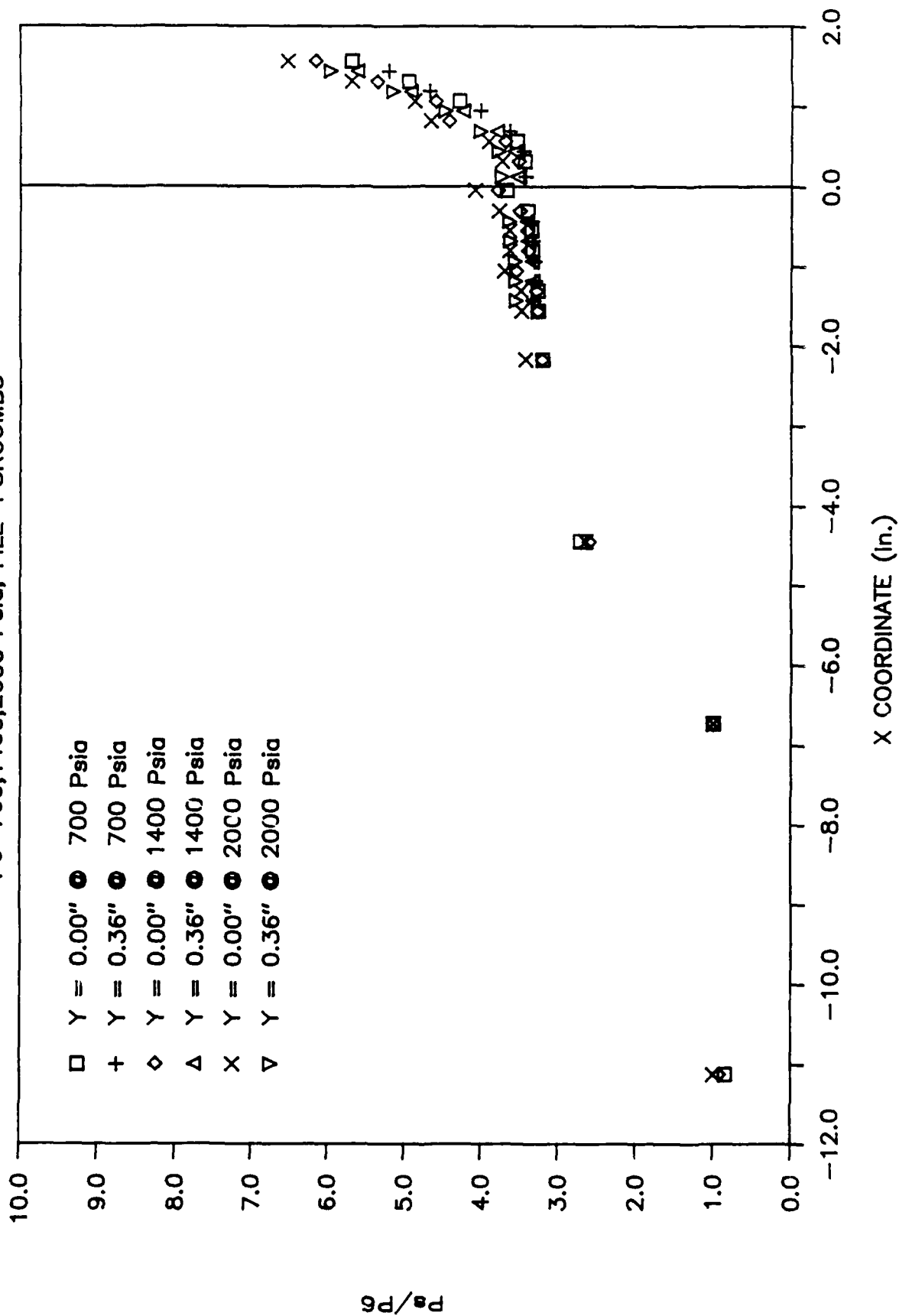


Figure 17 Combined Nondimensionalized Surface Pressures at a Given Ramp Angle

ROUGH PLATE 22,28 & 34 DEG. RAMP

Po=700 Psia, FILE=PSRCOMB4

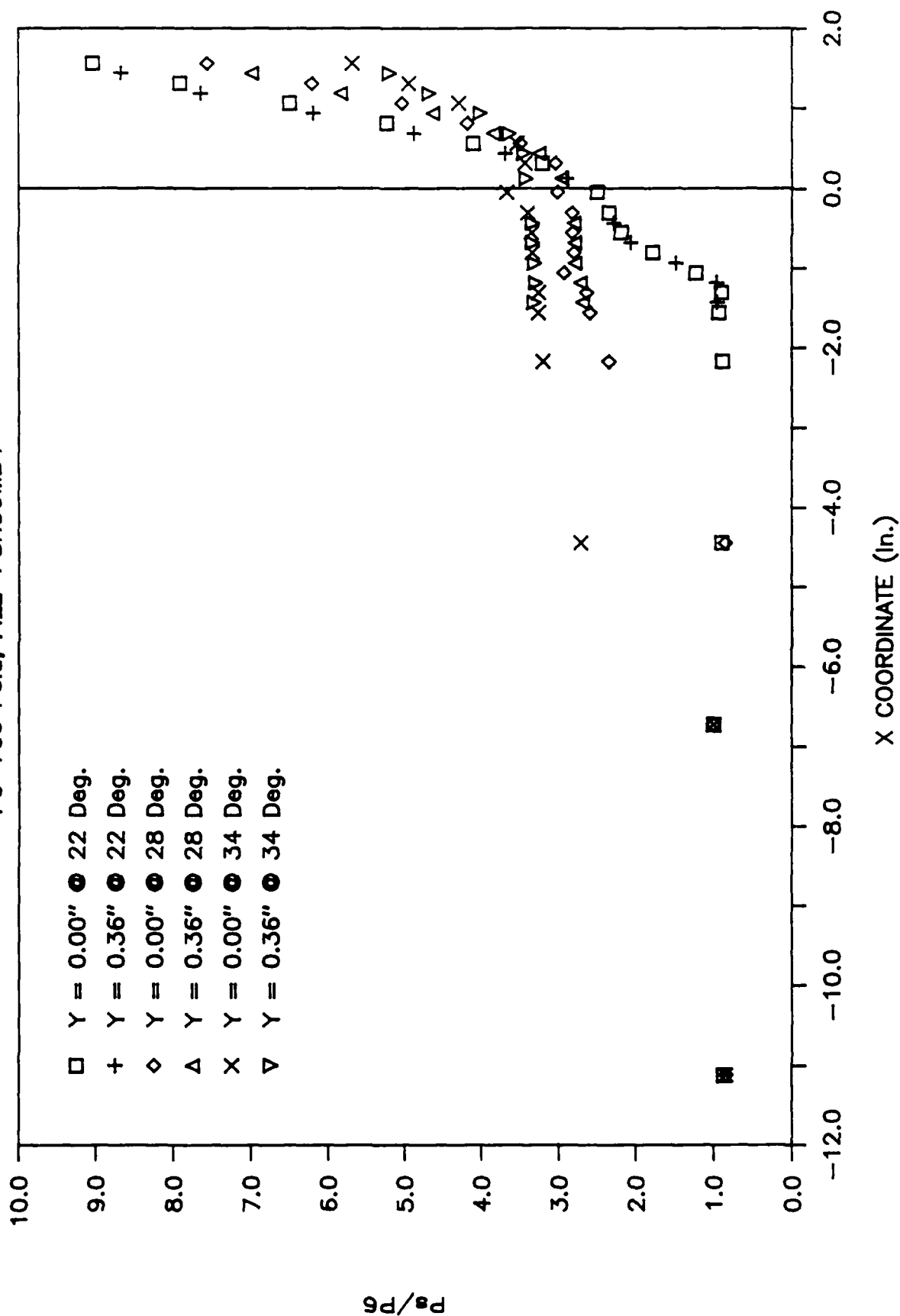


Figure 18 Combined Nondimensionalized Surface Pressures at a Single Station Pressure

ROUGH PLATE 22,28 & 34 DEG. RAMP

Po=1400 Psia, FILE=PSRCOMB5

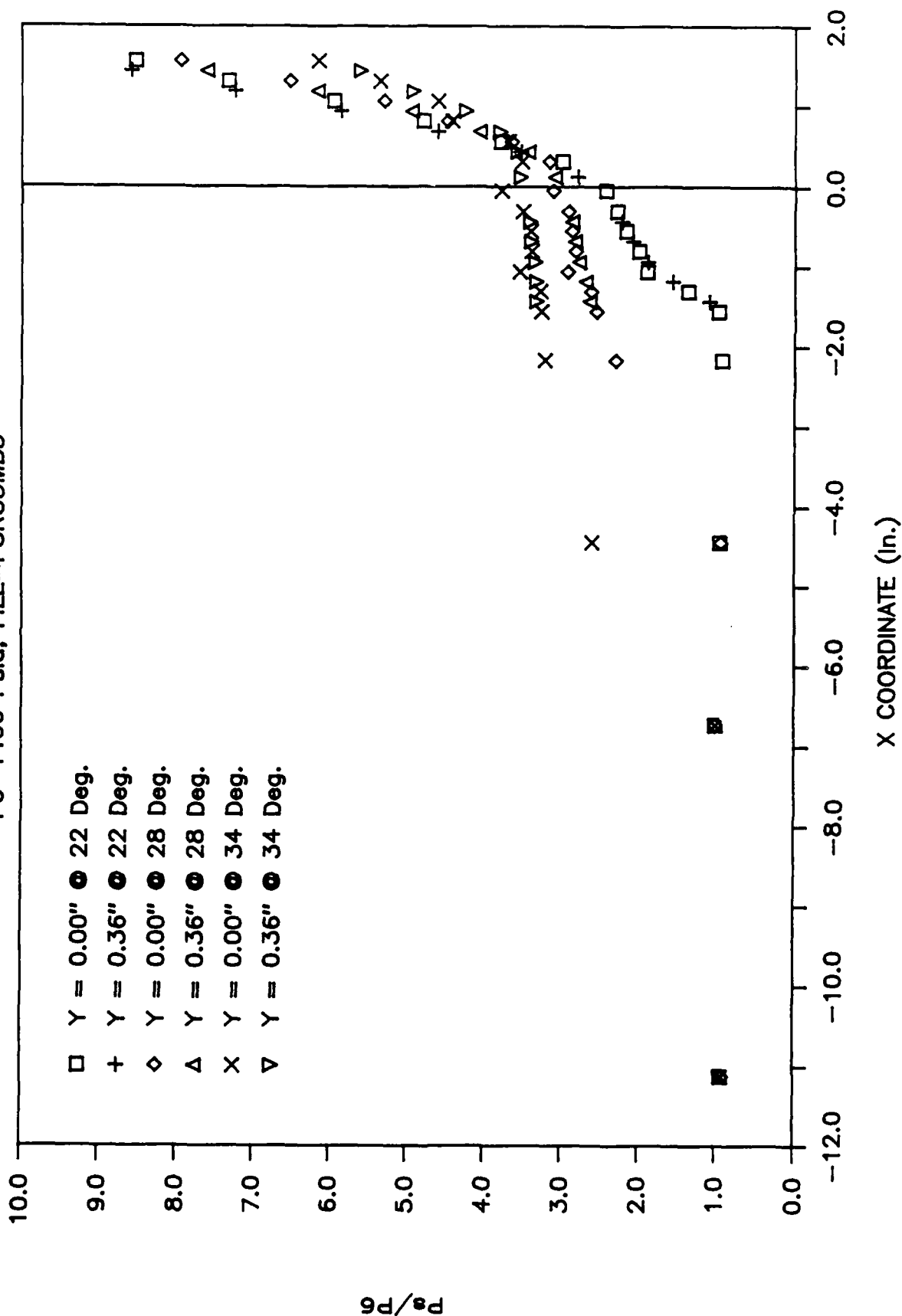


Figure 19 Combined Nondimensionalized Surface Pressures at a Single Stagnation Pressure

ROUGH PLATE 22,28 & 34 DEG. RAMP

$P_o=2000$ Psia, FILE=PSRCOMB6

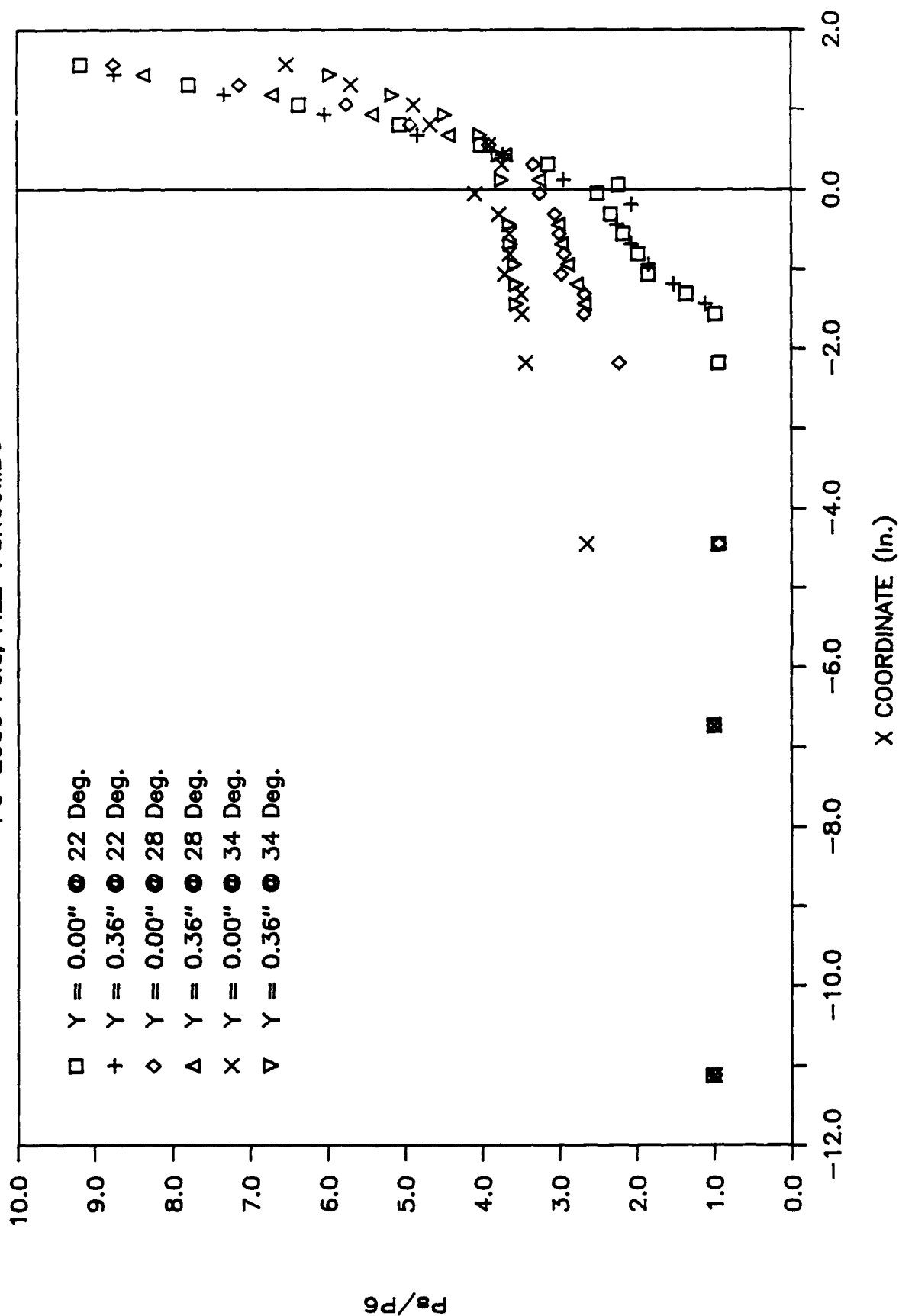


Figure 20 Combined Nondimensionalized Surface Pressures at a Single Stagnation Pressure

ROUGH PLATE 22 DEG. RAMP W/O FENCE

Po=700 Psia, FILE=PSRCOMB7

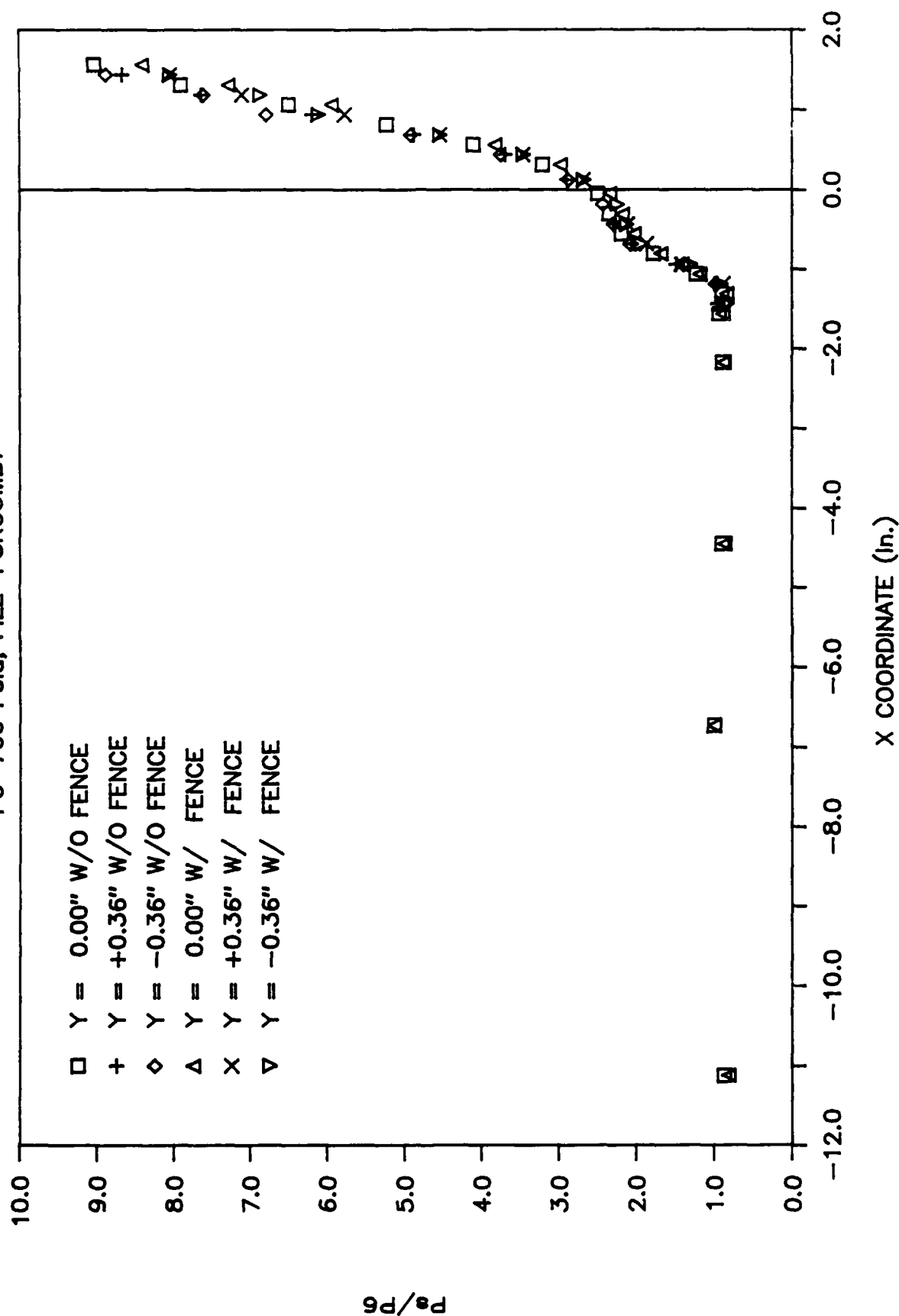


Figure 21 Comparison of the Nondimensionalized Surface Pressures with and without Side Fences

ROUGH PLATE

$P_o=700$ PSIA, $X=-6.484"$, FILE=HPTR2138

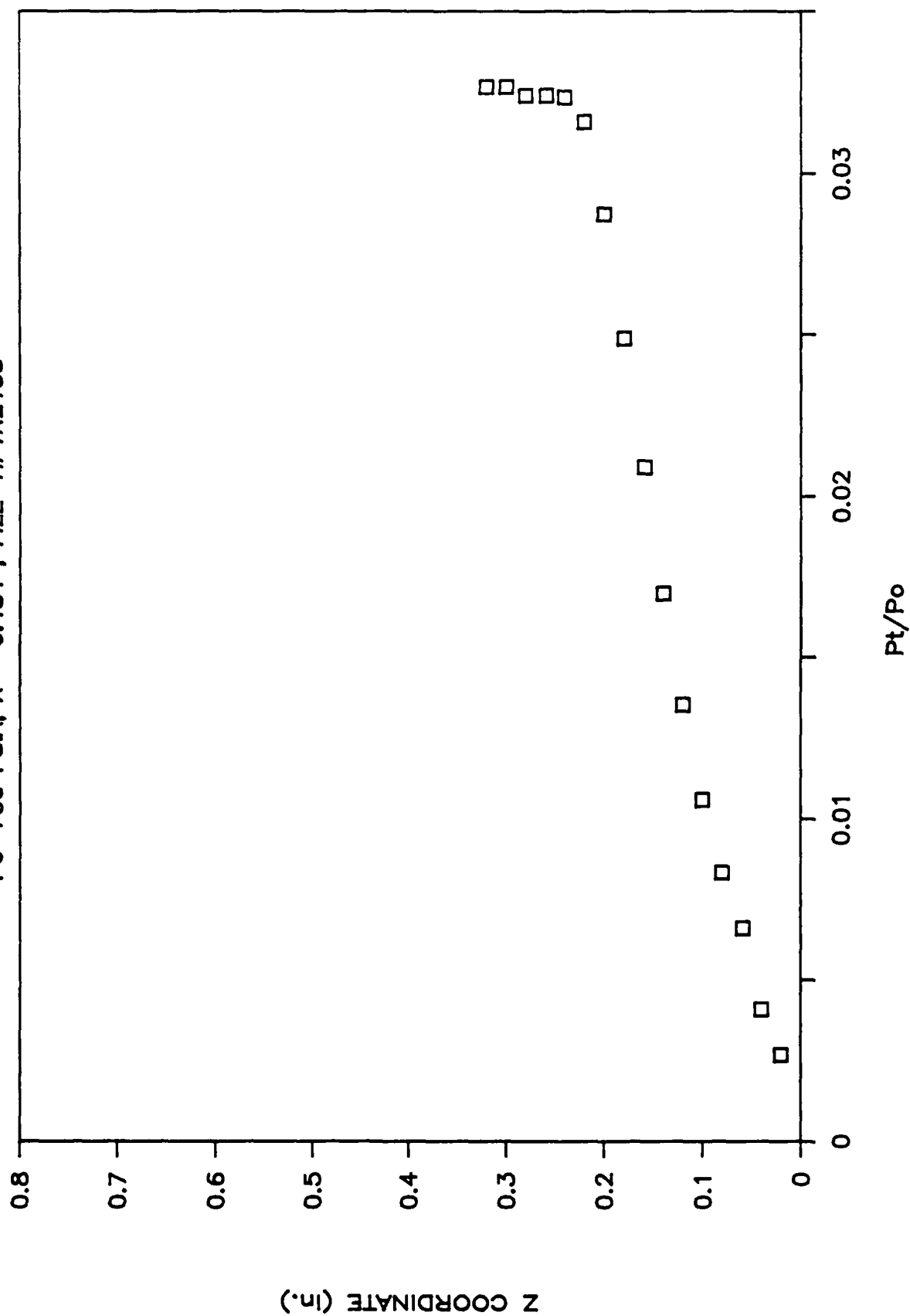


Figure 22a Nondimensionalized Pitot Pressure Distribution at a Given Location and Stagnation Pressure

ROUGH PLATE

$P_0=700$ PSIA, $X=-6.484"$, FILE=HPTR2138

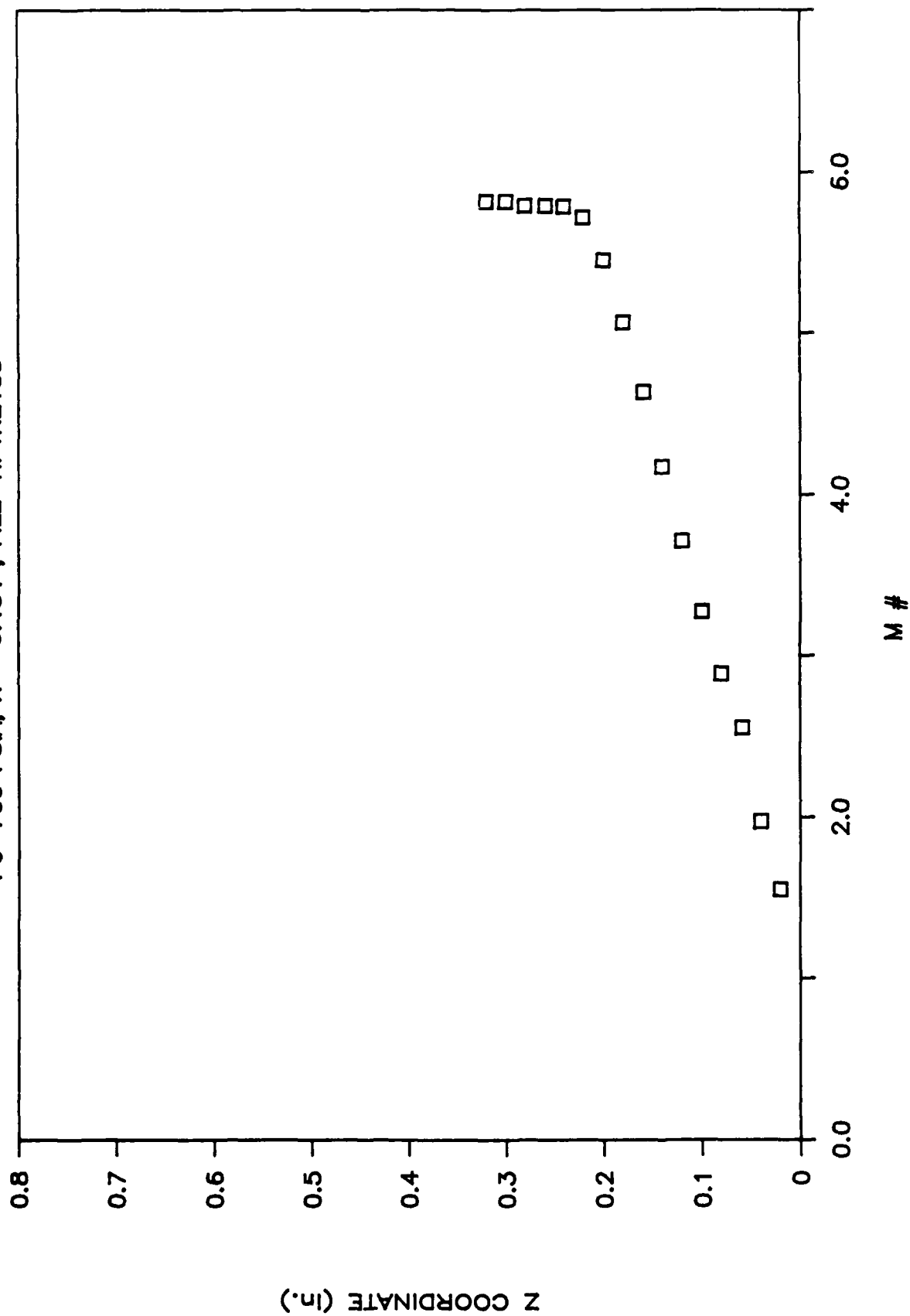


Figure 22b Mach Number Distribution at a Single Location

ROUGH PLATE 22 DEG RAMP

Po=700 PSIA, X=-6.484", FILE=HPTR2138

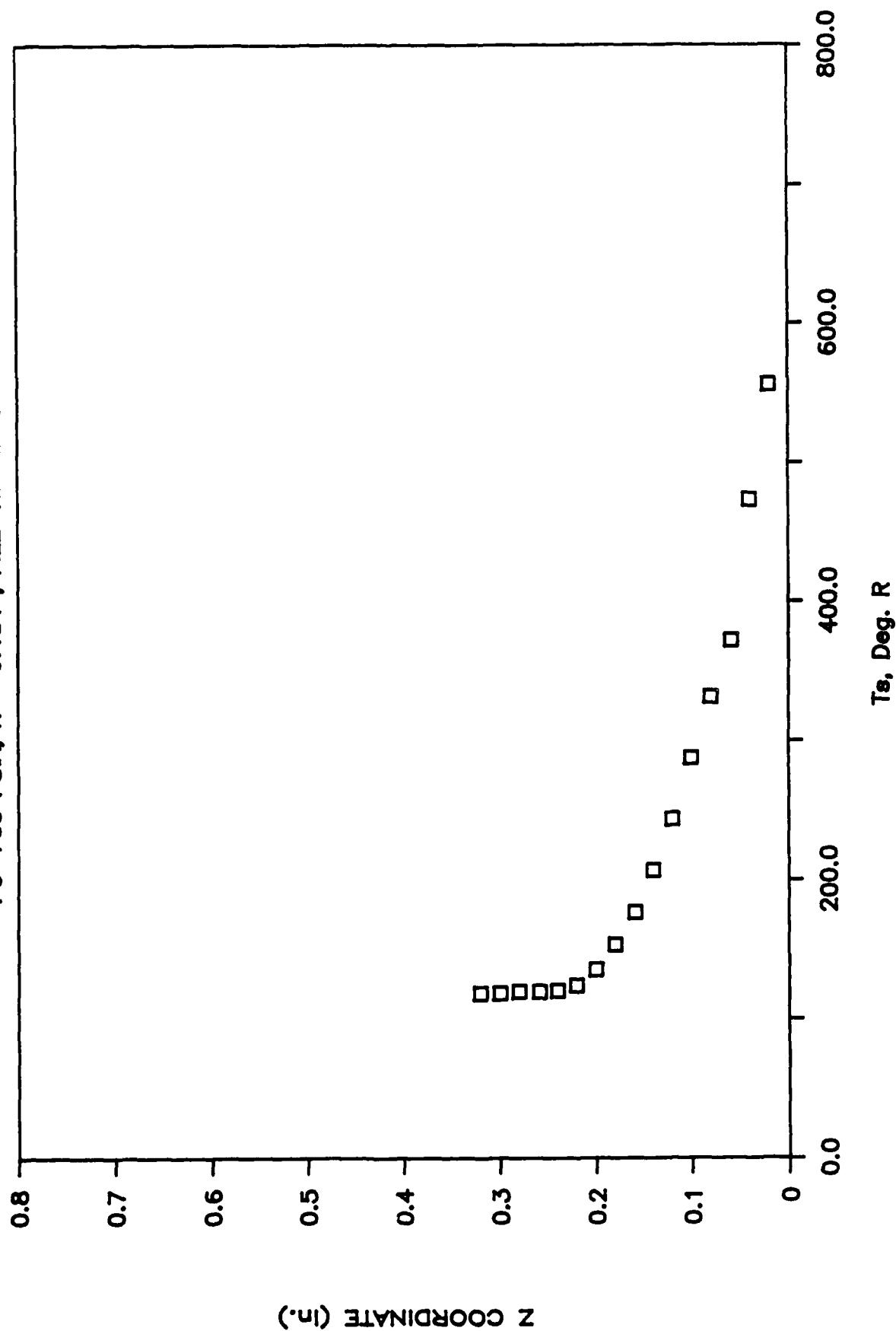


Figure 22c Static Temperature Distribution at a Given Location and Stagnation Pressure

ROUGH PLATE 22 DEG RAMP

Po=700 PSIA, X=-6.484", FILE=HPTR2138

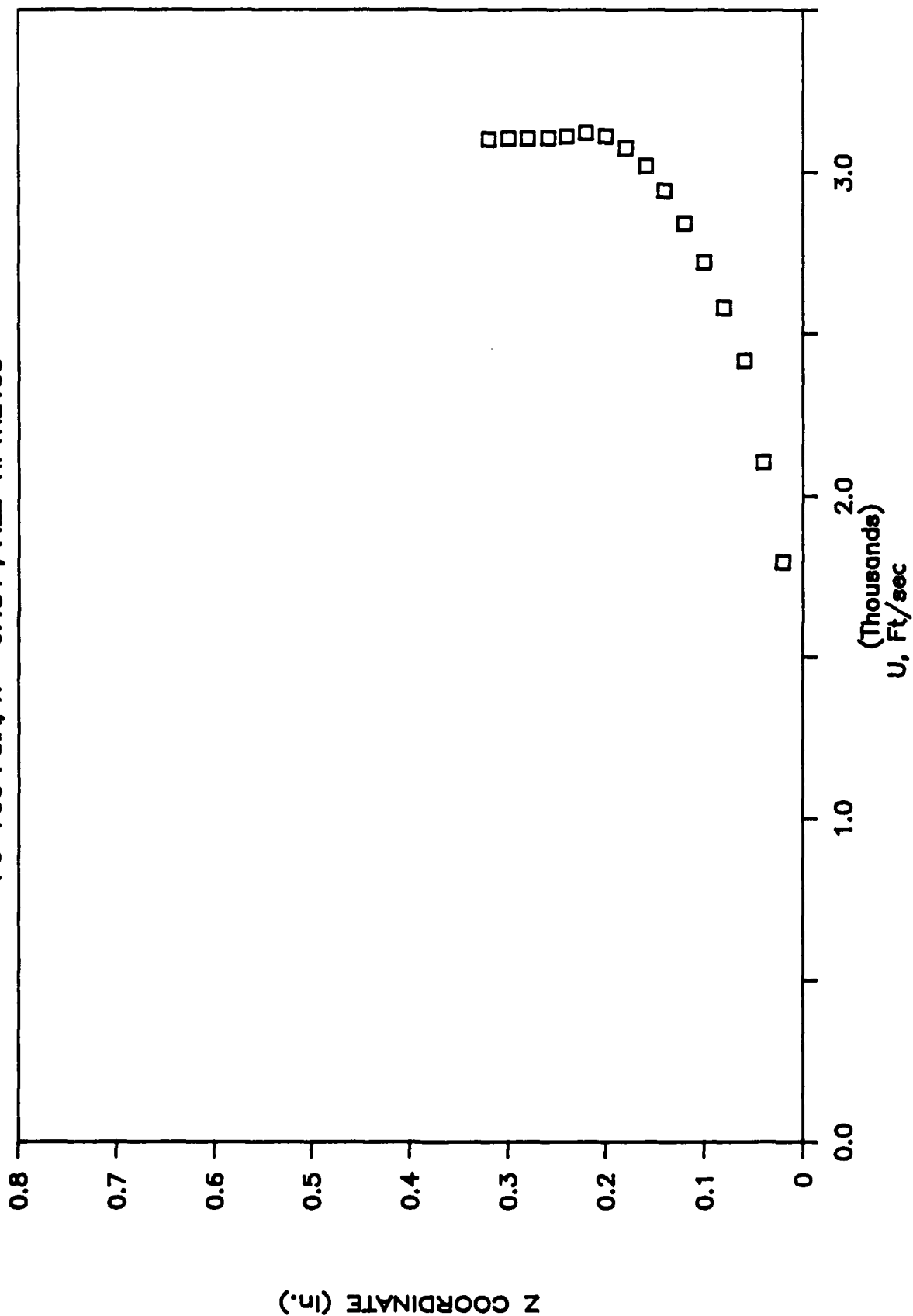


Figure 22d Local Mean Velocity Distribution at a Given Location and Stagnation Pressure

ROUGH PLATE

$P_o=1400$ PSIA, $X=-6.484"$, FILE=HPTR2141

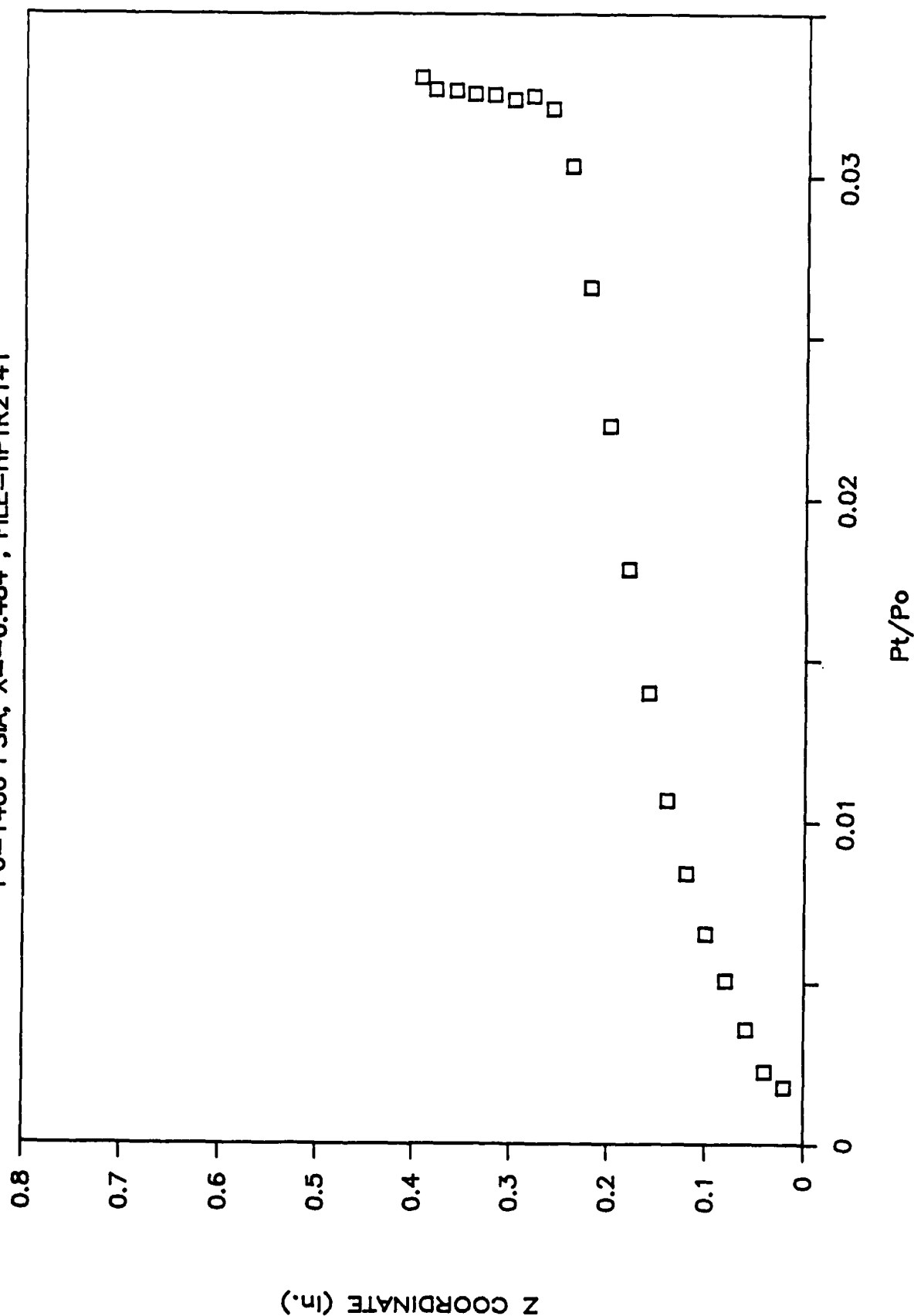


Figure 23a Nondimensionalized Pitot Pressure Distribution at a Given Location and Stagnation Pressure

ROUGH PLATE

Po=1400 PSIA, X=-6.484", FILE=HPTR2141

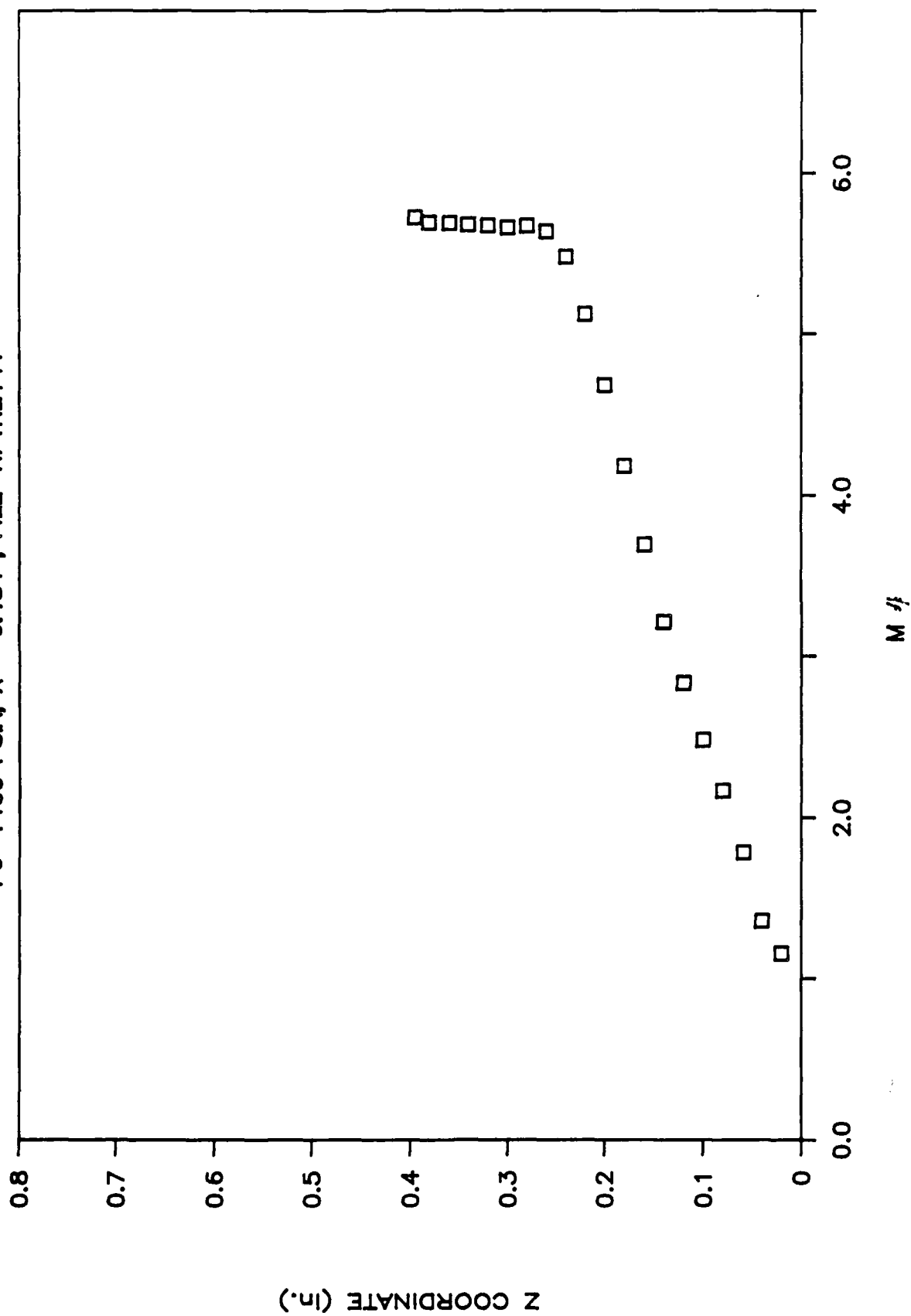


Figure 23b Mach Number Distribution at a Single Location

ROUGH PLATE 22 DEG RAMP

Po=1400 PSIA, X=-6.484", FILE=HPTR2141

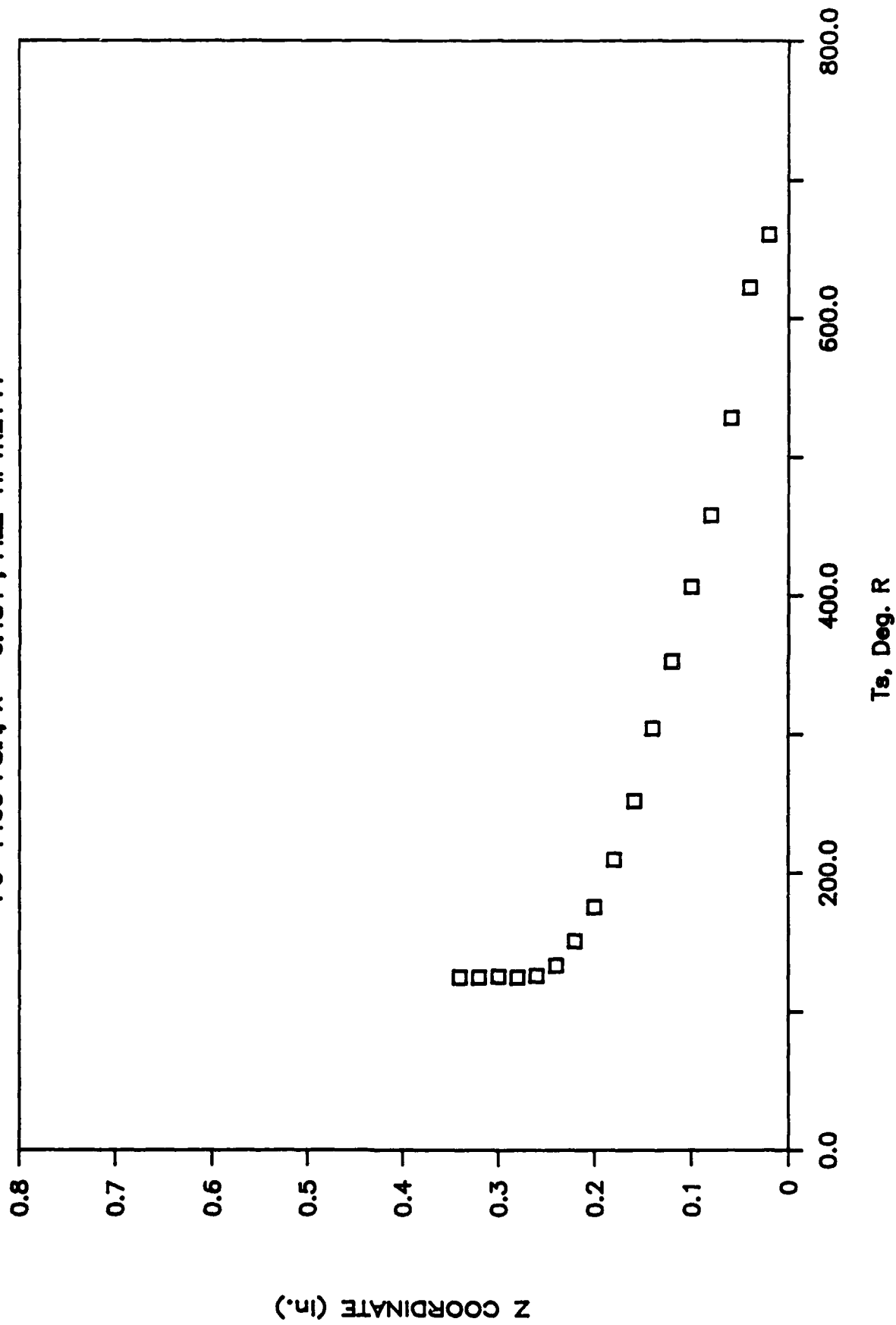


Figure 23c Static Temperature Distribution at a Given Location and Stagnation Pressure

ROUGH PLATE 22 DEG RAMP

Po=1400 PSIA, X=-6.484", FILE=HPTR2141

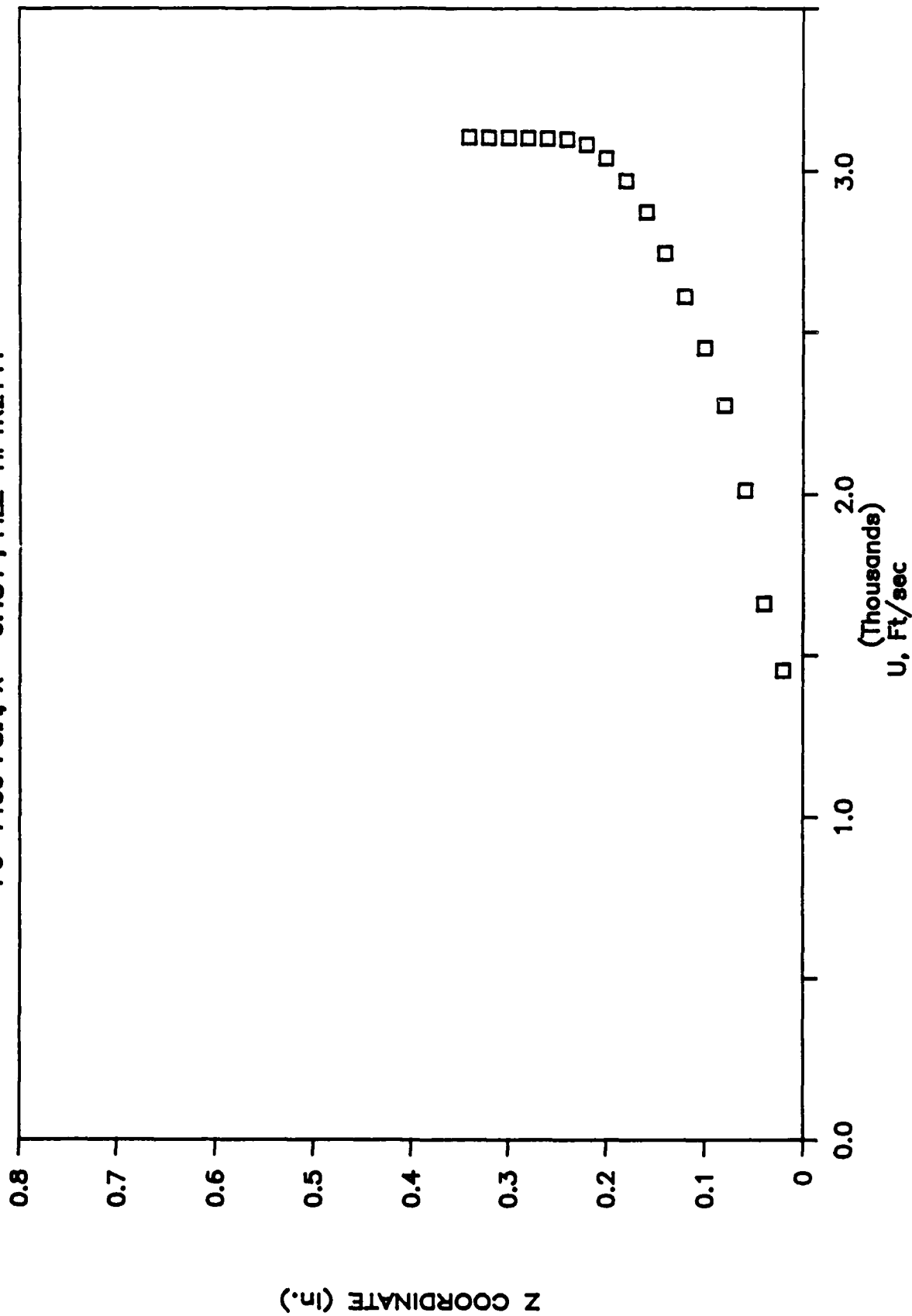


Figure 23d Local Mean Velocity Distribution at a Given Location and Stagnation Pressure

ROUGH PLATE

$P_o = 2000$ PSIA, $X = -6.484''$, FILE=HPTR2142

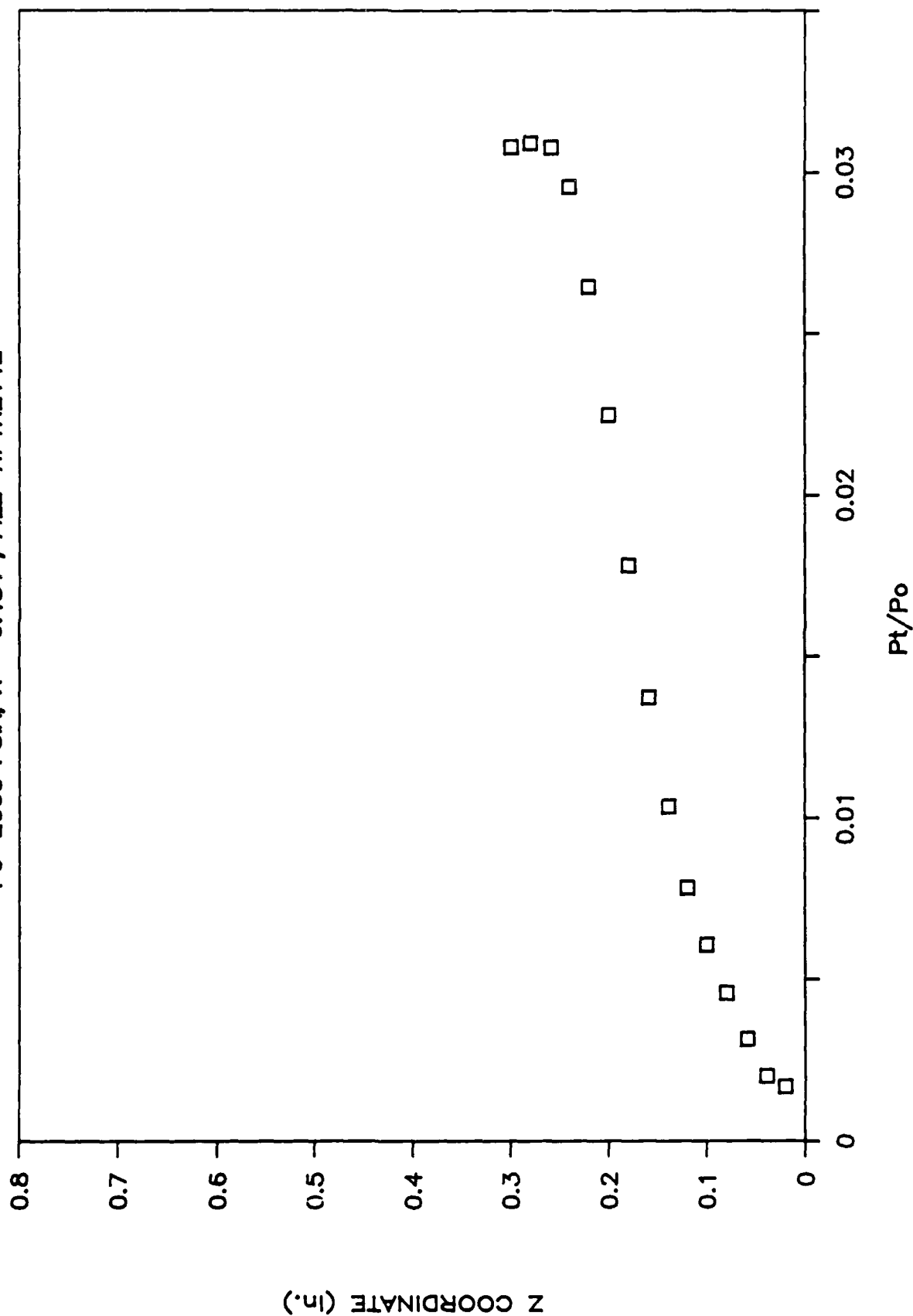


Figure 24a Nondimensionalized Pitot Pressure Distribution at a Given Location and Stagnation Pressure

ROUGH PLATE

Po=2000 PSIA, X=-6.484", FILE=HPTR2142

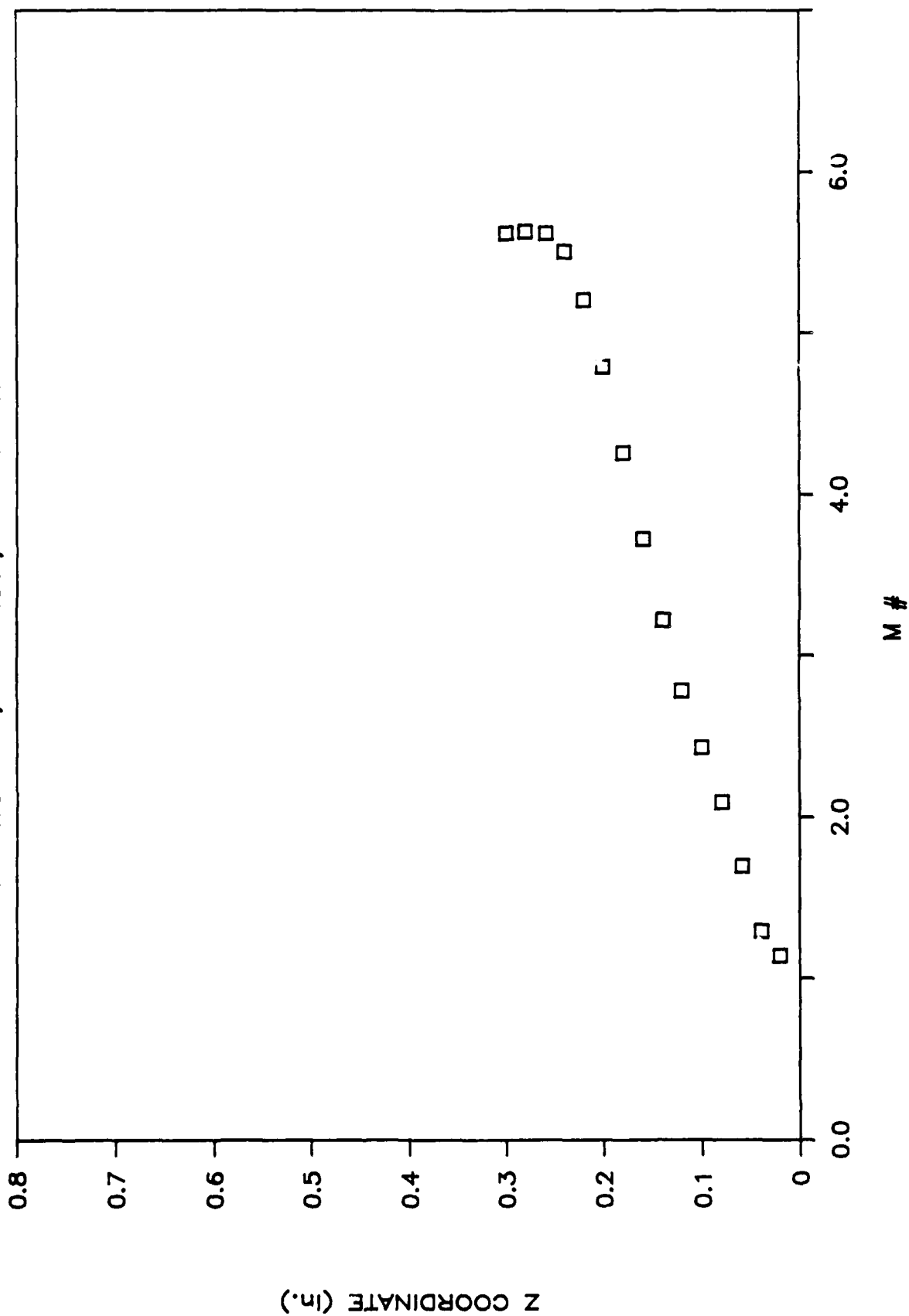


Figure 24b Mach Number Distribution at a Single Location

ROUGH PLATE 22 DEG RAMP

Po=2000 PSIA, X=-6.484, FILE=HPTR2142

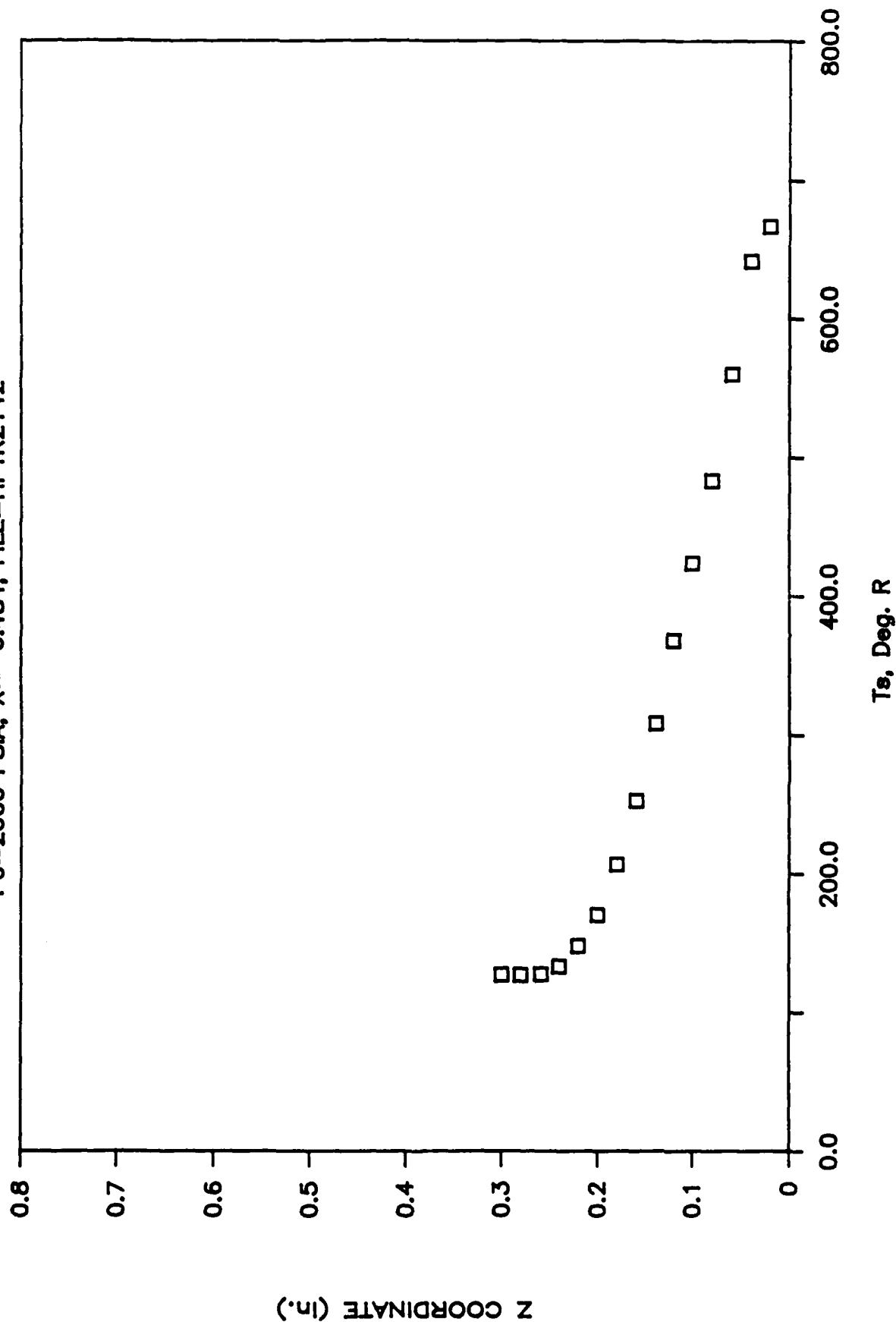


Figure 24c Static Temperature Distribution at a Given Location and Stagnation Pressure

ROUGH PLATE 22 DEG RAMP

$P_o=2000$ PSIA, $X=-6.484"$, FILE=HPTR2142

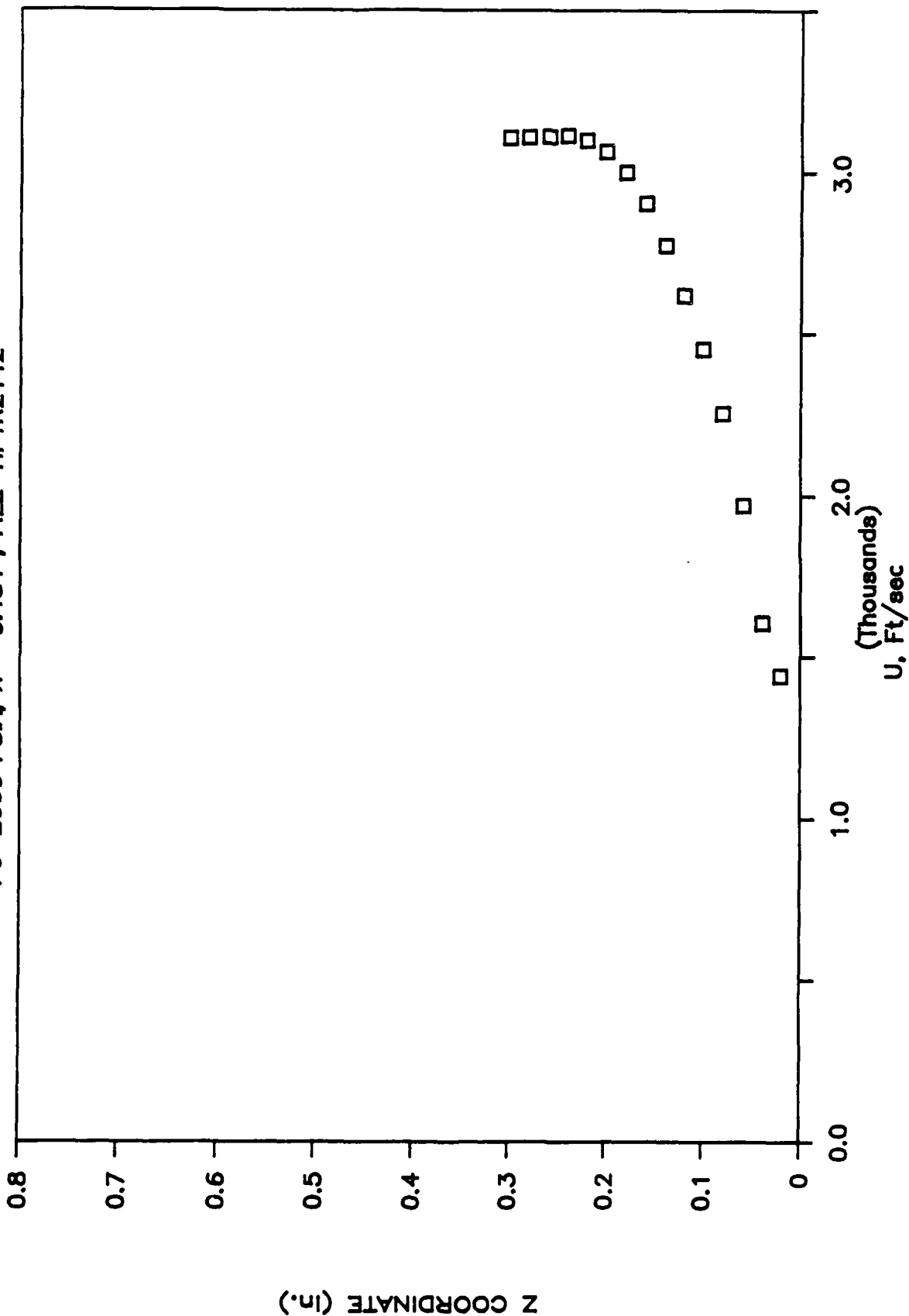


Figure 24d Local Mean Velocity Distribution at a Given Location and Stagnation Pressure

ROUGH PLATE

$P_0=700$ PSIA, $X=-2.172"$, FILE=HPTR2128

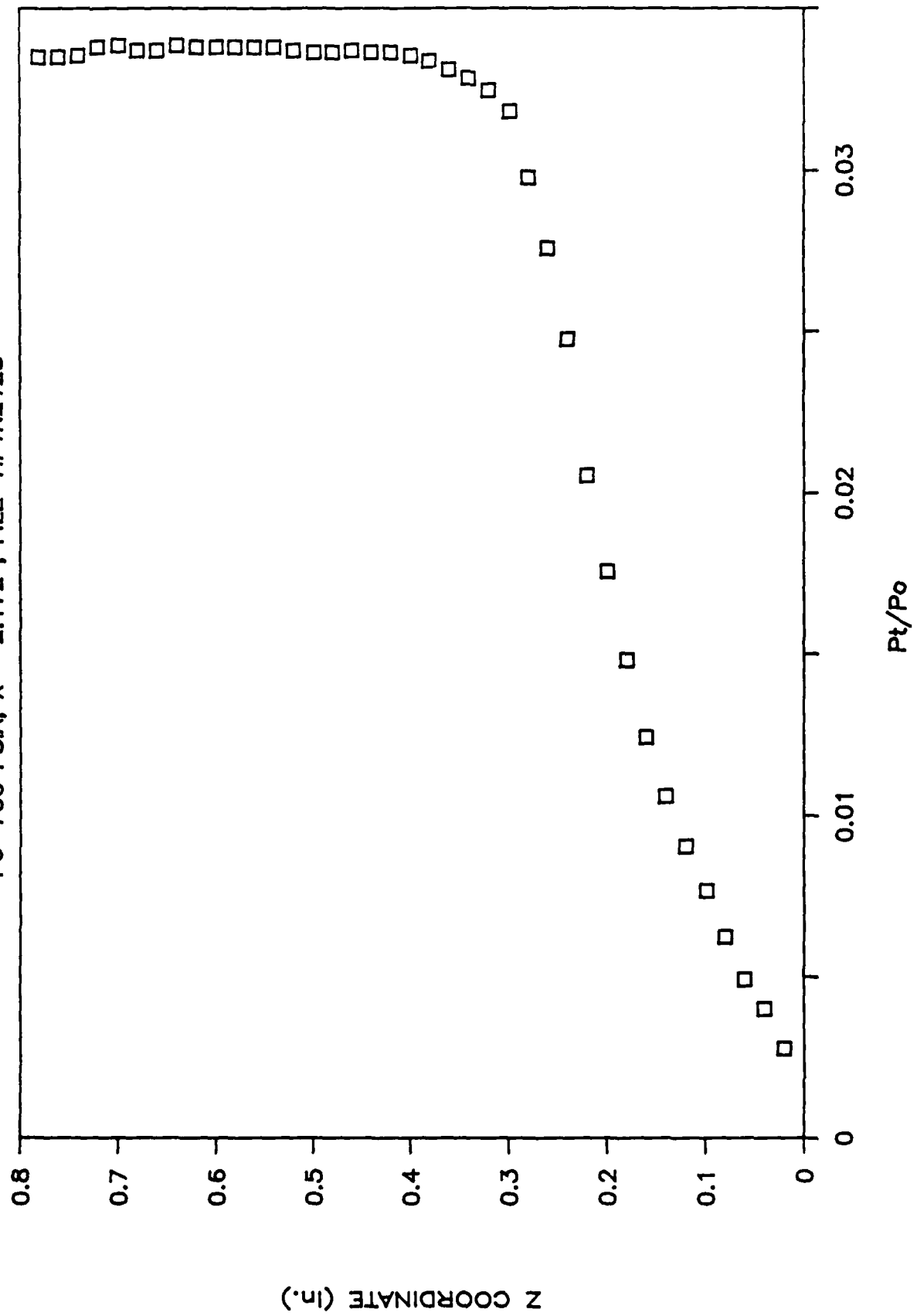


Figure 25a Nondimensionalized Pitot Pressure Distribution at a Given Location

ROUGH PLATE

Po=700 PSIA, X=-2.172", FILE=HPTR2128

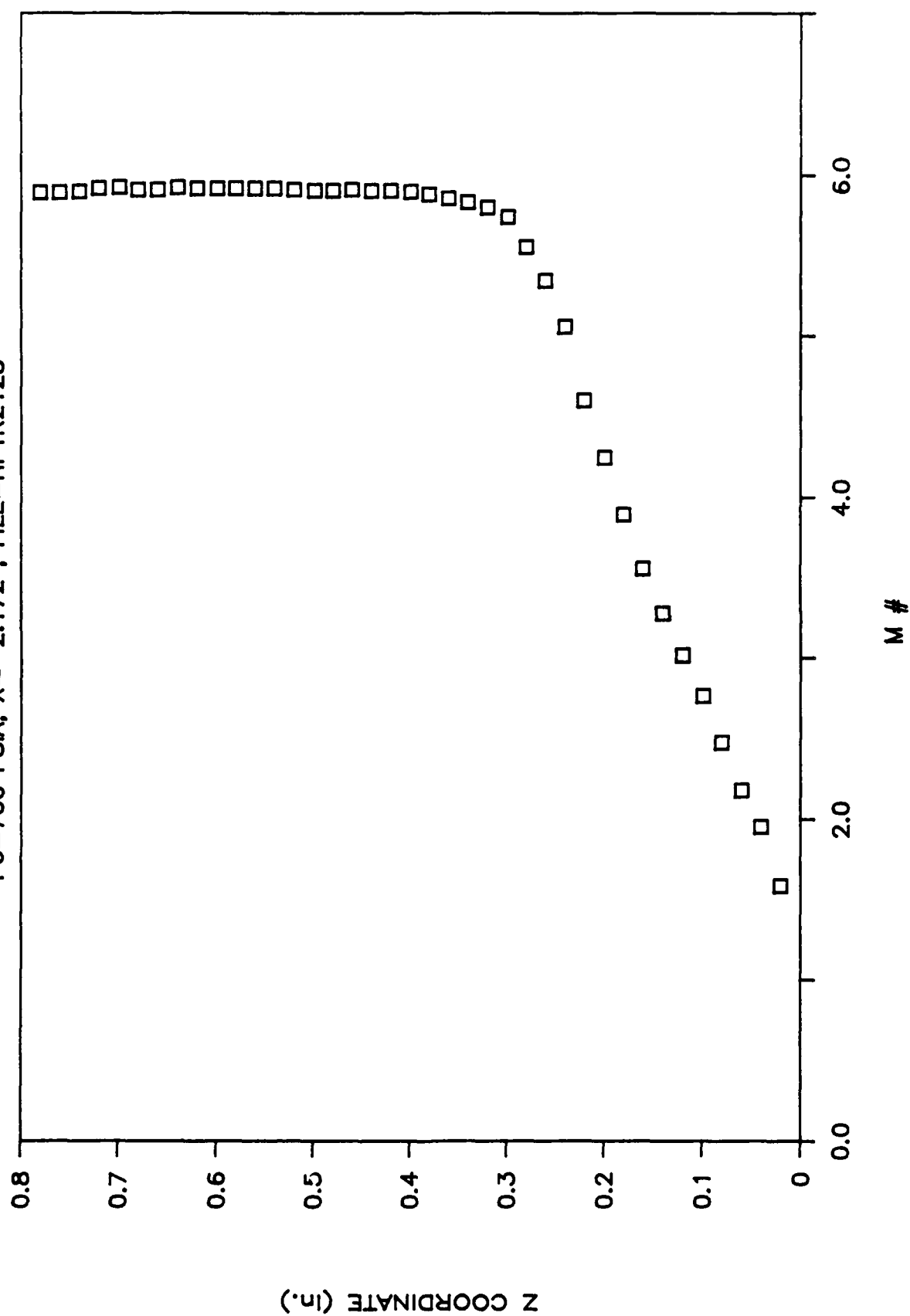


Figure 25b Mach Number Distribution at a Single Location

ROUGH PLATE 22 DEG RAMP

$P_o=700$ PSIA, $X=-2.172''$, FILE=HPTR2128

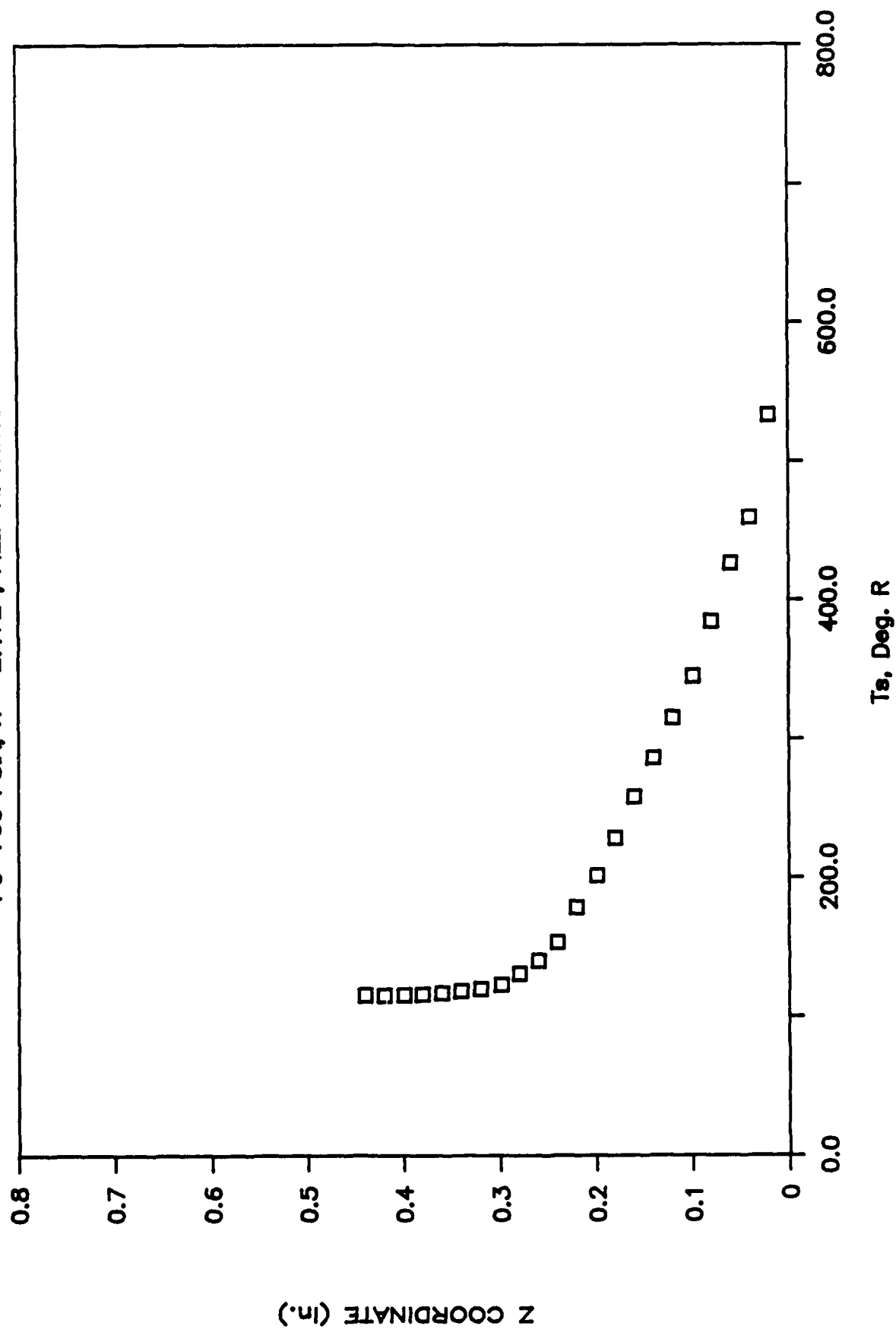


Figure 25c Static Temperature Distribution at a Given Location and Stagnation Pressure

ROUGH PLATE 22 DEG RAMP

$P_0=700$ PSIA, $X=-2.172"$, FILE=HPTR2128

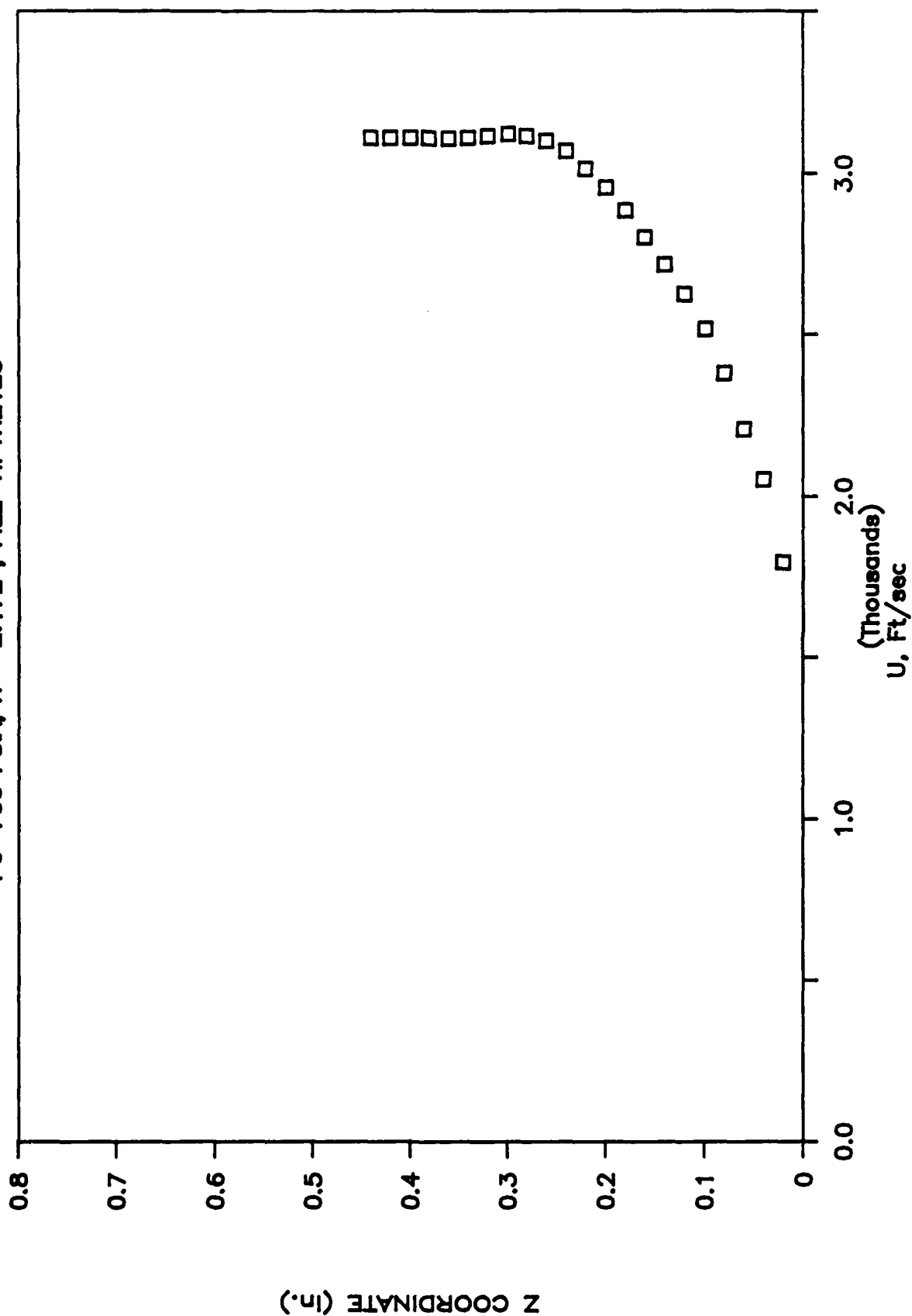


Figure 25d Local Mean Velocity Distribution at a Given Location and Stagnation Pressure

ROUGH PLATE

$P_o = 1400$ PSIA, $X = -2.172$ ", FILE=HPTr2139

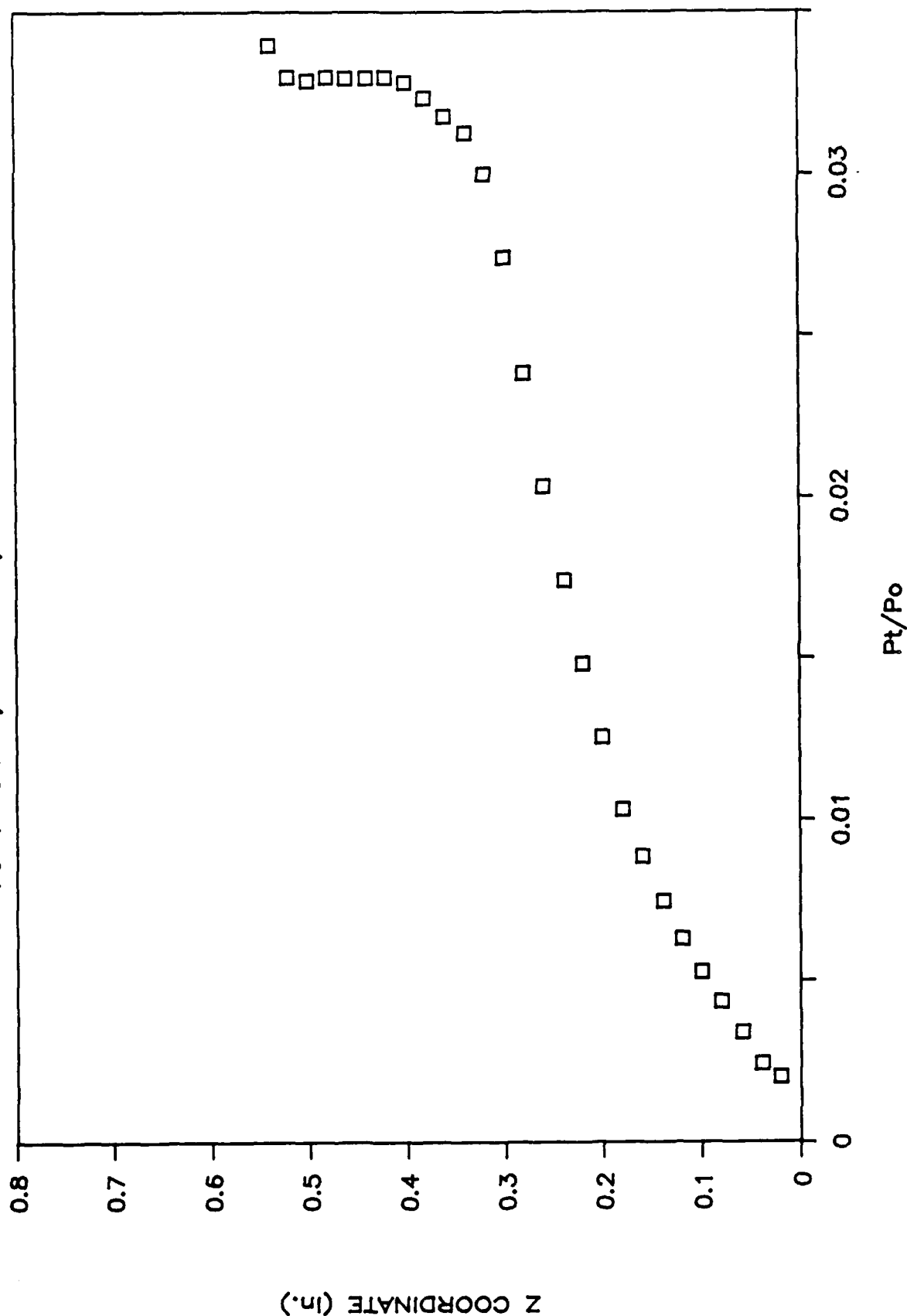


Figure 26a Nondimensionalized Pitot Pressure Distribution at a Given Location and Stagnation Pressure

ROUGH PLATE

$P_o=1400$ PSIA, $X=-2.172''$, FILE=HPTR2139

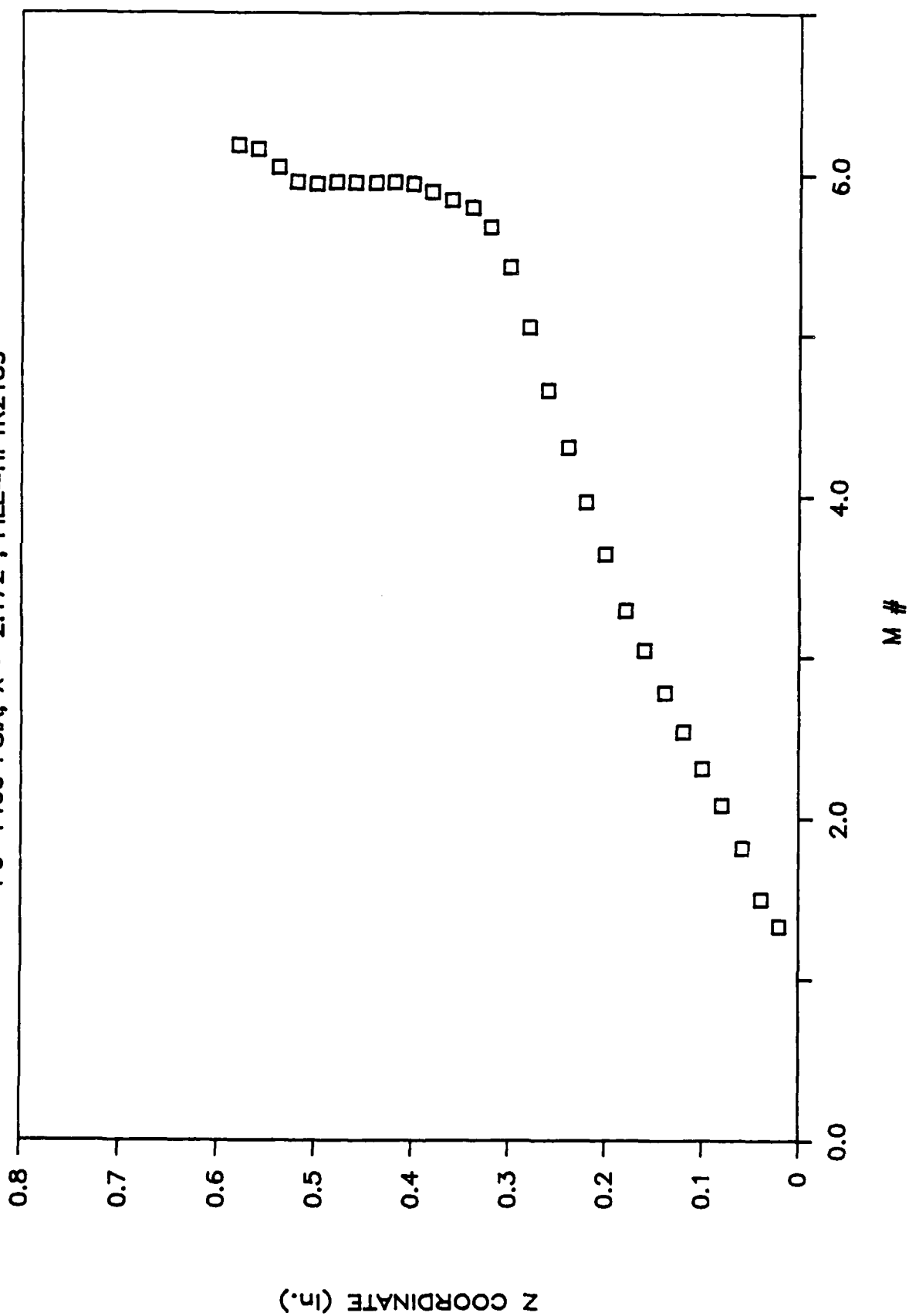


Figure 26b Mach Number Distribution at a Single Location

ROUGH PLATE 22 DEG RAMP

$P_o=1400$ PSIA, $X=-2.172"$, FILE=HPTR2139

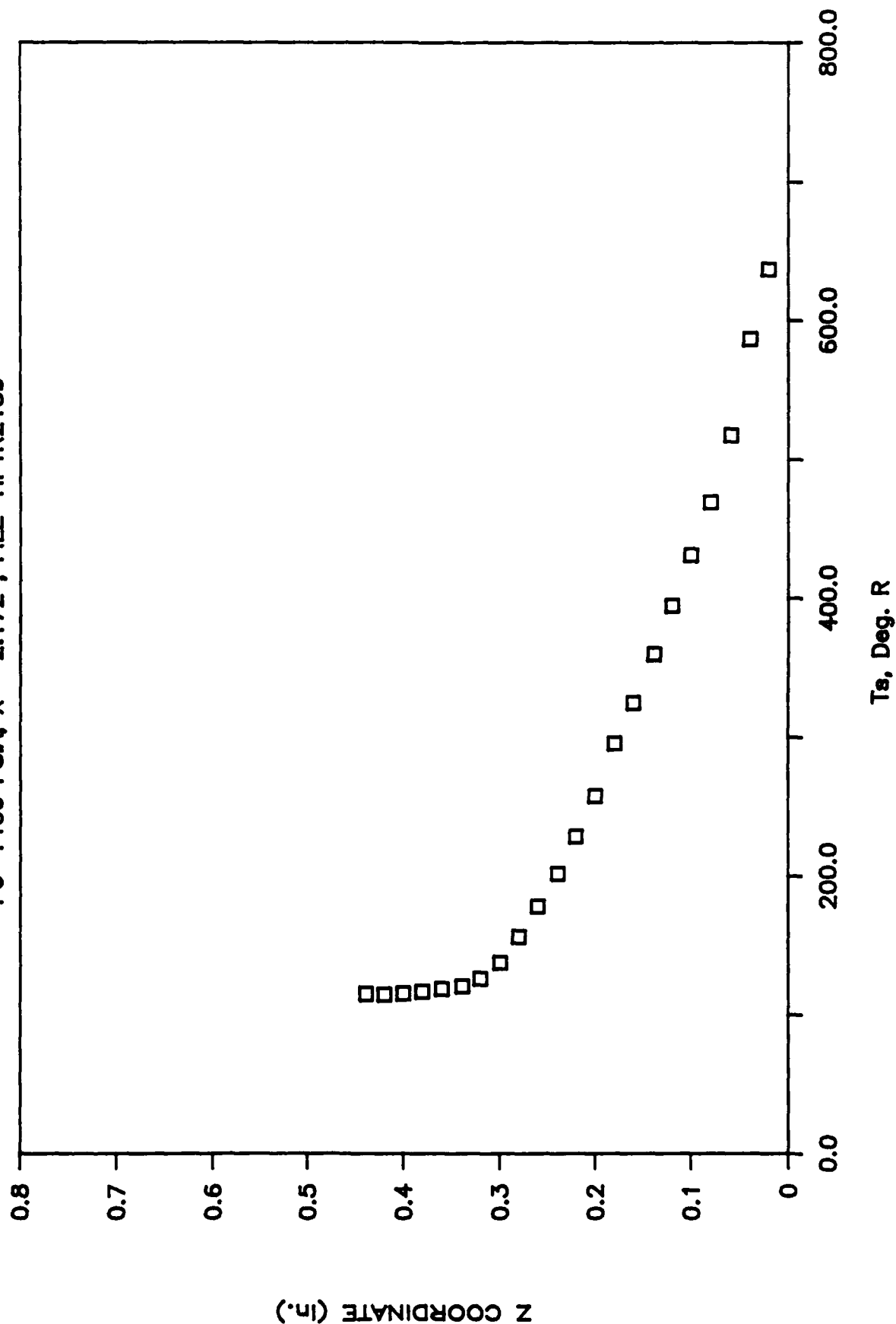


Figure 26c Static Temperature Distribution at a Given Location and Stagnation Pressure

BLANK PAGE

ROUGH PLATE 22 DEG RAMP

$P_0 = 1400$ PSIA, $X = -2.172''$, FILE=HPTR2139

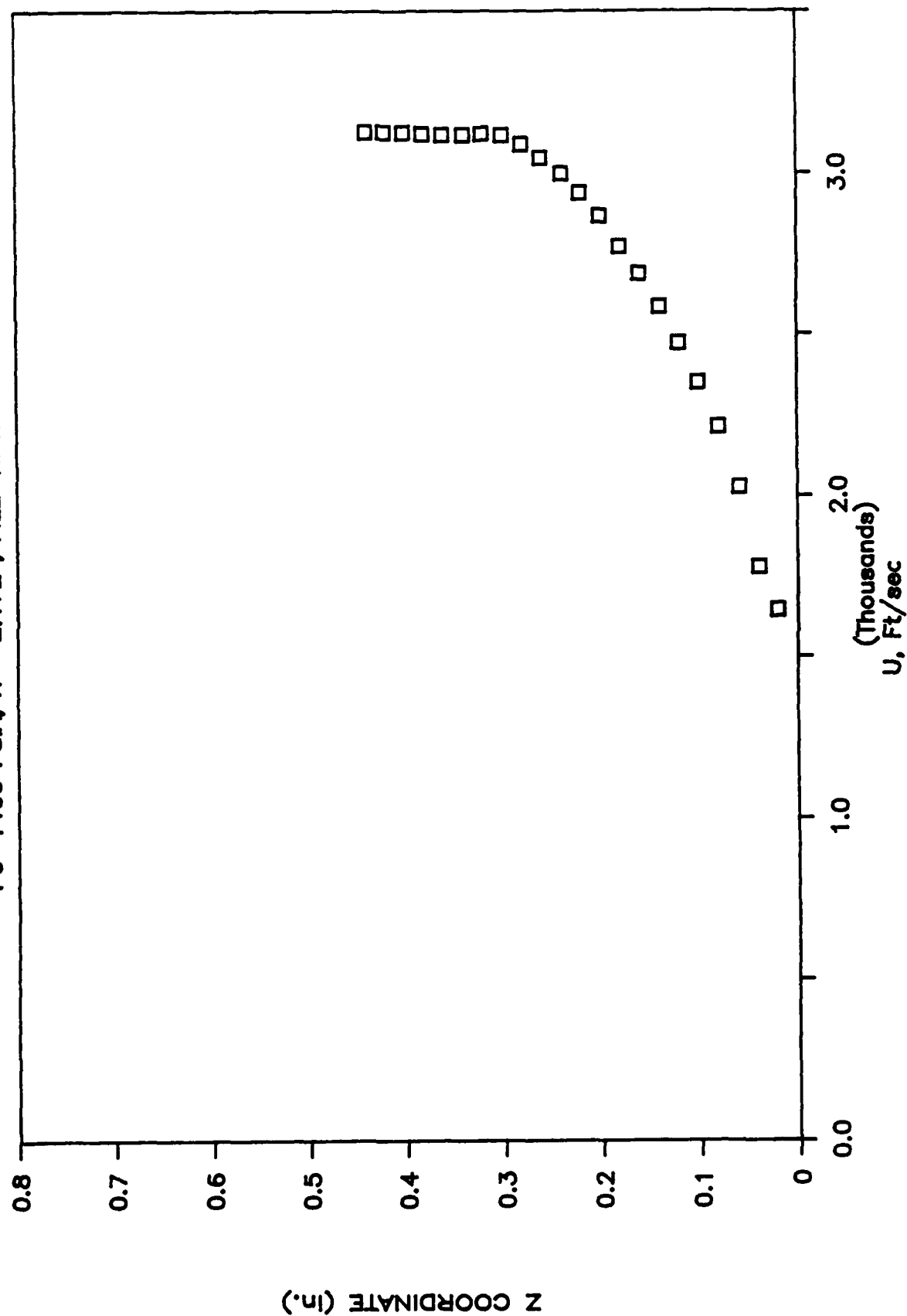


Figure 26d Local Mean Velocity Distribution at a Given Location and Stagnation Pressure

ROUGH PLATE

$P_o=2000$ PSIA, $X=-2.172"$, FILE=HPTR2151

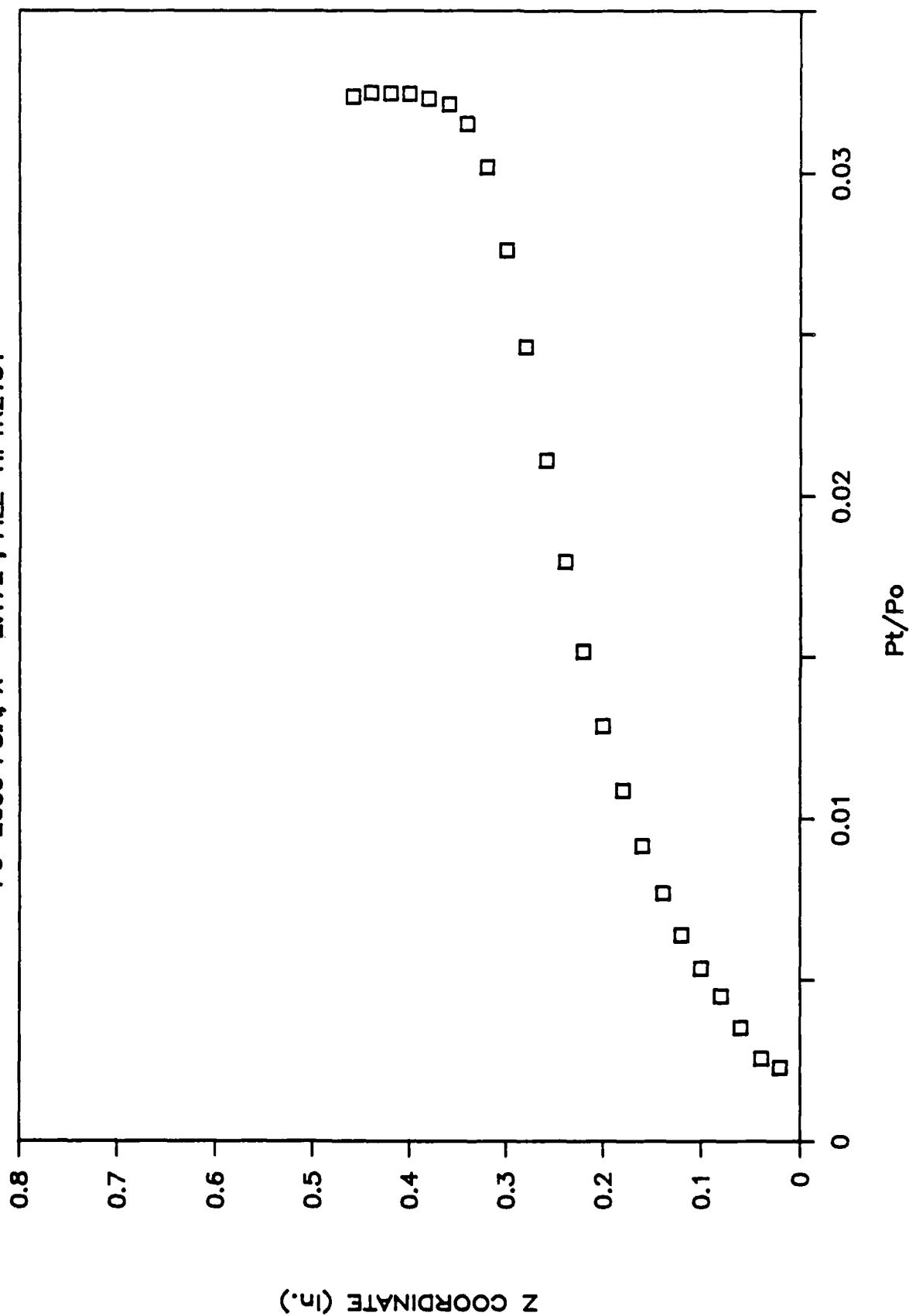
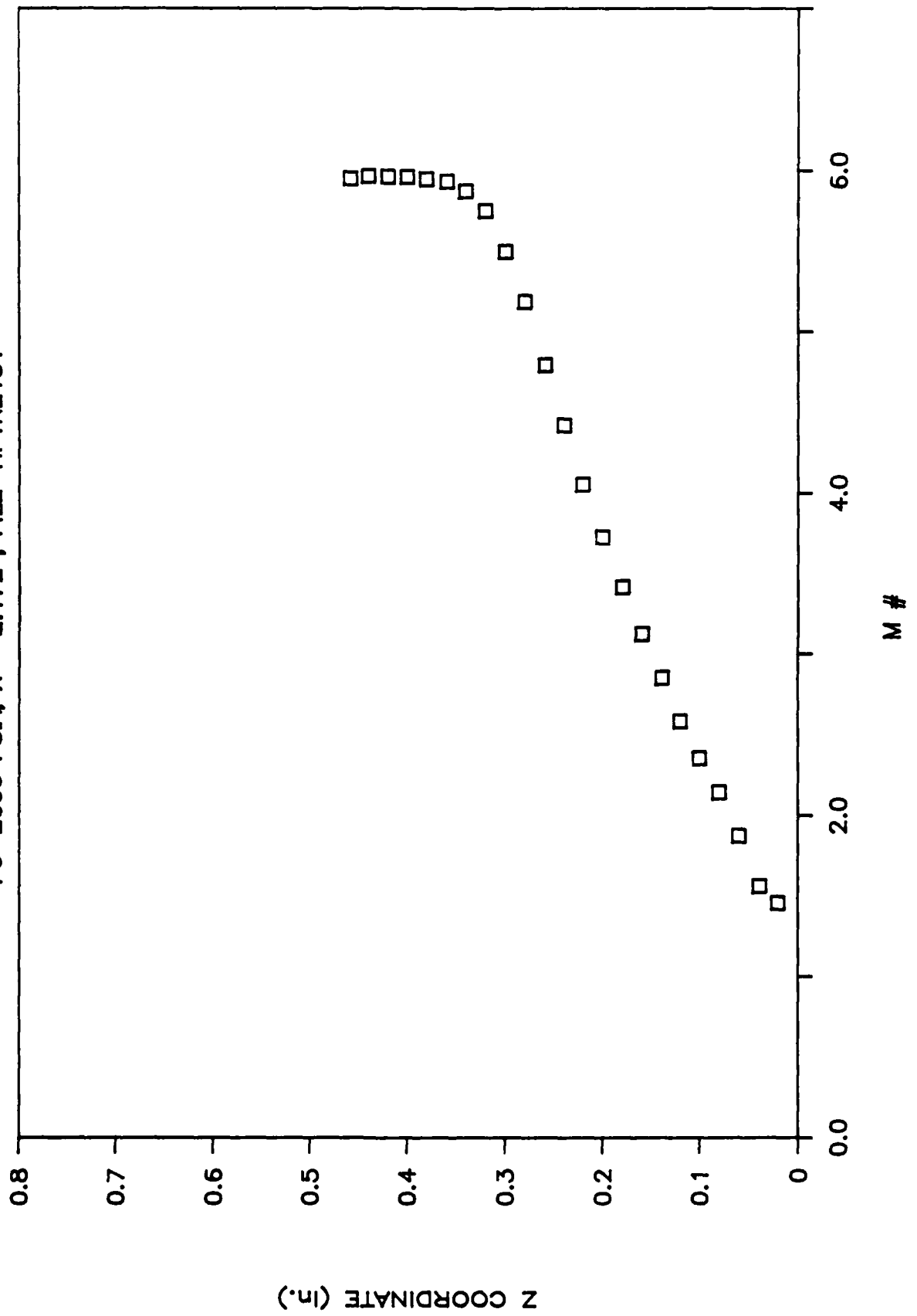


Figure 27a Nondimensionalized Pitot Pressure Distribution at a Given Location and Stagnation Pressure

ROUGH PLATE

Po=2000 PSIA, X=-2.172", FILE=HPTR2151



82-80

Figure 27b Mach Number Distribution at a Single Location

ROUGH PLATE 22 DEG RAMP

$P_0=2000$ PSIA, $X=-2.172"$, FILE=HPTR2151

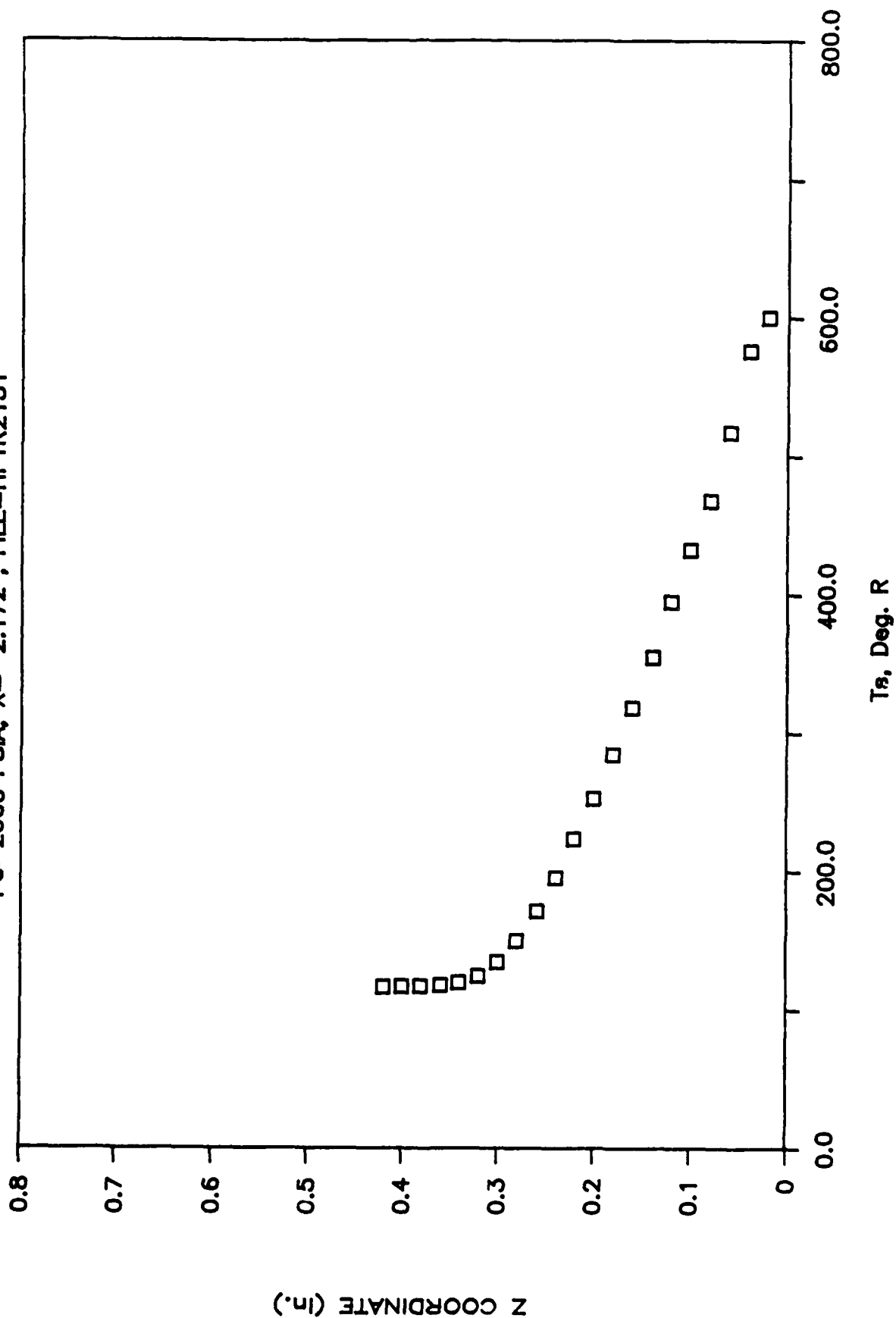


Figure 27c Static Temperature Distribution at a Given Location and Stagnation Pressure

ROUGH PLATE 22 DEG RAMP

$P_0=2000$ PSIA, $X=-2.172"$, FILE=HPTR2151

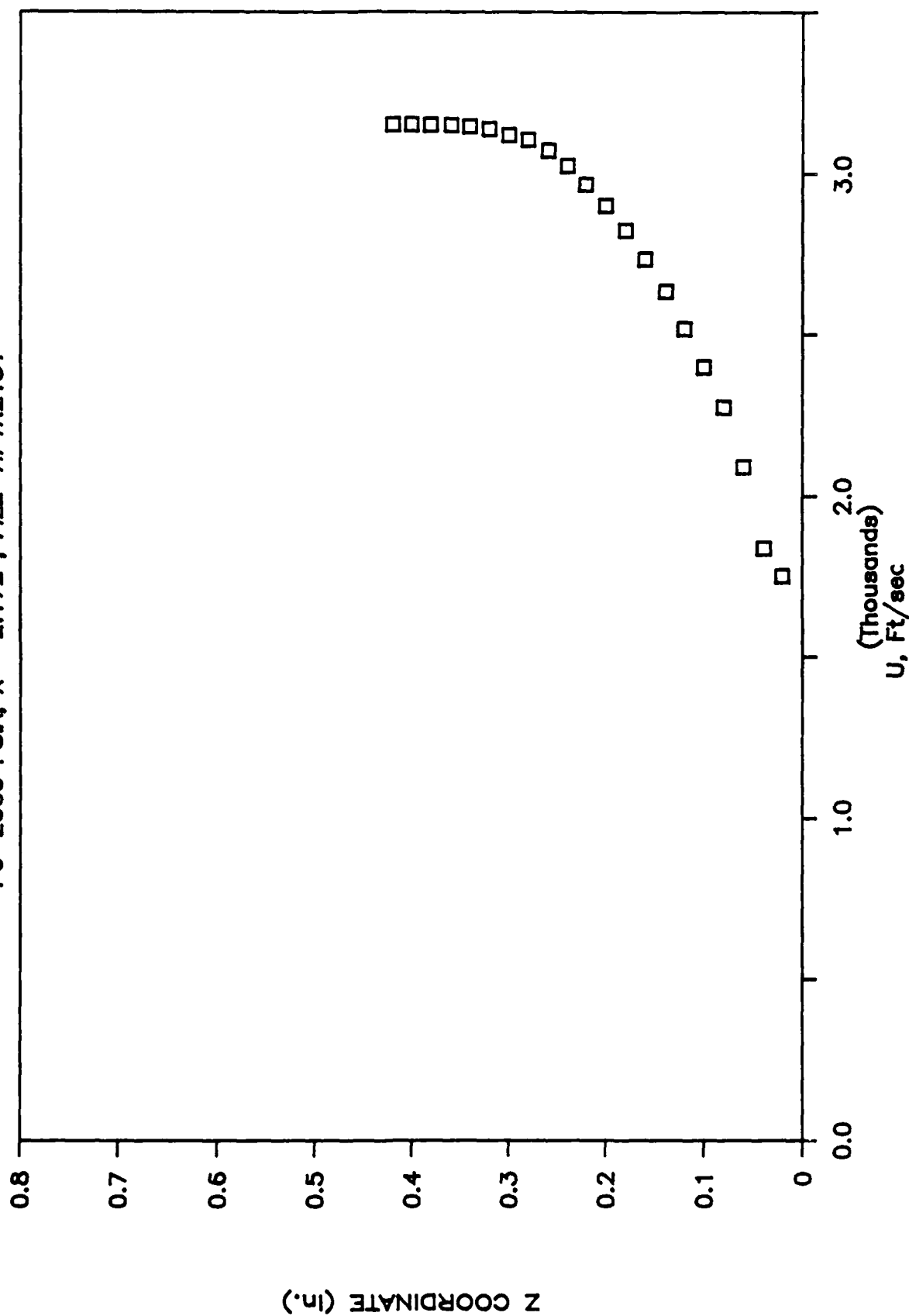


Figure 27d Local Mean Velocity Distribution at a Given Location and Stagnation Pressure

ROUGH PLATE 22 DEG RAMP

Po=700 PSIA, X=1.563", FILE=HPTR2165

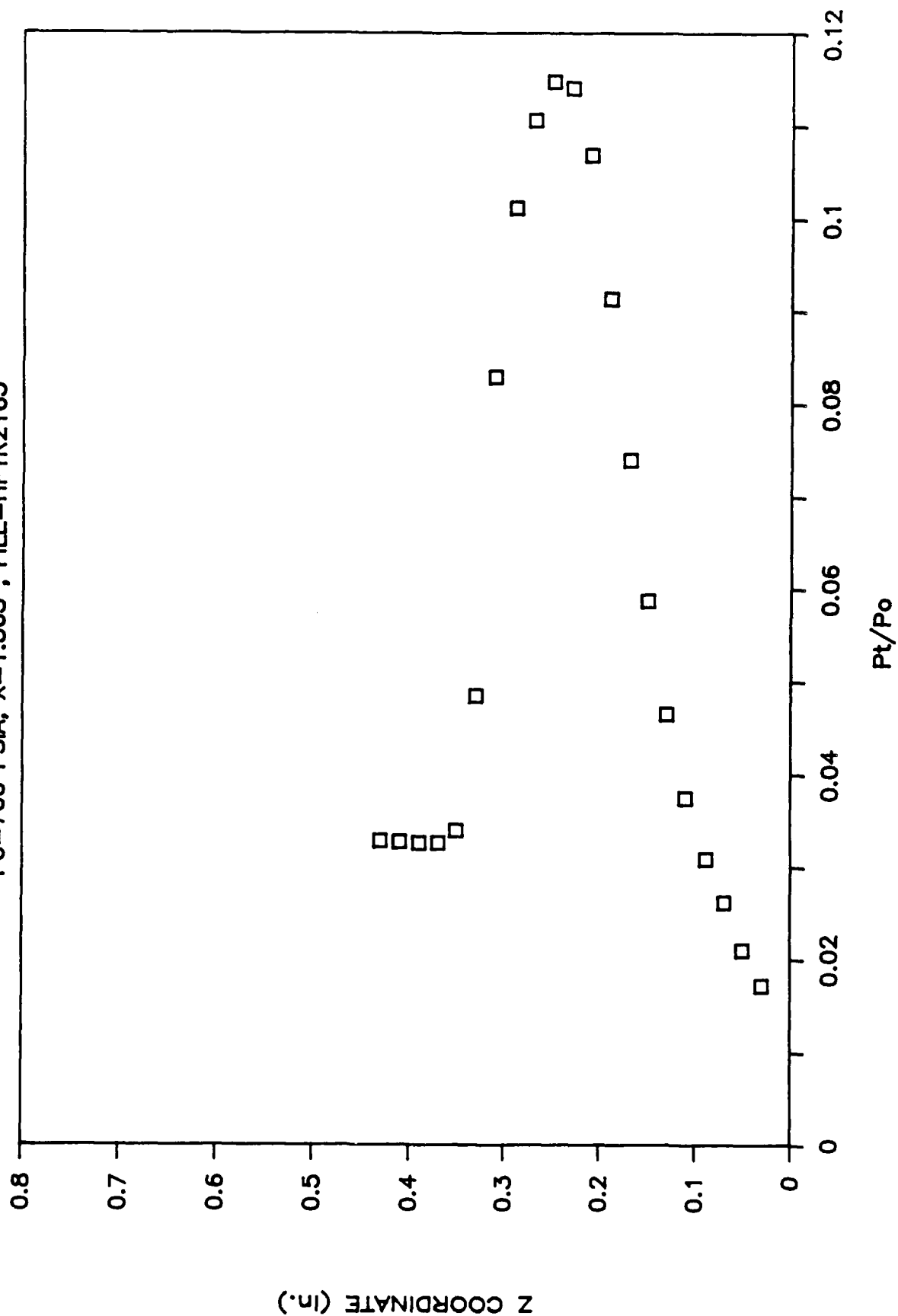


Figure 28 Nondimensionalized Pitot Pressure Distribution at a Given Location and Stagnation Pressure

ROUGH PLATE 22 DEG RAMP

$P_0=1400$ PSIA, $X=1.563$ ", FILE=HPTR2137

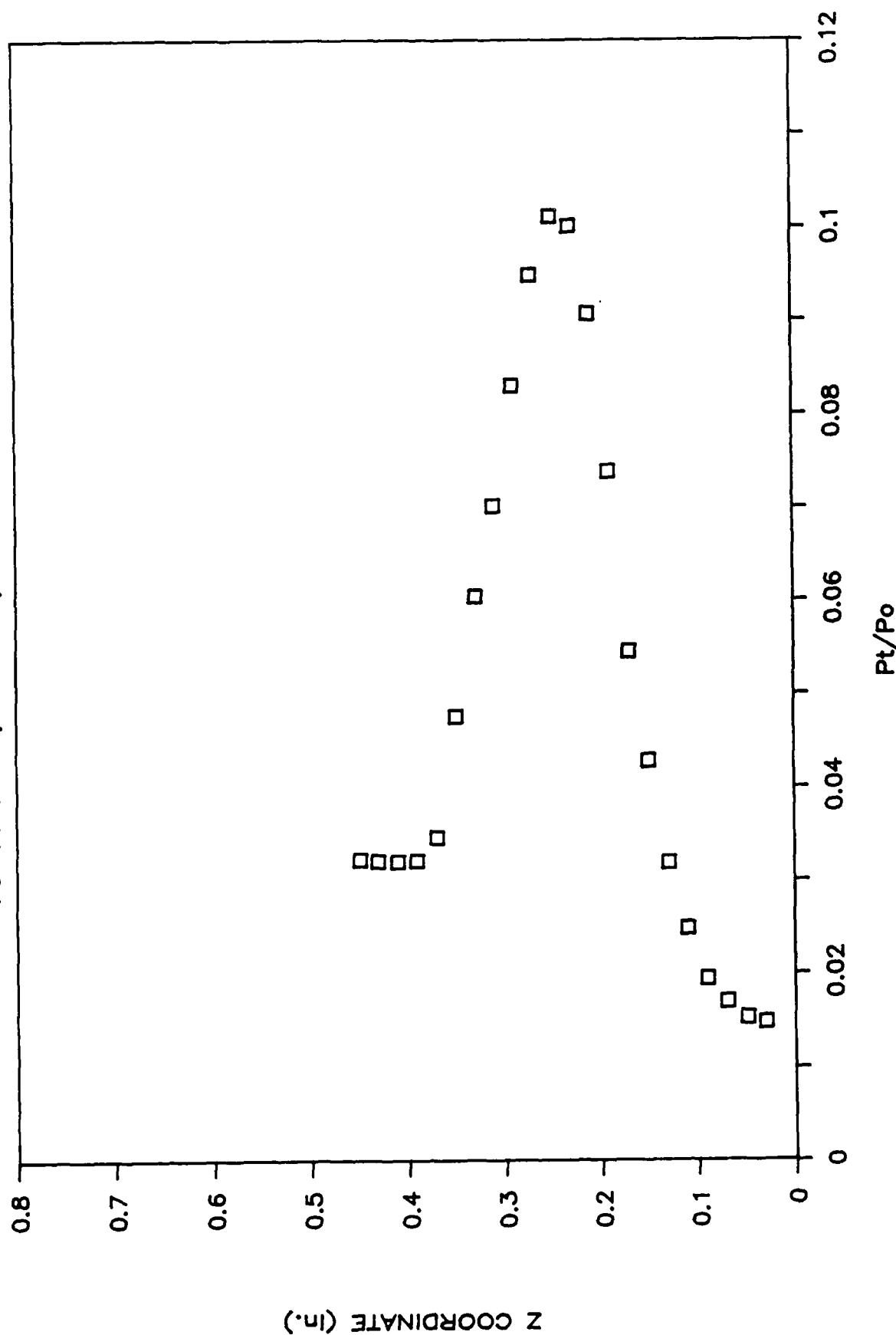


Figure 29 Nondimensionalized Pitot Pressure Distribution at a Given Location and Stagnation Pressure

ROUGH PLATE 22 DEG RAMP

$P_o=2000$ PSIA, $X=1.563$ ", FILE=HPTR2160

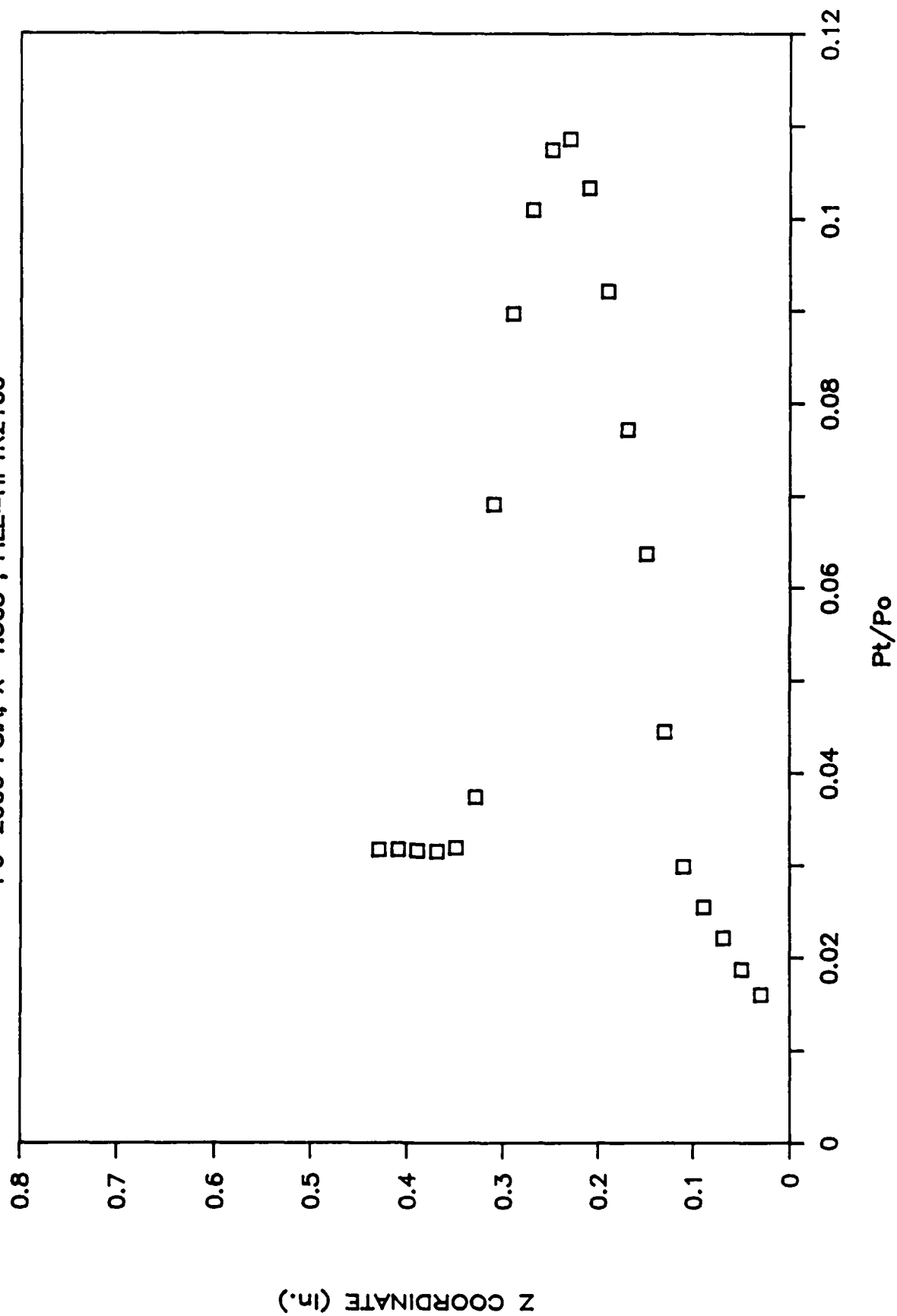
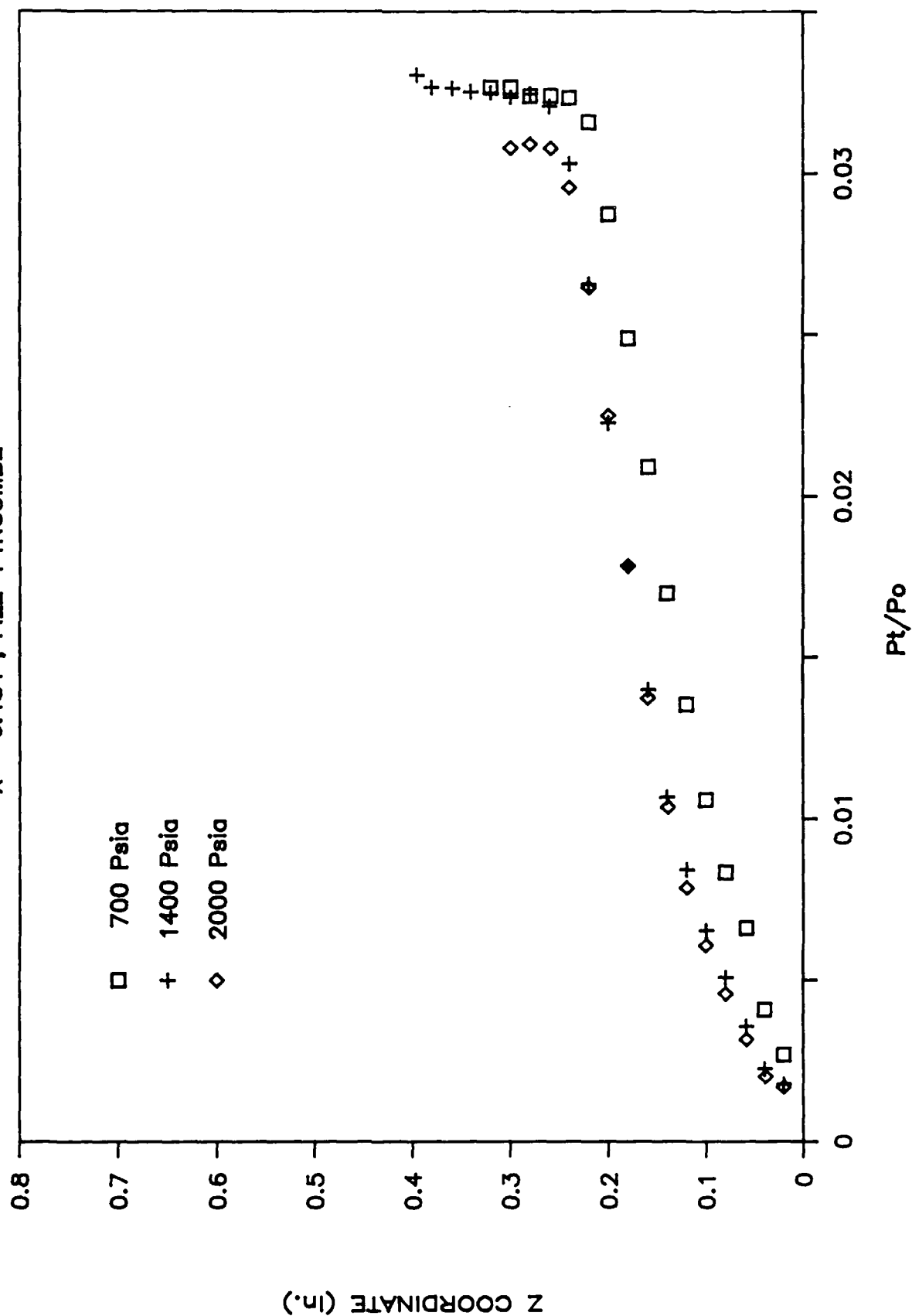


Figure 30 Nondimensionalized Pitot Pressure Distribution at a Given Location and Stagnation Pressure

ROUGH PLATE 22 DEG RAMP

X=-6.484", FILE=PTRCOMB2



ROUGH PLATE, 22 DEG RAMP

X=-2.172", FILE=PTRCOMB1

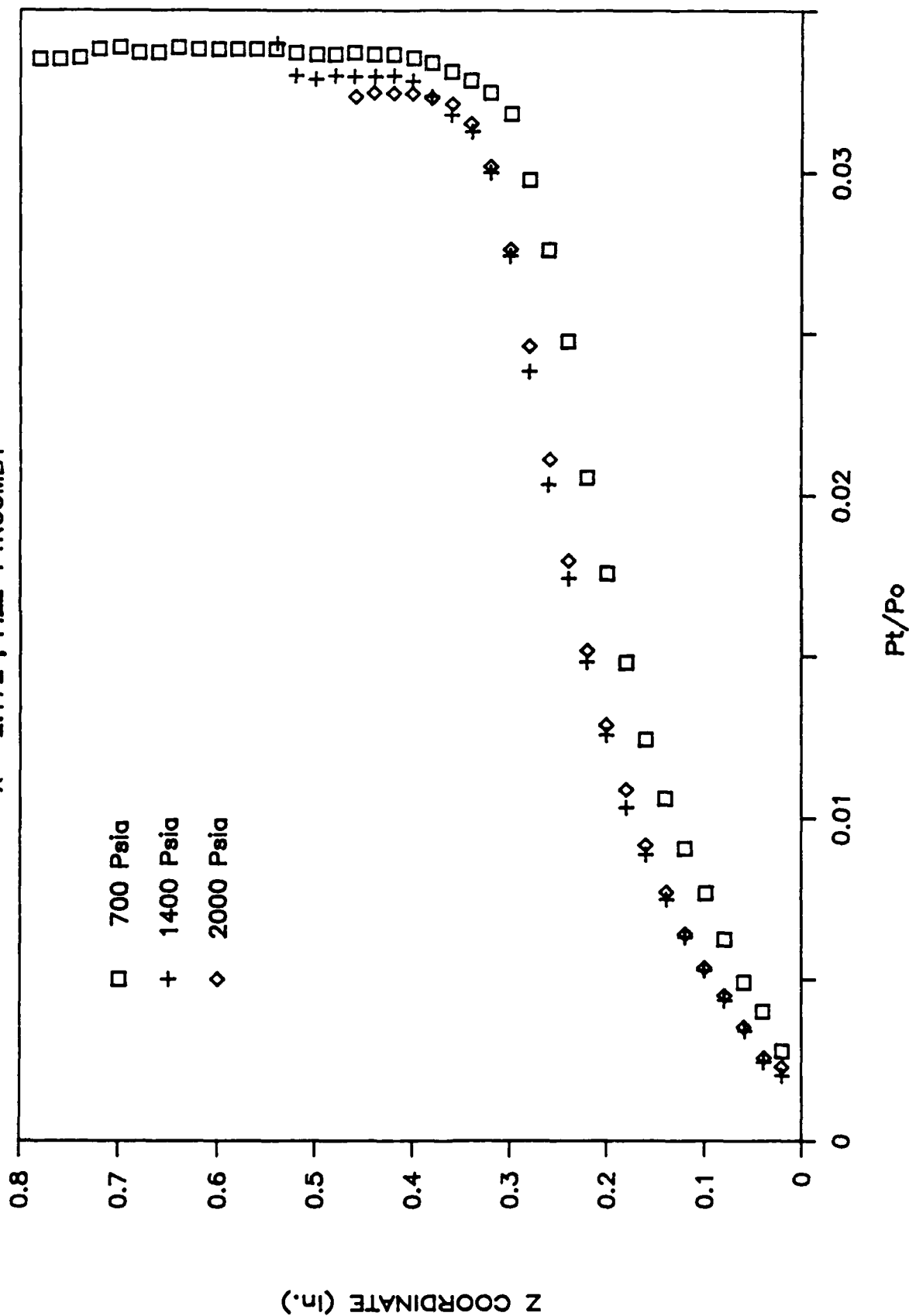


Figure 32 Combined Nondimensionalized Pitot Pressure Distributions at a Single Location

ROUGH PLATE 22 DEG RAMP

X=1.563", FILE=PTRCOMB3

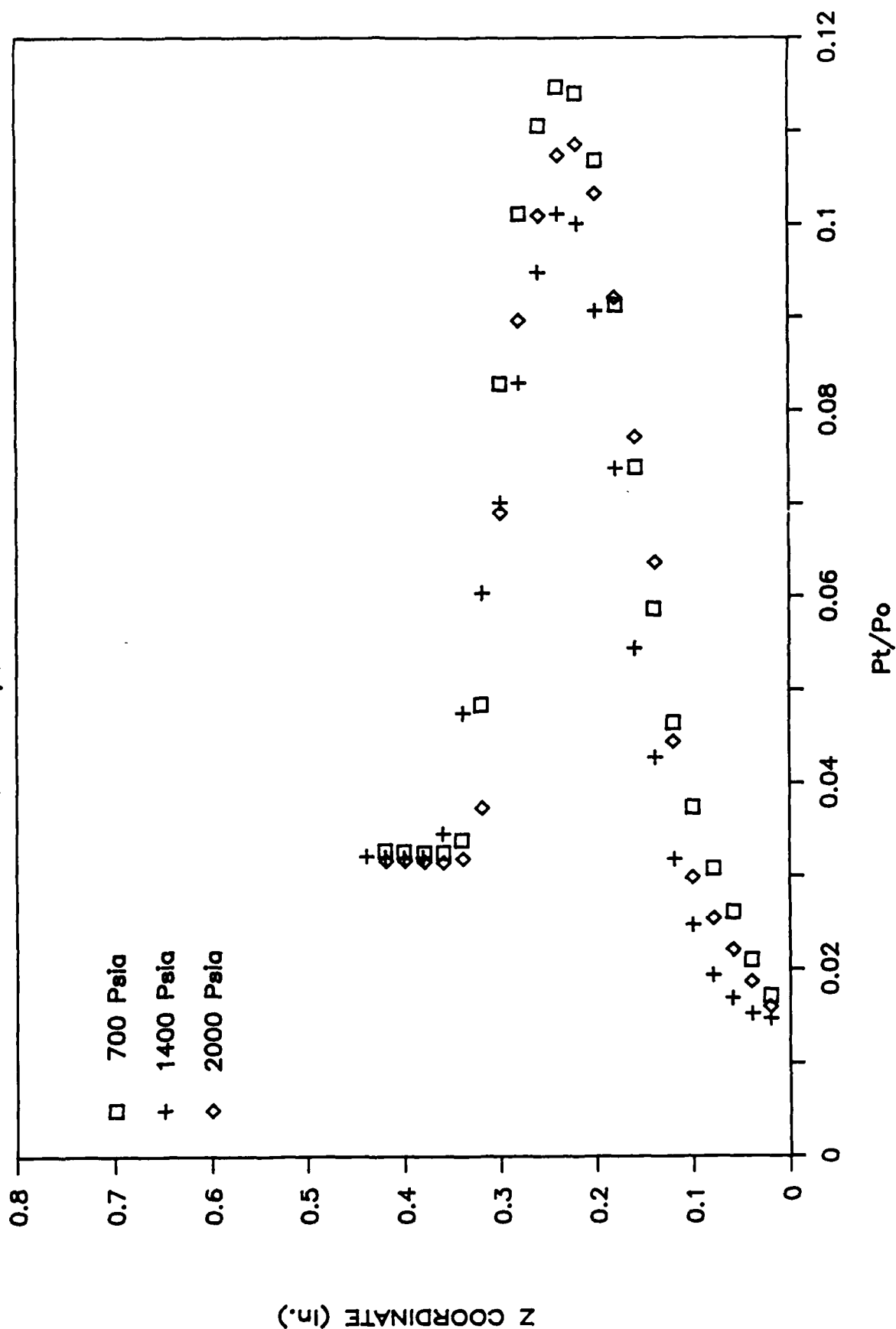


Figure 33 Combined Nondimensionalized Pitot Pressure Distributions at a Single Location

ROUGH PLATE 22 DEG RAMP

Po=700 PSIA, FILE=PTRCOMB4

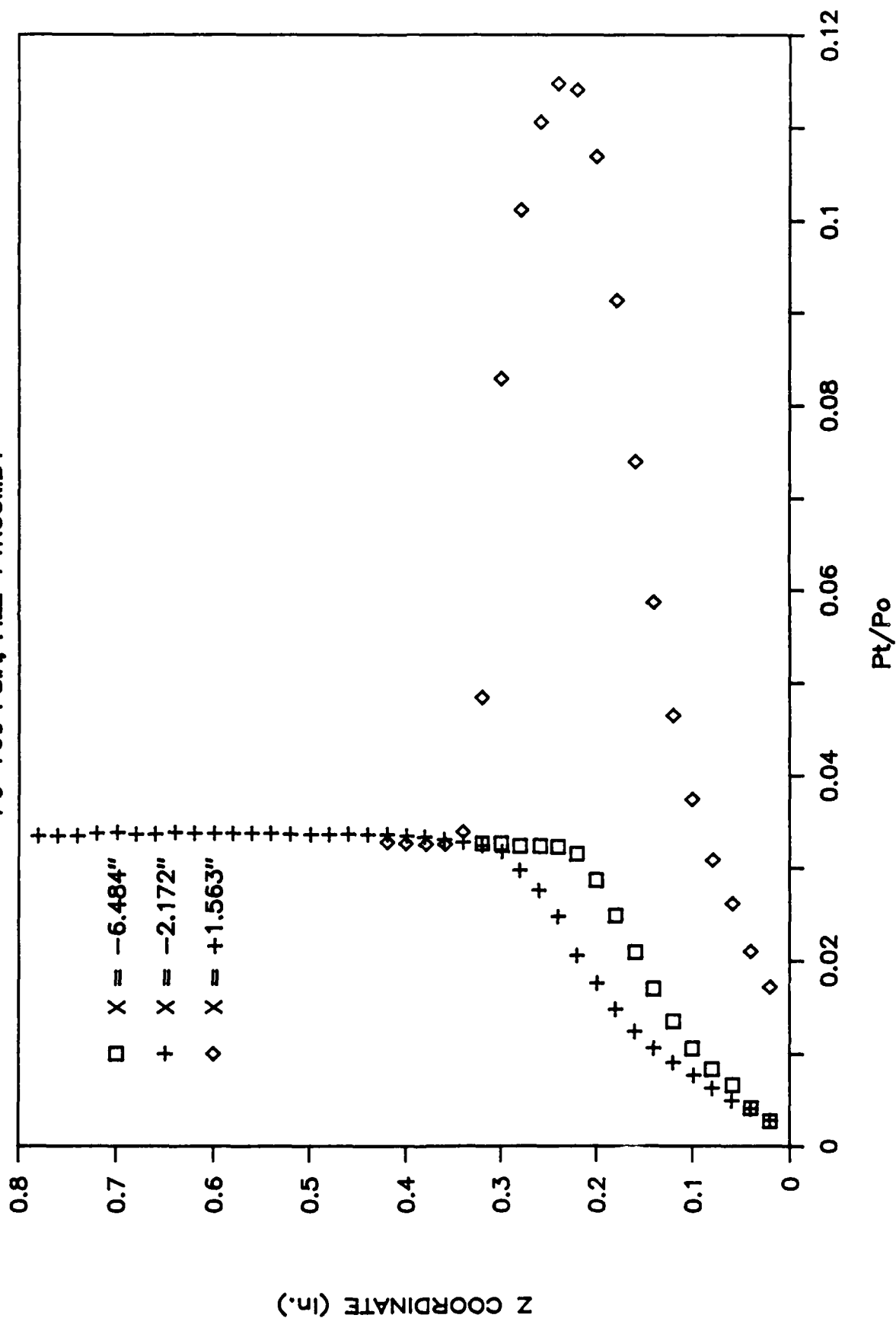


Figure 34 Combined Nondimensionalized Pitot Pressure Distributions at a Single Stagnation Pressure

ROUGH PLATE 22 DEG RAMP

$P_0=1400$ PSIA, FILE=PTRCOMB5

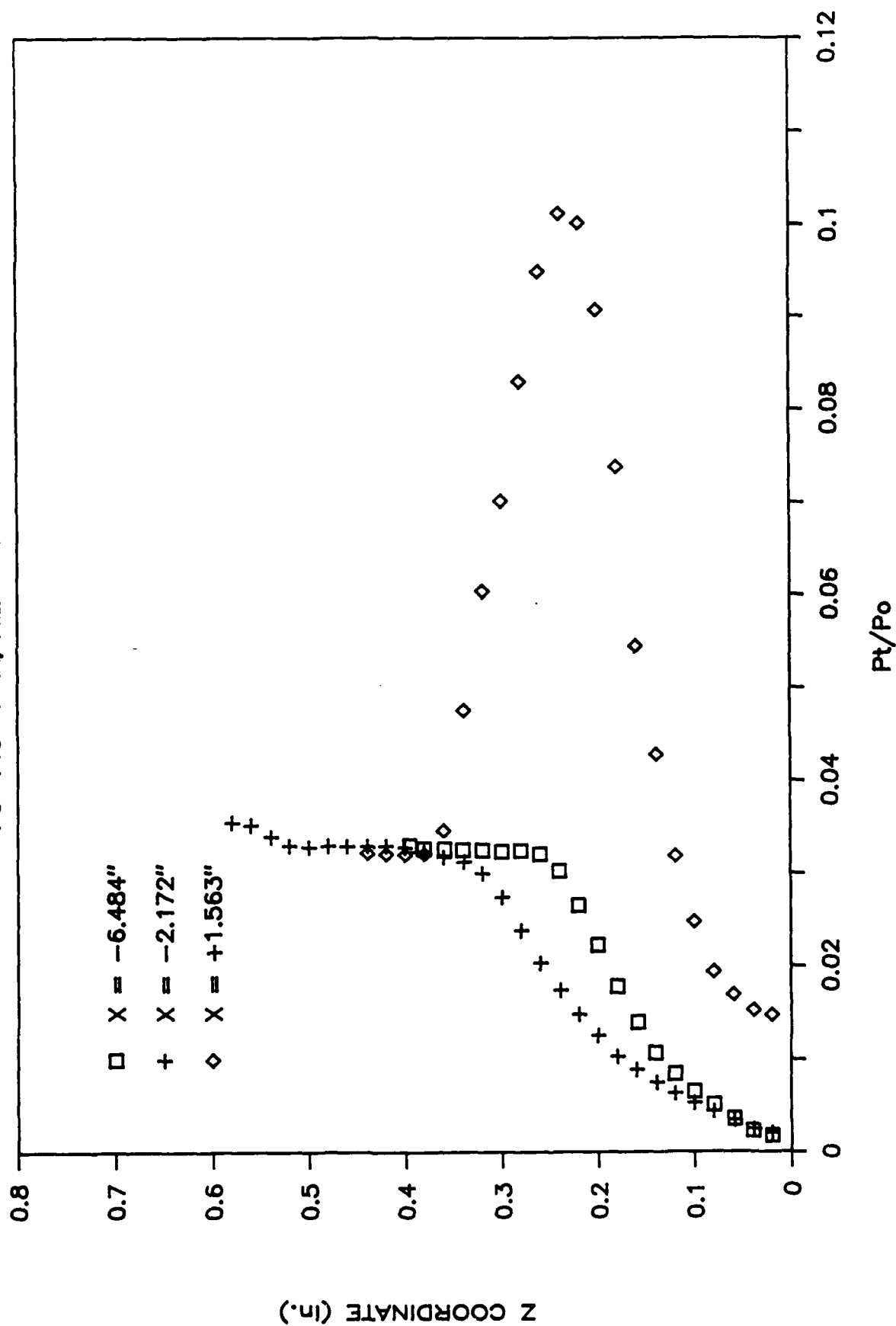


Figure 35 Combined Nondimensionalized Pitot Pressure Distributions

ROUGH PLATE 22 DEG RAMP

Po=2000 PSIA, FILE=PTRCOMB6

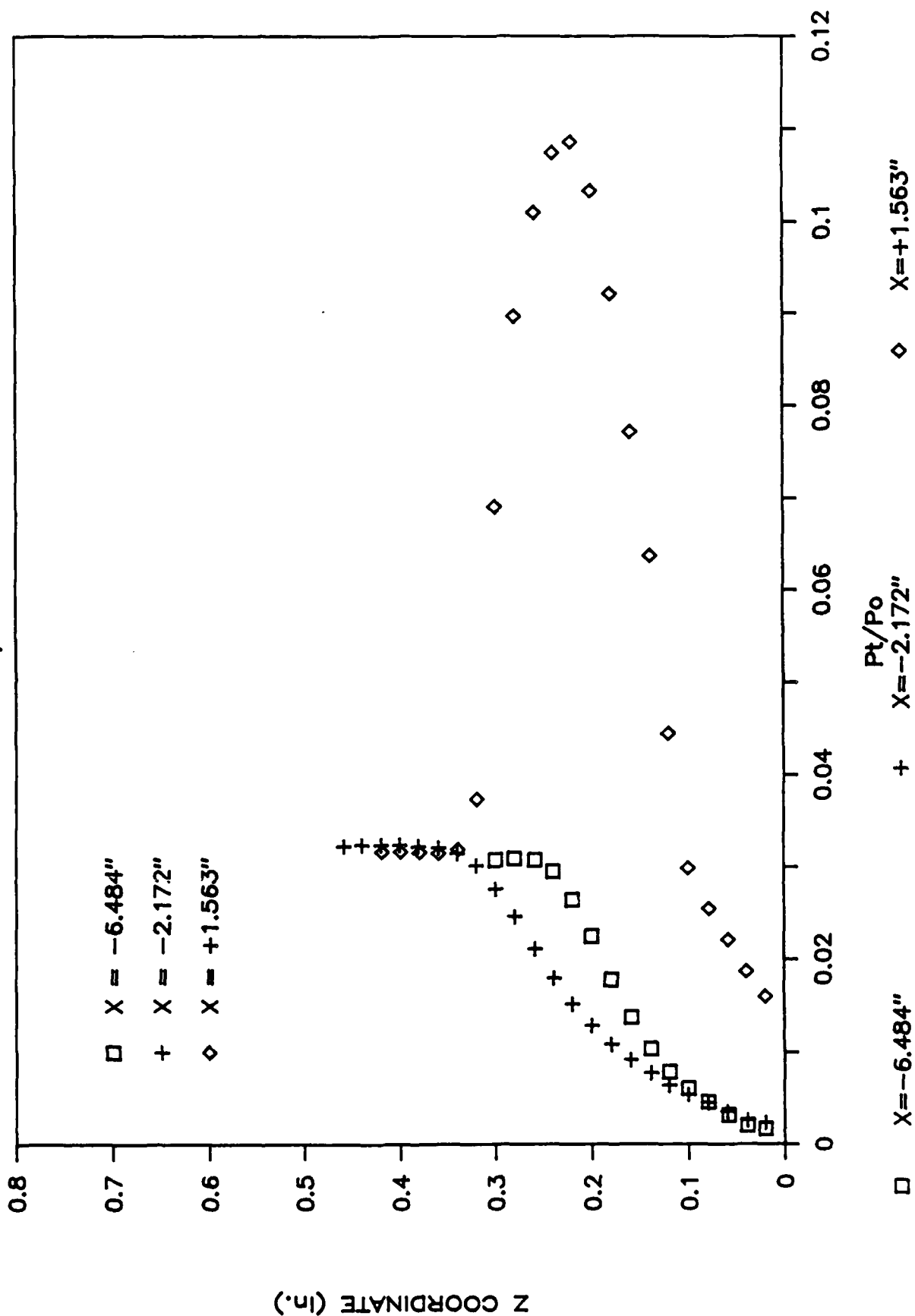


Figure 36 Combined Nondimensionalized Pitot Pressure Distributions at a Single Stagnation Pressure

ROUGH PLATE

X=-6.484", FILE=MRCOMB2

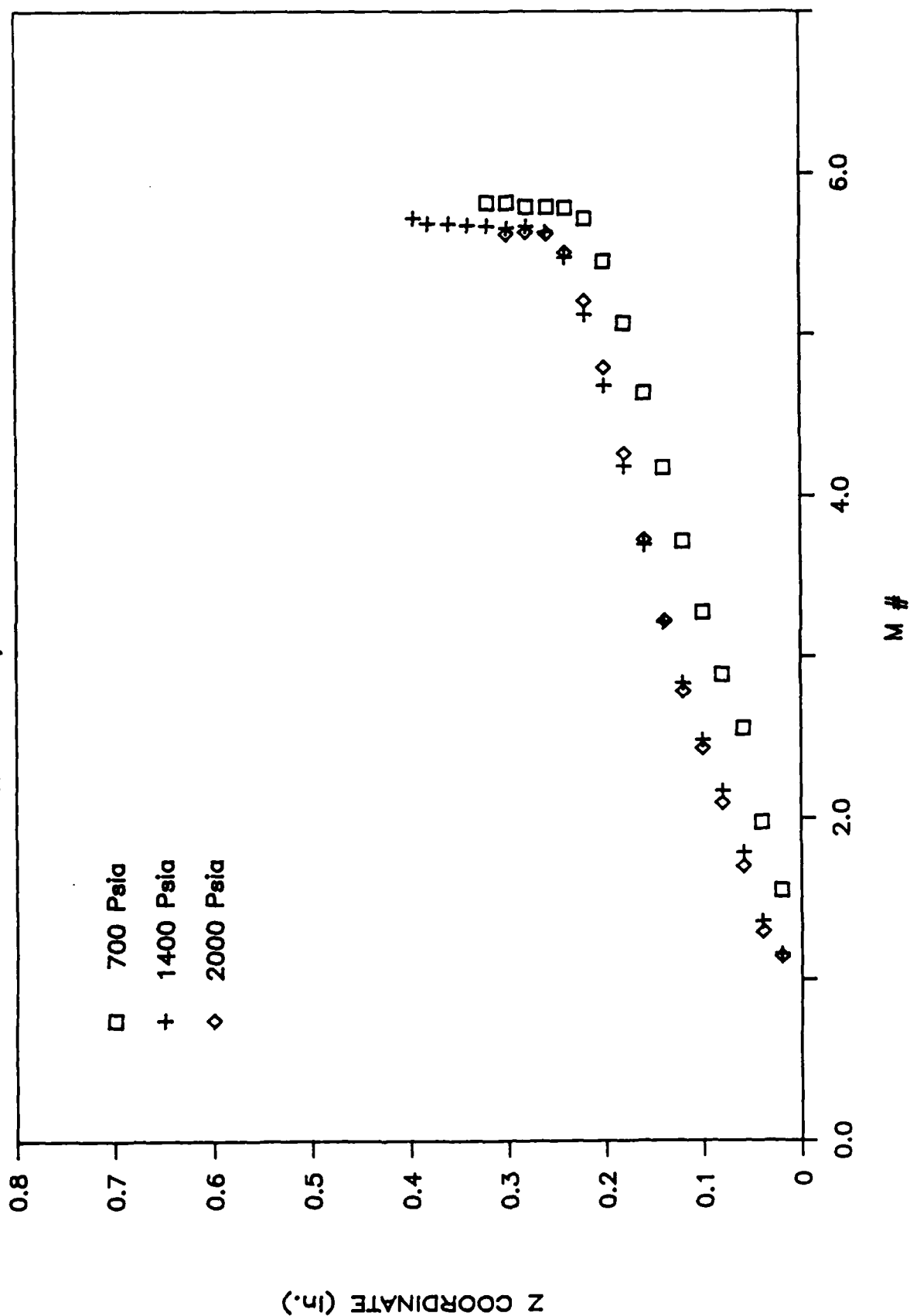


Figure 37 Combined Mach Number Distributions at a Single Location

ROUGH PLATE

X=-2.172", FILE=MRCOMB1

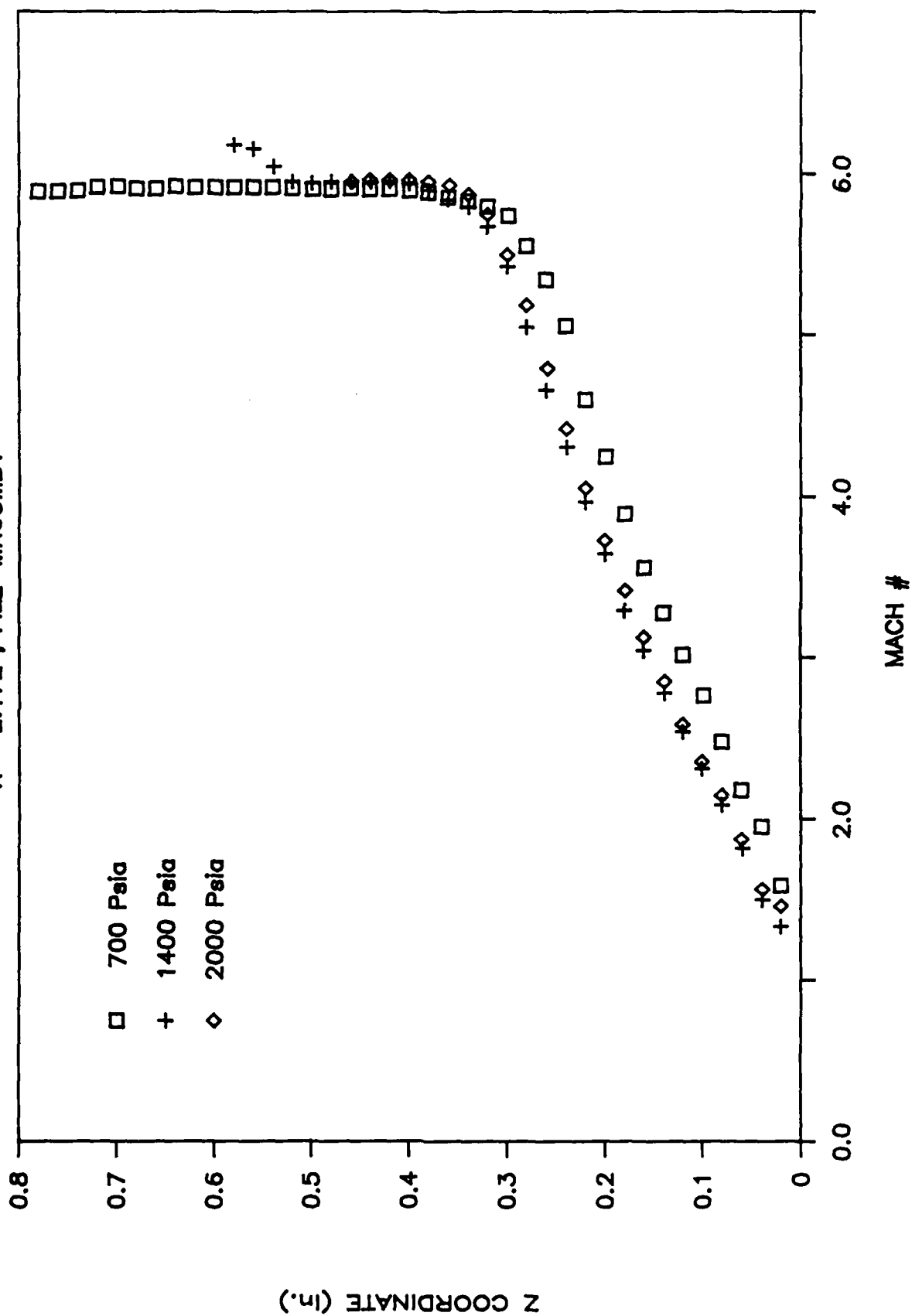


Figure 38 Combined Mach Number Distributions at a Single Location

ROUGH PLATE

$P_0=700$ PSIA, FILE=MRCOMB3

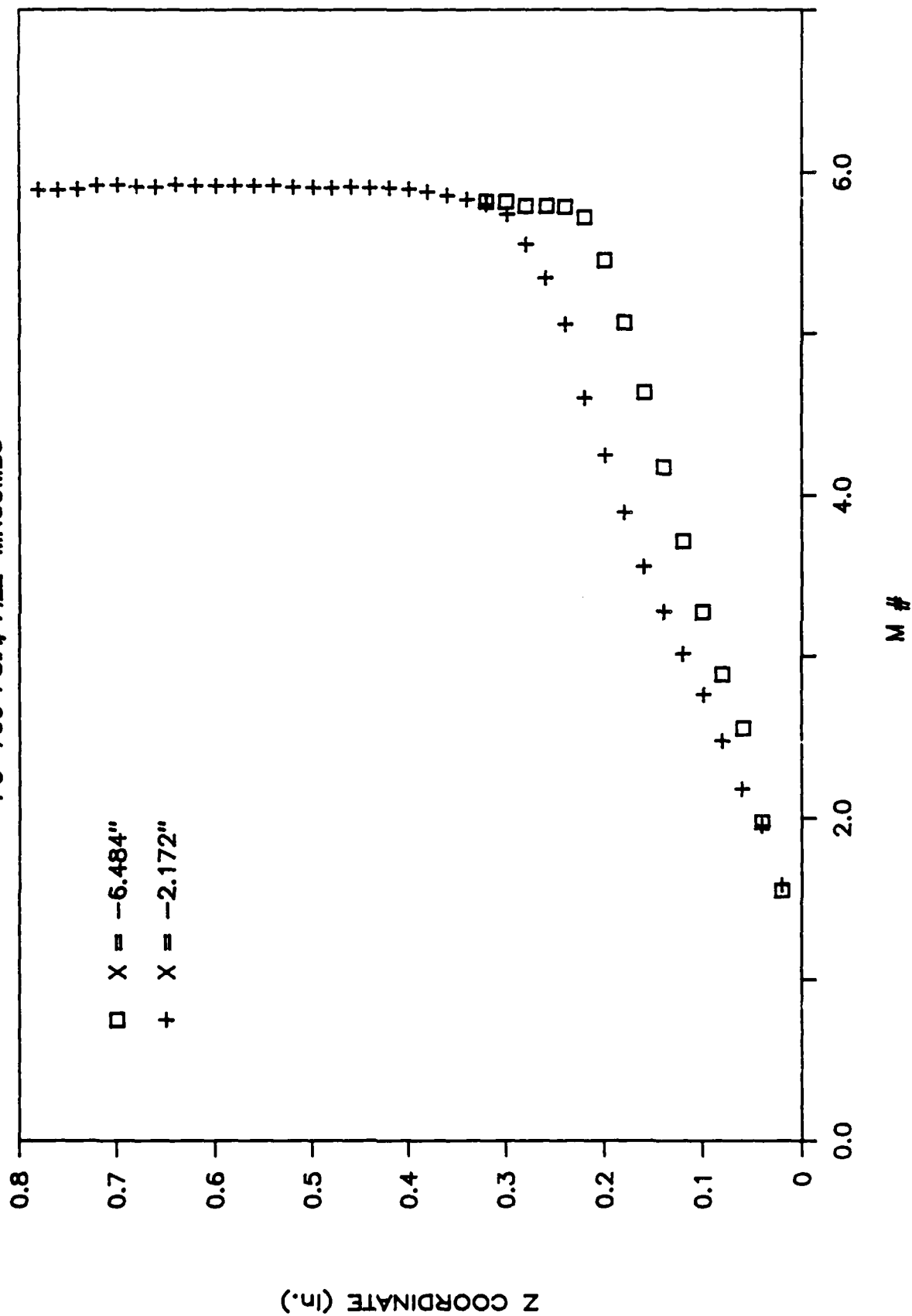


Figure 39 Combined Mach Number Distributions at a Single Stagnation Pressure

ROUGH PLATE

Po=1400 PSIA, FILE=MRCOMB4

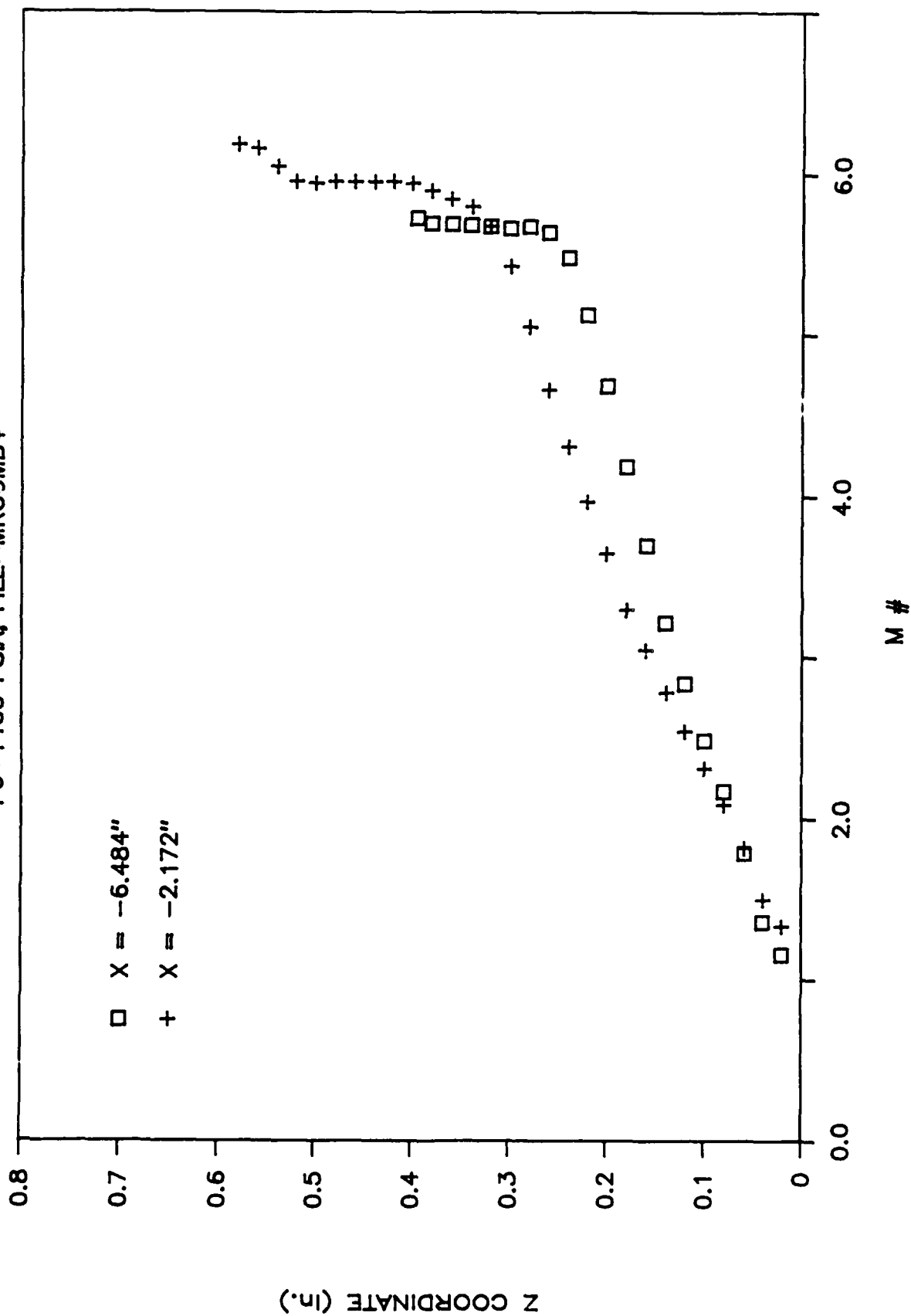
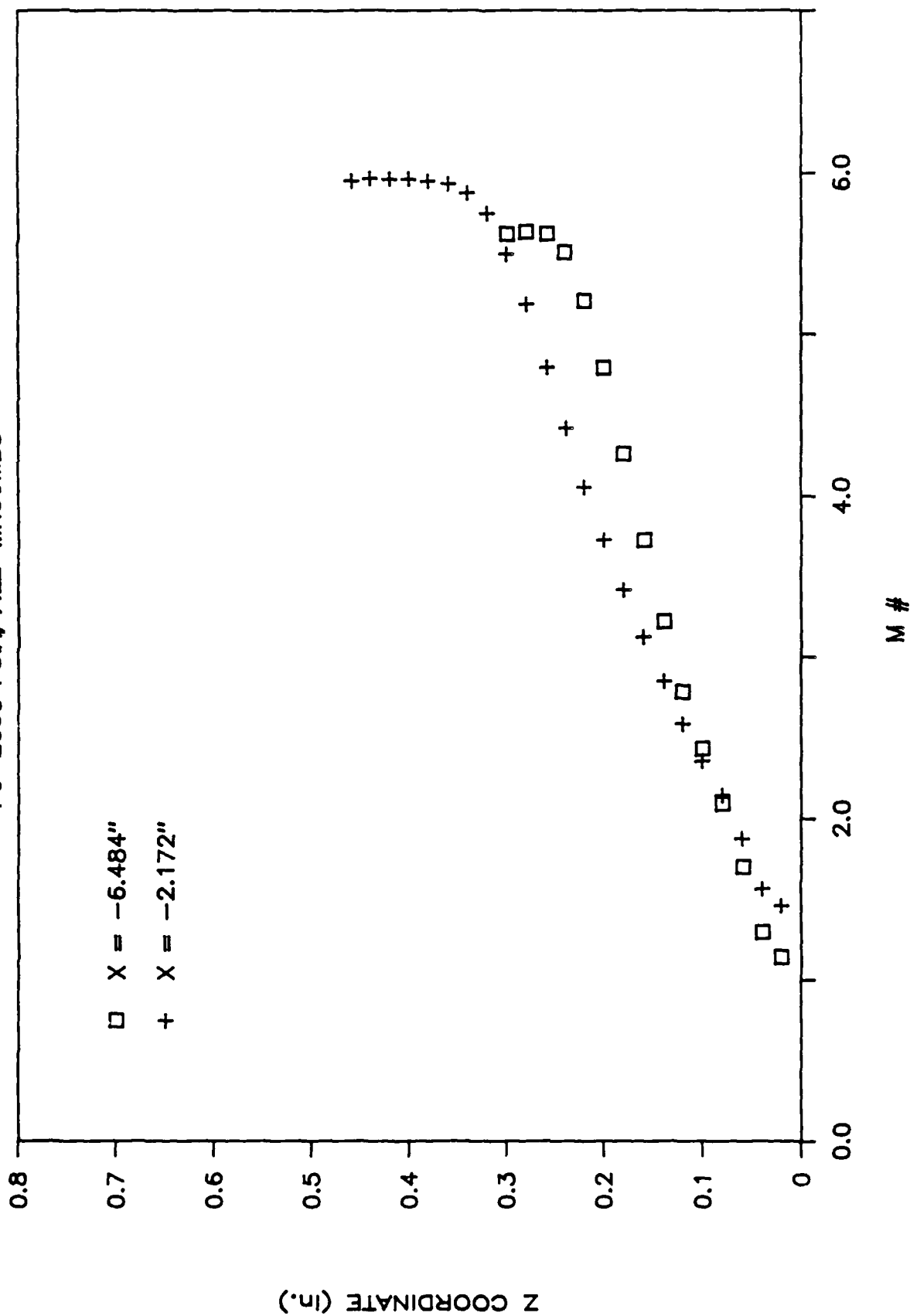


Figure 40 Combined Mach Number Distributions at a Single Stagnation Pressure

ROUGH PLATE

P₀=2000 PSIA, FILE=MRCOMB5



ROUGH PLATE

X=-6.484", P₀=700 PSIA, FILE=HTTR2174

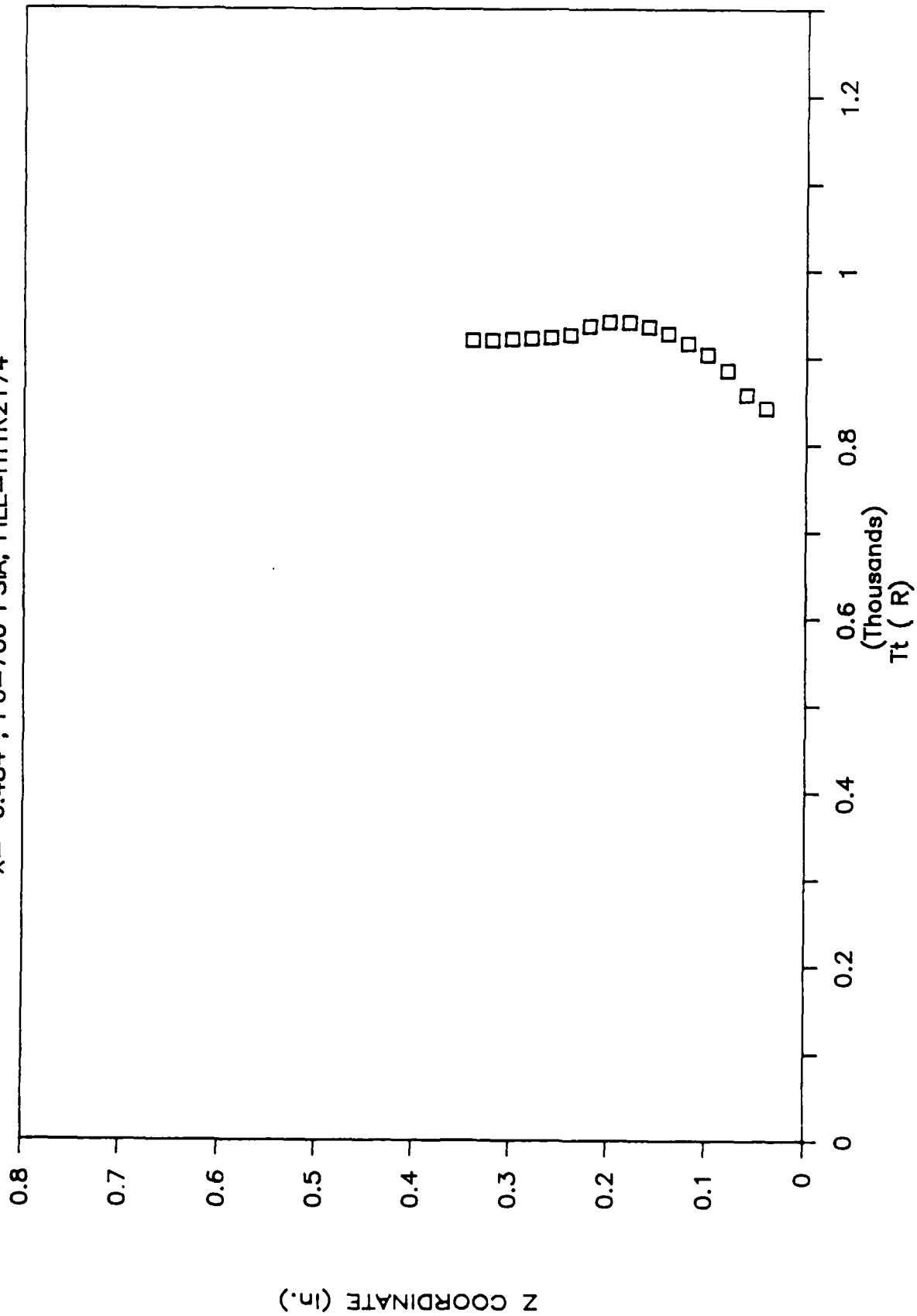


Figure 42a Total Temperature Distribution at a Given Location and Stagnation Pressure

ROUGH PLATE

X=-6.484", Po=700 PSIA, FILE=HTTR2174

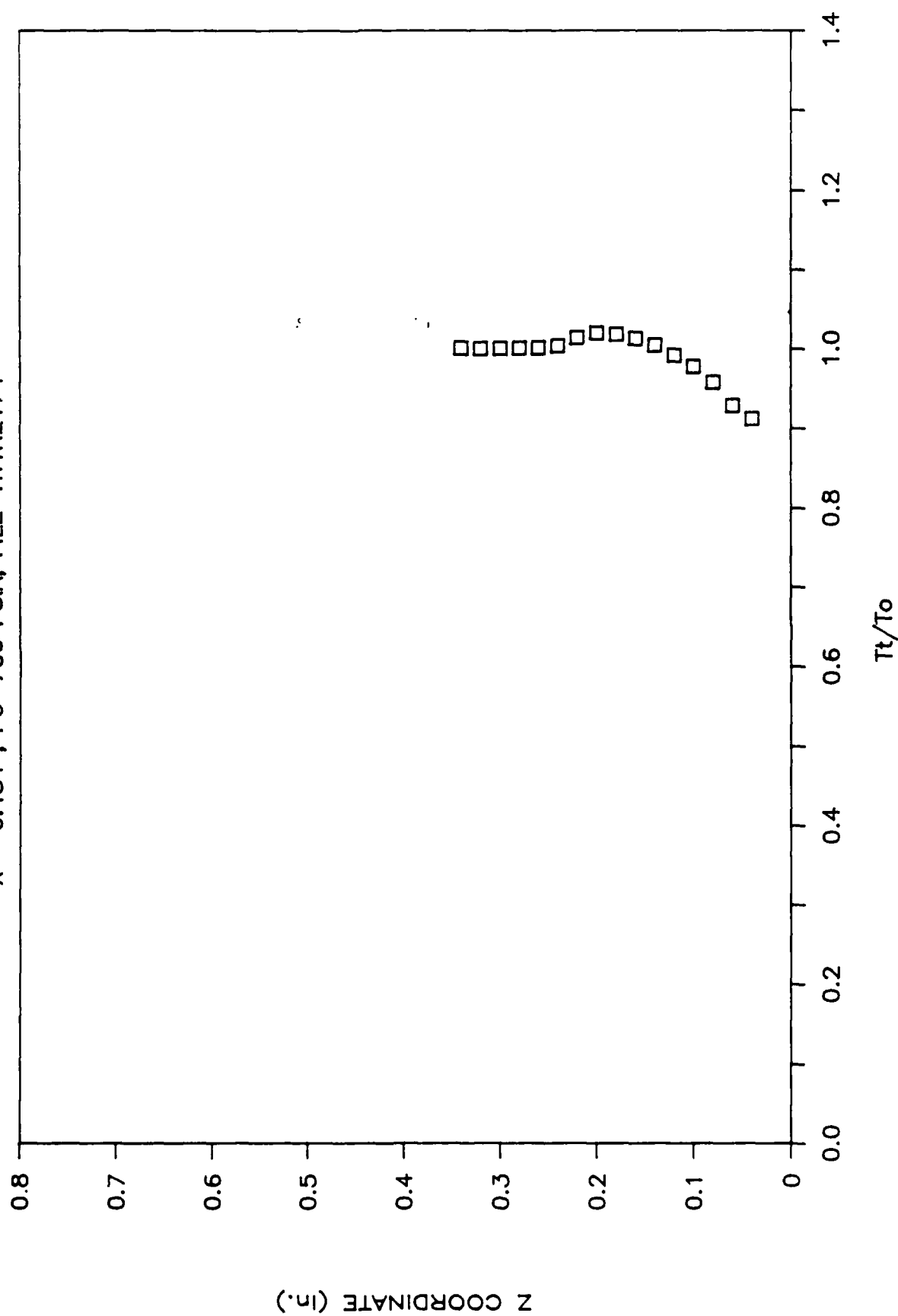


Figure 42b Normalized Total Temperature Distribution at a Given Location and

ROUGH PLATE

$X = -6.484"$, $P_o = 1400$ PSIA, FILE=HTTR2178

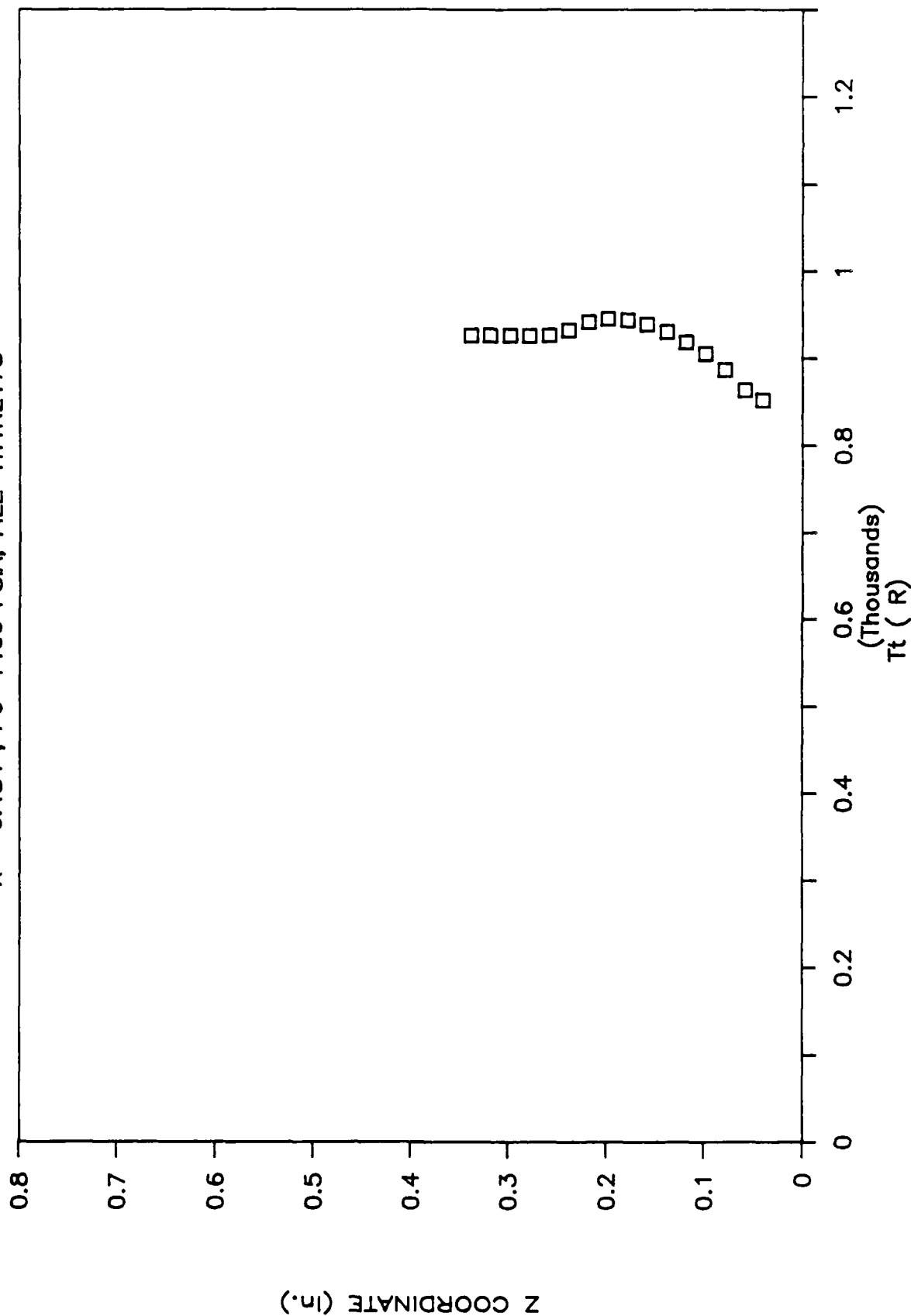


Figure 43a Total Temperature Distribution at a Given Location and Stagnation Pressure

ROUGH PLATE

X=-6.484", Po=1400 PSIA, FILE=HTTR2178

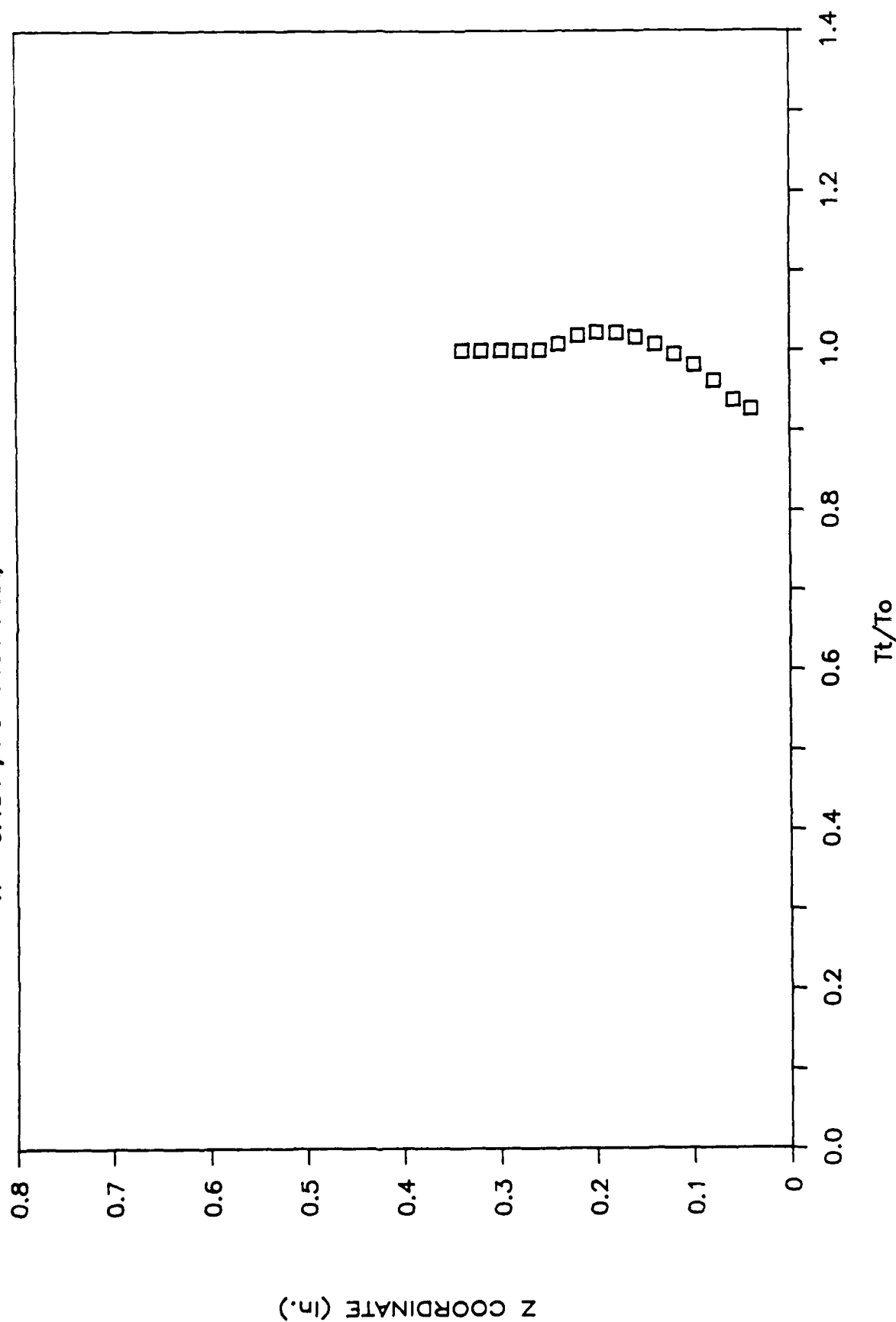


Figure 43b Normalized Total Temperature Distribution at a Given Location and Stagnation Pressure

ROUGH PLATE

X=-6.484", P₀=2000 PSIA, FILE=HTTR2177

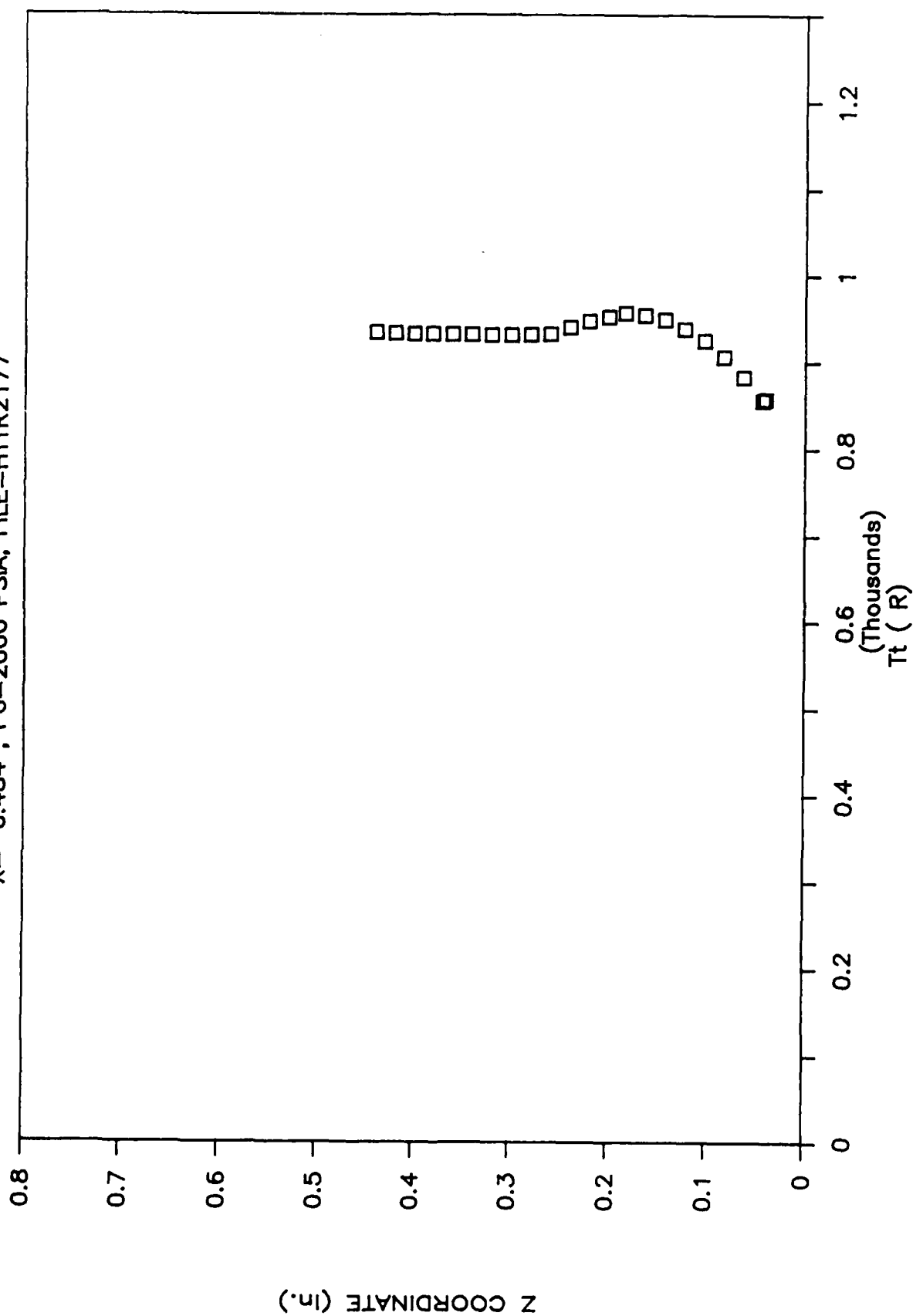


Figure 44a Total Temperature Distribution at a Given Location and Stagnation Pressure

ROUGH PLATE

X=-6.484", Po=2000 PSIA, FILE=HTTR2177

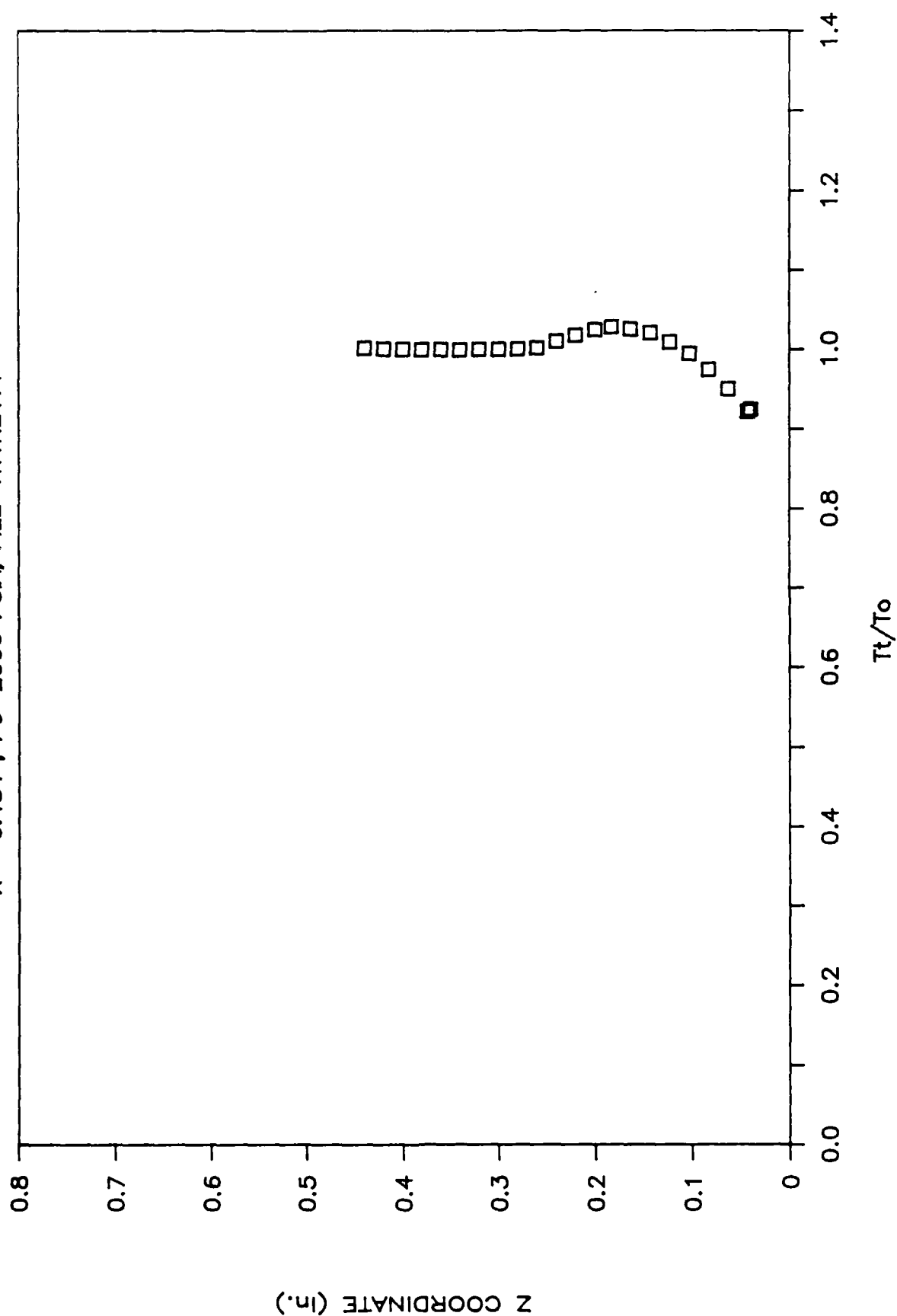


Figure 44b Normalized Total Temperature Distribution at a Given Location and

ROUGH PLATE

X=-2.172", P₀=700 PSIA, FILE=HTTR2168

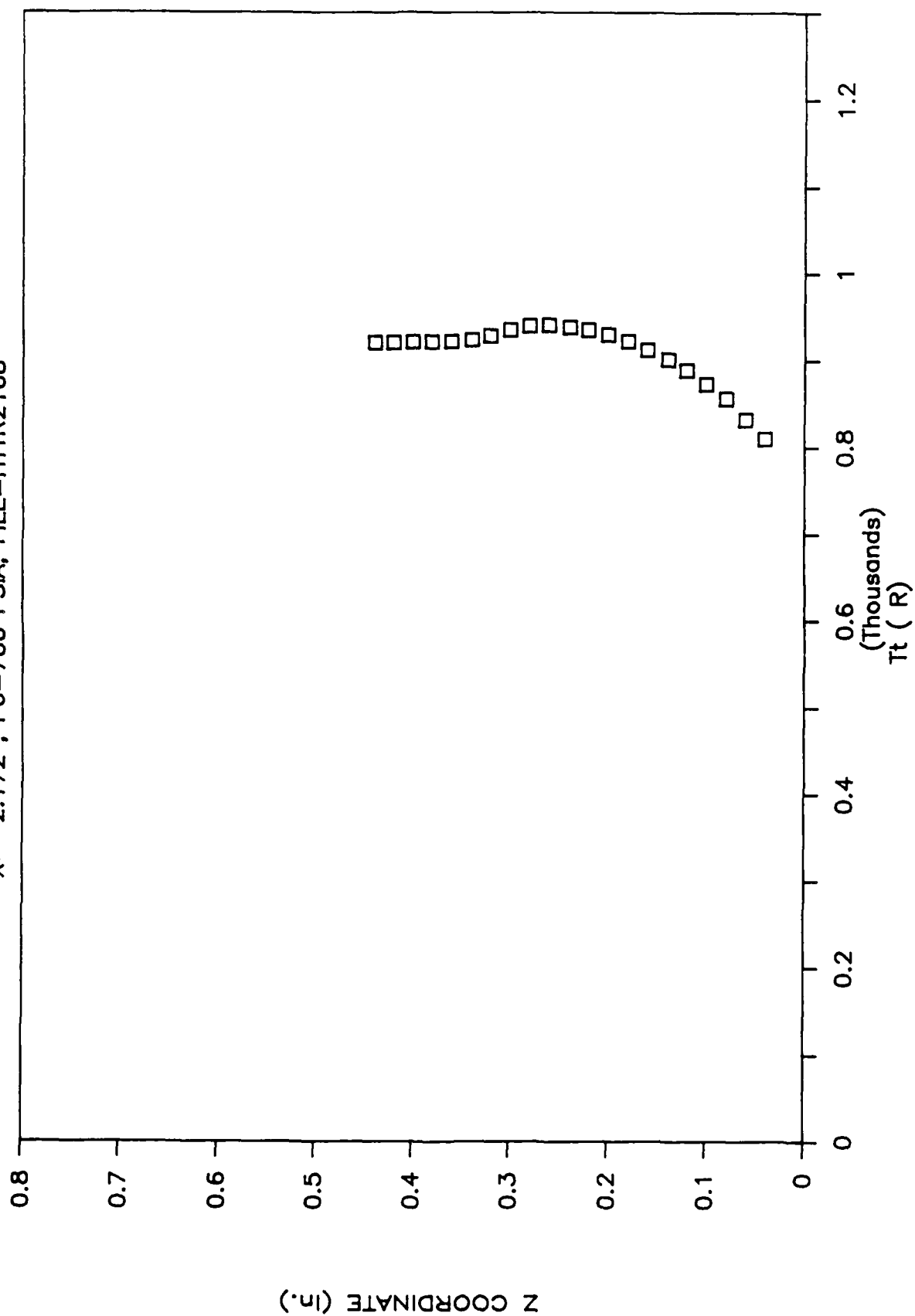


Figure 46a Total Temperature Distribution at a Given Location and Stagnation Pressure

ROUGH PLATE

X=-2.172", P₀=700 PSIA, FILE=HTTR2168

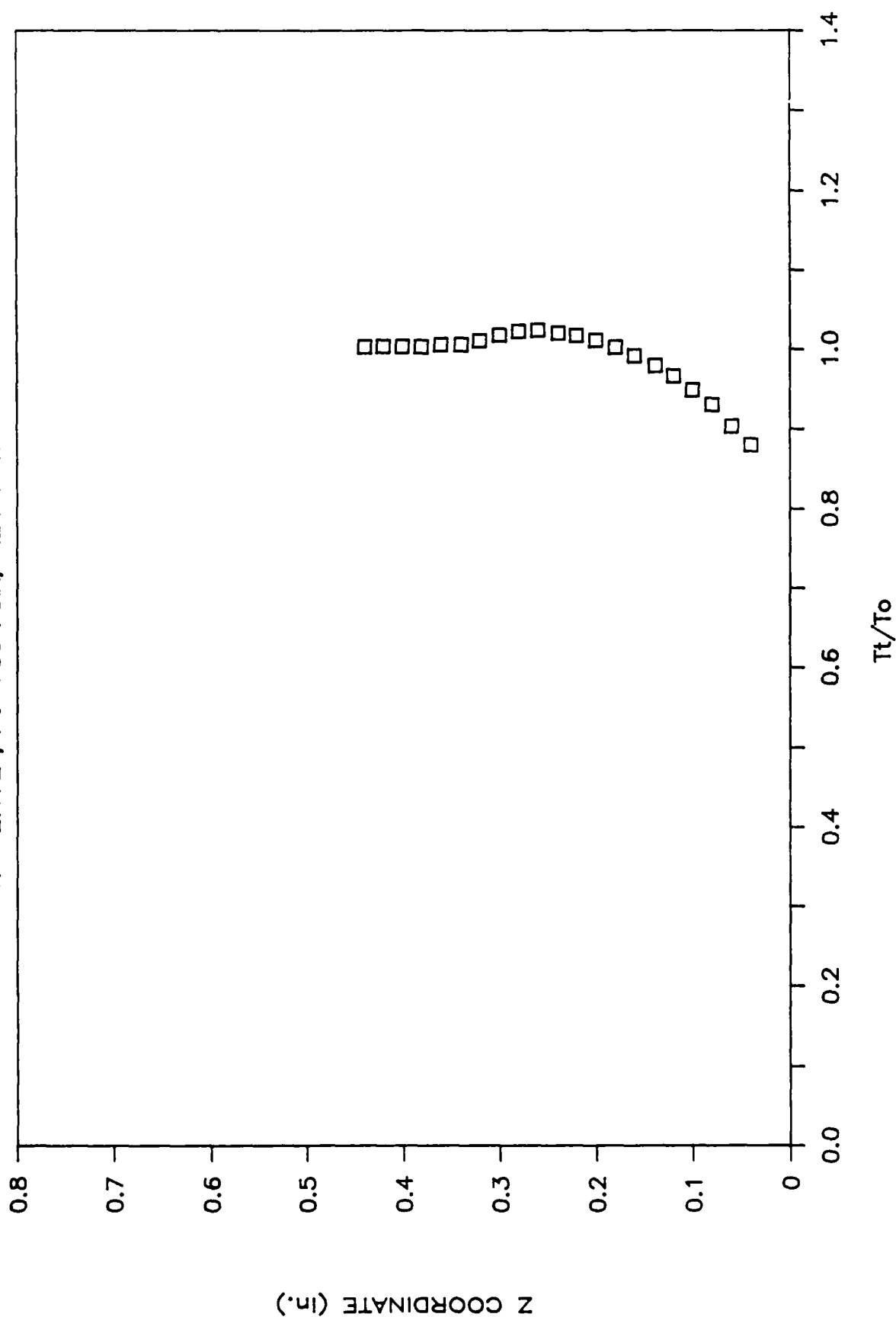


Figure 45b Normalized Total Temperature Distribution at a Given Location and

ROUGH PLATE

X=-2.172", Po=1400 PSIA, FILE=HTTR2171

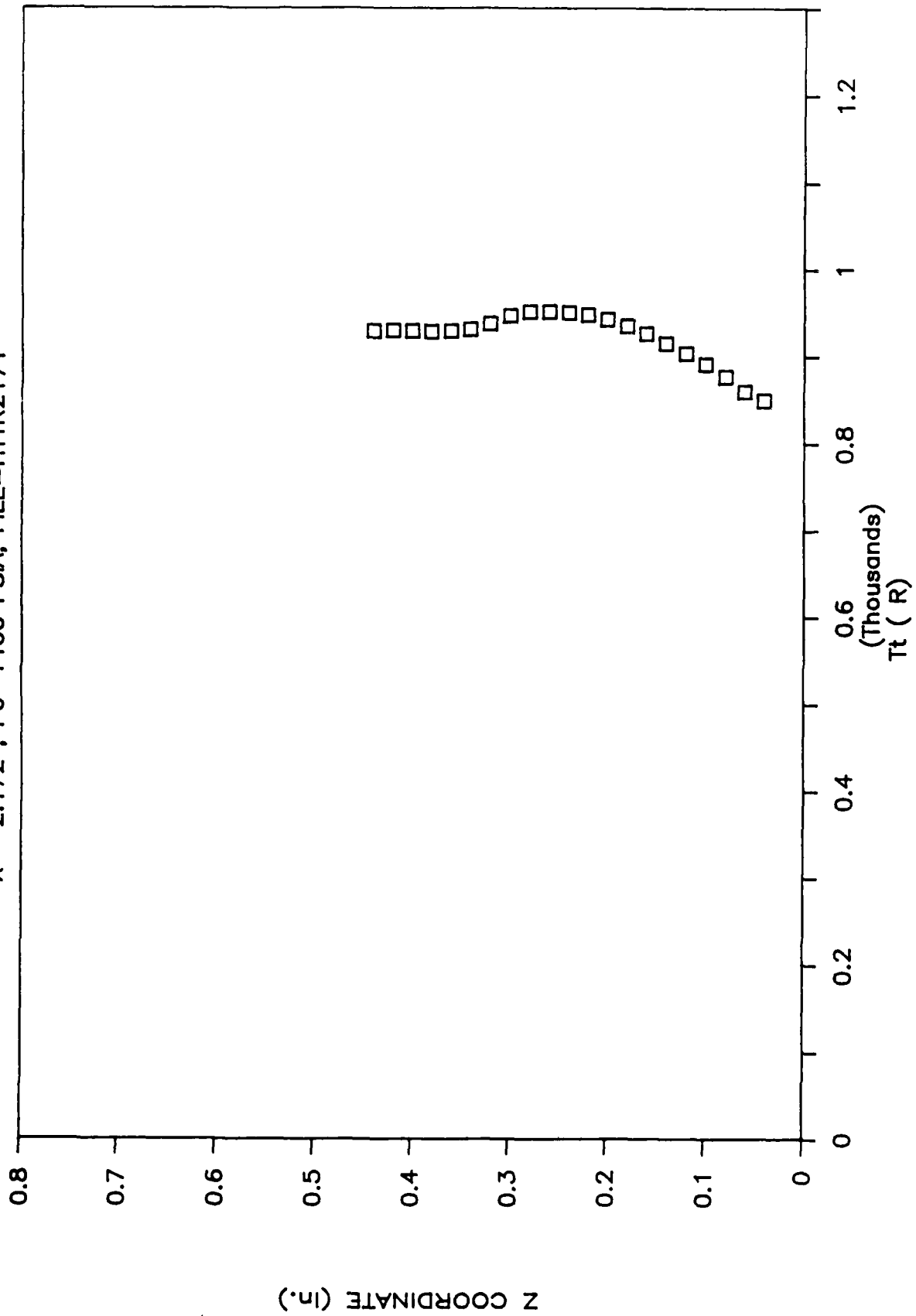


Figure 46a Total Temperature Distribution at a Given Location and Stagnation Pressure

ROUGH PLATE

X=-2.172", Po=1400 PSIA, FILE=HTTR2171

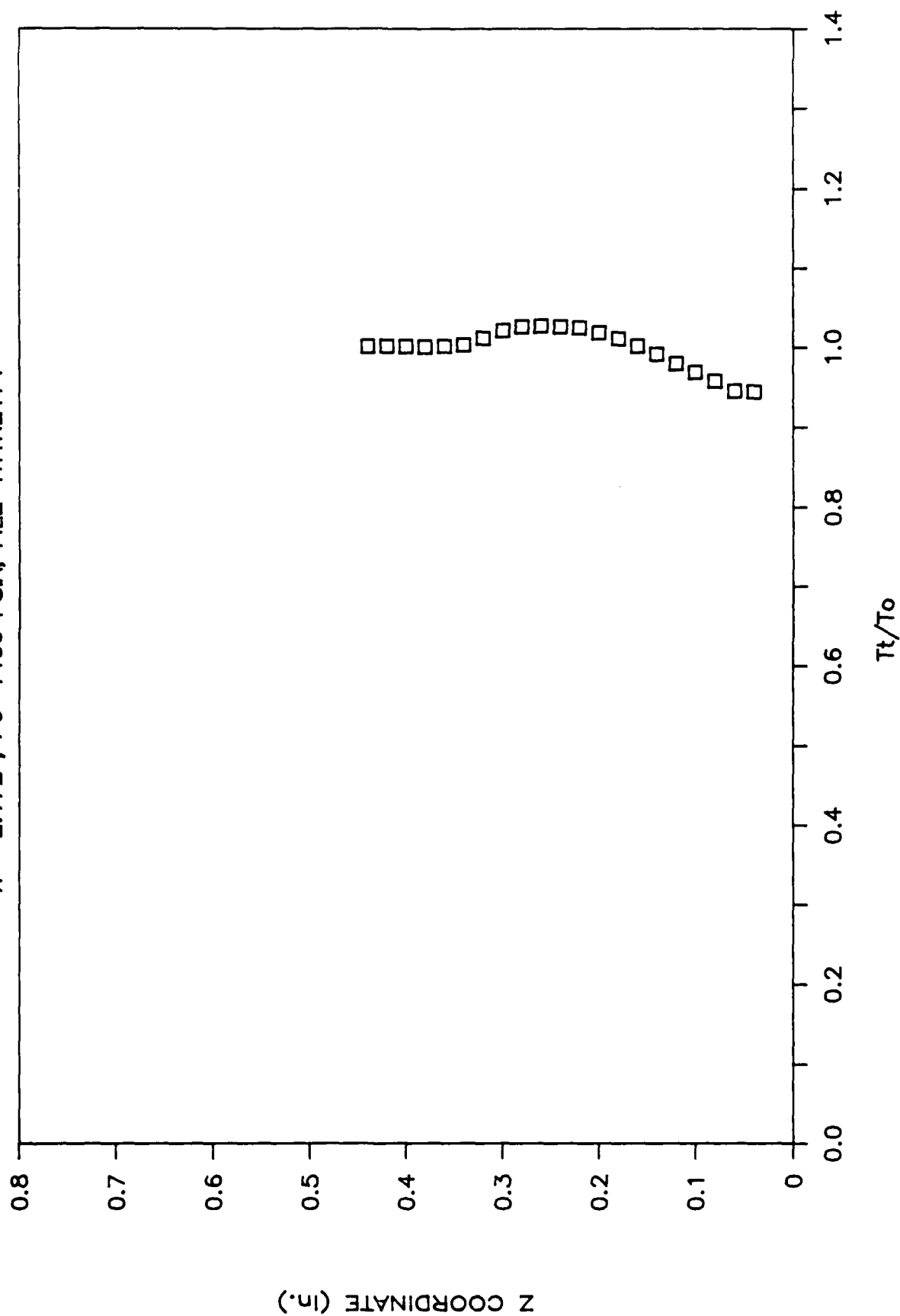


Figure 46b Normalized Total Temperature Distribution at a Given Location and

ROUGH PLATE

$X = -2.172''$, $P_o = 2000$ PSIA, FILE=HTRR2182

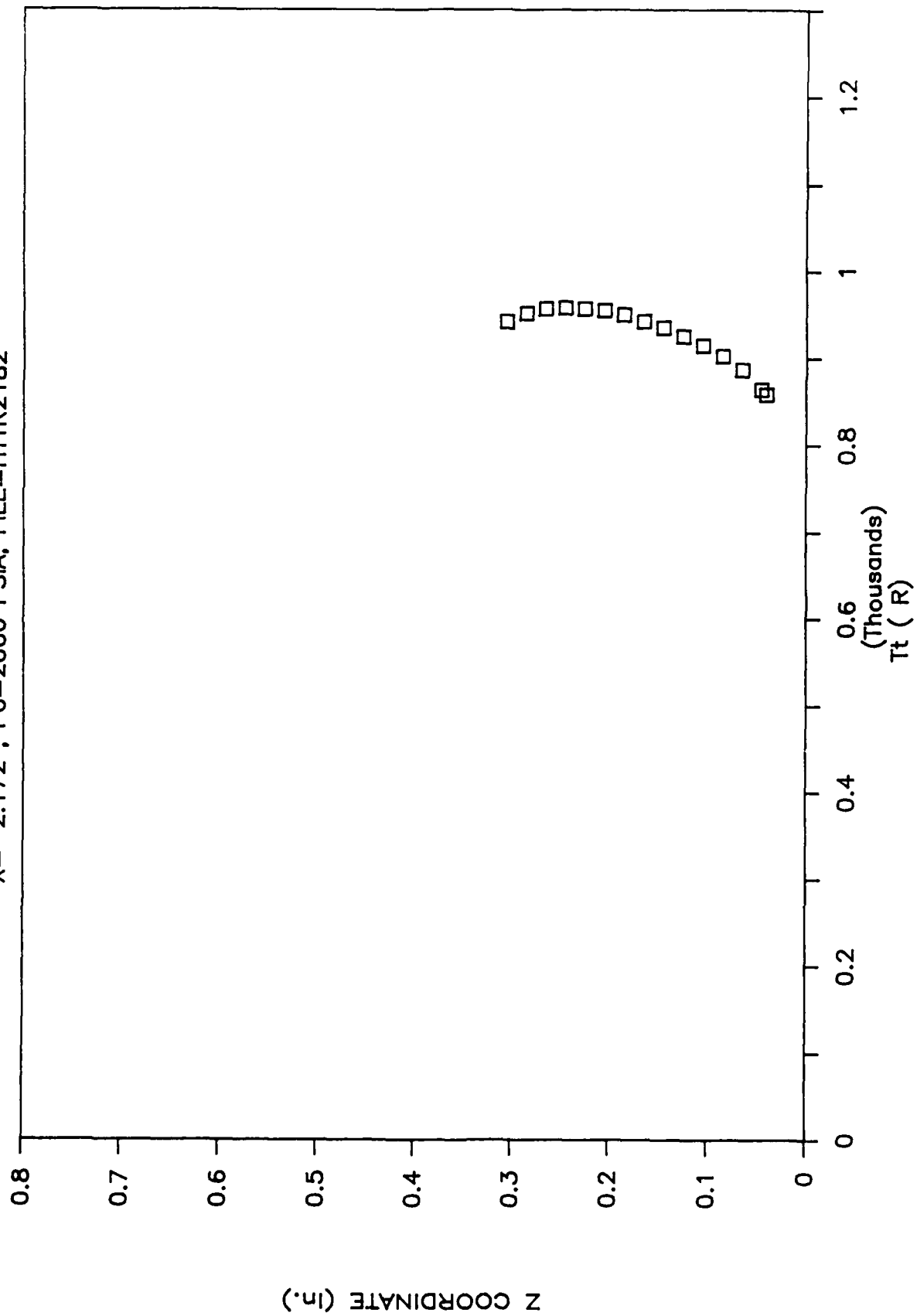


Figure 47a Total Temperature Distribution at a Given Location and Stagnation Pressure

ROUGH PLATE

X=-2.172", Po=2000 PSIA, FILE=HTTR2182

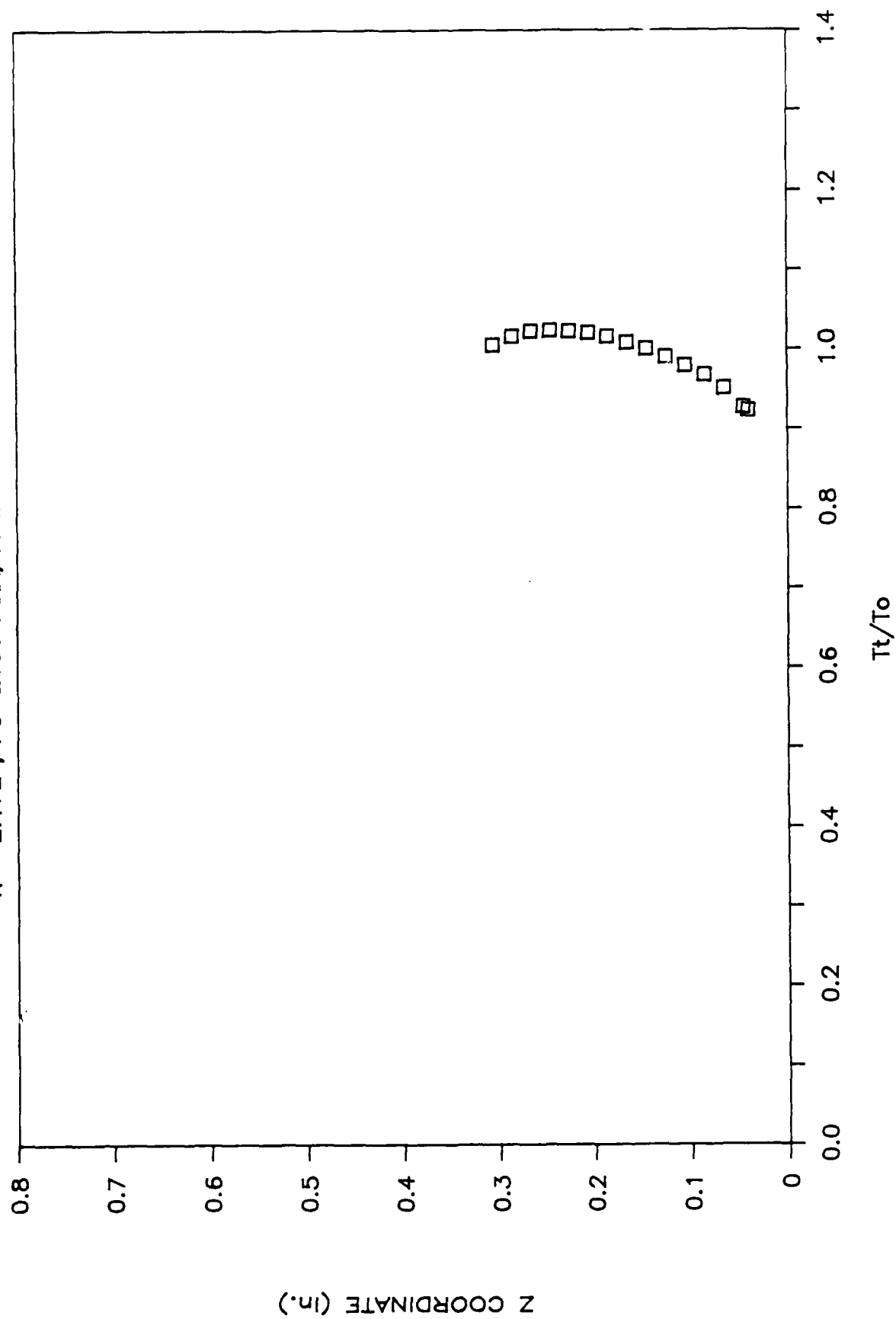


Figure 47b Normalized Total Temperature Distribution at a Given Location and

ROUGH PLATE

$X=+1.563"$, $P_0=700$ PSIA, FILE=HTTR2194

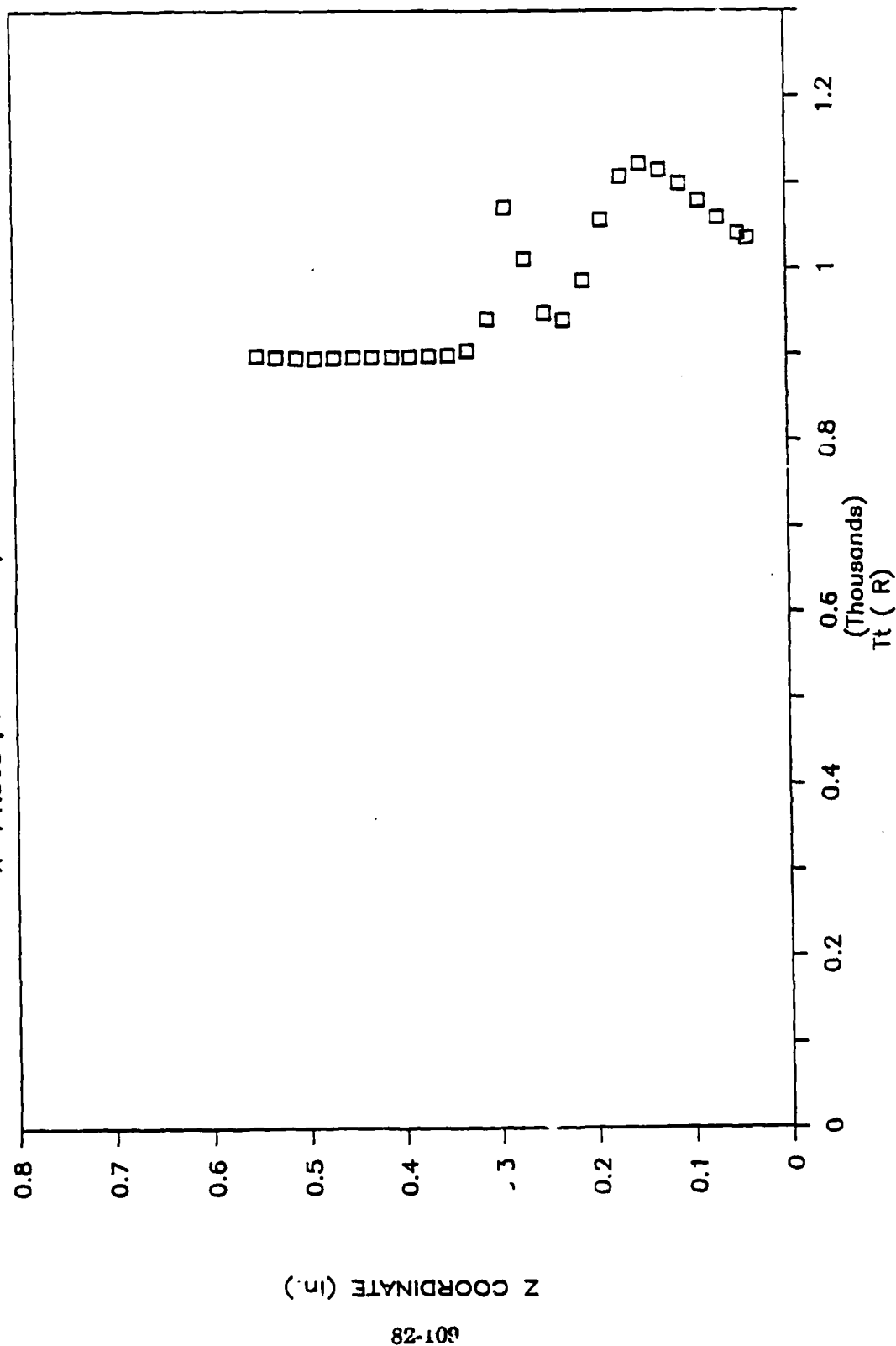


Figure 48a Total Temperature Distribution at a Given Location and Stagnation Pressure



ROUGH PLATE

X=+1.563", Po=700 PSIA, FILE=HTTR2194

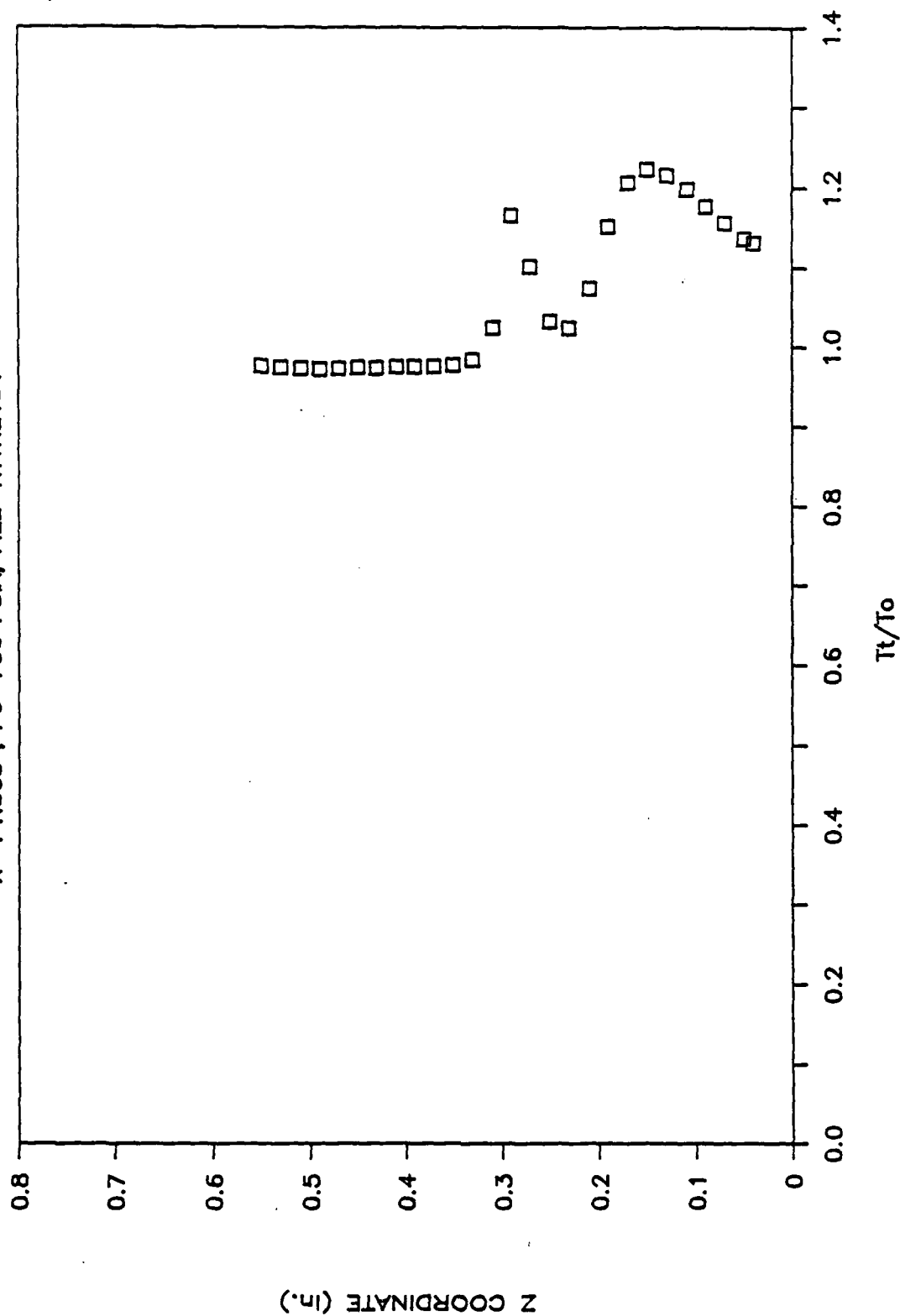


Figure 48b Normalized Total Temperature Distribution at a Given Location and

ROUGH PLATE

X=+1.563", $P_0=1400$ PSIA, FILE=HTTR2196

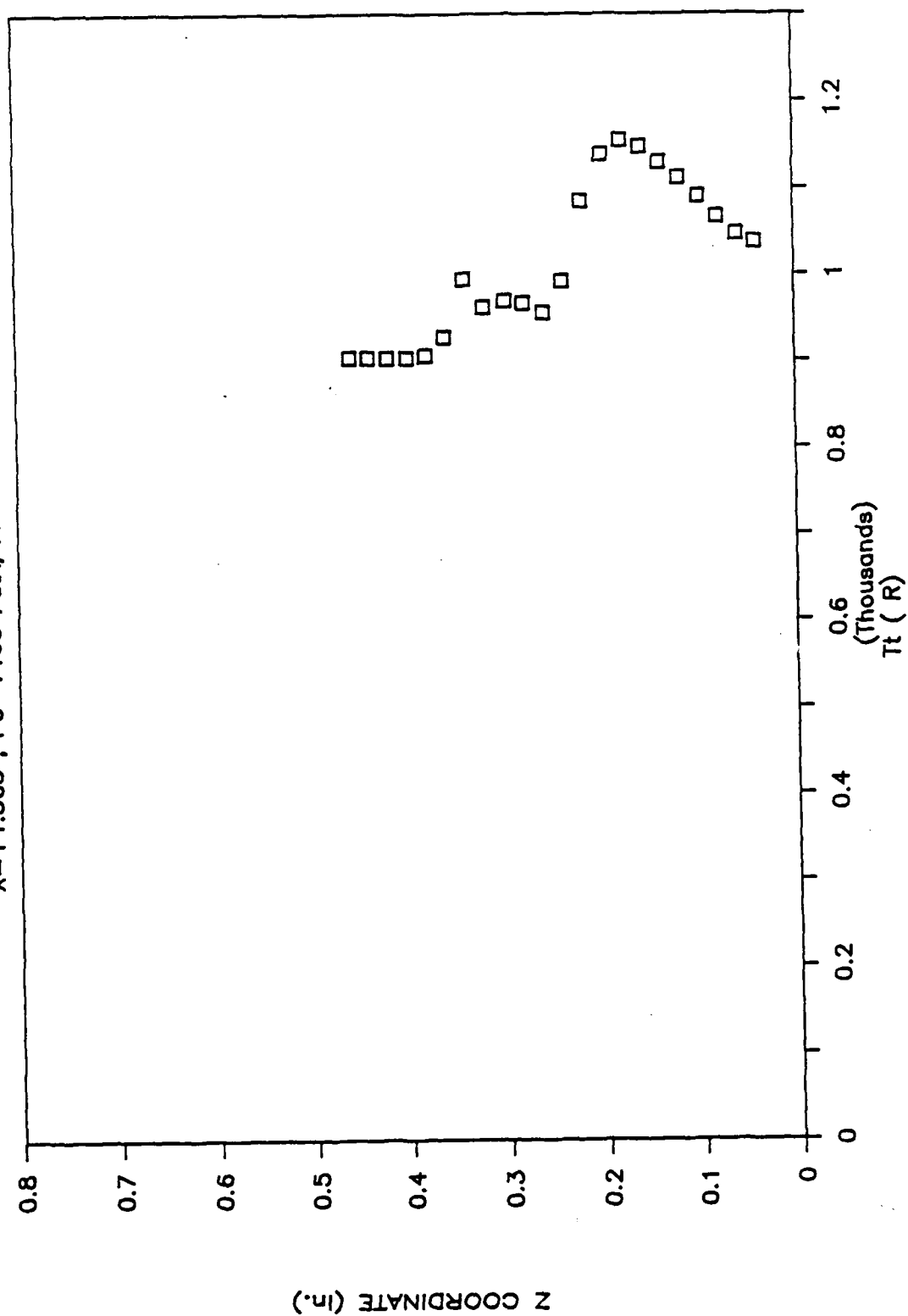
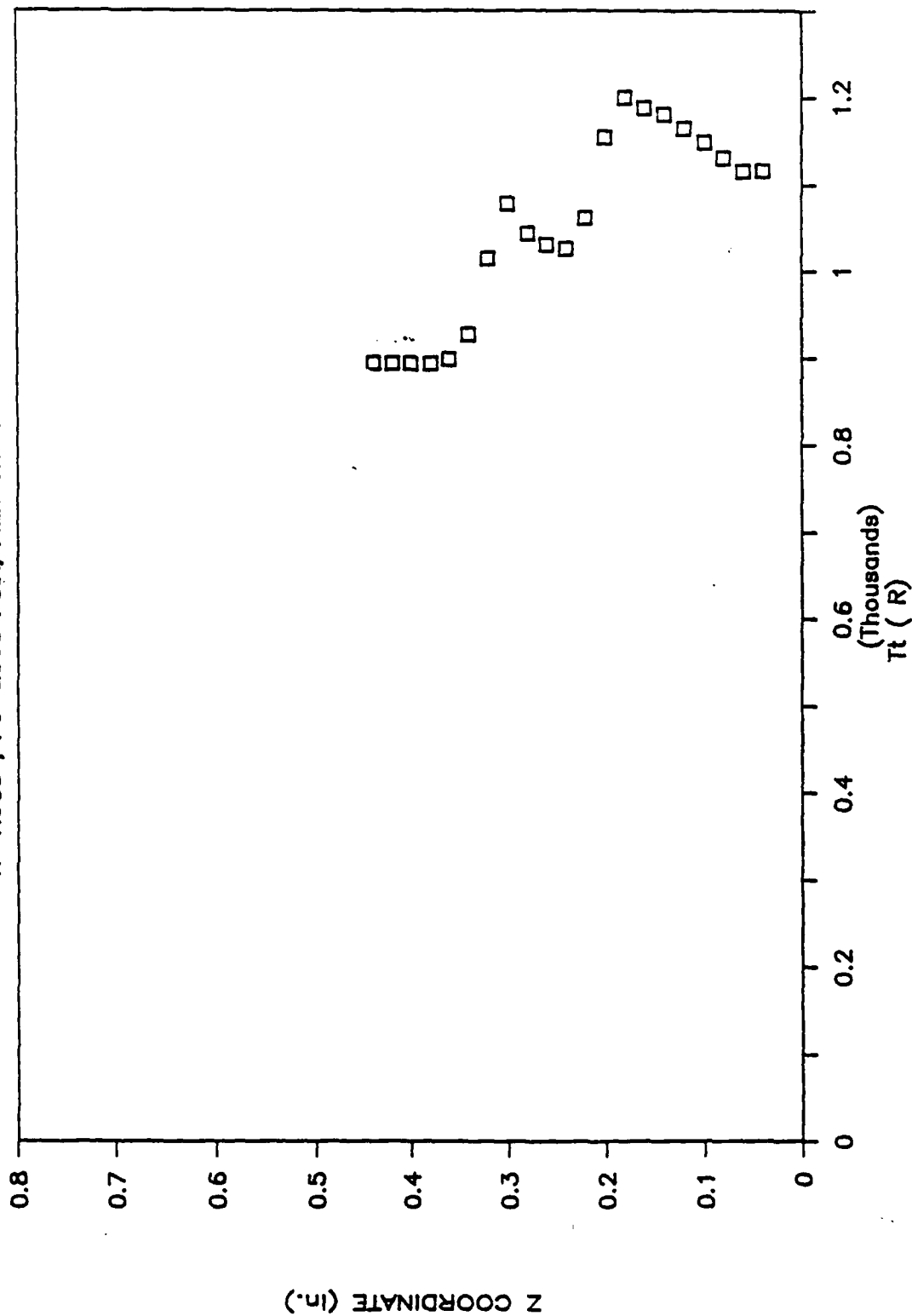


Figure 49a Total Temperature Distribution at a Given Location and Stagnation Pressure

ROUGH PLATE

X=1.563", Po=2000 PSIA, FILE=HTTR2197



ROUGH PLATE

X=1.563", Po=2000 PSIA, FILE=HTTR2197

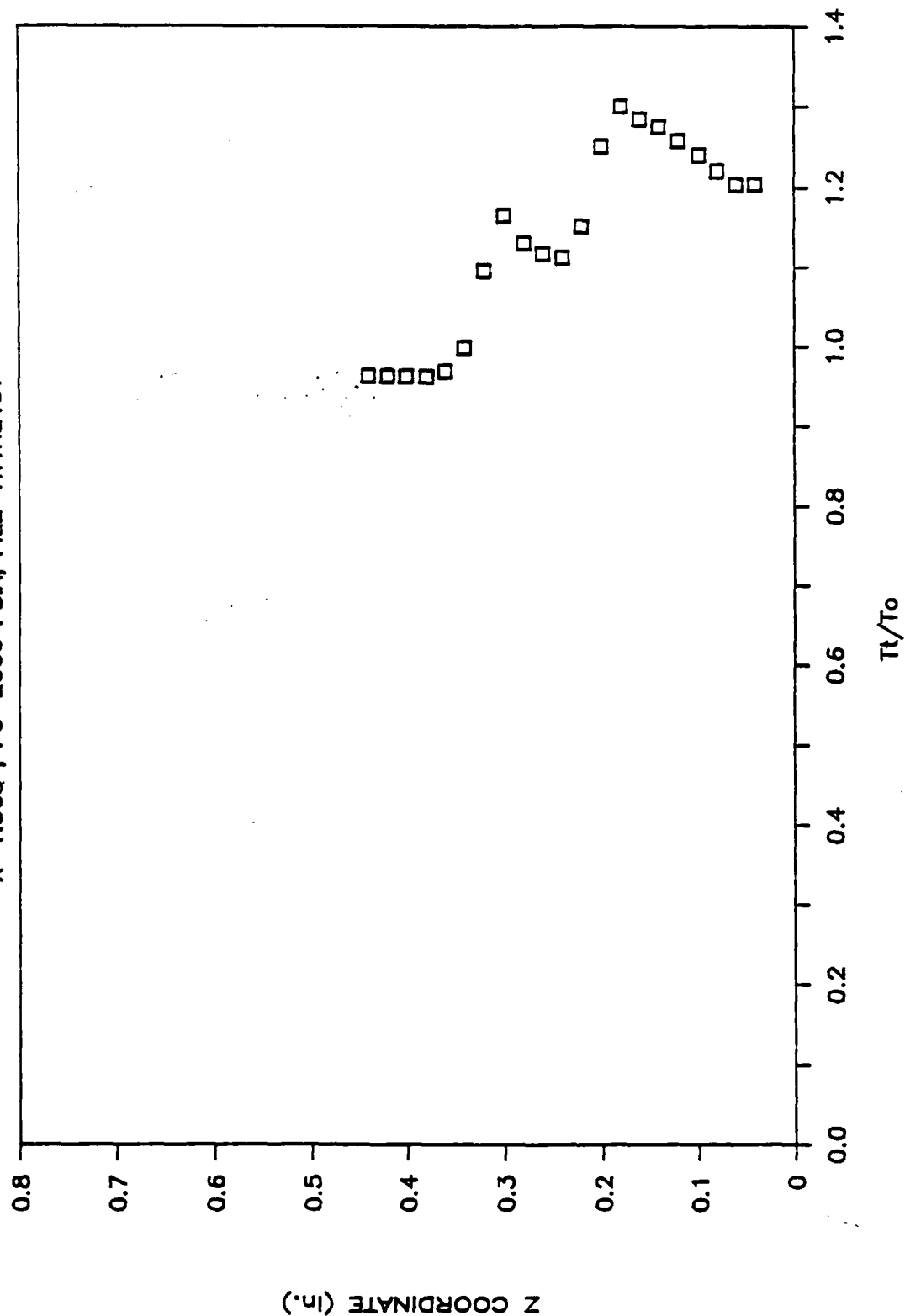


Figure 50b Normalized Total Temperature Distribution at a Given Location and Stagnation Pressure

ROUGH PLATE

X=-6.484", FILE=HTRCOMB1

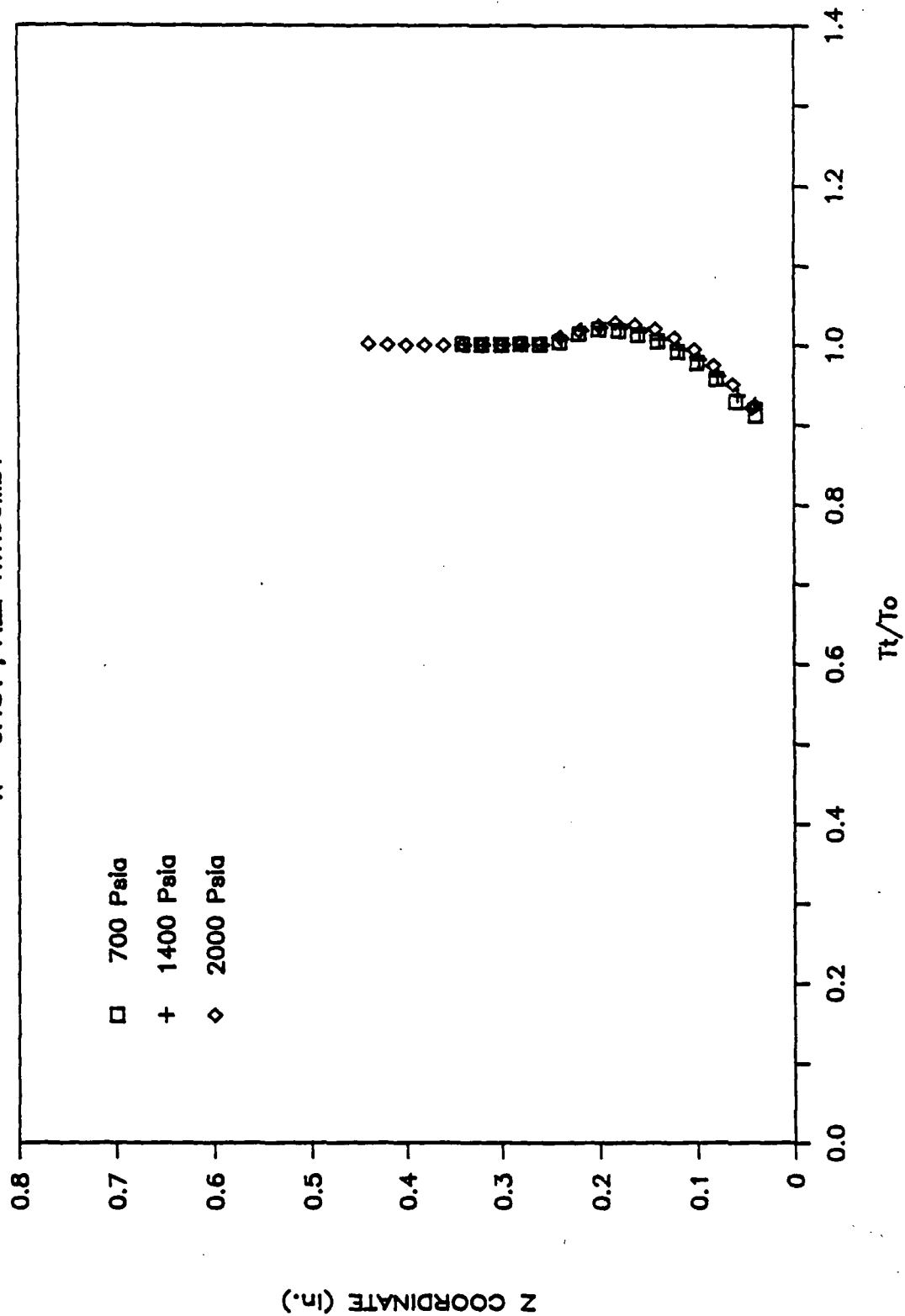


Figure 51 Combined Normalized Total Temperature Distributions at a Given Location

ROUGH PLATE

X=-2.172", FILE=HTRCOMB2

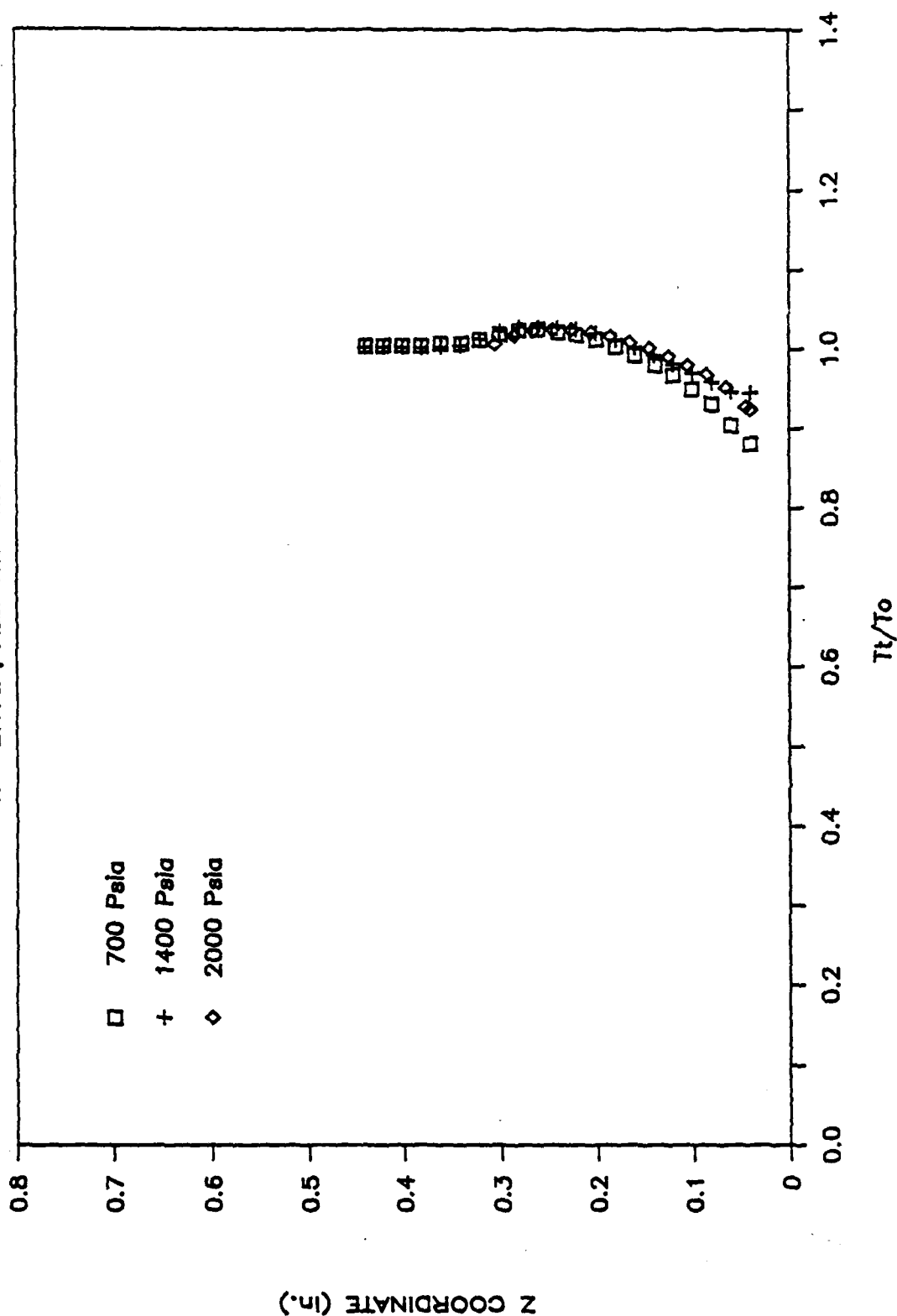


Figure 52 Combined Normalized Total Temperature Distributions at a Given Location

ROUGH PLATE

X=+1.563", FILE=HTRCOMB3

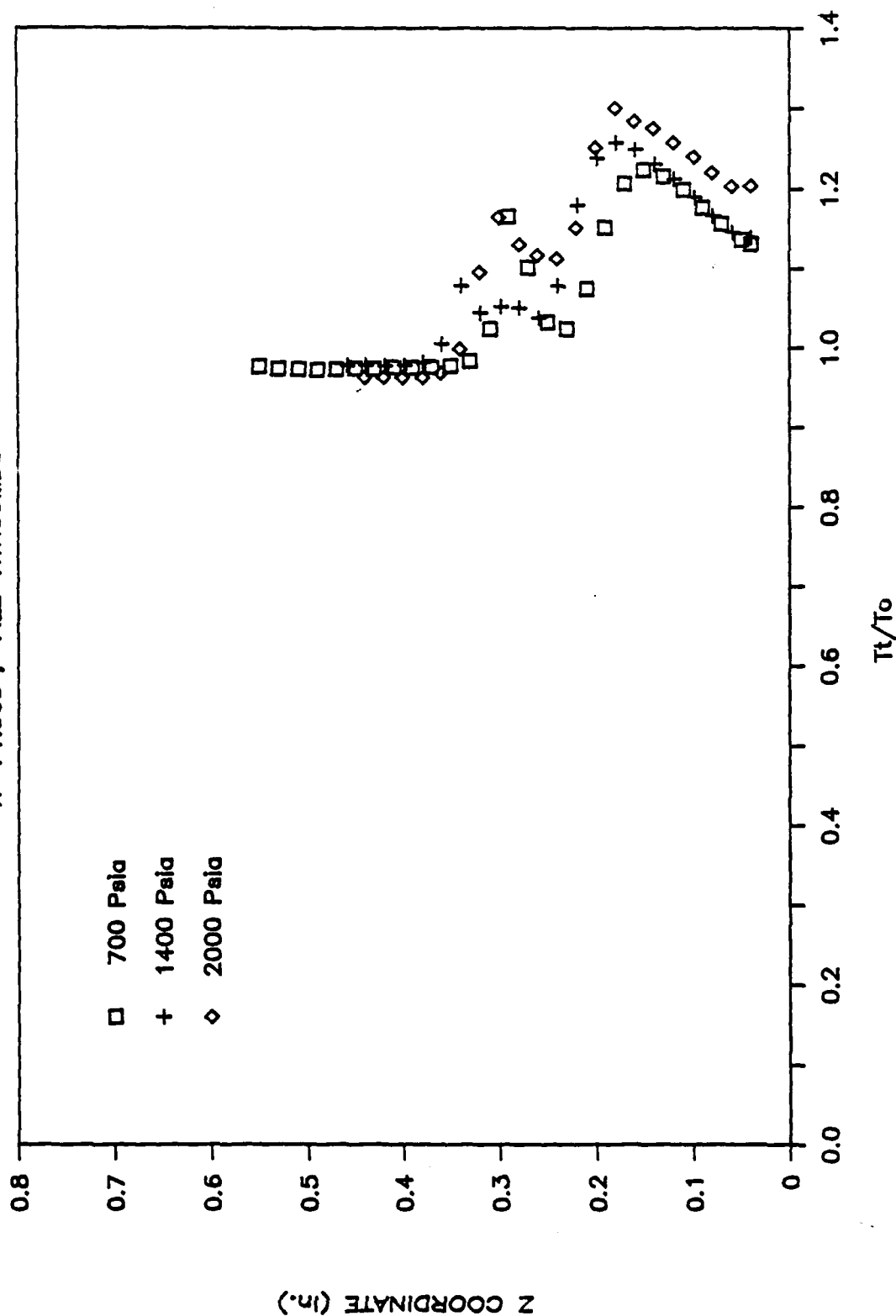
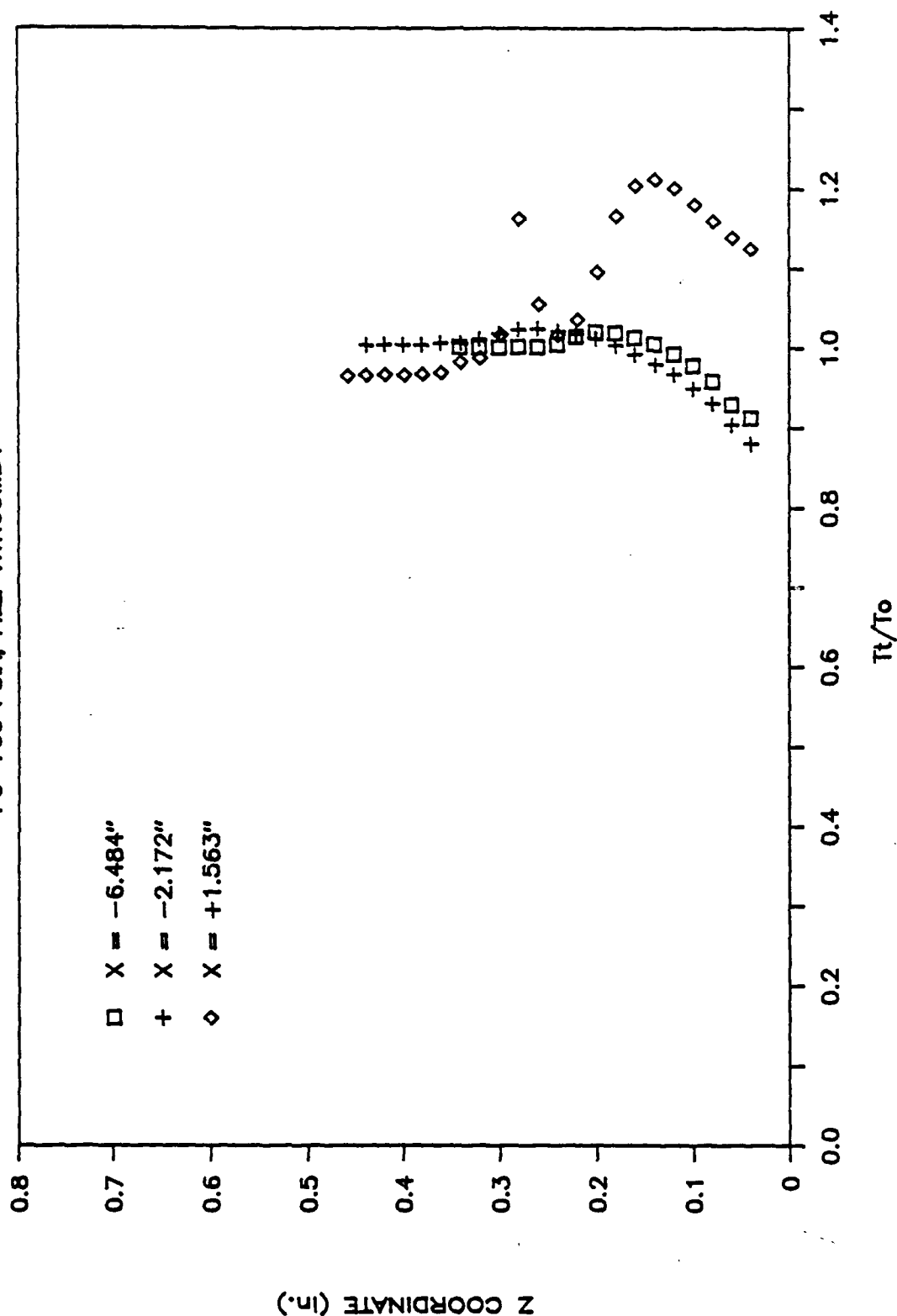


Figure 53 Combined Normalized Total Temperature Distributions at a Given Location

ROUGH PLATE

$P_0=700$ PSIA, FILE=HTRCOMB4



811-28

Figure 64 Combined Normalized Total Temperature Distributions at a Given Stagnation Pressure

ROUGH PLATE

$P_o=1400$ PSIA, FILE=HTRCOMB5

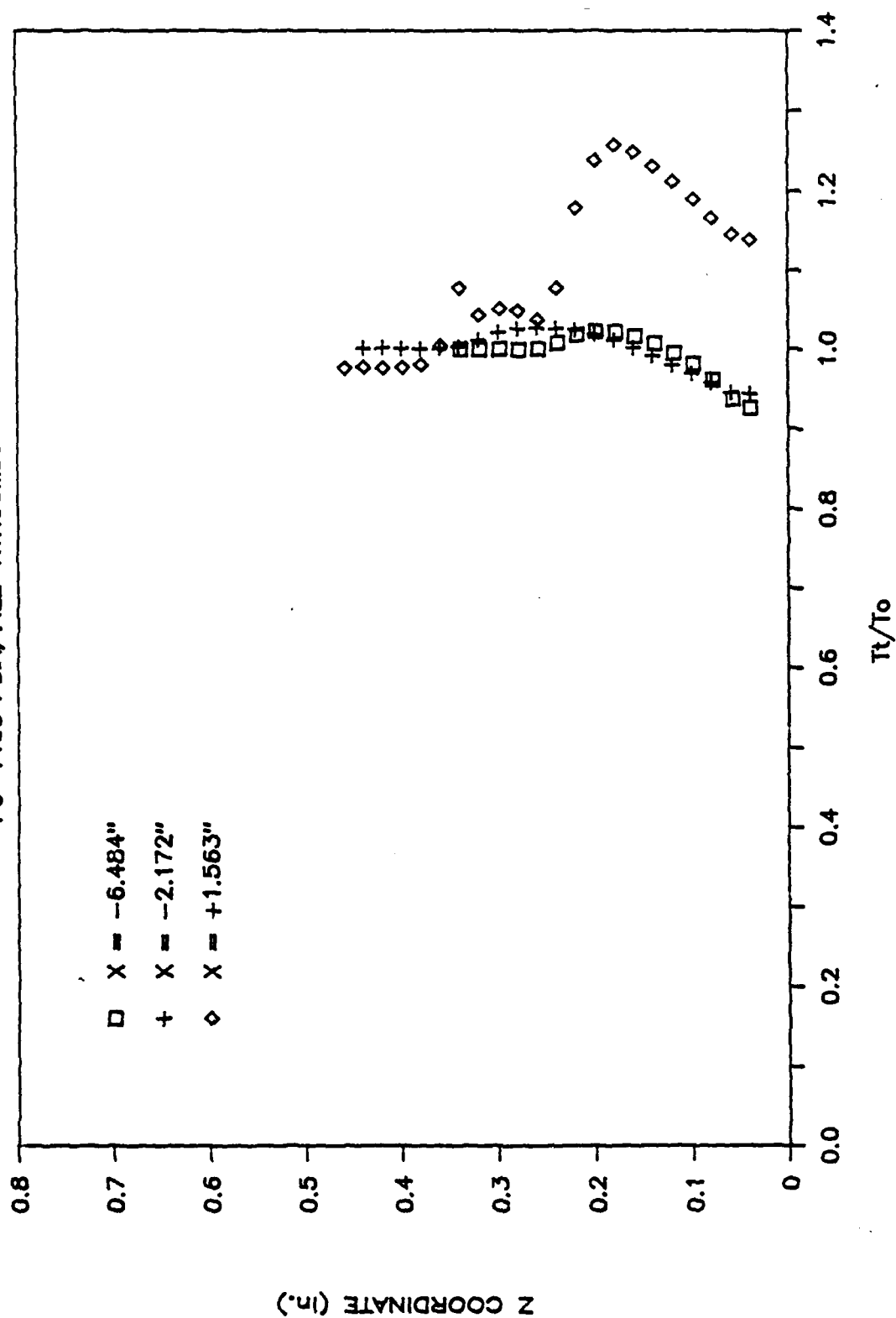


Figure 55 Combined Normalized Total Temperature Distributions at a Given Stagnation Pressure

ROUGH PLATE, 22 DEG. RAMP

Po=2000 PSIA, FILE=HTRCOMB6

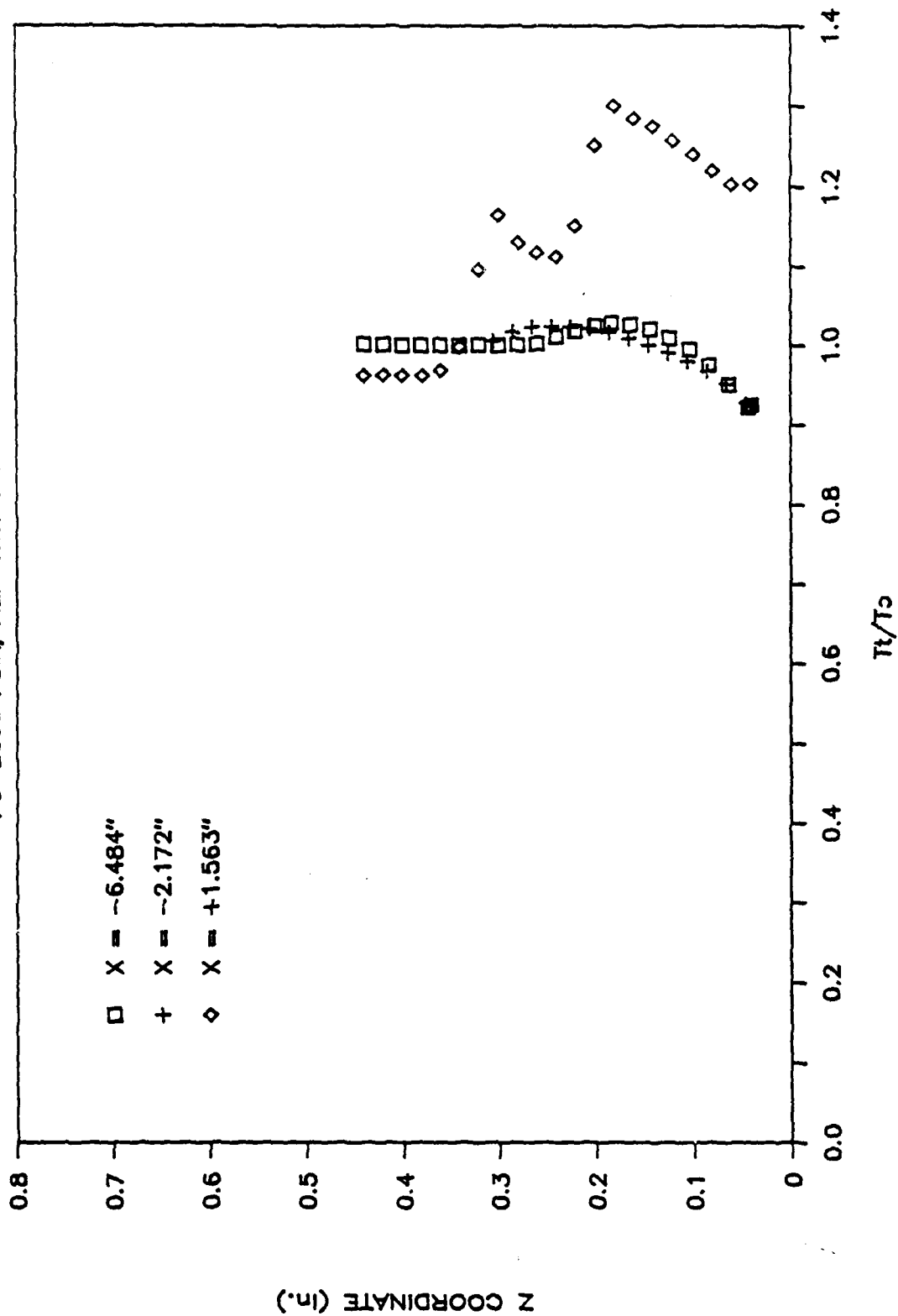


Figure 56 Combined Normalized Total Temperature Distributions at a Given Stagnation Pressure

ROUGH PLATE

X=-6.484", FILE=HTSRCOM2

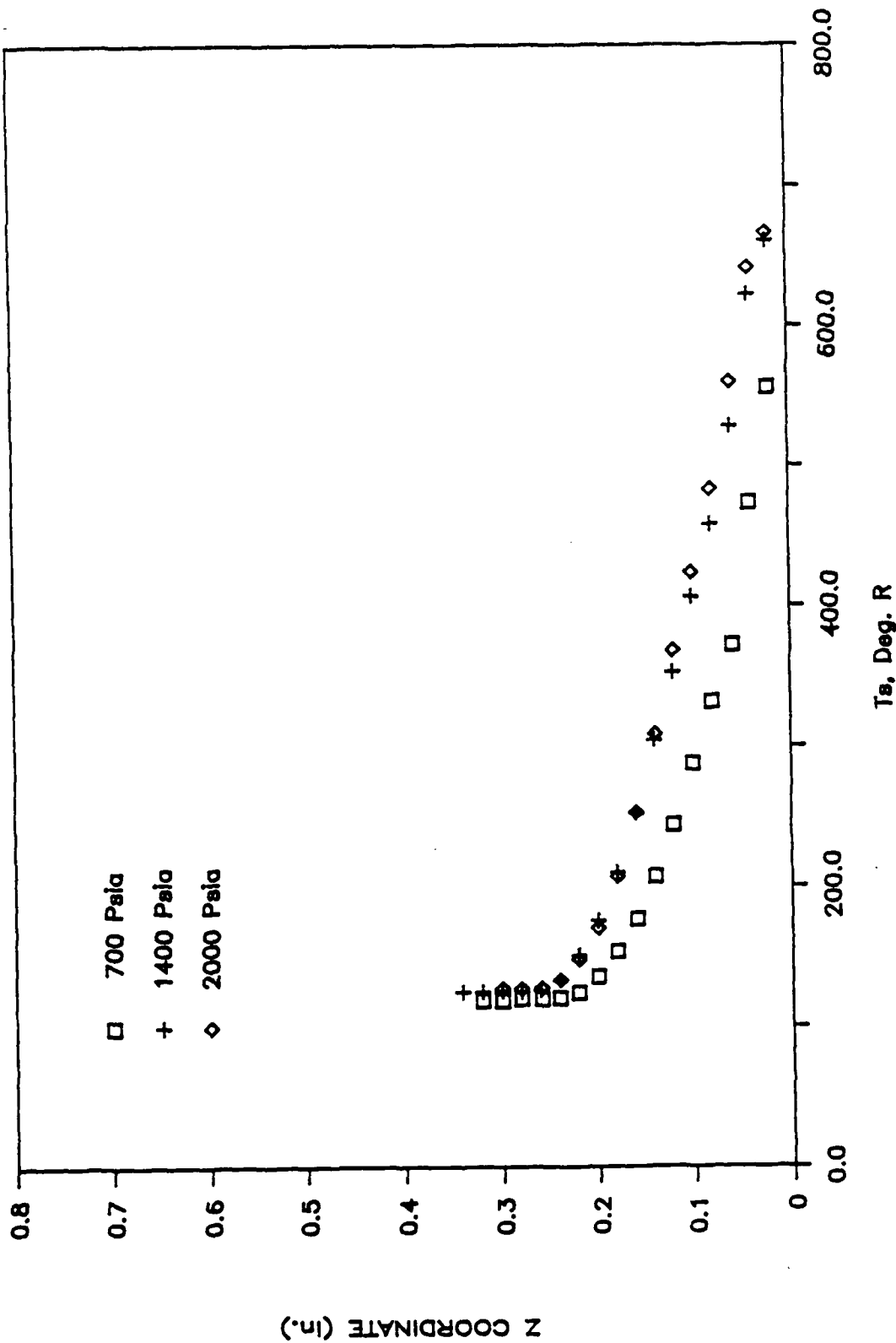


Figure 57 Combined Static Temperature Distributions at a Given Location

ROUGH PLATE

X=-2.172", FILE=HTSRCOM1

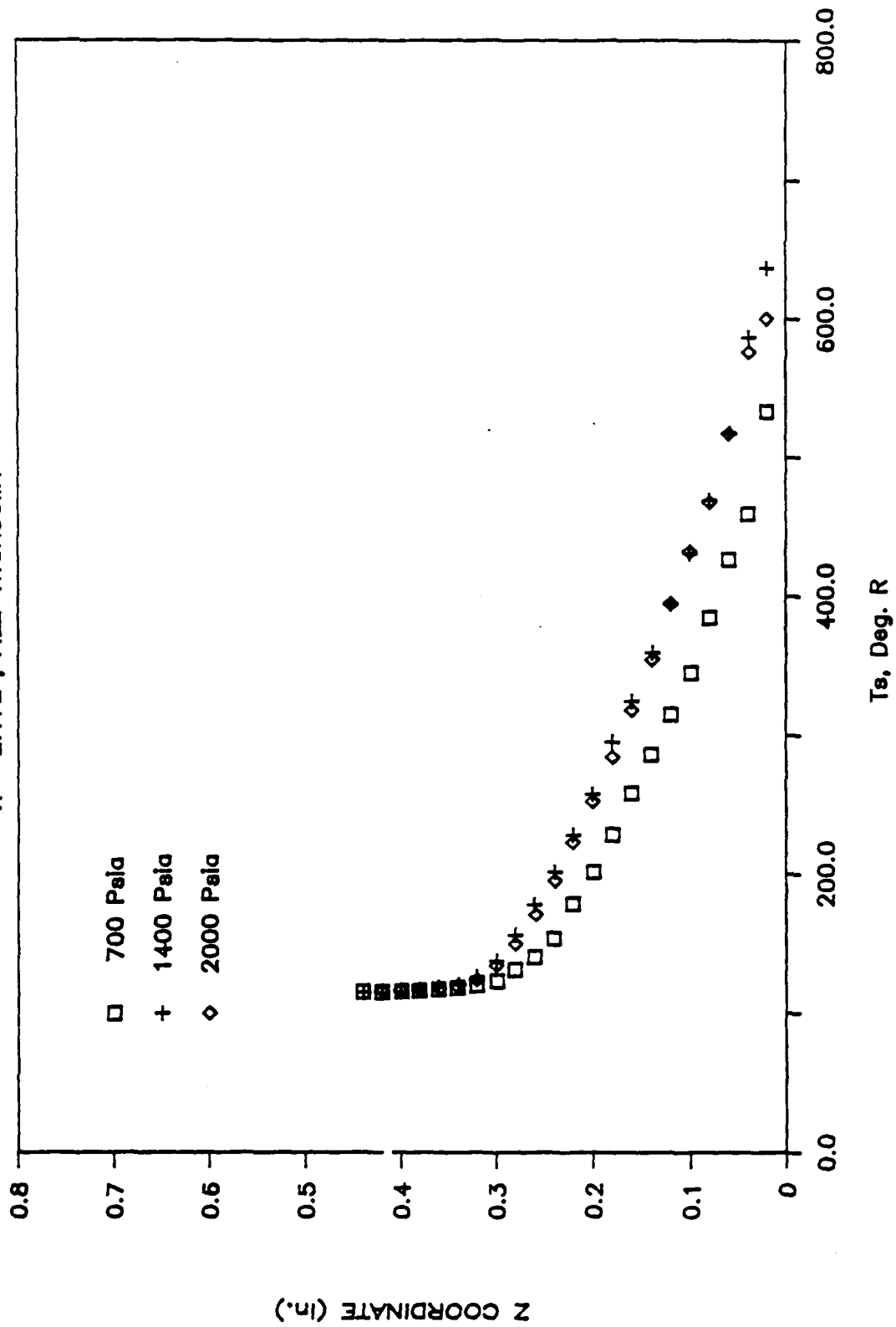


Figure 58 Combined Static Temperature Distributions at a Given Location

ROUGH PLATE

$P_0=700$ PSIA, FILE=HTSRCOM3

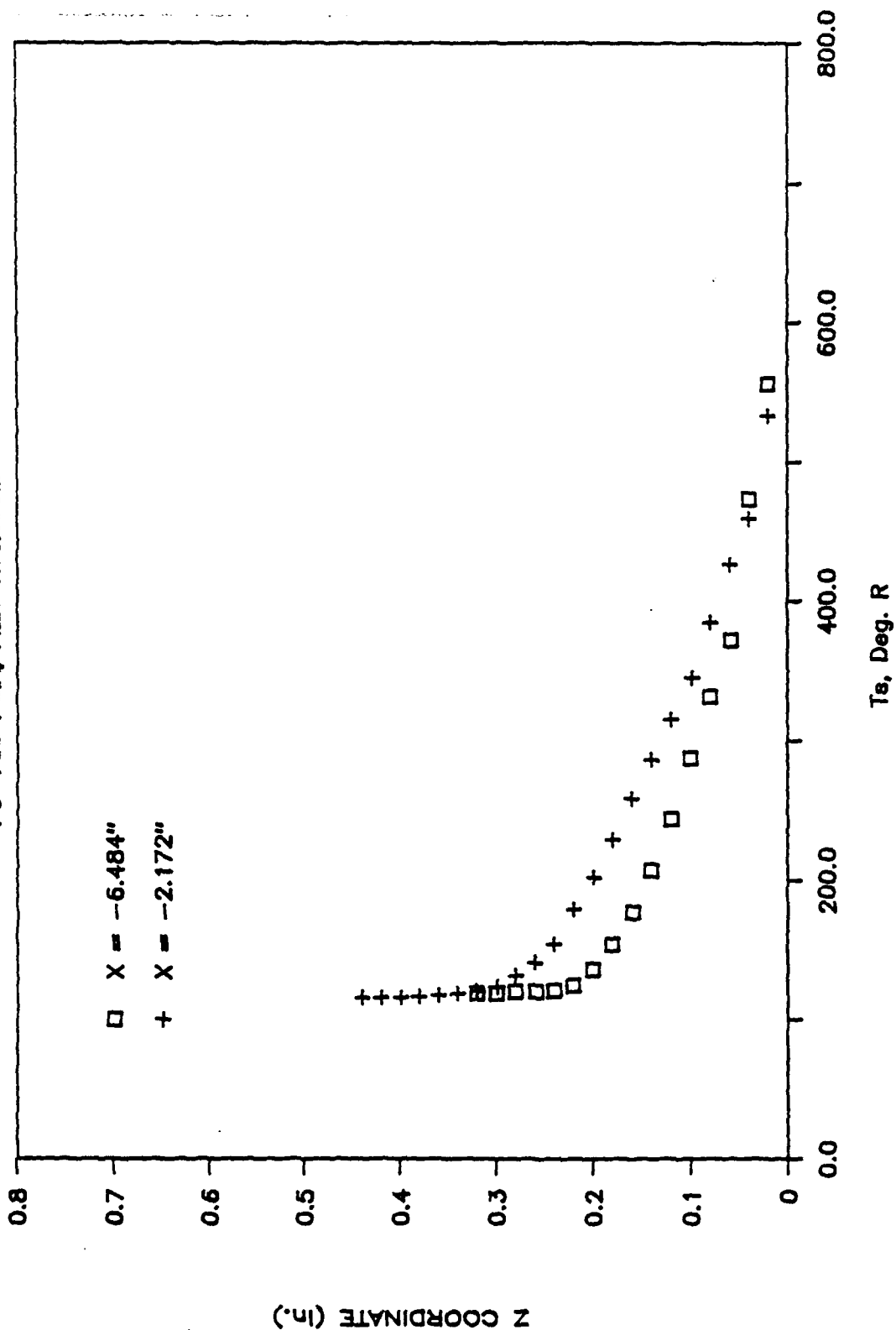


Figure 59 Combined Static Temperature Distributions at a Given Stagnation Pressure

ROUGH PLATE

Po=1400 PSIA, FILE=HTSRCOM4

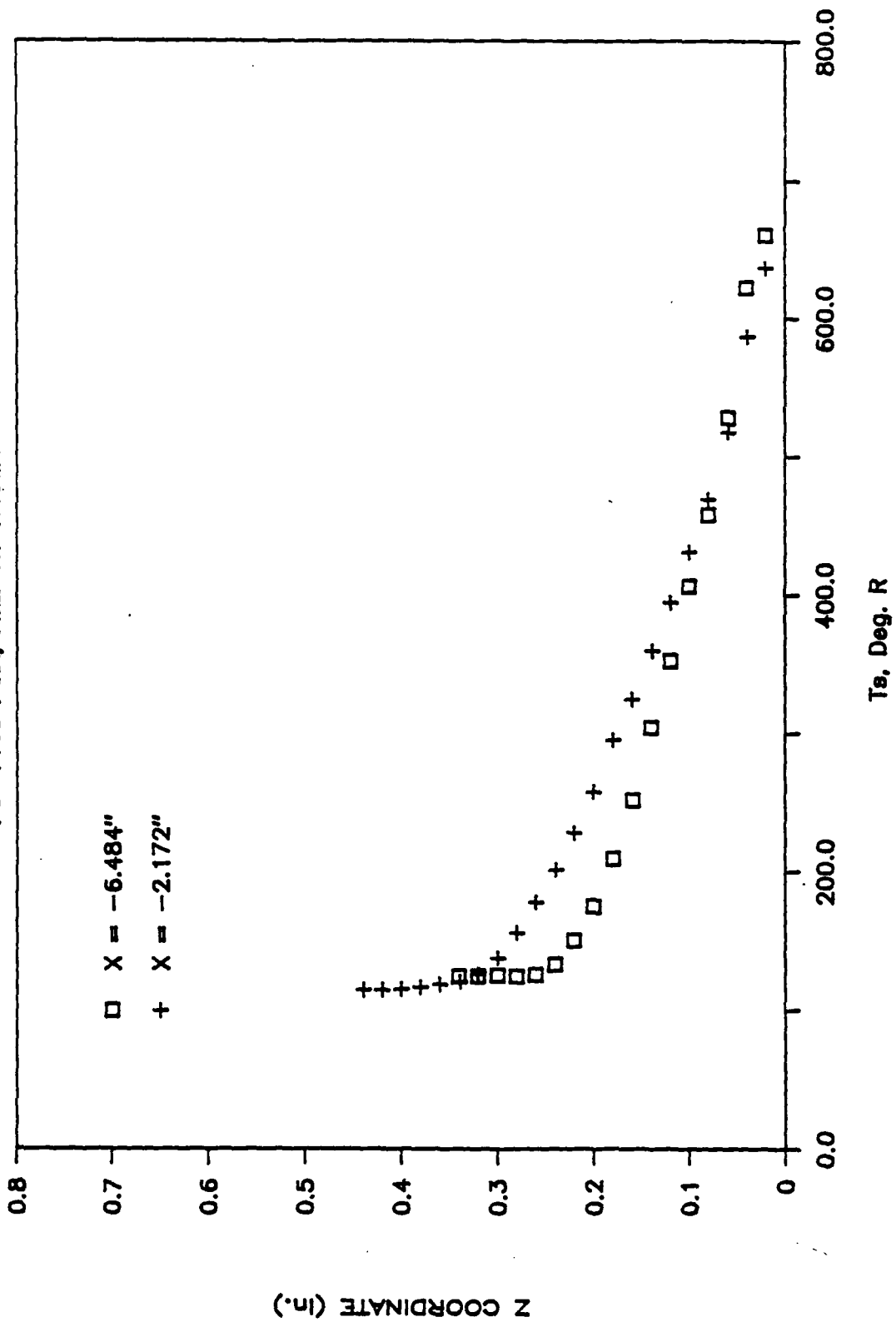


Figure 60 Combined Static Temperature Distributions at a Given Station Pressure

ROUGH PLATE

$P_0=2000$ PSIA, FILE=HTSRCOM5

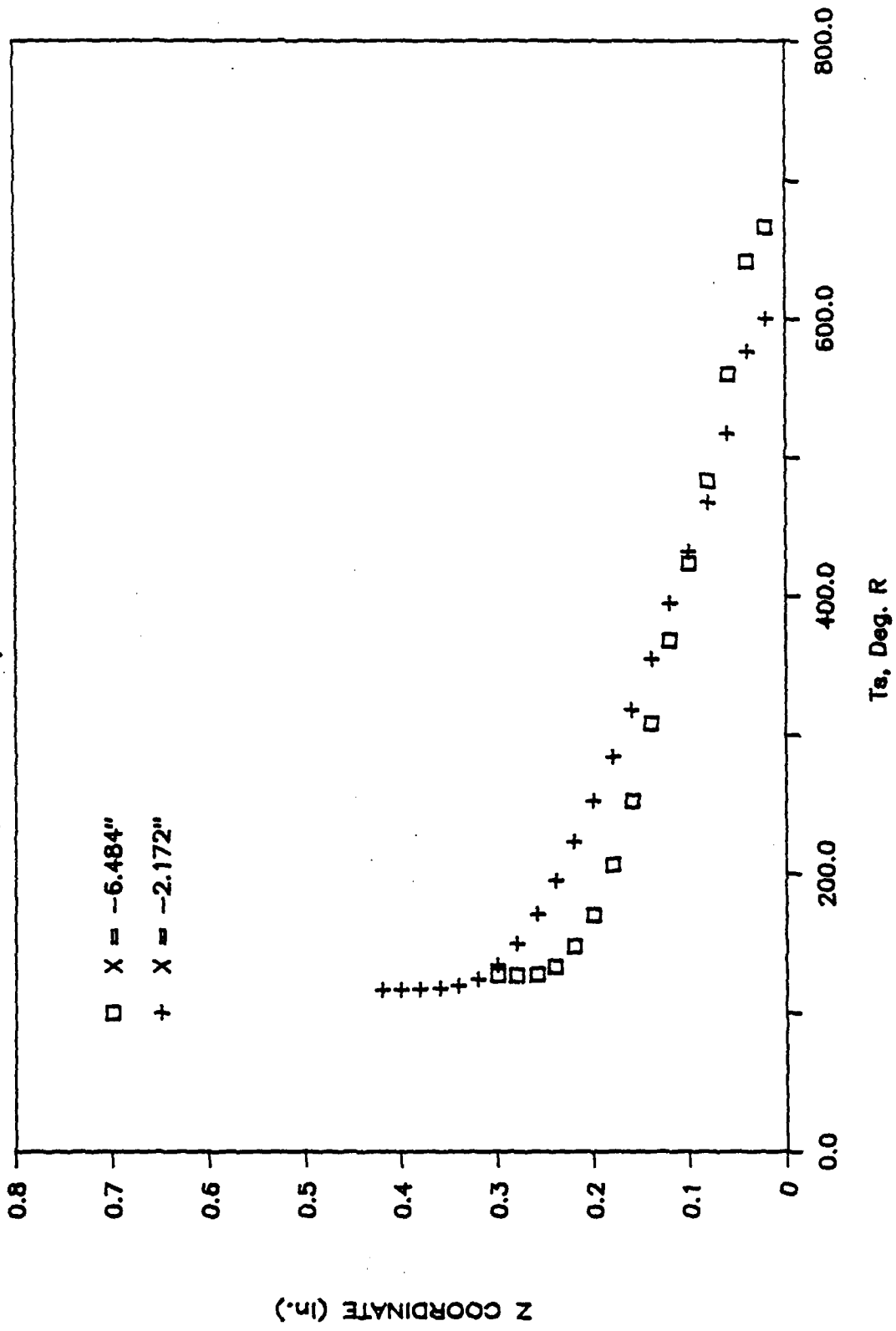


Figure 61 Combined Static Temperature Distributions at a Given Stagnation Pressure

ROUGH PLATE

X=-6.484", FILE=VLRCOMB2

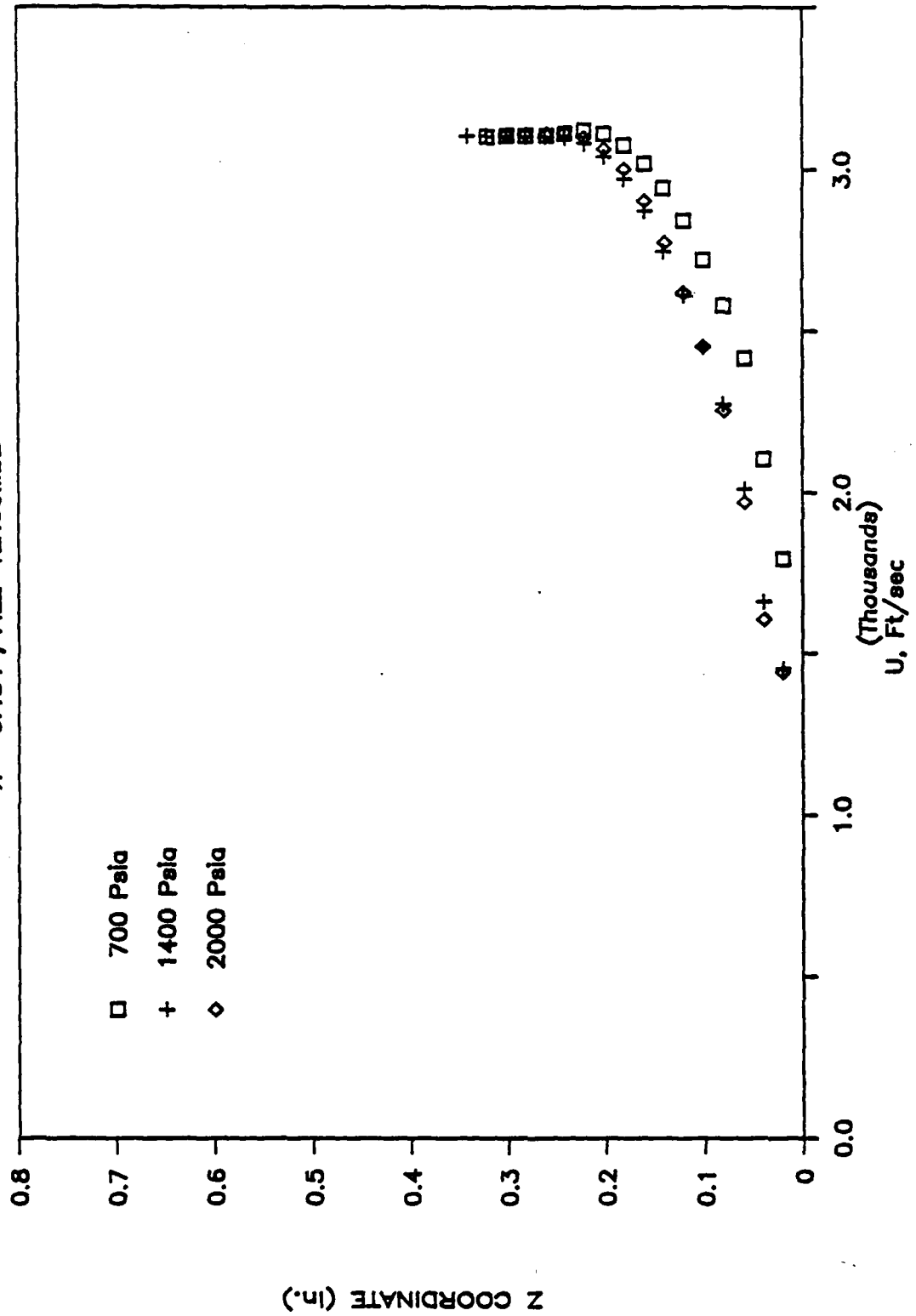


Figure 62 Combined Local Mean Velocity Distributions at a Given Location

ROUGH PLATE

X=-2.172", FILE=VLRCOMB1

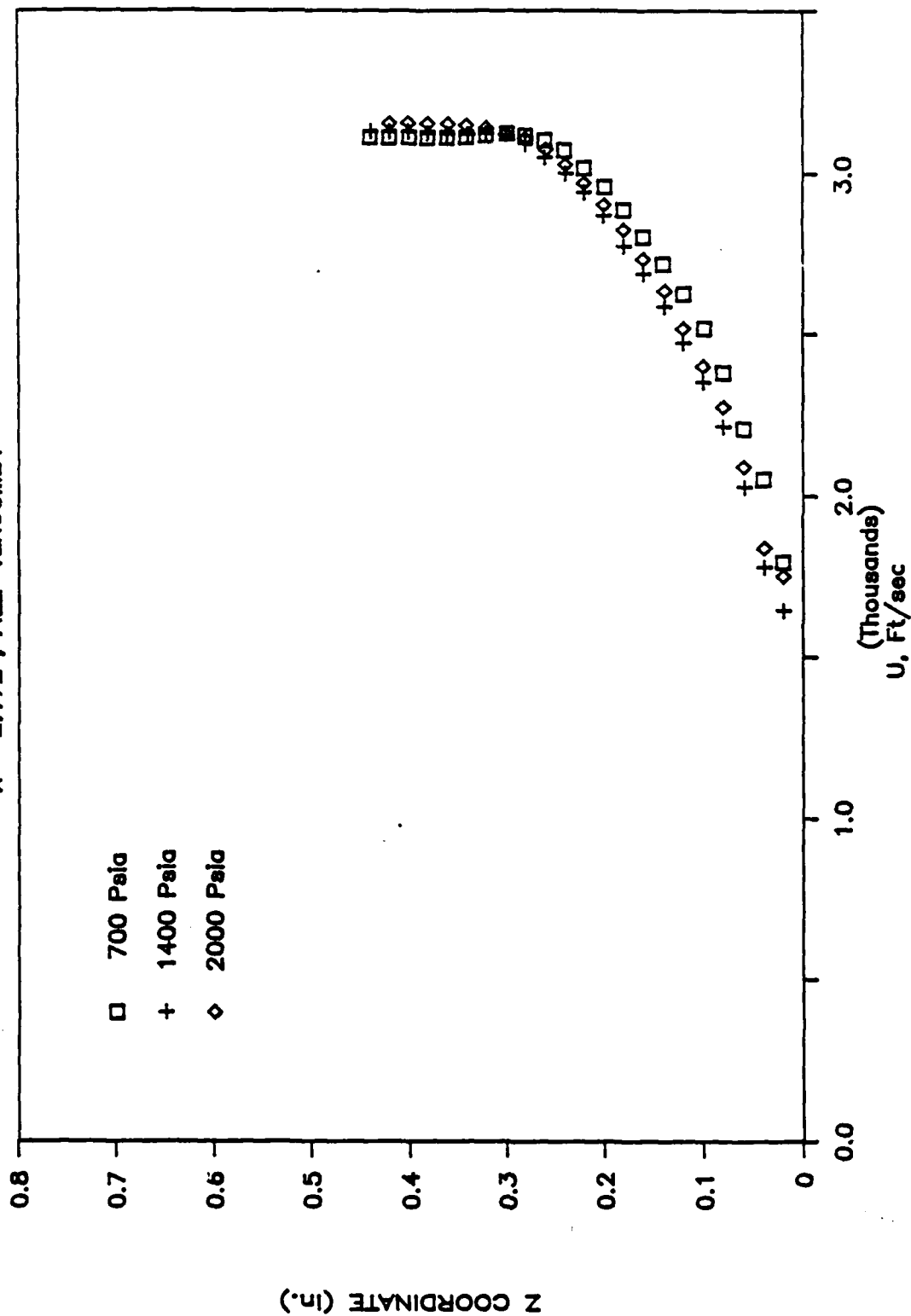


Figure 63 Combined Local Mean Velocity Distributions at a Given Location

ROUGH PLATE

Po=700 PSIA, FILE=VLRCOMB3

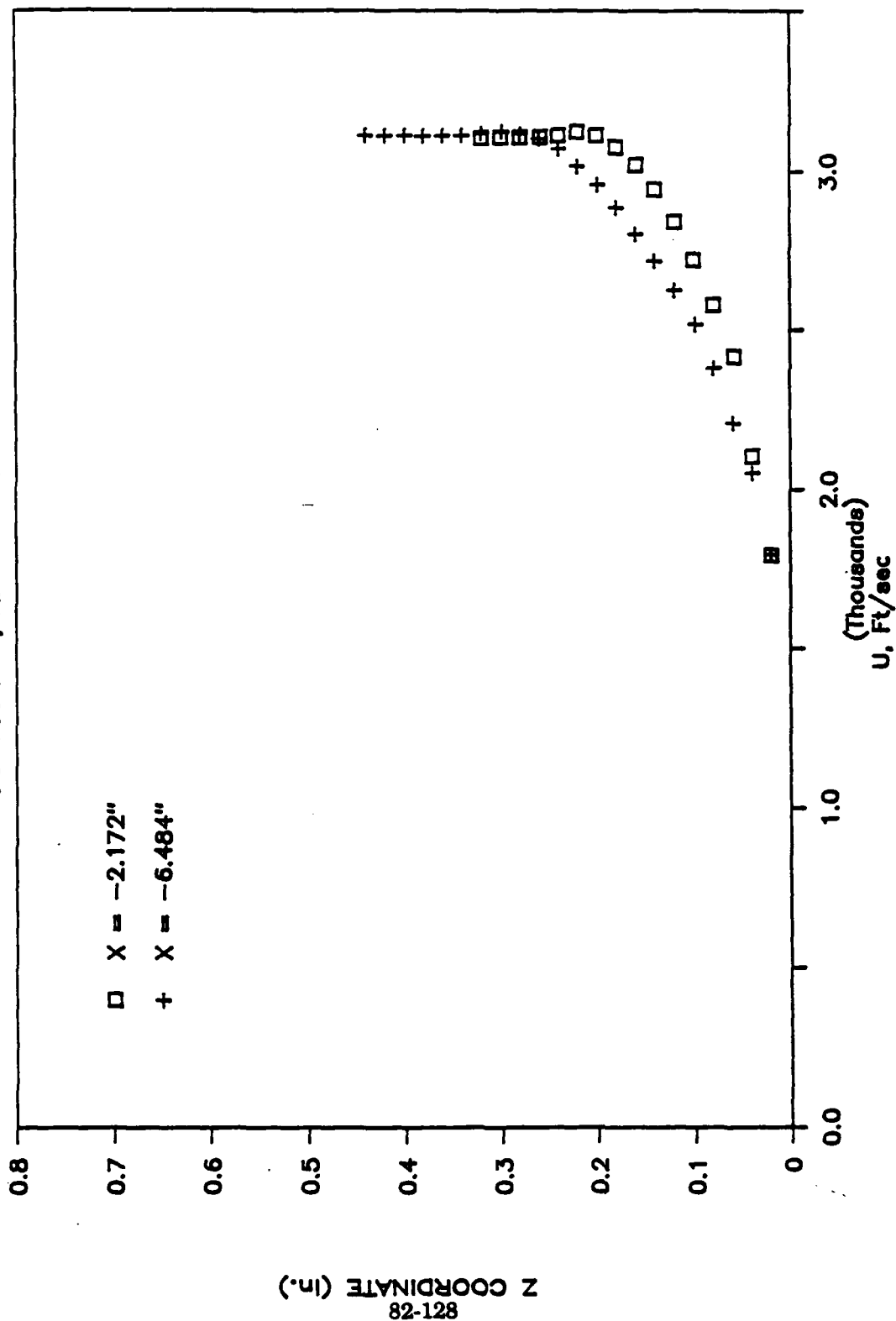


Figure 64 Combined Local Mean Velocity Distributions at a Given Stagnation Pressure

ROUGH PLATE

Po=1400 PSIA, FILE=VLRCOMB4

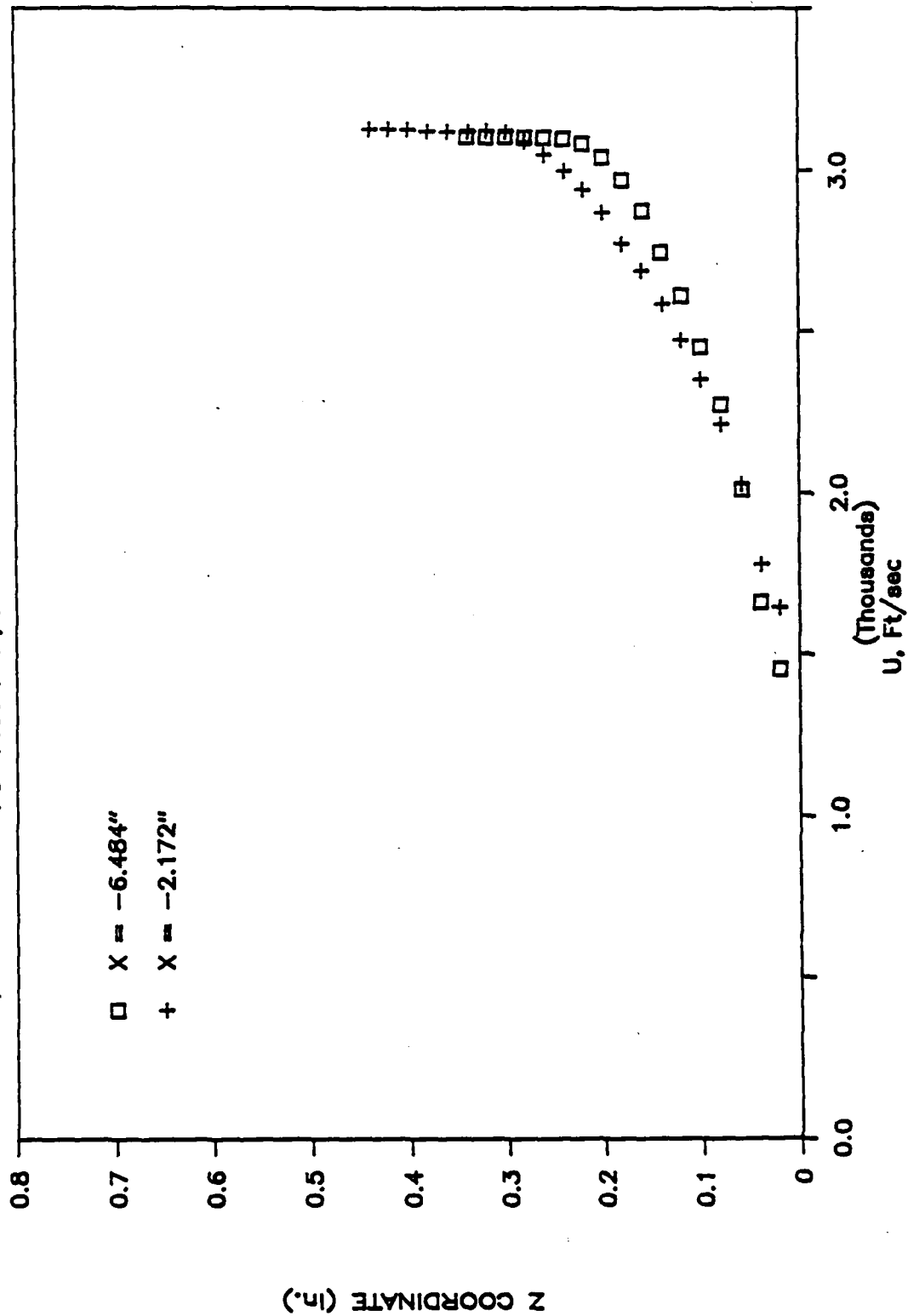


Figure 65 Combined Local Mean Velocity Distributions at a Given Stagnation Pressure

ROUGH PLATE

Po=2000 PSIA, FILE=VLRCOMB5

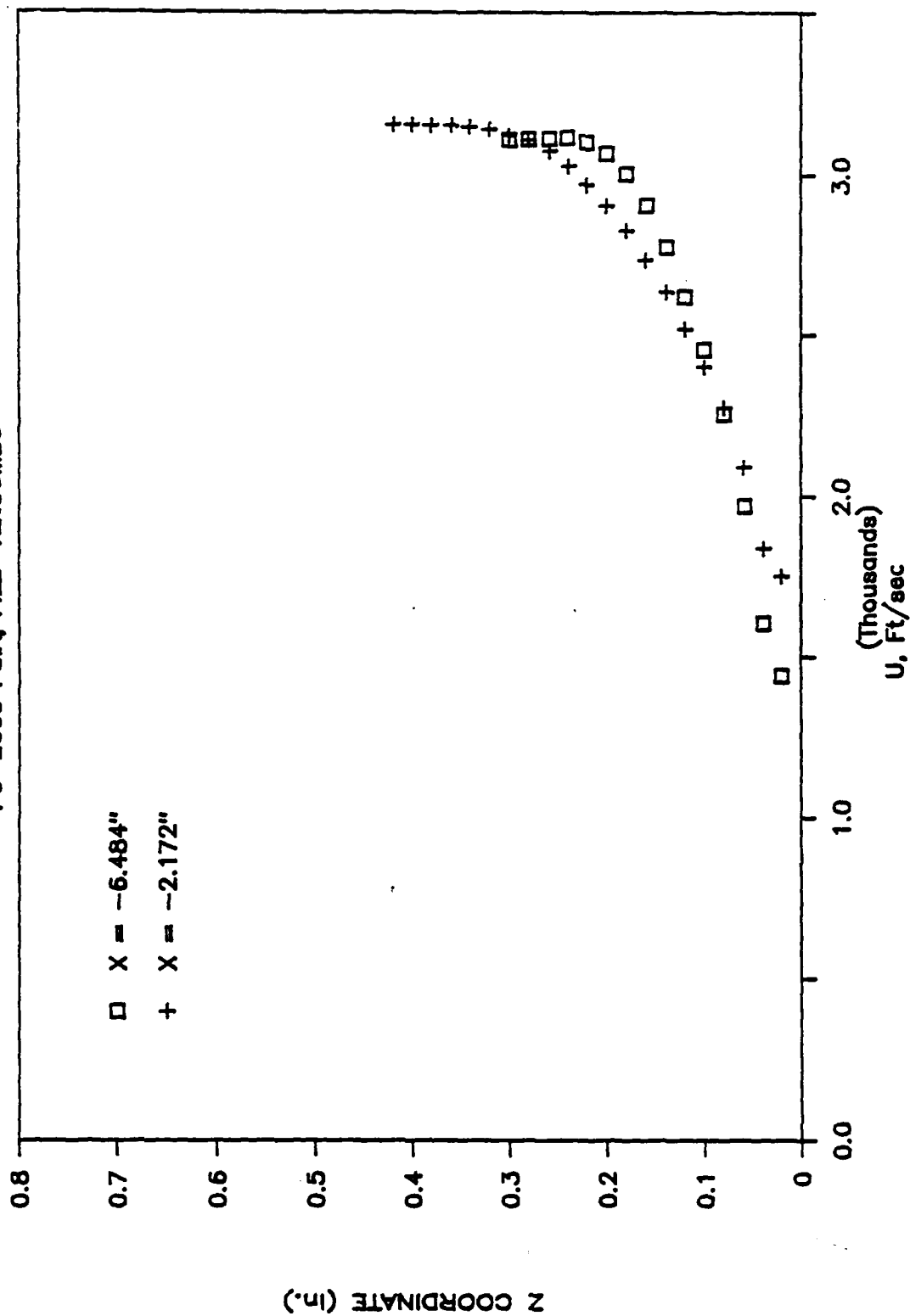


Figure 66 Combined Local Mean Velocity Distributions at a Given Stagnation Pressure

ROUGH PLATE

Po=700 PSIA, X=-2.172", FILE=HPTR2128

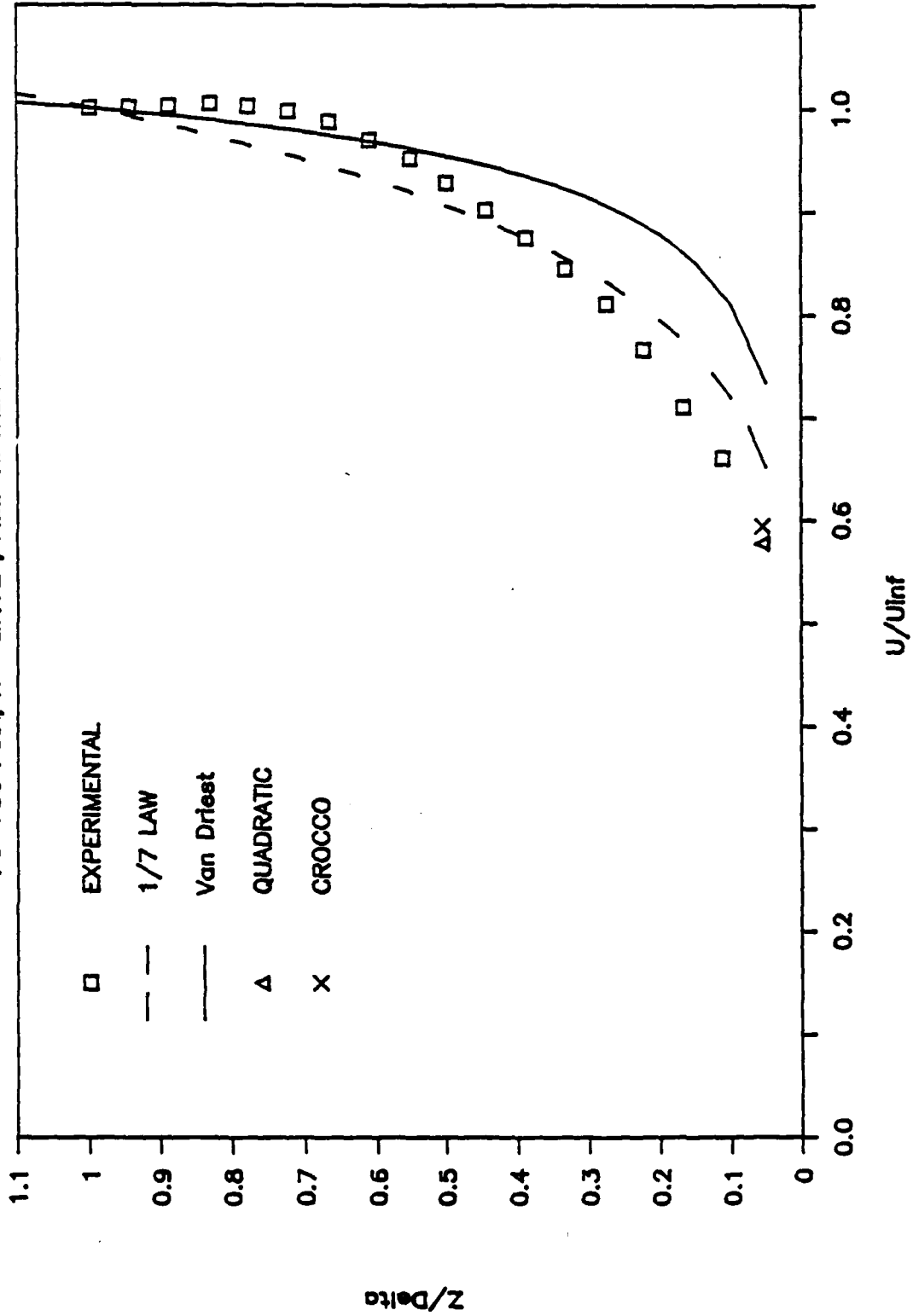


Figure 67 Boundary Layer Velocity Distribution Comparison at a Given Location and Stagnation Pressure

Z/Delta

82-131

ROUGH PLATE

$P_0=1400$ PSIA, $X=-2.172"$, FILE=HPTR2139

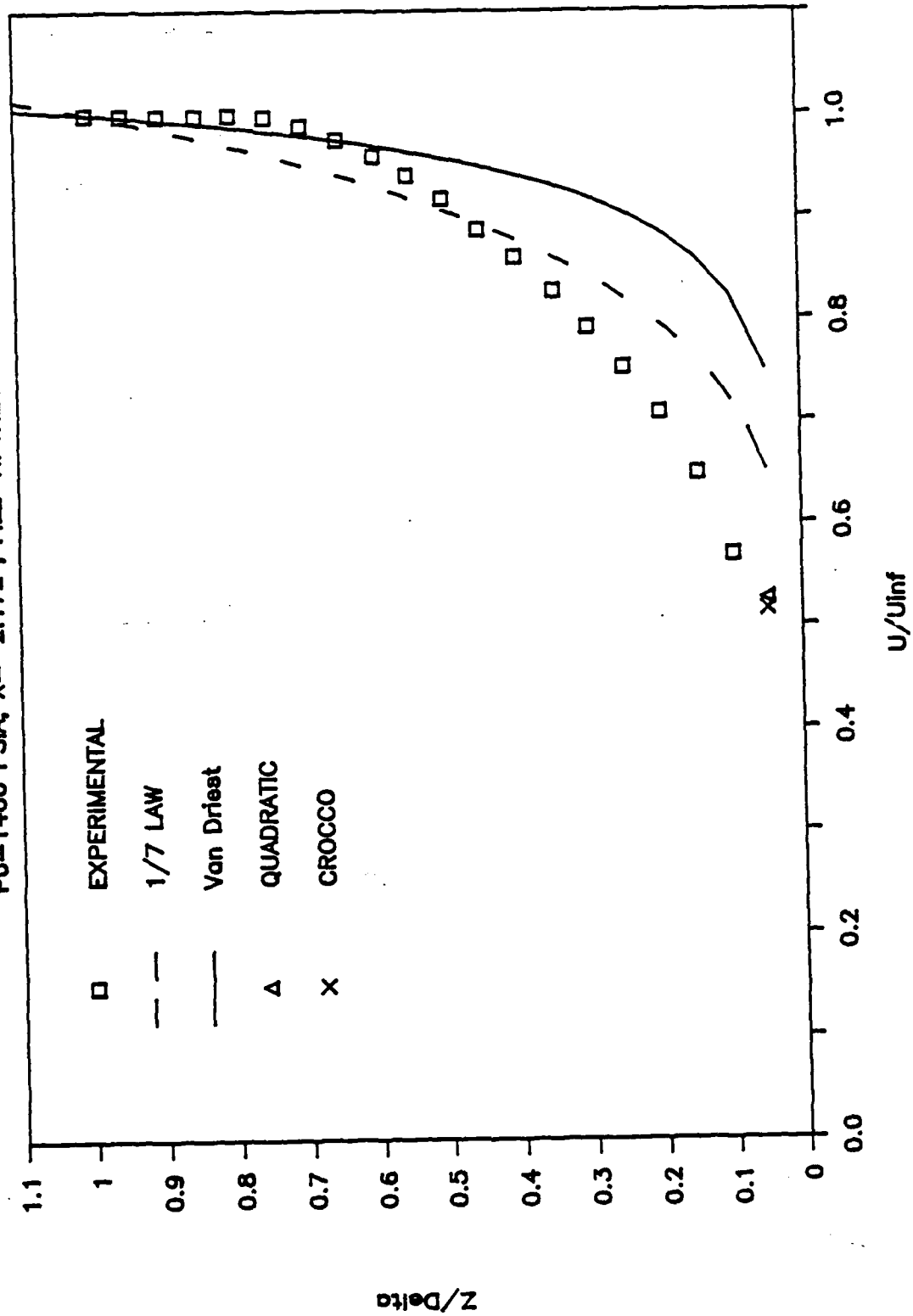


Figure 68 Boundary Layer Velocity Distribution Comparison at a Given Location and Stagnation Pressure

ROUGH PLATE

$P_0=2000$ PSIA, $X=-2.172''$, FILE=HPTR2151

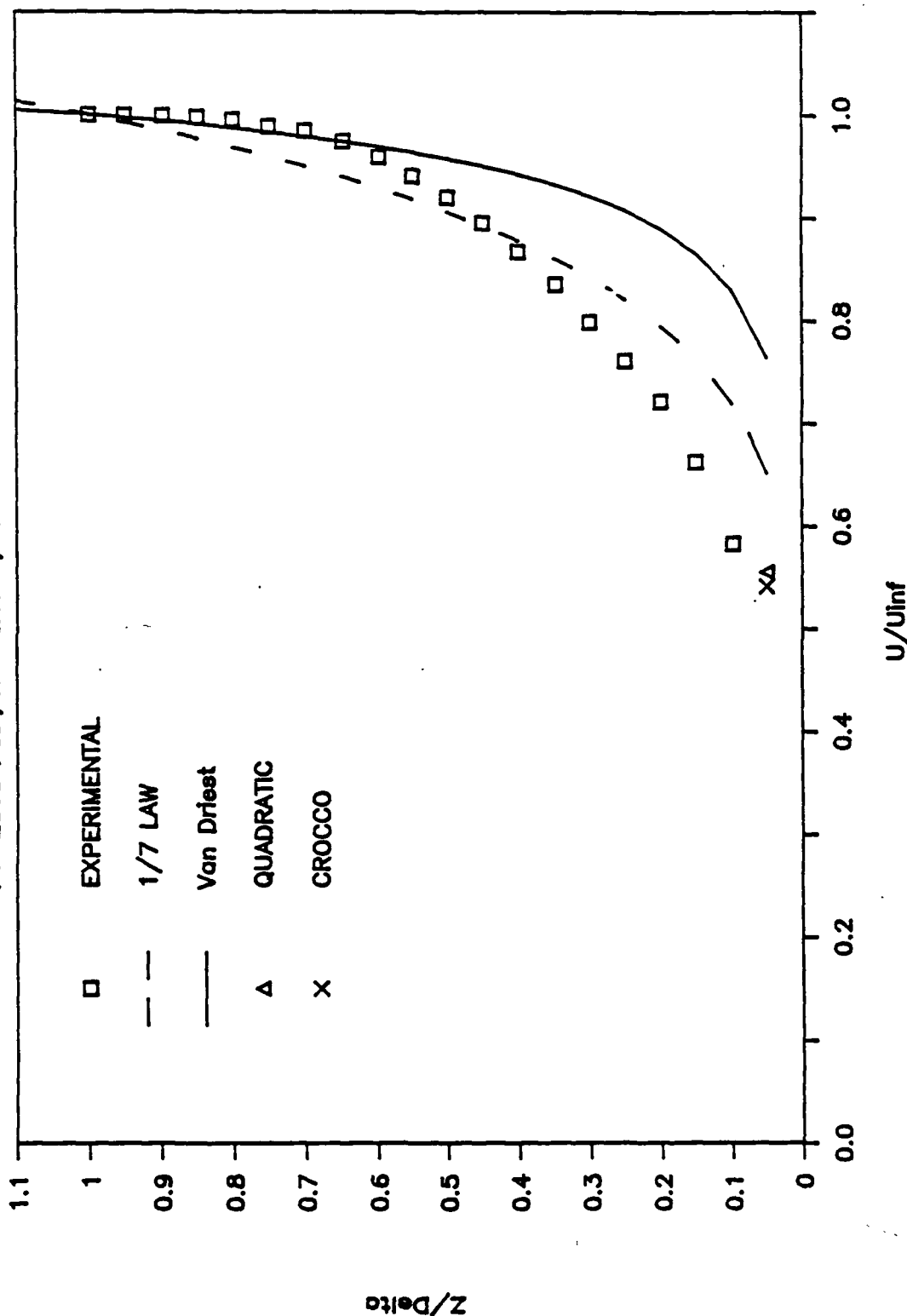


Figure 69 Boundary Layer Velocity Distribution Comparison at a Given Location and Stagnation Pressure

Table 1a Overall Model Instrumentation Coordinates

PRESSURE PORT	LATERAL POSITION (In.)	STREAMWISE POSITION (In.)
P1	0.000	-13.500
P2	0.000	-11.121
P3	-2.016	-9.656
P4	2.016	-9.656
P5	0.000	-8.937
P6	0.000	-6.727
P7	-2.016	-3.625
P8	2.016	-3.625
P9	0.000	-2.172
P10	0.050	-1.563
P11	-0.349	-1.434
P12	0.364	-1.434
P13	-0.034	-1.313
P14	-0.356	-1.186
P16	0.364	-1.188
P17	0.048	-1.063
P18	-0.351	-0.938
P19	0.367	-0.938
P20	-0.030	-0.803
P21	-0.360	-0.684
P23	0.364	-0.684
P24	0.051	-0.550
P25	-0.353	-0.433
P27	0.369	-0.433
P28	-0.033	-0.303
P29	-0.348	-0.181
P31	0.367	-0.188
P32	-2.032	-0.045
P33	0.044	-0.047
P34	2.018	-0.045
P35	0.000	-4.447
F1	-0.040	0.063
F2	0.360	0.188
F3	-0.360	0.188
F4	-0.040	0.313
F5	0.360	0.438
F6	-0.360	0.438
F7	-0.040	0.563
F8	0.360	0.688
F9	-0.360	0.688
F10	-0.040	0.813
F11	0.360	0.938
F12	-0.360	0.938
F13	-0.040	1.063
F14	0.360	1.188
F15	-0.360	1.188
F16	-0.040	1.313
F17	0.360	1.438
F18	-0.360	1.438
F19	-0.040	1.563
F20	2.000	0.063
F21	-2.000	0.063

Table 1a (conc'l)

THERMOCOUPLE NAME	LATERAL POSITION (In.)	STREAMWISE POSITION (In.)
1T	-0.359	-13.360
2T	-0.203	-9.656
3T	-0.203	-7.313
4T	-0.203	-6.528
5T	-0.203	-4.625
6T	-0.203	-2.906
7T	-0.203	-1.266
8T	-0.203	-0.203

Table 1b Interaction Zone Instrumentation Coordinates

PRESSURE PORT	LATERAL POSITION (In.)	STREAMWISE POSITION (In.)
P9	0.000	-2.172
P10	0.050	-1.563
P11	-0.349	-1.434
P12	0.364	-1.434
P13	-0.034	-1.313
P14	-0.356	-1.186
P16	0.364	-1.188
P17	0.048	-1.063
P18	-0.351	-0.938
P19	0.367	-0.938
P20	-0.030	-0.803
P21	-0.360	-0.684
P23	0.364	-0.684
P24	0.051	-0.550
P25	-0.353	-0.433
P27	0.369	-0.433
P28	-0.033	-0.303
P29	-0.348	-0.181
P31	0.367	-0.188
P32	-2.032	-0.045
P33	0.044	-0.047
P34	2.018	-0.045
P35	0.000	-4.447
F1	-0.040	0.063
F2	0.360	0.188
F3	-0.360	0.188
F4	-0.040	0.313
F5	0.360	0.438
F6	-0.360	0.438
F7	-0.040	0.563
F8	0.360	0.688
F9	-0.360	0.688
F10	-0.040	0.813
F11	0.360	0.938
F12	-0.360	0.938
F13	-0.040	1.063
F14	0.360	1.188
F15	-0.360	1.188
F16	-0.040	1.313
F17	0.360	1.438
F18	-0.360	1.438
F19	-0.040	1.563
F20	2.000	0.063
F21	-2.000	0.063

Table 1b (conc'l)

THERMOCOUPLE NAME	LATERAL POSITION (In.)	STREAMWISE POSITION (In.)
6T	-0.203	-2.906
7T	-0.203	-1.266
8T	-0.203	-0.203

Table 2 Surface Pressure Data at a Given Ramp Angle and Stagnation Press

CASE : ROUGH FLAT PLATE
 RAMP ANGLE (deg) : 22
 STAGNATION PRESSURE : 700 Psia
 FILE : HPSR2150

PORT ID #	Y COORD (In.)	X COORD (In.)	Ps (mm Hg)	Y= 0.00" Ps/P6	Y=+0.36" Ps/P6	Y=-0.36" Ps/P6	Y=+2.00" Ps/P6	Y=-2.00" Ps/P6
P2	0.000	-11.121	26.47	0.8724				
P3	-2.016	-9.656	31.32					1.0323
P4	2.016	-9.656	30.82				1.0158	
P6	0.000	-6.727	30.34	1.0000				
P35	0.000	-4.447	27.17	0.8855				
P9	0.000	-2.172	26.85	0.8850				
P10	0.050	-1.563	28.23	0.9305				
P11	-0.349	-1.434	26.56			0.8754		
P12	0.364	-1.434	28.92		0.9532			
P13	-0.034	-1.313	27.24	0.8978				
P16	0.364	-1.188	29.10		0.9591			
P14	-0.356	-1.186	29.60			0.9756		
P17	0.048	-1.063	37.08	1.2221				
P18	-0.351	-0.938	42.22			1.3916		
P19	0.367	-0.938	44.96		1.4819			
P20	-0.030	-0.803	54.00	1.7798				
P21	-0.360	-0.684	62.98			2.0761		
P23	0.364	-0.684	62.48		2.0593			
P24	0.051	-0.550	66.41	2.1889				
P25	-0.353	-0.433	69.60			2.2940		
P27	0.369	-0.433	69.56		2.2927			
P28	-0.033	-0.303	71.23	2.3477				
P29	-0.348	-0.181	73.81			2.4328		
P33	0.044	-0.047	75.78	2.4977				
PF17	-2.000	0.063	80.00					2.6368
PF19	2.000	0.063	78.21				2.5778	
PF1	0.360	0.125	88.03		2.9015			
PF20	-0.360	0.125	87.24			2.8754		
PF3	0.040	0.313	97.57	3.2159				
PF2	-0.360	0.438	113.85			3.7525		
PF4	0.360	0.438	112.11		3.6951			
PF6	0.040	0.563	124.58	4.1061				
PF5	-0.360	0.688	149.13			4.9153		
PF7	0.360	0.688	147.92		4.8754			
PF9	0.040	0.813	158.68	5.2301				
PF10	0.360	0.938	187.93		6.1941			
PF8	-0.360	0.938	206.14			6.7943		
PF12	0.040	1.063	197.21	6.5000				
PF11	-0.360	1.188	231.08			7.6163		
PF13	0.360	1.188	231.98		7.6460			
PF15	0.040	1.313	240.04	7.9117				
PF14	-0.360	1.438	269.53			8.8837		
PF16	0.360	1.438	263.19		8.6747			
PF18	0.040	1.563	274.02	9.0316				

Table 3 Surface Pressure Data at a Given Ramp Angle and Stagnation Pressure

CASE : ROUGH FLAT PLATE
RAMP ANGLE (deg) : 22
STAGNATION PRESSURE : 1400 Psia
FILE : HPSR2149

PORT ID #	Y COORD (In.)	X COORD (In.)	Ps (mm Hg)	Y= 0.00" Ps/P5	Y=+0.36" Ps/P6	Y=-0.36" Ps/P6	Y=+2.00" Ps/P6	Y=-2.00" Ps/P6
P2	0.000	-11.121	52.18	0.9296				
P3	-2.016	-9.656	63.40					1.1295
P4	2.016	-9.656	61.26				1.0914	
P6	0.000	-6.727	56.13	1.0000				
P35	0.000	-4.447	52.83	0.9412				
P9	0.000	-2.172	51.80	0.9229				
P10	0.050	-1.563	54.58	0.9724				
P11	-0.349	-1.434	57.68			1.0276		
P12	0.364	-1.434	61.23		1.0909			
P13	-0.034	-1.313	76.42	1.3615				
P16	0.364	-1.188	87.68		1.5621			
P14	-0.356	-1.186	90.30			1.6088		
P17	0.048	-1.063	106.31	1.8940				
P18	-0.351	-0.938	107.06			1.9074		
P19	0.367	-0.938	106.04		1.8892			
P20	-0.030	-0.803	112.18	1.9986				
P21	-0.360	-0.684	119.18			2.1233		
P23	0.364	-0.684	116.68		2.0787			
P24	0.051	-0.550	121.44	2.1635				
P25	-0.353	-0.433	126.03			2.2453		
P27	0.369	-0.433	124.46		2.2174			
P28	-0.033	-0.303	128.07	2.2817				
P29	-0.348	-0.181	132.02			2.3520		
P33	0.044	-0.047	136.41	2.4303				
PF17	-2.000	0.063	142.96					2.5469
PF19	2.000	0.063	142.51				2.5389	
PF1	0.360	0.125	156.88		2.7949			
PF20	-0.360	0.125	154.37			2.7502		
PF3	0.040	0.313	167.74	2.9884				
PF2	-0.360	0.438	196.20			3.4955		
PF4	0.360	0.438	197.88		3.5254			
PF6	0.040	0.563	212.39	3.7839				
PF5	-0.360	0.688	252.05			4.4905		
PF7	0.360	0.688	258.68		4.5086			
PF9	0.040	0.813	268.85	4.7898				
PF10	0.360	0.938	329.35		5.8676			
PF8	-0.360	0.938	344.70			6.1411		
PF12	0.040	1.063	334.31	5.9560				
PF11	-0.360	1.188	395.44			7.0451		
PF13	0.360	1.188	406.72		7.2460			
PF15	0.040	1.313	411.82	7.3369				
PF14	-0.360	1.438	471.59			8.4017		
PF16	0.360	1.438	482.07		8.5885			
PF18	0.040	1.563	479.15	8.5364				

Table 4 Surface Pressure Data at a Given Ramp Angle and Stagnation Pressure

CASE : ROUGH FLAT PLATE
 RAMP ANGLE (deg) : 22
 STAGNATION PRESSURE : 2000 Psia
 FILE : HPSR2148

PORT ID #	Y COORD (In.)	X COORD (In.)	Ps (mm Hg)	Y= 0.00" Ps/P6	Y=+0.36" Ps/P6	Y=-0.36" Ps/P6	Y=+2.00" Ps/P6	Y=-2.00" Ps/P6
P2	0.000	-11.121	78.65	1.0165				
P3	-2.016	-9.656	90.94					1.1754
P4	2.016	-9.656	84.56				1.0929	
P6	0.000	-6.727	77.37	1.0000				
P35	0.000	-4.447	73.21	0.9462				
P9	0.000	-2.172	72.60	0.9383				
P10	0.050	-1.563	76.03	0.9827				
P11	-0.349	-1.434	82.35			1.0644		
P12	0.364	-1.434	85.64		1.1069			
P13	-0.034	-1.313	104.80	1.3545				
P16	0.364	-1.188	117.54		1.5192			
P14	-0.356	-1.186	122.52			1.5836		
P17	0.048	-1.063	142.63	1.8435				
P18	-0.351	-0.938	144.76			1.8710		
P19	0.367	-0.938	142.01		1.8355			
P20	-0.030	-0.803	152.87	1.9758				
P21	-0.360	-0.684	162.94			2.1060		
P23	0.364	-0.684	159.59		2.0627			
P24	0.051	-0.550	167.36	2.1631				
P25	-0.353	-0.433	175.69			2.2708		
P27	0.369	-0.433	173.72		2.2453			
P28	-0.033	-0.303	179.98	2.3262				
P29	-0.348	-0.181	187.19			2.4194		
P33	0.044	-0.047	193.24	2.4976				
PF17	-2.000	0.063	207.29					2.6792
PF19	2.000	0.063	204.93				2.6487	
PF1	0.360	0.125	227.23		2.9369			
PF20	-0.360	0.125	222.64			2.8776		
PF3	0.040	0.313	243.17	3.1429				
PF2	-0.360	0.438	284.62			3.6787		
PF4	0.360	0.438	288.17		3.7246			
PF6	0.040	0.583	309.96	4.0062				
PF5	-0.360	0.688	366.99			4.7433		
PF7	0.360	0.688	373.22		4.8238			
PF9	0.040	0.813	391.43	5.0592				
PF10	0.360	0.938	466.99		6.0358			
PF8	-0.360	0.938	497.23			6.4267		
PF12	0.040	1.063	492.46	6.3650				
PF11	-0.360	1.188	573.37			7.4108		
PF13	0.360	1.188	566.77		7.3254			
PF15	0.040	1.313	601.98	7.7805				
PF14	-0.360	1.438	686.02			8.8667		
PF16	0.360	1.438	675.42		8.7297			
PF18	0.040	1.563	709.51	9.1704				

Table 5 Surface Pressure Data at a Given Ramp Angle and Stagnation Pressure

CASE : ROUGH FLAT PLATE
 RAMP ANGLE (deg) : 28
 STAGNATION PRESSURE : 700 Psia
 FILE : HPSR2186

PORT ID #	Y COORD (In.)	X COORD (In.)	Ps (mm Hg)	Y= 0.00" Ps/P6	Y=+0.36" Ps/P6	Y=-0.36" Ps/P6	Y=+2.00" Ps/P6	Y=-2.00" Ps/P6
P2	0.000	-11.121	26.71	0.8344				
P3	-2.016	-9.656	32.54					1.0166
P4	2.016	-9.656	31.33				0.9788	
P6	0.000	-6.727	32.01	1.0000				
P35	0.000	-4.447	27.09	0.8463				
P9	0.000	-2.172	75.18	2.3486				
P10	0.050	-1.563	82.92	2.5904				
P11	-0.349	-1.434	84.94			2.6535		
P12	0.364	-1.434	86.21		2.6932			
P13	-0.034	-1.313	84.28	2.6329				
P16	0.364	-1.188	86.82		2.7123			
P14	-0.356	-1.186	86.98			2.7173		
P17	0.048	-1.063	93.75	2.9288				
P18	-0.351	-0.938	87.92			2.7466		
P19	0.367	-0.936	89.26		2.7885			
P20	-0.030	-0.803	89.51	2.7963				
P21	-0.360	-0.684	91.07			2.8450		
P23	0.364	-0.684	89.20		2.7866			
P24	0.051	-0.550	90.30	2.8210				
P25	-0.353	-0.433	91.55			2.8600		
P27	0.369	-0.433	89.67		2.8013			
P28	-0.033	-0.303	90.44	2.8254				
P29	-0.348	-0.181	92.35			2.8850		
P33	0.044	-0.047	96.64	3.0191				
P32	-2.032	-0.045	96.42					3.0122
P34	2.018	-0.045	95.19				2.9738	
PF19	2.000	0.063	95.90				2.9959	
PF1	0.360	0.125	94.69		2.9581			
PF20	-0.360	0.125	94.86			2.9634		
PF3	0.040	0.313	97.37	3.0419				
PF2	-0.360	0.438	104.15			3.2537		
PF4	0.360	0.438	104.30		3.2584			
PF6	0.040	0.563	111.96	3.4977				
PF5	-0.360	0.688	122.86			3.8382		
PF7	0.360	0.688	122.95		3.8410			
PF9	0.040	0.813	133.81	4.1803				
PF10	0.360	0.938	148.20		4.6298			
PF8	-0.360	0.938	156.03			4.8744		
PF12	0.040	1.063	161.17	5.0350				
PF11	-0.360	1.188	180.30			5.6326		
PF13	0.360	1.188	186.66		5.8313			
PF15	0.040	1.313	198.80	6.2106				
PF14	-0.360	1.438	226.08			7.0628		
PF16	0.360	1.438	223.73		6.9894			
PF18	0.040	1.563	242.00	7.5601				

Table 6 Surface Pressure Data at a Given Ramp Angle and Stagnation Pressure

CASE : ROUGH FLAT PLATE
RAMP ANGLE (deg) : 28
STAGNATION PRESSURE : 1400 Psia
FILE : HPSR2185

PORT ID #	Y COORD (In.)	X COORD (In.)	Ps (mm Hg)	Y= 0.00" Ps/P6	Y=+0.36" Ps/P6	Y=-0.36" Ps/P6	Y=+2.00" Ps/P6	Y=-2.00" Ps/P6
P2	0.000	-11.121	51.93	0.9119				
P3	-2.016	-9.656	64.53					1.1331
P4	2.016	-9.656	60.79				1.0674	
P6	0.000	-8.727	56.95	1.0000				
P35	0.000	-4.447	53.07	0.9319				
P9	0.000	-2.172	130.74	2.2957				
P10	0.050	-1.563	145.20	2.5496				
P11	-0.349	-1.434	149.40			2.6234		
P12	0.364	-1.434	150.30		2.6392			
P13	-0.034	-1.313	149.25	2.6207				
P16	0.364	-1.188	153.25		2.6910			
P14	-0.356	-1.186	154.93			2.7205		
P17	0.048	-1.063	166.29	2.9199				
P18	-0.351	-0.938	157.82			2.7712		
P19	0.367	-0.938	158.48		2.7828			
P20	-0.030	-0.803	160.74	2.8225				
P21	-0.360	-0.684	164.08			2.8811		
P23	0.364	-0.684	161.32		2.8327			
P24	0.051	-0.550	163.06	2.8632				
P25	-0.353	-0.433	166.58			2.9250		
P27	0.369	-0.433	163.21		2.8658			
P28	-0.033	-0.303	165.63	2.9083				
P29	-0.348	-0.181	169.37			2.9740		
P33	0.044	-0.047	177.61	3.1187				
P32	-2.032	-0.045	176.71					3.1029
P34	2.018	-0.045	175.46				3.0809	
PF17	-2.000	0.063	180.94					3.1772
PF19	2.000	0.063	177.95				3.1247	
PF1	0.360	0.125	175.85		3.0878			
PF20	-0.360	0.125	175.96			3.0897		
PF3	0.040	0.313	179.70	3.1554				
PF2	-0.360	0.438	194.12			3.4086		
PF4	0.360	0.438	195.47		3.4323			
PF6	0.040	0.563	207.81	3.6490				
PF5	-0.360	0.688	231.15			4.0588		
PF7	0.360	0.688	231.74		4.0692			
PF9	0.040	0.813	254.87	4.4753				
PF10	0.360	0.938	281.43		4.9417			
PF8	-0.360	0.938	296.42			5.2049		
PF12	0.040	1.063	301.72	5.2980				
PF11	-0.360	1.188	344.88			6.0558		
PF13	0.360	1.188	351.20		6.1668			
PF15	0.040	1.313	371.82	6.5289				
PF14	-0.360	1.438	433.10			7.6049		
PF16	0.360	1.438	433.94		7.6197			
PF18	0.040	1.563	452.85	7.9517				

Table 7 Surface Pressure Data at a Given Ramp Angle and Stagnation Pressure

CASE : ROUGH FLAT PLATE
 RAMP ANGLE (deg) : 28
 STAGNATION PRESSURE : 2000 Psia
 FILE : HPSR2184

PORT ID #	Y COORD (In.)	X COORD (In.)	Ps (mm Hg)	Y= 0.00" Ps/P6	Y=+0.36" Ps/P6	Y=-0.36" Ps/P6	Y=+2.00" Ps/P6	Y=-2.00" Ps/P6
P2	0.000	-11.121	77.52	0.9871				
P3	-2.016	-9.656	91.71					1.1678
P4	2.016	-9.656	83.54				1.0638	
P6	0.000	-6.727	78.53	1.0000				
P35	0.000	-4.447	73.48	0.9357				
P9	0.000	-2.172	174.44	2.2213				
P10	0.050	-1.563	210.10	2.6754				
P11	-0.349	-1.434	209.01			2.6615		
P12	0.364	-1.434	209.52		2.6680			
P13	-0.034	-1.313	209.40	2.6655				
P16	0.364	-1.188	217.42		2.7686			
P14	-0.356	-1.186	218.39			2.7810		
P17	0.048	-1.063	232.88	2.9655				
P18	-0.351	-0.938	223.95			2.8518		
P19	0.367	-0.938	226.18		2.8802			
P20	-0.030	-0.803	230.48	2.9349				
P21	-0.360	-0.684	233.70			2.9759		
P23	0.364	-0.684	232.68		2.9629			
P24	0.051	-0.550	234.70	2.9687				
P25	-0.353	-0.433	239.37			3.0481		
P27	0.369	-0.433	235.99		3.0051			
P28	-0.033	-0.303	239.70	3.0523				
P29	-0.348	-0.181	246.01			3.1327		
P33	0.044	-0.047	254.84	3.2451				
P32	-2.032	-0.045	258.50					3.2917
P34	2.018	-0.045	253.85				3.2325	
PF17	-2.000	0.063	258.49					3.2916
PF19	2.000	0.063	258.49				3.2916	
PF1	0.360	0.125	255.51		3.2537			
PF20	-0.360	0.125	256.32			3.2640		
PF3	0.040	0.313	261.66	3.3320				
PF2	-0.360	0.438	283.34			3.6080		
PF4	0.360	0.438	289.64		3.6883			
PF6	0.040	0.563	306.29	3.9003				
PF5	-0.360	0.688	337.54			4.2982		
PF7	0.360	0.688	347.24		4.4217			
PF9	0.040	0.813	386.43	4.9208				
PF10	0.360	0.938	425.15		5.4139			
PF8	-0.360	0.938	429.36			5.4675		
PF12	0.040	1.063	451.27	5.7465				
PF11	-0.360	1.188	501.99			6.3923		
PF13	0.360	1.188	527.36		6.7154			
PF15	0.040	1.313	559.78	7.1282				
PF14	-0.360	1.438	626.67			7.9800		
PF16	0.360	1.438	656.54		8.3604			
PF18	0.040	1.563	686.59	8.7430				

Table 8 Surface Pressure Data at a Given Ramp Angle and Stagnation Pres

CASE : ROUGH FLAT PLATE
 RAMP ANGLE (deg) : 34
 STAGNATION PRESSURE : 700 Psia
 FILE : HPSR2192

PORT ID #	Y COORD (In.)	X COORD (In.)	Ps (mm Hg)	Y= 0.00" Ps/P6	Y=+0.36" Ps/P6	Y=-0.36" Ps/P6	Y=+2.00" Ps/P6	Y=-2.00" Ps/P6
P2	0.000	-11.121	26.73	0.8445				
P3	-2.016	-9.656	31.87					1.0070
P4	2.016	-9.656	31.34				0.9902	
P6	0.000	-6.727	31.65	1.0000				
P35	0.000	-4.447	85.85	2.7125				
P9	0.000	-2.172	101.58	3.2095				
P10	0.050	-1.563	103.33	3.2648				
P11	-0.349	-1.434	104.10			3.2891		
P12	0.364	-1.434	105.11		3.3210			
P13	-0.034	-1.313	103.32	3.2645				
P16	0.364	-1.188	104.34		3.2967			
P14	-0.356	-1.186	105.38			3.3295		
P18	-0.351	-0.938	105.05			3.3191		
P19	0.387	-0.938	104.98		3.3189			
P20	-0.030	-0.803	105.75	3.3412				
P21	-0.360	-0.684	107.41			3.3937		
P23	0.364	-0.684	105.63		3.3374			
P24	0.051	-0.550	106.07	3.3513				
P25	-0.353	-0.433	107.89			3.4088		
P27	0.369	-0.433	105.91		3.3463			
P28	-0.033	-0.303	107.73	3.4038				
P29	-0.348	-0.181	111.15			3.5118		
P33	0.044	-0.047	116.22	3.6720				
P32	-2.032	-0.045	116.80					3.6904
P34	2.018	-0.045	112.11				3.5422	
PF17	-2.000	0.063	117.81					3.7223
PF19	2.000	0.063	109.93				3.4733	
PF20	-0.360	0.125	109.48			3.4591		
PF1	0.360	0.125	108.43		3.4259			
PF3	0.040	0.313	108.81	3.4379				
PF4	0.360	0.438	109.34		3.4547			
PF2	-0.360	0.438	108.80			3.4376		
PF6	0.040	0.563	112.07	3.5409				
PF7	0.360	0.688	115.30		3.6430			
PF5	-0.360	0.688	115.99			3.6648		
PF8	-0.360	0.938	132.70			4.1927		
PF10	0.360	0.938	127.06		4.0145			
PF12	0.040	1.063	135.82	4.2913				
PF11	-0.360	1.188	143.04			4.5194		
PF13	0.360	1.188	148.13		4.6803			
PF15	0.040	1.313	156.51	4.9450				
PF14	-0.360	1.438	167.29			5.2856		
PF16	0.360	1.438	164.74		5.2051			
PF18	0.040	1.563	179.90	5.6840				

Table 9 Surface Pressure Data at a Given Ramp Angle and Stagnation Pressure

CASE : ROUGH FLAT PLATE
RAMP ANGLE (deg) : 34
STAGNATION PRESSURE : 1400 Psia
FILE : HPSR2191

PORT ID #	Y COORD (In.)	X COORD (In.)	Ps (mm Hg)	Y= 0.00" Ps/P6	Y=+0.36" Ps/P6	Y=-0.36" Ps/P6	Y=+2.00" Ps/P6	Y=-2.00" Ps/P6
P2	0.000	-11.121	52.72	0.9193				
P3	-2.016	-9.656	64.10					1.1177
P4	2.016	-9.656	60.82				1.0605	
P6	0.000	-6.727	57.35	1.0000				
P35	0.000	-4.447	149.03	2.5986				
P9	0.000	-2.172	184.62	3.2192				
P10	0.050	-1.563	187.50	3.2694				
P11	-0.349	-1.434	188.80			3.2921		
P12	0.364	-1.434	191.07		3.3316			
P13	-0.034	-1.313	188.05	3.2790				
P16	0.364	-1.188	190.91		3.3289			
P14	-0.356	-1.186	191.70			3.3426		
P17	0.048	-1.063	203.42	3.5470				
P18	-0.351	-0.938	191.65			3.3418		
P19	0.367	-0.938	192.15		3.3505			
P20	-0.030	-0.803	194.69	3.3948				
P21	-0.360	-0.684	196.36			3.4239		
P23	0.364	-0.684	194.92		3.3988			
P24	0.051	-0.550	195.34	3.4061				
P25	-0.353	-0.433	199.62			3.4807		
P27	0.369	-0.433	195.67		3.4119			
P28	-0.033	-0.303	200.91	3.5032				
P29	-0.348	-0.181	206.59			3.6023		
P33	0.044	-0.047	217.11	3.7857				
P32	-2.032	-0.045	212.19					3.6999
P34	2.018	-0.045	210.76				3.6750	
PF17	-2.000	0.063	209.36					3.6506
PF19	2.000	0.063	205.98				3.5916	
PF20	-0.360	0.125	204.07			3.5583		
PF1	0.360	0.125	202.56		3.5320			
PF3	0.040	0.313	201.81	3.5189				
PF4	0.360	0.438	204.79		3.5709			
PF2	-0.360	0.438	204.88			3.5724		
PF6	0.040	0.563	211.77	3.6926				
PF7	0.360	0.688	218.28		3.8061			
PF5	-0.360	0.688	222.22			3.8748		
PF9	0.040	0.813	253.63	4.4225				
PF8	-0.360	0.938	260.56			4.5433		
PF10	0.360	0.938	243.25		4.2415			
PF12	0.040	1.063	263.76	4.5991				
PF11	-0.360	1.188	284.95			4.9686		
PF13	0.360	1.188	282.38		4.9238			
PF15	0.040	1.313	307.04	5.3538				
PF14	-0.360	1.438	340.94			5.9449		
PF16	0.360	1.438	321.97		5.6141			
PF18	0.040	1.563	353.03	6.1557				

Table 10 Surface Pressure Data at a Given Ramp Angle and Stagnation Press

CASE : ROUGH FLAT PLATE

RAMP ANGLE (deg) : 34

STAGNATION PRESSURE : 2000 Psia

FILE : HPSR2188

PORT ID #	Y COORD (In.)	X COORD (In.)	Ps (mm Hg)	Y= 0.00" Ps/P6	Y=+0.36" Ps/P6	Y=-0.36" Ps/P6	Y=+2.00" Ps/P6	Y=-2.00" Ps/P6
P2	0.000	-11.121	78.34	0.9971				
P3	-2.016	-9.656	91.15					1.1601
P4	2.016	-9.656	83.21				1.0591	
P6	0.000	-6.727	78.57	1.0000				
P35	0.000	-4.447	207.75	2.6441				
P9	0.000	-2.172	269.51	3.4302				
P10	0.050	-1.563	273.55	3.4816				
P11	-0.349	-1.434	276.86			3.5237		
P12	0.364	-1.434	278.91		3.5498			
P13	-0.034	-1.313	274.27	3.4908				
P16	0.364	-1.188	279.37		3.5557			
P14	-0.356	-1.186	279.52			3.5576		
P17	0.048	-1.063	290.98	3.7034				
P18	-0.351	-0.938	279.37			3.5557		
P19	0.367	-0.938	280.83		3.5743			
P20	-0.030	-0.803	285.87	3.6384				
P21	-0.360	-0.684	286.06			3.6408		
P23	0.364	-0.684	284.97		3.6270			
P24	0.051	-0.550	286.10	3.6413				
P25	-0.353	-0.433	293.61			3.7369		
P27	0.369	-0.433	286.18		3.6424			
P28	-0.033	-0.303	296.71	3.7764				
P29	-0.348	-0.181	309.50			3.9392		
P33	0.044	-0.047	321.00	4.0855				
P32	-2.032	-0.045	309.84					3.9435
P34	2.018	-0.045	308.29				3.9238	
PF17	-2.000	0.063	306.15					3.8965
PF19	2.000	0.063	300.53				3.8250	
PF20	-0.360	0.125	299.40			3.8106		
PF1	0.360	0.125	294.05		3.7425			
PF3	0.040	0.313	293.88	3.7378				
PF4	0.360	0.438	297.22		3.7829			
PF2	-0.360	0.438	296.48			3.7735		
PF6	0.040	0.563	306.60	3.9023				
PF7	0.360	0.688	315.66		4.0176			
PF5	-0.360	0.688	317.57			4.0419		
PF9	0.040	0.813	366.56	4.6654				
PF8	-0.360	0.938	369.03			4.6968		
PF10	0.360	0.938	351.57		4.4746			
PF12	0.040	1.063	383.07	4.8755				
PF11	-0.360	1.188	402.52			5.1231		
PF13	0.360	1.188	405.38		5.1595			
PF15	0.040	1.313	447.08	5.6902				
PF14	-0.360	1.438	475.67			6.0541		
PF16	0.360	1.438	468.28		5.9600			
PF18	0.040	1.563	513.02	6.5295				

**Table 11 Surface Pressure Data at a Given Ramp Angle
and Stagnation Pressure with the Side Fences**

CASE : ROUGH FLAT PLATE
RAMP ANGLE (deg) : 22
STAGNATION PRESSURE : 700 Psia
FILE : HPSR2166

PORT ID #	Y COORD (In.)	X COORD (In.)	Ps (mm Hg)	Y= 0.00" Ps/P6	Y=+0.36" Ps/P6	Y=-0.36" Ps/P6	Y=+2.00" Ps/P6	Y=-2.00" Ps/P6
P2	0.000	-11.121	26.85	0.8149				
P3	-2.016	-9.656	33.23					1.0085
P4	2.016	-9.656	31.98				0.9706	
P6	0.000	-6.727	32.95	1.0000				
P35	0.000	-4.447	28.41	0.8622				
P9	0.000	-2.172	28.72	0.8716				
P10	0.050	-1.563	29.03	0.8810				
P11	-0.349	-1.434	27.37			0.8307		
P12	0.364	-1.434	29.67		0.9005			
P13	-0.034	-1.313	27.61	0.8379				
P16	0.364	-1.188	29.08		0.8825			
P14	-0.356	-1.186	29.93			0.9083		
P17	0.048	-1.063	38.86	1.1794				
P18	-0.351	-0.938	42.94			1.3032		
P19	0.367	-0.938	46.59		1.4140			
P20	-0.030	-0.803	55.58	1.6868				
P21	-0.360	-0.684	63.65			1.9317		
P23	0.364	-0.684	61.55		1.8680			
P24	0.051	-0.550	66.81	2.0276				
P25	-0.353	-0.433	69.95			2.1229		
P27	0.369	-0.433	69.54		2.1105			
P28	-0.033	-0.303	71.88	2.1815				
P29	-0.348	-0.181	74.01			2.2461		
P33	0.044	-0.047	77.12	2.3405				
P32	-2.032	-0.045	75.45					2.2898
P34	2.018	-0.045	74.54				2.2622	
PF17	-2.000	0.063	79.69					2.4185
PF19	2.000	0.063	78.56				2.3842	
PF1	0.360	0.125	88.42		2.6835			
PF20	-0.360	0.125	88.31			2.6801		
PF3	0.040	0.313	98.28	2.9821				
PF2	-0.360	0.438	114.10			3.4628		
PF4	0.360	0.438	114.27		3.4680			
PF6	0.040	0.563	126.04	3.8252				
PF5	-0.360	0.688	149.53			4.5381		
PF7	0.360	0.688	149.60		4.5402			
PF10	0.360	0.938	190.29		5.7751			
PF8	-0.360	0.938	201.58			6.1178		
PF12	0.040	1.063	195.91	5.9457				
PF11	-0.360	1.188	226.35			6.8695		
PF13	0.360	1.188	234.34		7.1120			
PF15	0.040	1.313	240.09	7.2865				
PF14	-0.360	1.438	265.35			8.0531		
PF16	0.360	1.438	265.41		8.0549			
PF18	0.040	1.563	277.03	8.4076				

**Table 12 Pitot Pressure Distribution Data for the 22 Degree Ramp Angle
at a Given Location and Stagnation Pressure**

CASE : ROUGH PLATE
 RAMP ANGLE (deg) : 22
 STAGNATION PRESSURE : 700 Psia
 STAGNATION TEMPERATURE : 919 - 923 Deg. R
 STATIC PRESSURE : 30.34 mm Hg @ X = -6.727 In.
 AVERAGE WALL TEMPERATURE (1) : 727.30 Deg. R.
 MOMENTUM THICKNESS : 0.007274 In.
 PROBE LOCATION : X = -6.484 In.
 TOTAL PRESSURE FILE : HPTR2138
 TOTAL TEMPERATURE FILE : HTTR2174

Z COORD (In.)	Pt (Psia)	Pt/Po	M #	Tt (2) Deg. R	Ts Deg. R	a (Ft/sec)	U (Ft/sec)
0.320	22.86	0.0327	5.82	919.61	118.39	533.27	3102.04
0.300	22.86	0.0327	5.82	920.90	118.56	533.64	3104.21
0.280	22.67	0.0324	5.79	921.87	119.58	535.93	3104.12
0.259	22.67	0.0324	5.79	922.85	119.70	536.22	3105.77
0.240	22.63	0.0323	5.79	926.07	120.30	537.56	3110.83
0.220	22.11	0.0316	5.72	935.75	124.08	545.93	3122.20
0.200	20.11	0.0287	5.45	941.24	135.53	570.56	3110.72
0.180	17.41	0.0249	5.07	940.27	153.22	606.65	3074.50
0.159	14.62	0.0209	4.64	935.44	176.49	651.09	3019.11
0.140	11.88	0.0170	4.17	928.01	207.09	705.29	2942.48
0.120	9.47	0.0135	3.72	916.38	243.70	765.10	2842.33
0.100	7.41	0.0106	3.27	903.77	287.60	831.15	2720.34
0.080	5.83	0.0083	2.89	885.66	331.80	892.74	2579.12
0.059	4.62	0.0066	2.56	858.13	372.03	945.31	2416.21
0.040	2.86	0.0041	1.97	842.26	473.57	1066.54	2104.28
0.020	1.88	0.0027	1.55	823.68	555.89	1155.53	1793.38
				Twall = 727.30			

(1) NOTE : TEMPERATURE IS THERMOCOUPLE 4

(2) NOTE : TEMPERATURE INTERPOLATED FROM TOTAL TEMPERATURE FILE

**Table 13 Pitot Pressure Distribution Data for the 22 Degree Ramp Angle
at a Given Location and Stagnation Pressure**

CASE : ROUGH PLATE
 RAMP ANGLE (deg) : 22
 STAGNATION PRESSURE : 1400 Psia
 STAGNATION TEMPERATURE : 851 - 945 Deg. R
 STATIC PRESSURE : 56.13 mm Hg @ X = -6.727 In.
 AVERAGE WALL TEMPERATURE (1) : 710.34 Deg. R.
 MOMENTUM THICKNESS : 0.008679 In.
 PROBE LOCATION : X = -6.484 In.
 TOTAL PRESSURE FILE : HPTR2141
 TOTAL TEMPERATURE FILE : HTTR2178

Z COORD (In.)	Pt (Psia)	Pt/Po	M #	Tt (2) Deg. R	Ts Deg. R	a (Ft/sec)	U (Ft/sec)
0.395	46.25	0.0330	5.72				
0.380	45.73	0.0327	5.69				
0.359	45.69	0.0326	5.69				
0.340	45.54	0.0325	5.68	926.75	124.47	546.79	3104.10
0.320	45.50	0.0325	5.67	926.42	124.54	546.94	3103.33
0.300	45.28	0.0323	5.66	926.68	125.11	548.19	3102.73
0.280	45.43	0.0325	5.67	925.85	124.61	547.10	3102.07
0.260	44.90	0.0321	5.64	926.33	125.98	550.10	3100.35
0.240	42.42	0.0303	5.48	931.92	133.14	565.51	3097.31
0.220	37.16	0.0265	5.12	941.24	150.72	601.69	3081.25
0.200	31.15	0.0223	4.68	945.11	175.53	649.33	3040.17
0.180	24.95	0.0178	4.18	944.28	209.94	710.12	2969.74
0.159	19.58	0.0140	3.69	939.24	251.87	777.81	2873.22
0.140	14.93	0.0107	3.21	931.43	304.18	854.77	2744.68
0.120	11.76	0.0084	2.84	919.83	352.62	920.32	2610.03
0.100	9.13	0.0065	2.48	906.71	406.40	988.02	2451.27
0.080	7.10	0.0051	2.17	888.79	458.34	1049.25	2273.72
0.059	5.00	0.0036	1.79	864.80	528.21	1126.39	2010.60
0.040	3.16	0.0023	1.36	851.98	622.41	1222.72	1660.45
0.020	2.48	0.0018	1.15	836.84	660.83	1259.89	1453.91

Twall = 710.34

(1) NOTE : TEMPERATURE IS THERMOCOUPLE 4

(2) NOTE : TEMPERATURE INTERPOLATED FROM TOTAL TEMPERATURE FILE

**Table 14 Pitot Pressure Distribution Data for the 22 Degree Ramp Angle
at a Given Location and Stagnation Pressure**

CASE : ROUGH PLATE
 RAMP ANGLE (deg) : 22
 STAGNATION PRESSURE : 2000 Psia
 STAGNATION TEMPERATURE : 928 - 933 Deg. R
 STATIC PRESSURE : 77.37 mm Hg @ X = -6.727 In.
 AVERAGE WALL TEMPERATURE (1) : 651.57 Deg. R.
 MOMENTUM THICKNESS : 0.008209 In.
 PROBE LOCATION : X = -6.484 In.
 TOTAL PRESSURE FILE : HPTR2142
 TOTAL TEMPERATURE FILE : HTTR2177+2181

Z COORD (In.)	Pt (Psia)	Pt/Po	M #	Tt (2) Deg. R	Ts Deg. R	a (Ft/sec)	U (Ft/sec)
0.300	61.58	0.0308	5.62	931.24	127.19	552.74	3107.50
0.280	61.81	0.0309	5.63	931.57	126.81	551.90	3108.88
0.259	61.55	0.0308	5.62	932.21	127.37	553.11	3108.04
0.240	59.12	0.0296	5.51	939.95	133.04	565.29	3113.04
0.220	52.88	0.0264	5.21	947.22	147.58	595.38	3098.97
0.200	44.96	0.0225	4.79	951.89	170.15	639.29	3064.11
0.180	35.65	0.0178	4.26	956.72	206.73	704.68	3001.22
0.159	27.47	0.0137	3.73	954.46	252.63	778.98	2903.27
0.139	20.7	0.0104	3.22	948.98	308.62	860.98	2773.23
0.120	15.66	0.0078	2.79	938.66	367.92	940.08	2618.12
0.100	12.11	0.0061	2.43	925.10	423.98	1009.16	2453.26
0.080	9.16	0.0046	2.09	906.36	483.53	1077.70	2253.48
0.059	6.32	0.0032	1.70	883.07	580.10	1159.89	1989.50
0.039	4.04	0.0020	1.29	855.86	641.40	1241.23	1604.90
0.020	3.36	0.0017	1.14	839.67	666.69	1265.46	1441.36
				Twall =	651.57		

(1) NOTE : TEMPERATURE IS THERMOCOUPLE 4

(2) NOTE : TEMPERATURE INTERPOLATED FROM TOTAL TEMPERATURE FILE

**Table 15 Pitot Pressure Distribution Data for the 22 Degree Ramp Angle
at a Given Location and Stagnation Pressure**

CASE : ROUGH PLATE
RAMP ANGLE (deg) : 22
STAGNATION PRESSURE : 700 Psia
STAGNATION TEMPERATURE : 917 - 921 Deg. R
STATIC PRESSURE : 26.85 mm Hg @ X = -2.172 In.
AVERAGE WALL TEMPERATURE (1) : 735.25 Deg. R.
MOMENTUM THICKNESS : 0.009992 In.
PROBE LOCATION : X = -2.172 In.
TOTAL PRESSURE FILE : HPTR2128
TOTAL TEMPERATURE FILE : HTTR2168

Z COORD (In.)	Pt (Psia)	Pt/Po	M #	Tt (2) Deg. R	Ts Deg. R	a (Ft/sec)	U (Ft/sec)
0.780	23.44	0.0335	5.89				
0.760	23.44	0.0335	5.89				
0.740	23.47	0.0335	5.90				
0.720	23.66	0.0338	5.92				
0.699	23.70	0.0339	5.92				
0.680	23.59	0.0337	5.91				
0.660	23.59	0.0337	5.91				
0.640	23.70	0.0339	5.92				
0.620	23.66	0.0338	5.92				
0.599	23.66	0.0338	5.92				
0.580	23.66	0.0338	5.92				
0.560	23.66	0.0338	5.92				
0.540	23.66	0.0338	5.92				
0.520	23.59	0.0337	5.91				
0.499	23.55	0.0336	5.91				
0.480	23.55	0.0336	5.91				
0.460	23.59	0.0337	5.91				
0.440	23.55	0.0336	5.91	920.25	115.41	526.51	3109.04
0.420	23.55	0.0336	5.91	920.58	115.45	526.60	3109.60
0.399	23.47	0.0335	5.90	920.90	115.83	527.48	3109.48
0.380	23.36	0.0334	5.88	920.90	116.32	528.57	3108.55
0.360	23.17	0.0331	5.86	921.54	117.27	530.73	3107.95
0.340	22.98	0.0328	5.83	923.49	118.36	533.20	3109.60
0.320	22.72	0.0325	5.80	928.01	120.12	537.15	3114.92
0.299	22.27	0.0318	5.74	934.79	123.17	543.92	3122.11
0.280	20.84	0.0298	5.55	939.31	131.14	561.24	3115.47
0.260	19.31	0.0278	5.34	940.27	140.23	580.37	3099.76
0.240	17.33	0.0248	5.06	938.02	153.46	607.13	3069.63
0.220	14.38	0.0205	4.60	935.11	178.79	655.33	3013.86
0.199	12.30	0.0178	4.25	929.62	201.77	696.16	2956.61
0.180	10.37	0.0148	3.89	921.87	228.78	741.30	2885.14
0.160	8.70	0.0124	3.56	912.17	258.48	787.95	2801.94
0.140	7.42	0.0106	3.28	900.86	286.31	829.29	2716.75
0.120	6.33	0.0090	3.02	889.22	315.41	870.41	2625.16
0.099	5.36	0.0077	2.77	873.03	345.20	910.59	2517.78
0.080	4.35	0.0062	2.48	856.19	384.61	961.16	2379.84
0.060	3.43	0.0049	2.18	831.88	426.69	1012.38	2205.97
0.040	2.81	0.0040	1.95	810.15	459.57	1050.66	2051.94
0.020	1.95	0.0028	1.59	801.57	533.29	1131.79	1795.02
				Twall = 735.25			

(1) NOTE : TEMPERATURE IS INTERPOLATION OF THERMOCOUPLES 6 & 7

(2) NOTE : TEMPERATURE INTERPOLATED FROM TOTAL TEMPERATURE FILE

**Table 16 Pitot Pressure Distribution Data for the 22 Degree Ramp Angle
at a Given Location and Stagnation Pressure**

CASE : ROUGH PLATE

RAMP ANGLE (deg) : 22

STAGNATION PRESSURE : 1400 Psia

STAGNATION TEMPERATURE : 927.35 - 900.12 Deg. R.

STATIC PRESSURE : 51.80 mm Hg @ X = -2.172 In.

AVERAGE WALL TEMPERATURE (1) : 716.50 Deg. R.

MOMENTUM THICKNESS : 0.010929 In.

PROBE LOCATION : X = -2.172 In.

TOTAL PRESSURE FILE : HPTR2139

TOTAL TEMPERATURE FILE : HTTR2171

Z COORD (In.)	Pt (Psia)	Pt/Po	M #	Tt (2) Deg. R	Ts Deg. R	a (Ft/sec)	U (Ft/sec)
0.580	49.70	0.0355	6.18				
0.560	49.32	0.0352	6.16				
0.539	47.56	0.0340	6.04				
0.520	46.17	0.0330	5.95				
0.500	46.02	0.0329	5.94				
0.480	46.17	0.0330	5.95				
0.460	46.13	0.0330	5.95				
0.439	46.13	0.0330	5.95	928.97	114.96	525.49	3126.69
0.420	46.17	0.0330	5.95	929.30	114.90	525.36	3127.44
0.400	45.94	0.0328	5.94	928.97	115.37	526.42	3125.91
0.380	45.26	0.0323	5.89	928.33	116.84	529.76	3121.86
0.360	44.47	0.0318	5.84	928.97	118.74	534.06	3119.43
0.339	43.76	0.0313	5.79	930.91	120.68	538.39	3119.44
0.320	41.99	0.0300	5.67	937.69	126.05	550.25	3122.14
0.300	38.38	0.0274	5.42	946.73	137.61	574.93	3117.29
0.280	33.35	0.0238	5.05	950.91	155.93	611.99	3089.95
0.260	28.46	0.0203	4.66	951.24	178.09	654.05	3047.21
0.239	24.36	0.0174	4.30	950.27	201.98	696.52	2997.84
0.220	20.75	0.0148	3.97	948.02	228.76	741.26	2939.11
0.200	17.59	0.0126	3.64	942.53	257.92	787.10	2867.42
0.180	14.43	0.0103	3.29	935.11	295.59	842.62	2771.39
0.160	12.41	0.0089	3.04	926.39	324.96	883.49	2687.59
0.139	10.45	0.0075	2.78	915.73	359.72	929.54	2584.12
0.120	8.80	0.0063	2.54	903.77	394.78	973.79	2472.44
0.100	7.37	0.0053	2.31	891.48	431.25	1017.77	2351.04
0.080	6.09	0.0044	2.08	877.25	469.68	1062.15	2212.46
0.059	4.77	0.0034	1.82	859.76	517.61	1115.03	2027.13
0.039	3.42	0.0024	1.50	850.03	586.71	1187.13	1778.32
0.020	2.82	0.0020	1.33	835.42	637.04	1237.00	1643.97

Twall = 716.50

(1) NOTE : TEMPERATURE IS INTERPOLATION OF THERMOCOUPLES 6 & 7

(2) NOTE : TEMPERATURE INTERPOLATED FROM TOTAL TEMPERATURE FILE

**Table 17 Pitot Pressure Distribution Data for the 22 Degree Ramp Angle
at a Given Location and Stagnation Pressure**

CASE : ROUGH PLATE
 RAMP ANGLE (deg) : 22
 STAGNATION PRESSURE : 2000 Psia
 STAGNATION TEMPERATURE : 936 - 930 Deg. R
 STATIC PRESSURE : 72.60 mm Hg @ X = -2.172 In.
 AVERAGE WALL TEMPERATURE (1) : 654.00 Deg. R.
 MOMENTUM THICKNESS : 0.011166 In.
 PROBE LOCATION : X = -2.172 In.
 TOTAL PRESSURE FILE : HPTR2151+2153+2154
 TOTAL TEMPERATURE FILE : HTTR2182

Z COORD (In.)	Pt (Psia)	Pt/Po	M #	Tt (2) Deg. R	Ts Deg. R	a (Ft/sec)	U (Ft/sec)
0.459	64.66	0.0323	5.95				
0.440	64.92	0.0325	5.96				
0.420	64.88	0.0324	5.96	943.90	116.43	528.84	3152.44
0.400	64.85	0.0324	5.96	943.90	116.47	528.92	3152.38
0.380	64.55	0.0323	5.95	943.90	116.95	530.01	3151.46
0.359	64.21	0.0321	5.93	943.90	117.50	531.27	3150.41
0.340	63.00	0.0315	5.87	943.90	119.51	535.77	3146.59
0.320	60.37	0.0302	5.75	943.90	124.07	545.91	3137.87
0.300	55.22	0.0276	5.49	943.90	134.14	567.63	3118.54
0.280	49.21	0.0246	5.18	952.37	149.44	599.14	3105.33
0.259	42.19	0.0211	4.79	956.91	171.04	640.97	3072.18
0.239	35.92	0.0180	4.42	957.17	195.26	684.85	3024.99
0.220	30.33	0.0152	4.05	956.15	223.29	732.35	2966.76
0.200	25.75	0.0129	3.73	953.25	252.51	778.80	2901.02
0.180	21.73	0.0109	3.41	947.77	284.52	826.70	2822.34
0.160	18.31	0.0092	3.12	940.35	318.56	874.75	2732.71
0.139	15.38	0.0077	2.85	931.78	354.72	923.06	2632.58
0.120	12.76	0.0064	2.59	922.19	394.70	973.69	2516.98
0.100	10.89	0.0053	2.35	911.45	432.52	1019.27	2398.33
0.080	9.00	0.0045	2.14	898.43	468.09	1060.36	2273.41
0.060	7.05	0.0035	1.87	880.72	517.35	1114.75	2089.04
0.039	5.14	0.0026	1.56	857.35	576.19	1176.44	1837.60
0.020	4.58	0.0023	1.46	855.36	600.43	1200.93	1749.76
Twall =				654.00			

- (1) NOTE : TEMPERATURE IS INTERPOLATION OF THERMOCOUPLES 6 & 7
 (2) NOTE : TEMPERATURE INTERPOLATED FROM TOTAL TEMPERATURE FILE

**Table 18 Pitot Pressure Distribution Data for the 22 Degree Ramp Angle
at a Given Location and Stagnation Pressure**

CASE : ROUGH PLATE
 RAMP ANGLE (deg) : 22
 STAGNATION PRESSURE : 700 Psia
 AVERAGE STAGNATION TEMPERATURE : 919.7
 PROBE LOCATION : X = 1.563 In.
 TOTAL PRESSURE FILE : HPTR2165
 TOTAL TEMPERATURE FILE : HTTR2194

Z COORD (In.)	Pt (Psia)	Pt/Po
-----	-----	-----
0.430	22.97	0.0328
0.410	22.86	0.0327
0.389	22.82	0.0326
0.369	22.82	0.0326
0.350	23.76	0.0339
0.330	33.91	0.0484
0.310	58.01	0.0829
0.289	70.81	0.1012
0.269	77.41	0.1106
0.250	80.33	0.1148
0.230	79.82	0.1140
0.210	74.81	0.1069
0.189	63.95	0.0914
0.169	51.77	0.0740
0.150	41.09	0.0587
0.130	32.56	0.0465
0.110	26.20	0.0374
0.089	21.62	0.0309
0.069	18.32	0.0262
0.050	14.70	0.0210
0.030	12.03	0.0172

**Table 19 Pitot Pressure Distribution Data for the 22 Degree Ramp Angl
at a Given Location and Stagnation Presure**

CASE : ROUGH PLATE
RAMP ANGLE (deg) : 22
STAGNATION PRESSURE : 1400 Psia
STAGNATION TEMPERATURE : 920.13 Deg. R
PROBE LOCATION : X = 1.583 In.
TOTAL PRESSURE FILE : HPT2137
TOTAL TEMPERATURE FILE : HTT2196

Z COORD (In.)	Pt (Psia)	Pt/Po
0.449	45.09	0.0322
0.430	44.98	0.0321
0.410	44.83	0.0320
0.390	44.98	0.0321
0.370	48.46	0.0346
0.349	66.64	0.0476
0.329	84.57	0.0604
0.310	98.21	0.0702
0.290	116.19	0.0830
0.270	132.81	0.0949
0.249	141.62	0.1012
0.229	140.13	0.1001
0.210	126.98	0.0907
0.190	103.30	0.0738
0.170	76.27	0.0543
0.149	58.90	0.0428
0.129	44.84	0.0319
0.110	34.87	0.0248
0.090	27.14	0.0194
0.070	23.69	0.0169
0.049	21.40	0.0153
0.030	20.65	0.0148

**Table 20 Pitot Pressure Distribution Data for the 22 Degree Ramp Angle
at a Given Location and Stagnation Pressure**

CASE : ROUGH PLATE

RAMP ANGLE (deg) : 22

STAGNATION PRESSURE : 2000 Psia

STAGNATION TEMPERATURE : 927.03 Deg. R.

PROBE LOCATION : X = 1.563 In.

TOTAL PRESSURE FILE : HPTR2160+2161+2164

TOTAL TEMPERATURE FILE : HTTR2197+2198+2199

Z COORD (In.)	Pt (Psia)	Pt/Po
0.429	63.38	0.0317
0.409	63.38	0.0317
0.389	63.23	0.0318
0.369	63.08	0.0315
0.349	63.87	0.0319
0.329	74.75	0.0374
0.310	138.20	0.0691
0.290	179.34	0.0897
0.269	201.95	0.1010
0.249	214.90	0.1075
0.230	217.19	0.1086
0.210	206.65	0.1033
0.190	184.29	0.0921
0.169	154.32	0.0772
0.149	127.32	0.0638
0.130	88.94	0.0445
0.110	59.80	0.0299
0.089	50.92	0.0255
0.069	44.22	0.0221
0.050	37.37	0.0187
0.030	32.03	0.0160

**Table 21 Total Temperature Distribution Data for the 22 Degree Ramp Angle
at a Given Location and Stagnation Pressure**

CASE : ROUGH PLATE
 RAMP ANGLE : 22 Deg
 STAGNATION PRESSURE : 700 Psia
 AVERAGE STAGNATION TEMPERATURE : 922.58 Deg. R.
 PROBE LOCATION : X = -8.484 In.
 FILE : HTR2174

Z COORD	INDICATED	CORRECTED	STAGNATION	T/To
In.	PROBE TEMP	PROBE TEMP	TEMP	
	Deg. R	Deg. R	Deg. R	
0.340	904.90	919.81	918.92	1.0008
0.320	904.90	919.81	919.24	1.0004
0.300	906.17	920.90	920.54	1.0004
0.280	907.12	921.87	921.19	1.0007
0.260	908.08	922.85	921.84	1.0011
0.240	911.25	926.07	922.81	1.0035
0.220	920.78	935.75	922.81	1.0140
0.200	926.18	941.24	923.13	1.0196
0.180	925.23	940.27	923.46	1.0182
0.160	920.47	935.44	923.78	1.0126
0.140	913.16	928.01	923.78	1.0046
0.120	901.72	916.38	924.11	0.9916
0.100	889.31	903.77	924.11	0.9780
0.080	871.49	885.66	924.43	0.9581
0.060	844.40	858.13	923.78	0.9289
0.040	828.78	842.26	923.46	0.9121

Table 22 Total Temperature Distribution Data for the 22 Degree Ramp Angle at a Given Location and Stagnation Pressure

CASE : ROUGH PLATE

RAMP ANGLE : 22 Deg

STAGNATION PRESSURE : 1400 Psia

AVERAGE STAGNATION TEMPERATURE : 924.03 Deg. R.

PROBE LOCATION : X = -6.484 In.

FILE : BTTR2178

Z COORD	INDICATED	CORRECTED	STAGNATION	T/To
In.	PROBE TEMP	PROBE TEMP	TEMP	
	Deg. R	Deg. R	Deg. R	
0.338	911.89	926.72	926.38	1.0004
0.318	911.57	926.39	926.38	1.0000
0.298	911.89	926.72	926.38	1.0004
0.278	910.94	925.75	926.05	0.9997
0.258	911.57	926.39	925.73	1.0007
0.238	917.61	932.53	925.08	1.0081
0.218	927.13	942.21	924.76	1.0189
0.198	930.31	945.44	924.43	1.0227
0.178	929.04	944.15	923.78	1.0220
0.158	923.96	938.98	923.78	1.0163
0.138	915.70	930.59	923.46	1.0077
0.118	903.94	918.64	923.13	0.9951
0.098	890.90	905.39	922.49	0.9815
0.078	872.78	888.95	922.16	0.9618
0.058	849.82	863.64	921.19	0.9375
0.040	838.35	851.98	919.24	0.9268

Table 23 Total Temperature Distribution Data for the 22 Degree Ramp Angle at a Given Location and Stagnation Pressure

CASE : ROUGH PLATE
 RAMP ANGLE : 22 Deg
 STAGNATION PRESSURE : 2000 Psia
 AVERAGE STAGNATION TEMPERATURE : 930.78 Deg. R.
 PROBE LOCATION : X = -8.484 In.
 FILE : HTR2177+2181

Z COORD	INDICATED	CORRECTED	STAGNATION	T/To
In.	PROBE TEMP	PROBE TEMP	TEMP	
	Deg. R	Deg. R	Deg. R	
0.440	919.20	934.15	932.86	1.0014
0.420	918.24	933.17	932.86	1.0003
0.400	917.61	932.53	932.54	1.0000
0.380	917.29	932.21	932.21	1.0000
0.360	917.29	932.21	932.21	1.0000
0.340	916.66	931.57	931.89	0.9997
0.320	916.34	931.24	931.56	0.9997
0.300	916.34	931.24	931.24	1.0000
0.280	916.66	931.57	930.92	1.0007
0.260	917.29	932.21	930.59	1.0017
0.240	924.91	939.95	930.27	1.0104
0.220	932.06	947.22	930.59	1.0179
0.200	936.66	951.89	929.62	1.0240
0.183	941.41	956.72	930.92	1.0277
0.163	939.19	954.46	930.92	1.0253
0.143	933.80	948.98	930.27	1.0201
0.123	923.84	938.66	930.27	1.0090
0.103	910.30	925.10	929.94	0.9948
0.083	891.86	908.36	929.94	0.9746
0.063	868.94	883.07	929.29	0.9503
0.043	842.17	855.86	928.65	0.9216
0.040	843.77	857.49	927.67	0.9243

**Table 24 Total Temperature Distribution Data for the 22 Degree Ramp An
at a Given Location and Stagnation Pressure**

CASE : ROUGH PLATE
RAMP ANGLE : 22 Deg
STAGNATION PRESSURE : 700 Psia
AVERAGE STAGNATION TEMPERATURE : 918.93 Deg. R.
PROBE LOCATION : X = -2.172 In.
FILE : HTR2168

Z COORD	INDICATED	CORRECTED	STAGNATION	T/To
In.	PROBE TEMP	PROBE TEMP	TEMP	
	Deg. R	Deg. R	Deg. R	
0.439	905.53	920.25	917.30	1.0032
0.420	905.85	920.58	917.30	1.0036
0.400	906.17	920.90	917.62	1.0036
0.380	906.17	920.90	917.95	1.0032
0.360	906.80	921.54	915.95	1.0061
0.339	908.71	923.49	918.27	1.0057
0.320	913.16	928.01	918.27	1.0106
0.300	919.83	934.79	918.60	1.0176
0.280	924.28	939.31	918.60	1.0225
0.260	925.23	940.27	918.60	1.0236
0.239	923.01	938.02	919.24	1.0204
0.220	920.15	935.11	919.24	1.0173
0.200	914.75	929.62	919.24	1.0113
0.180	907.12	921.87	919.57	1.0025
0.160	897.58	912.17	919.89	0.9916
0.139	886.45	900.86	919.89	0.9793
0.120	874.99	889.22	920.22	0.9663
0.100	859.06	873.03	920.22	0.9467
0.080	842.48	856.19	920.22	0.9304
0.060	818.57	831.86	920.54	0.9037
0.040	797.19	810.15	920.87	0.8798

**Table 25 Total Temperature Distribution Data for the 22 Degree Ramp Angle
at a Given Location and Stagnation Pressure**

CASE : ROUGH PLATE

RAMP ANGLE : 22 Deg

STAGNATION PRESSURE : 1400 Psia

AVERAGE STAGNATION TEMPERATURE : 923.21 Deg. R.

PROBE LOCATION : X = -2.172 In.

FILE : HTTR2171

Z COORD	INDICATED	CORRECTED	STAGNATION	T/To
In.	PROBE TEMP	PROBE TEMP	TEMP	
	Deg. R	Deg. R	Deg. R	
0.440	914.11	928.97	927.35	1.0018
0.420	914.43	929.30	927.35	1.0021
0.400	914.11	928.97	927.35	1.0018
0.380	913.48	928.33	927.35	1.0011
0.360	914.11	928.97	927.35	1.0018
0.340	916.02	930.91	927.35	1.0038
0.320	922.69	937.69	927.02	1.0115
0.300	931.58	946.73	926.70	1.0216
0.280	935.70	950.91	926.70	1.0261
0.260	936.02	951.24	926.38	1.0268
0.240	935.07	950.27	926.05	1.0262
0.220	932.85	948.02	925.40	1.0244
0.200	927.45	942.53	925.08	1.0189
0.180	920.15	935.11	924.76	1.0112
0.160	911.57	928.39	924.43	1.0021
0.140	901.08	915.73	923.46	0.9916
0.120	889.31	903.77	922.16	0.9801
0.100	877.22	891.48	919.57	0.9695
0.080	863.21	877.25	916.00	0.9577
0.060	846.00	859.76	909.52	0.9453
0.040	836.43	850.03	900.12	0.9444

**Table 26 Total Temperature Distribution Data for the 22 Degree Ramp At
at a Given Location and Stagnation Pressure**

CASE : ROUGH FLATE
 RAMP ANGLE : 22 Deg
 STAGNATION PRESSURE : 2000 Psia
 AVERAGE STAGNATION TEMPERATURE : 934.18 Deg. R.
 PROBE LOCATION : X = -2.172 In.
 FILE : HTTR2182

Z COORD	INDICATED	CORRECTED	STAGNATION	T/To
In.	PROBE TEMP	PROBE TEMP	TEMP	
	Deg. R	Deg. R	Deg. R	
0.305	926.50	941.57	936.43	1.0055
0.285	935.70	950.91	936.10	1.0158
0.265	941.41	956.72	935.45	1.0227
0.245	942.05	957.37	935.78	1.0231
0.225	941.41	956.72	935.45	1.0227
0.205	939.19	954.46	935.45	1.0203
0.185	934.43	949.62	934.81	1.0158
0.165	927.13	942.21	934.81	1.0079
0.145	919.83	934.78	934.46	1.0003
0.125	909.98	924.78	933.83	0.9903
0.105	899.81	914.44	933.51	0.9798
0.085	888.04	902.48	932.86	0.9674
0.065	872.12	886.30	932.21	0.9508
0.045	850.14	863.96	931.56	0.9274
0.040	844.72	858.46	929.94	0.9231

**Table 27 Total Temperature Distribution Data for the 22 Degree Ramp Angle
at a Given Location and Stagnation Pressure**

CASE : ROUGH PLATE
 RAMP ANGLE : 22 Deg
 STAGNATION PRESSURE : 700 Psia
 AVERAGE STAGNATION TEMPERATURE : 919.77 Deg. R.
 PROBE LOCATION : X = +1.563 In.
 FILE : HTTR2194

Z COORD	INDICATED	CORRECTED	STAGNATION	T/To
In.	PROBE TEMP	PROBE TEMP	TEMP	
	Deg. R	Deg. R	Deg. R	
0.550	884.86	899.25	921.84	0.9755
0.530	883.27	897.63	922.16	0.9734
0.509	882.31	896.66	921.84	0.9727
0.490	881.68	896.02	921.84	0.9720
0.470	881.99	896.33	921.84	0.9723
0.450	882.53	896.98	921.51	0.9734
0.430	882.95	897.31	921.51	0.9737
0.409	883.27	897.63	921.19	0.9744
0.390	883.27	897.63	921.19	0.9744
0.370	883.90	898.27	921.19	0.9751
0.350	885.18	899.57	920.87	0.9769
0.330	890.59	905.07	920.54	0.9832
0.309	926.82	941.88	920.54	1.0232
0.290	1054.38	1071.53	919.89	1.1649
0.270	995.21	1011.39	919.57	1.0999
0.250	933.17	948.34	919.57	1.0313
0.230	925.55	940.60	919.24	1.0232
0.209	970.24	986.02	918.92	1.0730
0.190	1040.26	1057.17	918.92	1.1505
0.170	1090.10	1107.83	918.60	1.2060
0.150	1104.78	1122.74	918.27	1.2227
0.130	1097.60	1115.45	917.95	1.2152
0.109	1081.97	1099.56	917.62	1.1983
0.090	1062.23	1079.50	917.62	1.1764
0.070	1043.09	1060.05	916.98	1.1560
0.050	1024.85	1041.51	916.65	1.1362
0.040	1019.18	1035.75	916.00	1.1307

**Table 28 Total Temperature Distribution Data for the 22 Degree Ramp An
at a Given Location and Stagnation Pressure**

CASE : ROUGH PLATE
RAMP ANGLE : 22 Deg
STAGNATION PRESSURE : 1400 Psia
AVERAGE STAGNATION TEMPERATURE : 920.13 Deg. R.
PROBE LOCATION : X = +1.563 In.
FILE : HITR2196

Z COORD	INDICATED	CORRECTED	STAGNATION	T/To
In.	PROBE TEMP	PROBE TEMP	TEMP	
	Deg. R	Deg. R	Deg. R	
0.459	889.31	903.77	924.78	0.9773
0.439	889.31	903.77	924.43	0.9777
0.419	888.68	903.13	924.43	0.9770
0.398	888.99	903.45	923.78	0.9780
0.379	891.54	906.04	923.46	0.9811
0.359	912.84	927.88	923.13	1.0049
0.339	978.15	994.05	922.81	1.0772
0.319	946.49	961.88	922.16	1.0431
0.298	953.46	968.96	921.84	1.0511
0.279	950.92	966.38	921.51	1.0487
0.259	940.14	955.43	921.19	1.0372
0.238	975.62	991.48	920.87	1.0767
0.219	1066.94	1084.29	919.89	1.1787
0.198	1119.74	1137.95	919.57	1.2375
0.179	1136.23	1154.71	918.92	1.2566
0.159	1126.46	1146.81	918.60	1.2484
0.139	1111.33	1129.40	917.95	1.2304
0.119	1093.54	1111.32	917.30	1.2115
0.098	1072.58	1090.02	916.33	1.1895
0.079	1049.68	1068.75	915.03	1.1658
0.059	1029.57	1046.31	913.73	1.1451
0.040	1021.07	1037.67	911.14	1.1389

**Table 29 Total Temperature Distribution Data for the 22 Degree Ramp Angle
at a Given Location and Stagnation Pressure**

CASE : ROUGH PLATE
 RAMP ANGLE : 22 Deg
 STAGNATION PRESSURE : 2000 Psia
 AVERAGE STAGNATION TEMPERATURE : 927.09 Deg. R.
 PROBE LOCATION : X = +1.563 In.
 FILE : BTTR2197+2198+2199

Z COORD	INDICATED	CORRECTED	STAGNATION	T/To
In.	PROBE TEMP	PROBE TEMP	TEMP	
	Deg. R	Deg. R	Deg. R	
0.440	880.72	895.04	929.94	0.9625
0.420	880.72	895.04	929.94	0.9625
0.400	880.40	894.72	929.94	0.9621
0.379	880.08	894.39	929.94	0.9618
0.360	885.18	899.57	929.26	0.9681
0.340	912.52	927.36	929.29	0.9979
0.320	999.31	1015.56	928.32	1.0940
0.300	1061.29	1078.55	926.86	1.1637
0.279	1027.36	1044.07	925.08	1.1286
0.260	1015.00	1031.50	924.76	1.1154
0.240	1010.04	1026.46	924.11	1.1108
0.220	1045.29	1062.29	923.78	1.1499
0.200	1136.53	1155.01	923.62	1.2505
0.180	1181.03	1200.23	923.30	1.2999
0.160	1189.43	1188.45	925.73	1.2838
0.140	1182.00	1180.89	926.70	1.2743
0.120	1146.49	1165.13	927.02	1.2569
0.099	1130.95	1149.34	927.35	1.2394
0.080	1113.20	1131.30	927.67	1.2195
0.060	1098.53	1116.39	928.00	1.2030
0.040	1099.16	1117.03	928.32	1.2033

REPORT TO UNIVERSAL ENERGY SYSTEMS

for research entitled

A STOCHASTIC MODEL OF FATIGUE CRACK GROWTH
DUE TO RANDOM LOADING
FOR APPLICATION TO AIRCRAFT WHEELS

By T.J. Enneking and B.F. Spencer, Jr.
Department of Civil Engineering
University of Notre Dame
Notre Dame, IN 46556

submitted to

Mr. Paul Ulrich

AFWAL/FIEMA, WPAFB, Ohio

April 27, 1989

1.0 Abstract

AFWAL/FIEMA initiated an in-house program in late 1986 to investigate experimental and analytical methods for wheel life estimation and verification. The applied loads on a wheel during a typical mission profile are by nature very random. In addition, corrosion and the effects of high temperature introduce even more uncertainty. Thus probabilistic analysis techniques are required to define the overall risk associated with a given wheel design. A detailed literature review was performed to identify current research involving aircraft wheels, fatigue studies and other key topics.

The research discussed herein focuses on developing a vectored diffusion model to account for the random nature of the loads present in a typical mission profile. A four-dimensional boundary value problem is developed which describes the distribution of the random time to reach a critical crack size. This approach will be capable of handling sequence effects and distinct overloads (e.g. landing impacts or severe turns applied to aircraft wheels). A row-by-row numerical marching solution methodology is discussed and shown to be highly effective in determining the solution for several two and three state problems in stochastic mechanics in an efficient and timely fashion. The method recognizes the specific form of the differential equation governing these problems and utilizes an efficient splitting technique to solve them. Unfortunately, although it appeared quite promising, this approach has not proven to be effective in the solution of the four-state random load fatigue crack growth problem.

Three alternative methods are being investigated for the solution of this four-state problem: Monte Carlo simulation, cell-to-cell mapping and closure methods. Monte Carlo simulation is a proven solution technique and is effective in helping understand the problem and its associated boundary conditions, however it cannot be considered as a viable solution approach due to the large amounts of computer time required for problem solution. Cell-to-cell mapping is a promising technique, used here with Monte Carlo simulation to develop a transitional probability matrix which can then be used to determine the time to reach a critical crack size given some initial parameters. Closure methods refer to the truncation of a set of stochastic differential equations to determine approximate values for lower order moments. These methods appear to be applicable to our four-state problem and will be pursued in conjunction with the cell-to-cell mapping technique in future research.

2.0 Introduction

Failure of structural components due to fatigue, especially those components associated with weight critical structures such as aircraft and space vehicles, has always been a major concern of the designers of these components. In a survey of U.S. Air Force maintenance records, cracking was reported to have the highest frequency of occurrence among corrosion, maintenance/manufacturing damage and other reported incidents. Thus fatigue crack growth is an important damage mechanism to consider when designing aircraft components. Although aircraft wheels are often overlooked as aircraft structural components, an FAA study [27] showed that more than 30% of the over 5000 operational failure reported from 1970-75 were due to wheel problems. This did not include wheels which were removed from service ahead of their expected service life due to cracks found during routine tire changes. Ground-to-tire loads are transmitted through the tire to the wheel giving rise to concentrated bending and tensile stress states. When the wheel is rotating, these cyclic stresses are superimposed on the mean stress due to tire inflation pressure and any residual stresses which are present. In addition to high impact and landing loads and significant lateral loads due to low speed turns and drift, aircraft wheels may be required to roll over 100,000 miles over the design life of an aircraft during routine taxiing, often in a highly corrosive environment.

It has become widely accepted that fatigue failure involves three stages: 1) crack initiation, 2) crack propagation and 3) fracture. An initial flaw size assumption for durability has been adopted by the Air Force [81] for fatigue design specifications. Thus the slow crack growth phase of fatigue failure is the major remaining factor to be considered in the design of fatigue critical components. The primary design method of the wheel vendors for fatigue life evaluation remains the traditional stress-life (S-N) method. However, high temperature, environmental effects, and overloads, all of which are possible occurrences in aircraft wheels, have an affect on the material, and consequently the S-N curve, which is very difficult to quantify deterministically. Load sequence effects are also neglected in these analyses. The applied loads on a wheel during a typical mission profile are by nature very random. Sharp taxi turns, uneven runway repair and landing impacts are all examples of overloads whose magnitude and time of occurrence can only be described in terms of some random measure. In addition, the random nature of wheel corrosion and consequently the time to crack initiation, or initial flaw size, introduces even more uncertainty. Thus it is evident that probabilistic analysis techniques are required to quantitatively assess this uncertainty and better define the overall risk for a given design.

The aircraft wheel life problem has been present in the aircraft industry for more than twenty five years and has been the subject of a number of other previous and ongoing studies. In order to understand this problem it is necessary to identify and understand as much of the previously published information as possible. In response to a specified logistic need, a program at AFWAL/FIEMA under the direction of Lt. David Treanor was initiated in late 1986 to investigate test and analytical methods for wheel life estimation and verification [86]. Its initial specific objective was to develop a methodology for determining representative loading spectra for military aircraft and experimental qualifications for verification of wheel life. In conjunction with this program, an additional ten-week study was initiated June 1, 1987 to explore analytical techniques for fatigue analysis and experimental methods to verify these analytical techniques [31]. In particular, the applicability and feasibility of applying fracture mechanics concepts to aircraft wheel assemblies was assessed. A detailed literature review was performed to identify current research activity involving aircraft wheels and fatigue studies. This was expanded to include finite element techniques and stochastic methods as applied to wheel life and reliability estimates along with solution algorithms. Several other key topics were identified and specifically addressed in this detailed literature review which is summarized in Table 1. Only articles pertinent to these key topics were included from the hundreds of articles identified using both traditional and computerized literature database search techniques.

A major conclusion from the ten week study was that a combined analytical and experimental program is required in order to understand the behavior of the wheel. The experimental tasks identified include fatigue tests and on-aircraft operational tests for load verification. The analytical program involves a significant effort in utilizing present analysis techniques, such as finite element modeling and linear elastic fracture mechanics, in addition to the development of the new probabilistic methods of life estimation for aircraft structures, in particular wheels, subject to random. The development of the probabilistic problem formulation and its associated solution is discussed in the following sections.

3.0 Stochastic Models for Fatigue Crack Growth

Stochastic crack propagation models and analyses have been the subject of considerable research efforts in recent years. This interest is due in part to the fact that, even in a controlled environment with a specimen subjected to simple constant amplitude cyclic loading, deterministic crack growth models fail to adequately explain the variability in the experimental results. Consider the Virkler data [88] depicted in Fig. (1). This data is from 68 identical 2.54 mm thick center cracked specimens cut from the same plate of 2024-T3 aluminum alloy. Each test was performed under identical loading, and the crack length was recorded from 9 mm to a final length of 49.8 mm. Tightly controlled laboratory conditions were present in this test, yet significant scatter is seen in the fatigue crack growth data. Thus it becomes apparent that deterministic models are inadequate for predicting the safety of a fatigue critical structure. To further complicate matters, there is usually considerable uncertainty in the applied loading.

3.1 Material Uncertainty Model

Deterministic models for fatigue crack propagation which have been suggested based upon the principles of fracture mechanics are generally of the form [59]

$$\frac{da(t)}{dt} = Q(\Delta K, K_{\max}, S, S_{op}, a, R) \quad (1)$$

where $a(t)$ is the deterministic crack size, t is time or number of cycles, Q is a non-negative function, ΔK is the stress intensity factor range, K_{\max} is the maximum stress intensity factor, S is the stress amplitude, S_{op} is the crack opening stress and R is the stress ratio. In order to account for the random nature of the crack growth, several researchers [52,53,55,80,96-99] have suggested the following model for deterministic loadings

$$\frac{dA(t)}{dt} = Q(\Delta K, K_{\max}, S, S_{op}, A, R) X(t) \quad (2)$$

where $A(t)$ is the random crack size, and $X(t)$ is ideally a non-negative random process. In this manner, random deviations in the crack growth rate are readily included. Virkler, et al. [88] conducted simulation studies and Sobczyk [77] conducted analytical studies in which the random process $X(t)$ was assumed to be uncorrelated at two different times (i.e. a white noise), whereas Yang and coworkers [96-99] have advocated that $X(t)$ be perfectly correlated or that $X(t)$ be taken as a random variable. As can be seen in Fig. (1), sample crack size paths cross, and thus dictate that $X(t)$ be a random process and not simply a random variable. Yang, et al. [98,99] indicated that if $X(t)$ is perfectly correlated, the

largest statistical dispersion of crack sizes at time t is obtained, and that an uncorrelated $X(t)$ would give the smallest dispersion of crack sizes. Experimental evidence indicates that the optimal situation for modeling fatigue crack propagation lies somewhere in between.

Lin and Yang [52,53] examined Eq. (2) and developed an analysis method which allows $X(t)$ to be a random process which is partially correlated. This is one of the first analyses in which a non-white noise random process was considered and represents a major step forward. In this work, the random crack size $A(t)$ was asserted to be nearly Markovian, and using stochastic averaging, the authors derived a Fokker-Planck-Kolmogorov equation which approximately governs the transition probability density function of crack length $A(t)$. However, $X(t)$ cannot be a non-negative random process in these methods, and thus, as pointed out by Kozin and Bogdanoff [47], there exists a finite probability of the occurrence of a physically impossible negative crack growth rate. Alternatively, in Lin, et al. [55] the Markovian assumption was removed and substituted by a Gaussian closure procedure to obtain approximate probability distributions of fatigue lives.

In a report to the Air Force, Yang, et al. [96] examined Eq. (2) and based on experimental evidence, assumed $X(t)$ to be the logarithm of an exponentially correlated stationary Gaussian random process. Excellent comparisons with experimental data were obtained via Monte Carlo simulation of this model; however analytical solutions for the distributions or statistics of the random time to reach a critical crack size were unobtainable. This report indicated that *"the white noise process is definitely not a valid model"* and that the lognormal random process *"model is demonstrated to be very flexible and it correlates excellently with all the experimental data considered"*.

Several authors have suggested alternative approaches to those mentioned above. Bogdanoff and Kozin [12] and their references contained therein presented an approach based upon Markov chain theory. The statistical dispersion in the fatigue crack growth damage accumulation is accounted for by assuming that $A(t)$ is a discrete Markov chain. However, the model is based on the crack size $A(t)$ and not the crack growth rate dA/dt as fracture mechanics theory would indicate. In addition, recent papers by Ortiz and Kiremidjian [63,64], Ditlevsen [23], and Ditlevsen and Olesen [24] have suggested that the scatter fatigue crack growth data is due to random variations across the sample of the specimens and to random process growth within a single specimen. These papers are,

however, fundamentally different. In the first two papers, the authors suggest that the random process $X(\cdot)$ in Eq. 2 be a function of a rather than t , and then they apply a combination of time series analysis techniques and concepts from linear system theory to obtain statistics of the crack growth process. This approach, however, requires a large number of replicate specimens be obtained and that the data be recorded at constant Δa intervals. The latter two papers employ an incremental analog of the Paris-Erdogan equation, and determine that under certain restrictions, the distribution of the random time to reach a given crack size asymptotically follows the inverse Gaussian distribution. The reader is directed to Palmberg, et al. [66] and Kozin and Bogdanoff [48] for further discussions of stochastic fatigue crack propagation models.

The formulation presented herein introduced by Spencer and Tang [81] augments the fatigue crack growth rate model given by Eq. (2) with an auxiliary equation in order to eliminate the possibility of a negative crack growth rate. In addition, the formulation of the boundary-value problem is consistent with physical phenomena, uses a fracture mechanics approach, implements the lognormal random process model with an exponential autocorrelation function, does not require the use of stochastic averaging, and gives the solution as a function of initial flaw size.

Consider the two-state lognormal random process model given by [81]

$$\frac{dA}{dt} = Q(A) \exp(Z) \quad (3)$$

$$\frac{dZ}{dt} = -\xi Z + \sigma_z(\xi/\pi)^{1/2} W(t) \quad (4)$$

$$A(0) = a_0, \quad Z(0) = z_0 \quad (5)$$

where A is the random crack length, ξ is the inverse of the correlation parameter for Z , Z is an auxiliary random variable, $Q(\cdot)$ is a deterministic fatigue crack growth law, σ_z is the standard deviation of Z , and $W(t)$ is a standard Gaussian white noise process. This formulation accounts for the history dependence exhibited by the data. It can be shown that the dependence of the solution on z_0 can be eliminated by utilizing the theorem of total probability and assuming stationary start conditions for $Z(t)$.

The recursive set of boundary value problems for the stochastic fatigue crack growth problem, are given by Spencer and Tang [81] as

$$-n T^{n-1} = Q(a_0) \exp(z_0) \frac{\partial T^n}{\partial a_0} - \xi z_0 \frac{\partial T^n}{\partial z_0} + \sigma_z^2 \xi \frac{\partial^2 T^n}{\partial z_0^2} \quad n=1,2,\dots \quad (6)$$

subject to

$$T^0(a_0, z_0) \equiv 1; \quad T^n(a_c, z_0) = 0 \quad \forall z_0 \quad (7a,b)$$

$$T^n(a_0, z_0) \rightarrow 0, z_0 \rightarrow \infty; \quad \frac{\partial T^n(a_0, z_0)}{\partial z_0} \rightarrow 0, z_0 \rightarrow -\infty \quad (7c,d)$$

where a_c is the critical crack length.

Solution of the boundary value problem described by Eqs. (6,7) will yield the statistical moments of the time to reach a critical crack size conditional on the initial flaw size. This problem does not appear to possess an analytical solution and is difficult to solve numerically due to the absence of the second partial derivative with respect to a_0 . A general Petrov–Galerkin weighted residual finite element solution technique has been shown to produce stable and convergent results [81]. However, a significant amount of computer time and storage is required. While this method works well for specified deterministic loadings, it fails to account for changes in loading.

3.2 Random Load Model

A new stochastic methodology for modeling of fatigue crack growth in structural components due to random and spectrum loading is developed herein. The research focuses on the development of a vectored diffusion model to account for the random nature of the loads present in actual operating environments. The load model employed will be capable of handling important sequence effects such as retardation; thus allowing the effects due to distinct overloads (e.g. landing impacts or severe turns applied to aircraft wheels) to be assessed. A large tensile load produces a plastic zone and residual compressive stresses at the crack tip which inhibit the re-opening of the crack thus retarding the crack growth. This retardation gradually dies out as the crack grows beyond the influence of the overload plastic zone. Several deterministic models have been developed which account for this

overload effect. The modeling method considered here is that introduced by Veers [87] which is based on a combination of Nelson's [61] and Willenborg's [92] models.

Consider the following Paris type law

$$\frac{dA}{dt} = C(\Delta K_{\text{eff}})^b \quad (8)$$

where ΔK_{eff} is the effective stress intensity range. In this crack growth model, sequence effects are included in the model by making the crack opening stress a function of the reset stress, and thus the magnitude of the retardation is correlated with the magnitude of the overload through the reset stress.

Consider the tensile overload S_{ol} applied when the crack has a length a_{ol} . The overload stress intensity factor is given by

$$K_{ol} = \sqrt{\pi a} Y(a) S_{ol}, \quad (9)$$

and the maximum extent of the influence of the overload can be approximated as

$$d_{ol} = \frac{K_{ol}^2}{\gamma \pi S_y^2}. \quad (10)$$

$Y(a)$ is a deterministic function of geometry and loading, γ is plane strain constraint factor, and S_y is the yield stress. We can define the reset stress S_r as the stress required to extend the influence zone past its current position

$$S_r = \frac{S_y}{Y(a)} \left(\frac{\gamma d_p}{a} \right)^{1/2} \quad (11)$$

where d_p is defined as $d_p = a_{ol} + d_{ol} - a$ (see Fig. 2). Then defining the crack opening stress as

$$S_{op} = q S_r, \quad (12)$$

the effective stress intensity range is defined as

$$\Delta K_{\text{eff}} = \begin{cases} Y(a) \sqrt{\pi a} (S - q S_r) & S > q S_r, S_{\min} < q S_r \\ Y(a) \sqrt{\pi a} (S - S_{\min}) & S > q S_r, S_{\min} \geq q S_r \\ 0 & S \leq q S_r \end{cases} \quad (13)$$

where S is the applied random stress, and S_{\min} is the effective stress minimum in a defined cycle. Substituting Eq. (13) into Eq. (8) and making the assumption that $S_{\min} < S_{op}$, we have

$$\frac{da}{dt} = C(Y(a) \sqrt{\pi a} \{S - q S_r\})^b \mu(S - q S_r) = Q(a, S_r, S) \quad (14)$$

where $\mu(\cdot)$ is the unit step function.

In order to model the crack growth as a vectored diffusion process, our governing equations must be cast into a system of first-order differential equations. Thus, taking the derivative of S_r we have

$$\frac{dS_r}{dt} = \frac{\partial S_r}{\partial a} \frac{da}{dt} + \dot{S} \mu(S - S_r) \quad (15)$$

where the first term in Eq. (15) is due to the gradual reduction in the reset stress, and the second term is due to the increase in the reset stress when the applied stress exceeds the reset stress. Substituting in the appropriate terms, Eq. (15) becomes

$$\begin{aligned} \frac{dS_r}{dt} = -\frac{S_r}{Y(a)} \left\{ \frac{dY(a)}{da} + (1/2a) \left[Y(a) + \frac{\gamma S_v^2}{Y(a) S_r^2} \right] \right\} C(Y(a) \sqrt{\pi a} \{S - qS_r\})^b \mu(S - qS_r) \\ + \dot{S} \mu(S - S_r) = G(A, S_r, S, \dot{S}) \end{aligned} \quad (16)$$

Upon examination of Eq. (16), we see that the applied stress rate must be one of the state variables. The random applied stress will be modeled as a filtered white noise. The second order filter can be either linear or nonlinear, and thus the applied stress can assume a broad range of probability distributions, correlation structures, and power spectral densities.

Repeating Eqs. (14,16) and including the filtered applied stress, we have

$$\frac{dA}{dt} = Q(A, S_r, S) \quad (17)$$

$$\frac{dS_r}{dt} = G(A, S_r, S, \dot{S}) \quad (18)$$

$$\frac{dS}{dt} = \dot{S} \quad (19)$$

$$\frac{d\dot{S}}{dt} = -H(S, \dot{S}) + W(t) \quad (20)$$

where $W(t)$ is a Gaussian white noise described by

$$E[W(t)] = 0 \quad (21a)$$

$$E[W(t) W(t+\tau)] = 2\pi I_0 \delta(\tau) \quad (21b)$$

Equations (17–20) are in the Ito form and as a result, all of the attendant theory of Markov processes becomes available to us, and a recursive set of four-dimensional boundary value problems for the statistics of the time to reach the critical crack size a_c can be derived. These boundary value problems are given by

$$\begin{aligned}
-nT^{n-1} = & Q(a_o, s_{ro}, s_o) \frac{\partial T^n}{\partial a_o} + G(a_o, s_{ro}, s_o, \dot{s}_o) \frac{\partial T^n}{\partial s_{ro}} + \dot{s}_o \frac{\partial T^n}{\partial s_o} \\
& - H(s_o, \dot{s}_o) \frac{\partial T^n}{\partial \dot{s}_o} + \pi I_o \frac{\partial^2 T^n}{\partial \dot{s}_o^2}.
\end{aligned} \quad (22)$$

where T^n is the n^{th} statistical moment of the random time to reach a_c . The initial solution and boundary conditions are given by

$$T^0(a_o, s_{ro}, s_o, \dot{s}_o) = 1 \quad \forall 0 \leq a \leq a_c; \forall s_{ro}, s_o < s_{ult}; \forall \dot{s}_o \quad (23)$$

$$T^n(a_o = a_c, s_{ro}, s_o, \dot{s}_o) = 0 \quad \forall s_{ro}, s_o < s_{ult}; \forall \dot{s}_o \quad (24)$$

$$\lim_{s_{ro} \rightarrow -\infty} \frac{\partial T^n(a_o, s_{ro} = -s_{ult}, s_o, \dot{s}_o)}{\partial s_{ro}} \rightarrow 0 \quad \forall 0 \leq a \leq a_c; \forall s_o < s_{ult}; \forall \dot{s}_o \quad (25)$$

$$T^n(a_o, s_{ro}, s_o = s_{ult}, \dot{s}_o) = 0 \quad \forall 0 \leq a \leq a_c; \forall s_{ro} < s_{ult}; \forall \dot{s}_o \quad (26)$$

$$\lim_{\dot{s}_o \rightarrow \infty} T^n(a_o, s_{ro}, s_o, \dot{s}_o) \rightarrow 0 \quad \forall 0 \leq a \leq a_c; \forall s_{ro}, s_o < s_{ult} \quad (27)$$

$$\lim_{\dot{s}_o \rightarrow -\infty} \frac{\partial T^n(a_o, s_{ro}, s_o, \dot{s}_o)}{\partial \dot{s}_o} \rightarrow 0 \quad \forall 0 \leq a \leq a_c; \forall s_{ro}, s_o < s_{ult} \quad (28)$$

Equation (22) is a four-dimensional convective-transport equation. For such problems, which have significant first partial derivatives relative to their respective second partial derivatives, solution is known to be impossible to obtain analytically and difficult to achieve numerically. It was proposed that the absence of the second partial derivative with respect to all state variables except \dot{s}_o in Eq. (22) be exploited and that a splitting technique be developed to solve this problem. This solution methodology is discussed in the following section.

4.0 Row-by-Row Numerical Marching Solution

It is well-known that the response of a system whose excitation can be approximated by a white noise is a Markov process and that the transitional probability density function is governed by the Fokker-Plank-Kolmogorov (FPK) equation [54]. Thus many problems in aerospace, civil structures, and other areas of engineering can be reduced to the solution of the two-dimensional FPK equation. A general closed form solution for this equation is however not presently available, and analytical solutions exist for only a limited number of specific cases. This has led several researchers to investigate other numerical solution techniques and simulation studies. Bhandari and Sherrer [10] utilized a Galerkin solution method where the joint probability density function was represented by a multiple series of Hermite polynomials. This method was applied successfully to weakly non-linear one and two degree of freedom systems. Wen [89] extended this method to the non-stationary case for the one degree of freedom system. A finite element solution to the FPK equation for stationary non-linear random vibration problems is presented by Langley [50] and applied to the Duffing oscillator problem and a ship rolling problem. Spencer and Tang [80] apply a general weighted residual finite element technique of the Petrov-Galerkin kind to solve a problem related to the FPK equation associated with stochastic fatigue crack growth. A major disadvantage of all of these methods is the amount of computer time and storage required for solution.

The method proposed herein recognizes the specific form of the differential equation governing these problems and utilizes an efficient splitting technique to solve them. The solution begins at a known boundary and uses a finite difference marching technique to move from row to row while the solution for each row is determined using a one-dimensional finite element or finite difference technique (see schematic in Fig. 3). It will be shown through the use of examples: a Duffing oscillator problem, a two-state stationary stochastic fatigue crack growth problem, and a three state non-stationary stochastic fatigue crack growth problem, that the use of this new solution approach produces a considerable reduction in the computer time and storage requirements without an associated loss of accuracy in the solution results. Unfortunately, although it appeared quite promising, this approach has not proven to be effective in the solution of the four state fatigue crack growth under random loading problems.

4.1 Solution Development

A two-state random vector Y is exactly Markovian for any system whose governing equations are of the form [54]

$$\dot{Y} = \begin{bmatrix} g_1(Y) \\ g_2(Y) \end{bmatrix} + \begin{bmatrix} 0 \\ \sqrt{s} \end{bmatrix} W(t) \quad (29)$$

where g_1, g_2 are general functions of the state vector Y , s is a constant, t is time, and $W(t)$ is a Gaussian white noise with zero mean and constant two-sided spectral density of magnitude one. For vectored Markov processes, the state transition probability density function $f = f(y, t | y_0, t_0)$ is governed by the Fokker-Planck-Kolmogorov (FPK) equation which for Eq. (29) reads

$$\frac{\partial f(y_1, y_2, t | y_{10}, y_{20}, t_0)}{\partial t} = - \frac{\partial}{\partial y_1} \left[g_1(y_1, y_2, t) f \right] - \frac{\partial}{\partial y_2} \left[g_2(y_1, y_2, t) f \right] + \pi \left[\frac{\partial^2}{\partial y_2^2} (s f) \right] \quad (30)$$

Here, the state transition probability density function $f(y_1, y_2, t | y_{10}, y_{20}, t_0)$ is the joint probability density function for the vectored random process $\begin{bmatrix} Y_1 \\ Y_2 \end{bmatrix}$ under the condition that $Y_1 = y_{10}$ and $Y_2 = y_{20}$ at time t_0 . Setting the left hand side of Eq. (30) equal to zero yields the stationary form of the FPK equation to be solved herein. This equation will also be utilized in the numerical example section to develop the specific partial differential equation governing the response of the Duffing oscillator.

The formal adjoint of the FPK equation, the backward Kolmogorov equation, is given in terms of the backward coordinates y_{10} and y_{20} by

$$\frac{\partial f(y_1, y_2, t | y_{10}, y_{20}, t_0)}{\partial t} = g_1(y_{10}, y_{20}, t_0) \frac{\partial f}{\partial y_{10}} + g_2(y_{10}, y_{20}, t_0) \frac{\partial f}{\partial y_{20}} + \pi s \frac{\partial^2 f}{\partial y_{20}^2} \quad (31)$$

A related problem in this class is the solution of the Pontriagin-Vitt equation which can be derived from Eq. (31) [80]. This is a recursive set of equations given by

$$-n T^{n-1} = g_1(y_{10}, y_{20}, t_0) \frac{\partial T^n}{\partial y_{10}} + g_2(y_{10}, y_{20}, t_0) \frac{\partial T^n}{\partial y_{20}} + \pi s \frac{\partial^2 T^n}{\partial y_{20}^2} \quad n=1, 2, \dots \quad (32)$$

which governs the statistical moments of the time to first passage of a response process. In particular, the solutions for this equation for the stochastic fatigue crack growth numerical example are the moments of the time required to reach a critical crack size.

Upon examining Eqs. (30–32), we see that due to the excitation in Eq. (29) being single source, i.e. directly influencing only Y_2 , there is only one second derivative in these equations. This specific nature of the governing equations will be exploited to obtain efficient numerical solutions. Equation (32) and the stationary form of Eqs. (30,31) can be represented by a partial differential equation of the following form

$$B \frac{\partial^2 f}{\partial y_2^2} + C \frac{\partial f}{\partial y_2} + D f + E = F \frac{\partial f}{\partial y_1} \quad (33)$$

subject to certain problem specific boundary conditions. The coefficients B through F may be functions of y_1 and/or y_2 . This equation is rewritten and discretized in the y_1 -direction using a variable weighted finite difference approach with weighting parameter θ as

$$\frac{f^{y_1+1} - f^{y_1}}{\Delta y_1} - \frac{B}{F} \frac{\partial^2 f^{y_1+\theta}}{\partial y_2^2} - \frac{C}{F} \frac{\partial f^{y_1+\theta}}{\partial y_2} - \frac{D}{F} f^{y_1+\theta} = \frac{E}{F} \quad (34)$$

where f^{y_1} is the state transition density function at row y_1 , Δy_1 is discretized interval width, and $y_1+1 \equiv y_1 + \Delta y_1$. Thus by using a variable weighted finite difference scheme, the terms in Eq. (33) are approximated as some weighted averages over the Δy_1 interval as opposed to being approximated entirely at the y_1+1 or y_1 point. The choice of $\theta = .5$ yields the well known Crank–Nicolson scheme. It can be shown that this method will be stable for values of $\theta \geq .5$. Stability when $\theta < .5$ is dependent on the value chosen for Δy_1 . A value of $\theta = .5$ was used in this study to minimize the truncation error in the finite difference approximation. A smooth solution was obtained when using this θ value. Then expressing $f^{y_1+\theta}$ as the weighted average $\theta f^{y_1+1} + (1-\theta)f^{y_1}$, Eq. (34) can be written as

$$(f^{y_1+1} - f^{y_1}) - \frac{\Delta y_1 B}{F} \left[\theta \frac{\partial^2 f^{y_1+1}}{\partial y_2^2} + (1-\theta) \frac{\partial^2 f^{y_1}}{\partial y_2^2} \right] -$$

$$\frac{\Delta y_1 C}{F} \left[\theta \frac{\partial f^{y_1+1}}{\partial y_2} + (1-\theta) \frac{\partial f^{y_1}}{\partial y_2} \right] - \frac{\Delta y_1 D}{F} \left[\theta f^{y_1+1} + (1-\theta) f^{y_1} \right] = \frac{\Delta y_1 E}{F} \quad (35)$$

We simplify Eq. (35) by combining like terms and moving all terms dependent only on the solution for the row at the previous y_1 location to the right hand side of the equation. The resulting second order differential equation for each row in the y_2 -direction at a specific y_1 location can then be expressed as

$$\frac{\partial^2 \delta f}{\partial y_2^2} + \frac{C}{B} \frac{\partial \delta f}{\partial y_2} + \frac{D\Delta y_1 - F/\theta}{\Delta y_1 B} \delta f = \frac{-1}{\theta} \left[\frac{\partial^2 f^{y_1}}{\partial y_2^2} + \frac{C}{B} \frac{\partial f^{y_1}}{\partial y_2} + \frac{D}{B} f^{y_1} + \frac{E}{B} \right] \quad (36a)$$

where

$$\delta f = f^{y_1+1} - f^{y_1} \quad (36b)$$

Notice that this equation is similar in form to a standard one-dimensional convection diffusion equation with the addition of a linear term and a non-zero right hand side which is dependent only on the solution for the row at the previous y_1 location. The governing differential equation given in Eq. (36) can be cast into the weak form using arbitrary weighting functions, W_i , defined to be zero on the boundaries. In this simple one-dimensional finite element case, integration by parts is used to eliminate the second derivative terms so that linear interpolation functions, N_n , can be readily applied. Linear functions are also used for the weighting functions. Thus the weak form can be expressed as follows

$$\begin{aligned} \int_{-\infty}^{\infty} W_i \left[\frac{\partial^2 \delta f}{\partial y_2^2} + \frac{C}{B} \frac{\partial \delta f}{\partial y_2} + \frac{D\Delta y_1 - F/\theta}{\Delta y_1 B} \delta f \right] dy_2 = \\ \frac{-1}{\theta} \int_{-\infty}^{\infty} W_i \left[\frac{\partial^2 f^{y_1}}{\partial y_2^2} + \frac{C}{B} \frac{\partial f^{y_1}}{\partial y_2} + \frac{D}{B} f^{y_1} + \frac{E}{B} \right] dy_2 \end{aligned} \quad (37)$$

or, after partial integration,

$$\begin{aligned}
& - \int_{-\infty}^{\infty} \left[\frac{\partial W_i}{\partial y_2} \frac{\partial \delta f}{\partial y_2} - \frac{W_i C}{B} \frac{\partial \delta f}{\partial y_2} - \frac{W_i (D \Delta y_1 - F/\theta) \delta f}{\Delta y_1 B} \right] dy_2 + W_i \frac{\partial \delta f}{\partial y_2} \Big|_{-\infty}^{\infty} = \\
& \frac{-1}{\theta} \left\{ \int_{-\infty}^{\infty} \left[- \frac{\partial W_i}{\partial y_2} \frac{\partial f}{\partial y_2} y_1 + \frac{W_i C}{B} \frac{\partial f}{\partial y_2} y_1 + \frac{W_i D}{B} f y_1 + \frac{W_i E}{B} \right] dy_2 + W_i \frac{\partial f}{\partial y_2} y_1 \Big|_{-\infty}^{\infty} \right\} \quad (38)
\end{aligned}$$

Note that the boundary terms in Eq. (38) are equal to zero due to the zero boundary conditions and the generally accepted practice of selecting weighting functions which are zero on the boundaries. Discretizing in space by letting $f = \sum N_n(y_2) f_n$, Eq. (38) is rewritten as

$$\begin{aligned}
& \sum \left\{ \int_{-\infty}^{\infty} \left[\frac{\partial W_i}{\partial y_2} \frac{\partial N_n}{\partial y_2} - \frac{W_i C}{B} \frac{\partial N_n}{\partial y_2} - \frac{W_i (D \Delta y_1 - F/\theta) N_n}{\Delta y_1 B} \right] dy_2 \right\} \delta f_n = \\
& \sum \frac{1}{\theta} \left\{ \int_{-\infty}^{\infty} \frac{W_i E}{B} dy_2 + \int_{-\infty}^{\infty} \left[- \frac{\partial W_i}{\partial y_2} \frac{\partial N_n}{\partial y_2} + \frac{W_i C}{B} \frac{\partial N_n}{\partial y_2} + \frac{W_i D N_n}{B} \right] dy_2 f_n y_1 \right\} \quad (39)
\end{aligned}$$

After transforming to the isoparametric coordinate, η , Eq. (39) can be expressed in matrix form as

$$[K_d - K_c - K_l] \{\delta f\} = \{P\} + \frac{1}{\theta} [-K_d + K_c + R H_1] \{f^{y_1}\} \quad (40)$$

where

$$[K_d] = \int_{-1}^1 [W']^T [N'] |J| d\eta \quad (41a)$$

$$[K_c] = \int_{-1}^1 \frac{C}{B} [W]^T [N'] |J| d\eta \quad (41b)$$

$$[K_I] = \int_{-1}^1 \frac{D\Delta y_1 - F/\theta}{\Delta y_1 B} [W]^T [N] |J| d\eta \quad (41c)$$

$$[RH_I] = \int_{-1}^1 \frac{D}{B} [W]^T [N] |J| d\eta \quad (41d)$$

$$[P] = \int_{-1}^1 \frac{E}{\theta B} [W]^T |J| d\eta \quad (41e)$$

Since the coefficients B through F may be functions of y_1 and y_2 , one should use $y_1 = \theta y_1^{y_1+1} + (1-\theta)y_1^{y_1}$ and $y_2 = \sum N_n(y_2) y_{2n}$ to represent y_1 and y_2 in these functions as required. $[W]$ and $[N]$ are column matrices which contain the weight and shape functions. $[W']$ and $[N']$ represent matrices of the derivatives with respect to y_2 of the weighting and shape functions respectively. $|J|$ is the determinant of the Jacobian matrix; half the element length in this one-dimensional case.

Before Eq. (40) can be solved using this one-dimensional finite element approach however, the boundary conditions must be addressed. The approach employed herein is problem specific and will be discussed in the solution application section. The solution of the matrix equation given in Eq. (40) is efficiently determined due to its tri-diagonal nature, using standard matrix solution techniques, such as, the Thomas algorithm [22].

4.2 Solution Application

Example problems will be addressed in this section to show the versatility and accuracy of this numerical technique and the corresponding reduction in the required computer time and storage. First the stationary response of the Duffing oscillator is studied. Current results for this problem are compared to those presented previously by Bhandari and Sherrer [10], Langley [50] and to the exact analytical solution. In the second example, results for the stationary two-dimensional stochastic fatigue crack growth problem, as formulated by Spencer and Tang [80], are compared to experimental results and the numerical results previously reported by Spencer, et al. [81]. A time and storage comparison is also presented for this example. Three dimensional non-stationary fatigue

crack growth results in the last successfully solved example are compared to the experimental data also previously reported by Tang and Spencer, et al. [81].

4.2.1 Non-Linear Duffing Oscillator

The equation of motion for the random vibration of a Duffing oscillator is

$$X + 2\beta\omega X + \omega^2(1+\gamma X^2)X = G(t) \quad (42)$$

where $G(t)$ is the forcing function, taken here to be a Gaussian white noise having a spectral density of $1/\pi$, ω is the natural frequency of the system, β is a damping coefficient and γ a non-linearity factor. Letting $Y_1 = X$ and $Y_2 = \dot{X}$, we have

$$Y_1 = Y_2 \quad (43a)$$

$$Y_2 = -2\beta\omega Y_2 - \omega^2(Y_1 + \gamma Y_1^3) + W(t)/(\pi)^{1/2} \quad (43b)$$

which, using Eqs. (29,30), leads to the stationary FPK equation [50] as

$$\frac{\partial}{\partial y_1} (y_2 f) - \frac{\partial}{\partial y_2} [2\beta\omega y_2 f + \omega^2(y_1 + \gamma y_1^3) f] - \frac{\partial^2 f}{\partial y_2^2} = 0 \quad (44)$$

where f is the stationary joint probability density function of the system response. After differentiation and simplification, Eq. (44) can be rewritten as

$$\frac{\partial^2 f}{\partial y_2^2} + (2\beta\omega y_2 + \omega^2 y_1 + \omega^2 \gamma y_1^3) \frac{\partial f}{\partial y_2} + 2\beta\omega f = y_2 \frac{\partial f}{\partial y_1} \quad (45)$$

This equation has an exact analytical solution given as

$$f(y_1, y_2) = k \exp \left[-\beta\omega (y_2^2 + \omega^2 y_1^2 + \frac{1}{2} \gamma \omega^2 y_1^4) \right] \quad (46)$$

where k is chosen to satisfy the normalization condition that the volume under the density function must equal one. This exact solution will be compared to the results using the proposed numerical approach.

Using the notation from Eq. (33) in the numerical solution description, the coefficients B through F for this example problem can be expressed as

$$B = 1; \quad C = 2\beta\omega y_2 + \omega^2 y_1 + \omega^2 \gamma y_1^3; \quad D = 2\beta\omega; \quad E = 0; \quad F = y_2.$$

The associated boundary conditions for this problem are

$$f = 0 \text{ at } y_1 = \infty \quad (47a)$$

$$f = 0 \text{ at } y_2 = \infty \quad (47b)$$

Moreover, due to the symmetry in the solution, we need to solve only one fourth of the problem domain. This results in the symmetry conditions

$$\frac{\partial f}{\partial y_2} = 0 \text{ at } y_2 = 0 \quad (48a)$$

$$\frac{\partial f}{\partial y_1} = 0 \text{ at } y_1 = 0 \quad (48b)$$

Due to the fact that the coefficient E is zero, the trivial zero solution state is determined if the solution is started at the known zero solution boundary at $y_1 = \infty$. Thus we will use the symmetry conditions in the numerical algorithm. Due to the statistical independence of displacement and velocity processes, we can first solve the $y_1 = 0$ row subject to the symmetry conditions, Eqs. (48a,b). That is, solve the partial differential equation

$$\frac{\partial^2 f}{\partial y_2^2} + 2\beta\omega (y_2 \frac{\partial f}{\partial y_2} + f) = 0 \quad (49)$$

using as boundary conditions for this row only

$$f = K \text{ at } y_1 = 0, y_2 = 0 \quad (50a)$$

and

$$f = 0 \text{ at } y_1 = 0, y_2 = \infty \quad (50b)$$

Then use this solution as the starting row, return to the original equation and march in the positive y_1 direction to determine f . The approach employed herein to account for the infinite boundary conditions is to place the boundary at a sufficiently large, but finite,

distance from the domain of interest so that the solution is not affected. This method has been shown to be effective for problems of this type [78].

Results for comparison to the exact solution and previous studies were generated using $\omega = 1$, $\beta = .5$ and $\gamma = .5$. These are shown in Table 2 along with the exact solution, results presented by Bhandari and Sherrer [10], and those reported by Langley [50]. Excellent comparisons are seen between the proposed solution method and the previously reported results with the maximum deviation from the exact solution being 0.001. Fig. (4) is a surface plot of a quarter section of the solution surface for this case. Figs. (5–8) are results for various values of β and γ (damping and non-linearity) plotted over the exact solution curves. In all cases, excellent comparison is again shown. Solutions were obtained quickly on a personal computer and as will be shown in the time and storage comparison of the following two-state stochastic fatigue crack growth example, significantly faster than previously used two-dimensional finite element approaches. As discussed above, this is due to the row by row solution technique proposed herein which results in a stiffness matrix of tri-diagonal form. A matrix of this form can be quickly and easily solved and requires only a row of storage rather than the entire finite element mesh.

4.2.2 Two-State Stochastic Fatigue Crack Growth

The solution of the first ordinary moment of the random time to reach the critical crack size will be investigated herein, however higher moments can be obtained in a similar fashion. Setting $n = 1$ in Eq. (6), the governing differential equation for the first ordinary moment boundary value problem becomes

$$-1 = Q(a_0) \exp(z_0) \frac{\partial T^1}{\partial a_0} - \xi z_0 \frac{\partial T^1}{\partial z_0} + \sigma_z^2 \xi \frac{\partial^2 T^1}{\partial z_0^2} \quad (51)$$

Again, using the notation from Eq. (33), the coefficients B through F are

$$B = \sigma_z^2 \xi; \quad C = -\xi z_0; \quad D = 0; \quad E = 1; \quad F = -H(a_0) \exp(z_0).$$

In order to create a problem with positive diffusion, which will ensure numerical stability, the solution must be obtained by marching backwards from a_c to a_0 . Note that this backwards marching scheme requires a coordinate transformation from a_0 to a_t where

$$a_t = a_c - a_0 \quad (52a)$$

$$\Delta a_t = -\Delta a_0 \quad (52b)$$

a_t is the transformed variable representing crack length. The solution process begins at the known zero boundary value when the initial crack length equals the critical crack length, $a_0 = a_c$, and uses the finite difference marching technique to move backwards in a to the minimum value considered. The solution in the z_0 direction for each row in a_0 is determined using a finite element approach. Contrary to the Duffing oscillator problem, this problem must be solved over its entire domain due to the lack of symmetry in the solution. As in the previous example, the boundary is placed at a distance sufficiently removed from the domain of interest so that the solution is not affected.

The results from the solution of the two-state stochastic fatigue crack growth problem using the proposed method were compared to the results presented by Spencer, et al. [81]. The Virkler fatigue crack growth data, shown in Fig. (1), was used in this comparison study.

Fatigue crack growth under constant amplitude loading is a function of the elastic stress intensity range given for a finite width plate as

$$\Delta K = \Delta S \sqrt{\pi a / \cos(\pi a / b)} \quad (53)$$

where b is the width of the plate, 152.4 mm in the Virkler study. A cubic polynomial fatigue crack growth law of the following form was used [62]

$$Q(a) = \exp[L_1 + L_2 \log \Delta K + L_3 (\log \Delta K)^2 + L_4 (\log \Delta K)^3]. \quad (54)$$

Values for the L parameters, the standard deviation of Z , and the correlation parameter were chosen to be consistent with the previous study [81] as: $L_1 = -74.087$, $L_2 = 60.276$, $L_3 = 21.39$, $L_4 = 2.6348$, $\sigma_z = .22732$, and $\xi = 9E-5$.

Deviation from the finite element results presented by Spencer, et al. [81] for the moments of the random time to reach the critical crack size is less than 1% for the same mesh size. Fig. (9) shows the solution for the first ordinary moment of the time to reach a critical crack size of $a_c = 49.8$ mm starting from an initial value of a_0 . Note that the

solution surface is smooth and, as expected, as the initial flaw size decreases, the time to reach the critical crack size increases, and as the initial flaw size approaches the critical crack size, the solution decreases to zero. In addition, note that the boundary conditions prescribed for z_0 at plus and minus infinity are well represented on this finite domain (-4 to 6). Fig. (10) compares results from this numerical solution with the experimental data. In this figure, it can be seen that the numerical solution results plot directly over the experimental data for the mean time to reach a_c even for small values of a_0 .

Time and storage comparison studies were performed using an IBM 9375 computer at the University of Notre Dame. Identical mesh sizes were used. Required computer time and storage are shown in Table 3. As can be seen, both the required storage and processing time are significantly reduced by the use of the proposed solution technique. Problem solution was obtained over 30 times faster through the use of the new numerical solution technique. Additionally, 50 times less storage is required due to the row by row solution marching scheme. In other words, only 3% of the processing time and 2% of the storage required by the previously used solution method is required when using this new numerical solution technique.

4.2.3 Three-State Non-Stationary Fatigue Crack Growth

Although the calculation of the statistical moments are of interest, the solution of the distribution is the most desirable result since it contains a complete description of the random variable. The mean, variance and skewness can all be derived from this distribution function.

A unique feature of the proposed two-state Markov process model is that a well-posed initial-boundary value problem can be formulated for the distribution function. Denoting the probability that the crack size is less than the critical crack size, conditional on the initial flaw size, as $R = R(t|a_0, z_0; 0 \leq a_0 < a_c)$, the backward Kolmogorov equation for R is given by [80].

$$\frac{\partial R}{\partial t} = Q(a_0)F_x^{-1}(\Phi(z_0)) \frac{\partial R}{\partial a_0} - \zeta z_0 \frac{\partial R}{\partial z_0} + \pi S_0 \frac{\partial^2 R}{\partial z_0^2} \quad (55)$$

The initial and boundary conditions are stated on physical grounds and given as follows

$$R(0|a_0, z_0) = 1 \quad 0 \leq a_0 < a_c \quad (56a)$$

$$R(t|a_c, z_0) = 0 \quad \text{for all } z_0 \quad (56b)$$

$$R(t|a_0, z_0) = 0 \quad z_0 \rightarrow \infty \quad (56c)$$

$$\frac{\partial R(t|a_0, z_0)}{\partial z_0} \rightarrow 0 \quad z_0 \rightarrow \infty \quad (56d)$$

The solution to all these problems is a function of z_0 , and as in the previous work [80,81] we average over z_0 using the fact that $Z(t)$ is a Gaussian random process.

Validation of a model using data is one of the most important steps in modeling. However, for the fatigue crack growth problem, not many reliable data sets are available. Perhaps the most widely used data set is the Virkler data [88]. Another recently published data set is the Ghonem and Dore data [37] in which results for three different stress levels are reported. Both of those sets of data will be employed herein to validate the model and solution procedure.

We will use two fatigue crack growth laws to study the Virkler data, the simplest one is the Paris law, which is randomized to give:

$$\frac{dA(t)}{dt} = C(\Delta K)^m X(t) \quad (57)$$

In order to find C and m , the ordinary least square method could be used. However, this method will produce bias in the parameters because of the numerical differentiation of the discrete data set a vs. t . Reference [65] gives a detailed analysis of this problem and a finite integral method which was introduced to eliminate the bias. The method is for deterministic crack growth laws and must be modified to account for the random nature of the crack growth process. The modified finite integral method does not need to differentiate the data in order to determine model parameters. It uses finite integration, and in doing so, the original data set can be used directly. Here, Eq. (57) is separated, integrated, and averaged to obtain,

$$\int_{a_0}^{a_i} \frac{dA}{C(\Delta K)^m} = E \left(\int_0^{T_{ri}} X(t) dt \right) = u_x E(T_{ri}) \quad (58)$$

where a_i is specified. Eq. (58) is numerically integrated through finite crack length levels, and the sum of square error (SSQ) is defined as

$$SSQ = \sum_{i=1}^N (E(T_{ai}) - E(T_{ri}))^2 \quad (59)$$

where $E(T_{ai})$ is the mean cumulative cycle count from the data and $E(T_{ri})$ is the value obtained from Eq. (58).

In order to obtain unbiased estimates of the parameters, we use 51 constant Δa increments for each sample in the Virkler data and there are 68 samples; thus N is equal to 51×68 here. The optimum C , m and μ_x will give the least SSQ, and it is found that $C = 6.3258E-11$, $m = 3.000$ and $\mu_x = 1$. It should be noted that setting $\mu_x = 1$ is consistent with the work by Ditlevsen [23]. For the model given by Eq. (55,56), we also need to estimate ζ and σ_x . ζ is chosen to be equal to $9.c-5$ as in reference [8] where σ_x can be calculated as follows. Let $da/dt = Q(A)X(t)$. Then we write $X(t) = [da/dt]/Q(A)$, and thus the variance can be given by

$$\text{Var}(X) = \frac{1}{N-2} \sum_{i=1}^N \left(\frac{(da/dt)_i}{Q(a_i)} - 1 \right)^2 \quad (60)$$

However we found that $\text{Var}(X)$ is too large via this equation. This is due to the fact that a few $(da/dt)_i$ data are unreasonably large. As we know, the majority of $X_i = (da/dt)_i/Q(a_i)$ should be within the range of a few standard deviations away from $\mu_x = 1$. Unreasonably large X_i could be considered as outliers [4] which should not be included in the statistical analysis. In this way, we find the variance is more reasonable. If we consider those $X > 2$ (approximately 4 standard deviations from the mean) as outliers, we will find 44 out of 11084 to be outliers, and $\sigma_x = 0.2405$ using Eq. (60) excluding the outliers. If we include the outliers, $\sigma_x = 0.2959$. $\text{Var}(X)$ can also be approximated by $\text{Var}(\log(x))$ for small $\text{Var}(X)$ [19], and we found $\text{Var}(\log(X)) = (0.24)^2$, which is very close to $\text{Var}(X)$ by the above calculation excluding the outliers.

The marginal distribution of X is also an unknown in the modeling of fatigue crack growth. However, because of the versatility of the two-state Markov process model, any reasonable probability distribution function can be considered. We consider X to be lognormal, normal and Weibull distributed. It turns out that the mean and variance of the random time to reach a critical crack size does not change much for different distribution assumptions. The skewness coefficient, however, does become larger using the normal and Weibull distribution assumptions. Here the skewness coefficient is defined as skewness divided by the cube of the standard deviation. Nevertheless, the normal assumption has

the drawback of allowing the possibility of negative crack growth rates. Fortunately, for the Virkler data σ_x is about 0.25, which means the negative crack growth rates are 4 standard deviations away from the mean crack growth rate. The Weibull distribution assumption will give similar results to the normal assumption.

The solution results for Eqs. (55,56) are given in Figs. (11) and (12). In Fig. (11), the initial crack size is held constant, and the distribution of times to reach several critical crack sizes is given. The marching solution results are to the left of the data when the critical crack size $a_c = 13$ mm. In Fig. (12), the critical crack size is held constant, and the initial crack size is varied. It can be seen that for the initial crack size $a_0 = 13$ mm, the marching solution results are to the right of the data. This is due to the inability of the Paris law to model the nonlinear behavior in the $\log(da/dt)$ vs. $\log(\Delta K)$ data as depicted in Fig. (13). The Paris law, however, necessarily implies that there exist a linear relationship between $\log(da/dt)$ and $\log(\Delta K)$. The results can be improved by using a more suitable crack growth law.

A recently proposed fatigue crack growth law which accounts for the nonlinear nature of the phenomena, the cubic law [63], will be considered here. This law takes the form

$$\log(da/dt) = b_0 + b_1 \log(\Delta K) + b_2 (\log(\Delta K))^2 + b_3 (\log(\Delta K))^3 \quad (61)$$

The modified finite integral method described above was used to find

$$b_0 = -74.060 \quad b_1 = 60.275 \quad b_2 = -21.390 \quad b_3 = 2.6348 \quad \mu_x = 1.$$

And as before, $\zeta = 9E-5$. Similarly, $\sigma_x = .227$ using the method described above.

Figs. (14) and (15) show the solutions corresponding to Figs. (13) and (14), respectively, by the marching solution method using the cubic law. We will notice improved results, particular when there are small initial flaws. In Fig. (14), the numerical solution results fit the data very well, and no bias is observed. This indicates that the cubic law has corrected the systematic error introduced by the Paris law. In Fig. (15), we also find that the numerical solution results fit the data very well, thus showing that the model is capable of describing the fatigue crack growth phenomenon for different initial crack length as well as different critical crack length.

These results are all based on the lognormal assumption for the random process $X(t)$. To see the effect of different assumptions for the marginal distribution of $X(t)$ on the distributions of the time to reach the critical crack size, we superimpose the results using a lognormal, normal and Weibull distribution assumption on the same figure (see Fig. 16) without the results from data. There is little difference in the solution for these three assumptions except for a very small difference in the tails of the probability distributions. Here, the results from the Weibull and normal distribution assumptions lie on top of each other, and are always slightly to the right of the results assuming X to be lognormally distributed. However, the difference is so small that, practically, we can ignore it.

The Ghonem and Dore Data was developed from tests conducted on aluminum 7075-T6 alloy, (the material is a different alloy from that in the Virkler data, so no direct comparison will be made). Three sets of data are collected at three different stress levels, each with 60 replicate specimens of rectangular shape with length of 320 mm, width of 101 mm and thickness of 3.175 mm [37]. A photographic technique was used to determine the crack length with an acceptable resolution. Data was recorded from a length of 9 mm to a length of 23 mm and are depicted in Figs. (17a-c). Here, we should note that the loading conditions for these tests are quite different. This will introduce additional difficulty in modeling. In Fig. (17a), the load range for test I is given by $\Delta P = 9.11$ KN, the maximum load is $P_{\max} = 22.79$ KN, and the stress ratio $R = 0.6$. Figure (17b) depicts test II in which $\Delta P = 11.12$ KN, $P_{\max} = 22.25$ KN, and $R = 0.5$, while in Fig. (17c), $\Delta P = 9.11$ KN, $P_{\max} = 15.19$ KN, and $R = 0.4$ for test III. We see that for test III the data has larger variation than that of in Figs. (17a) or (17b). This could be due to the fact that P_{\max} in test III is much smaller than that of test I or II.

The modified finite integral method discussed in the last section will be utilized to determine the parameters in several different fatigue crack growth laws. Four fatigue crack growth laws listed in reference [62], in addition to the cubic law, will be considered to account for the effect of stress ratio in fatigue crack growth. The crack closure concept is utilized herein which a function U , first introduced by Elber [29], is used to modify the randomized Paris and cubic laws to account for the crack closure phenomenon. Schijve [24] considered several materials and suggested the following formulas for U ,

2219-T851,	$U = 0.68 + 0.191R$
Ti-6al-4V,	$U = 0.73 + 0.82R$

7175-T651,	$U = 0.4 + 0.4R$
2024-T3,	$U = 0.55 + 0.33R + 0.12R^2$
mild steel I,	$U = 0.69 + 0.4R$
mild steel II,	$U = 1/(1.5 - R)$
7475-T73,	$U = 0.618 + 0.365R + 0.139R^2$

The form of U employed herein is $U = a_1R^2 + a_2R + a_3$.

The parameters obtained using the modified finite integral method are tabulated in Table 4. We can see that the modified cubic law gives the smallest SSQ, and thus it will be used in the remainder of the paper.

The other parameters can be found in the same way as in the previous section. As usual, $\zeta = 9E-5$, $\mu_x = 1$, and we found that $\sigma_x = 0.3800$. Here, we use one set of parameters for the fatigue crack growth model to describe all three sets of test results. The resulting model can then be used to predict the fatigue crack growth for different stress ratios.

The marching method solution results for the mean, standard deviation and the skewness coefficient of the random time to reach a critical crack size for the Ghonem and Dore data are shown in Fig. (18). As can be seen, the results are not as satisfactory as in the case of the Virkler data discussed in the previous section. Although Test I and II are acceptable, the error associated with Test III is quite large. Ghonem and Dore [37] utilized a different set of parameters for each of these three tests. Thus, it appears difficult to use their model as a prediction tool.

As indicated previously, the loading conditions are quite different for test III. In test III, P_{\max} 15.19 KN whereas in test I and II, P_{\max} is about 22 KN. Here, P_{\max} was not directly taken into account in the formulation of our model. Preliminary work indicates that considering ζ or σ_x as function of the maximum stress may have promise, but sufficient experimental data is presently not available to investigate this in greater depth.

In Fig. (19) the numerical solution results for the initial crack size $a_0 = 9$ mm, $a_c = 15$ mm for test I, II and III are given. Again, we can see that for test I and II, the results fit the data very well. For test II, the upper tail deviates somewhat from the data.

In Fig. (20) the numerical solution results for the initial crack size $a_0 = 15$ mm, $a_c = 22$ mm for test I, II and III are given. Here, we also see that the results fit the data very well. Small differences in the tails of the distribution function for test I can now be seen. For test III, some deviation can be observed in the upper tail, but in the toes, where the design is usually carried out, the finite difference solutions fit the data quite well. More research is needed, particularly on the influence of the maximum stress on the stochastic fatigue crack growth problem.

4.2.4 Four-State Fatigue Crack Growth Due to Random Loading

The stochastic model for fatigue crack growth which accounts for both material uncertainty and random loading was presented in Section 3.2. The resulting recursive set of four-dimensional boundary value problems for the statistics of the time to reach a critical crack size a_c is shown in Eq. (22-28). This convective-transport type equation is quite difficult to solve and the row-by-row numerical marching solution methodology discussed in the previous section was developed in an attempt to efficiently solve this set of problems. Unfortunately this method has proven to be unstable and thus ineffective in the solution of this four-state fatigue crack growth problem. Although we have not investigated in detail the cause of this instability, we feel it is related to the nature of Eqs. (19) and (20). These equations, with the application of appropriate boundary conditions, describe the first passage problem for a two-state system. We did attempt to solve this problem also in our efforts to develop an efficient yet robust solution algorithm. However, due to the offset nature of the boundary conditions in this first passage problem, the solution does not lend itself to a marching solution approach. Other numerical manipulations could be attempted here to stabilize the problem solution, eg. variable step sizes, upwind finite element techniques, however these would detract from the simplicity of this solution approach. Thus, we felt that alternative solution methods should be explored. Several methods were identified and will be discussed in the following sections. The most promising of these, a generalized cell mapping method, is currently being investigated in further detail.

5.0 Alternative Solution Methods

Several solution methods were identified and included in a preliminary study. These are as follows:

- 1) Monte Carlo Simulation: Although simulation can be used the results are computationally intensive and extensive parametric studies are required to generalize a solution. Veers [87] utilizes simulation in his studies, Spencer and Tang [80] compare their two-state fatigue crack growth model finite element results with simulation and we have simulated this four-state problem in order to better understand the boundary conditions but not to the extent required for a complete problem solution. Based on these preliminary results for a typical problem, approximately 3 hrs. of computer time are required for one sample and one set of initial conditions. Hundreds of samples and several sets of initial conditions are required to fully understand the complete solution. Thus, simulation can be used on a limited basis only and cannot be considered as a viable solution alternative.
- 2) Marching of a higher dimensional Finite Element Approach: This was considered as a natural extension of the row-by-row marching solution algorithm. However, large amounts of computer time and storage would again be required. Additionally, solution instabilities similar to those expressed by the row-by-row marching method are possible. Thus this approach was not pursued in any greater detail.
- 3) Generalized Cell-to-Cell Mapping: A cell-to-cell mapping theory for both non-linear deterministic and stochastic systems was introduced and discussed in detail by Hsu and Hsu et. al. [39-43]. These theories of both simple and generalized cell-to-cell mapping have been applied in the fields of nonlinear mediums, stochastic mechanics and optimal control [41]. Of particular significance to our study of the four-state fatigue crack growth problem which accounts for random loading is the application of a generalized cell mapping method to the solution of the first passage time probability for linear and non-linear dynamical systems by Sun and Hsu [83]. In this approach a one step transitional probability for a one-state problem transition from cell i to cell j is determined using simulation. This approach is quite similar to that which has been extensively applied to the stochastic fatigue crack growth problem by Kozin and Bogdanoff [47,48] referred to as the B model. These results lead us to select this approach for further immediate study and application to our four-state problem.
- 4) Closure Methods: The term closure here refers to the truncation of a set of stochastic differential equations in order to determine approximate values for lower order moments. The simplest closure scheme is the Gaussian closure scheme where higher moments are expressed in terms of the first and second moments as if they were Gaussian.

This approximation is sometimes referred to as linearization [94]. The non-Gaussian closure technique utilizes some non-Gaussian probability distribution assumption to approximate the higher order moments [82]. Second and fourth order cumulant neglect closure methods were applied to non-linear oscillators by Wu and Lui [94]. These closure methods seem to hold great promise for a solution to our four-state problem however it is felt that at this time the previously addressed generalized cell-to-cell mapping technique will lead to a more expedient solution.

6.0 Conclusions and On-Going Research

The following major conclusions can be drawn from the research work detailed in this report.

- 1) A stochastic model for fatigue crack growth which accounts for material uncertainty is available and can be solved using the row-by-row numerical marching solution algorithm presented herein.
- 2) The solution algorithm is very efficient in both time and storage requirements and produces considerable savings when applied to the two-state stationary fatigue crack growth problem and the non-linear duffing oscillator.
- 3) The three-state non-stationary fatigue crack growth problem using the material uncertainty model can also be accurately solved using the proposed solution algorithm.
- 4) A four-state stochastic model for fatigue crack growth which accounts for both material uncertainty and random loading has been developed and is presented herein.
- 5) The row-by-row numerical marching solution method is unstable and thus ineffective in the solution of this four-state fatigue crack growth problem.
- 6) Several alternative solution methods were investigated and a generalized cell mapping method is believed to hold the most promise for expedient problem solution and as such will be studied in greater detail.

Present research efforts involve the development of a generalized cell-mapping technique for the solution of the four-state fatigue crack growth problem which accounts for material uncertainty and random loading. Specific topics currently being studied include the required uniform or variable cell size, possible averaging of \dot{s} and s , the number of time steps required for the formation of the probability transition matrix and comparisons between this method and the B-model of Kozin and Bogdanoff [47,48].

7.0 References

1. Aerospace Information Report 4012, *Military Service Experience – Aircraft Wheels*, 1986.
2. Allison, J.E., "Measurement of Crack Tip Stress Distributions by X-Ray Diffraction", *Fracture Mechanics*, ASTM STP 677, C.W. Smith, Ed., 1979, pp. 550–562.
3. Ang, A. H-S. and Tang W.H., "Probability Concepts in Engineering Planning and Design," Vol. I, "Basic Principles", Wiley, New York, 1975.
4. Anscombe, F.J., "Rejection of Outliers", *Technometrics*, Vol. 2, pp. 123–146, 1960.
5. Arone, R., "On Retardation Effects During Fatigue Crack Growth Under Random Overloads", *Engineering Fracture Mechanics*, Vol. 27, No. 1, pp. 83–89, 1987.
6. Bannantine, J., Comer, J., and Handrock, J., "Fundamentals of Metal Fatigue Analysis", *University of Illinois Fracture Control Program*, 1987.
7. Battelle Columbus Division, *The Probabilistic Fracture Mechanics Program Technical Highlights*, Advanced Materials Department, Mechanical Section, June 1986.
8. Bergman, L.A. and Heinrich, J.C. (1980). "Solution of the Pontriagin–Vitt Equation for the Moments of Time to First Passage of the Randomly Accelerated Particle by the Finite Element Method." *International Journal for Numerical Methods in Engineering*, 14, 1408–1412.
9. Bergman, L.A. and Heinrich, J.C. (1981). "On the Moments of Time to First Passage of the Linear Oscillator." *Earthquake Engineering and Structural Dynamics*, 9, 197–204.
10. Bhandari, R.G. and Sherrer, R.E. (1968). "Random Vibrations in Discrete Non-Linear Dynamic Systems." *Journal of Mechanical Engineering Sciences*, Vol. 10, pp. 168–174.
11. Blankenship, D. (ASD/ENFSF), "A Fracture Mechanics Approach to the Durability Analysis of the Original A-10 Nose Wheel", *Fracture and Durability Branch, Structures Division*, April 1987.
12. Bogdanoff, J.L. and Kozin, F. (1985). *Probabilistic Models of Cumulative Damage*, John Wiley and Sons.
13. Botsis, J. Chudnovsky, A. and Moet A., "Fatigue Crack Layer Propagation in Polystyrene – Part I Experimental Observations", *International Journal of Fracture*, Vol. 33, pp. 263–276, 1987.
14. Botsis, J. Chudnovsky, A. and Moet A., "Fatigue Crack Layer Propagation in Polystyrene – Part II Analysis", *International Journal of Fracture*, Vol. 33, pp. 277–284, 1987.

15. Broek, D., *Elementary Engineering Fracture Mechanics*, Martinus Nijhoff Publishers, 1986.
16. Bruhn, E.F., *Analysis and Design of Flight Vehicle Structures*, Tri-State Offset Co., 1973, pp. C13.1-45.
17. Celia, M.A. and G.F. Pinder, "An Analysis of Alternate-Direction Methods for Parabolic Equations," *Numerical Methods for Partial Differential Equations*, Vol. 1, pp. 57-70, 1985.
18. Chand S. and Garg S.B.L., "Crack Propagation under Constant Amplitude Loadings", *Engineering Fracture Mechanics*, Vol. 21, No. 1, pp. 1-30, 1985.
19. Chiu, H.M. and Hsu, C.S., "A Cell Mapping Method for Nonlinear Deterministic and Stochastic Systems - Part II: Examples of Application", *Journal of Applied Mechanics*, Vol. 53, pp. 702-710, 1986.
20. Cox, B.N., Pardee, W.J. and Morris, W.L., "A Statistical Model of Intermittent Short Fatigue Crack Growth", *Fatigue Fracture Engng. Mater. Struct.*, Vol. 9, No. 6, pp. 435-455, 1987.
21. Currey, N.S., *Landing Gear Design Handbook, First Edition*, Lockheed-Georgia Co., 1982.
22. Dahlquist, G. and Bjorck, A. (1974). *Numerical Methods*. Translated by N. Anderson. Prentice-Hall, Englewood Cliffs, New Jersey, pp. 166-167.
23. Ditlevsen, O. (1986). "Random Fatigue Crack Growth - A First Passage Problem." *Engineering Fracture Mechanics*, 23, 467-477.
24. Ditlevsen, O. and Olesen, R. (1986). "Statistical Analysis of the Virkler Data on Fatigue Crack Growth," *Engineering Fracture Mechanics*, 25, 177-195.
25. Dolinski, K., "Fatigue Crack Growth with Retardation Under Stationary Stochastic Loading", *Engineering Fracture Mechanics*, Vol. 27, No. 3, pp. 279-290, 1987.
26. Dowling, N.E., "Fatigue at Notches and the Local Strain and Fracture Mechanics Approaches", *Fracture Mechanics*, ASTM STP 577, C.W. Smith, Ed., 1979, pp. 247-273.
27. Durup, P.C. and T.R. Brussat, "Wheel Performance Evaluation," FAA Technical Center, June, 1985.
28. Ekvall, J.C. and Young, L., "Converting Fatigue Loading Spectra for Flight-by-Flight Testing of Aircraft and Helicopter Components", *Journal of Testing and Evaluation*, Vol. 4, No. 4, July 1976, pp. 231-247.
29. Elber, W., "Fatigue Crack Closure Under Cyclic Tension," *Engineering Fracture Mechanics*, Vol. 2, pp. 37-45, 1970.
30. El Haddad, M.H., Smith, K.N., and Topper, T.H., "A Strain Based Intensity Factor Solution for Short Fatigue Cracks Initiating from Notches", *Fracture Mechanics*, ASTM STP 677, C.W. Smith, Ed., 1979, pp. 550-562.

31. Enneking, T.J., "Investigation into the Applicability of Fracture Mechanics Techniques to Aircraft Wheel Life Analysis - Final Report," performed for AFWAL/FIEMA, July 1987.
32. Enneking, T.J., Spencer, B.F., Jr. and Kinnmark, I.P.E. (1989) in press. "Computational Aspects of the Stochastic Fatigue Crack Growth Problem." *Computational Mechanics of Probabilistic and Reliability Analysis*, W.K. Liu and T. Belytscho, Editors, Elme Press International.
33. Fichera, G. (1960). "On a Unified Theory of Boundary Value Problems for Elliptic-Parabolic Equations of Second Order". *Boundary Problems in Differential Equations*, R.E. Langer Ed., University of Wisconsin Press, Wisconsin, pp. 97-102.
34. Gallagher, J.P., "Estimating Fatigue-Crack Lives for Aircraft: Techniques", *Experimental Mechanics*, Vol. 16, No. 11, Nov. 1976, pp. 425-433.
35. Garubisic, V. and Fischer, G., "Automotive Wheels, Methods and Procedure for Optimal Design and Testing", *SAE Technical Paper 830135*, 1983.
36. Gemma, A.E. and Snow, D.W., "Prediction of Fatigue Crack Growth Under Spectrum Loading", *Fracture Mechanics*, ASTM STP 677, C.W. Smith, Ed., 1979, pp. 320-338.
37. Ghonem, H. and Dore, S., "Experimental Study of the Constant Probability Crack Growth Curves under Constant Amplitude Loading," *Engineering Fracture Mechanics*, Vol. 27, No. 1, 1987, pp. 1-25.
38. Heinrich, J.C., Huyakorn, P.S., Zienkiewicz, O.C. and Mitchell, A.R. (1977). "An 'Upwind' Finite Element Scheme for Two Dimensional Convective Transport Equation." *International Journal for Numerical Methods in Engineering*, 11, 131-143.
39. Hsu, C.S. "A Generalized Theory of Cell-to-Cell Mapping for Nonlinear Dynamical Systems", *Journal of Applied Mechanics*, Vol. 48, pp. 634-642, 1981.
40. Hsu, C.S., "A Theory of Cell-to-Cell Mapping Dynamical Systems", *Journal of Applied Mechanics*, Vol. 47, pp. 931-939, 1980.
41. Hsu, C.S., and Chiu, H.M., "A Cell Mapping Method for Non-linear Deterministic and Stochastic Systems - Part I: The Method of Analysis", *Journal of Applied Mechanics*, Vol. 53, pp. 695-701, 1986.
42. Hsu, C.S., *Cell-to-Cell Mapping: A Method of Global Analysis for Nonlinear Systems*, Springer-Verlag, 1987.
43. Hsu, C.S. and Guttalu, R.S., "An Unraveling Algorithm for Global Analysis of Dynamical Systems: An Application of Cell-to-Cell Mapping", *Journal of Applied Mechanics*, Vol. 47, pp. 940-948, 1980.
44. Hudson, C.M., "A Root-Mean-Square Approach for Predicting Fatigue Crack Growth under Random Loading", *Methods and Models for Predicting Fatigue Crack Growth Under Random Loading*, ASTM Special Technical Publication 748, 1987.

45. Irwin, G.R., "Analysis of Stresses and Strains Near the End of a Crack Traversing a Plate," *Journal of Applied Mechanics*, Trans. ASME, Vol. 24, p. 351, 1957.
46. Iyengar, R.N. and Dash, P.K., "Study of the Random Vibration of Nonlinear Systems by the Gaussian Closure Technique", *Journal of Applied Mechanics*, Vol. 45, pp. 393-399, 1978.
47. Kozin, F. and Bogdanoff, J.L. (1984). "Analysis of Stochastic Equation Models of Crack Growth." *Proceedings of the IUTAM Symposium on 'Probabilistic Methods in Mechanics of Solids and Structures.'* Stockholm Sweden, June 19-21, 93-101.
48. Kozin, F. and Bogdanoff, J.L., "Probabilistic Methods in Fatigue Crack Growth: Results and Speculations," *Journal of Nuclear Engineering and Design*, 1988, in press.
49. Krause, G. and Mahnig, F., "A Comprehensive Method for Wheel Testing by Stress Analysis", *SAE Technical Paper 760042*, 1976.
50. Langley, R.S., (1985). "A Finite Element Method for the Statistics of Non-linear Random Vibration." *Journal of Sound and Vibration*, Vol. 101, No. 1, pp. 41-54.
51. Larson, C.E. and Shawver, W.R., "Method for Determining Probability of Structural Failure from Aircraft Counting Accelerometer Tracking Data", *Probabilistic Fracture Mechanics and Fatigue Methods: Application for Structural Design and Maintenance*, ASTM STP 798, J.M. Bloom and J.C. Ekvall, Eds., 1983, pp. 147-160.
52. Lin, Y.K. and J.N. Yang, "A Stochastic Theory of Fatigue Crack Propagation," *AIAA Journal*, Vol. 23, No. 1, pp. 117-124, 1985.
53. Lin, Y.K. and J.N. Yang, "On Statistical Moments of Fatigue Crack Propagation," *Journal of Engineering Fracture Mechanics*, Vol. 18, No. 2, pp. 243-256, 1983.
54. Lin, Y.K. (1967). *Probabilistic Theory of Structural Dynamics*. McGraw-Hill, New York. Reprinted by R.E. Krieger, 1976, New York.
55. Lin, Y.K., W.F. Wu and J.N. Yang, "Stochastic Modeling of Fatigue Crack Propagation," *Proceedings of the IUTAM Symposium on 'Probabilistic Methods in Mechanics of Solids and Structures'*, Stockholm Sweden, June 19-21, 1984, pp. 103-110.
56. Madsen, H.O., Krenk, S. and Lind, N.C., *Methods of Structural Safety*, Prentice-Hall, Inc. 1986.
57. MIL-W-5013K, *Military Specification Wheel and Brake Assemblies*, 1982.
58. Mitchell, M.R., "Fundamentals of Modern Fatigue Analysis for Design", *Fatigue and Microstructure*, ASM, 1979.
59. Mitler, M.S. and J.P. Gallagher, "An Analysis of Several Fatigue Crack Growth Rate (FCGR) Descriptions," *Fatigue Crack Growth MEasurement and Data Analysis*, ASTM-STP 738, pp. 205-251, 1981.

60. Nagar, A., "Fatigue Crack Growth in Aircraft Main Landing Gear Wheels", submitted for publication in *Fracture Mechanics Nineteenth Symposium ASTM*, April 1987.
61. Nelson, D.V. and Fuchs, H.O., "Prediction of Fatigue Crack Growth under Irregular Loading", *Fatigue Crack Growth under Spectrum Loads*, ASTM STP 595, pp. 276-291, 1976.
62. Ortiz, K. and Kung, C.J. (1987). "Modeling Errors in Fatigue Crack Growth Laws." *Materials and Member Behavior*, Proceedings of the Sessions at Structures Congress '87 related to Material and Member Behavior, Orlando, Florida, August 17-20, 1987.
63. Ortiz, K. and Kiremidjian, A.S., "Stochastic Modeling of Fatigue Crack Growth." *Engineering Fracture Mechanics*, to appear.
64. Ortiz, K. and Kiremidjian, A.S. (1986). "Time Series Analysis of Fatigue Crack Growth Data." *Engineering Fracture Mechanics*, 24, 657-676.
65. Ostergaard, D.F. and Hillberry, B.M., "Characterization of the Variability in Fatigue Crack Propagation Data," *Probabilistic Methods for Design and Maintenance of Structures*, ASTM-STP 798, American Society for Testing and Materials, 1983.
66. Palmberg, B., Blom, A.F., and Eggwertz, S. (1985,1987). "Probabilistic Damage Tolerance Analysis of Aircraft Structures." *The Aeronautical Research Institute of Sweden, Technical Report FFA TN 1985-68*, Bromma, Sweden, and in *Probabilistic Fracture Mechanics and Reliability*, edited by J. Provan, Martinus Nijhoff Publishers, The Netherlands.
67. Paris, P.C. and Erdogan, F., "A Critical Analysis of Crack Propagation Laws," *Transactions ASME, Journal of Basic Engineering*, Vol. 85, pp. 528-534, 1963.
68. Pavlik, J.V., "Experimental Stress Analysis of the A-7D Main Wheel to Determine Cause and Correction of Field Service Inboard Web Spoke Fatigue Cracking", *B.F. Goodrich Company Engineering Report No. ER-5106*, 1982.
69. Riesner, M. and Devries, R.I., "Finite Element Analysis and Structural Optimization of Vehicle Wheels", *SAE Technical Paper 880193*, 1983.
70. Roberts, J.B. (1981). "Response of Non-Linear Mechanical Systems to Random Excitation Part 1: Markov Methods." *Shock and Vibration Digest*, Vol. 13, No. 4, pp. 17-28.
71. Roberts, J.B. (1981). "Response of Non-Linear Mechanical Systems to Random Excitation Part 2: Equivalent Linearization and Other Methods." *Shock and Vibration Digest*, Vol. 13, pp. 15-29.
72. Rodriguez, A., *F/FB-111 Service Life Monitoring Summary Report, Vol. III, FB111A Technical Analysis*, December 1983, General Dynamics, Fort Worth Division.
73. Rolfe, T. and Barsom, J.M., *Fracture and Fatigue Control in Structures - Applications of Fracture Mechanics*, Prentice-Hall, Inc., 1977.

74. Schijve, J., "Fatigue Crack Closure: Observations and Technical Significance", *Mechanics of Fatigue Crack Closure*, ASTM STP 982, J.C. Newman, Jr. and W. Elber, Eds., American Society for Testing and Materials, Philadelphia, pp. 5-34, 1988.
75. Seward, L.R., "REDUCE User's Guide, for IBM 360 and Derivative Computers, Version 3.2", Rand Publication CP83, 1985.
76. Smith, S.M., "Aircraft Wheel Design and Proving", *Tech Air*, Vol. 44, 1986, pp. 1-4.
77. Sobczyk, K. (1984). "Stochastic Modelling of Fatigue Crack Growth." *Proceedings of the IUTAM Symposium on 'Probabilistic Methods in Mechanics of Solids and Structures'*. Stockholm, Sweden, June 19-21, 111-119.
78. Spencer, B.F., Jr. and Bergman, L.A. (1985). "On the Reliability of a Simple Hysteretic System", *Journal of Engineering Mechanics*, ASCE, Vol. 111, No. 12, pp. 1502-1514.
79. Spencer, B.F., Jr. (1986). *On the Reliability of Nonlinear Hysteretic Structures subjected to Broadband Random Excitation*, Lecture Notes in Engineering, 21 (series editors: C.A. Brebbia and S.A. Orszag), Springer-Verlag.
80. Spencer, B.F., Jr., and Tang, J. (1988). "A Markov Process Model for Fatigue Crack Growth." *Journal of Engineering Mechanics*, ASCE, Vol. 114, No. 12, pp. 2134-2157.
81. Spencer, B.F., Jr., Tang, J., and Artley, M.E. (1989). "A Stochastic Approach to Modeling Fatigue Crack Growth." *AIAA Journal*, to appear.
82. Sun, J.Q. and Hsu, C.S., "Cumulant-Neglect Closure Method for Nonlinear Systems Under Random Excitations", *Journal of Applied Mechanics*, Vol. 54, pp. 649-655, 1987.
83. Sun, J.Q. and Hsu, C.S., "First Passage Time Probability of Nonlinear Stochastic Systems by Generalized Cell Mapping Method", *Journal of Sound and Vibration*, Vol. 124, No. 2, pp. 233-248, 1988.
84. Tanaka, H. and Tsurui, A., "Reliability Degradation of Structural Components in the Process of Fatigue Crack Propagation Under Stationary Random Loading", *Engineering Fracture Mechanics*, Vol. 27, No. 5, pp. 501-516, 1987.
85. Technical Standard Order - C26c Aircraft Wheels and Wheel-Brake Assemblies, *Department of Transportation, Federal Aviation Administration*, 1984.
86. Treanor, D. and T.J. Carter, "Military Aircraft Wheel Life Improvement Assessment," Air Force Wright Aeronautical Laboratories, Flight Dynamics Lab, 1987.
87. Veers, P.S., "Fatigue Crack Growth Due to Random Loading", Ph.D. Dissertation, Stanford University, Stanford, California, 1987.

88. Virkler, D.A., Hillberry, B.M. and Goel, P.K. (1979). "The Statistical Nature of Fatigue Crack Propagation." *Journal of Engineering Materials and Technology*, Vol. 101, pp. 148-152.
89. Wen, Y.K. (1975). "Approximate Method for Non-linear Random Vibration." *Proceedings of the American Society of Civil Engineers, Journal of the Engineering Mechanics Division*, Vol. 101, pp. 389-401.
90. Wen, Y.K. (1976). "Method for Random Vibration of Hysteretic Systems." *Proceedings of the American Society of Civil Engineers, Journal of the Engineering Mechanics Division*, Vol. 102, pp. 249-263.
91. Wheeler, O.E., "Spectrum Loading and Crack Growth", *Journal of Basic Engineering, Transactions ASME*, Vol. 94, pp. 81, 1972.
92. Willenborg, J., Engle, R.M. and Wood, H.A., "A Crack Growth Retardation Model Using an Effective Stress Concept", *Report TM-71-1-FBR*, Wright Patterson Air Force Base, Ohio, 1971.
93. Wihterstein, S.R. and Ness, O.B., "Hermite Moment Analysis of Nonlinear Random Vibrations", *Computational Mechanics of Probabilistic and Reliability Analysis*, W.K. Liu and T. Belytscho, Editors, Elme Press International, 1989.
94. Wu, W.F. and Liu, Y.K., "Cumulant-Neglect Closure for Non-Linear Oscillators Under Random Parametric and External Excitations", *Int. J. of Non-Linear Mechanics*, Vol. 19, No. 4, pp. 349-362, 1984.
95. Yadav, D. and Nigam, N.C., "Reliability Analysis of Landing Gear Fatigue Life", *IUTAM Probabilistic Methods in the Mechanics of Solids and Structures*, S. Eggwertz and N.C. Lind, Eds., 1985, pp. 569-577.
96. Yang, J.N., W.H. Hsi and S.D. Manning, "Stochastic Crack Propagation with Application to Durability and Damage Tolerance Analyses," *Air Force Wright Aeronautical Laboratories - Flight Dynamics Laboratory, Technical Report AFLWA-TR-85-9062*, WPAFB, 1985 and in *Probabilistic Fracture Mechanics and Reliability*, edited by J. Provan, Martinus Nijhoff Publishers, The Netherlands.
97. Yang, J.N., G.C. Salivar, C.G. Annis, "Statistical Modeling of Fatigue-Crack Growth in a Nickel-Based Superalloy," *Journal of Engineering Fracture Mechanics*, Vol. 18, No. 2, pp. 257-270, 1983.
98. Yang, J.N., G.C. Salivar, C.G. Annis, "The Statistics of Crack Growth in Engine Materials, Vol. II: Spectrum Loading and Advanced Models," *AFWAL-TR-82-4040*, January, 1983.
99. Yang, J.N., and R.C. Donath, "Statistical Crack Propagation in Fastener Holes Under Spectrum Loading," *Journal of Aircraft*, Vol. 20, pp. 1028-1032, 1983.
100. Yang, J.N. and Trapp, W.J., "Reliability Analysis of Aircraft Structures Under Random Loading and Periodic Inspection", *AIAA Journal*, Vol. 12, No. 12, 1975, pp. 494-496.

Table 1 - Literature Review

Reference No.	Wheels and/or Landing Gear	Fracture Mechanics	Other Fatigue Study Methods	Finite Element Method	Wheel Load Determination	Material Properties	Experimental Methods	Stochastic Methods	Environmental Effects	Non-Destructive Inspection	Other Numerical Solution Methods
1	X		X		X		X		X		
2		X		X			X				
3								X			
4								X			X
5		X									
6		X	X			X	X		X	X	
7		X						X			
8				X				X			X
9				X				X			X
10								X			X
11	X	X	X		X	X	X		X		
12		X	X				X	X			X
13		X					X				
14		X					X				
15		X		X			X				
16	X		X			X					
17				X							X
18		X						X			X
19								X			X
20		X					X				
21	X				X						
22				X							X
23		X						X			
24		X						X			
25		X						X			
26		X						X			
27	X	X	X		X	X	X		X	X	
28			X		X	X	X		X		
29		X									
30		X									
31	X	X	X		X	X	X	X	X	X	
32		X		X				X			
33											X
34		X			X						
35	X		X		X		X				
36		X					X				
37		X					X				
38				X							X
39											X
40											X

Table 1 - Literature Review

Reference No.	Wheels and/or Landing Gear	Fracture Mechanics	Other Fatigue Study Methods	Finite Element Method	Wheel Load Determination	Material Properties	Experimental Methods	Stochastic Methods	Environmental Effects	Non-Destructive Inspection	Other Numerical Solution Methods
41								X			X
42											X
43											X
44		X									X
45		X	X								
46								X			X
47		X	X				X	X			X
48		X	X				X	X			X
49	X		X		X		X				
50				X				X			X
51		X	X					X			
52		X						X			
53		X						X			
54				X				X			X
55		X						X			
56		X	X					X			
57	X				X		X				
58		X	X			X			X		
59		X					X				
60	X	X			X		X				
61		X									
62		X				X		X			
63		X						X			
64		X						X			
65		X				X	X	X			
66		X		X	X	X		X		X	
67		X									
68	X		X		X		X				
69	X		X	X							
70								X			X
71								X			X
72	X		X		X		X				
73		X	X				X		X	X	
74		X									
75											X
76	X		X				X				
77		X						X			
78								X			X
79								X			X
80		X		X			X	X			X

Table 1 - Literature Review

Reference No.	Wheels and/or Landing Gear	Fracture Mechanics	Other Fatigue Study Methods	Finite Element Method	Wheel Load Determination	Material Properties	Experimental Methods	Stochastic Methods	Environmental Effects	Non-Destructive Inspection	Other Numerical Solution Methods
81		X		X			X	X			X
82								X			X
83								X			X
84		X									
85	X				X		X				
86	X		X	X	X		X				
87		X	X			X	X	X			X
88		X					X				
89								X			X
90								X			X
91		X									
92		X									
93								X			X
94								X			X
95	X	X						X			
96		X						X			
97		X						X			
98		X						X			
99		X						X			
100		X						X			

Table 2. Probability density function of response for a Duffing oscillator

Density function				
Response	Exact result	Bhandari and Sherrer [1968] method	Langley [1985] method	Present method
0.00	0.4757	0.4792	0.4762	0.4757
0.15	0.4703	0.4736	0.4709	0.4697
0.30	0.4543	0.4566	0.4550	0.4537
0.45	0.4277	0.4285	0.4285	0.4268
0.60	0.3910	0.3898	0.3919	0.3902
0.75	0.3452	0.3423	0.3462	0.3442
0.90	0.2923	0.2884	0.2932	0.2915
1.05	0.2355	0.2319	0.2361	0.2346
1.20	0.1787	0.1766	0.1788	0.1779
1.35	0.1263	0.1264	0.1259	0.1255
1.50	0.0820	0.0841	0.0811	0.0814
1.65	0.0483	0.0512	0.0471	0.0476
1.80	0.0254	0.0277	0.0242	0.0249

Table 3. Virtual CPU and storage comparison

	Storage	Virtual CPU
Existing Solution Method (Spencer and Tang, 1988)	12.3 MBytes	649 seconds
New Numerical Solution Technique	.25 MBytes	21 seconds

Table 4. Different crack growth law and the corresponding SSQ for the Ghonem and Dore Data

crack growth law	parameters	SSQ
Forman's $da/dt = C(\Delta K)^m / ((1-R)K_c - \Delta K)$	$C = 5.1204E-9$ $m = 2.9650$ $K_c = 34.461$	0.19279E9
Pearson's $da/dt = C(\Delta K)^m / ((1-R)K_c - \Delta K)^{1/2}$	$C = 5.5666E-10$ $m = 3.2571$ $K_c = 21.300$	0.87903E9
Modified Cubic $\log(da/dt) = C_4 + C_3 \log(U\Delta K) + C_2 (\log(U\Delta K))^2 + C_1 (\log(U\Delta K))^3$ where $U = a_1 R^2 + a_2 R + a_3$	$a_1 = 15.736$ $a_2 = -12.133$ $a_3 = 6.6525$ $C_1 = 7.6378$ $C_2 = -79.511$ $C_3 = 278.88$ $C_4 = -345.07$	0.53068E8
Modified Paris $da/dt = C(U\Delta K)^m$ where $U = a_1 R^2 + a_2 R + a_3$	$C = 5.8353E-10$ $a_1 = 2.4885$ $a_2 = -1.9710$ $a_3 = 0.9690$ $m = 3.8744$	0.11010E9
Chand and Garg $da/dt = C(U\Delta K)^2 / (1+R)^{3.8}$ where $U = \Delta K(8.8R+6)/1000/(1-R) + 1.3R + 0.2$	$C = 1.2719E-8$	0.76243E10

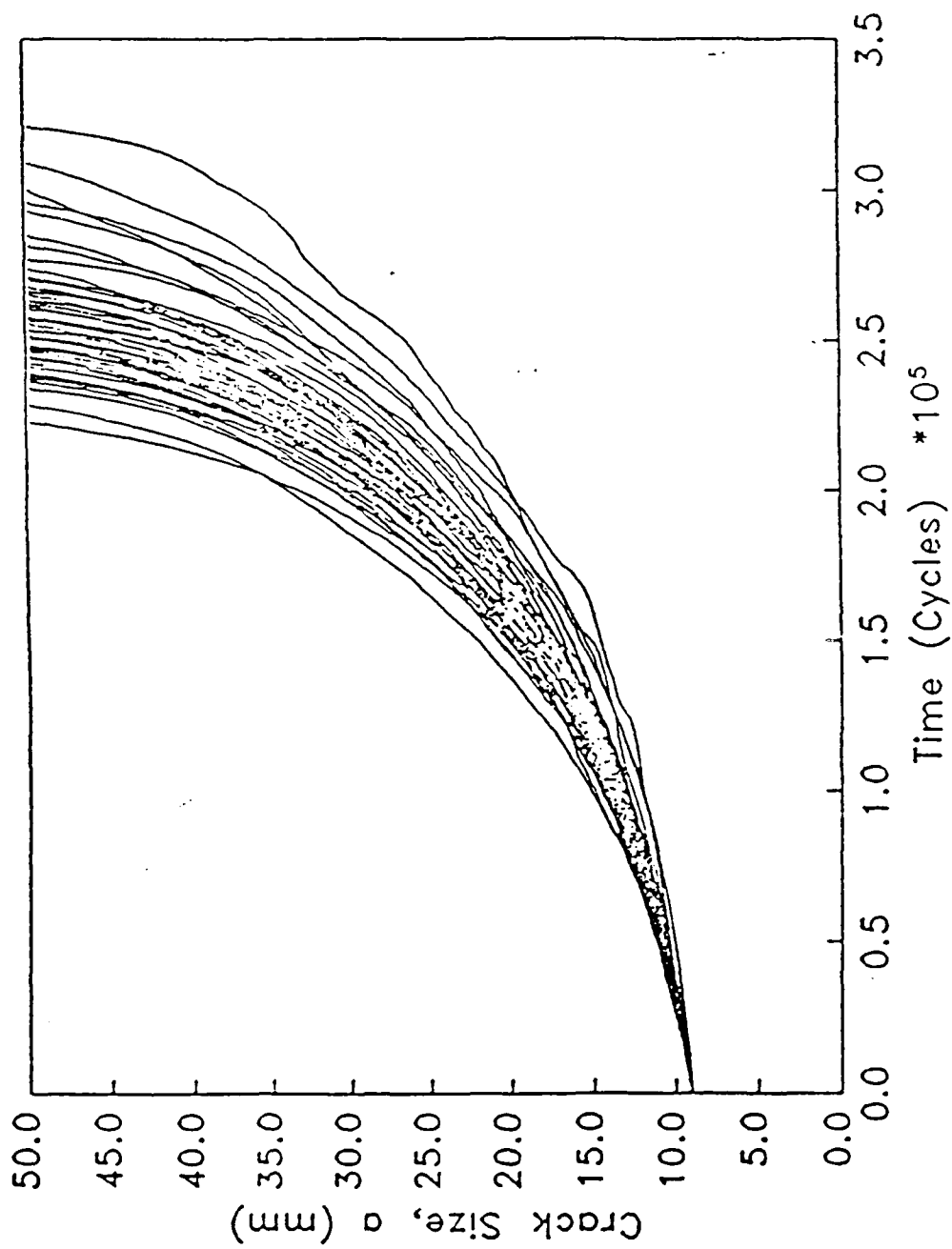


Figure 1 Virkler, et al. (1979) fatigue crack growth curves

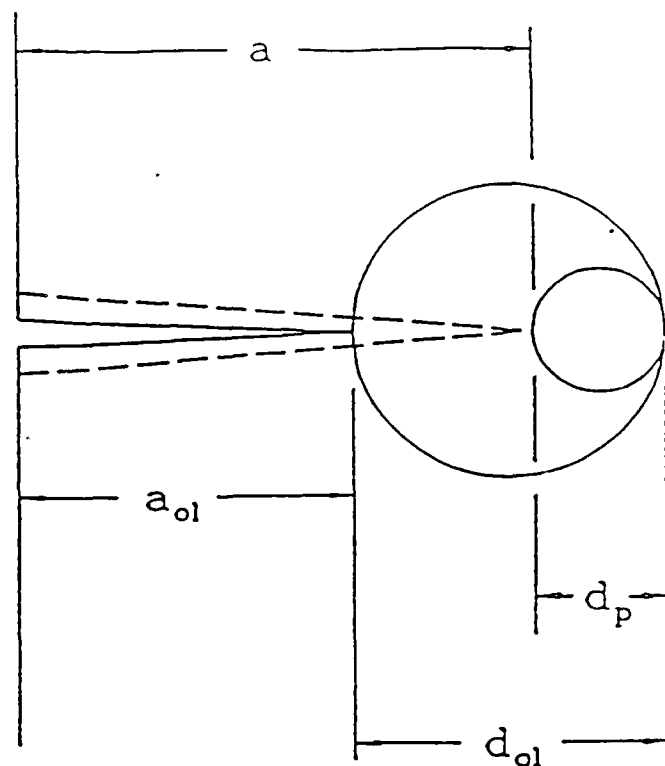


Figure 2(a) Schematic of crack growth through the overload affected zone from a_{ol} to $a_{ol} + d_{ol}$

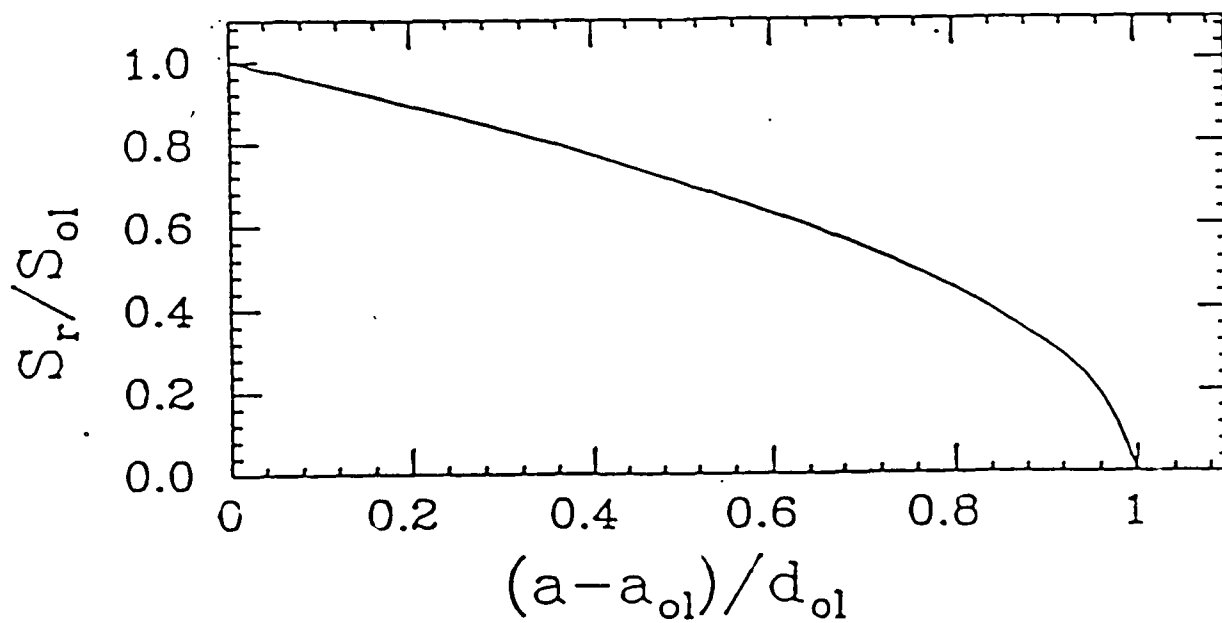


Figure 2(b) Variation in reset stress, S_r , as the crack grows through the overload affected zone from a_{ol} to $a_{ol} + d_{ol}$

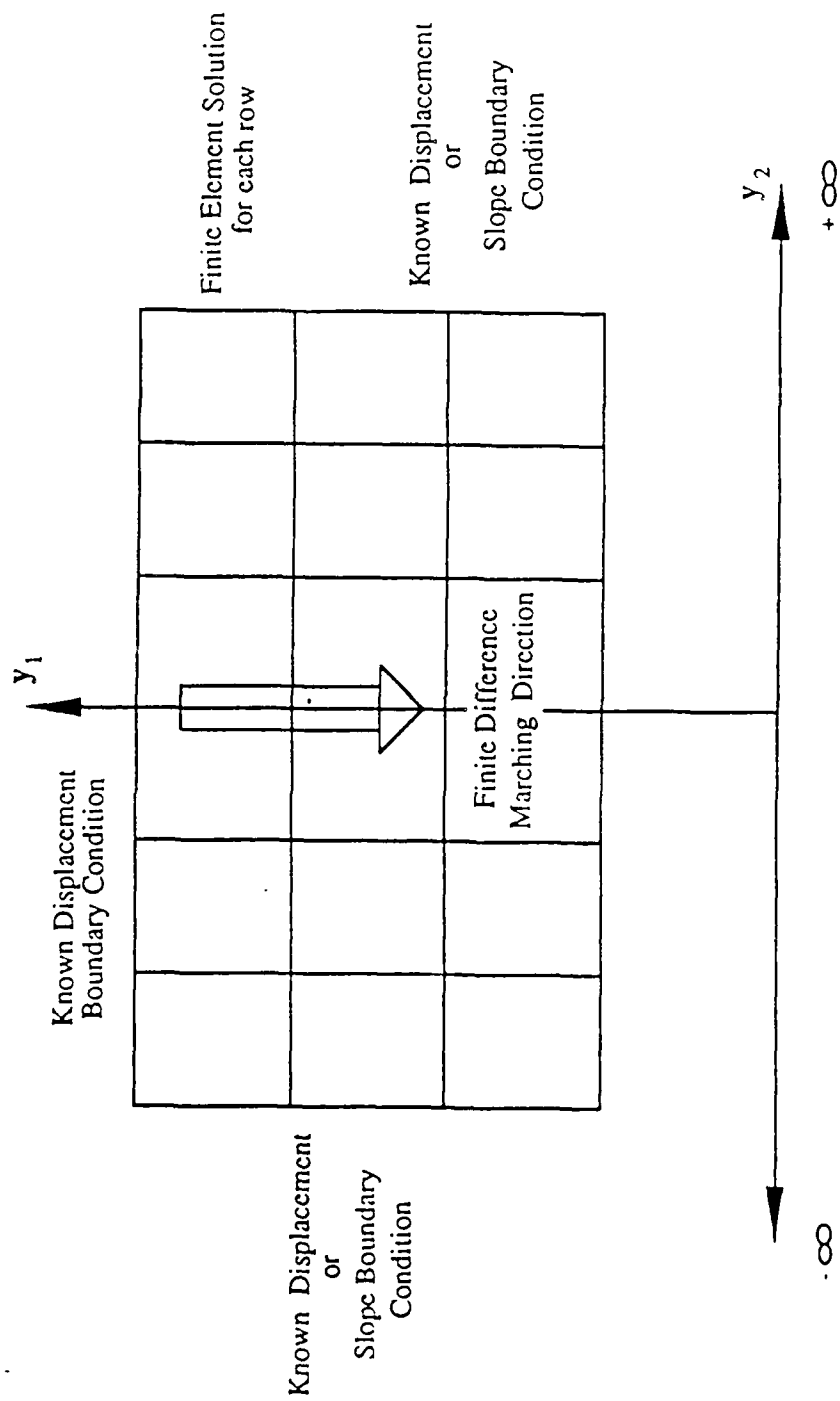


Figure 3 Schematic of problem solution methodology

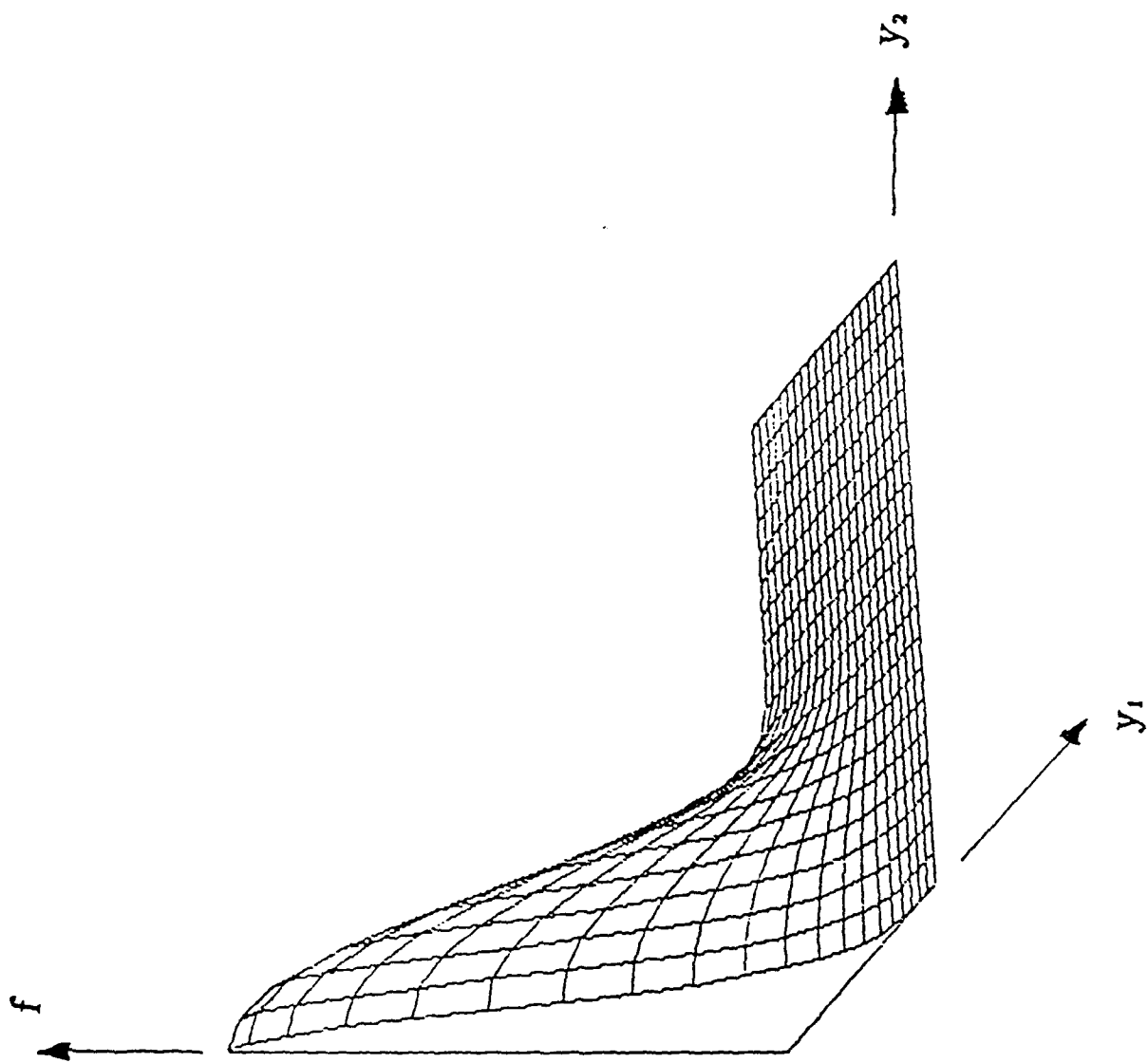


Figure 4 Numerical solution for quarter section of f as a function of y_1 and y_2 for $\omega \approx 1$, $\gamma = .5$, and $\beta = .5$

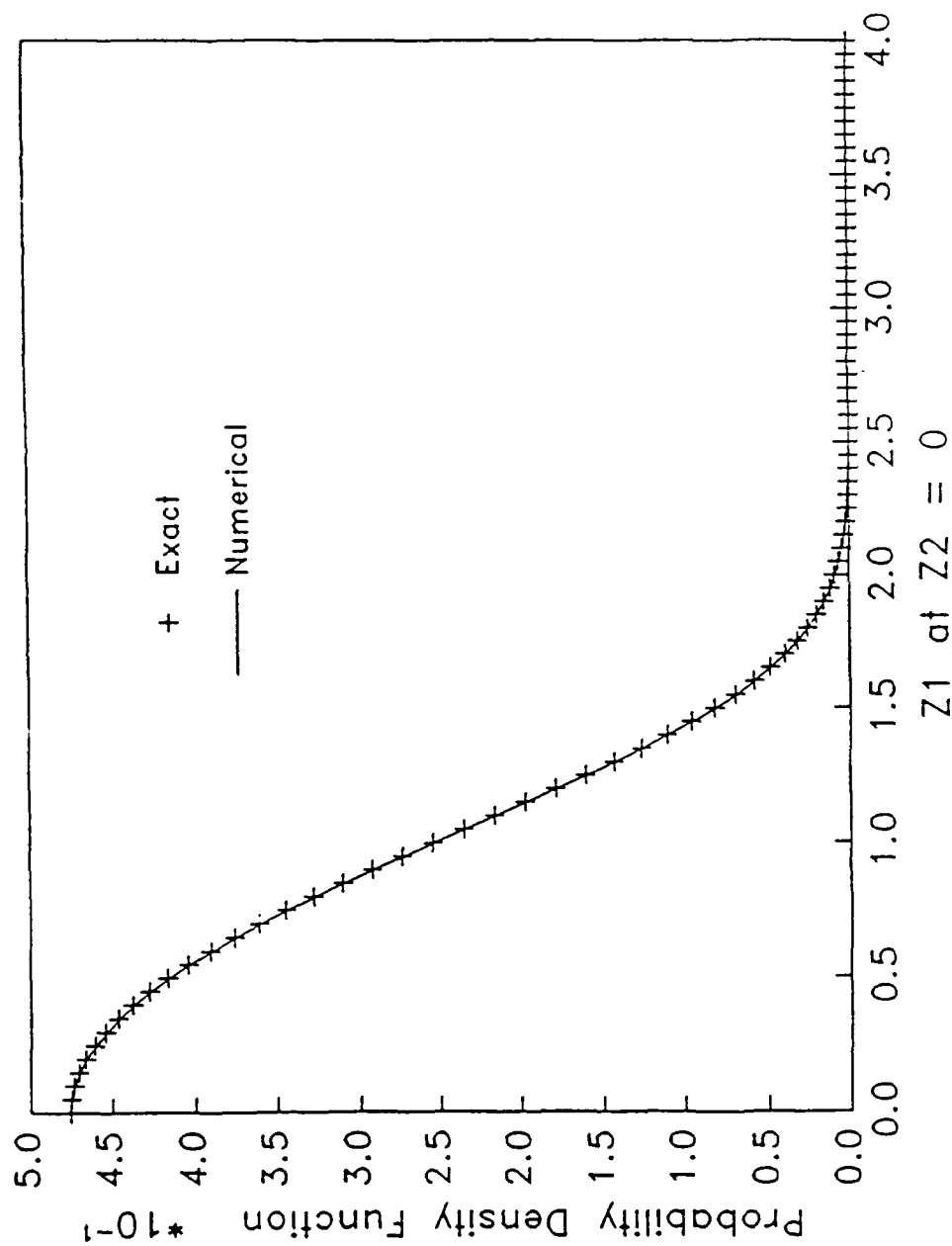


Figure 5 Numerical solution for quarter section of f as a function of y_1 at $y_2 = 0$ for $\omega = 1$, $\gamma = .5$, and $\beta = .5$ plotted over the exact solution curve

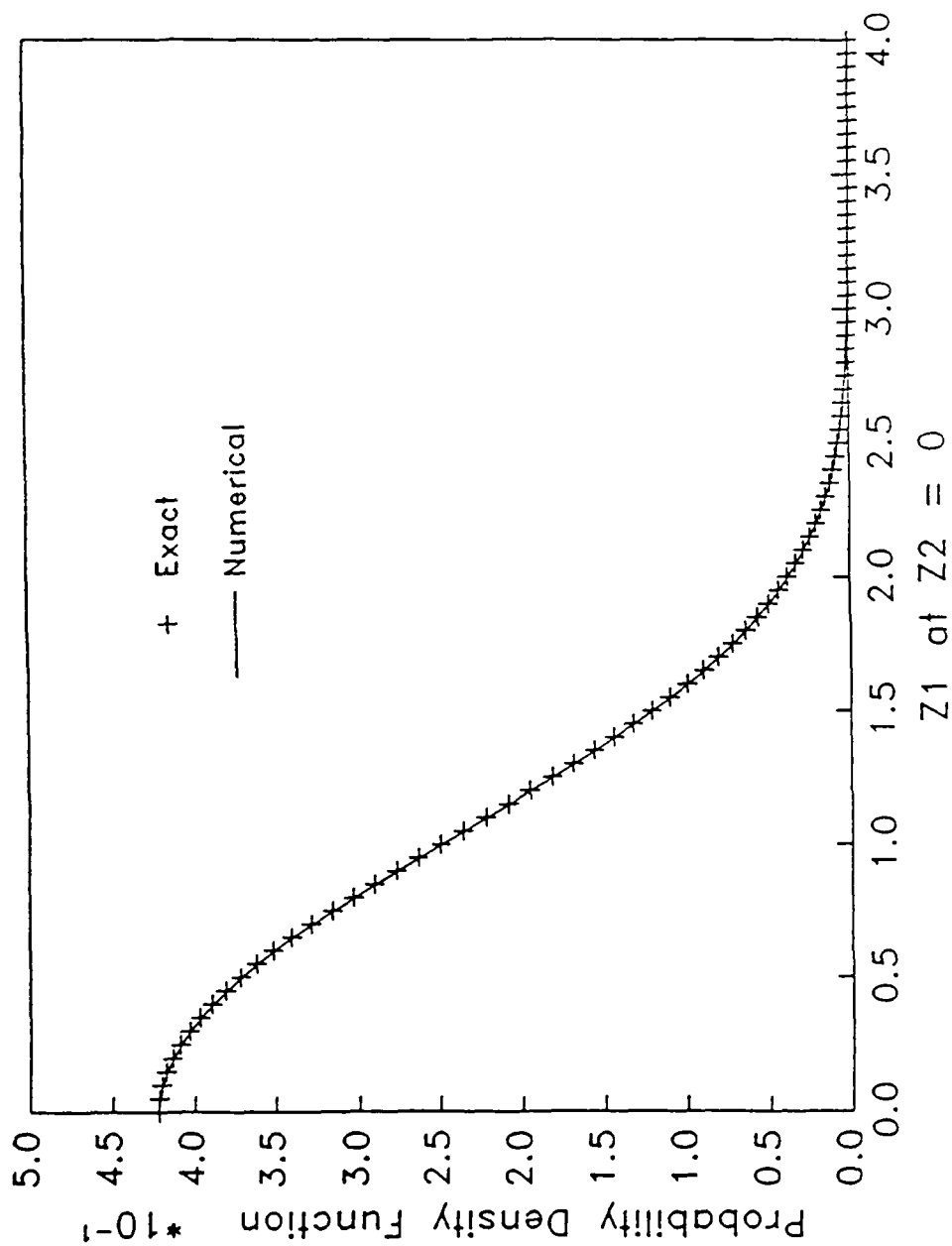


Figure 6 Numerical solution for quarter section of f as a function of y_1 at $y_2 = 0$ for $\omega = 1$, $\gamma = .1$, and $\beta = .5$ plotted over the exact solution curve

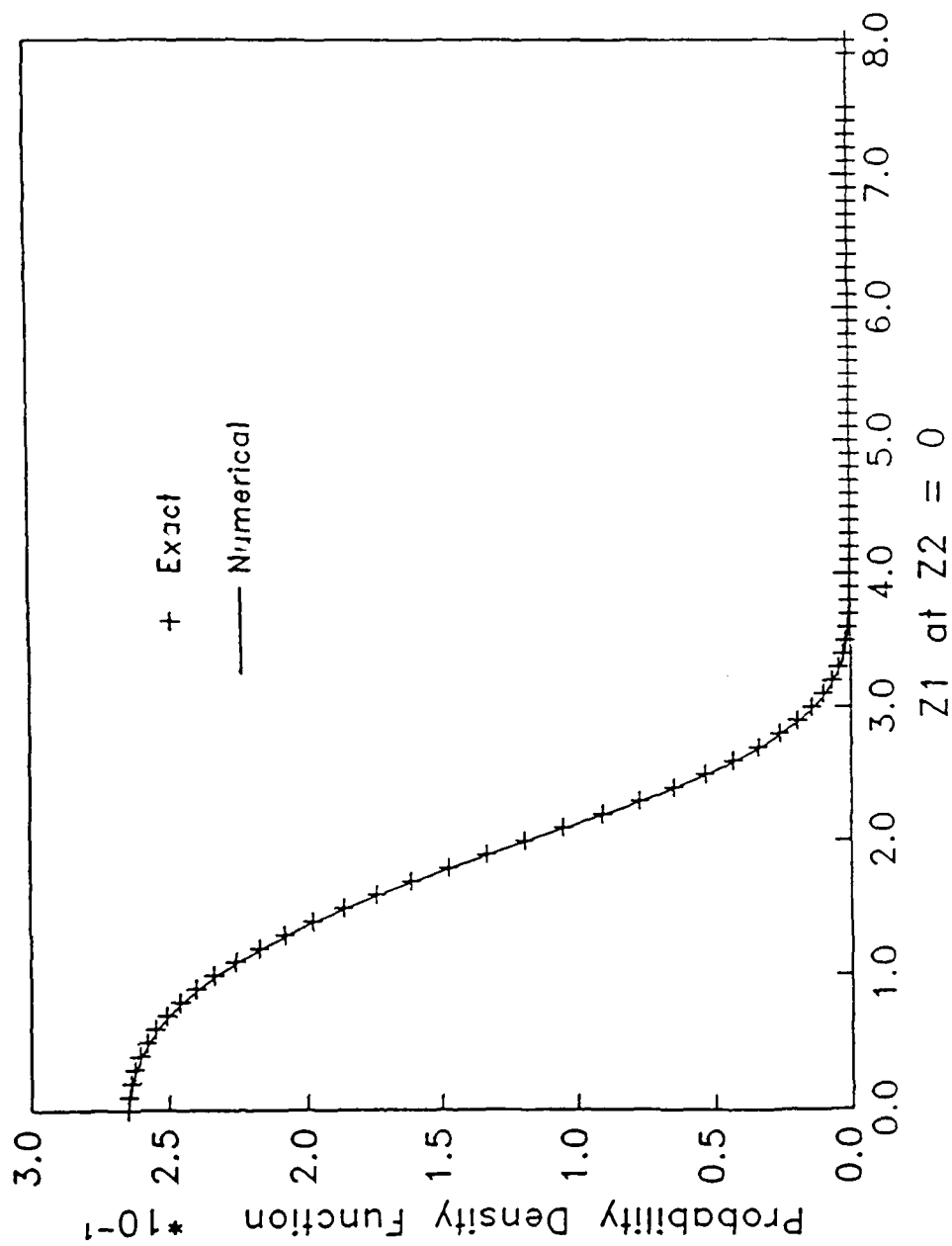


Figure 7 Numerical solution for quarter section of f as a function of y_1 at $y_2 = 0$ for $\omega = 1$, $\gamma = .5$, and $\beta = .1$ plotted over the exact solution curve

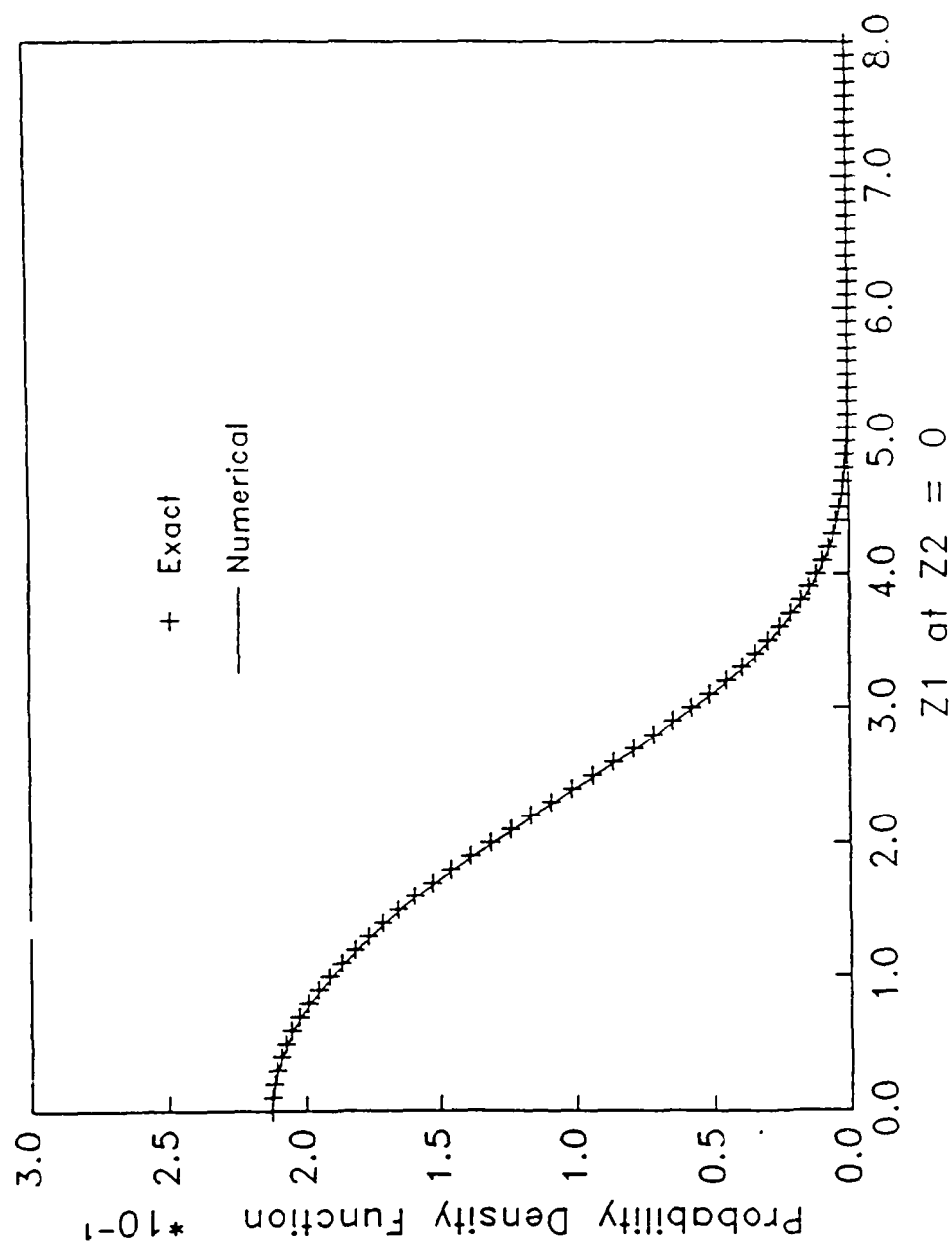


Figure 8 Numerical solution for quarter section of f as a function of y_1 at $y_2 = 0$ for $\omega = 1$, $\gamma = .1$, and $\beta = .1$ plotted over the exact solution curve

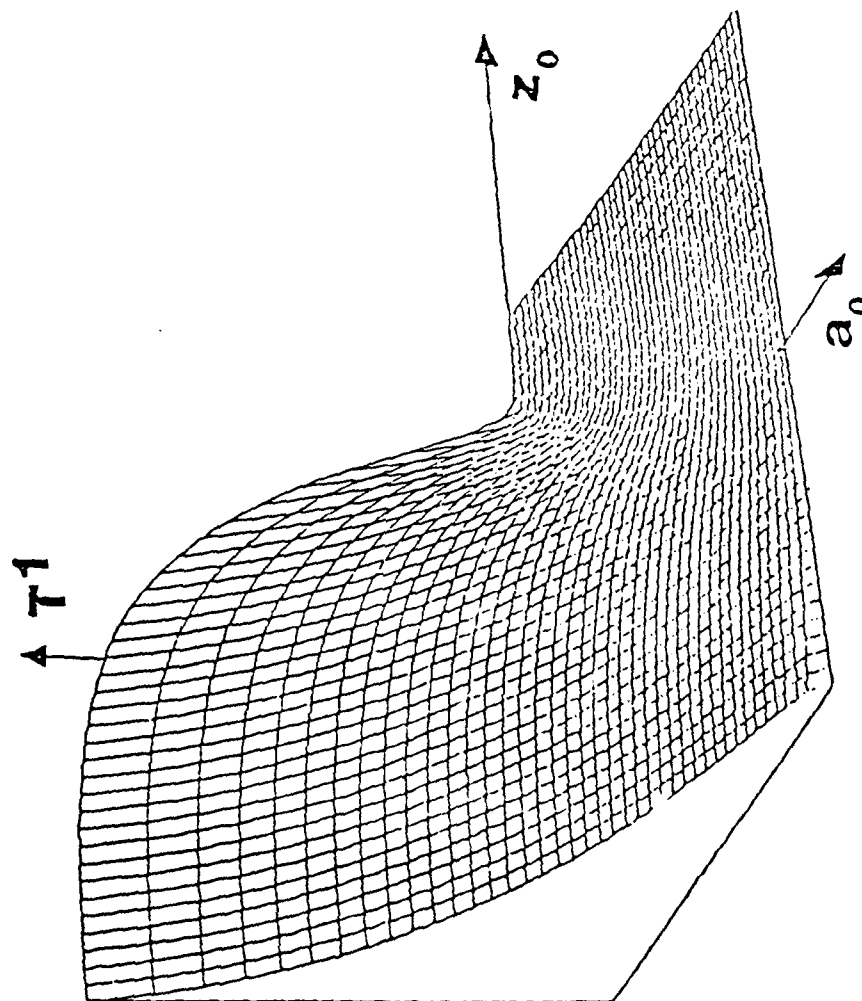


Figure 9

Numerical solution for $T^1(a_0, z_0)$, the mean time to reach $a_c = 49.8$ mm as a function of the initial flaw size and the initial value of the auxiliary process $Z(t)$

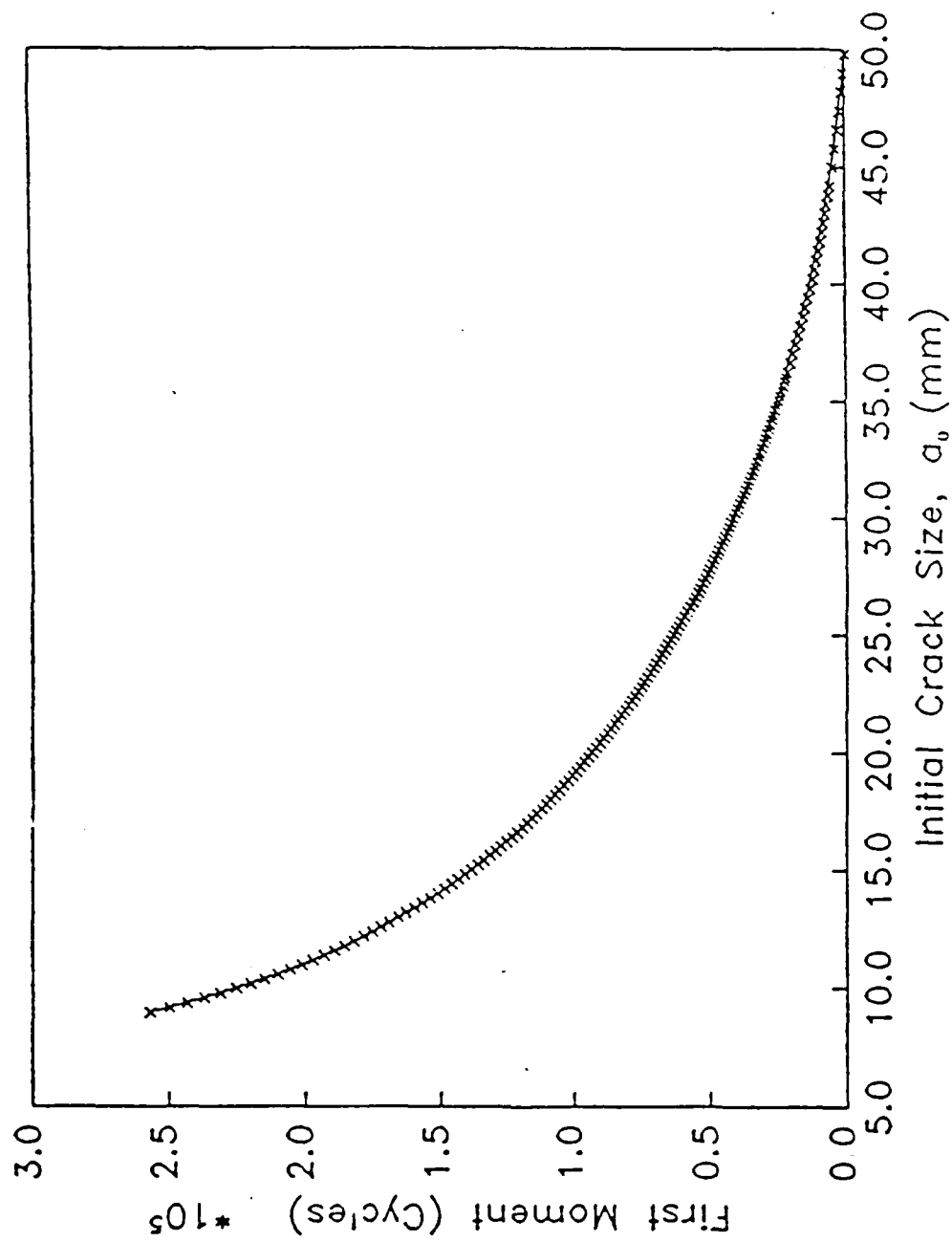


Figure 10 Comparison between the predicted mean time to reach $a_c = 49.8$ mm and the experimental data

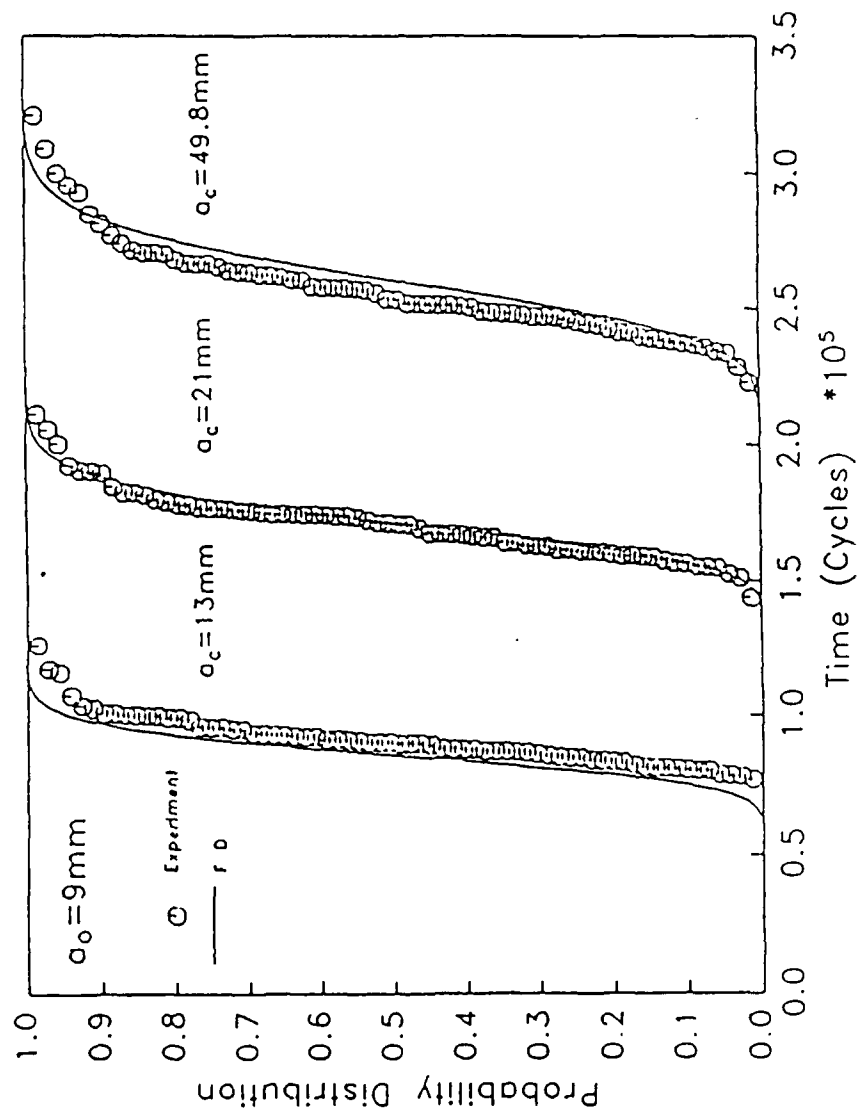
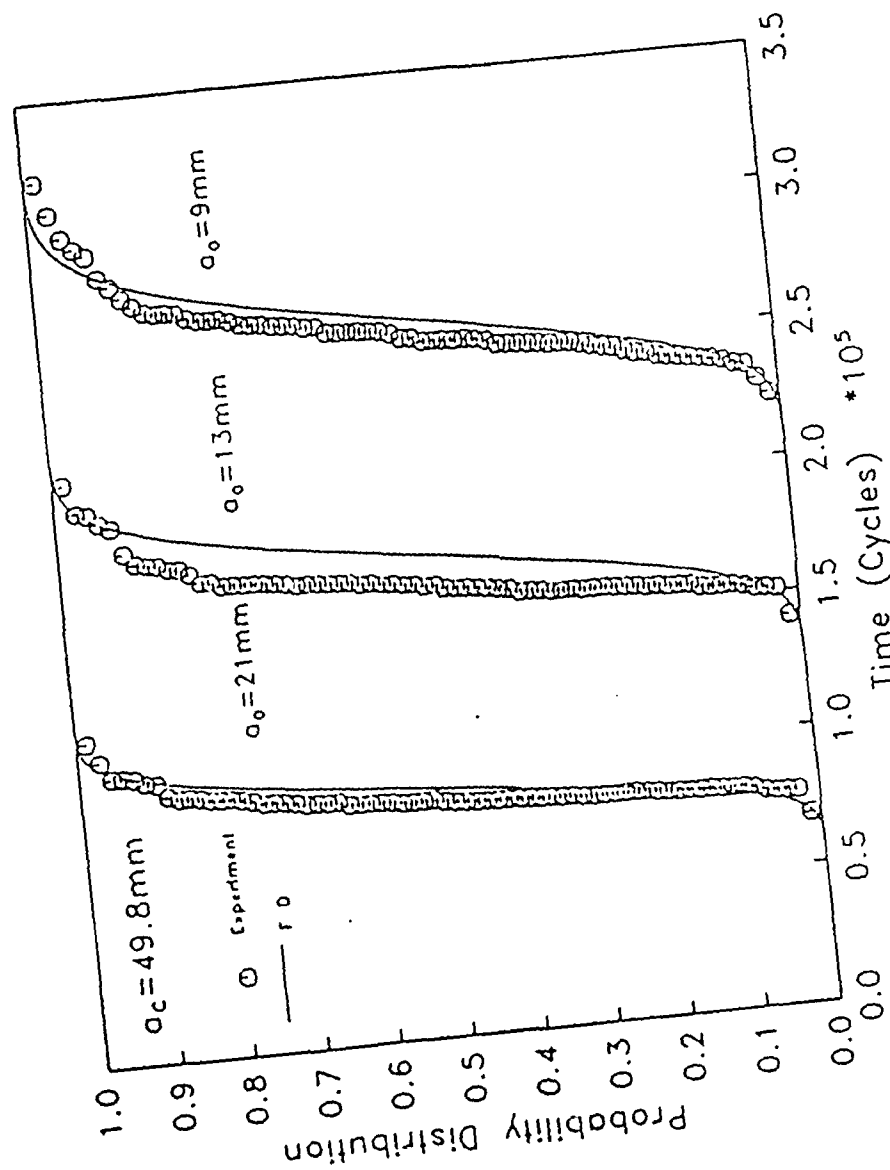


Figure 11 Finite difference solutions for the distribution function of the random time to reach critical crack sizes $a_c = 13$ mm, $a_c = 21$ mm and $a_c = 49.8$ mm with the initial crack size $a_0 = 9$ mm. Virkler data using the Paris law



Finite difference solutions for the distribution function of the random time to reach the critical crack size $a_c = 49.8$ mm with initial crack sizes $a_0 = 21$ mm, $a_0 = 13$ mm and $a_0 = 9$ mm. Virkler data using the Paris law

Figure 12

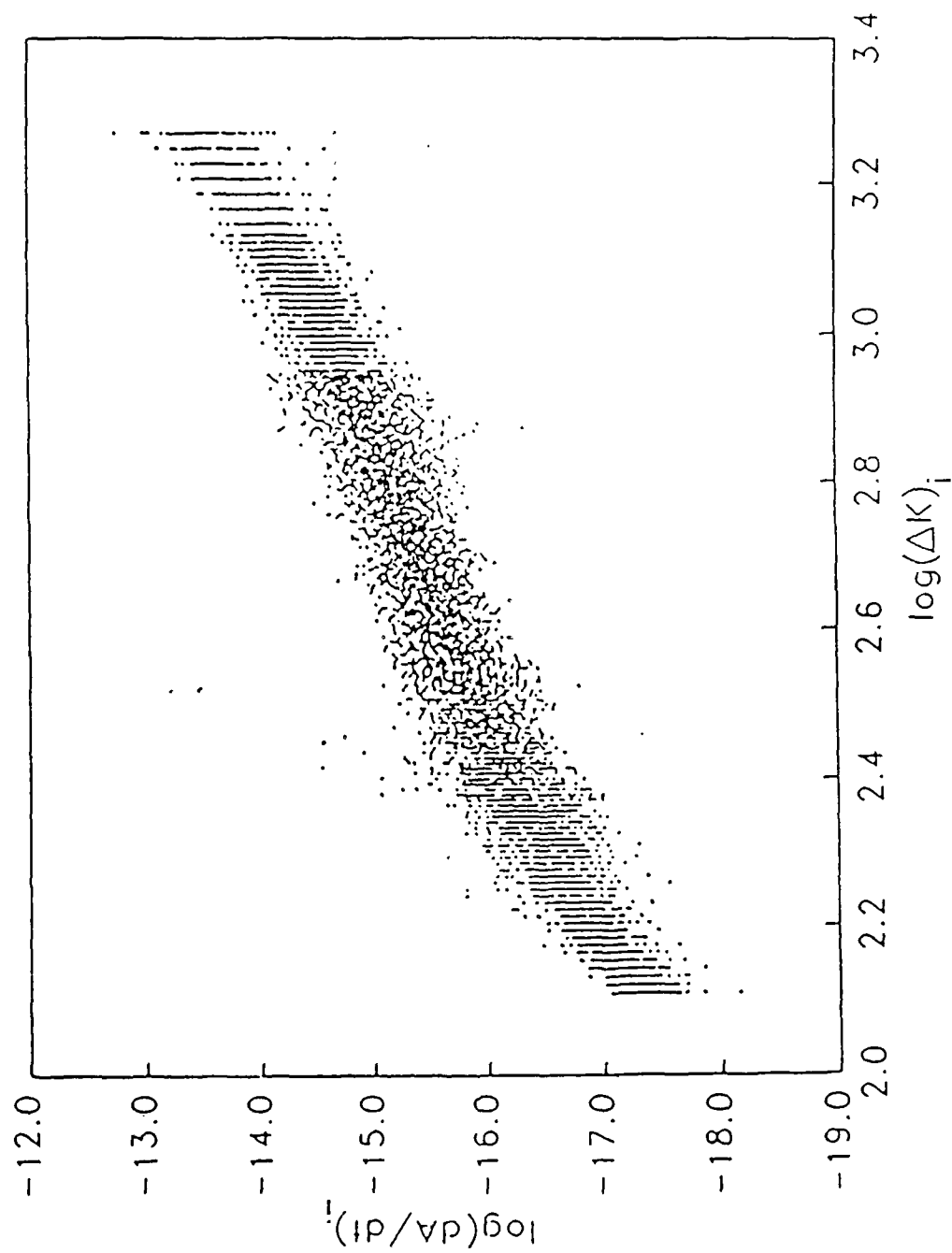


Figure 13 $\log(da/dt)_i$ versus $\log(\Delta K)_i$ for the Virkler data.

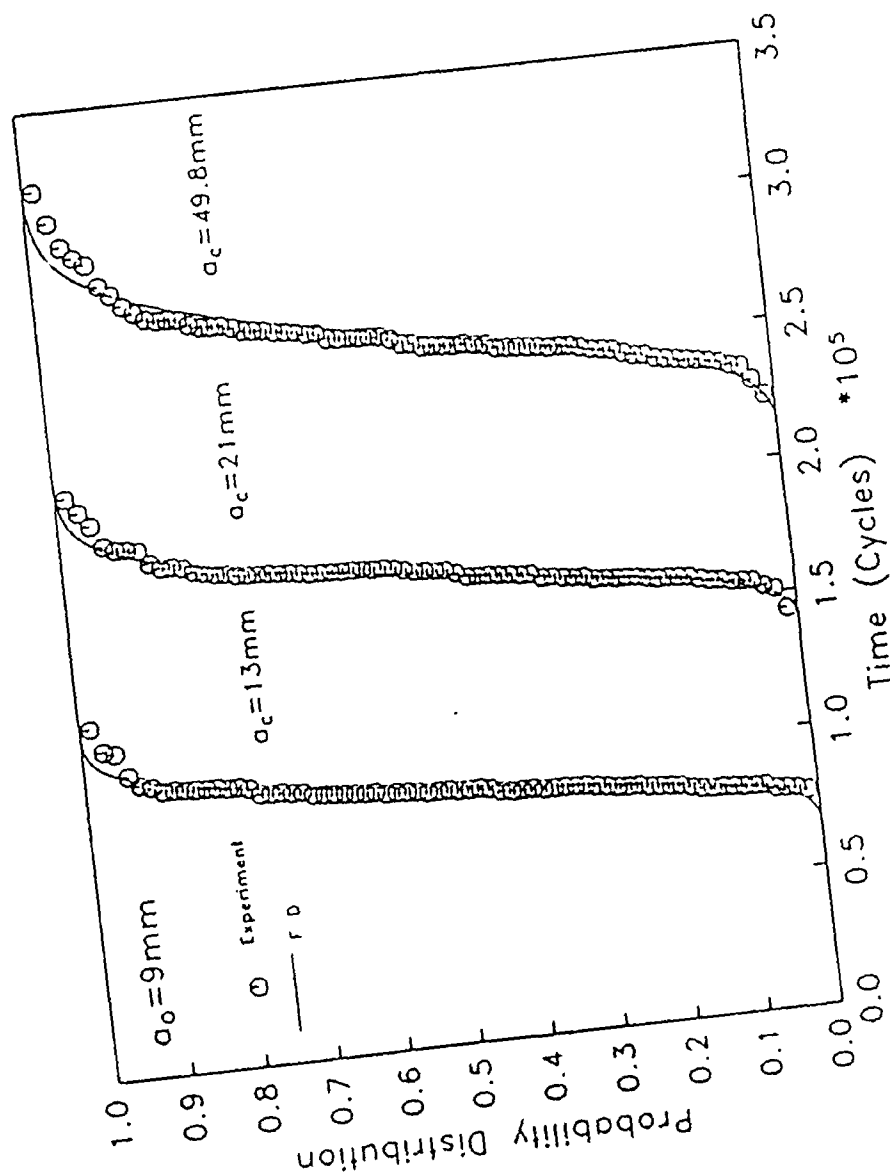
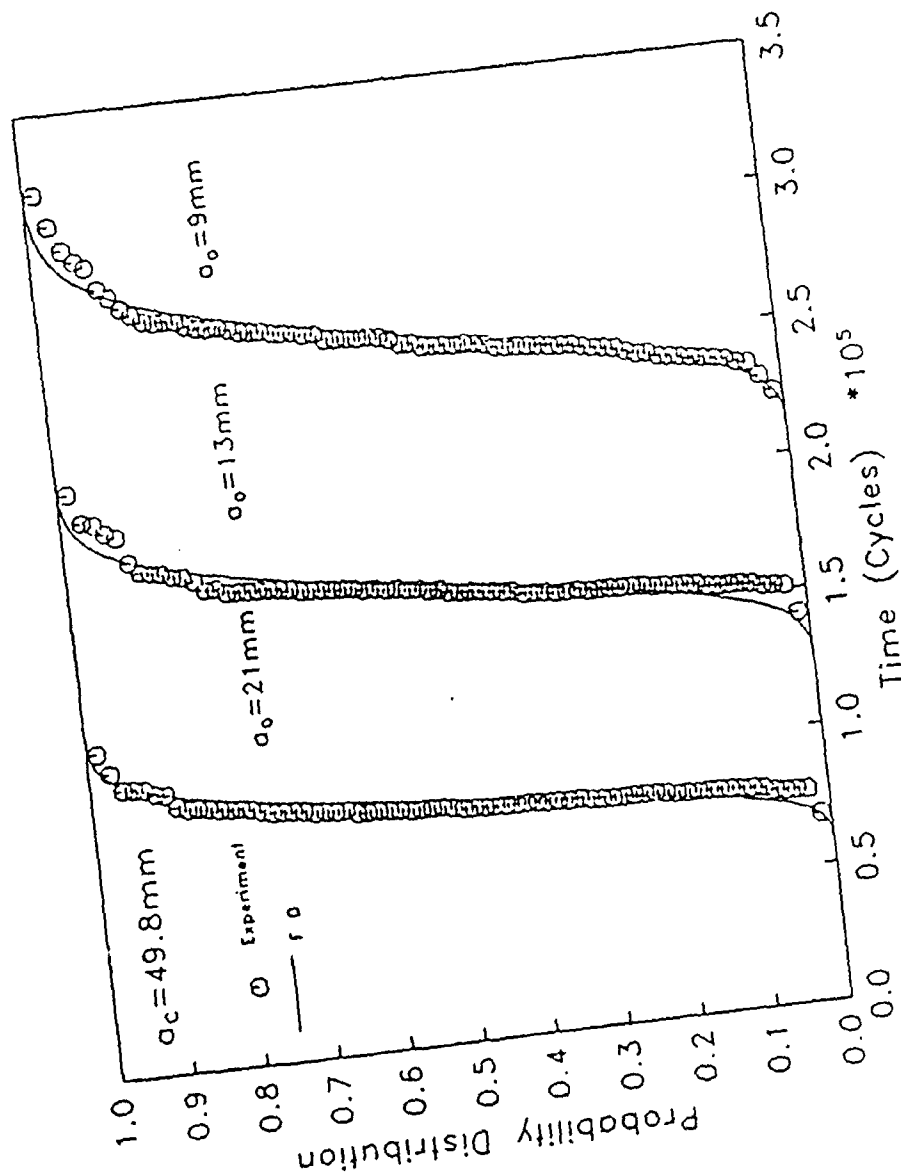


Figure 14

Finite difference solutions for the distribution function of the random time to reach the critical crack size $a_c = 13$ mm, $a_c = 21$ mm and $a_c = 49.8$ mm with the initial crack size $a_0 = 9$ mm. Virkler data using the cubic law



Finite difference solutions for the distribution function of the random time to reach the critical crack size $a_c = 49.8 \text{ mm}$, with the initial crack size $a_0 = 21 \text{ mm}$, $a_0 = 13 \text{ mm}$ and $a_0 = 9 \text{ mm}$. Virkler data using the cubic law

Figure 15

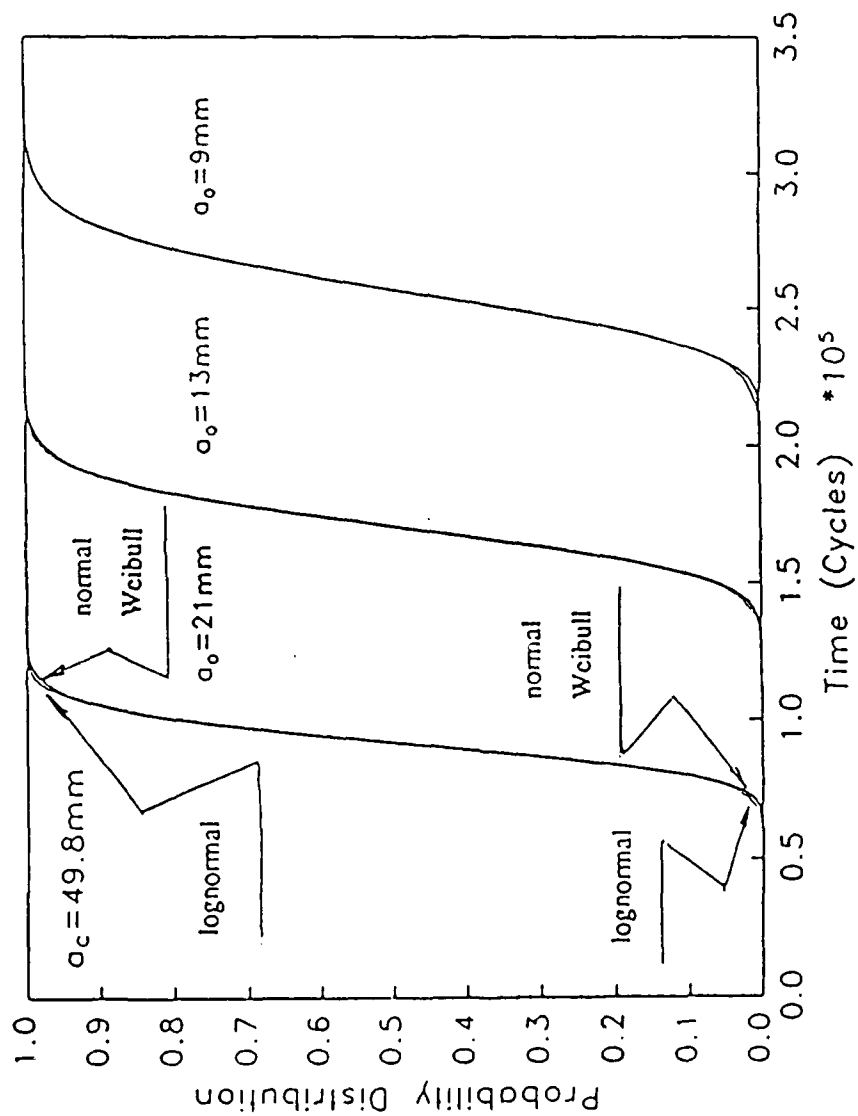


Figure 16 Comparison of finite difference solutions for the distribution function of the random time to reach the critical crack size $a_c = 49.8$ mm with the initial crack size $a_0 = 21$ mm, $a_0 = 13$ mm and $a_0 = 9$ mm. Virkler data using the cubic law and several distribution assumptions on the marginal distribution of the random process $X(t)$.

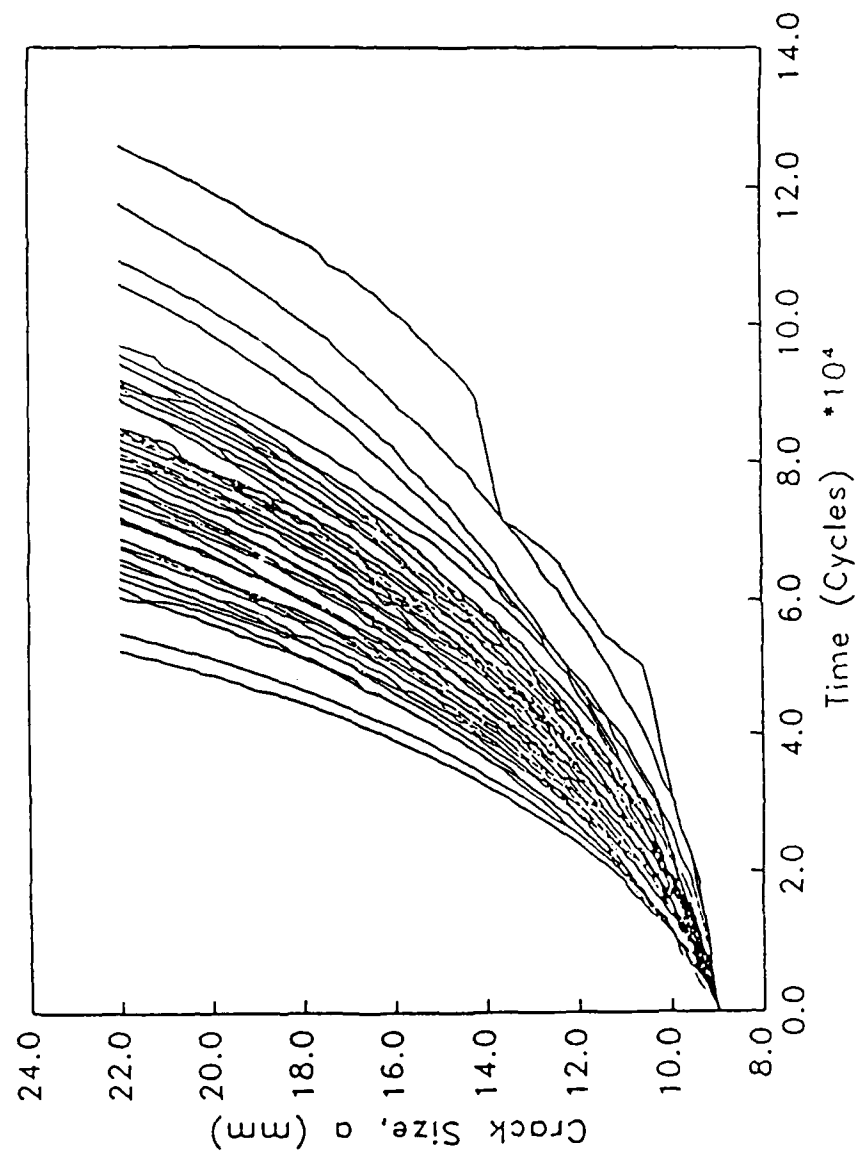


Figure 17(a) Crack growth curves for 60 replicate tests observed by Ghonem and Dore, test I. $R=0.6$

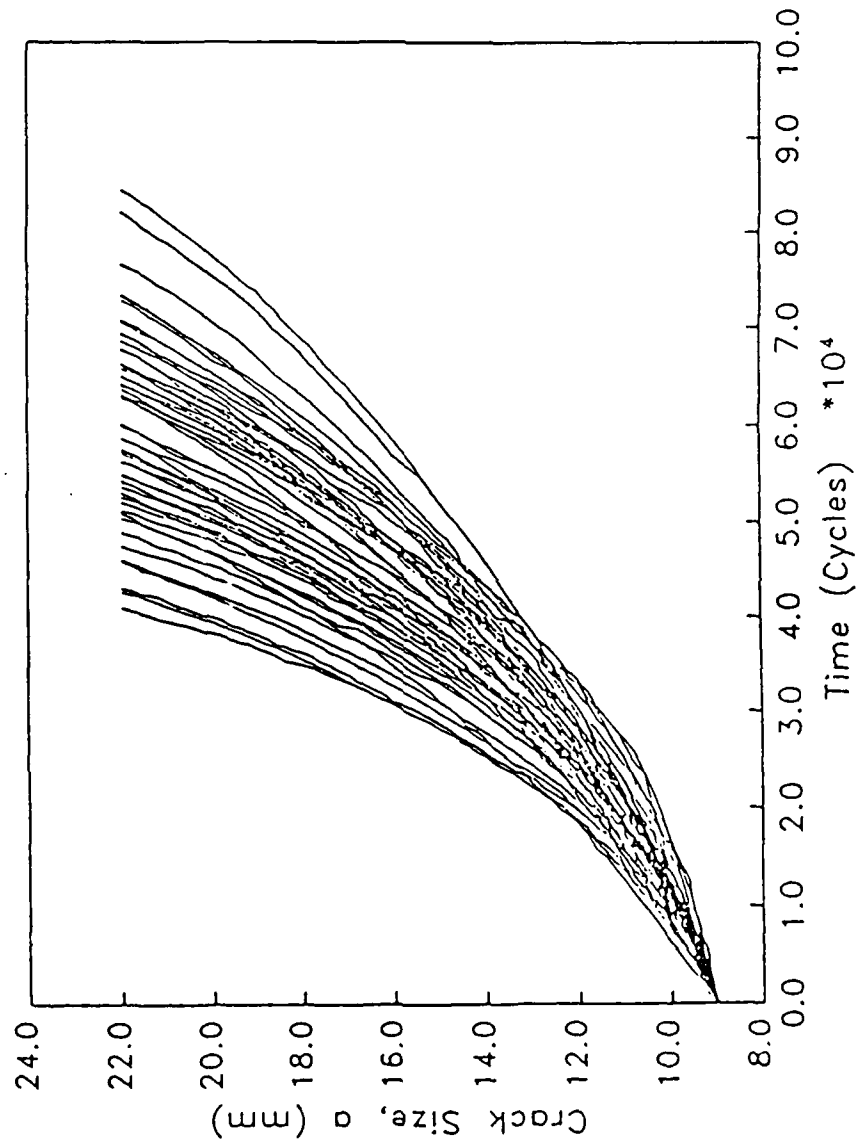


Figure 17(b) Crack growth curves for 60 replicate tests observed by Ghonem and Dore, test II. $R=0.5$

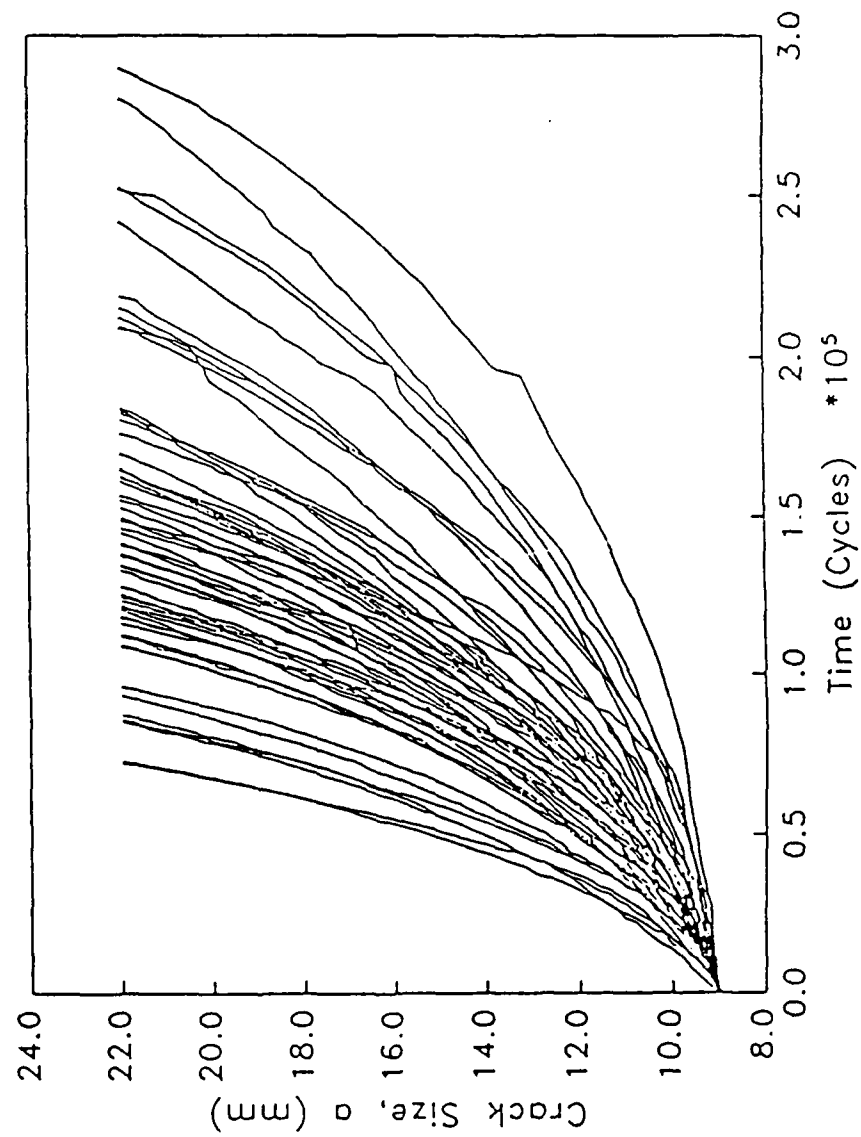


Figure 17(c) Crack growth curves for 60 replicate tests observed by Ghonem and Dore, test III. $R=0.4$

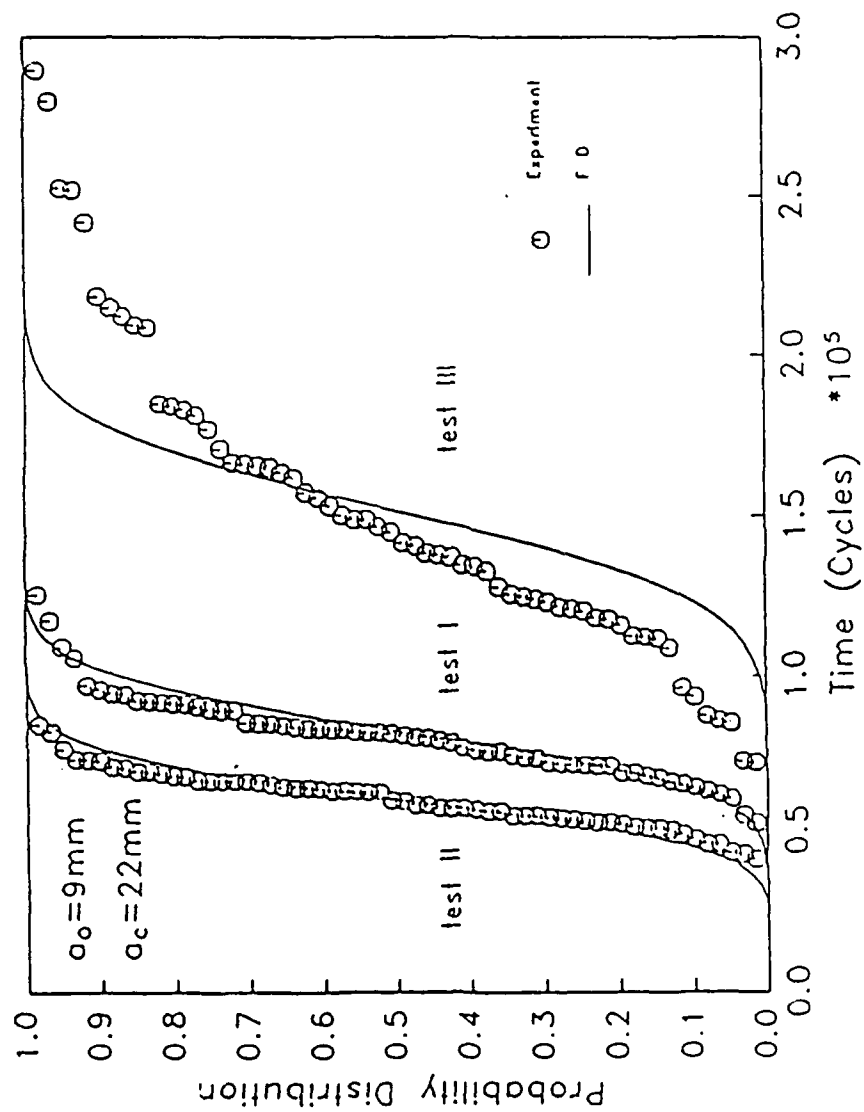


Figure 18

Finite difference solutions for the distribution function of the random time to reach the critical crack size $a_c = 22 \text{ mm}$ with the initial crack size $a_0 = 9 \text{ mm}$. Ghonem and Dore data using the cubic law. (test I, $R=0.6$, test II, $R=0.5$, test III, $R=0.4$)

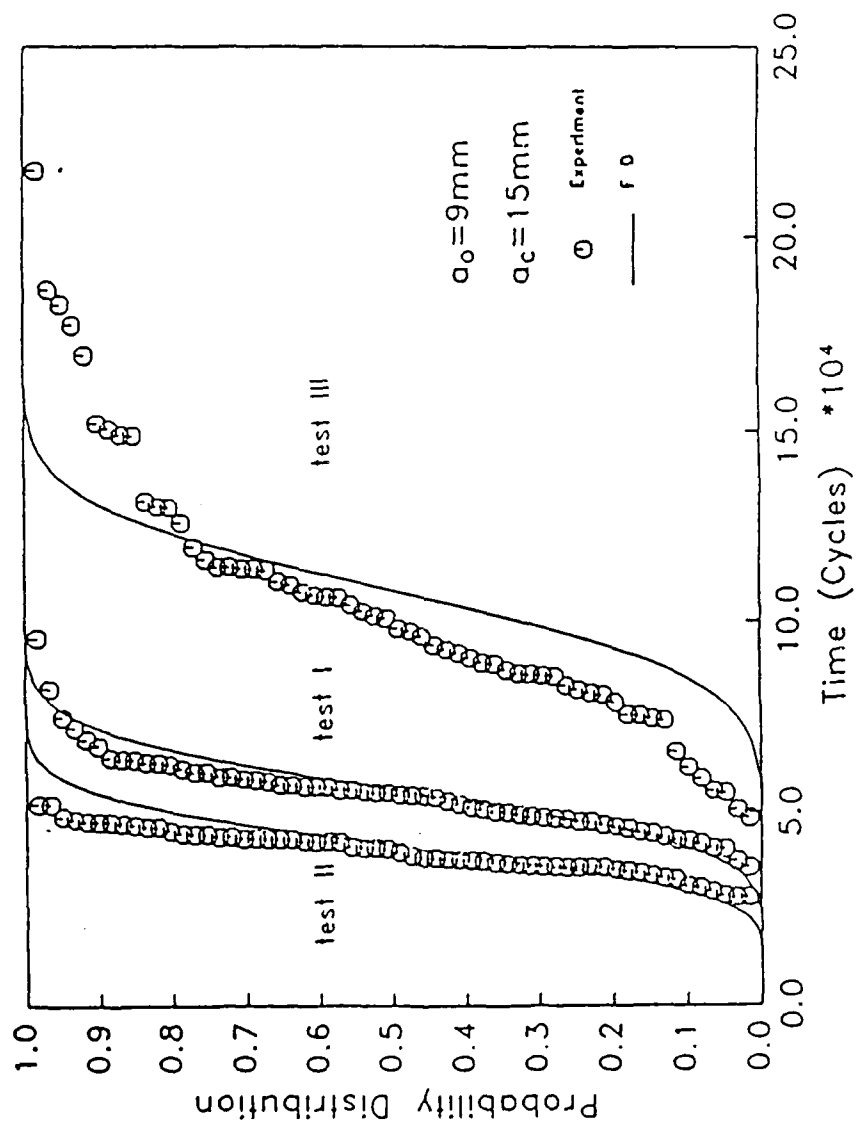


Figure 19

Finite difference solutions for the distribution function of the random time to reach the critical crack size $a_c = 15 \text{ mm}$ with the initial crack size $a_0 = 9 \text{ mm}$. Ghonem and Dore data using the cubic law. (test I, $R=0.6$, test II, $R=0.5$, test III, $R=0.4$)

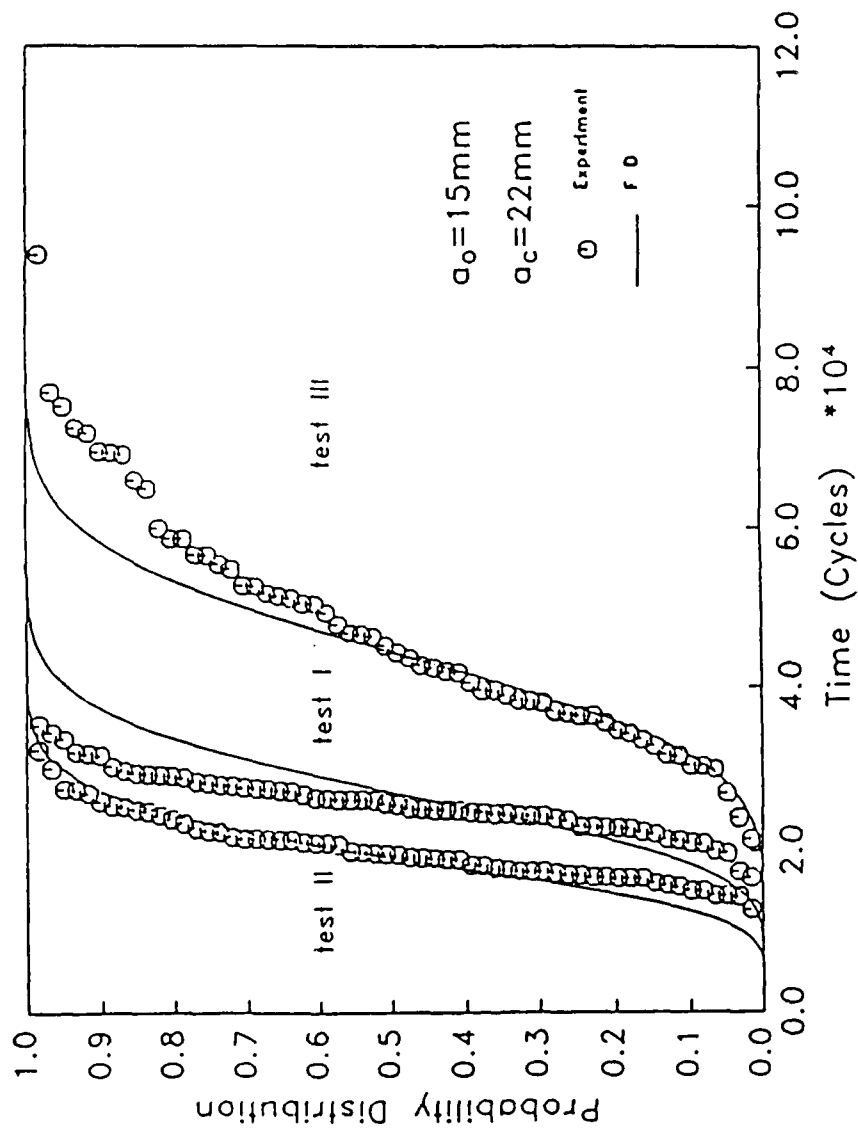


Figure 20

Finite difference solutions for the distribution function of the random time to reach the critical crack size $a_c = 22$ mm with the initial crack size $a_0 = 15$ mm. Ghonem and Dore data using the cubic law. (test I, $R=0.6$, test II, $R=0.5$, test III, $R=0.4$)

FINAL REPORT NUMBER 84
AN INVESTIGATION OF THE FLOW FIELD IN
SHOCK WAVE/BOUNDARY LAYER/BLEED INTERACTIONS
PENDING APPROVAL
Dr. Awatef Hamed
210-9MG-061

FATIGUE CHARACTERISTICS OF F-16 COMPOSITE TRANSPARENCY
MATERIAL DETERMINED BY LONG-TERM AND ACCELERATED METHODS

YULIAN B. KIN
ASSOCIATE PROFESSOR OF MECHANICAL ENGINEERING

PURDUE UNIVERSITY CALUMET
SCHOOL OF PROFESSIONAL STUDIES
ENGINEERING DEPARTMENT

THE PROJECT IS SPONSORED BY THE AIR FORCE OFFICE OF
SCIENTIFIC RESEARCH AND CONDUCTED BY THE UNIVERSAL ENERGY
SYSTEMS, INC.

GRANT NO. S-210-9MG-038

FEBRUARY 1990

ABSTRACT

There are complaints of fatigue failures of the F-16 transparencies and, therefore, a need to improve the design to prolong the canopy fatigue life and reliability. At present, no experimental fatigue statistics on the materials used for the F-16 transparency exist. Hence, it is necessary to obtain reliable long-term fatigue test data. The development of test procedures and the performance of such tests to obtain reliable fatigue parameters is the basic goal of this project. Note that the long-term test procedure requires the breaking of 20 to 30 identically prepared specimens and 15 days to one month to complete. Thus, manufacturers do not perform a conventional fatigue test in spite of its obvious utility. Therefore, there is a definite need for an accelerated fatigue test which can be completed in approximately one day. The fatigue parameters determined in this study can be used in the accelerated test procedure project development.

ACKNOWLEDGEMENTS

The project was initiated as a continuation of research started by the principal investigator at the Flight Dynamic Laboratory of the Wright-Patterson Air Force Base in the Summer of 1988.

Sponsorship by the AIR FORCE OFFICE OF SCIENTIFIC RESEARCH, BOLLING AFB, DC and financial support from Universal Energy Systems, Inc. (Mini Grant Award S-210-9 MG-038) is gratefully acknowledged.

Particular thanks to Dr. Arnold H. Mayer and Mr. Robert McCarty for their help in obtaining this award. Their interest and visits to Purdue University Calumet during different phases of the project served as a source of encouragement. Special thanks to Mr. Mike Gran for his technical support during the entire project.

PURDUE UNIVERSITY CALUMET provided financial and equipment support to make this project possible.

LIST OF FIGURES AND TABLES

Figure 1	Specimens used in the study
Figure 2	MTS flexure fatigue fixture
Figure 3	Loading diagram
Figure 4	S-N diagram plotted from the results of fatigue tests for the polycarbonate specimens with stress concentrators
Figure 5	S-N diagram plotted from the results of fatigue tests for the solid polycarbonate specimens
Figure 6	S-N diagram plotted from the results of fatigue tests for the polycarbonate specimens with and without stress concentrators
Figure 7	Failed Specimen
Figure 8	Failed Specimen
Figure 9	Failed Specimen
Table 1	Testing Regimes
Table 2	Test data sheet
Table 3	Test Results. Solid polycarbonate specimen.
Table 4	Test Results. Polycarbonate specimen with stress concentrator.

INTRODUCTION

There are recent complaints of F-16 transparency failures in flight [1, 2, 3]. The nature of failures is not quite clear, but some evidence implies that transparency life is limited by fatigue [4]. At present, no experimental fatigue statistics on the composite material used for F-16 transparency were found. Therefore, today no data exists that allows life prediction for a canopy based on fatigue or crack propagation, and thus no basis for comparison of new materials and designs taking into consideration their resistance to fatigue and crack propagation.

The F-16 transparency is manufactured from a laminated composite material. Components of the composite are an acrylic face ply, a polycarbonate ply, interlayers, and coatings with some variations among the vendors. Design of the canopy allows to unload an acrylic ply and hence the structural polycarbonate ply of the composite used is the primary concern during fatigue investigation.

Note that a long-term fatigue test procedure requires the breaking of 20 to 30 identically prepared specimens and 15 days to one month to complete. Thus, manufacturers do not perform a conventional fatigue test in spite of its obvious utility. Therefore, there is a definite need for an accelerated test which can be completed in approximately one shift and this is an important future goal which can be achieved using the fatigue test results described in this report.

OBJECTIVES

The major objectives of the study were:

- 1) Development of a long-term fatigue test procedure for specimens manufactured from F-16 transparency material, and performance of the test. During this part of the project a flexure fatigue failure mechanism was investigated because it was not clear what specimen conditions should be considered as a failure -- cracks, significant load drop, or complete breakage.
- 2) Determination of the families of S-N fatigue curves and basic fatigue parameters -- fatigue strength for specified life, knee points (if any), and fatigue curve slopes (for linear functions).
- 3) Test and comparison of fatigue parameters for specimens with stress concentrators (holes) and without stress concentrators.
- 4) Development of a draft of the procedure for an accelerated fatigue test using the statistics gained during the long-term fatigue test performed.

MATERIAL AND SPECIMENS

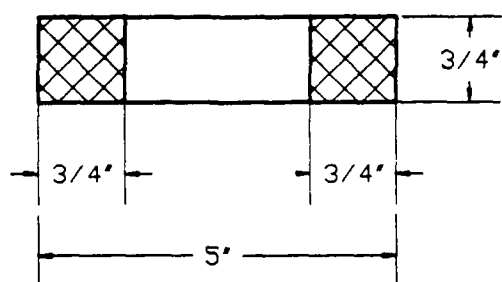
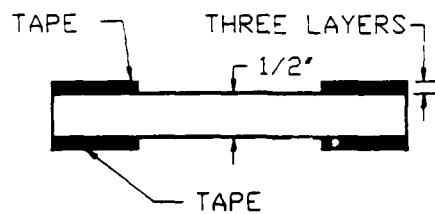
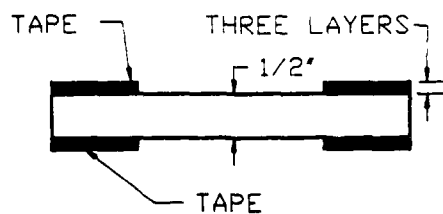
The material used was supplied by Wright-Patterson Air Force Base. The testing coupons were cut from the polycarbonate sheet extruded by Mobay Plastics. The 0.5-inch thick sheet was pressed and polished at Texstar Plastics in Dallas. The military specification for this type of polycarbonate is MIL - P - 83310.

The configuration and dimensions of the test specimens are shown in Fig. 1. The specimens were cut by a fine band saw with the lowest possible speed and using a cooling liquid. The holes were also drilled very slowly with intermittent stops and using cooling liquid. The hole edge burrs were not removed to prevent invisible damage. The cut specimens were divided into two groups. In the first group the edges were left as they were after machining. All machined specimens in the second group were polished on the edges by carbimet paper disks for automet attachment. The 8" x 2.5" self-adhesive back disks NO. 30-5158-120, grits 120-180, were manufactured by BUEHLER LTD. The 3/4" core-series 17-0310 scotch tape was used to protect from damage the gripping area of the specimens. The scotch tape was bonded in three layers on each end of the specimen. It took usually about 10-15 minutes after the beginning of the test to adjust the loading regime assigned due to formation of "bed" by hard jig rollers in relatively soft tape layers.

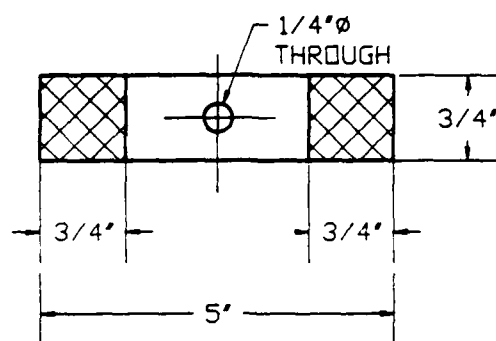
EQUIPMENT, FAILURE CRITERIA, TEST PROCEDURE

The flexure fatigue tests were conducted on an MTS machine using four point MTS flexure system to provide pure bending. Actual flexure fixture and loading diagram are shown in Figures 2 and 3.

Note that load reading on the MTS machine controller is P, in other words the load reading on the machine device doubled comparing with that shown in Figure 3. The appropriate support and load spans were selected to provide



SPECIMEN
WITHOUT STRESS
CONCENTRATION



SPECIMEN
WITH STRESS
CONCENTRATION

FIG. 1 SPECIMENS USED IN STUDY.

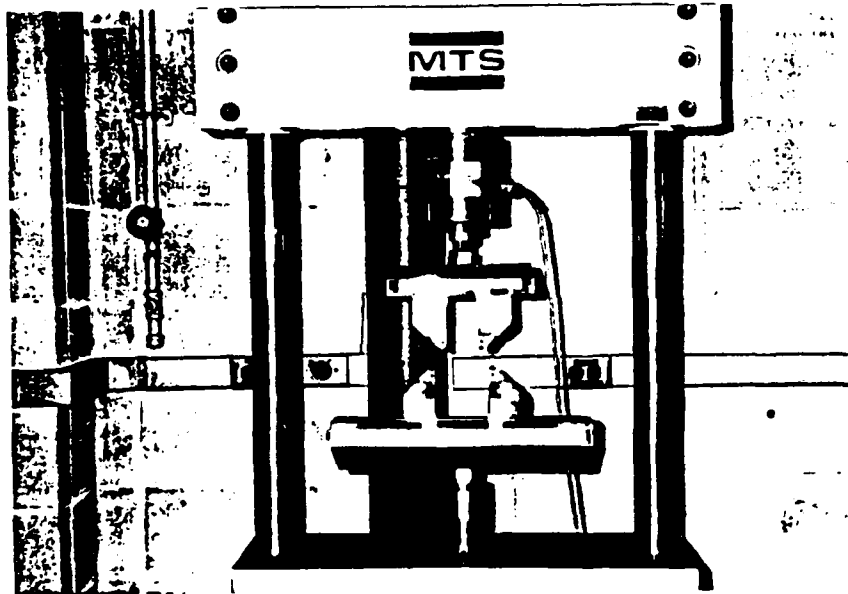
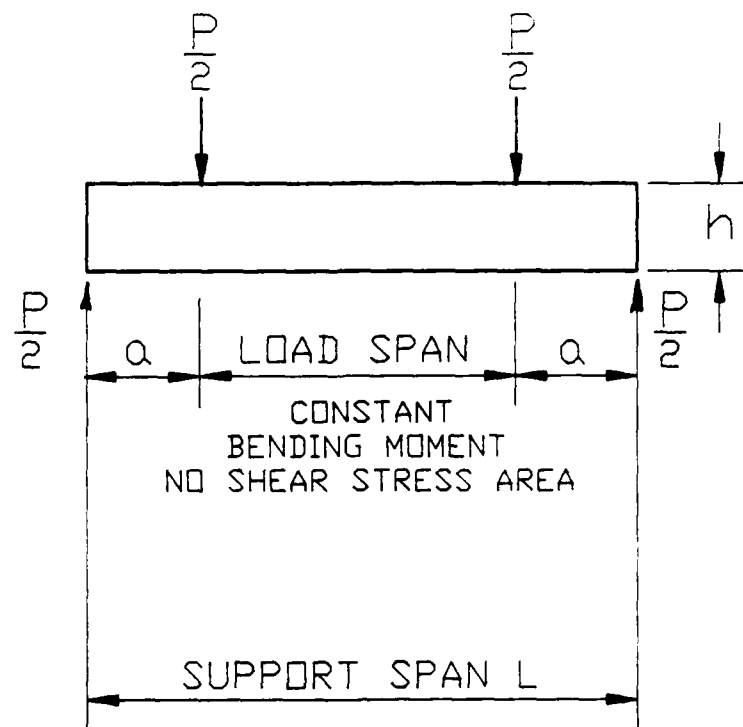


Figure 2. MTS Flexure Fatigue Fixture



MAX DEFLECTION:

$$Y_{\text{MAX}} = \frac{Pa}{48EI} (4a^2 - 3L^2)$$

MAX STRESS:

$$\sigma_{\text{MAX}} = \frac{3P(a)}{bh^2}$$

FIG. 3 LOADING DIAGRAM

minimum possible deflection of the specimens. The small deflections provide more stable position of the specimens between jig rollers and permit to assign greater testing frequency.

Three different options were analyzed prior to the assign a final failure criterion.

- 1) Certain percentage load drop can be considered as failure during constant stroke and hence controlled specimen deflection testing. This testing mode permitted crack growth observation and decreased creep influence. But non- uniform and inconsistent load drop did not permit to make a clear test result interpretation. Also constant deflection conditions do not reflect the actual situation.
- 2) During constant load testing the complete separation or certain percentage crack propagation can be considered as failure and the preliminary testing showed that the resultant scatter was significantly less than in the constant stroke test. The constant load mode also better simulates the actual loading.
- 3) Craizing and therefore visibility lost definitely can be considered as failures for the canopy material.
- 4) A minute crack detected by eye can also be considered as a failure because there is no data on how fast an

- 4) A minute crack detected by eye can also be considered as a failure because there is no data on how fast an initial crack will propagate in the polycarbonate sheet tested.

Taking this into consideration the decision was made to perform the test under constant load regime and develop S-N diagrams with different failure criteria (complete separation or 80% crack propagation over the specimen width, craizing, minute crack formation).

The pulsating bending tests were conducted in the laboratory atmosphere (about 75°F and 50% relative humidity). The tests were run at least at four load levels and four specimens were tested at each load level. The regimes are given in Table 1. The ratio of minimum load over maximum load was 0.2 for all tests. The frequency at each load level was set so that the product of the amplitude stress and frequency remained constant for all tests. The testing time per day was not more than 9 hours, hence the possible influence of stops was not considered in this project. The tests continued until specified damage was observed but not longer than 10^6 cycles. The testing data are collected in the form which is given in Table 2. Regression analysis was used to treat the test results.

TEST RESULTS AND DAMAGE DESCRIPTION

The test results are given in Tables 3 and 4 and in Figures 4, 5, and 6. The cracks were always started at the bottom tensile zone of the specimens (Figures 7, 8). In all

Table 1

Testing Regimes.

Variable Bending.

Amplitude Load Lb.		Amplitude Stress, psi	<u>Maximum Stress</u>	frequency
			<u>Minimum Stress</u>	
Plate with Hole	Solid Plate			
180	240	1440	0.2	12
	360	2160	0.2	8
360	480	2880	0.2	6
	600	3600	0.2	5
540	720	4320	0.2	4
750	990	5760	0.2	3

SPECIMEN TYPESPECIMEN NUMBERDIMENSIONROCKWELL HARDNESS NUMBER

MAXIMUM LOAD	MINIMUM LOAD	MEAN LOAD	AMPLITUDE LOAD

DATE	FREQ.	SPAN	SET PT.	CYCLES	COMMENTS
TOTAL NUMBER OF CYCLES					

Table 3

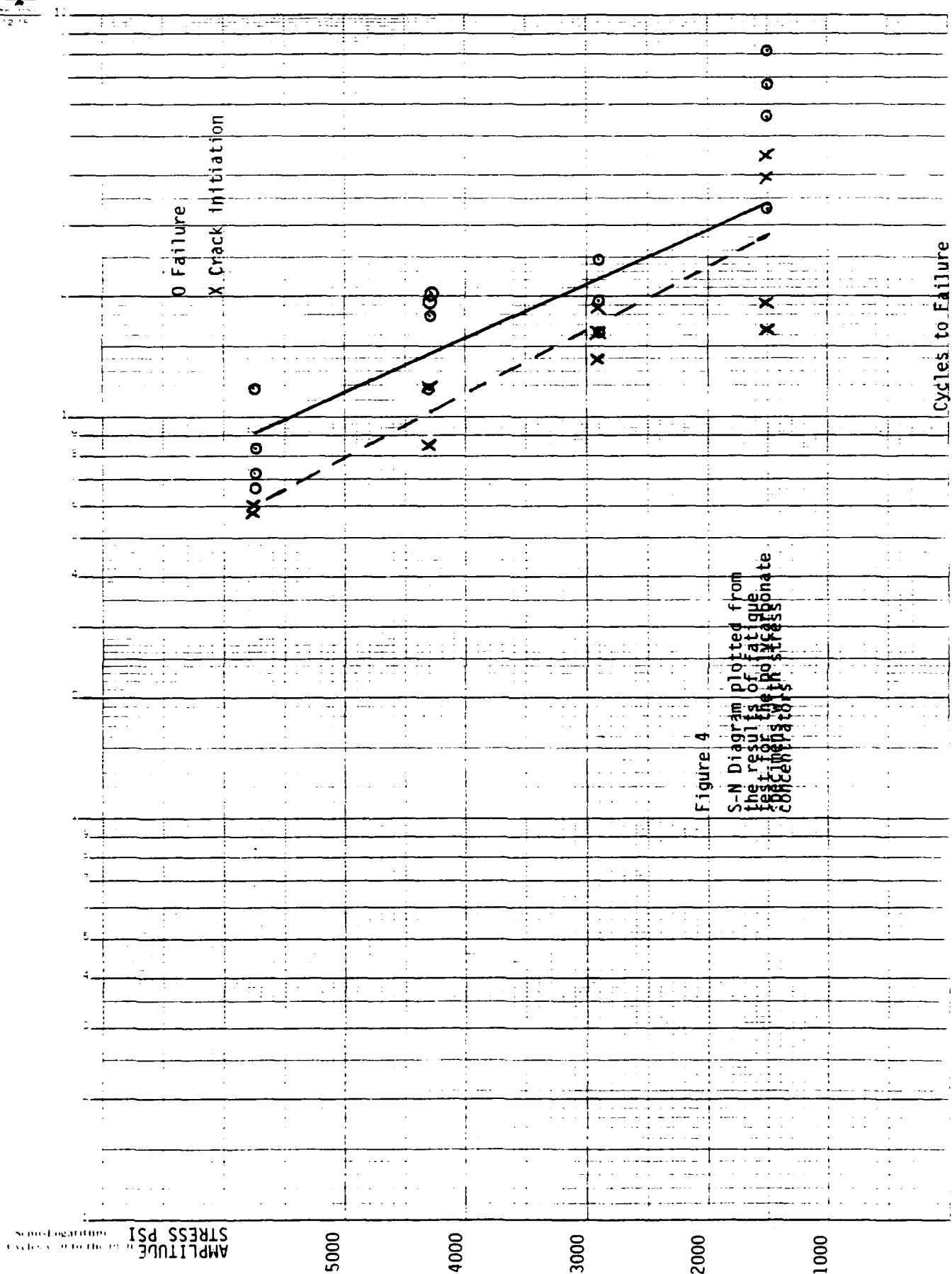
Test results for the solid polycarbonate specimen without stress concentrators. Variable bending.

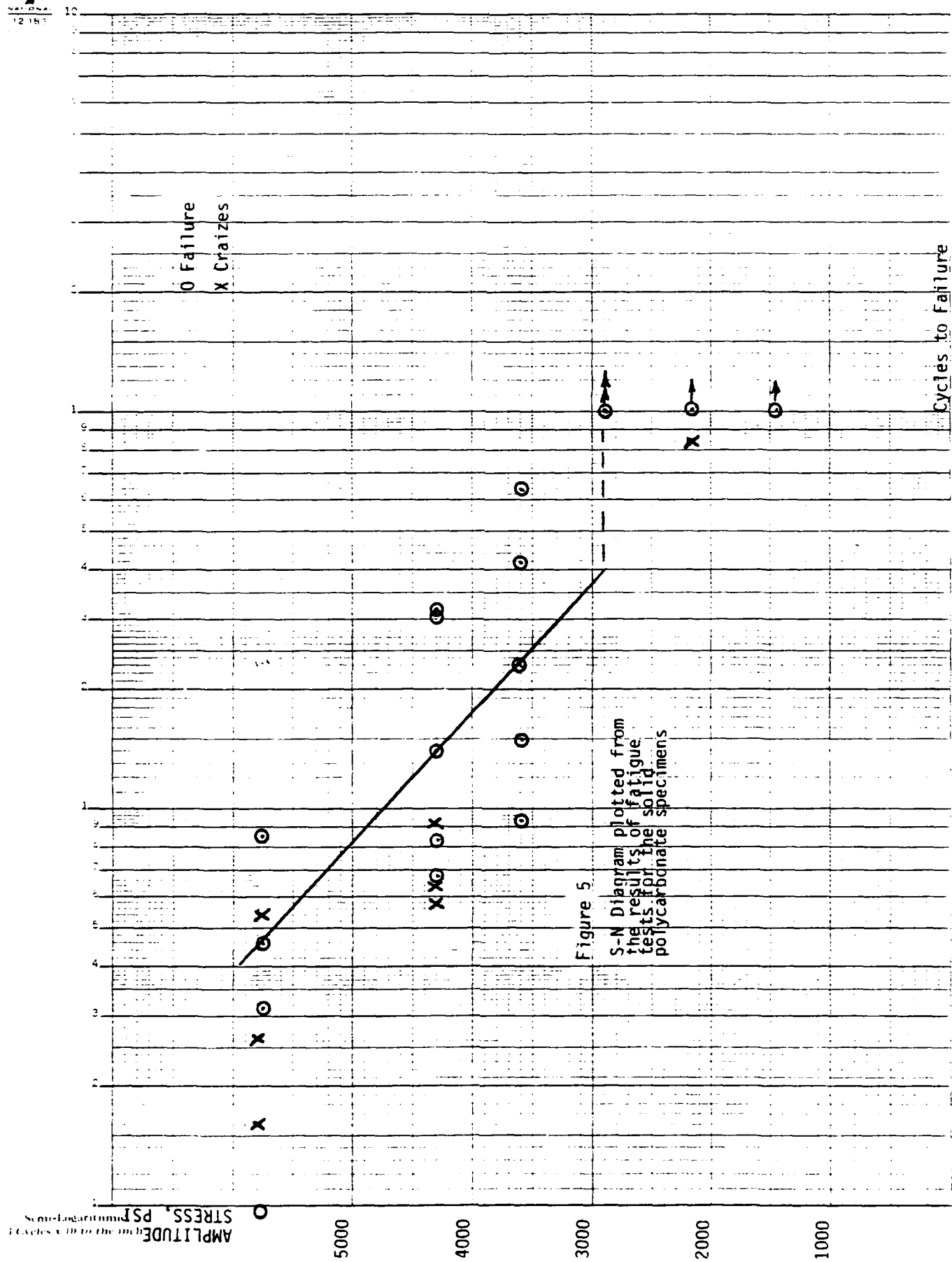
Amplitude load, lb	Amplitude stress, psi	Cycles to failure	Cycles to craizes	Comments
990	5760	8500		
		32200	15100	
		45000	26000	
		64300	53000	
		233700		
720	4320	68600	58300	
		82000	63000	
		140000		
		323000	91300	
		315000		
600	3600	82000		
		152300		
		413000		
		641100		
480	2880	1000000		No failure
		1000000		
360	2160	1187000	831200	Crack initiation
240	1440	1000000		No failure

Table 4

Test results for the polycarbonate specimen with the stress concentrator (1/4" Dia hole), variable bending.

Amplitude load, lb	Amplitude stress, psi	Cycles to failure	Cycles to crack initiation	Comments
750	5760	68600	58000	
		72100		
		84000		
		119000	56000	Craizes
540	4320	117800	75000	
		177900	121000	
		194900		
		201000		
360	2880	163000	140200	
		163200		
		196300	165000	
		245100	185000	
180	1440	331000	164000	
		561100	191000	
		683300	450000	
		811000	390000	





AMPLITUDE
STRESS, PSI

5000

4000

3000

2000

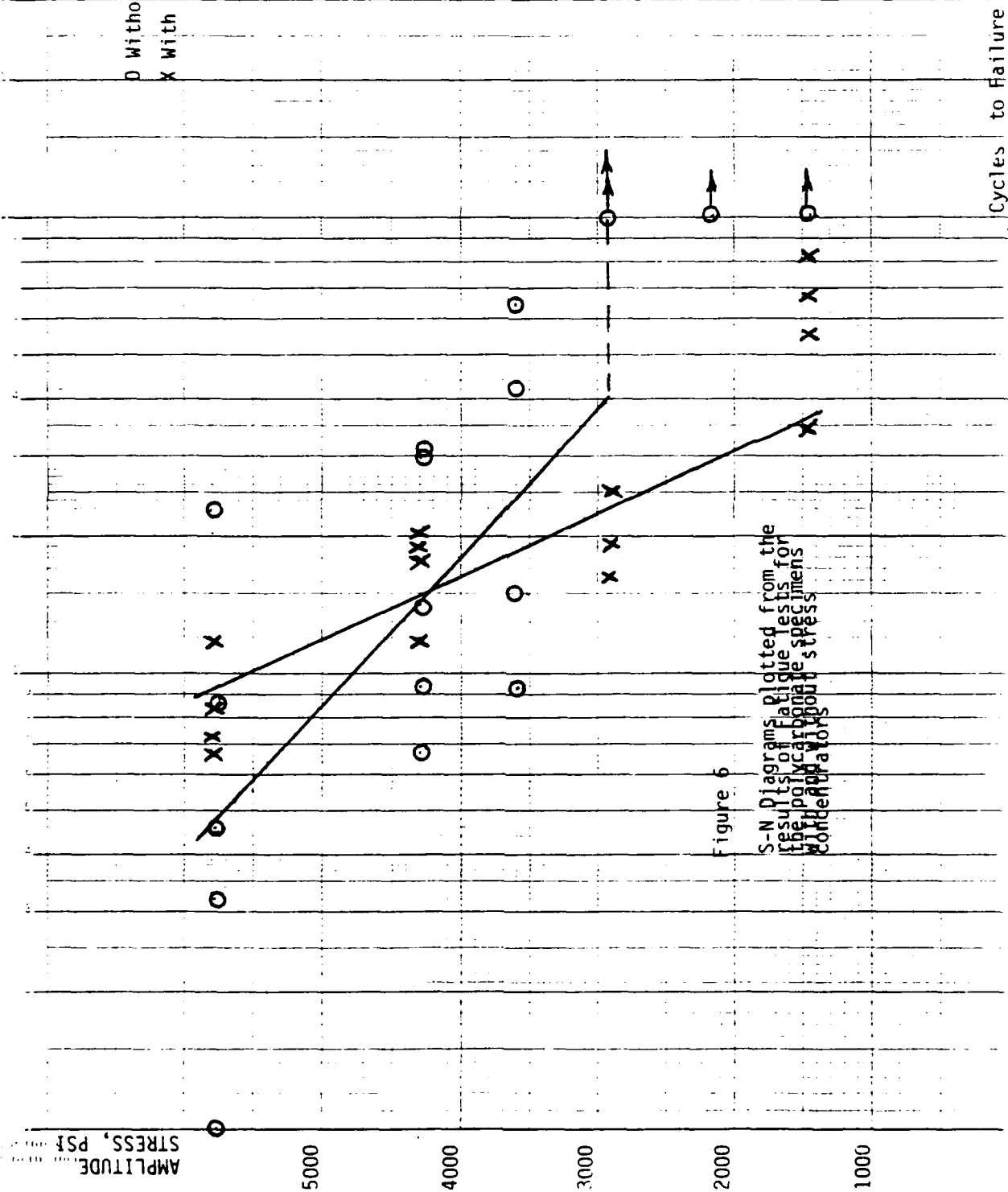
1000

O Without stress concentrator
X With stress concentrator

Cycles to Failure

Figure 6

S-N Diagrams Plotted from the
Results of Fatigue Tests for
the Polycarbonate Specimens
With and Without
Stress Concentrations



tested. Usually craze spot precedes the crack formation and propagates ahead of the crack tip during the entire damage process. Analyzing the photographs (Figures 7, 8, 9, 10, 11) of the specimens tested, we can conclude that damage mechanism is very similar to that described in [5] for crack propagation in polystyrene under fatigue loading. When the visible separate craizes were detected during the high load level testing, the massive craze zones developed after that very fast. It is interesting to note that the lives of specimens before the massive craze spot formation and after that (until complete breakage) are almost the same. For low load levels no massive craze zones were observed. But again in many cases after the initiated crack was easily visible we could detect almost the same number of cycles until breakage that specimen worked before crack initiation. Comparing the S-N diagrams in figures 4, 5, and 6 it can be noted that the stress concentration influence on fatigue life of the tested polycarbonate specimens is significant. The specimens without stress concentration have much longer fatigue life. In all specimens with holes cracks initiated at hole edge in tensile zone and propagated toward the side edge of the coupons tested.

CONCLUSIONS AND PROPOSALS

The results of this study permit to make the following conclusions:

1. The specimens (especially without stress concentrators) have significant life until complete separation after appearance of the massive craizes or minute cracks.

PHOTO 46
SPECIMEN # 10

20X

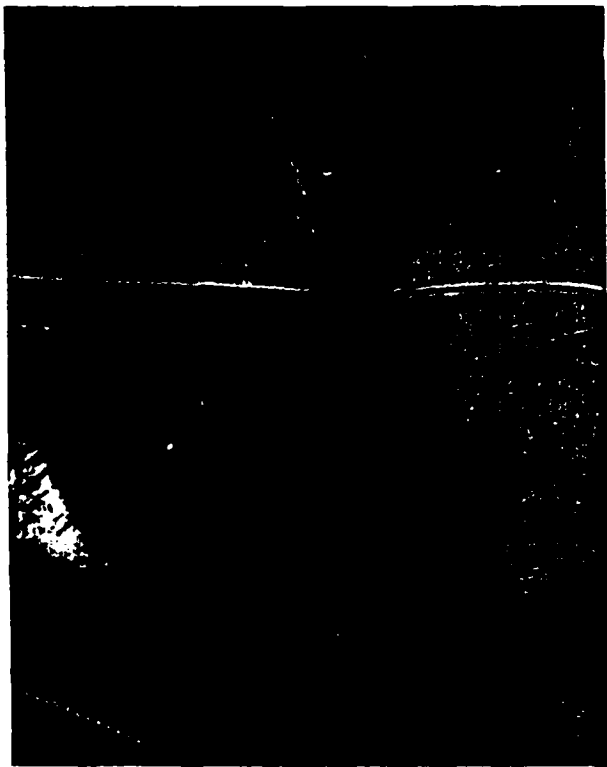


Figure 7. Crack at tensile zone of the solid polycarbonate specimen. Crack is initiated from the edge. Craze spot is located ahead of the crack tip.



SAMPLE 31 PHOTO A
163,000 cycles crack at hole

Figure 8. Crack at tensile zone of the specimen with the 1/4" Dia hole. Crack is started from the hole edge. Craze spot is located ahead of the crack tip.



PHOTO A of specimen 28
Taken at 179300 cycles (over)



PHOTO A of specimen 29
Taken at crack initiation 45,900
cycles

Figure 9. The specimens with stress concentrators. The Craize spot initiation is clear seen at the hole edge of the specimen \$29. Total number of cycles until complete separation for the specimen \$28 is 245000, for the specimen #29=119000.



Specimen 30 photo c
main crack @ 200,800 cycles



Specimen 30 photo A
crack @ 198,500 cycles

Figure 10. The crack propagation in the specimens with the stress concentrators.

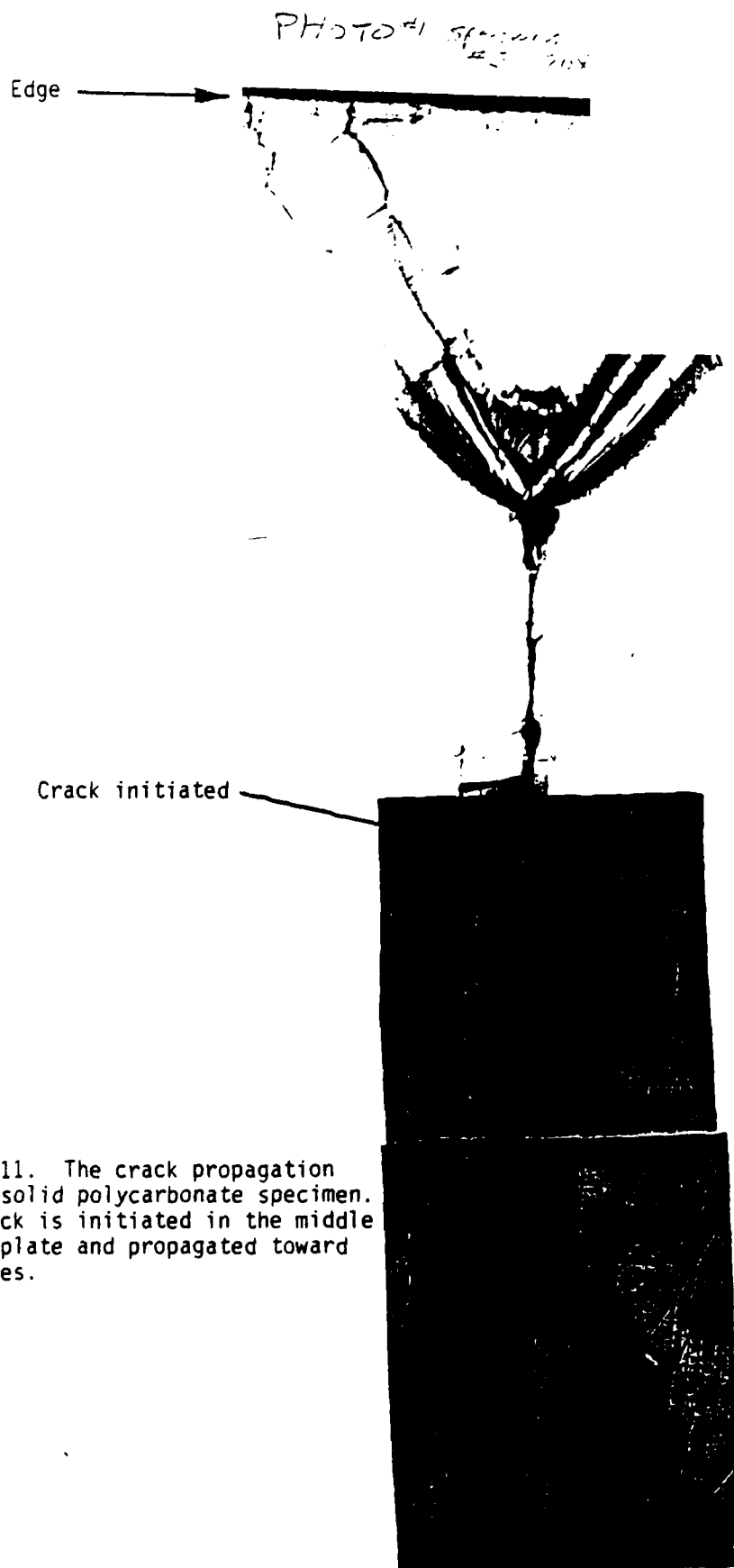


Figure 11. The crack propagation in the solid polycarbonate specimen. The crack is initiated in the middle of the plate and propagated toward the edges.

2. The craizes usually appear only on the specimens tested at high load levels. Therefore, it is possible to make certain judgment about load history by analyzing the specimens after failure.
3. The stress concentration influence on fatigue life of the tested polycarbonate specimens is very strong. The specimens without stress concentration have much longer fatigue life. From this point of view, the frameless canopies without holes for fasteners can be very promising. However, it is important to keep in mind that the scatter of test results for the specimens without stress concentration is greater than that for the specimens with holes. The high scatter of the solid polycarbonate specimen fatigue statistics can be caused by unevenness of the properties along the polycarbonate sheet (manufacturing defects).
4. Additional conventional fatigue tests of canopy materials manufactured by different companies should be run to make a comparison and gain more statistics for reliable conclusions.
5. The investigation of the fatigue characteristics of polycarbonate sheets with different thicknesses are very interesting. It appears and there is some evidence showing strong dependency of the material thickness on the polycarbonate fatigue strength and life. If it is correct, new fundamental changes of the canopy design can be discussed.

6. Using the fatigue parameters determined in this study (fatigue slope and fatigue strength for 10^6 cycles) the attempt to develop accelerated fatigue test technique can be continued. The preliminary draft accelerated technique is proposed in the Appendix to this report. The procedure proposed allows to receive fatigue parameters of the polycarbonate in one or two days and, therefore, allows to control the stability of the manufacturing process. It will be especially useful if the assumption about the unevenness of the properties along the polycarbonate sheet material is correct. The assumption is based on the considerable scatter of the fatigue test results.

REFERENCES

1. Contract No. F-33657-82-2035 Service Report
Investigations SR1 375 S/N 0308, F-16 FWD "C"
Transparency Texstar Plastics, August 22, 1986.
2. Contract No. F-42600-85-D-4910 Service Report
Investigations SR1 374 S/N 0217, F-16 FWD "C"
Transparency Texstar Plastics, August 4, 1986.
3. FIER, M. Kelley, Examination Report Wright-Patterson
AFB, June 27, 1986.
4. Yulian Kin, Contract No. F49620-87-R-009, Failures of
the F-16 Transparencies. Analysis and Failure
Prevention Recommendations.
5. Alexander Chudnovsky, Kamel Chaovi, Abdelsamie Moet,
"Curvilinear Crack Layer Propagation," Journal of
Material Science Letters 6 (1987) 1033-1038.

Appendix

ACCELERATED FATIGUE TEST PROCEDURE

INTRODUCTION

A conventional fatigue test requires breaking of from 20 to 30 carefully prepared specimens, and up to one month to complete. Because of this, many manufacturers do not perform a fatigue test in spite of its obvious utility and there is a definite interest in an accelerated fatigue test.

The accelerated technique for the specified type of specimens can be reliably developed if the statistics of conventional fatigue test of similar specimens are known. Therefore, the results of preliminary run conventional fatigue test will be used to assign certain parameters and estimate the error of the accelerated test.

Taking into account the fact that accelerated fatigue methods were never before applied to the F-16 transparency material, it is not clear what kind of accelerated technique (if any) can give the best results.

Locaty's accelerated technique can be recommended to start an investigation. It is assumed that time to run the proposing accelerated test will be within 10 hrs.

LOCATY'S METHOD FOR ACCELERATED DETERMINATION OF FATIGUE STRENGTH

1. The idea and short description of the method.

The method is based on the concept of cumulative fatigue

damage or Palmgren- Minor rule considering $\sum \frac{n_i}{N_i} = 1-5$,
 n_i = The number of cycles which specimen worked in the
 specified test regime.

N_i = The number of cycles which specimen could work
 according to fatigue curve received from the results of the
 conventional fatigue test of the same type of specimens.

The loading program and the treatment of results are
 presented in Fig. 1 and 2. Fig. 1 shows three fatigue
 curves (for example, 5%, 50%, and 95% probability of
 failure) received from a conventional fatigue test.

During an accelerated test the specimen works, for example,
 for 10^5 cycles at the first load level, then the load is
 increased and the specimen is again tested for 10^5 cycles.
 The procedure is repeated until the instant when the
 specimen fails. Then using Fig. 1, the magnitudes of

$$\sum \left(\frac{n_i}{N_i} \right)_C, \quad \sum \left(\frac{n_i}{N_i} \right)_B, \quad \sum \left(\frac{n_i}{N_i} \right)_A$$

determined. With these three parameters (or, if necessary,
 a greater number of points) and knowing corresponding
 stresses, we can find the coordinates of the points which
 result in the curve shown in Fig. 2. Now, if according to
 an accepted hypothesis fatigue strength corresponds to a
 definite value (for example, $\sum \frac{n_i}{N_i} = 1$), we can easily
 determine the fatigue strength magnitude (Fig. 2).

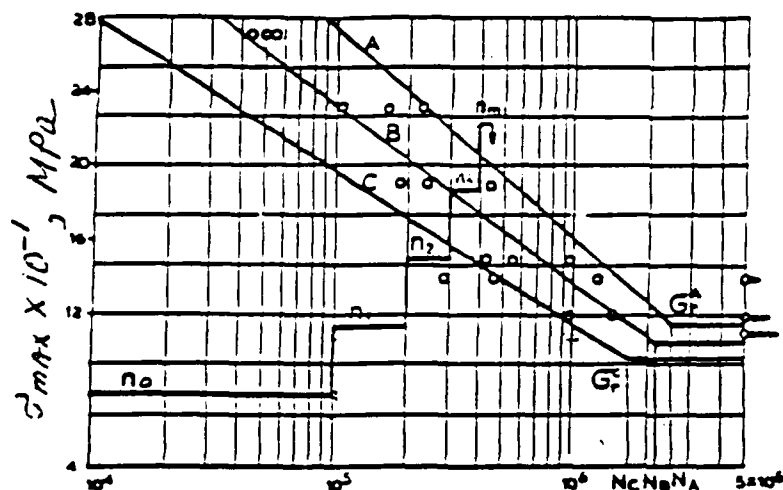


Fig. 1. Loading Program

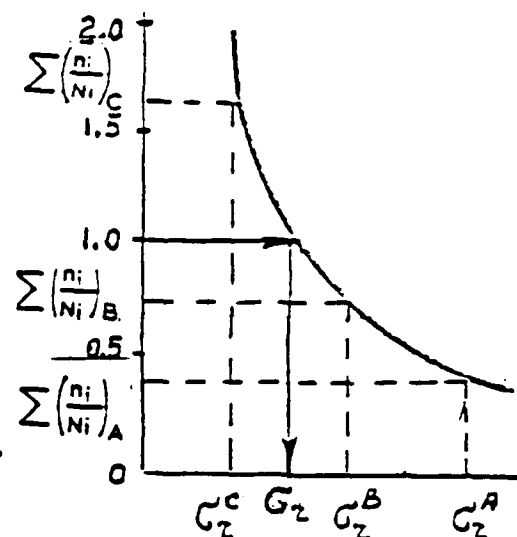


Fig. 2 Graphical Determination of Fatigue Strength

2. Nomenclature and symbols

Parameter	Symbol	Unit	Reference
Initial stress	σ_0	Pa	Fig. 1
Stress increment	$\Delta \sigma$	Pa	Fig. 1
Initial number of cycles	n_0	Cycle	Fig. 1
Number of cycles at ith level of stress	n_i	Cycle	Fig. 1
Rate of stress increment	λ	Pa/Cycle	
Stress at failure	σ_F	Pa	Fig. 1
Fatigue strength determined by acceler, method	σ_{Acc}	Pa	Fig. 2
Number of cycles at ith level of stress determined during conventional fatigue test	N_i	Cycle	
Sum of relative lives	$\sum \frac{n_i}{N_i}$		m is the total number of load levels

Fatigue strength corresponding to the curve A, B, C respectively: σ_F^A ; σ_F^B ; σ_F^C Pa

Expected fatigue strength

σ_{Exp} Pa

$$\sigma_{Exp} = \sigma_F^B$$

Knee points (if any) on curves A, B, C respectively

$$\begin{aligned} N_0^A \\ N_0^B \\ N_0^C \end{aligned} = N_{Exp}$$

Fig. 1

Slopes of curves A, B, C respectively

$$\begin{aligned} K_A \\ K_B \\ K_C \end{aligned}$$

$$K = \frac{\sigma_{m+1} - \sigma_m}{\log N_m - \log N_{m+1}}$$

3. Loading Regimes

Intervals of the initial load level are assigned from the inequality

$$\sigma_{Exp} < \sigma_0 < 1.2 \sigma_{Exp}$$

Magnitude of σ_{Exp} , N_{Exp} , and K_A , K_B , K_C are assigned

after the completion of the conventional test. Optimal

value α of the stress increment rate depends on the selected

ratio σ_0 / σ_{Exp} and can be found from the Fig. 8.

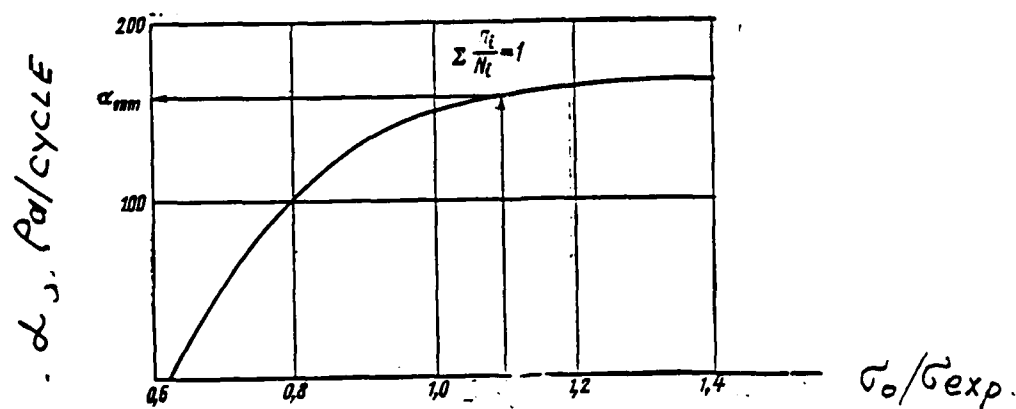


Fig. 8. Stress Increment Rate Versus σ_0 / σ_{Exp} Ratio

The selected ratio σ_0/σ_{exp} is located on the horizontal axis, then the perpendicular is drawn upwards until it intersects the curve. The vertical coordinate of this point represents the recommended stress increment rate. Optimal intervals for the stress increment are found from the expression

$$0.05 \sigma_{exp} < \Delta \sigma < 0.15 \sigma_{exp}$$

Value of n_i is determined from $n_i = \Delta \sigma / \Delta$

In case when n_i appears to be greater than 3×10^5 , it is necessary to decrease $\Delta \sigma$

Most of the recommendations are based on test experience with metal and corrections are quite possible.

4. Termination of the test and record of the test results.

Each specimen should be visually examined during stops before each load change. A specimen has to remain in clamping position during inspection and all observed crazes and cracks should be indicated. Only the tensile side of a specimen is inspected. The test is terminated complete breakage of a specimen. The forms to record test results are given below.

Protocol #1

Specimen number:

Specimen type: (size):

Frequency:

Eccentric number:

Initial stress σ_0 :

Stress increment rate Δ :

Table #1. Accelerated test results.

MAXIMUM STRESS, MPa	LIFE, CYCLES	CURVE A		CURVE B		CURVE C	
		N _i	$\frac{n_i}{N_i}$	N _i	$\frac{n_i}{N_i}$	N _i	$\frac{n_i}{N_i}$
1							
2							
3							
4							

$$\sum \left(\frac{h_i}{N_i} \right) = \sum \left(\frac{h_i}{N_i} \right) = \sum \left(\frac{h_i}{N_i} \right) =$$

The results of tests for all identical specimens are recorded in Table 2.

Table 2. Comparison of fatigue strength of specimens. Accelerated (Locaty's method) and conventional procedures.

Number of specimen	Accelerated method		Long Term Error method %
	Fatigue strength (Maximum stress) of the specimen, MPa	Average Fatigue Strength, MPa	Fatigue strength, MPa
1			
2			
3			
4			

CONVERGENCE OF UPPER-BOUND OPTIMUM
DESIGN OF LARGE-SCALE STRUCTURES
WITH SPECIFIED FREQUENCY BANDS

BY

Oliver G. McGee and Khing F. Phan
Department of Civil Engineering

Final Report to the
AIR FORCE OFFICE OF SCIENTIFIC RESEARCH
RESEARCH INITIATION PROGRAM

Period of Investigation: January 1, 1988 to April 30, 1989

Structural Engineering Report No. 34

The Ohio State University Research Foundation
1314 Kinnear Road, Columbus, Ohio 43212

FOREWORD

This report describes research carried out at the Ohio State University under the AFOSR Research Initiation Program. Dr. V.B. Venkayya was the program manager of the research effort. At the Ohio State University, the work was performed under the supervision of Dr. Oliver G. McGee during the investigative period starting January 1, 1988 and ending April 30, 1989. Mr. Khing F. Phan contributed significantly to the project as a Graduate Research Associate. Professor R.S. Sandhu of the Department of Civil Engineering provided valuable technical communications which enhanced the research effort.

ABSTRACT

Research in structural optimization has grown considerably in recent years, in part due to the emergence of powerful supercomputers. However, structural practitioners have achieved uneven success in controlling the convergence of optimum sizing parameters for large-scaled skeletal structures. The focus of this report is to present an optimality criteria (OC) procedure for improved convergence of minimum-weight design of large-scaled bar and frame structures having nonstructural mass and governed by constraints on natural frequencies, and restrictions on minimum and maximum gauge. Specific criteria using previous information in the design cycle is found to both promote and accelerate convergence of optimum structural design parameters. Design examples are presented to demonstrate the improved OC method. The method is also used to delineate convergence quality of existing OC recursive relations compositely used to resize and to evaluate the Lagrange multipliers. What is offered here is a robust OC method that quickly dissolves the (sometimes violent) oscillations of scaled weights in the iteration history, and that eliminates the need for adjustments of internal parameters during the redesign phase.

SECTION I

INTRODUCTION

1. BACKGROUND AND RELATED LITERATURE

Although much work has been done on the use of optimization algorithms for structural design, the number of applications to practical structures remains very small (Ashley, 1982). However, the emergence of powerful computers has stimulated renewed interest in this field. Practical structures typically have thousands of sizing variables subjected to multiple constraints. The design space can also possess multiple points of local extrema. While optimization continues to play an integral part of structural design, current algorithms must be further developed to increase their efficiency in large-scaled design applications.

Most design procedures begin with a conceptual design in which the physical characteristics are defined as a function of basic sizing variables (x_1, \dots, x_n) . The primary objective is to calculate these sizing variables through a minimization of an objective or cost function $f(x_1, \dots, x_n)$. A classical example is the total weight of a structure. In practice constraints drawn from various analyses are imposed. These constraints include displacements, stresses, global instability and natural frequencies. Hence, the nature of the structural optimization problem is highly nonlinear.

Structural optimization problems traditionally have been

solved by using iterative methods described as either mathematical programming (MP) or optimality criteria (OC) (to be discussed shortly). MP methods are called direct methods, because they seek the minimum of the objective function subject to both equality- and inequality-type constraints. MP methods were first applied to structural optimization in the late 1950s. Early contributions included Livesley's (1956) and Pearson's (1958) treatments of limit design as a linear-programming problem, and Schmit's (1960) casting of elastic design as the more general nonlinear programming problem. No attempt is made to delineate here the detailed historical development of MP methods of structural optimization, because exhaustive surveys exist in the published literature. The most complete and authoritative surveys of optimum structural design in the context of MP formulations have been provided by Schmit (1966,1970,1971), Carpenter and Smith (1975,1977), Sandgren and Ragsdell (1980), and more recently Belgundu and Arora (1985a,1985b).

Nonetheless, progress toward efficient MP applications to large structures can best be described as uneven. A primary reason for the slow success is that MP methods offer some generality of application at the expense of a large number of reanalyses. Schmit and Miura (1976) have proposed robust approximation techniques to improve MP applications, such as design variable linking, constraint deletion techniques, higher-order approximations for sensitivity analysis, and constraint approximation concepts. However, for large-scaled structural

applications, these techniques can be computationally impractical and can many times lead to local extrema which may not be a suitable optimum.

Alternatively, OC methods emerged in the early 1970's as an efficient method for optimum structural design. OC methods are called indirect methods, because the weight is minimized indirectly by satisfying a condition of optimality. The optimality condition is equivalent to the Kuhn-Tucker conditions of nonlinear MP methods. In addition, the optimality condition is used to develop recursive relations for redesign.

The OC optimization procedure may be divided into three main phases. First, a finite element analysis of the structure is performed to obtain the structural response, and essential cost function and constraint gradient information. Then, the design is scaled to satisfy the constraints. Finally, the design parameters are modified so that the total weight decreases to a minimum, while satisfying an appropriate optimality condition. In the later step a recursive relation is used to modify the design. The recursive relation contains two groups of unknowns: (1) the constraint gradients, and (2) the Lagrange multipliers. Both of these quantities must be known before the recursive relation can be used.

Several investigators are noted for early development of OC methods [Taylor (1969); Berke (1970); Prager, et.al. (1971);

Gellatly and Berke (1971); and Venkayya, et.al. (1969,1971)]. A multitude of papers were published afterwards, demonstrating design algorithms including stress and displacement constraints [Venkayya, et.al. (1973); Gellatly and Berke (1973); Gunnlaugsson (1974); Gellatly, Helenbrook and Kocher (1978); Allwood and Chang (1984); Levy and Parawnsky (1982); Khan, Willmert and Thorton (1979)]. Several surveys documenting design problems solved with stress and displacement constraints are given by [Khot, et.al. (1979,1981)].

A large amount of work related to structural design with frequency constraints is available [Pierson (1972); and Venkayya (1978)]. However, papers employing finite element and OC methods are few in number [Kamat, et.al. (1973); Levy, et.al. (1979); Spillers, et.al. (1981); Venkayya, et.al. (1971,1983)]. Most of the design algorithms reported in these papers imposed a single constraint on the fundamental frequency. Several investigators [Khot (1984); and Grandhi and Venkayya (1987)] extended the constraint base for multiple frequencies. Khan and Willmert (1981) derived recursive formulas for modifying minimum weight designs of beams and frames subjected to a single natural frequency constraint. Groundwork has been made in using OC methods for structural design with constraints on elastic stability (buckling) [Khot, (1973,1984)]. Notable work is a generalized optimality criteria approach for frequency and buckling constraints for bending elements by [Fleury and Sander (1980)].

2. PROBLEM STATEMENT

Little effort has been directed towards controlling the convergence of optimum sizing parameters for minimum-weight design of large-scaled bar and frame structures. For frame structures, robust approximation techniques to monitor constraint sensitivities and for design scaling are important issues requiring more developmental effort and testing. Moreover, existing OC recursive relations used in the redesign stage may become unstable early in the design cycle history or locally near the optimum. Consequently, they may converge slowly towards local extrema which may not be a suitable optimum. Several causes are: (1) poor selection of a proper step size in the early iterations of the design cycle, (2) the number of critical or potentially critical constraints used in the redesign phase, and (3) lack of information extracted from the local history of the design cycle to enhance the convergence to an optimal design. For large-scaled structural design, investigators are faced with a conflict between the desire to be mathematically rigorous and consistent, and the need to draw from intuition the information necessary to generate optimum member sizes within reasonable computer resources. Even though considerable research effort has been devoted to a suitable resolution of this conflict, the effort described here centered on improving the convergence quality of existing OC methods.

3. RESEARCH OBJECTIVES

This report describes an OC method for improved convergence of minimum-weight design of large-scaled bar and frame structures having nonstructural mass and governed by constraints on natural frequencies, and restrictions on minimum and maximum gauge. Specific criteria using previous information in the design cycle is found to both promote and accelerate convergence of optimum sizing parameters. Design examples are presented to demonstrate the improved OC method. The method is also used to delineate convergence quality of existing OC recursive relations collectively used to resize and to evaluate the Lagrange multipliers. What is offered here is a robust OC method that quickly dissolves the (sometimes violent) oscillations of scaled weights in the iteration history, and that eliminates the need for adjustments of internal parameters during the redesign phase.

4. STRUCTURE OF THE REPORT

Section II describes an adaptive OC method for stabilizing convergence quality of minimum-weight design of bar structures supporting nonstructural mass and subjected to multiple natural frequency constraints and minimum gauge restrictions. Section III describes an efficient OC method for crosssectional optimization of 2-D frame structures supporting large amounts of nonstructural mass, and subjected to multiple natural frequency constraints and minimum and maximum gauge restrictions. Section IV outlines the accomplishments of the effort report here and possible extension

of the research. Appendix A lists the publications and presentations produced during the period of investigation.

REFERENCES

- Ashley, H., "On Making Things the Best-Aeronautical Use of Optimization", J. of Aircraft, Vol. 19, No. 1, 1982, p. 5-28.
- Allwood, R.J. and Chung, Y.S. (1984), "Minimum weight design of trusses by an optimality criteria method", Int. J. Num. Meth. Engng., Vol. 20, p. 697-713.
- Bartolomew, P. and Morris, A.J. (1976), "A unified approach to fully stresses design", Engng. Optimization, Vol. 2, p. 3-15.
- Belgundu, A.D. and Arora, J.S. (1985a), "A study of mathematical programming methods for structural optimization, part 1: theory", Intl. J. for Num. Methods in Eng., Vol. 21, p. 1583-1599.
- Idem (1985b), "A study of mathematical programming methods for structural optimization, part 2: numerical results", ibid. Vol. 21, p. 1600-1623.
- Berke, L. (1970), "An efficient approach to the minimum weight design of deflection limited structures", AFFDL-TM-70-4-FDTR, Flight Dynamics Laboratory, Wright Patterson AF OH.
- Carpenter, W.C., and Smith, E.A. (1975), "Computational efficiency in structural optimization", Eng. Optimization, Vol. 1, p. 169-188.
- Idem (1977), "Computational efficiency of nonlinear programming methods on a class of structural problems", Int. J. for Num. Methods in Eng., Vol. 11, p. 1203-1223.
- Fleury, C. and Sander, G. (1980), "Generalized optimality criteria for frequency constraints, buckling constraints and bending elements", Tech. Rept., AFOSR-TR-80-107.
- Gellatly, R.A. and Berke, L. (1971), "Optimal structural design", AFFDL-TR-70-165.
- Gellatly, R.A. and Berke, L. (1973), "Optimality criterion based algorithms", In Proc. Optimum Strct. Design, Theory and Applications (ed. by R.H. Gallagher and O.C. Zienkiewicz), p. 33-49.
- Gellatly, R.A., Helenbrook, R.G., and Kocher, L.H. (1978), "Multiple constraints in structural optimization", Int. J. for Num. Meth. in Eng., Vol. 12, p. 297-309.
- Grandhi, R.V., and Venkayya, V.B. (1986), "Structural optimization with frequency constraints", SDM Conference Proceeding, 28th SDM Conference, Monterey, California.

Gunnlaugsson, G.A. (1974), "Optimality conditions for trusses with nonzero minimum cross-section", Engng. Optimization, Vol. 1, p. 29-35.

Khan, M.R., Willmert, K.D. and Thorton, W.A. (1979), "An optimality criterion method for large scaled structures", AIAA J., Vol. 17, p. 753-761.

Khan, M.R. and Willmert, K.D. (1981), "An efficient optimality criterion method for natural frequency constrained structures", Comp. and Struct., Vol. 14, No. 5-6, p. 501-507.

Khot, N.S., Berke, L. and Venkayya, V.B. (1979), "Comparison of optimality criteria algorithms for minimum weight design structures", AIAA J., Vol. 17, p. 182-190.

Khot, N.S. (1982), "Optimality criterion methods of structural optimization, foundations of structural optimization: a unified approach (ed. by A.J. Morris), p. 99-235.

Khot, N.S. (1985), "Optimization of structures with multiple frequency constraints", Computers and Structures, Vol. 20, No. 5, p. 869-876.

Kiusalaas, I.J. and Shaw, R.C.J. (1978), "An algorithm for optimal structural design with frequency constraints", Int. J. Num. Meth. Eng., Vol. 13, p. 283-295.

Levy, R. and Choi, K. (1979), "Implementation of natural frequency analysis and optimality criterion design", Computer and Structures, Vol. 10, p. 277-282.

Levy, R. and Parawnsky, W. (1982), "Optimality criteria solution strategies in multiple constraint design optimization", AIAA J. Vol. 20, p. 708-715.

Livesley, R.K. (1956), "The automatic design of structural frames", Quart. J. Mech. Appl. Math., Vol. 9, Part 3.

McGee, O.G. (1987), "Automated design of large-scaled frame structures with multiple frequency constraints", Final Rept., USAF-UES SFRP, AFOSR Contract No. F49620-85-C-0013.

McGee, O.G. and Phan, K.F. (1988), "An improved algorithm for optimum structural design with multiple frequency constraints", Proc. of Second NASA/Air Force Symposium on Multidisciplinary Analysis and Optimization, Raddison Hotel, Hampton, Virginia, September 28-30, 1988.

Pearson, C. (1958), "Structural design by high-speed computing machines", Proc. of ASCE Conf. on Electronic Computation, Kansas City, Missouri.

Pierson, B.L. (1972), "Survey of optimal structural design under dynamic constraints", Int. J. Num. Meth. Eng., Vol. 4, p.491-499.

Prager, W. and Marcal, P. (1971), "Optimality criteria in structural design", AFFDL-TR-70-166.

Sandgren, E. and Ragsdell, K.M. (1980), "The utility of nonlinear programming algorithms: a comparative study- parts 1 and 2", ASME J. of Mech. Design, Vol. 102, p. 540-552.

Schmit, L. (1960), "Structural design by systematic synthesis", Proc. of ASCE 2nd Conf. on Electronic Computation, Pittsburgh, Pa.

Idem (1966), "Automated design", Int. Sci. and Tech.

Idem (1970), "Structural engineering applications of mathematical programming techniques", in Symp. on Struc. Optimization, AGARD Conf. Proc. No. 36 (Ed. R. Gellatly), Advisory Group for Aero. Res. and Devel., NATO.

Idem (1971), "Structural synthesis: 1959-1969: a decade of progress", in Recent Advances in Matrix Methods of Structural Analysis and Design (Ed. R.H. Gallagher et.al.), Univ. of Alabama Press.

Spillers, W.R., Singh, S. and Levy, R. (1981), "Optimization with frequency constraint", ASCE J. Struct. Div. Vol. 107, p. 2337-2347.

Taylor, J. (1969), "Optimal design of structural systems: an energy formulation", AIAA J., Vol. 7, p. 1404-1406.

Venkayya, V.B. (1973), "Design of optimum structures", Computers and Structures, Vol. 1, No. 1-2, p. 265-309.

Venkayya, V.B., Khot, N.S., and Berke, L. (1973), "Application of optimality criteria approaches to automated design of large practical structures", AGARD Second Symposium on Structural Optimization, Milan, Italy.

Venkayya, V.B. (1978), "Structural optimization: a review and some recommendations", Int. J. Num. Meth. Eng., Vol. 13, p. 203-228.

Venkayya, V.B., and Tischler, V.A. (1983), "Optimization of structures with frequency constraints", Computer Methods for Nonlinear Solids and Structural Mechanics, ASME, AMD-54, p. 239-259.

Venkayya, V.B. (1988), "Optimality criteria: a basis for multidisciplinary design optimization", to be published.

Section II

AN ADAPTIVE PROCEDURE FOR STABILIZING CONVERGENCE
QUALITY IN FREQUENCY-CONSTRAINED DESIGN OPTIMIZATION¹

Khing F. Phan² and Oliver G. McGee³
Department of Civil Engineering
The Ohio State University
Columbus, Ohio 43210, U.S.A.

Submitted for publication in the International Journal of
Numerical Methods in Engineering

¹This work was presented in part at the Second NASA/Air Force
Symposium on Multidisciplinary Analysis and Optimization in
Hampton, Virginia on September 28-30, 1988.

²Graduate Research Associate

³Assistant Professor

SUMMARY

This paper presents an improved optimality criteria (OC) method for minimum-weight design of bar structures supporting nonstructural mass and subjected to multiple natural frequency constraints and minimum gauge restrictions. The convergence quality of the OC method hinges on both the number of active constraints retained and the choice of a proper step size. This being the case, a criterion, which uses previous scaled designs to "adaptively" tune the step size, is established with purpose of dissolving the (sometimes violent) oscillations of scaled design weights in the iteration history. As the step size is tuned, the convergence rate is decreased. Hence, a modified Aitken's accelerator, which extrapolates from previous scaled designs to obtain an improved one, is used. Its effect is to both increase the convergence rate and reduce the net cost of convergence by reducing the number of repeat finite element analyses. The method presented here is used to quantitatively survey the convergence of several OC recursive schemes compositely used to resize and to evaluate the Lagrange multipliers. Design examples are presented to demonstrate the method. The method is adaptable, as it eliminates the need for adjustments of internal parameters during the redesign stage.

1. INTRODUCTION

If an engineer has to either avert fatigue failure resulting from structural resonances, or circumvent interaction between structural responses and their control systems, the ideal placement of natural frequencies of complex structures having nonstructural mass and minimum gauge restrictions are meaningful design considerations. For this class of problem, efficient and reliable schemes employing robust approximation techniques for natural frequency constraints and nonlinear mathematical programming algorithms have been presented by a number of investigators [1-4]. In references [5-9], structural optimization algorithms combining finite element analyses and the Kuhn-Tucker conditions were devised, showing advantages of using exuberant approximations for the Lagrange multipliers.

In recent papers [10-12], broader iterative design strategies have been developed for large-scaled bar structures, by taking advantage of their special characteristics (e.g. structural matrices linearly proportional to a basic sizing parameter). The iterative approach based on alternately satisfying the constraints (scaling) and applying the Kuhn-Tucker optimality condition (resizing) may exhibit poor convergence quality at the expense of an increased number of design iterations.

Basically, the recurrence relations for resizing are derived from the optimality condition and contain unknown Lagrange multipliers each of which correspond to a specific constraint. Recurrence relations can also be used to efficiently evaluate these multipliers, which must be computed before the recurrence relations for resizing can be utilized. The concept of scaling involves changing the design variables (either by adding differential quantities or by multiplying the variables by constant factors) in order to place the constraints on their boundaries. Various OC methods in the published literature differ for the same design problem, both in the recurrence schemes used in the redesign phase and in whether or not scaling is used to predict the constraint surface. More importantly, the convergence quality of the OC method may be sharply influenced by the number of potentially critical (or "active") constraints retained, and by the choice of a proper step size (or sometimes called move limit) used in the resizing phase.

In the truss designs of references [10-12], the step size for resizing, which was used to stabilize convergence, was exponentially controlled. Ironically, the selection of a proper step size was an arbitrary process with much user-experimentation done on the same problem. For instance, one would initially fix the step size in design iterations where the scaled weight was continually reduced. If a sudden rise in the weight was observed,

then one would momentarily stall the design cycle, while the step size was reduced (ad hoc) until a decrease in the weight was obtained. However, it has now become necessary to establish a criteria which "adaptively" tunes the step size for smoother convergence of OC redesign methods.

The effect of properly tuned move limits in sequential linear programming and nonlinear programming methods has been recognized in the literature [13-15]. Unfortunately, no standards of choosing the appropriate step size that is availing to OC redesign methods has been established. Here, a criterion is offered for adaptively tuning the step size. The key idea is to adjust the step size by monitoring a localized history of the scaled weights calculated in the design cycle. The net effect of the criterion is to "damp-out" or stabilize the (sometimes violent) oscillatory convergence proclivity of the iteration process. As the step size is tuned, the net cost and rate of convergence is increased, mainly due to the number of repeat finite element analyses. Hence, a modified Aitken's accelerator, which extrapolates from previous scaled designs to obtain an improved design, is utilized.

The method offered here will be described in detail. Also, examples will be presented and compared with previously published results. The method is also used to quantitatively survey the convergence of OC recursive schemes collectively used to resize

and to evaluate the Lagrange multipliers. It is shown that the present approach is robust in that it is not dependent on adjustments of internal parameters during the redesign stage, and that it efficiently stabilizes the convergence of frequency-constrained design problems.

2. MATHEMATICAL STATEMENT OF THE PROBLEM

The optimization problem to be solved is:

minimize the structural weight of a bar structure

$$\min W(\mathbf{x}) = \rho_i l_i x_i \quad (i=1,2,\dots,n) \quad (1)$$

subject to m natural frequency constraints

$$g_j(\mathbf{x}) = \omega_j^2 - \omega_j^{2*} \geq 0 \quad (j=1,2,\dots,m) \quad (2)$$

and n side constraints

$$x_i \geq x_i^L \quad (i=1,2,\dots,n) \quad (3)$$

where in equation (1) a summation over n bar elements is implied. Furthermore, ρ_i is the i^{th} bar mass density; x_i is the i^{th} bar crosssectional area chosen as the basic sizing variable; and l_i is the i^{th} bar length. In equation (2), ω_j^2 and ω_j^{2*} are the squares of the actual and desired values of the j^{th} natural frequency, respectively, and m is the retained number of active constraints. In this work, the active frequency constraints are those within a specified minimum tolerance from their respective boundaries. The superscript (L) in equation (3) denotes the prescribed minimum gauge on the sizing variables.

3. FREQUENCY AND DESIGN SENSITIVITY ANALYSES

The square of the j^{th} natural frequency of a discretized bar structure is obtained by solving the following eigenvalue problem:

$$([K] - \omega_j^2 [M]) \{q_j\} = \{0\} \quad (4)$$

where $\{q_j\}$ is the j^{th} mode shape, $[K]$ is the global stiffness matrix, and $[M]$ is the total mass matrix consisting of structural mass, M_s , plus nonstructural mass, M_c . The normalization equation of the mode shape with respect to the total mass is written as

$$\{q_j\}^T [M] \{q_j\} = 1 \quad (5)$$

Differentiating equation (4) with respect to the i^{th} sizing variable results in the following equation

$$([K]_{,i} - \omega_j^2_{,i} [M] - \omega_j^2 [M_s]_{,i}) \{q_j\} + ([K] - \omega_j^2 [M]) \{q_j\}_{,i} = \{0\} \quad (6)$$

where $\omega_j^2_{,i}$ represents a gradient of the square of the j^{th} natural frequency with respect to the i^{th} sizing variable; $\{q_j\}_{,i}$ indicates the gradient of the corresponding j^{th} mode shape; and $[M_s]_{,i}$ and $[K]_{,i}$ denote respective gradients of the structural mass and stiffness matrices. Note that the nonstructural mass contribution to $[M]$ is independent of the sizing variable. First, by rearranging equation (6)

$$([K] - \omega_j^2 [M]) \{q_j\}_{,i} - \omega_j^2_{,i} [M] \{q_j\} = -([K]_{,i} - \omega_j^2 [M_s]_{,i}) \{q_j\} \quad (6a)$$

and then premultiplying equation (6a) by $\{q_j\}^T$, one obtains the following equation

$$\begin{aligned} \{q_j\}^T([K] - \omega_j^2[M])\{q_j\}_i - \omega_j^2 \{q_j\}^T[M]\{q_j\} = \\ - \{q_j\}^T[K]_i\{q_j\} + \omega_j^2 \{q_j\}^T[M_S]_i\{q_j\} \end{aligned} \quad (7)$$

Using equation (4) and considering the normalization of the mode shape (in equation 5), the j^{th} natural frequency gradient can be written as

$$\omega_j^2{}_{,i} = \{q_j\}^T[K]_i\{q_j\} - \omega_j^2 \{q_j\}^T[M_S]_i\{q_j\} \quad (8)$$

For bar structures, the element stiffness and structural mass matrices are the product of the sizing variable and an invariant matrix. Thus, it is generally recognized that the gradient equation (8) simplifies to

$$\omega_j^2{}_{,i} = (1/x_i)\{q_j\}_i^T[k_i]\{q_j\}_i - \omega_j^2(1/x_i)\{q_j\}_i^T[m_{Si}]\{q_j\}_i \quad (9)$$

where $\{q_j\}_i$ represents the component of the vibration mode associated with the i^{th} sizing variable, and $[k_i]$ and $[m_{Si}]$ correspond to the i^{th} element stiffness and structural mass matrices, respectively defined in the global coordinate system.

The frequency gradient equation (9) is comprised of two terms that are inversely proportional to the sizing variable: the

first being named the modal potential energy (MPE) and the second is designated the modal kinetic energy (MKE). For problems involving a substantial amount of nonstructural mass, the MKE term was disregarded in the gradient calculations of recent OC algorithms [11,12]. This was done to alleviate oscillatory convergence of solutions. Quantitative studies showing the effectiveness of the proposed damping criterion, when the MKE term is either retained or omitted, will be rendered in this work.

The gradient of the objective function (structural weight) with respect to the i^{th} sizing variable is simply given as

$$W_{,i} = \rho_i l_i \quad (10)$$

Equations (9) and (10) are used to define the optimality criteria in the next section.

4. OPTIMIZATION PROCEDURE

Using equations (1) and (2), the Lagrangian function, L , for constrained minimization is written as

$$L(x, \lambda) = \rho_i l_i x_i - \lambda_j (\omega_j^2 - \omega_j^{2*})$$

(summed over $i=1,2,\dots,n$ and $j=1,2,\dots,m$) (11)

where λ_j are the Lagrange multipliers and m is the retained number of active constraints.

Differentiating equation (11) with respect to the sizing variables and setting the resulting equations to zero, gives the n optimality conditions as

$$D_i = e_{ij} \lambda_j = 1 \quad (i=1,2,\dots,n)$$

(summed over $j=1,2,\dots,m$) (12)

The Lagrangian energy density, e_{ij} , which represents a ratio of the gradient for the active frequency constraint (equation 9) and the gradient of the objective function (equation 10), is written as follows

$$e_{ij} = \frac{-\omega_j^{2,i}}{W_i}$$

(13)

4.1 Previous OC Redesign Methods

Indeterminate complex structures, unlike determinate ones, require an iterative procedure to update the sizing variables. Using equation (12), one can write several recursive relations to

update these variables [16-18]. Two of the most commonly used ones are first, an exponential recursive relation, where the sizing variables are modified by a quantity that is equal to unity at the optimum

$$x_i^{k+1} = x_i^k [D_i]_k^{(1/a)} \quad (14)$$

and second, one of many linearized recursive relations in which the sizing variables are modified by an error quantity which is equal to zero at the optimum

$$x_i^{k+1} = x_i^k [1 + (1/a)(D_i - 1)]_k \quad (15)$$

In equations (14) and (15) the superscript and subscript k and $k+1$ indicate iteration numbers. These recursive relations drive the design from an infeasible to a feasible location in the design space. In order to use any one of the recursive relations, one must evaluate D_i (equation 12), which contains the unknown Lagrange multipliers (discussed later) and cost function and constraint gradient information. The quantity $(1/a)$ is the step size. The step size has to be reduced in order to give a stable convergence. It acts like a move limit on the sizing variables. A normal initial value of $a=2$ was typically used by investigators in references [10-12].

However, the writer's experience has shown that just arbitrarily increasing $a>2$ is not sufficient to improve convergence, particularly near an optimum. Numerical studies revealed that both the exponential and linear redesign methods gave smooth monotonic convergence when applied to a single-path

design problem with a constraint on the fundamental frequency. However, the convergence quality rapidly declined, when the redesign methods were applied to problems with constraints on the higher vibration modes or multiple number of modes. For example, Figures 1 and 2 tumultuously show that the upper-bound convergence exhibited by equations (14) and (15) had a (sometimes violent) oscillatory propensity without the selection of a proper step size. Until now, this selection was an arbitrary process with much experimentation done on the same problem. What is offered here is a criterion that adaptively tunes the step size for a smooth upper-bound convergence near an optimum.

4.2 Present Redesign Approach

The following simple redesign strategy is used in this work:

$$x_i^{k+1} = x_i^k + s \, dx_i \quad (16)$$

where s is an adaptively-controlled tuning parameter and $dx_i = (x_i^{k+1} - x_i^k)$ is the correction to the sizing variable calculated using any one of the OC redesign methods.

In the present algorithm, the quantity $(1/a)$ in equations (14) and (15) is immobilized by setting it to a constant value. Then, the parameter, s , is tuned both to control the step size and to "damp-out" or stabilize the oscillatory convergence nature of equations (14) and (15). At the beginning of the design cycle, the tuning parameter is set to unity. Henceforth, the value of s is adjusted by monitoring a localized history of scaled weights

calculated during the design cycle. Given any weight fluctuations, a tuned value of s is chosen by the following damping criterion at a current k^{th} design: If $w^{k+1} > C_s[w^k - w^{k-1}]$ or $w^{k+1} > w^k > w^{k-1}$, then s is reduced to $s/2$ (given that the tuned value of s is maintained above a specified minimum value). If the weight increases are more than say 10 percent, then the scaling constant, C_s , is set to $1/2$. Otherwise, if they are less than 10 percent, then the scaling constant is further tuned to a percent difference in scaled weight: $[(w^k - w^{k-1})/w^k] \times 100\%$.

With the above damping criterion, the bandwidth of weight oscillations decreases near the optimum. This assures a smoother quality of convergence. It will be shown in later examples that the damping criterion is appropriate to guide an adaptive OC approach.

4.3 Uncoupled Methods for Evaluating the Lagrange Multipliers

The unknown Lagrange multipliers used in the OC redesign methods indicate the relative importance of each active constraint. For single constraint problems, the Lagrange multiplier is a deterministic quantity. However, when several active constraints are retained, at least the relative values of the Lagrange multipliers corresponding to these constraints must be closely estimated to maintain a convincingly smooth quality of convergence.

For computational ease, several approximate methods for evaluating the Lagrange multipliers have been previously proposed. Recursive formulas can be written by assuming that the active constraints in equation (2) are equality constraints [16-18]. This uncoupled approach updates the multipliers in direct measure to the lack of satisfaction of the constraints and more importantly, the convergence of the method greatly depends on a good initial starting guess. This being the case, one can express the recursive relations in an exponential

$$\lambda_j^{k+1} = \lambda_j^k [\omega_j^2 / \omega_j^{2*}]_k^{(1/b)} \quad (17)$$

or a linearized form [16-18]

$$\lambda_j^{k+1} = \lambda_j^k [(b+1)/b - (1/b)(\omega_j^2 / \omega_j^{2*})]_k \quad (18)$$

where the subscript k indicates that the quantity in parenthesis is evaluated at the k^{th} iteration, and the parameter b is the step size. It can be shown that the step size $b=1/a$ [17,18], where the parameter, a , is defined in equations 14 and 15.

Another approximate method derived from a single constraint condition was proposed in references [11,12]

$$\lambda_j = W / \omega_j^{2*} m_{cj} \quad (19)$$

where m_{cj} is the j^{th} ratio of the nonstructural modal mass to the total modal mass.

$$m_{cj} = \frac{\{q_j\}^T [M_c] \{q_j\}}{\{q_j\}^T [M] \{q_j\}} \quad (20)$$

It will be shown in later examples that equation (19) is an

especially good approximation. Furthermore, it certainly serves as suitable starting values to enhance the recursive equations (16) and (17).

4.4 Present Approach to the Lagrange Multipliers

In this work, the convergence of either equation (16) or (17), is reinforced by adapting the same updating approach used for the sizing variables. Hence,

$$\lambda_j^{k+1} = \lambda_j^k + s \, d\lambda_j \quad (21)$$

where s is tuned according to the damping criterion, and $d\lambda_j = (\lambda_j^{k+1} - \lambda_j^k)$ is the correction to the j^{th} Lagrange multipliers.

A cogent source of uneven convergence of OC redesign methods originates in the assumptions made regarding the role of the Lagrange multipliers and active and passive constraints. Determining which constraints are critical or potentially critical must be made at the outset. As the number of active constraints is increased, more Lagrange multipliers participate in the redesign phase. This tends to overconstrain the system. Thus, the final design is an extreme upper-bound and that tuning the step size sometimes does not profoundly effect the already smooth quality of convergence of solution.

In this work, the active constraints are those within a

specified minimum tolerance near their respective boundaries. All other constraints are considered inactive (or passive). By maintaining such a tolerance around the constraint boundaries, the chances of mode switching (i.e., when passive frequencies cluster near active ones) is substantially reduced. Mode switching tends to curtail smoother convergence. Nonetheless, a somewhat liberal tolerance of 5 percent is used here to allow enough active constraints to participate in resizing, so as to demonstrate the effectiveness of the damping criterion.

4.5 Scaling Procedure

In the present OC method, a scaling procedure is used to drive infeasible designs to feasible ones. Presumably, all or some of the sizing variables may be scaled depending on how the formulation is derived. This is the subject of ongoing research. What is used here is simple scaling with the assumption that there exists a dominant active constraint. If one uniformly scales the design with respect to this constraint, then presumably all of the other constraints will be brought to the feasible region [19].

After the bar members are resized, they are uniformly scaled by a factor f_j corresponding to a j^{th} active frequency constraint. For instance, the relationship between the scaled sizing variables, x_{ni} , and the unscaled one, x_i , is

$$x_{ni} = f_j x_i \quad (22)$$

For bar structures, an exact expression for the scaling factor, f_j , is written as follows [11]:

$$f_j = \frac{m_{cj} R_j^2}{1 - R_j^2 m_{sj}} \quad , \quad R_j^2 m_{sj} < 1$$

$$f_j = R_j^2 \quad , \quad \text{otherwise} \quad (23)$$

where R_j^2 represents the square of the j^{th} target frequency ratio, given as

$$R_j^2 = \omega_j^{2*} / \omega_j^2 \quad (24)$$

In equation (23), $m_{sj} + m_{cj} = 1$, where m_{sj} is defined as the j^{th} ratio of the structural modal mass to the total modal mass

$$m_{sj} = \frac{(q_j)^T [M_s] (q_j)}{(q_j)^T [M] (q_j)} \quad (25)$$

and m_{cj} is defined in equation (20). It should be noted that all design weights reported in this paper are obtained from scaled designs.

5. MODIFIED AITKEN'S ACCELERATOR

Computational studies showed that the price of reducing the value of s in equations (16) and (21) was a considerably larger number of repeated finite element analyses. However, it was transparent that a numerical accelerator could be beneficial to the net cost and overall rate of convergence. Since the convergence propensity of the OC method here is mostly oscillatory, Aitken's accelerator, which extrapolates improved results from previous (slow-to-converge) oscillatory results, was conclusively the most adaptable choice.

With Aitken's accelerator [20], three consecutive results of an oscillatory nature are used to linearly extrapolate improved results based on an assumption that the error curve of the governing iterative process decays exponentially. However, computer adaptability of Aitken's accelerator is unpredictable, given the possibility of a singular denominator in the extrapolation algorithm. Nonetheless, the extrapolation algorithm of the modified Aitken's accelerator [21], which was developed for general multivariable iterative problems, requires a single division per vector update, as opposed to one for each variable.

Let $\{x\}^{k-3}$, $\{x\}^{k-2}$, and $\{x\}^{k-1}$ be design vectors exhibiting oscillatory convergence trends in three previous consecutive

iterations of the design cycle, and let $\{x\}^k$ be the desired vector for a current k^{th} design. If

$$\{d_1\} = \{x\}^{k-2} - \{x\}^{k-3} \quad \text{and} \quad \{d_2\} = \{x\}^{k-1} - \{x\}^{k-2} \quad (26)$$

then, an accelerated design, $\{x\}^a$, can be extrapolated as follows:

$$\{x\}^a = \{x\}^{k-1} + S\{d_2\} \quad (27)$$

where S , is defined as a scalar acceleration factor

$$S = ((\{d_2\} - \{d_1\})^T(-\{d_2\})[(\{d_2\} - \{d_1\})^T(\{d_2\} - \{d_1\})]^{-1} \quad (28)$$

In general, the accelerated design, $\{x\}^a$, violates both the optimality criteria and the frequency constraints. Nonetheless, the design cycle is continued after the extrapolation by resizing with the accelerated design, $\{x\}^a$. The k^{th} design is then scaled to satisfy the constraints using equations (22). The benefits of the modified Aitken's accelerator will be demonstrated later in the paper.

6. OPTIMIZATION ALGORITHM

The main steps of the present optimization algorithm are summarized as follows:

- (1) Assign uniform sizes to all elements (set $s=1$ and $k=0$).
- (2) Calculate natural frequencies of structure (eqs. 1-2)
- (3) Scale design until target frequencies are within a specified tolerance of the constraint surface (eq. 22).
- (4) Calculate the scaled weight of structure (eq. 1)
- (5) For iteration $k=4$ or greater, check for oscillations in the scaled weights of the last three consecutive $k-1$, $k-2$, $k-3$ designs. If so, then extrapolate an accelerated design using equation (27); Else continue.
- (6) Determine the Lagrange multipliers for m active frequency constraints (eq. 21).
- (7) Resize the design using (eq. 16).
- (8) Repeat steps 2, 3 and 4.
- (9) For iterations $k=4$ or greater, check damping criterion:
If $w^{k+1} > C_s [w^k - w^{k-1}]$ or $w^{k+1} > w^k > w^{k-1}$ and $s > a$ specified minimum value, then set s to $s/2$ and go to step 7; Else go to step 5.

Note: Steps 5-9 represent one iteration in the design cycle, which is repeated until either the difference in weight is less than a specified tolerance, or the parameter, s , reaches the specified minimum value (at which relative

convergence is implied in equation 16).

7. EXAMPLES

A computer program written in FORTRAN 77 was developed to execute the optimization algorithm summarized in the preceding section. Several example problems were used to demonstrate the method and the results were compared with previous results. While it was not possible to provide a direct comparison in all cases, due to differences in the mass formulations of the finite element models, the results show passable correlation to manifest a reasonably valid comparison. The method was also used to quantitatively map the convergence of OC recursive relations collectively used to resize and to evaluate the Lagrange multipliers. For simplicity, the resizing equations (14) and (15) are hereafter referred to as options 1 and 2, respectively, and equations (17), (18), and (19) as options A, B, and C, respectively. These recursive options were used in equations (16) and (21) in the present algorithm. Unless otherwise stated, the modal kinetic energy (MKE) term was disregarded in all frequency gradient calculations (in equation 9). This was done to provide better comparisons between the results present here and those previously reported [10,11]. An additional study was performed showing the effectiveness of the damping criterion, when the MKE term was either retained or disregarded in the frequency gradient calculations (equation 9). Results of this study are given in the last subsection. All natural frequencies in this work were

calculated using the subspace iteration method [19] with double precision (14 significant digit accuracy) on an IBM 3081-D machine.

7.1 Example 1. Ten bar truss

Figure 3 shows a ten bar truss, a classical problem in the structural synthesis literature. The Young's elastic modulus and weight density were specified at 10^7 psi and $0.1 \text{ lb-s}^2/\text{in}^3$, respectively. A nonstructural mass of $2.588 \text{ lb-s}^2/\text{in}$ was added to the four free nodes. For an initial starting design, the relative crosssectional areas of the members was set to 9.5318 in^2 . A minimum gauge value of 0.1 in^2 was imposed as a side constraint.

Table 1 compares initial and final design frequencies and scaled weight for several frequency constraint conditions. Table 2 gives the optimum bar sizes. (Comparable data extracted from reference [11] is shown in parentheses). As indicated in Tables 1 and 2, options 1C was used in the present method. The ten bar truss was designed to satisfy four constraint conditions. These were: (i) $\omega_2 = 10 \text{ Hz}$ (Case 1); (ii) $\omega_1 = 7 \text{ Hz}$, $\omega_2 \geq 15 \text{ Hz}$ (Case 2); (iii) $\omega_1 = 7 \text{ Hz}$, $\omega_2 \geq 15 \text{ Hz}$, $\omega_3 \geq 20 \text{ Hz}$ (Case 3); and finally (iv) $\omega_1 \geq 3.5 \text{ Hz}$, $\omega_2 \geq 10 \text{ Hz}$, $\omega_3 \geq 14 \text{ Hz}$ (Case 4).

The weight of the initial starting design was 4000 lbs. It should be noted that in this example a lump mass formulation was used, while a partially-coupled mass was used in reference [11].

This explains the slight differences in the predicted frequencies of the higher modes at the initial starting designs. Nonetheless, the present method spawned in some cases significantly lower upper-bounds on the optimum design than those obtained in reference [11]. For example, in Cases 1 and 4 (columns 3 and 6 in Table 1), lower upper-bounds of approximately 15 percent were gained. Whereas, in Cases 2 and 3 (columns 4 and 5), reductions of 4 percent at most were obtained.

Figure 4 shows the effect of modified Aitken's accelerator (equation 27) on the iteration history of the ten bar truss with the constraint Cases 1 and 4. Four curves are shown with or without acceleration. In all cases the step size (in equation 16 with option 1C) was adaptively tuned. Several observations can be made. First, Aitken's accelerator had a disparating effect on the path of convergence, particularly when more active constraints were allowed to participate in resizing (Case 4). Second, the price of reducing the step size without acceleration was paid through an increased number of repeat finite element analyses. For instance, a total of 54 (and 36) analyses were required for Cases 1 (and 4) to reach final design weights of 257.68 (and 404.68) lbs, respectively. By way of comparison, a reduced total of 39 (and 21) analyses were required to reach slightly lower upper-bound weights of 257.40 (and 403.94) lbs respectively, when Aitken's accelerator was used. It should be noted that with acceleration a substantial number of analyses were sometimes

required in the closing cycles to achieve a negligibly small change in a converged upper-bound weight. This was mainly due to the specified minimum tolerances used to delineate final convergence of solution in the algorithm. Figure 4 shows that when the algorithm was allowed to continue with acceleration, lower upper-bounds on the optimum weight were gained at 255.41 lbs (in 49 analyses for Case 1) and 398.74 lbs (in 35 analyses for Case 4). The lower upper-bound weights obtained with the use of the modified Aitken's accelerator were mainly attributed to numerical anomalies caused by extrapolation.

7.2 Example 2. Thirty-eighty bar truss

The thirty-eight bar truss problem was first reported by Khot [10]. Figure 5 gives a diagram and the element-joint connectivities for the bar structure. The elastic modulus and weight density of the material were set to 10^7 psi and $0.1 \text{ lb-s}^2/\text{in}^3$, respectively. At nodes 8 and 14 a concentrated nonstructural mass of $0.5 \text{ lb-s}^2/\text{in}$ was included. A minimum gauge constraint on the sizing variables was specified at 0.005 in^2 .

This example was solved using options 1C in the present method. Columns 1-4 in Tables 3 and 4 show iteration histories of the first 2 natural frequencies and scaled weight for two cases treated in reference [10]. These were: (i) $\omega_1^2 = 2500 \text{ rad}^2/\text{sec}^2$, $\omega_2^2 \geq 2500 \text{ rad}^2/\text{sec}^2$ (Case 1); and (ii) $\omega_1^2 = 2500 \text{ rad}^2/\text{sec}^2$, $\omega_2^2 \geq 3000 \text{ rad}^2/\text{sec}^2$ (Case 2). Analogous data was extracted from

reference [10], which is shown in columns 5-8 in Tables 3 and 4. The initial starting design weight for both analyses was 52.30 lbs. Although not shown in Columns 1-4 in Tables 3 and 4, the square of the first and second frequencies of the initial starting design were calculated at 2500 and 8560 $\text{rad}^2/\text{sec}^2$, respectively. By way of comparison with reference [10], the final designs listed in columns 1-4 show lower upper-bounds on the optimum by approximately 9 percent for Case 1 and nearly 8 percent for Case 2. (Note that the asterisk in column 4 in Tables 3 and 4 indicates those iterations where accelerated design vectors (equation 27) were extrapolated).

7.3 Example 3. Two-hundred bar truss

The two-hundred bar truss problem was examined in reference [11]. The model is shown in Figure 6. The elastic modulus and weight density of the material were specified at 30×10^6 psi and $0.283 \text{ lb-s}^2/\text{in}^3$, respectively. As an initial design, the relative crosssectional areas were set to a uniform value of 10 in^2 . A minimum gauge on the sizing variables was specified at 0.1 in^2 .

Table 5 compares initial and final design frequencies and scaled weight for a range of specified limits on the fundamental frequency. (Comparable data extracted from reference [11] is shown in parenthesis). As indicated in Table 5, options 1C was used in the present algorithm. Also, a lump mass formulation was used in the frequency calculations. Overall, the results appear

consistent, with a faster convergence rate in the present work.

Next, the truss model was designed for multiple frequency constraints (Table 6). Three cases were examined: (i) $\omega_1 = 3$ Hz, $\omega_2 \geq 9$ Hz (Case 1); (ii) $\omega_1 = 4$ Hz, $\omega_2 \geq 10$ Hz (Case 2); (iii) $\omega_1 \geq 3$ Hz, $\omega_2 \geq 9$ Hz, $\omega_3 \geq 14$ Hz (Case 3). Here, less dramatic reductions on the upper-bound to the optimum weight were realized, when the present results were compared to those reported in reference [11] (see Table 6). The results in Case (3) were supplied as benchmark values with which any future ones can be compared.

7.4 Quantitative convergence study of OC recursive schemes

The example ten bar truss was redesigned with the constraints of Case 4 in example 1. Figure 7 compares the iteration histories of scaled weights for six Cases A-F using options 1C, 2C, 1A, 2A, 1B, 2B, respectively. As the optimization process was "jump-started" in the early iterations, it was apparent that the convergence of the various recursive options used in equations (16) and (21) was quickly stabilized by the damping criterion used here. Final upper-bound weights are shown in Figure 7 with the number of complete finite element analyses given in parentheses. A design with the lowest upper-bound weight at 398.74 lbs was obtained with Case A (option 1C). It required 35 finite element analyses to converge. On the other hand, Case C (option 1A) converged to a design with the highest upper-bound

weight at 514.30 lbs in 42 analyses. It was surprising that Cases B, E, and F all produced designs, which converged to nearly the same weights. Although, their paths of upper-bound convergence were significantly dispersed. Nonetheless, Case F demanded the largest number of analyses (83) to achieve convergence of solution.

It was interesting to compare the effectiveness of the damping criterion on the iteration histories of Cases A-F, when the MKE term in the frequency gradient calculations (equation 9) was retained (see Figure 8). In reference [11], the MKE term was disregarded to alleviate oscillatory convergence of solutions. As can be seen, all of the recursive cases converged to nearly the same upper-bound weights, except for Case E. It not only converged to the highest upper-bound result (524.31 lbs), it also required the largest number of complete analyses (at 57). Also, the paths of convergence were less dispersed, when the MKE term was retained. Presumably, this appears to be a stabilizing characteristic in the present method.

The thirty-eight bar truss was redesigned with the constraints of Cases 1 and 2 in example 2. The iteration histories of scaled weight using the recursive options of Cases A-F is depicted in Figures 9 and 10. In Figure 9, most of the recursive schemes converged to nearly identical design weights (close to those reported in reference [10]). Again, the number of

finite element analyses is shown in parentheses. As the frequency band was increased (in Figure 10), all of the cases again converged to approximately the same weight, but the path of convergence was more dispersed. For constraint Case 1, a final design with the lowest weight at 24.93 lbs in 22 analyses was obtained by Case A (option 1C). For constraint Case 2, a final weight of 25.64 lbs in 21 analyses was also obtained by Case A.

Figures 11 and 12 show an overall stabilizing effect on the iteration history of the six recursive Cases A-F, when the MKE term was retained in conjunction with the damping criterion used here. Although, a small penalty of additional analyses was expended.

The two-hundred bar truss was redesigned with the constraints of Case 3 in example 3. The iteration history for the same six recursive options (A-F) is shown by the curves in Figure 13. As can be seen, the convergence paths of the various recursive strategies (A-F), although eventually stabilized by the present damping criterion, were significantly more dispersed. It is interesting that a "best" design with a weight of 7697.36 lbs was obtained in Case E (option 1B).

When this problem was resolved with the MKE term in the gradient calculations, the relative values of the sizing variables during redesign became prohibitively large. Therefore,

a maximum limit on the sizing variables ($x_i < x_i^U = 88 \text{ in}^2$) was imposed as an additional side constraint. This constraint consequently produced higher upper-bounds on the optimum. Figures 14 and 15 present iteration histories of upper-bound design weights, when the MKE terms was either disregarded or retained. A precursory conclusion is that by retaining the MKE term in the frequency gradient calculations, the damping criterion here generally produces a more stable convergence to a lower upper-bound solution.

8. CONCLUDING REMARKS

An "adaptive" technique has been offered for alleviating the convergence anomalies of the OC approach to structural synthesis. The key idea has been to tune the step size of OC redesign methods according to a damping criterion, which dissolves the (sometimes violent) oscillations of scaled weights in the iteration history. During optimization, a liberal number of active frequency constraints has been allowed to participate in the redesign phase. This has been done to fully demonstrate the effectiveness of the damping criterion. All designs have been uniformly scaled in order to satisfy the constraints. A modified Aitken's accelerator has been used both to increase the ecumenical rate and decrease the net cost of convergence by reducing the number of repeat finite element analyses.

The method presented here demonstrates the usefulness of creating specific criteria based on previous scaled designs to smooth convergence of OC methods. Overall, this method has been found to be efficient and reliable, as compared to previous OC methods. Also, it is an adaptive method, which does not require adjustments of numerous internal parameters. The goal here has been to create the most computationally robust OC technique possible.

A wide range of design examples have been presented. Reasonably smooth upper-bound convergence of optimum designs obtained by using various OC recursive schemes have been charted and compared for the first time within this class of design problem--i.e., the minimum-weight design of bar structures having nonstructural mass and subjected to multiple frequency constraints and minimum gauge restrictions. Globally speaking, the method has exhibited a stabilizing effect on the oscillatory convergence propensity of the various OC recursive strategies examined. Also, known results have been improved with optimum designs obtained here in early cycles of the iterative process. It is anticipated that the method can smooth the convergence of optimum designs with other types of constraints, and this is the subject of continuing research.

ACKNOWLEDGEMENTS

This research effort has been supported by grants from the Air Force Office of Scientific Research under their Research Initiation Program and the National Science Foundation under their Minority Research Initiation Program. The authors gratefully acknowledge the technical communications and helpful assistance given by Dr. V.B. Venkayya of the Design and Analysis Group at the Wright Research and Development Center, and by Dr. R.S. Sandhu, Professor, Department of Civil Engineering at The Ohio State University.

REFERENCES

1. Miura, H., and Schmit, L.A., "Second order approximation of natural frequency constraints in structural synthesis, Int. Journal Num. Meth. Eng., Vol. 13, 1978, p. 337-351.
2. Woo, T.H., "Space frame optimization subject to frequency constraints", Proc. 27th AIAA/ASME/ASCE/AHS Structures, Structural Dynamics, and Materials Conference, San Antonio, Texas, May 19-21, 1986, p. 103-115.
3. Vanderplaats, G.N., and Salajegheh, E., "An efficient approximation technique for frequency constraints in frame optimization", Int. J. Num. Meth. Eng., Vol. 26, 1988, p. 1057-1069.
4. Canfield, R.A., "An approximation function for frequency constrained structural optimization", Proc. of Second NASA/Air Force Symposium on Recent Advances in Multidisciplinary Analysis and Optimization, Hampton, Virginia, September 28-30, 1988.
5. Kiusalaas, I.J., and Shaw, R.C.J., "An algorithm for optimal structural design with frequency constraints", Int. J. Num. Meth. Eng., Vol. 13, 1978, p. 283-295.
6. Khan, M.R., and Willmert, K.D., "An efficient optimality criterion method for natural frequency constrained structures", Computers and Structures, Vol. 14, No. 5-6, p. 501-507.
7. Levy, R. and Choi, K., "Implementation of natural frequency analysis and optimality criterion design", Computers and Structures, Vol. 10, 1979, p. 277-282.
8. Spillers, W.R., Singh, S. and Levy, R., "Optimization with frequency constraint", ASCE J. Struct. Div. Vol. 107 2337-2345, 1981.
9. Venkayya, V.B., Khot, N.S., Tischler, V.A. and Taylor, R.F., "Design of optimum structures for dynamic loads", 3rd Conf. Matrix Meth., Wright-Paterson AFB, Ohio, 1971, p. 619-658.
10. Khot, N.S., "Optimization of structures with multiple frequency constraints", Computer and Structures, Vol. 20, No. 5, p. 869-876 (1985).
11. Grandhi, R.V. and Venkayya, V.B., "Structural optimization with frequency constraints", 26th Structural, Dynamics and Materials Conference, Monterey, California (1986).
12. Venkayya, V.B. and Tischler, V.A., "Optimization of structures with frequency constraints", Computer Meth. for

Nonlinear Solids and Structural Mech., ASME, AMD-54, p. 239-259, (1983).

13. Pedersen, P., "The integrated approach of FEM-SLP for solving problems of optimal design", Optimization of Distributed Parameter Structures, (Hang and Cea, Oeds) Sijthoff and Nourdhoff, 1981, p. 757-780.

14. Pedersen, P., "Design with several eigenvalue constraints by finite elements and linear programming", J. Struct. Mech., Vol 10, No. 3, 1982, p.243-271.

15. Wang, B.P., "Synthesis of structures with multiple frequency constraints", AIAA Paper 86-0951, 1986.

16. Khot, N.S., Berke, L., and Venkayya, V.B., "Comparison of optimality criteria algorithms for minimum weight design of structures", AIAA Journal, Vol. 17, No. 2, 1978, p. 182-190.

17. Khot, N.S. and Berke, L., "Structural optimization using optimality criteria methods", New Directions in Optimum Structural Design, (Ed. by E. Atek, R.H. Gallagher, K.M. Ragsdell, and O.C. Zienkiewicz), John Wiley, (1978), p. 47-74.

18. Khot, N.S., "Optimality criterion methods in structural optimization", Foundations of Structural Optimization: A Unified Approach" (Ed. by A.J. Morris), p. 99-235, Wiley, New York (1984).

19. Venkayya, V.B. and Tischler, V.A., "A compound scaling algorithm for mathematical optimization", WRDC-TR-89-3040 (1989).

20. Jennings, A., "Accelerating the convergence of matrix iterative processes", J. Inst. Maths. Applics., Vol. 8, p. 99-110 (1971).

21. Boyle, E.F. and Jennings, A., "Accelerating the convergence of elastic-plastic stress analysis", Int. J. Num. Meth. Engng., Vol. 7, p. 232-235 (1973).

22. Bathe, K.J., Finite Element Procedures in Engineering Analysis, Prentice-Hall, Inc., 1982.

Table 1 Ten Bar Truss
Initial and Final Frequencies (Hz.) in Different Constraint Conditions *

Frequency No.	Initial Design	$\omega_2 = 10.0$	$\omega_1 = 7.0$ $\omega_2 \geq 15.0$	$\omega_1 = 7.0$ $\omega_2 \geq 15.0$ $\omega_3 \geq 20.0$	$\omega_1 \geq 3.5$ $\omega_2 \geq 10.$ $\omega_3 \geq 14.0$
1	8.95 (8.96)	3.07 (3.26)	7.00 (7.00)	7.00 (7.00)	3.68 (4.40)
2	26.84 (27.08)	10.00 (10.00)	15.50 (15.58)	16.67 (15.61)	10.50 (12.14)
3	27.06 (27.45)	10.00 (10.19)	17.40 (16.93)	20.29 (20.17)	14.00 (14.00)
4	48.73 (51.25)	11.23 (16.01)	18.39 (18.75)	26.74 (20.77)	14.06 (17.89)
5	55.85 (58.00)	13.08 (18.08)	27.95 (29.13)	29.35 (28.76)	15.90 (19.58)
6	61.42 (64.73)	17.46 (22.96)	29.09 (30.30)	29.41 (29.76)	20.07 (22.96)
7	63.46 (66.87)	25.79 (25.21)	46.43 (46.93)	47.35 (53.88)	29.08 (34.01)
8	73.90 (80.85)	26.75 (27.25)	48.61 (49.67)	49.78 (56.03)	30.24 (35.72)
Weight (lbs.)	4000.0 (4000.0)	260.0 (304.5)	1162.7 (1172.6)	1256.6 (1308.4)	417.1 (489.17)

* present analysis using exponential resizing and approximate
Lagrange multiplier formulas
() via reference [1].

Table 2 Ten Bar Truss
*Optimum Design Variables (in.²) in Different Constraint Conditions**

Element No.	$\omega_2 = 10.0$	$\omega_1 = 7.0$ $\omega_2 \geq 15.0$	$\omega_1 = 7.0$ $\omega_2 \geq 15.0$ $\omega_3 \geq 20.0$	$\omega_1 \geq 3.5$ $\omega_2 \geq 10.0$ $\omega_3 \geq 14.0$
1	0.845 (0.910)	5.897 (5.511)	4.978 (5.672)	1.026 (2.306)
2	0.896 (0.821)	2.003 (1.937)	2.690 (3.823)	1.064 (1.304)
3	0.911 (0.910)	5.897 (5.511)	4.979 (5.672)	1.038 (2.306)
4	0.918 (0.821)	2.002 (1.937)	2.689 (3.823)	1.047 (1.304)
5	0.375 (0.768)	0.159 (0.207)	0.227 (0.646)	0.293 (0.639)
6	0.199 (0.570)	0.568 (0.414)	0.732 (0.321)	0.336 (0.557)
7	0.766 (0.712)	3.380 (3.616)	4.437 (4.191)	1.850 (1.029)
8	0.802 (0.712)	3.380 (3.616)	4.436 (4.191)	1.876 (1.029)
9	0.299 (0.581)	2.231 (2.414)	2.143 (1.604)	0.537 (0.800)
10	0.308 (0.581)	2.231 (2.414)	2.144 (1.604)	0.536 (0.800)
Weight (lbs.)	260.0 (304.5)	1162.7 (1172.6)	1256.6 (1308.4)	417.1 (489.17)

* present analysis using exponential resizing and approximate Lagrange multiplier formulae
 () via reference [11].

Table 3 Thirty Eight Bar Truss
Design Cycle History for $\omega_1^2 = 2500$ and $\omega_2^2 \geq 2500$ (rad./sec.)²

Iter.* No.	ω_1^2	ω_2^2	Weight (lbs.)	Iter.+ No.	ω_1^2	ω_2^2	Weight (lbs.)
1	2500	3671	27.74	1	2500	8560	52.30
2	2500	2907	25.74	2	2500	6451	39.41
3	2500	3111	30.65	3	2500	5061	33.29
4	2500	4495	* 28.56	4	2500	4326	31.01
5	2500	3435	26.29	5	2500	4033	29.83
6	2500	2759	25.26	6	2500	3706	28.94
7	2500	2507	24.93	7	2500	3314	28.26
				8	2500	2880	27.72
				9	2500	2537	27.36
				10	2500	2501	27.29
				11	2500	2500	27.28

* present analysis using exponential resizing and approximate Lagrange multiplier

+ via. reference [10]

* accelerated value

Table 4 Thirty Eight Bar Truss
Design Cycle History for $\omega_1^2 = 2500$ and $\omega_2^2 \geq 3000$ (rad./sec.)²

Iter.* No.	ω_1^2	ω_2^2	Weight (lbs.)	Iter.+ No.	ω_1^2	ω_2^2	Weight (lbs.)
1	2500	3668	27.74	1	2500	8560	52.30
2	2578	3000	26.58	2	2500	6451	39.41
3	2500	4467	28.33	3	2500	5061	33.29
4	2500	3715	* 26.76	4	2500	4326	31.01
5	2500	3011	25.64	5	2500	4033	29.83
				6	2500	3706	28.94
				7	2500	3314	28.26
				8	2500	3016	27.80
				9	2500	2998	27.72
				10	2500	2999	27.72
				11	2500	3000	27.72

* present analysis using exponential resizing and approximate Lagrange multiplier

+ via. reference [10]

* accelerated value

*Table 5 Two Hundred Bar Truss
Initial and Final Five Frequencies (Hz.) for a Specified
Fundamental Frequency*

	ω_1	ω_2	ω_3	ω_4	ω_5	Weight (lbs.)
Initial Design	2.87 (2.87)	13.01 (13.02)	13.70 (13.72)	31.80 (31.92)	37.41 (37.68)	99633.4 (99634.0)
<u>Frequency Limit</u>						
2.0	2.00 (2.00)	6.27 (6.24)	6.65 (6.66)	10.69 (10.69)	12.63 (12.64)	2366.5 (2365.7)
3.0	3.00 (3.00)	8.19 (8.19)	8.92 (8.92)	13.66 (13.67)	13.81 (13.81)	5006.5 (5004.7)
4.0	4.00 (4.00)	9.83 (9.79)	10.80 (10.90)	14.46 (14.43)	15.61 (15.66)	9196.7 (9198.4)
5.0	5.00 (5.00)	11.24 (11.24)	12.69 (12.71)	15.13 (15.13)	17.15 (17.17)	15508.3 (15500.9)
6.0	6.00 (6.00)	12.59 (12.61)	14.25 (14.28)	15.89 (15.90)	18.13 (18.13)	24846.4 (24830.6)
7.0	7.00 (7.00)	13.82 (13.93)	15.67 (15.86)	16.84 (16.90)	19.60 (19.65)	38701.7 (38683.3)
8.0	8.00 (8.00)	14.93 (16.74)	16.99 (19.08)	17.81 (20.15)	21.14 (24.16)	59560.0 (61186.7)

present analysis using exponential resizing and approximate
Lagrange multiplier formulae.
() via reference [1].

*Table 6 Two Hundred Bar Truss
Initial and Final Five Frequencies (Hz.)
in Different Constraint Conditions*

Frequency No.	Initial Design	$\omega_1 = 3.0$ $\omega_2 \geq 9.0$	$\omega_1 = 4.0$ $\omega_2 \geq 10.0$	$\omega_1 \geq 3.0$ $\omega_2 \geq 9.0$ $\omega_3 \geq 14.0$
1	2.87 (2.87)	3.00 (3.00)	4.00 (4.00)	3.12
2	13.01 (13.02)	9.39 (9.01)	10.44 (10.00)	9.37
3	13.70 (13.72)	9.67 (9.41)	11.22 (11.04)	14.00
4	31.80 (31.92)	14.43 (14.39)	14.97 (14.46)	14.25
5	37.41 (37.68)	14.76 (14.78)	15.99 (15.78)	16.22
Weight (lbs.)	99633.4 (99634.0)	5226.7 (5226.5)	9315.1 (9220.9)	7837.0

* present analysis using exponential resizing and
approximate Lagrange multiplier formulae.
() via reference [11].

Ten Bar Truss

$$\omega_2 = 10 \text{ Hz.}$$

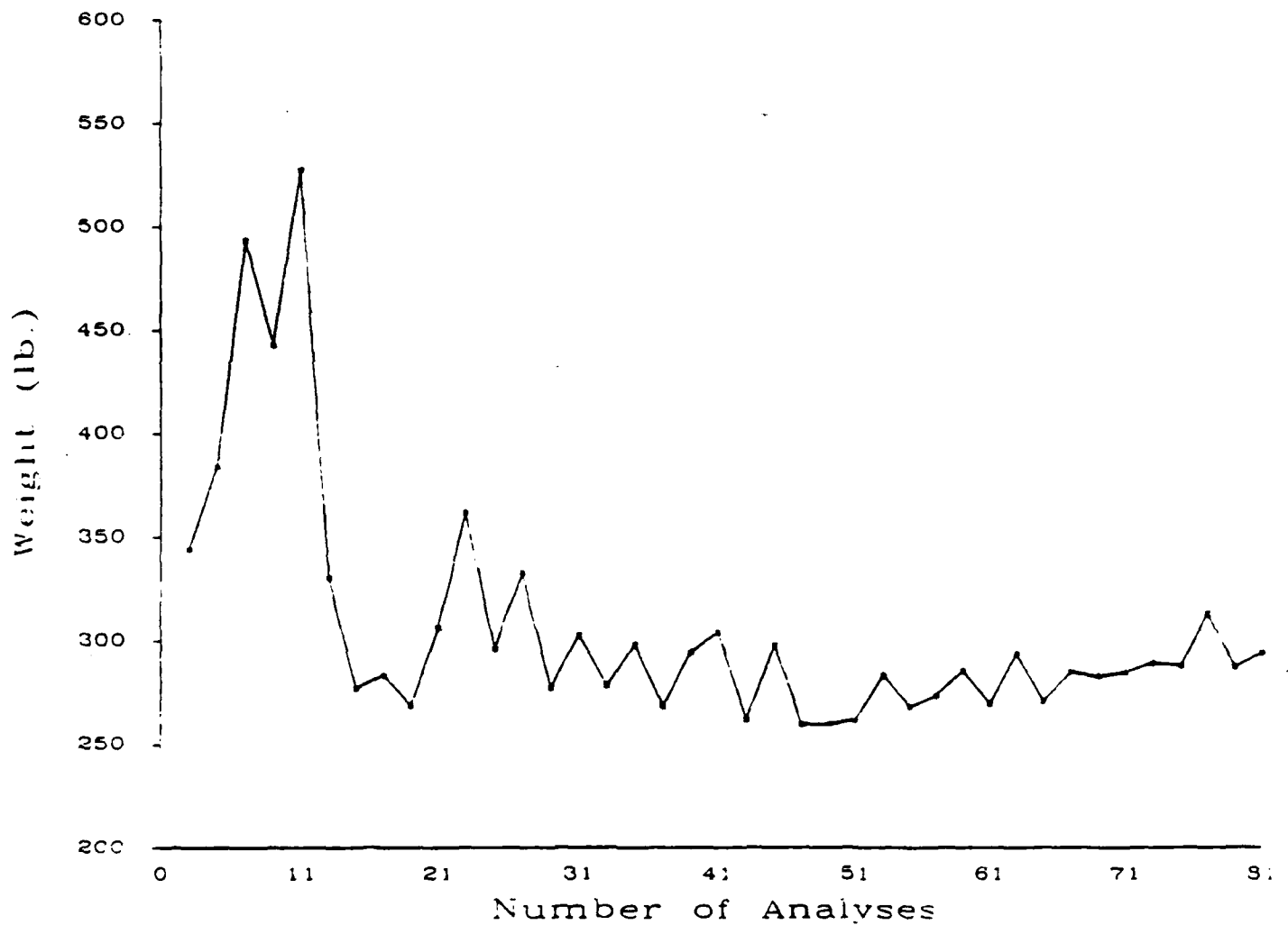


Figure 1 Convergence quality when arbitrarily reducing step size in single-constrained (higher vibration mode) problems

Ten Bar Truss

$$\omega_1 \geq 3.5 \text{ Hz.} \quad \omega_2 \geq 10 \text{ Hz.} \quad \omega_3 \geq 14 \text{ Hz.}$$

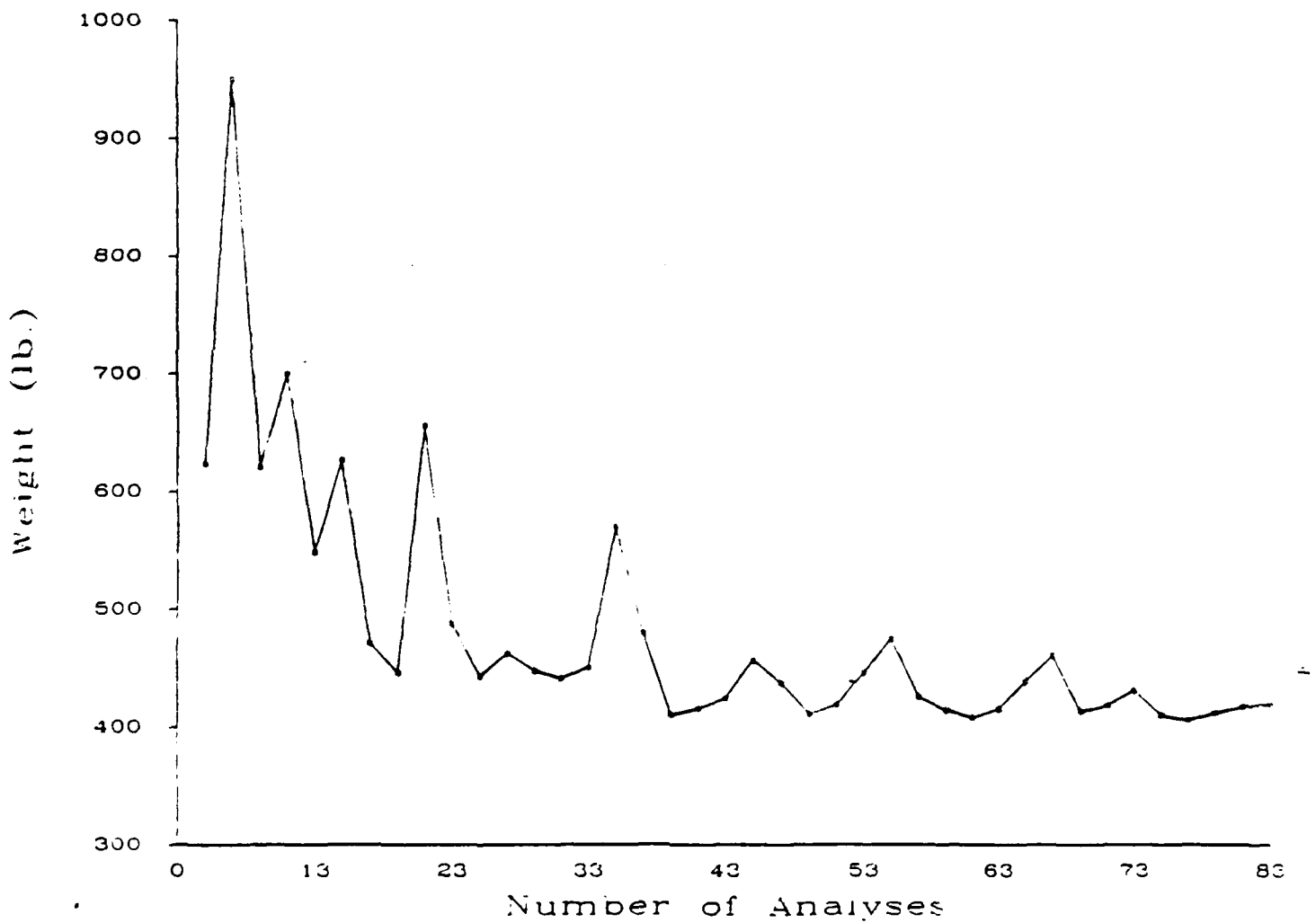


Figure 2 Convergence quality when arbitrarily reducing step size in multiple-constrained problem.

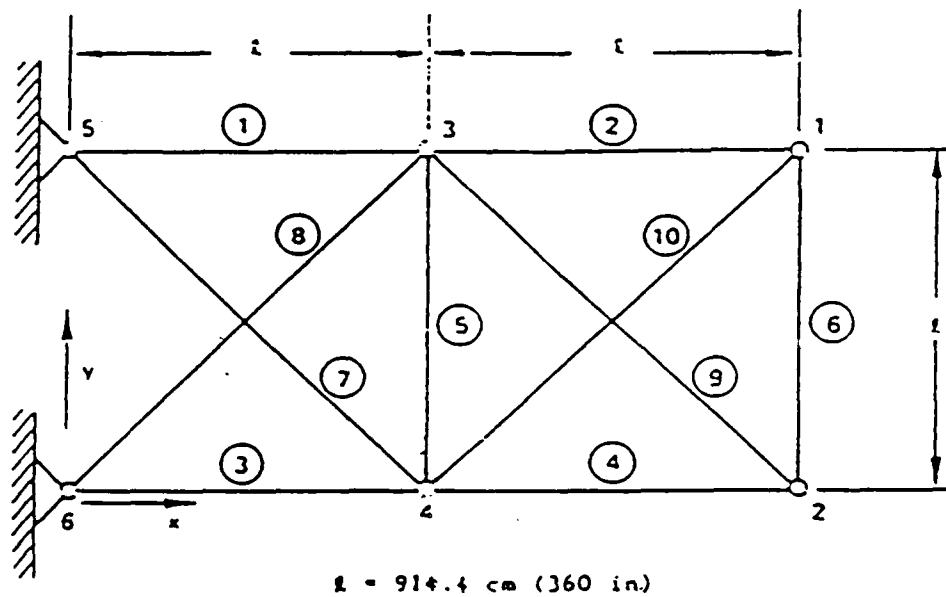


Figure 3 Ten bar truss

Ten Bar Truss

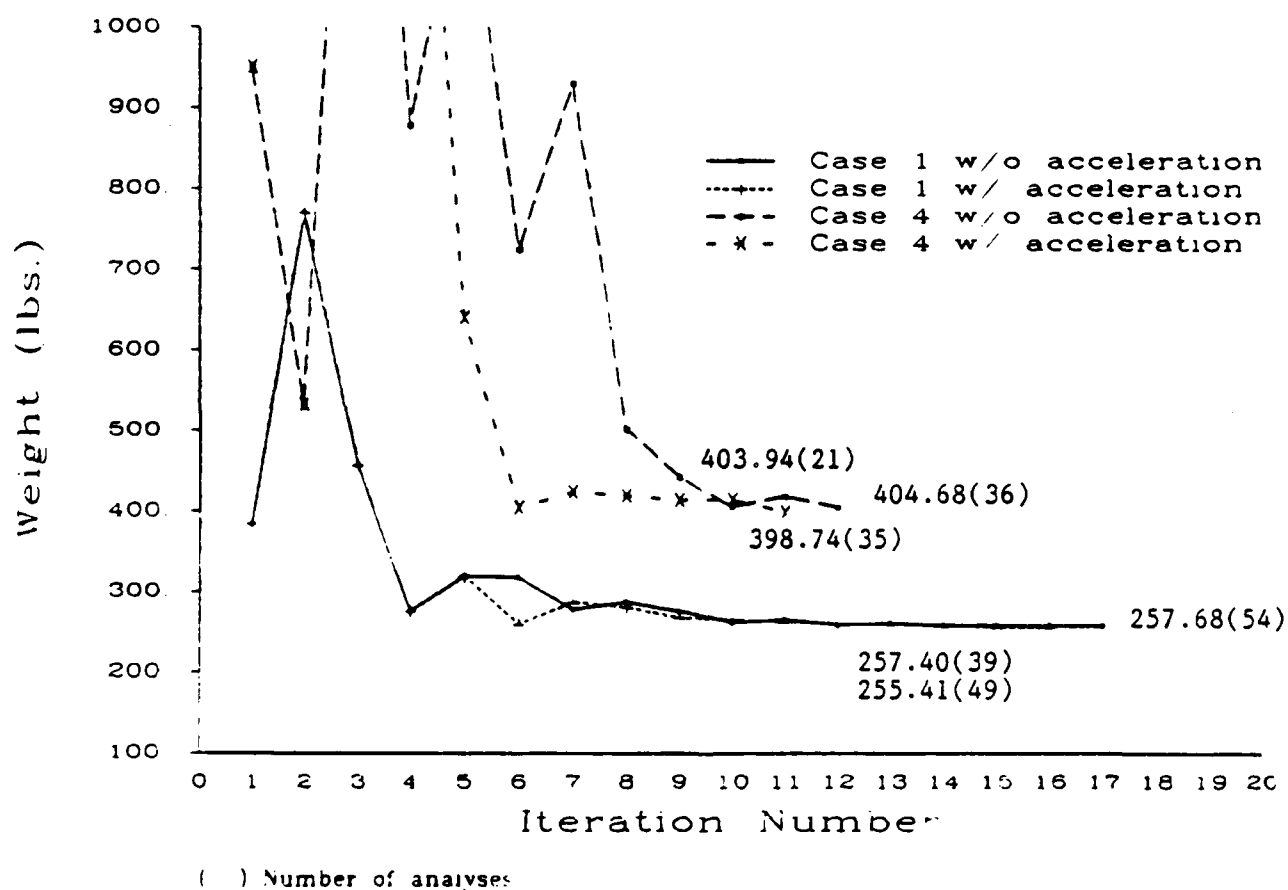


Figure 4 Effect of Aitken's accelerator on iteration history of ten-bar truss with multiple frequency constraints

Element	Connecting Nodes	Element	Connecting Nodes	Element	Connecting Nodes
1	1-2	14	7-9	27	13-16
2	1-3	15	7-10	28	14-15
3	1-4	16	8-9	29	14-16
4	2-3	17	8-10	30	15-17
5	2-4	18	9-11	31	15-18
6	3-5	19	9-12	32	16-17
7	3-6	20	10-11	33	16-18
8	4-5	21	10-12	34	17-19
9	4-6	22	11-13	35	17-20
10	5-7	23	11-14	36	18-19
11	5-8	24	12-13	37	18-20
12	6-7	25	12-14	38	19-20
13	6-8	26	13-15		

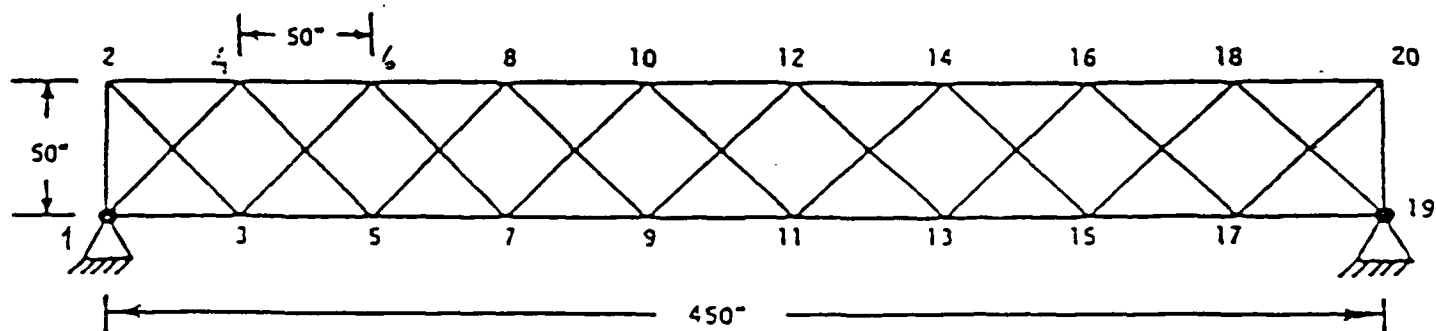


Figure 5 Thirty-eight bar truss

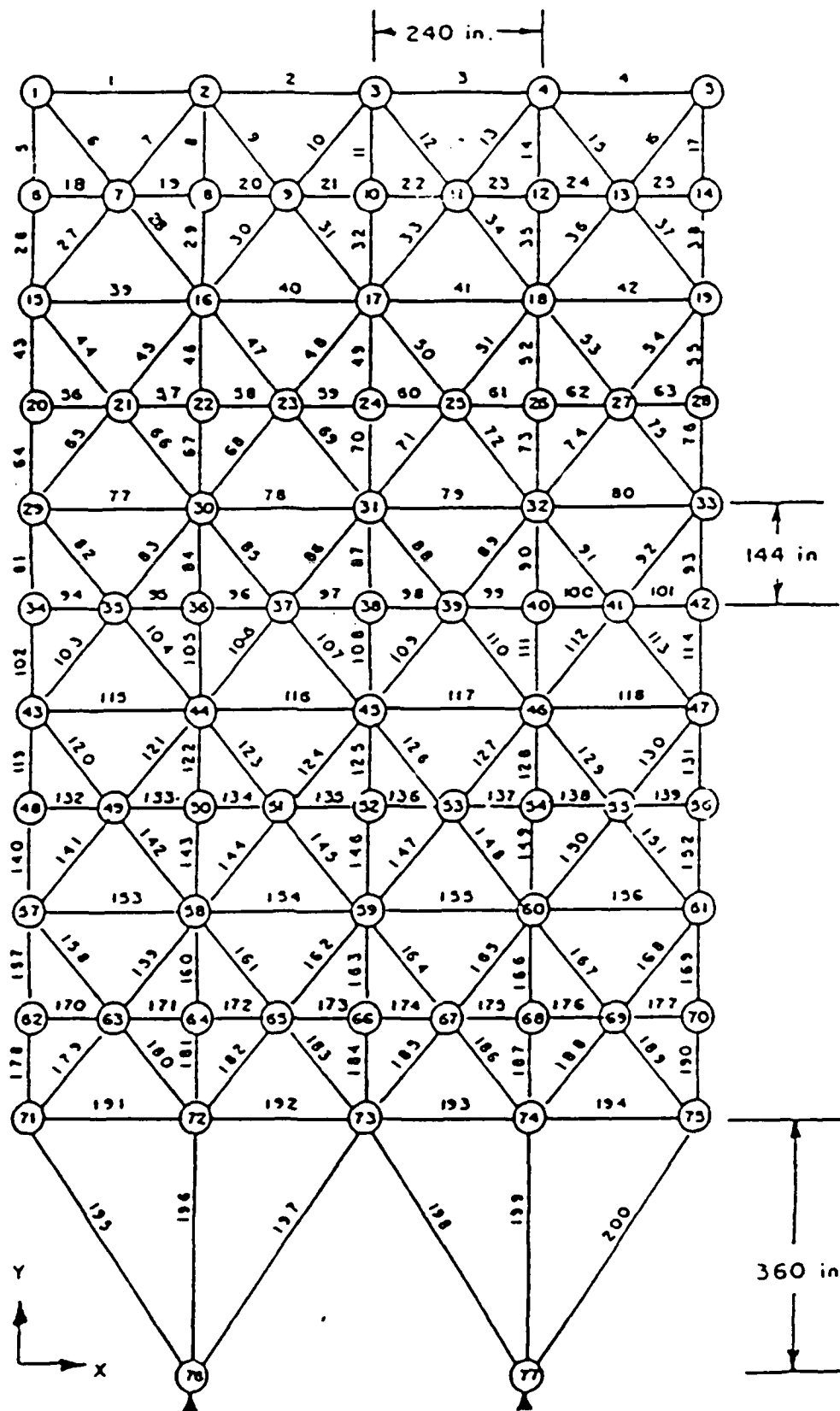
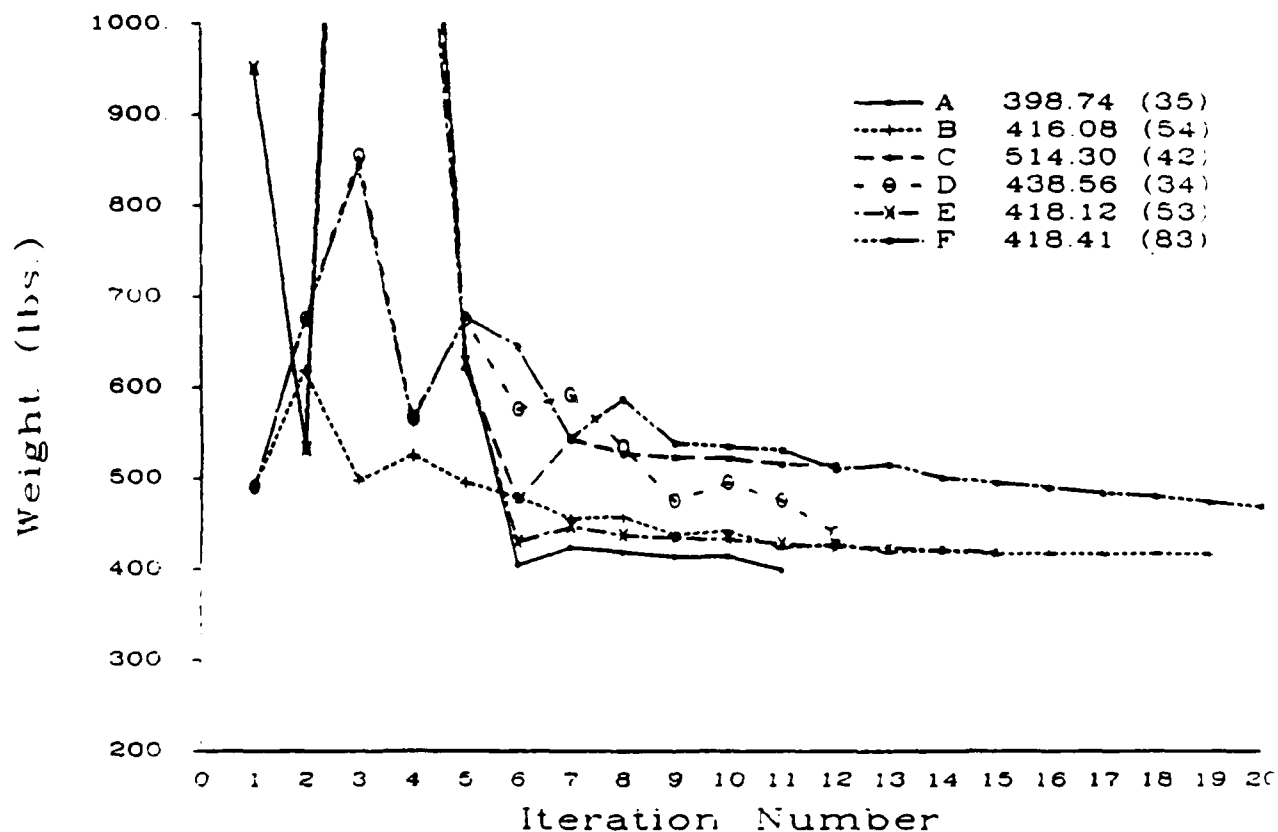


Fig. 6 Two Hundred Bar Truss Structure

Ten Bar Truss

$$\omega_1 \geq 3.5 \text{ Hz.} \quad \omega_2 \geq 10 \text{ Hz.} \quad \omega_3 \geq 14 \text{ Hz}$$



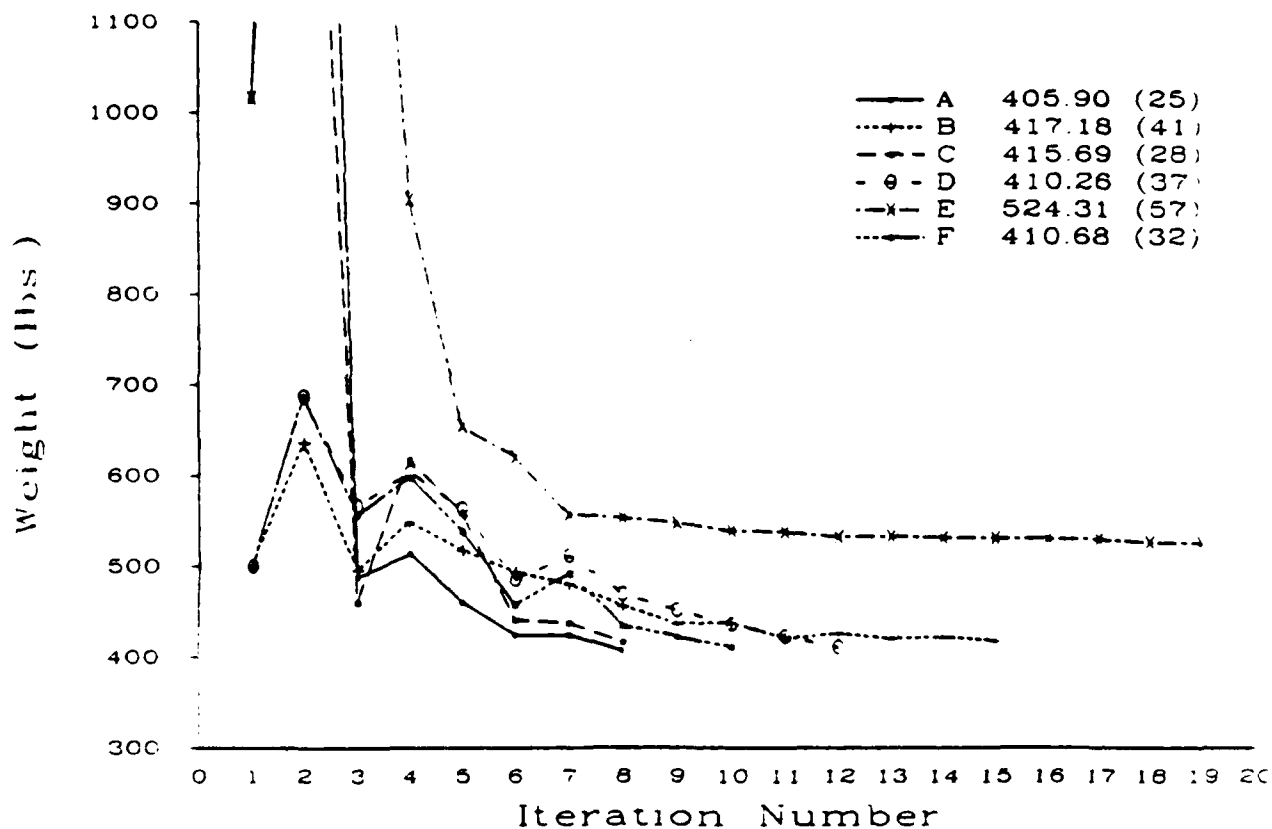
- A : exponential resizing/approximate Lagrange multiplier formulae
- B : linear resizing/approximate Lagrange multiplier formulae
- C : exponential resizing/exponential Lagrange multiplier formulae
- D : linear resizing/exponential Lagrange multiplier formulae
- E : exponential resizing/linear Lagrange multiplier formulae
- F : linear resizing/linear Lagrange multiplier formulae
- () number of analyses

Figure 7 Iteration history for ten-bar truss with multiple frequency constraints

Ten Bar Truss

$$\omega_1 \geq 3.5 \text{ Hz} \quad \omega_2 \geq 10 \text{ Hz} \quad \omega_3 \geq 14 \text{ Hz}$$

Including Modal Kinetic Energy

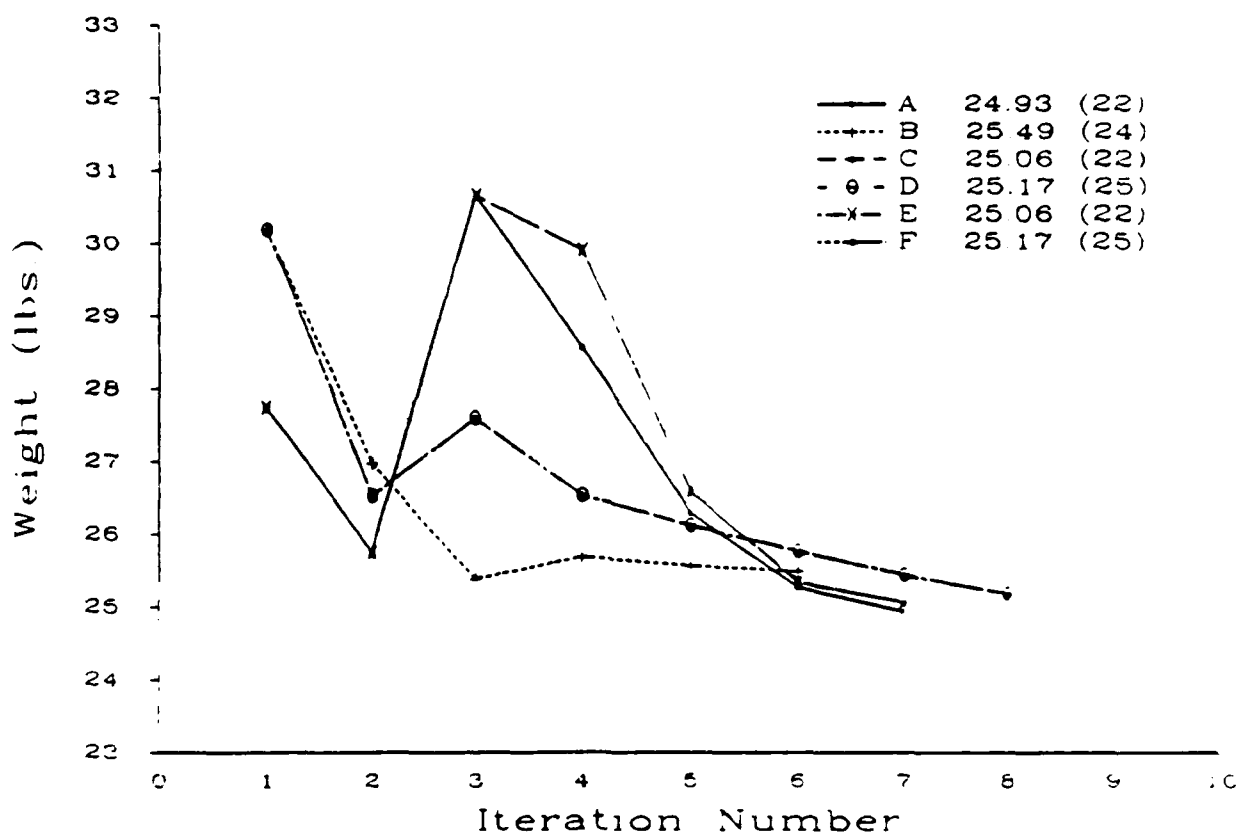


- A : exponential resizing/approximate Lagrange multiplier formulae
- B : linear resizing/approximate Lagrange multiplier formulae
- C : exponential resizing/exponential Lagrange multiplier formulae
- D : linear resizing/exponential Lagrange multiplier formulae
- E : exponential resizing/linear Lagrange multiplier formulae
- F : linear resizing/linear Lagrange multiplier formulae
- () : number of analyses

Figure 8 Iteration history for ten-bar truss with multiple frequency constraints

Thirty Eight Bar Truss

$$\omega_1 = 2500 \text{ Hz. } \omega_2 \geq 2500 \text{ Hz}$$

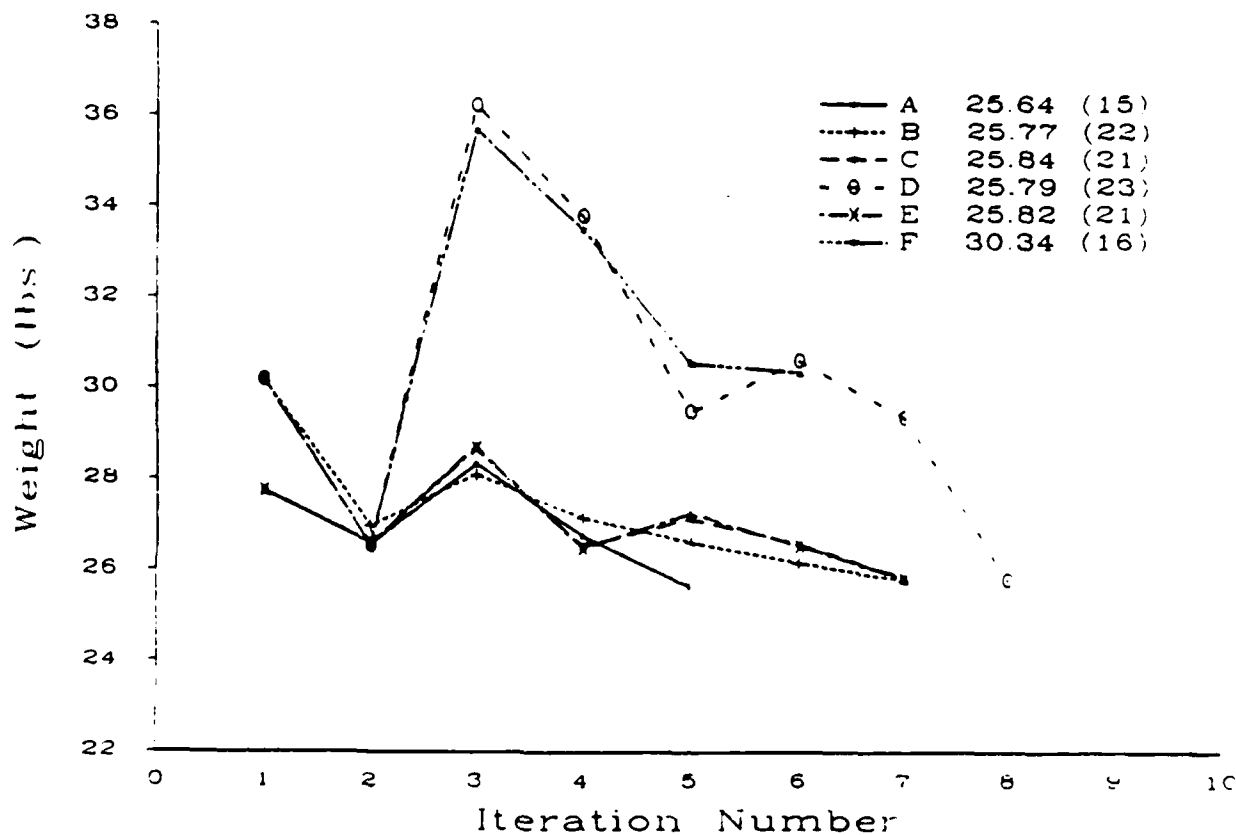


- A : exponential resizing/approximate Lagrange multiplier formulae
- B : linear resizing/approximate Lagrange multiplier formulae
- C : exponential resizing/exponential Lagrange multiplier formulae
- D : linear resizing/exponential Lagrange multiplier formulae
- E : exponential resizing/linear Lagrange multiplier formulae
- F : linear resizing/linear Lagrange multiplier formulae
- () number of analyses

Figure 9 Iteration history for thirty-eight bar truss with multiple frequency constraints

Thirty Eight Bar Truss

$$\omega_1 = 2500 \text{ Hz. } \omega_2 \geq 3000 \text{ Hz}$$



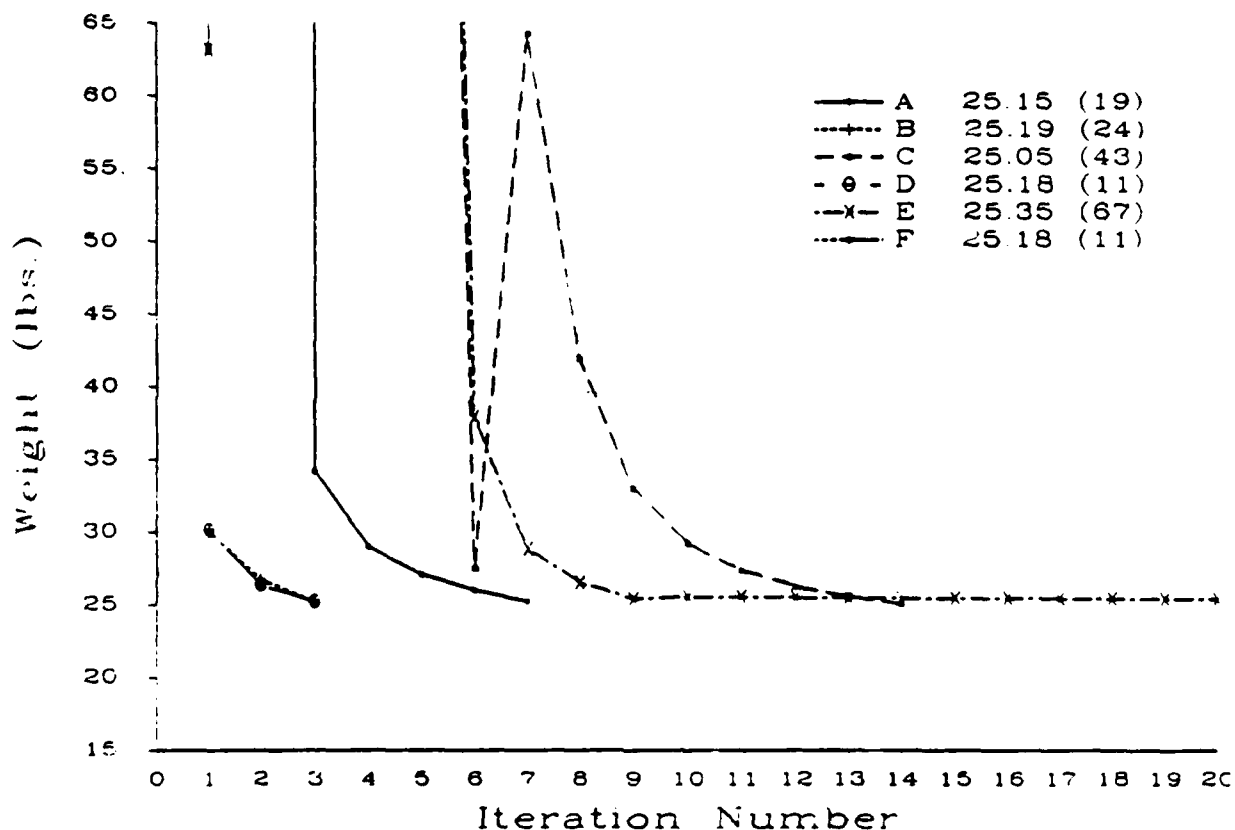
- A : exponential resizing/approximate Lagrange multiplier formulae
- B : linear resizing/approximate Lagrange multiplier formulae
- C : exponential resizing/exponential Lagrange multiplier formulae
- D : linear resizing/exponential Lagrange multiplier formulae
- E : exponential resizing/linear Lagrange multiplier formulae
- F : linear resizing/linear Lagrange multiplier formulae
- () number of analyses

Figure 10 Iteration history for thirty-eight bar truss with multiple frequency constraints

Thirty Eight Bar Truss

$$\omega_1 = 2500 \text{ Hz. } \omega_2 \geq 2500 \text{ Hz.}$$

Including Modal Kinetic Energy



- A . exponential resizing/approximate Lagrange multiplier formulae
- B . linear resizing/approximate Lagrange multiplier formulae
- C . exponential resizing/exponential Lagrange multiplier formulae
- D . linear resizing/exponential Lagrange multiplier formulae
- E . exponential resizing/linear Lagrange multiplier formulae
- F . linear resizing/linear Lagrange multiplier formulae
- () number of analyses

Figure 11 Iteration history for thirty-eight bar truss with multiple frequency constraints

Thirty Eight Bar Truss

$$\omega_1 = 2500 \text{ Hz. } \omega_2 \geq 3000 \text{ Hz.}$$

Including Modal Kinetic Energy

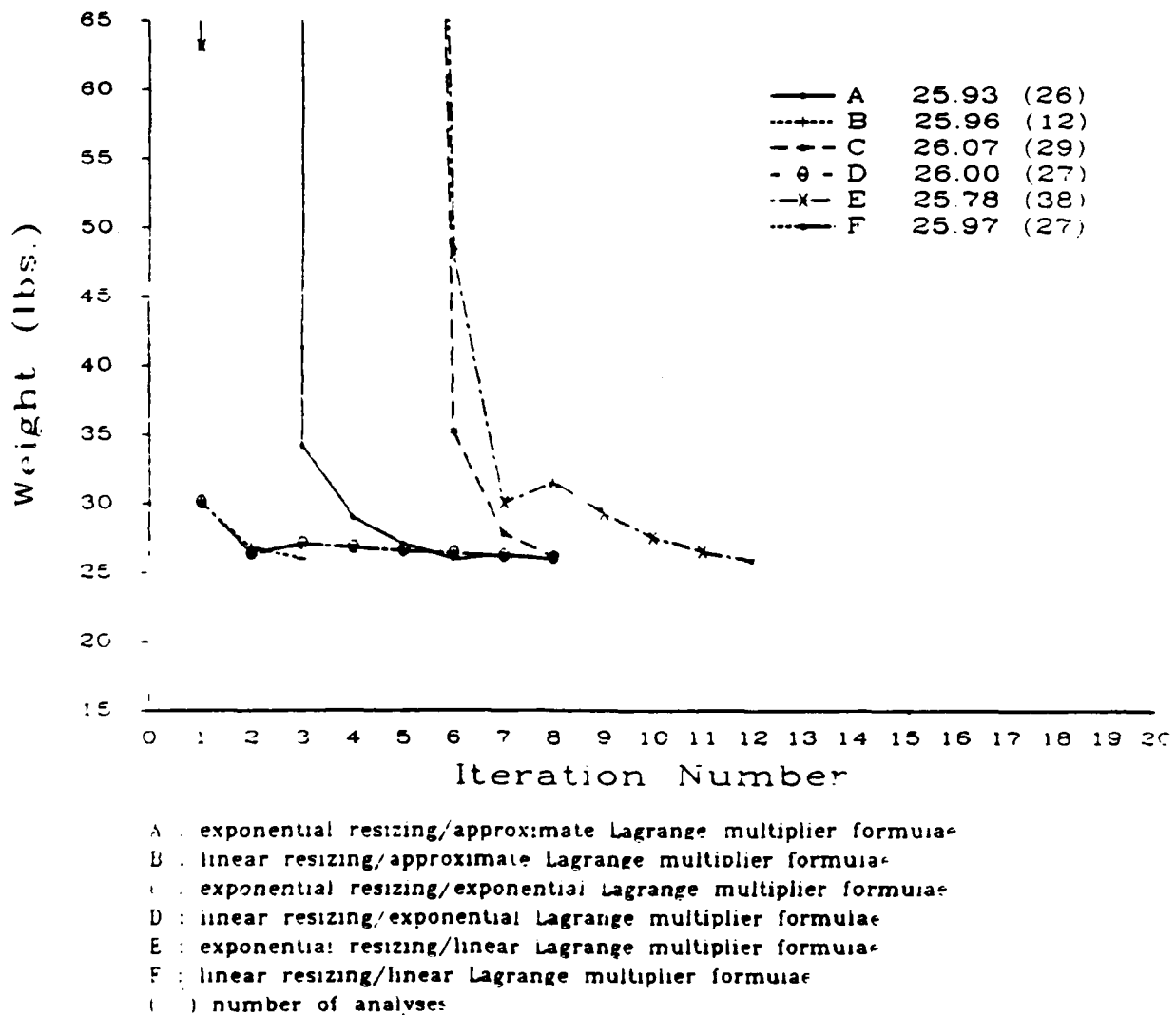
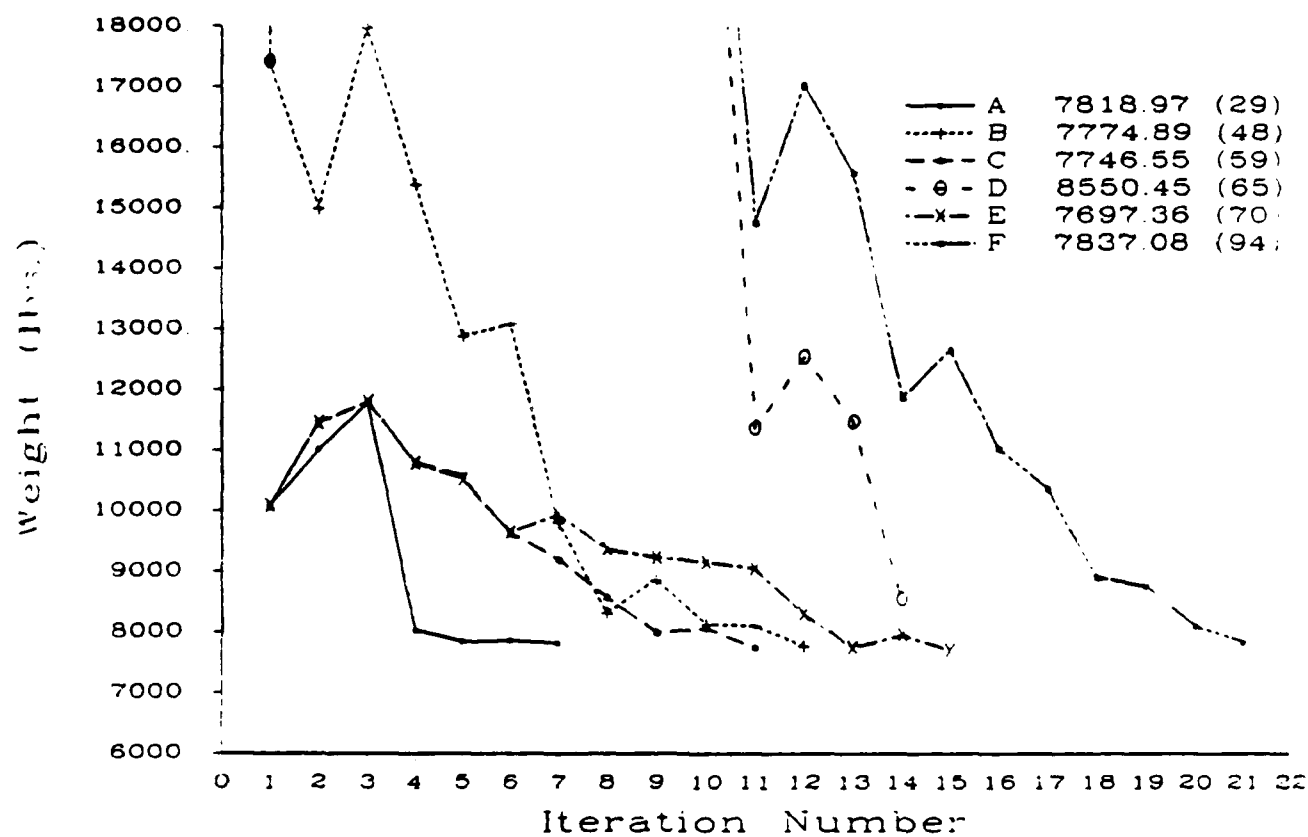


Figure 12 Iteration history for thirty-eight bar truss with multiple frequency constraints

Two Hundred Bar Truss

$\omega_1 \geq 3 \text{ Hz.}$ $\omega_2 \geq 9 \text{ Hz.}$ $\omega_3 \geq 14 \text{ Hz.}$



- A : exponential resizing/approximate Lagrange multiplier formulae
- B : linear resizing/approximate Lagrange multiplier formulae
- C : exponential resizing/exponential Lagrange multiplier formulae
- D : linear resizing/exponential Lagrange multiplier formulae
- E : exponential resizing/linear Lagrange multiplier formulae
- F : linear resizing/linear Lagrange multiplier formulae
- () number of analyses

Figure 13 Iteration history for two-hundred bar truss with multiple frequency constraints

Two Hundred Bar Truss

$$\omega_1 \geq 3 \text{ Hz.} \quad \omega_2 \geq 9 \text{ Hz.} \quad \omega_3 \geq 14 \text{ Hz}$$

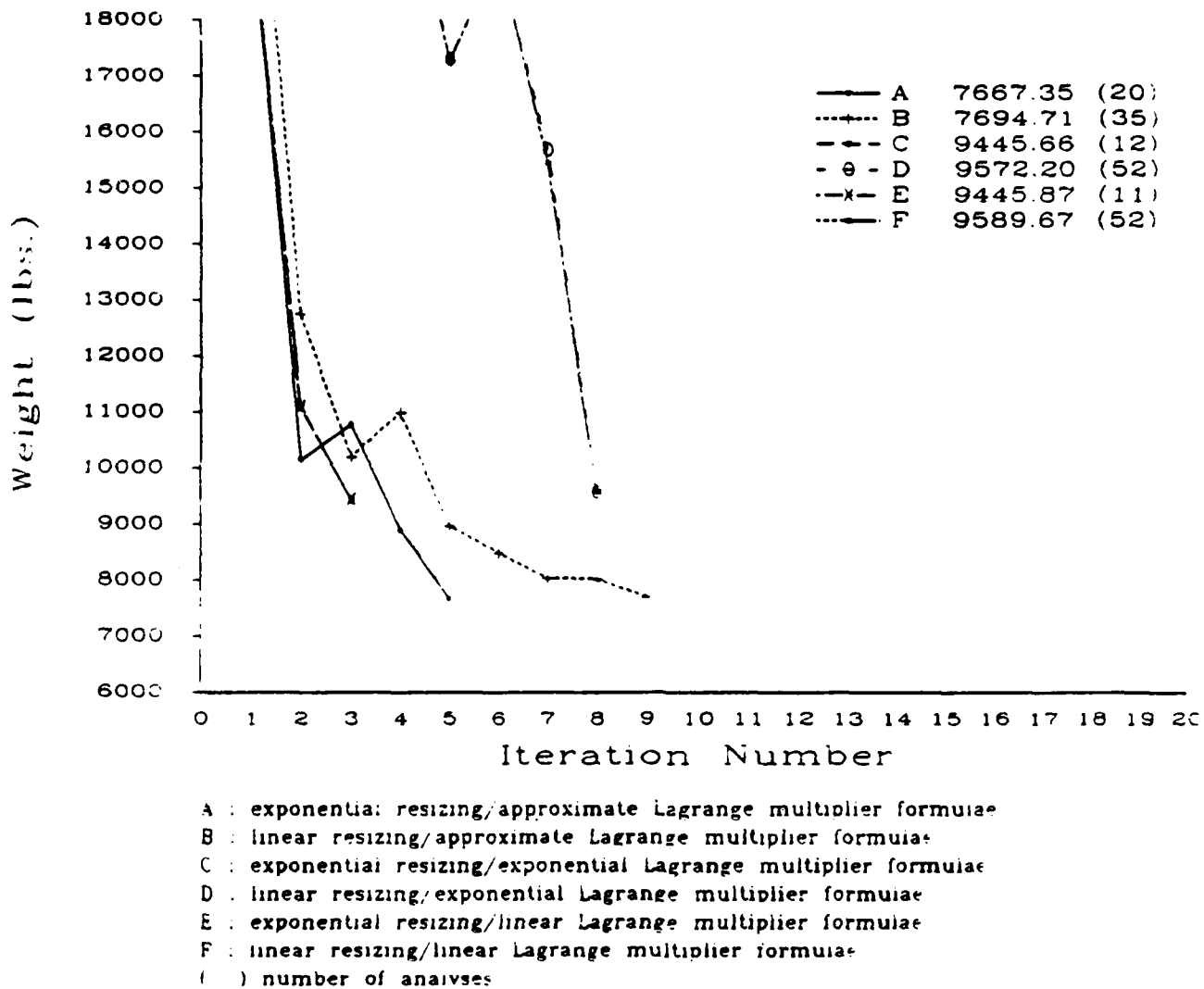
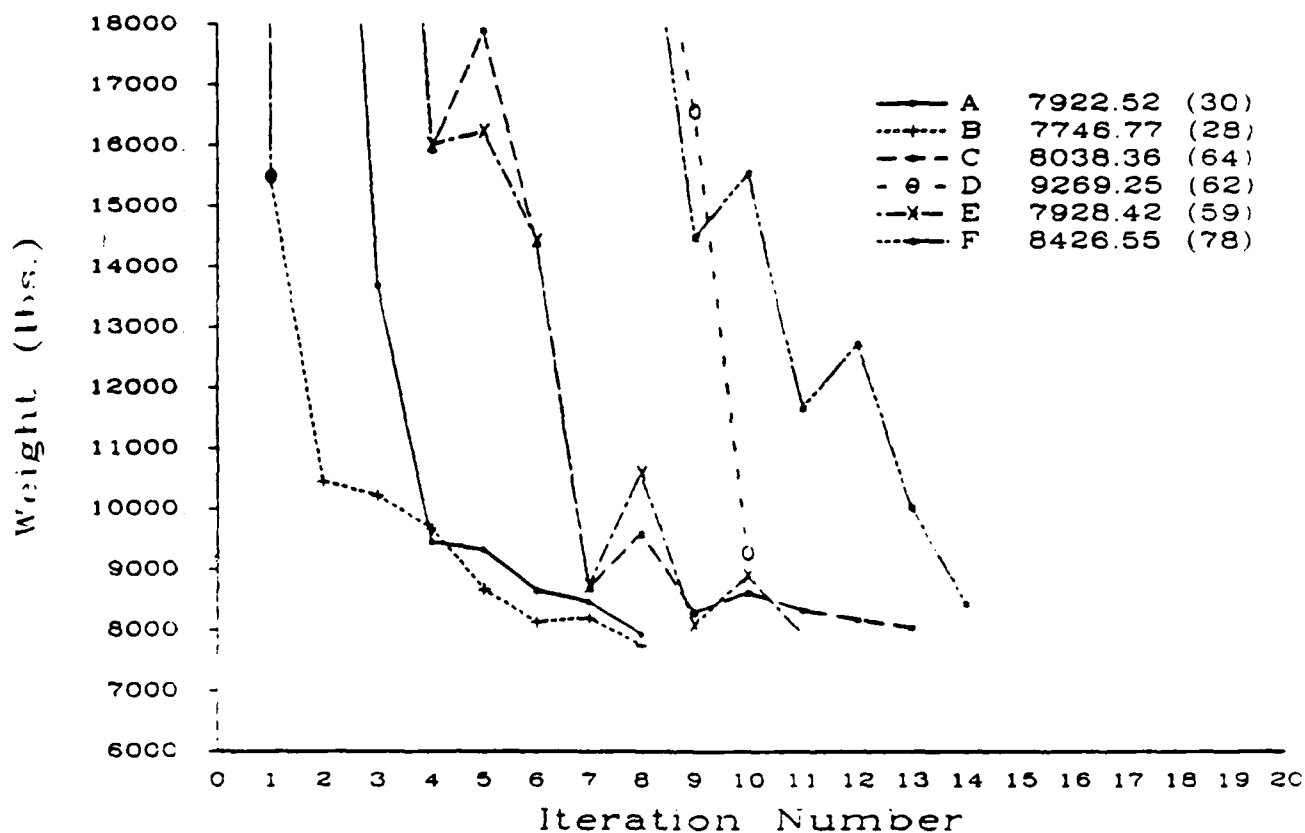


Figure 14 Iteration history for two-hundred bar truss with multiple frequency constraints and maximum gauge restriction.

Two Hundred Bar Truss

$$\omega_1 \geq 3 \text{ Hz} \quad \omega_2 \geq 9 \text{ Hz} \quad \omega_3 \geq 14 \text{ Hz}$$

Including Modal Kinetic Energy



- A : exponential resizing/approximate Lagrange multiplier formulae
 B : linear resizing/approximate Lagrange multiplier formulae
 C : exponential resizing/exponential Lagrange multiplier formulae
 D : linear resizing/exponential Lagrange multiplier formulae
 E : exponential resizing/linear Lagrange multiplier formulae
 F : linear resizing/linear Lagrange multiplier formulae
 () number of analyses

Figure 15 Iteration history for two-hundred bar truss with multiple frequency constraints and maximum gauge restriction

Section III

**A ROBUST OPTIMALITY CRITERIA PROCEDURE
FOR CROSSECTIONAL OPTIMIZATION OF FRAME STRUCTURES
WITH MULTIPLE FREQUENCY LIMITS**

Oliver G. McGee¹ and Khing F. Phan²
Department of Civil Engineering
The Ohio State University
Columbus, Ohio 43210, U.S.A.

Submitted for publication in the American Institute of
Aeronautics and Astronautics Journal

¹Assistant Professor

²Graduate Research Associate

ABSTRACT

An efficient optimality criteria (OC) method is presented for crosssectional optimization of 2-D frame structures supporting a sizeable amount of nonstructural mass, and subjected to multiple natural frequency constraints and minimum and maximum gauge restrictions. The iterative method involves alternately satisfying the constraints (scaling) and applying the Kuhn-Tucker (optimality) condition (resizing). This being the case, a criterion, which uses previous scaled designs to "adaptively" tune the step size, is established. As the step size is tuned, the convergence rate is decreased. Hence, a modified Aitken's accelerator, which extrapolates from previous scaled designs to obtain an improved one, is used. When the frequency constraints are to be satisfied, the sizing variables (crosssectional areas) are uniformly scaled to the constraint surfaces using a closed-form formulation. This exact formulation is introduced for the first time in the open literature. Design examples are presented to demonstrate the method. The method is also used to quantitatively survey the convergence of OC recursive relations compositely used to resize and to evaluate the Lagrange multipliers. The method is robust, as it quickly dissolves the (sometimes violent) oscillations of scaled weights in the iteration history. Also, it eliminates the need for adjustments of internal parameters during the redesign phase.

1. INTRODUCTION

Crosssectional optimization of frame structures having nonstructural mass subjected to natural frequency constraints and minimum and maximum gauge restrictions is a purposeful class of design problem. A pointed application is in controlling critical ranges of natural frequencies in situations of narrow-band forced excitations. Given the ability to manipulate a particular frequency value, a designer can realize substantial improvements in the overall forced response of the frame structure.

In the late sixties and early seventies the optimality criteria (OC) approach to structural synthesis was introduced [1]. Subsequently, many algorithms using OC procedures were proposed (see reference [2] for an excellent review), all of which demonstrated remarkable efficiency and reliability on design problems having a large number of sizing variables and multiple constraints. A few OC algorithms [3-8] slanted towards the approach of satisfying "one most critical constraint" to avoid scaling and to avoid calculating a large number of Lagrange multipliers. Nonetheless, modern OC algorithms [9-13] involve first choosing a suitable initial design, and then alternately satisfying multiple constraints (scaling) and applying the Kuhn-Tucker (optimality) condition (resizing).

Basically, the recurrence relations for resizing are derived from the optimality condition and contain unknown Lagrange multipliers each of which correspond to a critical or potentially critical (or better yet "active") constraint. A number of numerical procedures are available for efficient evaluation of these multipliers, which first must be computed before the recurrence relations for resizing can be used. Moreover, the concept of scaling involves changing the design variables (either by adding differential quantities or by multiplying the variables by constant factors) in order to place the violated constraints on or inside the constraint surface. Conversely, if no constraints are violated, then scaling will place the most critical constraints on the boundary. It is advantageous to evaluate the constraints on the boundaries, because this is where sensitivity information is most meaningful. Scaling is essential to the efficiency of the OC method, particularly when it is applied to structural problems involving both dependent and independent sizing variables per member. It has been suggested that when the crosssectional area and a principal moment of inertia of a 2-D frame member are nonlinearly related, scaling procedures normally used in OC methods are at most approximate in nature [8].

In this paper, a closed-form formula is developed for scaling frame structures with frequency constraints. The scaling formulation is tested for its accuracy in predicting the

constraint surface for a wide range of desired target frequencies. The closed-form scaling procedure is united with an "adaptive" design strategy in which Aitken's accelerator is coupled with "tuned" OC recursive methods [13]. What is offered here is a criterion, which uses previous scaled designs to "adaptively" tune the step size. Its purpose is to dissolve the (sometimes violent) oscillations of scaled design weights in the iteration history. As the step size is tuned, the convergence rate is decreased. Hence, a modified Aitken's accelerator, which extrapolates from previous scaled designs to obtain an improved one, is utilized. Its effect is to both increase the ecumenical rate and reduce the net cost of convergence by reducing the number of repeat finite element analyses.

The method presented here in detail is used to quantitatively survey the convergence of several OC recursive schemes compositely used to resize and to evaluate the Lagrange multipliers. Design examples are presented to demonstrate the method. The method is adaptable, as it eliminates the need for adjustments of internal parameters during the redesign stage.

2. MATHEMATICAL STATEMENT OF THE PROBLEM

The present design problem is defined mathematically as follows:

minimize the structural weight of a plane frame structure

$$\min W(\mathbf{x}) = \rho_i l_i x_i \quad (i=1,2,\dots,n) \quad (1)$$

subject to m natural frequency constraints

$$g_j(\mathbf{x}) = \omega_j^2 - \omega_j^{2*} \leq 0 \quad (j=1,2,\dots,m) \quad (2)$$

and n side constraints on minimum and maximum gauge

$$x_i^L \leq x_i \leq x_i^U \quad (i=1,2,\dots,n) \quad (3)$$

where in equation (1) a summation over n frame members is implied. Also, ρ_i is the i^{th} member mass density; x_i is the i^{th} member crosssectional area (chosen as the basic sizing variable); and l_i is the i^{th} member length. In equation (2), ω_j^2 and ω_j^{2*} are the squares of the actual and desired values of the j^{th} natural frequency, respectively, and m is the retained number of active constraints. In this work, the active frequency constraints are those within a specified minimum tolerance from their respective boundaries. Note that the superscripted variables (L) and (U) in equation (3) identify the prescribed minimum and maximum gauge values, respectively.

3. BASIC SIZING VARIABLES

The primary sizing variables, x_i (crosssectional area), and the secondary variables, I_i (principal moment of inertia), for the i th frame member are explicitly related in the following nonlinear form [12]:

$$I_i = c x_i^p \quad (4)$$

where c is a constant that depends on the shape of the member crosssection and p is a positive number. For a wide variety of practical sections, p is taken as an integer number equal to 1, 2, or 3. Explicit expressions for equation (4) are developed in references [14,15] for sections with numerous assumptions on width, depth, and thickness ratios.

In this paper, each frame member is designed as a wide-flange (WF) steel section according to the latest edition of the American Institute of Steel Construction (AISC) Code. Note that WF sections are exclusively used in this analysis, mainly because the crosssectional shape is kept relatively constant during redesign (dilatation or contraction). The principal moment of inertia and the crosssectional area of WF sections in the AISC Code are empirically related as follows [15]:

$$\begin{aligned} I_i &= 4.6206 x_i^2, & 0 \text{ in}^2 < x_i < 44.2 \text{ in}^2 \\ I_i &= 257.76 x_i - 2461.29, & 44.2 \text{ in}^2 < x_i < 88.28 \text{ in}^2 \end{aligned} \quad (5)$$

or according to references [16,17]

$$\begin{aligned} I_i &= 4.6206 x_i^2 & , & \quad 0 \text{ in}^2 < x_i < 44.2 \text{ in}^2 \\ I_i &= 257.76 x_i - 2461.29 & , & \quad 44.2 \text{ in}^2 < x_i < 88.28 \text{ in}^2 \end{aligned} \quad (6)$$

Both of these empirical formulas are used here with the later being used to compare with previously published results.

4. FREQUENCY AND DESIGN SENSITIVITY ANALYSES

The square of the j^{th} natural frequency of a frame structure is obtained by solving the following generalized eigenvalue problem:

$$([K] - \omega_j^2 [M]) \{q_j\} = \{0\} \quad (7)$$

where $\{q_j\}$ is the j^{th} mode shape, $[K]$ is the global stiffness matrix, and $[M]$ is the total mass matrix consisting of structural mass, M_s , plus nonstructural mass, M_c . The normalization equation of the mode shape with respect to the total mass is written as

$$\{q_j\}^T [M] \{q_j\} = 1 \quad (8)$$

Differentiating equation (7) with respect to the i^{th} sizing variable results in the following equation

$$([K]_{,i} - \omega_j^2_{,i} [M] - \omega_j^2 [M_s]_{,i}) \{q_j\} + ([K] - \omega_j^2 [M]) \{q_j\}_{,i} = \{0\} \quad (9)$$

where $\omega_j^2_{,i}$ represents a gradient of the square of the j^{th} natural frequency with respect to the i^{th} sizing variable; $\{q_j\}_{,i}$ indicates the gradient of the corresponding j^{th} mode shape; and $[M_s]_{,i}$ and $[K]_{,i}$ denote respective gradients of the structural mass and stiffness matrices. Note that the nonstructural mass contribution to $[M]$ is independent of the sizing variable. First, by rearranging equation (9)

$$([K] - \omega_j^2 [M]) \{q_j\}_{,i} - \omega_j^2_{,i} [M] \{q_j\} = -([K]_{,i} - \omega_j^2 [M_s]_{,i}) \{q_j\} \quad (10)$$

and then premultiplying equation (10) by $\{q_j\}^T$, one obtains the following equation

$$\begin{aligned} \{q_j\}^T([K] - \omega_j^2[M])\{q_j\},_i - \omega_j^2,_i \{q_j\}^T[M]\{q_j\} = \\ - \{q_j\}^T[K],_i\{q_j\} + \omega_j^2\{q_j\}^T[M_S],_i\{q_j\} \end{aligned} \quad (11)$$

By using equation (7) and considering the normalization of the mode shape (in equation 8), the j^{th} natural frequency gradient can be written as follows:

$$\omega_j^2,_i = \{q_j\}^T[K],_i\{q_j\} - \omega_j^2\{q_j\}^T[M_S],_i\{q_j\} \quad (12)$$

For 2-D frame structures, the element structural mass matrices are the product of the sizing variable and an invariant matrix. Therefore, the gradient matrix $[M_S],_i$ is known. However, the frame element stiffness matrix is not linearly proportional to the sizing variable. One can obtain the element stiffness gradient by first summing it into extensional plus flexural contributions:

$$[k_i] = [k_{ai}] + [k_{bi}] \quad (13)$$

where the $[k_{ai}]$ matrix is directly dependent on the i^{th} sizing variable (crosssectional area x_i), and the $[k_{bi}]$ matrix is dependent on the i^{th} principal moment of inertia, I_i . By factoring out the sizing variable from the $[k_{ai}]$ matrix and the principal moment of inertia from the $[k_{bi}]$ matrix, equation (13) is temporarily rewritten as

$$[k_i] = x_i [k_{ai}] + I_i [k_{bi}] \quad (14)$$

where $[k_{ai}]$ and $[k_{bi}]$ are invariant matrices. Substituting equation (4) into equation (14) gives

$$[k_i] = x_i [k_{ai}] + c x_i^p [k_{bi}] \quad (15)$$

Equation (15) expresses the element stiffness matrix in terms of the sizing variable explicitly. Thus, one can write the gradient of the element stiffness matrix with respect to the i^{th} sizing variable, as follows

$$[k_i]_{,i} = [k_{ai}] + cp x_i^{p-1} [k_{bi}] \quad (16)$$

And finally using equations (4) and (14), the stiffness gradient equation (16) can be recanted into a usable form:

$$[k_i]_{,i} = (1/x_i) [k_{ai}] + (p/x_i) [k_{bi}] \quad (17)$$

With the 2-D frame element stiffness gradient defined explicitly in terms of the sizing variable, the frequency gradient equation (12) reduces to

$$\omega_{j,i}^2 = (1/x_i) \{ (q_j)_i^T [[k_{ai}] + p[k_{bi}]] (q_j)_i - \omega_j^2 (1/x_i) (q_j)_i^T [m_{si}] (q_j)_i \} \quad (18)$$

where $(q_j)_i$ represents the component of the vibration mode associated with the i^{th} sizing variable, and $[k_{ai}]$, $[k_{bi}]$, and $[m_{si}]$ correspond to the i^{th} element axial and flexural stiffness and structural mass matrices, respectively defined in the global coordinate system.

The frequency gradient equation (18) is comprised of two terms, which are nonlinear functions of the primary sizing variable: the first being named the modal potential energy (MPE) and the second is designated the modal kinetic energy (MKE). For problems involving a considerable amount of nonstructural mass, the MKE term was disregarded in the gradient calculations of recent OC algorithms [10,11]. This was done to alleviate oscillatory convergence of solutions. Quantitative studies showing the effectiveness of the present method, when the MKE term is either retained or omitted, will be performed in this work.

Finally, the gradient of the objective function (structural weight) with respect to the i^{th} sizing variable is simply given as

$$W_{,i} = \rho_i l_i \quad (19)$$

Equations (18) and (19) are used to define the optimality criteria in the next section.

5. OPTIMALITY CONDITIONS

Using equations (1) and (2), the Lagrangian function, L , is stated as follows:

$$L(x, \lambda) = \rho_i l_i x_i - \lambda_j (\omega_j^2 - \omega_j^{2*})$$

(summed over $i=1,2,\dots,n$ and $j=1,2,\dots,m$) (20)

where λ_j are the Lagrange multipliers.

Differentiating equation (20) with respect to the sizing variables and setting the resulting equations to zero, the condition of optimality can be written as:

$$D_i = e_{ij} \lambda_j = 1 \quad ; \quad (i=1,2,\dots,n)$$

(summed over $j=1,2,\dots,m$) (21)

The Lagrangian energy density, e_{ij} , which represents a ratio of the gradient for the natural frequency constraint (equation 18) and the gradient of the objective function (equation 19), is written as follows

$$e_{ij} = - \frac{\omega_j^{2,i}}{W,i}$$

(22)

6. CLOSED-FORM SCALING PROCEDURE

In the OC method presented here, a closed-form scaling procedure is used to drive infeasible designs to feasible ones. Presumably, all or some of the sizing variables may be scaled depending on how the formulation is derived. This is the subject of ongoing research [18]. What is used here is simple scaling with the assumption that there exists a dominate (or most violated) constraint. If one uniformly scales the design with respect to this constraint, then presumably all of the other constraints will be brought to the feasible region [18]. After the frame members are resized, they are uniformly scaled by a factor f_j , whose value corresponds to a j^{th} target frequency constraint. For instance, the relationship between the scaled sizing values (x_{ni}, I_{ni}) and the unscaled ones (x_i, I_i) is

$$x_{ni} = f_j x_i \quad I_{ni} = f_j^p I_i \quad (23)$$

where f_j is the scaling factor corresponding to the j^{th} frequency constraint and the use of equation (4) is implied.

Using equations (13) and (23), the scaled global stiffness matrix, $[K]_n$, and the scaled global structural mass matrix, $[M_S]_n$, are written as

$$\begin{aligned} [K]_n &= f_j [K_a] + f_j^p [K_b] \\ [M_S]_n &= f_j [M_S] \end{aligned} \quad (24)$$

where $[K_a]$ and $[K_b]$ are the global axial and flexural stiffness matrices for the frame structure. Note that the nonstructural mass matrix $[M_C]$ is independent of the sizing variables and is

not affected by scaling.

To compute the scaling factor f_j , consider Rayleigh's quotient for the square of the natural frequency of the unscaled, ω_j^2 , and scaled, ω_{nj}^2 , designs:

$$\omega_j^2 = \frac{(q_j)^T [K_a] (q_j) + (q_j)^T [K_b] (q_j)}{(q_j)^T [M_s] (q_j) + (q_j)^T [M_c] (q_j)} \quad (25)$$

$$\omega_{nj}^2 = \frac{f_j (q_j)^T [K_a] (q_j) + f_j^p (q_j)^T [K_b] (q_j)}{f_j (q_j)^T [M_s] (q_j) + (q_j)^T [M_c] (q_j)} \quad (26)$$

If one divides both the numerators and denominators of equations (25) and (26) by the unscaled modal mass, $(q_j)^T [M] (q_j)$, then one can define the square of the j^{th} target frequency ratio, R_j^2 , as follows:

$$R_j^2 = (\omega_j^{2*} / \omega_j^2) = \frac{f_j s_{aj} + f_j^p s_{bj}}{(s_{aj} + s_{bj}) (f_j m_{sj} + m_{cj})} \quad (27)$$

where s_{aj} is the j^{th} ratio of the axial modal stiffness to the total modal mass, s_{bj} is the j^{th} ratio of the bending modal stiffness to the total modal mass, m_{sj} is the j^{th} ratio of the structural modal mass to the total modal mass, and m_{cj} is the j^{th} ratio of the nonstructural modal mass to the total modal mass. These nondimensional parameters are symbolically defined as

follows:

$$\begin{aligned}
 s_{aj} &= \frac{\{q_j\}^T [K_a] \{q_j\}}{\{q_j\}^T [M] \{q_j\}} & s_{bj} &= \frac{\{q_j\}^T [K_b] \{q_j\}}{\{q_j\}^T [M] \{q_j\}} \\
 m_{sj} &= \frac{\{q_j\}^T [M_s] \{q_j\}}{\{q_j\}^T [M] \{q_j\}} & m_{cj} &= \frac{\{q_j\}^T [M_c] \{q_j\}}{\{q_j\}^T [M] \{q_j\}}
 \end{aligned} \tag{28}$$

Note that

$$\begin{aligned}
 s_{aj} + s_{bj} &= \omega_j^2 \\
 m_{sj} + m_{cj} &= 1
 \end{aligned} \tag{29}$$

From equation (27), one obtains a closed-form nonlinear equation for the scaling factor, f_j , corresponding to the j^{th} frequency constraint:

$$f_j^p s_{bj} + f_j s_{aj} - R_j^2 (s_{aj} + s_{bj})(f_j m_{sj} + m_{cj}) = 0 \tag{30}$$

A specialization of equation (30) for the case of flexural members with WF sections (e.g. $p=2$ in equations 5-6) results in the following equations:

$$\begin{aligned}
 f_j^2 c_1 + f_j c_2 + c_3 &= 0 \\
 f_j &= A / B \\
 A &= (-c_2 + (c_2^2 - 4c_1c_3)^{1/2}) \\
 B &= 2c_1 \\
 c_1 &= s_{bj} \\
 c_2 &= s_{aj} - (s_{aj} + s_{bj}) (m_{sj}R_j^2) \\
 c_3 &= - (s_{aj} + s_{bj}) (m_{cj}R_j^2)
 \end{aligned} \tag{31a}$$

When ($p=1$) in equations (5) and (6), then equation (30) reduces to

$$f_j = m_{cj} R_j^2 / (1 - m_{sj} R_j^2) \quad (31b)$$

Equation (31b) is the exact scaling formula used for bar structures [9-11,13], where the principal moment of inertia of the bar elements are linearly related to the sizing variable.

A closed-form formulation that is analytically equivalent to equation (30) can be obtained if one instead divides both the numerators and denominators of equations (25) and (26) by the modal stiffness, $\{q_j\}^T [K] \{q_j\}$. Then, the square of the target frequency ratio, R_j^2 , can be written as

$$R_j^2 = (\omega_{nj}^2 / \omega_j^2) = \frac{f_j s_{1j} + f_j^p s_{2j}}{(f_j m_{sj} + m_{cj})} \quad (32)$$

where s_{1j} is the j^{th} ratio of the axial modal stiffness to the generalized stiffness, and s_{2j} is the j^{th} ratio of the bending modal stiffness to the generalized stiffness. These nondimensional parameters are written as follows:

$$s_{1j} = \frac{\{q_j\}^T [K_a] \{q_j\}}{\{q_j\}^T [K] \{q_j\}} \quad s_{2j} = \frac{\{q_j\}^T [K_b] \{q_j\}}{\{q_j\}^T [K] \{q_j\}} \quad (33)$$

Note that in this case

$$s_{1j} + s_{2j} = 1 \quad (34)$$

Equation (32) leads to another closed-form equation for the scaling factor, as follows:

$$f_j^p s_{2j} + f_j (s_{1j} - R_j^2 m_{sj}) - (R_j^2 m_{cj}) = 0 \quad (35)$$

A specialization of equation (35) for the case of flexural members with WF sections ($p=2$) yields the following equations:

$$\begin{aligned} f_j^2 k_1 + f_j k_2 + k_3 &= 0 \\ f_j &= A / B \\ A &= \{-k_2 + (k_2^2 - 4k_1k_3)^{1/2}\} \\ B &= 2k_1 \\ k_1 &= s_{2j} \\ k_2 &= s_{1j} - m_{sj} R_j^2 \\ k_3 &= -m_{cj} R_j^2 \end{aligned} \quad (36)$$

For the case of ($p=1$) in equations (5-6), equation (35) also reduces to equation (31b).

A first order (Taylor's series) approximation formula for the scaling factor was recently reported in references [18,19]. The approximate formula [18] is rewritten here in notation common to this paper, as follows:

$$f_j = \frac{s_{1j} + p s_{2j} - 1 + m_{cj} R_j^2}{s_{1j} + p s_{2j} - m_{sj} R_j^2} \quad (37)$$

It is interesting to compare the errors in predicting the constraint surface using either one of the closed-form scaling equations (30 or 35) and the approximate equation (37). For example, consider the axial-flexural frame model shown in Figure 1. The three member frame has two 60-degree inclined support columns. The elastic modulus and mass density of the material was specified at 30×10^6 psi and 7.2464×10^{-4} lb-s²/in⁴, respectively. As an initial design, the relative crosssectional areas of the three members were set to unity. A concentrated amount of nonstructural mass (2.3292 lb-s²/in) was placed at the free nodes to alleviate the triviality of scaling the initial design within a specified range of target frequency ratios, R_j . Three different member types (e.g., $p=1,2,3$ in equations 30,35, and 37) were examined.

Figure 2 shows a relative mapping of the error due to scaling only the initial design with equation (37) and the closed-form equations (30 and 35) in a defined range of target frequency ratios. The relative (rel.) error in the scale factor was computed as follows

$$\text{rel. error in } f = ((f_t - f_e)/f_t) \times 100 \quad (38)$$

where f_t and f_e are scale factors computed from equations (30 and

35) and equation (37), respectively. Note that when the actual frequency equals the desired frequency, the target frequency ratio equals unity. As can be seen in Figure 2, the prediction errors between the exact and approximate scaling formulations within reasonable limits of the target frequency ratio are acute. For $p=1$, equations 30, 35 and 37 all reduce to equation 31b, which is exact.

7. PRESENT OPTIMALITY CRITERIA APPROACH

Indeterminate complex structures, unlike determinate ones, require an iterative procedure to update the sizing variables. Using equation (21), one can write several recursive relations to update these variables [20-22]. These recursive relations drive the design from an infeasible to a feasible location in the design space. In order to use any one of the recursive relations, one must evaluate D_i (in equation 21), which contains the unknown Lagrange multipliers and cost function and constraint gradient information. For computational ease, several uncouple approaches for estimating the Lagrange multipliers have been reported in the open literature [20-22]. This work will focus on these uncouple approaches.

At any rate, the convergence characteristics of the existing OC recursive schemes [5,6,8-11,17,18-22] depended on the selection of a proper step size. Until recently, this selection was an arbitrary process with much experimentation done on the same problem. It became necessary to establish a criteria to tune the step size for a more assureable degree of convergence. To meet this need, some commonly used OC recursive schemes were fused into an "adaptive" redesign strategy [13]:

To modify the sizing variables:

$$x_i^{k+1} = x_i^k + s ((D_i)_k^{(1/a)} - 1) x_i^k \quad (39)$$

$$x_i^{k+1} = x_i^k + s (1 + (1/a) (D_i - 1)_k - 1) x_i^k \quad (40)$$

To update the Lagrange multipliers:

$$\lambda_j^{k+1} = \lambda_j^k + s ((\omega_j^2 / \omega_j^{2*})_k^{(1/b)} - 1) \lambda_j^k \quad ; \quad (b=1/a) \quad (41)$$

$$\lambda_j^{k+1} = \lambda_j^k + s ((b+1)/b - (1/b)(\omega_j^2 / \omega_j^{2*})_k^{(1/b)} - 1) \lambda_j^k \quad (42)$$

where the subscripts and superscripts, k and $k+1$, denote iteration numbers. The quantity $(1/a)$, is the step size commonly used in modern OC algorithms [9-11]. This step size is immobilized in this paper by setting it to a constant value. Alternatively, a more adaptive parameter, s , is tuned both to control the step size and to "damp out" oscillations of scaled weights in the iteration history. At the beginning of the design cycle, the tuning parameter is set to unity. Henceforth, the value of s is adjusted by monitoring a localized history of scaled weights calculated during the design cycle. Given any weight fluctuations, a tuned value of s is chosen by the following damping criterion at a current k^{th} design: If $w^{k+1} > C_s [w^k - w^{k-1}]$ or $w^{k+1} > w^k > w^{k-1}$, then s is reduced to $s/2$ (given that the tuned value of s is maintained above a specified minimum value). If the weight increases are more than say 10 percent, then the scaling constant, C_s , is set to $1/2$. Otherwise, if they are less than 10 percent, then the scaling constant is further tuned to a percent difference in scaled weight, given as follows: $[(w^k - w^{k-1})/w^k] \times 100\%$.

With the above damping criterion, the bandwidth of weight oscillations decreases near the optimum. This assures a smoother quality of convergence. It will be shown in later examples that

the damping criterion is appropriate to guide an adaptive OC approach.

Initial values in the recursive equations (41) and (42) are approximated by a simple expression for multiple constraint conditions that was generalized from a single constraint condition [10,11,18]

$$\lambda_j = W / \omega_j^{2*} (s_{aj} + s_{bj} - m_{sj}) \quad (43)$$

where the nondimensional parameters, s_{aj} , s_{bj} , and m_{sj} are defined in equations (28).

A cogent source of uneven convergence of OC redesign methods originates in the assumptions made regarding the role of the Lagrange multipliers and active and passive constraints. Determining which constraints are critical or potentially critical must be made at the outset. As the number of active constraints is increased, more Lagrange multipliers participate in the redesign phase. This tends to overconstrain the system. Thus, the final design is an extreme upper-bound and that tuning the step size sometimes does not profoundly effect the already smooth quality of convergence of solution.

In this work, the active constraints are those within a specified minimum tolerance near their respective boundaries. All other constraints are consider inactive (or passive). By maintaining such a tolerance around the constraint boundaries,

the chances of mode switching (i.e., when passive frequencies cluster near active ones) are significantly reduced. Mode switching tends to diminish smoother convergence. An extremely close tolerance of 0.001 percent was used in the work here to produce the smoothest least upper-bound convergence of solution.

Computational studies showed that the price of reducing the value of s in equations (39-42) was a considerably larger number of repeated finite element analyses. However, it has been shown that a modified Aitken's accelerator is quite beneficial to the net cost and overall rate of convergence [13].

Let $\{x\}^{k-3}$, $\{x\}^{k-2}$, and $\{x\}^{k-1}$ be design vectors exhibiting oscillatory convergence trends in three previous consecutive iterations of the design cycle, and let $\{x\}^k$ be the desired vector for a current k^{th} design. If

$$\{d_1\} = \{x\}^{k-2} - \{x\}^{k-3} \quad \text{and} \quad \{d_2\} = \{x\}^{k-1} - \{x\}^{k-2} \quad (44)$$

then, an accelerated design vector, $\{x\}^a$, can be extrapolated as follows:

$$\{x\}^a = \{x\}^{k-1} + S\{d_2\} \quad (45)$$

where S , is defined as the acceleration factor

$$S = (\{d_2\} - \{d_1\})^T (-\{d_2\}) [(\{d_2\} - \{d_1\})^T (\{d_2\} - \{d_1\})]^{-1} \quad (46)$$

In general, the accelerated design vector $\{x\}^a$, violates both the optimality criteria and the frequency constraints. However, the

design cycle is continued after an acceleration by resizing with the accelerated design vector $\{x\}^a$. The k^{th} design is then scaled to satisfy the constraints using the closed-form procedure outlined in the preceding section.

8. OPTIMIZATION ALGORITHM

The main steps of the present optimization algorithm are summarized as follows:

- (1) Assign uniform sizes to all elements (set $s=1$ and $k=0$).
- (2) Calculate natural frequencies of structure (eqs. 7-8)
- (3) Scale design until target frequencies are within a specified tolerance of the constraint surface (eq. 30)
- (4) Calculate the scaled weight of structure (eq. 1)
- (5) For iteration $k=4$ or greater, check for oscillations in the scaled weights of the last three consecutive $k-1$, $k-2$, $k-3$ designs. If so, then extrapolate an accelerated design using equation (45); Else continue.
- (6) Determine the Lagrange multipliers for m active frequency constraints using either one of equations (41-43).
- (7) Resize the design using either one of equations (39-40).
- (8) Repeat steps 2, 3 and 4.
- (9) For iterations $k=4$ or greater, check damping criterion: If $w^{k+1} > C_s [w^k - w^{k-1}]$ or $w^{k+1} > w^k > w^{k-1}$ and $s > a$ specified minimum value, then set s to $s/2$ and go to step 7; Else go to step 5.

Note: Steps 5-9 represent one iteration in the design cycle, which is repeated until either the difference in weight is less than a specified tolerance, or the parameter, s , reaches the specified minimum value (at which relative convergence is implied in equations 39-42).

9. EXAMPLES

A computer program [23] written in FORTRAN 77 was developed to execute the optimization algorithm summarized in the preceding section. Several example problems were used to demonstrate the method and the results were compared with previous results. While it was not possible to provide a direct comparison in all cases, due to either inextensibility assumptions or differences in the mass formulations of the finite element models, the results show passable correlation to manifest a reasonably valid comparison. The method was also used to chart the convergence of OC recursive relations collectively used to resize and to evaluate the Lagrange multipliers. For simplicity, the resizing equations (39) and (40) are hereafter referred to as combinations 1 and 2, respectively, and equations (41), (42), and (43) as combinations A, B, and C, respectively. All constraints were met by uniformly scaling the design to the constraint surface with the closed-form equation (30). An additional study was performed showing the effectiveness of the damping criterion, when the MKE term was either retained or disregarded in the frequency gradient calculations (equation 9). This study was done to establish the validity of disregarding the MKE term, a common practice in modern OC applications [10,11]. In this paper, all natural frequencies were calculated using the subspace iteration method [24] with double precision (14 significant digit accuracy) on an IBM 3081-D machine and single precision (14 significant digit

accuracy) on the Cray X-MP/24 and the Cray Y-MP8/864 supercomputers.

9.1 Example 1. Two-story and one-bay frame problem

This six member frame, studied in references [17,25], is depicted in Figure 3. A uniformly distributed nonstructural weight of 10 lb/in. was superimposed on the horizontal members of the frame. This problem was solved with a weight density of 0.28 lb-s²/in³ and an elastic modulus of 30x10⁶ psi. The lowest allowable natural frequency was 78.5 rad/sec. Uniform member sizes were assumed for an initial design. A minimum gauge constraint on the sizing variables was specified at 7.9187 in² and a maximum gauge was set to 88.28 in².

Columns 2-4 in Table 1 list optimum designs "tuned" for isolated step size values in the OC method of reference [17]. The final designs obtained in the present method with the previously defined combination 1C are listed in the last two column. The MKE term was included in the sensitivity calculations for the results listed in column 5, while in column 6 the MKE term was omitted. As one can see, including the MKE term resulted in nearly a 0.33 percent lower design weight. A pointed observation is that member 5 did not reach minimum gauge (in the present analysis). This indirectly accounts for the approximately 3 percent higher weights obtained against those reported in reference [17].

Table 2 presents initial and final frequencies and structural weight at the optimum design for several constraint conditions. These were: (i) $\omega_1 = 5.0\text{Hz}$ (Case 1); (ii) $\omega_2 = 18.0\text{Hz}$ (Case 2); (iii) $\omega_1 \geq 5.0\text{Hz}$, $\omega_2 \geq 18.0\text{Hz}$ (Case 3); (iv) $\omega_1 \geq 5.0\text{Hz}$, $\omega_2 \geq 18.0\text{Hz}$, $\omega_3 \geq 35.0\text{ Hz}$ (Case 4). The material data and the nonstructural weight remained unchanged. In all cases, uniform member sizes were assumed for an initial starting design with the results shown in column 2 of Table 2. In addition, side constraints on minimum and maximum gauge were specified at 3 in² and 88.28 in², respectively. The MKE term was retained in the sensitivity calculations for the results listed in parenthesis. It was apparent that when the MKE term was retained, lower upper bounds on the optimum weight were obtained, primarily in the multiple constraint conditions (columns 5 and 6 in Table 2). Although, these quantitative changes in weight are minimal, given the small size of this problem. The distribution of member crosssectional areas for the four final designs are given in Table 3.

Figure 4 shows the effect of modified Aitken's accelerator on the iteration history of the example frame with the constraint Case 4. Four curves are shown with and/or without the MKE term and the use of Aitken's accelerator (equation 45). In all cases the step size (in equations 39 and 41) was adaptively tuned. The price of reducing the step size without the MKE term and

acceleration was paid through an increased number of repeat finite element analyses. For instance, a total of 96 analyses were required to reach a converged upper-bound on the optimum weight at 3291.90 lbs. By way of comparison, a reduced total of 52 analyses were required to reach a slightly higher weight of 3292.77 lbs, when Aitken's accelerator was employed without the MKE term. When the algorithm was allowed to continue, a lower weight of 3287.38 lbs was gained in 55 analyses. Finally, a converged upper-bound on the optimum weight was obtained at 3280.24 lbs in 62 analyses. The lower upper-bound weight obtained with the use of the modified Aitken's accelerator were mainly attributed to numerical anomalies caused by extrapolation.

With the MKE term, Figure 4 shows that the scaled weight oscillations in the early iterations were more noticeable. However, the oscillations were quickly stabilized by the damping criterion used in the present method. Without acceleration, a total of 66 analyses were required to reach a final design weight of 3284.22 lbs. With acceleration, a reduced total of 61 analyses were required to reach a converged upper-bound on the optimum weight at 3267.17 lbs. Presumably, the MKE term appears to have a beneficial effect in the present method.

9.2 Example 2. Seven-story and one-bay frame

This example, also studied in reference [17], is shown in Figure 5. The fundamental natural frequency was specified at 10.2

rad/sec. The material data, nonstructural weight and gauge constraints assigned the same values as those used in Table 1 of Example 1.

Columns 2-6 in Table 4 show final designs tuned for isolated step size values in the OC method of reference [17]. The final designs obtained in the present analysis with combination 1C are shown in the last two columns. A uniform starting design of 80 in² was assumed for each member size. One can see in Table 4 that the present method (with the MKE term) produced an optimum design weight at 16,537 lbs, which was approximately 2.5% lower than the average value of weights reported in reference [17]. The improved design was gained by reducing the top floor to the minimum gauge limit and increasing the sizes of the base columns. This looks to be a stronger design for this frame in its fundamental vibration mode. No substantial changes in the final design were obtained, when the MKE term was disregarded (see column 8 in Table 4).

9.3 Example 3. Ten-story and three-bay frame

The present OC algorithm with combination 1C was applied to the 70 member frame shown in Figure 6. The elastic modulus and weight density of the material were given values of 30×10^6 psi and 0.28 lbs/in³, respectively. A uniformly distributed nonstructural weight of 10 lb/in was placed on each floor level. The relative crosssectional area of all the members was set to

unity, as an initial design. The minimum gauge constraint was specified at 3 in², while the maximum gauge constraint was limited to 88.28 in². The frame was designed to satisfy four constraint conditions: (i) $\omega_1 = 2.0\text{Hz}$ (Case 1); (ii) $\omega_2 = 7.0\text{Hz}$ (Case 2); (iii) $\omega_1 \geq 2.0\text{Hz}$, $\omega_2 \geq 7.0\text{Hz}$ (Case 3); and finally (iv) $\omega_1 \geq 2.0\text{Hz}$, $\omega_2 \geq 7.0\text{Hz}$, $\omega_3 \geq 15.0\text{Hz}$ (Case 4).

Table 5 lists the first 5 natural frequencies obtained for the initial and final designs subjected to the four constraint conditions. As can be seen, all constraint conditions were met quite well, largely due to the closed-form scaling equation (30). As before, the MKE term was retained in the gradient calculations for the results listed in parenthesis. Given the intermediate size of this problem, the quantitative effect of the MKE term was fairly significant in some cases. For example, a 2 percent lower upper-bound weight was gained in constraint Case 3, while in Case 4, a 3 percent optimum weight reduction was obtained. It was surprising that a higher optimum weight was obtained in Case 1, when the MKE term was retained.

9.4 Example 4. Three-hundred and thirteen member frame

A 313 member frame structure [14] (Figure 7) was designed using combination 1C in the present OC algorithm. Supercomputer capabilities were needed to solved this large-scaled problem. The elastic modulus and weight density of the material were given values of 30×10^6 psi and $0.28 \text{ lb-s}^2/\text{in}^3$, respectively. A

concentrated amount of nonstructural mass equal to $0.1 \text{ lb-s}^2/\text{in}$ was placed at all free nodes. The relative crosssectional area of all the members was set to unity for the initial iteration. The minimum gauge constraint was specify at 3 in^2 , while the maximum gauge constraint was set to 88.28 in^2 . The frame was designed to satisfy four constraint conditions: (i) $\omega_1 = 1.0\text{Hz}$ (Case 1); (ii) $\omega_2 = 5.0\text{Hz}$ (Case 2); (iii) $\omega_1 \geq 1.0\text{Hz}, \omega_2 \geq 5.0\text{Hz}$ (Case 3); and (iv) $\omega_1 \geq 1.0\text{Hz}, \omega_2 \geq 5.0\text{Hz}, \omega_3 \geq 9.0\text{Hz}$ (Case 4).

Table 6 lists the first 5 natural frequencies obtained for the initial and final designs under the four constraint conditions. As in the previous example, all constraint conditions were met completely. Again, the results in parenthesis included the MKE term. In some cases, nearly a 2 percent change in final design weights were obtained, when the MKE term was retained in the gradient calculations. Given the large size of this problem, this may be significant for engineering design purposes. The results of this example were submitted as benchmark values with which any future ones could be compared.

9.5 Quantitative convergence study of OC recursive schemes

All six combinations of the two recursive relations and the three approaches to evaluate the Lagrangian multipliers were surveyed on the example frames studied in this paper. The damping criteria (outlined in section 6) was used to adaptively tune the step size for improved convergence of the OC recursive

combinations (1A,2A,1B,2B,1C,2C) previously defined.

The two-story and one-bay frame was redesigned with the constraints of Case 4 (in example 1). Figure 8 compares the iteration histories of scaled weights using combinations 1C,2C,1A,2A,1B,2B (Cases A-F, respectively) in the present OC method. Here, the MKE term was not retained in the gradient calculations. A minimum value of s was specified at 0.001 in the damping criterion in order to reduce the number of unnecessary reanalyses once relative convergence was achieved. (Note that the parameter, s , was not used in equation (43) of Cases A and B.)

As the optimization process was "jump-started" in the first-four iterations, one can see in Figure 8 that the convergence of the various recursive schemes used in Cases A-F was quickly stabilized. Ironically, all the recursive cases converged to final designs with relatively similar upper-bound weights. It was apparent that Cases A,C, and E required fewer number of repeated analyses to achieve relative convergence. This is to be expected, since equation (15) is an approximation of equation (14). It was surprising that a final design with the lowest upper-bound weight of 3240.83 lbs was obtained in 90 analyses in Case B (combination 2C). In all the cases surveyed, the final weights did not improve with additional iterations. The one exception was in Case E (combination 1B), where in this case the algorithm aborted because the specified minimum value of s was reached. Still, the

listed weight of 3291.93 lbs in 61 analyses was within a few pounds of its final converged value.

Figure 9 compares the iteration histories of scaled weights for the six member frame using Cases A-F, when the MKE term was retained in the frequency gradient calculations. Here, one can see that the weight oscillations in the early cycles of Cases A, C, and E were slightly more obtrusive. Still, the convergence of all the cases were quickly stabilized by the damping criterion. Figure 9 shows that by including the MKE term in the sensitivity calculations, lower upper-bounds on the optimum weight were gained in all cases, except Case E. Although, a sporadic change in the number of repeated analyses required by the various cases was apparent.

The ten-story and three-bay frame problem was reexamined with the constraints of Case 4 (in example 3). The iteration history of scaled weights for Cases A-F are shown in Figures 10 and 11. The MKE term was retained in the cases shown in Figure 11. As one can see in both graphs, the erratic oscillatory behavior of Cases A-F was promptly steadied by the adaptive OC approach used here. Figure 11 shows that by including the MKE term, lower upper-bounds on the optimum weight were gained in some cases. Case A resulted in the highest gain by approximately 3 percent. A couple of exceptions were Cases B and F, which produced approximately 0.25 percent higher upper-bounds than

those shown in Figure 10.

Finally, the 313 member frame was resolved with the constraints of Case 4 (in example 4). The iteration histories for Cases A-F without the MKE term are shown in Figure 12. The MKE term was retained in the cases shown in Figure 13. As exhibited by both graphs, the violent oscillations of scaled weights in the early cycles of Cases A-F were rapidly steadied after the 4th iteration. Figure 13 shows that by retaining the MKE term the path of convergence was less dispersed amongst the various cases. Presumably, this appears to be a more stabilizing characteristic in the present method. The one exception was in Case C, which was within a few pounds of its converged upper-bound, when the minimum s gauge was imposed in the algorithm.

10. CONCLUDING REMARKS

An "adaptive" OC technique has been offered for dealing with frequency constraints in frame optimization. The key idea has been to tune the step size of OC redesign methods according to a damping criterion, which dissolves the (sometimes violent) oscillations of scaled design weights in the iteration history. Aitken's accelerator is then used both to increase the ecumenical rate and decrease the net cost of convergence by reducing the number of repeat finite element analyses. During optimization, a closed-form nonlinear scaling procedure has been utilized. It also has been tested for its accuracy in predicting the constraint surface of a wide range of desired target frequencies. This closed-form approach is introduced for the first time in the open literature.

The method presented here demonstrates the usefulness of creating specific criteria based on previous scaled designs to smooth convergence of OC methods. Overall, this method has been found to be efficient and reliable as compared to previous OC methods. Also, it is an adaptive method which does not require adjustments of numerous internal parameters. The goal here has been to create the most computationally robust OC technique possible.

A wide range of design examples have been presented. The

convergence of final designs obtained by various OC recursive methods have been charted and compared for the first time for this class of problem--i.e., the crosssectional optimization of a 2-D frame structure having nonstructural mass with multiple frequency constraints and minimum and maximum gauge restrictions. Globally speaking, the method has exhibited a stabilizing effect on the oscillatory convergence propensity of the various OC recursive strategies surveyed. It is anticipated that the method can smooth the convergence of optimum designs with other types of constraints, and this is the subject of continuing research.

ACKNOWLEDGEMENTS

This research effort has been supported by grants from the Air Force Office of Scientific Research under the Research Initiation Program and the National Science Foundation under the Minority Research Initiation Program. The authors gratefully acknowledge the technical communications and helpful assistance given by Dr. V.B. Venkayya and Captain R. Canfield of the Design and Analysis Group in the Wright Research and Development Center at WPAFB, Ohio. This work was performed in part on the Cray X-MP/24 and the Cray Y-MP8/864 at The Ohio Supercomputer Center on the campus of The Ohio State University. A great deal of appreciation and respect is extended to the governing board and operating officials for services rendered.

REFERENCES

1. Venkayya, V.B., "Design of optimum structures", Computer and Structures, Vol. 1 (1971), p. 265-309.
2. Venkayya, V.B., "Structural optimization: a review and some recommendations", Int'l. Journal for Num. Meth. in Eng., Vol. 13, No. 2 (1978), p. 203-228.
3. Khan, M.R., Willmert, K.D., and Thornton, W.A., "A new optimality criterion method for large-scale structures", Proc. of AIAA/ASME 19th Structures, Structural Dynamics, and Materials Conference, Bethesda, Md., April (1978), p. 47-50.
4. Idem, "Optimality criterion techniques applied to mechanical design", Journal of Mechanical Design, Trans. of ASME, Vol. 100, No. 1 (1978), p. 319-327.
5. Idem, "Optimality criterion techniques for structures with multiple design variables per member", Proceedings of the AIAA/ASME/ASCE/AHS 20th Structures, Structural Dynamics, and Materials Conference, St. Louis, Mo., April (1979), p. 87-95.
6. Syed, M.I., Willmert, K.D., and Khan, M.R., "Optimality criterion techniques applied to structures composed of different element types", Proc. of AIAA/ASME/ASCE/AHS 21st Structures, Structural Dynamics, and Materials Conference, Seattle, Wash., May (1980), p. 345-351.
7. Tabak, E. and Wright, P.M., "Optimality criteria method for building frames", Journal of Structures ASCE, p. 1327-1337, July (1981).
8. Khan, M.R., "Optimality criterion techniques applied to frames having general cross-sectional relationships", AIAA Journal, Vol. 22, No. 5, May (1984), p. 669-676.
9. Khot, N.S., "Optimization of structures with multiple frequency constraints", Computer and Structures, Vol. 20, No. 5, p. 869-876 (1985).
10. Grandhi, R.V., and Venkayya, V.B., "Structural optimization with frequency constraints", Proc. 26th Structural, Dynamics and Materials Conference, Monterey, California (1986).
11. Venkayya, V.B. and Tischler, V.A., "Optimization of structures with frequency constraints", Computer Meth. for Nonlinear Solids and Structural Mech., ASME, AMD-54, p. 239-259 (1983).
12. Fleury, C. and Sander, G., "Generalized optimality criteria for frequency constraints, buckling constraints, and bending

elements", AFOSR TR-80-0107 (1979).

13. Phan, K.F. and McGee, O.G., "An adaptive procedure for stabilizing convergence quality in frequency-constrained design optimization", Int. J. Num. in Eng., to appear (1989).

14. Kolonay, R.M., Venkayya, V.B., Tischler, V.A., and Canfield, R.A., "Structural optimization of framed structures using generalized optimality criteria", Proc. Second NASA/Air Force Symposium on Recent Advances in Multidisciplinary Analysis and Optimization, Hampton, Virginia, September (1988).

15. Kalonay, R.M., "Structural optimization of large-scale structures under multiple loading conditions subjected to stress and displacement constraints", M.S. Thesis, The Ohio State University (1987).

16. Brown, D.M. and Ang, A.H., "Structural optimization by nonlinear programming, J. Struct. Div., ASCE Vol. 92 (ST6), p. 319-340 (1966).

17. Khan, M.R. and Willmert, K.D., "An efficient optimality criterion method for natural frequency constrained structures", Computer and Structures, Vol. 14, No. 5-6 (1981), p. 501-507.

18. Venkayya, V.B., "Aerospace structures design on computers", WRDC-TR-89-3045 (1989).

19. Venkayya, V.B. and Tischler, V.A., "A compound scaling algorithm for mathematical optimization", WRDC-TR-89-3040 (1989).

20. Khot, N.S., Berke, L., and Venkayya, V.B., "Comparison of optimality criteria algorithms for minimum weight design of structures", AIAA Journal, Vol. 17, No. 2, 1978, p. 182-190.

21. Khot, N.S. and Berke, L., "Structural optimization using optimality criteria methods", New Directions in Optimum Structural Design, (Ed. by E. Atek, R.H. Gallagher, K.M. Ragsdell, and O.C. Zienkiewicz), John Wiley, (1978), p. 47-74.

22. Khot, N.S., "Optimality criterion methods in structural optimization", Foundations of Structural Optimization: A Unified Approach" (Ed. by A.J. Morris), p. 99-235, Wiley, New York (1984).

23. McGee, O.G. and Phan, K.F., "PACSOP" Promotion and acceleration of convergence of structural optimization procedures, OSURF Structural Engineering Rept. No. 35 (1989).

24. Bathe, K.J., "Finite element procedures in engineering analysis", Prentice-Hall, Inc. (1982).

25. Da-Sen Yu, "Optimum design of structures subjected to transient dynamic ground motion", M.S. Dissertation, Mechanical and Industrial Engineering Department, Clarkson College of Technology, (1981).

Table 1 Two-Story and One-Bay Frame
Optimum Design Variables (in.²) $\omega_1 = 78.5$ rad/sec

Element No.	Via Reference [17]			Present Analysis* w/ MKE	Present Analysis* w/o MKE
1	20.331	20.411	20.412	17.549	17.637
2	20.331	20.411	20.412	17.549	17.637
3	39.325	38.776	38.965	39.485	39.380
4	39.325	38.776	38.965	39.485	39.380
5	7.9187	7.9187	7.9187	14.829	15.299
6	34.089	34.557	34.355	31.357	31.248
Weight (lbs.)	9565	9562	9561	9815	9847

* present analysis using exponential resizing and approximate Lagrange multiplier formulae

*Table 2 Two-Story and One-Bay Frame
Initial and Final Five Frequencies ($\frac{H}{s}$.)
in Different Constraint Conditions*

Frequency No.	Initial Design	$\omega_1 = 5.0$	$\omega_2 = 18.0$	$\omega_1 \geq 5.0$ $\omega_2 \geq 18.0$	$\omega_1 \geq 5.0$ $\omega_2 \geq 18.0$ $\omega_3 \geq 35.0$
1	0.54 (0.54)	5.00 (5.00)	3.10 (3.11)	5.00 (5.00)	5.00 (5.00)
2	2.30 (2.30)	15.69 (15.58)	18.00 (18.00)	18.45 (18.28)	19.71 (19.51)
3	13.29 (13.29)	36.38 (36.67)	47.65 (47.64)	34.12 (34.06)	35.01 (35.00)
4	18.38 (18.38)	49.79 (49.80)	49.27 (49.27)	51.94 (51.85)	52.66 (52.59)
5	19.24 (19.24)	58.48 (58.59)	57.51 (57.57)	64.94 (64.89)	65.61 (65.51)
Weight (lbs.)	369.6 (369.6)	3366.9 (3361.9)	2380.5 (2380.5)	3224.0 (3219.5)	3280.2 (3267.2)

* present analysis using exponential resizing and approximate Lagrange multiplier formulae

() results with MKE term

*Table 3 Two-Story and One-Bay Frame
Optimum Design Variables (in.²) in Different Constraint Conditions**

Element No.	$\omega_1 = 5.0$	$\omega_2 = 18.0$	$\omega_1 \geq 5.0$ $\omega_2 \geq 18.0$	$\omega_1 \geq 5.0$ $\omega_2 \geq 18.0$ $\omega_3 \geq 35.0$
1	6.139 (6.100)	10.651 (10.593)	5.908 (5.805)	6.659 (6.563)
2	6.139 (6.100)	10.651 (10.594)	5.908 (5.805)	6.659 (6.563)
3	12.958 (13.041)	10.515 (10.554)	19.237 (19.442)	18.279 (18.415)
4	12.958 (13.041)	10.515 (10.555)	19.239 (19.444)	18.281 (18.417)
5	5.464 (5.266)	3.000 (3.000)	5.808 (5.627)	6.821 (6.620)
6	10.887 (10.979)	3.000 (3.000)	3.000 (3.000)	3.000 (3.000)
Weight (lbs.)	3366.9 (3361.9)	2380.5 (2380.5)	3224.0 (3219.5)	3280.2 (3267.2)

* present analysis using exponential resizing and
approximate Lagrange multiplier formulae

() results with MKE term

Table 4 Seven-Story and One-Bay Frame
Optimum Design Variables (in.²) $\omega_1 = 10.2$ rad/sec

Element No.	Via Reference [17]					Present Analysis* w/ MKE	Present Analysis* w/o MKE
1	7.9187	7.9187	7.9187	7.9187	7.9187	7.9187	7.9187
2	7.9187	7.9187	7.9187	7.9187	7.9187	7.9187	7.9187
3	7.9187	7.9187	7.9187	7.9187	7.9187	7.9187	7.9187
4	7.9187	7.9187	7.9187	7.9187	7.9187	7.9187	7.9187
5	8.1644	8.2330	8.4045	8.0937	8.3065	7.9187	7.9187
6	8.1644	8.2330	8.4045	8.0937	8.3065	7.9187	7.9187
7	9.4956	9.4987	9.5212	9.3640	9.5818	8.7612	8.7792
8	9.4956	9.4987	9.5212	9.3640	9.5818	8.7612	8.7792
9	10.4700	10.4470	10.4220	10.3130	10.5300	9.6766	9.6742
10	10.4700	10.4470	10.4220	10.3130	10.5300	9.6766	9.6742
11	11.1950	11.2290	11.2790	11.0870	11.3140	10.2988	10.2850
12	11.1950	11.2290	11.2790	11.0870	11.3140	10.2988	10.2850
13	17.2150	17.2970	17.2740	17.5070	17.1860	25.5192	25.4635
14	17.2150	17.2970	17.2740	17.5070	17.1860	25.5192	25.4635
15	7.9187	7.9187	8.2283	7.9187	7.9187	7.9187	7.9187
16	7.9187	7.9187	7.9187	7.9187	7.9187	7.9187	7.9187
17	10.8080	10.7440	10.7900	10.7220	10.7770	10.4736	10.5563
18	12.9640	12.8260	12.5990	12.8020	12.8440	13.0765	13.0753
19	14.8050	14.8820	14.8840	14.9460	14.8500	14.5608	14.5533
20	15.6980	15.7860	15.8020	15.8780	15.7360	15.7920	15.7716
21	15.0050	15.1390	15.2570	15.0900	15.1580	7.9187	7.9187
Weight (lbs.)	16882	16909	16997	16901	16918	16537	16539

* present analysis using exponential resizing and approximate Lagrange multiplier formula:

*Table 5 Ten-Story and Three-Bay Frame
Initial and Final Five Frequencies (Hz.)
in Different Constraint Conditions*

Frequency No.	Initial Design	$\omega_1 = 2.0$	$\omega_2 = 7.0$	$\omega_1 \geq 2.0$ $\omega_2 \geq 7.0$	$\omega_1 \geq 2.0$ $\omega_2 \geq 7.0$ $\omega_3 \geq 15.0$
1	0.11 (0.11)	2.00 (2.00)	1.10 (1.10)	2.00 (2.00)	2.22 (2.17)
2	0.34 (0.34)	3.74 (3.63)	7.00 (7.00)	7.00 (7.00)	7.00 (7.00)
3	0.59 (0.59)	7.07 (6.95)	7.76 (7.77)	9.71 (9.57)	15.00 (15.00)
4	0.88 (0.88)	9.85 (9.30)	9.08 (9.09)	14.99 (14.77)	17.88 (17.39)
5	1.21 (1.21)	10.66 (10.32)	9.90 (9.91)	15.98 (15.81)	17.87 (17.70)
Weight (lbs.)	4213.4 (4213.4)	66222.5 (66672.7)	80023.0 (80020.2)	102503.2 (100433.6)	135295.6 (131648.5)

* present analysis using exponential resizing and approximate Lagrange multiplier formulae

() results with MKE term

Table 6 313 Member Frame
Initial and Final Five Frequencies (Hz.)
in Different Constraint Conditions

Frequency No.	Initial Design	$\omega_1 = 1.0$	$\omega_2 = 5.0$	$\omega_1 \geq 1.0$ $\omega_2 \geq 5.0$	$\omega_1 \geq 1.0$ $\omega_2 \geq 5.0$ $\omega_3 \geq 9.0$
1	0.39 (0.39)	1.00 (1.00)	0.88 (0.87)	1.00 (1.00)	1.26 (1.20)
2	1.13 (1.13)	2.51 (2.56)	5.00 (5.00)	5.00 (5.00)	5.00 (5.00)
3	2.15 (2.15)	4.69 (4.79)	5.36 (5.30)	5.72 (5.58)	9.00 (9.00)
4	2.20 (2.20)	4.83 (4.93)	6.47 (6.47)	6.56 (6.61)	9.00 (9.00)
5	3.03 (3.03)	6.88 (7.01)	7.56 (7.41)	7.72 (7.52)	11.29 (11.10)
Weight (lbs.)	10458.2 (10458.2)	44316.9 (46007.0)	78707.7 (77549.8)	85918.2 (84830.4)	118850.9 (116658.2)

* present analysis using exponential resizing and approximate Lagrange multiplier formulae

() results with MKE term

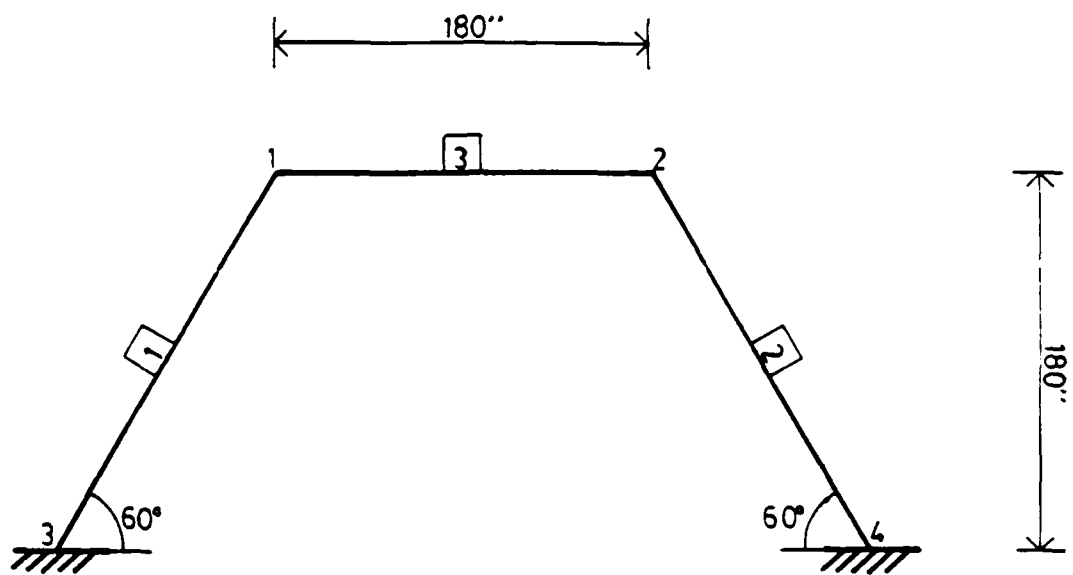


Figure 1 Three member frame with inclined support columns

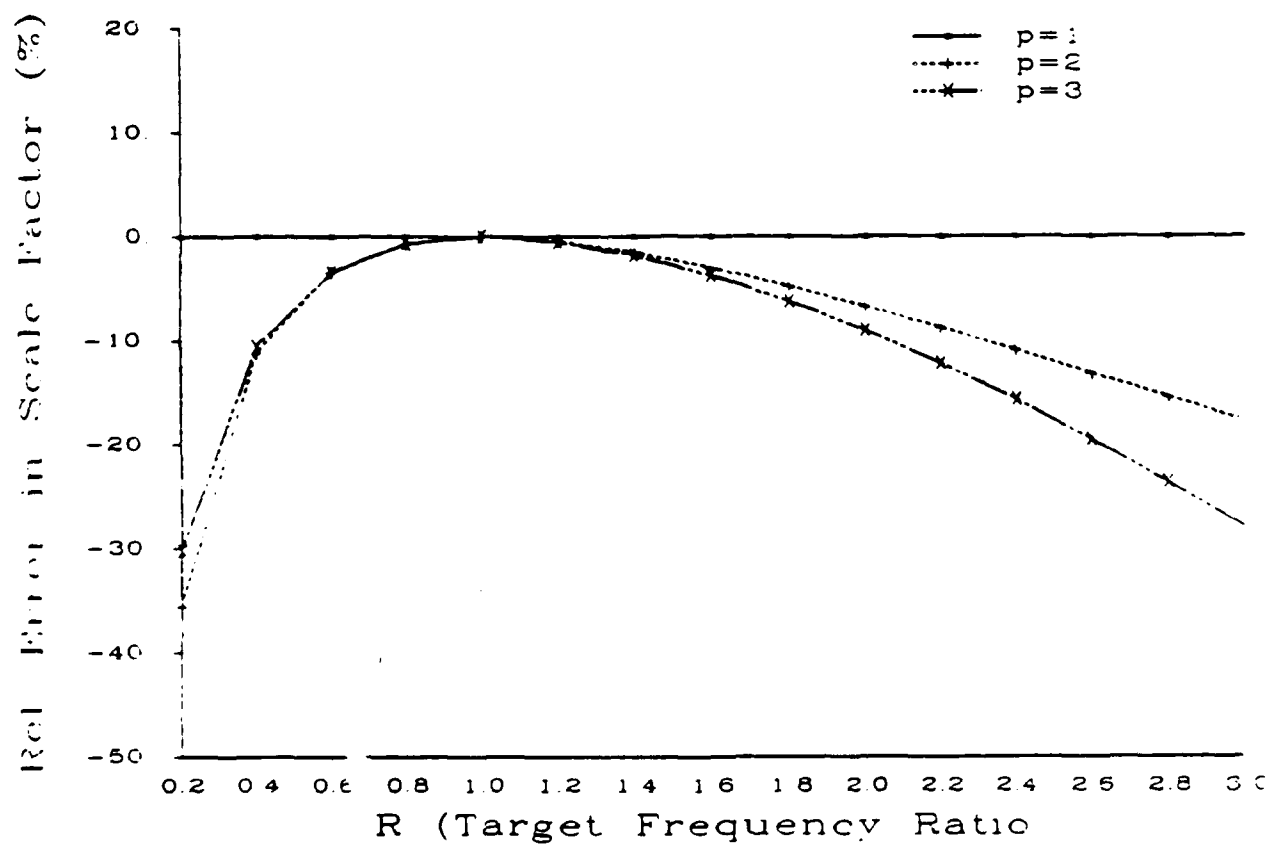


Figure 2 Relative expected error due to scaling

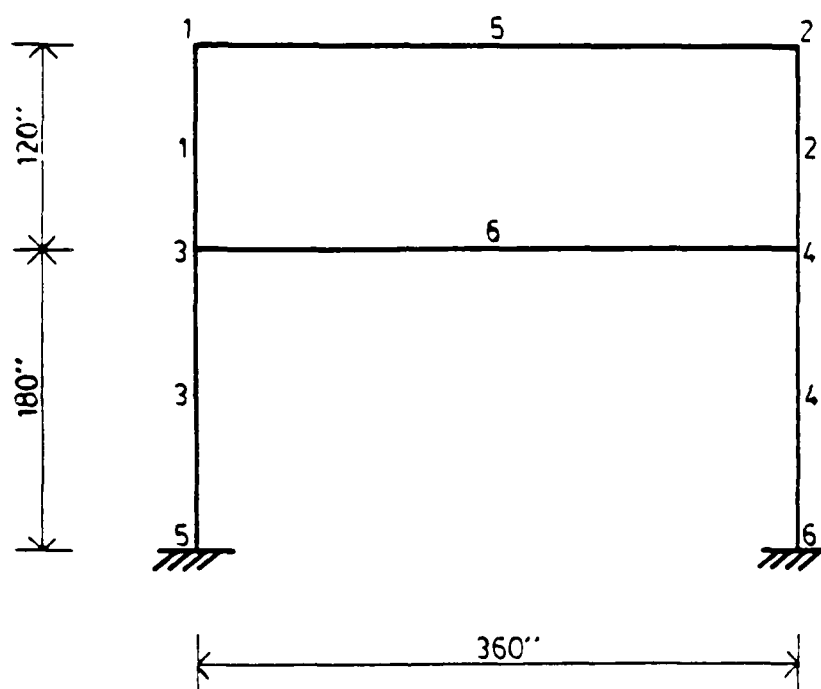


Figure 3 Two-story and one-bay frame

Two-Story and One-Bay Frame

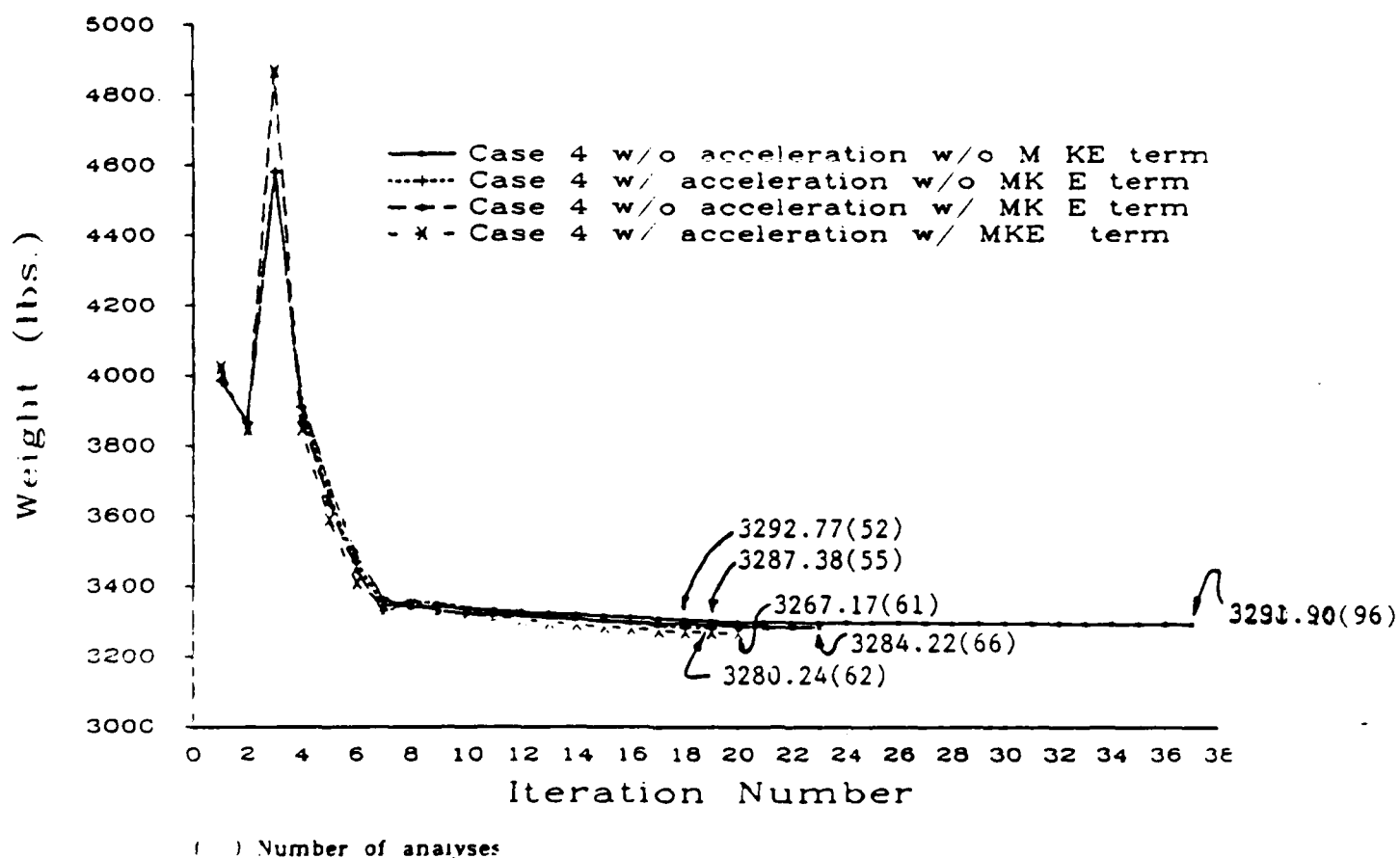


Figure 4 Effect of Aitken's accelerator on iteration history of six-member frame with multiple frequency constraints

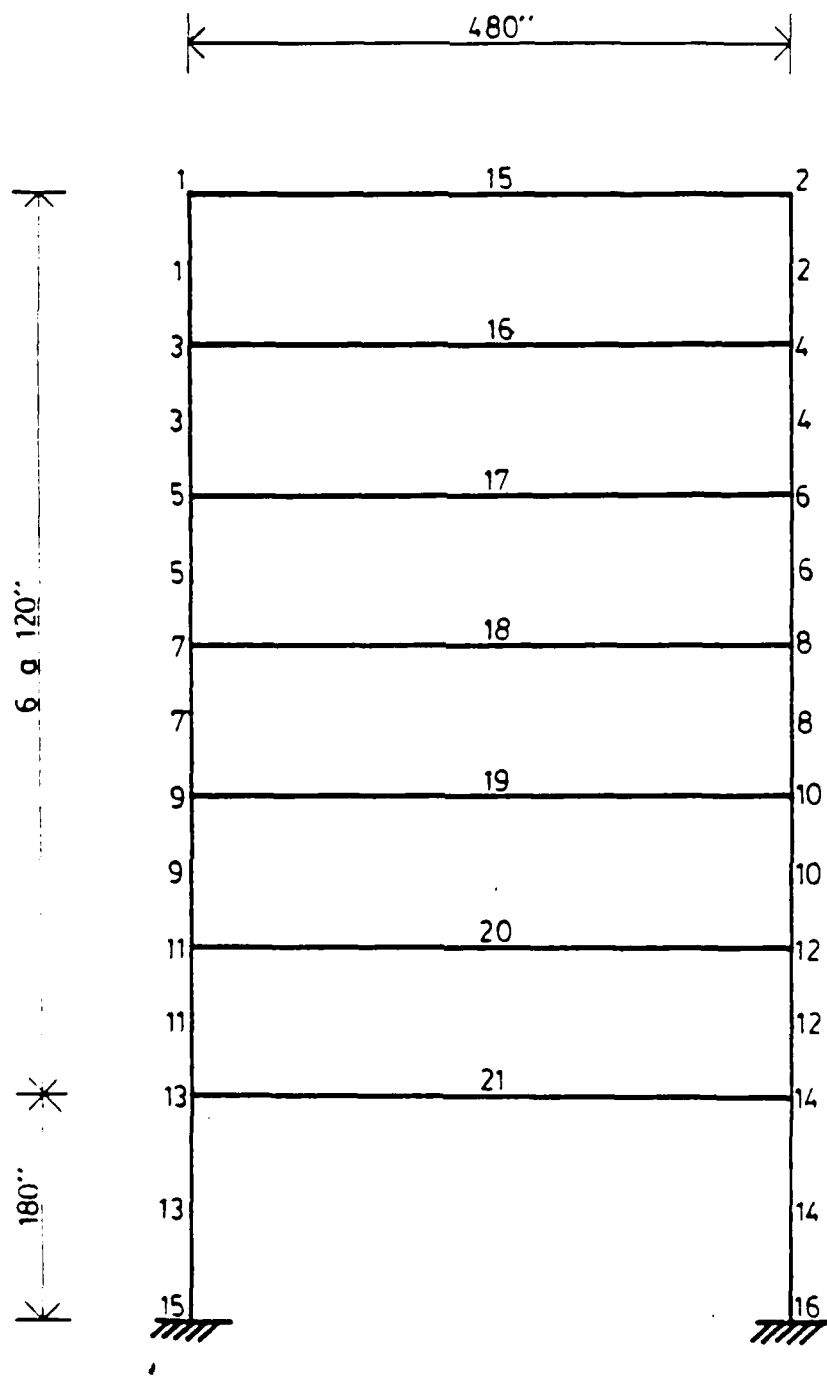


Figure 5 Seven-story and one-bay frame

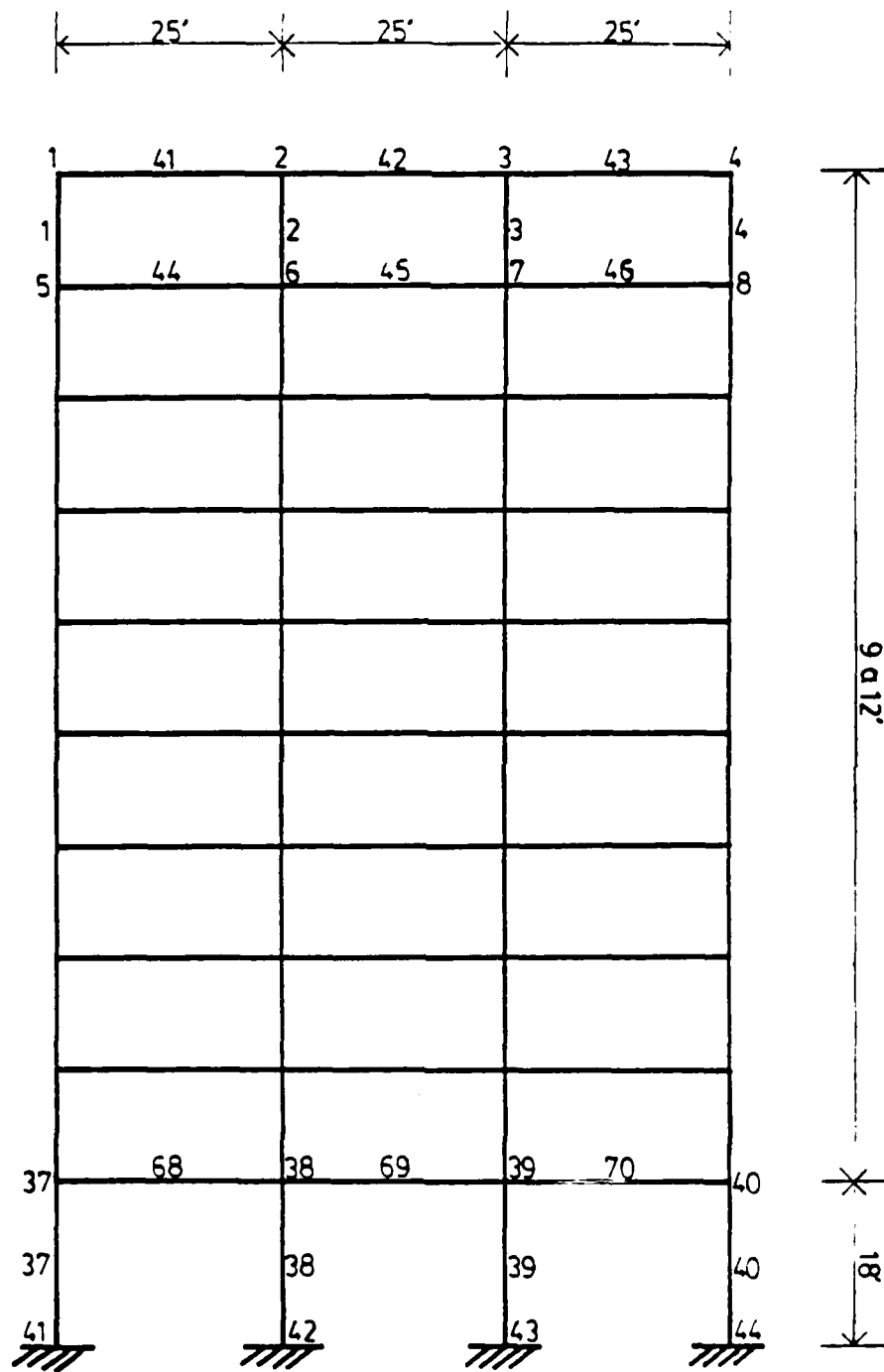


Figure 6 Ten-story and three-bay frame

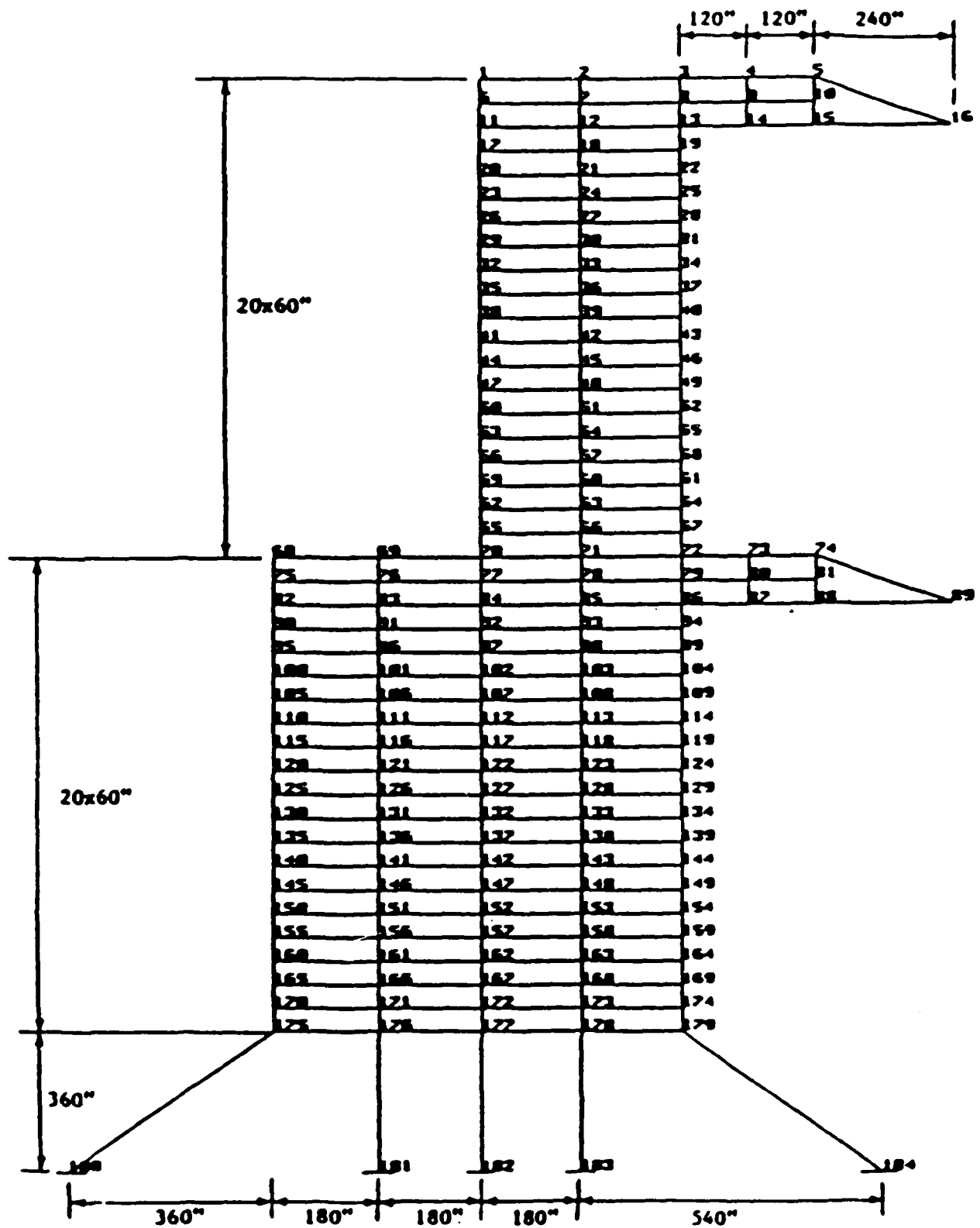
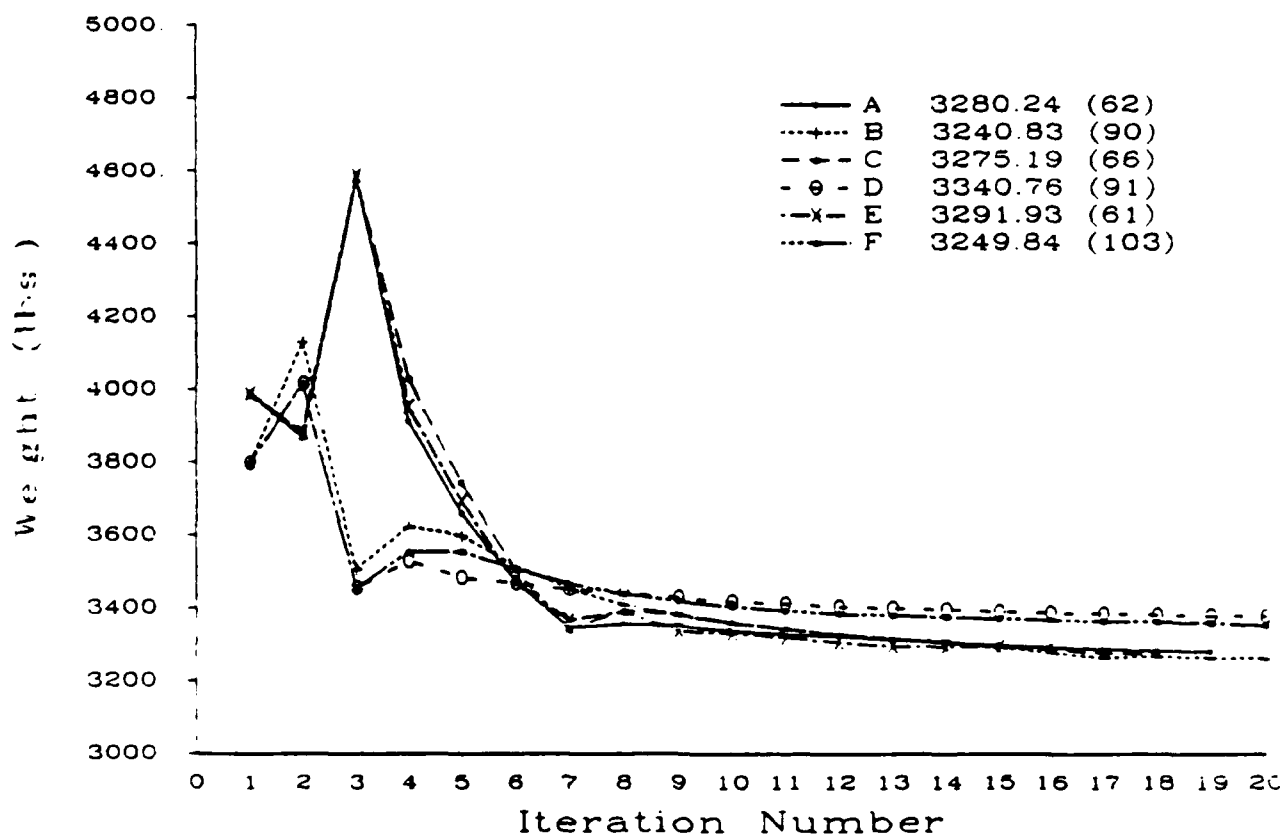


Figure 7 Three hundred and thirteen member frame

Two-Story and One-Bay Frame

$$\omega_1 \geq 5 \text{ Hz.} \quad \omega_2 \geq 18 \text{ Hz.} \quad \omega_3 \geq 35 \text{ Hz.}$$



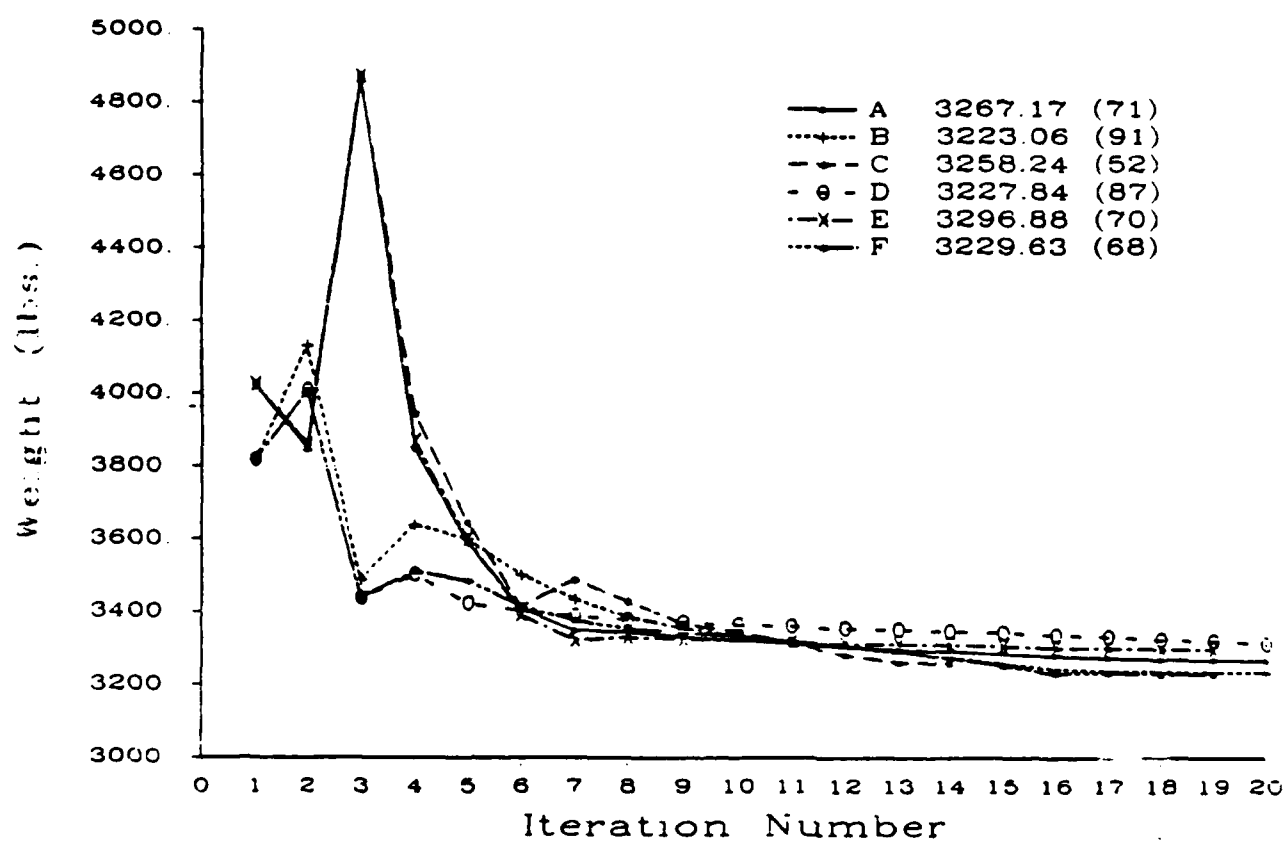
- A : exponential resizing/approximate Lagrange multiplier formulae
- E : linear resizing/approximate Lagrange multiplier formulae
- C : exponential resizing/exponential Lagrange multiplier formulae
- D : linear resizing/exponential Lagrange multiplier formulae
- E : exponential resizing/linear Lagrange multiplier formulae
- F : linear resizing/linear Lagrange multiplier formulae
- () : number of analyses

Figure 8 Iteration history for two-story and one-bay frame-

Two-Story and One-Bay Frame

$\omega_1 \geq 5 \text{ Hz.}$ $\omega_2 \geq 18 \text{ Hz.}$ $\omega_3 \geq 35 \text{ Hz.}$

• Including Modal Kinetic Energy

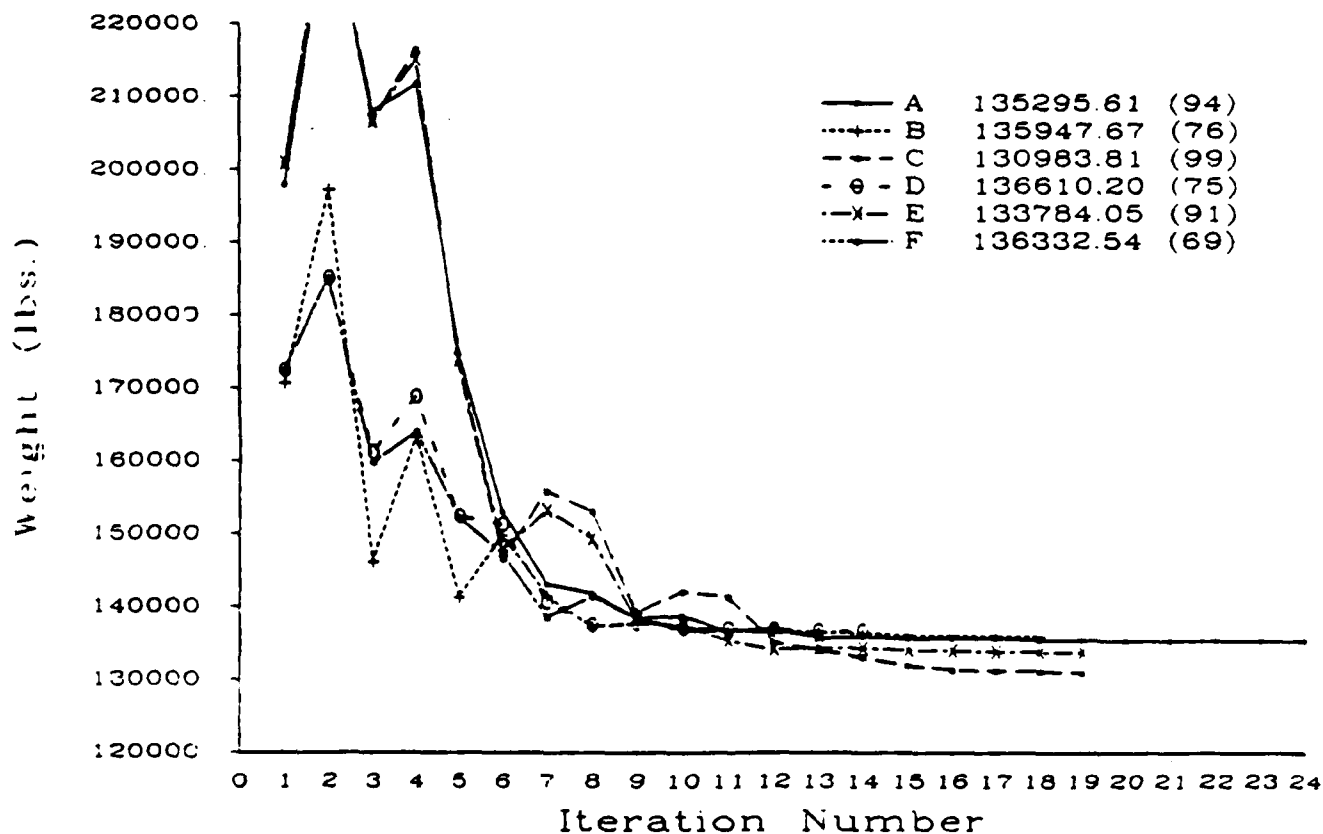


- A : exponential resizing/approximate Lagrange multiplier formulae
- B : linear resizing/approximate Lagrange multiplier formulae
- C : exponential resizing/exponential Lagrange multiplier formulae
- D : linear resizing/exponential Lagrange multiplier formulae
- E : exponential resizing/linear Lagrange multiplier formulae
- F : linear resizing/linear Lagrange multiplier formulae
- () number of analyses

Figure 9 Iteration history for two-story and one-bay frame

Ten-Story and Three-Bay Frame

$$\omega_1 \geq 2 \text{ Hz.} \quad \omega_2 \geq 7 \text{ Hz.} \quad \omega_3 \geq 15 \text{ Hz.}$$



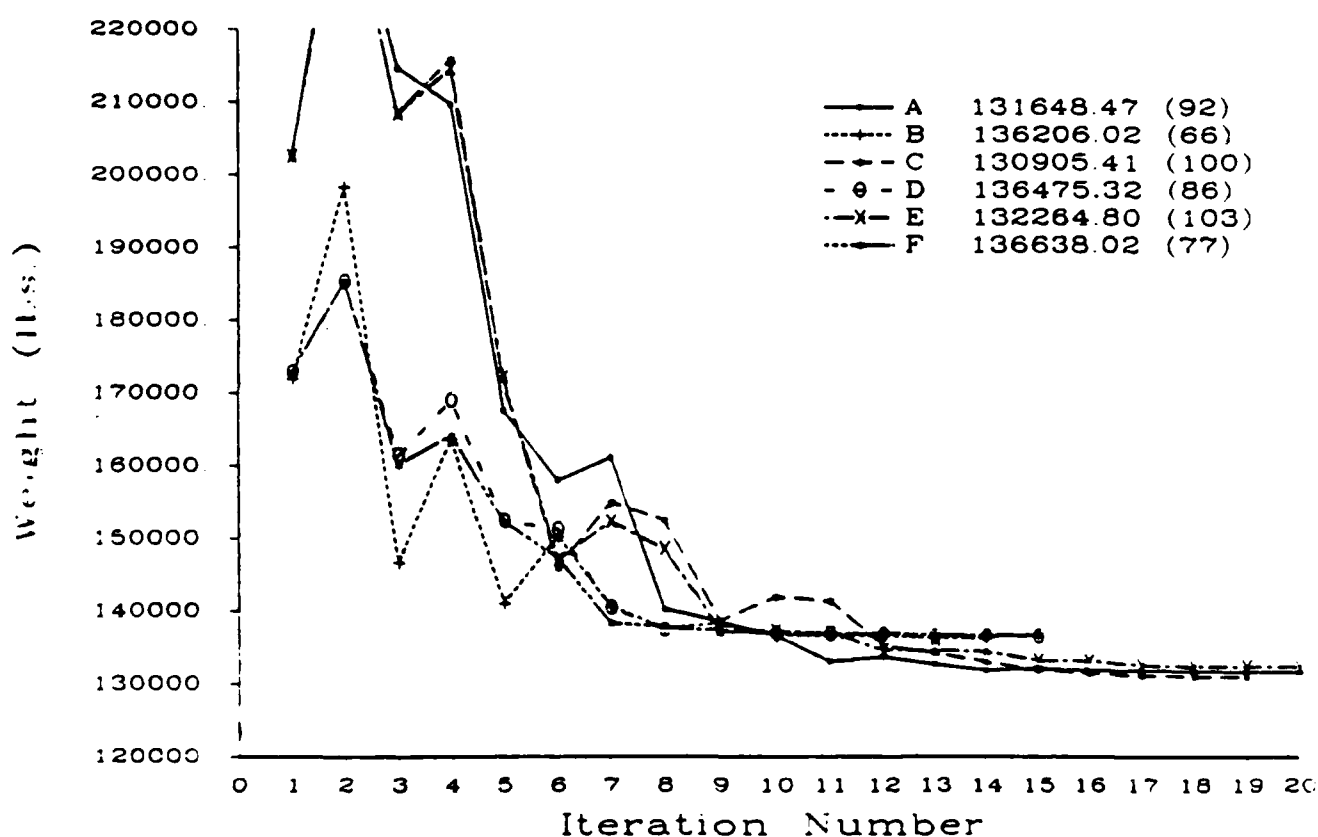
- A : exponential resizing/approximate Lagrange multiplier formulae
 B : linear resizing/approximate Lagrange multiplier formulae
 C : exponential resizing/exponential Lagrange multiplier formulae
 D : linear resizing/exponential Lagrange multiplier formulae
 E : exponential resizing/linear Lagrange multiplier formulae
 F : linear resizing/linear Lagrange multiplier formulae
 () number of analyses

Figure 10 Iteration history for ten-story and three-bay frame

Ten-Story and Three-Bay Frame

$\omega_1 \geq 2 \text{ Hz}$ $\omega_2 \geq 7 \text{ Hz}$ $\omega_3 \geq 15 \text{ Hz}$

Including Modal Kinetic Energy

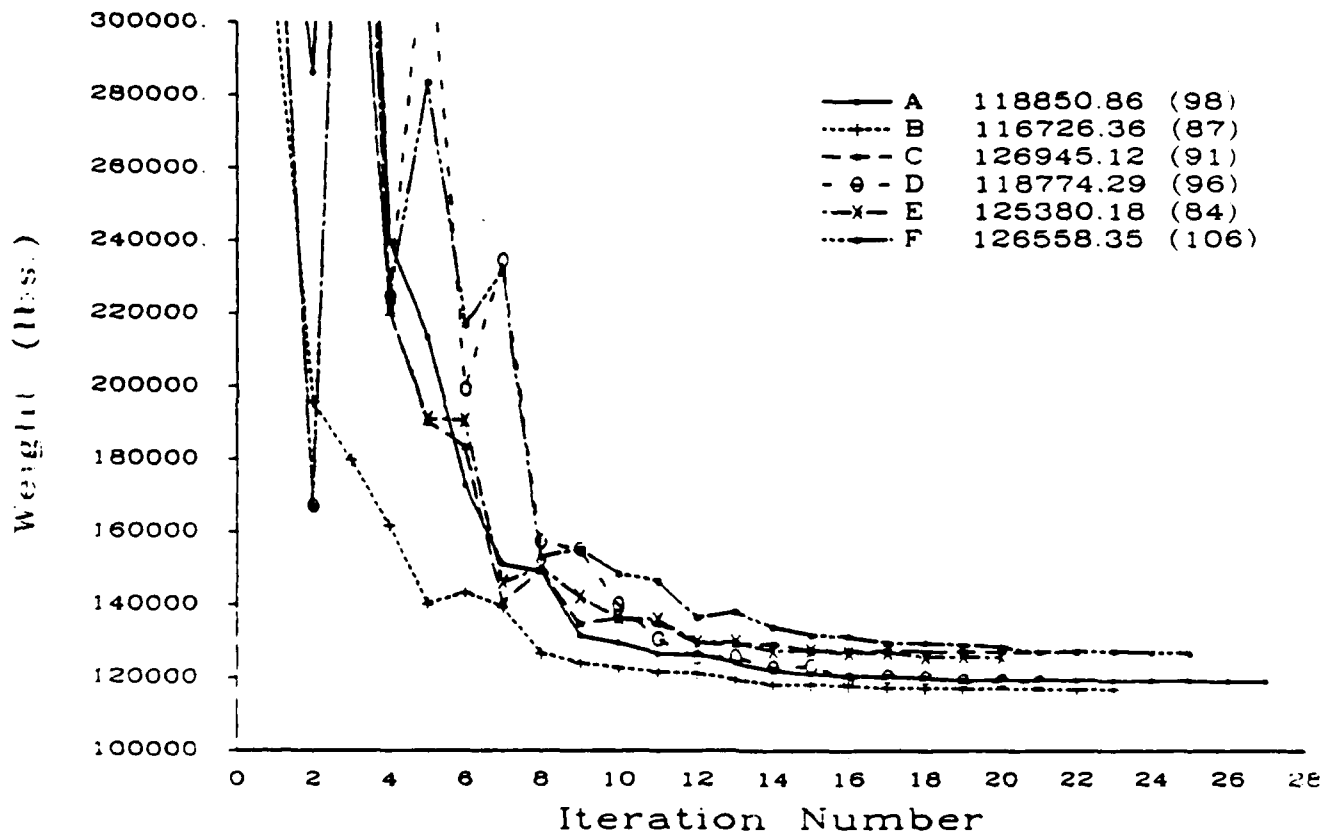


- A : exponential resizing/approximate Lagrange multiplier formulae
- B : linear resizing/approximate Lagrange multiplier formulae
- C : exponential resizing/exponential Lagrange multiplier formulae
- D : linear resizing/exponential Lagrange multiplier formulae
- E : exponential resizing/linear Lagrange multiplier formulae
- F : linear resizing/linear Lagrange multiplier formulae
- () number of analyses

Figure 11 Iteration history for ten-story and three-bay frame

313 Member Frame

$$\omega_1 \geq 1 \text{ Hz.} \quad \omega_2 \geq 5 \text{ Hz.} \quad \omega_3 \geq 9 \text{ Hz.}$$



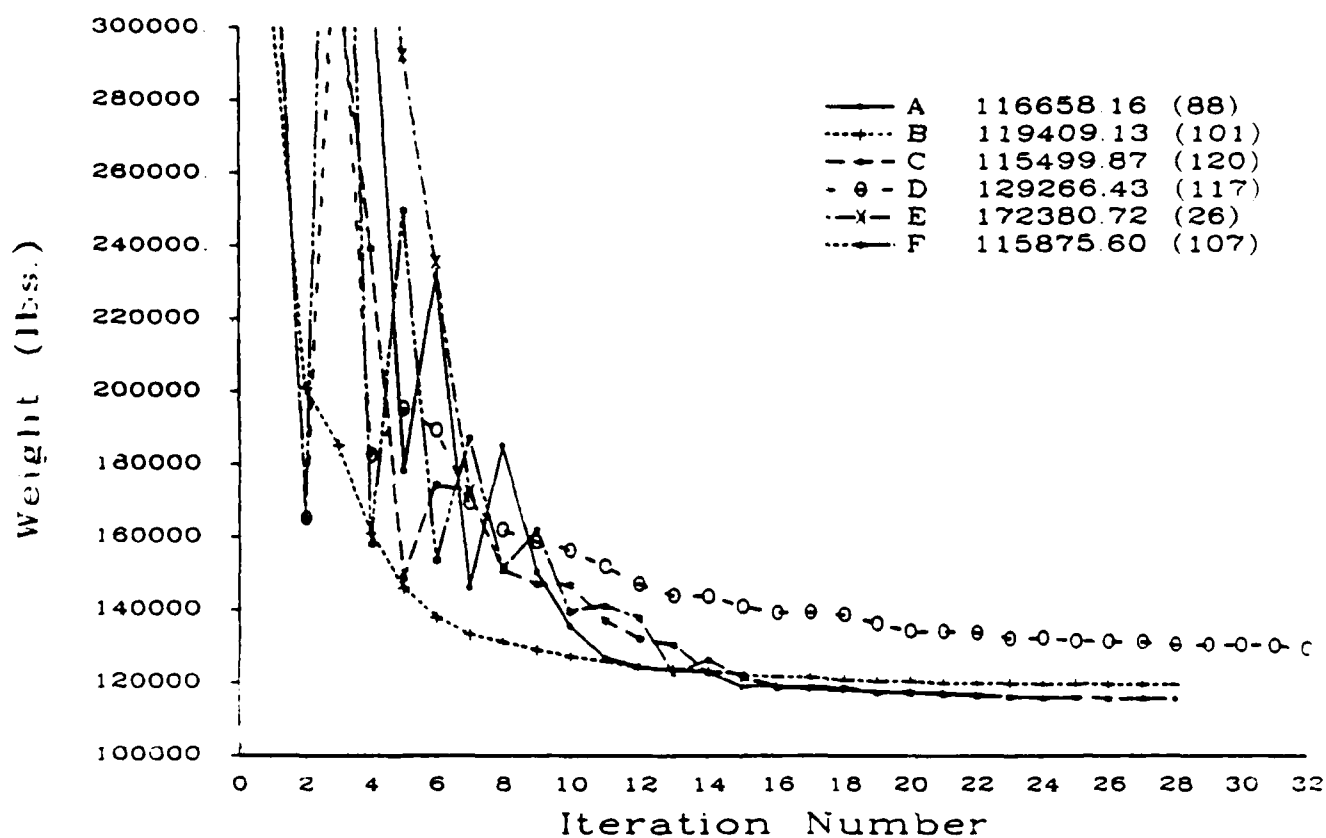
- A : exponential resizing/approximate Lagrange multiplier formulae
- B : linear resizing/approximate Lagrange multiplier formulae
- C : exponential resizing/exponential Lagrange multiplier formulae
- D : linear resizing/exponential Lagrange multiplier formulae
- E : exponential resizing/linear Lagrange multiplier formulae
- F : linear resizing/linear Lagrange multiplier formulae
- () number of analyses

Figure 12 Iteration history for 313 member frame

313 Member Frame

$\omega_1 \geq 1 \text{ Hz.}$ $\omega_2 \geq 5 \text{ Hz.}$ $\omega_3 \geq 9 \text{ Hz.}$

Including Modal Kinetic Energy



A : exponential resizing/approximate Lagrange multiplier formulae
 B : linear resizing/approximate Lagrange multiplier formulae
 C : exponential resizing/exponential Lagrange multiplier formulae
 D : linear resizing/exponential Lagrange multiplier formulae
 E : exponential resizing/linear Lagrange multiplier formulae
 F : linear resizing/linear Lagrange multiplier formulae
 () number of analyses

Figure 13 Iteration history for 313 member frame

SECTION IV

CONCLUDING REMARKS

The OC method is a powerful tool for large-scaled structural optimization. Many investigators have intuitively applied it to frequency-constrained bar and frame structures with uneven degrees of convergence. We note here specifically the recent work by Venkayya, Khot, Grandhi, Tischler, Khan, and Willmert. While it was not possible to provide a direct comparison of results in all cases, due to differences in the optimization algorithms used, the results given in this report show passable correlation to manifest a reasonably valid concern regarding the convergence quality of OC methods. A competent OC procedure must establish specific criteria based on previous scaled designs to automatically select the proper step size in the redesign phase. Also, the numerical procedure must be an adaptive one, which does not require adjustments of numerous internal parameters.

In this report, the above improvement components of the OC method have been developed. A computer program PACSOP (Promotion and Acceleration of Convergence of Structural Optimization Procedures), written in FORTRAN 77, was developed to execute the optimization algorithm described in this report. (Complete documentation of PACSOP is currently in preparation as a follow-on report.) Several example problems were used to demonstrate the method and the results were compared with previous results. Overall, the improved OC method exhibited a stabilizing effect on the oscillatory convergence propensity of the various OC

recursive strategies reviewed here. It is anticipated that the method can enhance the convergence of minimum-weight designs involving displacement, stress, and buckling constraints, and this is the focus of continuing research.

APPENDIX A

PUBLICATIONS AND PRESENTATIONS

The research program has resulted in the following publications and presentations.

A.1 RESEARCH REPORTS

1.1 "Convergence of upper-bound optimum design of large-scaled structures with specified frequency bands", (with K.F. Phan), OSURF Structural Eng. Rept. No. 34, Dept. of Civil Eng. (1989).

1.2 "PACSOP--Promotion and Acceleration of Convergence of Structural Optimization Procedures", (with K.F. Phan), OSURF Structural Eng. Rept. No. 35, Dept. of Civil Eng. (in preparation).

A.2 CONFERENCE PROCEEDINGS

2.1 "An improved algorithm for optimum structural design with multiple frequency constraints" (with K.F. Phan), Proceedings of the Second NASA/Air Force Symposium on Multidisciplinary Analysis and Optimization in Hampton, Virginia, September 28-30, 1988, NASA-CP 3031 (Part 3).

A.3 REFERRED JOURNAL ARTICLES

3.1 "An adaptive procedure for stabilizing convergence quality in frequency-constrained design optimization" (with K.F. Phan), International Journal of Numerical Methods in Engineering (in review) (1989).

3.2 "A robust optimality criteria procedure for crosssectional optimization of plane frames with multiple frequency limits", (with K.F. Phan), Computers and Structures, (in review) (1989).

A.4 DISSERTATIONS AND THESES

4.1 Khing F. Phan, "Optimal design of large-scaled structures with multiple displacement and frequency constraints", Ph.D. Dissertation (Completion date: March 1990).

A.5 OTHER PRESENTATIONS

In addition to the publications and presentations listed above, the principal investigator presented results of the

Research to the Structural Dynamics Branch at NASA Lewis Research
Center in February 1989.

FINAL REPORT NUMBER 87
REPORT NOT AVAILABLE AT THIS TIME
Dr. James A. Sherwood
210-9MG-088

FINAL REPORT

Robustness with Positive Real Controllers
for Large Space Structures

sponsored by

UNIVERSAL ENERGY SYSTEMS

Contract P.O. #S-760-7MG-088

prepared by

G.L. Slater, Principal Investigator

contributing authors

Q. Zhang, Research Professor,
A. Bosse, Graduate Student,

June 13, 1989
University of Cincinnati
Cincinnati, Ohio, 45221

Abstract

The robustness of a continuous positive real controller design is established by linking the positivity theory to the standard singular value robustness tests. By application of the singular value test to a model of the deviation from positivity induced by actuators, computational delays, etc., the global stability of the control design can be assured, even with significant modeling errors due to modal uncertainty. Both theoretical and experimental verification of this stability result is presented.

1. INTRODUCTION

The design of controls for large space structures (LSS) is a difficult task due to the complexity of these dynamical systems. The structural model of these flexible bodies has a large number of vibration modes which are widely spaced in frequency and are characterized by a very low inherent damping. Generally, the dynamic model is poorly defined leading to considerable uncertainty (especially in the higher modes) in the modal frequencies, damping and mode shapes. In addition, the control design model is usually based on a low order modal representation of the finite element model in order to reduce the complexity and sensitivity of the control design. This modal truncation leads to observation and control spillover which can destabilize one or more of the poorly damped modes. Controllers are expected to be implemented using digital systems although many analysis techniques utilize only a continuous system theoretical approach. All of these approximations used in the process of control design make the robustness of the control laws a matter of particular interest for the control system designer.

The existing literature on the space structure control problem is extensive, see e.g. Refs. [1-4]. Numerous investigators have proposed techniques for dealing with the uncertainties inherent in the structural dynamic model. A powerful technique which can mathematically guarantee stability in the presence of significant modeling uncertainty is the "positive real" approach, [5, 6] which is based on the positive real property of the input-output relationship between collocated force actuator and velocity sensors. The positivity approach has been used to (theoretically) design stable controls for spacecraft models which give good

structural model and are insensitive to failures in multiple actuators and/or sensors [6].

A fundamental limitation remains however in the strictness of the positive real property, a mathematical condition which can be satisfied for ideal sensors and actuators, but which fails for real components due to phase lag, excessive high frequency attenuation and computational delays. In fact it is easily shown that no digitally controlled continuous system can satisfy the fundamental positive real stability theorem. [7]

Currently in the controls field, the robustness of multivariable systems is one of the major research areas. The seminal article by Doyle and Stein [8] showed the importance of the singular values of the return difference matrix $\sigma(I+GH)$ for investigating robustness to various perturbative models. A succession of articles by Doyle and other researchers [9-12] has led to an abundance of information on structured and unstructured perturbations, stability analyses and even design procedures to ensure robustness.

Unfortunately the form of the perturbation models for the conventional unstructured perturbation are inappropriate for the large space structure model and generally fail to give significant results. For example, in a design for the DRAPER II space telescope, Kissel and Hegg [13] were unable to achieve desired stable performance due to the modal perturbations encountered. The essence of the problem lies in the nature of the assumed perturbations. The conventional singular value analysis is oriented toward high frequency unstructured perturbations in magnitude and phase. LSS control has these problems caused by the sensors and actuators, but the

modal uncertainty is not of this form. A possible approach is to use a structured perturbation model and in particular, to use real perturbations to capture this problem. Current work in this direction has been reported by Doyle [12], Jones [14], Tahk [15], and Yedavelli [16], yet much remains to be done before a general theory is complete. Much of the difficulty encountered in the robustness research is caused by the generality of the systems which must be considered. By focusing on the structural control problem, we can take advantage of the special mathematical structure of this problem to yield important results.

For large space structures the dynamic model is characterized by a large number of 'significant' structural modes in a frequency range which is within the desired bandwidth of the system. These modes are characterized by a fairly low damping and the primary goal of the controller is to add damping to these modes. Mathematical models of these systems are generally constructed from a finite element representation or from a simplified continuum approach. In either case it has been common knowledge that while the first few low frequency modes can be predicted fairly well, higher frequency modes are extremely difficult to accurately predict. In addition these modes may be extremely sensitive to small parameter changes (e.g., stiffness, mass) which may be expected to occur over the life of the structure. Finally in terms of constructing a control design model, it is often not the lowest frequency modes which are of interest. Often these low frequency modes may be associated with the vibration of appendages or other "local modes". Alternately, the mode shape associated with such a vibration may not be easily excited by the applied forces, or is not a significant component in the controller cost function. Even though such a mode may not contribute greatly to the overall system response, the maximum singular

value of the perturbation matrix $\delta(L)$ will generally be quite large at the unmodeled modal frequency, warning of a potential stability problem. Mathematically this is correct - a small (unstructured) change in the system dynamics at this frequency could cause the system poles to go unstable. Nevertheless, since this mode is within the control system bandwidth, the conventional approach of reducing system gains at this frequency is not appropriate.

For higher frequencies the unmodeled mode problem remains serious, although outside the control bandwidth stability robustness can be assured through high frequency gain attenuation. This permits the unstructured singular value bounds to be met so long as unmodeled modal damping is not arbitrarily small. Another source of modeling errors (particularly) at high frequency is in the area of actuator dynamics. In most preliminary analyses, actuation dynamics are neglected. Tests of "proof mass" type of actuators indicate significant amounts of phase shift are often present as well as non-linear effects due to friction and hysteresis. So long as this uncertainty is restricted to a higher frequency range then the unstructured singular value analysis can accommodate this error source.

For low frequency error sources, the primary conclusion to be drawn is that there must be additional information available regarding the system if some stability robustness is to be ensured. Our work in the area of positive real controls indicates that this approach offers additional robustness criteria not available through unstructured singular value analysis. In this paper we outline the theory of positive real control (Section 2) and the standard robustness results (Section 3). Finally in Section 4 we propose a methodology to combine these analyses to produce

meaningful stability results and in Section 5 we demonstrate theoretical and experimental results verifying the robustness of the positive real laws.

2. REVIEW OF POSITIVITY

The formal definition of a positive real system is as follows [17]:

Def. 1 Positive Real System

(a) A system with $m \times m$ transfer matrix $G(s)$ is positive real if for $\text{Re}(s) > 0$, then

$$[G(s) + G^*(s)] \geq 0 \quad (1)$$

where $()^*$ indicates conjugate transpose and where the inequality in (1) means that the matrix on the left side of (1) is non-negative definite.

(b) Equivalent to (a) are the conditions:

- (i) The elements of $G(s)$ have no poles in $\text{Re}(s) > 0$.
- (ii) Poles of $G(s)$ on the imaginary axis are simple and such that the residue matrix is non-negative definite Hermitian.
- (iii) For all real ω with $s = j\omega$ not a pole of an element of $G(s)$, then

$$[G(j\omega) + G^*(j\omega)] \geq 0$$

If the inequalities above are strictly satisfied ($>$) then the system is referred to as 'strictly positive real'. In network theory, positive

realness is commonly related to a property of passive networks; viz. that the system is dissipative in that the (generalized) energy in the system at time t , minus the energy added to the system by the input function, is bounded (above) by the initial energy. (See Anderson [18].) Thus positive realness implies a rather strong type of stability.

The test for positive realness in Definition 1 is seen to be fairly restrictive in terms of the type of transfer functions commonly encountered in engineering. For a scalar transfer function to be positive real the Nyquist plot of $G(j\omega)$ must remain in the first and fourth quadrants, i.e., it must exhibit less than $\pm 90^\circ$ of phase shift, at all frequencies. Thus, e.g., the transfer functions $1/(s + p)$ and $s/(s^2 + \zeta\omega_n s + \omega_n^2)$ can easily be shown to be positive real. The transfer function $\omega_n^2/(s^2 + 2\zeta\omega_n s + \omega_n^2)$ is seen to be not positive real since it exhibits phase shift approaching -180° for large ω .

The positivity tests on transfer matrices may be replaced with an equivalent criterion applicable to systems in state variable form [17].

Test for Positive Real System: Let a system with transfer matrix $G(s)$ have a minimal realization with

$$\dot{\underline{x}} = \underline{F} \underline{x} + \underline{G} \underline{u}$$

$$\underline{y} = \underline{H} \underline{x} + \underline{D} \underline{u} \quad (2)$$

Then $G(s)$ is positive real if and only if there exists a symmetric positive definite matrix P and matrices W_0 and L such that

$$PF + F^T P = -LL^T \quad (3a)$$

$$PG = H^T - LW_0 \quad (3b)$$

$$W_0^T W_0 = D + D^T \quad (3c)$$

For a given realization, equation (3c) determines W_0 to within an arbitrary orthogonal transformation (if W_0 satisfies (3c) and Q is an orthogonal matrix, then (QW_0) also satisfies (3c)). In the normal case where $D = 0$, then $W_0 = 0$. The determination of L and P to satisfy (3a) and (3b) is a non-trivial task, hence to test a system for positive realness may be quite difficult using this approach.

An alternate problem which we encounter in control design is to construct a positive real system given certain fixed elements. For example, we may be given a matrix F and either G or H and seek the remaining matrix required to impose positive realness (Assume $D = 0$). Such a problem is solved fairly easily by choice of an L such that (F^T, L) is controllable. This guarantees a positive definite P (F must of course be stable) which can be easily obtained from (3a). Given G or H the remaining matrix can be obtained from (3b).

Stability of Positive Real Feedback Systems

The importance of positivity is due to the strong stability theorems for feedback systems with positive transfer functions. This theorem can be stated as follows (Popov, Reference 19).

Theorem: The feedback combination of blocks G and H, where one block is strictly positive real and the other block is at least positive real, is also strictly positive real and hence is stable.

Note in Popov's notation positive realness is equivalent to "hyperstability".

Application to Structural Control

A flexible structure may be modeled as having a large (theoretically infinite) number of vibration modes which govern the motion of the structure. In practice only a few modes are modeled accurately; the remaining modes have uncertain frequency, damping and mode shape. The important fact to observe about the structure - control problem is the following: **The transfer function matrix between colocated velocity sensor - force actuator pairs is positive real.** A proof of this can be found in Benhabib [5] and will not be repeated here. This implies that for ideal velocity sensors and force actuators, then any strictly positive real feedback function can stabilize the structure. This is independent of any knowledge or model of the flexible modes. In a realistic application we require satisfactory performance in addition to stability, and for this a realistic system model is generally required. The important stability result however is that for a positive real control design then the model

uncertainty can not cause an instability with loop closure. The primary difficulty in applying this concept is the strict phase requirement of the positive real assumption. In reality no physical system can meet these requirements exactly and to consider true stability then we consider the effect of deviations from the positive real assumption.

3. ROBUSTNESS RESULTS

In this section we review the robustness results of Doyle et al [8-10] and show how these results can be integrated with the positivity concepts to yield strict stability results. The problem considered by Doyle is based on the Nyquist stability criteria, which for single input-single output (SISO) systems can be phrased in terms of encirclements of the origin by the return difference function $(1 + GH)$ evaluated along the $j\omega$ axis (ie. the Nyquist contour). To ascertain the stability in the presence of unmodeled changes in the system transfer matrix we consider a perturbed system as shown in Figure 1 where the actual transfer function differs from the model G by the multiplicative relation

$$G_{act} = (I + L)G \quad (4)$$

The multiplication perturbation $L(s)$ represents changes in magnitude and phase of the actual system from the nominal design model. A sufficient condition for the perturbed system to be stable is that the perturbation does not produce any change in encirclements of the origin. (We do not care about the absolute encirclements as the nominal closed loop system is stable). We may state this mathematically as

$$1 + (1 + \epsilon_0 L) GH \neq 0 \quad (5)$$

for all $0 \leq \epsilon_0 \leq 1$.

For the multivariable case, a sufficient condition for the perturbation "L" to not produce instability is, in analogy with our SISO result

$$\det[I + (I + \epsilon_0 L)GH] \neq 0 \quad (6)$$

for all $0 \leq \epsilon_0 \leq 1$

To relate this easily to the size of "L" requires recourse to the singular values of the return difference matrix. Now for (6) to hold we can equivalently require that

$$\underline{\sigma}(I + (I + \epsilon_0 L)GH) > 0 \quad (7)$$

for all ϵ_0 , where $\underline{\sigma}(\)$ indicates the minimum singular value.

Using various singular value relations, Doyle showed that (7) implies the sufficiency condition

$$\underline{\sigma}[(I+GH)(GH)^{-1}] = \underline{\sigma}[I+(GH)^{-1}] > L_m(\omega) \quad (8a)$$

or

$$\bar{\sigma}[GH(I+GH)^{-1}] < \frac{1}{L_m(\omega)} \quad (8b)$$

where $L_m(\omega) = \bar{\sigma}(L)$

(9)

Equations (8) represents a fundamental bound on the size of perturbation allowed for the MIMO system to maintain stability. This last statement is a precise quantification of a familiar SISO result, namely that the closed loop gain should be small if the perturbation in G is likely to be large. It is precisely at this point that the conventional application of the robustness results breaks down.

4. A Combined Positivity-Robustness Theorem

Using the multiplicative perturbation approach, the maximum singular value of the perturbation matrix $\bar{\sigma}(L)$ will have numerous peaks corresponding to the shifted modes. Because of the relatively low frequency of these perturbations, application of the singular value bound (8) to a modal uncertainty problem is useless. For example, a standard test model for flexible system control design is the tetrahedral truss model referred to as DRAPER I (see Ref. [20]). A model of the DRAPER I structure is shown in Figure 2. The system possesses 12 degrees of freedom with six inputs and six sensors. The nominal frequencies range from about 1 - 10 rad/sec. Randomly perturbing the truss elements (areas and mass) by $\leq 5\%$ produces a different set of frequencies and mode shapes. The singular value plot $L_m(\omega)$ for one 'typical' perturbation is shown in Figure 3. Each double peak in this plot corresponds to a slightly displaced modal frequency. The classic singular value robustness requirement is that the closed loop transfer function must be below the inverse of this curve which is clearly inappropriate considering the height of these peaks. (Note we have arbitrarily assumed a nominal modal damping of 0.2% and have not perturbed

this number). In spite of the inability to satisfy the singular value requirement, a positive real control design with ideal actuators is guaranteed stable since even for the perturbed model, the positive real stability theorems are satisfied.

The primary stability question then comes when additional error sources are considered, in particular those modeling errors that invalidate the positive real assumption. Most commonly these may be attributed to actuator dynamics. Other sources of error could be included, as for example, sampling delays in a digitally controlled system. The key to considering the stability problem then is to evaluate the singular value bounds on the deviation from positivity - not on the deviation from an apriori model. Using this philosophy then, extended stability results can be obtained for a class of realistic problems.

The combined application of the positivity-robustness theorems can be stated as follows:

Theorem: Define the perturbation matrix $L(s)$ as the deviation from the positive real condition for the feedback system shown in Figure 1. The closed loop system is stable then if the singular value inequality (8) holds.

The proof of this theorem follows almost trivially from a careful, sequential application of the positivity theorem, then the Doyle robustness theorem. This result is significant however, since it gives important verification of the extended range of validity of positive real control design. Caution must be used in applying this theorem for arbitrary modal

perturbations since the inequality (8) can only be evaluated using a modeled $G(s)$, not necessarily the 'actual', $G(s)$. In particular, if high frequency modes have arbitrary small damping then this extension will be invalid. Nevertheless, this result can be an important technique to establish stability for problems with high frequency actuator/sensor dynamics and to estimate the effect of various perturbation models on closed loop stability.

One additional application considered in this paper is to apply this result to a digital control system implementation. In applying this result to digital systems, the effect of digitization on continuous frequency response can be approximated crudely as a pure phase delay. This approximation is not 'sharp' however and can not be used to establish conservative boundaries for the stability problem. Details of this application are explained in the next section.

5. Application

Using a controller designed by the positive real method, the actuator effects, and the computational delays can be modeled as a high frequency perturbation $L(j\omega)$. Modal perturbations due to uncertainties in mass and stiffness are not included in this perturbative model. Applying the fundamental robustness result (8) to the nominal closed loop design implies in a physical sense that the stability of the controlled structure can be guaranteed if the controller bandwidth is sufficiently low, and with enough high frequency roll-off such that the phase and magnitude perturbations occur sufficiently outside the nominal system bandwidth. Formally we also require that outside this bandwidth, the inherent damping of any unmodeled modes must be large enough that the product of $GH(j\omega)$ is still small. In our simulation examples this does not seem to present any difficulties, and

in fact with damping ratios characteristic of these high frequency modes ($\approx .02-.10$) our results have been verified with a high degree of success.

We demonstrate this methodology with several examples, including an aircraft flutter control problem, control of the DRAPER I model truss structure with actuator dynamics, and finally an experimentally controlled beam demonstrated in the laboratory.

Example 1: An Aircraft Flutter Problem

A simple example demonstrating this concept was shown by Slater [21] using an aircraft flutter problem originally formulated by Takahashi [22]. In this example the nominal transfer function between sensor and control deflection was 'almost' positive real if actuator dynamics were neglected. The presence of the actuator added significant phase shift destroying the positivity at the high frequency range (see Figure 4). Nevertheless, a positive real design (see Figure 5) which neglected the actuator was successful in controlling the structural oscillations.

This success was justified initially [22] using heuristic arguments based on bandwidth. Using Theorem 1 allows us to guarantee the stability of this control design for both the nominal model and a perturbed model. In this and in many other cases, a reasonable first assumption is to model the deviation from positivity for the vehicle transfer function strictly as a phase change, i.e.

$$I + L = e^{j\phi} I \quad (10)$$

hence

$$L_m(\omega) = 2 \left| \sin\left(\frac{\phi}{2}\right) \right| \quad (11)$$

which clearly is bounded by

$$\begin{aligned} L_m(\omega) &< 2 \\ &< 6 \text{ db} \end{aligned} \quad (12)$$

Note that inequality (12) is only applied for frequencies outside the positive real range, and that the more precise bound (11) may be applied if desired. Combining the system and controller models, the nominal closed loop plant for the flutter example is shown in Figure 6. Applying perturbation (11) to the closed loop plant as shown by the dashed line on Figure 6 we see that the criterion (8) is satisfied (except for a small intersection at a resonant peak), giving a sufficiency condition that guarantees stability for this problem. This stability had previously been verified by a numerical procedure for the given modal data, but in fact we can now guarantee stability for additional modal variations from the base positive real model.

Example 2: Analytical Study of the DRAPER I Structure

For the DRAPER I structural model previously mentioned, the normal singular value inequality bound (8) clearly can not be satisfied for the type of modal uncertainty depicted in Figure 3. Using a positive real control design we know however that such variations will not harm the closed loop stability of the nominal design. We have chosen a nominal design here from Reference 21, and the singular value plot $\sigma[GH(I+GH)^{-1}]$ is shown in

Figure 7. For the control design used to generate Figure 7, we assume that the actual system has actuation dynamics modeled by the second order transfer function

$$G(s) = \frac{g\omega s + \omega^2}{s^2 + g\omega s + \omega^2} \quad (13)$$

Using $g = 1.4$ and a natural frequency of 30 rad/sec the resultant perturbation plot is superimposed on Figure 7. Again this plot demonstrates satisfaction of the robustness condition (8) everywhere (except for one zero damping peak introduced by an unobservable mode). Hence from a theoretical point of view this positive-real design can be guaranteed stable even with significant modeling errors in the modal model. A time simulation of the actual truss structure (12 modes) controlled by a reduced order model (three modes), and with modeling errors introduced by random perturbations of the truss elements is shown in Figure 8. As predicted by the stability theorem, this system is stable; and in this case, performance is not degraded by the presence of the actuator.

Example 3. A Laboratory Beam

A third example involves the laboratory control of a simple cantilever beam (see Figure 9), using a fixed mechanical shaker as the controller device. The controller includes compensation for the shaker so as to reduce actuator phase shift within the control bandwidth. The control is implemented using accelerometer inputs. These are sampled using an HP digital computer, integrated to produce a velocity signal, and a (continuous) positive real controller design is implemented in discrete form within the computer system. A trial result, using a two degree of freedom analog computer model to replace the actual beam was also used to more

precisely quantify our predictions. The analog model had modal frequencies at 0.259Hz and 1.095Hz, respectively while damping was .30% and 1.3%. The robustness results are applied using the continuous formulation. The effect of the digital controller was approximated as a pure time delay.

$$I + L(s) \approx e^{-(sT/2)} \quad (14)$$

applied to the continuous system plus controller. This approximation can be considered valid at frequencies significantly below the Nyquist frequency $\omega_s/2 = \pi/T$.

The two mode analog system was experimentally verified to be unstable for a sampling periods greater than about 140msec. A singular value plot and the approximate perturbation are shown in Figure 10 and representative time histories are shown in Figure 11. The robustness theorem is not conservative in this case but does predict stability well beyond the range of validity of the approximation (14).

A similar approach was used with the physical beam. In this problem actuator dynamics were neglected completely and only the approximation (14) was used to model the perturbation. Note that one advantage of the positive real theorem is that stability can normally be assured for a multivariable design even if one (or more) of the scalar feedback paths is broken due to a failed actuator or sensor. In the laboratory two controller designs were tested. The first was a single-input-single-output design based on a two mode model of the beam. The second controller was based on a four mode beam model and additionally was a two-input-two-output design. In the experiment, only one shaker was available, so this latter controller was used with one of the paths failed. In this way it acted similar to the SISO design only with four modes considered in the design rather than two. Both of the positive real controllers were designed using a pole placement

algorithm as described in [22] such that the positivity criteria (c) are satisfied. The transfer functions for the beam and the controllers are shown in Figure 12. The singular value plots for these cases are shown in Figure 13. Using a standard discretization and zero order hold assumption, the digital implementation of the four mode continuous controller design is predicted to go unstable at a sampling rate of about 5msec (as determined by an eigenvalue analysis). Similarly, the two mode controller is predicted to become unstable at a sampling rate of about 10msec. Using the approximate phase perturbation (14) produces the 'unmodeled' perturbation as shown by the solid line on Figure 13. The singular value plot for this case shows that both controllers are near the limiting stability boundary. Since the phase approximation is not accurate at these high frequencies, this is not a conservative approximation. In the actual experimental test, the two mode controller was stable at a sampling period of about 3msec. (See figure 14). This was the fastest sampling period possible for the computer setup and slower sample rates were not investigated for this controller. The four mode controller design required over 5msec per cycle and was unstable (as predicted by the eigenvalue analysis). We are currently investigating application of these principles to a digital design to see if these robustness bounds can be applied in a more general sense for the digital problem.

5. CONCLUSION

This paper shows that the use of unstructured singular value tests can be combined with a positive real control design to extend stability results for systems with uncertainties in the modal parameters and with multiplicative uncertainties due to actuator and sensor dynamics. The effect of high frequency actuator and sensor dynamics can be included in a positive real design using this approach. Caution must be exercised when using the continuous theory to model the computational delays introduced by a digital controller.

These results should be a valuable aid in control design for large space structures and other flexible systems with significant structure-control interaction.

REFERENCES

1. Arbel, A. and Gupta, N.K., "Robust Colocated Control for Large Flexible Space Structures", J. Guidance & Control, vol 4, #5, Sept-Oct 1981, pp 480-486.
2. Hablani, H.B., "Stochastic Response Analysis, Order Reduction, and Output Feedback Controllers for Flexible Spacecraft", J. Guidance Control & Dynamics, vol 8, #1, Jan-Feb 1985, pp 94-103.
3. Inman, D.J., "Modal Decoupling Conditions for Distributed Control of Flexible Structures", J. Guidance Control & Dynamics, Vol 7, #6, Nov-Dec 1984, pp 750-752.
4. Venkayya, V.B., Tischler, V.A., Khot, N.S., "Dynamics and Control of Space Structures", Engineering Optimization, Vol. 11, 1987, pp 251-264.
5. Benhabib, R.J., Iwens, R.P. and Jackson, R.L., "Stability of LSS Control Systems Using Positivity Concepts", J. Guidance & Control, Vol 4, #5, Sept-Oct 1981, pp 487-494.
6. McLaren, M., Slater, G.L., "Robust Multivariable Control of Large Space Structures Using Positivity", J. Guidance, Control, and Dynamics, vol.10, #4, July-August 1987, pp 393-400.
7. Slater G.L., "Flutter Mode Suppression Using Hyperstable Feedback," AIAA Paper #82-0368 Aerospace Sciences Mtg. January 1982.

8. Doyle, J.C., Stein, G., "Multivariable System Design: Concepts for a Classical/Modern Synthesis", IEEE Transactions on Auto. Control, vol. AC-26, #1, Feb. 1981, pp 4-16.
9. Doyle, J., "Multivariable Design Techniques Based on Singular Value Generalizations of Classical Control", AGARD Lecture Series 117 Multivariable Analysis and Design Techniques, Sept. 1981.
10. Safanov, M.G., Laub, A.J. and Hartmann, G.L., 'Feedback Properties of Multivariable Systems: The Role and Use of the Return Difference Matrix', IEEE Trans. on Auto. Control, Vol AC- 26, No 1, 1981, pp 57-65.
11. Mukhopadhyay, V. and Newsom, J.R., 'Application of Matrix Singular Value Properties for Evaluating Gain and Phase Margins of Multiloop Systems', AIAA Guidance and Control Conference, San Diego Ca., Aug 9-11, 1982.
12. Doyle, J. "Analysis of feedback systems with structured uncertainty", IEE Proc., vol. 129, Pt. D, #6, Nov. 1982, pp242-250.
13. Kissel, G.J., Hegg, D.R. , "Stability Enhancement for Control of Flexible Space Structures", IEEE Control Systems Magazine, Vol. 6, #3, June 1986, pp19-26.
14. Jones, R.D. "Structured Singular Value Analysis for Real Parameter Variation", AIAA Paper 87-2589CP, Guidance and Control Meeting, Monterey, CA., August 1987.

15. Tahk, M., Speyer, J. "Modeling of Parameter Variations and Asymptotic LQG Synthesis", IEEE Trans. on Auto. Control, vol. AC-32, #9, Sept. 1987, pp 793-801.
16. Yedavelli, R.K., "Robust Control for Linear Systems with Structured Uncertainty", AFWAL-TR-88-3077, Nov., 1988.
17. Anderson, B.D.O., "A System Theory Criteria for Positive Matrices", SIAM J. Control, vol. 5, #2, 1967, pp 171-182.
18. Anderson, B.D.O., "A Simplified View of Hyperstability", IEEE Transactions on Automatic Control, TAC-13, #3, 1968, pp 292-294.
19. Popov, V.M., "The Solution of a New Stability Problem for Controlled Systems", Automation and Remote Control, vol. 24, #1, 1963, pp 1-23.
20. Sesak, J. ACOSS ONE (Active Control of Space Structures) Phase I, Report RADC TR-80-79 March 1980.
21. Slater, G.L., et al., "Robustness and Positive Real Control Design for Large Space Structures", 3rd Int'l Conference on Recent Advances in Structural Dynamics, Southampton, England, July, 1988.
22. Takahashi, M.D., Slater, G.L., "Design of a Flutter Mode Controller Using Positive Real Feedback" J. Guidance, Control, and Dynamics, vol.9, #3, May-June 1986, pp 339-345.
23. McLaren, M., Slater, G.L. "Estimator Eigenvalue Placement in Positive Real Control", J. Guidance, Control and Dynamics, to be published, 1989.

FIGURE CAPTIONS

- Figure 1 Perturbation Model for Singular Value Robustness Bounds
- Figure 2 Model of the DRAPER I Structure (from Ref. [20])
- Figure 3 $L_m(\omega)$ for a Typical Perturbation of the Draper I Spacecraft Model
- Figure 4 Transfer Function of Flexible Aircraft Model (a) Without, and
(b) With Actuator Dynamics (from Ref. 22)
- Figure 5 Positive Real Feedback Transfer Function for Control of Flexible Aircraft Model (from Ref. 22)
- Figure 6 Nominal Closed Loop Transfer Function for Flutter Problem and Actuator Perturbation
- Figure 7 Singular Values for Draper I Nominal Closed Loop Design Model and $L_m(\omega)$ for Actuator Model
- Figure 8 Time Response of Draper I Model Including a Second Order Actuator Showing Stable Response
- Figure 9 Set-up of Laboratory Beam Control Experiment
- Figure 10 Robustness Plot for Two Mode Analog Model
- Figure 11 Controlled Time Responses for Analog Model (a) $T = 67.3$ msec;
(b) 142.2 msec Controller.

Figure 12 Transfer Function for Beam Experiment: (a) Modeled Beam Transfer Function. (b) Two Mode controller. (c) Four Mode controller.

Figure 13 Singular Value Plot for Nominal Closed Loop Beam Control System. $L_m(\omega)$ for time delay approximation.

Figure 14 Time Response for Beam Experiment: (a) Two Mode Controller. (b) Four Mode Controller.

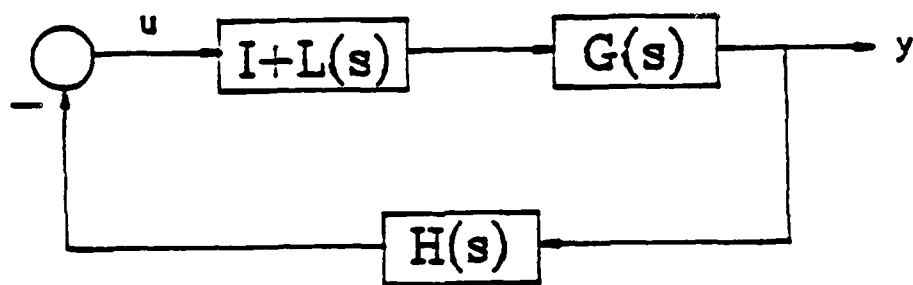


Figure 1 Perturbation Model for Singular Value Robustness Bounds

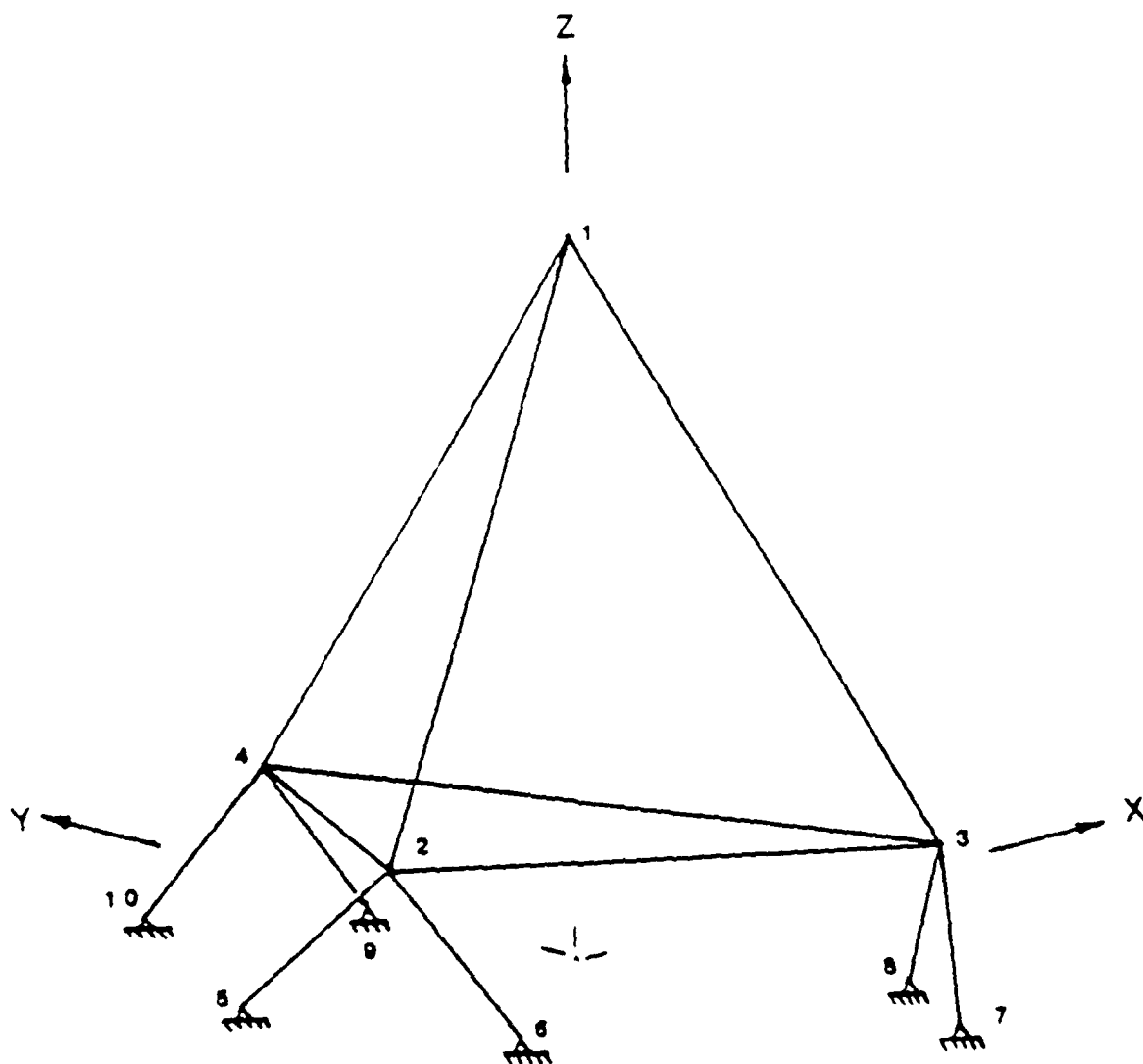


Figure 2 Model of the DRAPER I Structure (from Ref. [20])

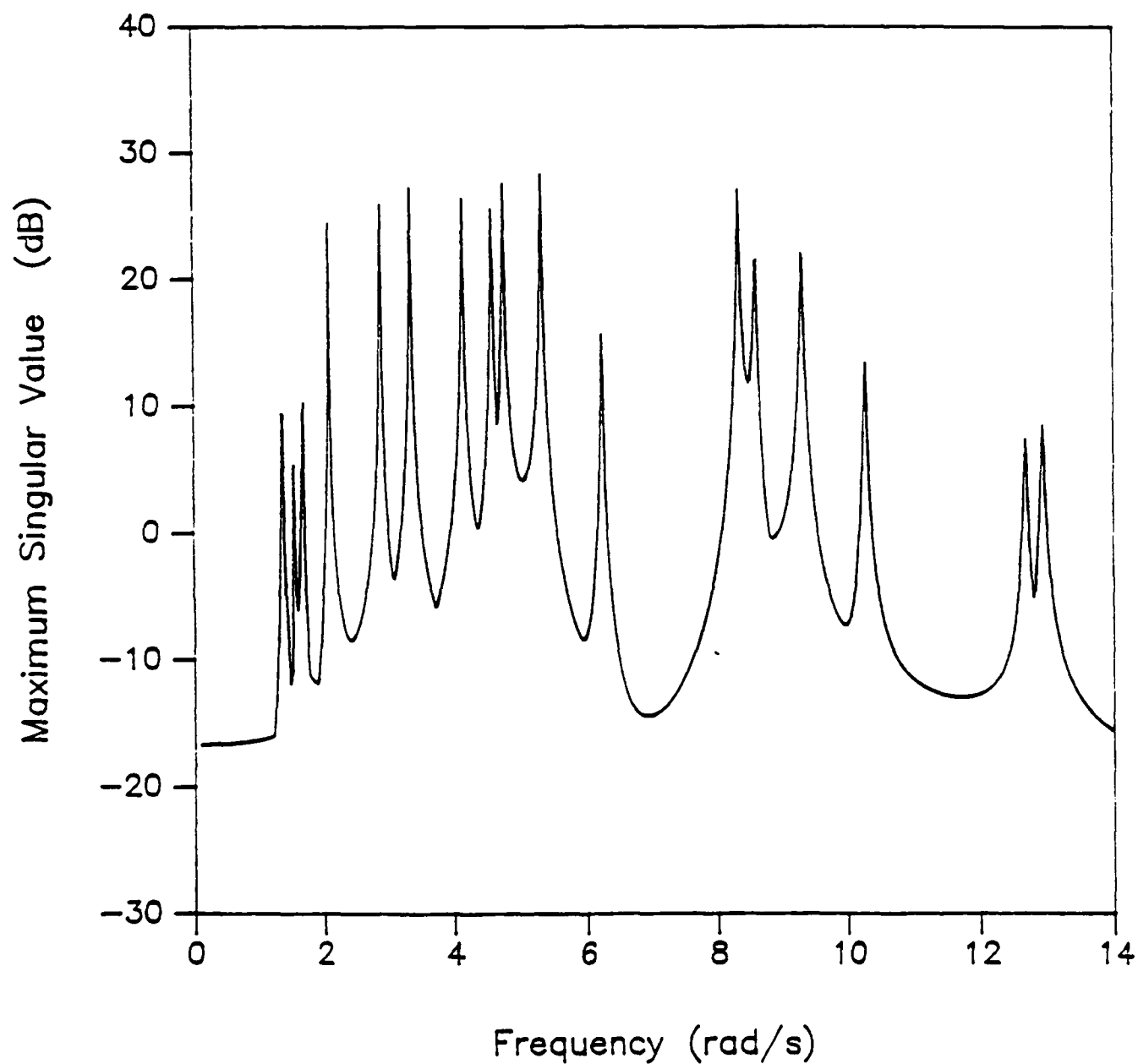


Figure 3 $L_m(\omega)$ for a Typical Perturbation of the Draper I Spacecraft Model

Figure 4(a)

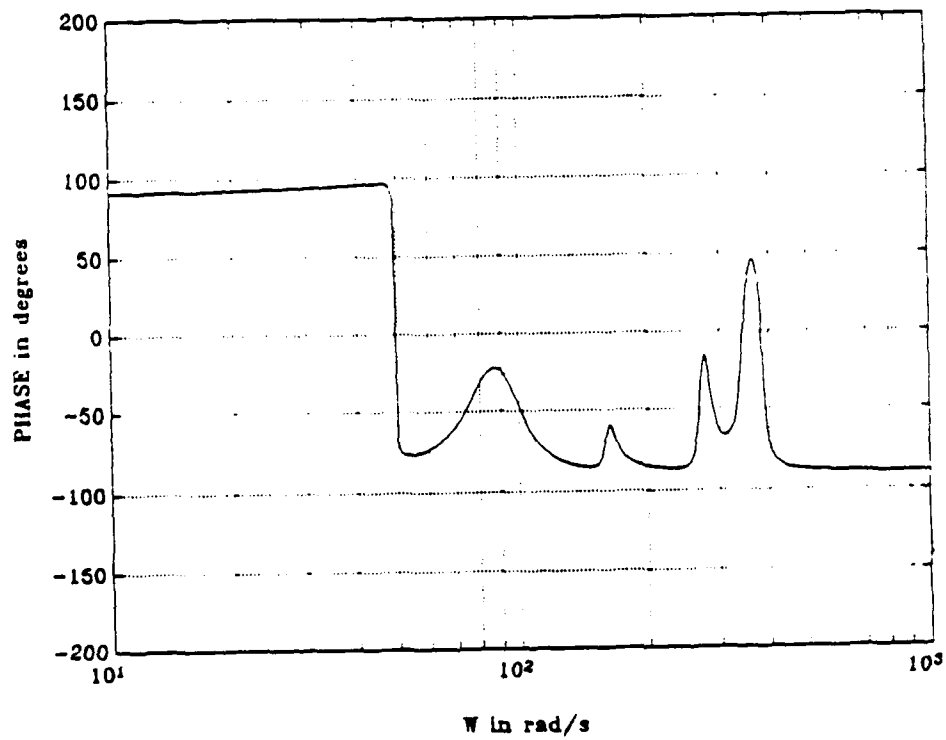
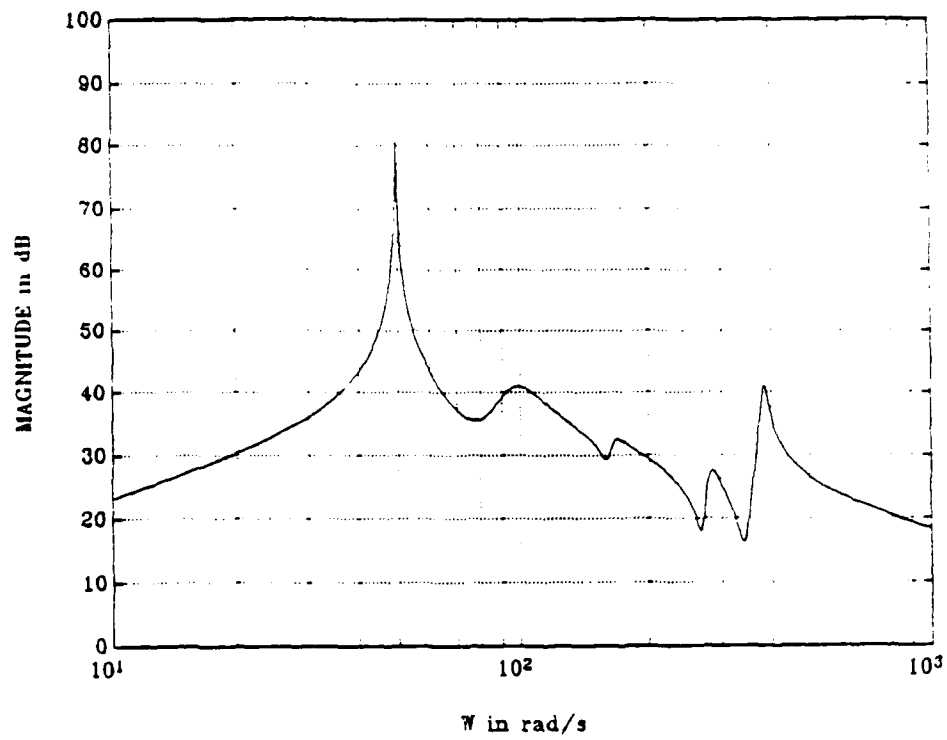
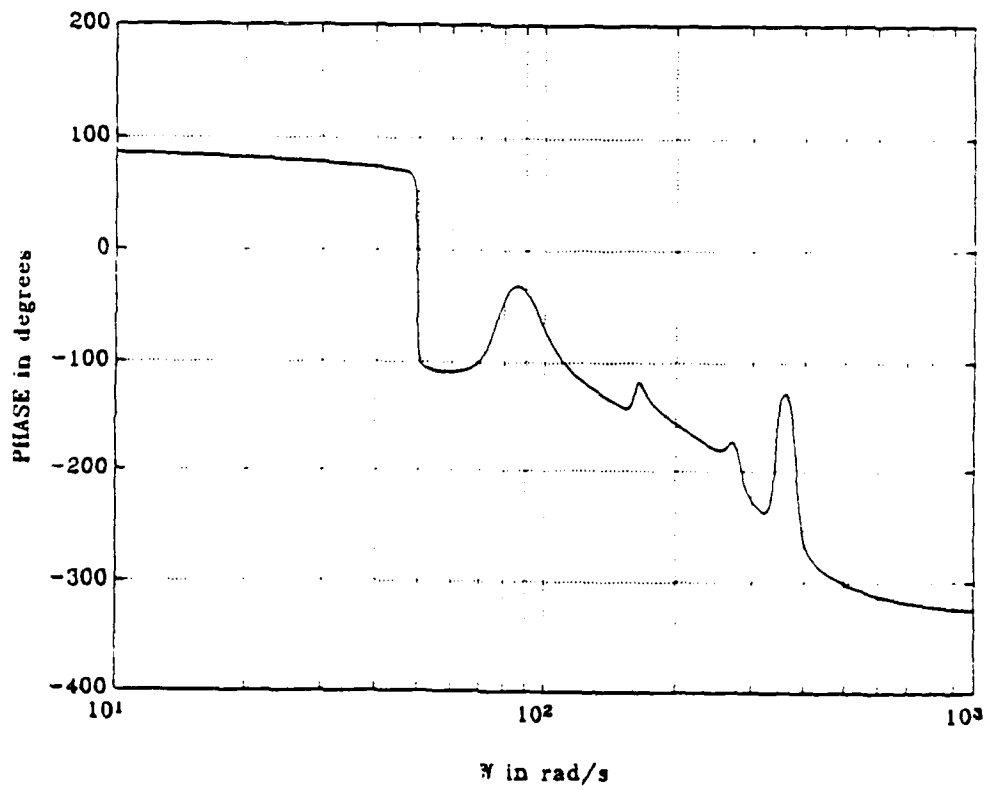
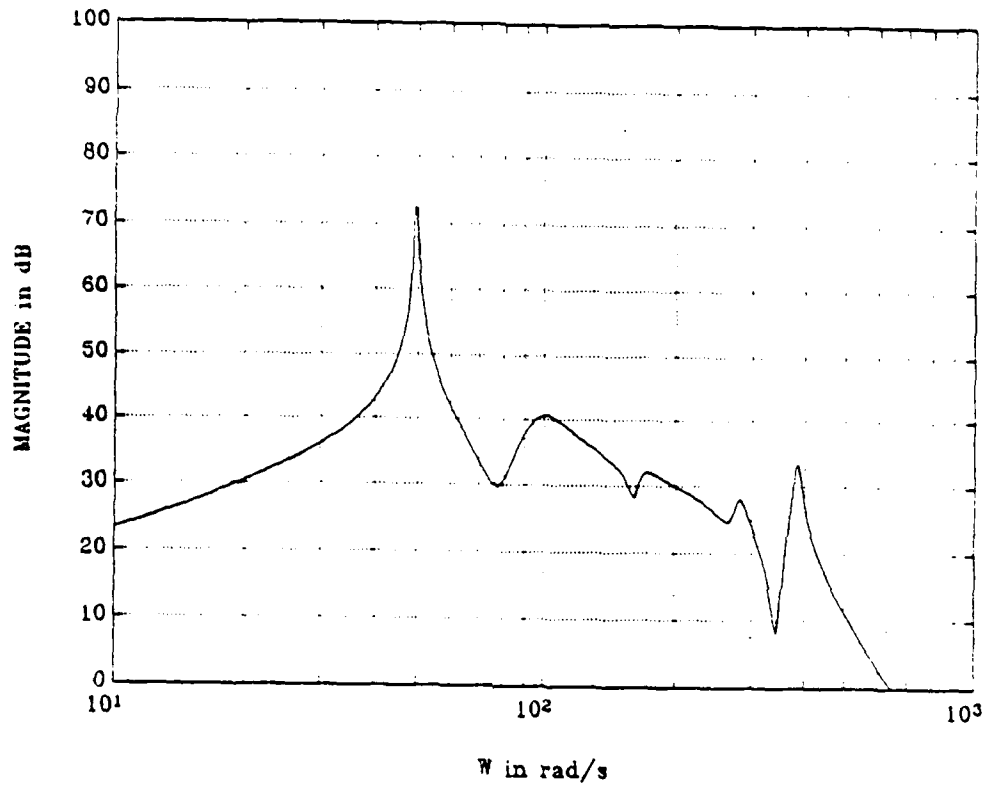


Figure 4 Transfer Function of Flexible Aircraft Model (a) Without, and
(b) With Actuator Dynamics (from Ref. 22)

Figure 4(b)



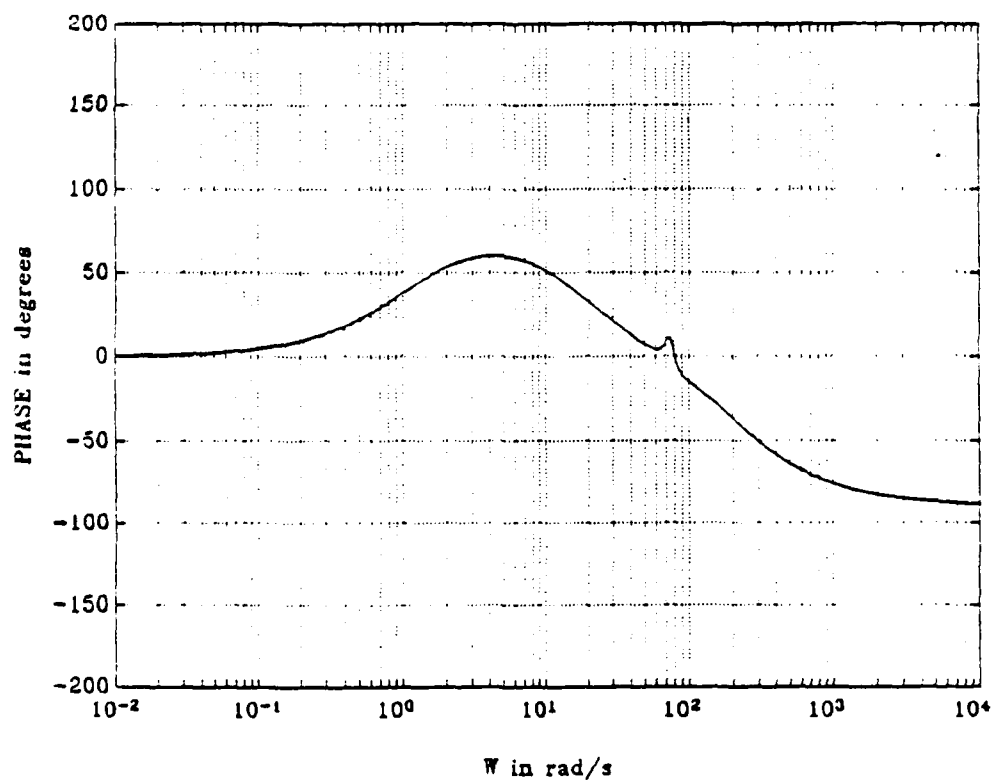
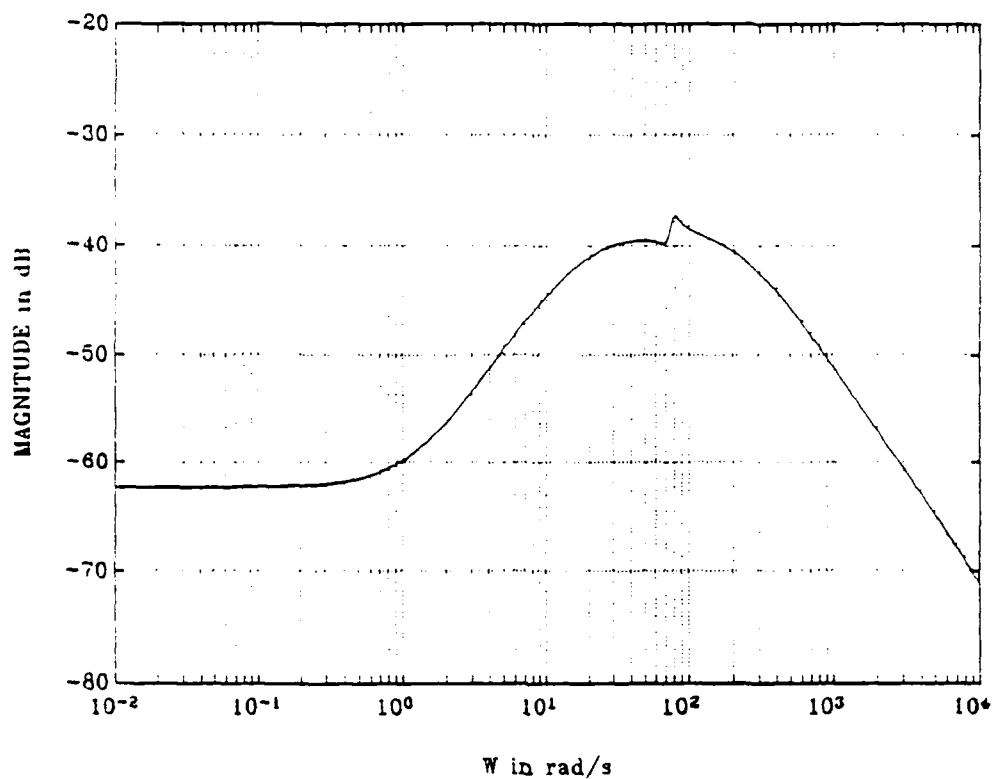


Figure 5 Positive Real Feedback Transfer Function for Control of Flexible Aircraft Model (from Ref. 22)

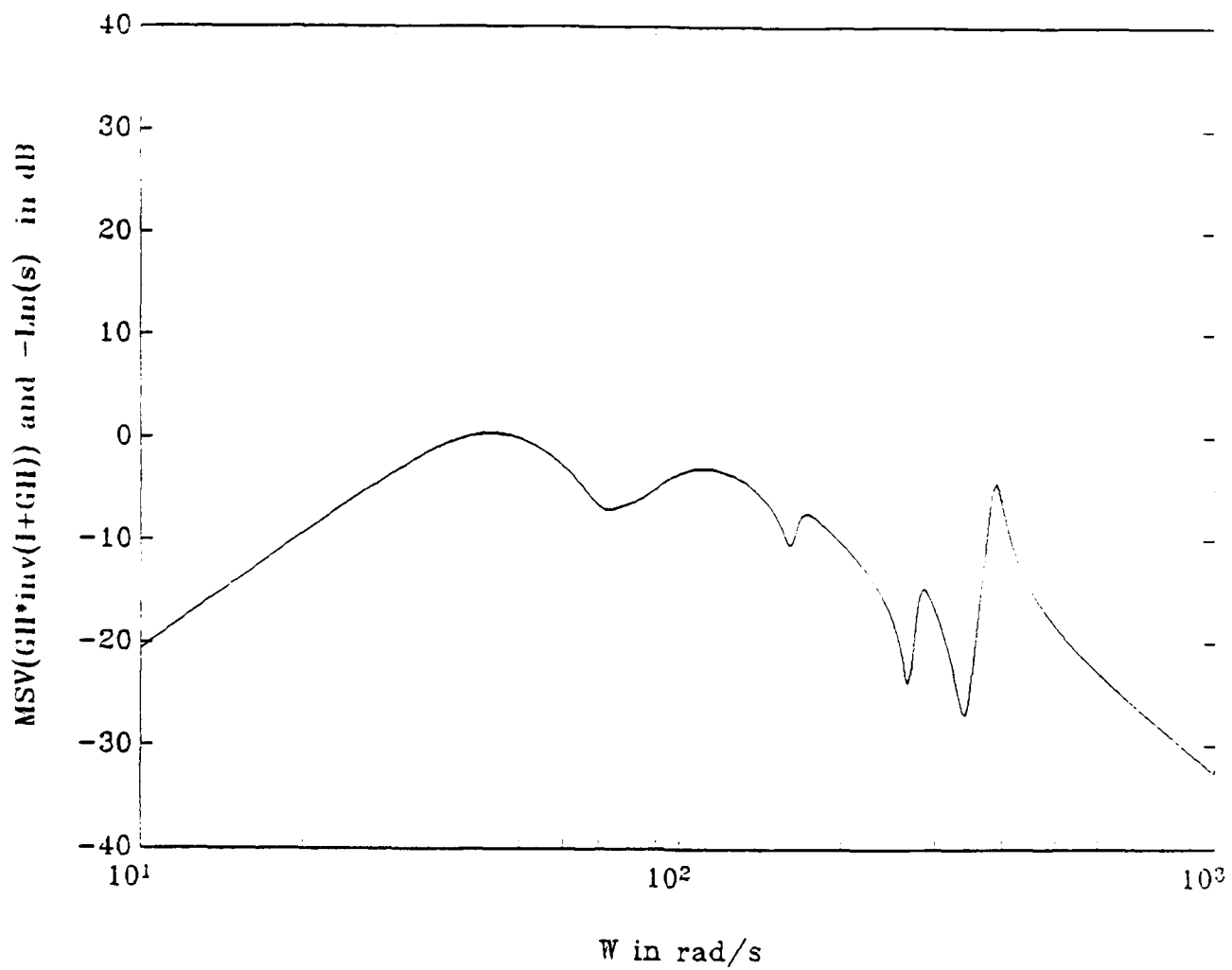


Figure 6 Nominal Closed Loop Transfer Function for Flutter Problem and
Actuator Perturbation

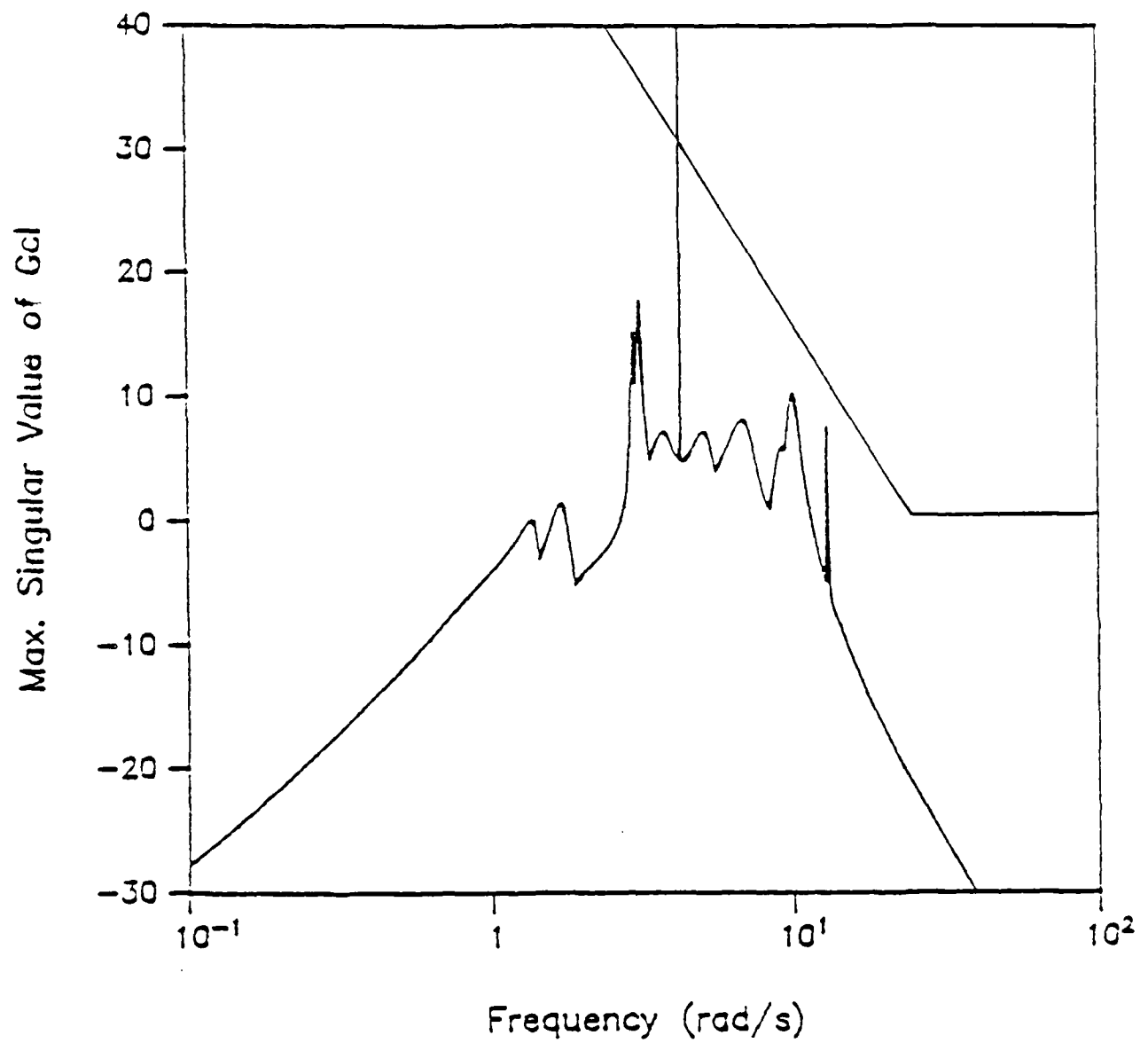


Figure 7 Singular Values for Draper I Nominal Closed Loop Design Model and $L_m(\omega)$ for Actuator Model

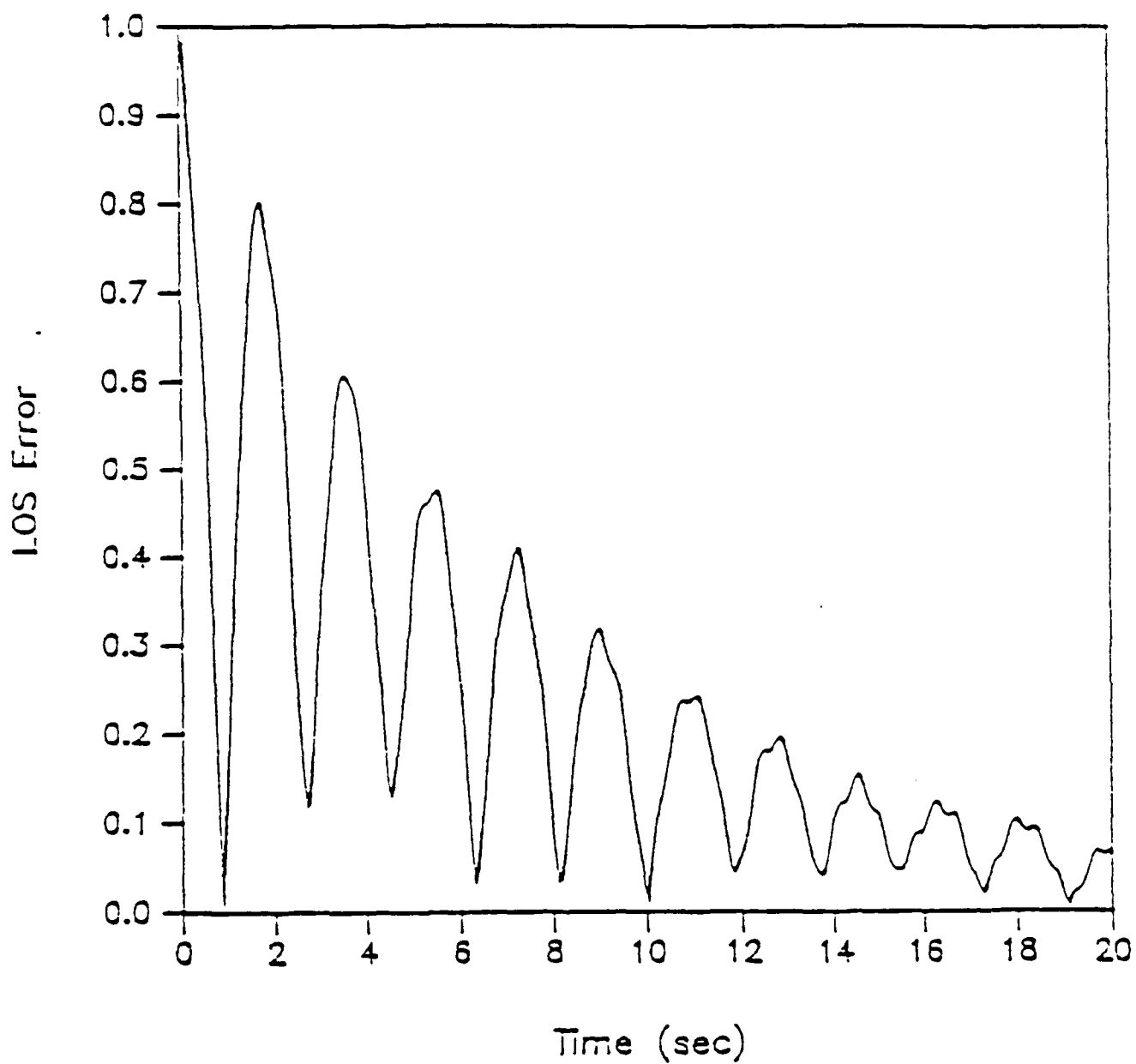


Figure 8 Time Response of Draper I Model Including a Second Order Actuator
Showing Stable Response

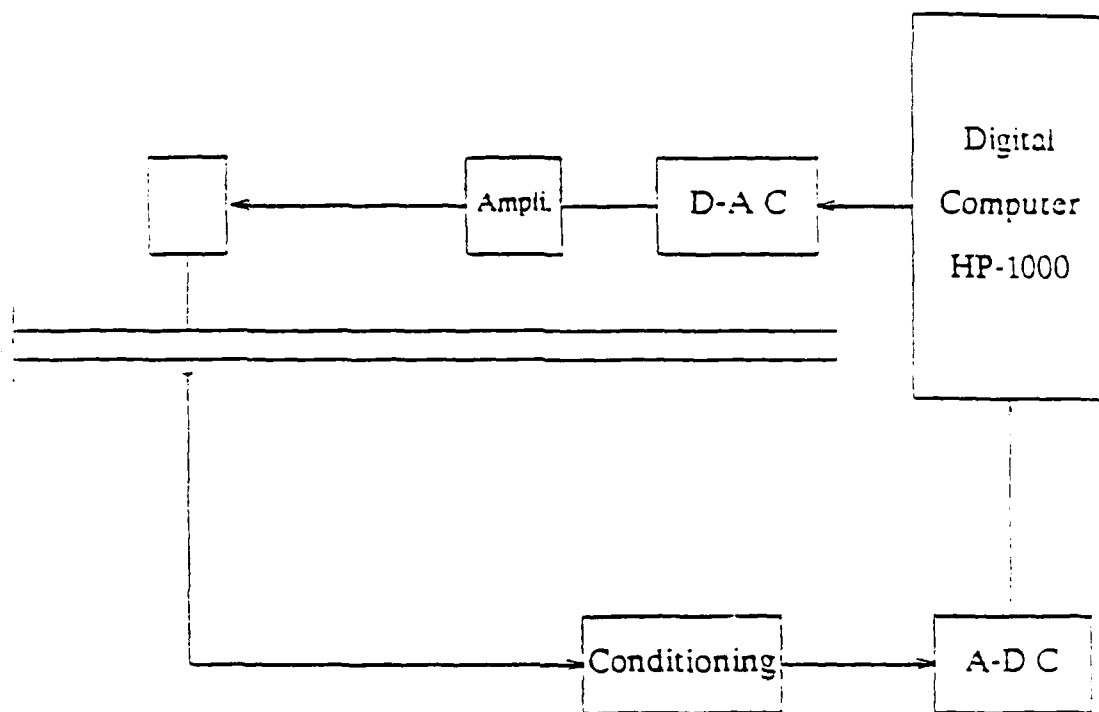


Figure 9 Set-up of Laboratory Beam Control Experiment

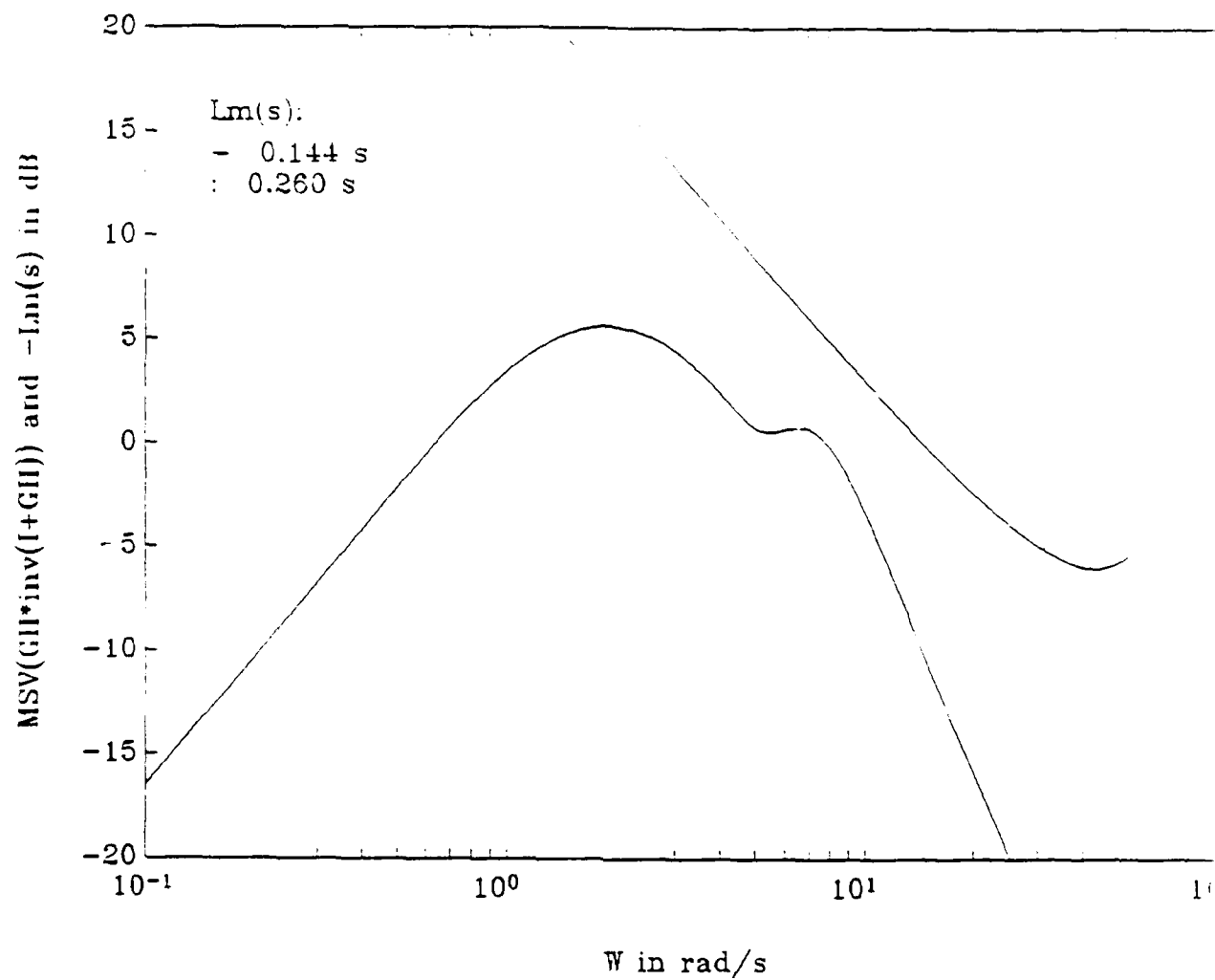
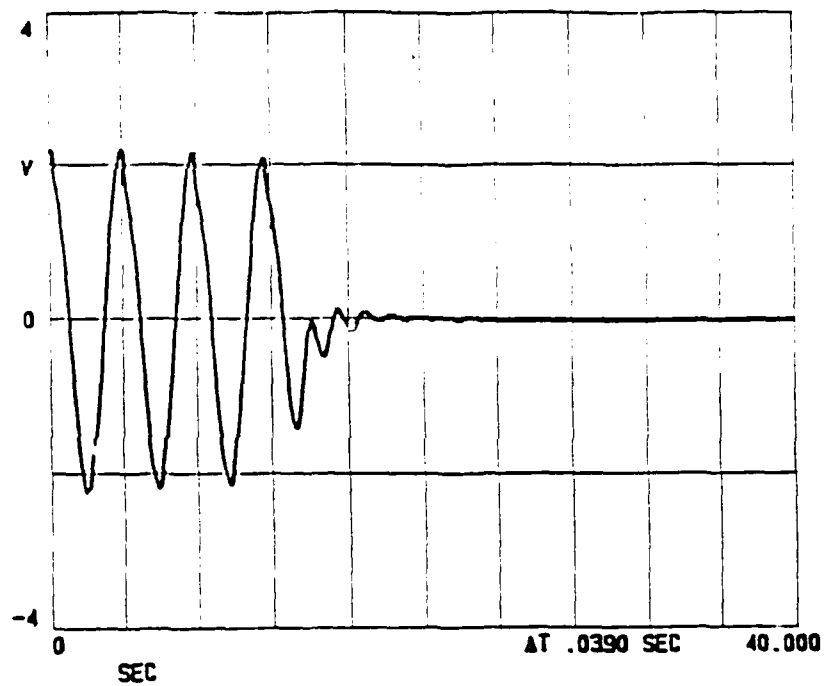


Figure 10 Robustness Plot for Two Mode Analog Model

(a)



(b)

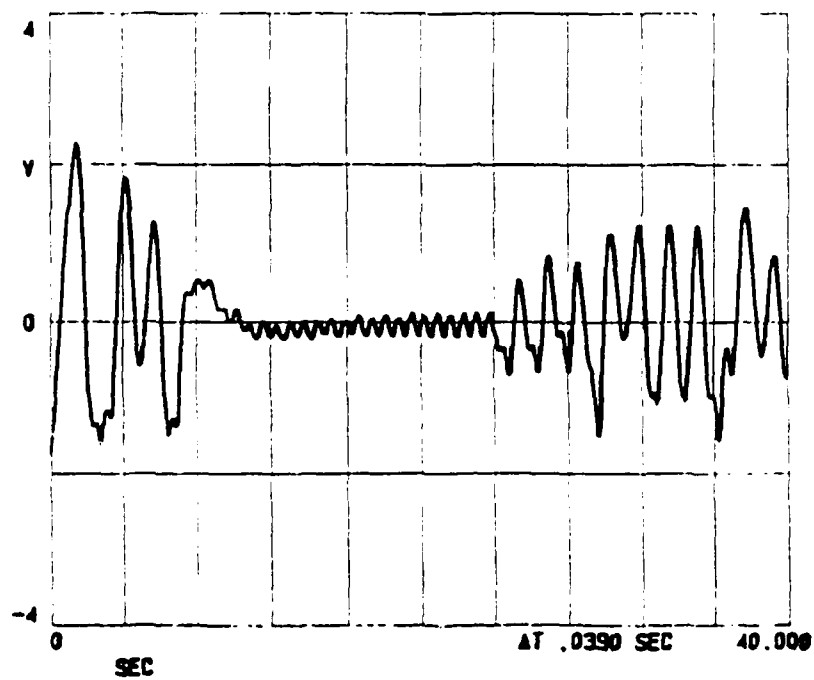


Figure 11 Controlled Time Responses for Analog Model (a) $T = 67.3$ msec;
(b) 142.2 msec Controller.

Figure 12(a)

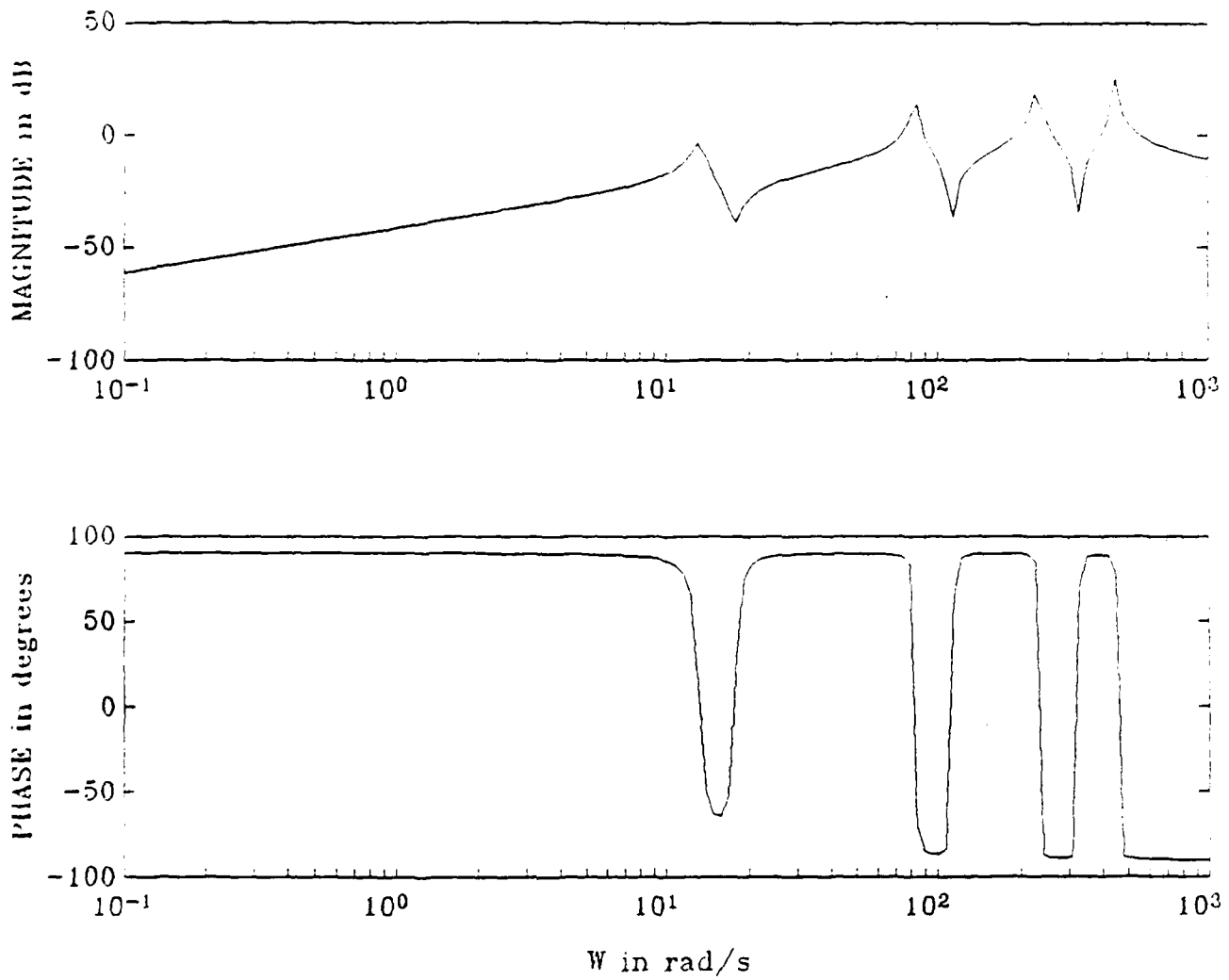


Figure 12 Transfer Function for Beam Experiment: (a) Modeled Beam Transfer Function. (b) Two Mode controller. (c) Four Mode controller.

Figure 12(b)

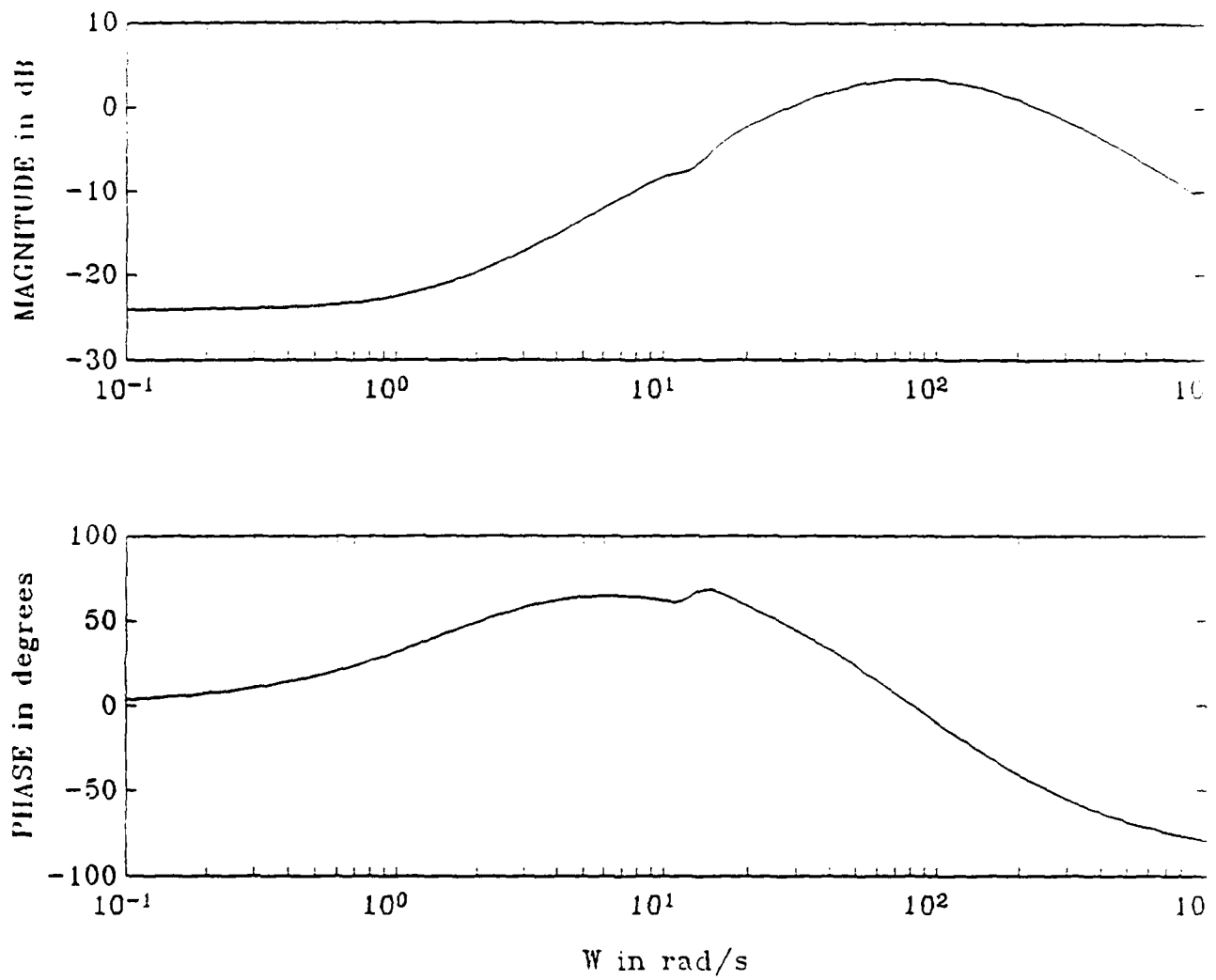
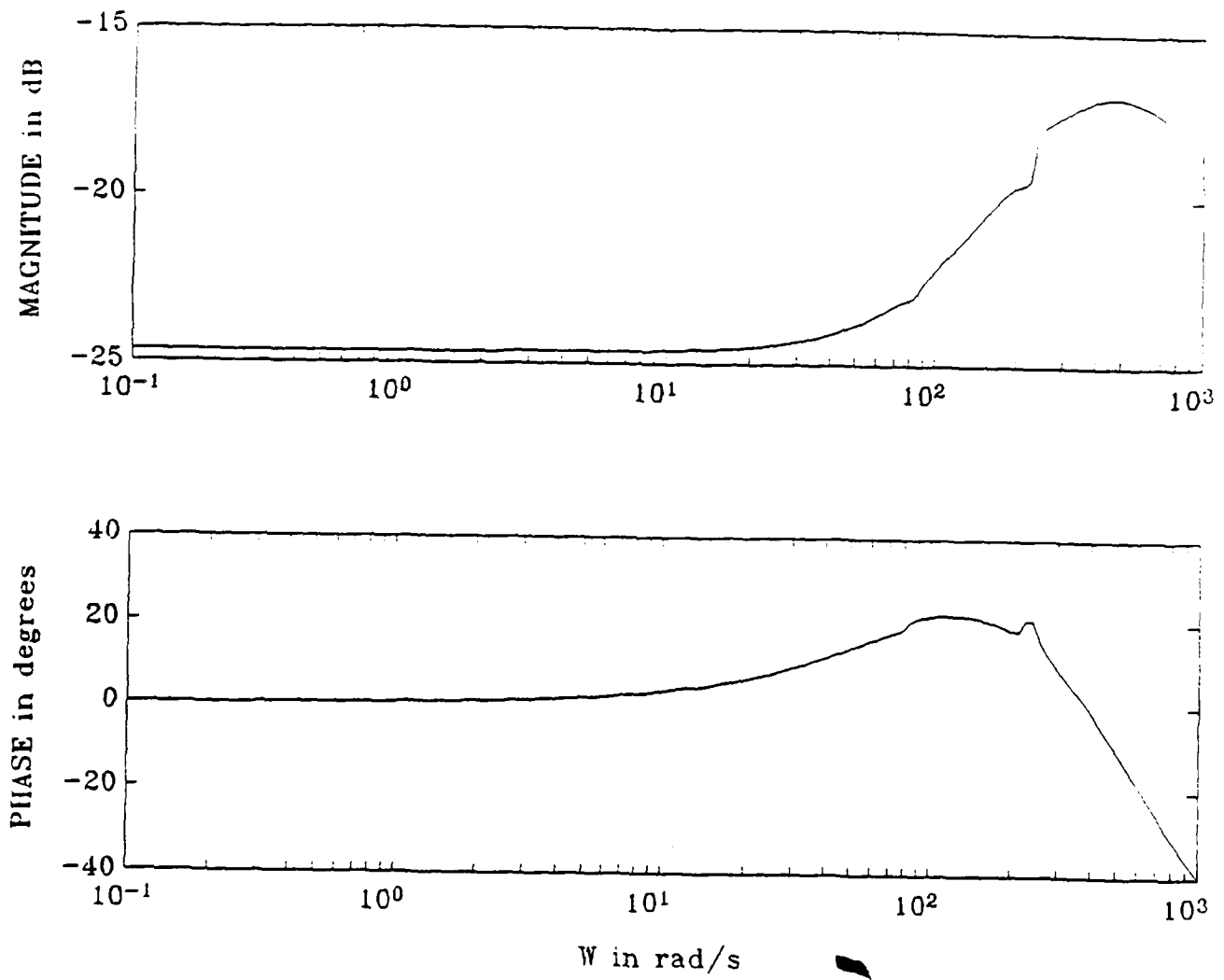


Figure 12(c)



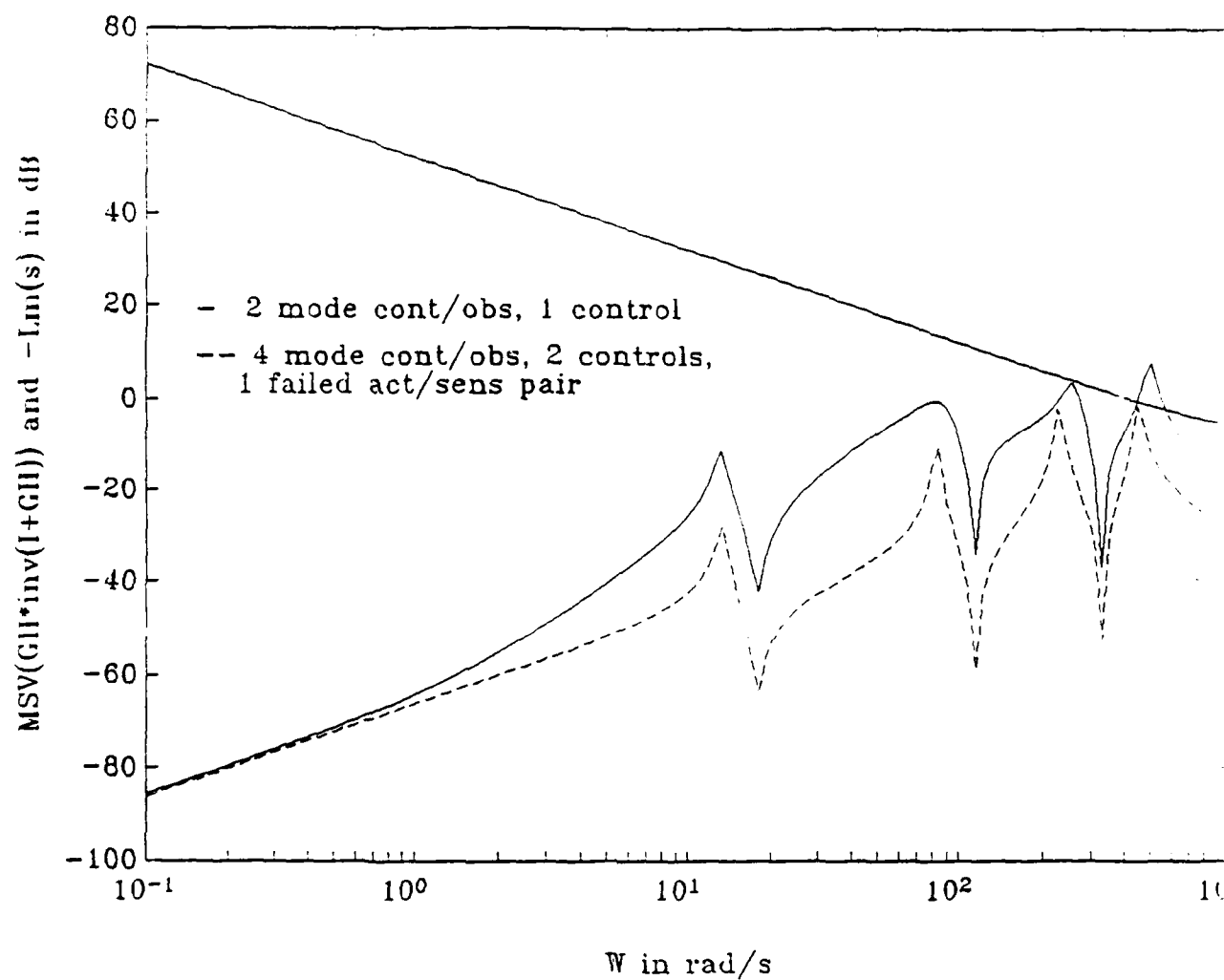
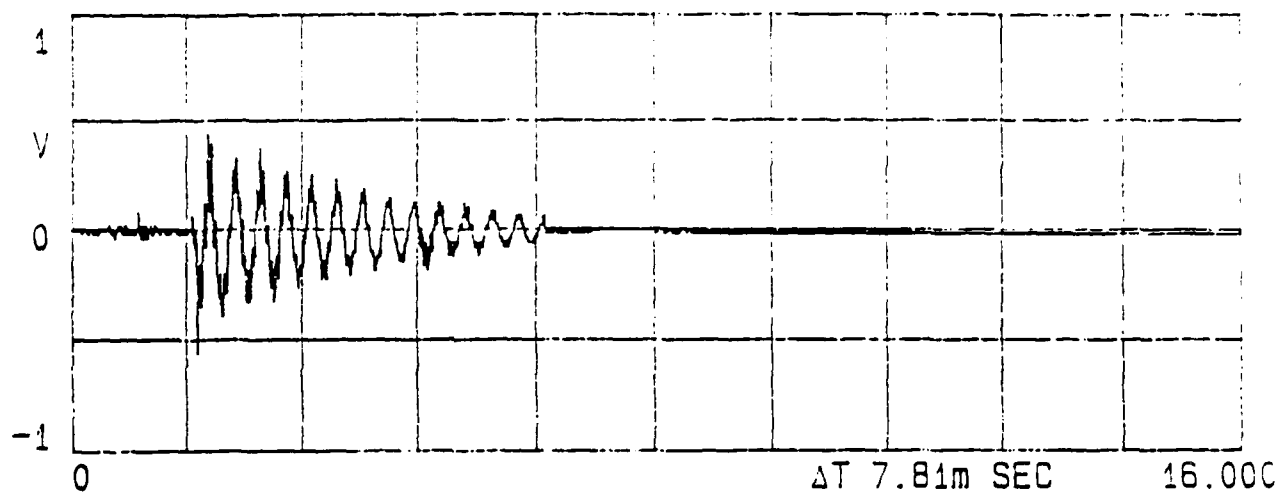


Figure 13 Singular Value Plot for Nominal Closed Loop Beam Control System.

$L_m(\omega)$ for time delay approximation.

(a)



(b)

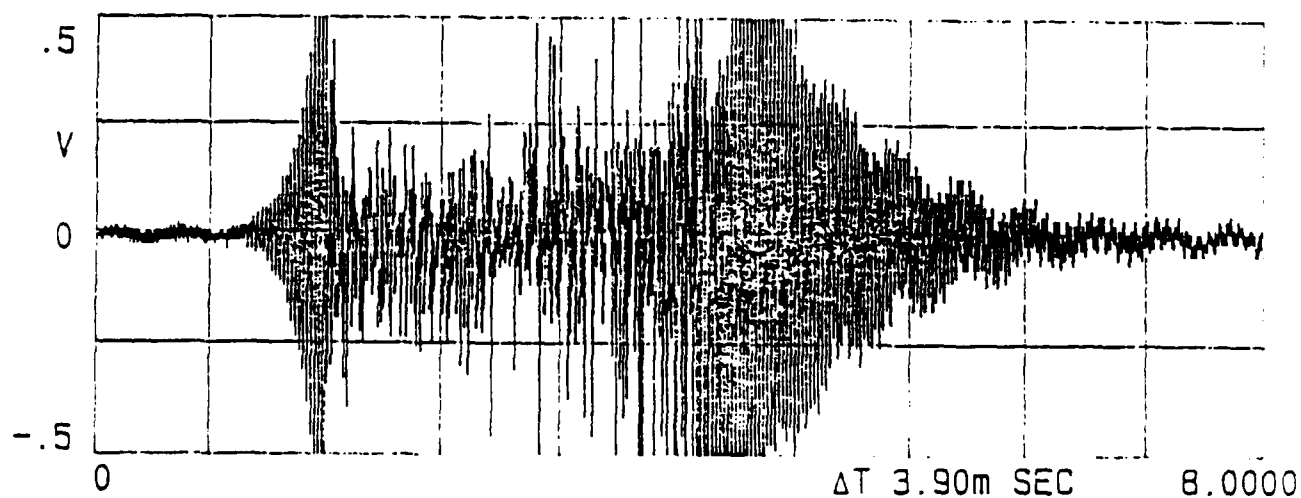


Figure 14 Time Response for Beam Experiment: (a) Two Mode Controller. (b) Four Mode Controller.

1988 USAF-UES RESEARCH INITIATION PROGRAM

Sponsored by the
AIR FORCE OFFICE OF SCIENTIFIC RESEARCH

Conducted by
Universal Energy Systems, Inc.

FINAL REPORT FOR THE PERIOD 1/1/89 TO 12/31/89

ROBUST EIGENSTRUCTURE ASSIGNMENT FOR FLIGHT CONTROL DESIGN

Prepared by:	Kenneth Sobel, Ph.D.
Academic Rank:	Associate Professor
Department and	Electrical Engineering
University:	The City College of New York
Summer Research	
Location:	WRDC/FIGC Wright-Patterson AFB Dayton OHIO 45433
USAF Researcher:	Dr. Siva S. Banda
Date:	31 Dec 89
Contract No:	F49620-88-C-0053 S-210-9MG-035

ROBUST EIGENSTRUCTURE ASSIGNMENT FOR FLIGHT CONTROL DESIGN

by

Kenneth M. Sobel

ABSTRACT

A recent stability robustness sufficient condition for LTI systems with structured state space uncertainty is extended to ensure that the closed loop eigenvalues lie within chosen performance regions. The conservatism of both the stability and performance robustness conditions is addressed by introducing both a unitary weighting matrix and a state transformation in addition to the earlier real positive diagonal weighting. These sufficient conditions are utilized to obtain a robust eigenstructure assignment flight control design method. This approach optimizes either of the two sufficient conditions while constraining the dominant nominal eigenvalues to lie within chosen regions in the complex plane. This constrained optimization problem is solved by using the sequential unconstrained minimization technique with a quadratic extended interior penalty function. An alternative approach using the steepest descent method is also considered. Two examples are presented which illustrate the design of a robust eigenstructure assignment controller for a pitch pointing/vertical translation maneuver for the AFTI F-16 aircraft and a stability augmentation system for the linearized lateral dynamics of the L-1011 aircraft. Finally, a new theorem is presented for robust stability of an LTI system with both structured state space uncertainty and a class of unmodelled dynamics which may be represented by an unknown nonlinear function of the plant input.

Acknowledgements

I wish to thank the Air Force Systems Command and the Air Force Office of Scientific Research for sponsorship of this research. Universal Energy Systems must be mentioned for their help in all administrative aspects of the Research Initiation Program. I would also like to thank Dr. Siva Banda of the Wright Research and Development Center for his support of my research. I also acknowledge Mr. Wangling Yu, a Ph.D. student under my supervision, whose work constitutes a significant portion of this report.

This work was partially supported by computer resources provided by The City University of New York/University Computer Center.

I. INTRODUCTION

Eigenstructure assignment is a method for incorporating classical specifications on damping, settling time, and mode decoupling into a modern multivariable control framework. However, this design approach does not guarantee stability when the plant is subject to structured state space uncertainty. This uncertainty may arise from errors in the identification method which is used to obtain the linearized models of the plant. Another source of uncertainty is caused by errors in the dynamic pressure computations which result in the gain schedule choosing the wrong linearized model.

During the summer research period, the author of this report derived a sufficient condition for the robust stability of LTI systems which are subjected to linear time-varying structured state space uncertainty. This result, which is based upon the Gronwall lemma, ensures robust stability if the nominal eigenvalues lie to the left of a vertical line in the complex plane which is determined by a norm involving the structure of the uncertainty and the nominal closed loop eigenvector matrix.

The Flight Control Analysis Group of the Wright Research and Development Center at Wright-Patterson Air Force Base is interested in robust control methods for flight control design. Thus, we have a mutual interest in combining the robust stability condition with eigenstructure assignment and applying this new robust eigenstructure assignment method to flight control design.

II. OBJECTIVES OF THE RESEARCH EFFORT

The primary objective of this research is to combine eigenstructure assignment with the sufficient condition for robust stability to obtain a robust eigenstructure assignment design method. One approach is to solve a nonlinear constrained optimization problem by using the sequential unconstrained minimization technique with an extended interior penalty function. An alternative approach is to use the steepest descent method in which the optimization proceeds in the direction of the negative gradient. In each of these methods, the parameters to be optimized will include both the closed loop eigenvectors and the closed loop eigenvalues. The robust eigenstructure assignment method will be utilized to design flight control laws for (1) the linearized lateral dynamics of the L-1011 aircraft and (2) the linearized longitudinal dynamics of the AFTI F-16 aircraft for a pitch pointing/vertical translation maneuver.

A robust eigenstructure assignment feedback gain matrix will be computed in which certain outputs are not fed back to certain inputs. This is equivalent to constraining some elements of the feedback gain matrix to be zero. By suppressing certain gains to zero, we reduce controller complexity and improve reliability. However, it may not always be possible to achieve the dual goals of performance and robustness with a constant gain controller using only output feedback. Thus, the use of low order dynamic compensators will be studied for designing robust eigenstructure assignment control laws with desirable nominal performance specifications. Flight control laws will be computed for the linearized lateral dynamics of the L-1011 aircraft using robust eigenstructure assignment with either gain suppression or dynamic compensation.

The robust stability sufficient condition will be extended to ensure that the closed loop eigenvalues lie within chosen performance regions when the LTI system is subjected to time-invariant structured state space uncertainty. The conservatism of both the stability and performance robustness conditions will be addressed by introducing a state transformation. Also to be considered is the use of a new weighting matrix in addition to the real positive diagonal weighting. Finally, the stability robustness of LTI systems with simultaneous time-varying structured state space

uncertainty and unstructured uncertainty will be considered. An important issue to be considered is the choice of the mathematical representation for the unstructured uncertainty.

III. PROBLEM FORMULATION

Consider a nominal linear time invariant multi-input multi-output system described by

$$\dot{x} = Ax + Bu \quad (1a)$$

$$y = Cx \quad (1b)$$

where $x \in R^n$ is the state vector, $u \in R^m$ is the input vector, $y \in R^r$ is the output vector, and A, B, C are constant matrices.

Suppose that the nominal system is subject to linear time-varying uncertainties in the entries of A, B described by $\Delta A(t)$ and $\Delta B(t)$, respectively. Then, the system with uncertainty is given by

$$\dot{x} = Ax + Bu + \Delta A(t)x + \Delta B(t)u \quad (2a)$$

$$y = Cx \quad (2b)$$

Further, suppose that bounds are available on the absolute values of the maximum variations in the elements of $\Delta A(t)$ and $\Delta B(t)$. That is,

$$|\Delta a_{ij}(t)| \leq (a_{ij})_{\max}; i=1, \dots, n; j=1, \dots, n \quad (3a)$$

$$|\Delta b_{ij}(t)| \leq (b_{ij})_{\max}; i=1, \dots, n; j=1, \dots, m \quad (3b)$$

Define $\Delta A^+(t)$ and $\Delta B^+(t)$ as the matrices obtained by replacing the entries of $\Delta A(t)$ and $\Delta B(t)$ by their absolute values. Also, define A_m and B_m as the matrices with entries $(a_{ij})_{\max}$ and $(b_{ij})_{\max}$, respectively. Then,

$$\{ \Delta A(t): \Delta A^+(t) \leq A_m \} \quad (4a)$$

$$\text{and } \{ \Delta B(t): \Delta B^+(t) \leq B_m \} \quad (4b)$$

where " \leq " is applied element by element to matrices and $A_m \in R_+^{n \times n}$, $B_m \in R_+^{n \times m}$ where R_+ is the field of non-negative numbers.

Consider the constant gain output feedback control law described by

$$u(t) = Fy(t) \quad (5)$$

Then, the nominal closed loop system is given by

$$\dot{x}(t) = (A + BFC)x(t) \quad (6)$$

and the uncertain closed loop system is given by

$$\dot{x}(t) = (A + BFC)x(t) + [\Delta A(t) + \Delta B(t)FC]x(t) \quad (7)$$

Problem I: Given a feedback gain matrix $F \in \mathbb{R}^{m \times r}$ such that the nominal closed loop system exhibits desirable dynamic performance, determine if the uncertain closed loop system is asymptotically stable for all $\Delta A(t)$ and $\Delta B(t)$ described by Eq.(4).

Problem II: A feedback gain matrix $F \in \mathbb{R}^{m \times r}$ is chosen such that all of the eigenvalues of the nominal closed loop system are inside a region R . Determine if all of the eigenvalues of the uncertain closed loop system are inside the region R for all time-invariant ΔA and ΔB described by (4).

IV. REVIEW OF THE STABILITY ROBUSTNESS SUFFICIENT CONDITION

Theorem: Suppose that F is such that the nominal closed loop system described by Eq. (6) is asymptotically stable with distinct eigenvalues. Then, the uncertain closed loop system given by Eq.(7) is asymptotically stable for all $\Delta A(t)$ and $\Delta B(t)$ described by Eq.(4) if

$$\alpha > || (M^{-1})^+ [A_m + B_m(FC)^+] M^+ ||_2 \quad (8)$$

where $\alpha = -\max_i \operatorname{Re}[\lambda_i(A + BFC)]$

and M is the modal matrix of $(A + BFC)$.

Remark: This theorem presents a sufficient condition for the robust stability in terms of the eigenstructure of the nominal closed loop system. Robust stability is ensured provided that the nominal closed loop eigenvalues lie to the left of a vertical line in the complex plane which is determined by a norm involving the structure of the uncertainty and the nominal closed loop modal matrix.

The conservatism inherent in the sufficient condition can be reduced by the use of a diagonal weighting. Let D be a diagonal matrix with real non-negative entries. Then, given a nominal closed loop modal matrix M , another valid modal matrix is MD . This is because the matrix D just serves to scale the nominal closed loop eigenvectors. Therefore, Eq.(8) may be replaced by the sufficient condition given by

$$\alpha > || D^{-1} (M^{-1})^+ [A_m + B_m(FC)^+] M^+ D ||_2 \quad (13)$$

or equivalently by the D -weighted 2-norm described by

$$\alpha > || (M^{-1})^+ [A_m + B_m(FC)^+] M^+ ||_{2D} \quad (14)$$

We now state a lemma which gives the infimum of the right hand side of Eq.(14) which has been attributed to Stoer and Witzgall (1964).

Lemma: Define the Perron eigenvalue of the non-negative matrix A^+ , denoted by $\pi(A^+)$, to be the real non-negative eigenvalue $\lambda_{\max} \geq 0$ such that $\lambda_{\max} \geq |\lambda_i|$ for all eigenvalues ($i=1, \dots, n$) of A^+ . Then,

$$\inf_D \|A^+\|_{2D} = \pi(A^+) \quad (15)$$

We observe that the matrix inside the norm on the right hand side of Eq.(14) is a non-negative matrix. Therefore, our sufficient condition becomes

$$\alpha > \inf_D \| (M^{-1})^+ [A_m + B_m (FC)^+] M^+ \|_{2D} \quad (16)$$

or, by using the lemma

$$\alpha > \pi [(M^{-1})^+ [A_m + B_m (FC)^+] M^+] \quad (17)$$

By taking the infimum on the right hand side of Eq.(14), we have placed the vertical line in the complex plane as close to the imaginary axis as possible with a real positive diagonal weighting. Recall that the sufficient condition for robust stability requires that the nominal eigenvalues lie to the left of this vertical line. In this sense, we have reduced the conservatism of the sufficient condition.

V. PERFORMANCE ROBUSTNESS FOR LTI SYSTEMS WITH STRUCTURED STATE SPACE UNCERTAINTY

A. Overview

An important design criterion for the design of uncertain LTI systems is performance robustness. A sufficient condition has been proposed by Juang, Hong, and Wang (1989) by using the Lyapunov approach to robustness. The closed loop eigenvalues are guaranteed to lie within chosen performance regions when the LTI system is subjected to time-invariant structured state space uncertainty. However, this approach requires the solution of a Lyapunov matrix equation involving complex matrices.

In this section, we use a lemma of Juang, Hong, and Wang (1989) to obtain a sufficient condition for performance robustness by using the Gronwall lemma approach. The closed loop eigenvalues are guaranteed to lie within chosen performance regions when the LTI system is subjected to time-invariant structured state space uncertainty. If the performance region is chosen as the entire left half plane, then the new result reduces to the stability robustness condition described in section IV. The required computations include the nominal eigenvalues/eigenvectors and a matrix norm involving the uncertainty structure and the closed loop eigenvector matrix.

We also address the problem of the conservatism of the new sufficient condition for performance robustness based upon the Gronwall lemma. In section IV, we utilized a diagonal weighting matrix D whose real positive entries were chosen by using Perron weightings in order to reduce the conservatism. In this section, we introduce an additional matrix Q which can further reduce the conservatism. Although a simple closed form solution for the optimal matrix Q is not yet known, we propose a choice based upon obtaining a unitary Q from the singular value decomposition of the product of the nominal closed loop eigenvector matrix and the weighting matrix D .

An example of the lateral dynamics of the L-1011 aircraft is utilized to illustrate the use of the sufficient condition for performance robustness using the region corresponding to a minimum damping ratio of 0.15 and a maximum time constant of 4 seconds. This example also illustrates the need for the unitary matrix Q in order to satisfy the sufficient condition for performance robustness.

B. Preliminary Results

First, we review the following result which is attributed to Juang, Hong, and Wang (1989): Consider a line L which separates the complex plane into two open half planes, namely H and \bar{H} as shown in Figure 1. The line L intersects the real axis at point 'a' and makes an angle θ with respect to the positive imaginary axis, where θ is assumed positive in a counterclockwise sense and $-\pi < \theta \leq \pi$. Denote a specific region H by $H(a, \theta)$.

Lemma 1: All the eigenvalues of a constant matrix E lie in the H region if and only if the eigenvalues of the matrix $e^{-j\theta}(E - aI)$ lie in the open left half plane.

Proof: see Juang, Hong, and Wang (1989)

Next, we present two new definitions which relate the so-called transformed uncertain system to the uncertain system described by (7). Then, we propose a lemma which shows that the transformed uncertain system is asymptotically stable if and only if the eigenvalues of the uncertain system of (7) are in the H region.

Note: When we refer to the uncertain system in the context of performance robustness, we implicitly assume that the uncertainty is time-invariant.

Definition 1: The transformed uncertain system is given by

$$\dot{\tilde{x}}(t) = e^{-j\theta}(A + BFC - aI)\tilde{x}(t) + e^{-j\theta}(\Delta A + \Delta BFC)\tilde{x}(t) \quad (18)$$

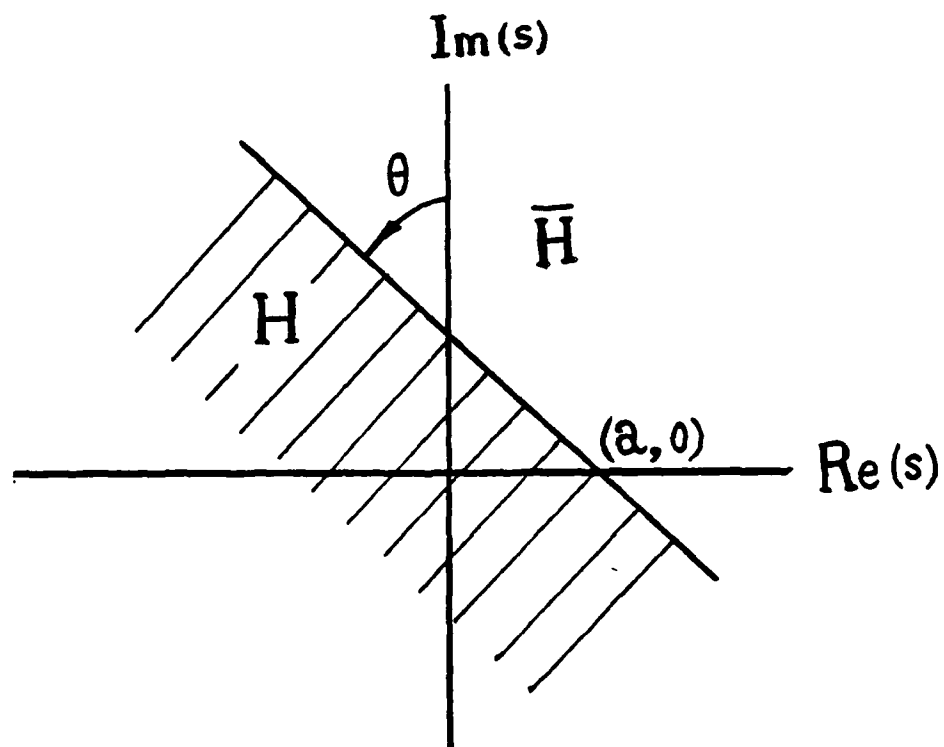


Figure 1. Description of H Region

Definition 2: The nominal closed loop system matrix A_c , the uncertainty matrix ΔA_c , the transformed closed loop system matrix \tilde{A}_c , and the transformed uncertainty matrix $\Delta \tilde{A}_c$ are defined by

$$\begin{aligned} A_c &= A + BFC \\ \Delta A_c &= \Delta A + \Delta BFC \\ \tilde{A}_c &= e^{-j\theta}(A_c - aI) \\ \Delta \tilde{A}_c &= e^{-j\theta} \Delta A_c \end{aligned}$$

Then, the uncertain closed loop system is given by

$$\dot{\hat{x}}(t) = A_c \hat{x}(t) + \Delta A_c \hat{x}(t) \quad (19)$$

and the transformed uncertain closed loop system is given by

$$\dot{\tilde{x}}(t) = \tilde{A}_c \tilde{x}(t) + \Delta \tilde{A}_c \tilde{x}(t) \quad (20)$$

Lemma 2: The eigenvalues of (19) are in the H region for all $\Delta A, \Delta B$ described by (4) if and only if the eigenvalues of (20) are in the open left half complex plane for all $\Delta A, \Delta B$ described by (4).

Proof: The uncertain closed loop system may be written as

$$\dot{\hat{x}}(t) = (A_c + \Delta A_c) \hat{x}(t) \quad (21)$$

and the transformed uncertain closed loop system may be written as

$$\dot{\tilde{x}}(t) = e^{-j\theta}(A_c + \Delta A_c - aI) \tilde{x}(t) \quad (22)$$

Then, the result follows by using lemma 1 with $E = A_c + \Delta A_c$.

End of proof

Now suppose that the real matrix A_c has distinct eigenvalues. Then, the next lemma shows that the modal matrix of A_c will also diagonalize the complex matrix \tilde{A}_c .

Lemma 3: Suppose that the matrix A_c has distinct eigenvalues. Let M be a modal matrix of A_c such that $\Lambda = M^{-1}A_c M$ is a diagonal matrix with the eigenvalues of A_c on the diagonal of Λ . Then, $\tilde{\Lambda} = M^{-1}\tilde{A}_c M$ is a diagonal matrix with the eigenvalues of \tilde{A}_c on the diagonal of $\tilde{\Lambda}$.

Proof: Consider the transformed uncertain closed loop system which is described by

$$\dot{\tilde{x}}(t) = \tilde{A}_c \tilde{x}(t) + \Delta \tilde{A}_c \tilde{x}(t)$$

where $\tilde{A}_c = e^{-j\theta}(A_c - aI)$ and $\Delta \tilde{A}_c = e^{-j\theta} \Delta A_c$.

Let λ_i be the i -th eigenvalue of A_c and let $\tilde{\lambda}_i$ be the corresponding eigenvalue of \tilde{A}_c .

Then, $\det[\tilde{\lambda}_i I - \tilde{A}_c] = 0$

$$\det[\tilde{\lambda}_i I - e^{-j\theta}(A_c - aI)] = 0$$

$$\det[(\tilde{\lambda}_i I + e^{-j\theta} a)I - e^{-j\theta} A_c] = 0$$

$$\det[e^{-j\theta} I] \det[e^{j\theta}(\tilde{\lambda}_i + e^{-j\theta} a)I - A_c] = 0$$

$$\lambda_i = e^{j\theta} \tilde{\lambda}_i + a$$

$$\tilde{\lambda}_i = e^{-j\theta}(\lambda_i - a)$$

$$\tilde{\Lambda} = e^{-j\theta}(\Lambda - aI)$$

Let $A_c = M\Lambda M^{-1}$

Since $\tilde{A}_c = e^{-j\theta}(A_c - aI)$, it follows that

$$\begin{aligned} \tilde{A}_c &= e^{-j\theta}(M\Lambda M^{-1} - aI) \\ &= e^{-j\theta}M(\Lambda - aI)M^{-1} \\ &= M[e^{-j\theta}(\Lambda - aI)]M^{-1} \\ &= M\tilde{\Lambda}M^{-1} \end{aligned}$$

Therefore, $\tilde{A}_c = M\tilde{\Lambda}M^{-1}$

and $\tilde{\Lambda} = M^{-1}\tilde{A}_c M$

End of proof

The final preliminary result (lemma 4) will establish an upper bound on $\|M^{-1}\Delta\tilde{A}_c M\|_2$ which will be required in the proof of the main performance robustness result. We observe that the upper bound of the norm of the complex matrix $M^{-1}\Delta\tilde{A}_c M$ is given by the norm of a real matrix.

Lemma 4: Let \tilde{A}_c be given by definition 2, M is the modal matrix of A_c , and A_m, B_m are given by (4). Then,

$$||M^{-1}\Delta\tilde{A}_cM||_2 \leq ||(M^{-1})^+[A_m + B_m(FC)^+M^+]|_2 \quad (23)$$

Proof: Use the result given by Kouvaritakis and Latchman (1985) that for any matrix $A \in C^{n \times m}$

$$||A||_2 \leq ||A^+||_2$$

Thus,

$$\begin{aligned} ||M^{-1}\Delta\tilde{A}_cM||_2 &\leq ||[M^{-1}\Delta\tilde{A}_cM]^+||_2 \\ &= \sup \frac{||[M^{-1}\Delta\tilde{A}_cM]^+x^+||_2}{||x^+||_2} \\ &= \sup \frac{||[M^{-1}e^{-j\theta}\Delta A_cM]^+x^+||_2}{||x^+||_2} \\ &= \sup \frac{||\{M^{-1}e^{-j\theta}[\Delta A + \Delta BFC]M\}^+x^+||_2}{||x^+||_2} \\ &\leq \sup \frac{|e^{-j\theta}| \cdot ||\{(M^{-1})^+[\Delta A + \Delta BFC]^+M^+x^+||_2}{||x^+||_2} \\ &\leq \sup \frac{||(M^{-1})^+[A_m + B_m(FC)^+M^+]|_2}{||x^+||_2} \\ &= ||(M^{-1})^+[A_m + B_m(FC)^+M^+]|_2 \end{aligned}$$

End of proof

C. Performance Robustness Sufficient Condition

Theorem 1: Suppose that F is such that the nominal closed loop system described by (6) has only distinct eigenvalues all of which lie in some $H(a, \theta)$ region. Let M be the modal matrix of A_c , let D be a diagonal matrix with positive entries, and let Q be a nonsingular matrix. Then, the eigenvalues of the uncertain closed loop system given by (7) will be in the $H(a, \theta)$ region for all ΔA and ΔB described by (4) if

$$\alpha \geq \kappa_2(Q) \cdot \|[(MDQ)^{-1}]^+ [A_m + B_m(FC)^+] [MDQ]^+\|_2 \quad (24)$$

where $\alpha = -\max_i \operatorname{Re}[\lambda_i(\tilde{A}_c)]$

$$= -\max_i \operatorname{Re}[e^{-j\theta}(\lambda_i - a)]$$

and where $\kappa_2(Q) = \|Q^{-1}\|_2 \cdot \|Q\|_2$ is the 2-norm condition number of the matrix Q .

Proof: The transformed uncertain closed loop system is described by

$$\dot{\tilde{x}}(t) = \tilde{A}_c \tilde{x}(t) + \Delta \tilde{A}_c \tilde{x}(t)$$

Let $\tilde{x}(t) = MDQz(t)$ where M and MD are both modal matrices of A_c .

$$z(t) = Q^{-1}D^{-1}M^{-1}\tilde{A}_c MDQz(t) + Q^{-1}D^{-1}M^{-1}\Delta \tilde{A}_c MDQz(t)$$

use lemma 3 to obtain

$$z(t) = Q^{-1}\tilde{\Lambda}Qz(t) + Q^{-1}D^{-1}M^{-1}\Delta \tilde{A}_c MDQz(t)$$

which has a solution described by

$$z(t) = \exp(Q^{-1}\tilde{\Lambda}Qt)z(0) + \int_0^t \exp(Q^{-1}\tilde{\Lambda}(t-\tau)Q)Q^{-1}D^{-1}M^{-1}\Delta \tilde{A}_c MDQz(\tau)d\tau$$

use $\exp(Q^{-1}\tilde{\Lambda}Qt) = Q^{-1}\exp(\tilde{\Lambda}t)Q$ to obtain

$$z(t) = Q^{-1} \exp(\tilde{\lambda} t) Q z(0) + \int_0^t Q^{-1} \exp(\tilde{\lambda}(t-\tau)) Q Q^{-1} D^{-1} M^{-1} \Delta A_c M D Q z(\tau) d\tau$$

In the remainder of the proof, the subscript '2' on the norms is omitted for notational convenience,

$$\begin{aligned} \|z(t)\| &\leq \|Q^{-1}\| \cdot \|\exp(\tilde{\lambda} t)\| \cdot \|Q\| \cdot \|z(0)\| \\ &\quad + \int_0^t \|Q^{-1}\| \cdot \|\exp(\tilde{\lambda}(t-\tau))\| \cdot \|Q\| \cdot \|Q^{-1} D^{-1} M^{-1} \Delta \tilde{A}_c M D Q\| \cdot \|z(\tau)\| d\tau \end{aligned}$$

use $\|\exp(\tilde{\lambda} t)\| \leq \exp(-\alpha t)$ where $\alpha = -\max_i \operatorname{Re}[\lambda_i(\tilde{A}_c)] = -\max_i \operatorname{Re}[e^{-j\theta}(\lambda_i - a)]$

Also, use $\kappa_2(Q) = \|Q\| \cdot \|Q^{-1}\|$ and $Q^{-1} D^{-1} M^{-1} = (M D Q)^{-1}$

Then, $\|z(t)\| \leq \kappa_2(Q) \exp(-\alpha t) \|z(0)\|$

$$+ \int_0^t \kappa_2(Q) \exp(-\alpha(t-\tau)) \cdot \|(M D Q)^{-1} \Delta \tilde{A}_c M D Q\| \cdot \|z(\tau)\| d\tau$$

Multiply both sides by $\exp(\alpha t)$ to obtain

$$\|z(t)\| \exp(\alpha t) \leq \kappa_2(Q) \|z(0)\| + \int_0^t \kappa_2(Q) \cdot \|(M D Q)^{-1} \Delta \tilde{A}_c M D Q\| \cdot \exp(\alpha \tau) \|z(\tau)\| d\tau$$

Use the Gronwall lemma (see Vidyasagar 1978) to obtain

$$\|z(t)\| \exp(\alpha t) \leq \kappa_2(Q) \|z(0)\| \cdot \exp\left[\int_0^t \kappa_2(Q) \cdot \|(M D Q)^{-1} \Delta \tilde{A}_c M D Q\| d\tau\right]$$

Use lemma 4 to obtain

$$\|z(t)\| \exp(\alpha t) \leq \kappa_2(Q) \|z(0)\| \cdot \exp\left[\kappa_2(Q) \cdot \|[(M D Q)^{-1}]^+ [A_m + B_m(FC)^+][M D Q]^+ \| t\right]$$

or

$$\|z(t)\| \leq \kappa_2(Q) \|z(0)\| \exp[-\alpha + \|[(M D Q)^{-1}]^+ [A_m + B_m(FC)^+][M D Q]^+ \| t]$$

Thus, $\|z(t)\| \rightarrow 0$ if $\alpha > \|[(M D Q)^{-1}]^+ [A_m + B_m(FC)^+][M D Q]^+ \|^+$

Then, $z(t)$ is asymptotically stable

→ $\tilde{x}(t)$ is asymptotically stable

→ $\tilde{A}_c + \Delta \tilde{A}_c$ has all its eigenvalues in the open left half complex plane.

Then, by using lemma 2, it follows that $A_c + \Delta A_c$ has all its eigenvalues in the H region.

End of proof

Remark 1

Theorem 1 presents a sufficient condition for robust performance in terms of the eigenstructure of the nominal closed loop system. Robust performance is ensured provided that the eigenvalues of the transformed system matrix \tilde{A}_c lie to the left of a vertical line in the complex plane. The phrase 'robust performance', as used here, means that the eigenvalues of the matrix $A_c + \Delta A_c$ lie inside the $H(a, \theta)$ region for all time-invariant ΔA and ΔB described by (4).

Remark 2

Consider the special case where the H region is the entire open left half complex plane which corresponds to $a = \theta = 0$ and let Q be the identity matrix. Then (24) reduces to

$$\alpha > \|D^{-1}(M^{-1})^+[A_m + B_m(FC)^+]M^+D\|_2; \quad \alpha = -\max_i \operatorname{Re} \lambda_i \quad (25)$$

which is the result shown in section IV for stability robustness. Thus, Theorem 1 includes the earlier stability robustness sufficient condition as a special case. However, the stability robustness result given by (25) is applicable to time-varying uncertainty while the performance robustness result of Theorem 1 requires that the uncertainty be time-invariant.

Corollary 1: Multiple H regions

Let the region R be the intersection of $H_k(a_k, \theta_k)$ for $k=1, 2, \dots, q$. Suppose F is such that the nominal closed loop system described by (6) has distinct eigenvalues all of which are inside R . Let M and Q be defined as in Theorem 1. Then, the eigenvalues of the uncertain closed loop system given by (7) will be in R for all ΔA and ΔB described by (4) if

$$\min_k \alpha_k > \kappa_2(Q) \cdot \|[(MDQ)^{-1}]^+[A_m + B_m(FC)^+][MDQ]^+\|_2 \quad (26)$$

where $\alpha_k = -\max_i \operatorname{Re}[e^{-j\theta_k}(\lambda_i - a_k)]$

Proof:

Using Theorem 1, it follows that the eigenvalues of the system matrix of (7) are in H_k if

$$\alpha_k > \kappa_2(Q) \cdot \|[(MDQ)^{-1}]^+[A_m + B_m(FC)^+][MDQ]^+\|_2$$

The eigenvalues of the system matrix of (7) are in R if they are simultaneously in each H_k ; $k=1,2,\dots,q$. This will be true if (26) is satisfied.

End of proof

Corollary 2: Special Case

Let the region R be the intersection of $H_1(a_1, 0)$, $H_2(0, \theta_2)$, and $H_3(0, -\theta_2)$ as shown in Figure 2. Suppose that the matrices F , M , and Q satisfy the conditions of Theorem 1. Then, the eigenvalues of the uncertain closed loop system given by (7) will be in R for all ΔA and ΔB described by (4) if

$$\min[\alpha_1, \alpha_2] > \kappa_2(Q) \cdot \|[(MDQ)^{-1}]^+[A_m + B_m(FC)^+][MDQ]^+\|_2 \quad (27)$$

where $\alpha_1 = -\max_i [\operatorname{Re} \lambda_i] + a_1$

and $\alpha_2 = -\max_i \operatorname{Re}[e^{-j\theta_2} \lambda_i]$

Proof:

From Corollary 1 we have

$$\min[\alpha_1, \alpha_2, \alpha_3] > \kappa_2(Q) \cdot \|[(MDQ)^{-1}]^+[A_m + B_m(FC)^+][MDQ]^+\|_2$$

where $\alpha_k = -\max_i \operatorname{Re}[e^{-j\theta_k}(\lambda_i - a_k)]$

Thus,

$$\alpha_1 = -\max_i \operatorname{Re}[e^{-j0}(\lambda_i - a_1)]$$

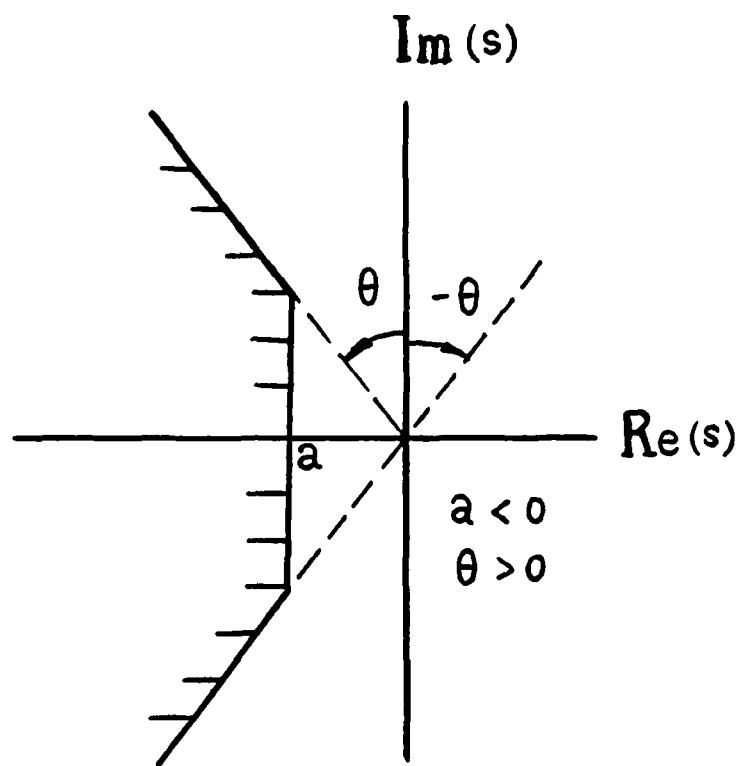


Figure 2. Region for Special Case of Corollary 2

$$= -\max_i \operatorname{Re}[\lambda_i - a_1]$$

$$= -\max_i [\operatorname{Re} \lambda_i] + a_1$$

Also,

$$\alpha_2 = -\max_i \operatorname{Re}[e^{-j\theta/2}(\lambda_i - 0)]$$

$$= -\max_i \operatorname{Re}[e^{-j\theta/2}\lambda_i]$$

$$= -\max_i [\operatorname{Re}(\lambda_i)\cos\theta + \operatorname{Im}(\lambda_i)\sin\theta]$$

and

$$\alpha_3 = -\max_i \operatorname{Re}[e^{j\theta/2}(\lambda_i - 0)]$$

$$= -\max_i \operatorname{Re}[e^{j\theta/2}\lambda_i]$$

$$= -\max_i [\operatorname{Re}(\lambda_i)\cos\theta - \operatorname{Im}(\lambda_i)\sin\theta]$$

Since λ_i are the eigenvalues of the real matrix A_c , the λ_i are either real or they occur in complex conjugate pairs. If λ_i is real, then $\operatorname{Im}(\lambda_i) = 0$ and $\alpha_2 = \alpha_3$. Consider the complex pair $\lambda_i = a_i + jb_i$; $\lambda_{i+1} = \bar{\lambda}_i = a_i - jb_i$. In this case,

$$\alpha_2 = -\max_i \{a_i\cos\theta + b_i\sin\theta, a_i\cos\theta - b_i\sin\theta\}$$

$$\alpha_3 = -\max_i \{a_i\cos\theta - b_i\sin\theta, a_i\cos\theta + b_i\sin\theta\}$$

So it follows that $\alpha_2 = \alpha_3$. In general, α_2 and α_3 are the maximum of sets with the same members which appear in a different order. Thus, the maximum of the two sets is equal and $\alpha_2 = \alpha_3$.

End of proof

Remark 3

The region R in Corollary 2 ensures that a system with a dominant pair of complex conjugate eigenvalues has a damping ratio $\zeta \geq \zeta_{\min}$ and a settling time $t_s \leq (t_s)_{\max}$.

D. Choice of Matrices D and Q

First, we consider the optimal choice of the diagonal real positive matrix D in (24) when Q is the identity matrix. Thus, we seek D_{opt} which yields the infimum of

$$||[(MD)^{-1}]^+ [A_m + B_m(FC)^+] [MD]^+ ||_2 \quad (28)$$

or equivalently

$$||D^{-1}(M^{-1})^+ [A_m + B_m(FC)^+] M^+ D ||_2 \quad (29)$$

We now state a lemma that gives the optimal matrix D_{opt} which yields the infimum of (29). This result is attributed to Stoer and Witzgall (1964).

Lemma 5: Define the Perron eigenvalue of the non-negative matrix A^+ , denoted by $\pi(A^+)$, to be the real non-negative eigenvalue $\lambda_{\max} \geq 0$ such that $\lambda_{\max} \geq |\lambda_i|$ for all eigenvalues ($i=1, \dots, n$) of A^+ . Define the right and left eigenvectors corresponding to λ_{\max} to be the right and left Perron eigenvectors, denoted by x and y , respectively. Normalize the Perron eigenvectors such that $\pi x = Ay$ and $\pi y^T = y^T A$ with $||x||_{\infty} = ||y||_{\infty} = 1$. Then, the matrix D_{opt} which yields the infimum of $||D^{-1}A^+D||_2$ is given by

$$D_{\text{opt}} = \text{diag} \{ [y(1)/x(1)]^{\frac{1}{2}}, \dots, [y(n)/x(n)]^{\frac{1}{2}} \} \quad (20)$$

Proof: see Stoer and Witzgall (1964)

Remark 4

Lemma 5 applies to the performance robustness problem because the matrix $(M^{-1})^+[A_m + B_m(FC)^+]M^+$ in (29) is non-negative. Also (28) and (29) are equivalent because $[MD]^+ = M^+D$ and $[(MD)^{-1}]^+ = D^{-1}(M^{-1})^+$. These last two equalities hold because D is a real diagonal matrix.

Conjecture 1

A choice for the matrix Q which will reduce the norm in (24) is given by

$$Q = UV^T \quad (31)$$

where $U\Sigma V^T$ is the singular value decomposition of the matrix $(MD)^T$.

Remark 5

An optimal choice for the matrix Q is not yet available. However, the choice of (31) results in $\kappa_2(Q)$ equal to its minimum value of unity because U and V are unitary due to the property of the singular value decomposition. Furthermore, the choice of (31) solves (see Golub and Van Loan 1983) the following problem:

$$\begin{aligned} \min \quad & ||MDQ - I||_F \\ \text{subject to} \quad & Q^T Q = I \end{aligned} \quad (32)$$

where $||\cdot||_F$ denotes the Frobenius norm. This provides some motivation for the conjecture that the choice of Q in (31) will reduce the value of the norm in (24)

Remark 6

The proposed method is to first compute D_{opt} using (30) and then compute

Q using (31). Then, these matrices are used to compute the norm in the performance robustness condition given by (24).

E. Example

Consider the linearized lateral dynamics of an aircraft described by

$$\begin{bmatrix} \dot{\phi} \\ \dot{r} \\ \dot{p} \\ \dot{\beta} \end{bmatrix} = \begin{bmatrix} 0 & 0 & 1 & 0 \\ 0 & N_r & N_p & N_\beta \\ 0 & L_r & L_p & L_\beta \\ g/V & (Y_r/V)-1 & Y_p/V & Y_\beta/V \end{bmatrix} \begin{bmatrix} \phi \\ r \\ p \\ \beta \end{bmatrix} + \begin{bmatrix} 0 & 0 \\ N_{\delta_r} & N_{\delta_a} \\ L_{\delta_r} & L_{\delta_a} \\ Y_{\delta_r}/V & Y_{\delta_a}/V \end{bmatrix} \begin{bmatrix} \delta_r \\ \delta_a \end{bmatrix}$$

The example shown here is similar to the example which was utilized by Sobel, Banda, and Yeh (1989) to illustrate the stability robustness condition which was described in section IV. The example shown here uses a different feedback gain matrix and it is assumed here that the uncertainty is time-invariant.

The nominal parameter values and the maximum absolute values of the uncertainty are shown in Table 1 for the L-1011 aircraft at some cruise flight condition. These maximum absolute values of the uncertainty are the entries in the matrices A_m and B_m which are defined in (4). The feedback gain matrix F using state feedback is chosen as

$$F = \begin{bmatrix} 0.426 & -4.13 & 0.176 & 5.57 \\ -4.24 & -1.46 & -2.63 & 6.32 \end{bmatrix}$$

with nominal closed loop eigenvalues given by

$$\begin{aligned} \lambda_{1,2} &= -1.75 \pm j1.75 && \text{(dutch roll mode)} \\ \lambda_{3,4} &= -2.0 \pm j1.0 && \text{(roll mode)} \end{aligned}$$

The region R is chosen to be the intersection of $H_1(-0.25, 0)$, $H_2(0, 8.63 \text{ deg})$.

Table 1. Stability and Control Derivatives for L-1011 Aircraft

Parameter	Nominal Values	Maximum of Absolute Value of Uncertainty
N_r	-0.154	0.01925 (12.5%)
L_r	0.249	0.031125 (12.5%)
$(Y_r/V)-1$	-0.996	0.0
N_p	-0.0042	0.0021 (50%)
L_p	-1.00	0.125 (12.5%)
Y_p/V	-0.000295	0.0001475 (50%)
N_B	1.54	0.1155 (7.5%)
L_B	-5.20	0.26 (5%)
Y_B/V	-0.177	0.0146 (12.5%)
g/V	0.0386	0.0
N_{δ_r}	-0.744	0.093 (12.5%)
N_{δ_a}	-0.032	0.004 (12.5%)
L_{δ_r}	0.337	0.042125 (12.5%)
L_{δ_a}	-1.12	0.084 (7.5%)
Y_{δ_r}/V	0.02	0.01 (50%)
Y_{δ_a}/V	0.0	0.0

and $H_3(0, -8.63 \text{ deg})$. This region guarantees that (1) the damping ratio of the dominant mode is $\zeta \geq \zeta_{\min} = 0.15$ and (2) the time constant of the dominant mode is less than or equal to four seconds.

Then, according to Corollary 2

$$\begin{aligned}\alpha_1 &= -\max_i [\operatorname{Re} \lambda_i] - 0.25 \\ &= -\max_i [-1.75 - 0.25, -2.0 - 0.25] \\ &= 1.50\end{aligned}\tag{34}$$

$$\begin{aligned}\alpha_2 &= -\max_i \operatorname{Re}[e^{-j8.63\pi/180} \lambda_i] \\ &= -\max_i \operatorname{Re}[e^{-j0.1506} \lambda_i] \\ &= -\max_i [-1.4676, -1.8273] \\ &= 1.4676\end{aligned}\tag{35}$$

The matrix D_{opt} is computed using (30) and it is given by

$$D_{\text{opt}} = \operatorname{diag}(1.9291, 1.9291, 0.4861, 0.4861)\tag{36}$$

Then, using Corollary 2 we require that

$$\min[\alpha_1, \alpha_2] > \kappa_2(Q) \cdot \|[(MDQ)^{-1}]^+ [A_m + B_m(FC)^+][MDQ]^+\|_2\tag{37}$$

and with $Q=I$ (the identity matrix), we obtain from (37) that

$$1.4676 \not> 1.5843$$

and the robust performance sufficient condition is not satisfied.

Next, we use D_{opt} from (36) to compute a unitary matrix Q by using (31).

The matrix Q is given by

$$Q = \begin{bmatrix} -0.2238+j0.6706 & -0.0025+j0.0029 & 0.6708+j0.2238 & 0.0021-j0.0123 \\ -0.2238-j0.6706 & -0.0025-j0.0029 & 0.6708-j0.2238 & 0.0021+j0.0123 \\ -0.0010-j0.0128 & 0.6935+j0.1382 & 0.0018-j0.0015 & 0.1383-j0.6933 \\ -0.0010+j0.0128 & 0.6935-j0.1382 & 0.0018+j0.0015 & 0.1383+j0.6933 \end{bmatrix}$$

Then, (37) yields

$$1.4676 > 1.4572$$

and the performance robustness is guaranteed for the chosen region R .

That is, the eigenvalues of the uncertain closed loop system will remain within R for all possible combinations of the time-invariant uncertainty described by ΔA and ΔB .

V. ROBUST EIGENSTRUCTURE ASSIGNMENT (CONSTRAINED OPTIMIZATION)

A. Overview

We present a robust eigenstructure assignment design method which optimizes either the sufficient condition for robust stability or robust performance while constraining the dominant eigenvalues to lie within chosen regions in the complex plane. Constraints may also be placed on entries of the eigenvectors to emphasize the need for mode decoupling. The constrained optimization problem is solved by using the sequential unconstrained minimization technique with a quadratic extended interior penalty function (Haftka and Starnes, 1976). We also introduce a similarity transformation on the uncertain plant which can reduce the conservatism of the sufficient condition. The first example illustrates the design of a robust eigenstructure assignment controller for a pitch pointing/vertical translation maneuver of the AFTI F-16 aircraft. The second example considers the linearized

lateral dynamics of the L-1011 aircraft using state feedback, gain suppression, and a dynamic compensator.

B. Review of Eigenstructure Assignment

Consider the linear time invariant system described by (1). We shall assume that the matrices B and C have full rank. With these assumptions, the constant gain output feedback problem using eigenstructure assignment can be stated as follows: Given a set of desired eigenvalues $\{\lambda_i^d\}$, $i=1,2,\dots,r$ and a corresponding set of desired eigenvectors, v_i^d , $i=1,2,\dots,r$ find a real $(m \times r)$ matrix F such that the eigenvalues of $A+BFC$ contain λ_i^d as a subset and the corresponding eigenvectors of $A+BFC$ are close to the respective members of the set $\{v_i^d\}$.

The following theorem, due to Srinathkumar (1976), describes the number of eigenvalues and eigenvectors entries that can be exactly assigned.

Theorem: Given the controllable and observable system described by (1) and the assumptions that the matrices A and B are full rank, then $\max(m,r)$ closed loop eigenvalues can be assigned and $\max(m,r)$ eigenvectors can be partially assigned with $\min(m,r)$ entries in each eigenvector arbitrarily chosen using constant gain output feedback.

In general, we may desire to exercise some control over more than $\min(m,r)$ entries in a particular eigenvector. Therefore, we shall now discuss the problem of first characterizing desired eigenvectors v_i^d that can be assigned as closed loop eigenvectors and of then determining the best possible set of achievable eigenvectors in case a desired eigenvector v_i^d is not achievable.

The solution to these problems was shown by Andry et. al. (1983) and begins with the closed loop system described by

$$\dot{x}(t) = (A + BFC)x(t) \quad (38)$$

For an eigenvalue/eigenvector pair, λ_i and v_i

$$(A + BFC)v_i = \lambda_i v_i \quad (39)$$

or

$$v_i = (\lambda_i I - A)^{-1} BFCv_i \quad (40)$$

Define the m vector m_i as

$$m_i = FCv_i \quad (41)$$

Then, (40) becomes

$$v_i = (\lambda_i I - A)^{-1} Bm_i \quad (42)$$

The importance of (42) is the need for the eigenvector v_i to be in the subspace spanned by the columns of $(\lambda_i I - A)^{-1} B$. This subspace is of dimension m , which is the number of independent control variables. Therefore, the number of control variables determines the dimension of the subspace in which the achievable eigenvectors must reside. We conclude that if we choose an eigenvector v_i that lies precisely in the subspace spanned by the columns of $(\lambda_i I - A)^{-1} B$ it will be achieved exactly.

In general, however, a desired eigenvector v_i^d will not reside in the prescribed subspace and, hence, cannot be achieved. Instead, a "best possible" choice for an achievable eigenvector is made. It is suggested by Andry et. al. (1983) that this "best possible" eigenvector is the projection of v_i^d onto the subspace spanned by the columns of

$(\lambda_i I - A)^{-1}B$. We remark that the desired eigenvectors v_i^d are chosen based upon mode decoupling specifications. By using an orthogonal projection to obtain the achievable eigenvectors v_i^a , we are minimizing the 2-norm error between a desired eigenvector and its corresponding achievable eigenvector. It is important to note that the concept of stability robustness was not considered in the design approach proposed by Andry et. al. (1983).

To further complicate the situation, complete specification of v_i^d is neither required nor known in most practical situations. When the designer is interested in only certain elements of the eigenvector, we assume that the desired eigenvector has a structure given by

$$v_i^d = [v_{i1}, x, x, x, x, v_{ij}, x, x, x, v_{in}]^T$$

where v_{ij} are the designer specified components and "x" the unspecified components. We define a reordering operator $\{ \}^R_i$ as follows (see Harvey and Stein, 1978):

$$\{v_i^d\}^R_i = \begin{bmatrix} l_i^d \\ d_i \end{bmatrix}$$

where l_i^d is the vector of specified components of v_i^d and d_i is the vector of unspecified components of v_i^d .

We begin the computation of an achievable eigenvector v_i^a by defining

$$L_i = (\lambda_i I - A)^{-1}B \quad (43)$$

Since an achievable eigenvector must lie in the subspace spanned by the columns of L_i , we require that

$$v_i^a = L_i z_i \quad (44)$$

where the vectors z_i are the eigenvector design parameters.

We reorder the rows of L_i to conform with the reordered components of v_i^d . Thus, as shown by Harvey and Stein (1978), we have

$$\{L_i\}^{R_i} = \begin{bmatrix} \tilde{L}_i \\ D_i \end{bmatrix} \quad (45)$$

It is suggested by Andry et. al. (1983) that the value of the vector z_i be computed so that it corresponds to the orthogonal projection onto the so-called "achievability subspace". Hence, z_i is chosen to minimize

$$J = \|l_i^d - l_i^a\|_2^2 = \|l_i^d - L_i z_i\|_2^2 \quad (46)$$

Then, the i -th achievable eigenvector is given by (44). Once all r achievable eigenvectors are computed, the output feedback gain matrix is easily calculated, as shown by Andry et. al. (1983). We conclude with the remark that this approach should yield achievable eigenvectors v_i^a which are closest in the 2-norm sense to the desired eigenvectors v_i^d . Recall that the desired eigenvectors are chosen for mode decoupling performance specifications.

C. Review of the Sequential Unconstrained Minimization Technique (see Haftka and Starnes, 1976)

The constrained optimization to be considered is to find a vector v^* of design variables that minimizes the function $m(v)$ subject to the constraints

$$g_i(v) \geq 0; i=1, \dots, n \quad (47)$$

It is assumed that at least one of the constraints of (47) is critical at the minimum v^* , that is, $g_i(v^*) = 0$ for some i . This constrained optimization problem may be transformed into a series of unconstrained minimization problems by introducing a penalty function associated with

the constraints, and the transformed problem can be solved by the sequence of unconstrained minimizations technique. The resulting transformed problem is to find the minimum of a function $P(r)$ as r goes to zero where

$$P(r) = m(v) + r \sum_{i=1}^n f_i(v) \quad (48)$$

and $f_i(v)$ is defined by

$$f_i(v) = 1/g_i(v) \quad \text{if } g_i(v) > 0 \quad (49)$$

The term $rf_i(v)$ represents the penalty associated with the i -th constraint, and is an interior penalty function in the sense that it is defined only if v is inside the feasible design domain. With v^r denoting the point in the design space where $P(r)$ attains its minimum value for a given value of r , it may be shown that as r goes to zero

$$\begin{aligned} \min P(r) &\rightarrow m(v^*) \\ v^r &\rightarrow v^* \end{aligned}$$

Next, a quadratic extended interior penalty function is introduced to permit the use of design points that are outside the feasible domain. The definition of the f_i in (48) for the quadratic extended penalty function is

$$f_i = \begin{cases} 1/g_i & \text{if } g_i \geq g_0 \\ 1/g_0 [(g_i/g_0)^2 - 3(g_i/g_0) + 3] & \text{if } g_i \leq g_0 \end{cases} \quad (50)$$

To complete the definition of the quadratic extended penalty function, a relation that defines the transition point g_0 between the two constraint functions in (50) is required. This definition is described by

$$g_0 = Cr^p; \quad 1/2 \leq p < 1/3 \quad (51)$$

D. AFTI F-16 Pitch Pointing/Vertical Translation Design

Consider the LTI model of the AFTI F-16 aircraft described by

$$\begin{bmatrix} \dot{\gamma} \\ \dot{q} \\ \dot{\alpha} \\ \dot{\delta}_e \\ \dot{\delta}_f \end{bmatrix} = \begin{bmatrix} 0 & 0.00665 & 1.3411 & 0.16897 & 0.25183 \\ 0 & -0.86939 & 43.223 & -17.251 & -1.5766 \\ 0 & 0.99335 & -1.3411 & -0.16897 & -0.25183 \\ 0 & 0 & 0 & -20.0 & 0 \\ 0 & 0 & 0 & 0 & -20.0 \end{bmatrix} \begin{bmatrix} \gamma \\ q \\ \alpha \\ \delta_e \\ \delta_f \end{bmatrix} + \begin{bmatrix} 0 & 0 \\ 0 & 0 \\ 0 & 0 \\ 20 & 0 \\ 0 & 20 \end{bmatrix} \begin{bmatrix} \delta_{ec} \\ \delta_{fc} \end{bmatrix} \quad (52)$$

A pitch pointing/vertical translation controller was proposed by Sobel and Shapiro (1985) to decouple the pitch attitude and flight path responses. The zero entries in the short period eigenvectors are for pitch pointing (θ command with no coupling to γ) while the zero entry in the γ mode eigenvector is for vertical translation (γ command with no coupling to θ or q). The desired eigenvectors are shown in Table 2 where we observe the zero entries which are chosen to obtain the required decoupling. The feedback gains described by Sobel and Shapiro (1985) are for the outputs $y^T = [q, n_{zp}, \gamma, \delta_e, \delta_f]$. However, for simplicity, in this report, we will use full state feedback. The full state feedback gain matrix is shown in Table 3 and it is obtained by applying a transformation to the feedback gain matrix described by Sobel and Shapiro (1985). The achievable eigenvectors are shown in Table 4 where we observe that the three zero entries have been exactly achieved. Thus, we expect excellent decoupling in both pitch pointing and vertical translation responses. Finally, feedforward gains based upon Broussard's (1978) command generator tracker are computed to obtain zero steady state error to a step command. The vertical translation and pitch pointing step responses are shown in Figures 3 and 4, respectively. As expected,

the decoupling is excellent for both cases. However, the design of Sobel and Shapiro (1985) does not consider stability robustness when the aircraft is subject to linear time-varying state space uncertainty.

Table 2. Desired Eigenvectors

Short Period	Gamma Mode	Actuator Mode	Actuator Mode
0 0	1	x	x
1 x	0	x	x
x 1	x	x	x
x x	x	1	x
x x	x	x	1

Next, we consider a robust eigenstructure assignment pitch pointing/vertical translation control law. First, to reduce the conservatism in (17), we use a constant similarity transformation to obtain the transformed state given by

$$\tilde{x}(t) = [\theta, q, \alpha, \delta_e, \delta_f]^T$$

The utilization of such a transformation is valid because the stability of a linear time-varying system is preserved when subjected to a constant similarity transformation (Chen, 1970, pp. 143-146). The use of such a similarity transformation to reduce conservatism was used by Yedavalli and Liang (1986) in connection with a Lyapunov approach to robustness.

In the transformed coordinates, the equation $\dot{\theta} = q$ is a physical relationship without uncertain parameters. Thus, the first row of A_m will contain all zeros. The matrices A_m and B_m for the transformed system are given by

$$A_m = \begin{bmatrix} 0 & 0 & 0 & 0 & 0 \\ 0 & .0869 & 1.08 & .4313 & .158 \\ 0 & 0 & .1341 & .0169 & .0252 \\ 0 & 0 & 0 & 0.1 & 0 \\ 0 & 0 & 0 & 0 & 0.1 \end{bmatrix} \quad (53a)$$

Table 3. Closed Loop Eigenvalues and Control Gains

	Closed Loop Eigenvalues	Feedforward Gains (γ_c, θ_c)		Feedback Gains ($u=-Fx$)				
Non- Robust Design	-5.60±j4.19 -1.00 -19.0 -19.5	-.375 4.12	-2.87 1.98	-3.25 6.10	-.891 .898	-7.11 10.02	.526 -.420	.0840 -.102
Robust Design	-3.62±j5.18 -2.66 -19.0 -19.5	-.992 10.93	-1.62 -6.47	-2.61 4.47	-.581 .0642	-5.31 1.11	.288 .0131	.0555 .0204
Robust Design v_i constraint	-3.62±j5.14 -3.00 -19.0 -19.5	-1.11 12.37	-2.01 -1.83	-3.12 10.54	-.606 .361	-5.72 5.97	.291 -.0239	.0543 .0342
Robust with matrix Q	-3.61±j5.18 -2.40 -19.0 -19.5	-.890 9.90	-1.68 -5.76	-2.57 4.14	-.552 -.243	-5.29 .925	.259 .331	.0540 .0363
Perform- ance Robust	-3.61±j5.18 -2.71 -19.0 -19.5	-1.01 11.14	-1.68 -5.67	-2.69 5.47	-.557 -.183	-5.31 1.23	.262 .290	.0529 .0476

Table 4. Closed Loop Eigenvectors (normalized $\|x\|_{\infty} = 1$)

	short period		gamma mode	actuator mode	actuator mode
Non-	0.0	0.0	.3089	-.0054	-.0135
Robust	.5954	-.7679	.0001	1.0	.0343
Design	-.1339	.0369	-.3090	-.0472	.0118
	-.4502	-.2629	-.8656	.9317	-.0249
	1.0	0.0	1.0	.0081	1.0
Robust	-.0434	.0301	-.2668	-.0052	-.0137
Design	1.0	0.0	-.0038	1.0	.0631
	-.0472	-.1598	.2682	-.0475	.0104
	.0215	-.7004	.5802	.9316	.0029
	.2153	-.0044	1.0	-.0060	1.0
Robust	-.0200	.0077	-.1911	-.0053	-.0137
Design	1.0	0.0	.0010	1.0	.0599
v_i	-.0716	-.1378	.1908	-.0474	.0106
constraint	-.0685	-.7063	.3868	.9312	-.0002
	.5301	.6895	1.0	-.0018	1.0
Robust	-.0418	.0119	-.3711	-.0053	-.0137
with	1.0	0.0	.0008	1.0	.0587
matrix Q	-.0486	-.1419	.3708	-.0473	.0106
	-.0177	-.6719	.8377	.9325	-.0013
	.5985	.1743	1.0	.0018	1.0
Perform-	-.0421	.0119	-.2528	-.0053	-.0137
ance	1.0	0.0	-.0026	1.0	.0599
Robust	-.0485	-.1420	.2537	-.0473	.0106
Design	-.0180	-.6714	.5440	.9374	-.0001
	.6023	.1711	1.0	.0027	1.0

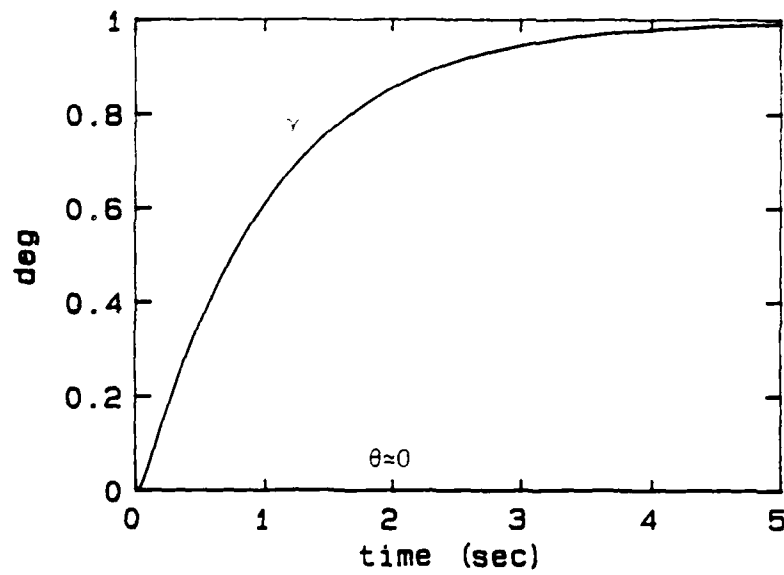


Figure 3. AFTI F-16 Non-Robust Design (Vertical Translation)

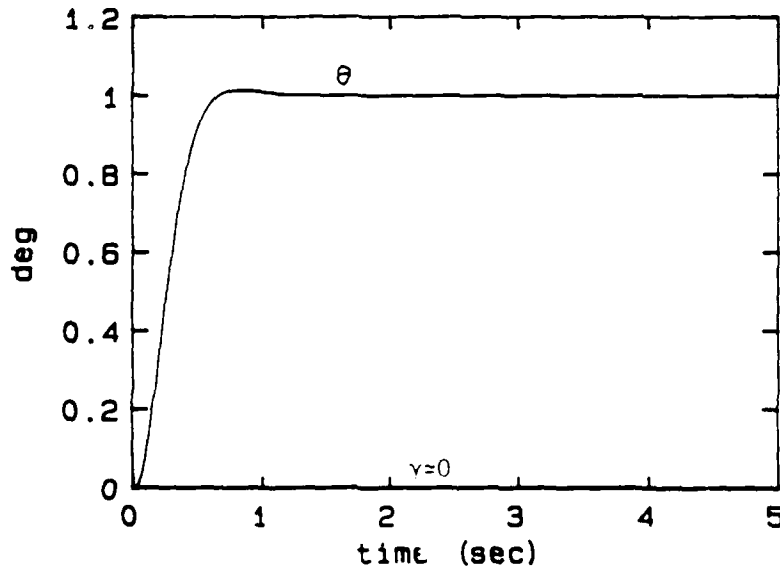


Figure 4. AFTI F-16 Non-Robust Design (Pitch Pointing)

$$B_m = \begin{bmatrix} 0 & 0 \\ 0 & 0 \\ 0 & 0 \\ 0.1 & 0 \\ 0 & 0.1 \end{bmatrix} \quad (53b)$$

We emphasize that the transformed system is only used for computation of (17), while the original system of (52) is used for eigenvalue/eigenvector selection and gain computation. For the design of Sobel and Shapiro (1985), $\alpha = 1.0$ while the right hand side of (17) equals 4.28 which indicates that the sufficient condition for robust stability is not satisfied. We use a constrained optimization to solve

$$\min \lambda_{\max} [(M^{-1})^+ (A_m + B_m F^+) M^+] - \alpha \quad (54)$$

while constraining some of the eigenvalues and eigenvectors. First, we choose to assign the actuator eigenvalues and eigenvectors to the same values as in the design presented by Sobel and Shapiro (1985). Then, an optimization is performed over a subset of the short period eigenvector parameters, short period eigenvalues, and the gamma mode eigenvalue. This choice of optimization parameters is chosen by examining the gradient at the initial point corresponding to the design of Sobel and Shapiro (1985). The term "eigenvector parameters" is the vector z_i , where an eigenvector v_i is defined by $v_i = L_i z_i$ and where the columns of L_i are an orthonormal basis for the i -th eigenvector subspace. So during the optimization, the first entry (both real and imaginary parts) of the vector z_{sp} for the short period mode is allowed to change, the short period eigenvalues are allowed to change subject to the constraints $-7.6 \leq \text{Re}[\lambda_{sp}] \leq -3.6$, $3.2 \leq \text{Im}[\lambda_{sp}] \leq 5.2$, and the gamma mode eigenvalue is allowed to change subject to the constraint $-2.65 \leq \lambda_\gamma \leq -0.5$. Each

time λ_γ is changed, its eigenvector is computed as the orthogonal projection of the desired gamma mode eigenvector onto the current achievable gamma mode subspace. In this way, the zero entry in the gamma mode eigenvector might be achieved in which case the vertical translation decoupling may be nearly the same as in the design of Sobel and Shapiro (1985).

When the optimization is complete $\alpha = 2.65$ and the right hand side of (17) equals 2.57; thus, the sufficient condition for robust stability is satisfied. The closed loop eigenvectors are shown in Table 4 from which we observe that the zero entry in the gamma mode eigenvector has been achieved. This suggests that the vertical translation decoupling will be the same as in Sobel and Shapiro (1985). However, the entries in the short period eigenvectors which were zero in Sobel and Shapiro (1985), are now non-zero. This suggests that the pitch pointing decoupling will not be as good as in Sobel and Shapiro (1985). The closed loop eigenvalues and feedback gains are shown in Table 3. Observe that the short period eigenvalues have moved to the boundary of the constraint region corresponding to the largest settling time and smallest damping ratio. The gamma mode eigenvalue has moved to the leftmost point in its constraint interval which is to be expected since λ_γ appears explicitly in (17). Also observe that the magnitude of the feedback gains has been reduced. The vertical translation and pitch pointing responses are shown in Figures 5 and 6, respectively. As expected, the vertical translation decoupling is virtually identical to the Sobel and Shapiro (1985) design while the pitch pointing decoupling has been degraded. Table 5 shows that the new robust eigenstructure assignment design exhibits a significantly improved minimum singular value of the return

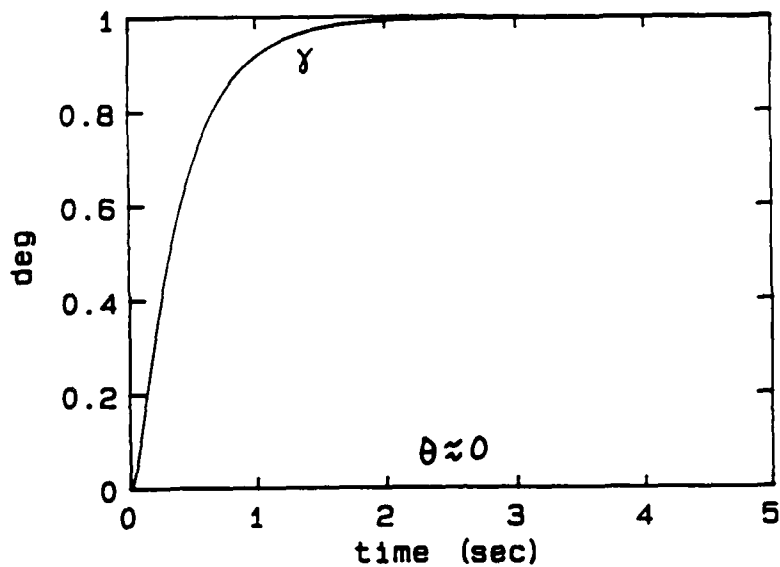


Figure 5. AFTI F-16 Robust Design (Vertical Translation)

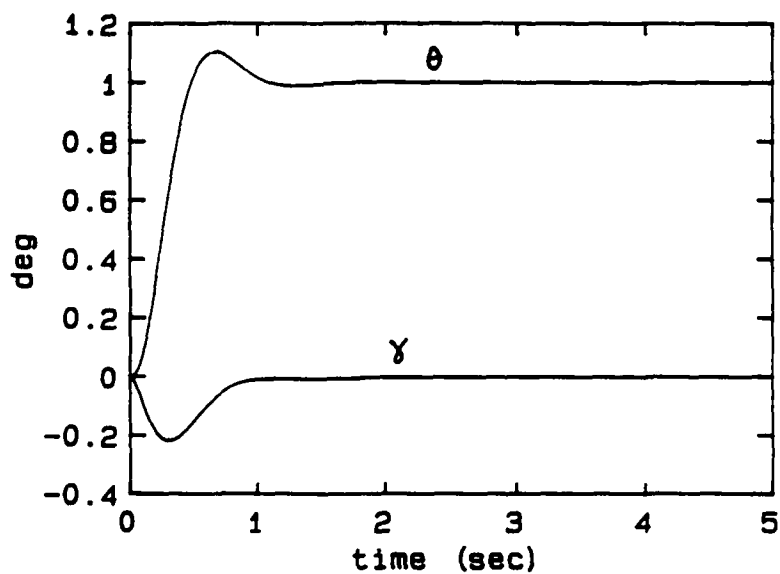


Figure 6. AFTI F-16 Robust Design (Pitch Pointing)

Table 5. Comparison of Robustness Measures

	Max $ \gamma $ $\theta_c = 1$	Min $\underline{\sigma}(I+FG)$	Cond(M)
Non- Robust Design	6.66×10^{-4}	0.1983	56.00
Robust Design	0.2171	0.5021	27.30
Robust Design v_i constraint	0.0787	0.2802	36.80
Robust Design with matrix Q	0.1617	0.4244	27.11
Perform- ance Robust Design	0.1596	0.4143	27.84

difference matrix at the inputs and an improved condition number of the closed loop modal matrix as compared to the Sobel and Shapiro (1985) design.

Next, we place a constraint on the first entry of the complex conjugate short period eigenvectors. This will allow us to place additional emphasis on the mode decoupling which is required for the pitch pointing maneuver. The constraints are chosen to be $|\operatorname{Re} v_{sp}| \leq 0.01$ and $|\operatorname{Im} v_{sp}| \leq 0.01$ where the eigenvectors are normalized to unit length in the 2-norm sense. A solution could not be obtained for the eigenvalue constraints which were used in the previous design. Therefore, the gamma mode eigenvalue constraint is relaxed to become $-3.0 \leq \lambda_\gamma \leq -0.5$ which will have the effect of moving the gamma mode eigenvalue farther into the left half of the complex plane. The new closed loop eigenvectors are shown in Table 4 where we observe that the real and imaginary parts

of the first entry of the short period eigenvectors are significantly smaller than in the previous design. Thus, we should expect that the pitch pointing response will be improved. The vertical translation and pitch pointing responses are shown in Figures 7 and 8, respectively. We observe that the coupling between γ and θ has been reduced by approximately 50% as compared to the previous design. However, we observe from Table 3 that the feedback gains are larger in magnitude. Also, from Table 5 we observe that we no longer have a significant improvement in the minimum singular value of the return difference matrix.

Next, we remove the additional short period eigenvector constraints, but we introduce the unitary weighting matrix Q in order to reduce the conservatism in the robust stability condition. Due to the use of the matrix Q , we can tighten the constraint on the gamma eigenvalue to

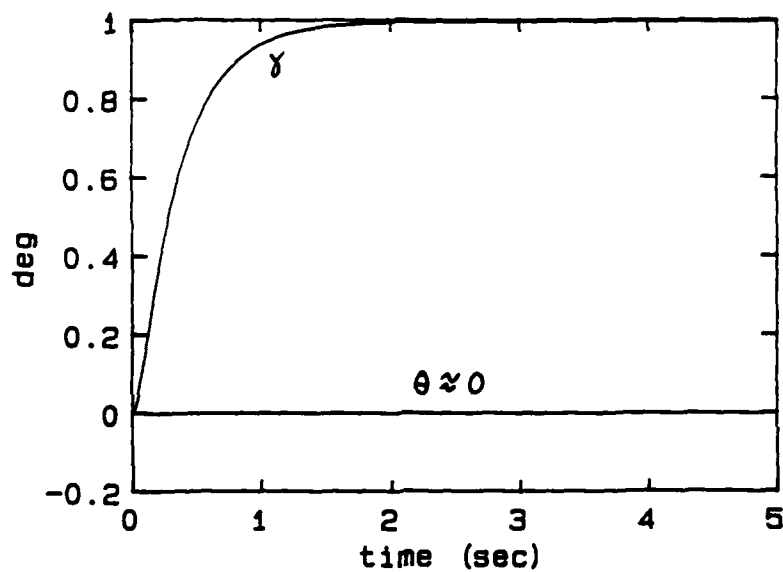


Figure 7. AFTI F-16 Robust Design with v_i Constraints (Vertical Translation)

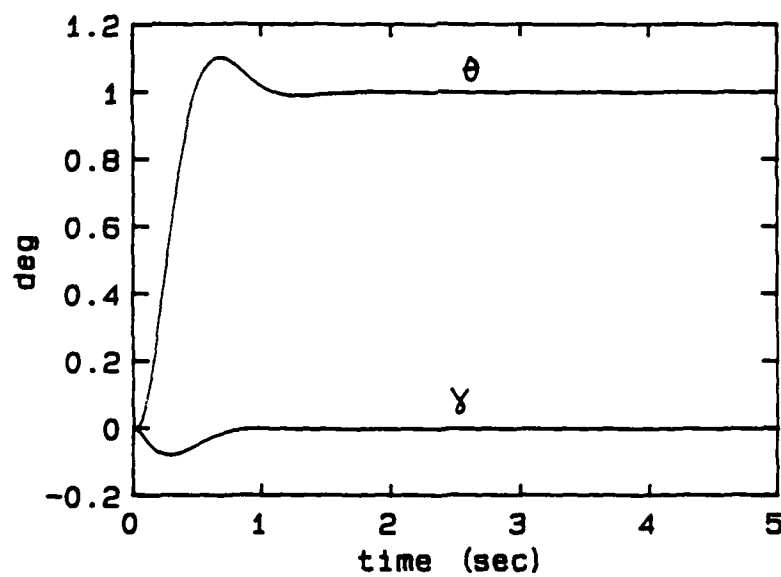


Figure 8. AFTI F-16 Robust Design with v_i Constraints (Pitch Pointing)

$-2.4 \leq \lambda_Y \leq -0.5$. Thus, we obtain a solution with $\lambda_Y = -2.4$ which is to be compared with the previous solution with $\lambda_Y = -2.65$. So we do not need to move the gamma mode eigenvalue as far left in the complex plane as before. The vertical translation and pitch pointing responses are shown in Figures 9 and 10, respectively. The vertical translation response exhibits slightly less coupling than the previous design which did not utilize the unitary matrix Q .

Finally, we design a controller by optimizing the performance robustness condition of (24). We choose $a = -0.25$ and $\theta = 8.63$ deg which corresponds to a region with $\zeta = 0.15$ and $t_s = 4$ sec. The constraint for the gamma mode eigenvalue is chosen to be $-2.70 \leq \lambda_Y \leq -0.5$. The vertical translation and pitch pointing responses are shown in Figures 11 and 12, respectively. We observe that these responses are almost identical to the robust stability responses which were shown in Figures 9 and 10, respectively. However, we now guarantee that the closed loop eigenvalues remain in the performance region for all uncertainty which satisfies the A_m and B_m bounds. We observe from Table 5 that this design has the smallest coupling of all the robust designs which do not use constraints on the first entry of the complex conjugate short period eigenvectors.

E. L-1011 Aircraft with State Feedback

Consider the L-1011 aircraft described in section V.E. with stability and control derivatives shown in Table 1. An eigenstructure assignment controller was designed in Sobel and Shapiro (1987a) which decouples the dutch roll mode from the roll mode while assigning the eigenvalues to the following:

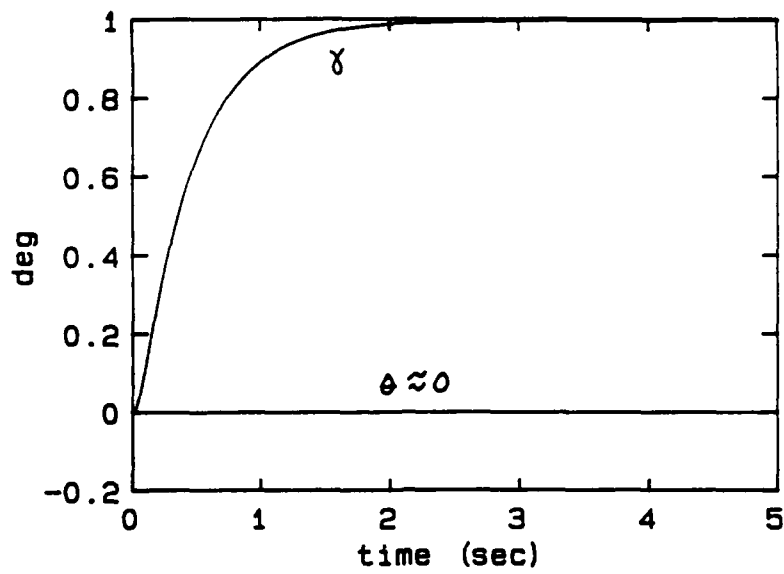


Figure 9. AFTI F-16 Robust Design with Matrix Q (Vertical Translation)

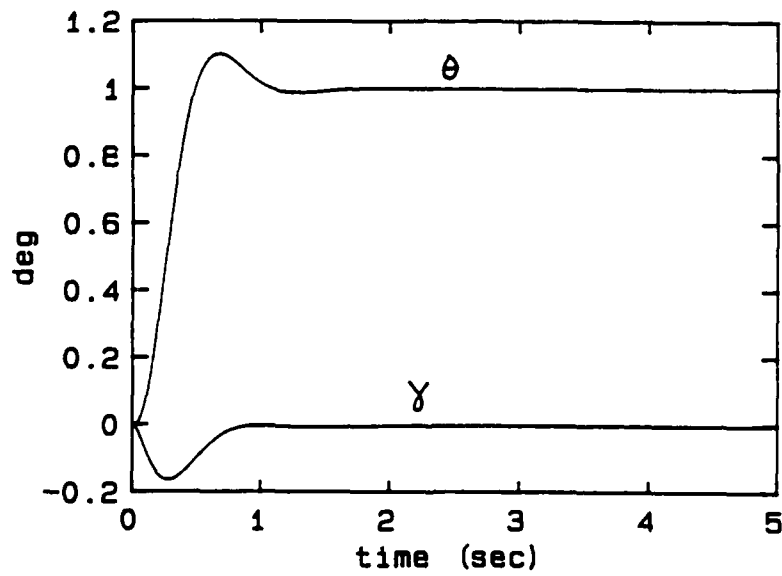


Figure 10. AFTI F-16 Robust Design with Matrix Q (Pitch Pointing)

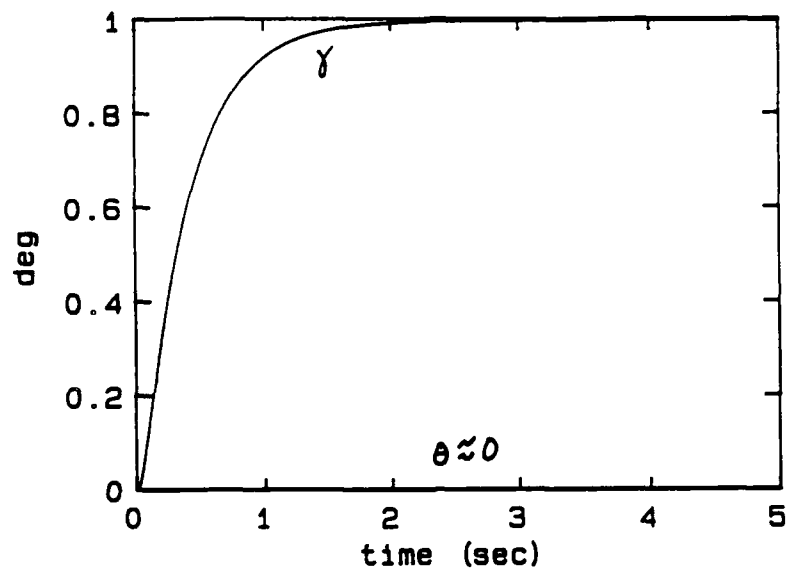


Figure 11. AFTI F-16 Performance Robust Design (Vertical Translation)

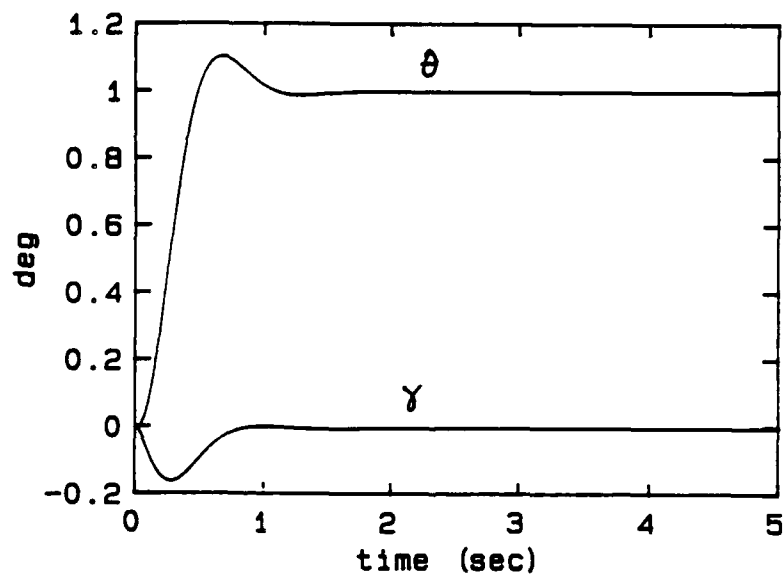


Figure 12. AFTI F-16 Performance Robust Design (Pitch Pointing)

$$\lambda_{dr} = -1.5 \pm j1.5$$

$$\lambda_{roll} = -2.0 \pm j1.0$$

The feedback gain matrix is given by

$$F = \begin{bmatrix} -0.367 & 3.52 & -0.163 & -3.46 \\ 4.35 & 1.28 & 2.63 & -5.68 \end{bmatrix} \quad (55)$$

We evaluate the stability robustness condition of (17) where $\alpha = 1.5$ and the right hand side of (17) equals 1.46. Therefore, the stability robustness sufficient condition is satisfied. Nonetheless, we choose to optimize (54) in order to increase the stability margin. That is, to guarantee stability for larger uncertainty than shown in Table 1. The gradient is computed at the design described by (55) to determine which parameters should be varied during the optimization. The chosen parameters are $\text{Re}[z_{dr}(1)]$, $\text{Im}[z_{dr}(1)]$, $\text{Re}[\lambda_{dr}]$, $\text{Re}[z_{roll}(2)]$, $\text{Im}[z_{roll}(2)]$, $\text{Re}[\lambda_{roll}]$, and $\text{Im}[\lambda_{roll}]$. The constraints are $-1.4 \leq \text{Re}[\lambda_{dr}] \leq -1.9$, $-1.95 \leq \text{Re}[\lambda_{roll}] \leq -3.0$, and $0.5 \leq \text{Im}[\lambda_{roll}] \leq 1.45$. The optimal solution has eigenvalues given by

$$\begin{aligned} \lambda_{dr} &= -1.87 \pm j1.5 \\ \lambda_{roll} &= -1.95 \pm j1.45 \end{aligned}$$

with feedback gain matrix given by

$$F = \begin{bmatrix} -0.411 & 4.47 & -0.161 & -5.07 \\ 5.16 & 1.57 & 2.54 & -6.17 \end{bmatrix} \quad (56)$$

We find that $\alpha = 1.87$ while the right hand side of (17) equals 1.50. Thus, the system is robustly stable for larger uncertainty than shown in Table 1. Also of interest is that the design of (55) has a closed loop modal matrix with condition number equal to 5.83 as compared with 4.56 for the

design of (56). Thus, as we have also seen in the F-16 example, optimizing (54) seems to provide other desirable system characteristics. The time responses to an initial sideslip of one degree are shown for the designs of (55) and (56) in Figures 13 and 14, respectively. We observe that the new design has a slighter larger peak in yaw rate and a slightly faster response.

F. L-1011 Aircraft with Gain Suppression

We consider computing a robust eigenstructure assignment feedback gain matrix where certain outputs are not fed back to certain inputs. This is equivalent to constraining some elements of the feedback gain matrix to be zero. By suppressing certain gains to zero, we reduce controller complexity and improve reliability.

Mathematically, the output feedback gain matrix F using eigenstructure assignment satisfies (see Andry et. al., 1983)

$$F \Omega = \Psi \quad (57)$$

where Ω and Ψ depend upon the open loop system, the closed loop eigenvalues, and the closed loop eigenvectors. As shown by Andry et. al.(1983), each row of feedback gains (f_i) can be computed independently of all other rows. That is,

$$f_i = \psi_i \Omega^{-1} \quad (58)$$

If we were to constrain f_{ij} to be zero, then we delete f_{ij} from f_i^T and delete the j -th column of Ω^T . We now solve the reduced problem given by

$$\tilde{\Omega}^T \tilde{f}_i^T = \psi_i^T \quad (59)$$

where $\tilde{\Omega}^T$ is the matrix Ω^T with its j -th column deleted and \tilde{f}_i^T is the

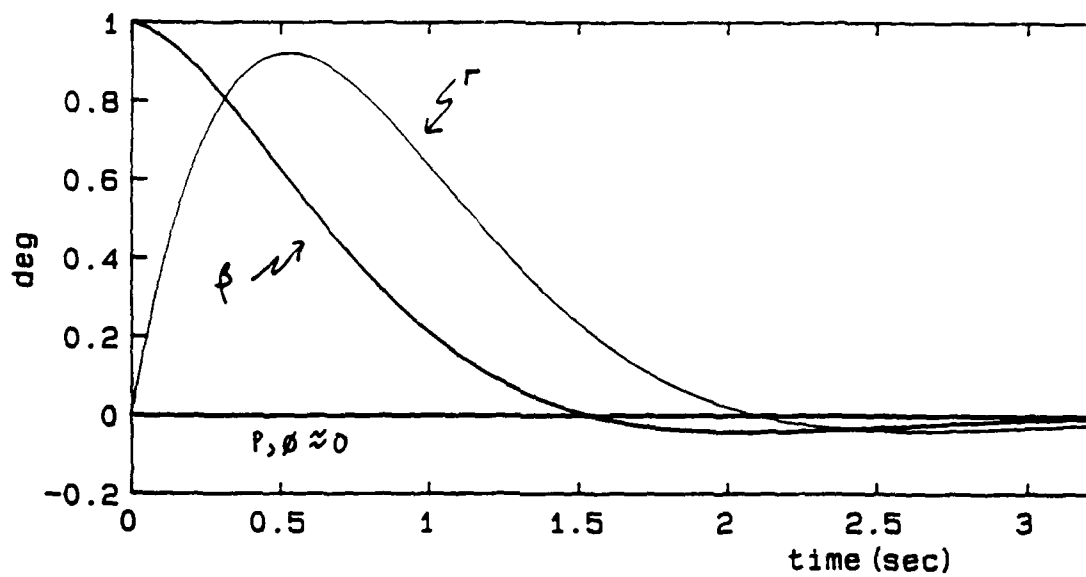


Figure 13. L-1011 State Feedback Initial Design

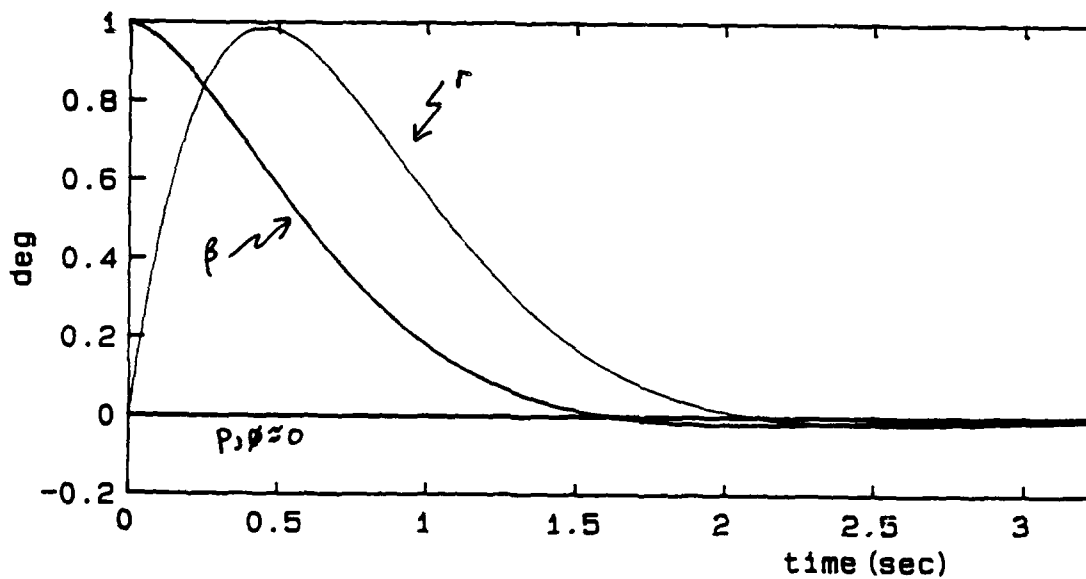


Figure 14. L-1011 State Feedback Robust Design

vector f_i^T with its j -th element deleted. Eq.(59) may be solved for \tilde{f}_i , the remaining active gains in the i -th row, as shown by Andry et. al. (1983). If more than one gain in a row of F is to be set to zero, then (59) should be appropriately modified.

First, we determine which gains may be set to zero while having the least impact on the closed loop eigenvalues and eigenvectors. We compute the eigenvalue decision matrix D^λ and the eigenvector decision matrix D^v as described by Sobel et. al. (1990). The eigenvalue decision matrix is given by

$$D^\lambda = \begin{bmatrix} .02185 & \underline{.64226} & .02173 & \underline{.29302} \\ \underline{.86204} & .00786 & \underline{1.16413} & .02358 \end{bmatrix} \quad (60)$$

and the eigenvector decision matrix is given by

$$D^v = \begin{bmatrix} .05228 & .51731 & .05201 & .23612 \\ .15345 & \underline{.60016} & .20723 & \underline{1.23568} \end{bmatrix} \quad (61)$$

The large entries in (60), denoted by an underline, are the elements of F which need to be non-zero based upon eigenvalue considerations. Thus, we could constrain f_{11} , f_{13} , f_{22} , f_{24} to be zero based solely upon their small effect on the closed loop eigenvalues. However, from (61) we observe that f_{22} and f_{24} are important for eigenvector considerations. Therefore, we choose to constrain only f_{11} and f_{13} to be zero.

An eigenstructure assignment feedback gain matrix with $f_{11}=f_{13}=0$ is computed using the same choice for the desired eigenvalues and eigenvectors which were used in section E. The closed loop eigenvalues are given by

$$\begin{aligned} \lambda_{dr} &= -1.5 \pm j1.5 \\ \lambda_{roll} &= -1.97 \pm j0.20 \end{aligned}$$

and the feedback gain matrix is given by

$$F = \begin{bmatrix} 0.0 & 3.52 & 0.0 & -3.46 \\ 4.45 & 1.28 & 2.63 & -5.68 \end{bmatrix}$$

We evaluate the stability robustness condition of (17) where $\alpha = 1.50$ and the right hand side of (17) equals 1.67. Therefore, the stability robustness sufficient condition is not satisfied. We optimize (54) with the additional parameter of $\text{Im}[\lambda_{dr}]$ as compared with the full state robust design. We also include the constraint given by $1.0 \leq \text{Im}[\lambda_{dr}] \leq 2.0$ in addition to the constraints which were used in the full state robust design. However, an important difference is that now the constraints apply only to the eigenvalues used for subspace computation and not to the actual closed loop eigenvalues. The optimized design has eigenvalues for subspace computation given by

$$\begin{aligned} \lambda_{dr} &= -1.74 \pm j1.96 \\ \lambda_{roll} &= -2.00 \pm j0.958 \end{aligned}$$

and closed loop eigenvalues given by

$$\begin{aligned} \lambda_{dr} &= -1.77 \pm j1.85 \\ \lambda_{roll} &= -1.77 \pm j1.01 \end{aligned}$$

The robust feedback gain matrix is given by

$$F = \begin{bmatrix} 0.0 & 4.62 & 0.0 & -6.11 \\ 3.69 & 1.47 & 2.27 & -6.48 \end{bmatrix}$$

We now find that $\alpha = 1.77$ while the right hand side of (17) equals 1.63. Therefore, robust stability is ensured for the uncertainty described in Table 1. Also of interest is that we have reduced the condition

number of the closed loop modal matrix from 5.78 to 4.99 which indicates that optimizing (54) yields other desirable closed loop system characteristics. The non-robust and robust time responses for an initial sideslip of one degree are shown in Figures 15 and 16, respectively. We observe that both designs exhibit perfect decoupling between the dutch roll mode and the roll mode.

G. L-1011 Aircraft with Dynamic Compensation

The use of constant gain output feedback is desirable because of the simplicity of the resulting control structure. However, it may not always be possible to achieve the dual goals of performance and robustness with a constant gain controller using only output feedback. In fact, if the number of outputs is too small, it may not even be possible to achieve the performance specifications using constant gain output feedback.

Sobel and Shapiro (1987b) have considered flight control design using eigenstructure assignment with low order dynamic compensators. This allows performance specification to be achieved in the case of very limited measurements. Mathematically, the linear time-invariant dynamical controller is described by

$$\dot{z} = Dz + Ey \quad (62)$$

$$u = Fz + Gy \quad (63)$$

where the controller state z is of dimension ℓ , $0 \leq \ell \leq n-r$.

It is convenient to model the plant and compensator by the composite system originally proposed by Johnson and Athans (1970). Thus, define

$$\dot{\bar{x}} = \bar{A} \bar{x} + \bar{B} \bar{u} \quad (64a)$$

$$\bar{y} = \bar{C} \bar{x} \quad (64b)$$

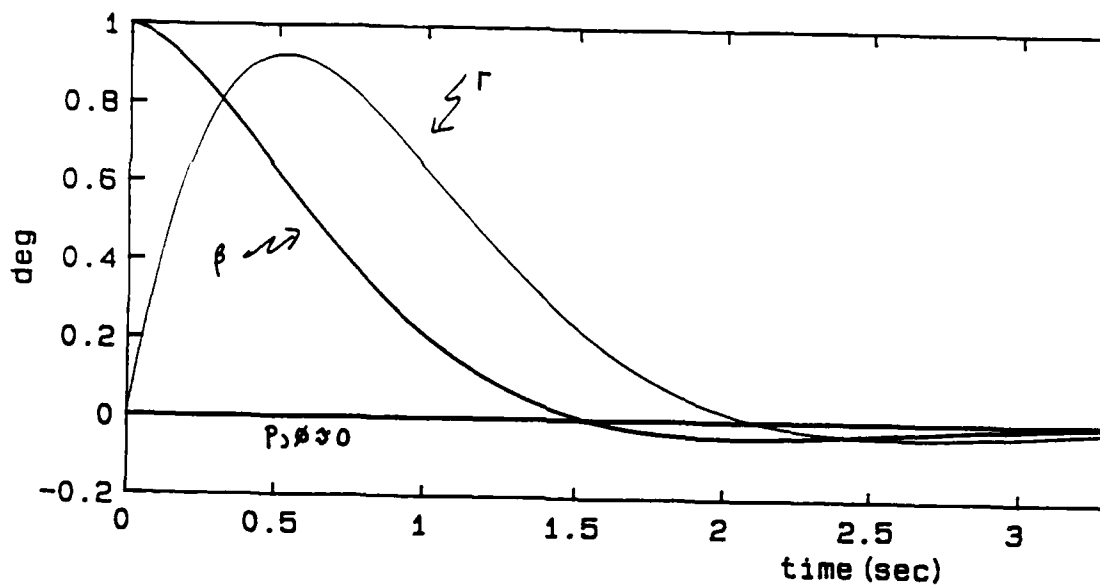


Figure 15. L-1011 Gain Suppression Initial Design

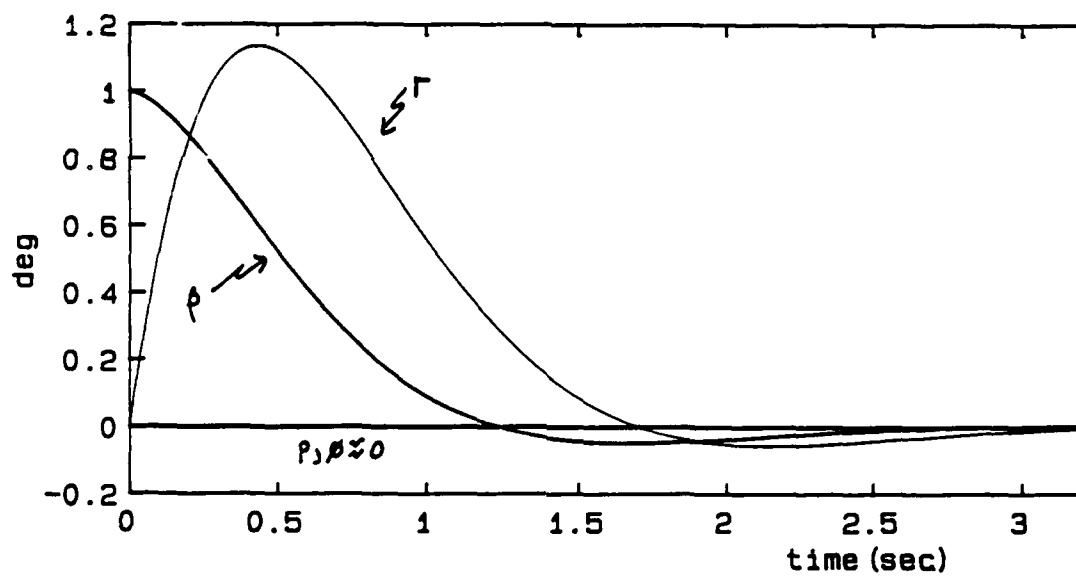


Figure 16. L-1011 Gain Suppression Robust Design

$$\bar{u} = \bar{F} \bar{y} \quad (65)$$

$$\text{where } \bar{x} = \begin{bmatrix} x \\ z \end{bmatrix}; \bar{A} = \begin{bmatrix} A & 0 \\ 0 & 0 \end{bmatrix}; \bar{B} = \begin{bmatrix} B & 0 \\ 0 & I \end{bmatrix}$$

$$\bar{C} = \begin{bmatrix} C & 0 \\ 0 & I \end{bmatrix}; \bar{F} = \begin{bmatrix} G & F \\ E & D \end{bmatrix}$$

Consider the L-1011 aircraft where we assume that sideslip angle may not be measured. For a second order dynamic compensator, the structure is described by

$$\bar{A} = \begin{bmatrix} A_{4 \times 4} & 0 \\ 0 & 0_{2 \times 2} \end{bmatrix}; \bar{B} = \begin{bmatrix} B_{4 \times 2} & 0 \\ 0 & I_{2 \times 2} \end{bmatrix}; \bar{C} = \begin{bmatrix} C_{3 \times 4} & 0 \\ 0 & I_{2 \times 2} \end{bmatrix}$$

$$\bar{A}_m = \begin{bmatrix} A_m & 0 \\ 0 & 0_{2 \times 2} \end{bmatrix}; \bar{B}_m = \begin{bmatrix} B_m & 0 \\ 0 & 0_{2 \times 2} \end{bmatrix}$$

where A, B, A_m, B_m are the same as before and

$$C = \begin{bmatrix} 0 & 1 & 0 & 0 \\ 0 & 0 & 1 & 0 \\ 0 & 0 & 0 & 0 \end{bmatrix}$$

corresponding to $y^T = [p, \beta, \phi]$.

The desired closed loop eigenvalues are (five can be chosen because we have five outputs)

$$\lambda_{dr} = -1.5 \pm j1.5$$

$$\lambda_{roll} = -2.0 \pm j1.0$$

$$\lambda_5 = -3.0 \text{ (compensator eigenvalue)}$$

The achievable closed loop eigenvalues are

$$\begin{aligned}\lambda_{dr} &= -1.5 \pm j1.5 \\ \lambda_{roll} &= -2.0 \pm j1.0 \\ \lambda_5 &= -3.0 \text{ (compensator)} \\ \lambda_6 &= -3.64 \text{ (compensator)}\end{aligned}$$

The dynamic compensator is described by

$$\begin{bmatrix} \delta_r \\ \delta_a \end{bmatrix} = \begin{bmatrix} 2.90 & 2.00 & 1.86 \\ 0.26 & 6.18 & 8.02 \end{bmatrix} \begin{bmatrix} r \\ p \\ \phi \end{bmatrix} + \begin{bmatrix} 2.13 & -2.13 \\ 3.51 & -3.51 \end{bmatrix} \begin{bmatrix} z_1 \\ z_2 \end{bmatrix} \quad (66)$$

$$\begin{bmatrix} \dot{z}_1 \\ \dot{z}_2 \end{bmatrix} = \begin{bmatrix} -2.46 & -0.54 \\ -1.50 & -1.50 \end{bmatrix} \begin{bmatrix} z_1 \\ z_2 \end{bmatrix} + \begin{bmatrix} 0.96 & 1.54 & 3.54 \\ 0.0 & -0.50 & -0.50 \end{bmatrix} \begin{bmatrix} r \\ p \\ \phi \end{bmatrix} \quad (67)$$

We evaluate the stability robustness condition to find $\alpha = 1.5$ and the right hand side of (17) equals 13.6 which indicates that the sufficient condition is not satisfied.

A robust design is computed by optimizing (54) over all 25 possible parameters. These include the eigenvalues $\lambda_1, \dots, \lambda_5$ and their corresponding eigenvector parameter vectors z_1, \dots, z_5 . The constraints on the eigenvalues are $-\infty < \text{Re}[\lambda_i] \leq -0.5$ for $i=1, \dots, 5$ which are chosen to ensure some degree of nominal relative stability. The optimized design has closed loop eigenvalues given by

$$\begin{aligned}\lambda_{dr} &= -1.03 \pm j1.08 \\ \lambda_{roll} &= -1.98 \pm j1.13 \\ \lambda_5 &= -6.61 \\ \lambda_6 &= -5.01\end{aligned}$$

and the dynamic compensator is described by

$$\begin{bmatrix} \dot{\delta}_r \\ \dot{\delta}_a \end{bmatrix} = \begin{bmatrix} 1.92 & .070 & -.005 \\ -2.57 & 4.23 & 0.456 \end{bmatrix} \begin{bmatrix} r \\ p \\ \phi \end{bmatrix} + \begin{bmatrix} 0.405 & -.0005 \\ 0.083 & -3.94 \end{bmatrix} \begin{bmatrix} z_1 \\ z_2 \end{bmatrix} \quad (68)$$

$$\begin{bmatrix} \dot{z}_1 \\ \dot{z}_2 \end{bmatrix} = \begin{bmatrix} -7.45 & -3.71 \\ 0.618 & -2.87 \end{bmatrix} \begin{bmatrix} z_1 \\ z_2 \end{bmatrix} + \begin{bmatrix} 5.12 & 0.442 & 0.758 \\ -1.41 & 1.28 & -5.41 \end{bmatrix} \begin{bmatrix} r \\ p \\ \phi \end{bmatrix} \quad (69)$$

Unfortunately, we find $\alpha = 1.03$ while the right hand side of (17) equals 1.97 which indicates that the sufficient condition for robust stability is not satisfied. However, note that the difference between the right and left hand sides of (17) is significantly smaller than for the initial design. We conclude that the sufficient condition cannot be satisfied for the A_m and B_m described in Table 1. However, if we let A_m and B_m be replaced by $A_m/2$ and $B_m/2$ then we find that $\alpha = 1.03 > 0.986$ so that robust stability can be ensured for uncertainty which equals one-half the uncertainty shown in Table 1. The time responses for the initial and optimized designs for an initial one degree sideslip are shown in Figures 17 and 18, respectively. We observe that both designs exhibit similar and acceptable time responses.

VI. ROBUST EIGENSTRUCTURE ASSIGNMENT (STEEPEST DESCENT)

A. Overview

In this section, a subset of the nominal eigenvalues and eigenvectors will be changed by moving in the direction of the negative gradient of (54). Suppose that the chosen parameters for the steepest descent search are placed in a vector p . Then, the parameters are updated according to

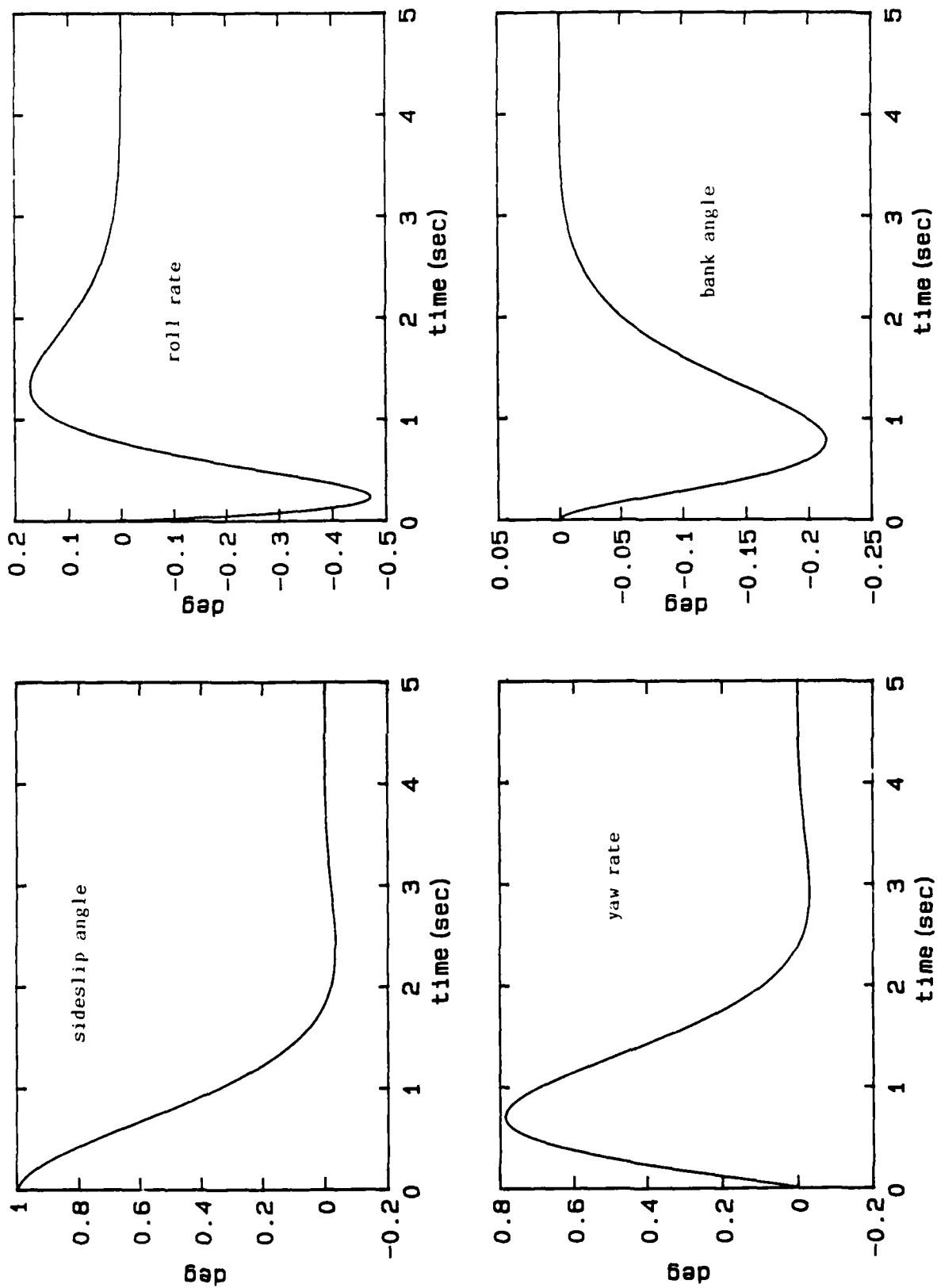


Figure 17. L-1011 Compensator Initial Design

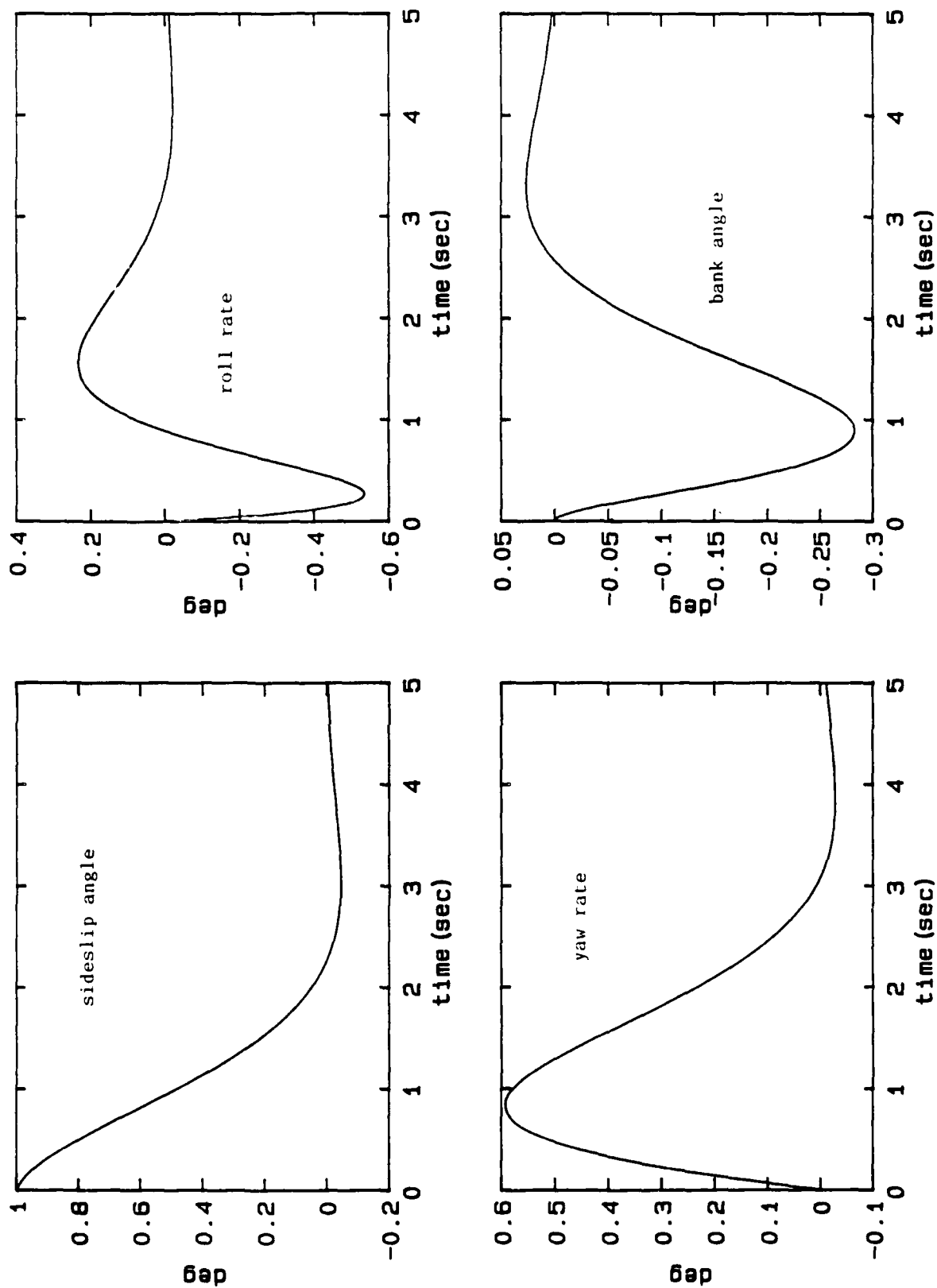


Figure 18. L-1011 Compensator Robust Design

the following: Given the vector p_k at step k , we find the vector p_{k+1} at step $k+1$ by using

$$p_{k+1} = p_k - \varepsilon_k g_k; \varepsilon_k > 0 \quad (70)$$

We stop the search when the stability robustness condition is just satisfied or equivalently when (54) becomes negative. The gradient g_k is computed numerically by calling IMSL subroutine ZXMIN with MAXFN = 1.

We compute robust eigenstructure assignment control laws for (1) the AFTI F-16 without Q weighting and (2) the L-1011 with gain suppression. These new designs will be compared to the designs in section V which utilized a constrained optimization.

B. AFTI F-16 Design

We return to the robust pitch pointing/vertical translation design of the AFTI F-16 aircraft which was considered in section V.D. We proceed in the negative gradient direction starting at the non-robust design with the parameters to be varied chosen to be the same as before. The condition given by (54) becomes negative with $\alpha = 3.3967$ and the right hand side of (17) equal to 3.3965. The closed loop eigenvalues are given by

$$\lambda_{sp} = -4.19 \pm j5.18$$

$$\lambda_y = -3.397$$

$$\lambda_{act} = -19.0$$

$$\lambda_{act} = -19.5$$

with feedback gain matrix given by

$$F = \begin{bmatrix} 2.699 & 0.6173 & 5.259 & -.3297 & -.0558 \\ -2.791 & 0.3412 & 3.8055 & -.1887 & -.0739 \end{bmatrix}$$

The condition number of the closed loop modal matrix is 40.77 which compares with 27.30 when using the constrained optimization. Thus, there is some advantage to optimizing (54) rather than just varying the parameters until (54) is negative. This is because a small condition number of the closed loop modal matrix is advantageous in terms of reducing an upper bound on the incremental eigenvalue sensitivity. We also observe that since the steepest descent method is an unconstrained approach, $\text{Re}[\lambda_{sp}]$ and λ_y have undergone a larger change than was the case in the constrained optimization. Therefore, using the method shown in this section results in a larger change in the nominal system performance. Overall, we recommend using the constrained optimization approach which was shown in section V.

C. L-1011 Aircraft with Gain Suppression

We now return to the robust design of a control law for the L-1011 aircraft with gain suppression which was considered in section V.F. We proceed in the negative gradient direction starting at the non-robust design with the parameters to be varied chosen to be the same as in section V.F. The condition given by (54) just becomes negative with $\alpha = 1.5098$ and the right hand side of (17) equal to 1.5098.

The robust design has eigenvalues for subspace computation described by

$$\begin{aligned}\lambda_{dr} &= -1.51 \pm j1.68 \\ \lambda_{roll} &= -1.81 \pm j1.15\end{aligned}$$

and closed loop eigenvalues described by

$$\begin{aligned}\lambda_{dr} &= -1.51 \pm j1.68 \\ \lambda_{roll} &= -1.79 \pm j1.14\end{aligned}$$

The robust feedback gain matrix is given by

$$F = \begin{bmatrix} 0.0 & 3.53 & 0.0 & -4.24 \\ 4.00 & 1.26 & 2.29 & -5.85 \end{bmatrix}$$

The condition number of the closed loop modal matrix is 4.60 which compares with 4.99 when using the constrained optimization approach. So the unconstrained steepest descent solution has a slightly smaller condition number. This is in contrast to the F-16 problem where the constrained optimization approach yielded a significantly smaller condition number. Also, the steepest descent method has slightly smaller gains and eigenvalues which are closer to the non-robust design. We conjecture that this behavior may be caused by choosing the constraint intervals to be larger than needed when using the constrained optimization in section V.F. When considering the results of both examples, we recommend using the constrained optimization approach. However, several designs may be required in order to obtain a good choice for the constraint intervals.

VII. SIMULTANEOUS STRUCTURED STATE SPACE UNCERTAINTY AND UNMODELLED DYNAMICS

A. Problem Formulation

We now consider the stability robustness of linear time-invariant systems with simultaneous time-varying structured state space uncertainty and unmodelled dynamics. Consider a nominal linear time-invariant multi-input multi-output plant described by (1). Suppose that the nominal plant is subject to linear time-varying uncertainties $\Delta A(t)$ and $\Delta B(t)$, as shown by (2). Furthermore, suppose that the unmodelled dynamics may be represented by an unknown nonlinear function $\Delta h(u)$ which affects the

output. Then, the uncertain plant may be described by

$$\dot{x} = Ax + Bu + \Delta A(t)x + \Delta B(t)u \quad (71a)$$

$$y = Cx + \Delta h(u) \quad (71b)$$

Further, suppose that $\|\Delta h(u)\|$ is bounded by

$$\|\Delta h(u)\| \leq \gamma \cdot \|u(t)\| \quad (72)$$

This representation of the plant with structured state space uncertainty and unmodelled dynamics is shown in Figure 19.

Problem III: Given a feedback gain matrix $F \in \mathbb{R}^{m \times r}$ such that the nominal closed loop system exhibits desirable dynamic performance, determine if the uncertain closed loop system is asymptotically stable for all $\Delta A(t)$ and $\Delta B(t)$ described by (4) and all $\Delta h(u)$ described by (72).

B. Stability Robustness Result

We present a sufficient condition for the robust stability of a linear time-invariant system subjected to simultaneous time-varying parametric uncertainty and the class of unmodelled dynamics described by (72).

Theorem: Suppose F is such that the nominal closed loop system described by

$$\dot{x}(t) = (A+BFC)x(t)$$

is asymptotically stable with distinct eigenvalues. Then, the uncertain closed loop system given by

$$\dot{x}(t) = (A+BFC)x(t) + [\Delta A(t) + \Delta B(t)FC]x(t) + [B + \Delta B(t)]F \cdot \Delta h$$

is asymptotically stable for all $\Delta A(t)$ and $\Delta B(t)$ described by (4) and all $\Delta h(u)$ described by (72) if

$$\alpha > ||(M^{-1})^+ [A_m + B_m(FC)^+ M^+]||_2 + \beta ||(M^{-1})^+ (B^+ + B_m) F^+||_2 \quad (73)$$

where $\alpha = -\max_i \operatorname{Re}[\lambda_i(A + BFC)]$

$$\beta = \frac{\gamma \cdot ||F|| \cdot ||CM||}{1 - \gamma \cdot ||F||}$$

and $||F|| < 1/\gamma$

Proof:

$$\dot{x}(t) = Ax(t) + Bu(t) + \Delta A(t)x(t) + \Delta B(t)u(t) \quad (74)$$

$$y(t) = Cx(t) + \Delta h(u) \quad (75)$$

$$u(t) = Fy(t) \quad (76)$$

Combine (74), (75), and (76) to obtain

$$\begin{aligned} \dot{x}(t) &= Ax(t) + BFCx(t) + \Delta A(t)x(t) + \Delta BFCx(t) + [B + \Delta B]F\Delta h(u) \\ &= (A + BFC)x(t) + (\Delta A + \Delta BFC)x(t) + [B + \Delta B]F\Delta h(u) \\ &= A_c x(t) + \Delta A_c(t)x(t) + [B + \Delta B]F\Delta h(u) \end{aligned} \quad (77)$$

where $A_c = A + BFC$

and $\Delta A_c(t) = \Delta A(t) + \Delta BFC$

Let $x(t) = Mz(t)$

where M is a modal matrix for A_c .

Then,

$$\dot{z}(t) = M^{-1}A_c Mz(t) + M^{-1}\Delta A_c(t)Mz(t) + M^{-1}[B + \Delta B]F\Delta h(u)$$

which has a solution given by

$$z(t) = \exp(\Lambda t)z(0) + \int_0^t \exp(\Lambda(t-\tau)) [M^{-1}\Delta A_c(\tau)Mz(\tau) + M^{-1}[B+\Delta B(\tau)]F\Delta h(u)] d\tau$$

use $||\exp(\Lambda t)|| \leq \exp(-\alpha t)$ where $\alpha = -\max_i \operatorname{Re}[\lambda_i(A+BFC)]$

$$\begin{aligned}
||z(t)|| \leq & ||\exp(\Lambda t)|| \cdot ||z(0)|| + \int_0^t ||\exp(\Lambda(t-\tau))|| \cdot ||M^{-1}\Delta A_c(\tau)M|| \cdot ||z(\tau)|| d\tau \\
& + \int_0^t ||\exp(\Lambda(t-\tau))|| \cdot ||M^{-1}[B+\Delta B(\tau)]F\Delta h(u)|| d\tau \quad (78)
\end{aligned}$$

Consider the second integral in (78) which satisfies

$$\begin{aligned}
& \int_0^t ||\exp(\Lambda(t-\tau))|| \cdot ||M^{-1}[B + \Delta B(\tau)]F\Delta h(u)|| d\tau \\
& \leq \int_0^t \exp(-\alpha(t-\tau)) ||M^{-1}[B+\Delta B(\tau)]F|| \cdot ||\Delta h(u)|| d\tau \quad (79)
\end{aligned}$$

Recall that (72) is given by

$$||\Delta h(u)|| \leq \gamma \cdot ||u(t)||$$

Therefore,

$$\begin{aligned}
||\Delta h(u)|| & \leq \gamma \cdot ||u(t)|| \leq \gamma \cdot ||F|| \cdot ||y(t)|| = \gamma \cdot ||F|| \cdot ||CMz(t) + \Delta h(u)|| \\
& \leq \gamma \cdot ||F|| (||CMz(t)|| + ||\Delta h(u)||)
\end{aligned}$$

$$(1 - \gamma ||F||) ||\Delta h(u)|| \leq \gamma ||F|| \cdot ||CM|| \cdot ||z(t)||$$

which yields the following bound on $\Delta h(u)$

$$||\Delta h(u)|| \leq \beta ||z(t)|| \quad \text{if } 1 - \gamma ||F|| > 0 \quad (80)$$

$$\text{where } \beta = \frac{\gamma ||F|| \cdot ||CM||}{1 - \gamma ||F||}$$

Therefore, the second integral in (78) satisfies the following:

$$\begin{aligned}
& \int_0^t ||\exp(\Lambda(t-\tau))|| \cdot ||M^{-1}[B+\Delta B(\tau)]F\Delta h(u)|| d\tau \\
& \leq \int_0^t \exp(-\alpha(t-\tau)) \beta [||M^{-1}[B+\Delta B(\tau)]F||] \cdot ||z(\tau)|| d\tau \quad (81)
\end{aligned}$$

Substitute (81) into (78) to obtain

$$\begin{aligned}
||z(t)|| & \leq \exp(-\alpha t) ||z(0)|| + \int_0^t \exp(-\alpha(t-\tau)) [||M^{-1}\Delta A_c(\tau)M|| + \beta ||M^{-1}[B+\Delta B(\tau)]F||] ||z(\tau)|| d\tau \\
||z(t)|| \exp(\alpha t) & \leq ||z(0)|| + \int_0^t [||M^{-1}\Delta A_c(\tau)M|| + \beta ||M^{-1}[B+\Delta B(\tau)]F||] \exp(\alpha \tau) ||z(\tau)|| d\tau
\end{aligned}$$

Use the Gronwall lemma to obtain

$$||z(t)|| \exp(\alpha t) \leq ||z(0)|| \exp\left[\int_0^t \{ ||M^{-1} \Delta A_c(\tau) M|| + \beta ||M^{-1} [B + \Delta B(\tau)] F|| \} d\tau \right]$$

$$||z(t)|| \exp(\alpha t) \leq ||z(0)|| \exp\left[\int_0^t \{ ||(M^{-1})^+ [A_m + B_m (FC)^+] M^+|| + \beta ||(M^{-1})^+ [B^+ + B_m] F^+|| \} d\tau \right]$$

$$\leq ||z(0)|| \exp\{ \{ ||(M^{-1})^+ [A_m + B_m (FC)^+] M^+|| + \beta ||(M^{-1})^+ [B^+ + B_m] F^+|| \} t \}$$

Thus,

$$||z(t)|| \leq ||z(0)|| \exp\{ \{ -\alpha + ||(M^{-1})^+ [A_m + B_m (FC)^+] M^+|| + \beta ||(M^{-1})^+ [B^+ + B_m] F^+|| \} t \}$$

Thus, $||z(t)||$ goes to zero, and hence $||x(t)||$ goes exponentially to zero

$$\text{if } \alpha > ||(M^{-1})^+ [A_m + B_m (FC)^+] M^+|| + \beta ||(M^{-1})^+ [B^+ + B_m] F^+||$$

where

$$\beta = \frac{\gamma ||F|| \cdot ||CM||}{1 - \gamma ||F||} ; \gamma < ||F||^{-1} \text{ or } ||F|| < 1/\gamma$$

End of proof

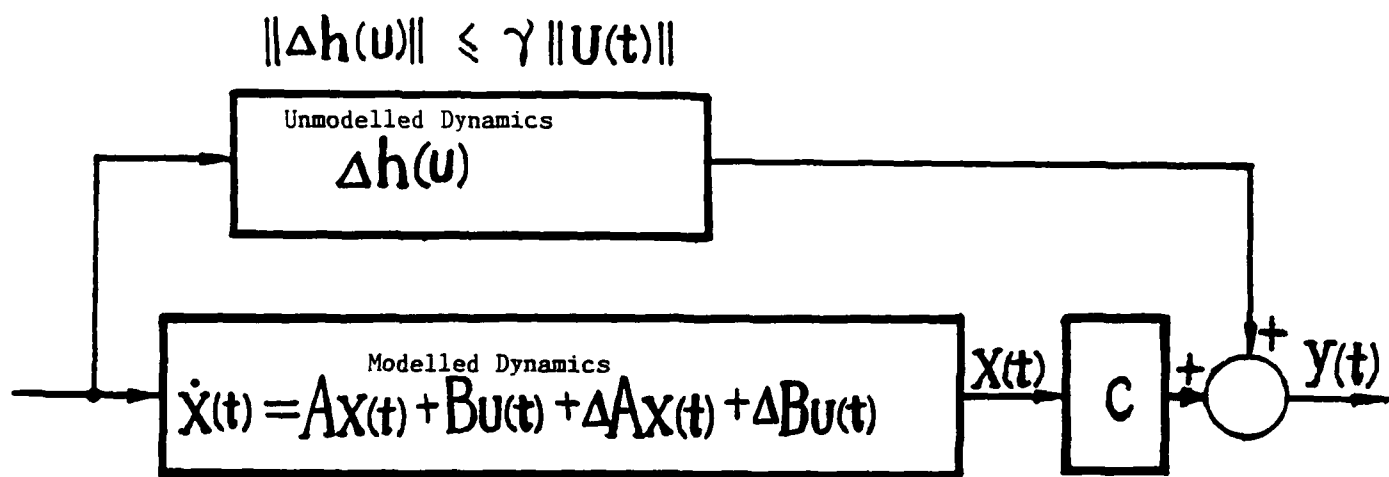


Figure 19. Representation for Unmodelled Dynamics

VIII. RECOMMENDATIONS

The optimization problem was solved by using a DFP algorithm with a numerically computed gradient which is obtained via a finite difference method. The optimization would be more efficient if analytical expressions could be obtained for the gradient and the Hessian matrix. If an analytic expression can only be found for the gradient, then perhaps the conjugate gradient method could be utilized.

Future work should consider methods for further reducing the conservatism of the sufficient conditions. A systematic method needs to be found for computing the state transformation matrix T . A proof is needed for the conjecture which is currently used to obtain the unitary weighting matrix Q .

Other representations for the unmodelled dynamics need to be considered. One potential candidate is to consider the output to be affected by a convolution operation between $\Delta h(t)$ and the plant input. The relationship between unmodelled high frequency dynamics represented in the frequency domain and the function $\Delta h(t)$ needs to be studied.

Robustness results in the frequency domain are usually stated in terms of the singular values of some matrix. The relationship between the robustness conditions derived from the Gronwall lemma and the singular values of a suitable matrix should be studied.

PAPERS PREPARED DURING THE 1988 RIP PROGRAM

W. Yu and K. M. Sobel, "Performance Robustness for LTI Systems with Structured State Space Uncertainty", International Journal of Control, in review; also submitted to the 1990 American Control Conference, San Diego, California, May 1990

K. M. Sobel and W. Yu, "Flight Control Application of Eigenstructure Assignment with Optimization of Robustness to Structured State Uncertainty", Proceedings of the 28th IEEE Conference on Decision and Control, Tampa, Florida, December 1989

W. Yu and K. M. Sobel, "Robust Eigenstructure Assignment with Structured State Space Uncertainty", Journal of Guidance, Control, and Dynamics, in preparation

W. Yu and K. M. Sobel, "Stability Robustness of LTI Systems with Structured State Space Uncertainty and a Class of Unmodelled Dynamics, 29th IEEE Conference on Decision and Control, Honolulu, Hawaii, December 1990, in preparation

REFERENCES

- Andry, A. N., Jr., Shapiro, E. Y., and Chung, J.C., 1983, IEEE Transactions on Aerospace and Electronic Systems, 19, 711
- Chen, C. T., 1970, Introduction to Linear System Theory (New York, NY: Holt, Rinehart, and Winston, Inc.)
- Golub, G. H., and Van Loan, C. F., 1983, Matrix Computations (Baltimore, MD: The Johns Hopkins University Press)
- Haftka, R. T., and Starnes, J. H., Jr., 1976, AIAA Journal, 14, 718
- Harvey, C. H., and Stein, G., 1978, IEEE Transactions on Automatic Control, 23, 378
- Juang, Y. T., Hong, Z. C., and Wang, Y. T., 1989, IEEE Transactions on Automatic Control, 34, 758
- Kouvaritakis, B., and Latchman, H., 1985, International Journal of Control, 41, 1381
- O'Brien, M. J., and Broussard, J. R., 1978, Feedforward Control to Track the Output of a Forced Model, Proceedings of the 17th IEEE Conference on Decision and Control, 1149-1155
- Sobel, K. M., and Shapiro, E. Y., 1985, Journal of Guidance, Control, and Dynamics, 8, 181
- Sobel, K. M., and Shapiro, E. Y., 1987a, Flight Control Examples of Robust Eigenstructure Assignment, Proceedings of the 26th IEEE Conference on Decision and Control, Los Angeles, California
- Sobel, K. M., and Shapiro, E. Y., 1987b, Journal of Guidance, Control, and Dynamics, 10, 73

Sobel, K. M., Banda, S. S., and Yeh, H. H., 1989, Structured State Space Robustness with Connection to Eigenstructure Assignment, Proceedings of the 1989 American Control Conference, Pittsburgh, 966-973

Sobel, K. M., Yu, W., and Lallman, F. J., 1990, Eigenstructure Assignment with Gain Suppression Using Eigenvalue and Eigenvector Derivatives, Journal of Guidance, Control, and Dynamics, to appear

Srinathkumar, S. 1976, Spectral Characterization of Multi-Input Dynamic Systems, Ph.D. Thesis, Oklahoma State University

Stoer, J., and Witzgall, C., 1964, Numerical Mathematics, 4, 458

Vidyasagar, M., 1978, Nonlinear Systems Analysis (Englewood Cliffs, NJ: Prentice Hall)

Yedavalli, R. K., and Liang, Z., 1986, IEEE Transactions on Automatic Control, 31, 863

RESEARCH INITIATION PROGRAM MINI-GRANT

1988

Sponsored by the
AIR FORCE OFFICE OF SCIENTIFIC RESEARCH

Administered by
Universal Energy Systems, Inc.

Supported by the
AFWAL/FIES
Flight Dynamics Laboratory

FINAL REPORT

COMPARATIVE BURNING RATES

AND

DUPLEX LOADS OF SOLID PROPELLANTS

Prepared by:	Forrest D. Thomas II
Academic Rank:	Professor of Chemistry
Department:	Department of Chemistry
University:	University of Montana
Research Location:	Department of Chemistry University of Montana and Missoula County Sheriff's Department Firearms Training Facility, Missoula, Montana
Researchers:	Forrest D. Thomas II Edward J. Keller
Date:	31 December 1988
Contract No.:	#F49620-85-C-0013/SB585-0360

COMPARATIVE BURNING RATES
AND
DUPLEX LOADS OF SOLID PROPELLANTS

By

Forrest D. Thomas II and Edward J. Keller

ABSTRACT

A barrel mount was made from railroad ties and a 1/2 inch steel plate.

A golf cart was modified for barrel transportation.

Three PACT chronographs were used. Velocity printouts obtained via a Hewlett-Packard Infrared printer.

Three Hewlett-Packard power converters provided 90 volts D.C. for the firing system.

Projectiles were 565 grain black polyethylene cylinders, except where noted for IMR-4831. Velocities were measured 20ft from the muzzle.

IMR-4831: 1500 through 2500 grains, case failure, maximum load, velocity over 7000 ft./sec.

IMR-4350: 1900 through 2400 grains, some case failure, near maximum load, velocity near 7000 ft./sec.

IMR-4320: 1800 through 2300 grains, case failure, maximum load, velocity over 7000 ft./sec.

IMR-4895: 1700 through 2000 grains, some case failure, near maximum load, velocity over 7000 ft./sec.

IMR-4064: 1800 grains to compare current results with previous data, Summer 1987, WPAFB.

IMR-3031: 1300 through 1700 grains, under maximum load, velocity to 6000 ft./sec.

IMR-4831: 1500 through 2400 grains, 1130 grain projectile, case failure, over maximum load, velocity to 7000 ft./sec.

Velocities over 7000 ft./sec. 20ft from the muzzle would calculate to over 8000 ft./sec. muzzle velocity.

ACKNOWLEDGEMENTS

Our thanks and appreciation are due to the Air Force Office of Scientific Research who sponsored this program. Thanks also to Mr. Rodney C. Durrah from Universal Energy Systems, Inc., who administered the program.

Captain Larry Ehle and his staff from the Flight Dynamics Laboratory, AFWAL/FIES. He and his staff provided equipment, supplies and support that were absolute necessities to successfully conduct this research project.

Personnel from the Missoula County Sheriff's Office and the Johnson-Bell airport security service were more than helpful in providing access to, and use of, the outdoor firing range.

Mr. Bob Evans, supervisor and Mr. Bruce C. Young of Omark Industries, provided information on ballistics, firing and pressure measurements.

I. Facilities Construction and Procedures

Barrel Mount. Four tiers of railroad ties were bolted together. A one-half inch thick steel plate was bolted to the top row of ties. The barrel recoil plate was bolted to the steel plate for firing.

Barrel Transportation. A golf cart trailer was modified by welding steel tube to the undercarriage to support a hydraulic hoist. Two sections of railroad tie with 4-inch notches were bolted to the trailer bed to cradle the barrel for transportation to and from the range.

Velocity Measurements. Two, then three PACT chronographs were placed in a foam padded 11" x 7" x 5.5" steel ammunition container. The chronographs were placed 15ft (the length of the skyscreen leads) to the side of the skyscreen array. Muzzle blast affected the chronographs resulting in multiple and erroneous readings. A box, 18" x 12" x 22", was made of 3/4-inch plywood and lined with 3-4 inches of styrofoam and foam padding. The steel container with the chronographs was placed in the insulated wood box. This seemed to sufficiently protect the chronographs from the muzzle blast shock.

A Hewlett-Packard HP82240A Infrared Printer was used to obtain a printout of the chronographs memories. The chronographs retained all triggered data, even erroneous data but only displayed the last stimulation. Sometimes, muzzle blast and/or adjusting the skyscreen bracket for barrel sighting would trigger the skyscreens. Before and after each shot, the chronograph display was recorded. A full memory printout was then necessary to determine which readings were projectile velocities and which were erroneous data. (Once, the shadow of an airplane leaving the airport triggered the skyscreens).

Skyscreens. Initially, a skyscreen bracket was constructed from wood to accommodate two sets of skyscreens spaced 24-inches apart for 2 chronographs. When velocities above 7000 ft./sec. were achieved, it became necessary to construct another bracket to allow 48-inch separations. The chronographs were factory set to record velocities up to 6999 ft./sec. with 24-inch spacings. The factory recommended 48-inch spacings and doubling the chronographs output. Finally, a third bracket, 5.5 feet long was made to accommodate 3 sets of skyscreens with 48-inch spacings for 3 chronographs. The skyscreen brackets were designed to be mounted on a camera tripod. The skyscreens had to be positioned before each shot to line up with the barrel. Dust thrown up by the muzzle blast sometimes seemed to affect the skyscreens. Black plastic

sheet, laid from the muzzle to the skyscreens, seemed to resolve that problem.

Electrical System to Fire Electric Primers. The range house provided 110-120 volt A.C. power. Three Hewlett-Packard 6216A 30 volt D.C. power supplies in series fired the electric primers. Preliminary tests showed that 30 volts D.C. was insufficient to fire the primers, while 60 volts did fire the primers. A series of three power supplies (90 volts) was used for firing. The power supply output was wired to a power supply firing off-on switch. From there, leads were run to the barrel mount and connected to the barrel off-on switch. From the barrel off-on switch, the power leads went to the barrel and the primer wire. The power supply and firing switch were located 50ft from the side of the barrel.

The Barrel. See Figure I. This is the same 30mm smooth bore barrel used at WPAFB during the Summer of 1987 for the study of "High Velocity Projectiles."

Case Loading. Cases were used 30mm GAU-8 aluminum cases.

Depriming. The fired cases were set on a 4" x 4" x 4" wood block above a 1/2" x 3" hole. An iron rod was placed in the case on top of the flash tube and the ram of a hydraulic press gently pushed the spent primer and flash tube out the bottom of the case.

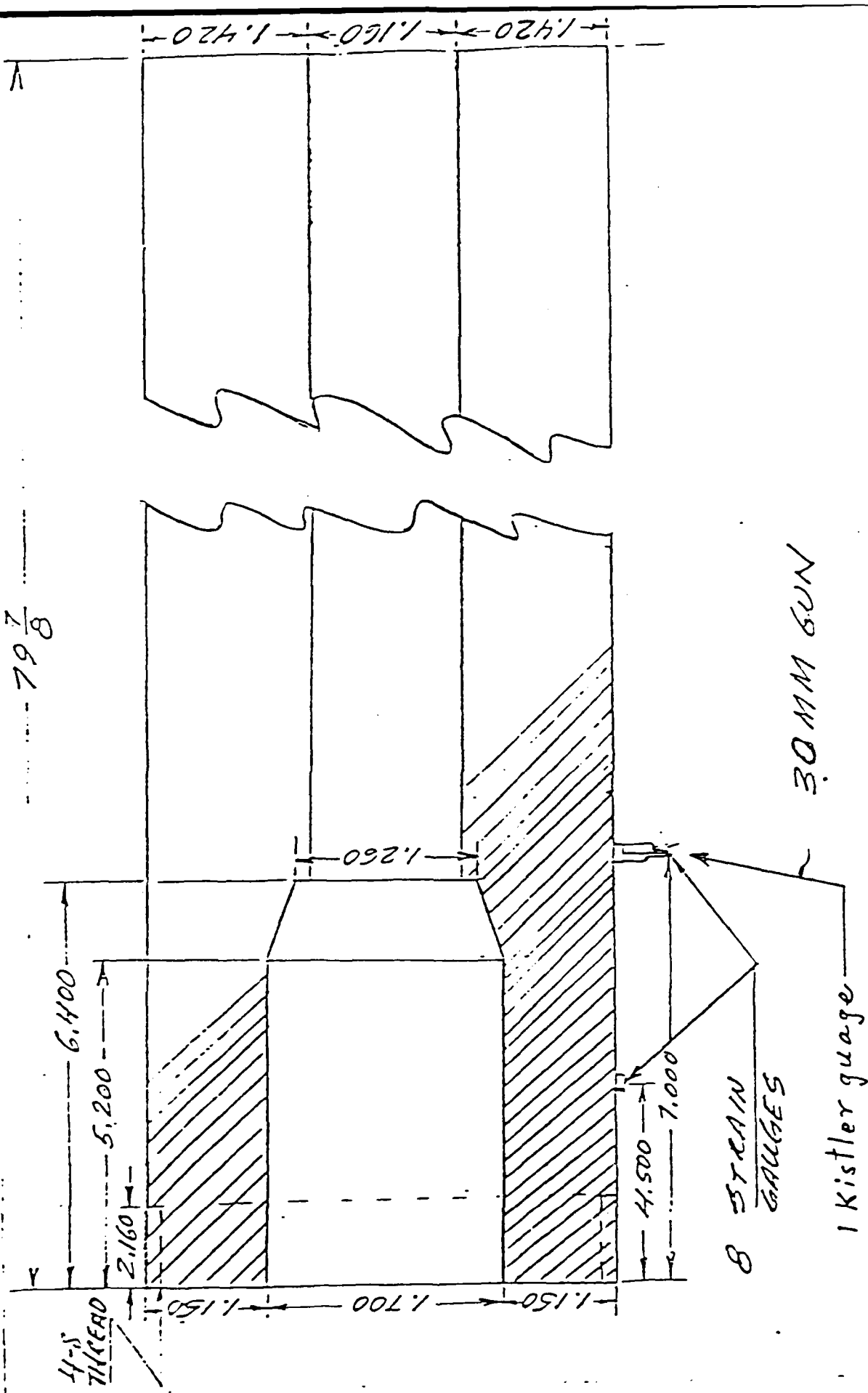
Priming. The mouth of the flash tube was sealed with a cellophane dot and filled with Pyrodex P powder. The flash tube was inserted into the primer pocket, with the case neck down. The live primer was placed onto the primer pocket opening. A 1/2" x 10" metal tube was inserted up into the case, around the flash tube, to the inside base of the case. This assembly was placed on a wood block under the ram of the hydraulic press. The ram was lowered down against the primer to set it flush with the outside base of the case, support being provided by the metal tube inside the case.

Powder. All powder charges were weighed on a Ohaus Dial-O-Grain 3100 scale. A thin circular sheet of plastic foam was used as an over the powder wad to hold the powder in place when the case was loaded into the chamber of the barrel. Space, if any, above the powder wad to the base of the projectile was filled with puffed rice.

Projectiles. Initially, projectiles were machined from 1-1/4" white polyethylene rod to 565 grains. These white projectiles against a dark blue clear sky did not appear to consistently trigger the skyscreens. For most of

Figure 1

797/8



the tests, the projectiles were machined from 1-1/4" black polyethylene rod to 565 grains and 1130 grains. The black projectiles seemed to work better than the white ones. Each was weighed before loading. Since a case neck-sizing die was not available, the projectiles were machined to fit the unsized case necks. Generally, cases are sized to adequately hold standard projectiles. But because these cases, even after firing, easily fit into the chamber of the barrel, it was just as convenient to make the plastic projectiles to fit the unsized cases. The projectiles were seated into the case necks by the ram of the hydraulic press.

Range Facilities. The Missoula County Sheriff's outdoor shooting range, about 5 miles west of Missoula, was used for testing. The range is located off the west end of the Johnson-Bell airport in a small canyon that provides a large soft dirt bank for the impact area. The gun mount was left at the firing point and the barrel and the rest of the equipment were transported to the range for each test session. The usual live range protocols were followed during testing.

Firing Procedures. After all the equipment had been set up:

1. Power supply firing switch off.
2. Barrel switch off.
3. Power leads grounded to barrel.
4. One person loads one round.
5. Connect ground wire to breach, live wire to primer wire.
6. Double check power supply firing switch off.
7. Turn barrel switch on, retire to power supply point.
8. Five second count down to fire, power supply firing switch on.
9. After firing, power supply firing switch off, barrel switch off, disconnect power leads and ground to barrel, and remove empty case.
10. Record data.
11. Repeat sequence for next shot.

Misfire

1. Power supply firing switch off.
2. Five minute delay.
3. Barrel switch off.

4. Disconnect, ground and reconnect power leads.
5. Repeat firing sequence, from step 6 on.

Repeat Misfire

1. Power supply firing switch off.
2. Five minute delay.
3. Barrel switch off.
4. Disconnect and ground lead wires.
5. Remove breach cap.
6. Replace primer wire. (The few misfires that occurred were all due to faulty primer wires).
7. Repeat firing sequence.

II. Results

All tests were run with used 30mm GAU-8 aluminum cases of unknown background. During these current tests, all cases were numbered and their sequence of use noted. With the heavier powder charges, severe physical erosion of the inside case shoulders and especially the inside of the case necks occurred. This appears to be due to unburnt powder granules being forcefully ejected from the case mouth by the initial combustion of the powder at the base of the charge. Thus, when case necks begin to disappear, it is not necessarily a true measure of a new cases' ability or capacity to withstand the effects of what appears to be a maximum or near-maximum load compared to second, third or more firings for used cases.

IMR-4831, relative burning rate 95, was tested from 1500 grains through 2500 grains in 100 grain increments with 565 grain projectiles. 2500 grains appears to be a maximum load for the aluminum cases. (See Table I for results).

IMR-4350, relative burning rate 100, was tested from 1900 grains through 2400 grains in 100 grain increments with 565 grain projectiles. 2400 grains appears to be near maximum load for aluminum cases. (See Table II for results).

IMR-4320, relative burning rate 110, was tested from 1800 grains through 2300 grains in 100 grain increments with 565 grain projectiles. 2300 grains does not appear to be a maximum load for aluminum cases. (See Table III for results).

IMR-4895, relative burning rate 115, was tested from 1700 grains through 2000 grains in 100 grain increments with 565 grain projectiles. 2000 grains appear to be near maximum load for aluminum cases. (See Table IV for results).

IMR-4064, relative burning rate 120, was tested only at 1800 grains with 565 grain projectiles in order to compare these results with data obtained at WPAFB during the Summer of 1987. (See Table V for results).

IMR-3031, relative burning rate 135, was tested from 1300 grains through 1700 grains in 100 grain increments with 565 grain projectiles. This series was not completed to maximum loads. (See Table VI for results).

IMR-4831 was also tested from 1500 grains through 2400 grains in 100 grain increments with 1130 grain projectiles. 2400 grains appears to be over the maximum load for aluminum cases. (See Table VII for results).

In the Summer of 1987 at WPAFB, 2300 grains of IMR-4064 fired from heavy steel cases gave velocities of 7100 ft./sec. measured 18ft from the muzzle. Calculated muzzle velocity was 8200 ft./sec.

Several tests from this current study gave recorded velocities in excess of 7000 ft./sec. (see Table VIII), measured 20ft from the muzzle from the same barrel. These would also calculate to better than 8000 ft./sec. muzzle velocity. From used aluminum cases and single powders, these results are quite encouraging.

Table VIII compares velocity results for all powders tested at all loads with 565 grain projectiles.

Table IX compares velocity results for loads of IMR-4831 between the 565 grain and 1130 grain projectiles.

TABLE I
IMR-4831 (95)¹
ALUMINUM CASES, 30 mm GAU-8, USED

<u>Test No.</u>	<u>Velocity², ft/sec</u>	<u>Powder, gr.</u>	<u>Projectile⁵, gr.</u>
2	5380 5340	1500	~565
3	5801 -- ³	1600	~565
4	5270 5917	1700	~565
5	-- 4298	1800	~565
6	-- 5939	1900	~565
8	5789 --	2000	567 ⁶
10	5552 5588	2000	567
11	5988 --	2000	561
28	6040 --	2000	567
70	6230 6197 6250	2100 2nd case firing (31&70) some neck gone	570
71	6357 7204 6397	2100 2nd case firing (32&71) some neck gone	570
72	6962 6846 6757	2200 2nd case firing (33&72) some neck gone	571
73	6509 6509 6491	2200 2nd case firing (36&73) most neck gone	575
78	-- 6233 6337	2300	570

Table I cont.
Page -2-

79	-- 6966 6838	2300	569
90	-- 8270 ³ 8068	2300 neck eroded, but intact	560
91	-- 5970 6436	2300 neck eroded, but intact	562
92	-- 6517 6501	2400 neck eroded	562
93	-- 7711 7801	2400 neck eroded	561
102	6658 6636 6683	2500 neck gone, maximum load	569
103	7020 6899 6832	2500 neck gone, maximum load	565

1. Relative burning rate compared to the standard burning rate of 100 for IMR-4350.
2. Two PACT chronographs for 2 readouts, three PACT chronographs for 3 readouts. Velocities measured 20 ft from the muzzle.
3. No chronograph readout.
4. Although a high velocity reading, 2 of the 3 chronographs recorded these values.
5. Initial projectiles were machined from white plastic rod. Each was not weighed prior to use.
6. Projectiles machined from black plastic rod and each weighed prior to use.

TABLE II
IMR-4350 (100)¹
ALUMINUM CASES, 30 mm GAU-8, USED

<u>Test No.</u>	<u>Velocity², ft/sec</u>	<u>Power, gr.</u>	<u>Projectile⁴, gr.</u>
44	5569 5337	1900	565
45	5848 5930	1900	563
46	6216 6201	2000	563
47	6457 -- 3	2000	563
48	6433 6449	2100	565
49	6156 6374	2100	565
84	5438 5323 5405	2200	571
85	-- 5208 5224	2200	571
98	-- 6774 6737	2200	557
99	-- 6708 6309	2200	562
100	6849 6855 6170	2300	562
101	6808 6777 6625	2300	562
110	6680 6725 6667	2400 some neck gone, near maximum	565

Table II cont.

Page -2-

111	6565	2400	570
	6255	some neck gone, near maximum	
	6359		

1. Standard IMR - powder assigned a burning rate of 100.
2. Two PACT chronographs for 2 readouts, three PACT chronographs for 3 readouts. Velocities measured 20 ft. from the muzzle.
3. No chronograph readout.
4. Projectiles machined from black plastic rod and each weighed prior to use.

TABLE III
IMR-4320 (110)¹
ALUMINUM CASES, 30 mm GAU-8, USED

<u>Test No.</u>	<u>Velocity², ft/sec</u>	<u>Powder, gr.</u>	<u>Projectile⁴, gr.</u>
12	6488 6541	1800	566
13	6446 6463	1800	~560
18	6342 6374	1800	562
19	5165 4689	1800	565
14	7079 7084	1900	563
15	7162 7162	1900	560
20	6544 6395	1900	565
21	5138 5140	1900	563
32	6579 7162	1900	562
33	5099 5128	1900	565
16	7037 7026	2000	564
17	7225 7271	2000	563
22	5289 5385	2000	562
23	6678 --3	2000	565
34	6647 6720	2000	564
35	8188 7048	2000	564

Table III cont.
Page -2-

24	7207 --	2100	566
25	6861 --	2100	561
36	4932 5532	2100	553
37	6962 7083	2100	564
38	7925 7346	2200	566
39	7191 7253	2200	563
43	5733 5726	2200	565
54	6923 6820 6908	2200 2nd case firing (2&54) neck erosion, primer setback	~565
55	7010 6969 7014	2200 2nd case firing (3&55) 1/3 neck gone, primer setback	573
56	8159 6431 6491	2300 2nd case firing (4&56) some neck gone, good primer	572
57	7383 6147 6182	2300 2nd case firing (5&57) most neck gone, good primer	570

1. Relative burning rate compared to the standard burning rate of 100 for IMR-4350.
2. Two PACT chronographs for 2 readouts, three PACT chronographs for 3 readouts. Velocities measured 20 ft from the muzzle.
3. No chronograph readout.
4. Projectiles machined from black plastic rod and each weighed prior to use.

TABLE IV
IMR-4895 (115)¹
ALUMINUM CASES, 30 mm GAU-8, USED

<u>Test No.</u>	<u>Velocity², ft/sec</u>	<u>Powder, gr.</u>	<u>Projectile⁴, gr.</u>
50	5810 6038	1700	565
51	6439 5737	1700	564
52	6858 6462	1800	564
53	6757 6896	1800	562
58	6001 6109 6156	1900 2nd case firing (6&58) 2/3 neck gone, primer setback	573
59	7274 7067 7042	1900 2nd case firing (7&59) most neck gone, good primer	572
60	7299 7269 7276	2000 2nd case firing (8&60) 1/2 neck gone, good primer	574
61	8329 7014 8036	2000 2nd case firing (9&61) most neck gone, primer gas leakage	576
112	-- ³ 6379 5990	2000 some neck gone, near maximum	567
113	4227 ⁵ 4030 3918	2000 some neck gone, near maximum	565

1. Relative burning rate compared to the standard burning rate of 100 for IMR-4350.
2. Two PACT chronographs for 2 readouts, three PACT chronographs for 3 readouts. Velocities measured 20 ft. from the muzzle.
3. No chronograph readout.
4. Projectiles machined from black plastic rod and each weighed prior to use.
5. No specific reasons for these types of velocity variations, only suspicions.

TABLE V
IMR-4064 (120)¹
ALUMINUM CASES, 30 mm GAU-8, USED

<u>Test No.</u>	<u>Velocity², ft/sec</u>	<u>Powder, gr.</u>	<u>Projectile⁵, gr.</u>
26	6079 -- ₃	1800	568
27	6107 --	1800	565
40	6555 6672	1800	565
41	6565 6669	1800	564
	6423 ⁴	1800	~565 ⁶
	6313	1800	~565
	6219	1800	~565
	6339	1800	~565

1. Relative burning rate compared to the standard burning rate of 100 for IMR-4350.
2. Velocities measured 20 ft from the muzzle, two PACT chronographs.
3. No chronograph readout.
4. These velocities were obtained at WPAFB, Summer 1987. Shown for comparison to data from this project.
5. Projectiles machined from black plastic rod and weighed prior to use.
6. Projectiles machined from white plastic rod.

TABLE VI
IMR-3031 (135)¹
ALUMINUM CASES, 30 mm GAU-8, USED

<u>Test No.</u>	<u>Velocity², ft/sec</u>	<u>Powder, gr.</u>	<u>Projectile³, gr.</u>
66	5073 4579 4578	1300	571
67	5191 5122 5078	1300	568
68	5596 5554 5596	1400	573
69	5180 5180 5217	1400	573
86	4582 4607 4532	1500	569
87	4992 4887 4792	1500	574
88	5567 5373 5389	1600	569
89	5997 5793 5852	1600	569
108	5935 5919 5919	1700	569
109	5928 5878 5882	1700	564

1. Relative burning rate compared to the standard burning rate of 100 for IMR-4350.
2. Velocities measured 20 ft from the muzzle, three PACT chronographs.
3. Projectiles machined from black plastic rod and each weighed prior to use.

TABLE VII
IMR-4831 (95)¹
ALUMINUM CASES, 30 mm GAU-8, USED

<u>Test No.</u>	<u>Velocity², ft/sec</u>	<u>Powder, gr.</u>	<u>Projectile⁴, gr.</u>
62	4905 4756 4865	1500	1127
63	4564 4196 4174	1500	1131
64	4888 4725 4490	1600	1131
65	4838 4850 4878	1600	1136
74	5328 5314 5346	1700 2nd case firing (37&74) some neck gone	1131
75	5020 4994 4987	1700 neck eroded but intact	1141
76	5321 5319 5294	1800 neck eroded but intact	1134
77	5099 5016 5016	1800 2nd case firing (43&77) some neck gone	1132
80	.. ³ 5527 5618	1900	1130
81	6074 5148 5241	1900	1136
82	5793 5772 5787	2000	1139
83	5835 5298 5820	2000	1138

Table VII cont.
Page -2-

94	-- 5863 5863	2100 neck eroded but intact	1130
95	-- 5782 5871	2100 neck gone	1132
96	-- 6102 6204	2200	1130
97	-- 6001 6054	2200 neck badly eroded, retire case	1132
104	7236 6873 6981	2300 severe neck erosion near maximum load	1130
105	6478 6067 6247	2300 severe neck erosion, near maximum load	1135
106	7763 6426 6439	2400 case very stuck in chamber, very severe neck erosion, over maximum load. Did not fire second test round.	1135

1. Relative burning rate compared to the standard burning rate of 100 for IMR-4350.
2. Velocities measured 20 ft from the muzzle, three PACT chronographs.
3. No chronograph readout.
4. Projectiles machined from black plastic rod and each weighed prior to use.

TABLE VIII
Velocity Comparisons - 565 Gr. Projectile
Table I through Table VI

	IMR-4831	IMR-4350	IMR-4320	IMR-4895	IMR-4064	IMR-3031
Powder gr.	(95) ¹	(100)	(110)	(115)	(120)	(135)
1300	--	--	--	--	--	5073 4579 4578 5191 5122 5078
1400	--	--	--	--	--	5596 5554 5596 5180 5180 5217
1500	--	--	--	--	--	4582 4607 4537 4992 4887 4792
1600	5801 --	--	--	--	--	5567 5373 5389 5997 5793 5852
1700	5270 5917	--	--	5810 6038 6439 5737	--	5935 5919 5919 5928 5878 5882

Table VIII

Page -2-

<u>Powder gr.</u>	IMR- <u>4831</u>	IMR- <u>4350</u>	IMR- <u>4320</u>	IMR- <u>4895</u>	IMR- <u>4064</u>	IMR- <u>3031</u>
1800	-- 4298	--	6488 6541	6558 6462	6079 --	--
			6446 6463	6757 6896	6107 --	
			6342 6374		6555 6672	
			5165 4689		6565 6669	
1900	-- 5939	5569 5337	7079 7084	6001 6109 6156	--	--
		5848 5930	7162 7162	7274 7067 7042		
			6544 6395			
			5138 5140			
			6579 7162			
			5099 5128			
2000	5789 --	6216 6201	7037 7026	--	--	--
	5552 5588	6457 --	7225 7271			
	5988 --		5289 5385			
	6040 --		6678 --			
			6647 6720	7299 7269 7276		
			8188 7048	8329		

Table VIII
Page -3-

<u>Powder gr.</u>	IMR- <u>4831</u>	IMR- <u>4350</u>	IMR- <u>4320</u>	IMR- <u>4895</u>	IMR- <u>4064</u>	IMR- <u>3031</u>
				7014 8036		
				-- 6379 5990		
				4227 4030		
2100	6230 6197 6250	6433 6449	7209 --	--	--	--
	6357 7204 6397	6156 6374	6861 -- 4932 5532			
			6962 7083			
2200	6962 6846 6757	5438 5323 5405	7925 7346			
	6509 6509 6491	-- 5208 5224	7191 7253 5733 5726			
		-- 6774 6737	6923 6820 6909			
		-- 6708 6309	7010 6969 7014			
2300	-- 6233 6337	6849 6855 6170	8159 6431 6491	--	--	--

Table VIII
Page -4-

<u>Powder gr.</u>	IMR- <u>4831</u>	IMR- <u>4350</u>	IMR- <u>4320</u>	IMR- <u>4895</u>	IMR- <u>4064</u>	IMR- <u>3031</u>
2300	-- 6966 6838	6808 6777 6625	7383 6147 6182			
	-- 8270 8068					
	-- 5970 6436					
2400	-- 6517 6501	6680 6725 6667	--	--	--	--
	-- 7711 7801	6565 6255 6359				
2500	6658 6636 6683	--	--	--	--	--
	7020 6899 6832					

1. Relative burning rates.

TABLE IX
IMR-4831 (95)
Comparison of Velocities Between 565 gr. and 1130 gr. Projectiles
Table I and Table VII

<u>Powder, gr.</u>	<u>Velocity, 565 gr. Projectile</u>	<u>Velocity, 1130 gr. Projectile</u>
1500	5380	4905
	5340	4756
		4865
		4564
		4196
		4174
1600	5801	4888
	--	4725
		4490
		4838
		4850
		4878
1700	5270	5328
	5917	5314
		5346
		5020
		4994
		4987
1800	--	5321
	4298	5319
		5294
		5099
		5016
		5016
1900	--	--
	5939	5527
		5618
		6074
		5148
		5241

Table IX cont.
Page -2-

2000	5789	5793
	--	5772
		5787
	5552	
	5588	5835
		5298
	5988	5820
	--	
	6040	
	--	
2100	6230	--
	6197	5863
	6250	5863
	6357	--
	7204	5782
	6397	5871
2200	6962	--
	6846	6102
	6757	6204
	6509	--
	6509	6001
	6491	6054
2300	--	7236
	6233	6873
	6337	6981
	--	6478
	6966	6067
	6838	6247
	--	
	8270	
	8068	
2400	--	7763
	6517	6426
	6501	6439
	--	
	7711	
	7801	

III. Conclusions and Comments

Powders and Loads. As this study progressed, it became obvious that velocity characteristics of slow to fast burning powders of one manufacturer should be determined for low to heavy weight charges, ranging from around 400 grain to case capacity or case failure. Most manufacturers develop a series of powders ranging from fast burning pistol powders to slow burning large rifle powders. The burning rates and characteristics are usually determined in closed powder bombs. However, these characteristics determined in a closed system cannot necessarily be extrapolated to general use in cartridges using various charges and projectiles of varying weights. W.L. Godfrey noted that some powders changed positions in burning rates during his studies for his two loading manuals, "The 30-06" and ".243 + 6mm". It should be noted that for commercial cartridges, a powder charge of 100 grains is very large and relatively unusual except for the largest rifles. For the 30mm cases, starting charges range from 1200 to 1500 grains and increase in 100 grain increments to as high as 2500 grains. It is more unlikely that closed bomb data or even commercial loading data could be used any more than to merely indicate a possible starting point to study the characteristics of the powders used in the quantities for the 30mm cases. These large weights and volumes of powders must certainly develop heats, pressures and burning characteristics in a much different manner than they would in the closed bomb or in the smaller quantities common to most commercial cartridges. Acceleration of the 500 to 1100 grain projectiles would also be of considerable influence. To determine the velocity characteristics for the 30mm cases, 30mm cases have to be used with the various powders from low to capacity charges and preferably with projectiles of various weights. In the sense of a basic, fundamental research project, the characteristics of each single powder should first be determined before any layered or mixed charges are studied. It makes little sense, for example, to test a 2000 grain load of 400 grains (20%) of powder A layered or mixed with 1600 grains (80%) of powder B, whatever the results, without first knowing what the separate effects are. The net results may be additive, subtractive or synergistic. Only testing will tell.

Thus, a loading table such as Table VIII should be completed for a manufacturer or for each manufacturers' series of powders starting with low

weight charges of about 400 grains and working up to case capacity or case failure. For other than a project designed specifically to accomplish this goal, it would be a long, tedious, difficult process. But without this tedious systematic approach, results would be rather haphazard. Firing only two to four shots per test at most indicates trends and in themselves are certainly not statistically valid. Nonetheless, the loading data derived from a study of this type could be useful in the form of a loading manual listing velocities for various weights of a number of powders using several standard weight projectiles. A manual of this type could save development time for testing laboratories whose main goal is impact studies.

Velocity Variations

As stated previously, firing two to four shots per load at most would indicate trends in velocity and would by no means be statistically valid. As data in Tables I through VII show, there are some velocity variations that stand out.

Instrumentation could be at fault. More replicas per test could help determine this. Also conductive papers could be substituted for some sets of skyscreens and the results of both systems compared. Velocity variations could also be the result of the inherent burning characteristics of the powder being used under these test conditions and in these quantities.

The nature of the charge ignition is another variable. The opening of the flash tube can be changed through repeated depriming and cleaning. If the flash hole becomes smaller, larger, or lopsided, the ignition flash would be directed differently into the powder charge. Variations in the ignition of these large masses of powder could be reflected in velocity variations. To finalize test velocities, extremely uniform flash tubes should be used, probably new unused ones.

Another consideration is to determine if the flash tube could be omitted and a layer of very fast pistol powder substituted. If the electric primer alone could ignite this layer of powder, then the main charge could be ignited at the base rather than having the ignition flash shot into the powder mass. Varying the mass and type of ignition could well affect the resulting velocities.

After near maximum loads are reached with the used aluminum cases, final velocity determination and absolute case capacity should be obtained using new cases, with or without new flash tubes, and projectiles machined to fit the

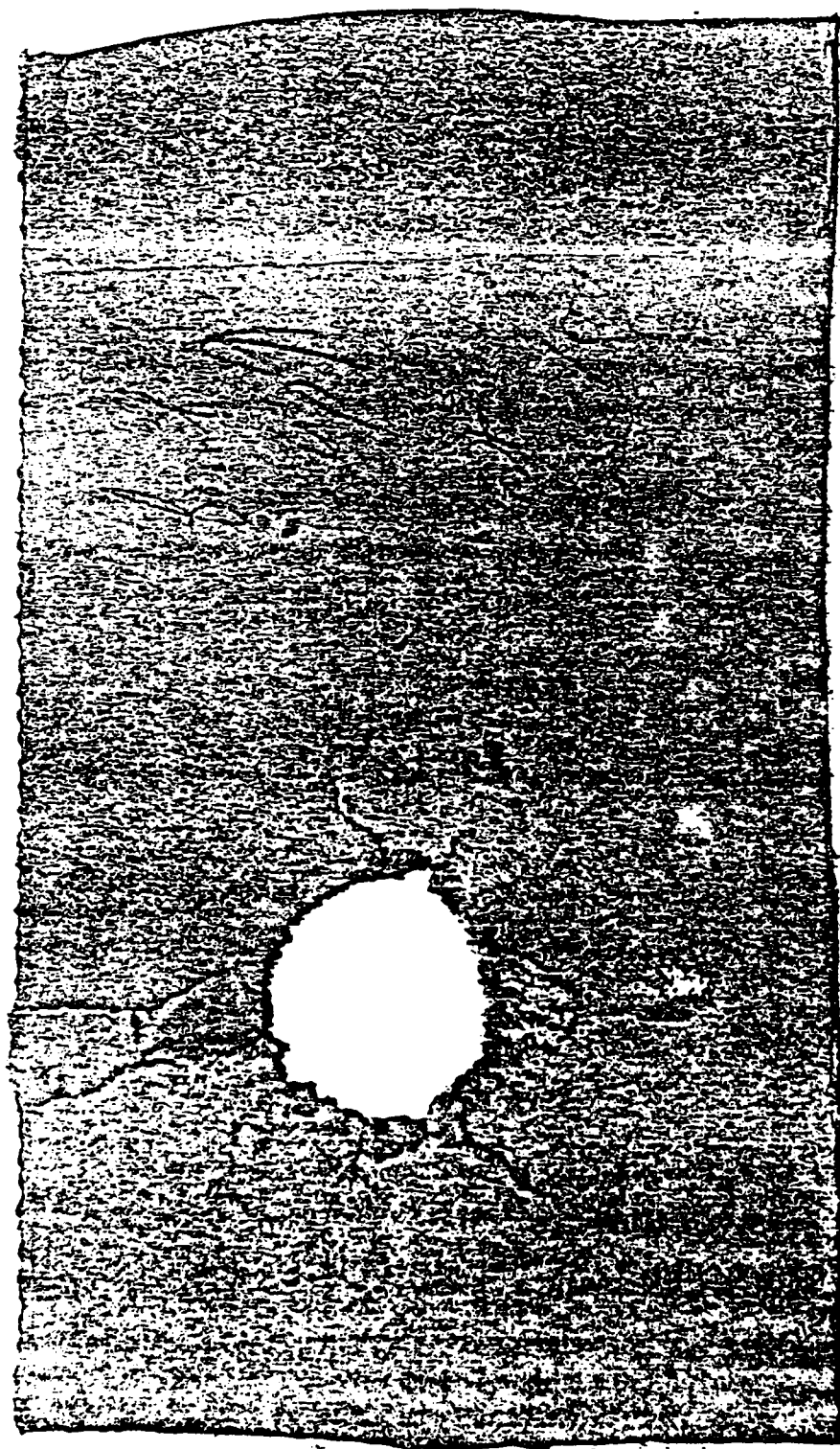
new cases. To that end, 200 new aluminum cases have been obtained from Honeywell, Inc., Joliet, Illinois.

Muzzle velocities could be determined by replacing a start skyscreen with a resistor and mounting a break wire at the muzzle, with the stop skyscreen mounted in the middle of the other skyscreens located 20ft from the muzzle.

During the Summer of 1987 at WPAFB, cardboard panels were placed in back of the timing screens. Holes in the panels showed that the projectiles were tumbling (Fig. 2 and 3). The 565 grain projectiles are 2.25 inches long. For ideal circumstances, if the tumbling projectile triggered one set of skyscreens in the horizontal position and another set in the verticle position, roughly this would be reflected as a projectile length difference of several inches over a 48-inch travel length or about a 2-3% difference in velocities. Thus, chronograph readings, per shot, differing by several hundred feet/second for velocities in the 6000 to 7000 ft./sec. range should not be unexpected.

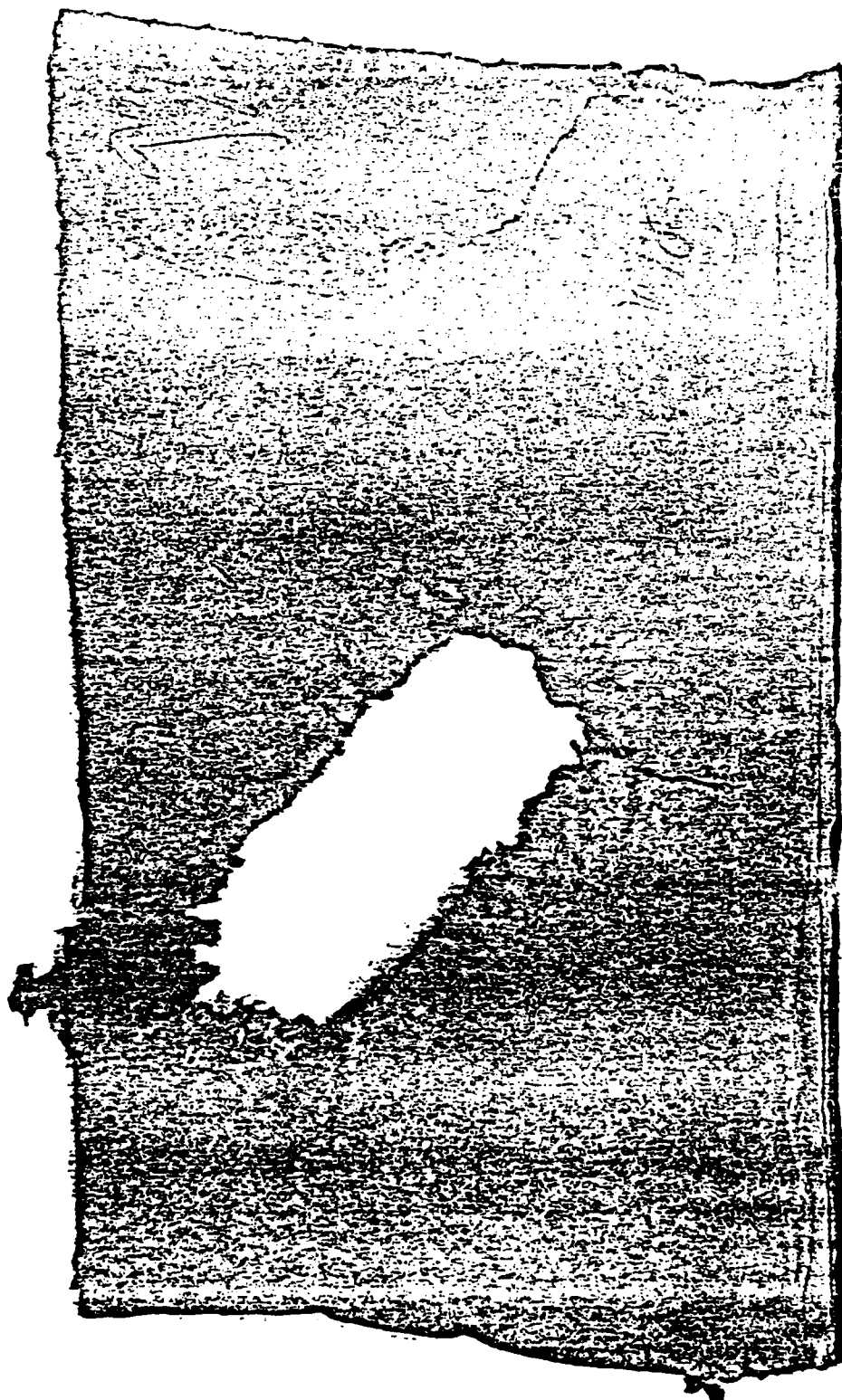
Fig. 2

Tip of
paw
#102



4/21/63
11/05

Fig. 3



**FINAL REPORT NUMBER 91
OPTIMAL AND SUB-OPTIMAL LOOP SHAPING IN
QUANTITATIVE FEEDBACK THEORY
PENDING APPROVAL
Mr. David F. Thompson
210-9MG-106**



Low Velocity Impact Of Composite Materials

William E. Wolfe and Gregory A. Schoeppner
Department of Civil Engineering

Universal Energy Systems, Inc.
Dayton, Ohio 45432

Grant Nos. S-760-7MG-102 and S-210-9MG-082
Final Report
RF Projects 766585/720514 and 767235/721759

January 1990

LOW VELOCITY IMPACT OF COMPOSITES

ABSTRACT

The behavior of graphite/epoxy composites plates during low velocity impact was investigated in a series of experiments. In the experimental program plates of different ply orientations and thicknesses were fabricated and impacted using an instrumented falling weight. Load and energy time histories were recorded for each test. A damage scale developed during the project was used to correlate the visible damage with the impact energy. Additional correlations between the impact energy, visible damage and the internal damage as identified in post-test ultrasonic scans of the test plates were presented. The experimental program was augmented by an analytical study. Pagano's discrete laminate model for the determination of stresses in a loaded laminate were thoroughly studied. The method was then extended to include a proper description of the inertia terms necessary to accommodate a dynamic analysis. Proper application of a discrete laminate theory is required if a consistent treatment of the transverse stresses at each ply interface is to be attempted. The work described will provide a basis for the development of an analytical capability to reasonably simulate results obtained by tests and then to design more reliable damage tolerant structures.

FOREWORD

This report describes research carried out in the Civil Engineering Department at The Ohio State University under the AFOSR Research Initiation Program and administered by Universal Energy Systems under contract numbers S-76J-7MG-102 and S-210-9MG-082. Dr. Raghubir S. Sandhu AFWAL/FIBCA was the technical monitor for the program. The work was supervised by Dr. William E. Wolfe during the time period January, 1988 to December 31, 1989. The authors are grateful to Dr. Sandhu for his advice throughout the course of the program. The authors also wish to thank those individuals who worked on this project. Much of the experimental work was performed by Graduate Research Associates Ibrahim Kandalaft and Bryan Foos. The OSU test panels were fabricated by Mr. Jason Roberson from graphite/epoxy prepreg tape supplied by the Flight Dynamics Laboratory. As always Mr. Lennart Claussan provided valuable support throughout the duration of the project.

Chapter I

INTRODUCTION

Fiber reinforced organic resin composites have become an important part of the advanced materials industry, primarily due to the high strength to weight and stiffness to weight ratios possessed by structures made from these composites. Structural properties can be tailored by orienting the fibers to provide the strength and stiffness required by the design. The growth in the use of structural composites has been particularly dramatic in the aerospace industry where the combination of high strength and light weight many times controls the design. Currently, the most common composite used in the aerospace industry consists of graphite fibers embedded in an epoxy matrix. Although the high strength to weight and stiffness to weight ratios make graphite/epoxy composites attractive, the users of laminated composites have long been concerned about this material's susceptibility to damage from low velocity impact.

In laminated composite structures, small amounts of impact energy can lead to localized stresses large enough to cause significant damage growth, possibly leading to failure through progressive ply delamination. Often this damage is internal to the

structural section, and therefore no visible indication that the material is damaged exists. Graphite/epoxy composites appear to be especially vulnerable to this type of loading. For example, damage to the internal structure of an impacted plate can be quite extensive with the effect on strength being as much as a fifty percent loss without any surface expression of the damage. Structural members of different thicknesses, and stacking sequences will experience different levels of damage when subjected to an impact load. Therefore, post-impact strengths can be expected to be specific to a particular laminate. Without a satisfactory analytical predictive tool, each material system, layup and panel thickness must be tested individually. As the use of composite materials grows, an increasing variety of designs will require an ever expanding number of laboratory tests for the measurement of stiffness and strength.

The research effort described in this report was divided in two phases. In the first phase, low velocity impact tests were performed in the laboratory on square graphite/epoxy plates of various thicknesses and ply configurations. The purpose of these tests was to develop a procedure for relating both visible damage and the extent of internal damage as measured by delamination area to the impact load parameters. In the second phase, an analytical program aimed at describing the stress field induced in a composite material by an impact load was begun. In this program, the boundary conditions for a laminated composite plate subjected to an impact load are specified and the stress field in the plate is

determined at the individual ply level. The results of these two work efforts will be presented in Chapters 2, 3 and 4. In Chapter 2, the pertinent literature is reviewed. In the third chapter the experimental program is described and the results of that program are presented. In Chapter 4, the equations for the stress field at the ply level are derived for the case of a plate subjected to a dynamic load.

The goals of the work presented are an improved description of the effects of the impact event on the behavior of laminated composite plates and a reduction in the time and expense required to determine the material properties necessary to make accurate predictions of the response of these plates to impact.

Chapter II

LITERATURE REVIEW

2.1 Introduction

Criteria used to set the requirements for the performance of laminated composites subjected to low velocity impact are often based on the effects of a specified impact event. Estimates of energy levels of up to 100 ft-lbs have been associated with an accidental tool drop, a threat which has been widely used as a typical example of a low velocity impact [23]. This value of 100 ft-lbs has for many purposes been defined as the design standard for low velocity impact threat. Alternatively, a threshold of visible damage has been used by maintenance personnel to define the minimum design impact. Currently a surface indentation of 0.1 inches is considered the limiting value for visible damage during routine inspections of structures made from graphite/epoxy laminates. The standard recommends that when a depression of this size is found, a damage survey be conducted to determine strength degradation. NASA Reference Publications 1092 [1] and 1142 [2] describe procedures to be followed to determine the effect of low velocity impact on the measured static strength of composite

plates. However, since the specifications are based on an expected event rather than a material performance requirement, it is likely that plates of different thicknesses and/or stacking sequences will experience different levels of damage resulting in post impact strengths specific to the geometry of the laminate. Therefore, while these procedures serve a useful function by requiring minimum acceptable values for design residual strength, they may not be able to accurately predict the extent of damage, given an impact event. Reports to Universal Energy Systems by the authors [101,102], have presented preliminary data that showed significant delamination occurring at impact energy levels well below current design levels.

Due to the complexity of the impact problem, a static analysis is oftentimes conducted in preference to a more general dynamic analysis. A common position taken by investigators studying low velocity impact of composite materials [33,55,66,88] is that when load duration during impact is large in comparison with the time of travel of stress waves through the structure, or large in comparison to the natural periods of the member, then static loading may be assumed.

Several studies have been conducted to determine the differences between low velocity impact loading and static or quasi-static loading. These include studies to determine how the strains, deflections and damage compare between the two types of loading. Elber [27] found that the deformation mechanics and fracture mechanics for panels subjected to low velocity impact was

essentially equivalent to the deformation and fracture mechanics of statically loaded specimens. One reason given for this phenomenon was that for the thin laminates tested, the higher modes of vibration have little effect on the mechanics of low velocity impact.

Hudock [39] compared test specimens based on the damage initiation load for both impact and static type loading. She stated that the results show a difference between impact and static test results. Her results showed that, for graphite/epoxy specimens, the static damage initiation load was greater than the impact damage initiation load for eight ply specimens, but not as great as the impact load for 16, 24 and 32 ply specimens.

Hudock's [39] and Elber's [27] somewhat contradictory results demonstrate that the data do not consistently substantiate the assumption that low velocity impact can be effectively modelled by static or quasi-static loading analyses. What these results may be suggesting is that low velocity impact cannot simply be defined as an event that excites primarily the first mode of vibration (as it would be expected to do in thin specimens). The same impact event may for thicker (stiffer) specimens excite higher modes of vibration. Considering these arguments, a quasi-static analysis may not be valid, particularly when the behavior of thick composite specimens is to be characterized.

Greszczuk [33] described three distinct problems that must be resolved in order to predict the level of damage resulting from projectile impact. These three problems are: 1) The determination

of the magnitude, distribution and duration of the surface pressure induced by the impactor. 2) The evaluation of the internal stresses resulting from the surface pressure. 3) The identification of failure modes caused by the induced internal stresses.

Over the past twenty years, there has been a significant amount of research conducted on each of Greszczuk's three problems with the aim of gaining a better understanding of the dynamic behavior of composite material systems. The reader is referred to Bert [8,9], Gibson [31] and Sierakowski and Chaturvedi [78], for extensive reviews of current and past theoretical, experimental and numerical research programs.

2.2 Experimental Contributions

Requirements for the performance of laminated composites are given in terms of strength and stiffness. Many variables that affect the response of composite materials under impact loading have been identified during numerous investigations [4,13,33,36, 43,61,66,74,88] but although the list of variables is not exhaustive, to investigate the effect and relationship of each of these parameters would require a test program of unprecedented complexity and size for every material system. Therefore, only those parameters which are believed to have the greatest effect on impact performance have been investigated. The parameters having a significant influence on impact damage (both visible and nonvisible) of composites laminates include laminate, impactor and

structure parameters. The important laminate parameters include material system [61], ply layup, stacking sequence [13] and thickness [4,15,33,84]. The impactor parameters include type of impactor (hard or soft), mass, velocity, nose shape and size [67], and energy. The structure parameters include support conditions, impact location relative to supports, prestress prior to impact [6,43,73] and surrounding environmental conditions.

Although the low velocity impact problem has been the subject of many studies, there is presently no standardized test method for evaluating composite behavior for low velocity impact [1,78,100,106]. Three devices which are used to perform the impact tests are the pendulum impact system, the vertical drop tower, and the gas gun system. The pendulum impact system has successfully been used by Cordell and Sjoblom [23]. The pendulum impactor is a simple device which provides reproducible impacts and is typically instrumented to record the load history for impact tests. The vertical drop tower is similar in concept to the pendulum impactor. As with the pendulum, the weight and drop height of the impactor are user selected, but unlike the pendulum, where the target is struck horizontally, the direction of impact is vertical. Impactors for typical drop towers are also instrumented to record the load history for the impact event.

The third device which is use to perform impact tests is the gas gun which propels a projectile at the composite target. The gas gun is limited for use in impact testing since the impactor is not instrumented and therefore the load history of the impact is not

recorded and thus must be inferred from indirect measurements. This type of impact facility is also limited by its inability to consistently reproduce a specified impact event. It does have the advantage of being able to simulate a wider range of impact velocities than either the pendulum or the drop tower. Results of impacts on composite plates using a gas gun have been reported by Sierakowski and Chaturvedi [78]. The instrumented impact systems have the critical advantage of being able to record the load-time history of the impact [19,40,53,79,94]. Thus instrumented impact tests provide a powerful tool to observe the impact event and to identify the impact mechanics.

Guyann and O'Brien [36] conducted drop tower impact tests on graphite/epoxy panels of varying thickness using a 0.5-in diameter aluminum impactor. They investigated the size, shape, and distribution of delamination on a ply by ply basis by using a combination of X-ray radiography, ultrasonic evaluations and deply techniques. They found that the delaminations were "peanut" shaped at almost every interface through the thickness. They also found that damage initiation began with intraply cracking which then led to delamination. The propagation direction of the delamination for a given interface was found to be controlled by the direction of the fibers in the ply furthest from the impact face. Wu and Springer [104] investigated the internal damage of 16 ply graphite/epoxy composites of various ply orientations by dissecting the impacted plates and by mapping the damage using ultrasonic methods. They observed that delaminations appeared to occur only

at changes in ply orientation. They also found the delamination were oblong with the major axis of the delaminations nearly parallel to the fiber direction in the ply further from the impact face. Nixon et.al. [58], conducted drop tower tests on carbon fiber composites in a PEEK matrix to investigate to effect of impact energy levels on material behavior. Ultrasonic evaluation of the post impacted plates was chosen as the method to investigate the progression of damage development with increasing impact energy levels. Similar investigations were conducted by Ghandhe and Griffin [30]. Both studies showed that a threshold impact energy level is required for the onset of delamination. Chaturvedi and Sierakowski [18] in tests using a gas gun to fire projectiles at composites plates found that the damage area increases with increasing impact energy. They also found that for a constant impact energy, increasing the impactor mass caused the size of the damage area to decrease.

Liu et al. [52] studied the damage of impacted graphite/epoxy specimens by edge replication and found that the delamination areas had characteristic shapes based on the composite stacking sequence. Liu et al. [52] found that the delaminations at every interface were peanut shaped. He attributed the occurrence of these delaminations to the bending stiffness mismatching of one lamina with respect to the next. Dost et al. [26] studying the particular case of spirally stacked quasi-isotropic laminates found impact damage consisted of a spiral array of transverse matrix cracks and delaminations forming four ply thick circular sublaminae.

Recent experimental studies [23,49] have tried to correlate visible front and back face damage to the impact event. Levin [49] defined barely visible impact damage as a one millimeter deep dent on the impacted surface of the test specimen. Cordell and Sjoblom [23] defined four different failure regions (labelled I through IV), distinguished primarily by the amount of damage the composite specimen sustained during the impact. Failure region I was characterized by, at most, minor intra-ply cracking. Failure regions II and III were associated with increasing levels of damage up to and including back face splitting and fiber breakage. In Region IV the extent of the resulting damage sustained by the composite structure increased to through penetration.

Techniques employed by several authors to relate the extent of impact damage in test specimens to residual structural properties include ultrasonic C-scan [12,14,17,37,64,65,72,75,82,83,92,98], dye penetrant X-ray radiography [5,36,49,52,60,76,105,108], moire interferometry [16,47,108], thermographic and laser holographic [5,108], acoustic emissions [32,35,58,97,99] thermal oxidant deply [28,29,36,38,60,76], edge replication [81], and microscopy techniques [22,67].

Jang et al. [42] surveyed various approaches for improving impact resistance including matrix modification by chemical additives and tougheners, fiber/matrix interfacial adhesion, laminate design including stacking sequence; introduction of through the thickness reinforcements such as braiding, 3-D weaving, and stitching; insertion of interlaminar interleaf layers, fiber

hybridization, and the utilization of high-strain fibers.

2.3 Analytical Contributions

2.3.1 Determination of Contact Forces

Numerous investigators have used the Hertzian contact law or a modified Hertz equation to predict contact force and duration for low velocity impact problems [33,34,56,77,84,88,90,93,103]. The Hertzian contact relationship was originally derived for the case of a perfectly elastic material subjected to static loading from a spherical indenter with small contact forces, but has been adopted for problems of low velocity impact because solutions to the Hertzian problem have been shown to approximate test data [56]. Since the equation was developed for a static contact force, it is only valid when the contact time is much greater than the time required for elastic waves to traverse the object. When Hertzian theory is used to predict contact forces in a body subjected to low velocity impact, several approximations must be made. Commonly recognized limitations of the theory include the fact that since the contact stresses predicted often exceed the elastic limit of most materials, they can form only an upper bound on the actual stresses. Also, if the surface of the target can move, the predicted contact times become lower bound estimates [56]. Gu and Sun [34] used the Hertzian contact law but determined the contact constant by experimentation. They found that the experimentally

obtained parameter was not constant but was a function of loading rate. Sun and Chattopadhyay [88] and Thangjitham, Libresch and Cedarbaum [93] developed double Fourier sine series representations of the Hertzian contact law in order to implement it into a double series plate solution. The impact force at a given time was then found by a simple numerical iteration scheme.

2.3.2 Determination of Internal Stresses

2.3.2.1 Dynamics of Laminated Plates

Finding the internal stresses caused by a surface pressure, has received a considerable amount of attention. However, due to the complexity of the stress fields in laminated composites, a closed form three dimensional solution to this problem has been slow in development. The plate models used to analyze laminated composite plates subjected to dynamic loads are, in general extensions of the models used for static analyses. One of the earliest studies describing the vibration of laminated plates is due to Pister [63] in which he used a plane stress analysis to calculate the natural vibration frequencies of layered isotropic materials. Since this work, the development of theory for the dynamics of laminated plates has been extended, refined and tailored to composite material systems.

2.3.2.2 Classical Thin Plate Theory (CPT)

The fundamental assumptions of CPT are that: 1) Inplane displacements are small compared to the plate thickness. 2) Kirchhoff's hypothesis that plane sections before deformation remain plane and perpendicular after deformation. 3) Transverse normal stress and transverse normal strain are negligible.

Using a variant of CPT, Bert and Mayberry [11] applied the Rayleigh-Ritz method to evaluate the natural frequencies of rectangular plates of two orthotropic layers and compared their results to experimental results. For the antisymmetric angle-ply and cross-ply laminates, it was reported that the calculated fundamental frequency matched well with experimental results but matched only fair for higher frequencies.

Using an asymptotic method to solve the eigenvalue problem, Lin and King [50] used CPT to estimate the free vibration frequencies of unsymmetric cross-ply and antisymmetric angle-ply laminates for various boundary conditions. Comparing the results with those reported in [11] and with exact solutions they observed that the method provides excellent estimates of fundamental frequencies and they expected that higher modes could be found with increased accuracy (within the framework of CPT).

To study the validity of CPT, Jones [44] found an exact solution for the natural frequencies of a laminate composed of orthotropic layers simply supported on two edges and infinite in the other direction. Jones observed that CPT accurately predicts

frequencies and mode shapes well for plates at low frequencies and long wave lengths. However, CPT accuracy decreases with increasing plate thickness and with increasing degree of material orthotropy. Bert [7], in a review of plate theories, stated that the classical plate theory suffers from the same deficiencies as the Bernoulli-Euler beam theory, namely that transverse shear and normal strains are neglected and in-plane normal strain is distributed linearly through the thickness, rather than nonlinearly. Neglecting the effects of the transverse shear deformation in CPT, implies infinite shear rigidity leading to an overestimation of plate stiffness. As a result, the theory gives an underprediction of lateral deflection and an overprediction of natural frequencies. It is also noted that CPT neglects rotary inertia and inertias associated with in-plane displacement components.

2.3.2.3 First Order Shear Deformation Theory (FSDT)

A theory proposed by Yang, Norris and Stavsky [107] was developed to eliminate the inadequacies of the CPT. The theory which is called first order shear deformation theory (FSDT) is an extension of Mindlin's [54] theory for homogeneous plates in which corrections for transverse shear and rotary inertia were included in CPT. Yang et al. [107] extended Mindlin's theory to laminated plates consisting of bonded anisotropic layers.

The theory is derived from the assumption that the transverse strains are constant through the plate thickness. This assumption leads to an inplane displacement which is linear through-the-thickness while the transverse displacement is constant through-the-thickness. It is noted that the theory assumes that individual layer rotations are equal. However, the theory does not address the assumption, as made in CPT, that the transverse normal stress is zero through-the-thickness of the laminate.

Whitney and Pagano [95] built upon the bending theory for anisotropic plates developed by Yang, Norris and Stavsky [107]. Instead of assuming the transverse normal stress is zero, Whitney and Pagano employed a generalized plane stress assumption, i.e. the transverse normal stress is not necessarily zero at every point, but its integral over the thickness of each layer vanishes. This leads to plane-stress reduced stiffness in the formulation. They also incorporated the Mindlin type shear correction factor k of FSDT into the governing equations to account for the transverse shear deformation. This Smeared Laminate Model has the drawback that the shear angle does not vary from layer to layer through the thickness.

Whitney and Pagano applied their FSDT to static and dynamic problems of laminated plates in cylindrical bending. The cylindrical bending of antisymmetric cross-ply and angle-ply plate strips under sinusoidal load distribution and free vibration of antisymmetric angle-ply plate strips were analyzed. Selected results were compared with exact solutions to determine the best

value for the shear correction parameter. Results showed that the FSDT gives accurate estimates of deflections in bending problems but the stresses calculated by FSDT are identical to those of classical laminated theory.

To study the validity and limitations of FSDT, Kulkarni and Pagano [48] obtained exact dispersion curves and thickness modes by dynamic elasticity theory for the vibration of a laminate in cylindrical bending. In general, FSDT was accurate in representing the first three modes of vibration for material with low anisotropy. It was found that the agreement with exact values is significantly affected by the fiber orientations. Kulkarni and Pagano pointed out that FSDT is essentially a bending theory and that flexural modes are generally in good agreement with exact solution. For laminates where flexural motion predominates, extensional motion is reasonably predicted and extensional modes are in close agreement with the exact solution provided the materials have low anisotropy.

The results of an investigation presented by Perry, Adams and Miller [62] outlined the significance of the transverse shear term on the calculation of flexural modulus and strain energy of laminated plates. They stated that one measure of the degree of anisotropy of a material, which is important in quantifying the amount of deformation due to transverse shear, is the ratio of the longitudinal tensile modulus E_x to the longitudinal transverse shear modulus G_{xz} , the larger the ratio the more pronounced the shear effects become. Since this ratio is usually large for

composite materials, it is expected that the deflection due to transverse shear stresses would be significant for thick composite panels. Comparing the classical plate theory with the shear deformation plate theory presented by Whitney and Pagano [95], Perry et.al. found that when transverse shear stresses are considered, the midspan deflection for beams with span-to-depth ratio less than 10, may be 1.5 times larger than the value obtained when transverse shear stress is neglected. Strain energies which were calculated using stresses due to flexure only account for about 1/2 of the energy obtained by integrating the area under the experimental load-deflection curve to the point of peak load. Strain energies which were calculated using both stresses due to flexure and transverse shear stresses compared well with strain energies from experimental load deflection curves. They concluded that almost half of the strain energy is due to transverse shear stress and strain.

Using the equations of Yang, Norris and Stavsky [107], Bert and Chen [10] investigated the effect of eliminating in-plane and rotary inertia terms from the formulation. They found that the effect of neglecting the in-plane and rotary inertia terms introduces very little error in prediction of the fundamental frequency as was found by Chow [20].

A parametric study was presented by Reddy [69] in which a finite element formulation of the governing equations presented by Yang et al. in Reference [107] was used. The results of the finite element analysis for free vibration were compared to a three

dimensional elasticity solution, CPT and the closed form solution of [10]. As found by other investigators, the error in CPT for predicting the fundamental frequency compared with FSDT, increases very severely with an increase in either the longitudinal or transverse wave numbers. The FSDT requires a correction to the transverse shear which is determined by matching results of the approximate theory with the exact solution to a dynamic problem, if Mindlin's [54] form is followed. The values used for the parameter k that have appeared in the literature range from $2/3$ to about 0.9.

Using a Rayleigh-Ritz analysis, and a finite strip method to solve the equations of [95], Craig and Dawe [24] found that there is very close correspondence between the fundamental frequency predicted by FSDT and the elasticity theory, provided the appropriate shear correction factors are used in the shear deformation theory.

FSDT has been used by several investigators to analyze laminated plates subjected to impact [68,78,88]. Ramkumar and Chen [68] used Whitney and Pagano's model to analyze a laminated plate subjected to transverse impact load. The in-plane displacements were assumed to be negligible in comparison to the transverse displacement and the rotary inertia terms were not included. The load history was based on available experimental data from instrumented impact tests using a linear variation of the contact force with time while the contact area was assumed to vary with time. Predicted maximum transverse displacements at the impact

location agreed well with experimental and finite element results. Computed longitudinal and transverse strains on the back surface of the impacted laminate directly below the impact location, also agree well with available experimental results.

Sun and Chattopadhyay [88] also used Whitney and Pagano's model [95] to investigate the central impact of a mass on a simply supported laminated composite plate. The authors incorporated into the theory initial stress and neglected rotary inertia terms. Shear stress which is prominent in impact problems was accounted for since the transverse shear deformation was included. The theory was found to be adequate in describing the transient wave propagation in an anisotropic plate subjected to an impulsive loading. Hertzian contact was modelled by a series representation of the contact load. The stiffening effect of initial inplane stresses was found to decrease deflections and the impact stresses in the plate. Also, it was found that impact induced stress waves propagate faster under a higher initial stress.

2.3.2.4 Higher Order Shear Deformation Theory (HSDT)

Thangjitham, Libresch and Cedarbaum [93] developed a higher order transverse shear deformation theory to describe the low velocity impact of anisotropic plates. They pointed out that there are several limitations of the first order transverse shear deformation theories including; 1) the introduction of a transverse

shear correction factor, whose determination is non-trivial, is required, 2) the effect of transverse normal stress is neglected, and 3) a constant distribution of transverse shear stresses across the thickness of the laminate is assumed. This assumption prevents fulfillment of static boundary conditions at the top and bottom surfaces of the plate. Their investigation showed that there is a strong influence of the transverse normal stress term when calculating flexural stress. As reported in Reference [62], it was found that as the thickness of the plate increases, the influence of the transverse normal stress on deflection increases. For example, for a plate with a span to thickness ratio $l/h = 5$, the analysis of flexural stress in which transverse normal stress is included was found to be twice that when transverse normal stress is not included.

A simplified higher order theory was proposed by Reddy and Phan [71] to determine the natural frequencies of orthotropic and antisymmetric angle-ply laminated plates. The displacement field, which satisfies the stress-free boundary conditions, gives parabolic distribution of transverse shear strains through-the-thickness of the plate. Eliminating the shear correction factors and using plane stress reduced elastic constants, as done by Whitney and Pagano [95], the solution was found to be in excellent agreement with the exact three dimensional analysis of Srinivas et al. [80]. Reddy and Phan found the refined shear deformation theory is as good as FSDT for predicting the fundamental frequency but not better than FSDT in predicting higher

natural frequencies.

A higher order theory by Whitney and Sun [96] extended the theory of Reference [95] to include the first symmetric thickness shear and thickness stretch modes by including higher order terms in the displacement expansion. Where FSDT, which is essentially a bending theory, failed to predict accurate in-plane modes for extensional vibration, the HSDT succeeded.

For cross-ply laminates composed of four layers a higher order theory to obtain dispersion relations and thickness mode shapes was derived by Nelson and Lorch [57]. The theory gave good representations of the two lowest natural frequencies for moderately small wave numbers, but did not predict thickness modes of stress accurately unless the wave number was extremely small. However, the theory requires the determination of nine shear correction parameters.

Theories based on an assumed displacement field will not, in general, satisfy equilibrium, guaranteeing discontinuous tractions at interlaminar boundaries for practical composites. Since kinematic relations are, in general, satisfied in the shear deformation theories, displacement predictions are acceptable, stress predictions however, are not. In general, the short comings of shear deformation theories are; the introduction of transverse shear deformation correction parameters whose determinations are uncertain, the disregarding of the effects of the transverse normal stress, and the assumption of a constant distribution of shear stress through-the-thickness.

2.3.2.5 Discrete Laminate Theory

Sun and Whitney [89] were the first to use the discrete laminated plate theory considering hybrid cross-ply laminates in which shearing rigidities of adjacent layers were quite different. Three theories based on FSDT were compared. The first theory allows for distinct shear deformation in the individual layers while enforcing continuity of displacements at the interfaces. The second theory enforces shear stress continuity at the interfaces of the layers and the third theory requires local rotations in the individual layers to be identical, making it equivalent to the FSDT discussed previously. The three theories are compared to an exact analysis for one-way harmonic vibration of a two layer plate of infinite extent [107]. Kirchhoff's assumption that plane sections remain plane after deformation was found to be acceptable in the case where differences in the shear rigidities of the layers are small. However, they found that for large differences in shear rigidity of the layers, the effect of local transverse deformation cannot be neglected.

A static laminate theory presented by Pagano [59] in which the assumed in-plane stress resultants are linear through-the-thickness of the plate overcomes many of the difficulties in the theories previously discussed. Pagano's theory which is based on a stress formulation, has given results that closely approximate stress fields in composite laminates. This theory, however, has not been extended to dynamics.

All of the theories presented in the preceding paragraphs are considered effective modulus theories in which the properties of the fibers and matrix are smeared to give a representative single material. In contrast, the effective stiffness theory separates the effects of the fiber and matrix of the laminate and replaces a fiber/matrix lamina with two separate homogeneous isotropic layers, one representing the fiber and the other representing the matrix. Sun, Achenbach and Herrmann [3,86,87] compared the effective stiffness theory with the effective modulus theory. They found that for high values of the ratio of layer stiffnesses typical of practical laminates, the lowest two modes show considerable dispersion even at very long wave lengths. They stated that since the effective modulus theory can not account for dispersion, its applicability for wave propagation in practical laminates is very limited, however, the effective stiffness theory is able to predict dispersion relations for composite laminates.

The displacements of the reinforcing layers and the matrix layers are approximated by linear expansions in terms of the thickness coordinate. It is noted that no consideration is given to the continuity of tractions across the interfaces.

The inclusion of initial stress into the formulation was later given by Sun [85] in which each layer behaves as a Mindlin plate under initial stress. What is common among the existing theories that have been used to describe the vibration characteristics of laminated plates is that the displacement behavior of the plate through-the-thickness is specified.

2.3.2.6 Other Approaches

Three dimensional elasticity solutions for vibration of laminated plates have been presented in literature [41,70,80]. An exact free and forced vibration analysis for harmonic oscillation, of rectangular three ply symmetric laminated plates, simply supported on all edges with no restrictions on thickness variations of stresses or displacements was given by Srinivas et al. [80]. A comparison of the lowest vibration frequencies for different material and geometric parameters was made with the CPT results presented by Pister [63] and the limitations of CPT were discussed.

Reddy and Kuppusamy [70] used a three dimensional elasticity solution that assumes continuous displacements at the interfaces and compared it to FSDT. They found that FSDT predicts higher frequencies for given modes than does the three dimensional elasticity solution. As found in other investigations, the degree of material anisotropy as well as plate aspect ratio adversely affect the accuracy of the frequencies predicted by the plate theory. Since the computational expense of the more accurate three dimensional elements is formidable in problems that require a large number of elements, Reddy and Kuppusamy stated that a higher order plate theory should give as accurate results, but less expensive, than the three dimensional element.

A formulation for the analysis of thin laminated plates subjected to low velocity impact was presented by Kelkar, Elber

and Raju [46]. In order to obtain large deflection behavior, the authors used a simple plate-membrane coupling model with low-velocity impact type point loading. To obtain the large deflection shape for thin circular plates, the plate and membrane problems were solved independently and the two solutions were then coupled. Kelker et al. [46] pointed out that classical solutions to the large deflection problem only represent a membrane correction to plate stiffness. Solutions of the coupling model were compared with the classical plate solution and with experimental results and it was observed that the coupled model gave solutions which compared well with experimental results while the classical solution did not.

Although the variety of formulations discussed above have provided a major contribution to the analysis capability, considerable work remains to be done to develop new theories or to make the modifications to existing theories necessary for the accurate prediction of the response of laminated plates to transient loading.

2.4 Determination of Failure

The solution of the third of Greszczuk's impact problems requires a criterion capable of describing behavior in any one of the several possible failure modes that can be associated with low velocity impact. Several failure models have been used (e.g. Tsai-Wu, Tsai-Hill, Max. Stress, Max. Strain, etc) but each is limited

to specific failure modes and often to specific loading conditions. In order to fully describe the behavior and failure of a composite during loading, a description of the stress field through the thickness on a ply by ply basis must be made. This requires adopting a discrete laminate theory in preference to a smeared laminate analysis.

CHAPTER III

EXPERIMENTAL PROGRAM

3.1 Introduction

Low velocity impact tests on the graphite/epoxy plates of different thicknesses and ply orientations were conducted. A visual inspection of each target plate was performed immediately after impact. The results of these inspections along with C-scan, X-ray, and deply results obtained from selected specimens are presented. Correlations between the instrumented impact tests and plate damage as measured visually and by ultrasonic techniques are made to determine a relationship between the impact event and the progression of damage. The experimental program was designed to determine the progression of impact damage with increasing amounts of impact energy. The size, shape, and location of damage areas were recorded for tested plates impacted at damage levels ranging from the threshold level up to the point where visible splitting in the far side plies occurred.

3.2 Specimens

Specimens were panels of graphite/epoxy composites fabricated from prepreg tapes. The panels were manufactured in the Structural Composites Laboratory in The Civil Engineering Department at The Ohio State University and in the Composites Facility of the Flight Dynamics Laboratory at Wright-Patterson Air Force Base. The specimens were vacuum-bag cured according to the manufacturer's recommendations. All specimens were symmetric about their midsurface.

The panels were scanned ultrasonically for delaminations, cracks, or foreign inclusions prior to testing. They were also measured for thickness uniformity. A resin analysis was conducted to determine the resin content, fiber fraction, and void fraction.

3.3 Test Equipment

3.3.1 Drop Tower

A model 8250 impact drop tower designed and built by Dynatup Products, and located in the Structural Composites Laboratory at OSU was used to load the specimens. The loading system consists of three basic components: a drop tower with weighted crosshead and impactor which is guided by rails to the target, a load transducer mounted in the impactor and hardware and software for data acquisition and reduction. Specimens up to 19" wide (48.3 cm) can

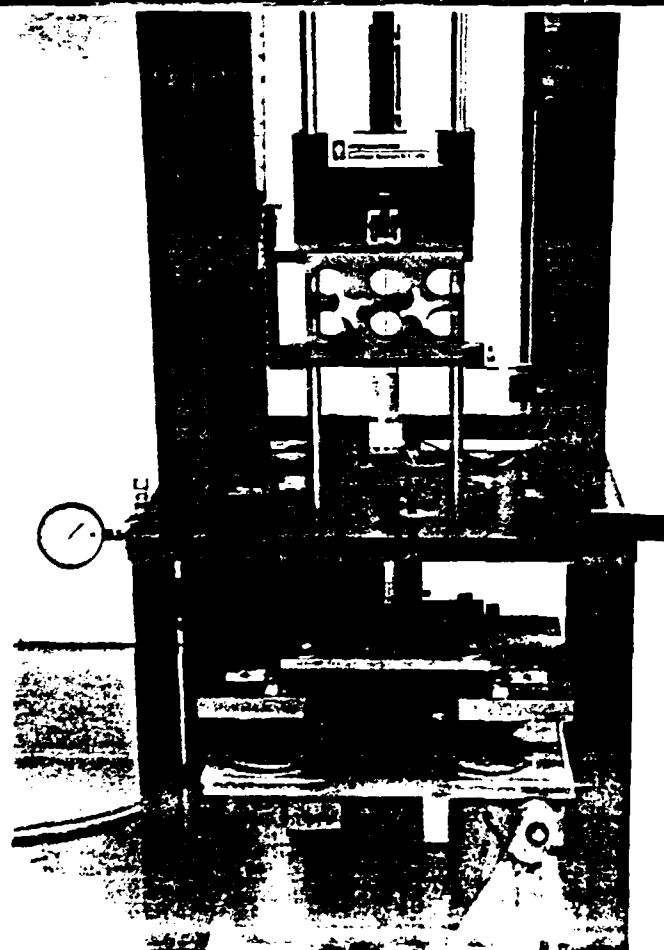
be tested using an adjustable platform installed under the drop tower baseplate. Impact energies of 0.47 to 223.6 ft-lb. (0.64 to 303.2 J) can be achieved by varying the crosshead weight (from 5.5 lb (2.5 kg) to 100 lb (45.5 kg)) and the impact velocity (from 2.0 to 12.0 ft/s (0.61 to 3.66 m/s)). The impactor used in all the impact tests was a 1.0 in (2.54 cm) diameter cylindrical shaft with a 1 inch hemispherical tip made of stainless steel. The drop tower is shown in Figure 1.

3.3.2 Data Acquisition

Data acquisition and analysis were accomplished with software provided by the manufacturer specifically for use in instrumented impact testing with the drop tower. Data acquisition was triggered when a flag, attached to the crosshead, passed through a light beam/photodetector. The velocity of the impactor was measured by recording the time required for the flag to pass through the detector.

3.4 System Calibration

The weight of the impactor was measured using a Sensotec model GM load cell with a range of 0 to 100 lb. (0 to 45.4 kg.) and a precision of ± 0.01 lb. The load-time history was measured directly from the impactor load cell, the impact energy, absorbed energy and



PICTURE IN PHOTOGRAPH IS PRESS TOWER

displacement time histories were computed from the measurements of impact velocity, crosshead mass, and the load-time history.

3.5 Impact Test Procedure

Low velocity impact tests were conducted on graphite/epoxy plates of different stacking sequence and thickness. Each specimen was bolted between two metal plates in a NASA holding fixture [2]. The target area was a 5.0 inch (12.7 cm) square. The crosshead was raised to a predetermined height and released to strike the center of the specimen normal to the plate surface. The crosshead was caught by a machine break after the initial impact in order to prevent multiple impacts. By adjusting the crosshead weight and/or the drop height, the impact energy could be controlled. Immediately after the load cell recorded the impact response, the test data were viewed and plotted. The record was then stored to be retrieved later for test comparisons.

3.6 Post Impact Damage Detection Techniques

Of the several destructive and non-destructive methods mentioned in Section 2.2 to detect internal damage in composite plates, the techniques used in this program included ultrasonic C-scan, thermal-oxidant deply, visual inspection, and penetrant enhanced X-ray. No single method can give a complete description of the internal damage in a composite specimen. The methods that

were incorporated in the investigation described in this report are summarized below.

3.6.1 Ultrasonic C-scan

Following the impact at the center of each test specimen, the extent of the damage was studied visually and recorded by the through transmission C-scan technique. This approach identifies damaged regions in the target panel by measuring changes in the attenuation of an ultrasonic wave as the wave passes from intact areas to damaged zones in the plate. This method is useful for identifying the areal extent of the damaged region but does not provide the detail needed to characterize the damage on a ply by ply basis.

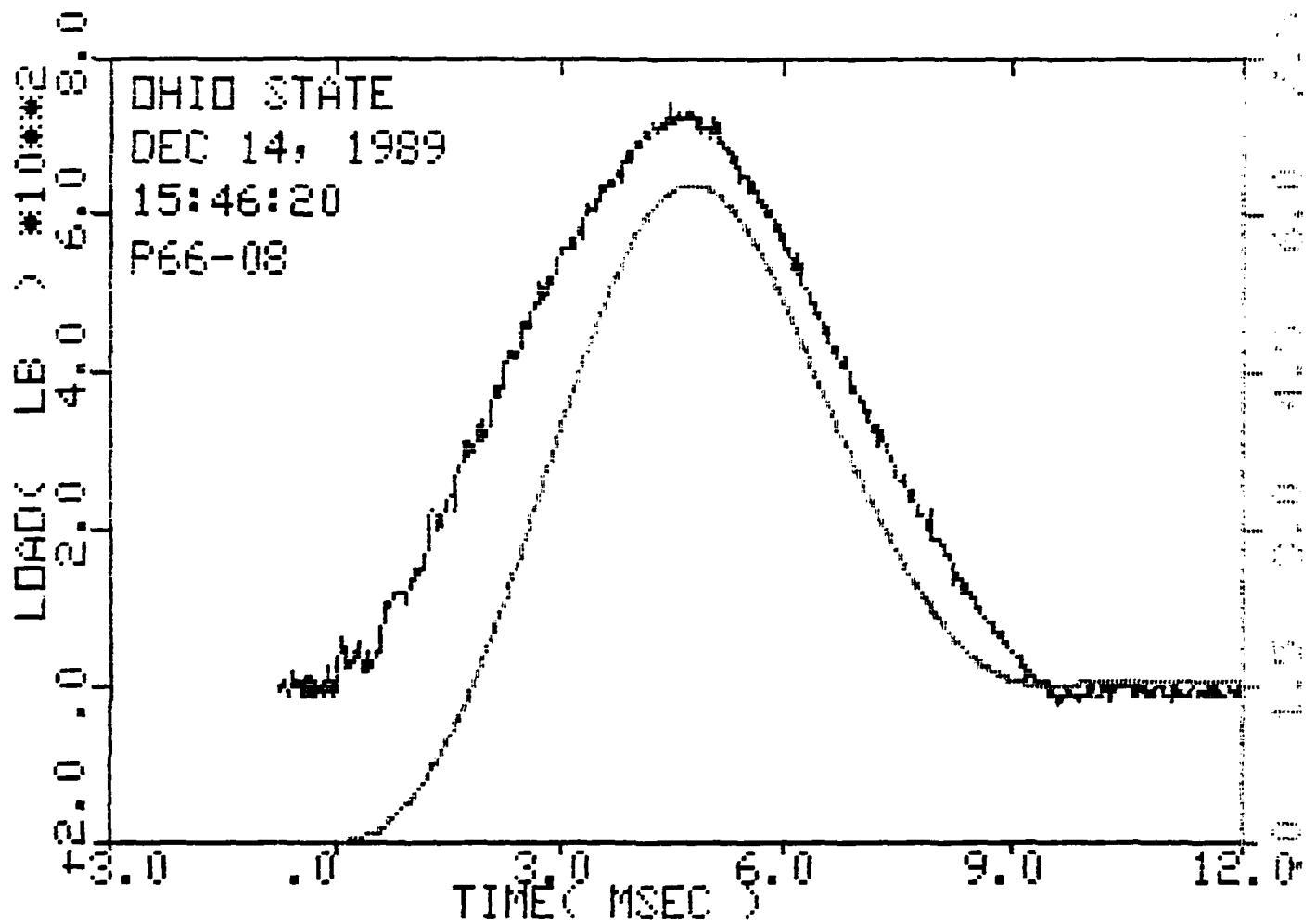
3.6.2 Thermal Oxidant Penetrant Deply

The deply technique is a destructive inspection technique developed by Freeman [28,29] to investigate through-the-thickness damage distribution. The technique involves partially pyrolyzing the resin matrix, permitting the individual plies of the laminated composite to be separated. In this program, square segments of the target plate containing the damage area as determined from the C-scan results, were studied. To maintain the proper orientation, a small notch was cut from the upper right hand corner of each deply specimen. The deply specimen was placed in a screen mesh

holder with a screen cover. The four corners of the screen holder were set on crucibles inside the furnace to allow for even heating of the specimen. The furnace temperature was maintained at the recommended temperature of 780 F (C) for between 60 and 90 minutes. After the sample was removed from the oven and allowed to cool at room temperature, the individual plies could be lifted one at a time and placed on a thin piece of plexiglass. Each lamina was visually inspected for damage.

3.7 Impact Test Results:

The data obtained from the impactor load cell was plotted as force and energy time histories. A typical plot combining the two time histories is shown in Figure 2. At the beginning of the record, a spike in the load time history reflecting the inertial load required to accelerate the specimen from zero to the velocity of the falling impactor can be clearly identified. Typically, this sharp spike is followed by a decaying oscillation caused by ringing in the load cell. At low levels of impact energy wherein the specimen does not experience any detectable damage, the load time history curve exhibits a smooth decrease in load beyond the peak as shown in Figure 2. From Figure 3 it is seen that as the impact energy is increased, a high frequency spike at or near the peak in the load time history curve indicates the onset of local failure,. The rapid unloading that typically followed this spike causes the load cell to oscillate, as seen in the load data following the peak



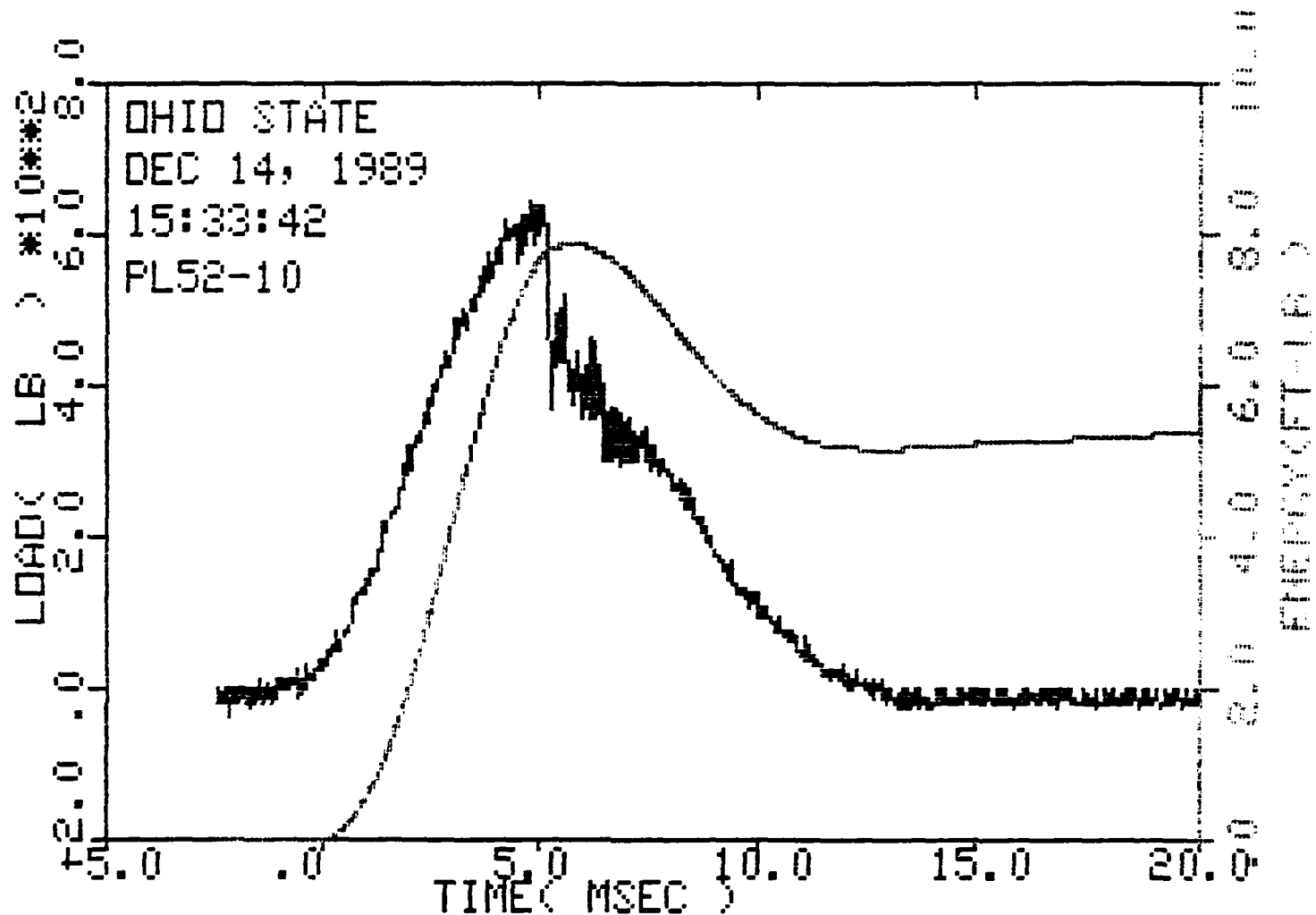
Specimen Id	Temp (f)	Impact Veloc. (ft/sec)	Energy (ft-lb)	Time (msec)		Load (lb)		Energy (ft-lb)	
				Max	Total	Max	Max Id	Total	
P66-08	70.	6.51	6.13	4.45	9.37	746.5	6.231	7.716	

Filter No. = 1, No Smoothing.

Comments:

barely dented top

FIGURE 2: FORCE AND ENERGY TIME HISTORY (NO DAMAGE)



Specimen Id	Temp (°)	Impact		Time		Load		Energy	
		Veloc. (ft/sec)	Energy (ft-lb)	(msec)	(msec)	(lb)	(lb)	(ft-lb)	(ft-lb)
PL52-10	70.	7.28	7.66	Max	Ld Total	Max	Max	Max	Total
				4.82	12.17	649.0	7.509		3.906

Filter No. = 1, No Smoothing.
Comments:
dentel top, some split bottom

FIGURE 3: FORCE AND ENERGY TIME HISTORY (DAMAGE)

load in Figure 3. Examples of the energy time histories resulting from the impact are also shown on Figures 2 and 3. Load parameters and target responses for the various plate configurations tested are presented in the Appendix.

3.7.1 Visual Inspection

To assess the effects of the impact on the graphite/epoxy plate a damage scale, shown in Figure 4, was developed. The scale is divided into six major damage levels ranging from no detectable damage to fiber breakage on the impact face and fiber breakage and matrix fracture on the back face (away from the impact site) of the panel. In order of increasing severity (damage) the proposed levels are as follows:

1. No Damage
2. Dented top surface
3. Discolored dented top surface
4. Dented top surface, split bottom surface
5. Dented top surface, broken and split bottom fibers
6. Broken top surface

Damage levels were plotted against the total energy at impact and net energy absorbed (impact minus rebound) for each of the ply configurations studied in the test program. To account for the different laminate thicknesses, the impact and net energies were each normalized by dividing by the number of plies in the plate and presented as either impact or net energy per ply. Figure 5 is a compilation of the damage vs. impact energy data for 0/90 crossply panels. A similar plot for +45/-45 panels is presented in

DAMAGE LEVELS

Increasing Damage

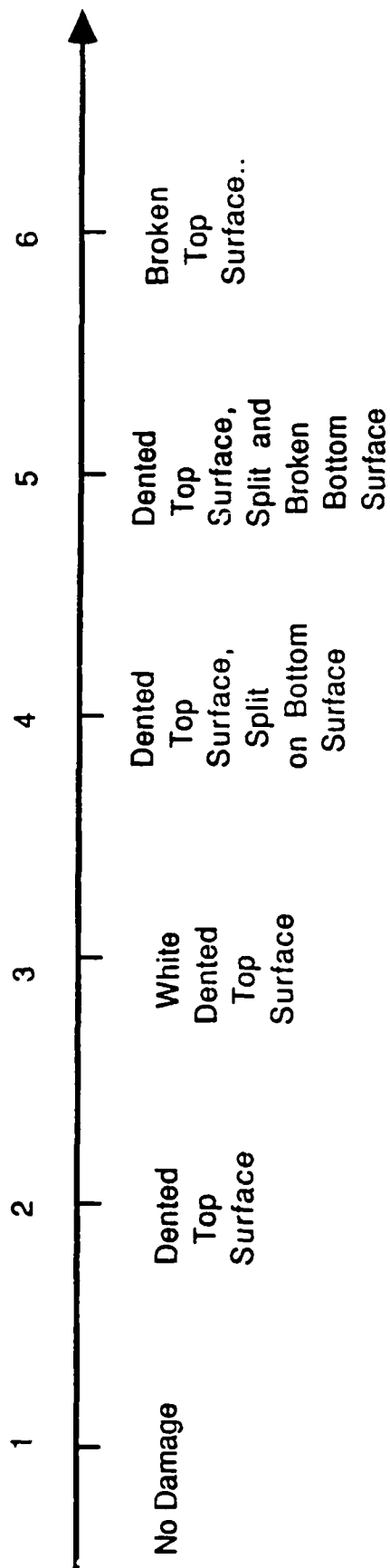


FIGURE 4: VISIBLE DAMAGE SCALE

Damage level vs. Impact Energy

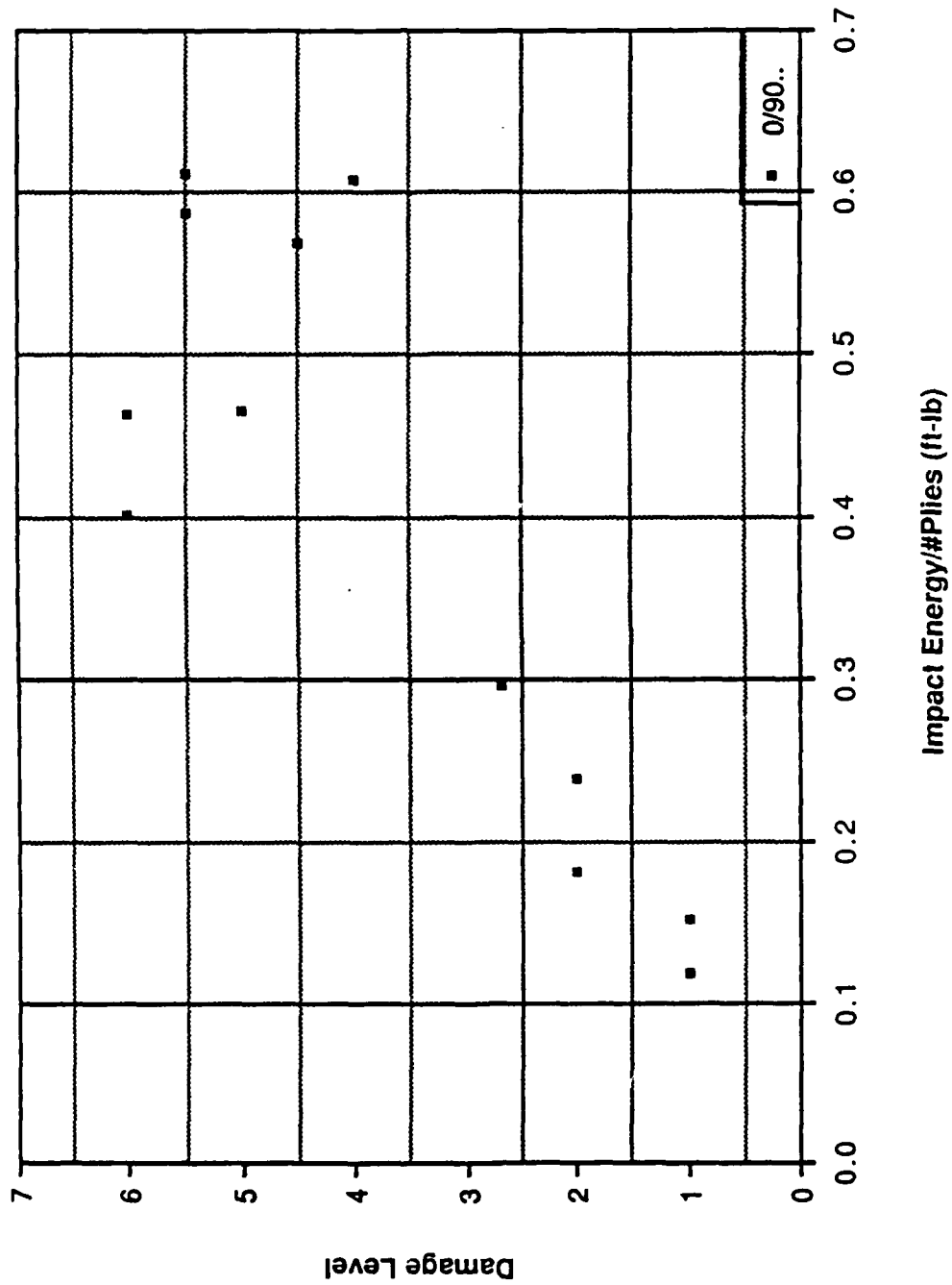


FIGURE 5: VISIBLE DAMAGE VS. IMPACT ENERGY 0/90 PLATES

Figure 6. The results of the tests for both ply orientations are combined in Figure 7. It is clear that increased impact energy results in higher levels of damage as described by the damage scale and, although there is considerable scatter in the data, a relationship between energy and damage can be specified. Such an expression for damage level as a function of impact energy is presented in Figure 7. Plotting the net energy vs. damage level results in figures similar to those presented for impact energy in Figures 5-7. Figures 8-10 show that although the data are scattered, increased levels of net (absorbed) energy result in increased damage levels as defined by the proposed damage scale and that a prediction can be made of the level of damage to be expected from a given amount of energy specified on a per ply basis.

Taking the ratio of the net energy to the impact energy defines the energy ratio. In Figure. 11, the damage levels are plotted against the energy ratio. Clearly, increasing levels of damage can be associated with higher levels of the energy ratio.

3.7.2. Ultrasonic Evaluation of Damage

Each of the panels included in the Appendix was interrogated ultrasonically. Each resulting plot (C-scan) provided a two dimensional representation of the damage zone by outlining its

Damage Level vs. Impact Energy

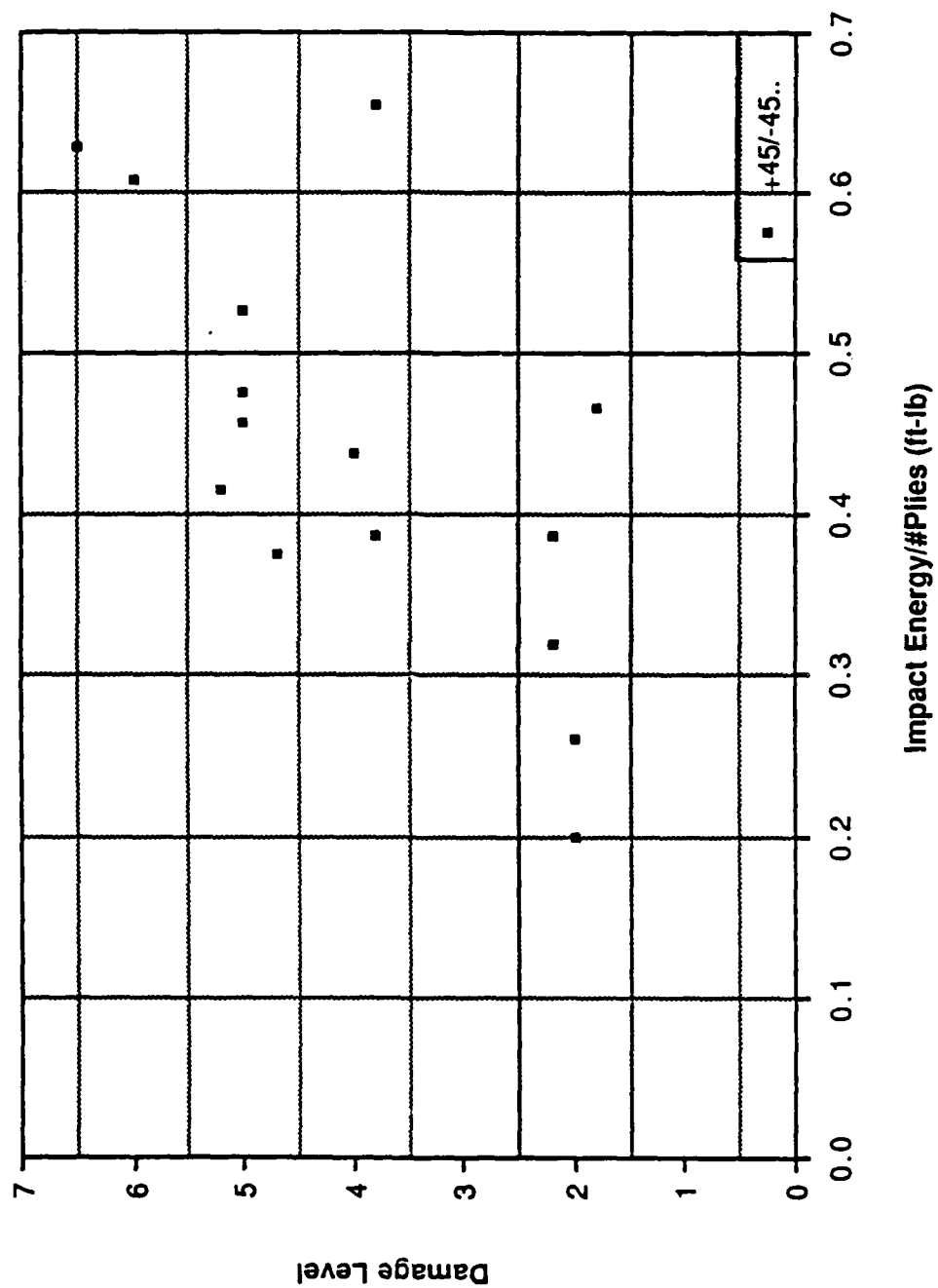


FIGURE 6: VISIBLE DAMAGE VS. IMPACT ENERGY +45/-45 PLATES

Damage Level vs. Net Energy

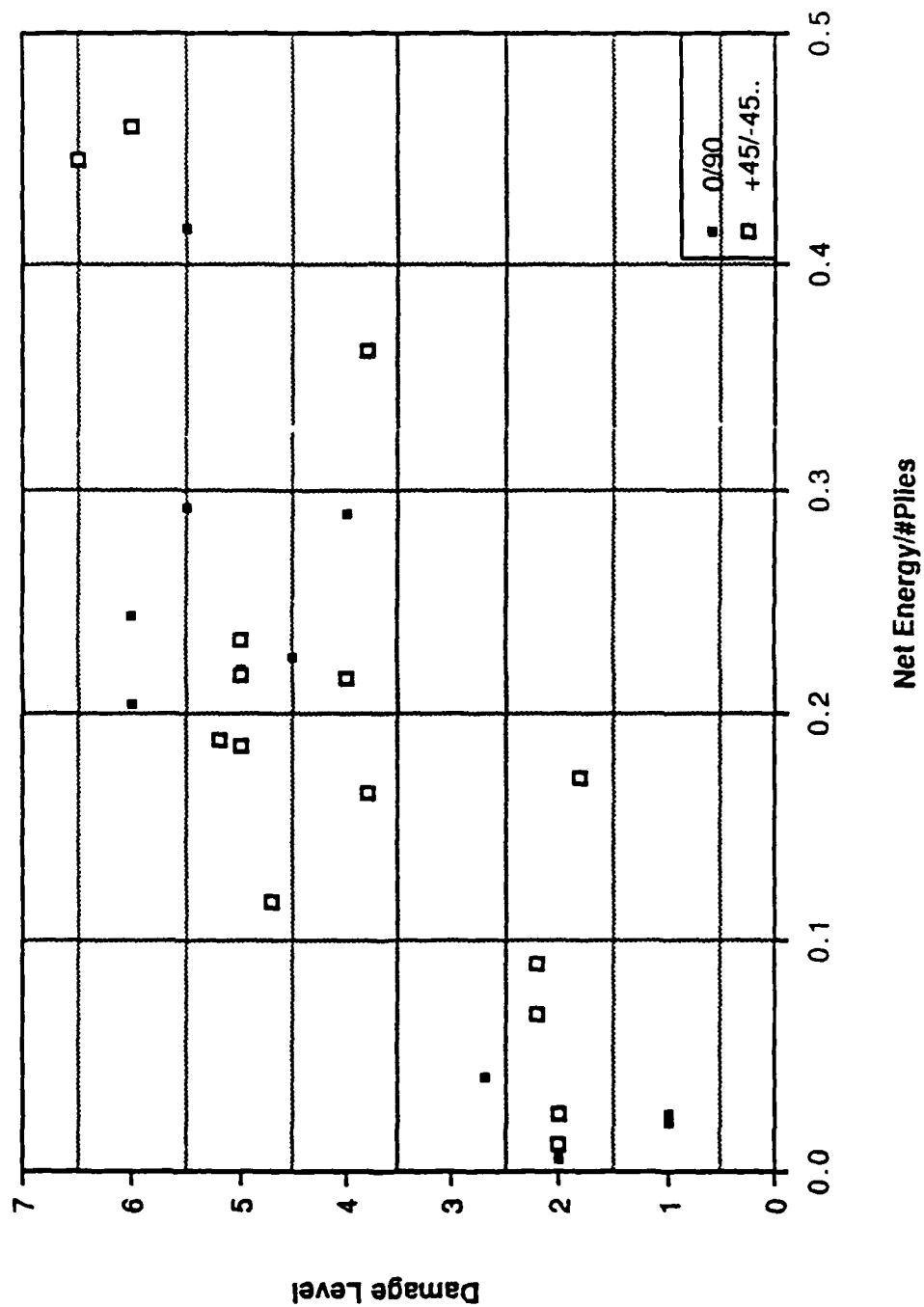


FIGURE 7: VISIBLE DAMAGE VS. IMPACT ENERGY 0/90 AND +45/-45 PLATES

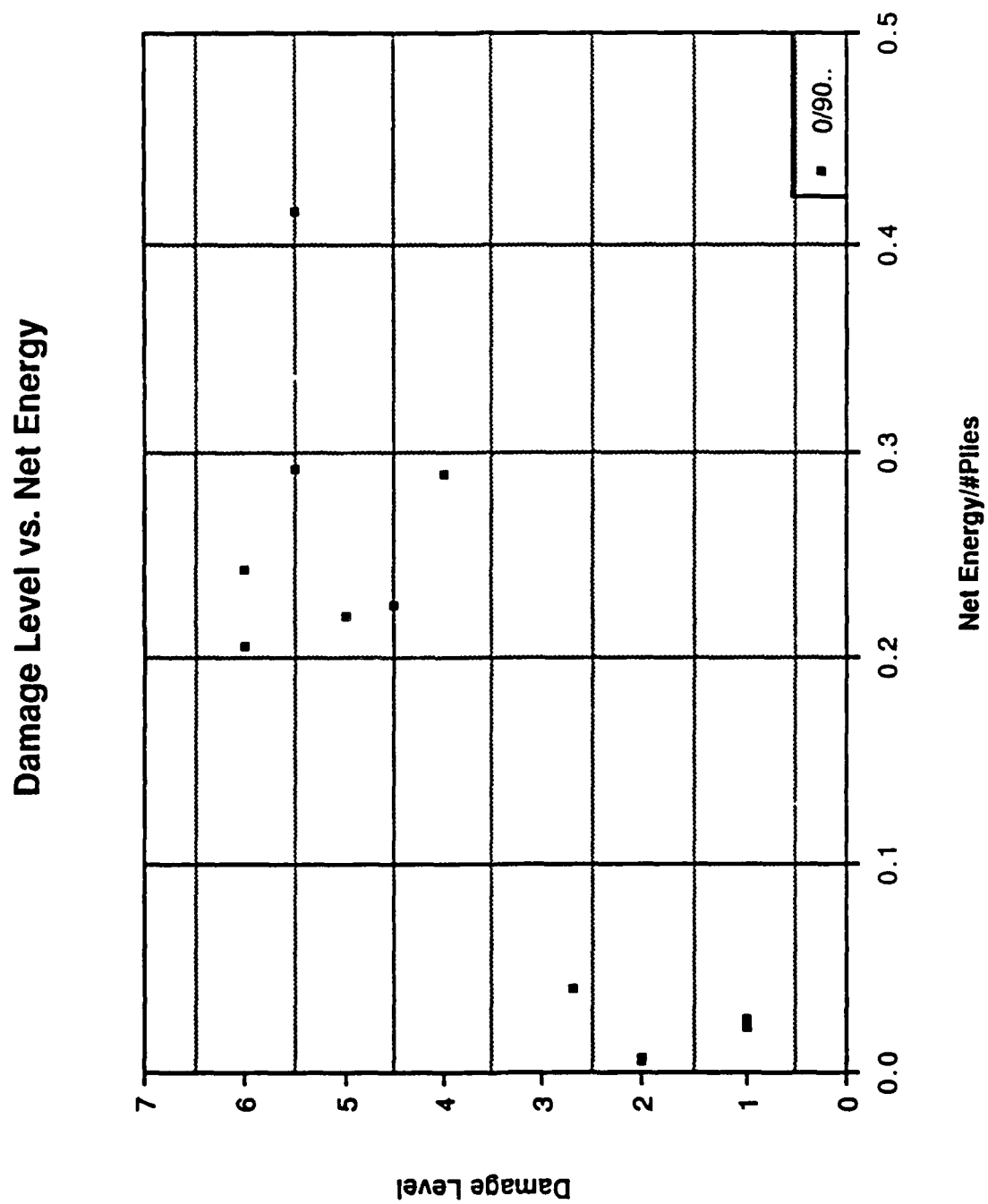


FIGURE 8: VISIBLE DAMAGE VS. NET ENERGY 0/90 PLATES

Damage Level vs. Net Energy

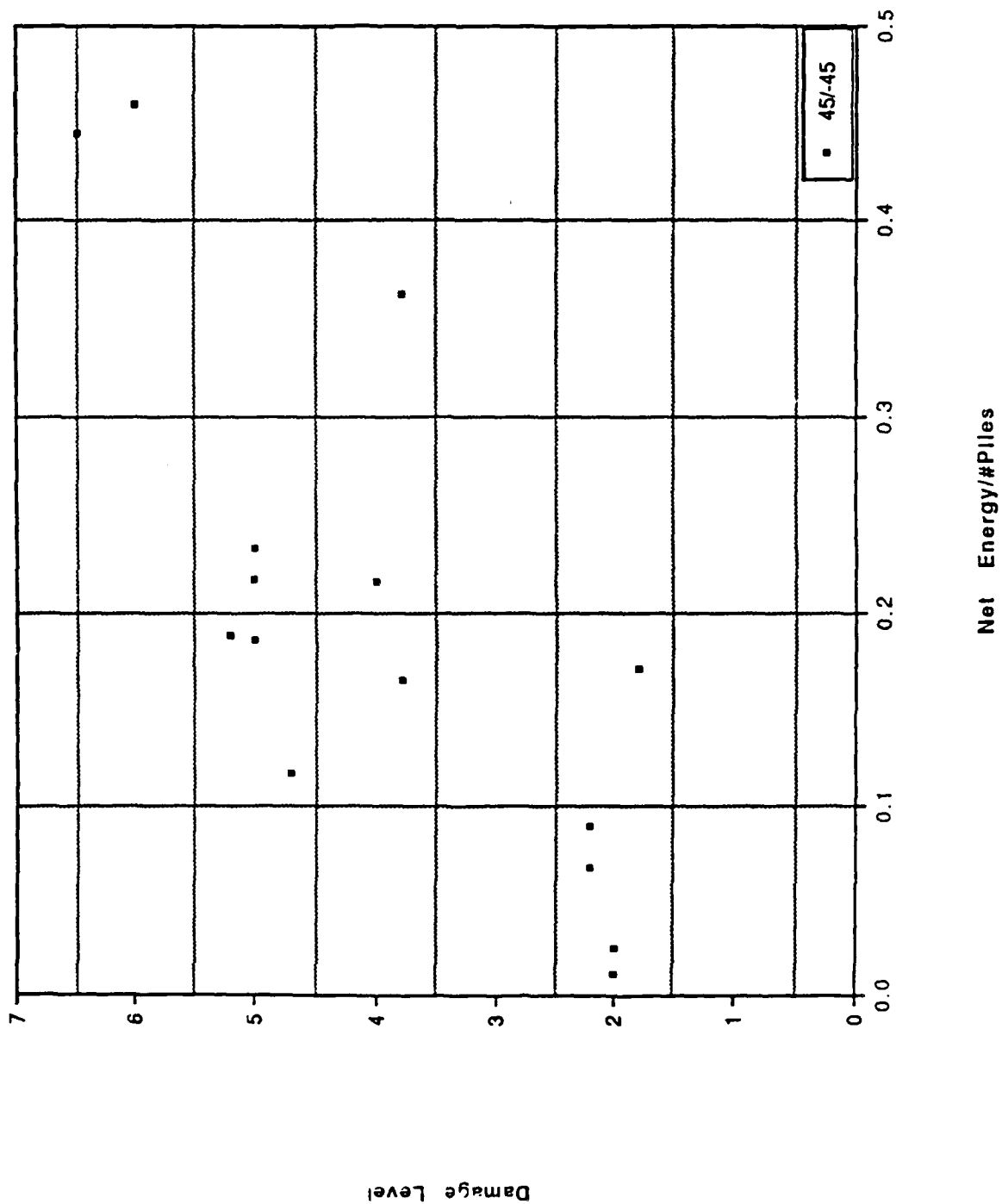


FIGURE 9: VISIBLE DAMAGE VS. NET ENERGY +45/-45 PLATES

Damage Level vs. Net Energy

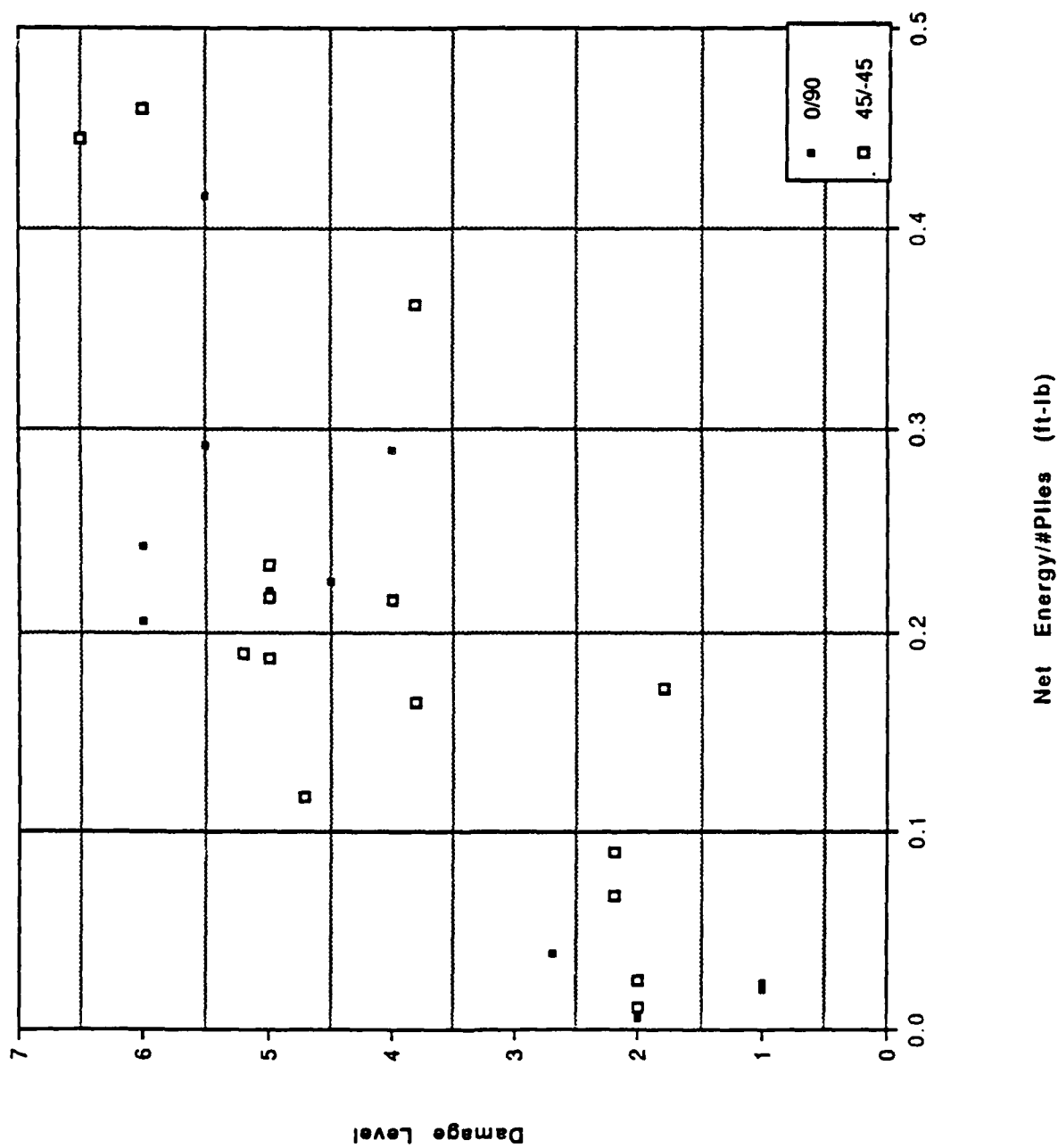


FIGURE 10: VISIBLE DAMAGE VS. NET ENERGY 0/90 AND +45/-45 PLATES

Damage vs. Energy Ratio

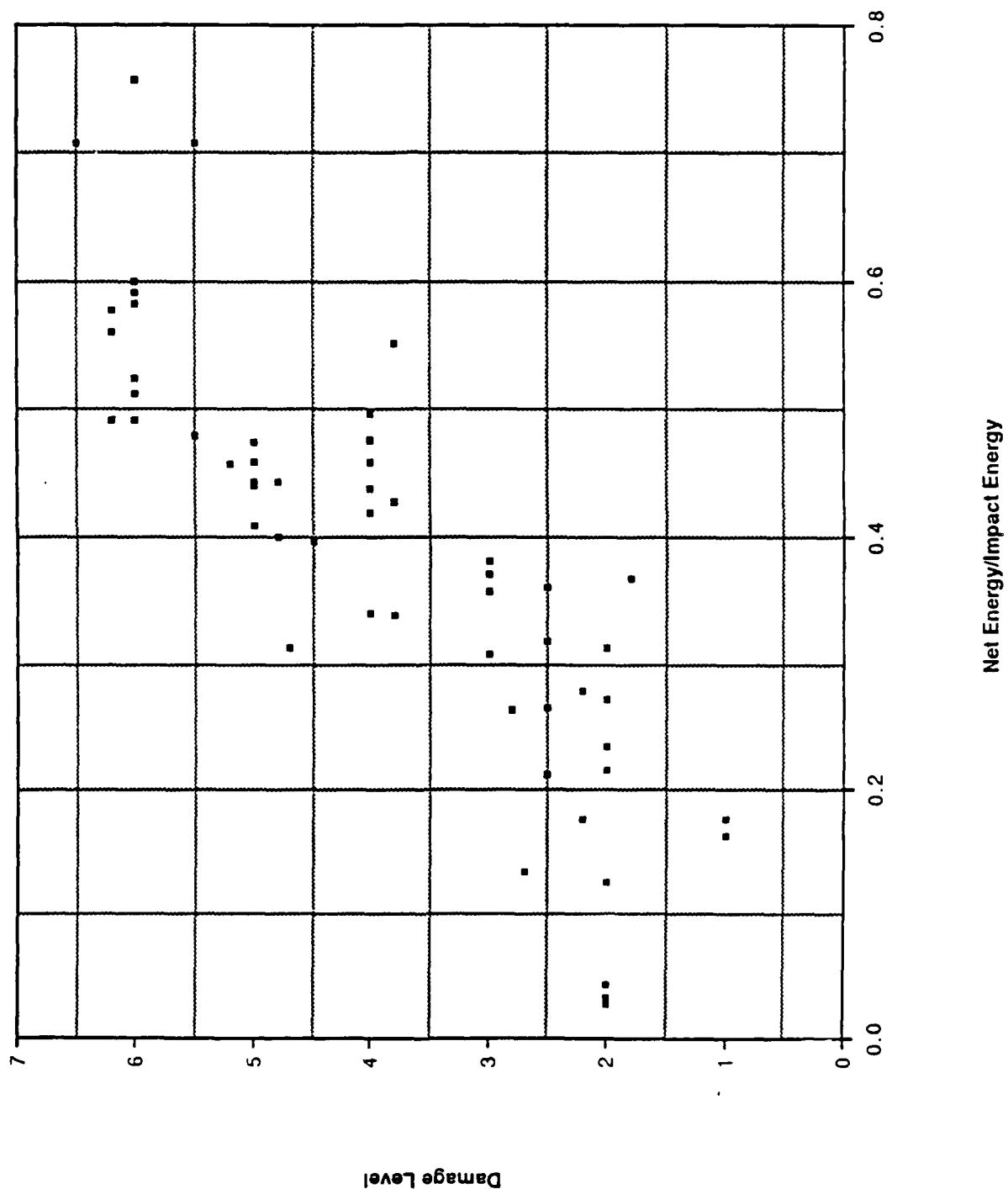


FIGURE 11: ENERGY RATIO VS. DAMAGE LEVEL

areal extent. Damage area could then be measured and correlated with the loading parameters. An example of a C-scan plot for a typical panel is shown in Figure 12. Figures 13, 14, and 15 show the damage area versus the impact energy per ply. Notice that there is clearly a threshold level of energy below which no damage is detected. This damage threshold for the (± 45) plates occurs roughly at impact energy per ply of 0.4 ft-lb (0.40 ft-lb for 12 ply plates, 0.39 ft-lb for 24 ply plates, and 0.37 for 48 ply plates). Notice also that for approximately the same impact energy per ply, the damage area is the largest for the thicker 48 ply plates and smallest in the 12 ply specimens. Figure 16 shows the damage area per ply for the (0/90) plates of 12, 24 and 48 ply thicknesses. Again it appears that a threshold energy level can be identified at about 0.3 ft-lbs.

As was done in the development of the visual damage classification scale, the damage as determined by ultrasonic methods can be plotted as a function of the net energy. Figure 17 shows the damage versus net energy per ply for the (± 45) 12, 24, and 48 ply specimens. The threshold damage level can be seen to occur at approximately 0.1 ft-lb. Damage area vs. net energy per ply is plotted in Figure 18 for the (0/90) specimens. The data indicate a threshold damage level of approximately 0.05 ft-lb for this ply configuration.

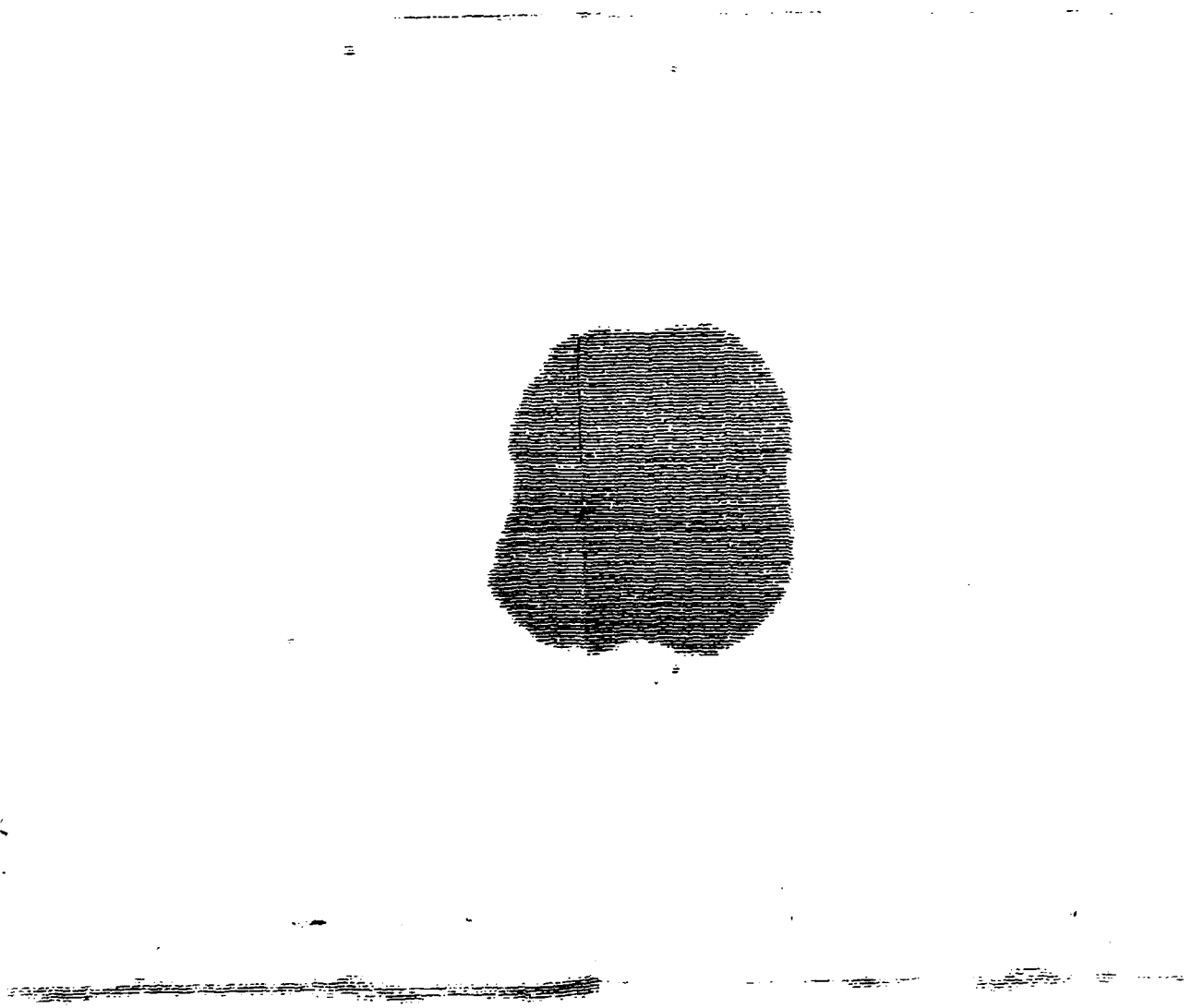


FIGURE 12: TYPICAL C-SCAN PLOT

Damage Area -vs- Impact Energy/Ply
($\pm 45^\circ$)3s

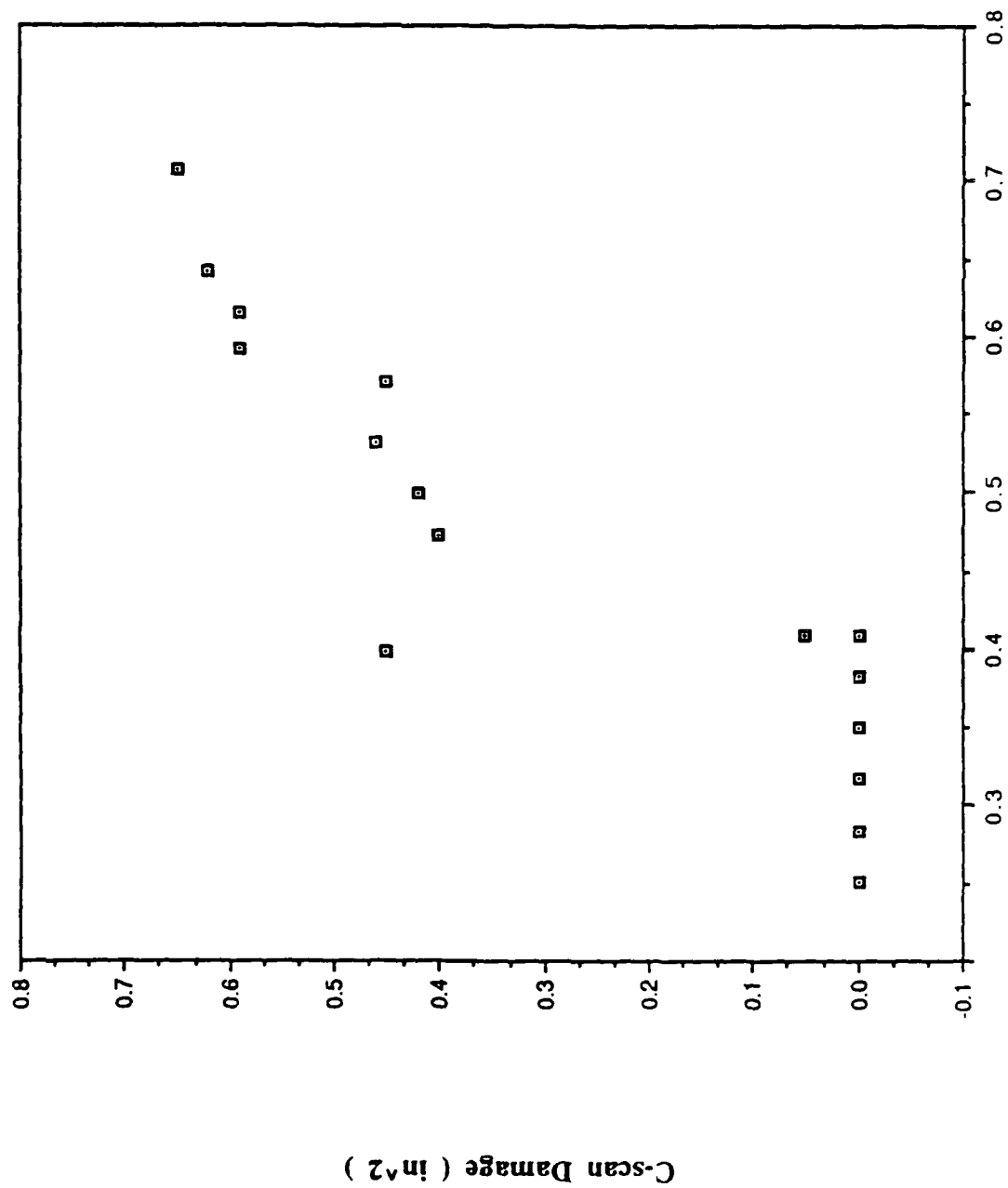


FIGURE 13: DAMAGE AREA VS. IMPACT ENERGY PER PLY

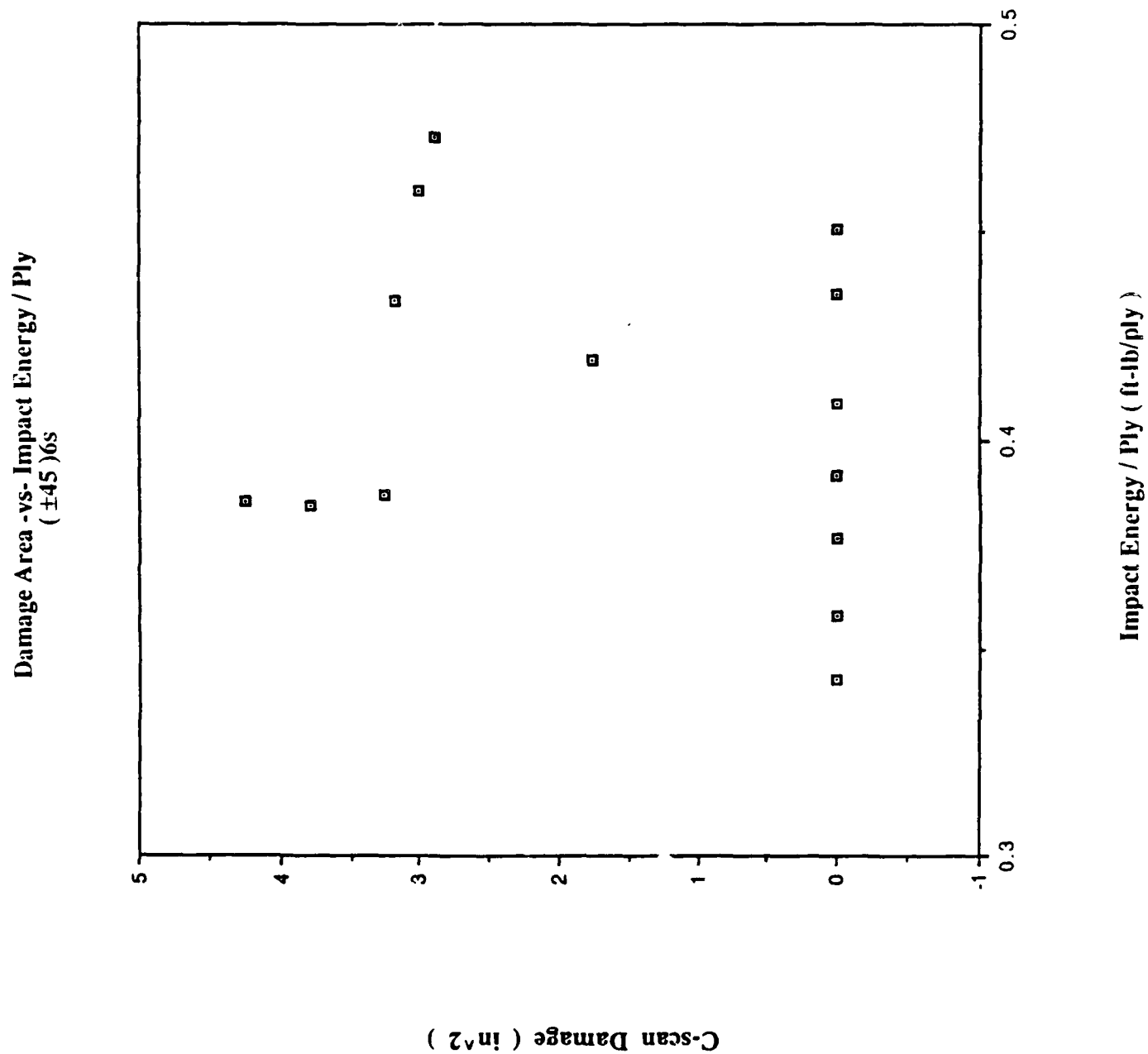


FIGURE 14: DAMAGE AREA VS. IMPACT ENERGY PER PLY

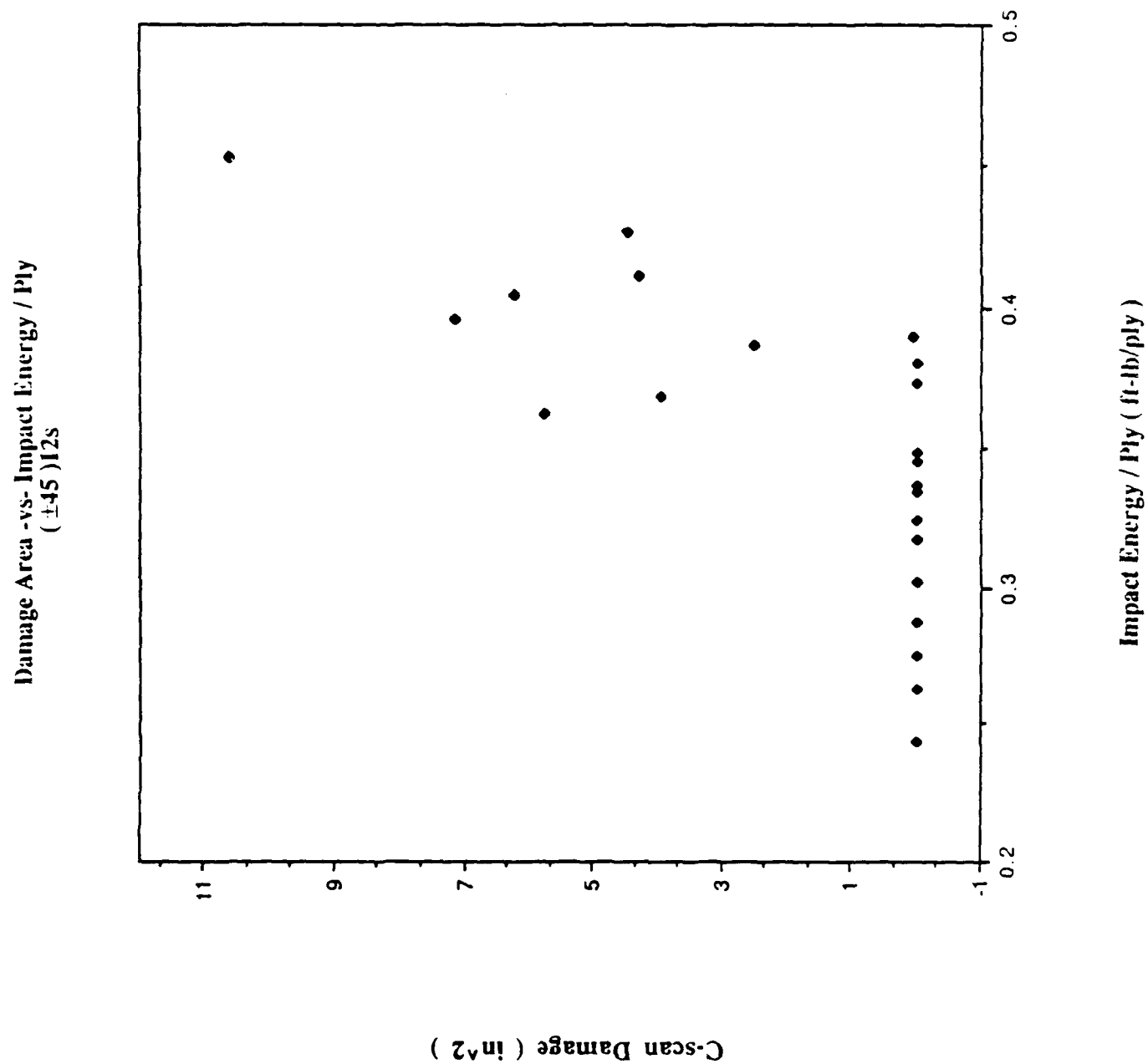


FIGURE 15: DAMAGE AREA VS. IMPACT ENERGY PER PLY

Damage Area -vs- Impact Energy / Ply
(0/90)3,6,12s

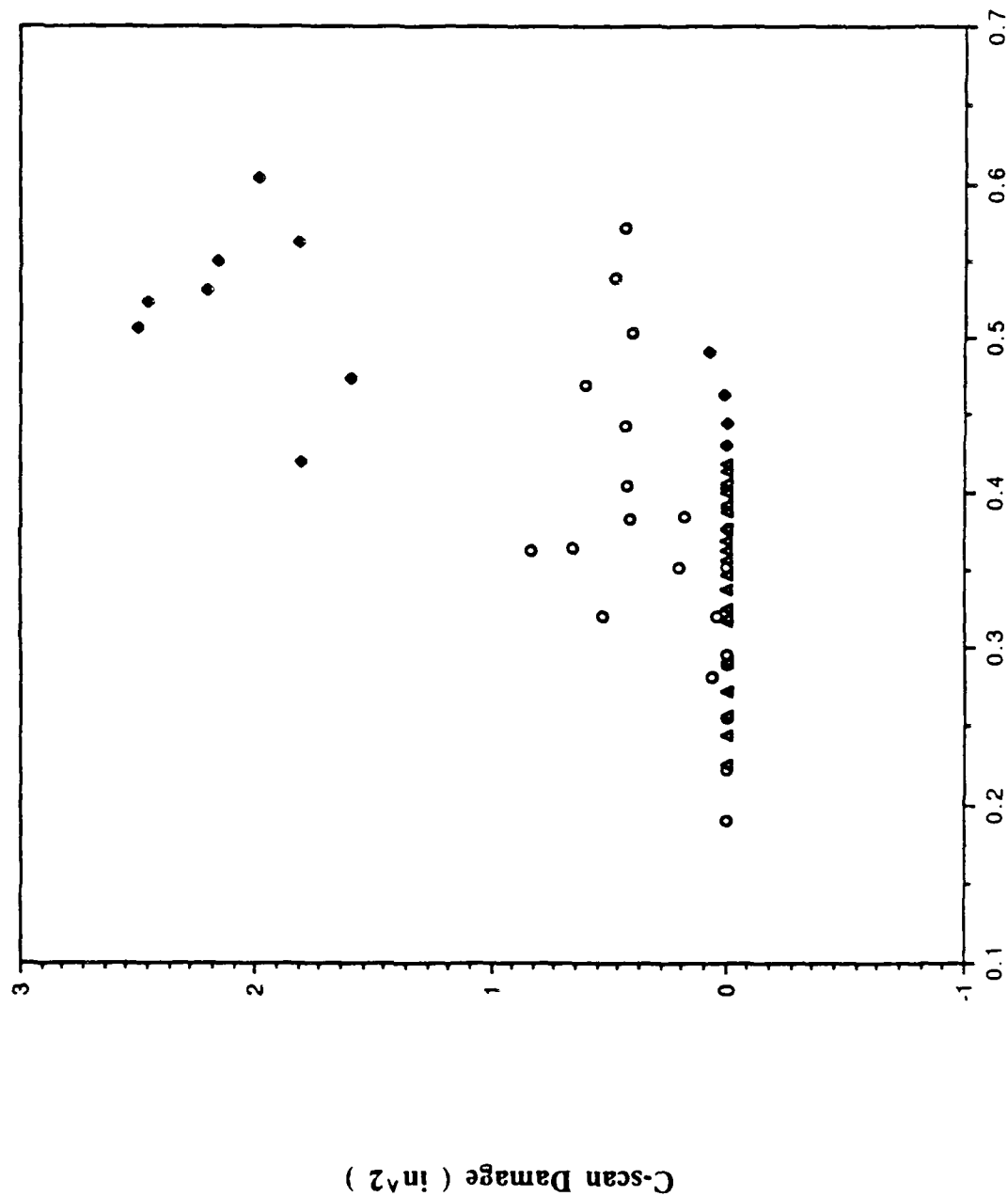


FIGURE 16: DAMAGE AREA VS. IMPACT ENERGY PER PLY COMBINED THICKNESSES

Damage Area -vs- Net Energy/Ply
(± 45) 3,6,12s

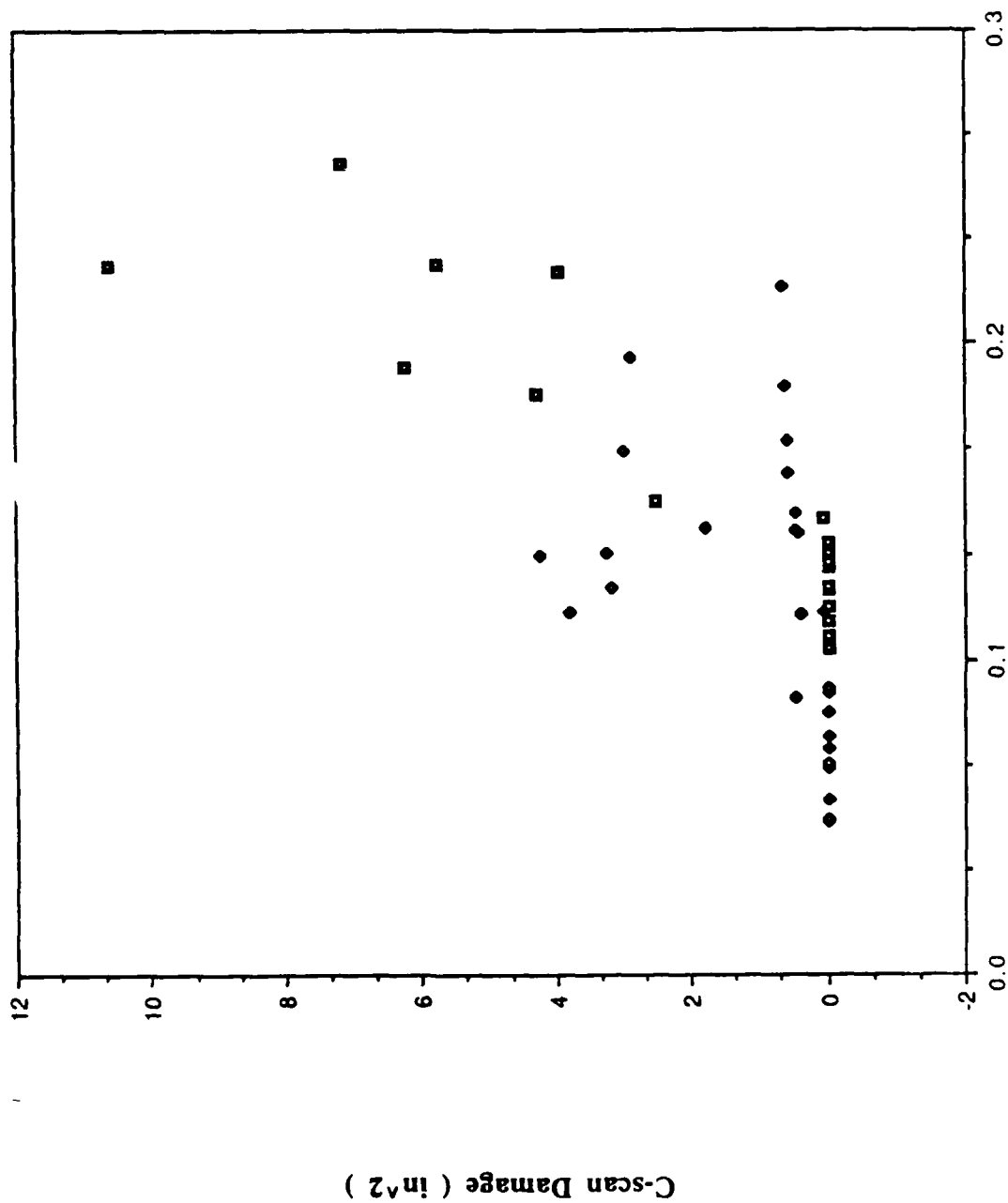


FIGURE 17: DAMAGE AREA VS. NET ENERGY PER PLY COMBINED THICKNESSES

± 45 PANELS

Damage Area -vs- Net Energy/Ply
(0/90) 3,6,12s

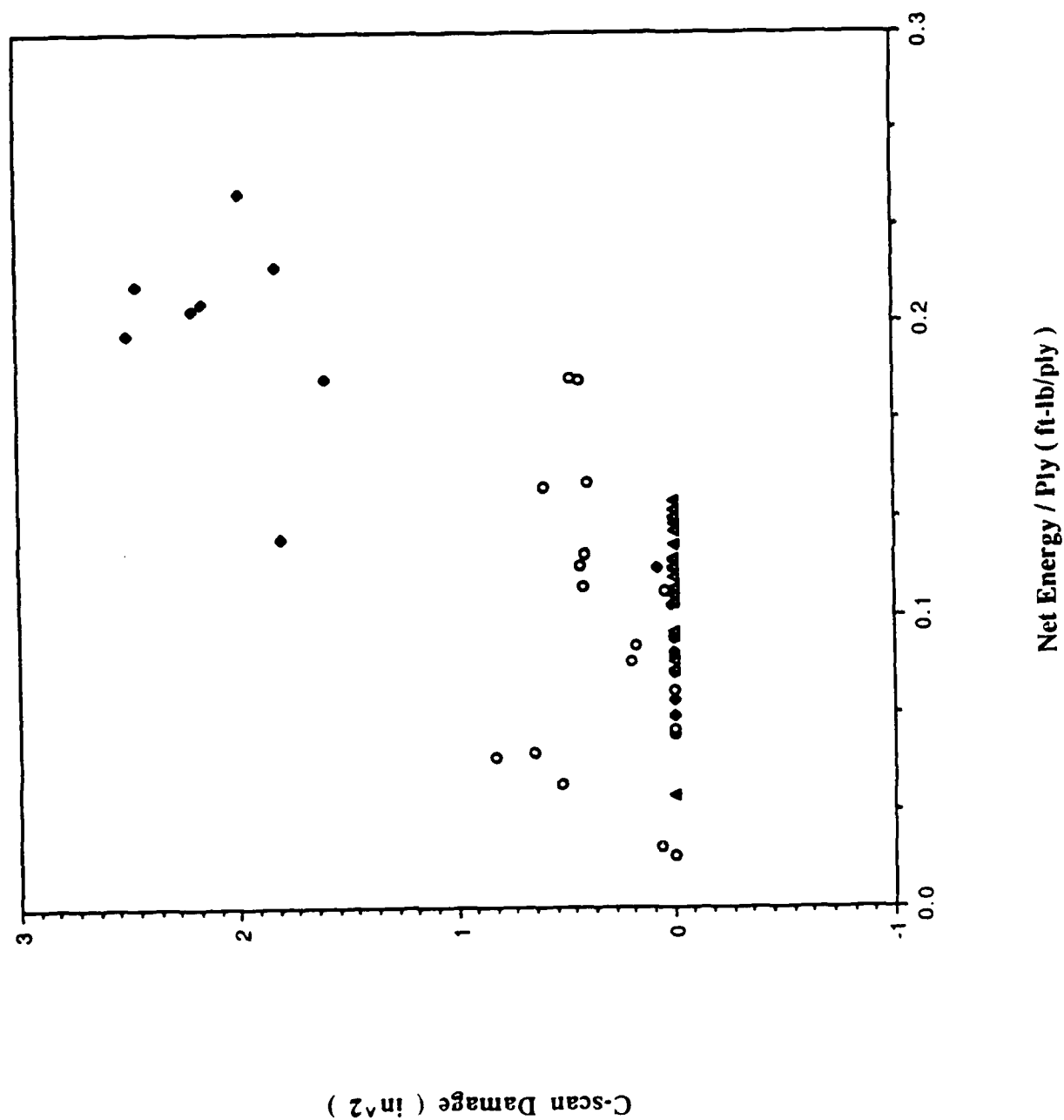


FIGURE 18: DAMAGE AREA VS. NET ENERGY PER PLY COMBINED THICKNESSES

0/90 PANELS

3.7.3 X-ray and Deply techniques

In addition to subjecting the impacted plates to visual and ultrasonic detection, selected specimens were x-rayed and then deplied in order to have a three dimensional description of damage.

Chapter IV

ANALYTICAL PROGRAM

After reviewing the present state of the art in the analysis of dynamics of laminate composites, the authors feel there is no completely acceptable solution to modelling and tracking through-the-thickness stress. However, the shortcomings of the present state of the art are not necessarily in laminate plate theory, but the application and extension of the available theories to dynamic problems.

4.1 *Equations of Motion of an Elastic Body*

Since transient loads on laminates often produce high stress gradients leading to failure, an accurate description of the stress field for such problems is imperative. The following theory is an extension of Pagano's [59] theory for stress fields in composite laminates to including inertia effects.

Consider a rectangular plate of uniform thickness h which is assumed to be homogeneous, linear elastic. The origin of the rectangular cartesian coordinate system is located in the midplane of the plate which is bounded by $x_1 = \pm a$, $x_2 = \pm b$, and $x_3 = \pm h/2$. See Figure 19.

The formulation begins with the differential equations of motion for three dimensional elasticity which are written as;

$$\sigma_{ij,j} + f_i - \rho_i = 0 \quad (1)$$

or separately

$$\sigma_{\alpha\beta,\beta} + \sigma_{\alpha 3,3} + f_\alpha - \rho_\alpha = 0 \quad (2)$$

$$\sigma_{\alpha 3,\alpha} + \sigma_{33,3} + f_3 - \rho_3 = 0 \quad (3)$$

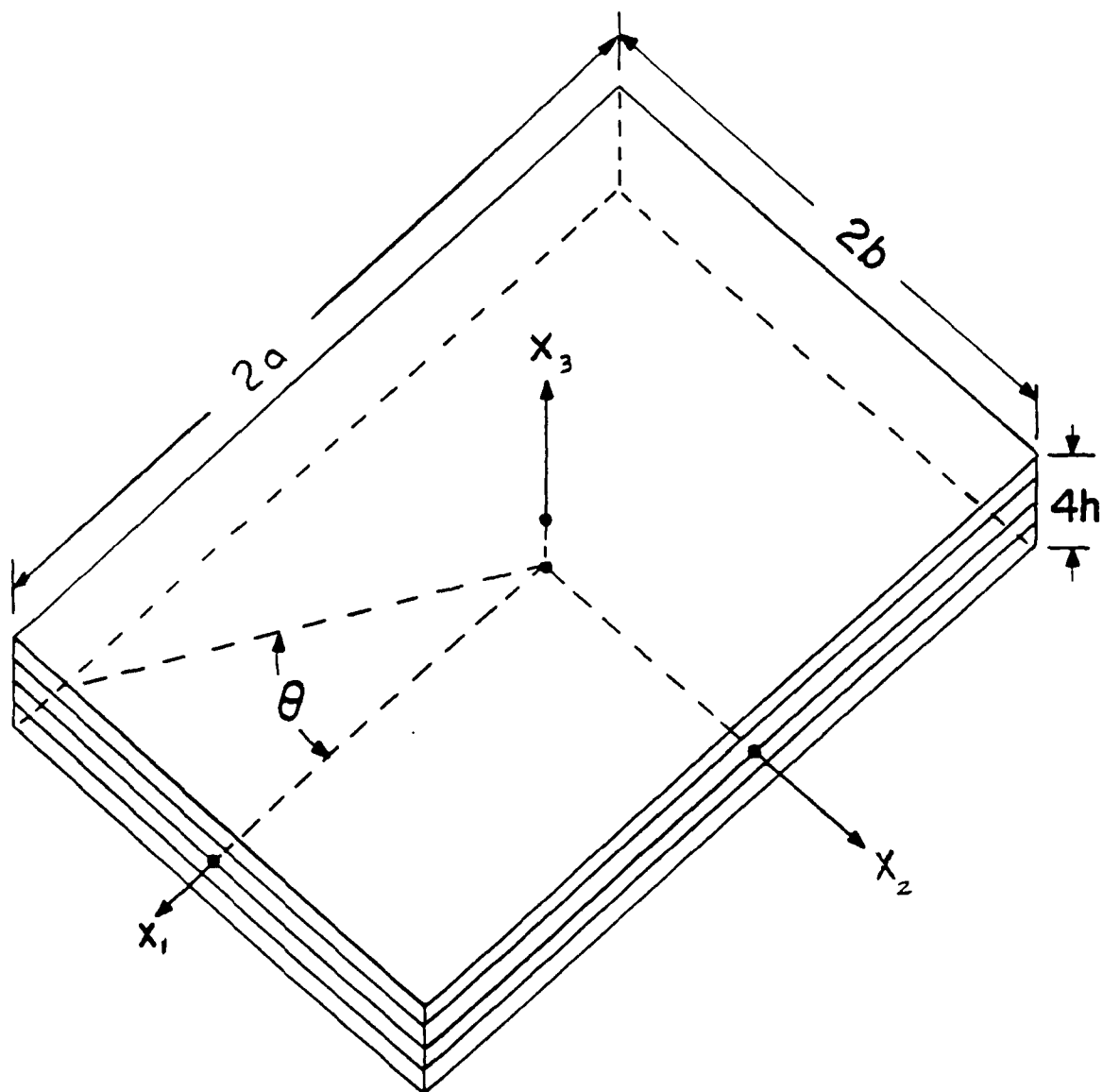


Figure 19: SIGN CONVENTION

where σ_{ij} are the components of the symmetric Cauchy stress tensor, f_i are the components of the body force vector per unit volume, and p_i are the momentum densities of the medium (mass density times the velocity vector). Standard index notation is used in which latin indices take on values from 1 to 3 and greek indices take on values 1 and 2. If we assume that the mass density is independent of time we can write

$$p_i = \rho \ddot{u}_i \quad (4)$$

where the superposed dots represent differentiation with respect to time.

4.2 Constitutive Relations

The generalized Hooke's law for an anisotropic linear elastic material is

$$\sigma_{ij} = E_{ijkl} \epsilon_{kl}$$

where E_{ijkl} are components of the isothermal elasticity tensor. In the absence of body couples, due to symmetry of σ_{ij} and ϵ_{ij} and the existence of a strain energy function

$$E_{ijkl} = E_{jikl} = E_{klij} = E_{ijlk}$$

and the number of independent constants is 21. For a monoclinic material, with symmetry about $x_3 = 0$, the number of independent constants is 13 and the constitutive equations are of the form

$$\sigma_{\alpha\beta} = E_{\alpha\beta\gamma\delta} \epsilon_{\gamma\delta} + E_{\alpha\beta 33} \epsilon_{33}$$

$$\sigma_{\alpha 3} = \sigma_{3\alpha} = 2E_{\alpha 3\beta 3} \epsilon_{\beta 3}$$

$$\sigma_{33} = E_{33\gamma\delta} \epsilon_{\gamma\delta} + E_{3333} \epsilon_{33}$$

Inversely these relationships can be expressed as

$$\epsilon_{\alpha\beta} = S_{\alpha\beta\gamma\delta} \sigma_{\gamma\delta} + S_{\alpha\beta 33} \sigma_{33}$$

$$\epsilon_{\alpha 3} = \epsilon_{3\alpha} = 2S_{\alpha 3\beta 3} \sigma_{\beta 3} \quad (5)$$

$$\epsilon_{33} = S_{33\alpha\beta} \sigma_{\alpha\beta} + S_{3333} \sigma_{33}$$

where S_{ijkl} are the components of the elastic compliance tensor with the properties

$$S_{ijkl} = S_{klij} = S_{jikl} = S_{ijlk}$$

4.3 Kinematics

For small deformation theory, the kinematic relations for linear elasticity are

$$\epsilon_{ij} = u_{(i,j)} \quad (6)$$

where ϵ_{ij} is the symmetric strain tensor. Integrating equations (6) we obtain

$$\begin{aligned} u_1(x_i) &= u_1^-(x_2, x_3) + \int_{-a}^{x_1} \epsilon_{11} d\eta_1 \\ u_2(x_i) &= u_2^-(x_1, x_3) + \int_{-b}^{x_2} \epsilon_{22} d\eta_2 \\ u_3(x_i) &= u_3^-(x_1, x_2) + \int_{-\frac{h}{2}}^{x_3} \epsilon_{33} d\eta_3 \end{aligned} \quad (7)$$

where u_1^- , u_2^- and u_3^- are values of the displacements u_1 , u_2 and u_3 at $-a$, $-b$ and $h/2$ respectively.

4.4 Plate Equilibrium Equations

Substituting equations (7) into equations (2) and (3) gives

$$\sigma_{1\beta,\beta} + \sigma_{13,3} + f_1 - \rho \left(u_1^-(x_2, x_3) + \int_{-a}^{x_1} \dot{\epsilon}_{11} d\eta_1 \right) = 0$$

$$\sigma_{2\beta,\beta} + \sigma_{23,3} + f_2 - \rho \left(\dot{u}_2^-(x_1, x_3) + \int_{-\frac{h}{2}}^{\frac{h}{2}} \ddot{e}_{22} d\eta_2 \right) = 0 \quad (8)$$

$$\sigma_{\alpha 3, \alpha} + \sigma_{33,3} + f_3 - \rho \left(\dot{u}_3^-(x_1, x_2) + \int_{-\frac{h}{2}}^{\frac{h}{2}} \ddot{e}_{33} d\eta_3 \right) = 0$$

Substituting equations (5) into equations (8) yields

$$\sigma_{1\beta,\beta} + \sigma_{13,3} + f_1 - \rho \left(\dot{u}_1^-(x_2, x_3) + \int_{-\frac{h}{2}}^{\frac{h}{2}} [S_{11\gamma\delta} \ddot{\sigma}_{\gamma\delta} + S_{1133} \ddot{\sigma}_{33}] d\eta_1 \right) = 0$$

$$\sigma_{2\beta,\beta} + \sigma_{23,3} + f_2 - \rho \left(\dot{u}_2^-(x_1, x_3) + \int_{-\frac{h}{2}}^{\frac{h}{2}} [S_{22\gamma\delta} \ddot{\sigma}_{\gamma\delta} + S_{2233} \ddot{\sigma}_{33}] d\eta_2 \right) = 0 \quad (9)$$

$$\sigma_{\alpha 3, \alpha} + \sigma_{33,3} + f_3 - \rho \left(\dot{u}_3^-(x_1, x_2) + \int_{-\frac{h}{2}}^{\frac{h}{2}} [S_{33\gamma\delta} \ddot{\sigma}_{\gamma\delta} + S_{3333} \ddot{\sigma}_{33}] d\eta_3 \right) = 0$$

Equations (9) can be written in the form

$$\sigma_{\alpha\beta,\beta} + \sigma_{\alpha 3,3} + f_\alpha - \rho \dot{u}_\alpha^- = 0 \quad (10)$$

$$\sigma_{\alpha 3, \alpha} + \sigma_{33,3} + f_3 - \rho \dot{u}_3^- = 0 \quad (11)$$

where

$$\dot{u}_1^-(x_i) = \dot{u}_1^-(x_2, x_3) + \int_{-\frac{h}{2}}^{\frac{h}{2}} [S_{11\gamma\delta} \ddot{\sigma}_{\gamma\delta} + S_{1133} \ddot{\sigma}_{33}] d\eta_1 \quad (12)$$

$$\dot{u}_2^-(x_i) = \dot{u}_2^-(x_1, x_3) + \int_{-\frac{h}{2}}^{\frac{h}{2}} [S_{22\gamma\delta} \ddot{\sigma}_{\gamma\delta} + S_{2233} \ddot{\sigma}_{33}] d\eta_2 \quad (13)$$

$$\dot{u}_3^-(x_i) = \dot{u}_3^-(x_1, x_2) + \int_{-\frac{h}{2}}^{\frac{h}{2}} [S_{33\gamma\delta} \ddot{\sigma}_{\gamma\delta} + S_{3333} \ddot{\sigma}_{33}] d\eta_3 \quad (14)$$

To reduce the equilibrium to an equality in two dimensions, the equilibrium equations are integrated over the transverse dimension. Integrating equations (10) and (11) over the thickness of the plate

$$\int_{-\frac{h}{2}}^{\frac{h}{2}} \sigma_{\alpha\beta,\beta} dx_3 + \int_{-\frac{h}{2}}^{\frac{h}{2}} \sigma_{\alpha 3,3} dx_3 + \int_{-\frac{h}{2}}^{\frac{h}{2}} f_\alpha dx_3 - \int_{-\frac{h}{2}}^{\frac{h}{2}} \rho \ddot{u}_\alpha dx_3 = 0 \quad (15)$$

$$\int_{-\frac{h}{2}}^{\frac{h}{2}} \sigma_{\alpha 3,\alpha} dx_3 + \int_{-\frac{h}{2}}^{\frac{h}{2}} \sigma_{33,3} dx_3 + \int_{-\frac{h}{2}}^{\frac{h}{2}} f_3 dx_3 - \int_{-\frac{h}{2}}^{\frac{h}{2}} \rho \ddot{u}_3 dx_3 = 0 \quad (16)$$

and integrating the first moment of equations (10) over the thickness of the plate gives

$$\int_{-\frac{h}{2}}^{\frac{h}{2}} \sigma_{\alpha\beta,\beta} x_3 dx_3 + \int_{-\frac{h}{2}}^{\frac{h}{2}} \sigma_{\alpha 3,3} x_3 dx_3 + \int_{-\frac{h}{2}}^{\frac{h}{2}} f_\alpha x_3 dx_3 - \int_{-\frac{h}{2}}^{\frac{h}{2}} \rho \ddot{u}_\alpha x_3 dx_3 = 0 \quad (17)$$

where the inplane stress and moment resultants are defined as

$$N_{\alpha\beta} = \int_{-\frac{h}{2}}^{\frac{h}{2}} \sigma_{\alpha\beta} dx_3 \quad (18)$$

$$M_{\alpha\beta} = \int_{-\frac{h}{2}}^{\frac{h}{2}} \sigma_{\alpha\beta} x_3 dx_3 \quad (19)$$

$$V_\alpha = \int_{-\frac{h}{2}}^{\frac{h}{2}} \sigma_{\alpha 3} dx_3 \quad (20)$$

$$\sigma_{i3}^+ = \sigma_{i3}\left(\frac{h}{2}\right)$$

$$\sigma_{i3}^- = \sigma_{i3}\left(-\frac{h}{2}\right)$$

Assuming that the body force per unit volume is constant, we define

$$F_i = hf_i \quad (21)$$

Using definitions (18), (19), (20) and (21), equations (15), (16) and (17) are written, respectively, as

$$N_{\alpha\beta,\beta} + (\sigma_{\alpha 3}^+ - \sigma_{\alpha 3}^-) + F_\alpha - \rho \int_{-\frac{h}{2}}^{\frac{h}{2}} \ddot{u}_\alpha dx_3 = 0 \quad (22)$$

$$V_{\alpha,\alpha} + (\sigma_{33}^+ - \sigma_{33}^-) + F_3 - \rho \int_{-\frac{h}{2}}^{\frac{h}{2}} \ddot{u}_3 dx_3 = 0 \quad (23)$$

$$M_{\alpha\beta,\beta} + \frac{h}{2}(\sigma_{\alpha 3}^+ + \sigma_{\alpha 3}^-) - V_\alpha - \rho \int_{-\frac{h}{2}}^{\frac{h}{2}} \ddot{u}_\alpha x_3 dx_3 = 0 \quad (24)$$

Equations (22), (23) and (24) are the integral form of the generalized equilibrium equations. It is noted here that since the force resultant are not functions of x_3 , the equations are applicable to wave propagation in the x_α plane only. However, once the plate is discretized through its thickness, the transfer of stress and displacement between the discretized layers allows mapping of transverse wave propagation. Evaluating the last terms of (22) we have

$$\rho \int_{-\frac{h}{2}}^{\frac{h}{2}} \ddot{u}_1 dx_3 = \rho \int_{-\frac{h}{2}}^{\frac{h}{2}} \left\{ \ddot{u}_1(x_2, x_3) + \int_{-\alpha}^{\alpha} [S_{11\gamma\delta} \ddot{\sigma}_{\gamma\delta} + S_{1133} \ddot{\sigma}_{33}] d\eta_1 \right\} dx_3 \quad (25)$$

Since linear elasticity is assumed and the integrals of equation (25) are not taken over or through any boundaries, the order of integration is changed as

$$\rho \int_{-\frac{h}{2}}^{\frac{h}{2}} \ddot{u}_1 dx_3 = \rho \left(\int_{-\frac{h}{2}}^{\frac{h}{2}} \ddot{u}_1(x_2, x_3) dx_3 + \int_{-\alpha}^{\alpha} [S_{11\gamma\delta} \ddot{N}_{\gamma\delta} + S_{1133} \ddot{N}_{33}] d\eta_1 \right) \quad (26)$$

Define

$$\bar{u}_1 = \int_{-\frac{h}{2}}^{\frac{h}{2}} \bar{u}_1(x_2, x_3) dx_3 + \int_{-\frac{h}{2}}^{\frac{h}{2}} [S_{11\gamma\delta} \dot{N}_{\gamma\delta} + S_{1133} \dot{N}_{33}] d\eta_1 \quad (27)$$

Similarly for the second of equations (22) and for (23) the following definitions are made

$$\bar{u}_2 = \int_{-\frac{h}{2}}^{\frac{h}{2}} \bar{u}_2(x_1, x_3) dx_3 + \int_{-\frac{h}{2}}^{\frac{h}{2}} [S_{22\gamma\delta} \dot{N}_{\gamma\delta} + S_{2233} \dot{N}_{33}] d\eta_2 \quad (28)$$

$$\bar{u}_3 = \bar{u}_3(x_1, x_2)h + \int_{-\frac{h}{2}}^{\frac{h}{2}} \int_{-\frac{h}{2}}^{\frac{h}{2}} [S_{33\gamma\delta} \ddot{\sigma}_{\gamma\delta} + S_{3333} \ddot{\sigma}_{33}] d\eta_3 dx_3 \quad (29)$$

Then equations (22) and (23) are written in simplified form as

$$N_{\alpha\beta} + (\sigma_{\alpha 3}^+ - \sigma_{\alpha 3}^-) + F_\alpha - \rho \bar{u}_\alpha = 0 \quad (30)$$

$$V_{\alpha\alpha} + (\sigma_{33}^+ - \sigma_{33}^-) + F_3 - \rho \bar{u}_3 = 0 \quad (31)$$

Evaluating the last terms of equations (24) in a similar manner

$$\begin{aligned} \rho \int_{-\frac{h}{2}}^{\frac{h}{2}} \bar{u}_1 x_3 dx_3 &= \rho \int_{-\frac{h}{2}}^{\frac{h}{2}} \left(\bar{u}_1(x_2, x_3) x_3 + \int_{-\frac{h}{2}}^{\frac{h}{2}} [S_{11\gamma\delta} \ddot{\sigma}_{\gamma\delta} + S_{1133} \ddot{\sigma}_{33}] d\eta_1 x_3 \right) dx_3 \\ &= \rho \left(\int_{-\frac{h}{2}}^{\frac{h}{2}} \bar{u}_1(x_2, x_3) x_3 dx_3 + \int_{-\frac{h}{2}}^{\frac{h}{2}} [S_{11\gamma\delta} \dot{M}_{\gamma\delta} + S_{1133} \dot{M}_{33}] d\eta_1 \right) \end{aligned}$$

the following definitions are made

$$\bar{u}_1^* = \int_{-\frac{h}{2}}^{\frac{h}{2}} \bar{u}_1(x_2, x_3) x_3 dx_3 + \int_{-\frac{h}{2}}^{\frac{h}{2}} [S_{11\gamma\delta} \dot{M}_{\gamma\delta} + S_{1133} \dot{M}_{33}] d\eta_1 \quad (32)$$

$$\dot{u}_2^* = \int_{-\frac{h}{2}}^{\frac{h}{2}} \dot{u}_2^-(x_1, x_3) x_3 dx_3 + \int_{-b}^{x_2} [S_{22\gamma\delta} \dot{M}_{\gamma\delta} + S_{2233} \dot{M}_{33}] d\eta_1 \quad (33)$$

Then equation (24) can be expressed as

$$M_{\alpha\beta,\beta} + \frac{h}{2}(\sigma_{\alpha 3}^+ + \sigma_{\alpha 3}^-) - V_\alpha - \rho \dot{u}_\alpha^* = 0 \quad (34)$$

Two new terms have been introduced in definitions (27) and (32) which are

$$N_{33} = \int_{-\frac{h}{2}}^{\frac{h}{2}} \sigma_{33} dx_3 \quad (35)$$

$$M_{33} = \int_{-\frac{h}{2}}^{\frac{h}{2}} \sigma_{33} x_3 dx_3 \quad (36)$$

Equations (30), (31) and (34) are a restatement of the integral form of the generalized equilibrium equations. The terms defined by (27), (28), (29), (32) and (33) represent weighted displacements over the thickness of the plate. No assumptions regarding the distribution of displacements, invoked in the so called displacement based theory, or distribution of stresses have been made thus far.

4.5 Equilibrium Stress Field

Equations (18), (19) and (20) express $N_{\alpha\beta}$, V_α and $M_{\alpha\beta}$ as force resultants, over the thickness of the plate, of the inplane components of the stress tensor. The inverse relationship i.e. the stress distribution for given $N_{\alpha\beta}$, V_α and $M_{\alpha\beta}$ is not uniquely defined. However, if an assumption is made regarding distribution of some components of σ_{ij} , the distribution of others can be determined. For a homogeneous plate, Reissner assumed a linear distribution of $\sigma_{\alpha\beta}$ over the thickness. Substituting $\sigma_{\alpha\beta} = \bar{\sigma}_{\alpha\beta} + H_{\alpha\beta}x_3$ into the definitions for inplane stress and moment resultants and solving for $\bar{\sigma}_{\alpha\beta}$ and $H_{\alpha\beta}$ in terms of the stress and moment resultants, yields

$$\sigma_{\alpha\beta} = \frac{N_{\alpha\beta}}{h} + \frac{12M_{\alpha\beta}}{h^3}x_3 \quad (37)$$

Integrating equations (2) over the thickness of the plate and rearranging,

$$\sigma_{\alpha 3} = \int_{-\frac{h}{2}}^{\frac{h}{2}} -\sigma_{\alpha\beta,\beta} d\eta_3 + \sigma_{\alpha 3}^- - \int_{-\frac{h}{2}}^{\frac{h}{2}} f_\alpha d\eta_3 + \rho \int_{-\frac{h}{2}}^{\frac{h}{2}} \ddot{u}_\alpha d\eta_3 \quad (38)$$

Substituting equations (37) into (38) gives

$$\sigma_{\alpha 3} = - \int_{-\frac{h}{2}}^{\frac{h}{2}} \left(\frac{N_{\alpha\beta}}{h} + \frac{12M_{\alpha\beta}}{h^3} \eta_3 \right) d\eta_3 + \sigma_{\alpha 3}^- - \int_{-\frac{h}{2}}^{\frac{h}{2}} f_\alpha d\eta_3 + \rho \int_{-\frac{h}{2}}^{\frac{h}{2}} \ddot{u}_\alpha d\eta_3 \quad (39)$$

Combining equations (30) and (34) with equations (39) and simplifying gives

$$\begin{aligned} \sigma_{\alpha 3} = & \frac{3}{2h} (V_\alpha - \frac{h}{2} S_\alpha) \left(1 - \left(\frac{2x_3}{h} \right)^2 \right) + \sigma_{\alpha 3}^- + (x_3 + \frac{h}{2}) \frac{P_\alpha}{h} \\ & - \frac{\rho}{h} \left(\ddot{u}_\alpha (x_3 + \frac{h}{2}) + \ddot{u}_\alpha^* \left(\frac{6x_3^2}{h^2} - \frac{3}{2} \right) \right) + \rho \int_{-\frac{h}{2}}^{\frac{h}{2}} \ddot{u}_\alpha d\eta_3 \end{aligned} \quad (40)$$

where

$$S_\alpha = (\sigma_{\alpha 3}^+ + \sigma_{\alpha 3}^-) \quad \text{and} \quad P_\alpha = (\sigma_{\alpha 3}^+ - \sigma_{\alpha 3}^-)$$

Integrating the third equation of motions, equation (3), over the thickness of the plate gives

$$\sigma_{33} = \sigma_{33}^- - \int_{\frac{h}{2}}^{\frac{h}{2}} \sigma_{\alpha 3, \alpha} d\eta_3 - \int_{\frac{h}{2}}^{\frac{h}{2}} f_3 d\eta_3 + \rho \int_{\frac{h}{2}}^{\frac{h}{2}} \ddot{u}_3 d\eta_3 \quad (41)$$

Differentiating equations (40) with respect to x_α and substituting into equation (41) gives an expression for the transverse normal stress as

$$\begin{aligned} \sigma_{33} = & \frac{(\sigma_{33}^+ + \sigma_{33}^-)}{2} - \{ (\sigma_{\alpha 3, \alpha}^+ - \sigma_{\alpha 3, \alpha}^-) \left(\frac{x_3^2}{2h} - \frac{h}{8} \right) + (\sigma_{\alpha 3, \alpha}^+ + \sigma_{\alpha 3, \alpha}^-) \left(\frac{x_3^3}{h^2} - \frac{x_3}{4} \right) \right. \\ & - \frac{3}{2} (\sigma_{33}^+ - \sigma_{33}^-) \left(\frac{x_3}{h} - \frac{4x_3^3}{3h^3} \right) \} + \frac{\rho}{h} \left(\ddot{u}_{\alpha, \alpha} \left(\frac{x_3^2}{2} + \frac{hx_3}{2} + \frac{h^2}{8} \right) + \ddot{u}_{\alpha, \alpha} \left(\frac{2x_3^3}{h^2} - \frac{3x_3}{2} - \frac{h}{2} \right) \right. \\ & \left. + \ddot{u}_3 \left(\frac{2x_3^3}{h^2} - \frac{3x_3}{2} - \frac{h}{2} \right) \right) - \rho \int_{\frac{h}{2}}^{\frac{h}{2}} \int_{\frac{h}{2}}^{\frac{h}{2}} \ddot{u}_{\alpha, \alpha} d\zeta_3 d\eta_3 + \rho \int_{\frac{h}{2}}^{\frac{h}{2}} \ddot{u}_3 d\eta_3 - f_3 \left(\frac{2x_3^3}{h^2} - \frac{x_3}{2} \right) \end{aligned} \quad (42)$$

In order to express the three stress components (40) and (42) in terms of stress resultants and boundary stresses terms, expressions for the weighted displacement terms must be developed. We can simplify equations (40) by substituting the following known relationships

$$\begin{aligned} \int_{\frac{h}{2}}^{\frac{h}{2}} \ddot{u}_1 d\eta_3 = & \int_{\frac{h}{2}}^{\frac{h}{2}} \ddot{u}_1(x_2, \eta_3) d\eta_3 + \int_{-\frac{a}{2}}^{\frac{a}{2}} S_{11, \eta_3} \left(\frac{\dot{N}_{\eta_3}}{h} (x_3 + \frac{h}{2}) + \frac{12 \dot{M}_{\eta_3}}{h^3} (\frac{x_3^2}{2} - \frac{h^2}{8}) \right) d\eta_1 \\ & + \int_{-\frac{a}{2}}^{\frac{a}{2}} \int_{\frac{h}{2}}^{\frac{h}{2}} S_{1133} \ddot{\sigma}_{33} d\eta_3 d\eta_1 \end{aligned} \quad (43)$$

and

$$\int_{\frac{h}{2}}^{\frac{h}{2}} \ddot{u}_2 d\eta_3 = \int_{\frac{h}{2}}^{\frac{h}{2}} \ddot{u}_2(x_1, \eta_3) d\eta_3 + \int_{-\frac{b}{2}}^{\frac{b}{2}} S_{22, \eta_3} \left(\frac{\dot{N}_{\eta_3}}{h} (x_3 + \frac{h}{2}) + \frac{12 \dot{M}_{\eta_3}}{h^3} (\frac{x_3^2}{2} - \frac{h^2}{8}) \right) d\eta_2$$

$$+ \int_{-\frac{h}{2}}^{\frac{h}{2}} \int_{-\frac{h}{2}}^{\frac{h}{2}} S_{2233} \ddot{\sigma}_{33} d\eta_3 d\eta_2 \quad (44)$$

Using relationships (27), (28), (32), (33), (43) and (44) equations (40) can be written as

$$\begin{aligned} \sigma_{13} = & \frac{3}{2h} \left(V_1 - \frac{h}{2} S_1 \right) \left(1 - \left(\frac{2x_3}{h} \right)^2 \right) + \sigma_{13}^- + \left(x_3 + \frac{h}{2} \right) \frac{P_1}{h} \\ & - \frac{\rho}{h} \int_{-\frac{h}{2}}^{\frac{h}{2}} S_{1133} \left(\dot{N}_{33} + \frac{6\dot{M}_{33}}{h^2} \left(x_3 - \frac{h}{2} \right) \right) \left(x_3 + \frac{h}{2} \right) d\eta_1 \\ & + \rho \int_{-\frac{h}{2}}^{\frac{h}{2}} \int_{-\frac{h}{2}}^{\frac{h}{2}} S_{1133} \ddot{\sigma}_{33} d\eta_3 d\eta_1 - \frac{\rho}{h} \int_{-\frac{h}{2}}^{\frac{h}{2}} \bar{u}_1(x_2, x_3) dx_3 \left(x_3 + \frac{h}{2} \right) \\ & - \frac{\rho}{h} \int_{-\frac{h}{2}}^{\frac{h}{2}} \bar{u}_1(x_2, x_3) x_3 dx_3 \left(\frac{6x_3^2}{h^3} - \frac{3}{2h} \right) + \rho \int_{-\frac{h}{2}}^{\frac{h}{2}} \bar{u}_1(x_2, \eta_3) d\eta_3 \end{aligned} \quad (45)$$

and

$$\begin{aligned} \sigma_{23} = & \frac{3}{2h} \left(V_2 - \frac{h}{2} S_2 \right) \left(1 - \left(\frac{2x_3}{h} \right)^2 \right) + \sigma_{23}^- + \left(x_3 + \frac{h}{2} \right) \frac{P_2}{h} \\ & - \frac{\rho}{h} \int_{-\frac{h}{2}}^{\frac{h}{2}} S_{2233} \left(\dot{N}_{33} + \frac{6\dot{M}_{33}}{h^2} \left(x_3 - \frac{h}{2} \right) \right) \left(x_3 + \frac{h}{2} \right) d\eta_2 \\ & + \rho \int_{-\frac{h}{2}}^{\frac{h}{2}} \int_{-\frac{h}{2}}^{\frac{h}{2}} S_{2233} \ddot{\sigma}_{33} d\eta_3 d\eta_2 - \frac{\rho}{h} \int_{-\frac{h}{2}}^{\frac{h}{2}} \bar{u}_2(x_1, x_3) dx_3 \left(x_3 + \frac{h}{2} \right) \\ & - \frac{\rho}{h} \int_{-\frac{h}{2}}^{\frac{h}{2}} \bar{u}_2(x_1, x_3) x_3 dx_3 \left(\frac{6x_3^2}{h^3} - \frac{3}{2h} \right) + \rho \int_{-\frac{h}{2}}^{\frac{h}{2}} \bar{u}_2(x_1, \eta_3) d\eta_3 \end{aligned} \quad (46)$$

To simplify equation (42) substitute the following relationships

$$\bar{u}_{1,1} = S_{11\gamma\delta} \dot{N}_{\gamma\delta} + S_{1133} \dot{N}_{33} \quad (47)$$

$$\bar{u}_{2,2} = S_{22\gamma\delta} \dot{N}_{\gamma\delta} + S_{2233} \dot{N}_{33} \quad (48)$$

$$\dot{u}_{1,1}^* = S_{11\gamma\delta} \dot{M}_{\gamma\delta} + S_{1133} \dot{M}_{33} \quad (49)$$

$$\dot{u}_{2,2}^* = S_{22\gamma\delta} \dot{M}_{\gamma\delta} + S_{2233} \dot{M}_{33} \quad (50)$$

and

$$\bar{u}_3 = \bar{u}_3(x_1, x_2)h + S_{33\gamma\delta} \left[\frac{h}{2} \dot{N}_{\gamma\delta} - \dot{M}_{\gamma\delta} \right] + \int_{-\frac{h}{2}}^{\frac{h}{2}} \int_{-\frac{h}{2}}^{\frac{h}{2}} S_{3333} \sigma_{33} d\eta_3 dx_3 \quad (51)$$

Substituting equations (37) into equation (12) and differentiating with respect to x_1 yields

$$\ddot{u}_{1,1} = S_{11\gamma\delta} \left[\frac{\dot{N}_{\gamma\delta}}{h} + \frac{12 \dot{M}_{\gamma\delta}}{h^3} x_3 \right] + S_{1133} \ddot{\sigma}_{33} \quad (52)$$

To obtain the terms required in equation (42), integrate equation (52) twice through-the-thickness,

$$\begin{aligned} \int_{-\frac{h}{2}}^{\frac{h}{2}} \int_{-\frac{h}{2}}^{\frac{h}{2}} \ddot{u}_{1,1} d\zeta_3 d\eta_3 &= S_{11\gamma\delta} \left(\frac{\dot{N}_{\gamma\delta}}{h} \left(\frac{x_3^2}{2} + \frac{hx_3}{2} + \frac{h^2}{8} \right) + \frac{12 \dot{M}_{\gamma\delta}}{h^3} \left(\frac{x_3^3}{6} - \frac{h^2 x_3}{8} - \frac{h^3}{24} \right) \right) \\ &+ \int_{-\frac{h}{2}}^{\frac{h}{2}} \int_{-\frac{h}{2}}^{\frac{h}{2}} S_{1133} \ddot{\sigma}_{33} d\zeta_3 d\eta_3 \end{aligned} \quad (53)$$

similarly

$$\begin{aligned} \int_{-\frac{h}{2}}^{\frac{h}{2}} \int_{-\frac{h}{2}}^{\frac{h}{2}} \ddot{u}_{2,2} d\zeta_3 d\eta_3 &= S_{22\gamma\delta} \left(\frac{\dot{N}_{\gamma\delta}}{h} \left(\frac{x_3^2}{2} + \frac{hx_3}{2} + \frac{h^2}{8} \right) + \frac{12 \dot{M}_{\gamma\delta}}{h^3} \left(\frac{x_3^3}{6} - \frac{h^2 x_3}{8} - \frac{h^3}{24} \right) \right) \\ &+ \int_{-\frac{h}{2}}^{\frac{h}{2}} \int_{-\frac{h}{2}}^{\frac{h}{2}} S_{2233} \ddot{\sigma}_{33} d\zeta_3 d\eta_3 \end{aligned} \quad (54)$$

Substituting equations (37) into equation (14) and integrating through-the-thickness gives

$$\int_{-\frac{h}{2}}^{\frac{h}{2}} \ddot{u}_3 d\eta_3 = \ddot{u}_3^-(x_3 + \frac{h}{2}) + S_{33\gamma\delta} \left(\frac{\dot{N}_{\gamma\delta}}{h} \left(\frac{x_3^2}{2} + \frac{hx_3}{2} + \frac{h^2}{8} \right) + \frac{12 \dot{M}_{\gamma\delta}}{h^3} \left(\frac{x_3^3}{6} - \frac{h^2 x_3}{8} - \frac{h^3}{24} \right) \right) + \int_{-\frac{h}{2}}^{\frac{h}{2}} \int_{-\frac{h}{2}}^{\frac{h}{2}} S_{3333} \ddot{\sigma}_{33} d\zeta_3 d\eta_3 \quad (55)$$

Substituting the developed weighted displacement expressions (47) - (55) into (42) and simplifying gives the following integral equation for σ_{33} as

$$\begin{aligned} \sigma_{33} = & \frac{(\sigma_{33}^+ + \sigma_{33}^-)}{2} - ((\sigma_{\alpha 3, \alpha}^+ - \sigma_{\alpha 3, \alpha}^-) \left(\frac{x_3^2}{2h} - \frac{h}{8} \right) + (\sigma_{\alpha 3, \alpha}^+ + \sigma_{\alpha 3, \alpha}^-) \left(\frac{x_3^3}{h^2} - \frac{x_3}{4} \right) \\ & - \frac{3}{2} (\sigma_{33}^+ - \sigma_{33}^-) \left(\frac{x_3}{h} - \frac{4x_3^3}{3h^3} \right) + \frac{\rho}{h} \{ S_{33\gamma\delta} \dot{N}_{\gamma\delta} \left(\frac{x_3^3}{h} + \frac{x_3^2}{2} - \frac{hx_3}{4} - \frac{h^2}{8} \right) \\ & + S_{\alpha\alpha 33} \dot{N}_{33} \left(\frac{x_3^2}{2} + \frac{hx_3}{2} + \frac{h^2}{8} \right) + S_{\alpha\alpha 33} \dot{M}_{33} \left(\frac{2x_3^3}{h^2} - \frac{3x_3}{2} - \frac{h}{2} \right) \\ & + \int_{-\frac{h}{2}}^{\frac{h}{2}} \int_{-\frac{h}{2}}^{\frac{h}{2}} S_{3333} \ddot{\sigma}_{33} d\eta_3 dx_3 \left(\frac{2x_3^3}{h^2} - \frac{3x_3}{2} - \frac{h}{2} \right) + h \int_{-\frac{h}{2}}^{\frac{h}{2}} \int_{-\frac{h}{2}}^{\frac{h}{2}} (S_{3333} - S_{\alpha\alpha 33}) \ddot{\sigma}_{33} d\zeta_3 d\eta_3 \} \\ & + \rho \ddot{u}_3^-(x_1, x_2) \left(\frac{2x_3^3}{h^2} - \frac{x_3}{2} \right) - f_3 \left(\frac{2x_3^3}{h^2} - \frac{x_3}{2} \right) \end{aligned} \quad (56)$$

4.6 Pagano's Equations of Equilibrium

Pagano's equations of equilibrium are determined by substituting the integral equation for σ_{33} , equation (56), into expressions for N_{33} and M_{33} , equations (35) and (36).

$$\begin{aligned}
 N_{33} = & \frac{h}{2}(\sigma_{33}^+ + \sigma_{33}^-) + \frac{h^2}{12}(\sigma_{\alpha 3, \alpha}^+ - \sigma_{\alpha 3, \alpha}^-) + \frac{\rho}{h} \left\{ -\frac{h^3}{12} S_{33\gamma\delta} \dot{N}_{\gamma\delta} \right. \\
 & + \frac{h^3}{6} S_{\beta\beta 33} \dot{N}_{33} - \frac{h^2}{2} S_{\beta\beta 33} \dot{M}_{33} - \frac{h^2}{2} \int_{-\frac{h}{2}}^{\frac{h}{2}} \int_{-\frac{h}{2}}^{\frac{h}{2}} S_{3333} \ddot{\sigma}_{33} d\eta_3 dx_3 \\
 & \left. + h \int_{-\frac{h}{2}}^{\frac{h}{2}} \int_{-\frac{h}{2}}^{\frac{h}{2}} \int_{-\frac{h}{2}}^{\frac{h}{2}} (S_{3333} - S_{\beta\beta 33}) \ddot{\sigma}_{33} d\zeta_3 d\eta_3 dx_3 \right\}
 \end{aligned} \quad (57)$$

and

$$\begin{aligned}
 M_{33} = & \frac{h^3}{120}(\sigma_{\alpha 3, \alpha}^+ + \sigma_{\alpha 3, \alpha}^-) + \frac{h^2}{10}(\sigma_{33}^+ - \sigma_{33}^-) + \frac{\rho}{h} \left\{ -\frac{h^4}{120} S_{33\gamma\delta} \dot{N}_{\gamma\delta} \right. \\
 & + \frac{h^4}{24} S_{\beta\beta 33} \dot{N}_{33} - \frac{h^3}{10} S_{\beta\beta 33} \dot{M}_{33} - \frac{h^3}{10} \int_{-\frac{h}{2}}^{\frac{h}{2}} \int_{-\frac{h}{2}}^{\frac{h}{2}} S_{3333} \ddot{\sigma}_{33} d\eta_3 dx_3 \\
 & + h \int_{-\frac{h}{2}}^{\frac{h}{2}} \int_{-\frac{h}{2}}^{\frac{h}{2}} \int_{-\frac{h}{2}}^{\frac{h}{2}} (S_{3333} - S_{\beta\beta 33}) \ddot{\sigma}_{33} d\zeta_3 d\eta_3 dx_3 \\
 & \left. + \frac{h^3}{60} [f_3 - \dot{u}_3(x_1, x_2)] \right\}
 \end{aligned} \quad (58)$$

Rearranging, equation (57) is written as

$$(\sigma_{\alpha 3, \alpha}^+ - \sigma_{\alpha 3, \alpha}^-) = \frac{12}{h^3} \left\{ N_{33} - \frac{h}{2}(\sigma_{33}^+ + \sigma_{33}^-) - \frac{\rho}{h} \left[-\frac{h^3}{12} S_{33\gamma\delta} \dot{N}_{\gamma\delta} \right. \right.$$

$$\begin{aligned}
& + \frac{h^3}{6} S_{\beta\beta 33} \dot{N}_{33} - \frac{h^2}{2} S_{\beta\beta 33} \dot{M}_{33} - \frac{h^2}{2} \int_{\frac{h}{2}}^{\frac{h}{2}} \int_{\frac{h}{2}}^{\frac{h}{2}} S_{3333} \ddot{\sigma}_{33} d\eta_3 dx_3 \\
& + h \int_{\frac{h}{2}}^{\frac{h}{2}} \int_{\frac{h}{2}}^{\frac{h}{2}} \int_{\frac{h}{2}}^{\frac{h}{2}} (S_{3333} - S_{\beta\beta 33}) \ddot{\sigma}_{33} d\zeta_3 d\eta_3 dx_3]
\end{aligned} \quad (59)$$

Similarly, equation (58) is rewritten as

$$\begin{aligned}
(\sigma_{\alpha 3, \alpha}^+ + \sigma_{\alpha 3, \alpha}^-) &= \frac{120}{h^3} \{ M_{33} - \frac{h^2}{10} (\sigma_{33}^+ - \sigma_{33}^-) - \frac{\rho}{h} [-\frac{h^4}{120} S_{3333} \dot{N}_{33} \\
& + \frac{h^4}{24} S_{\beta\beta 33} \dot{N}_{33} - \frac{h^3}{10} S_{\beta\beta 33} \dot{M}_{33} - \frac{h^3}{10} \int_{\frac{h}{2}}^{\frac{h}{2}} \int_{\frac{h}{2}}^{\frac{h}{2}} S_{3333} \ddot{\sigma}_{33} d\eta_3 dx_3 \\
& + h \int_{\frac{h}{2}}^{\frac{h}{2}} \int_{\frac{h}{2}}^{\frac{h}{2}} \int_{\frac{h}{2}}^{\frac{h}{2}} (S_{3333} - S_{\beta\beta 33}) \ddot{\sigma}_{33} d\zeta_3 d\eta_3 dx_3] \\
& - 2[f_3 - u_3^-(x_1, x_2)] \}
\end{aligned} \quad (60)$$

Substituting equations (59) and (60) into equation (56) yields the final form of the integral equation for σ_{33}

as

$$\begin{aligned}
\sigma_{33} &= \frac{(\sigma_{33}^+ + \sigma_{33}^-)}{4} \left(\frac{12x_3^2}{h^2} - 1 \right) + \frac{(\sigma_{33}^+ - \sigma_{33}^-)}{4} \left(\frac{40x_3^3}{h^3} - \frac{6x_3}{h} \right) + \frac{3N_{33}}{2h} \left(1 - \frac{4x_3^2}{h^2} \right) \\
& + \frac{15M_{33}}{h^2} \left(\frac{2x_3}{h} - \frac{8x_3^3}{h^3} \right) + \frac{\rho}{h} \{ [S_{\alpha\alpha 33} (\frac{h}{2} \dot{N}_{33} - \dot{M}_{33}) - S_{3333} \int_{\frac{h}{2}}^{\frac{h}{2}} \int_{\frac{h}{2}}^{\frac{h}{2}} \ddot{\sigma}_{33} d\eta_3 dx_3] \\
& \times \left(\frac{10x_3^3}{h^2} + \frac{3x_3^2}{h} - \frac{3x_3}{2} - \frac{h}{4} \right) \}
\end{aligned} \quad (61)$$

$$\begin{aligned}
& + \frac{\rho}{h} (S_{3333} - S_{\alpha\alpha 33}) \left[\int_{\frac{h}{2}}^{\frac{h}{2}} \int_{\frac{h}{2}}^{\frac{h}{2}} \int_{\frac{h}{2}}^{\frac{h}{2}} \ddot{\sigma}_{33} d\zeta_3 d\eta_3 dx_3 \left(\frac{6x_3^2}{h^2} - \frac{3}{2} \right) + h \int_{\frac{h}{2}}^{\frac{h}{2}} \int_{\frac{h}{2}}^{\frac{h}{2}} \ddot{\sigma}_{33} d\eta_3 dx_3 \right. \\
& \left. + \int_{\frac{h}{2}}^{\frac{h}{2}} x_3 \int_{\frac{h}{2}}^{\frac{h}{2}} \int_{\frac{h}{2}}^{\frac{h}{2}} \ddot{\sigma}_{33} d\zeta_3 d\eta_3 dx_3 \left(\frac{120x_3^3}{h^4} - \frac{30x_3}{h^2} \right) \right]
\end{aligned}$$

An approximation for the integral equation can be found by selecting the static terms of (61) as a first approximation and substituting back into (61). Repeated substitution yields the following approximation for

σ_{33} ,

$$\begin{aligned}
\sigma_{33} = & \frac{(\sigma_{33}^+ + \sigma_{33}^-)}{4} \left(\frac{12x_3^2}{h^2} - 1 \right) + \frac{(\sigma_{33}^+ - \sigma_{33}^-)}{4} \left(\frac{40x_3^3}{h^3} - \frac{6x_3}{h} \right) \\
& + \frac{3N_{33}}{2h} \left(1 - \frac{4x_3^2}{h^2} \right) + \frac{15M_{33}}{h^2} \left(\frac{2x_3}{h} - \frac{8x_3^3}{h^3} \right) \\
& + \frac{\rho}{h} (S_{\alpha\alpha 33} - S_{3333}) \left\{ \left[\frac{h}{4} (\ddot{\sigma}_{33}^+ + \ddot{\sigma}_{33}^-) - \frac{1}{2} \ddot{N}_{33} \right] \left(\frac{3x_3^2}{10} - \frac{x_3^4}{h^2} - \frac{h^2}{80} \right) \right. \\
& \left. + \left[\frac{h^2}{12} (\ddot{\sigma}_{33}^+ - \ddot{\sigma}_{33}^-) - \ddot{M}_{33} \right] \left(\frac{15x_3^3}{7h^2} - \frac{6x_3^5}{h^4} - \frac{9x_3}{56} \right) \right\} \quad (62) \\
& + \frac{\rho^2}{h^2} (S_{\alpha\alpha 33} - S_{3333})^2 \left\{ \left[\frac{h}{4} (\sigma_{33}^{(4)+} + \sigma_{33}^{(4)-}) - \frac{1}{2} N_{33}^{(4)} \right] \right. \\
& \left. \times \left(\frac{x_3^6}{30h} - \frac{hx_3^4}{40} + \frac{27h^3x_3^2}{5600} - \frac{11h^5}{67,200} \right) \right. \\
& \left. + \left[\frac{h^2}{12} (\sigma_{33}^{(4)+} - \sigma_{33}^{(4)-}) - M_{33}^{(4)} \right] \left(\frac{x_3^7}{7h^3} - \frac{3x_3^5}{28h} + \frac{55hx_3^3}{2352} - \frac{13h^3x_3}{9408} \right) \right\} \\
& + \frac{\rho^3}{h^3} (S_{\alpha\alpha 33} - S_{3333})^3 \left\{ \left[\frac{h}{4} (\sigma_{33}^{(6)+} + \sigma_{33}^{(6)-}) - \frac{1}{2} N_{33}^{(6)} \right] \right.
\end{aligned}$$

$$\times \left(\frac{h^2 x_3^6}{1200} - \frac{x_3^8}{1680} - \frac{9h^4 x_3^4}{22,400} + \frac{19h^6 x_3^2}{288,000} - \frac{67h^8}{32,256,000} \right) \\ + \left[\frac{h^2}{12} (\sigma_{33}^{(6)*} - \sigma_{33}^{(6)}) - M_{33}^{(6)} \right] \left(\frac{x_3^7}{392} - \frac{x_3^9}{504h^2} - \frac{11h^2 x_3^5}{9408} + \frac{905h^4 x_3^3}{4,346,496} - \frac{257h^6 x_3}{23,181,312} \right)$$

where superposed (n) denotes the nth derivative with respect to time. To evaluate the contributions of the various terms of the approximation, we can look at the multiplicative factors for subsequent higher order approximations. We know

$$S_{13} = \frac{-v_{31}}{E_{33}}, \quad S_{23} = \frac{-v_{32}}{E_{33}}, \quad S_{33} = \frac{1}{E_{33}}$$

Representative values for material constants are

$$v_{31} = v_{32} = 0.21$$

$$E_{33} = 2.1 \times 10^6 \text{ psi}$$

Then the factors for subsequent higher order terms in the approximation take on the values

$$(S_{\alpha\alpha 33} - S_{3333}) = \frac{1}{E_{3333}} (-v_{3\alpha} - 1) = -5.7619 \times 10^{-7} \frac{\text{in}^2}{\text{lb}}$$

$$(S_{\alpha\alpha 33} - S_{3333})^2 = 3.3199 \times 10^{-13} \frac{\text{in}^4}{\text{lb}^2}$$

$$(S_{\alpha\alpha 33} - S_{3333})^3 = -1.9129 \times 10^{-19} \frac{\text{in}^6}{\text{lb}^3}$$

Based on the exponential indices, the contribution of the higher order terms appears to become negligible. Additionally, through spatial discretization, we may select h to be as small as necessary to make the higher order terms negligible. For high stress gradients, the higher order terms may become important and can be included to account for higher modes of vibration. Since lamina thickness or h may be the same for thick and thin laminates, the theory is not limited by plate thickness. Therefore the following approximation is used to develop the constitutive relations

$$\begin{aligned}
\sigma_{33} = & \frac{(\sigma_{33}^+ + \sigma_{33}^-)}{4} \left(\frac{12x_3^2}{h^2} - 1 \right) + \frac{(\sigma_{33}^+ - \sigma_{33}^-)}{4} \left(\frac{40x_3^3}{h^3} - \frac{6x_3}{h} \right) \\
& + \frac{3N_{33}}{2h} \left(1 - \frac{4x_3^2}{h^2} \right) + \frac{15M_{33}}{h^2} \left(\frac{2x_3}{h} - \frac{8x_3^3}{h^3} \right) \\
& + \frac{\rho}{h} (S_{\alpha\alpha 33} - S_{3333}) \left(\left[\left(\frac{h}{4} (\ddot{\sigma}_{33}^+ + \ddot{\sigma}_{33}^-) - \frac{1}{2} \ddot{N}_{33} \right) \left(\frac{3x_3^2}{10} - \frac{x_3^4}{h^2} - \frac{h^2}{80} \right) \right. \right. \\
& \left. \left. + \left(\frac{h^2}{12} (\ddot{\sigma}_{33}^+ - \ddot{\sigma}_{33}^-) - \ddot{M}_{33} \right) \left(\frac{15x_3^3}{7h^2} - \frac{6x_3^5}{h^4} - \frac{9x_3}{56} \right) \right] \right)
\end{aligned} \tag{63}$$

4.7 Constitutive Relations for Generalized Displacements

Let

$$(\bar{f}, \bar{f}, \hat{f}) = \int_{-\frac{h}{2}}^{\frac{h}{2}} f \left(1, \frac{2x_3}{h}, \frac{4x_3^2}{h} \right) \frac{2}{h} dx_3 \tag{64}$$

The constitutive equations given by Pagano, neglecting the expansional strains, were derived by integrating the quantities $\epsilon_{\alpha\beta}$, $x_3\epsilon_{\alpha\beta}$, ϵ_{33} , $x_3\epsilon_{33}$, $x_3^2\epsilon_{33}$, $x_3^3\epsilon_{33}$, $\epsilon_{\alpha\alpha}$, $x_3\epsilon_{\alpha\alpha}$ and $x_3^2\epsilon_{\alpha\alpha}$ with respect to x_3 . In evaluation, repeated use of integration by parts and substitution for stresses $\sigma_{\alpha\beta}$ and σ_{33} was required. The resulting equations are

$$\begin{aligned}
\int_{-\frac{h}{2}}^{\frac{h}{2}} \epsilon_{\alpha\beta} dx_3 &= \int_{-\frac{h}{2}}^{\frac{h}{2}} u_{(\alpha,\beta)} dx_3 = \int_{-\frac{h}{2}}^{\frac{h}{2}} (S_{\alpha\beta\gamma\delta} \sigma_{\gamma\delta} + S_{\alpha\beta 33} \sigma_{33}) dx_3 \\
\Rightarrow \frac{h}{2} \bar{u}_{(\alpha,\beta)} &= S_{\alpha\beta\gamma\delta} N_{\gamma\delta} + S_{\alpha\beta 33} N_{33}
\end{aligned} \tag{65}$$

$$\int_{-\frac{h}{2}}^{\frac{h}{2}} x_3 \varepsilon_{\alpha\beta} dx_3 = \int_{-\frac{h}{2}}^{\frac{h}{2}} u_{(\alpha\beta)} x_3 dx_3 = \int_{-\frac{h}{2}}^{\frac{h}{2}} (S_{\alpha\beta\gamma\delta} \sigma_{\gamma\delta} + S_{\alpha\beta 33} \sigma_{33}) x_3 dx_3$$

$$\Rightarrow \frac{h^2}{4} \bar{u}_{(\alpha\beta)} = S_{\alpha\beta\gamma\delta} M_{\gamma\delta} + S_{\alpha\beta 33} M_{33} \quad (66)$$

$$\int_{-\frac{h}{2}}^{\frac{h}{2}} \varepsilon_{33} dx_3 = \int_{-\frac{h}{2}}^{\frac{h}{2}} u_{3,3} dx_3 = \int_{-\frac{h}{2}}^{\frac{h}{2}} (S_{33\alpha\beta} \sigma_{\alpha\beta} + S_{3333} \sigma_{33}) dx_3$$

$$\Rightarrow u_3^+ - u_3^- = S_{33\alpha\beta} N_{\alpha\beta} + S_{3333} N_{33} \quad (67)$$

$$\int_{-\frac{h}{2}}^{\frac{h}{2}} x_3 \varepsilon_{33} dx_3 = \int_{-\frac{h}{2}}^{\frac{h}{2}} u_{3,3} x_3 dx_3 = \int_{-\frac{h}{2}}^{\frac{h}{2}} (S_{33\alpha\beta} \sigma_{\alpha\beta} + S_{3333} \sigma_{33}) x_3 dx_3$$

$$\Rightarrow \bar{u}_3 = u_3^+ + u_3^- - \frac{2}{h} S_{33\alpha\beta} M_{\alpha\beta} - \frac{2}{h} S_{3333} M_{33} \quad (68)$$

$$\int_{-\frac{h}{2}}^{\frac{h}{2}} x_3^2 \varepsilon_{33} dx_3 = \int_{-\frac{h}{2}}^{\frac{h}{2}} u_{3,3} x_3^2 dx_3 = \int_{-\frac{h}{2}}^{\frac{h}{2}} (S_{33\alpha\beta} \sigma_{\alpha\beta} + S_{3333} \sigma_{33}) x_3^2 dx_3$$

$$\Rightarrow 6\bar{u}_3 = - S_{33\alpha\beta} N_{\alpha\beta} - \frac{h}{5} S_{3333} (\sigma_{33}^+ + \sigma_{33}^-) - \frac{3}{5} S_{3333} N_{33} + 3(u_3^+ - u_3^-) \quad (69)$$

$$- \frac{h^3}{175} S_{3333} \frac{\rho}{h} (S_{\alpha\alpha 33} - S_{3333}) \left[\frac{h}{4} (\ddot{\sigma}_{33}^+ + \ddot{\sigma}_{33}^-) - \frac{1}{2} \ddot{N}_{33} \right]$$

$$\int_{-\frac{h}{2}}^{\frac{h}{2}} x_3^3 \varepsilon_{33} dx_3 = \int_{-\frac{h}{2}}^{\frac{h}{2}} u_{3,3} x_3^3 dx_3 = \int_{-\frac{h}{2}}^{\frac{h}{2}} (S_{33\alpha\beta} \sigma_{\alpha\beta} + S_{3333} \sigma_{33}) x_3^3 dx_3$$

$$\Rightarrow \dot{u}_3 = \frac{1}{3} (u_3^+ + u_3^-) - \frac{2}{5h} S_{33\alpha\beta} M_{\alpha\beta} - \frac{2}{7h} S_{3333} M_{33} - \frac{h}{105} S_{3333} (\sigma_{33}^+ - \sigma_{33}^-)$$

$$- \frac{h^2}{2205} S_{3333} \frac{\rho}{h} (S_{\alpha\alpha 33} - S_{3333}) \left(\frac{h^2}{12} (\ddot{\sigma}_{33}^+ - \ddot{\sigma}_{33}^-) - \dot{M}_{33} \right) \quad (70)$$

$$\int_{-\frac{\hbar}{2}}^{\frac{\hbar}{2}} \varepsilon_{\alpha 3} dx_3 = \int_{-\frac{\hbar}{2}}^{\frac{\hbar}{2}} \frac{1}{2} (u_{\alpha 3} + u_{3,\alpha}) dx_3 = \int_{-\frac{\hbar}{2}}^{\frac{\hbar}{2}} 2S_{\alpha 3 \beta 3} \sigma_{\beta 3} dx_3$$

$$\Rightarrow \bar{u}_{3,\alpha} = \frac{8}{h} S_{\alpha 3 \beta 3} V_{\beta} - \frac{2}{h} (u_{\alpha}^{+} - u_{\alpha}^{-}) \quad (71)$$

$$\int_{-\frac{\hbar}{2}}^{\frac{\hbar}{2}} \varepsilon_{\alpha 3} x_3 dx_3 = \int_{-\frac{\hbar}{2}}^{\frac{\hbar}{2}} \frac{1}{2} (u_{\alpha 3} + u_{3,\alpha}) x_3 dx_3 = \int_{-\frac{\hbar}{2}}^{\frac{\hbar}{2}} 2S_{\alpha 3 \beta 3} \sigma_{\beta 3} x_3 dx_3$$

$$\Rightarrow \frac{h}{4} \bar{u}_{3,1} - \frac{1}{2} \bar{u}_1 = \frac{h}{3} S_{13 \beta 3} (\sigma_{\beta 3}^{+} - \sigma_{\beta 3}^{-}) - \frac{1}{2} (u_1^{+} + u_1^{-})$$

$$- S_{13 \beta 3} \rho \int_{-\frac{\hbar}{2}}^{\frac{\hbar}{2}} S_{\beta \beta 33} \frac{2h}{15} \left(\frac{h}{4} (\ddot{\sigma}_{33}^{+} + \ddot{\sigma}_{33}^{-}) - \frac{1}{2} \dot{N}_{33} \right) d\eta_1 \quad (72)$$

$$- S_{13 \beta 3} \rho \int_{-\frac{\hbar}{2}}^{\frac{\hbar}{2}} (S_{\beta \beta 33} - S_{3333}) \frac{h^3}{1050} \left(\frac{h}{4} (\sigma_{33}^{(4)+} + \sigma_{33}^{(4)-}) - \frac{1}{2} N_{33}^{(4)} \right) d\eta_1$$

$$\Rightarrow \frac{h}{4} \bar{u}_{3,2} - \frac{1}{2} \bar{u}_2 = \frac{h}{3} S_{23 \beta 3} (\sigma_{\beta 3}^{+} - \sigma_{\beta 3}^{-}) - \frac{1}{2} (u_2^{+} + u_2^{-})$$

$$- S_{23 \beta 3} \rho \int_{-\frac{\hbar}{2}}^{\frac{\hbar}{2}} S_{\beta \beta 33} \frac{2h}{15} \left(\frac{h}{4} (\ddot{\sigma}_{33}^{+} + \ddot{\sigma}_{33}^{-}) - \frac{1}{2} \dot{N}_{33} \right) d\eta_2 \quad (73)$$

$$- S_{23 \beta 3} \rho \int_{-\frac{\hbar}{2}}^{\frac{\hbar}{2}} (S_{\beta \beta 33} - S_{3333}) \frac{h^3}{1050} \left(\frac{h}{4} (\sigma_{33}^{(4)+} + \sigma_{33}^{(4)-}) - \frac{1}{2} N_{33}^{(4)} \right) d\eta_2$$

$$\int_{-\frac{\hbar}{2}}^{\frac{\hbar}{2}} \varepsilon_{\alpha 3} x_3^2 dx_3 = \int_{-\frac{\hbar}{2}}^{\frac{\hbar}{2}} \frac{1}{2} (u_{\alpha 3} + u_{3,\alpha}) x_3^2 dx_3 = \int_{-\frac{\hbar}{2}}^{\frac{\hbar}{2}} 2S_{\alpha 3 \beta 3} \sigma_{\beta 3} x_3^2 dx_3$$

$$\Rightarrow \hat{u}_{3,1} = \frac{8}{15} S_{13 \beta 3} (\sigma_{\beta 3}^{+} + \sigma_{\beta 3}^{-}) + \frac{8}{5h} S_{13 \beta 3} V_{\beta} + \frac{4}{h} \bar{u}_1 - \frac{2}{h} (u_1^{+} - u_1^{-})$$

$$- \frac{16}{35h} S_{13 \beta 3} \rho S_{\beta \beta 33} \int_{-\frac{\hbar}{2}}^{\frac{\hbar}{2}} \left(\dot{N}_{33} - \frac{h^2}{12} (\ddot{\sigma}_{33}^{+} - \ddot{\sigma}_{33}^{-}) \right) d\eta_1 \quad (74)$$

$$\begin{aligned}
& + \frac{4h}{2205} S_{13\beta 3} \rho (S_{\beta\beta 33} - S_{3333}) \int_{-\frac{\pi}{2}}^{\frac{\pi}{2}} \left(M_{33}^{(4)} - \frac{h^2}{12} (\ddot{\sigma}_{33}^{(4)+} - \ddot{\sigma}_{33}^{(4)-}) \right) d\eta_1 \\
\Rightarrow \hat{u}_{3,2} &= \frac{8}{15} S_{23\beta 3} (\sigma_{\beta 3}^+ + \sigma_{\beta 3}^-) + \frac{8}{5h} S_{23\beta 3} V_{\beta} + \frac{4}{h} \bar{u}_2 - \frac{2}{h} (u_2^+ - u_2^-) \\
& - \frac{16}{35h} S_{23\beta 3} \rho S_{\beta\beta 33} \int_{-\frac{\pi}{2}}^{\frac{\pi}{2}} \left(\dot{M}_{33} - \frac{h^2}{12} (\ddot{\sigma}_{33}^+ - \ddot{\sigma}_{33}^-) \right) d\eta_2 \\
& + \frac{4h}{2205} S_{23\beta 3} \rho (S_{\beta\beta 33} - S_{3333}) \int_{-\frac{\pi}{2}}^{\frac{\pi}{2}} \left(M_{33}^{(4)} - \frac{h^2}{12} (\ddot{\sigma}_{33}^{(4)+} - \ddot{\sigma}_{33}^{(4)-}) \right) d\eta_2
\end{aligned} \tag{75}$$

The above equations contain quantities u_i^+ and u_i^- which are aprior unknowns. To eliminate $u_3^+ + u_3^-$ we can write equation (68) as

$$u_3^+ + u_3^- = \bar{u}_3 + \frac{2}{h} S_{33\alpha\beta} M_{\alpha\beta} + \frac{2}{h} S_{3333} M_{33} \tag{76}$$

Substituting equation (76) into equation (70) and rearranging we get

$$\begin{aligned}
3\hat{u}_3 - \bar{u}_3 &= \frac{4}{5h} S_{33\alpha\beta} M_{\alpha\beta} + \frac{8}{7h} S_{3333} M_{33} - \frac{h}{35} S_{3333} (\sigma_{33}^+ - \sigma_{33}^-) \\
& - \frac{h}{735} S_{3333} \rho (S_{\alpha\alpha 33} - S_{3333}) \left(\frac{h^2}{12} (\ddot{\sigma}_{33}^+ - \ddot{\sigma}_{33}^-) - \dot{M}_{33} \right)
\end{aligned} \tag{77}$$

Combining equations (67) and (69) gives

$$\begin{aligned}
6\bar{u}_3 &= 2S_{33\alpha\beta} N_{\alpha\beta} + \frac{12}{5} S_{3333} N_{33} - \frac{h}{5} S_{3333} (\sigma_{33}^+ + \sigma_{33}^-) \\
& - \frac{h^2}{175} S_{3333} \rho (S_{\alpha\alpha 33} - S_{3333}) \left(\frac{h}{4} (\ddot{\sigma}_{33}^+ + \ddot{\sigma}_{33}^-) - \frac{1}{2} \dot{N}_{33} \right)
\end{aligned} \tag{78}$$

To eliminate $u_\alpha^+ - u_\alpha^-$ we can write equation (71) as

$$-\frac{2}{h} (u_\alpha^+ - u_\alpha^-) = \bar{u}_{3,\alpha} - \frac{8}{h} S_{\alpha 3\beta 3} V_{\beta} \tag{79}$$

Substituting equation (79) into equations (74) and (75) and rearranging gives

$$\begin{aligned}\hat{u}_{3,1} - \bar{u}_{3,1} - \frac{4}{h}\bar{u}_1 &= \frac{8}{15}S_{13\beta 3}(\sigma_{\beta 3}^+ + \sigma_{\beta 3}^-) - \frac{32}{5h}S_{13\beta 3}V_{\beta} \\ &+ \frac{16}{35h}S_{13\beta 3}\rho S_{\beta\beta 33}\int_{-a}^a\left(\frac{h^2}{12}(\ddot{\sigma}_{33}^+ - \ddot{\sigma}_{33}^-) - \ddot{M}_{33}\right)d\eta_1\end{aligned}\quad (80)$$

$$\begin{aligned}&- \frac{4h}{2205}S_{13\beta 3}\rho(S_{\beta\beta 33} - S_{3333})\int_{-a}^a\left(\frac{h^2}{12}(\sigma_{33}^{(4)+} - \sigma_{33}^{(4)-}) - M_{33}^{(4)}\right)d\eta_1 \\ \hat{u}_{3,2} - \bar{u}_{3,2} - \frac{4}{h}\bar{u}_2 &= \frac{8}{15}S_{23\beta 3}(\sigma_{\beta 3}^+ + \sigma_{\beta 3}^-) - \frac{32}{5h}S_{23\beta 3}V_{\beta} \\ &+ \frac{16}{35h}S_{23\beta 3}\rho S_{\beta\beta 33}\int_{-a}^a\left(\frac{h^2}{12}(\ddot{\sigma}_{33}^+ - \ddot{\sigma}_{33}^-) - \ddot{M}_{33}\right)d\eta_2 \\ &- \frac{4h}{2205}S_{23\beta 3}\rho(S_{\beta\beta 33} - S_{3333})\int_{-a}^a\left(\frac{h^2}{12}(\sigma_{33}^{(4)+} - \sigma_{33}^{(4)-}) - M_{33}^{(4)}\right)d\eta_2\end{aligned}\quad (81)$$

Equations (65), (66), (77), (78), (80) and (81) are the elastodynamic form of Pagano's constitutive equations for weighted displacement functions.

4.8 Interface Displacement Equations and Interface Conditions

The displacement at the interface can be obtained by combining some of the equations previously developed. Expressions for the inplane and transverse displacements at the interfaces are defined. Equations (72) and (73) can be written as

$$\begin{aligned}u_1^+ + u_1^- &= -\frac{h}{2}\bar{u}_{3,1} + \bar{u}_1 + \frac{2h}{3}S_{13\beta 3}(\sigma_{\beta 3}^+ - \sigma_{\beta 3}^-) \\ &- S_{13\beta 3}\rho S_{\beta\beta 33}\int_{-a}^a\left(\frac{4h}{15}\left(\frac{h}{4}(\ddot{\sigma}_{33}^+ + \ddot{\sigma}_{33}^-) - \frac{1}{2}\ddot{N}_{33}\right)\right)d\eta_1\end{aligned}\quad (82)$$

$$\begin{aligned}
& -S_{13\beta 3} \rho (S_{\beta\beta 33} - S_{3333}) \int_{-\frac{\pi}{2}}^{\frac{\pi}{2}} \frac{h^3}{525} \left(\frac{h}{4} (\sigma_{33}^{(4)+} + \sigma_{33}^{(4)-}) - \frac{1}{2} N_{33}^{(4)} \right) d\eta_1 \\
& u_2^+ + u_2^- = -\frac{h}{2} \bar{u}_{3,2} + \bar{u}_2 + \frac{2h}{3} S_{23\beta 3} (\sigma_{\beta 3}^+ - \sigma_{\beta 3}^-) \\
& -S_{23\beta 3} \rho S_{\beta\beta 33} \int_{-\frac{\pi}{2}}^{\frac{\pi}{2}} \frac{4h}{15} \left(\frac{h}{4} (\dot{\sigma}_{33}^+ - \dot{\sigma}_{33}^-) - \frac{1}{2} \dot{N}_{33} \right) d\eta_2 \\
& -S_{23\beta 3} \rho (S_{\beta\beta 33} - S_{3333}) \int_{-\frac{\pi}{2}}^{\frac{\pi}{2}} \frac{h^3}{525} \left(\frac{h}{4} (\sigma_{33}^{(4)+} + \sigma_{33}^{(4)-}) - \frac{1}{2} N_{33}^{(4)} \right) d\eta_2
\end{aligned} \tag{83}$$

Rearranging equations (71) gives

$$-\frac{2}{h} (u_\alpha^+ - u_\alpha^-) = \bar{u}_{3,\alpha} - \frac{8}{h} S_{\alpha 3\beta 3} V_\beta \tag{84}$$

Equations (74) and (75) are rearranged and written as

$$\begin{aligned}
-\frac{2}{h} (u_1^+ - u_1^-) &= \hat{u}_{3,1} - \frac{8}{15} S_{13\beta 3} (\sigma_{\beta 3}^+ + \sigma_{\beta 3}^-) - \frac{8}{5h} S_{13\beta 3} V_\beta - \frac{4}{h} \bar{u}_1 \\
& - \frac{16}{35h} S_{13\beta 3} \rho S_{\beta\beta 33} \int_{-\frac{\pi}{2}}^{\frac{\pi}{2}} \left(\frac{h^2}{12} (\dot{\sigma}_{33}^+ - \dot{\sigma}_{33}^-) - \dot{M}_{33} \right) d\eta_1 \\
& + \frac{4h}{2205} S_{13\beta 3} \rho (S_{\beta\beta 33} - S_{3333}) \int_{-\frac{\pi}{2}}^{\frac{\pi}{2}} \left(\frac{h^2}{12} (\sigma_{33}^{(4)+} - \sigma_{33}^{(4)-}) - M_{33}^{(4)} \right) d\eta_1
\end{aligned} \tag{85}$$

$$\begin{aligned}
-\frac{2}{h} (u_2^+ - u_2^-) &= \hat{u}_{3,2} - \frac{8}{15} S_{23\beta 3} (\sigma_{\beta 3}^+ + \sigma_{\beta 3}^-) - \frac{8}{5h} S_{23\beta 3} V_\beta - \frac{4}{h} \bar{u}_2 \\
& - \frac{16}{35h} S_{23\beta 3} \rho S_{\beta\beta 33} \int_{-\frac{\pi}{2}}^{\frac{\pi}{2}} \left(\frac{h^2}{12} (\dot{\sigma}_{33}^+ - \dot{\sigma}_{33}^-) - \dot{M}_{33} \right) d\eta_2 \\
& + \frac{4h}{2205} S_{23\beta 3} \rho (S_{\beta\beta 33} - S_{3333}) \int_{-\frac{\pi}{2}}^{\frac{\pi}{2}} \left(\frac{h^2}{12} (\sigma_{33}^{(4)+} - \sigma_{33}^{(4)-}) - M_{33}^{(4)} \right) d\eta_2
\end{aligned} \tag{86}$$

Following Chyou's [21] form, multiplying equations (84) by $\frac{h}{4}$ and multiplying equation (85) by $-\frac{3h}{4}$ then

adding the results gives

$$\begin{aligned} u_1^+ - u_1^- = & -\frac{3h}{4}\hat{u}_{3,1} + \frac{h}{4}\bar{u}_{3,1} + 3\bar{u}_1 + \frac{2h}{5}S_{13\beta 3}(\sigma_{\beta 3}^+ + \sigma_{\beta 3}^-) \\ & - \frac{4}{5}S_{13\beta 3}V_{\beta} + \frac{12}{35}S_{13\beta 3}\rho S_{\beta\beta 33} \int_{-\infty}^{\infty} \left(\frac{h^2}{12} (\ddot{\sigma}_{33}^+ - \ddot{\sigma}_{33}^-) - \dot{M}_{33} \right) d\eta_1 \\ & - \frac{h^2}{735}S_{13\beta 3}\rho(S_{\beta\beta 33} - S_{3333}) \int_{-\infty}^{\infty} \left(\frac{h^2}{12} (\sigma_{33}^{(4)+} - \sigma_{33}^{(4)-}) - M_{33}^{(4)} \right) d\eta_1 \end{aligned} \quad (87)$$

similarly

$$\begin{aligned} u_2^+ - u_2^- = & -\frac{3h}{4}\hat{u}_{3,2} + \frac{h}{4}\bar{u}_{3,2} + 3\bar{u}_2 + \frac{2h}{5}S_{23\beta 3}(\sigma_{\beta 3}^+ + \sigma_{\beta 3}^-) \\ & - \frac{4}{5}S_{23\beta 3}V_{\beta} + \frac{12}{35}S_{23\beta 3}\rho S_{\beta\beta 33} \int_{-\infty}^{\infty} \left(\frac{h^2}{12} (\ddot{\sigma}_{33}^+ - \ddot{\sigma}_{33}^-) - \dot{M}_{33} \right) d\eta_2 \\ & - \frac{h^2}{735}S_{23\beta 3}\rho(S_{\beta\beta 33} - S_{3333}) \int_{-\infty}^{\infty} \left(\frac{h^2}{12} (\sigma_{33}^{(4)+} - \sigma_{33}^{(4)-}) - M_{33}^{(4)} \right) d\eta_2 \end{aligned} \quad (88)$$

Adding equations (82) and equations (87) we get

$$\begin{aligned} u_1^+ = & -h \left(\frac{3}{8}\hat{u}_{3,1} - \frac{1}{8}\bar{u}_{3,1} - \frac{3}{2h}\bar{u}_1 \right) - \left(\frac{h}{4}\bar{u}_{3,1} - \frac{1}{2}\bar{u}_1 \right) \\ & + 4S_{13\beta 3} \left(\frac{(4\sigma_{\beta 3}^+ - \sigma_{\beta 3}^-)}{30} - \frac{V_{\beta}}{10} \right) \\ & - S_{13\beta 3}\rho S_{\beta\beta 33} \int_{-\infty}^{\infty} \left(\frac{2h}{15} \left(\frac{h}{4} (\ddot{\sigma}_{33}^+ + \ddot{\sigma}_{33}^-) - \frac{1}{2}\dot{N}_{33} \right) - \frac{6}{35} \left(\frac{h^2}{12} (\ddot{\sigma}_{33}^+ - \ddot{\sigma}_{33}^-) - \dot{M}_{33} \right) \right) d\eta_1 \\ & - S_{13\beta 3}\rho(S_{\beta\beta 33} - S_{3333}) \int_{-\infty}^{\infty} \left(\frac{h^3}{1050} \left(\frac{h}{4} (\sigma_{33}^{(4)+} + \sigma_{33}^{(4)-}) - \frac{1}{2}N_{33}^{(4)} \right) \right. \\ & \quad \left. + \frac{h^2}{1470} \left(\frac{h^2}{12} (\sigma_{33}^{(4)+} - \sigma_{33}^{(4)-}) - M_{33}^{(4)} \right) \right) d\eta_1 \end{aligned} \quad (89)$$

Similarly, adding equations (83) and equations (88) we get

$$\begin{aligned}
 u_2^+ = & -h \left(\frac{3}{8} \hat{u}_{3,2} - \frac{1}{8} \bar{u}_{3,2} - \frac{3}{2h} \bar{u}_2 \right) - \left(\frac{h}{4} \bar{u}_{3,2} - \frac{1}{2} \bar{u}_2 \right) \\
 & + 4S_{23\beta 3} \left(\frac{(4\sigma_{\beta 3}^+ - \sigma_{\beta 3}^-)}{30} - \frac{V_{\beta}}{10} \right) \\
 & - S_{23\beta 3} \rho S_{\beta\beta 33} \int_{-\frac{h}{2}}^{\frac{h}{2}} \left(\frac{2h}{15} \left(\frac{h}{4} (\ddot{\sigma}_{33}^+ + \ddot{\sigma}_{33}^-) - \frac{1}{2} \ddot{N}_{33} \right) - \frac{6}{35} \left(\frac{h^2}{12} (\ddot{\sigma}_{33}^+ - \ddot{\sigma}_{33}^-) - \ddot{M}_{33} \right) \right) d\eta_2 \\
 & - S_{23\beta 3} \rho (S_{\beta\beta 33} - S_{3333}) \int_{-\frac{h}{2}}^{\frac{h}{2}} \left(\frac{h^3}{1050} \left(\frac{h}{4} (\sigma_{33}^{(4)+} + \sigma_{33}^{(4)-}) - \frac{1}{2} N_{33}^{(4)} \right) \right. \\
 & \quad \left. + \frac{h^2}{1470} \left(\frac{h^2}{12} (\sigma_{33}^{(4)+} - \sigma_{33}^{(4)-}) - M_{33}^{(4)} \right) \right) d\eta_2
 \end{aligned} \tag{90}$$

Subtracting equation (87) from (82) we get

$$\begin{aligned}
 u_1^- = & h \left(\frac{3}{8} \hat{u}_{3,1} - \frac{1}{8} \bar{u}_{3,1} - \frac{3}{2h} \bar{u}_1 \right) - \left(\frac{h}{4} \bar{u}_{3,1} - \frac{1}{2} \bar{u}_1 \right) \\
 & - 4S_{13\beta 3} \left(\frac{(4\sigma_{\beta 3}^- - \sigma_{\beta 3}^+)}{30} - \frac{V_{\beta}}{10} \right) \\
 & - S_{13\beta 3} \rho S_{\beta\beta 33} \int_{-\frac{h}{2}}^{\frac{h}{2}} \left(\frac{2h}{15} \left(\frac{h}{4} (\ddot{\sigma}_{33}^+ + \ddot{\sigma}_{33}^-) - \frac{1}{2} \ddot{N}_{33} \right) + \frac{6}{35} \left(\frac{h^2}{12} (\ddot{\sigma}_{33}^+ - \ddot{\sigma}_{33}^-) - \ddot{M}_{33} \right) \right) dx_1 \\
 & - S_{13\beta 3} \rho (S_{\beta\beta 33} - S_{3333}) \int_{-\frac{h}{2}}^{\frac{h}{2}} \left(\frac{h^3}{1050} \left(\frac{h}{4} (\sigma_{33}^{(4)+} + \sigma_{33}^{(4)-}) - \frac{1}{2} N_{33}^{(4)} \right) \right. \\
 & \quad \left. - \frac{h^2}{1470} \left(\frac{h^2}{12} (\sigma_{33}^{(4)+} - \sigma_{33}^{(4)-}) - M_{33}^{(4)} \right) \right) dx_1
 \end{aligned} \tag{91}$$

Similarly, subtracting equation (88) from (83) we get

$$\begin{aligned}
 \bar{u}_2^- = & h \left(\frac{3}{8} \hat{u}_{3,2} - \frac{1}{8} \bar{u}_{3,2} - \frac{3}{2h} \bar{u}_2 \right) - \left(\frac{h}{4} \bar{u}_{3,2} - \frac{1}{2} \bar{u}_2 \right) \\
 & - 4S_{23\beta 3} \left(\frac{(4\sigma_{\beta 3}^- - \sigma_{\beta 3}^+)}{30} - \frac{V_{\beta}}{10} \right)
 \end{aligned} \tag{92}$$

$$\begin{aligned}
& -S_{23\beta 3}\rho S_{\beta\beta 33}\int_{-\frac{h}{2}}^{\frac{h}{2}}\left(\frac{2h}{15}\left(\frac{h}{4}(\ddot{\sigma}_{33}^{+} + \ddot{\sigma}_{33}^{-}) - \frac{1}{2}\ddot{N}_{33}\right) + \frac{6}{35}\left(\frac{h^2}{12}(\ddot{\sigma}_{33}^{+} - \ddot{\sigma}_{33}^{-}) - \ddot{M}_{33}\right)\right)dx_2 \\
& -S_{23\beta 3}\rho(S_{\beta\beta 33} - S_{3333})\int_{-\frac{h}{2}}^{\frac{h}{2}}\left\{\frac{h^3}{1050}\left(\frac{h}{4}(\sigma_{33}^{(4)+} + \sigma_{33}^{(4)-}) - \frac{1}{2}N_{33}^{(4)}\right) \right. \\
& \quad \left. - \frac{h^2}{1470}\left(\frac{h^2}{12}(\sigma_{33}^{(4)+} - \sigma_{33}^{(4)-}) - M_{33}^{(4)}\right)\right\}dx_2
\end{aligned}$$

To eliminate $N_{\alpha\beta}$ write equation (67) as

$$N_{\alpha\beta} = \frac{1}{S_{33\alpha\beta}}(u_3^{+} - u_3^{-} - S_{3333}N_{33})$$

substituting into equation (69) and rearranging

$$\begin{aligned}
u_3^{+} - u_3^{-} &= 3\bar{u}_3 - \frac{1}{5}S_{3333}N_{33} + \frac{h}{10}S_{3333}(\sigma_{33}^{+} + \sigma_{33}^{-}) \\
&+ \frac{h^2}{350}S_{3333}\rho(S_{\alpha\alpha 33} - S_{3333})\left(\frac{h}{4}(\ddot{\sigma}_{33}^{+} + \ddot{\sigma}_{33}^{-}) - \frac{1}{2}\ddot{N}_{33}\right)
\end{aligned} \tag{93}$$

To eliminate $M_{\alpha\beta}$ write equation (68) as

$$M_{\alpha\beta} = \frac{h}{2S_{33\alpha\beta}}\left(-\bar{u}_3 + (u_3^{+} + u_3^{-}) - \frac{2}{h}S_{3333}M_{33}\right)$$

Substituting into equation (70) and rearranging

$$\begin{aligned}
u_3^{+} + u_3^{-} &= \frac{15}{2}\hat{u}_3 - \frac{3}{2}\bar{u}_3 - \frac{6}{7h}S_{3333}M_{33} + \frac{h}{14}S_{3333}(\sigma_{33}^{+} - \sigma_{33}^{-}) \\
&- \frac{h}{294}S_{3333}\rho(S_{\alpha\alpha 33} - S_{3333})\left(\frac{h^2}{12}(\ddot{\sigma}_{33}^{+} - \ddot{\sigma}_{33}^{-}) - \ddot{M}_{33}\right)
\end{aligned} \tag{94}$$

Adding equations (93) and equations (94) we get

$$\begin{aligned}
u_3^{+} &= \frac{3}{4}(5\hat{u}_3 - \bar{u}_3) + \frac{3}{2}\bar{u}_3 + \frac{S_{3333}}{70h}((6\sigma_{33}^{+} + \sigma_{33}^{-}) - 7hN_{33} - 30M_{33}) \\
&+ S_{3333}\rho(S_{\alpha\alpha 33} - S_{3333})\left(\frac{h^2}{700}\left(\frac{h}{4}(\ddot{\sigma}_{33}^{+} + \ddot{\sigma}_{33}^{-}) - \frac{1}{2}\ddot{N}_{33}\right) \right.
\end{aligned} \tag{95}$$

$$- \frac{h}{588} \left(\frac{h^2}{12} (\ddot{\sigma}_{33}^+ - \ddot{\sigma}_{33}^-) - \dot{M}_{33} \right)$$

Similarly subtracting equations (93) from equations (94) we get

$$\begin{aligned} \bar{u}_3 = & \frac{3}{4}(5\hat{u}_3 - \bar{u}_3) - \frac{3}{2}\bar{u}_3 - \frac{S_{3333}}{70h} ((6\bar{\sigma}_{33} + \bar{\sigma}_{33}^-) - 7hN_{33} + 30M_{33}) \\ & - S_{3333}\rho(S_{\alpha\alpha 33} - S_{3333}) \left\{ \frac{h^2}{700} \left(\frac{h}{4} (\ddot{\sigma}_{33}^+ + \ddot{\sigma}_{33}^-) - \frac{1}{2} \dot{N}_{33} \right) \right. \\ & \left. + \frac{h}{588} \left(\frac{h^2}{12} (\ddot{\sigma}_{33}^+ - \ddot{\sigma}_{33}^-) - \dot{M}_{33} \right) \right\} \end{aligned} \quad (96)$$

The interface continuity conditions are

$$\sigma_{i3}^{-(k)} = \sigma_{i3}^{+(k+1)} \quad (97)$$

$$u_i^{(k)} \left(-\frac{l_k}{2} \right) = u_i^{(k+1)} \left(\frac{l_{k+1}}{2} \right) \quad (98)$$

and the initial conditions

$$u_i^{(k)} = u_{i0}^{(k)} \quad (99)$$

$$\dot{u}_i^{(k)} = \dot{u}_{i0}^{(k)} \quad (100)$$

4.9 Summarizing the Field Equations

The theory developed herein, is an extension of Pagano's theory to include both inertia and body [59] force terms. It is believed by the authors that Pagano's theory has been restricted to the static case due to the formidable task of deriving and solving the governing equations. The following is a summary of the derived governing equations. It is noted that the equations of reference [59] are recovered if the time dependence is eliminated. The equilibrium equations are (30), (31) and (34).

$$N_{\alpha\beta,\beta} + (\sigma_{\alpha 3}^+ - \sigma_{\alpha 3}^-) + F_{\alpha} - \rho \ddot{u}_{\alpha} = 0$$

$$V_{\alpha,\alpha} + (\sigma_{33}^+ - \sigma_{33}^-) + F_3 - \rho \ddot{u}_3 = 0$$

$$M_{\alpha\beta,\beta} + \frac{h}{2}(\sigma_{\alpha 3}^+ + \sigma_{\alpha 3}^-) - V_{\alpha} - \rho \dot{\ddot{u}}_{\alpha} = 0$$

The constitutive relations are given by (65), (66) and (77), (78), (80) and (81)

$$\frac{h}{2} \ddot{u}_{(\alpha,\beta)} = S_{\alpha\beta\gamma\delta} N_{\gamma\delta} + S_{\alpha\beta 33} N_{33}$$

$$\frac{h^2}{4} \ddot{u}_{(\alpha,\beta)} = S_{\alpha\beta\gamma\delta} M_{\gamma\delta} + S_{\alpha\beta 33} M_{33}$$

$$3\hat{u}_3 - \ddot{u}_3 = \frac{4}{5h} S_{33\alpha\beta} M_{\alpha\beta} + \frac{8}{7h} S_{3333} M_{33} - \frac{h}{35} S_{3333} (\sigma_{33}^+ - \sigma_{33}^-) \\ - \frac{h}{735} S_{3333} \rho (S_{\alpha\alpha 33} - S_{3333}) \left(\frac{h^2}{12} (\ddot{\sigma}_{33}^+ - \ddot{\sigma}_{33}^-) - \dot{M}_{33} \right)$$

$$6\ddot{u}_3 = 2S_{33\alpha\beta} N_{\alpha\beta} + \frac{12}{5} S_{3333} N_{33} - \frac{h}{5} S_{3333} (\sigma_{33}^+ + \sigma_{33}^-) \\ - \frac{h^2}{175} S_{3333} \rho (S_{\alpha\alpha 33} - S_{3333}) \left(\frac{h}{4} (\ddot{\sigma}_{33}^+ + \ddot{\sigma}_{33}^-) - \frac{1}{2} \dot{N}_{33} \right)$$

$$\hat{u}_{3,1} - \ddot{u}_{3,1} - \frac{4}{h} \ddot{u}_1 = \frac{8}{15} S_{13\beta 3} (\sigma_{\beta 3}^+ + \sigma_{\beta 3}^-) - \frac{32}{5h} S_{13\beta 3} V_{\beta} \\ + \frac{16}{35h} S_{13\beta 3} \rho S_{\beta\beta 33} \int_{-\frac{h}{2}}^{\frac{h}{2}} \left(\frac{h^2}{12} (\ddot{\sigma}_{33}^+ - \ddot{\sigma}_{33}^-) - \dot{M}_{33} \right) d\eta_1 \\ - \frac{4h}{2205} S_{13\beta 3} \rho (S_{\beta\beta 33} - S_{3333}) \int_{-\frac{h}{2}}^{\frac{h}{2}} \left(\frac{h^2}{12} (\sigma_{33}^{(4)+} - \sigma_{33}^{(4)-}) - M_{33}^{(4)} \right) d\eta_1$$

$$\hat{u}_{3,2} - \ddot{u}_{3,2} - \frac{4}{h} \ddot{u}_2 = \frac{8}{15} S_{23\beta 3} (\sigma_{\beta 3}^+ + \sigma_{\beta 3}^-) - \frac{32}{5h} S_{23\beta 3} V_{\beta} \\ + \frac{16}{35h} S_{23\beta 3} \rho S_{\beta\beta 33} \int_{-\frac{h}{2}}^{\frac{h}{2}} \left(\frac{h^2}{12} (\ddot{\sigma}_{33}^+ - \ddot{\sigma}_{33}^-) - \dot{M}_{33} \right) d\eta_2$$

$$- \frac{4h}{2205} S_{23\beta 3} \rho (S_{\beta\beta 33} - S_{3333}) \int_{-b}^b \left(\frac{h^2}{12} (\sigma_{33}^{(4)+} - \sigma_{33}^{(4)-}) - M_{33}^{(4)} \right) d\eta_2$$

The surface displacement components are given by (89) - (92), (95) and (96).

$$\begin{aligned} u_1^+ = & -h \left(\frac{3}{8} \hat{u}_{3,1} - \frac{1}{8} \bar{u}_{3,1} - \frac{3}{2h} \bar{u}_1 \right) - \left(\frac{h}{4} \bar{u}_{3,1} - \frac{1}{2} \bar{u}_1 \right) \\ & + 4S_{13\beta 3} \left(\frac{(4\sigma_{\beta 3}^+ - \sigma_{\beta 3}^-)}{30} - \frac{V_{\beta}}{10} \right) \\ & - S_{13\beta 3} \rho S_{\beta\beta 33} \int_{-a}^a \left(\frac{2h}{15} \left(\frac{h}{4} (\ddot{\sigma}_{33}^+ + \ddot{\sigma}_{33}^-) - \frac{1}{2} \dot{N}_{33} \right) - \frac{6}{35} \left(\frac{h^2}{12} (\ddot{\sigma}_{33}^+ - \ddot{\sigma}_{33}^-) - \dot{M}_{33} \right) \right) d\eta_1 \\ & - S_{13\beta 3} \rho (S_{\beta\beta 33} - S_{3333}) \int_{-a}^a \left(\frac{h^3}{1050} \left(\frac{h}{4} (\sigma_{33}^{(4)+} + \sigma_{33}^{(4)-}) - \frac{1}{2} N_{33}^{(4)} \right) \right. \\ & \quad \left. + \frac{h^2}{1470} \left(\frac{h^2}{12} (\sigma_{33}^{(4)+} - \sigma_{33}^{(4)-}) - M_{33}^{(4)} \right) \right) d\eta_1 \end{aligned}$$

$$\begin{aligned} u_2^+ = & -h \left(\frac{3}{8} \hat{u}_{3,2} - \frac{1}{8} \bar{u}_{3,2} - \frac{3}{2h} \bar{u}_2 \right) - \left(\frac{h}{4} \bar{u}_{3,2} - \frac{1}{2} \bar{u}_2 \right) \\ & + 4S_{23\beta 3} \left(\frac{(4\sigma_{\beta 3}^+ - \sigma_{\beta 3}^-)}{30} - \frac{V_{\beta}}{10} \right) \\ & - S_{23\beta 3} \rho S_{\beta\beta 33} \int_{-b}^b \left(\frac{2h}{15} \left(\frac{h}{4} (\ddot{\sigma}_{33}^+ + \ddot{\sigma}_{33}^-) - \frac{1}{2} \dot{N}_{33} \right) - \frac{6}{35} \left(\frac{h^2}{12} (\ddot{\sigma}_{33}^+ - \ddot{\sigma}_{33}^-) - \dot{M}_{33} \right) \right) d\eta_2 \\ & - S_{23\beta 3} \rho (S_{\beta\beta 33} - S_{3333}) \int_{-b}^b \left(\frac{h^3}{1050} \left(\frac{h}{4} (\sigma_{33}^{(4)+} + \sigma_{33}^{(4)-}) - \frac{1}{2} N_{33}^{(4)} \right) \right. \\ & \quad \left. + \frac{h^2}{1470} \left(\frac{h^2}{12} (\sigma_{33}^{(4)+} - \sigma_{33}^{(4)-}) - M_{33}^{(4)} \right) \right) d\eta_2 \end{aligned}$$

$$u_1^- = h \left(\frac{3}{8} \hat{u}_{3,1} - \frac{1}{8} \bar{u}_{3,1} - \frac{3}{2h} \bar{u}_1 \right) - \left(\frac{h}{4} \bar{u}_{3,1} - \frac{1}{2} \bar{u}_1 \right)$$

$$\begin{aligned}
& -4S_{13\beta 3} \left(\frac{(4\sigma_{\beta 3}^- - \sigma_{\beta 3}^+)}{30} - \frac{V_{\beta}}{10} \right) \\
& - S_{13\beta 3} \rho S_{\beta\beta 33} \int_{-\frac{h}{2}}^{\frac{h}{2}} \left(\frac{2h}{15} \left(\frac{h}{4} (\ddot{\sigma}_{33}^+ + \ddot{\sigma}_{33}^-) - \frac{1}{2} \dot{N}_{33} \right) + \frac{6}{35} \left(\frac{h^2}{12} (\ddot{\sigma}_{33}^+ - \ddot{\sigma}_{33}^-) - \dot{M}_{33} \right) \right) dx_1 \\
& - S_{13\beta 3} \rho (S_{\beta\beta 33} - S_{3333}) \int_{-\frac{h}{2}}^{\frac{h}{2}} \left(\frac{h^3}{1050} \left(\frac{h}{4} (\sigma_{33}^{(4)+} + \sigma_{33}^{(4)-}) - \frac{1}{2} N_{33}^{(4)} \right) \right. \\
& \quad \left. - \frac{h^2}{1470} \left(\frac{h^2}{12} (\sigma_{33}^{(4)+} - \sigma_{33}^{(4)-}) - M_{33}^{(4)} \right) \right) dx_1 \\
u_2^- &= h \left(\frac{3}{8} \hat{u}_{3,2} - \frac{1}{8} \bar{u}_{3,2} - \frac{3}{2h} \bar{u}_2 \right) - \left(\frac{h}{4} \bar{u}_{3,2} - \frac{1}{2} \bar{u}_2 \right) \\
& - 4S_{23\beta 3} \left(\frac{(4\sigma_{\beta 3}^- - \sigma_{\beta 3}^+)}{30} - \frac{V_{\beta}}{10} \right) \\
& - S_{23\beta 3} \rho S_{\beta\beta 33} \int_{-\frac{h}{2}}^{\frac{h}{2}} \left(\frac{2h}{15} \left(\frac{h}{4} (\ddot{\sigma}_{33}^+ + \ddot{\sigma}_{33}^-) - \frac{1}{2} \dot{N}_{33} \right) + \frac{6}{35} \left(\frac{h^2}{12} (\ddot{\sigma}_{33}^+ - \ddot{\sigma}_{33}^-) - \dot{M}_{33} \right) \right) dx_2 \\
& - S_{23\beta 3} \rho (S_{\beta\beta 33} - S_{3333}) \int_{-\frac{h}{2}}^{\frac{h}{2}} \left(\frac{h^3}{1050} \left(\frac{h}{4} (\sigma_{33}^{(4)+} + \sigma_{33}^{(4)-}) - \frac{1}{2} N_{33}^{(4)} \right) \right. \\
& \quad \left. - \frac{h^2}{1470} \left(\frac{h^2}{12} (\sigma_{33}^{(4)+} - \sigma_{33}^{(4)-}) - M_{33}^{(4)} \right) \right) dx_2 \\
u_3^+ &= \frac{3}{4} (5\hat{u}_3 - \bar{u}_3) + \frac{3}{2} \bar{u}_3 + \frac{S_{3333}}{70h} ((6\sigma_{33}^+ + \sigma_{33}^-) - 7hN_{33} - 30M_{33}) \\
& + S_{3333} \rho (S_{\alpha\alpha 33} - S_{3333}) \left(\frac{h^2}{700} \left(\frac{h}{4} (\ddot{\sigma}_{33}^+ + \ddot{\sigma}_{33}^-) - \frac{1}{2} \dot{N}_{33} \right) \right. \\
& \quad \left. - \frac{h}{588} \left(\frac{h^2}{12} (\ddot{\sigma}_{33}^+ - \ddot{\sigma}_{33}^-) - \dot{M}_{33} \right) \right) \\
u_3^- &= \frac{3}{4} (5\hat{u}_3 - \bar{u}_3) - \frac{3}{2} \bar{u}_3 - \frac{S_{3333}}{70h} ((6\sigma_{33}^- + \sigma_{33}^+) - 7hN_{33} + 30M_{33})
\end{aligned}$$

$$\begin{aligned}
& -S_{3333}\rho(S_{\alpha\alpha 33} - S_{3333})\left\{\frac{h^2}{700}\left(\frac{h}{4}(\ddot{\sigma}_{33}^+ + \ddot{\sigma}_{33}^-) - \frac{1}{2}\ddot{N}_{33}\right)\right. \\
& \quad \left. + \frac{h}{588}\left(\frac{h^2}{12}(\ddot{\sigma}_{33}^+ - \ddot{\sigma}_{33}^-) - \dot{M}_{33}\right)\right\}
\end{aligned}$$

The governing equations for the extension of Pagano's [59] theory to include inertia and body force terms has been presented.

Primary emphasis will be placed on theoretical and analytical development of a method to simulate stress fields in a laminate composite subjected to transient loading. The theory is being formulated for implementation into a computer program. Various numerical and finite element schemes are being reviewed to determine the feasibility of the computational techniques for solving the governing equations. A verification of the solution procedure will be based on available published results, exact solutions and experimental results. This will be followed by a parametric study to determine the effect of panel thickness, stacking sequence, and material system, etc. on the behavior of the laminate.

Chapter 5

SUMMARY

The behavior of graphite fiber reinforced epoxy composites during low velocity impact has been studied both experimentally and analytically. In the experimental program described in this report graphite/epoxy plates of different ply orientations and thicknesses were fabricated in the laboratories at WPAFB and at OSU. Prior to testing, the plates were checked to make sure they were free of fabrication defects. Each plate was then impacted a single time using an instrumented falling weight. Load and energy time histories were recorded for each test. The energy was correlated with the visible damage using a damage scale developed during the project, and with the internal damage as identified in post-test ultrasonic scans of the test plates. When the energy levels were normalized to a per ply basis, relationships were clearly identified between the amount of impact energy or absorbed energy imparted to the specimens and the damage levels. These relationships were presented in graphical form. Some plates were also subjected to interrogation by x-rays and then deplied. The purpose of these additional tests was to try to develop a three dimensional picture of the damage done to a laminated plate during the impact event. Work will continue in this area.

In the analytical portion of the project, we have sought to identify methods for determining the complete stress field in a loaded laminated plate. To this end, Pagano's model for the determination of stresses in a laminate subjected to a static in-plane load were thoroughly studied. Pagano's method was then extended to include a proper description the inertia terms necessary to accommodate a dynamic analysis. Pagano's formulation is a discrete laminate theory which allows for a thorough description of the stresses on a ply by ply basis. Such a presentation is required if a consistent treatment of the transverse stresses at each ply interface is to be attempted. It is believed that the work presented in this report will provide a basis for the development of an analytical capability to reasonably simulate results obtained by tests and then to design more damage tolerant structures.

Chapter 6

REFERENCES

1. ACEE Composites Project Office, "Standard Tests for Toughened Resin Composites - Revised Edition," NASA Reference Publication 1092, July, 1983.
2. ACEE Composites Project Office, "NASA/Aircraft Industry Standard Specification for Graphite Fiber/Toughened Thermoset Resin Composite Materials," NASA Reference Publication 1142, 1985.
3. Achenbach, J. D., Sun, C. T. and Herrmann, G., "On the Vibrations of a Laminated Body," *Journal of Applied Mechanics, Transactions, ASME*, Vol. 35, 1968, pp. 689-696.
4. Adams, D. F., "Impact Response of Polymer-Matrix Composite Materials," *Composite Materials: Testing and Design, ASTM STP 617*, 1977, pp 409-426.
5. American Society for Testing and Materials, "Nondestructive Evaluation and Flaw Criticality for Composite Materials," *ASTM STP 696*, 1979.
6. Avva, V. S., Vala, J. R. and Jeyaseelan, M., "Effect of Impact on the Strength of Graphite/Epoxy Composites," *ASTM STP 893*, 1986, pp 196-206.
7. Bert, C. W., "A Critical Evaluation of New Plate Theories Applied to Laminated Composites," *Office of Naval Research, Report OU-AMNE-83-3*, 1983.
8. Bert, C. W., "Dynamic Behavior of Composites: An Overview," *Proceedings Society of Experimental Mechanics Conference*, 1985, pp. 747-751, 1985.
- 9.. Bert, C. W., "Research on Dynamic Behavior of Composite and Sandwich Plates-IV," *Shock and Vibration Digest*, Vol. 17, No. 11, 1985, pp 3-15.
10. Bert, C. W. and Chen, T. L. C., "Effect of Shear Deformation on Vibration of Antisymmetric Angle-Ply Laminated Rectangular Plates," *Int. J. Solids Structures*, Vol. 14, pp. 465-473, 1978.

11. Bert, C. W. and Mayberry, B. L., "Free Vibration of Unsymmetrically Laminated Anisotropic Plates with Clamped Edges," *Journal of Composite Materials*, Vol.3, pp. 282-293, 1969.
12. Broughton, W. R., and Chester, R. J., "The Development of a Portable Ultrasonics Facility for NDI of Graphite/Epoxy Composites," *Non-Destructive Testing Australia*, Vol. 23, No. 2, 1986, pp. 38-40.
13. Broutman, L. J. and Mallick, P., "Impact Strength and Toughness of Fiber Composite Materials," AFSOR TR 0051, 1974.
14. Cantwell, W. J., and Morton, J., "Detection of Impact Damage in CFRP Laminates," *Composite Structures*, Vol. 3, 1985, pp. 241-257.
15. Cantwell, W. J. and Morton, J., "Low Velocity Impact Damage in Carbon Fiber Reinforced Plastic Laminates," *Proceedings of the 5th International Congress in Experimental Mechanics, Society of Experimental Stress Analysis, Montreal, 1984.*
16. Chai, H., Knauss, W. G., and Babcock, C. D., "Observation of Damage Growth in Compressively Loaded Laminates," *Experimental Mechanics*, September 1983, pp. 329-337.
17. Chang, F. G., Gordon, D. E., and Gardner, A. H., "A Study of Fatigue Damage in Composite by Non-Destructive Techniques," Fatigue of Filamentary Composite Materials, ASTM STP 636, 1977, pp. 57-72.
18. Chaturvedi, S.K. and Sierakowski, R.L., "Effects of Impactor Size on Impact Damage Growth and Residual Properties in an SMC-R50 Composite," *Journal of Composite Materials*, Vol. 19, 1985, pp. 100-113.
19. Cheresh, M., and McMichael, S., "Instrumented Impact Test Data Interpretation," Instrumented Impact Testing of Plastic and Composite Materials, ASTM STP 936, S. L. Kessler, G. C. Adams, S. B. Driscoll, and D. R. Ireland, Eds., American Society for Testing and Materials, Philadelphia, 1987, pp. 9-23.
20. Chow, T. S., "On the Propagation of Flexural Waves in an Orthotropic Laminated Plate and Its Response to an Impulsive Load," *Journal of Composite Materials*, Vol. 5, 1971, pp. 306-319.
21. Chyou, H. A., Variational Formulation and Implementation of Pagano's Theory of Laminated Plates, Ph.D. Dissertation, The Ohio State University, Columbus, Ohio, 1989

22. Clark, G. and Blaricum, T. J., Carbon Fiber Composite Coupons - Static and Fatigue Behaviour after Impact Damage, Structures Division Report 422, Aeronautical Research Laboratories, Melbourne, Australia, 1986.
23. Cordell, T. M. and Sjoblom, P. O., "Low Velocity Impact Testing of Composites," Proceedings of the American Society for Composites, 1st Technical Conference, Dayton, OH., 1986, pp 297-312.
24. Craig, T. J. and Dawe, D. J., "Flexural Vibration of Symmetrically Laminated Composite Rectangular Plates including Transverse Shear Effects," International Journal of Solids and Structures, Vol.22, No.2, 1986, pp. 155-169.
26. Dost, E. F., Ilcewicz, L. B., and Gosse, J. H., "Sublaminar Stability Based Modeling of Impact-Damaged Composite Laminates,".....
27. Elber, W., Failure Mechanics in Low-Velocity Impact on Thin Composite Plates, NASA TP 2152, 1983.
28. Freeman, S.M., Damage Progression in Graphite-Epoxy by a Depleting Technique, Air Force Wright Aeronautical Laboratory Technical Report, AFWAL-TR-81-3157, December 1981.
29. Freeman, S. M., "Characterization of Lamina and Interlaminar Damage in Graphite/Epoxy Composites by the Depley Technique," Composite Materials : Testing and Design, 6th Conference, ASTM 787, Daniel, I. M., Eds., American Society for Testing and Materials, 1982, pp. 50-62.
30. Ghandhe, G.V. and Griffin, O.H., "Post Impact Characterization of Interleafed Composite Materials," SAMPE Quarterly, July 1989, pp. 55-58
31. Gibson, R.F., "Dynamic Mechanical Properties of Advanced Composite Materials and Structures: A Review," Shock and Vibration Digest, Vol. 19, No. 7, 1987.
32. Green, A. T., "Acoustic Emission for NDT for Advanced Composite Structures," The Conference on Advanced Composites - Special Topics, December 1979, El Segundo, California, pp. 228-245.
33. Greszczuk, B., "Damage in Composite Materials Due to Low Velocity Impact," Impact Dynamics, J. A. Zukas Ed., John Wiley Publ., 1982, pp 55-94.

34. Gu, Z. L. and Sun, C. T., "Prediction of Impact Damage Region in SMC Composites," *Composite Structures*, Vol. 7, 1987, pp 179-190.
35. Guild, F. J., Phillips, M. G., and Harris, B., "Acoustic Emission Study of Damage in GRP, NDT International, October, 1980, pp. 209-217.
36. Guynn, E. G., and O'Brien, T. K., "The Influence of Lay-Up and Thickness on Composite Impact Damage and Compression Strength," AIAA/ASME/SAE, 26th Structures Structural Dynamics and Materials Conference, Orlando, Florida, 1985, pp. 187-196.
37. Hagemmaier, D. J., and Fassbender, R. H., "Nondestructive Testing of Advanced Composites," *Materials Evaluation*, June 1979, pp. 43-49.
38. Harris, C.E., and Morris, D.H., "An Evaluation of the Effect of Stacking Sequence and Thickness on the Fatigue Life of Quasi-Isotropic Graphite/Epoxy Laminates," Recent Advances in Composites in the United States and Japan, ASTM STP 864, 1985, p. 153.
39. Hudock, M. F., Low Velocity Impact, Research Report, Univ. of Dayton Research Institute
40. Ireland, D.R., "Procedures and Problems Associated with Reliable Control of the Instrumented Impact Test," ASTM STP 563, 1974, pp. 3-29.
41. Iyengar, N. G. R. and Umaretiya, J. R., "Transverse Vibrations of Hybrid Laminated Plates," *J. Sound Vibration*, Vol. 104, 1986, pp. 425-435.
42. Jang, B.Z., Chen, L.C., Wang, C.Z., Lin, H.T., and Zee, R.H., "Impact Resistance and Energy Absorption Mechanisms in Hybrid Composites," *Composite Science and Review*, Vol. 34, 1989, pp. 305-335.
43. Jaques, Capt. W., "Soft Body Impact Damage Effects on Boron-Aluminum Composites," AFML-TR-74-155, 1975.
44. Jones, A. T., "Exact Natural Frequencies and Modal Functions for a Thick Off-Axis Lamina," *Journal of Composite Materials*, Vol. 5, 1971, pp. 504-520.
46. Kelkar, A., Elber, W. and Raju, I. S., "Large Deflection Behavior of Quasi-Isotropic Laminates Under Low-Velocity Impact Type Point Loading," 26th Struc., Struc. Dynam. Malts. Conf., Orlando, FL, Pt. 1, 1985, pp 432-441.

47. Knauss, W.G., Babcock, C.D., and Chai, H., Visualization of Impact Damage of Composite Plates by Means of the Moire' Technique, NASA CR 159261, April, 1980.
48. Kulkarni, S. V. and Pagano, N. J., "Dynamic Characteristics of Composite Laminates," *Journal of Sound and Vibration*, Vol.23, 1972, pp. 127-143.
49. Levin, K., "Effects of Low-Velocity Impact on Compressive Strength of Quasi-Isotropic Laminate," *Proceedings of the American Society of Composites, First Technical Conference*, October 1986, pp. 313-326.
50. Lin, C. C. and King, W. W., "Free Transverse Vibrations of Rectangular Unsymmetrically Laminated Plates," *J. Sound Vibration*, Vol. 36, 1974, pp. 91-103.
51. Liu, D., "Impact-Induced Delamination - A View of Bending Stiffness Mismatching," *Journal of Composite Materials*, Vol. 22, July 1988, pp. 674-692.
52. Liu, D., Lillycrop, L.S., Malvern L.E. and Sun C.T., "The Evaluation of Delamination - An Edge Replication Study," *Experimental Techniques*, Vol. 11, No. 5, May 1987, pp. 20-25.
53. Miller, A.G., Herztberg, P.E., and Rantula, V.W., "Toughness Testing of Composite Materials," *Society of Aerospace Materials and Process Engineers Quarterly*, Vol. 12, No. 2, January, 1981, pp. 36-42.
54. Mindlin, R. D., "Influence of Rotary Inertia and Shear on Flexural Motions of Isotropic, Elastic Plates," *J. of Applied Mechanics*, Vol. 18, 1951, pp. 31-38.
55. Moon, F. C., A Critical Survey of Wave Propagation and Impact in Composite Materials, NASA CR-121226, Lewis Research Center, 1973.
56. Moon, F. C., Theoretical Analysis of Impact in Composite Plates, NASA CR-121110, Lewis Research Center, 1972.
57. Nelson, R. B. and Lorch, D. R., "A Refined Theory for Laminated Orthotropic Plates," *J. Appl. Mech., Trans. ASME*, Vol. 41, pp. 177-183, 1974.
58. Nixon, J.A., Phillips, M.G., Moore, D.R. and Prediger, R.S., "A Study of the Development of Impact Damage in Cross-Ply Carbon Fibre/PEEK Laminates Using Acoustic Emission," *Composite Science and Technology*, Vol. 31, 1988, pp. 1-14.

59. Pagano, N. J., "Stress Fields in Composite Laminates," Int. J. Solids and Structures, Vol. 14, 1978, pp. 385-400.
60. Palazotto, A., Maddux, G.E. and Horban, B., "The Use of Stereo X-Ray and Depty Techniques for Evaluating Instability of Composite Cylindrical Panels with Delaminations," Experimental Mechanics, June, 1989, Presented at the 1987 SEM Spring Conference on Experimental Mechanics, Houston, Texas, June 14-19.
61. Palmer, R. J., Investigation of the Effect of Resin Material on the Impact Damage to graphite/Epoxy Composites, NASA CR 165677, 1981.
62. Perry, J. L., Adams, D. F. and Miller, A. K., Effect of Low Level Impact on Advanced Hybrid Composites, N00019-74-0229, Naval Air Systems Command, 1975.
63. Pister, K. S., "Flexural Vibration of Thin Laminated Plates," J. Acoustical Soc. Am., Vol. 31, No. 2, 1959, pp. 233-234.
64. Preuss, T.E., The Development of a Thickness C-Scan Ultrasonic Technique for the Non-Destructive Inspection of Composite Materials, Technical Memorandum ARL-TM-395, Aircraft Materials Division, Aeronautical Research Laboratories, Melbourne, Australia, 1987.
65. Preuss, T.E., and Clarck, G., "Use of Time-of-Flight C-Scanning for Assessment of Impact Damage in Composites," Composites, Vol. 19, No. 2, March, 1988, pp. 145-148.
66. Ramkumar, R. L., Composite Impact Damage Susceptibility, NADC-79068-60, Naval Air Development Center, 1981.
67. Ramkumar, R. L., "Effect of Low-Velocity Impact Damage on the Fatigue Behavior of graphite/Epoxy Laminates," Long-Term Behavior of Composites, ASTM STP 813, T. K. O'Brien Ed., ASTM, 1983, pp 116-135.
68. Ramkumar, R. L. and Chen, P. C., "Low-Velocity Impact Response of Laminated Plates," AIAA, Vol. 21, No. 10, 1982, pp 1448-1452.
69. Reddy, J. N., "Free Vibration of Antisymmetric, Angle-Ply Laminated Plates Including Transverse Shear Deformation by the Finite Element Method," J. Sound Vibration, Vol. 66, No. 4, pp. 565-576, 1979.
70. Reddy, J. N. and Kuppusamy, T., "Natural Vibrations of Laminated Anisotropic Plates," J. Sound and Vibration, Vol. 94, pp. 63-69, 1984.

71. Reddy, J. N. and Phan, N. D., "Stability and Vibration of Isotropic, Orthotropic and Laminated Plates According to a Higher-Order Shear Deformation Theory," J. Sound Vibration, Vol. 98, No. 2, pp. 157-170, 1985.
72. Reifsnider, K.L., Henneke, E.G. and Stinchcomb, W.W., "The Mechanics of Vibrothermography," Mechanics of Nondestructive Testing, W.W. Stinchcomb, Eds., Plenum Press, N. Y., 1980.
73. Rhodes, M. D., Williams, J. G. and Starnes, Jr., J. H., Effect of Low Velocity Impact Damage on the Compressive Strength of Graphite/Epoxy Hat-Stiffened Panels, NASA TM X-73988, 1976.
74. Sandhu, R. S., Impact Damage of Composite Laminates Preloaded in Tension, AFWAL-TM-85-254-FIBC, 1985.
75. Schulte, K. and Stinchcomb, W.W., "Damage Development Near the Edge of a Composite Specimen During Quasi Static and Fatigue Loading," Composite Technology Review, Vol. 6, 1984, pp. 3-9.
76. Sendekyj, G., Maddux, E., and Porter, E., "Damage Documentation in Composites by Stereo Radiography," ASTM STP 775, 1982, pp. 16-26.
77. Shivakumar, K. N., Elber, W. and Illg, W., "Prediction of Impact Forces and Duration to Low-Velocity Impact on Circular Composite Laminates," Journal of Applied Mechanics, Vol. 52, 1985, pp 674-680.
78. Sierakowski, R. L. and Chaturvedi, S. K., "Impact Loading in Filamentary Structural Composites," Shock and Vibration Digest, Vol. 15, pp 13-33, 1986.
79. Sjoblom, P.O., Hartness, J.T. and Cordell, T.M., "On Low-Velocity Impact Testing of Composite Materials," Journal of Composite Materials, Vol. 22, January 1988, pp. 30-52.
80. Srinivas, S., Roa, C. V. and Roa, A. K., "An Exact Analysis for Vibration of Simply-Supported Homogeneous and Laminated Thick Rectangular Plates," J. Sound Vibration, Vol. 12, No. 2, pp. 187-199, 1970.
81. Stevanovic, M.M., Stecenko, T.B., Kostic, M.C., and Bris'ki-Gudic', "Effect of Impactor Shape on Residual Tensile Strength and Tensile Fatigue Failure of Carbon/Epoxy Laminates," Composite Structures, Proceedings of the 5th International Conference on Composite Structures, Paisley College of Technology, Scotland, July 24-26, 1989, I.H. Marshall, Ed.

82. Stinchcomb, W.W., "Nondestructive Evaluation of Damage Accumulation Processes in Composite Laminates," Composite Science and Technology, Vol. 25, 1986, pp. 103-118.
83. Subramanian, K., and Rose, J.L., "C-Scan Testing for Complex Parts," Advanced Materials and Processes (Metal Progress), Vol. 2, 1987, pp.40-43.
84. Sun, C. T., "An Analytical Method for Evaluation of Impact Damage Energy of Laminated Composites," ASTM STP 617, 1977, pp 427-440.
85. Sun, C. T., "Incremental Deformations in Orthotropic Laminated Plates Under Initial Stress," J. Appl. Mech., Trans. ASME, Vol. 40, pp. 193-200, 1973.
86. Sun, C. T., Achenbach, J. D. and Herrmann, G., "Continuum Theory for a Laminated Medium," J. Appl. Mech., Trans. ASME, Vol. 35, pp. 467-475, 1968.
87. Sun, C. T., Achenbach, J.D. and Herrman, G., "Time Harmonic Waves in Stratified Medium Propagating in the Direction of the Layering," Journal of Applied Mechanics, Transactions ASME, Vol. 35, 1968, pp. 408-411.
88. Sun, C. T. and Chattopadhyay, S., "Dynamic Response of Anisotropic Laminated Plates Under Initial Stress to Impact of a Mass," Journal of Applied Mechanics, Transactions ASME, Vol.42, 1975, pp.693-698.
89. Sun, C.T. and Whitney, J.M., "Theories for the Dynamic Response of Laminated Plates," AIAA J., Vol.11, No.2, 1973, pp. 178-183.
90. Sun, C.T. and Yang, S.H., Contact Law and Impact Response of Laminated Composites, NASA CR 159884, 1980.
92. Teagle, P.R., "The Quality Control and Non-Destructive Evaluation of Composite Aerospace Components," Composites, Vol.14, No.2, April, 1983, pp. 115-128.
93. Thangjitham, S., Libresch, L. and Cedarbaum, G., "Low Velocity Impact Response of Orthotropic Plates using a Higher-Order Theory," AIAA/ASME/ASCE/AHS, 28th Structures, Structural Dynamics and Materials Conference, 1987, pp. 448-457.
94. Wardle, M.W. and Tokarsky, E.W., "Drop Weight Impact Testing of Laminates Reinforced with Kevlar Aramid Fibers, E-Glass, and Graphite," Composite Technology Review, Vol.5, No.1, Spring 1983, pp. 4-10

95. Whitney, J. M. and Pagano, N. J., "Shear Deformation in Heterogeneous Anisotropic Plates," Journal of Applied Mechanics, Vol.37, 1970, pp. 1031-1036.
96. Whitney, J.M. and Sun, C.T., "A Higher Order Theory for Extensional Motion of Laminated Composites," Journal of Sound and Vibration, Vol.30, 1973, pp. 85-97.
97. Williams, J.H., Jr., and Egan, D.M., "Acoustic Emission Spectral Analysis of Fiber Composite Failure Mechanisms," Materials Evaluation, Vol. 37, 1979, pp. 43-47.
98. Williams, J.H., and Lampert, N.R., Ultrasonic Nondestructive Evaluation of Impact Damaged Graphite Fiber Composites, " NASA Contract Report, NASA CR-3293, 1980.
99. Williams, J.H., and Lee, S.S., "Acoustic Emission Monitoring of Fiber Composite Materials and Structures," Journal of Composite Materials, Vol. 12, 1978, pp. 348-370.
100. Winkel, J.D. and Adams, D.F., The Instrumented Drop Weight Impact Testing of Composite Materials, Department Report UWME-DR-301-108-0, University of Wyoming, December, 1983.
101. Wolfe, W. E. and Schoeppner, G. S., LOW VELOCITY IMPACT OF GRAPHITE/EPOXY PLATES, Final Report, USAF-UES Summer Faculty and Graduate Student Research Program, 1987.
102. Wolfe, W. E. and Schoeppner, G. S., DAMAGE IN GRAPHITE/EPOXY PLATES SUBJECTED TO LOW VELOCITY IMPACT, Final Report, USAF-UES Summer Faculty and Graduate Student Research Program, 1988.
103. Wu, H.T. and Springer, G. S., "Impact Damage of Composites," Proceedings of the American Society for Composites, 1st Technical Conference, Dayton, OH., 1986, pp 297-312.
104. Wu, H.Y. and Springer, G.S., "Measurements of Matrix Cracking and Delamination Caused by Impact of Composite Plates," Journal of Composite Materials, Vol. 22, June 1988, pp. 518-532.
105. Wyrick, D.A. and Adams, D.F., "Damage Sustained by a Carbon/Epoxy Composite Material Subjected to Repeated Impact," Composites, Vol. 19, No. 1, January 1988.
106. Wyrick, D.A. and Adams, D.F., "Residual Strength of a Carbon/Epoxy Composite Material Subjected to Repeated Impact," Journal of Composite Materials, Vol. 22, August 1988, pp. 749-764.

107. Yang, P. C., Norris, C. H., and Stavsky, Y., "Elastic Wave Propagation in Heterogeneous Plates," International Journal of Solids and Structures, Vol. 2, 1966, pp 534-547.
108. Ye, L., "Role of Matrix Resin in Delamination Onset and Growth in Composite Laminates," Composite Science and Technology, Vol. 33, 1988, pp. 257-277.

APPENDIX

The following Tables contain a summary of the experimental results obtained from the impact test performed during this investigation. Specimens were panels of graphite/epoxy composites fabricated from prepreg tapes. The panels were manufactured in the Structural Composites Laboratory in The Civil Engineering Department at The Ohio State University and in the Composites Facility of the Flight Dynamics Laboratory at Wright-Patterson Air Force Base.

0/90	PLATE #	Test	# plies	ImpactE(ft-lb)	Vel (ft/sec)	Rebnd ht(in)	RebndE(ft-lb)	Net E(ft-lb)	ImpE/#plies	RebndE/#plies	NetE/#plies	Damage
10	PL10-3		16	1.9	3.61	2	1.57	0.34	0.12	0.10	0.02	1
10	PL10-37		16	2.43	4.08	2.6	2.03	0.40	0.15	0.13	0.02	1
10	PL10-45		16	2.91	4.46	3.6	2.82	0.09	0.18	0.18	0.01	2
10	PL10-60		16	3.82	5.12	4.75	3.72	0.10	0.24	0.23	0.01	2
10	PL10-16		16	9.72	8.16	6.5	5.09	4.63	0.61	0.32	0.29	4
10	PL10-15		16	9.39	8.02	3.5	2.74	6.65	0.59	0.17	0.42	5.5
10	PL10-12		16	7.44	7.14	5	3.91	3.53	0.47	0.24	0.22	5
12	PL12-16		32	9.49	8.07	10.5	8.22	1.27	0.30	0.26	0.04	2.7
12	PL12-25		32	14.82	10.08	9	7.01	7.78	0.46	0.22	0.24	6
12	PL12-20		32	12.82	9.37	8	6.26	6.56	0.40	0.20	0.21	6
1	PL01-08		8	4.88	5.78	3.25	2.54	2.34	0.61	0.32	0.29	5.5
1	PL01-75		8	4.54	5.58	3.5	2.74	1.80	0.57	0.34	0.23	4.5
0/0/90/90												
51	P51-06		8	4.56	5.62	4	3.13	1.43	0.57	0.39	0.18	2
51	P51-08		8	6.12	6.51	5	3.91	2.21	0.77	0.49	0.28	2.5
51	P51-10		8	7.48	7.19	6	4.70	2.79	0.94	0.59	0.35	3
60	P60-10		16	7.43	7.17	7	5.48	1.95	0.46	0.34	0.12	2.8
60	P60-15		16	11.11	8.77	8.5	6.65	4.46	0.69	0.42	0.28	4.8
60	P60-16		16	11.87	9.06	10.5	8.22	3.65	0.74	0.51	0.23	3
60	P60-19		16	13.86	9.79	9	7.04	6.82	0.87	0.44	0.43	6
62	P62-15		32	10.21	8.41	9.5	7.43	2.78	0.32	0.23	0.09	2
62	P62-19		32	13.85	9.79	13	10.17	3.68	0.43	0.32	0.11	2.5
62	P62-25		32	18.27	11.24	15	11.74	6.53	0.57	0.37	0.20	3
62	P62-32		32	23.13	12.65	13	10.17	12.96	0.72	0.32	0.40	6.2

45/45	PLATE #	Test	# piles	ImpctE(ft-lb)	Vel (ft/sec)	Rebnd ht(in)	RebndE(ft-lb)	Net E(ft-lb)	ImpE/#piles	RebndE/#piles	NetE/#piles	Damage
11	PL11-5		16	3.22	4.7	3.6	2.82	0.40	0.20	0.18	0.03	2
11	PL11-65		16	4.17	5.35	5.1	3.99	0.18	0.26	0.25	0.01	2
11	PL11-8		16	5.11	5.92	4.7	3.68	1.43	0.32	0.23	0.09	2.2
11	PL11-12		16	7.29	7.07	5.5	4.30	2.99	0.46	0.27	0.19	5
11	PL11-16		16	9.71	8.16	3	2.35	7.36	0.61	0.15	0.46	6
13	PL13-24		32	13.96	9.78	9	7.04	6.92	0.44	0.22	0.22	4
13	PL13-29		32	16.86	10.75	12	9.39	7.47	0.53	0.29	0.23	5
13	PL13-34		32	20.11	11.74	7.5	5.87	14.24	0.63	0.18	0.45	6.5
2	PL02-06		8	3.72	5.05	3	2.35	1.37	0.47	0.29	0.17	1.8
2	PL02-08		8	5.24	5.99	3	2.35	2.89	0.66	0.29	0.36	3.8
16	PL16-13		16	7.59	7.21	5.25	4.11	3.48	0.47	0.26	0.22	5
16	PL16-11		16	5.99	6.41	5.25	4.11	1.88	0.37	0.26	0.12	4.7
31	PL31-14		20	8.28	7.53	5.75	4.50	3.78	0.41	0.22	0.19	5.2
22	PL22-20		32	12.34	9.2	13	10.17	2.17	0.39	0.32	0.07	2.2
22	PL22-26		32	12.33	9.19	9	7.04	5.29	0.39	0.22	0.17	3.8
45/45/45/45												
52	P52-08		8	6.06	6.48	4.5	3.52	2.54	0.76	0.44	0.32	4
52	P52-09		8	6.96	6.94	5.5	4.30	2.66	0.87	0.54	0.33	3
52	PL52-11		8	7.66	7.28	4	3.13	4.53	0.96	0.39	0.57	6
52	P52-95		8	7.23	7.07	5	3.91	3.32	0.90	0.49	0.41	4
66	P66-08		16	6.13	6.51	6	4.70	1.43	0.38	0.29	0.09	2
66	P66-11		16	8.29	7.57	7	5.48	2.81	0.52	0.34	0.18	3.8
66	P66-12		16	8.9	7.85	7.5	5.87	3.03	0.56	0.37	0.19	4
66	P66-14		16	10.49	8.52	7.5	5.87	4.62	0.66	0.37	0.29	5
81	P81-12		24	8.97	7.88	9	7.04	1.93	0.37	0.29	0.08	2
81	P81-14		24	10.44	8.5	10.5	8.22	2.22	0.44	0.34	0.09	2.5
81	P81-17		24	12.52	9.31	9	7.04	5.48	0.52	0.29	0.23	4
81	P81-19		24	13.86	9.79	9	7.04	6.82	0.58	0.29	0.28	6.2
63	P63-20		32	14.62	10.06	7.5	5.87	8.75	0.46	0.18	0.27	6
63	P63-18		32	13.12	9.53	7	5.48	7.64	0.41	0.17	0.24	6
63	P63-16		32	11.49	8.92	10	7.83	3.67	0.36	0.24	0.11	2.5
63	P63-23		32	16.69	10.75	9	7.04	9.65	0.52	0.22	0.30	6.2

	A	B	C	D	E	F	G	H	I	J	K	L
	Specimen	#plies	Impct E (ft-lb)	Vel (ft/s)	Rebnd Ht (in)	Damage (in ²)	Max Load	Rebnd E (ft-lb)	Impct E (#plies)	Rebnd E (#plies)	Net E (#plies)	Max Ld/# plies
1	45-3S-1-A	12.00	3.02	4.57	2.75	0.00	443.30	2.15	0.25	0.18	0.07	36.94
2	45-3S-2-A	12.00	3.41	4.86	3.50	0.00	481.20	2.74	0.28	0.23	0.06	40.10
3	45-3S-3-A	12.00	3.82	5.14	3.50	0.00	512.40	2.74	0.32	0.23	0.09	42.70
4	45-3S-4-A	12.00	4.21	5.40	4.00	0.00	550.70	3.13	0.35	0.26	0.09	45.89
5	45-3S-5-A	12.00	4.60	5.64	4.50	0.00	581.80	3.52	0.38	0.29	0.09	48.48
6	45-3S-6-A	12.00	4.92	5.83	5.00	0.00	602.90	3.91	0.41	0.33	0.08	50.24
7	45-3S-7-A	12.00	4.91	5.83	4.50	0.05	606.60	3.52	0.41	0.29	0.12	50.55
8	45-3S-8-A	12.00	4.78	6.02	4.75	0.45	596.90	3.72	0.40	0.31	0.09	49.74
9	45-3S-1-C	12.00	5.68	6.27	5.50	0.40	653.30	4.30	0.47	0.36	0.11	54.44
10	45-3S-2-C	12.00	5.99	6.44	5.50	0.42	628.60	4.30	0.50	0.36	0.14	52.38
11	45-3S-3-C	12.00	6.39	6.65	6.00	0.46	666.60	4.70	0.53	0.39	0.14	55.55
12	45-3S-4-C	12.00	6.84	6.93	6.50	0.45	704.60	5.09	0.57	0.42	0.15	58.72
13	45-3S-5-C	12.00	7.11	7.02	6.50	0.59	725.60	5.09	0.59	0.42	0.17	60.47
14	45-3S-6-C	12.00	7.38	7.15	7.00	0.59	753.30	5.48	0.62	0.46	0.16	62.78
15	45-3S-7-C	12.00	7.71	7.31	7.00	0.62	777.50	5.48	0.64	0.46	0.19	64.79
16	45-3S-8-C	12.00	8.48	7.66	7.50	0.65	827.70	5.87	0.71	0.49	0.22	68.98
17	90-3S-1-A	12.00	4.34	5.45	4.75	0.83	695.30	3.72	0.36	0.31	0.05	57.94
18	90-3S-2-A	12.00	2.28	3.97	2.00	0.00	360.10	1.57	0.19	0.13	0.06	30.01
19	90-3S-3-A	12.00	3.40	5.13	4.25	0.52	604.30	3.33	0.28	0.28	0.01	50.36
20	90-3S-4-A	12.00	2.67	4.30	2.50	0.00	408.60	1.96	0.22	0.16	0.06	34.05
21	90-3S-5-A	12.00	3.06	4.60	3.00	0.00	453.40	2.35	0.26	0.20	0.06	37.78
22	90-3S-6-A	12.00	3.47	4.90	3.50	0.00	488.10	2.74	0.29	0.23	0.06	40.68
23	90-3S-7-A	12.00	3.85	5.16	3.25	0.04	519.30	2.54	0.32	0.21	0.11	43.28
24	90-3S-8-A	12.00	4.22	5.40	4.25	0.00	567.80	3.33	0.35	0.28	0.07	47.32
25	90-3S-1-C	12.00	3.38	5.06	4.00	0.06	563.50	3.13	0.28	0.26	0.02	46.96
26	90-3S-2-C	12.00	4.22	5.41	4.10	0.20	547.00	3.21	0.35	0.27	0.08	45.58
27	90-3S-3-C	12.00	3.54	4.92	4.25	0.00	578.50	3.33	0.30	0.28	0.02	48.21
28	90-3S-4-C	12.00	4.60	5.64	4.50	0.18	605.90	3.52	0.38	0.29	0.09	50.49
29	90-3S-5-C	12.00	4.58	5.63	4.00	0.41	588.50	3.13	0.38	0.26	0.12	49.04
30	90-3S-6-C	12.00	4.84	5.79	4.50	0.42	612.80	3.52	0.40	0.29	0.11	51.07
31	90-3S-7-C	12.00	5.32	6.07	5.00	0.43	640.20	3.91	0.44	0.33	0.12	53.35
32	90-3S-8-C	12.00	5.63	6.24	5.00	0.60	640.50	3.91	0.47	0.33	0.14	53.38
33	90-3S-1-B	12.00	4.36	5.46	4.75	0.65	658.30	3.72	0.36	0.31	0.05	54.86
34	90-3S-2-B	12.00	6.04	6.46	5.50	0.40	696.10	4.30	0.50	0.36	0.14	58.01
35	90-3S-3-B	12.00	6.47	6.69	5.50	0.47	709.70	4.30	0.54	0.36	0.18	59.14
36	90-3S-4-B	12.00	6.85	6.88	6.00	0.43	730.80	4.70	0.57	0.39	0.18	60.90
37	90-3S-5-B	12.00	7.12	7.02	6.50	0.60	779.30	5.09	0.59	0.42	0.17	64.94
38	90-3S-6-B	12.00	7.04	6.98	5.50	0.54	765.20	4.30	0.59	0.36	0.23	63.77
39	90-3S-7-B	12.00	8.13	7.50	7.00	0.64	852.00	5.48	0.68	0.46	0.22	71.00
40	90-3S-8-B	12.00	8.13	7.50	7.00	0.64	852.00	5.48	0.68	0.46	0.22	71.00
41	90-6S-1-A	24.00	10.32	8.45	11.00	0.00	1146.30	8.61	0.43	0.36	0.07	47.76
42	90-6S-2-A	24.00	10.67	8.59	11.00	0.00	1191.20	8.61	0.44	0.36	0.09	49.63
43	90-6S-3-A	24.00	11.10	8.76	11.00	0.01	1218.20	8.61	0.46	0.36	0.10	50.76
44	90-6S-4-A	24.00	11.38	8.91	9.00	1.59	1226.20	7.04	0.47	0.29	0.18	51.09
45	90-6S-5-A	24.00	11.79	9.03	11.50	0.07	1265.20	9.00	0.49	0.37	0.12	52.72
46	90-6S-6-A	24.00	12.15	9.17	9.50	2.50	1235.50	7.43	0.51	0.31	0.20	51.48
47	90-6S-7-A	24.00	12.55	9.32	9.50	2.45	1276.10	7.43	0.52	0.31	0.21	53.17
48	90-6S-8-A	24.00	12.74	9.39	10.00	2.20	1309.60	7.83	0.53	0.33	0.20	54.57
49	90-6S-1-B	24.00	13.18	9.55	10.50	2.16	1257.30	8.22	0.55	0.34	0.21	52.39
50	90-6S-2-B	24.00	13.48	9.66	10.50	1.81	1434.00	8.22	0.56	0.34	0.22	59.75

	A	B	C	D	E	F	G	H	I	J	K	L
	Specimen	#plies	Impact E (ft-lb)	Vel (ft/s)	Rebnd Ht (in)	Damage (in ²)	Max Load	Rebnd E (ft-lb)	Impd E (ft-lb)	Rebnd E (ft-lb)	Net E (ft-lb)	Max Ld/# plies
51	90-6S-3-B	24.00	14.48	10.01	11.00	1.98	1361.40	8.61	0.60	0.36	0.24	56.73
52	90-6S-4-B	24.00	9.01	7.89	9.50	0.00	1118.60	7.43	0.38	0.31	0.07	46.61
53	90-6S-5-B	24.00	9.36	8.05	9.50	0.00	1103.20	7.43	0.39	0.31	0.08	45.97
54	90-6S-6-B	24.00	9.65	8.17	9.50	0.00	1136.80	7.43	0.40	0.31	0.09	47.37
55	90-6S-7-B	24.00	10.08	8.35	9.00	1.80	1123.00	7.04	0.42	0.29	0.13	46.79
56	90-6S-8-B	24.00	10.32	8.45	10.50	0.00	1199.00	8.22	0.43	0.34	0.09	49.96
57	45-6S-1-A	24.00	8.23	7.55	9.00	0.00	1081.50	7.04	0.34	0.29	0.05	45.06
58	45-6S-2-A	24.00	8.60	7.72	9.50	0.00	1075.00	7.43	0.36	0.31	0.05	44.79
59	45-6S-3-A	24.00	9.05	7.91	9.50	0.00	1123.40	7.43	0.38	0.31	0.07	46.81
60	45-6S-4-A	24.00	9.29	7.98	7.75	3.25	1319.80	6.06	0.39	0.25	0.13	54.99
61	45-6S-5-A	24.00	9.41	8.07	10.00	0.00	1161.40	7.83	0.39	0.33	0.07	48.39
62	45-6S-6-A	24.00	9.82	8.24	10.50	0.00	1185.30	8.22	0.41	0.34	0.07	49.39
63	45-6S-7-A	24.00	10.06	8.34	8.50	1.77	1130.00	6.65	0.42	0.28	0.14	47.08
64	45-6S-8-A	24.00	10.40	8.48	9.50	3.18	1203.30	7.43	0.43	0.31	0.12	50.14
65	45-6S-1-B	24.00	10.44	8.50	11.00	0.00	1243.90	8.61	0.44	0.36	0.08	51.83
66	45-6S-2-B	24.00	10.81	8.65	11.00	0.00	1247.90	8.61	0.45	0.36	0.09	52.00
67	45-6S-3-B	24.00	11.03	8.74	9.00	3.00	1285.90	7.04	0.46	0.29	0.17	53.58
68	45-6S-4-B	24.00	11.34	8.86	8.50	2.90	1223.70	6.65	0.47	0.28	0.20	50.99
69	45-6S-5-B	24.00	9.23	7.95	8.25	3.78	1359.70	6.46	0.38	0.27	0.12	56.65
70	45-6S-6-B	24.00	9.26	7.97	7.75	4.25	1496.50	6.06	0.39	0.25	0.13	62.35
71	90-12S-1-A	48.00	10.86	8.67	11.50	0.00	2130.10	9.00	0.23	0.19	0.04	44.38
72	90-12S-2-A	48.00	11.72	9.00	10.00	0.00	2247.70	7.83	0.24	0.16	0.08	46.83
73	90-12S-3-A	48.00	12.29	9.22	10.50	0.00	2365.00	8.22	0.26	0.17	0.08	47.19
74	90-12S-4-A	48.00	13.08	9.52	11.00	0.00	2354.00	8.61	0.27	0.18	0.09	49.04
75	90-12S-5-A	48.00	13.94	9.82	12.00	0.00	2538.20	9.39	0.29	0.20	0.09	52.88
76	90-12S-6-A	48.00	14.40	9.98	10.50	4.16	2424.10	8.22	0.30	0.17	0.13	50.50
77	90-12S-7-A	48.00	15.29	10.28	13.00	0.00	2379.70	10.17	0.32	0.21	0.11	53.74
78	90-12S-8-A	48.00	15.20	10.26	13.00	0.00	2520.90	10.17	0.32	0.21	0.10	52.52
79	90-12S-9-A	48.00	15.62	10.40	13.00	0.00	2690.60	10.17	0.33	0.21	0.11	56.05
80	90-12S-1-B	48.00	16.15	10.57	13.50	0.00	2714.80	10.56	0.34	0.22	0.12	56.56
81	90-12S-2-B	48.00	16.63	10.73	14.00	0.00	2694.10	10.96	0.35	0.23	0.12	56.13
82	90-12S-3-B	48.00	17.07	10.87	14.50	0.00	2884.00	11.35	0.36	0.24	0.12	60.08
83	90-12S-4-B	48.00	17.36	10.96	15.50	0.00	2662.70	12.13	0.36	0.25	0.11	55.47
84	90-12S-5-B	48.00	17.67	11.06	15.50	0.00	2724.90	12.13	0.37	0.25	0.12	56.77
85	90-12S-6-B	48.00	18.08	11.18	15.50	0.00	2773.30	12.13	0.38	0.25	0.12	57.78
86	90-12S-7-B	48.00	18.54	11.33	15.50	0.00	2828.70	12.13	0.39	0.25	0.13	58.93
87	90-12S-8-B	48.00	18.80	11.41	15.50	0.00	2872.80	12.13	0.39	0.25	0.14	61.93
88	90-12S-1-C	48.00	19.19	11.52	16.50	0.00	3076.80	12.91	0.40	0.27	0.13	64.10
89	90-12S-2-C	48.00	19.48	11.61	17.00	0.00	2987.70	13.30	0.41	0.28	0.13	62.24
90	90-12S-3-C	48.00	19.82	11.71	17.00	0.00	3108.80	13.30	0.41	0.28	0.14	64.77
91	90-12S-4-C	48.00	20.07	11.79	17.50	0.00	3048.70	13.69	0.42	0.29	0.13	63.51
92	45-12S-5-C	48.00	11.09	8.76	8.50	0.00	2504.20	6.65	0.23	0.14	0.09	52.17
93	45-12S-1-A	48.00	11.67	8.99	8.00	0.00	2628.50	6.26	0.24	0.13	0.11	54.76
94	45-12S-2-A	48.00	12.60	9.34	9.50	0.00	2718.30	7.43	0.26	0.15	0.11	56.63
95	45-12S-3-A	48.00	13.20	9.56	10.50	0.00	2680.70	8.22	0.28	0.17	0.10	56.06
96	45-12S-4-A	48.00	13.82	9.78	10.50	0.00	2846.10	8.22	0.29	0.17	0.12	59.29
97	45-12S-5-A	48.00	14.53	10.03	11.00	0.00	2901.40	8.61	0.30	0.18	0.12	60.45
98	45-12S-6-A	48.00	15.27	10.28	12.00	0.00	3033.00	9.39	0.32	0.20	0.12	63.19
99	45-12S-7-A	48.00	15.60	10.39	12.00	0.00	3133.10	9.39	0.33	0.20	0.13	65.27
100	45-12S-8-A	48.00										

	A	B	C	D	E	F	G	H	I	J	K	L
	Specimen	#plies	ImpctE (ft-lb)	Vel. (ft/s)	Rebnd Ht(in)	Damage (in ²)	Max Load	Rebnd E(11-lb)	Impct E/#plies	Rebnd E/#plies	Net E/#plies	Max Ld/# plies
101	45-12S-1-B	48.00	16.06	10.54	12.50	0.00	3064.00	9.78	0.33	0.20	0.13	63.83
102	45-12S-2-B	48.00	16.20	10.59	12.50	0.00	3040.70	9.78	0.34	0.20	0.13	63.35
103	45-12S-3-B	48.00	16.58	10.71	13.00	0.00	3140.00	10.17	0.35	0.21	0.13	65.42
104	45-12S-4-B	48.00	16.76	10.77	13.00	0.00	3181.20	10.17	0.35	0.21	0.14	66.28
105	45-12S-5-B	48.00	17.43	10.98	8.50	5.74	3060.30	6.65	0.36	0.14	0.22	63.76
106	45-12S-6-B	48.00	17.73	11.07	9.00	3.95	3346.90	7.04	0.37	0.15	0.22	69.73
107	45-12S-7-B	48.00	17.94	11.14	14.50	0.00	3554.20	11.35	0.37	0.24	0.14	74.05
108	45-12S-8-B	48.00	18.28	11.25	15.00	0.00	3464.20	11.74	0.39	0.24	0.14	72.17
109	45-12S-9-B	48.00	18.58	11.34	14.50	2.52	3367.70	11.35	0.39	0.24	0.15	70.16
110	45-12S-1-C	48.00	18.70	11.38	15.00	0.07	3633.60	11.74	0.39	0.24	0.15	75.70
111	45-12S-2-C	48.00	19.00	11.47	8.50	7.14	3286.00	6.65	0.40	0.14	0.26	68.46
112	45-12S-3-C	48.00	19.41	11.59	13.00	6.22	3440.20	10.17	0.40	0.21	0.19	71.67
113	45-12S-5-C	48.00	19.77	11.70	14.00	4.30	3523.10	10.96	0.41	0.23	0.18	73.40
114	45-12S-6-C	48.00	20.51	11.91	7.50	4.45	3533.80	5.87	0.43	0.12	0.31	73.62
115	45-12S-7-C	48.00	21.76	12.27	14.00	10.61	3157.00	10.96	0.45	0.23	0.23	65.77
116	45-12S-8-C	48.00	1.95	3.65	2.25	0.00	337.80	1.76	0.16	0.15	0.02	28.15
117	J90-3S-1-A	12.00	3.04	4.80	3.50	0.17	549.60	2.74	0.25	0.23	0.03	45.80
118	J90-3S-2-B	12.00	3.86	5.15	3.75	0.24	587.80	2.93	0.32	0.24	0.08	48.98
119	J90-3S-1-B	12.00	5.48	6.13	2.00	0.85	623.70	1.57	0.46	0.13	0.33	51.98
120	J45-3S-1-A	12.00	1.95	3.65	2.25	0.00	372.60	1.76	0.16	0.15	0.02	31.05
121	J45-3S-1-B	12.00	3.39	5.06	4.00	0.00	558.70	3.13	0.28	0.26	0.02	46.56
122	J45-3S-2-A	12.00	4.35	5.46	4.00	0.29	580.20	3.13	0.36	0.26	0.10	48.35
123	J45-3S-2-B	12.00	6.23	6.53	4.75	0.46	657.20	3.72	0.52	0.31	0.21	54.77
124	J90-6S-1-B	24.00	5.44	6.11	6.00	0.00	1035.00	4.70	0.23	0.20	0.03	43.13
125	J90-6S-2-A	24.00	6.90	6.88	8.25	0.00	1183.50	6.46	0.29	0.27	0.02	49.31
126	J90-6S-2-B	24.00	8.75	7.74	10.00	0.00	1371.50	7.83	0.36	0.35	0.04	57.15
127	J45-6S-1-A	24.00	3.18	4.67	3.50	0.00	771.90	2.74	0.13	0.11	0.02	32.16
128	J45-6S-1-B	24.00	10.52	8.49	8.75	1.74	1399.30	6.85	0.44	0.29	0.15	58.30
129	J90-12S-1-A	48.00	4.99	5.85	5.00	0.00	1899.40	3.91	0.10	0.08	0.02	39.36
130	J90-12S-1-B	48.00	10.79	8.60	9.50	0.00	2795.60	7.43	0.22	0.15	0.07	58.24
131	J90-12S-2-A	48.00	14.43	9.94	6.50	0.00	3895.90	5.09	0.30	0.11	0.19	80.96
132	J90-12S-2-B	48.00	21.59	12.14	9.75	3.15	3896.00	7.63	0.45	0.16	0.29	81.17
133	J45-12S-1-A	48.00	5.02	5.86	4.50	0.00	2132.10	3.52	0.10	0.07	0.03	44.42
134	J45-12S-2-B	48.00	18.30	11.20	8.75	3.30	3698.80	6.85	0.38	0.14	0.24	77.02

AIRCRAFT AVAILABILITY MODEL:
FEASIBILITY STUDY FOR POM FORECASTING
January, 1989

Submitted by: Dr. Ming S. Hung
Department of Administrative Sciences
Kent State University

Contract No. F49620-95-C-0013/SB5851-0360
Purchase Order No. S-760-6MG-105

PREFACE

Program Objective Memorandum (POM) forecasting is done by every command in the Air Force. It is difficult because of long forecast horizons and voluminous, complex input. The Air Force Logistics Command (AFLC) is now facing the task of determining a reliable approach for making forecasts.

The current study is part of an attempt to determine the feasibility of using a model such as the Aircraft Availability Model (AAM) in conjunction with economic forecasts to improve long range forecasting ability. The AAM is run with various combinations of model inputs to determine the model sensitivity with respect to future year forecasted data.

SUMMARY OF OUR EFFORTS

We began receiving tapes containing data sets and programs from AFLC/XRS late in 1986. Unfortunately, we had a great deal of trouble reading the tapes. Data tapes were returned and new ones supplied by AFLC/XRS. The initial FORTRAN programs received contained numerous non-IBM-standard conventions. These problems required line-by-line editing, aided by program listings from AFLC/XRS. We wrote new JCL programs in REXX to conform as closely as possible to the JCL supplied by the XRS.

Late in 1987 AFLC/XRS sent a new set of FORTRAN programs which followed IBM conventions. We then began using this set of programs instead of the older versions. The JCL was modified to run these new programs. We had received a test data base and a sample run of the Aircraft Availability Model. We were able to successfully run the model and our output was close to that of the XRS sample run. We continued to have problems reading some of the D041 data tapes.

During 1988 we began running the Aircraft Availability Model with the D041 data bases. Since the programs and data sets were quite large, we had some problems in obtaining sufficient resources on Kent State's IBM 3081-D computer. We also had problems with our sorting software because of the size of the intermediate output files that had to be

sorted between levels. The Kent State computer center then installed a newer version of the sorting software and we were able to successfully run the programs with most of the D041 data bases. In addition, we had to write programs specifically to sort the input level of indenture and buypoint files in accordance with IBM (vs. Honeywell) precedence rules.

In Spring of 1988 the AAM FORTRAN programs were changed to a double precision version, aided by sample listings supplied by AFLC/XRS. Although the test data base run did not exactly match the results supplied by AFLC/XRS, it was much closer. Using these programs we successfully ran the model with the D041 September 1984 and September 1985 data sets (Buypoint, Termpoint, and POM). We were never able to get the model to work with the 1986 data (we always got permanent I/O errors when trying to read the data files.)

During the summer and fall of 1988 several sets of experimental runs were made to determine the sensitivity of the input data. The results of these runs are explained in a later section.

OVERVIEW OF MODEL

The following overview is primarily from the Aircraft Availability User's Manual [2]. The Aircraft Availability model computes the optimal mix of reparable parts to meet prestatated aircraft availability objectives. The mix is optimal in the sense that the model minimizes the amount of money spent on reparable parts while ensuring that aircraft availability goals are met. Availability goals are set by mission or model designations (MD's). The MD's concentrated on in this project are the C5, C135, F4, and F15. The definition of availability considers only the impact of the availability of reparable parts for which demands are forecasted. Therefore, the availability rate used is the percentage of aircraft with a complete set of reparable parts. The definition of availability does not consider scheduled or unscheduled on-aircraft maintenance, shortages of consumables, or shortages of NSQ/insurance reparable parts. Also, the model does not consider maintenance actions which consolidate reparable item shortages on the aircraft (cannibalization).

The reparable part requirement computed by the model is a worldwide requirement. It explicitly models a multiple base, one depot, two-echelon system. It also explicitly models reparable part hierarchical (component/subcomponent)

relationships. In the present study, this hierarchical relationship consists of five different levels (known as levels of indenture). The five different levels include one level of line replaceable units (LRU's) and four different levels of shop replaceable units (SRU's).

The basic Aircraft Availability Model is made up of three parts: a preprocessor module, a procurement module, and an assessment module. The preprocessor module is used primarily to combine input data into the files that are read by the other two modules. The procurement module consists of the main procurement program and various other programs to produce a number of files and reports on availability, investment, etc. The assessment module uses the stock level files produced by the procurement module to determine the actual availability achieved by these stock levels. Since there are common items, the target availabilities of the procurement module tend to understate the actual availability achieved. The assessment model run estimates actual availabilities.

INPUT DATA

The data used in the model runs was provided by AFLC/XRS. Sets of D041 data tapes were provided for three comps: September of 1984, 1985, and 1986. For each of those three years, three sets of files were provided the buypoint, termoint, and POM files. The buypoint files represent forecasts for approximately 18 months after the asset cutoff date. Therefore, for the September 1984 comp the buypoint files are forecasts for March 1986. The termoint files represent forecasts approximately one year beyond the buypoint. Thus, the September 1984 termoint files are for March 1987. Finally, the POM files represent forecasts approximately one year beyond the termoint. Therefore, the September 1984 POM forecasts are for March 1988. Following these definitions, the buypoint, termoint, and POM forecasted data for the September 1985 comp are for (approximately) March of 1987, 1988, and 1989, respectively. For the September 1986 comp, they represent forecasts for March of 1988, 1989, and 1990.

The model was successfully run with the September 1984 and September 1985 data tapes (buypoint, termoint, and POM). Unfortunately, we could not run the model with the September 1986 data tapes.

Each data set consists of nine input files. They are briefly described below.

1.) Flying Hour Program File. This file provides the flying hours and number of aircraft per model designation series (MDS). It also tells how the MDS's are grouped within MD's. The file consists of four elements: the model designation (MD), the model designation series (MDS), the flying hours for the MDS, and the number of aircraft in the MDS.

2.) Amdahl Buypoint File. This file contains the asset and pipeline information for each stock number. It is created from the D041 Buypoint tape from the AMDAHL computer. For each stock number it contains information on price, number of users, available non-installed assets, daily demand rate, leadtime, and other pertinent information.

3 - 7.) Levels of Indenture Application Files. These files describe the component/sub-component relationships. The Level 1 file consists of header records and MDS records. Levels 2 through 5 have header and MDS records, as well as records indicating the stock number of the next higher assembly in the indenture system. The header records provide information on the stock number, the number of MDS applications, and the number of next higher assembly applications. There is one MDS record for each application

indicated in the header record. MDS records contain the quantity per application to the MDS and the future application percentage to the MDS. Finally, the next higher assembly records provide data on the quantity per application and future application percentage to the next higher assembly, along with flying hours and the total installed in the next higher assembly.

8.) MD Goal File. This file contains availability and fill rate goals for each MD. A default fill rate goal of .92 is set for MD's with no goal provided.

9.) Program Options File. This file includes factors used in initializing stock by MD. These factors are then multiplied by the pipeline data to determine the minimum stock levels for each item.

Another input file that may be used when running the AAM is the SMC (system management code) grouping file. This file is used to group the SMC's so that items with different SMC's can be combined into a group when computing stock levels required to reach fill rate goals. These files were not provided on the D041 tapes. A null file was used when running the model since, according to correspondence from the XRS, currently no grouping occurs.

OUTPUT REPORTS

A number of reports are produced by the model. The two basic ones are the One Percent Tables and the Investment Report. The One Percent Tables are produced for each MD. The tables show what it would cost to achieve varying levels of availability, including the first increment that exceeds the specified goal. The Investment Report estimates the dollars spent on each MD. These values are greater than those in the One Percent Tables, since simplifying assumptions are made in constructing the One Percent Tables. Other reports provide information on initialization costs, prorated cost to MD's, actual availabilities, expected back orders, and various other information. The model also prints out information from several of the input files, including data from the Flying Hour Program File and the Options File.

PRIOR WORK

A somewhat related study was undertaken by the Logistics Management Institute (LMI) in late 1984 [1]. In their study the LMI analyzed and documented the sensitivity of gross requirements for reparable spares for the F-16 weapon system. The LMI project involved a simulated life-cycle approach using D041 data bases from September 1983 and 1984. Data was extracted for the components that were applicable to the F-16A and F-16B weapon systems. Using this data the LMI used the Aircraft Availability Model to estimate the data base "churn" for the F-16 over several years. Churn is defined as those dynamic items in the D041 data bases that change over time. It includes changes in demand rates, condemnation rates, resupply times, costs, and the composition of items used in the weapon system.

The LMI study used the 1983 data base to estimate the costs in fiscal years 1984 and 1985 of achieving an 80-percent availability rate. In addition, the 1984 data base was used to compute the 1985 requirement. The churn was estimated as the difference between the two 1985 estimates. The study was replicated using 1982 - 1983 data bases. The LMI found that the data base churn was mainly the result of two factors: (1) significant changes in actual stock numbers applicable to the F-16 from data base to data base and (2)

significant changes in individual component factors (demand rates, resupply times, etc.). The LMI further analyzed condemnation and additive requirement costs and found considerable variation from one data base to another. They concluded that modification programs, reliability catastrophes resulting in 100-percent replacement of some items, and dramatic changes in pipeline factors represented a significant part of the Peacetime Operating Stock (POS) requirement for reparable spares.

RESULTS

Tables 1 through 4 summarize the output from our runs of the Aircraft Availability Model with the three sets of data each for 1984 and 1985. Table 1 summarizes significant output from the preprocessor reports. For the four MD's examined, in both the 1984 and 1985 comps the C5 and F15 are expected to increase in flying hours and total aircraft, while the C135 and F4 are expected to decrease. Note that the SEP84T forecasts represent approximately the same time as the SEP85B forecasts (March of 1987). Also, SEP84P is analogous to SEP85T (forecasts for March of 1988). Table 1 shows that in every case flying hours and total aircraft estimates were decreased from 1984 to 1985. In the case of the F4 for example, the flying hour estimate in SEP84T is 817. For the same time period using the 1985 comp projected flying hours are decreased to 573 (in SEP85B), representing a drop in expected flying hours of almost 30 percent.

It would perhaps be of some value to analyze the forecasted flying hours and total aircraft for each MD over a longer time period, as well as comparing the forecasts to the actual numbers for those times. That may aid in determining the amount of variability in these forecasts from year to year and the possible effects on model results from this variability. It would be interesting to run the AAM

model using the actual flying hours for the years in question and compare the results to the results with forecasted data.

Table 2 shows that the total initialization cost for insurance items remained the same for the three forecasted periods within the comp. However, the amount was reduced dramatically between the 1984 and 1985 comps, largely due to differences in the buypoint files. Total initialization costs to prevent negative assets increased significantly both within and between comps. Total initialization costs for negotiated assets increased within the comp (in most cases), and these costs increased dramatically between the 1984 and 1985 comps. Total initialization costs to buy to the pipeline increased dramatically during the 1984 comp, but they increased much less dramatically in the 1985 comp.

Table 3 shows that total costs (taken from the investment reports) increased steadily within comps, and the 1985 costs were much higher than those from the 1984 comp.

Table 4 provides specific initialization costs and dollars invested broken down by the four MD s: C5, C135, F4, and F15. For the C5 MD initialization costs and dollars invested increased within comps, but decreased from one comp to the next for the same forecasted time periods. In the case of the C135, costs increased both within and between comps. The F4 and C5 were similar to the C5, in that costs increased within comps but decreased between. The fact that, in general, total dollars spent for each MD decreased between

comps is consistent with the fact that flying hours and total aircraft also decreased between comps in Table 1.

Several sets of experimental runs were made to try to ascertain the effects of changes in the input data. Three basic types of experiments were done:

- 1.) The Goals files were changed for the four MD's of interest, with goals increased and decreased by 5 percent for these MD's, to determine the effect on the model.

- 2.) The model was run using different Buypoint files, to determine the effect of updated asset and pipeline information on the overall results.

- 3.) The Program Options file, containing factors used in initializing stock by MD, was changed.

Some significant differences in results were noted from the first two sets of experiments, but the changes in factors in the Program Options files had no effect by themselves.

The changes in the Goals files were made simultaneously for the four MD series C5, C135, F4, and F15. Goals were lowered by .05 and then raised by .05 for both SEP84B and SEP85B. These two data sets were chosen since they represent the budget year forecast, which is the shortest time into the future. Table 5 summarizes the results from these changes. As it can be seen in the table, changing the goals caused a greater difference in the total dollars invested at the higher fill rate goals, as in the case of the C5. This can also be seen in examining the One Percent Tables from the

original runs, which show the effects of changing fill rate goals for each item. It may be beneficial to see how the expenditures grow as more MD goals are changed simultaneously or in varying combinations.

The final set of experiments conducted involved running the AAM model with different Buypoint files. Cost data remains the same within one set of Buypoint files (budget year, termoint year, and POM year). Information that changes involves the total available non-installed assets, various pipeline information, and demand rate. Cost data does change from the 1984 data sets to the 1985 data sets, in some cases dramatically. For example, looking at the first twelve stock numbers, nine of the prices remain the same from 1984 to 1985. The other three differ as follows:

<u>Part No.</u>	<u>1984</u>	<u>1985</u>
100500431167	\$ 1,796.00	\$ 3,912.88
1005001027987	1,041.00	16,040.00
1005001136208	6,370.00	16,040.00

It seems rather unusual that some prices should change so dramatically, while others do not change at all. Perhaps the price changes and the methods used for updating prices need to be analyzed more fully to determine their impact.

Table 6 contains summary information from several of the combination runs that were tried. It is apparent from Table 6 that the Buypoint file is a critical input file in the AAM runs. Since the costs are the same within years, the other differences in the buypoint file account for most of the differences in dollars spent from one run to the next. Note that when the 1984 POM buypoint file was used with the 1984 budget year data, total costs more than doubled. When the 1985 POM buypoint file was used with 1985 budget year data total costs nearly doubled.

Another reason for the increased expenditures between comps is the differences that exist between level of indenture files. These files contain the relationships between components and subcomponents. They specify which MD's the parts are applied to and the quantity of these applications. We found that while the files for each level remained similar within comps, there were large differences between comps. For example, a comparison of the Level 5, or lowest level of indenture, files revealed that the files remained the same for the three data sets in the 1984 comp (51 identical records in each). On the other hand, the 1985 comp Level 5 indenture files each contain about 970 records. These files contained many more part numbers with more applications per part. Similar findings can be seen by looking at the higher levels of indenture files.

CONCLUSIONS

Based on the work completed so far, it appears that a number of factors affect the results of the Aircraft Availability Model and warrant further investigation. The Buypoint file data is critical in the model results. From Table 6, the differences in pipeline data and demand rates in the Buypoint file are critical to the results in our runs. In addition, levels of indenture files reveal that part numbers and application information can change rather dramatically from one comp to the next. These findings support conclusions reached in the Logistics Management Institute report described earlier.

Differences in prices may need to be explored further. The Air Force Logistics Command implemented a price updating procedure in December 1984. The September 1984 unit price was overwritten with the December 1984 unit price. We found that for some part numbers the 1985 price was significantly higher than the 1984 price.

Differences in flying hours and number of aircraft may also need to be examined further to see why they change so much from one forecast to the next. A comparison with actual flying hours might prove useful.

TABLE 1

Selected Output From Preprocessor Reports

	<u>C5</u>	<u>C135</u>	<u>F4</u>	<u>F15</u>
SEP84B				
Flying hours	157	655	906	523
Total aircraft	80	646	1496	689
SEP84T				
Flying hours	176	634	817	540
Total aircraft	97	621	1375	717
SEP84P				
Flying hours	191	600	745	578
Total aircraft	118	588	1259	750
SEP85B				
Flying hours	145	577	573	512
Total aircraft	97	576	964	693
SEP85T				
Flying hours	155	555	512	535
Total aircraft	117	547	869	718
SEP85P				
Flying hours	156	520	431	559
Total aircraft	118	503	720	744

B = budget year
 T = termpoint year
 P = POM year

TABLE 2

Overall Initialization Cost Results

Total initialization cost insurance items:

SEP84B	819,683,921.
SEP84T	819,683,921.
SEP84P	819,683,921.
SEP85B	173,078,392.
SEP85T	173,078,392.
SEP85P	173,078,392.

Total initialization cost to prevent negative assets:

SEP84B	310,710,968.
SEP84T	542,891,139.
SEP84P	908,671,143.
SEP85B	754,976,363.
SEP85T	2,021,970,028.
SEP85P	2,800,640,829.

Total initialization costs for negotiated assets:

SEP84B	39,895,614.
SEP84T	48,304,040.
SEP84P	47,610,203.
SEP85B	117,643,446.
SEP85T	133,617,740.
SEP85P	134,561,598.

Total initialization costs to buy to pipeline:

SEP84B	796,966,492.
SEP84T	1,805,006,650.
SEP84P	4,045,480,273.
SEP85B	2,373,334,343.
SEP85T	2,827,338,298.
SEP85P	3,296,167,277.

TABLE 3

Total Costs from Investment Report

SEP84B	3,020,026,697.49
SEP84T	4,449,324,633.27
SEP84P	7,135,543,771.11
SEP85B	4,494,259,601.22
SEP85T	6,302,268,485.93
SEP85P	7,658,221,707.74

TABLE 4

Aircraft Availability Results for MD's:

C5

SEP84B:

Initialization cost:	107,861,560.
Dollars invested:	173,644,303.

SEP84T:

Initialization cost:	122,039,797.
Dollars invested:	179,226,570.

SEP84P:

Initialization cost:	135,845,788.
Dollars invested:	191,211,092.

SEP85B:

Initialization cost:	71,317,468.
Dollars invested:	129,393,305.

SEP85T:

Initialization cost:	95,854,733.
Dollars invested:	153,378,333.

SEP85P:

Initialization cost:	129,616,540.
Dollars invested:	208,164,197.

SEP84B:

Initialization cost:	61,239,896.
Dollars invested:	128,399,110.

SEP84T:

Initialization cost:	86,628,359.
Dollars invested:	159,747,061.

SEP84P:

Initialization cost:	112,399,189.
Dollars invested:	190,070,979.

SEP85B:

Initialization cost:	359,548,325.
Dollars invested:	408,064,585.

SEP85T:

Initialization cost:	476,643,571.
Dollars invested:	533,103,433.

SEP85P:

Initialization cost:	589,777,714.
Dollars invested:	652,798,071.

F4

SEP84B:

Initialization cost:	100,828,208.
Dollars invested:	107,919,490.

SEP84T:

Initialization cost:	152,437,362.
Dollars invested:	166,273,264.

SEP84P:

Initialization cost:	211,673,460.
Dollars invested:	231,214,163.

SEP85B:

Initialization cost:	63,461,694.
Dollars invested:	71,852,398.

SEP85T:

Initialization cost:	99,925,348.
Dollars invested:	110,335,865.

SEP85P:

Initialization cost:	110,376,122.
Dollars invested:	124,620,575.

F15

SEP84B:

Initialization cost:	94,033,846.
Dollars invested:	118,781,614.

SEP84T:

Initialization cost:	496,599,185.
Dollars invested:	546,359,131.

SEP84P:

Initialization cost:	1,708,853,473.
Dollars invested:	1,762,293,491.

SEP85B:

Initialization cost:	233,299,672.
Dollars invested:	271,663,940.

SEP85T:

Initialization cost:	522,041,184.
Dollars invested:	563,695,105.

SEP85P:

Initialization cost:	664,739,556.
Dollars invested:	710,664,145.

TABLE 5
Changes in Goals File

	Availability Goal	Total Investment
<u>C5</u>		
SEP84B	.93	173,644,303
-.05	.88	153,540,684
+.05	.98	222,558,581
SEP85B	.93	128,399,110
-.05	.88	114,553,998
+.05	.98	170,247,995
<u>C135</u>		
SEP84B	.94	128,399,110
-.05	.89	125,031,528
+.05	.99	143,243,309
SEP85B	.94	408,064,585
-.05	.89	403,567,006
+.05	.99	431,537,791
<u>F4</u>		
SEP84B	.81	107,919,490
-.05	.76	106,305,345
+.05	.86	113,416,319
SEP85B	.81	71,852,398
-.05	.76	70,768,353
+.05	.86	74,625,679
<u>F15</u>		
SEP84B	.77	118,781,614
-.05	.72	116,952,833
+.05	.87	121,065,390
SEP85B	.77	271,663,940
-.05	.72	270,139,112
+.05	.87	273,424,474

TABLE 6
Changes in Buypoint Files

Total costs from Investment Report:

1984B	3,020,026,697
1984B with 84P Buypoint	7,297,964,168
1984P	7,135,543,771
1985B	4,494,259,601
1985B with 85P Buypoint	7,705,750,004
1985P	7,658,221,708
1985B with 85T Buypoint	6,329,659,704
1985T	6,302,268,486

BIBLIOGRAPHY

1. King, Randall M. and Virginia A. Mattern. The Effects of Data-Base Dynamics in Estimating Spares Costs: An Analysis of the F-16. Logistics Management Institute Working Note AF501-2, December 1985.

2. Stokes, Major Ronald. Aircraft Availability Model User's Manual, HQ AFLC/XRS , Wright Patterson AFB, OH 45433, AV 787-6920, June 1986.

10 July, 1989

SUBMITTED BY:

UNIVERSITY OF DAYTON
PHYSICS DEPARTMENT
DAYTON, OHIO 45469

760-7MG-097

TUNABLE ABSORPTION IN DOPING SUPERLATTICES

FINAL REPORT

PREPARED FOR:

Research Initiation Program
Universal Energy Systems
Dayton, Ohio 45469

SPONSORED BY:

Air Force Office of Scientific Research
Special Faculty Programs AFOSR/XOT
United States Air Force

PRINCIPAL INVESTIGATOR: Dr. Bruce A. Craver

PROPOSED STARTING DATE: 31 December 1987

PROPOSED COMPLETION DATE: 31 December 1988

1987 USAF RESEARCH COLLEAGUE: Dr. P. Hemenger
AFWAL/MLPO
Materials Laboratory
Wright-Patterson Air Force Base, OH
(513) 255-4474

ABSTRACT

In this report we have treated two closely related problems, that of computing the tunable absorption coefficient of a room temperature GaAs doping or "nipi" superlattice, and calculating the reflectance and transmittance of both absorbing and nonabsorbing optically nonlinear thin films. The superlattice absorption calculations employ the phenomenological model introduced by Dohler, Kunzel and Ploog. A representative set of calculations indicate that there is tunable absorption at room temperature, with roughly a one to two order magnitude modulation, which is somewhat smaller than that predicted by Dohler at 4 K. The calculations of the reflectance of optically nonlinear thin films uses a new technique, invariant imbedding, to obtain R directly as a function of the film thickness and incident intensity. Our results help resolve a contradiction in the literature, indicating there is bistable behavior for thin films, and not the hysteresis behavior claimed by Y.E. Band. The results with the inclusion of absorption suggest that this bistability may be shifted to higher intensities or eliminated, but some numerical instabilities preclude an unambiguous conclusion.

I. INTRODUCTION

The development of fast, low-power electro-optical devices for applications in image processing and optical computing are of great importance to the USAF. Nonlinear optical materials are likely to play a central role in the development of such devices. These nonlinear materials are characterized by a dielectric function ϵ which is a function of the local electric field strength E , and are capable of fast switching or changes in state, modulation or tuning of its properties, and self-interaction effects.

A previous review of the literature revealed that a class of structures known as superlattices (SLs) exhibit nonlinear optical behavior, and a potential for application to a wide range of electro-optical devices such as tunable light sources, lasers, and spatial light modulators. In particular, the ability to modulate, or tune, the absorption coefficient of doping, or nipi, SLs by modulating some external stimulus to the SL appears to be well suited for light modulation.

In the present work we were to concentrate on a particular class of SLs known as nipi's, or doping SLs, and direct our efforts along two directions. First, we intended to develop the capability to compute the absorption coefficient of the SL for a given set of materials parameters such as doping levels and physical dimensions. These calculations are based on the phenomenological model of Dohler, Kunzel, and Ploog.¹ This computer code would then assist in the in-house manufacture of

such SLs. Secondly, we were to develop the capability to compute the reflection, transmission, and absorption properties of films of SLs. The intention here was to investigate the way in which these properties of nonlinear films are altered by the changing intensity of an incident beam, i.e. their self-interaction effects. In a traditional approach one must solve a nonlinear wave equation subject to boundary conditions at two different locations in space. The solution is quite difficult because one can no longer use the superposition principle to construct solutions. It was proposed that this problem be addressed by using a numerical technique known as invariant imbedding. This approach allows one to compute the reflectance, etc. in an exact, nonperturbative manner. More importantly it allows us to include absorption, whether it be intensity-dependent or intensity-independent, in a straightforward manner.

II. TUNABLE ABSORPTION IN NIPIS

II.1 SEMI-CLASSICAL MODEL

In this section we present a brief overview of the model used to calculate the tunable absorption of nipi's, which was presented by Dohler et al. We avoid lengthy derivations, and include only details needed to understand the model or clarify assumptions or approximations we have employed. Doping SLs are constructed by alternately doping a single semiconductor material n-type and p-type along the SL axis. In addition, undoped or intrinsic, layers can be sandwiched between the doped layers, as desired. In the present calculations it is assumed that we have a layer of n-type material, an intrinsic layer, a p-type layer, and another intrinsic layer which taken together constitutes one period of the SL. The thicknesses of these layers are taken to be d_n , d_i , d_p , and d_i respectively, and the period of the SL is

$$d = d_n + d_p + 2d_i. \quad (2.1)$$

In the donor and acceptor regions the impurity concentrations, n_D and n_A are assumed constant. As a result of the diffusion between the donor and acceptor regions there is a space charge of ionized impurity sites in these regions. In the semi-classical model presented by Dohler et al¹ it is assumed that in the donor region, for example, the remaining unionized impurities form a layer of thickness d_n^0 in the center of the n-type layer,

surrounded by a layer of thickness d_n^+ of completely ionized impurities on either side. This thickness d_n^+ is just that of the depletion layer on either side of the n-type region. An analogous situation exists for the p-type layer. This is illustrated in Fig. 1.

In this model the donor layer, for example, can be thought of as a layer of electrons with a thickness d_n^0 and carrier density n_D superimposed on a background layer of ionized impurity sites with a thickness d_n and density n_D . One could then define as a measure of the amount of diffusion of electrons from the donor region an effective density of carriers (electrons) per unit cross sectional area as viewed along the axis of the SL. This two-dimensional carrier density is

$$n^{(2)} = n_D d_n^0. \quad (2.2)$$

The corresponding carrier density in the acceptor region is

$$p^{(2)} = n_A d_p^0. \quad (2.3)$$

As a result of this space charge distribution there is a periodic electrostatic potential set up in the crystal that modulates the conduction and valence band edges, as illustrated in Fig. 2. Note that this SL potential tends to localize electrons and holes in different spatial regions. In the semiclassical model one assumes these wells are of sufficient width to allow one to ignore any quantum effects due to the localization of the

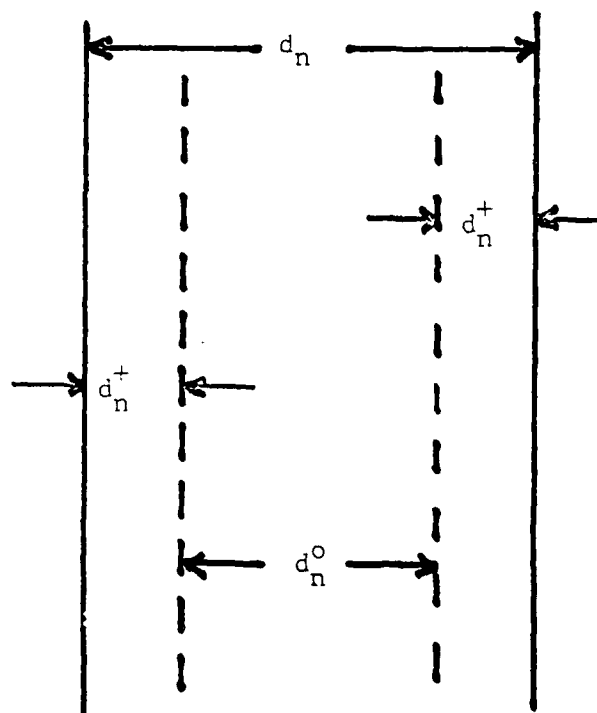


Fig. 1 The donor region with thickness d_n is assumed to consist of an unionized region of thickness d_n^o , surrounded by regions of completely ionized donors with thickness d_n^+ .

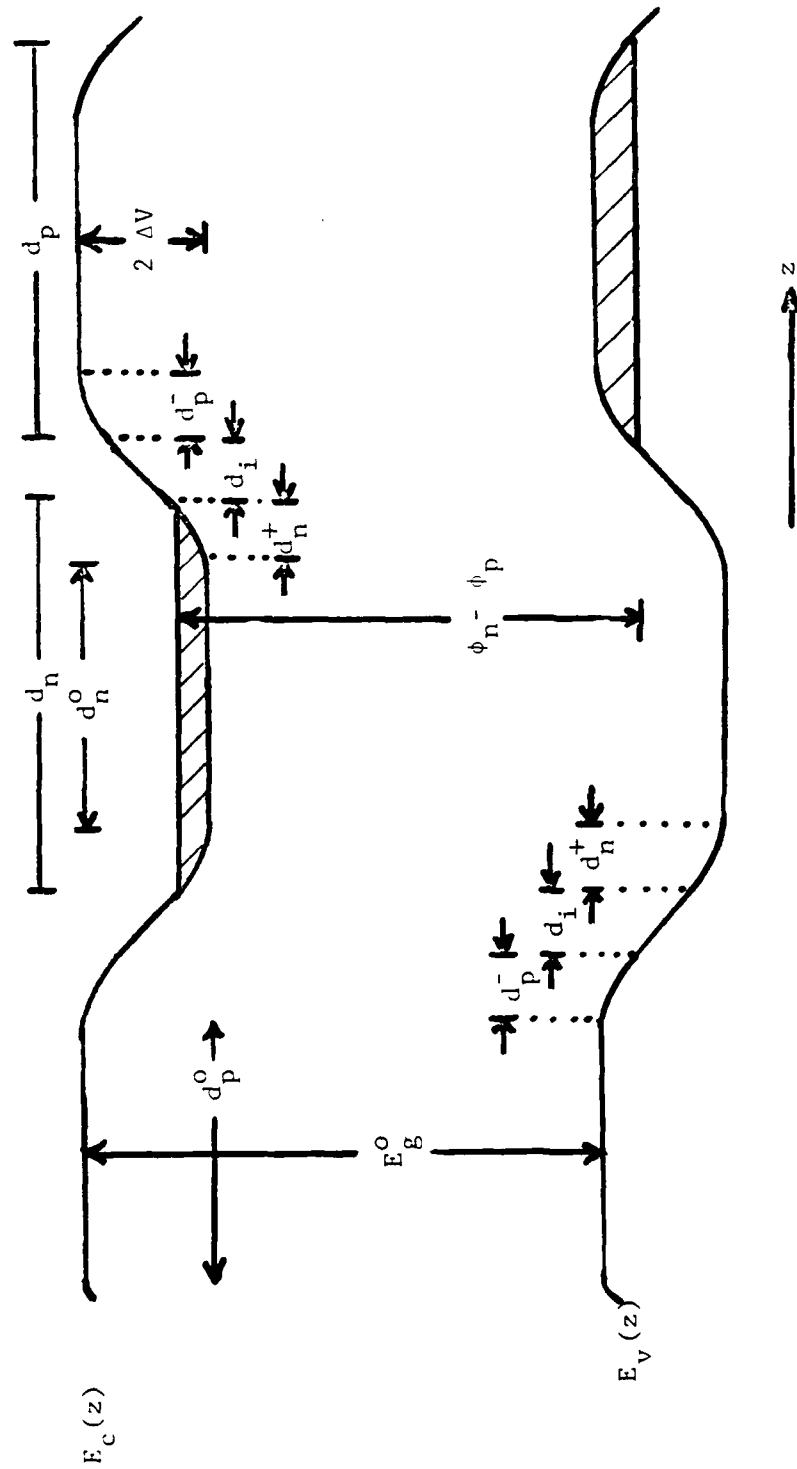


Figure 2. Superlattice band structure along the axis of the superlattice.

particles. This separation of electrons and holes results in recombination lifetimes which can be much longer than those in bulk materials, and one can imagine the electrons and holes separately achieve quasi-equilibrium which can be characterized by quasi-Fermi levels ϕ_n and ϕ_p respectively.

As a result of this SL potential the effective band gap E_g^{SL} of the SL is now less than the band gap E_g^0 of the bulk material. From Fig. 2 we can see that

$$E_g^{SL} = E_g^0 - 2\Delta V \quad (2.4)$$

where ΔV is the amplitude of the oscillation in the SL potential. It is therefore possible for photon absorption to occur for energies below the traditional band edge, but this process is inhibited by the spatial separation of electrons and holes. This transition can be most easily thought as a Franz-Keldysh effect,² i.e. absorption below the band edge in the presence of an electric field F . An electron absorbs a photon with energy less than the spatially direct gap E_g^0 , and then tunnels through the remaining barrier to the conduction band. The absorption coefficient α then depends on the field F , which is due to the SL potential.

Clearly, α is dependent on the state of excitation of the SL, which is most directly represented by ΔV or E_g^{SL} . Alternatively, the thicknesses d_n^+ and d_p^- , the carrier densities $n^{(2)}$ and $p^{(2)}$, or the quasi-Fermi levels ϕ_n and ϕ_p , are a direct measure of the level of excitation of the SL. As more electrons and holes are excited out of their wells and returned to their impurity sites

these sites become neutralized, and the amplitude ΔV decreases, thereby increasing E_g^{SL} and altering α . These carrier concentrations can be modified by electro-injection or photo-excitation. The unique feature of nipi's that makes this possible is the spatial separation of electrons and holes, greatly increasing their recombination lifetimes. The tunability of α is achieved by controlling the level of excitation of the SL.

Although the excitation may be described by ΔV , $\{n^{(2)}, p^{(2)}\}$, or $\Delta\phi_{np} = \phi_n - \phi_p$, one may be more convenient. Certainly, while discussing the dynamics of the electron and hole carrier concentrations the difference in the quasi-Fermi levels is important, since various reaction mechanisms are generally dependent upon it. Given $n^{(2)}$ and $p^{(2)}$, $2\Delta V$ can be found from a straightforward solution of Poisson's equation for the charge distribution described previously.

$$2\Delta V = \frac{4\pi e^2}{\epsilon_1} \left\{ \frac{1}{2} n_D d_n^{+2} + \frac{1}{2} n_A d_p^{-2} + n_D d_n^+ d_i \right\} \quad (2.5)$$

Furthermore,

$$\Delta\phi_{np} = \phi_n - \phi_p = (\phi_n - \epsilon_c) + E_g^{SL} + (\epsilon_v - \phi_p), \quad (2.6)$$

where ϵ_c and ϵ_v are the conduction and valence band edges at the center of the donor and acceptor layers. In this portion of the layer, of thickness d_n^0 or d_p^0 , the impurities are assumed fully

ionized, so that there is a carrier concentration n_D or n_A , depending on whether the layer is a donor or acceptor region. It is assumed that the location of the quasi-Fermi level relative to the band edge in this region is approximately the same as the location of the Fermi level relative to the band edge in bulk material with a carrier density $n_c = n_D$ or $n_h = n_A$. For the donor

$$\phi_n - E_c \approx (\phi - E_c)_{n_D;T}, \quad (2.7)$$

where ϕ and E_c are the Fermi level and conduction band edge in bulk material with a carrier concentration n_D at temperature T . Making a similar approximation for the acceptor region, we have

$$\Delta\phi_{np} \approx E_g^{SL} + (\phi - E_c)_{n_D;T} + (E_v - \phi)_{n_A;T} \quad (2.8)$$

or

$$\Delta\phi_{np} \approx V_{bi} - 2\Delta V. \quad (2.9)$$

where

$$V_{bi} = E_g^O + (\phi - E_c)_{n_D;T} + (E_v - \phi)_{n_A;T}. \quad (2.10)$$

The difference $(\phi - E_c)_{n_D;T}$ can be computed assuming a parabolic band approximation with an effective mass m_c . The

carrier concentration in a semi-conductor with a Fermi level φ and conduction band edge E_c is

$$n_c = \int_{E_c}^{\infty} g_c(E) f(E) dE, \quad (2.11)$$

where the density of states is

$$g_c(E) = \frac{1}{2\pi^2} \left[\frac{2m_c}{\hbar^2} \right]^{3/2} (E - E_c)^{1/2}, \quad (2.12)$$

$f(E)$ is the Fermi-Dirac distribution function,

$$f(E) = \frac{1}{1 + \exp(\beta(E - E_c))}, \quad (2.13)$$

and $\beta = 1/kT$. This can be expressed as

$$n_c = 2 \left[\frac{m_c}{2\pi\hbar^2} \right]^{3/2} \mathcal{F}_{1/2}(\beta(\varphi - E_c)) = N_c \mathcal{F}_{1/2}(\beta(\varphi - E_c)), \quad (2.14)$$

with $\mathcal{F}_{1/2}(x_0)$ one of the Fermi integrals

$$\mathcal{F}_j(x_0) = \frac{1}{\Gamma(j+1)} \int_0^{\infty} \frac{x^j dx}{1 + \exp(x - x_0)}. \quad (2.15)$$

To find $\phi - E_c$ we recall that in the neutralized region of the donor layer the impurities are all ionized, so the carrier concentration is $n_c = n_D$. To obtain $\phi - E_c$ we must then solve the equation

$$\mathcal{F}_{1/2}(\beta(\phi - E_c)) = n_D/N_c. \quad (2.16)$$

Unlike many cases, here the value of the Fermi integral is known, so that what is needed is a way to express the argument of this function in terms of the value of this function. There are available a variety of expansions, each with its own range of applicability. In the present work we have considered different ranges of arguments, and used approximations appropriate to each range. For $x_0 < 0$ the expansion

$$\mathcal{F}_{1/2}(x_0) \approx e^{x_0} - .3e^{2x_0} + .06e^{3x_0} \quad (x_0 < 0) \quad (2.17)$$

is accurate to within 0.75%. With $\mathcal{F}_{1/2} = n_D/N_c$ we have a cubic equation for $\exp(x_0)$ which can easily be solved. In the limit $x_0 \ll -1$, the nondegenerate regime, this reduces to the Maxwell-Boltzmann statistics. When $\mathcal{F}_{1/2} = n_D/N_c > 20$, the strongly degenerate region, a power law representation is sufficiently accurate,

$$F_{1/2}(x_0) = \frac{1}{\Gamma(3/2) (3/2)} x_0^{3/2} = \frac{4}{3\sqrt{\pi}} x_0^{3/2} \quad (2.18)$$

This can easily be inverted to find x_0 . Finally, in the region $0 < F_{1/2} < 20$ Abidi and Mohammad³ have developed an expansion of the argument x_0 in terms of the value of $u = n_D/N_C = F_{1/2}(x_0)$.

$$x_0 = 0.9985 \ln(u) - 1.048E-4 + 35.46250E-2 u - 4.958417E-3 u^2 \\ + 1.199012E-4 u^3 - 1.532784E-6 u^4 \quad (2.19)$$

Depending upon the value of n_D/N_C one of the above forms may be used to obtain $(\Delta - E_C)$. A similar calculation gives $E_V - \Delta$ for a hole concentration $n_h = n_A/N_V$ in the acceptor region.

In this semiclassical model it is assumed that spatial variations in the SL potential, and the resultant internal field F , are gradual. One can then define locally in the SL an absorption coefficient $\alpha(\omega, F(z))$, with z the spatial coordinate along the SL axis and $F(z)$ the local field. The effective absorption coefficient for the SL is then taken to be a spatial average over one SL period.

$$\alpha^{SL}(\omega, \Delta E_{np}) = d^{-1} \int_d \alpha_B(\omega, F(z)) dz \quad (2.20)$$

where the integration is to extend over one period of the SL, and

ΔV_{np} is a measure of the excitation of the SL. The result of this is

$$\alpha^{SL}(\omega, \Delta V_{np}) = \frac{1}{d} \left(d_n^0 \alpha_B^n(\omega, 0) + d_p^0 \alpha_B^p(\omega, 0) + 2d_1 \alpha_B(\omega, F_{max}) \right) \\ \frac{2(d_n^+ + d_p^-)}{F_{max}} \int_0^{F_{max}} \alpha_B(\omega, F) dF \quad (2.21)$$

where $\alpha_B^n(\omega, 0)$ and $\alpha_B^p(\omega, 0)$ are the absorption coefficient for bulk material doped either n-type or p-type, at frequency ω and $F = 0$, and $\alpha_B(\omega, F)$ is the absorption coefficient in bulk undoped material in the presence of an electric field F . F_{max} is the maximum internal field strength arising from the SL potential,

$$F_{max} = 4\pi e n_D d_n^+ / \epsilon_1 \quad (2.22)$$

and ϵ_1 is the real part of the dielectric constant $\epsilon = \epsilon_1 + i\epsilon_2$ for the material.

In order to determine α^{SL} we must know the bulk absorption coefficient for both doped and pure material, and also have a model for the absorption in the presence of electric fields. In the absence of any reliable and simple model of impurity dependence for α_B we will here approximate α_B^n and α_B^p near the band edge by fits to a limited amount of experimental data. The graphical representations of the spectral behavior of α_B^n and α_B^p near and below the band edge given by Casey, Sell, and Wecht⁴

for a range of doping levels was enlarged and then digitized with the aid of a plotter connected to a small computer. The spectral dependence was fit employing the functional form

$$\alpha_B(\omega, 0) = a_0 + \frac{a_1}{1 + \exp(a_2 - a_3 E_\gamma)} + \frac{a_4}{1 + \exp(a_5 - a_6 E_\gamma)} \quad (2.23)$$

Here $E_\gamma = \hbar\omega$ is the photon energy, and the $\{a_i\}$ are viewed as functions of the impurity concentrations. The quality of these approximations is illustrated in Fig. 3, which are representative. The criteria for the quality of these fits was to minimize the least squares difference in the parameter space.

The concentration dependence of these parameters is shown in Figs. 4-6. Although the approximations are quite good in the region of the band edge the dependence of the $\{a_i\}$ is not very smooth, thereby introducing some degree of uncertainty in the determination of $\alpha_B(\omega, 0)$ at impurity levels that would require us to interpolate for the constants $\{a_i\}$.

The dependence of the absorption on electric field strength is described in detail by Aspnes⁵ and Aspnes and Bottka.⁶ There it is shown that $\alpha_B(\omega, F)$ is related to the imaginary part of $\epsilon = \epsilon_1 + i\epsilon_2$ by

$$\alpha = \omega \epsilon_2 / nc, \quad (2.24)$$

where n is the refractive index, and

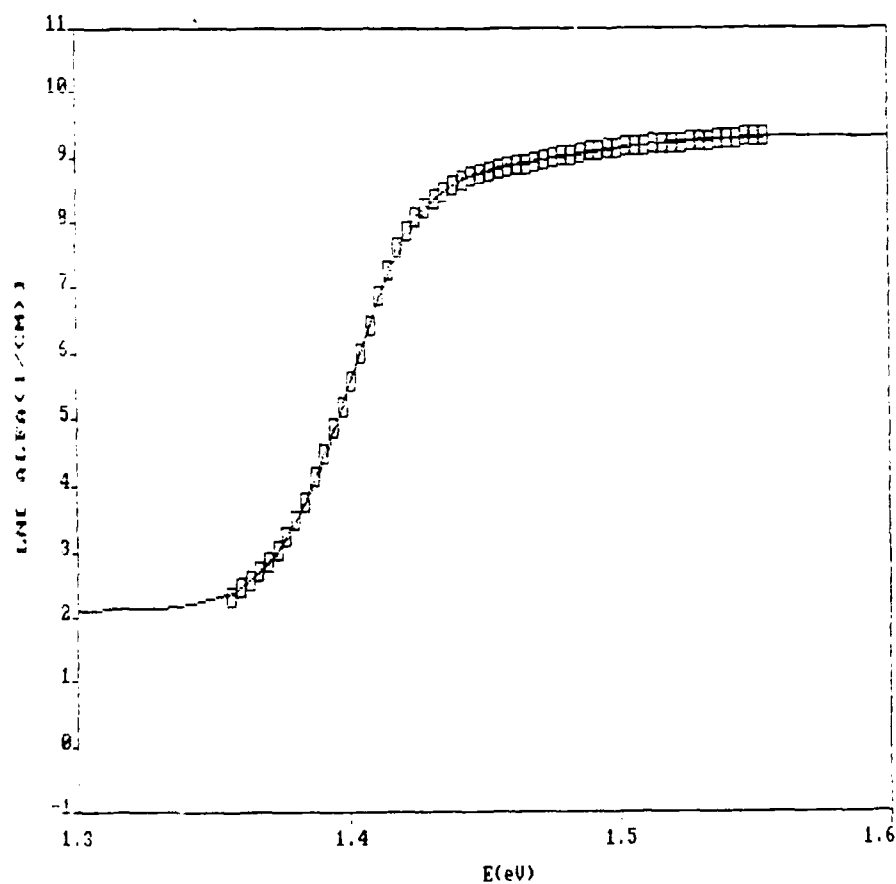


Fig. 3 Typical fit to absorption edge for doped bulk GaAs. The boxes are data from ref. 4 for n-type GaAs with $n=5.9 \times 10^{17}/\text{cm}^3$, and the solid line is a least squares fit using (2.23).

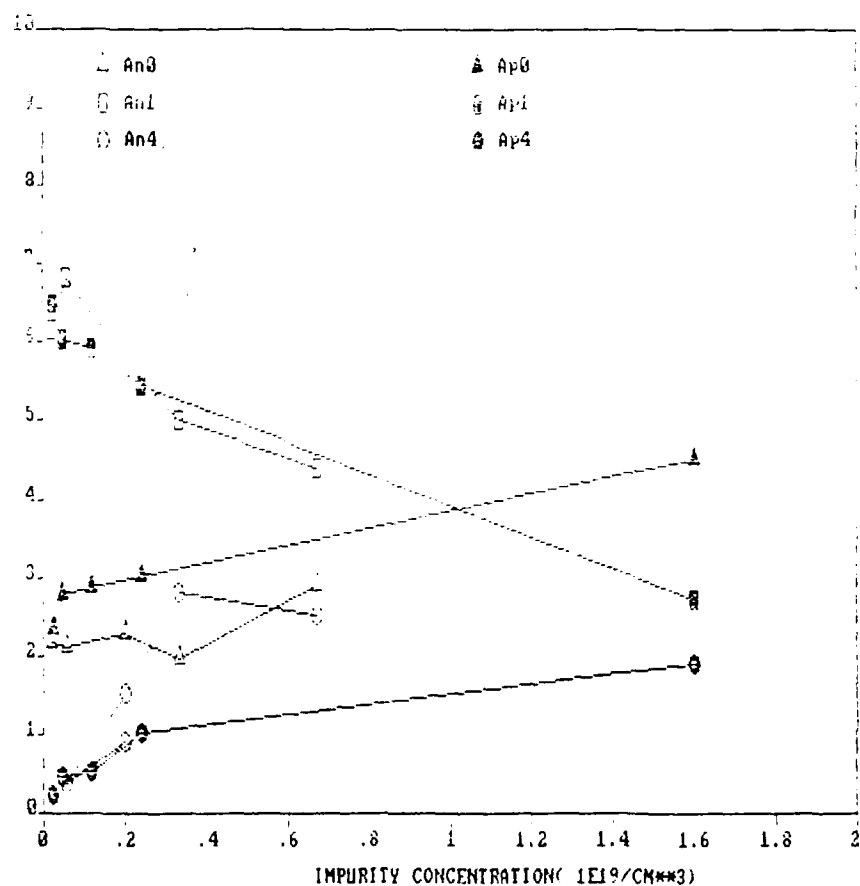


Fig. 4 Impurity concentration dependence of the parameters a_0 , a_1 , and a_4 . Subscripts n and p denote parameters for n-type or p-type doping.

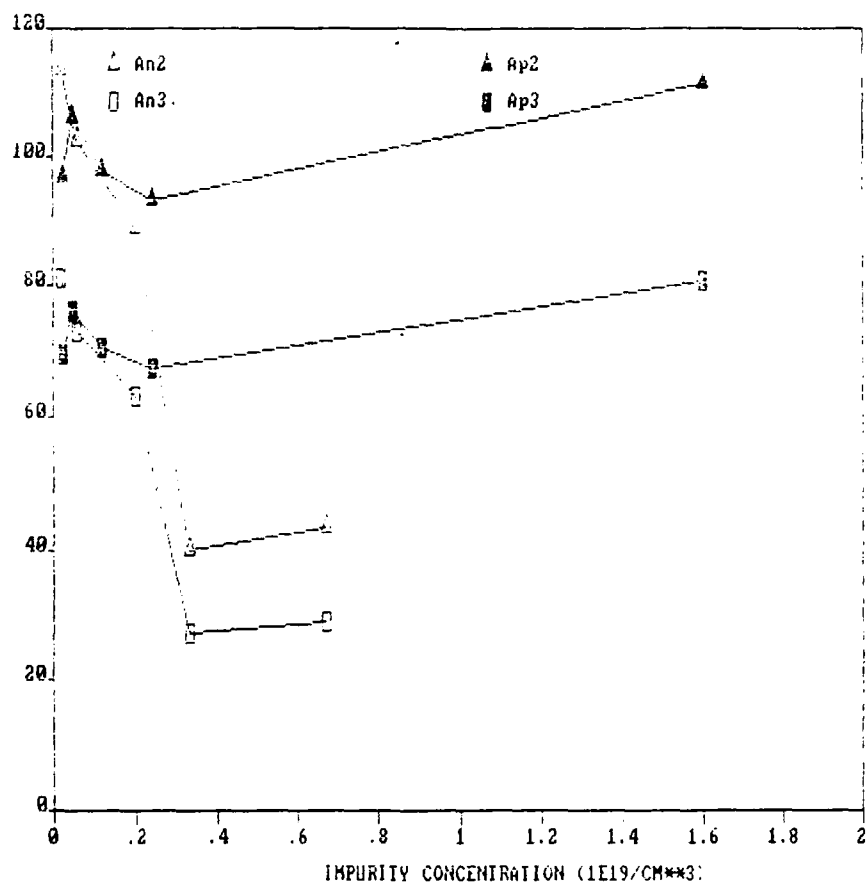


Fig. 5 Impurity concentration dependence of a_2 and a_3 . Subscripts n and p denote parameters for n-type and p-type doping.

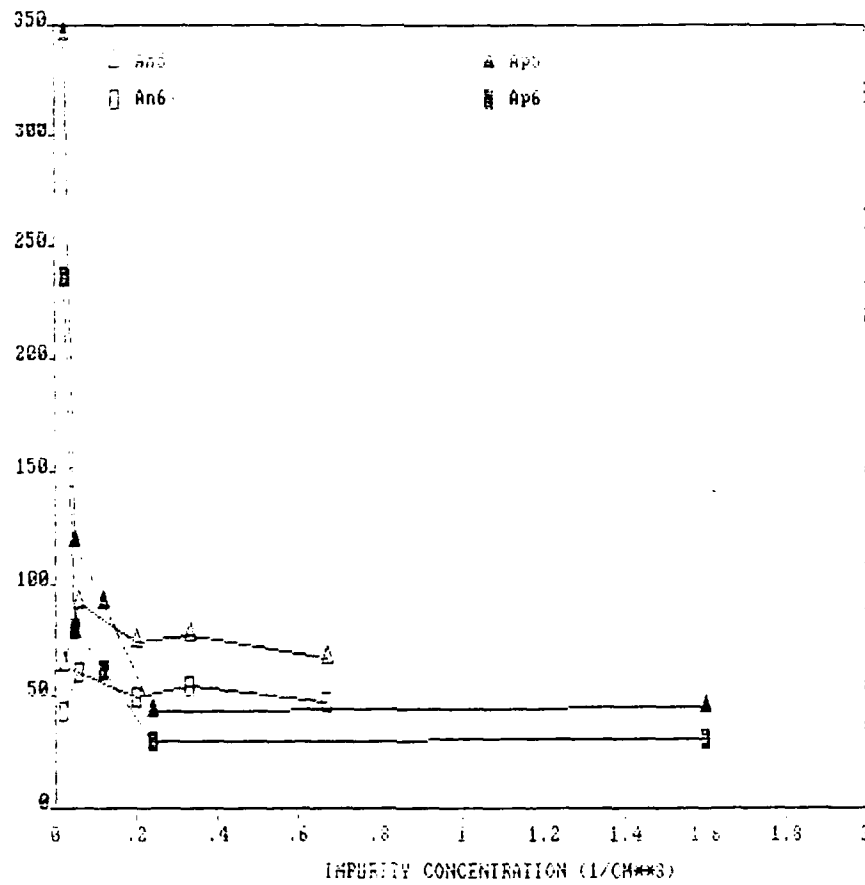


Fig. 6 Impurity concentration dependence of a_5 and a_6 . Subscripts n and p denote parameters for n-type and p-type doping.

$$\epsilon_2 = \frac{2e^2 |a_\lambda|^2 |P_{cv}|^2 (2\mu)^{3/2} (\hbar\Omega)^{1/2}}{m \omega \hbar^3} \int_0^\infty x^{1/2} \text{Ai}(x+x_0) dx. \quad (2.25)$$

In (2.25), a_λ is the photon polarization vector, $\text{Ai}(x)$ is the Airy function,⁷ $\mu = m_c m_v / (m_c + m_v)$, $x_0 = (E_g^0 - \hbar\omega) / (\hbar\Omega)$, P_{cv} is the momentum matrix element between Bloch states for the conduction and valence bands, and

$$\hbar\Omega = \left[\frac{\hbar^2 e^2 F^2}{8\mu} \right]^{1/3}. \quad (2.26)$$

With this the integral in the last term of (2.21) becomes

$$\int_0^{F_{\max}} \alpha_B(\omega, F) dF = \frac{2e^2 |a_\lambda|^2 |P_{cv}|^2 (2)^{3/2}}{m \omega \hbar^3} \frac{3\omega}{2nc} \left[\frac{8\mu}{\hbar^2 e^2} \right]^{1/2} \delta^2 G, \quad (2.27)$$

where $\delta = E_g^0 - E_\gamma$, and G is a dimensionless integral

$$G = \int_{y_{\min}}^{\infty} y^{-3} dy \int_0^{\infty} x^{1/2} Ai(x+y) dx, \quad (2.28)$$

and

$$y_{\min} = \delta \left[\frac{8\mu}{2 \frac{2}{\hbar} \frac{2}{e} \frac{2}{F_{\max}}} \right]^{1/3}. \quad (2.29)$$

Kane^{8,9} has shown that averaging (2.27) over the photon polarizations results in the substitution

$$|a_{\gamma} \cdot P_{CV}|^2 = \frac{2}{3} |\langle S | p_Z | Z \rangle|^2 = \frac{2}{3} \frac{m^2}{\hbar^2} P^2 \quad (2.30)$$

in equation (2.27), where the real matrix element $P = -i(\hbar/m) \langle S | p_Z | Z \rangle$ defined by Kane is

$$P = \frac{\hbar^2}{2m_c} \frac{E_g(E_g + \Delta)}{(E_g + 2\Delta/3)}, \quad (2.31)$$

and Δ is the spin-orbit splitting of the valence band. This procedure has been followed by Moss and Hawkins.¹⁰ They have computed α in the absence a field F , and above the band edge, using the model of Kane, and then fit their data with this analytic form.

II.2 RESULTS

We present some selective results to illustrate some general features of the SL absorption. These results are not optimized in any manner, and all calculations correspond to room temperature since this was considered to correspond to the most likely applications. Furthermore, in view of the limited success in obtaining a smooth concentration dependence of the fitting parameters $\{a_i\}$, we have considered impurity levels equal to those in the data of ref. 4, and not considered concentrations that would require interpolations for $\{a_i\}$. Furthermore, in view of the results of ref. 1 showing a larger sensitivity to excitation level in SL's with no intrinsic layer, we consider only cases where $d_i = 0$.

Figs. 7-8 show respectively the contribution from the last term in eq. (2.21), which we refer to as the Franz-Keldysh (F-K) contribution to α^{SL} , and α^{SL} itself. We see in Fig. 7 the dramatic variation in the F-K term that can be produced by changes in the excitation level of the SL. This also is present in the effective absorption coefficient α^{SL} , although it is clear from Fig. 8 that the modulation is not as dramatic. This modulation is also less than that reported in ref. 1 for similar doping levels and layer dimensions. This is so because the band edge is not nearly as sharp at room temperature and for these impurity levels. Consequently, the F-K term is only comparable to the bulk contribution terms in (2.21) rather than dominating them.

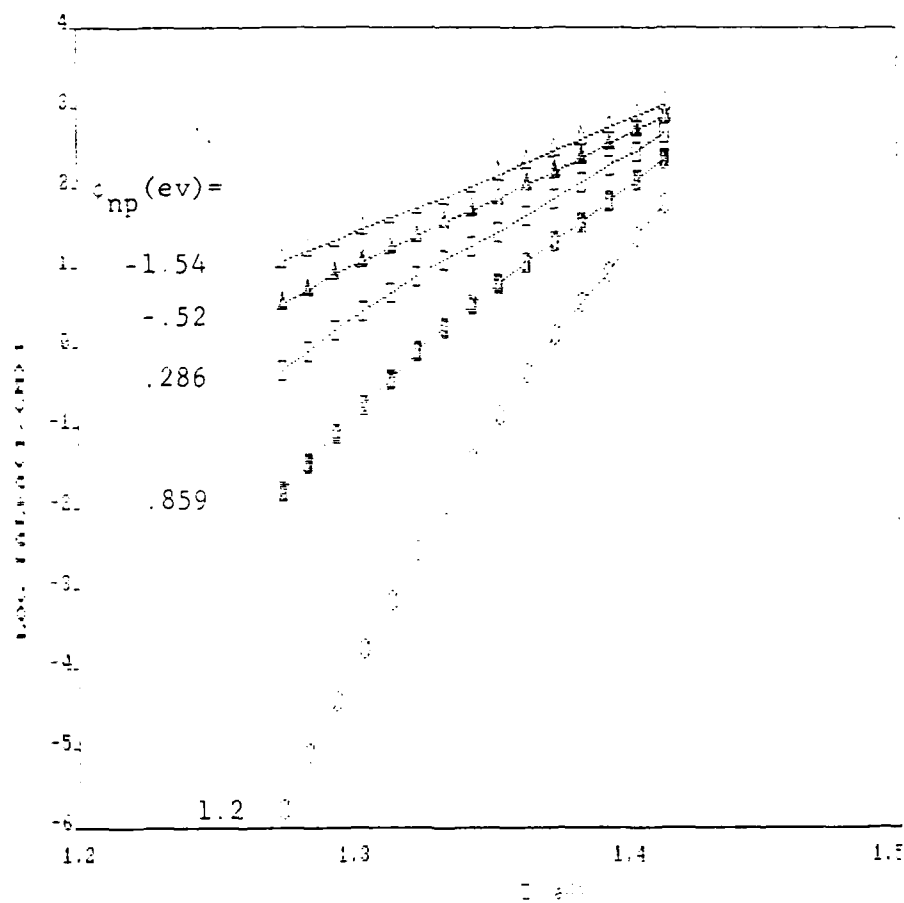


Fig. 7 Tunable Franz-Keldysh contribution to a^{SL} for $n_D = 2 \times 10^{17} / \text{cm}^3$, $n_A = 2.2 \times 10^{17} / \text{cm}^3$, $d_n = d_p = 1.9 \times 10^{-5} \text{ cm}$, and $(2\Delta V)_{\text{max}} = 2.87 \text{ eV}$.

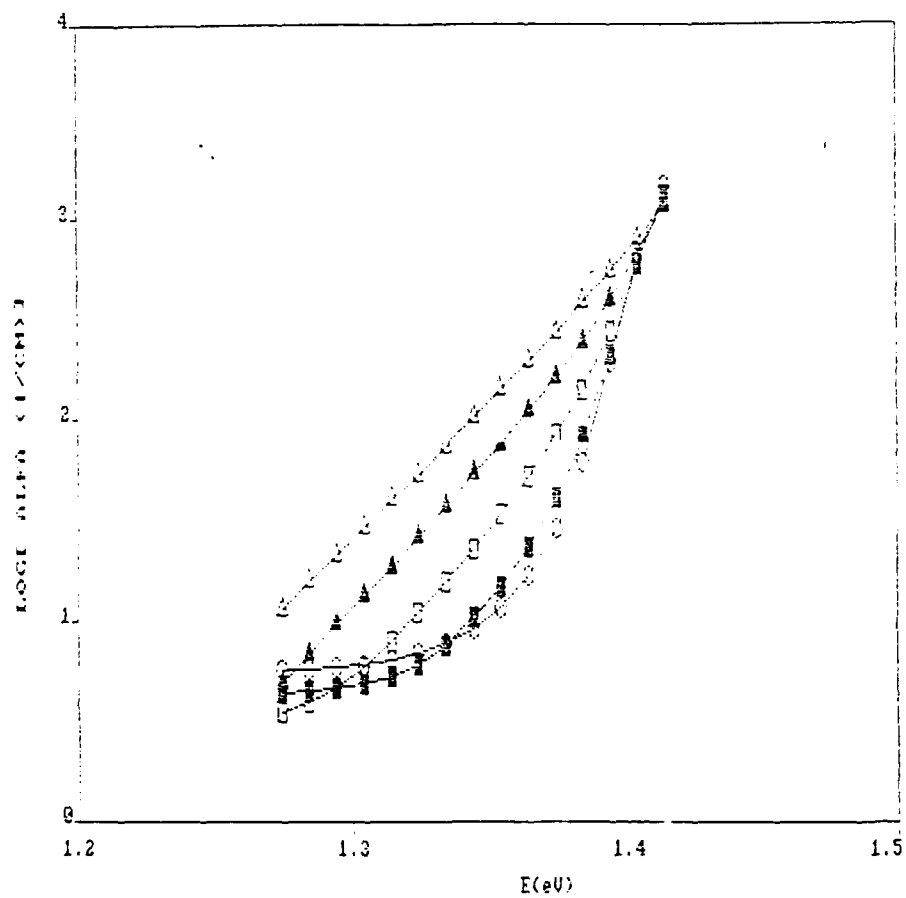


Fig. 8 α^{SL} for the same device parameters as in fig. 7.

The results for the same doping concentrations but with d_n and d_p a factor of ten smaller are shown in Figs. 9-10. As one would expect, this greatly enhances the modulation of the F-K contribution, Fig. 9, since the tunneling barrier is much smaller. Nevertheless, the overall modulation of α^{SL} , Fig. 10, is still comparable to the previous case. Once again, the F-K contribution is not the dominant one.

Finally, in Fig. 11 we have computed α^{SL} corresponding to more than a ten-fold increase in the impurity concentrations, and to thicknesses $d_n = 2 \times 10^{-6}$ cm, $d_p = 4 \times 10^{-6}$ cm. The maximum peak-to-peak modulation in the band edges is $(2\Delta V)_{\max} = 2.1$ eV. Making the layers much thicker greatly increases $(2\Delta V)_{\max}$ beyond realistic values. Here one finds a greater modulation, on the order two orders of magnitude, compared with the roughly one order of magnitude in Fig. 8.

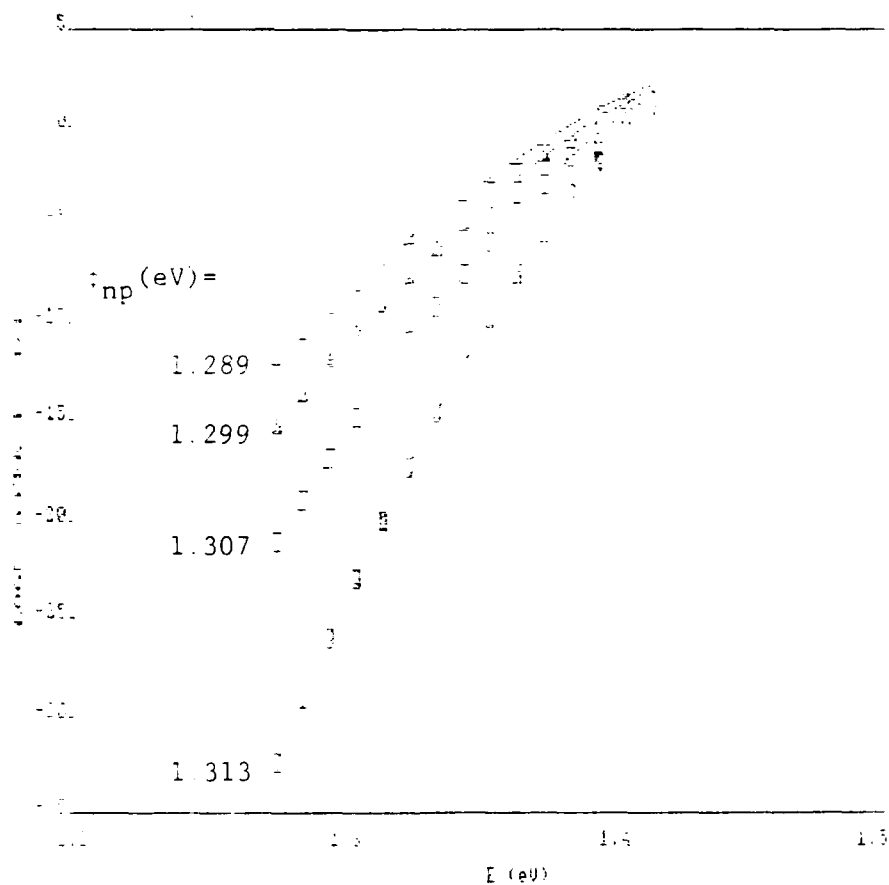


Fig. 9 Tunable Franz-Keldysh contribution to χ^{SL} for $n_D = 2 \times 10^{17} / \text{cm}^3$, $n_A = 2.2 \times 10^{17} / \text{cm}^3$, $d_n = d_p = 1.9 \times 10^{-6} \text{ cm}$, and $(2\Delta V)_{\text{max}} = 0.0286 \text{ eV}$.

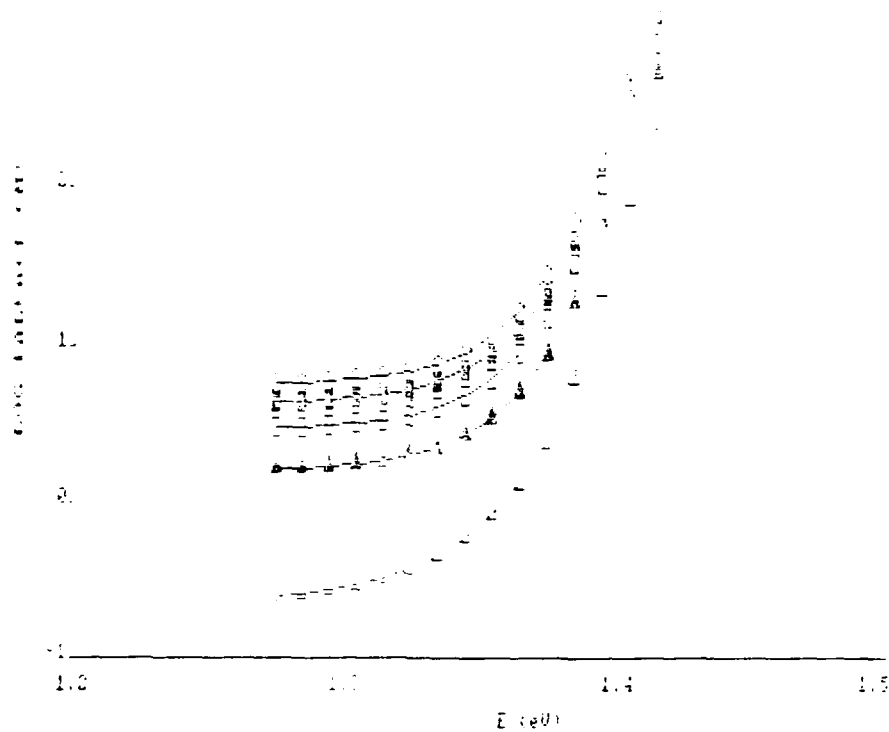


Fig. 10 J^{SL} for the same device parameters as in fig. 9.

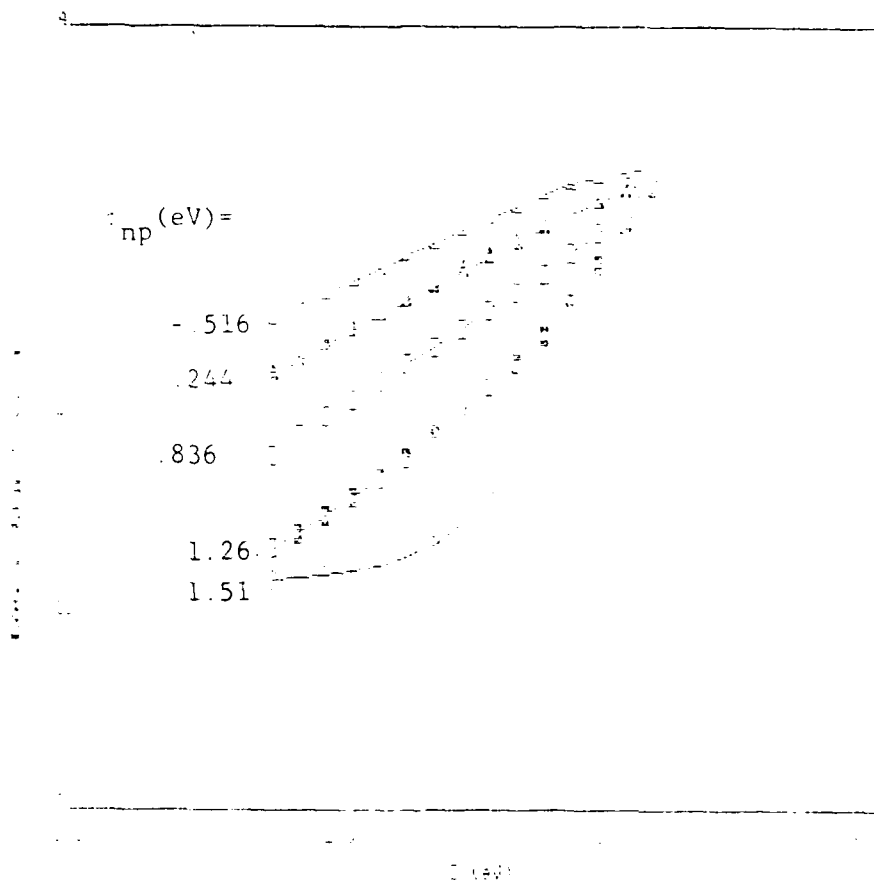


Fig 11 a^{SL} for $n_D = 6.7 \times 10^{18} / \text{cm}^3$, $n_A = 2.4 \times 10^{18} / \text{cm}^3$,
 $d_n = 2 \times 10^{-6} \text{ cm}$, $d_p = 4 \times 10^{-6} \text{ cm}$ and $(2\Delta V)_{\text{max}} = 2.11 \text{ eV}$

III. REFLECTANCE AND ABSORBANCE OF A NONLINEAR FILM

In the previous discussion we have seen that α^{SL} can be adjusted or tuned by changing the level of excitation of the SL, which can be accomplished by photoexcitation. When the SL absorbs some portion of the light incident upon it the level of excitation of the SL changes, and so does α . The absorption can be viewed as dependent on the intensity of radiation. In this section we wish to examine the manner in which such a nonlinear absorption coefficient effects the reflection, absorption and transmission properties of a film of such material. Here we will use a relatively new technique referred to as invariant imbedding^{11,12} to solve this problem in an essentially exact, albeit numerical manner. This approach is in contrast to perturbative treatments used in the past. Once again, we will present only the steps essential to understanding this approach.

III.1 DYNAMICAL EQUATIONS FOR REFLECTION AND TRANSMISSION AMPLITUDES

The basic geometry of the problem is shown in Fig. 12. A film of nonlinear optical material is placed between $Q=0$ and $Q=x$, where Q is the spatial variable along the direction perpendicular to the film, and x is the thickness of the film. For our purpose we simply note that the nonlinear properties originate from the dependence of the polarization of the material

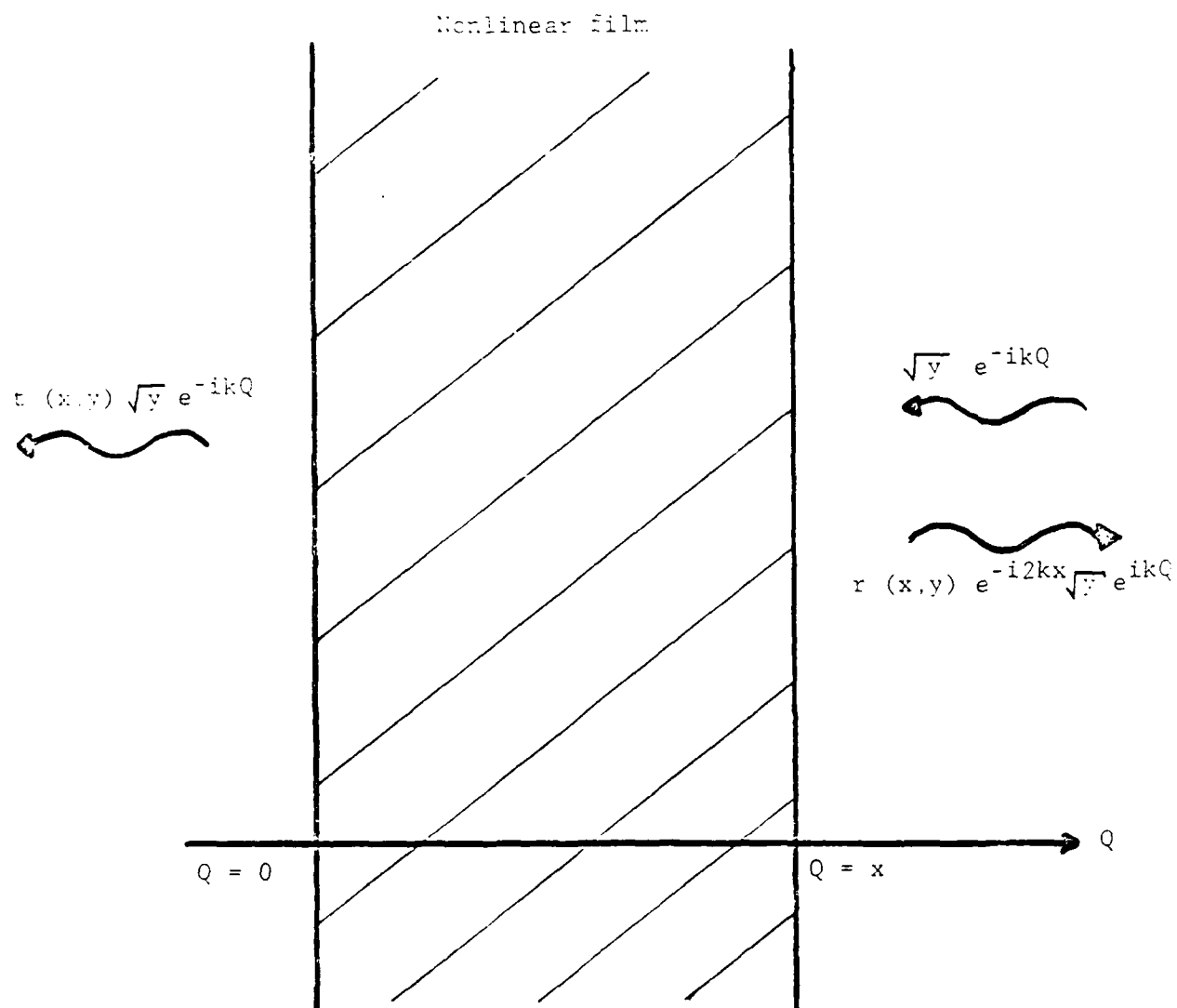


Figure 12. Incident, reflected and transmitted waves for an optically nonlinear film of thickness x .

on the total field in the material. We assume this dependence to be of the form

$$P = E (\chi_1 + \chi_3 \langle E^2 \rangle + \dots) \quad (3.1)$$

where $\langle E^2 \rangle$ is the time-averaged local field in the material. In linear materials χ_3 would be zero, and in general will be small compared to χ_1 . Also these susceptibilities are to be considered complex. The dielectric function is then of the form

$$\epsilon = \epsilon_1 + i \epsilon_2 = (\epsilon_{1,L} + \epsilon_{1,NL} I) + i(\epsilon_{2,L} + \epsilon_{2,NL} I). \quad (3.2)$$

In (3.2) I is the time-averaged local intensity in the medium, and the subscripts L and NL denote the intensity-independent and intensity-dependent portions of these functions. These functions can be related to the often used index of refraction and extinction coefficient,

$$\epsilon_1 = n^2 - \kappa^2, \quad \epsilon_2 = 2n\kappa. \quad (3.3)$$

In the limit of low intensity, $n_{NL} I \ll n_L$, and $\kappa \ll n_L$,

$$n_L + n_{NL} I \approx n_L + \epsilon_{1,NL} I / 2 \sqrt{\epsilon_{1,L}}. \quad (3.4)$$

A plane wave in vacuum

$$\sqrt{y} h^-(Q) = \sqrt{y} \exp(-ikQ) \quad (3.5)$$

is incident in the $-Q$ direction on this film. The vacuum wave number of this wave is k . In addition, there is a transmitted wave

$$t(x,y)\sqrt{y} h^-(Q) \quad (3.6)$$

and a reflected wave

$$r(x,y)\exp(-i2kx)\sqrt{y} h^+(Q) = r(x,y)\exp(-i2kx)\sqrt{y} \exp(ikQ). \quad (3.7)$$

Here, y is proportional to the intensity incident on the film, and the reflection and transmission coefficients are considered to be functions of the film thickness x and the "intensity" y .

The problem is to determine the reflectance $R = |r(x,y)|^2$, the transmittance $T = |t(x,y)|^2$, and the absorbance A , which must be defined from energy conservation, $A = 1 - R - T$. Within the film the field satisfies the wave equation

$$\left(\frac{d^2}{dQ^2} + k^2\right) E(Q) = -k^2 \chi(Q, E(Q)) E(Q) = V[Q, E(Q)^2] E(Q), \quad (3.8)$$

where $\chi = (-1$ is the (nonlinear) susceptibility for the film.

The traditional approach to such problems, for linear materials, would be to write the general solution within the film, and match the boundary conditions at each surface. The general solution can be written down in terms of the superposition of two counter-propagating beams, and this solution is independent of the intensity. This method is correct even if ϵ is a function of position. In the case of nonlinear materials one cannot write down a general solution within the film, and therefore cannot explicitly impose the boundary conditions. Furthermore, the principle of superposition is no longer valid since the wave equation is nonlinear. This makes it very difficult to write down the general solution in the film and to impose the boundary conditions at either side of the film. As a result, it is difficult to use the traditional approach, except in a perturbative fashion.

The invariant imbedding approach seeks to avoid these questions by eliminating the intermediate stage of computing the field within the film. In the traditional approach the field is used as an intermediate step in the calculation of $r(x,y)$ and $t(x,y)$. The objective of the invariant imbedding approach is to obtain equations that directly describe the dependence of these coefficients on the film thickness and intensity. The wave equation (3.8), subject to the above boundary conditions, can be written as an integral equation,

$$r(Q;x,y) = h^-(Q) + \int_0^x dq' G(Q|Q') V(Q',y) |r(Q';x,y)|^2 r(Q';x,y), \quad (3.9)$$

where $G(Q|Q')$ is the Green's function, a solution to

$$\left(\frac{d^2}{dQ^2} + k^2\right) G(Q|Q') = \delta(Q-Q'), \quad (3.10)$$

$$E(Q) = \sqrt{y} \psi(Q; x, y), \quad (3.11)$$

and $\psi(Q; x, y)$ is a renormalized field corresponding to a thickness x and incident field \sqrt{y} . Evaluating this expression at $Q = x$ and at $Q = 0^-$ and comparing with the previous forms for the reflected and transmitted waves gives

$$r(x, y) = \frac{e^{i2kx}}{2ik} \int_0^x h^-(Q') V[Q', y] |\psi(Q'; x, y)|^2 \psi(Q'; x, y) dQ' \quad (3.12)$$

$$t(x, y) = 1 + \frac{1}{2ik} \int_0^x h^+(Q') V[Q', y] |\psi(Q'; x, y)|^2 \psi(Q'; x, y) dQ'. \quad (3.13)$$

Band¹² has shown that by evaluating the derivatives of r and t with respect to x and y one obtains partial differential equations for r and t ,

$$\frac{\partial r}{\partial x} = \left(2ik - \frac{iV}{k}\right) r - \frac{iV}{2k} (1+r^2) + \frac{y}{k} \frac{\partial r}{\partial y} \operatorname{Im}\{(1+r)V\}, \quad (3.14)$$

and

$$\frac{\partial t}{\partial x} = \frac{-iV}{2k} (1+r) \tau - \frac{y}{k} \frac{\partial t}{\partial y} \text{Im}\{(1+r)V\}. \quad (3.15)$$

It is important to note that in these equations $V = -(\epsilon - 1)k^2$ should be understood to be

$$V = V[x, y | 1+r|^2]. \quad (3.16)$$

This means V is being evaluated at an intensity $y | 1+r|^2$ rather than the incident intensity y . Also, Im refers to the imaginary part of the argument. The solutions to these coupled, nonlinear partial differential equations (PDE's) for the complex coefficients are subject to the boundary conditions

$$r(0, y) = 0, \quad t(0, y) = 1. \quad (3.17)$$

Notice that the boundary conditions on the solutions in the x - y plane are now in the form of an initial-value problem in the sense that the conditions are imposed along only one line, the line corresponding to zero thickness.

The equations (3.14) and (3.15) were integrated by using a software package IDSS2 from Lehigh University. This package uses the numerical method of lines (NMOL), which is well suited to the type of initial-value posed by these equations and the boundary conditions (3.17). The algorithm begins with the solution along

the intensity (y) axis for $x = 0$. The variable y is discretized, and all partials with respect to y are approximated by finite differences. This transforms the PDE's into a system of coupled ordinary differential equations (ODE's). These are integrated, by any one of a variety of ODE solvers, in the direction of increasing thickness (x). As this integration proceeds the solutions in the y - x plane are returned along lines corresponding to a given thickness x .

III.2 RESULTS

The goal here is to study intensity-dependent absorption, but the absorbance can only be defined as $A = 1 - R - T$. In order to ensure that our solutions are reliable we must compare them with the literature wherever possible. The only other calculation using invariant imbedding that the author is aware of is that of Band¹³ for a nonabsorbing, spatially uniform nonlinear film. Not until some time after we had begun these calculations did we become aware of an exact solution to the spatially uniform film problem published by Chen and Mills.¹⁴ We will first report the results of the present calculations for this type film, and compare with those of Band, and Chen and Mills. Finally, we present the results including absorption.

III.2.1 NONLINEAR FILM WITHOUT ABSORPTION

Band solved the equations (3.14)-(3.15), but only for an

$\epsilon_{1,NL}$ corresponding to InSb, with no absorption included. His results indicated that even very thin films, with a thickness much smaller than the wavelength in the medium, show a nonlinear behavior which is most accurately described as hysteresis. He found that as the incident intensity is increased and then reduced to zero, the path of decreasing intensity was not the same as for increasing intensity. This was true regardless of how large the maximum intensity was. Chen and Mills have also treated this same problem for two types of materials, positive materials for which $\epsilon_{1,NL}$ is positive and negative ones for which $\epsilon_{1,NL}$ is negative. These correspond, respectively, to materials with indices of refraction that increase or decrease with increasing intensity. They have found that R exhibits bifurcations, or bistable, behavior for both type films, but only when the films are sufficiently thick. Their approach is applicable only to films without absorption or spatial variation of the optical properties, but has the advantage that T can be expressed in terms of Jacobi elliptic integrals, for which there are computer codes to evaluate them. Hence, they have an essentially exact treatment. There is no indication of the hysteretic behavior reported by Band.

We have computed R for $\epsilon_{1,L} = 4, 16, \text{ and } 36$, and for $\epsilon_{1,NL} = 4.6 \times 10^{-2} \text{ m}^2/\text{MW}$. Of these the choice $\epsilon_{1,L} = 16$ and $\epsilon_{1,NL} = -0.048 \text{ m}^2/\text{MW}$ correspond to the parameters chosen by Band. All of these may be compared with Chen and Mills. We find good comparison with Chen and Mills for both type films and all parameter combinations below certain thicknesses. Two cases,

$\epsilon_{1,L} = 16$ and $\epsilon_{1,NL} = 4.8 \times 10^{-2}$, are shown in the plots of R versus I and x in Figs. 13-14. These results are identical near $I = 0$, as they should be since that is the limit of linear behavior. The solutions at $I = 0$ are in excellent agreement with known results for linear films. Furthermore, one can clearly see the general increase (decrease) in R with increasing intensity for the positive(negative) films, as expected.

For these cases, with no absorption, energy conservation dictates that

$$R + T = 1. \quad (3.18)$$

Since this condition is not explicitly incorporated into the equations (3.14)-(3.15), so that an evaluation of $R + T$ is a direct means of checking the consistency of the solutions. Although it is not apparent from Figs. 13 and 14, in both cases (3.18) is not satisfied when the film thickness x approaches roughly $0.4 \lambda_f = 0.4 \lambda / n_L$, where λ_f is the wavelength in the film in the linear regime. This indicates the integration has become unstable.

A clue to what is happening comes from Figs. 15 and 16. In these figures the real and imaginary parts of $r(x,y)$ and $t(x,y)$ as a function of thickness are plotted for a low and a high intensity. Clearly, the derivatives $\partial r / \partial x$ and $\partial t / \partial x$ are diverging as I increases. Fig. 17 shows the dependence of R on x and I , which are curves formed by cuts through the $R(x,y)$ by planes perpendicular to the intensity axis. These cuts suggest

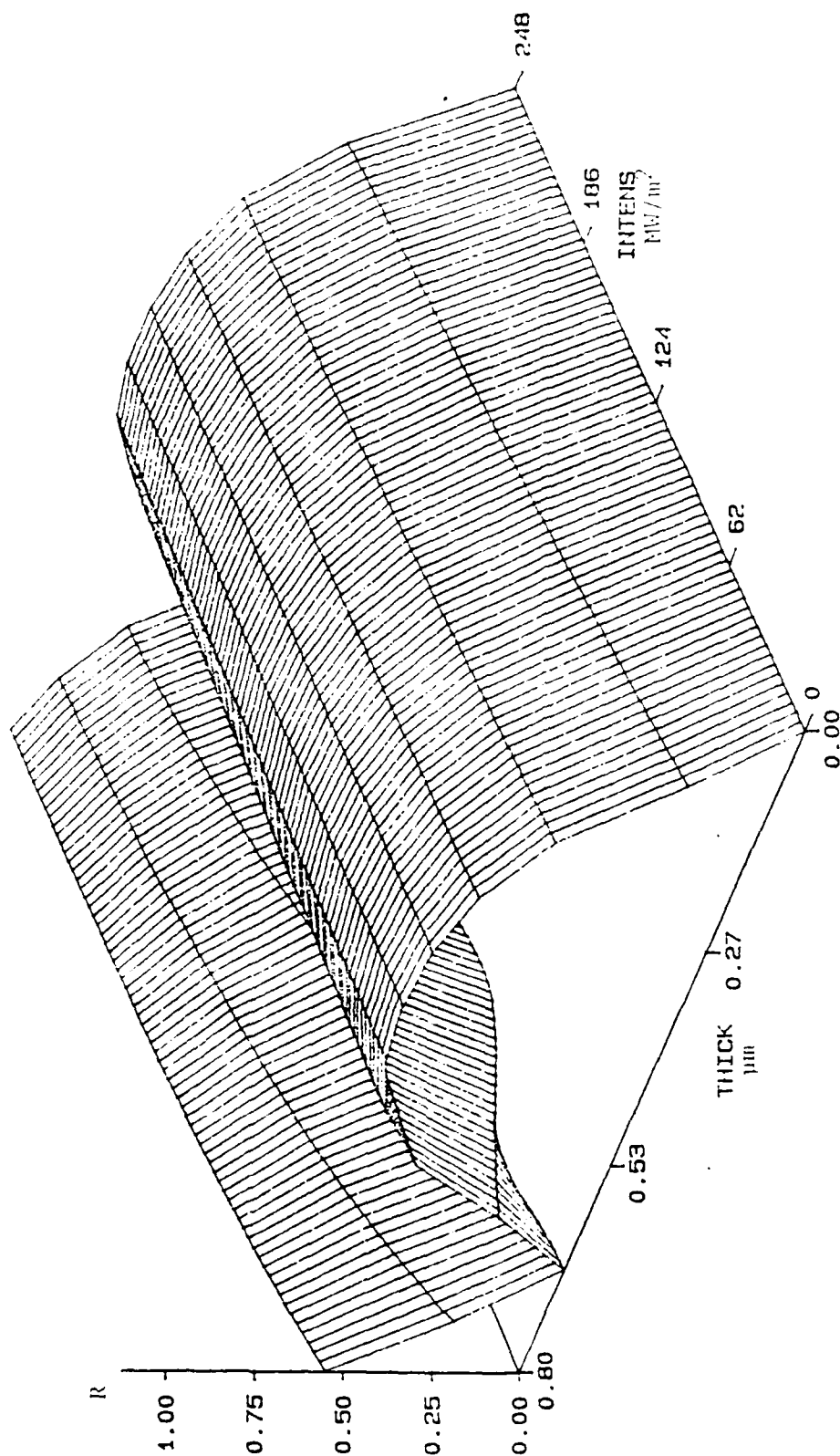


Fig. 13 Reflectance R for a positive film as a function of thickness and intensity for $\epsilon_1, \epsilon_2 = 16, \epsilon_3 = 1, n_L = 0.048 \text{ m}^2/\text{MW}$.

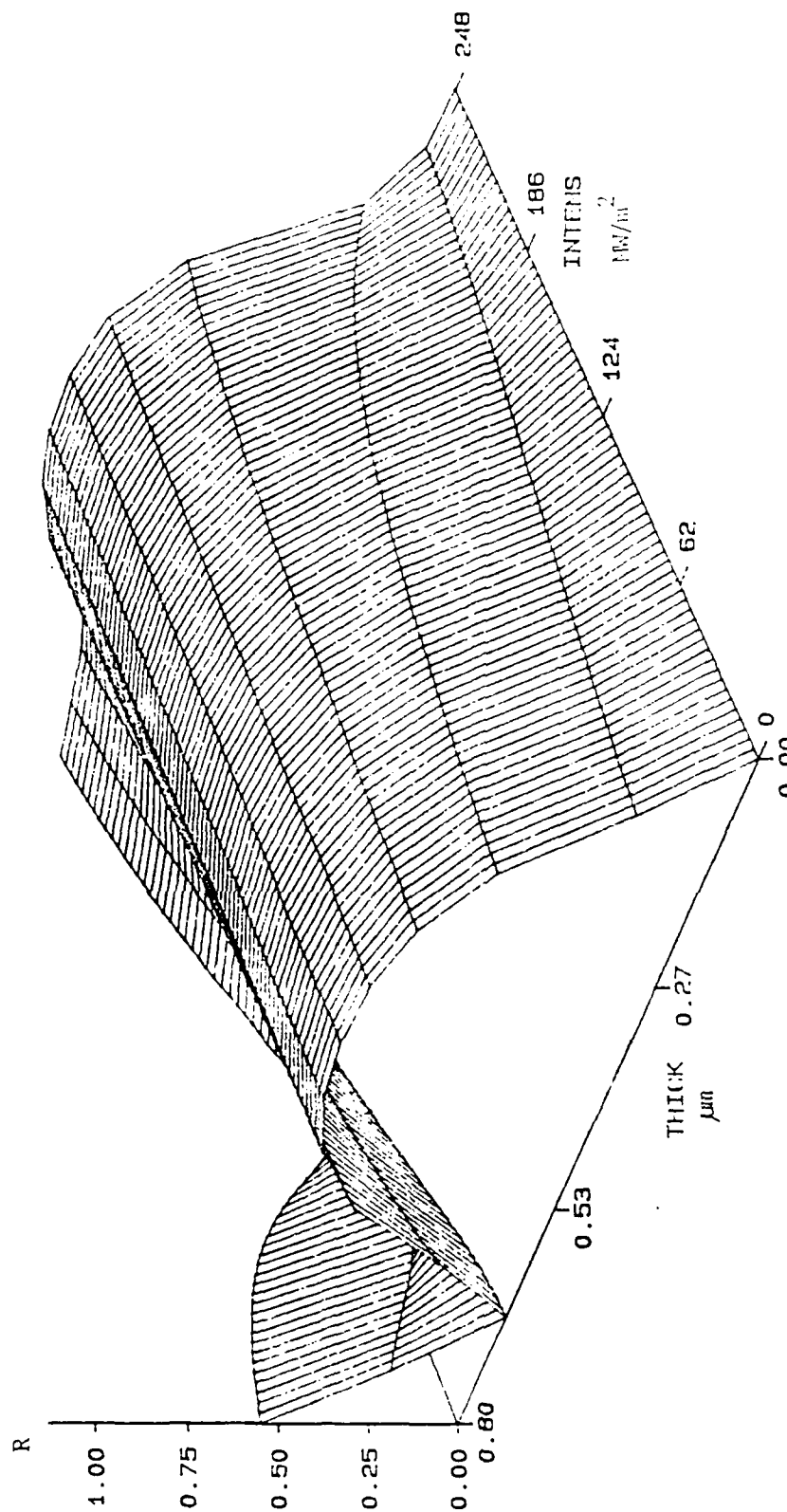
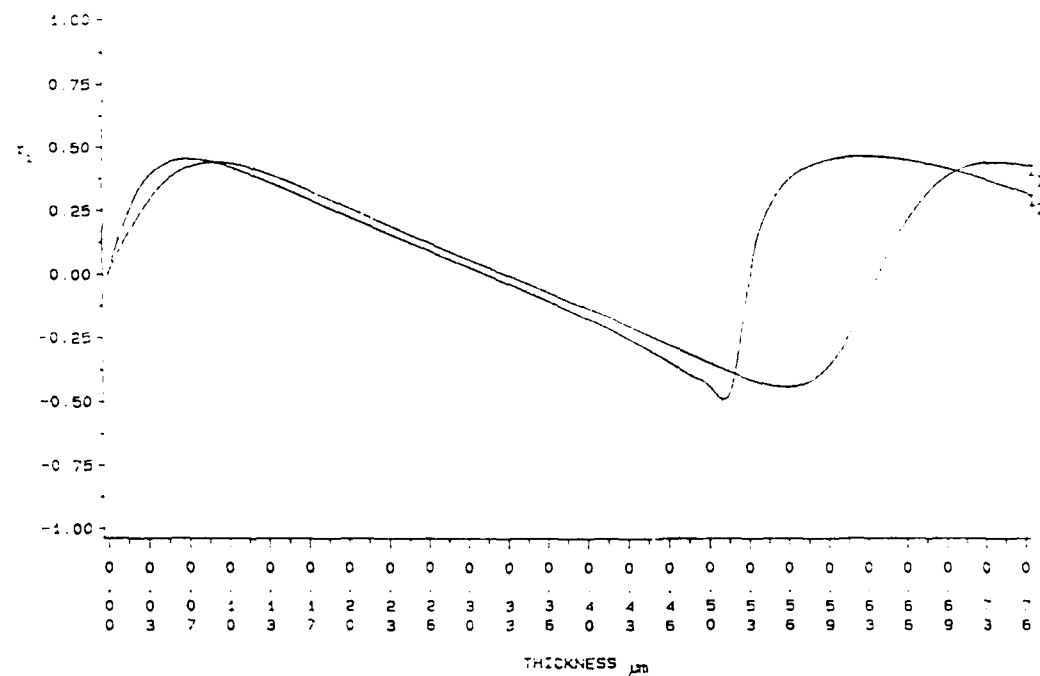


Fig. 14 Reflectance R for a negative film as a function of thickness and intensity for $\lambda = 16.7 \mu\text{m}$, $n = 1.48$, $k = 0.048$ m^2/MW



94-42

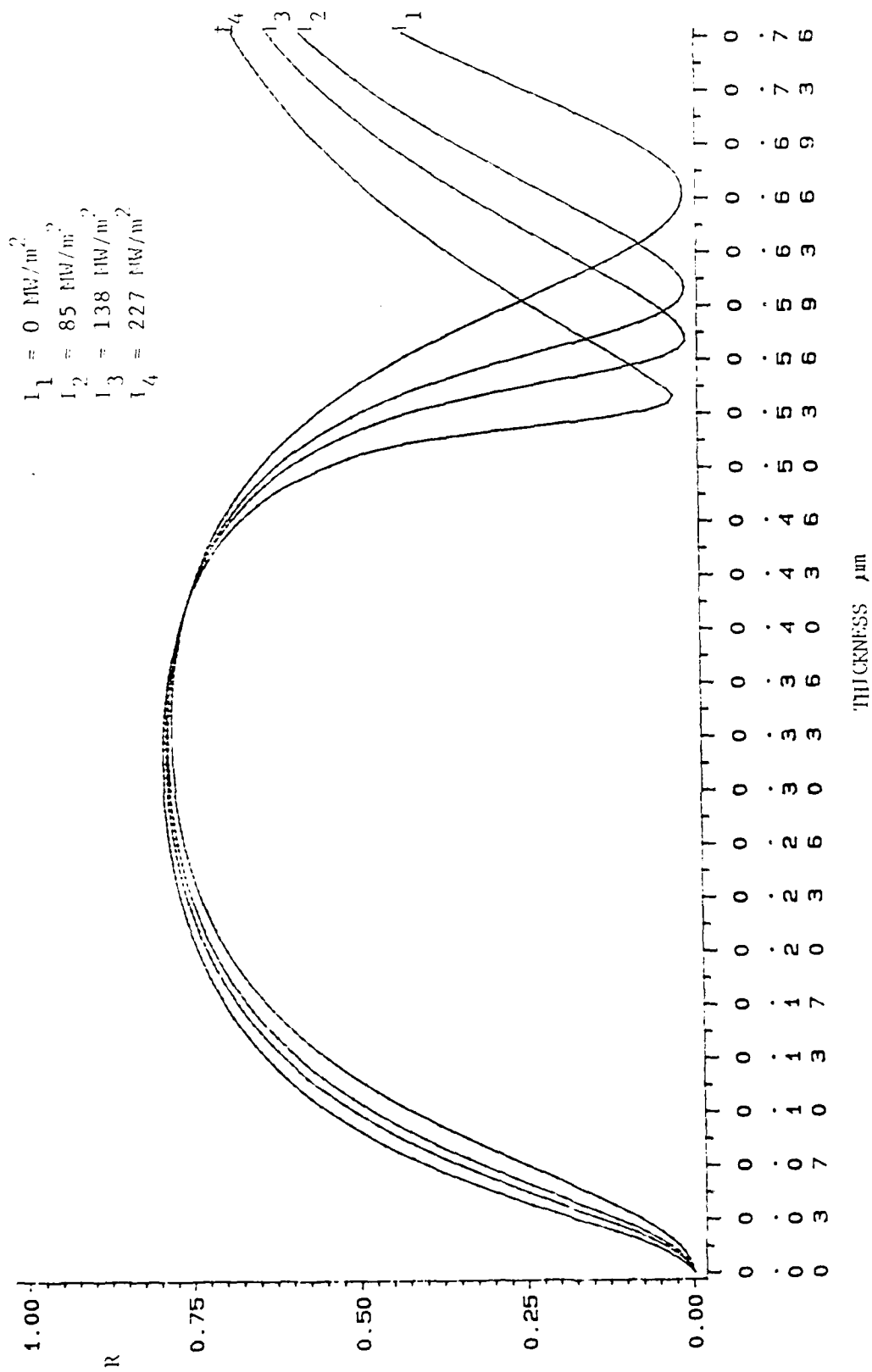


Fig. 17 Thickness dependence of R at various intensities, for the positive film of fig. 13

the following picture of this surface. For sufficiently thin films there is smooth dependence on x and y , but as x and y increase the surface develops a "fold" characteristic of a bifurcation or bistable state.

This behavior is in excellent qualitative agreement with the results of Chen and Mills.¹⁴ They observe bistability for films with a sufficiently high index of refraction for a thickness slightly smaller than $\lambda_f/2$. However, they find that $n_L \geq 6$ in order to show bistability, whereas we see it for $n_L = 4$. It should be noted that up to moderate intensities our calculations are in excellent quantitative agreement with theirs for all values of n_L . This is not surprising since this integration of the PDE's is bound to fail as one approaches such a fold. In this region the gradients become extraordinarily large, introducing instabilities into the computations which eventually propagate throughout the calculations. We have, in fact, been able to follow this.

The situation for the negative films is somewhat more disconcerting. Once again, there is excellent numerical agreement with their work over a wide intensity range up to $0.4 \lambda_f$, where we again see the emergence of instabilities, indicated by the violation of (3.18). Chen and Mills do not see this behavior until the film thickness is slightly larger than $\lambda_f/2$. Furthermore, the amplitudes $r(x,y)$ and $t(x,y)$, plotted in Figs. 18-19, show none of the singular behavior we witnessed for the positive film. This obviously implies a flaw in the computer code or solution algorithm, but this result persists despite all

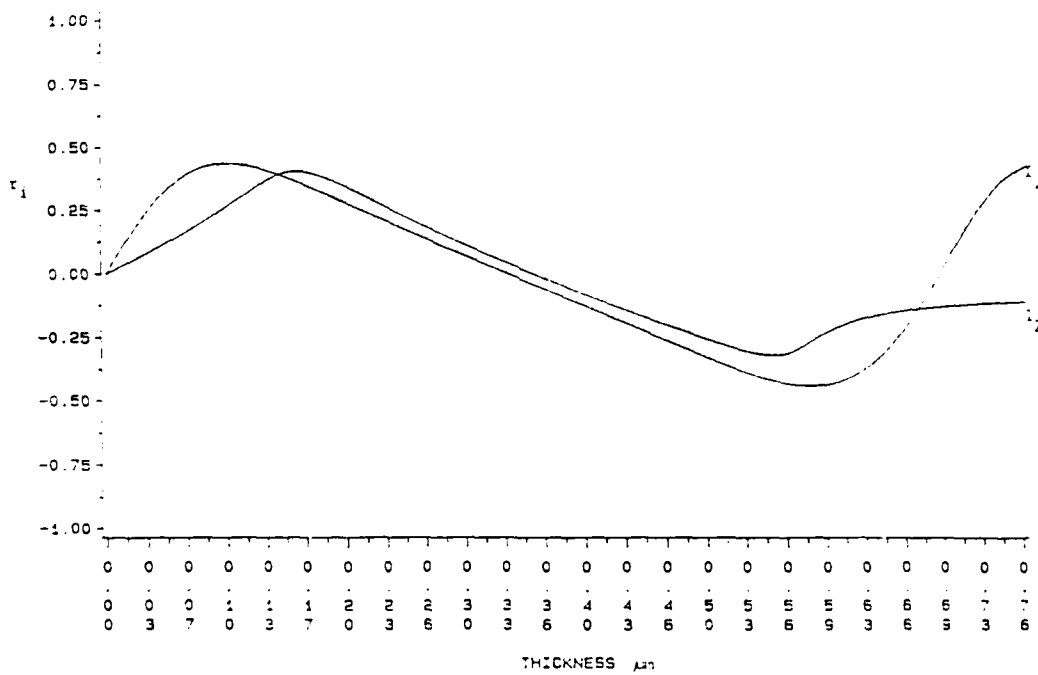
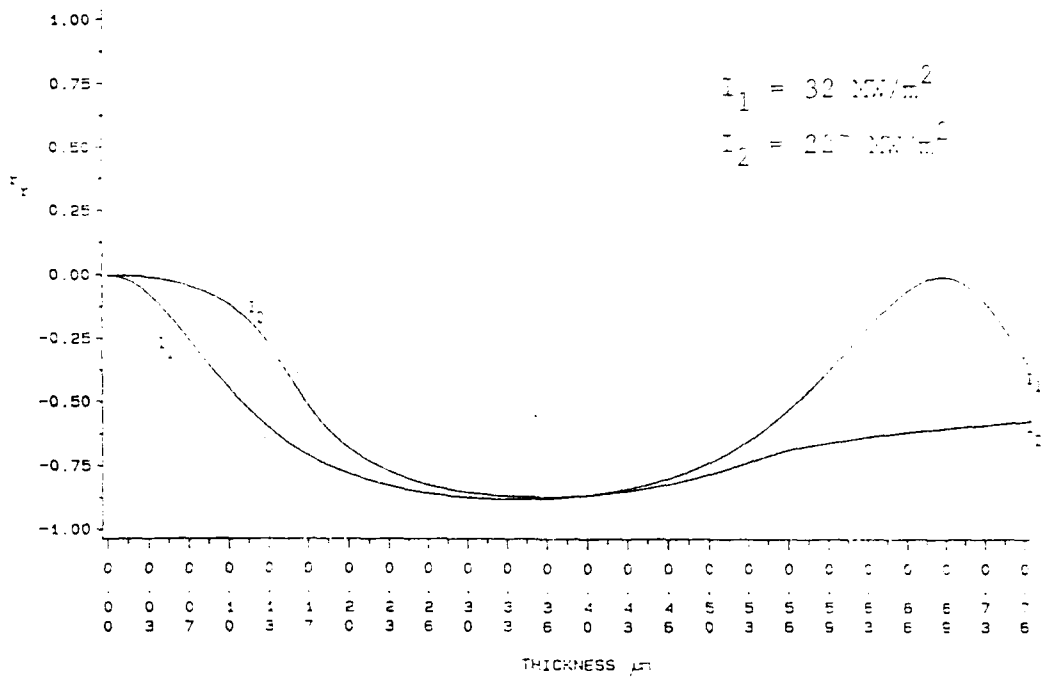


Fig. 15 Real and imaginary parts of the reflection coefficient for the negative film of Fig. 14

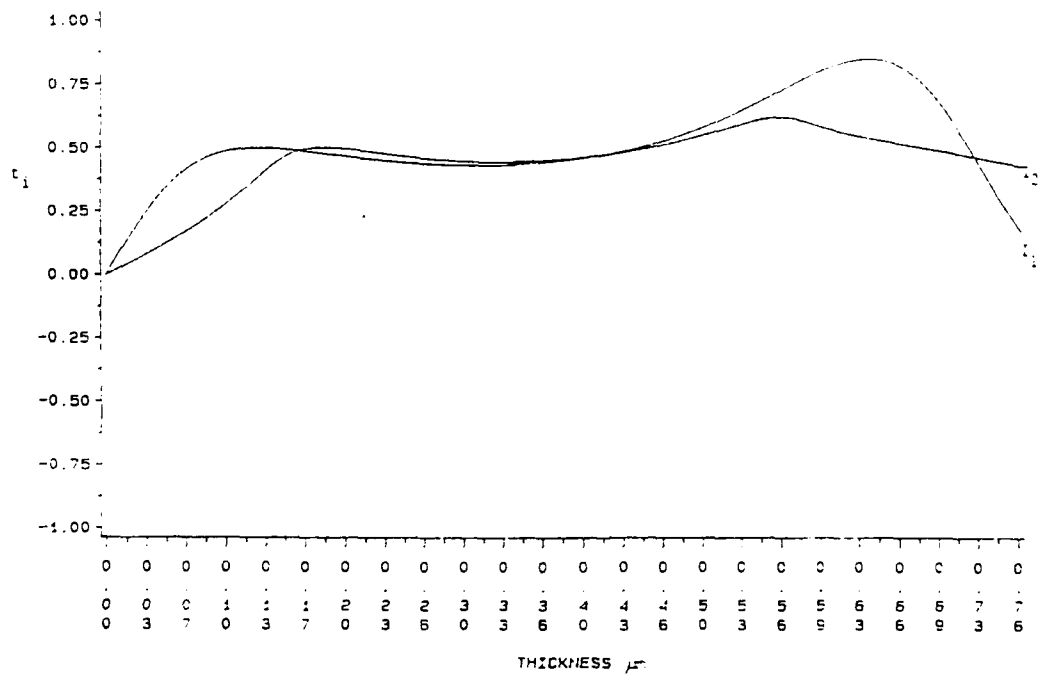
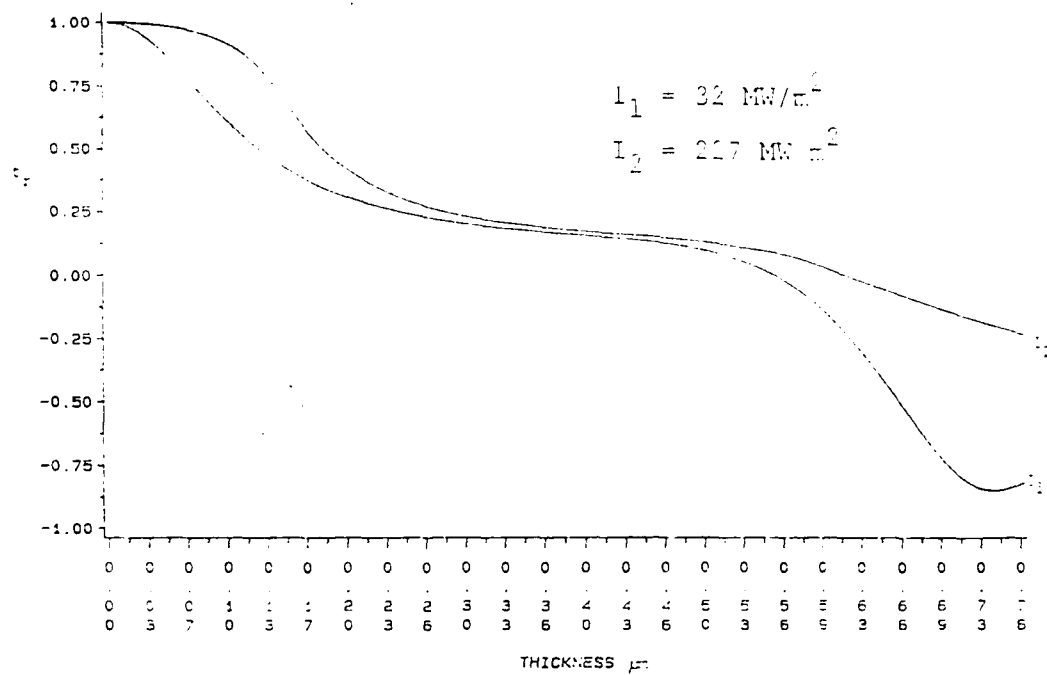


Fig. 19 Real and imaginary parts of the transmission coefficient for the negative film of fig. 14.

attempts to remedy it by using different grid sizes, integration step sizes, and different ODE solver algorithms. At this point we simply can not explain this behavior.

III.2.2 NONLINEAR FILM WITH ABSORPTION

We have mentioned that one of the attractive points about Band's formulation is that one can quite easily incorporate absorption, whether linear or nonlinear. We will present some results of calculations which include absorption, but one should note that it is difficult to interpret them. In the presence of absorption condition (3.18) is no longer valid, but must be replaced by

$$R + T + A = 1, \quad (3.19)$$

but this actually serves as the definition of the absorbance A , and as such no longer provides a gauge of the accuracy of the solutions. Given the preceding discussion we must view these results with some caution.

In general, the presence of absorption implies the loss of electromagnetic energy, and would imply a reduction of the field strength within the medium. Consequently, we would expect that adding absorption tends to dampen any effects observed in the absence of it. This is illustrated in Fig. 20, which compares the solutions for a linear film, ϵ_1 constant, for the cases of no absorption, $\epsilon_2 = 0$, and linear absorption, $\epsilon_2 = \text{constant}$. These

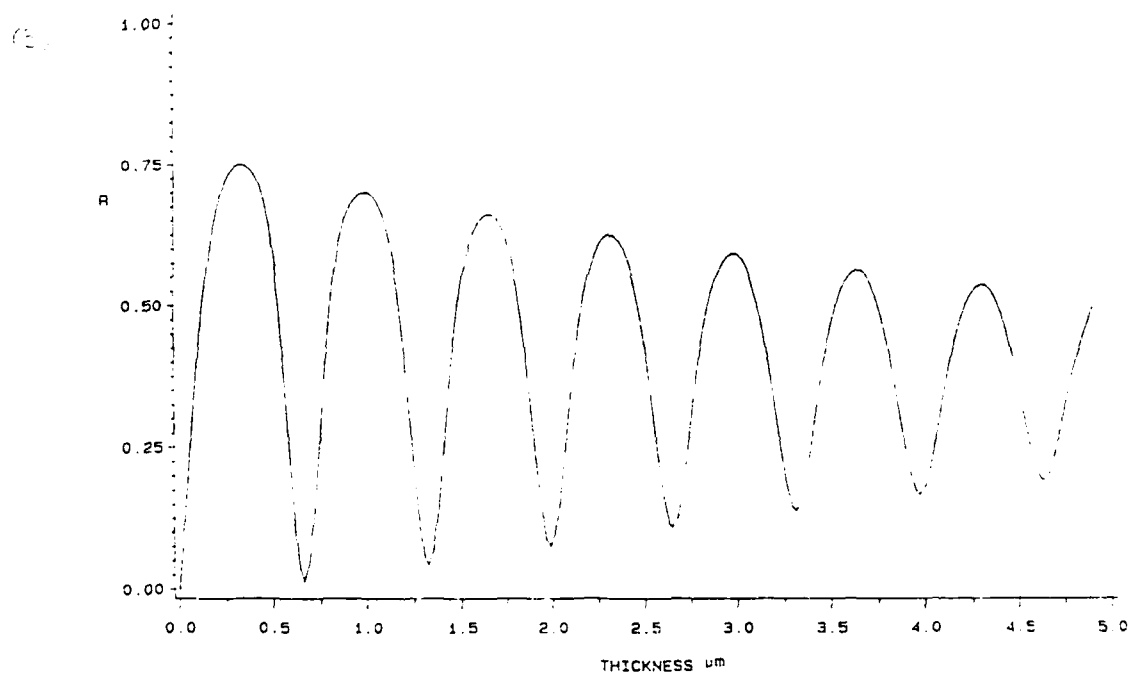
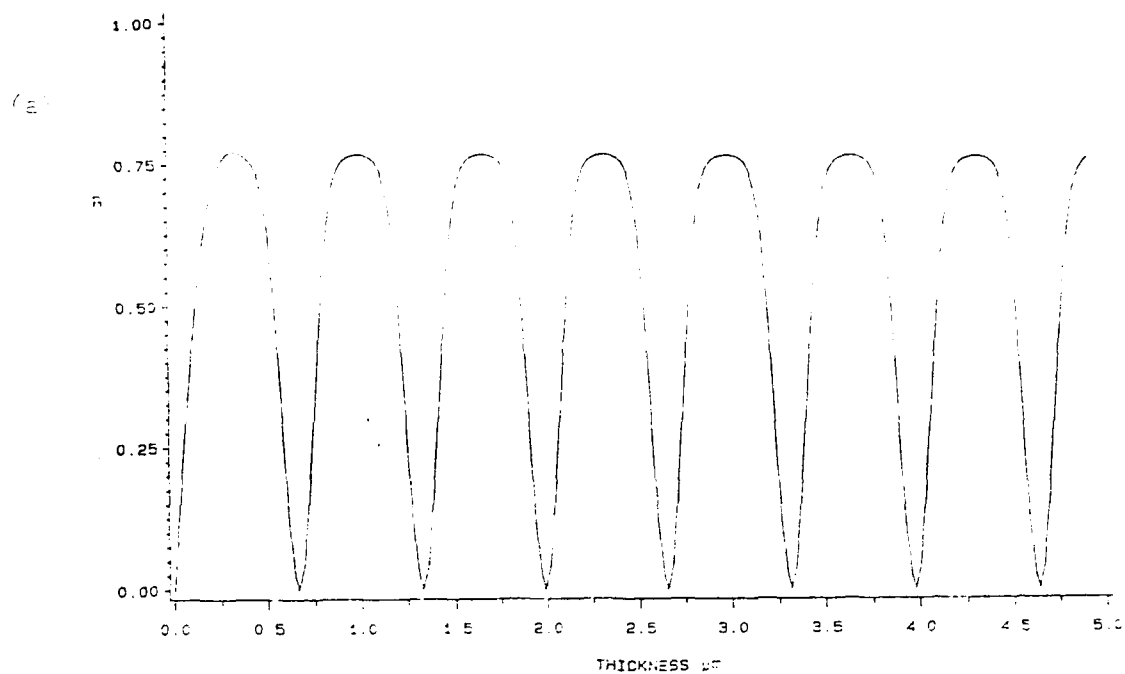


Fig. 20 Reflectance vs. film thickness for (a) a linear, non-absorbing film and (b) a linear, absorbing film.

solutions, which are in excellent agreement with well-known closed-form solutions, illustrate how absorption tends to damp the oscillatory behavior associated with standing wave resonances.

This same behavior is seen to carry over into the cases of nonlinear optical behavior. The effect of a linear, or constant absorption, in conjunction with a nonlinear dispersion is shown in Fig. 21. The parameters $\epsilon_{1,L}$ and $\epsilon_{1,NL}$ are as in Fig. 13, and $\epsilon_{2,L} = 0.728$, corresponding to InSb. As x increases the surface R for the absorbing film falls below the surface for the nonabsorbing film. The plots of Fig. 22 are of even more interest since they show that the divergent behavior of the gradient of $r(x,y)$ is no longer present, at least not at the thicknesses shown. This suggests that the absorption might delay or eliminate the onset of bistability.

Finally, in Fig. 23 we show the effect of nonlinear absorption in conjunction with linear dispersion. For these calculations $\epsilon_{1,L} = 16$, $\epsilon_{1,NL} = 0$, $\epsilon_{2,L} = .728$ and $\epsilon_{2,NL} = 0.05$ and $0.5 \text{ m}^2/\text{MW}$ respectively. This would approximately correspond to the SL with tunable absorption if one ignores the related changes in the index. In the latter case we see a dramatic damping in the reflectance behavior with increasing intensity.

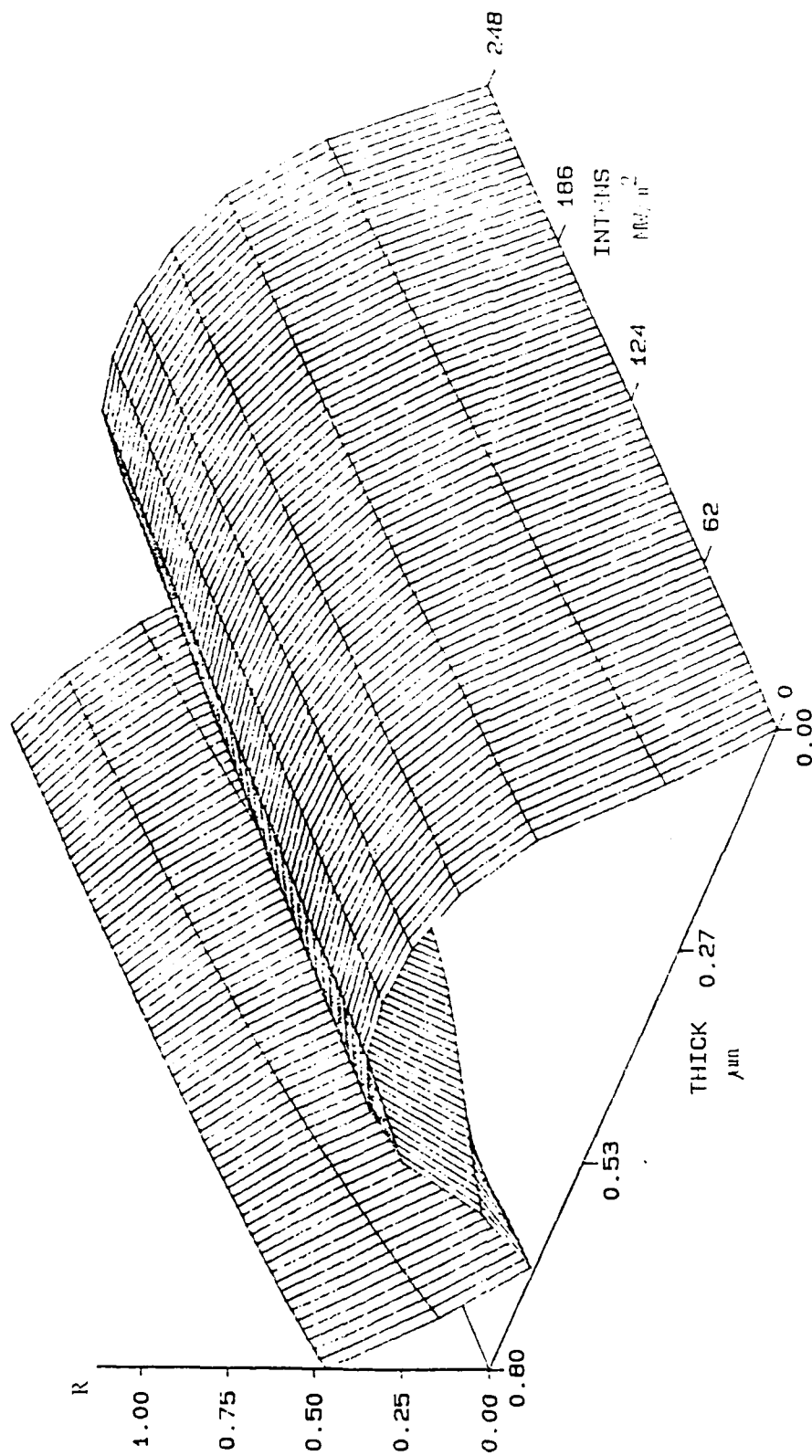
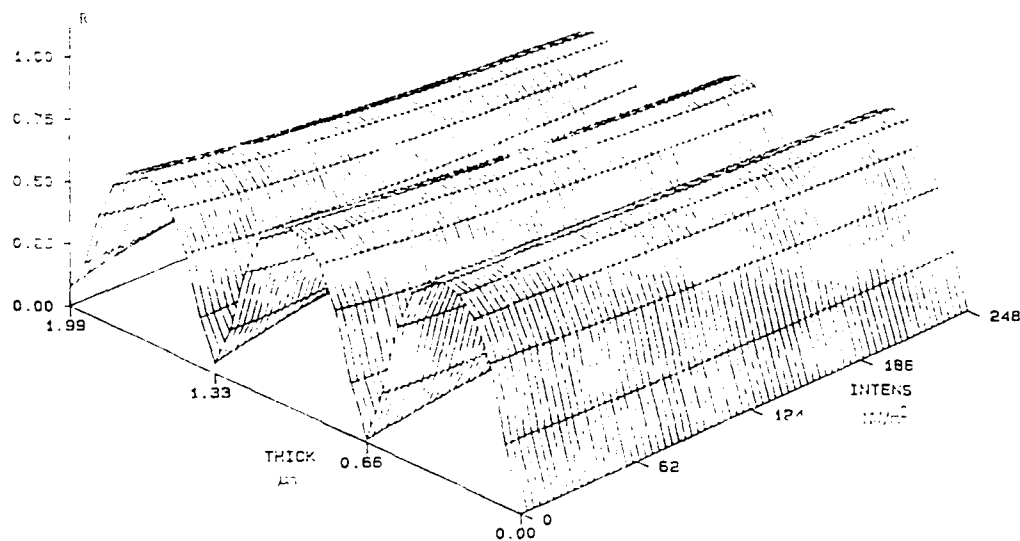


Fig. 21 Reflectance for a film with nonlinear dispersion and constant absorption; $\epsilon_{1,L} = 16$, $\epsilon_{1,NL} = .048 \text{ m}^2/\text{MW}$, and $\epsilon_{2,L} = .728$.

(a)



(b)

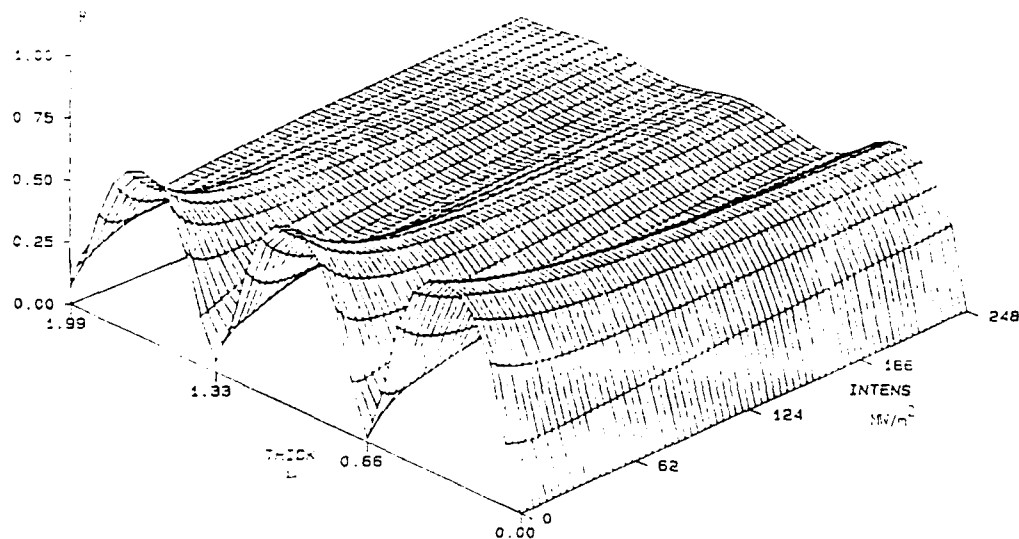


Fig. 23 Reflectance for films with linear dispersion and non-linear absorption: $\epsilon_{1,L} = 16$, $\epsilon_{1,NL} = 0$, $\epsilon_{2,L} = 0.728$. (a) Results for $\epsilon_{2,NL} = 0.05$ and (b) $\epsilon_{2,NL} = 0.5 \text{ m}^2/\text{MW}$

IV. SUMMARY

In this work we have successfully developed the computer codes necessary to compute the absorption coefficient α for a doping SL, within the framework of the semiclassical model of ref. 1. With this code we have studied the absorption for room temperature GaAs SL's, and demonstrated the tunability of these structures, although it is somewhat smaller than that calculated in ref. 1 for 4 K. This is largely attributable to the appreciable absorption tails of bulk material below the band edge for these doping levels at room temperature. Consequently, the contributions to (2.21) from the neutralized donor and acceptor sites in the layers of thicknesses d_n^0 and d_p^0 are larger, thereby reducing the relative importance of the tunable Franz-Keldysh term. This would appear to be unavoidable at these temperatures.

With this code one can now conduct a systematic series of calculations to search for the SL specifications providing the optimum tunability. At this stage, however, this program is not suitable for characterizing existing SL's. The main source of difficulty is in the determination of the contributions α_B^p and α_B^n from the doped bulk material. There is some inconsistency in the absorption data from various sources. Additionally, we have found that the fitting parameters of eq. (2.23) used to model the doping concentration of the absorption, do not show a smooth dependence on doping levels. It would appear that more absorption data near the band edge at a wider range of impurity

levels is desirable.

We can see that the invariant imbedding technique provides a direct and useful way to study wave propagation in nonlinear media, and, in particular, to include (nonlinear) absorption. Nevertheless, the presence of bistability or multistability in nonabsorbing media presents limitations to this approach. These PDE's are still useful, but require additional analytical methods to locate the regions of bistability and to modify the PDE's in these regions. The present results hint that absorption may delay, or even eliminate the bistability, but this conclusion is tentative. The solutions in the range of small absorption at low intensity, i.e. the linear absorption regime, agree excellently with known results, but there are few ways to check the code in the presence of strong nonlinear absorption.

Any future effort should concentrate on the computation of the reflectance, transmittance, and absorbance of thin films of SL material. This will require combining the previous results. It will be necessary to link the algorithm for finding c^{SL} to the method of excitation, in this case photoexcitation, to find the intensity dependence of α^{SL} . This will become input into the PDE's of the invariant imbedding method. The much more difficult stage will be finding computational methods to allow one to find solutions to these nonlinear PDE's in the regions of these "catastrophes" representing the transitions between bistable or multistable states.

IV. SUMMARY

In this work we have successfully developed the computer codes necessary to compute the absorption coefficient α^{SL} for a doping SL, within the framework of the semiclassical model of ref. 1. With this code we have studied the absorption for room temperature GaAs SL's, and demonstrated the tunability of these structures, although it is somewhat smaller than that calculated in ref. 1 for 4 K. This is largely attributable to the appreciable absorption tails of bulk material below the band edge for these doping levels at room temperature. Consequently, the contributions to (2.21) from the neutralized donor and acceptor sites in the layers of thicknesses d_n^0 and d_p^0 are larger, thereby reducing the relative importance of the tunable Franz-Keldysh term. This would appear to be unavoidable at these temperatures.

With this code one can now conduct a systematic series of calculations to search for the SL specifications providing the optimum tunability. At this stage, however, this program is not suitable for characterizing existing SL's. The main source of difficulty is in the determination of the contributions α_B^D and α_B^N from the doped bulk material. There is some inconsistency in the absorption data from various sources. Additionally, we have found that the fitting parameters of eq. (2.23) used to model the doping concentration of the absorption, do not show a smooth dependence on doping levels. It would appear that more absorption data near the band edge at a wider range of impurity

levels is desirable.

We can see that the invariant imbedding technique provides a direct and useful way to study wave propagation in nonlinear media, and, in particular, to include (nonlinear) absorption. Nevertheless, the presence of bistability or multistability in nonabsorbing media presents limitations to this approach. These PDE's are still useful, but require additional analytical methods to locate the regions of bistability and to modify the PDE's in these regions. The present results hint that absorption may delay, or even eliminate the bistability, but this conclusion is tentative. The solutions in the range of small absorption at low intensity, i.e. the linear absorption regime, agree excellently with known results, but there are few ways to check the code in the presence of strong nonlinear absorption.

Any future effort should concentrate on the computation of the reflectance, transmittance, and absorbance of thin films of SL material. This will require combining the previous results. It will be necessary to link the algorithm for finding ϵ^{SL} to the method of excitation, in this case photoexcitation, to find the intensity dependence of α^{SL} . This will become input into the PDE's of the invariant imbedding method. The much more difficult stage will be finding computational methods to allow one to find solutions to these nonlinear PDE's in the regions of these "catastrophes" representing the transitions between bistable or multistable states.

REFERENCES

1. Dohler, G.H., H. Kunzel, and K. Ploog, "Tunable absorption coefficient in GaAs doping superlattices," Phys. Rev. B, 1982, Vol. 25(4), pp. 2616-2626.
2. Keldysh, L.V., "The effect of a strong electric field on the optical properties of insulating crystals," Soviet Phys. JETP, 1958, Vol. 34(7), pp. 788-790.
3. Abidi, S.T.H. and S. Noor Mohammad, "Approximation for the Fermi-Dirac integral with applications to degenerately doped solar cells and other semiconductor devices," J. Appl. Phys., 1984, Vol. 56(11), pp. 3341-3343.
4. Casey Jr., H.C., D.D. Sell and K.W. Wecht, "Concentration dependence of the absorption coefficient for n- and p-type GaAs between 1.3 and 1.6 eV," J. Appl. Phys., 1975, Vol. 46, pp. 250-257.
5. Aspnes, David E., "Electric-field Effects on Optical Absorption near Thresholds in Solids," Phys. Rev., 1966, Vol. 147(2), pp. 554-565.
6. Aspnes, D.E. and N. Bottka, "Electric-Field Effects on the Dielectric Function of Semiconductors and Insulators," Semiconductors and Semimetals, Vol. 9, Modulation Techniques, R.K. Willardson and A.C. Beer eds., Academic Press, New York, 1972, pp. 457-543.
7. Abramowitz, M. and I.A. Stegun, Handbook of Mathematical Functions, Dover Publ., New York, 1970, pp. 446-450.
8. Kane, E.O., "Band Structure of Indium Antimonide," J. Phys. Chem. Solids, 1957, Vol. 1, pp. 249-261.
9. Kane, E.O., "Energy Band Structure in p-Type Germanium and Silicon," J. Phys. Chem. Solids, 1956, Vol. 1, pp. 82-99.
10. Moss, T.S. and T.D.F. Hawkins, "Infrared Absorption in Gallium Arsenide," Infrared Physics, 1961, Vol. 1, pp. 111-115.
11. Bellman, R and R. Vasudevan, Wave propagation: An Invariant Imbedding Approach, D. Reidel Publishing Co., 1986.
12. Band, Y.H., "Reflection and transmission coefficients for nonlinear media: Self-induced transmission, amplified reflection, phase conjugation, third harmonic generation, second harmonic generation," J. Appl. Phys., 1982, Vol. 53, pp. 7240-7246.
13. Band, Y.H., "Optical bistability in nonlinear media: An exact method of calculation," J. Appl. Phys., 1984, Vol. 56, pp. 656-659.
14. Chen, W., and D.L. Mills, "Optical response of a nonlinear dielectric film," Phys. Rev. B, 1986, Vol. 35(2), pp. 524-532.

JOINING OF CARBON-CARBON
COMPOSITES

FINAL REPORT

to

Universal Energy Systems, Inc.

4401 Dayton-Xenia Road

Dayton, Ohio 45432

for

Air Force Office of Scientific Program

Research Initiation Program

by

Parviz Dadras

Mechanical and Materials Engineering

Wright State University

Dayton, Ohio 45435

(November 14, 1989)

JOINING OF CARBON-CARBON COMPOSITES

by

P. Dadras

ABSTRACT

Solid-state diffusion bonding and brazing of c-c composites have been investigated. Molybdenum disilicide (MoSi_2) and titanium (Ti) have been used as interlayers. The effects of processing parameters such as diffusion time and temperature, and the interface contact pressure on the strength of the joints have been evaluated. The shear strength of the joints has been determined by conducting double-notch shear tests at room and at elevated temperatures. Other joint geometries such as T-joints and butt-joints have also been examined. The microstructures of the joints have been studied and a selected number of joints has been analyzed by electron microprobe.

It has been determined that strong joints can be produced by using MoSi_2 interlayers. In these cases, the shear strength of the joints have been found to exceed the interlaminar shear strength of the c-c composite materials. The shear strengths of the titanium joints have been found to be lower and for most cases they are less than 1000 psi (6.895 MPa).

I. ACKNOWLEDGEMENT

This project was supported by a Research Initiation Program Mini-Grant under the follow-on to the Summer Faculty Research Program sponsored by Universal Energy Systems for the Air Force Office of Scientific Research. The assistance and guidance of Mr. Steve Szaruga. AFVAL/MLBC is greatly appreciated.

II. Introduction

Joining of carbon-carbon components to each other and to other materials is becoming increasingly important as new applications for larger and more complex c-c composite structures are encountered. New developments in the science and technology of c-c composite joining are needed so that reliable joints can be produced which will retain their strength at elevated temperatures and will withstand thermal cyclings and other service conditions expected for c-c materials. At present, only some information on joining graphite can be found in the open literature [1-9]. In most of these works, however, the strength of the joint under different modes of loading and at high temperatures have not been evaluated.

In this project joining of c-c composites has been investigated. The employed processes and materials are based on the available knowledge on joining graphite and ceramic materials. Therefore, some preliminary steps such as wettability and flow characterizations have not been attempted in this project. Molybdenum disilicide (MoSi_2) and titanium (Ti) interlayers under different conditions for solid-state diffusion bonding and brazing have been investigated. Only uncoated c-c composites have been used, as it is assumed that the coating process will normally follow the joining operation. The strength of the joints at different temperatures have been determined and the microstructures of the bonded regions have been examined.

III. OBJECTIVES

Joining of c-c composite material to itself is the objective of this project. The joints are required to retain sufficient strength at the expected service temperatures. It is the objective of this project to produce joints and to evaluate them with respect to microstructure and mechanical properties.

IV. Experimental

The bonding operations and the high temperature mechanical tests were conducted in a front loaded graphite vacuum furnace. The hot zone for this furnace is 4 inches in diameter and 8 inches high. The furnace is designed for operation under vacuum at temperatures up to 2200°C (3992°F) and in an inert gas atmosphere up to 2400°C (4352°F). The furnace is equipped with thermocouple gauge tubes, a high vacuum ionization gauge and digital autoranging ionization controller. A Honeywell digital controller programmer DCP-700 is used to generate the desired heating schedules. Temperature was measured by a tantalum sheathed tungsten 5% Rh/tungsten 26% Rh thermocouple for $T < 1700^{\circ}\text{C}$. An Ircon Modline R dual-wave length optical pyrometer was also used for measuring temperatures $1100^{\circ}\text{C} < T < 2500^{\circ}\text{C}$. The furnace is mounted on an 1123 Instron with 25 KN load capacity. The load train inside the furnace consist of T-6 graphite push rods and c-c composite fixtures.

Solid-state diffusion bonding and brazing operations were performed on c-c composite specimens of various geometries. Double-notch shear specimens (Fig. 1) were used most often. In these tests two rectangular

pieces of c-c composite were bonded flatwise together in vacuum under controlled pressure and temperature conditions. After the bonding operation and cooling down to room temperature, the specimens were removed from the test chamber and two half-depth notches (Fig. 1) were machined on each specimen. In cutting these notches it is of primary importance that the notches extend accurately to the plane of the bonding so that a preferred fracture plane along the bonded surface would exist. The double-notch shear specimens were tested under compressive loading at different temperatures and the shear strength of the bond, based on the fracture load and the area between the two notches, was determined.

A limited number of tension specimens were tested for evaluating butt joints in tension. These specimens consisted of two halves of a tension specimen which were butt jointed together while under compressive loading applied through two 0.25 inch diameter c-c loading pins, shown in Fig. 2. Tensile loading of the joints was accomplished by applying tensile loading through the same c-c loading pins.

T-joints and modified T-joints (Fig. 3) were also investigated. These joints were tested in tension in a special fixture developed for high temperature testing of these specimens (Fig. 4).

Three disk-and-rod shear tests (Fig. 5) were also performed. In these tests c-c composite round bars of 0.5 inch diameter were machined from a 1 inch thick K-Karb c-c panel. These bars were brazed to 1 inch thick c-c composite disks which were made from the same K-Karb panel. The joints were then tested in shear (Fig. 5B) at 1400⁰ C.

The c-c composite materials used in this project were provided by

different manufacturers. A K-Karb Type A panel of 0.25 inch thickness was provided courtesy of Kaiser Aerotech. A C-CAT-4 panel was obtained from Carbon-Carbon Advanced Technologies, Inc. This panel was made of 22 plies of heat stabilized (4800⁰F) T-300, 8 harness satin weave fabric. The fabric was pre-pregged with Fiberite K 641 and the ply orientations were 0⁰ and 90⁰. A 3 x 8 x 0.2 inch panel of ACC-4 c-c composite material 1107/K604 was provided courtesy of LTV Aerospace and Defense Company. This panel consisted of 17 plies all 0⁰ warp aligned.

The machined specimens were outgassed at 2000⁰C for 10 minutes prior to the brazing operation. The outgassing step is needed because the maximum processing temperatures for some of the c-c materials are lower than the employed bonding temperatures. Also, any contaminants picked up during handling and fabrication can be burned off in this stage.

Different interlayer materials were used for bonding. Molybdenum disilicide MoSi₂ and titanium were investigated more extensively. Both 99.+% and 99.9% MoSi₂ powders were used. The -200 mesh titanium powder was 99.7% pure. Other interlayers consisted of -325 mesh silicon powder (99%) and -250 mesh, 99.9% purity molybdenum powder. In each case, an ethanol slurry of the powder was prepared and brushed on the faying surfaces of the specimen. The specimen was then placed in the vacuum furnace between the graphite push rods and force was applied until the desired interfacial pressure was reached. After achieving a vacuum of 2×10^{-5} torr or better, power was applied to the graphite heating elements at the programmed heating rates of 50 to 70⁰C per minute and for the appropriate soak times to perform bonding or testing of the

specimen.

During the heating process, due to thermal expansion of the specimen and the push rods, the contact force tends to increase steadily with temperature. To maintain a constant force, the load cycling unit of the Instron in the hold mode was used. In this manner, the applied load was maintained at a constant mean level with superimposed cyclic fluctuations of about 8N (1.8 lb) amplitude. Since the amplitude of the fluctuations was less than 4 percent of the mean load in all the experiments, a constant load condition was assumed to exist.

V. Results and discussions

1. Double-notched shear specimens

a. Molybdenum disilicide interlayers

The bondings were performed at different temperatures from 1270⁰C (2318⁰F) to 2050⁰C (3722⁰F). Solid-state diffusion bonding of a K-Karb specimen at 1270⁰C for 30 minutes and under an interfacial contact pressure of 90 psi (0.62 MPa) produced a joint shear strength of 893 psi (6.16 MPa) at room temperature. This value represents the lowest joint strength for bonding with a 99.+% MoSi₂ interlayer. This indicates that at this relatively low temperature ($T/T_m=0.67$, where $T_m=2303$ K) only a weak bond can be produced. Increasing the bonding temperature to 1700⁰C, and the interface pressure to 360 psi (2.48 MPa), while decreasing the diffusion time to 20 minutes produced a room-temperature joint shear strength of 2446 psi (16.87 MPa). This strength is substantially larger than the room-temperature interlaminar

shear strength (ILSS) of K-Karb, 2-D, c-c composites which is reported at an average value of 1258 psi (8.67 MPa) [10]. For this specimen the fracture surface consisted of about sixty percent c-c material and forty percent MoSi_2 . This indicates that because of the higher strength of the bond, the fracture path deviates from the plane of maximum shear stress, i.e. the plane of the bond, and progresses for the most part through the c-c material. As long as the fracture planes are composed of c-c and bond materials, the actual shear strength of the bond will depend on the ILSS of the c-c material, and its value will be different from the joint shear strength which is the average shear stress based on the load at fracture and the area between the two notches. An estimate of the bond shear strength can be obtained by using a simple model shown in Fig. 6. In this figure, A_c and A_b represent portions of the fracture surface which consist of the c-c and bonding materials, respectively. For the limiting case when $A_b = A$, fracture occurs entirely through the bonded interface. In this case the average bond strength is

$$\tau_b = (F_f/A) \quad (1)$$

where F_f is the fracture load and A is the area between the roots of the notches in double-notch shear specimen. This limiting case will happen for weak bonds when the strength of the bond τ_b is less than or equal to (τ_c/η) , where $\eta < 1$ is a factor associated with a lower value of shear stress acting on a possible c-c fracture plane which commonly lies one ply thickness away from the bonded interface where the maximum shear stress occurs, and τ_c is the ILSS of the c-c composite. For a case when

τ_b is much greater than (τ_c/η) the fracture may become entirely limited to the c-c material, away from the bonded interface. In such a case, $A=A_c$ and the stress on the fracture plane will be equal to τ_c . Therefore, the bond strength in this limiting case is

$$\tau_b \geq (\tau_c/\eta) \quad (2)$$

For the more prevalent cases where the fracture surface consists of patches of c-c and some regions of the bonded material, a linear interpolation between the limiting cases results in the following relationship

$$\tau_b = (A_b/A) (F_f/A) + (A_c/A) (\tau_c/\eta) \quad (3)$$

An estimate of η is required in order to use the above equation. The average ply spacing for 2-D, c-c composites is about 0.012 inch (0.305 mm) [10]. For a plane located 0.012 inch from the bonded interface (plane of maximum shear stress) a very rough estimate of the average shear stress is $\tau = 0.5 \tau_{\max}$ [11]. For the specimen under consideration, based on $\eta=0.5$, and experimental values for $A= 0.125 \text{ in}^2$ (80.64mm^2), $A_c=0.6A$, $A_b=0.4A$, $\tau_c=1258 \text{ psi}$ (8.67 MPa), and $F_f=305.8 \text{ lb}$ (1360N), the estimated bond shear strength is $\tau_b=2488 \text{ psi}$ (7.15 MPa). This value is only slightly higher than the nominal joint shear strength which is $\tau = (F_f/A) = 2446 \text{ psi}$ (16.87 MPa) for this specimen.

Interfacial pressure enhances bond formation by promoting stress-assisted solid-state diffusion, and by providing for greater intimacy at

the interfaces between the interlayer and the faying surfaces. Additionally, a denser and stronger bonded region can be produced due to the effect of pressure on compaction in the hot sintering of the interlayer powder that occurs during the bonding operation. An exhaustive study of the effect of pressure was not attempted in this project. This was decided because in most industrial bonding operations, due to the complexity of part geometry and equipment limitations, it is not possible to apply high interfacial pressures. In any case, for the present system it was found that by increasing the interface pressure from 92 psi (0.62 MPa) to 360 psi (2.48 MPa) the joint shear strength at 1200°C increased from 1404 psi (9.68 MPa) to 2068 (14.26 MPa). These specimens were diffusion bonded at 1700°C for 30 minutes durations.

In addition to interface pressure, bonding time and temperature also affect the strength and characteristics of the bond. Numerous experiments are required to determine the optimum bonding conditions for any given system. Moreover, since the strength of the bond varies with testing temperature, the optimum bonding conditions for producing maximum bond strengths at different temperatures will also depend on the intended service temperatures. In this project the shear strength of the joints were determined at room temperature, 1200°C, 1400°C, and 1600°C. Also, bonding temperatures for solid-state diffusion bonding and for brazing were investigated. It is to be noted that the melting point of MoSi_2 is commonly stated either as $2030 \pm 20^\circ\text{C}$, or 2010°C [12]. However, according to Johnson Matthey-Alpha Products, the supplier of 99.9% MoSi_2 , the melting point is 1870-2030°C. In this project

evidences of melting, such as flow of molten MoSi_2 out of the bonded area, and a definite change of fracture surface from a coarse, dull gray to a smoother and shinier appearance were observed for all the specimens which were bonded at 1900°C and higher.

Amongst the many factors that affect the bond strength are the specific c-c material characteristics such as porosity and surface morphology. Three c-c materials, namely ACC-4, K-Karb, and C-CAT were bonded at 1700°C for 20 minutes, under an interfacial pressure of 100 psi (0.69 MPa), and they were all double-notch shear tested at 1400°C . 99.+% MoSi_2 was used in all cases. The results are shown in Fig.7. The highest strength value of 2986 psi (20.59 MPa) was obtained for the C-CAT specimen. The reported open porosity for heat treated C-CAT is 10%, while for ACC-4 and K-Karb it is 7% [10,13]. As already mentioned, for a specimen whose fracture surface consists of patches of c-c and the bonding material, the overall nominal joint shear strength is a function of bond strength and the interlaminar shear strength of the c-c composite material. The reported ILSS values for ACC-4, K-Karb, and C-CAT 2D c-c composites are 1200 psi (8.27 MPa), 1258 psi (8.67 MPa), and 840 psi (5.79 MPa) [10,13], respectively. It then seems reasonable to assume that the contribution of a higher open porosity to the joint shear strength for C-CAT more than compensates the effect of a lower ILSS for the composite material. Obviously, more tests are needed to substantiate these results more definitely.

Two ACC-4 specimens were solid-state diffusion bonded with 99.+% MoSi_2 at 1700°C for 20 minutes under 100 psi (0.69 MPa) interfacial pressure. These specimens were double-notch shear tested at 1200°C and

1400°C and the joint shear strengths were found as 2468 psi (17.02 MPa) and 1925 psi (13.27 MPa), respectively. This indicates a 22% decrease in strength as a result of 200°C increase in the test temperature. Later in this section it will be shown that the pattern of dependence of shear strength on the test temperature is somewhat complicated and that it does not follow the variations in the strength of MoSi₂ with temperature. The yield strength of MoSi₂ is 170 MPa (24.66 ksi) at 22°C, 138.8 MPa (20.1 ksi) at 1200°C, and it drops sharply to 18.6 MPa (2.7 ksi) at 1400°C [12].

Another unique characteristic of MoSi₂ is that it undergoes brittle-to-ductile transition at about 1000°C. Therefore, while it is brittle at room temperature, it has pronounced plasticity at temperatures greater than 1000°C. In addition to the changes in the mechanical properties of MoSi₂, the variations of the interlaminar shear strength of the C-C material with temperature will also affect the observed differences in the joint shear strength values. The ILSS of ACC-4 increases from 1200 psi (8.27 MPa) at room temperature to about 1900 psi (13.1 MPa) at 1600°C. As a result, an increase in the observed joint shear strength due to higher ILSS values at higher temperatures is expected.

The effect of bonding temperature was investigated for solid-state bonding and for brazing. Two K-Karb specimens were bonded, one by solid-state diffusion at 1700°C and the other by brazing at 1930°C, both for a bonding duration of 30 minutes, and under 360 psi (2.48 MPa) interface pressure. The shear strength of these joints at 1200°C were 2068 psi (14.26 MPa) and 2198 psi (15.16 MPa), respectively, indicating

a slightly higher strength for the brazed specimen. In subsequent sections it will be shown that due to the scatter in the experimental data, a distinct pattern of temperature dependence cannot be obtained. Furthermore, the effect of test temperature on the joint shear strength introduces added complexity to this problem.

A number of C-CAT c-c specimens were bonded with 99.9% MoSi₂ at different temperatures for 10 minutes diffusion time, and under an interfacial contact pressure of 100 psi. Double-notched shear specimens were prepared and they were subsequently tested at 1400°C (2552°F) and 1600°C (2912°F). The results are shown in Fig.8. It is noticed that the joint shear strengths at 1600°C are generally lower. Also, for the employed bonding methods, a decrease in the joint shear strength with bonding temperature is observed. It has already been mentioned that for specimens bonded at 1900°C and 2050°C some flow of molten MoSi₂ out of the interfaces have been noticed. A study of the fracture surfaces of these specimens revealed some MoSi₂ depleted areas where the interlayer had been lost due to side flow and evaporation. To diminish the loss of interlayer due to flow, a specimen was bonded at 1900°C for 10 minutes with 100 psi interface pressure applied during heat-up to 1830°C, at which point the pressure was reduced to zero and heating was then continued to 1900°C. By removing the interfacial pressure before the start of melting, a reduction in outflow of molten MoSi₂ was achieved and an increase in strength from 1282 psi (8.4 MPa) to 2137 psi (14.73 MPa) was obtained (Fig.8.). In view of this result, higher joint shear strength values may be expected for all the specimens brazed at 1900°C. Excessive MoSi₂ evaporation was noticed for brazing at 2050°C. The

effect of interfacial contact pressure on the extent of this evaporation has not been investigated. Nevertheless, compared with 1900°C, for brazing at 2050° a lower joint shear strength is expected, unless the excessive evaporation is prevented by conducting the bonding operation in a pressurized inert atmosphere.

In Fig.8. it is shown that for bonding at 1700°C and 1800°C, higher joint shear strength values are obtained when the diffusion time is increased from 10 to 20 minutes. Also, by using a 99.+% MoSi₂ interlayer, a still higher joint shear strength of 2986 psi (20.6 MPa) is produced for bonding at 1700°C (Fig.8.).

The microstructure of the interfacial layers consisted mainly of sintered MoSi₂ for specimens that were solid-state diffusion bonded at 1800°C and lower. A typical microstructure for a specimen bonded at 1800°C for 20 minutes and under 100 psi interfacial pressure is shown in Fig.9. The porous nature of the sintered MoSi₂ powder is demonstrated in the inset of Fig. 9. The average Knoop microhardness for this interlayer measured at 5 locations by using 100 g load was 1323 Kg/mm². This hardness value corresponds closely to the reported Knoop microhardness of MoSi₂ which is 1257 Kg/mm² [12]. For a specimen which was also bonded at 1800°C, but for a shorter diffusion time of 10 minutes, the Knoop microhardness dropped to 1119 Kg/mm², mainly as a result of a reduced sintering time and the consequent increase in porosity. A drop in the joint shear strength from 1930 psi (13.31 MPa) to 1629 psi (11.23 MPa) was associated with the reduction in the microhardness value.

For specimens brazed at 1900°C and higher a multiphase microstructure was generally noticed (Fig.10). Two predominant phases

appear as dark gray connected zones which are located toward the outer boundaries of the interlayer and a lighter gray connected central region. Another possible phase is the smaller isolated patches which are dispersed throughout the interlayer. For a specimen brazed at 1900°C, 10 minutes diffusion time, and 100 psi interfacial pressure, the average Knoop microhardness of the outer dark gray regions was found as 3166 Kg/mm² which is in the range of microhardness values for SiC (2500-3225 Kg/mm² [14]). For the lighter gray central regions the Knoop microhardness was 1671 Kg/mm² which is higher than the microhardness of MoSi₂ and is in the range of microhardness values reported for Mo₂C (1500-1800 Kg/mm² [14]). A small decrease in the microhardness of similar phases was observed when the brazing temperature was increased to 2050°C (3722°F). For this specimen the average Knoop microhardness values were 1602 Kg/mm² for the light gray central regions, and 3091 Kg/mm² for the darker gray border regions. These hardness values, nevertheless, correspond to reported values for Mo₂C and SiC, respectively.

As has already been mentioned, a specimen was brazed at 1900°C for 10 minutes with 100 psi interface pressure applied during heat up to 1830°C, at which point the pressure was released and heating was continued to 1900°C without interfacial pressure. This procedure was adopted to diminish the loss of molten MoSi₂ as a result of outflow from the interface. The microstructure of this specimen, in contrast to that of the previously mentioned specimen which was also brazed at 1900°C and 10 minutes diffusion time, but under a sustained pressure of 100 psi, consisted only of one phase. This single phase microstructure resembled the microstructure of interlayers which were bonded at 1800°C. The

Knoop microhardness was 1269 Kg/mm² which is very close to the reported value of MoSi₂ (1257 Kg/mm² [12]). This observation reveals the significance of interfacial pressure in promoting SiC and Mo₂C formation at temperatures above the melting point of MoSi₂. The drop in the joint shear strength for the specimen bonded with sustained interfacial pressure, in comparison to the specimen bonded with interrupted pressure application (1282 psi vs. 2127 psi) is, for the most part, due to the depletion of MoSi₂ from the interface and may not be strongly dependent on carbide formation as the results seem to suggest.

The mechanisms responsible for bond formation in the MoSi₂ carbon-carbon system have not been investigated in detail. For specimens brazed at 1900°C and higher temperatures, the existence of SiC and Mo₂C phases has been identified by Knoop microhardness measurements and optical microscopy (Fig. 10). For these specimens carbide formation is obviously the prevalent mechanism for producing bonds. At lower bonding temperatures ($T \leq 1800^{\circ}\text{C}$) carbide phases were not discernible by regular light microscopy. Also, due to the very irregular and jagged interface boundaries between the MoSi₂ interlayer and c-c surroundings, and because of a large beam size ($\sim 2 \mu\text{m}$), a clear indication of Si and Mo diffusion gradients at the boundaries by electron microprobe was not obtained.

The formation of SiC at the interface boundaries as a possible means of bond formation was examined by using an ethanol slurry of -325 mesh silicon powder (99% purity) as the interlayer in four bonding experiments. Two C-CAT c-c specimens were solid-state diffusion bonded at 1385°C (2525°F) for 10 minutes and under 100 psi interface pressure.

The remaining two specimens were brazed at 1460°C (2660°F). Substantial Si evaporation was observed in all four cases. Bond formation was not observed in any of these specimens. The interface for the first two specimens consisted of densely packed silicon powder layers with little or no bonding to the c-c substrates. For the brazed specimens, the faying surfaces were covered with hard, shiny coatings of adherent silicon carbide, but with no bonding developed between the two rectangular c-c pieces.

The role of molybdenum in bond formation was investigated by bonding two C-CAT c-c specimens and using a mixture of Mo and Si powders as interlayers. The weight percent of Mo was 63.07 and that of Si was 36.93, corresponding to the elemental weight ratios in MoSi_2 . These specimens were also bonded at 1700°C , 10 minutes diffusion time, and 100 psi interface pressure. The double-notched shear strength for these specimens at 1400°C and 1600°C were 1349 psi (9.30 MPa) and 1145 psi (7.89 MPa), respectively. The microstructures of these bonds consisted of scattered narrow zones of fully densified MoSi_2 surrounded by porous regions of sintered powder. Due to the small size of the fully-densified MoSi_2 zones, accurate determination of Knoop microhardness was not possible and the approximate measured value of 814 kg/mm^2 is lower than the reported microhardness for MoSi_2 . The microstructure and the microhardness value for these two specimens were similar to those observed for specimens bonded by MoSi_2 interlayers of 1700°C .

From the results of the bonding experiments with Si and Si-Mo mixture it becomes apparent that silicon reacts preferentially with molybdenum to form MoSi_2 and, in general, it does not react with carbon

to form SiC when molybdenum is present. In fact, the first discernible evidences of a SiC phase were observed only at temperatures greater than the melting point of molybdenum (Fig. 10).

b. Titanium interlayers

Solid-state diffusion bonding and brazing of K-Karb, ACC-4, and C-CAT specimens were conducted by using an ethanol slurry of 99.7% purity, -200 mesh titanium powder as an interlayer. A limited number of bondings was also made by using 99.9% purity, 0.025 mm (0.001 inch) thick titanium foils. The bondings were made between $0.85 T_m$ and $1.037 T_m$ where $T_m = 1941$ K is the absolute melting temperature of titanium. The interfacial contact pressure was 100 psi (0.69 MPa) for all the titanium specimens.

Bonding of two C-CAT specimens at 1377° and 30 minutes were attempted. Titanium powder for one, and Ti foil for the other specimen were used. Upon cooling to room temperature, it was noticed that bond formation had not taken place under these conditions. At a higher diffusion temperature of 1495°C (2723°F) and for a shorter diffusion time of 15 minutes, bond formation was obtained for a K-Karb specimen. The double-notch shear strength of this specimen at room temperature was 165 psi (1.138 MPa). About 95% of the fracture surface for this specimen consisted of the bonding material and only small isolated patches of c-c material were observed. The joint shear strength increased to 306 psi (2.11 MPa) when bonding was performed at 1600°C for a diffusion time of 10 minutes. Further increase of temperature to 1685°C in order to provide for a brazing condition, while maintaining

diffusion time constant at 10 minutes, resulted in a decrease of joint shear strength to 183 psi (1.26 MPa). As would be expected, brazing at the same temperature ($T=1685^{\circ}\text{C}$) but using a shorter time of 3 minutes, resulted in an improved joint shear strength of 455 psi (3.14 MPa). For a specimen brazed at 1740°C for five minutes a joint shear strength of 306 psi (2.11 MPa) was obtained.

A number of ACC-4 and C-CAT specimens were bonded at different temperatures while keeping the diffusion time at 10 minutes and the interfacial contact pressure at 100 psi (0.689 MPa). These specimens were subsequently double-notch shear tested at room temperature and at 1200°C . The results are shown in Figs.11 and 12. The joint shear strength at room temperature for all the cases examined is relatively low. Also, the scatter in data for these specimens is considerable (Fig.11) and a well-defined pattern of dependence between the bonding temperature and joint shear strength does not emerge.

The joint shear strength values at 1200°C are generally higher than the corresponding values at room temperature (Figs.11 and 12). Also, the joint shear strength at 1200°C increases with bonding temperature for both ACC-4 and C-CAT materials (Fig.12). The observed higher shear strength for the specimens tested at 1200°C , in spite of an additional heating cycle experienced by these specimens, is not well understood. A contributing factor to the increased strength is the higher interlaminar shear strength of the c-c material at elevated temperatures. As shown in equation (3), the bond strength τ_b increases as τ_c becomes larger. For ACC-4 the ILSS increases from 1200 psi at room temperature to 2300 psi at 1200°C [13]. On the other hand, a decrease in the strength of Ti

and titanium carbide with temperature is to be expected which will have an opposite effect on the joint strength.

Microscopical observations of the fracture surfaces revealed no discernible differences between the room- and high-temperature tested specimens. In all cases, the shear strength was directly related to the percentage of the fracture area which consisted of sheared c-c laminates. Also, fracture always occurred either by shear separation of the c-c laminates or by shear fracture of the bonding material. In other words decohesion of the bonding material from c-c laminates was never observed. This observation is indicative of the higher shear strength of titanium carbide which forms at the outer regions of the bonded zone, compared with the weaker c-c material or the sintered titanium layer in the inner zones of the bond.

In general, two types of joint microstructures were observed for the six specimens that were examined. The determining factor in this regard was the thickness of the titanium interlayers. For three of the specimens where the interlayers were thicker than 90 μm , a three-zone microstructure (Fig.13) was observed, while for the other three specimens with interlayers thinner than 60 μm , a single zone microstructure was noticed. For two of the latter specimens, the Knoop microhardness values of the interlayers were 2057 Kg/mm^2 and 2259 Kg/mm^2 . These specimens were bonded at 1740°C and 1600°C, respectively, each with a diffusion time of 10 minutes and an interfacial contact pressure of 100 psi. Different Knoop hardness values have been reported for titanium carbide [14], but in general, these values are greater than 1800 Kg/mm^2 . It is then likely that the observed single zone for these

two specimens were composed entirely of titanium carbide. The joint shear strength for these two specimens were the highest values of all the Ti-bonded specimens. The third specimen for which a single zone microstructure was observed was bonded at 1495°C for 10 minutes. This specimen fractured while cutting the specimen notches. Although occurrence of some bonding was evident from the fracture surfaces, the shear strength of this specimen must have been very small, perhaps less than 70 psi. The Knoop microhardness for this specimen was about 1340 Kg/mm^2 . This value is below the reported minimum value for TiC, and it is higher than the value for titanium. Since TiC is the only known carbide in the Ti-C system, the identity of this zone as a carbide phase cannot be established. The solubility of carbon in titanium is very small (less than 0.6 atomic percent at 1600°C). The hardness of this solid solution is not known. Therefore, positive identification of this microstructure is not established, even though the existence of a carbon concentration gradient in titanium is inevitable.

The Knoop microhardness values for three specimens with three-zone microstructure were also determined. These specimens were bonded at 1600, 1650, and 1685°C for 10 minutes diffusion time. The microhardness values for the two outer regions were 1452, 1530, and 1764 Kg/mm^2 , respectively. The corresponding values for the inner zones were 1045, 709, and 965 Kg/mm^2 . Once again, positive identification of these zones on the basis of microhardness measurements is not possible.

The specimen which was bonded at 1650°C for 10 minutes was analyzed by electron microprobe and the results are shown in Fig.14. It is noticed that the concentration gradient of titanium at the interface

with c-c material is very sharp, perhaps varying from zero to 100% Ti concentration over a distance less than the beam size of about 2 μm . The gradual concentration drop of carbon, on the other hand, is due to the presence of Al_2O_3 powder which was lodged at the Ti-C boundaries during polishing and which resisted the ultrasonic cleaning of the specimen prior to the electron microprobe examinations. In regard to carbon profile, it is of particular interest that the concentration of carbon drops to about 24% at regions corresponding to the outer zones of the three-zone microstructure, further dropping to about 20% at the inner zone of the interface. It is noticed that a corresponding small increase in Ti concentration occurs at this inner zone. Since the carbon concentration in TiC is 20.05 atomic percent, it can be inferred that it is likely that both the outer and the inner zones are composed of TiC. A possible explanation for the observed low Knoop microhardness values may be the very narrow geometry of the interface layer and the presence of voids in the microstructure, particularly for specimens bonded by solid-state diffusion bonding.

The distribution of impurity elements Mn and Fe are also shown in Fig.14. It is noticed that very small quantities of these elements are present in the interlayer. Of particular significance is the narrow concentration peak for Fe at the center of the interlayer. Corresponding to this concentration peak, a central discontinuous phase is observed in the microstructure of the interlayer (Fig.13) and a small drop in the Ti concentration is also noticed (Fig.14). This peak is probably due to the differences in the activation energies for TiC and Fe_3C formations and for diffusion of carbon in Ti and Fe. It is likely

that with a purer interlayer (99.9% Ti) this peak may be eliminated or substantially reduced.

2. Butt joints in tension

Three K-Karb tension specimens were solid-state diffusion bonded at 1700°C (3092°F) for a diffusion time of 20 minutes. As already mentioned, each specimen consisted of two halves of a tension specimen which were butt joined together by a 99.+% MoSi_2 interlayer. The specimen was then loaded in tension, with the load applied through two 0.25 inch diameter c-c composite pins at each end. The specimen cross section at the joint was a square of 0.25 inch side. Due to axial misalignment in the load train, the two end planes of the specimen halves, even though parallel to each other, did not coincide on each other completely. As a result, contact and bonding occurred on only about 64 percent of the total cross-sectional area.

The interfacial contact force for the first specimen was 50 N (11.25 lb) and for the second and third specimens it was 104 N (23.38 lb). The first and the third specimens, after joining at 1700°C for 20 minutes, were cooled to 1200°C and were pulled in tension at 1200°C without cooling to room temperature prior to testing. The tensile fracture load for these specimens were 244 N (54.86lb) and 217 N (48.79 lb), respectively. The smaller fracture load for the third specimen, in spite of the higher interfacial contact pressure, is contrary to the usual expected result and can possibly be attributed to worsening misalignment at higher contact forces. Bases on 64 percent coincidence area (bonded region) and a calculated eccentricity of 0.707 inches

(1.796 mm), a resulting bending stress of 2908 psi (20 MPa), a direct tension of 1371 psi (9.45 MPa), and a combined stress of 4279 psi (29.50 MPa) were obtained for the first specimen. The corresponding stresses for the third specimen were 2587 psi (17.84 MPa), 1219 psi (8.40 MPa), and 3806 psi (26.24 MPa), respectively.

The second specimen was cooled from the bonding temperature (1700°C) to room temperature and was then pulled at room temperature to a fracture load of 150 N (33.7 lb). The fracture load for this specimen is substantially lower than the other two specimens. An examination of the fracture surfaces revealed more fiber pull out and ledge formations for the first and the third specimens. In view of the limited data, it is probably premature to attribute the observed differences in strength and microstructural details to the effect of cooling the second specimen to room temperature before testing. However, in regard to the effect of cooling it is to be appreciated that the problem of thermal expansion mismatch between the c-c material and MoSi₂ for butt and lap joints will not be the same. For the lap joints the thermal expansion coefficients in the plane of the bond, i.e. the thermal expansion coefficients in the warp and fill directions, are approximately the same and are about $2.6 \times 10^{-6}/^{\circ}\text{C}$ [13]. The thermal expansion coefficients in the plane of the butt joints at temperatures of interest are approximately $2.6 \times 10^{-6}/^{\circ}\text{C}$ for the fill direction and $6.7 \times 10^{-6}/^{\circ}\text{C}$ in the across-ply orientation [10,13], rendering the c-c thermal expansion anisotropic for the butt joints. The thermal expansion coefficient for MoSi₂ in the temperature range of interest is about $8.8 \times 10^{-6}/^{\circ}\text{C}$ [12]. In any case, due to the complexity of the problem, particularly on a microstructural basis, only

speculative assessments are possible at this point. Further investigations are needed to elucidate this problem in more detail.

The combined strength values for specimens one and three are indicative of the potential for obtaining high bond strength values for butt joints in c-c composites. A more appropriate specimen geometry and better fixtures are needed to investigate this potential further.

3. T-joints and modified T-joints

A limited number of T-joints and modified T-joints were prepared by using 0.25 inch thick K-Karb c-c composite and 99.+% MoSi_2 interlayers. The configuration of these specimens and a test fixture for tensile testing of these joints are shown in Figs.3 and 4, respectively. A T-joint bonded at 1700°C for a diffusion time of 30 minutes and under an interfacial pressure of 500 psi, was pulled in tension at 1200°C and a joint tensile strength of 504 psi (3.48 MPa) was obtained. Increasing the diffusion time to 60 minutes and the interfacial pressure to 1000 psi resulted in a lower tensile strength of 414 psi (2.85 MPa). A third specimen bonded under the same conditions as the first specimen, but tested at room temperature, had a lower tensile strength of only 281 psi (1.94 MPa). For these specimens fracture occurred predominantly by interlaminar tensile separation of one ply of c-c composite bonded to the MoSi_2 interlayer from the rest of the specimen. The room-temperature interlaminar tensile strength (ILTS) of K-Karb is reported at 650 psi (4.48 MPa) [10,15] which is higher than the room-temperature strength of the T-joint. Also, the higher T-joint strength values at 1200°C are less than the expected ILTS of the c-c

composites at 1200°C [16]. It is likely that, due to the presence of the bonding layer and the consequent stress concentration effects, fracture at nominal stress values lower than the ILTS of the material has occurred.

The modified T-joints were designed to avoid the tensile delamination of the regular T-joints. Two specimens were bonded at 1700°C, 500 psi (3.45 MPa) interfacial pressure, and diffusion times of 30 and 60 minutes. The joint tensile strength of these specimens were 349 psi (2.41 MPa) and 369 psi (2.54 MPa), respectively. The third specimen was bonded at 1900°C for 30 minutes and had a joint tensile strength of 338 psi (2.33 MPa). The tensile strength of these joints were lower than expected and they were, in general, smaller than the values for the T-joints. A preliminary examination of the fracture surfaces revealed that in all the three specimens actual contact and bonding between the faying surfaces had occurred only on isolated patches, with the remainder of the slanted surfaces coated but not bonded during the joining operation. Perhaps a better means of MoSi₂ application to the slanted surfaces is needed, so that a smooth and uniform thickness coating can be produced. More investigations on this type of joint are needed so that the tensile properties of MoSi₂ bonds can be adequately characterized.

4. Disk-and-rod shear specimens

The geometries of the disk-and-rod shear specimens and their test fixture are shown in Fig.5. 99.+% MoSi₂ was used as the brazing compound for joining three of these specimens. In each case, a very

thick paste of MoSi_2 powder in ethanol was applied to the top bowl-like portion of the disk in such a way that MoSi_2 particles will not enter the clearance gap between the disk and the rod. In this fashion, preplacing of the brazing compound in the joint was avoided and an indication of flow and wettability was also obtained by these experiments.

The radial clearance C (Fig.5) was 0.005 inch (0.127 mm) for the first specimen. This specimen was brazed at 2100°C (3812°F) for five minutes. Upon cooling and removal from the furnace, it was noticed that a coating of MoSi_2 had covered the concave surface of the top bowl and the part of the rod inside the bowl. The specimen was subsequently tested at 1400°C to a fracture load of 856 N (192.5 lb). It was observed that due to a large clearance and because of excessive evaporation at 2100°C very small amounts of MoSi_2 had remained entrapped in the joint gap. As a result, the joint strength for this specimen, based on a total shear area of $\pi(0.5)(0.5) \text{ in}^2$, was very low (245 psi = 1.69 MPa).

A smaller radial clearance of $C=0.002$ in (0.051 mm) was used for the second specimen. Also, the brazing time was reduced to about 10 seconds, while the brazing temperature was maintained at 2100°C . Once again, very good flow and wettability were observed. The amount of residual MoSi_2 in the joint gap, however, was very small. Consequently, the shear strength of the joint at 1400°C was only 305 psi (2.1 MPa).

The brazing temperature was lowered to 1948°C (3538°F) for the third specimen. The heating rate for this specimen, similar to the other two specimens, was 50°C per minute. Heating was discontinued as soon as the target temperature (1948°C) was reached. Upon cooling to

room temperature, it was noticed that a substantial amount of MoSi_2 was still present inside the top bowl. Some overflow over the top flat surface of the specimen was also observed. This specimen was subsequently tested at 1400°C to a fracture load of 5730 N (1288 lb). The joint shear strength, based on a shear area of $\pi(0.5)(0.5) \text{ in}^2$, was 1640 psi (11.31 MPa). A study of the separated parts revealed that only partial penetration of MoSi_2 into the joint gap had taken place and less than thirty percent of the contact surfaces was wetted and covered with MoSi_2 .

The above results indicate that the optimum brazing temperature for MoSi_2 is obviously higher than 1948°C , more likely about 2050°C . However, due to excessive evaporation brazing in an inert atmosphere, rather than vacuum, is advantageous. Another outcome of the above results is the likelihood of achieving joint shear strength values much larger than those obtained from the double-notch shear tests. The limiting influence of the ILSS of the c-c composite material on the double-notch shear strength is the major factor in this respect. Further investigations on the disk-and-rod specimens are needed so that the optimum process conditions and geometrical characteristics for the brazing with MoSi_2 can be determined.

VI. RECOMMENDATIONS

The potential of MoSi_2 as an interlayer for joining C-C materials has been demonstrated. It is recommended that other aspects of this problem such as joint thermal stability, effect of thermal cycling and thermal shock, and the influence of various fiber and matrix inhibitors to be investigated.

VII. REFERENCES

1. Moorhead, A.J., and C.R. Kennedy, Metals Handbook, ninth edition, Vol. 6, 1984, pp. 1061-1063.
2. Takamori, T., and M. Akanuma, "Possible Braze Compositions of Pyrolytic Graphite", Am. Ceramic Soc., Bulletin, Vol. 48, No. 7, 1969, pp. 734-736.
3. Anikin, L. T., et al., "The High Temperature Brazing of Graphite", Welding Production, Vol. 24, No. 1, 1977, pp. 39-41.
4. Amato, I., P.G. Cappeli and P.C. Martinengo, "Brazing of Special Grade Graphite to Metal Substrates", Welding Journal, Vol. 53, No. 10, 1974, pp. 623-628.
5. Werner, W.J., and G.M. Slaughter, "Brazing Graphite to Hastelloy N for Nuclear Reaction", Welding Engineer, March 1968, p. 65.
6. Hammond, J.P., and G.M. Slaughter, "Bonding Graphite to Metals with Transition Pieces", Welding Journal, Vol. 50, No. 1, 1971, pp. 33-40.
7. Fox, C.W., and G.M. Slaughter, "Brazing of Ceramics", Welding Journal, Vol. 43, No. 7, 1964, pp. 591-597.
8. Carnonico, D.A., N.C. Cole, and G.M. Slaughter, "Direct Brazing of Ceramics, Graphite, and Refractory Metals", Welding Journal, Vol. 56, No. 8, 1977, pp. 31-38.
9. Pattee, H.E., R.M. Evans, and R.E. Monroe, Joining Ceramics and Graphite to Other Materials, NASA SP-5052, NASA, Washington, D.C., 1968.
10. Iannuzzi, F.A., H.S. Starrett, and M.A. Sherman, Evaluation of Carbon-Carbon Composites for Advanced Turbine Engine Application, AFWAL-TR-88-4144, 1988.
11. Dadras, P., and J.S. McDowell, "Stress Analysis of Double-Notch Shear Specimens", submitted to Experimental Mechanics.
12. Carter, D.H., SiC Whisker-Reinforced MoSi₂, La-11411-T, Los Alamos National Laboratory, 1988.
13. Starrett, H.S. and F.A. Iannuzzi, Preliminary Data for Structural Carbon-Carbon Composites (ACC-4), AFWAL-TR-88-4145, 1988.
14. Metals and Ceramics Information Center, Battelle, Columbus Laboratories, Engineering Property Data on Selected Ceramics, Vol. 2, Carbides, MCIC Report, 1979.

15. Dadras, P., Determination of Across-Ply Strength of Carbon-Carbon Composites at High Temperatures, AFWAL-TR-88-4074, 1988.
16. Dadras, P., "High-Temperature Interlaminar Tensile Strength of Carbon-Carbon Composite Materials", in Metal Matrix, Carbon, and Ceramic Matrix Composites, NASA Conference Publication 3018, pp. 361-367, 1988.

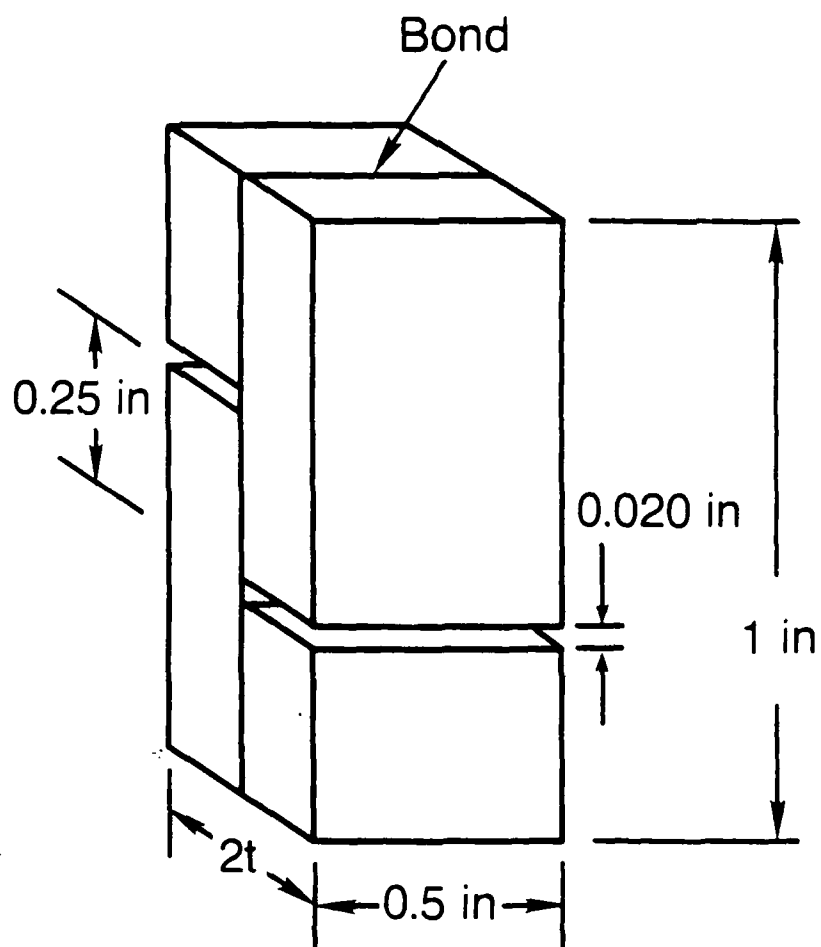


FIG. 1 GEOMETRY OF DOUBLE-NOTCH SHEAR SPECIMENS

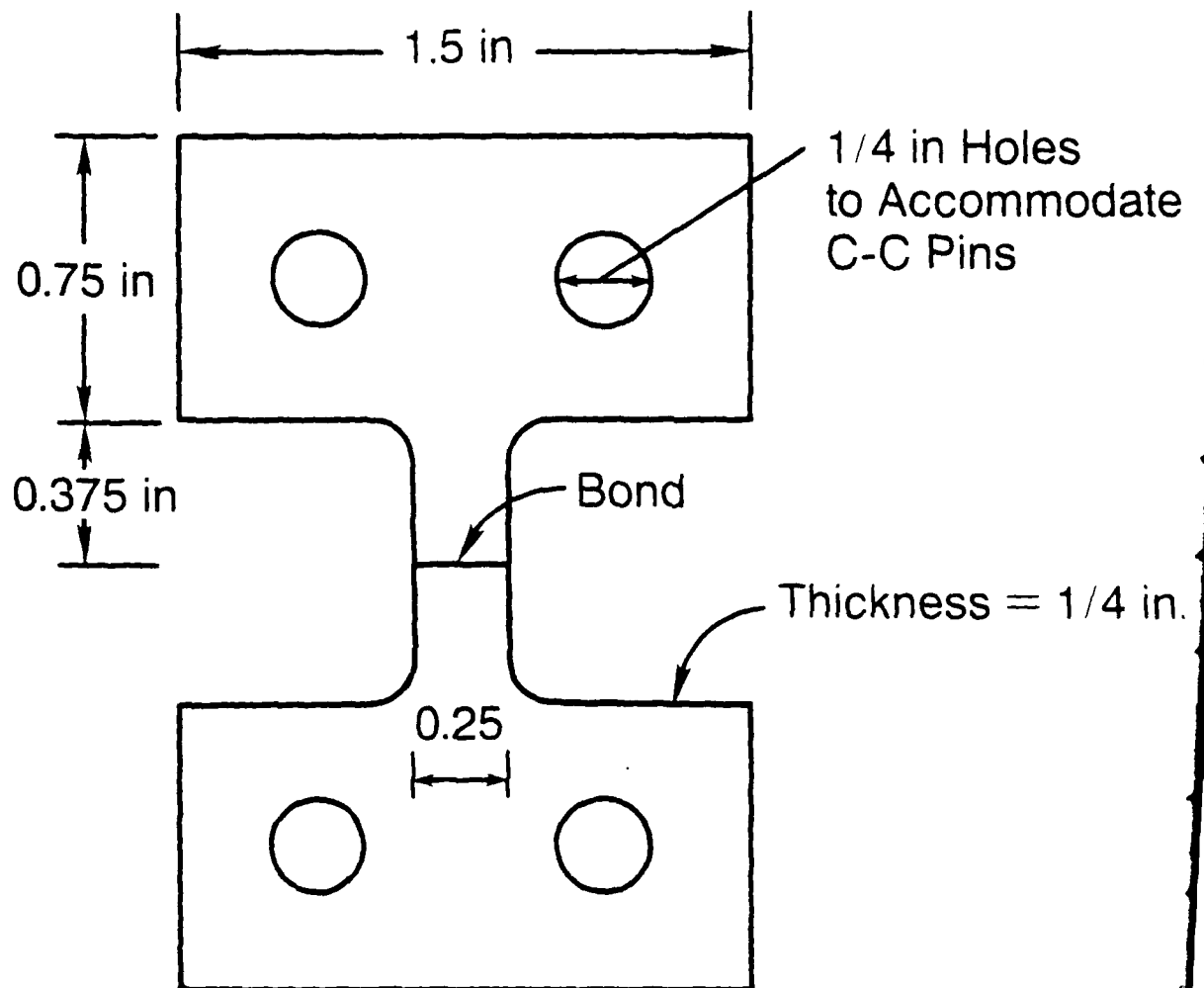


FIG. 2 GEOMETRY OF TENSION SPECIMENS

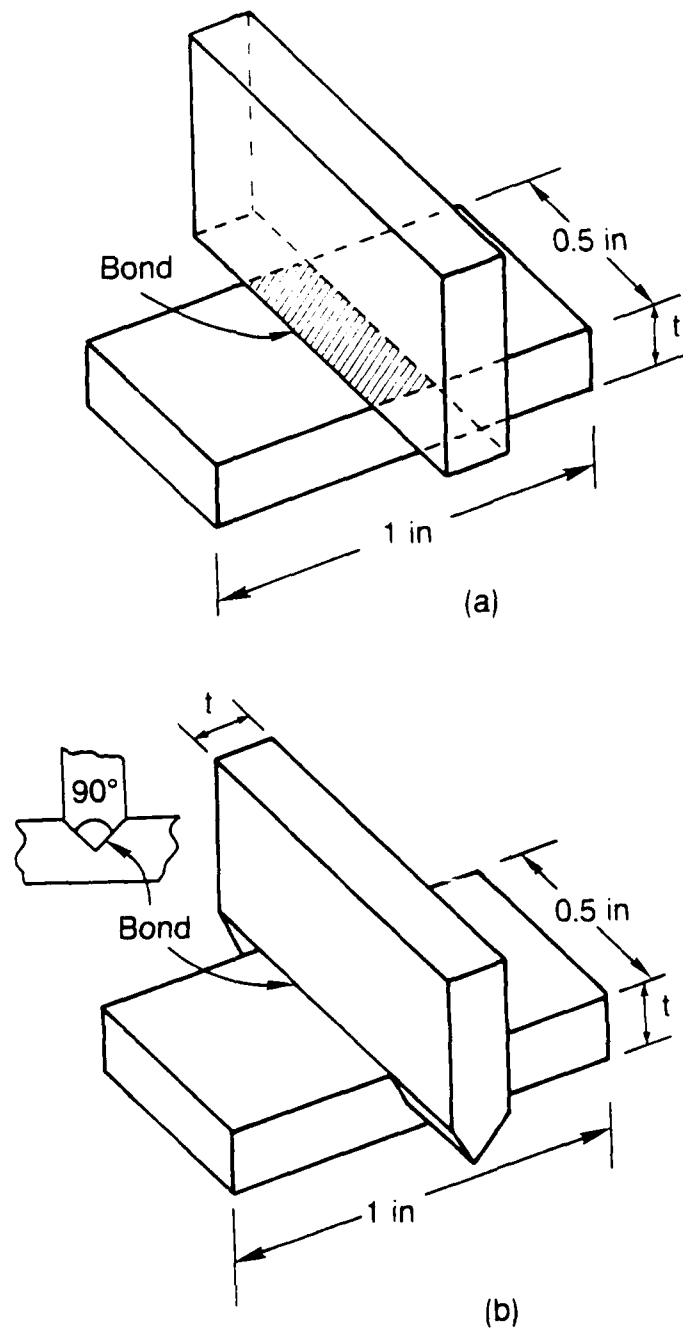


FIG. 3 (A) T-JOINT, AND (B) MODIFIED T-JOINT SPECIMENS

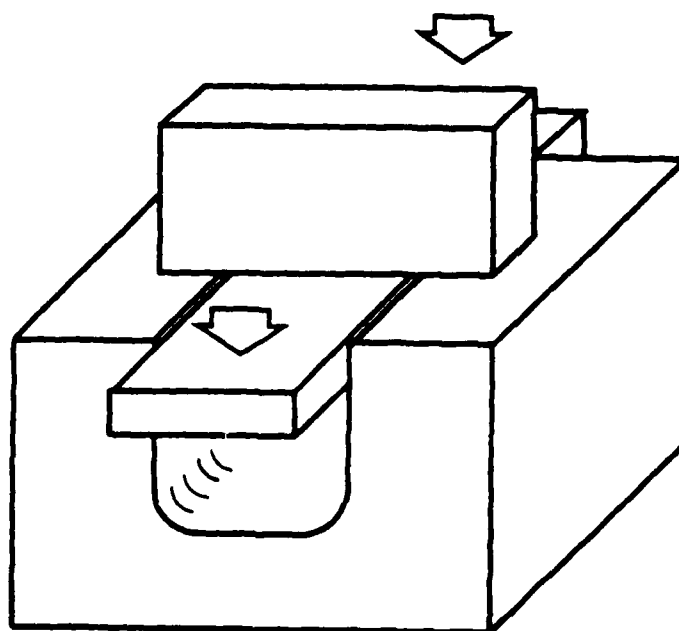
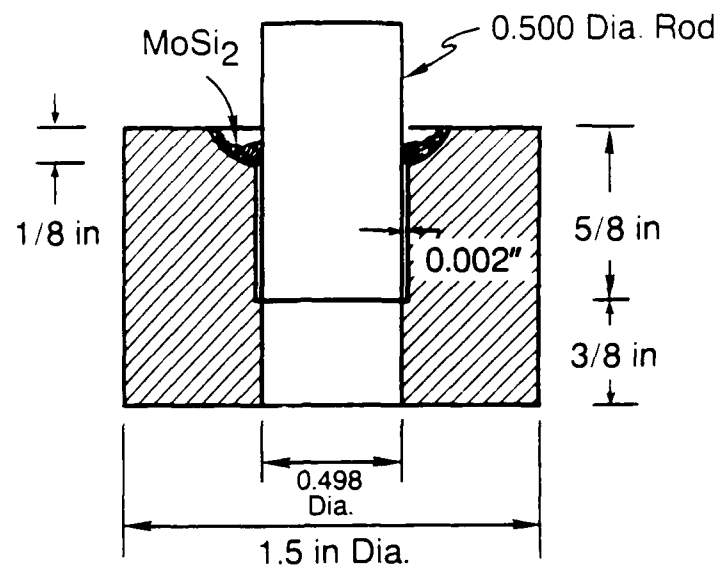
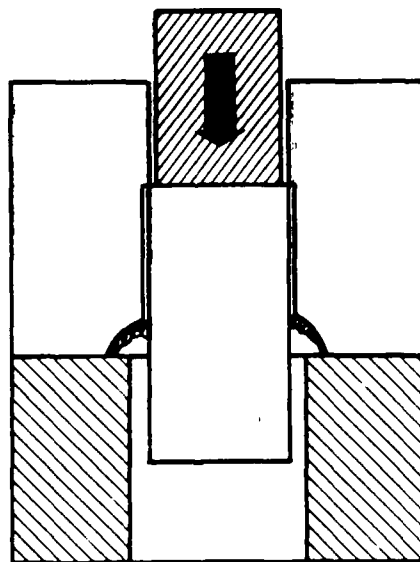


FIG. 4 FIXTURE FOR TESTING T-JOINTS AND MODIFIED T-JOINT SPECIMENS

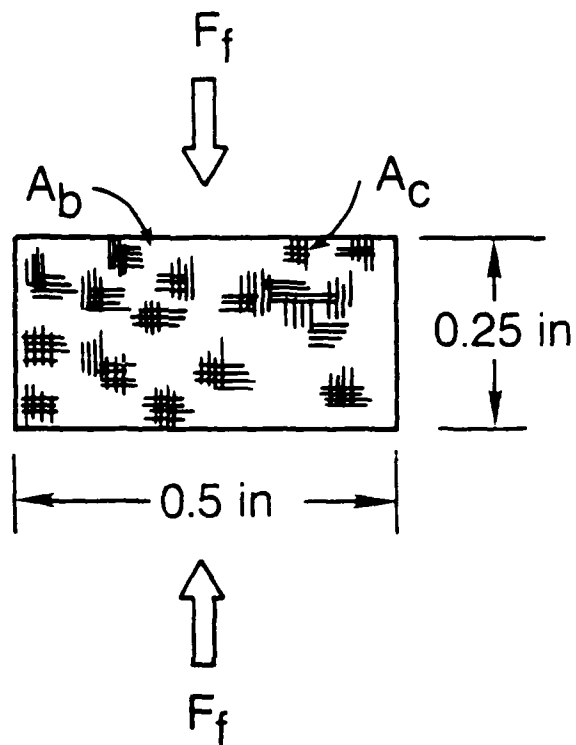


(a)



(b)

FIG. 5 (A) DISK-AND-ROD SPECIMENS, AND (B) TEST FIXTURE



A_c = Fracture Area of C-C Composite
 A_b = Fracture Area of Bond Material
 F_f = Fracture Load

FIG. 6 MODEL FOR BOND SHEAR STRENGTH DETERMINATION

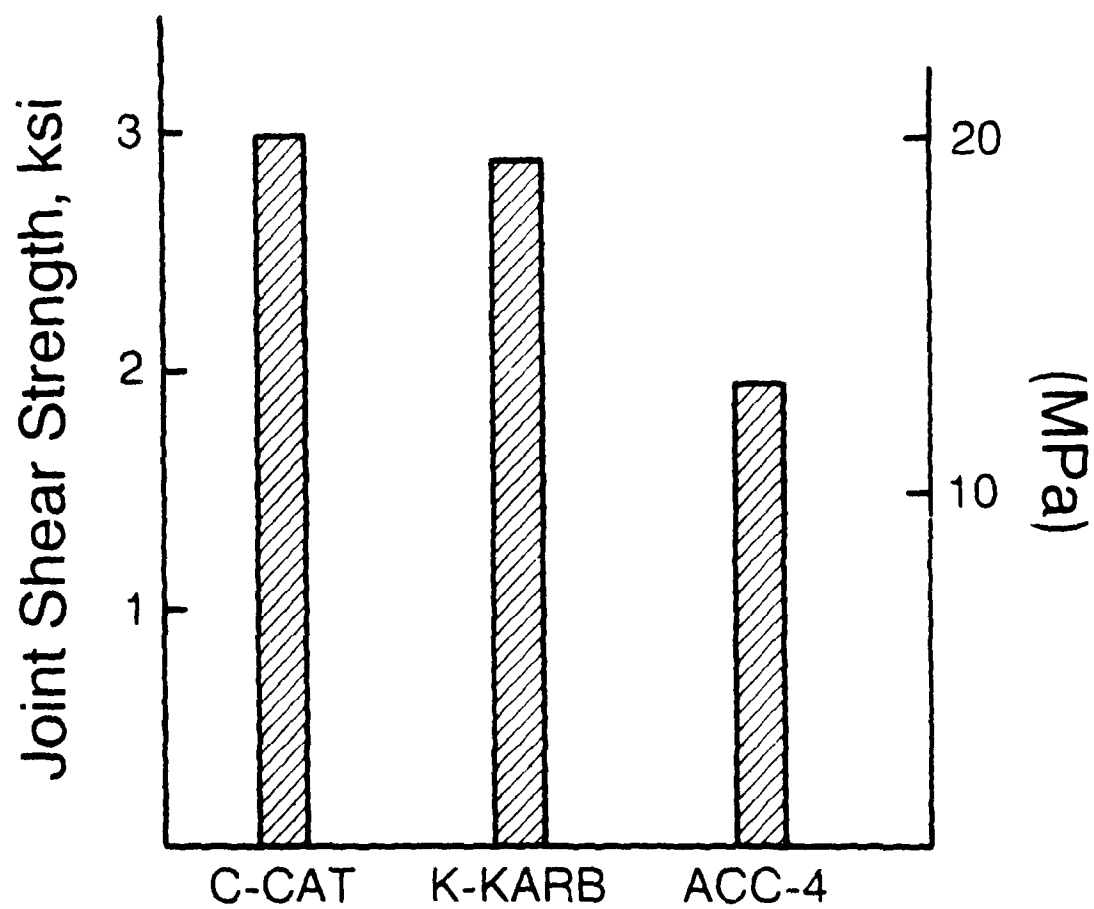


FIG. 7 DOUBLE-NOTCH JOINT SHEAR STRENGTH FOR THREE C-C COMPOSITES AT 1400°C (MoSi₂ INTERLAYER, 1700°C, 20 MINUTES)

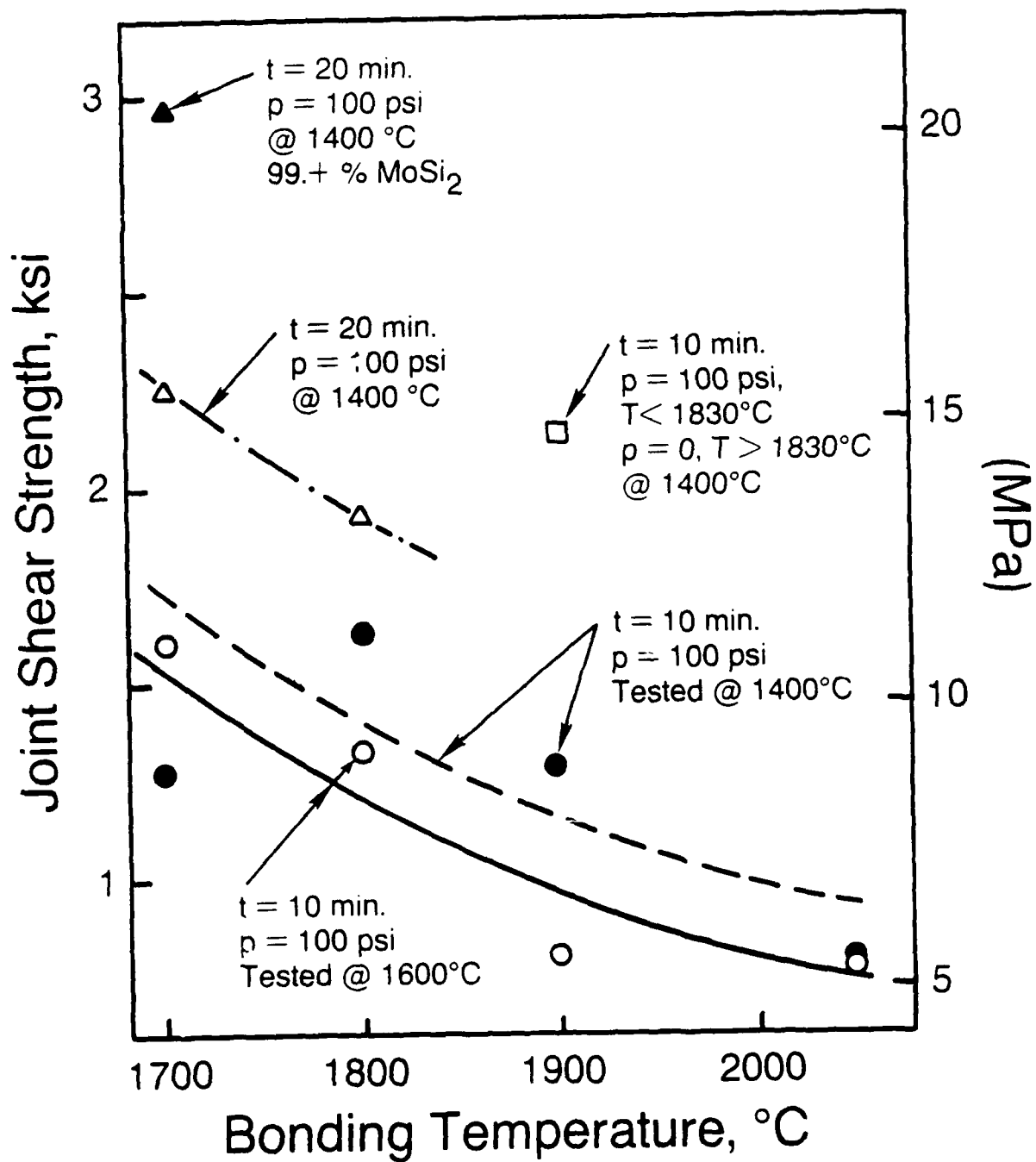


FIG. 8 VARIATIONS OF JOINT SHEAR STRENGTH WITH BONDING TEMPERATURE.
(MoSi_2 INTERLAYER)



FIG. 9 JOINT MICROSTRUCTURE OF C-CAT C-C SPECIMEN BONDED WITH MoSi_2 AT 1800°C , 20 MIN., 100 PSI.



FIG. 10 JOINT MICROSTRUCTURE OF C-CAT C-C SPECIMEN BRAZED WITH MoSi_2 AT 1900°C, 10 MIN., 100 PSI.

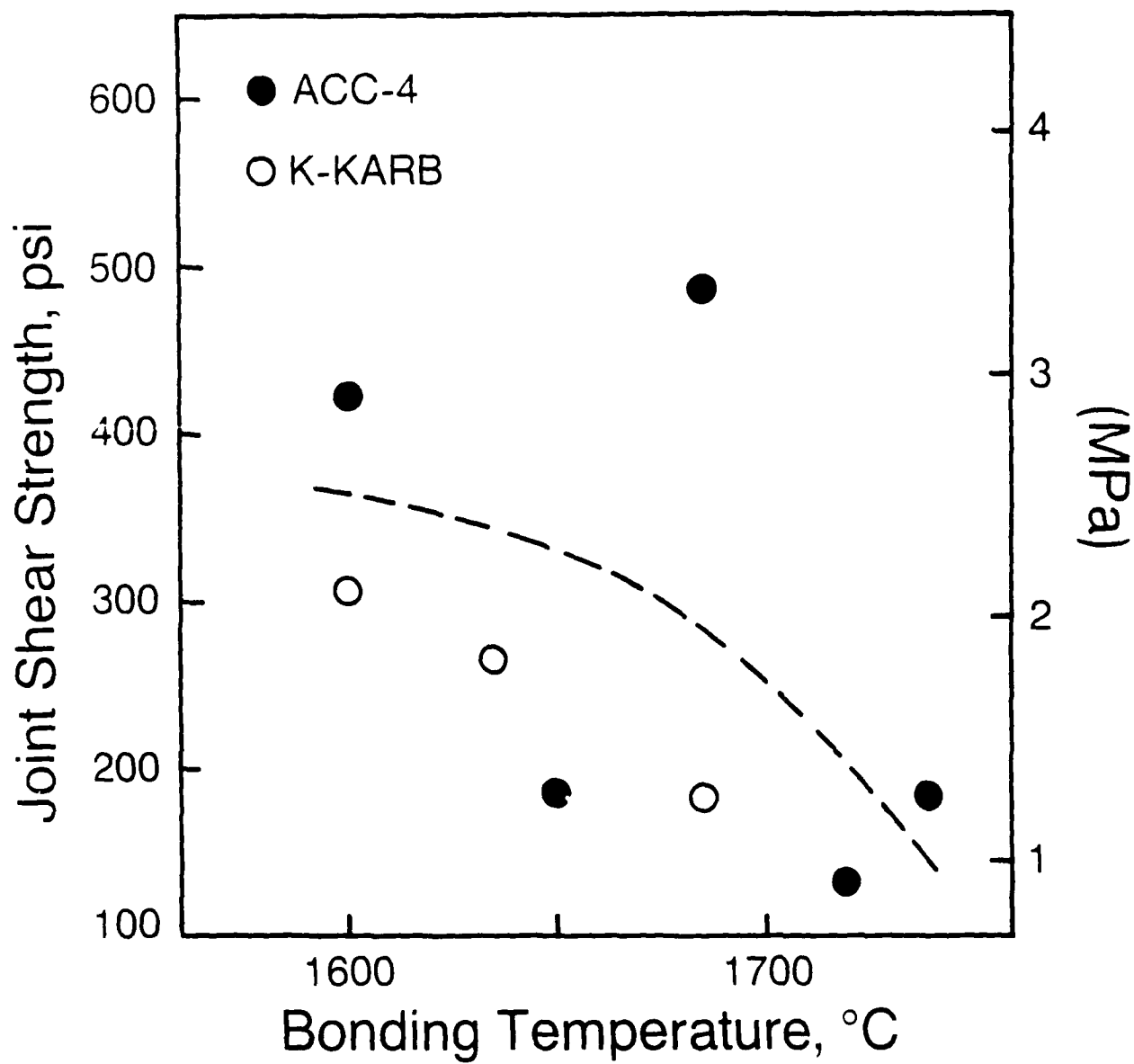


FIG. 11 VARIATIONS OF ROOM-TEMPERATURE JOINT SHEAR STRENGTH WITH BONDING TEMPERATURE. (T_I INTERLAYER)

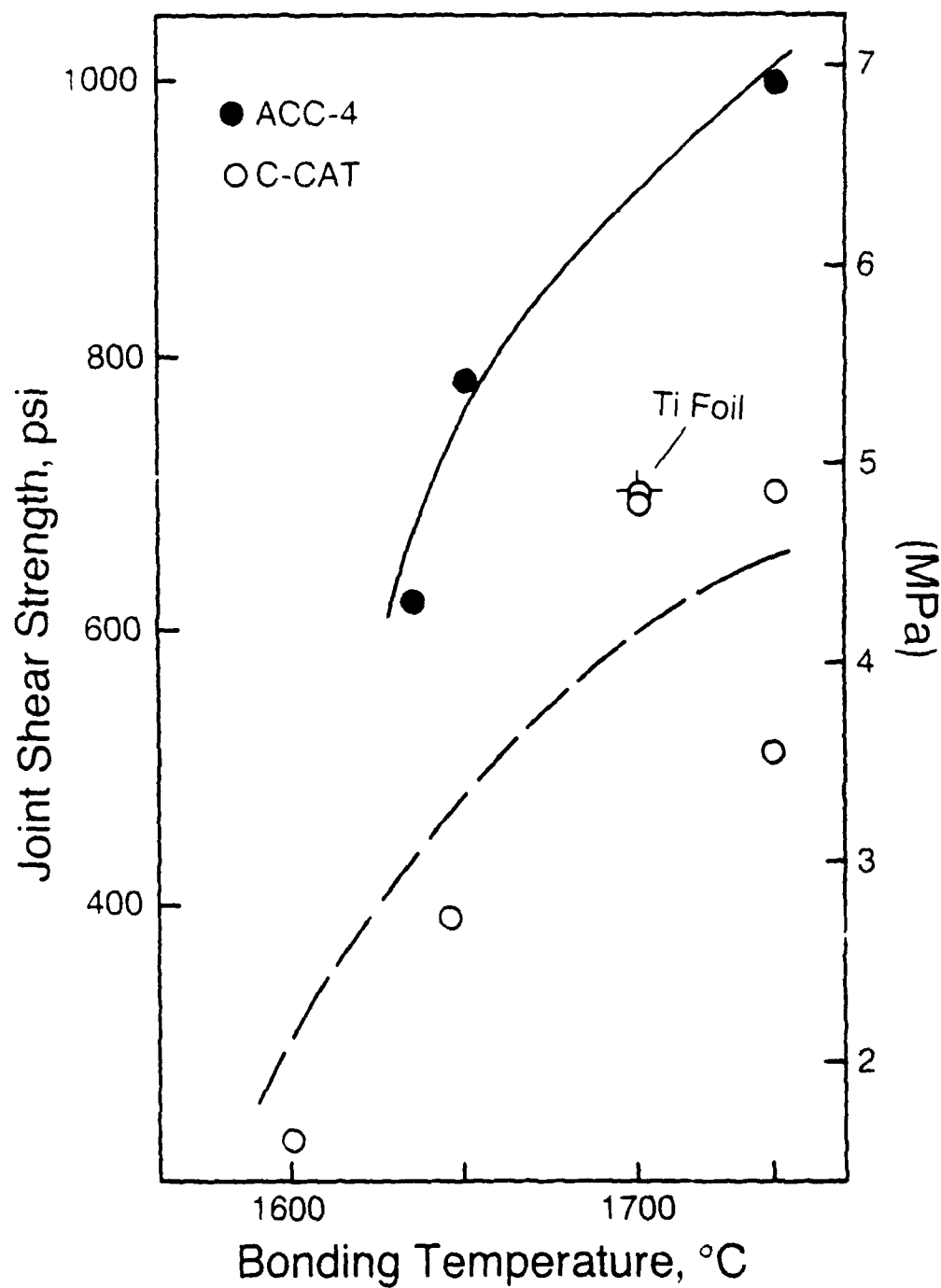


FIG. 12 VARIATIONS OF JOINT SHEAR STRENGTH AT 1200°C WITH BONDING TEMPERATURE. (Ti INTERLAYER)



FIG. 13 JOINT MICROSTRUCTURE OF ACC-4 C-C SPECIMEN BONDED AT 1685°C, 1 MIN., 100 PSI WITH Ti INTERLAYER.

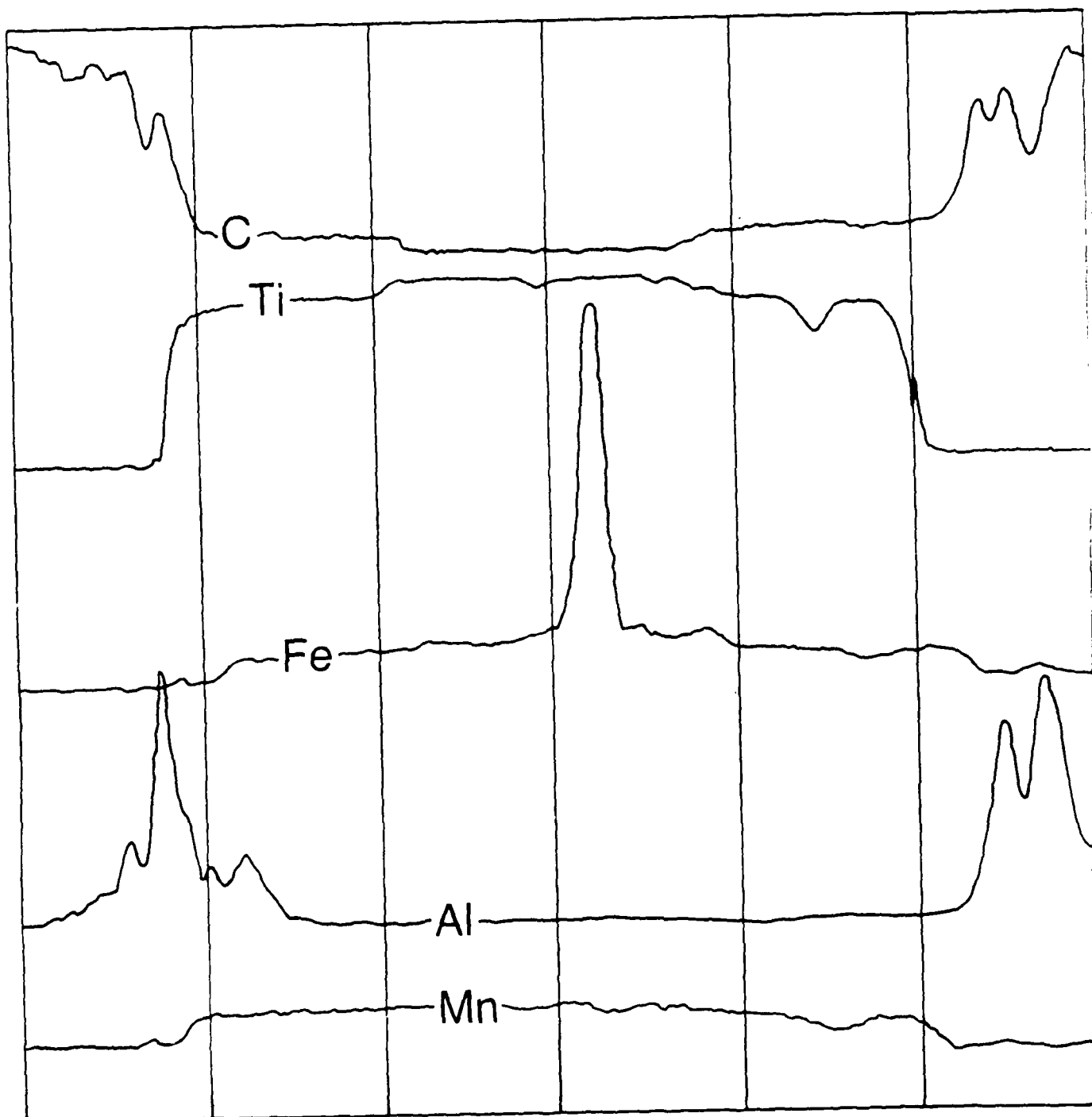


FIG. 14 CONCENTRATION GRADIENTS FOR Ti-BONDED SPECIMEN (1650°C, 10 MIN., 100 PSI) DETERMINED BY MICROPROBE

FINAL REPORT NUMBER 96
REPORT NOT AVAILABLE AT THIS TIME
Dr. Barry K. Fussell
210-9MG-064

1988 USAF-UES UNIVERSITY FACULTY MINIGRANT PROGRAM

Sponsored by the
AIR FORCE OFFICE OF SCIENTIFIC RESEARCH

Conducted by the
Universal Energy Systems, Inc.

FINAL REPORT

Prepared by:	John W. Gilmer
Department and	Department of Materials Science and Engineering
University:	The Pennsylvania State University
Date:	16 February 1990
Contract No:	760-7MG-013

Characterization of the Phase Separation Behavior of Poly(p-phenylene benzobisthiazole)/Amorphous Nylon Molecular Composites by Small Angle Light Scattering

Abstract

Rigid rod molecular composite films of poly(p-phenylene benzobisthiazole) (PBZT) and Zytel 330®, an amorphous nylon, have been produced by a coagulation process to ensure that the rods are molecularly dispersed in the coils. Since concentrated PBZT/Nylon blends are thermodynamically incompatible at all temperatures, the system begins spontaneously to phase separate when heated above its glass transition temperature. Time resolved small angle laser light scattering was utilized to characterize the phase separation of these blends. A very rapid phase separation process was found to occur which gave rise to a broad scattering maximum in the small angle region. Very little subsequent ripening of the domain structure was observed for these materials due to the immobility of the PBZT rich phase.

A rigid rod molecular composite utilizes a rigid rod polymer to reinforce a flexible coil polymer in which it is molecularly dispersed. The presence of the flexible coil component gives the material greater moldability than the rigid rod component itself possesses. The molecular dispersion of each rod molecule assures the maximum utilization of the reinforcing ability of rigid rod component. By utilizing fibers that are molecular in size, the interfacial area between the rod and coil is greatly increased leading to a decrease in the interfacial stress and better transfer of stress from the matrix material to the fibers. In addition, the molecular composite material is more like a conventional polymer than a composite in many aspects of its utility.

The rigid rod PBZT utilized in this study has a theoretical modulus of 600 GPa in the axial direction for a perfectly oriented fiber.^{1,2} Actual fibers yield values of 4.2 GPa and 330 GPa for the tensile strength and modulus, respectively.^{2,3} With the molecular composite films analyzed in this study, for which the orientation of the PBZT molecules is believed to be far less than in the case of neat fiber, values of 190 MPa and 7.8 GPa were obtained for strength and modulus values for a 50/50 PBZT/Zytel 330® mixture.⁴ This indicates marked reinforcement by the rigid component, in spite of the fact that this molecular composite falls far short of being competitive with PBZT or other high performance fibers. Considerably more promising reinforcement was achieved with 30% PBZT in poly-2,5(6) benzimidazole where a modulus of 72 GPa was reported.⁵

Experimental

With blends of PBZT and amorphous nylon, thermodynamic incompatibility is experienced both for solutions of the two materials above the critical concentration and for concentrated bulk films of the two materials. In order to assure individual dispersion of the rods in the coil-like material, the films are produced, as previously described,⁶ by extruding solutions of slightly less than the critical concentration through a coat-hanger die into a deionized water nonsolvent. In this manner molecular composites containing 30% PBZT in a Zytel 330® matrix were formed. These films were basically clear with slightly gold color. If the molecular composite films are then heated above their glass transition temperature to allow for molecular mobility and moldability, immediately phase separation begins to occur, and thus the benefit in properties obtained from the molecular dispersion of the rods is gradually lost.

The kinetics of phase separation was studied using small angle light scattering (SALS) equipped with a Mettler Hot Stage and a two dimensional vidicon detector controlled by an EG&G Optical Multichannel Analyzer III (OMA III). A helium neon laser was utilized as a light source and a three lense system was employed to focus the scattering pattern onto the the detector. Kinetic studies were then performed by preheating the hot stage which has been installed in the SALS apparatus to the temperature of interest. The sample, which is mounted between a microscope slide and cover glass, is then preheated to 200° C prior to insertion into the hot stage. The OMA III is then programmed so that the entire SALS profile is

automatically taken once or twice each second depending on the speed of the phase demixing at a given temperature.

Results and Discussion

A glass transition temperature of 30% PBZT in polyamide molecular composite was determined by H. Chuah using DSC (differential scanning calorimetry) to be a few degrees below 300° C.⁴ The molecular mobility of a rod/coil blend usually does not start to become appreciable until about 50° C above the T_g . Thus to examine the phase separation behavior of these materials, temperatures of 250°, 255° and 265° C were selected.

For blends which have been forced together in spite of thermodynamic inclination to form two phases, they would not be expected to need a critical nucleus for phase separation to occur and would undergo spontaneous phase separation. the early stages of such a process are readily described by the Cahn-Hilliard model of spinodal decomposition.^{7,8}

The change in the light scattering profile with time at 265° is shown in Fig. 2. The scattering profile at this temperature as well as at 250° and 255° was broad and diffuse, more a shoulder in the scattering curve than a separate well defined peak. The scattering at very low values of q is due to voids present in the film resulting from the great amount of shrinkage accompanying the coagulation process utilized to produce these samples. The light scattering profile of PBZT/Nylon-6,6 molecular composites undergoing phases separation exhibited a maximum which was considerably more pronounced than that exhibited by the PBZT/Zytel 330® material.

This possibly indicates that the materials analyzed in this study are considerably less well ordered in their phase separated morphology than are the PBZT/Nylon-6,6 materials, which, to a good first order approximation, seem to follow the predictions of the spinodal theory.^{7,8}

In utilizing scattering to follow the kinetics of phase separation in the unstable region, it has been shown that the change in the concentration fluctuation with time, t , can be followed by the scattered intensity, $I(q,t)$:

$$I(q,t) = I(q,t=0) \exp[2R(q)t]$$

In examining the growth rate, of the scattered intensity at q_{\max} at all three temperatures, it seems that a linear region exists for the initial stages of phase separation (Fig. 1-3). Quite pronounced at the higher temperatures is a rather abrupt transition from this linear region to a later stage in which very little change takes place in the phase separated molecular composite. Unlike conventional polymer blends in which appreciable coarsening occurs by a variety of mechanisms, in molecular composites, the mobility of the rod rich phase becomes negligible, thus greatly limiting the amount of coarsening possible.

In Fig. 4, $R(q_{\max})$ is presented as a function of temperature. The rate of domain growth increases with temperature, primarily due to an increase in the mobility of the system with increased elevation above the T_g of the blend.

The background light scattering intensity from the molecular composite films investigated in this study was quite high, primarily

due to the presence of voids in these films which were induced during the coagulation process. Thus, it is very difficult to determine with certainty which portion of the scattered light results from the concentration fluctuations in the blend and which portion is due to background factors such as voids or impurities present in the film.

In polymer blends, the assumption can be made that the background scattering contribution does not change appreciably during the process of phase separation. By making this assumption, the light scattering data can be replotted in a method utilized by T.P. Russel⁹ which automatically separates out the background scattering contributions from those of the blend undergoing phase separation. In this approach, referred to by Russell as the $t^{1/3}$ plot, the quantity $[t / (I(t) - I(0))]^{1/3}$ is plotted as a function of time. Thus all of the scattering data obtained for the blends of 30% PBZT in the amorphous polyamide matrix were replotted in this form. In Fig. 5 the scattering results during phase separation at 250° C are presented in a $t^{1/3}$ plot. These results are very similar in appearance to those obtained at other temperatures in the relative amount of noise present in the results obtained. Clearly it is possible to draw a straight line through the data as would be indicative of the early stages of spinodal decomposition. However, on all the plots, the noise present in the data is too great for the claim of the presence of a linear region to be made.

Therefore, for further work to be done on this blend system using the light scattering method, the signal to noise ratio must be markedly increased. The most direct way of achieving this would be

by changing the processing conditions in such a way that fewer voids are present in the molecular composite film obtained. To prepare small films suitable for light scattering, a method utilized by T. Kyu¹⁰ with reasonably good success is to shear a solution of the molecular composite material between two glass slides while it is immersed in deionized water. Another approach which could also be tried is that of filling the voids with an inert material which would approximately match the average refractive index of the blend.

As a molecular composite prototype, this system was disappointing since phase separation occurs rapidly enough to rule out the possibility of remolding or reshaping this material after its initial spinning process. Two methods currently being pursued in several laboratories to enhance compatibility are, firstly, increasing attractive secondary interactions between components and secondly, utilizing copolymers which entropically are more difficult to (micro)phase separate.

REFERENCES

1. Wierschke, S. G., Private Communication.
2. Adams, W. W., and R. K. Eby, MRS Bulletin, 12(8), 22, (1987).
3. E. Chenevey, Private Communication.
4. Chuah, H. H., Private Communication.
5. Hwang, W.-F., et al., Macrom. Sci., B22, 231 (1983).
6. Chuah, H. H., T. Kyu, and T. E. Helminiak, Polymer, 28, 2129 (1987).
7. Cahn, J. W. and J. E. Hilliard, J. Chem. Phys., 31, 688 (1959).
8. Cahn, J. W. , J. Chem. Phys., 42, 93 (1965).
9. T. P. Russell, American Physical Society Meeting , New Orleans, 1989.
10. T. Kyu, Private Communication.

1988 USAF-UES RESEARCH INCENTIVE PROGRAM

Sponsored by the
AIR FORCE OFFICE OF SCIENTIFIC RESEARCH

Conducted by the
Universal Energy Systems, Inc.

FINAL REPORT

STRUCTURAL ANALYSIS OF MODEL COMPOUNDS WITH POTENTIAL
SECOND AND THIRD ORDER NONLINEAR OPTICAL PROPERTIES

Prepared by:	David A. Grossie, Ph.D.
Academic Rank:	Assistant Professor
Department and	Department of Chemistry
University:	Wright State University
Date:	31 Dec 89
Contract No:	F49620-88-C-0053

ACKNOWLEDGEMENTS

I would like acknowledge the Air Force Systems Command and the Air Force Office of Scientific Research for sponsorship of this research. Additionally, acknowledgement of Universal Energy Systems must be given for their assistance in the administrative aspects of the program.

I wish to thank the Polymer Branch of the Materials Laboratory for access to the Enraf-Nonius CAD4 single-crystal diffraction system, on which all data was collected.

STRUCTURAL ANALYSIS OF MODEL COMPOUNDS WITH POTENTIAL
SECOND AND THIRD ORDER NONLINEAR OPTICAL PROPERTIES

by

David A. Grossie, Ph.D.

ABSTRACT

Single-crystal x-ray diffraction data was collected on 2-amino-5,8-dimethylbenzothiazole and 5,8-dimethyl-2-[3'-methoxyphenyl]benzothiazole, compounds designed to model of a polymer chain, with an electron-withdrawing group available for attachment of a pendent having potential nonlinear optical (NLO) properties. The former compound is an intermediate in the synthesis of such a NLO compound, whereas the latter should exhibit NLO properties. The synthetic intermediate crystallizes in an orthorhombic crystal lattice with cell constants of $a=8.188(2)$, $b=13.756(2)$, and $c=16.487(2)$ Å. The observed space group is $Pbca$, a centric space group. The structure was solved and refined, yielding a R-factor of 0.053. The compound is planar with little distortion in the internal bond distances and angles.

The latter compound crystallizes in a monoclinic crystal lattice having cell constants of $a=7.622(2)$, $b=12.188(4)$, $c=14.588(4)$ Å, and $\beta=92.04(2)^\circ$. The space group was determined to be $P2_1/c$. The completed structure yielded an R-factor of 0.063. The benzothiazole and methoxyphenyl ring structures are each planar, but lie in the molecule with a 16.32° interplanar angle. The bond distances and angles are normal for the phenyl and benzothiazole ring system, showing minimal distortion.

I. INTRODUCTION:

The Polymer Branch of the Materials Laboratory at the Wright Aeronautical Laboratory, Wright-Patterson Air Force Base and the Department of Chemistry at Wright State University are interested in the synthesis and characterization of polymeric materials. Basic research is also conducted in the structure of polymeric materials and the correlation of the structure and physical properties. The emphasis of this area is to predict the properties of a polymer prior to its synthesis. In this way, the synthesis problem can have greater direction and produce new and better materials with more efficiency. One of the techniques used in determining the structure of polymers is to examine by single-crystal x-ray diffraction methods compounds that may be used to form the backbone, pendants, or cross-links of the polymer. By knowing the structure of a small, repeating portion of the polymer, the polymer itself may be mathematically modeled, yielding the physical properties.

II. OBJECTIVES OF THE RESEARCH EFFORT:

A study of model compounds of polymeric materials that have potential nonlinear optical properties will be conducted. This study will involve the structural analysis of several compounds by single-crystal x-ray diffraction techniques, with the intent to amass data which may be used to correlate the observed structure and the magnitude of the nonlinear optical response. The primary structural information that is needed by the currently accepted theories is the centricity of the crystal lattice in which the compound of interest crystallizes and the extent of π -orbital conjugation. To this end, the study will examine derivatives of 2-methyl-4-nitroaniline, a compound with known nonlinear optical properties, and other conjugated systems with separated electron donor and acceptor groups. In addition, the analysis will be conducted into the means of attaching the NLO active compound to a polymer chain through the examination of polymeric models with available electron donor or acceptor functionalities.

III.

- a. Crystalline samples of a series of compounds were examined using an optical microscope to determine the size and quality of the individual crystals. Two of the compounds examined showed promise of containing suitable crystals for diffraction analysis, whereas the remainder were of insufficient size to be analyzed. Single crystals of 2-amino-5,8-dimethylbenzothiazole and 5,8-dimethyl-2-[3'-methoxyphenyl]-benzothiazole were prepared for analysis by attaching them to a thin glass fiber and placing them at the center of an Enraf-Nonius CAD-4 automated diffractometer. Preliminary x-ray analysis of each of the selected crystals was made. These results are summarized in Table 1, along with the parameters of the subsequent data collections.
- b. Data collected on each of the crystalline samples was examined for the presence of space-group-determining systematic absences using the program LOOK (Chapius, 1984). For each sample, an appropriate space group was determined--Pbca for 2-amino-5,8-dimethylbenzothiazole, and P2₁/c for 5,8-dimethyl-2-[3'-methoxyphenyl]benzothiazole.
- c. Using the direct methods routines contained in the XTAL system of crystallographic programs (Grossie, 1988; Hall and Stewart, 1989), the initial structures were determined. These structures were refined using SFLSX (Hall, Spadaccini, Olthoff-Hazekamp, and Dreissig, 1989) a full-matrix least-squares refinement program contained in XTAL (Hall and Stewart, 1989).
- d. Figure 1 shows an ORTEP (Johnson, 1971; Davenport, Hall, and Dreissig, 1989) drawing of the refined structure of 2-amino-5,8-dimethylbenzothiazole. A listing of the interatomic distances and angles is presented in Table 2. The molecule is completely planar, with a maximum deviation from planarity of 0.072 Å.

e. Figure 2 shows an ORTEP (Johnson, 1971; Davenport, Hall, and Dreissig, 1989) drawing of 5,8-Dimethyl-2-[3'-methoxyphenyl]benzothiazole. Intramolecular distances and angles are presented in Table 3. The molecule consists of two planar ring systems, benzothiazole moiety and a methoxyphenyl moiety. The two groups are planar, with maximum deviations from planarity of 0.028 Å and 0.024 Å, respectively. The two planes intersect with an angle of 16.32°. The phenyl ring of the methoxyphenyl group is very regular with minimal variance in the distances and angles. The average values found for the internal distances and angles are 1.382 Å and 120.0°

f. The benzothiazole ring system in each compound is virtually the same, with only minor variations in specific distances and angles. The five-membered thiazole rings are distorted as expected, with the sulfur atom having a more acute angle than the 108° of an idea pentagon. The other four angles are found to be more oblique, two slightly more oblique (109 - 110°) and two greatly oblique (115 - 116°).

IV.

From the completed analysis of 2-amino-5,8-dimethylbenzothiazole and 5,8-dimethyl-2-[3'-methoxyphenyl]benzothiazole, certain conclusions can be made regarding to the nonlinear optical properties of these compounds. Since both crystallize in lattices that are centrosymmetric, the second-order term of the polarizability equation must be zero. The two compounds do show however, that it is possible to place a NLO active fragment in a model of a polymerizable material.

V. RECOMMENDATIONS:

There is a need to improve the synthesis of nonlinear optical materials, with one of the improvements being in the selection of potential compounds for synthesis. Included in this area is the ability to attach the NLO active molecular fragment to a polymer chain. A second area where improvement is needed is in the quantification of the molecular parameters that produce a nonlinear optical response. This second area can potentially provide the information needed to make the improvement in the selection of synthesis candidates.

Currently, there are three factors that are assumed to produce the desired NLO response, with one factor being quantitative and a second based on a relative scale. These two factors are the centricity of the crystal lattice and the electron-donating and withdrawing effects of the commonly used functional groups. The third factor, the extent of conjugation within the molecule, is currently unquantified. Molecular planarity is normally taken as the first clue that a non-fused, π -bonded ring system is conjugated. Since this information, like the centricity, is directly obtainable from the structural analysis of a crystalline compound, the extent of conjugation can be quantified by this process.

As a final step, the same compounds examined by x-ray diffraction need to be tested for a nonlinear optical response and the magnitude of that response. With the above pieces of data obtained and analyzed, the synthesis of nonlinear optical materials can be by rational design. This will allow the physical properties of the material to be optimized without compromising the desired nonlinear optical properties.

REFERENCES

Chapius, G., "LOOK. A FORTRAN Program for Generating Simulated Precession Photographs from Diffractometer Data," University of Lausanne, Switzerland, 1984.

Davenport, G., Hall, S. R., and Dreissig, W., "ORTEP, XTAL 2.6 User's Manual," Hall, S. R. and Stewart, J. M., Eds., Universities of Western Australia and Maryland, 1989.

Grossie, D., "Desktop Crystallography: XTAL on a Personal Computer," American Crystallographic Association Meeting, 1988.

Hall, S. R. and Stewart, J. M., Eds., "XTAL 2.6 User's Manual," Universities of Western Australia and Maryland, 1989.

Hall, S. R., Spadaccini, N., Olthof-Hazekamp, R., and Dreissig, W., "SFLSX, XTAL 2.6 User's Manual," Hall, S. R. and Stewart, J. M., Eds., Universities of Western Australia and Maryland, 1989.

Johnson, C.K., ORTEP II. Report ORNL-3794, revised. Oak Ridge National Laboratory, Tennessee, 1971.

Table 1. Experimental Details for 2-Amino-5,8-dimethylbenzothiazole and 5,8-Dimethyl-2-[3'-methoxyphenyl]benzothiazole.

	2-Amino	2-[3'-methoxyphenyl]
Formula:	$C_9H_8N_2S$	$C_{16}H_{15}NOS$
Formula weight:	176.2	269.4
F(000):	736	568
Crystal dimensions:	0.35 x 0.40 x 0.50 mm	0.20 x 0.30 x 0.40 mm
Radiation:	Mo $K\alpha$	Mo $K\alpha$
Wavelength:	0.71073 Å	0.71073 Å
Temperature:	23°	23°
Crystal form:	orthorhombic	monoclinic
Space group:	Pbca	$P2_1/c$
Cell constants:	a = 8.188(2) Å b = 13.756(4) Å c = 16.487(2) Å	a = 7.622(2) Å b = 12.188(4) Å c = 14.588(4) Å β = 92.04(2)°
Volume:	1857.0 Å ³	1354.3 Å ³
Z:	8	4
Density:	1.26 g/cm ³	1.32 g/cm ³
Absorption coefficient:	2.80 cm ⁻¹	2.19 cm ⁻¹
Scan type:	$\omega/2\theta$	$\omega/2\theta$
Scan rate:	0.51 - 5.58°/min	0.51 - 4.19°/min
Scan width:	1.00 + 0.344 tan θ	1.00 + 0.344 tan θ
Maximum 2 θ :	62.0°	44.0°
Reflections measured:	3505 total 3341 unique	1909 total 1750 unique
Corrections:	Lorentz-polarization Reflection averaging (agreement on I = 4.4%)	Lorentz-polarization Reflection averaging (agreement on I = 3.3%)
Observations:	1327 with I > 3 σ (I)	1298 with I > 3 σ (I)
Parameters:	109	172
R:	0.053	0.063
wR:	0.055	0.063
Goodness-of-fit:	3.187	1.497
Maximum shift/error:	0.0008	0.0006
Residual density		
maximum:	0.3 e/Å ³	0.4 e/Å ³
minimum:	0.3 e/Å ³	0.5 e/Å ³

Table 2. Interatomic Bond Distances (Å) and Angles (°) for 2-Amino-5,8-dimethylbenzothiazole.

Atom 1	Atom 2	Distance	Atom 1	Atom 2	Atom 3	Angle
S(1)	C(2)	1.746(4)	C(2)	S(1)	C(9)	88.9(2)
S(1)	C(9)	1.736(3)	S(1)	C(2)	N(3)	116.7(3)
C(2)	N(3)	1.309(4)	S(1)	C(2)	N(10)	119.9(3)
C(2)	N(10)	1.352(5)	N(3)	C(2)	N(10)	123.4(3)
N(3)	C(4)	1.399(4)	C(2)	N(3)	C(4)	109.5(3)
C(4)	C(5)	1.398(5)	N(3)	C(4)	C(5)	124.9(3)
C(4)	C(9)	1.402(5)	N(3)	C(4)	C(9)	115.4(3)
C(5)	C(6)	1.380(5)	C(5)	C(4)	C(9)	119.6(3)
C(5)	C(11)	1.494(5)	C(4)	C(5)	C(6)	116.9(3)
C(6)	C(7)	1.385(6)	C(4)	C(5)	C(11)	120.3(3)
C(7)	C(8)	1.391(5)	C(6)	C(5)	C(11)	122.8(3)
C(8)	C(9)	1.392(5)	C(5)	C(6)	C(7)	122.8(3)
C(8)	C(12)	1.495(6)	C(6)	C(7)	C(8)	121.7(4)
			C(7)	C(8)	C(9)	115.3(4)
			C(7)	C(8)	C(12)	123.3(4)
			C(9)	C(8)	C(12)	121.3(3)
			S(1)	C(9)	C(4)	109.5(3)
			S(1)	C(9)	C(8)	126.9(3)
			C(4)	C(9)	C(8)	123.6(3)

Table 3. Interatomic Bond Distances (Å) and Angles (°) for 5,8-Dimethyl-2-[3'-methoxyphenyl]benzothiazole.

Atom 1	Atom 2	Distance	Atom 1	Atom 2	Atom 3	Angle
S(1)	C(2)	1.762(4)	C(2)	S(1)	C(9)	89.2(2)
S(1)	C(9)	1.716(4)	S(1)	C(2)	N(3)	114.7(3)
C(2)	N(3)	1.500(5)	S(1)	C(2)	C(10)	119.5(3)
C(2)	C(10)	1.467(6)	N(3)	C(2)	C(10)	125.8(4)
N(3)	C(4)	1.387(5)	C(2)	N(3)	C(4)	110.9(3)
C(4)	C(5)	1.403(6)	N(3)	C(4)	C(5)	124.0(4)
C(4)	C(9)	1.389(6)	N(3)	C(4)	C(9)	115.1(4)
C(5)	C(6)	1.379(6)	C(5)	C(4)	C(9)	120.9(4)
C(5)	C(17)	1.503(6)	C(4)	C(5)	C(6)	116.5(4)
C(6)	C(7)	1.393(7)	C(4)	C(5)	C(17)	121.6(4)
C(7)	C(8)	1.369(7)	C(6)	C(5)	C(17)	121.8(4)
C(8)	C(9)	1.409(6)	C(5)	C(6)	C(7)	121.8(4)
C(8)	C(16)	1.496(7)	C(6)	C(7)	C(8)	123.0(4)
C(10)	C(11)	1.390(6)	C(7)	C(8)	C(9)	115.3(4)
C(10)	C(15)	1.381(6)	C(7)	C(8)	C(16)	123.3(4)
C(11)	C(12)	1.381(6)	C(9)	C(8)	C(16)	121.3(4)
C(12)	C(13)	1.374(6)	S(1)	C(9)	C(4)	110.0(3)
C(12)	O(18)	1.375(6)	S(1)	C(9)	C(8)	127.5(4)
C(13)	C(14)	1.380(7)	C(4)	C(9)	C(8)	122.4(4)
C(14)	C(15)	1.387(7)	C(2)	C(10)	C(11)	118.7(4)
O(18)	C(19)	1.434(5)	C(2)	C(10)	C(15)	121.3(4)
			C(11)	C(10)	C(15)	119.9(4)
			C(10)	C(11)	C(12)	119.8(4)
			C(11)	C(12)	C(13)	120.3(4)
			C(11)	C(12)	O(18)	115.2(4)
			C(13)	C(12)	O(18)	124.5(4)
			C(12)	C(13)	C(14)	120.2(4)
			C(13)	C(14)	C(15)	120.0(4)
			C(10)	C(15)	C(14)	119.8(4)
			C(12)	O(18)	C(19)	117.2(3)

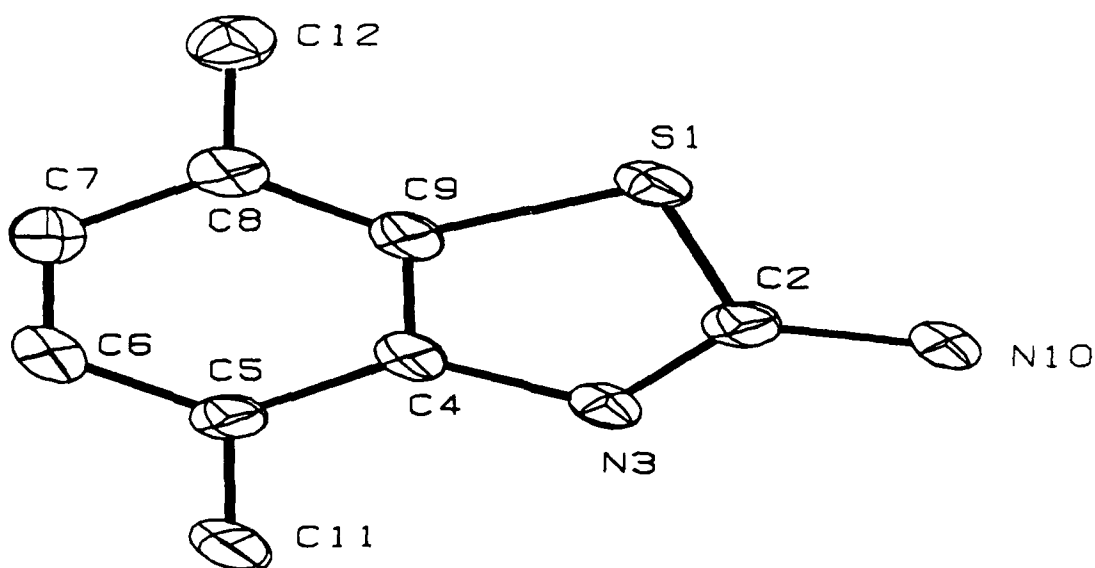


Figure 1. ORTEP drawing of 2-amino-5,8-dimethylbenzothiazole. Atoms are shown at 20% thermal probability. Hydrogen atoms have been omitted for clarity.

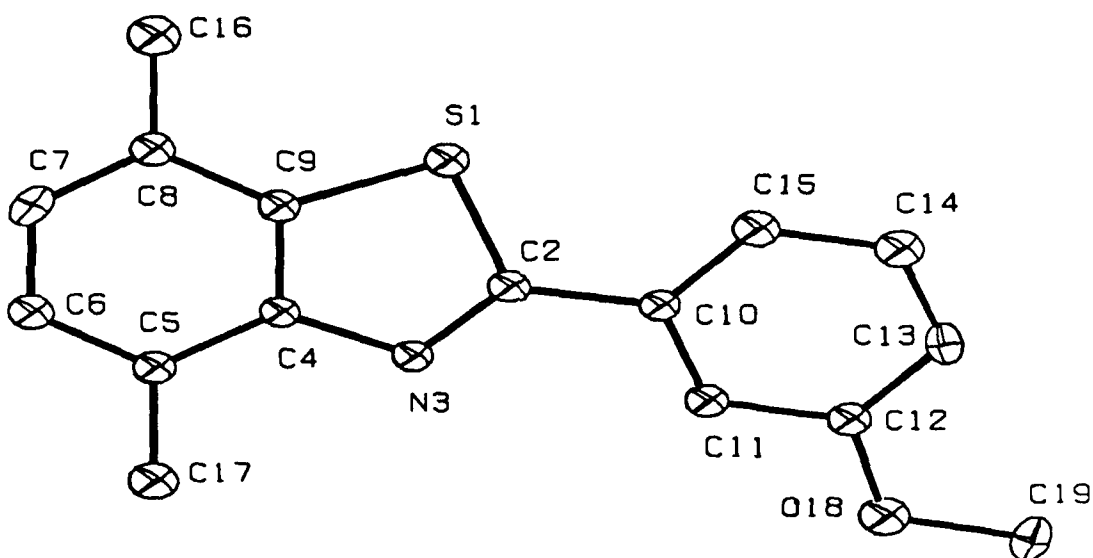


Figure 2. ORTEP drawing of 5,8-dimethyl-2-[3'-methoxyphenyl]benzothiazole. Atoms are shown at 20% thermal probability. Hydrogen atoms have been omitted for clarity.

1717s

RESEARCH INITIATION PROGRAM MINI-GRANT

Sponsored by the
AIR FORCE OFFICE OF SCIENTIFIC RESEARCH
BOLLING AFB, DC

LIQUID CRYSTAL BIOMOLECULES FOR USE AS OPTICAL FILTERS

FINAL REPORT

Submitted

by

Gordon O. Johnson, Ph. D.

Physics Department
Walla Walla College
204 S. College Avenue
College Place, WA 99324

December 23, 1988

Contract Number: S-760-7MG-075

LIQUID CRYSTAL BIOMOLECULES FOR USE AS OPTICAL FILTERS

by

Gordon O. Johnson

ABSTRACT

Cholesteric liquid crystals have a helical structure that when aligned properly will reflect light of a particular wavelength. The shorter the period of the helical structure (the so-called Grandjean lines); the shorter the wavelength reflected. Two biomolecules, poly-gamma-benzyl-L-glutamate (PBLG) and poly-gamma-ethyl-L-glutamate (PELG), were investigated in several different solvent systems. For PBLG in dioxane the minimum Grandjean line spacing was 3 microns at 50 wt.% PBLG. More concentrated solutions are so viscous that homogeneity is difficult to achieve. For PBLG in dimethylformamide a minimum spacing of 1 micron was achieved at 45 wt.% PBLG. These solutions are also less viscous than those in dioxane, but they are easily contaminated by water. By extrapolation Grandjean spacings appropriate for visible light reflections should occur at 65 wt.% PBLG. The only apparent barrier to achieving this is more stringent control of preparation and handling to avoid contamination. Alignment studies on PBLG/dioxane solutions sandwiched between two glass slides did show that etching the glass with hydrofluoric acid was somewhat effective in aligning the biomolecules parallel to the glass surface. PELG in various solvents resulted in transparent gels which showed some iridescent colors, but had no visible Grandjean lines.

I. INTRODUCTION

The work under the current grant focused on the study of the liquid crystal biomolecules, poly-gamma-benzyl-L-glutamate (PBLG) and poly-gamma-ethyl-L-glutamate (PELG). To make a thin optical coating that will reflect a particular wavelength of light due to the helical nature of the liquid crystal structure requires that the helices of the cholesteric liquid crystals be oriented perpendicular to the surface. The cholesteric structure of these molecules is really that of successive parallel layers that are rotated slightly with respect to each other thus forming a helical rotation of the molecules at any point in the layer. The so-called Grandjean spacing is the distance necessary for the molecules to rotate 180 degrees. The desired reflection is obtained when the light is parallel to the axes of these helices.[1] This stipulates that the structure should be oriented such that the molecules are parallel to the surface which is to be coated.

Previous work by Robinson [2] verified the fact that the Grandjean spacing of PBLG molecules in the solvent dioxane varies with PBLG concentration, the spacing becoming smaller as the concentration increases. His work includes a study of the effect of the molecular weight of the PBLG molecules on the phase diagram. A typical phase diagram (see Fig. 1) for these cholesteric liquid crystal solutions at room temperature shows an isotropic noncrystalline phase at low concentrations with a well-defined transition to a mixed phase at a higher concentration. Further increases in concentration result in a

transition to the desired liquid crystal phase. From Robinson's work the transition to the liquid crystal phase at room temperature occurs at 12 wt.% PBLG in dioxane if the molecular weight of the PBLG molecules is greater than 80,000. For smaller molecules the minimum concentration of PBLG required to be in the liquid crystal phase increases sharply; however, the Grandjean spacing in this phase remains constant at a given concentration of PBLG, irrespective of the molecular weight of the PBLG molecules. Our observations have confirmed that this is the case.

Another factor to consider is that the viscosity of the PBLG solutions increases dramatically as the concentration increases, but a solution of smaller molecules at a given concentration is less viscous than a solution of larger molecules. Since the Grandjean spacing is not a function of molecular weight, this can be a method to obtain more workable solutions still having small Grandjean spacings.

Studying the characteristics of PBLG in other solvents such as dimethylformamide (DMF) where previous workers have found smaller Grandjean spacings [3] is prompted by the desire to have Grandjean spacings on the order of visible light wavelengths. Solutions of PELG molecules in ethyl acetate have also been reported to have small Grandjean spacings.[4] Sandwich structures consisting of layers of liquid crystal solution between glass slides were made to study the alignment of the molecules with respect to the glass surface. Various surface treatments were used to optimize the desired parallel configuration.

The present work was twofold: 1) make solutions of

biomolecules with Grandjean spacings on the order of visible wavelengths of light, and 2) determine methods of aligning the molecules parallel to the glass surfaces.

II. EXPERIMENTS

Grandjean Spacing in Solutions of PBLG in Dioxane

To verify the conformity of PBLG solutions in dioxane to previous work using molecules with molecular weights of 200,000 or greater, solutions of 15, 20, 30, and 40 wt.% PBLG in dioxane were prepared. After allowing the solutions ample time to dissolve and become homogeneous, capillary tubes were filled with the solutions and sealed with a flame. The long range liquid crystal structure was then allowed to form over periods of hours or days. Microscope photographs were then made, usually with crossed polarizers, to obtain measurements of the Grandjean spacing.

Figure 2 shows the dependence of the Grandjean spacing on the concentration of PBLG in solutions of dioxane. These results are in quite good agreement with previous work.[2, 5] The figure includes the data for three different molecular weights 23,000, 196,000, and 260,000. No data is available for the 23,000 molecular weight below 40 wt.% because of the transition to the mixed phase region and the appearance of spherulites.[2, 4] Spherulites are indicative of the mixed phase in the phase diagram. Although they do show a circular Grandjean pattern, the spacing is equal to that of the concentration at the transition from the mixed phase to the

liquid crystal phase and is thus independent of the actual concentration of the solution. The minimum Grandjean spacing seen with this system, PBLG in dioxane, is about 3 microns.

Grandjean Spacing in Solutions of PBLG in DMF

DMF is highly hygroscopic so careful handling is necessary to prevent contamination with water. Consequently, solutions were mixed inside gloveboxes filled with dry nitrogen. Capillary tubes for observing the Grandjean spacing were also filled in the gloveboxes, but the sealing of the capillary tubes was completed outside. Figure 3 shows the results found with the solvent DMF and PBLG molecules with a molecular weight of 196,000. In agreement with Miller et al. [3], it was found that the spacing of the Grandjean lines decreased more rapidly with concentration than in the PBLG/dioxane system. The spacing at 45 wt.% PBLG in DMF was just resolvable with a magnification of 400x on the microscope and is right at 1 micron. No particular barrier to attaining even smaller spacings was evident. They were not explored since they would be too small to observe and verify. Contrary to the PBLG/dioxane system which exhibited more random orientations the Grandjean lines for the various solutions of PBLG in DMF were always observed to be nearly parallel to the walls of the capillary tubes.

At the higher concentrations of PBLG in DMF the solutions were an opaque white gel at room temperature. These solutions could be made transparent by heating them above room temperature. The process was quite reversible. An obvious

question is whether this represents the phase change from the mixed phase to the liquid crystal phase shown in Fig. 1. The transition temperature from the opaque to clear states varied from below room temperature at 20 wt.% PBLG to about 50°C at 60 wt.% PBLG for PBLG molecules with molecular weights >196,000. Furthermore the transition temperature increased as the solution aged making definite determinations of transition temperatures difficult. Since the solutions were stored in air in tubes sealed with a screw-on cap, slow contamination with water vapor is suspect. The same behavior also began to occur in samples pulled into capillary tubes (probably due to imperfect sealing or some adsorbed water on the capillary surfaces). The capillary tubes were cycled from the transparent state to the opaque state and back to the transparent state without any noticeable changes in the Grandjean patterns at a particular observation point. Other authors [6] have also used a transition from an opaque state to a transparent state to determine the phase boundary in PBLG solutions.

PBLG Solutions in Thin Sandwich Structures

Sandwich structures using glass slides with spacers of various thicknesses to define the thickness of the sandwich were studied in detail. Along with varying the sandwich thickness the surface treatment of the glass slides was changed as well. Spacers to fit between the glass slides were cut from aluminum foil with a thickness of approximately 16 microns. Spacers up to 96 microns thick were made by using

multiple layers of the foil. Scribing and breaking cover glass with a thickness of 200 microns provided even thicker spacers. These procedures gave well-defined sandwich spacings. Microscope slides were used for the bottom layer and cover glass slides were used on the top.

Work performed during the summer of 1987 [5] seemed to indicate that the desired orientation of the biomolecules parallel to the surface could be preferentially enhanced by etching the glass slides with dilute hydrofluoric acid (HF). To study this in detail and to optimize the procedure a series of sandwich structures were made using unetched glass slides as controls and etched glass slides as the subjects for comparison. Liquid crystal solutions of PBLG in dioxane were used for most of these observations because they had been characterized most completely and were not so sensitive to the presence of water vapor. Solutions containing 20% PBLG (molecular weights of 196,000 and 248,000) and 40% PBLG (molecular weights of 20,000 and 26,000) by weight were placed in sandwiches with spacer thicknesses of 16, 32, 64, 96, and 200 microns. The concentrations studied were chosen because more concentrated solutions of the heavy molecules are very viscous and thus are difficult to spread evenly and less concentrated solutions of the light molecules are not in the liquid crystal phase.

To determine the optimum etching process, slides were etched in 2-5% solutions of HF for periods of 20 seconds, 3 minutes, and 30 minutes. Control samples consisting of unetched slides were used for comparison. Observations of the sandwich structures were made with the polarizing microscope.

Since alignment of the molecules parallel to the glass surface would make the Grandjean layers lie parallel to the surface as well, light passing perpendicularly through the sandwich should not reveal the presence of Grandjean lines. Thus the primary criterion used for judging the degree of alignment was the absence of the striped Grandjean lines.

Before making the sandwiches the glass slides were cleaned carefully. Several different cleaning procedures were used with indistinguishable results. A typical procedure consisted of: 1) 5-10 minute rinse in acetone with ultrasonic agitation, 2) etch in HF for the desired time, 3) rinse with distilled water, 4) wash with Micro(TM) lab soap, 5) rinse with distilled water, 6) rinse with acetone for 1-3 minutes with ultrasonic agitation, and 7) dry overnight in vacuum oven at about 200°C. Control samples were prepared by omitting the etch in HF.

Microscope photographs of both control samples and etched samples were compared visually. Results at spacer thicknesses of 16 and 32 microns seemed to indicate that the 20 second etch was the most effective in suppressing the appearance of Grandjean lines in the sandwiches, therefore the remainder of the studies were done only with etch times of 20 seconds. To prevent the solutions in the sandwiches from drying out the samples were stored in petri dishes with dioxane in the bottom which were then kept in sealed plastic bags. Using this technique the sandwich samples could be kept for periods of weeks without degradation. Observations were made periodically with the microscope and photographs were taken. Summaries of the results are shown in Table I for 20% PBLG in dioxane and in Table II for 40% PBLG in dioxane. The term "worm structure" is

indicative of a pattern of meandering lines seen with the microscope at the boundary of the glass and the liquid crystal solution. It appears to be a pattern similar to that observed in other liquid crystal systems at the glass surface which has been interpreted to mean that the molecules are nearly perpendicular to the surface.[7] If this interpretation is correct, then suppression of the "worm structure" also indicates that the desired alignment parallel to the surface has been obtained.

PELG in Various Solvents

PELG molecules with a molecular weight of 160,000 were mixed with the solvents ethyl acetate, DMF, dioxane, and methylene chloride in concentrations varying from 5-30 wt.% PELG. Some early work by Robinson [4] indicated that Grandjean spacings on the order of visible wavelengths could be obtained using ethyl acetate as the solvent. All our attempts to duplicate this work resulted in transparent gels with viscosities so great that no flowing was visible during a period of days. In a couple of instances capillary tubes were partially filled with solution, but no Grandjean lines or other familiar structures were visible even though iridescent colors were observed through the microscope with crossed polarizers. Knowing that smaller molecules of PBLG result in solutions having much less viscosity suggested that smaller molecules of PELG might be the answer. All efforts to find a supplier of lighter molecules were without success.

III. CONCLUSIONS

The most important results can be summarized as follows:

1) PBLG in the solvent DMF looks like a very good candidate for achieving helical pitches in the range of visible wavelengths. The only problem lies in the fact that great care must be used to prevent contamination of the solutions after they are made.

2) The alignment of the biomolecules with respect to the glass surface is not an all or nothing matter. Although etching the glass lightly with hydrofluoric acid seems to give a greater probability of the molecules aligning with the surface, it by no means works 100% of the time. The thinner sandwich structures seem to be most affected by it. If PBLG/DMF solutions are used, the glass surfaces seem to favor parallel alignment of the molecules more than with the PBLG/dioxane system. This should reduce the need for special surface treatments.

3) PELG may very well be a molecule of interest, but the molecular weight presently obtainable does not even go into solution.

Several areas for additional work are also suggested by these results. Higher concentrations of PBLG in DMF should be tried using care to minimize any possible contamination. Our results would indicate by extrapolation that a 65 wt.% solution of PBLG in DMF should give Grandjean spacings appropriate to reflect visible light. Some of the lighter weight molecules may be useful here in making solutions that are not so viscous. Temperatures may need to be maintained above room temperature

to insure that the solutions remain in the liquid crystal phase.

Although a few open face sandwiches were tried, getting smooth, uniform coatings on a single glass slide is difficult, even when the film is placed in a solvent atmosphere for several days. Spin coating and other techniques should be utilized for this process.

The nature of the "worm structure" needs to be confirmed for our liquid crystal systems. Electric and/or magnetic fields applied to samples with such structures should conclusively show the orientation of the molecules at the surface. This is crucial for clearly understanding the surface effects on the liquid crystal layers.

ACKNOWLEDGMENTS

I would like to thank Melanie Thongs and Mark Pratt, both undergraduate students, for their hard work in carrying out many of the experimental details contained in this report. Their assistance was invaluable.

The sponsorship of the Air Force Office of Scientific Research and the administrative support of United Energy Systems are also much appreciated.

TABLE I

20 wt.% PBLG in Dioxane
(Molecular Weight 248,000 or 260,000)

<u>Spacer thickness</u>	<u>Control sample</u>	<u>Etched sample (20" in HF)</u>
16 microns	worm structure	no visible structure; uniformly magenta with tint plate
32 microns	Grandjean lines	Grandjean lines
64 microns	some Grandjean lines; cloudy	large regions without visible structure
96 microns	some Grandjean lines and worm structure	worm structure but no Grandjean lines
200 microns	some Grandjean with clear patches	Grandjean lines with some clear patches

TABLE II

40 wt.% PBLG in Dioxane
(Molecular Weight 20,000 or 26,000)

<u>Spacer thickness</u>	<u>Control sample</u>	<u>Etched sample (20" in HF)</u>
16 microns	Grandjean lines; bubbly	no visible structure; uniformly magenta with tint plate
32 microns	grainy; some Grandjean lines	grainy; some Grandjean lines
64 microns	Grandjean lines; grainy	no picture
96 microns	Grandjean lines; cloudy; bubbly	Grandjean lines; cloudy, bubbly
200 microns	very cloudy; grainy	very cloudy; grainy

FIGURE CAPTIONS

Fig. 1 - The phase diagram of the PBLG/DMF system. The temperature in Celcius is the vertical scale and the weight fraction of PBLG to DMF is the horizontal scale. I = isotropic phase; LC = liquid crystal phase; I + LC = mixed phase. (Data from Miller et al., Pure Appl. Chem., Vol. 38, 37 (1974))

Fig. 2 - Experimentally determined Grandjean line spacing in microns versus weight percent of PBLG in the PBLG/dioxane system.

Fig. 3 - Experimentally determined Grandjean line spacing in microns versus weight percent of PBLG in the PBLG/DMF system.

PBLG-DMF

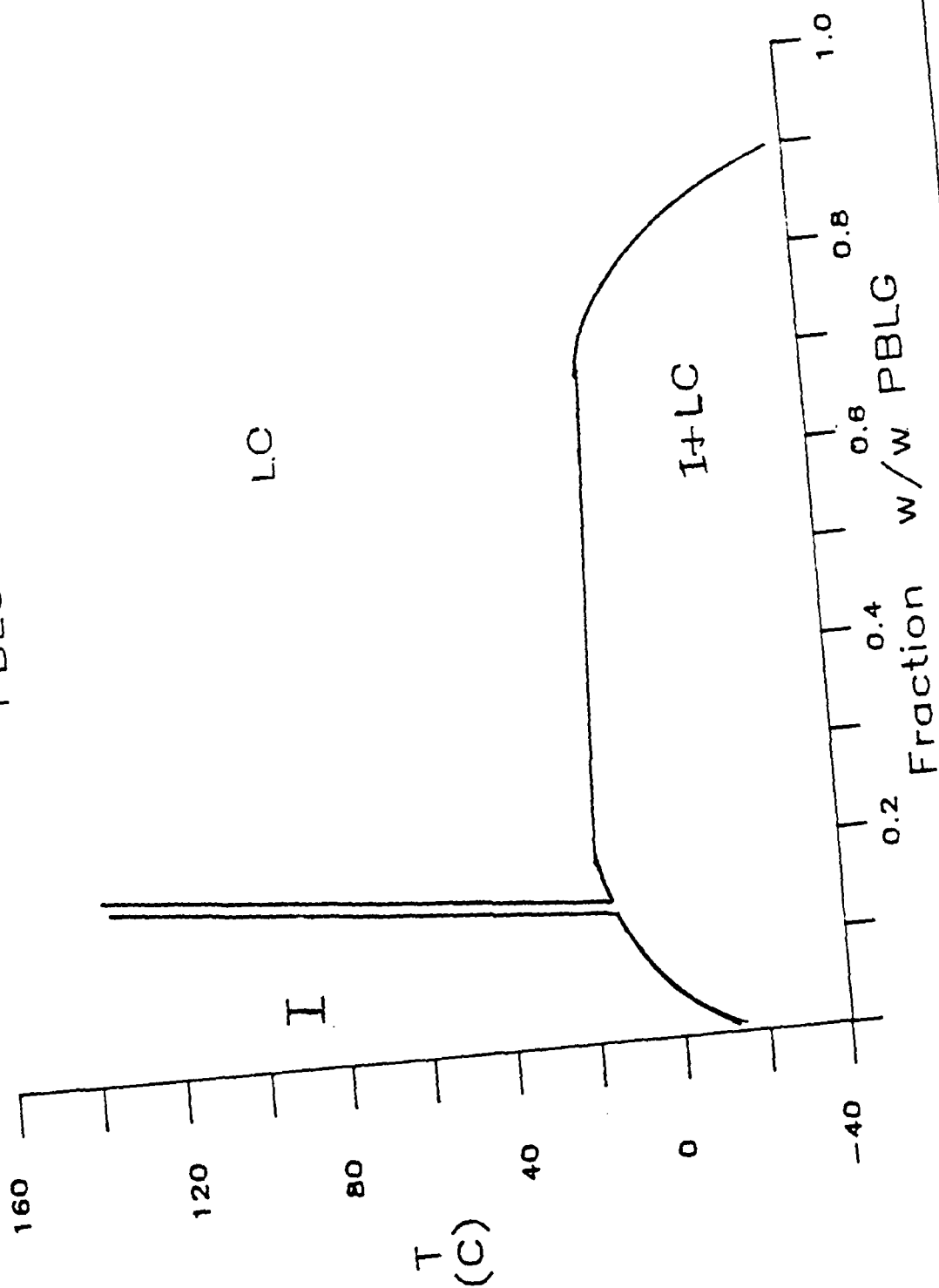


Fig. 1

Concentration Dependence of Spacing PBLG / Dioxane System

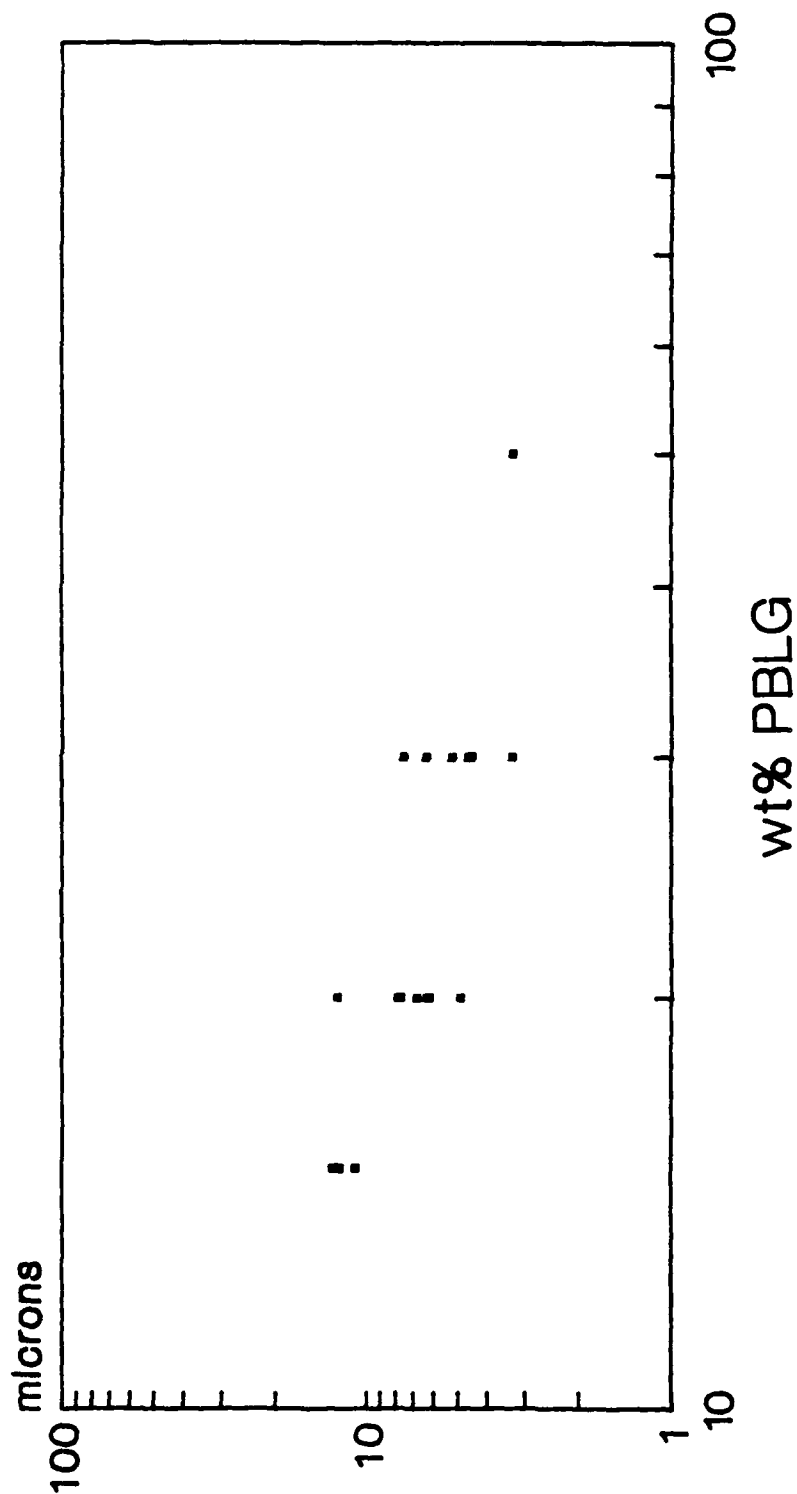


Fig. 2

Concentration Dependence of Spacing PBLG / DMF System

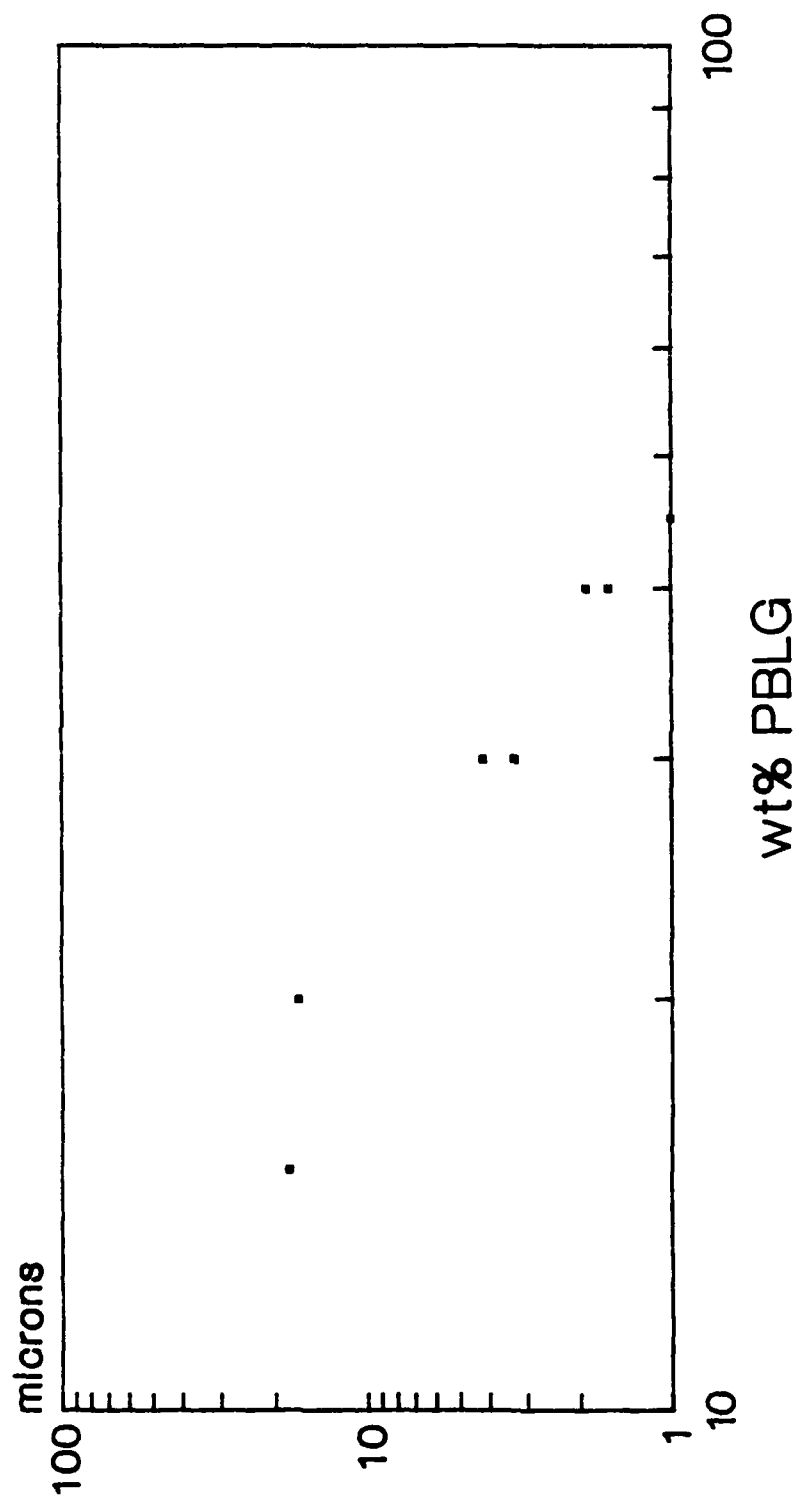


Fig. 3

REFERENCES

1. G. Gray and P. Winsor (editors), Liquid Crystals & Plastic Crystals, Vol. 2 (Ellis Horwood Limited, Chichester, 1973)
2. Conmar Robinson, J. C. Ward, and R. B. Beevers, Discussions Faraday Society, Vol. 25, 29-42 (1958)
3. Wilmer G. Miller, Paul S. Russo, and Sumana Chakrabarti, Journal of Applied Science: Applied Polymer Symposium 41. 49-63 (1985)
4. Conmar Robinson, Molecular Crystals, Vol. 1, 467-494 (1966)
5. Gordon Johnson, Report submitted to United Energy Systems for Air Force SFRP Program (1987)
6. Akio Nakajima, T. Hayashi, and M. Ohmori, Biopolymers, Vol. 6, 973-982 (1968)
7. W. Greubel, U. Wolff, and H. Kruger, Molecular Crystals and Liquid Crystals, Vol. 24, 103-111 (1973)

1989 Research Initiation Program (RIP)

sponsored by the
Air Force Office of Scientific Research

conducted by the
Universal Energy Systems, Inc.

FINAL REPORT

Prepared by:	L. James Lee, Ph.D.
Academic Rank:	Associate Professor
Department and	Chemical Engineering
University:	The Ohio State University
Research Location:	140 W. 19th Avenue
	Columbus, Ohio 43210
Date:	December 19, 1989
Contract No.:	F49620-88-C-0053/SB5881-0378

Knowledge Development for the Rule Based Process

Automation of Resin Transfer Molding

by

L. James Lee

ABSTRACT

This report covers two parts. One is the characterization of fibrous reinforcement mats in resin transfer molding and the other is the application of a dual heat flux sensor for on-line cure monitoring of graphite/epoxy composites. Mold filling experiments were conducted using two or more different fiber types in the mat stack, which created transverse porosity, permeability, and compressibility variations. The effect of these variations was studied by taking flow pressure measurements and observing the progress of the flow front of a non-reactive fluid filling a clear acrylic mold that contained the reinforcement mat stack.

The temperature distribution and the degree of cure of graphite/epoxy composites are governed by heat conduction and the exothermic reaction of epoxy resins. Determination of the major heat transfer and reaction characteristics was carried out by a scaling analysis. Exothermic reaction is best described by a lumped parameter, Damkohler number (Da). The value and/or change of Da can be used to establish rules for the control of heat transfer in order to reduce the cycle time and prevent the thermal runaway problem. The change of Da

at any given spot in the composite can be estimated by two heat flux sensors or by three closely displaced thermocouples. Experimental verification of this technique is presented.

Acknowledgements

I wish to thank the Air Force Office of Scientific Research for sponsorship of this research. Universal Energy Systems must be mentioned for their concern and help to me in all administrative and directional aspects of this program.

I would also like to thank Dr. Charles Lee and Ms. Frances Abrams at AFWAL/MLBC for their encouragement and technical support. Professor Bill Lee's (University of Dayton) interest in this project truly served as a source of stimulation. His help clearly added to this research project.

I. INTRODUCTION

Continuous fiber reinforced thermoset polymeric composites can be produced by injecting reactive liquid resins into molds with preplaced fiber mats. One process used in industry is resin transfer molding (RTM) where resin streams are mixed by mechanical means and then pumped into the mold containing fiber mats. Although RTM is already being used in industry, the process has not been thoroughly studied. Most technologies developed to date are based on experience or adapted from similar processes such as conventional reaction injection molding. As a result, there is considerable potential for improving these processes through a greater understanding. Part of this work seeks to develop a knowledge base of this process. Because of the time limit, the effort was concentrated on characterization of various fiber mats. The other part of this work seeks to develop a new method for the cure monitoring of thermoset resin based composites.

The manufacture of advanced thermosetting materials requires careful attention to heat transfer and exothermic reaction characteristics of the resin material. Often, productivity and the efficiency of time and energy use suffer because of slow and meticulous processing cycles. Cure temperature and pressure are normally set to follow some standard, pre-determined cycle. The standard cycles have been developed from years of processing experience. The difficulties associated with empirically determined cycles include the expensive trial and error experimentation, inflexibility to property variations from batch to

batch, and precautions cycles resulting in excessive processing times. In more sophisticated schemes, analytical process models have been utilized to aid in the design of new processing cycles. The analytical models are used to simulate the process, (i.e. temperature profile and degree of cure), based on imposed boundary conditions of temperature and pressure (1). The models allow for a less expensive manner to predict a suitable processing cycle. Process models or simulations are limited, however, by the simplifying assumptions that are necessary to achieve a solution. Again restrictive in this cycle design is the inflexibility to property variations from batch to batch and the simplified representation of the functional dependence of properties. A further limitation of process cycle design utilizing analytical models is the need to use simplified boundary conditions.

Recent developments have been made in the use of simple process models to go beyond design and attempt to automate the autoclave curing of composite materials (2). One such system developed is called Qualitative Process Automation (QPA) (2) and centers on the concept of using rule based models to yield qualitative results instead of the full quantitative solutions. The QPA system applies the qualitative results to a series of expert system rules in order to determine a proper control action to send to the molding machine. One specific application of the QPA concept has been in the identification of the reaction acceleration in curing graphite/epoxy composites from on-line temperature measurements. Accelerated reaction is the case when the rate at which the heat generated by reaction is greater than heat which

can be dissipated by conduction. This is represented as the point when the temperature gradient is positive (i.e. $\frac{dT}{dt} > 0$) and the second derivative of temperature indicates an inflection point, (i.e. $\frac{d^2T}{dt^2} > 0$) (2).

This work seeks to further expand the applicability of the QPA system through a more detailed identification of the major reaction characteristics which include the on-set of the cure reaction, reaction acceleration, and thermal runaway. This involves the development of a new sensor, on-line property estimation, and the use of dimensionless parameters to indicate the progress of the cure process. Specifically, the Fourier number (Fo), and the Damkohler number (Da), two dimensionless heat transfer parameters, are used. The on-line measurements and dimensionless numbers can be used to generate information which can be applied directly to an automation scheme such as the QPA system. In this study, the cure of a graphite/epoxy composite is used to demonstrate the concept and a dual heat flux sensor is developed for on-line measurements.

II. OBJECTIVES OF THE RESEARCH EFFORT

I participated in the 1988 Summer Faculty Research Program (SFRP) at AFWAL/MLBC, Dayton, Ohio. Working with several USAF researchers: Frances L. Abrams and Dr. Charles Lee, and Dr. Bill Lee from the University of Dayton. I learned the basic principles of the QPA system and autoclave curing. After a discussion with Dr. Charles Lee and

Frances Abrams, I decided to propose a research plan aimed at applying the rule based QPA system to the resin transfer molding (RTM) process, with particular emphasis on the development of a knowledge base. The reasons for choosing the RTM process are: (i) RTM is a relatively new composite manufacturing process with a great potential for Air Force applications because it is a faster and more economic processing method. (ii) There is necessary equipment in my laboratory for experimental work. And (iii) many governing phenomena in RTM are very similar to those in autoclave curing, e.g., heat generation, degree of cure and resin flow; therefore, the knowledge and sensors developed in the proposed research can be very useful for autoclave curing, as well.

The proposed research includes process characterization and the development of an on-line cure monitoring sensor.

The specific objectives are:

1. to carry out a detailed process characterization on laboratory RTM equipment such that the relationship among manipulated variables (i.e., mold temperature, injection rate or pressure, mold clamping force and mold vacuum), controlled variables (i.e., resin and fiber temperatures, resin pressure and mat porosity), governing phenomena (i.e., reaction kinetics, rheological changes, mat permeability and resin flow pattern), and process issues (i.e., cycle time, residual stresses, incomplete reaction, incomplete fill, void formation, fiber distortion and mold leakage) can be established.
2. to develop a knowledge base from scaling analysis and design a new on-line sensor for QPA application.

III. RESEARCH RESULTS

Because of time limitations, previously listed research objectives have only been partially finished. For process characterization, a detailed measurement of fiber mat permeability and compressibility has been carried out. The results are presented in Part I. For cure monitoring, the feasibility of using a dual heat flux sensor in conjunction with scaling analysis to detect the reaction progress has been investigated. The results are presented in Part II.

Part I: Fiber Mat Characterization in RTM

A. Apparatus for Permeability Measurements

The planar permeabilities of the fiber mats (i.e. k_x and k_y) were measured using the mold filling apparatus shown schematically in Figure 1 and the transverse permeability, k_z , measurement device is shown in Figure 2. A constant speed pump was constructed by mounting a 3-1/4 inch (8.25 cm) diameter, 3 inch (7.62 cm) stroke stainless steel hydraulic cylinder (Lynair Model H-3-1/4C01-3-SS) on an Instron Universal Testing Instrument (Model 1137). High pressure hydraulic tubing (9.5 mm O.D., 6.35 mm I.D.) was used to connect the cylinder to the permeability measurement device. The hydraulic cylinder was filled with a non-reactive fluid (DOP oil) by means of a rotary pump (Blackmer Model AT210A) and driven at a constant speed by the action (i.e. closing) of

the Instron crosshead. The fluid flow rates were varied by changing the closing speed of the Instron crosshead.

The 31.5 inch by 8 inch (80 cm by 20 cm) platens of the mold were constructed from 1/2 inch (1.27 cm) thick acrylic sheet. A 1/4 inch (6.35 mm) diameter inlet and a 1/4 inch (6.35 mm) diameter outlet (i.e. vent) separated by a distance of 21.25 inches (54 cm) were drilled into the upper platen. The mold cavity was formed by inserting a rectangular spacer of 1/16 inch (1.6 mm) thick aluminum. The mold was sealed by placing a 1/32 inch (0.8 mm) thick rubber gasket between the mold halves and the spacer and then clamping the entire assembly together with "C" clamps. In order to prevent the channeling of fluid between the edge of the fiber mats and the containing edge of the mold cavity, 1/4 inch (6.35 mm) wide strips of 1.16 inch (1.6 mm) thick neoprene rubber were pre-placed around the perimeter of the mold cavity to compress and clamp the edges of the fibers mats. A pressure transducer (Omega, Model PX302, 0-150 psi) located near the inlet was connected to a chart recorder. A vacuum pump can also be connected to this experimental set-up. The pressure measurements for k_x and k_y were made by placing the fiber mats in the mold cavity without covering the inlet and outlet allowing for a unidirectional flow in the machine direction.

The transverse permeability measurement device, which is similar to the one used by Miller and Clark (3), is shown in Figure 2. It consists of two pieces of aluminum pipe such that the inner pipe of 2.5 inch (6.35 mm) I.D. is mounted inside the outer pipe of 3.49 inch (8.87 cm) I.D. A circular specimen of fiber mat of any porosity is mounted

inside the inner pipe. A screen with 1 inch (2.54 cm) diameter hole in the center is placed at the bottom of the inside pipe in order to provide flow rates similar to those generated in the rectangular mold. The specimen is held by two stainless steel screens of 1/4 inch (6.35 mm) thickness and the thickness of the sample is fixed by a spacer of 1/8 inch (3.2 mm). A pressure transducer (Omega, Model PX 302, 0-5, 0-50, 0-150 or 0-300 psi) which is connected to a chart recorder (Houston Instruments, Omniscribe D5000) is located at the bottom of the outside pipe. In order to have a uniform flow, a "T" connector was placed near the liquid entrance at the bottom of the outside pipe. The transverse permeability k_z was calculated from the pressure-flow rate relationship for random, bidirectional and unidirectional fiber mats at different values of porosity. The porosity was varied by changing the number of fiber layers inside the device, maintaining sample thickness of 1/8 inch.

B. Apparatus for Compressibility Measurements

A head operated tensile/compression tester was used to determine the relationship of applied pressure and mat thickness. The tester has a 1000 pound (453.59 kg) load cell mounted on it. For these tests, the mats were slightly larger than the steel platens so the area of force application to the mats was the surface area of the platens. After compression, the distance between the platens was measured at each of the four corners with a dial caliper, and a force reading was taken. It took about one minute for the force to decline to a fairly steady

value; therefore, the force reading was taken at one minute after compression.

C. Results and Discussion

The permeability measurements (k_x , k_y , and k_z) were determined using pressure measurements by forcing the flow in the pre-specified direction for random, bidirectional and unidirectional fiber mats. The steady state pressure drop for a single type of reinforcement is often described by Darcy's Law.

$$Q = k A \Delta P / \mu \Delta L \quad (1)$$

Where Q = volumetric flow rate (ml/sec), μ = fluid viscosity (Pa-s), A = cross sectional area of the medium (cm²), $\Delta P/\Delta L$ = pressure drop per unit length (Pa/cm), and k = permeability of the porous medium (cm²). The unit most widely used for permeability measurement is the darcy. For a material of one darcy permeability, a pressure differential of one atmosphere will produce a flow rate of 1 cm/sec of fluid with a 1 cp viscosity through a cube having sides of 1 cm in length. Therefore,

$$1 \text{ darcy} = \frac{1 \text{ (cm}^3 \text{ sec)}}{1 \text{ (cm}^2) 1 \text{ (atm / cm)}} \frac{1 \text{ (cp)}}{1 \text{ (atm / cm)}}$$

For laminates consisting of a single type of fiber mat, the porosity can be found using the following equation.

$$\Phi = 1.0 - \frac{\rho_b}{\rho_f} \quad (2)$$

where ρ_b is the bulk density of the reinforcement inside the mold cavity, while ρ_f is the density of the fiber in the reinforcement. The bulk density of the reinforcement, ρ_b , was found by dividing the weight of fiber mats used in each run by the volume of the mold cavity.

Equation 2 can be expressed as

$$\Phi = 1 - \frac{n \xi}{t \rho_f} \quad (3)$$

where n is the number of reinforcement layers inside the mold, ξ is the surface density and t is the thickness of the mold cavity. The linear velocities were calculated from the superficial velocities of the fluid flows using the following equations:

$$v' = Q/A \quad (4)$$

$$v = v'/\Phi \quad (5)$$

where: v' = superficial velocity (cm/sec), Q = volumetric flow rate (ml/sec), A = cross-sectional area (cm²), v = linear velocity (cm/sec), Φ = porosity.

A relationship between porosity and permeability can be obtained by calculating the values of permeabilities at different porosities for a single type of reinforcement. Figure 3 shows the pressure drop versus

superficial velocity for the flow of DOP oil through different porosities (# of layers) of random, bidirectional and unidirectional fiber mats in the x direction in a 73.5 cm by 13.5 cm and 3.2 mm thick mold cavity. Figure 4 shows the results of pressure drop versus superficial velocity for bidirectional and unidirectional fiber mats in the y direction. For random fiber mats, it is not necessary to measure k_y because the flow pattern during the initial part of the mold filling shows a circular shape meaning that k_x and k_y are the same. Figure 5 shows plots of pressure drop versus superficial velocity at different porosities (# of layers) in the thickness direction for the flow of DOP oil through multi-layers of random, bidirectional, and unidirectional fiber mats.

Figure 6 compares permeability as a function of porosity in each direction of x, y and z for random, bidirectional and unidirectional fiber mats. The permeabilities in the x and y directions are function of the superficial velocity for random, bidirectional and unidirectional fiber mats because the relationship between ΔP and v' is curvilinear. The permeabilities in x and y directions shown in Figure 6 were calculated from the slopes of the lower portions of the curves of ΔP versus v' for the three types of fiber mats. Figure 6a shows that k_x is larger for bidirectional fiber mats than for unidirectional fiber mats. The permeability in the x direction for random fiber mats is similar to that of bidirectional fiber mats at low values of porosity, but is similar to that of unidirectional fiber mats at high values of porosity. For the three types of fiber mats, the permeability in the x

direction decreases significantly when the porosity decreases. In Figure 6b, the results of k_y as a function of porosity are presented. They follow the same trend as the permeabilities in the x direction. The permeability in the z direction for random and bidirectional fiber mats is independent of the superficial velocity because the relationship between ΔP and v' is linear. Therefore, the permeability in the z direction may be calculated at different porosities from the slopes of the lines of ΔP vs v' . In the case of unidirectional fibers mats, the permeability in the z direction is calculated from the lower portion of the curves of ΔP vs v' because the relationship between ΔP and v' is non-linear. For random fiber mats, k_z was found independent of the mat stack thickness, but for directional fiber mats, the mat stack has a synergistic effect on the transverse permeability. Increasing the number of mat layers at the same porosity tended to dramatically increase the flow pressure. All results shown in Figure 6c were based on a fixed mat stack thickness, i.e. 3.2 mm. Figure 6c shows that k_z is smaller in unidirectional fiber mats than in random and bidirectional fiber mats at the same values of porosity. Also, the permeability in the z direction is always higher in random fiber mats than in bidirectional fiber mats at the same values of porosity. The k_z for random glass fiber mats decreases greatly when the porosity decreases.

Figure 7 compares the permeability as a function of porosity for each fiber mat in x, y and z directions. The permeability in the x direction is larger than the permeability in the z direction for all

three types of fiber mats. However, the difference between the permeability in the x direction and that in the z direction (i.e. $k_x - k_z$) is larger for bidirectional fiber mats than for unidirectional and random fiber mats. Figures 7a and 7b show some differences between k_x and k_y for bidirectional and unidirectional fiber mats.

Compression tests showed that the compression force decayed with time. This implies that the mats reveal a visco-elastic type response and that closing speed may be an important factor in determining the peak pressure obtained during compression. The plots of steady pressure versus porosity for three types of fiber mats are shown in Figure 8. It can be seen that as compression pressure increased, the porosity of each of these mats was reduced. The porosity of the bidirectional fiber mat was reduced from about 70% to 45% as the pressure was increased from .1 to 150 psi ($6.9E2$ to $1.0E6$ n/m^2). Over the same pressure range the porosity of the random fiber mat dropped from 95% to 60%. It appears from examining the pressure vs. porosity plots in Figure 9 that the porosity of the random fiber mat remains higher than the porosity of directional fiber mats even at significantly higher pressure levels. Therefore, when these random and directional reinforcing mats are included in the same mat stack, the porosity in the random fiber mat will be significantly higher than that in the directional fiber mats. Due to the difference in porosity levels, when these mats are compressed with the same pressure, the in-plane permeability of the random fiber mats will also be higher than that of the

directional fiber mats, as shown in later experiments, although the in-plane permeabilities of the directional fiber mats are higher than those of the random fiber mats at the same porosity level.

To develop an accurate mathematical relationship between compression pressure and mat thickness, pressure was plotted against the fiber volume fraction (V_f). Logarithmic curves were then fitted to the plots of \log pressure versus V_f . Logarithmic equations were found to fit fairly well the plots of V_f versus pressure as shown in Figure 9. It can be seen that the first data point at $1.17\text{E}3 \text{ N/m}^2$ did not fall on the curve with the others when plotted in this manner. The compression pressure for this data point was created by laying 1.27 cm steel plate on the stack of fiber mats when no additional force was applied by the compression tester. With such a low compression pressure the fiber mats can easily be displaced during filling. Therefore, a compression pressure this low should not be used in actual molding processes. The equations describing the compression behavior of the mats tested are as follows:

Random Fiber Mat;

$$\log(V_f) = 0.2832 * \log(P) - 0.0916 \quad (6)$$

Bidirectional Fiber Mat;

$$\log(V_f) = 0.0954 * \log(P) - 1.177 \quad (7)$$

Unidirectional Fiber Mat;

$$\log (V_f) = 0.1031 * \log(P) - 1.057 \quad (8)$$

where P has a unit of N/m².

When only one type of reinforcement mat is present in the mold, the porosity can easily be calculated by determining the total volume of the mold cavity and the volume occupied by the reinforcement. Using multiple types of reinforcement in the mat stack requires a method to determine the porosity and thickness of each layer of reinforcement mat. If it is assumed that all mats of the same type have the same compression behavior regardless of their positions in the mat stack then the total thickness can be shown to be:

$$T = \sum_{i=1,j} (n_i * t_i) \quad (9)$$

where,

T = total thickness

n_i = number of mats of type i

t_i = thickness of a mat of type i

In the previous equation all the functions were defined in terms of volumes, i.e.

$$V_{f,i} = a_i * p^{b_i} \quad (10)$$

where,

a_i, b_i = compression constants for a mat of type i

$V_{f,i}$ = volume fraction of a layer of type i mat

Combining Equations 9 and 10 yields

$$T = \sum_{i=1,j} (X_i * p_{bi}) \quad (11)$$

where,

$$X_i = (100.0 * n_i * t_{\text{fibers},i}) / a_i$$

and $t_{\text{fibers},i}$ = thickness of a mat of type i with porosity = 0

For a mold cavity with fixed thickness, the only unknown in Equation 11 is pressure, once the total thickness and mat stack are specified. After the pressure has been determined it can be put back into Equation 10 to determine the porosity and thickness of each mat type used. In Equation 11 each pressure term will be raised to a different fractional power making the equation solvable by either the use of an equation solver, expansion of the terms, or by iteration. An iterative computer program was written to solve this equation.

Part II.: Cure Monitoring of Graphite/Epoxy Composites by Scaling Analysis and Heat Flux Sensors

A. Concept Development

Both the Damkohler number and the Fourier number can be developed from the one-dimensional heat transfer equation. This development assumes the other two dimensions are infinite in comparison. The Damkohler number is a dimensionless number representing the ratio of the rate of heat generation to the rate of heat conduction. The Fourier number is a dimensionless time representation. The heat transfer equation in one dimension is:

$$\rho C_p \frac{\partial T}{\partial t} = k \frac{\partial^2 T}{\partial x^2} + (\Delta H)(R) \quad (12)$$

where R is the reaction rate and ΔH is the heat of reaction. Defining dimensionless variables for temperature $\bar{T} = T/T_{ref}$, position $\bar{x} = x/L$, and reaction rate $\bar{R} = R/R_{ref}$, and substituting into Equation 12 yields:

$$\frac{\partial \bar{T}}{\partial t} = \frac{k}{\rho C_p L^2} \frac{\partial^2 \bar{T}}{\partial \bar{x}^2} + \frac{(\Delta H)R_{ref}}{\rho C_p T_{ref}} \bar{R} \quad (13)$$

Defining a characteristic time for heat conduction (λ_C) and heat generation (λ_G) such that:

$$\lambda_C = \frac{\rho C_p L^2}{k} \quad \text{and} \quad \lambda_G = \frac{\rho C_p T_{ref}}{(\Delta H)R_{ref}} \quad (14)$$

and defining a dimensionless time as:

$$\bar{t} = \frac{t}{\lambda_C} = \frac{tk}{\rho C_p L^2} \quad (15)$$

then Equation 13 becomes:

$$\frac{1}{\lambda_C} \frac{\partial \bar{T}}{\partial \bar{t}} = \frac{1}{\lambda_C} \frac{\partial^2 \bar{T}}{\partial \bar{x}^2} + \frac{1}{\lambda_G} \bar{R} \quad (16)$$

Multiplying Equation 16 by (λ_C) and defining,

$$Da = \frac{\lambda_C}{\lambda_G} = \frac{L^2(\Delta H)R_{ref}}{kT_{ref}} = \frac{\text{heat generation rate}}{\text{heat conduction rate}} \quad (17)$$

the heat transfer equation becomes:

$$\frac{\partial \bar{T}}{\partial \bar{t}} = \frac{\partial^2 \bar{T}}{\partial \bar{x}^2} + (Da)\bar{R} \quad (18)$$

To determine the Damkohler number on-line, without referring to any kinetic model, some way to measure $(\Delta H)(R)$ must be developed. When $(\Delta H)(R)$ is expressed as a heat generation rate, $\frac{dQ}{dt}$, Equations 12 and 17 become:

$$\rho C_p \frac{dT}{dt} = k \frac{d^2 T}{dx^2} + \frac{dQ}{dt} \quad (19)$$

and

$$Da = \frac{L^2}{kT} \frac{dQ}{dt} \quad (20)$$

Equation 19 can be rewritten in terms of heat flux and the result is:

$$\rho C_p \frac{dT}{dt} = -\frac{dq}{dx} + \frac{dQ}{dt} \quad (21)$$

Equations 20 and 21 can be discretized, assuming the sampling interval (Δt) and space interval (δx) are small such that:

$$Da = \frac{L^2}{kT} \frac{\Delta Q}{\Delta t} \quad (22)$$

and

$$\rho C_p \frac{\Delta T}{\Delta t} = -\frac{\delta q}{\delta x} + \frac{\Delta Q}{\Delta t} \quad (23)$$

Isolating the heat generation term gives:

$$\Delta Q = \rho C_p \Delta T + \left[\frac{\Delta t}{\delta x} \right] \delta q \quad (24)$$

To estimate the change in flux, two heat flux sensors may be used (4).

Thus,

$$\delta q = q_{in} - q_{out} = -k \left[\frac{dT}{dx}_{in} - \frac{dT}{dx}_{out} \right] \quad (25)$$

To circumvent the cost of disposing of expensive sensors each time a composite is fabricated, three thermocouples are used to estimate the

change in flux. Figure 10 illustrates the design for the dual heat flux sensor using three thermocouples. Assuming equal displacement of thermocouples in the dual heat flux sensor, Equation 25 can be discretized as:

$$\delta q = -k \left[\frac{T_i - T}{\delta x_i} - \frac{T - T_o}{\delta x_o} \right] = \frac{-k}{\delta x} [T_i + T_o - 2T] \quad \text{for } \delta x = \delta x_i = \delta x_o \quad (26)$$

where "i" represents in and "o" represents out. The temperature profile between adjacent thermocouples is assumed to be linear. Furthermore, it is assumed that the thermocouples are sensitive enough to detect temperature variations at such close spacing. In order to complete the determination of the Damkohler number, a means to measure properties on-line is developed. Substituting Equation 26 into Equation 24 and dividing by ρC_p yields:

$$\frac{\Delta Q}{\rho C_p} = \Delta T - \left[\frac{k \Delta t}{\rho C_p (\delta x)^2} \right] [T_i + T_o - 2T] \quad (27)$$

Substitution for the Fourier number, $Fo = \left(\frac{k \Delta t}{\rho C_p (\delta x)^2} \right)$ yields:

$$\frac{\Delta Q}{\rho C_p} = \Delta T - Fo [T_i + T_o - 2T] \quad (28)$$

The Fourier number is a dimensionless time which combines the thermophysical properties with the time interval for sampling and the spacing interval of the three thermocouples in the dual heat flux sensor, as in Figure 10. Supposing the heat up period of the composite material does not involve any reaction (i.e. $\Delta Q = 0$), Fo can be estimated as:

$$Fo|_{\Delta Q=0} = \left[\frac{k \Delta t}{\rho C_p (\delta x)^2} \right] = \frac{\Delta T}{T_i + T_o - 2T} \quad (29)$$

Thus the properties are determined from Equation 29 in the early part of processing or the heat-up period. The properties and dual heat flux sensors give δq in Equation 26, which is used to determine ΔQ in Equation 24 and finally Da in Equation 22.

B. Reaction Characteristics

The three significant reaction characteristics in the cure of a thermosetting composite material include the start of the cure reaction, the acceleration of the reaction, and in unfavorable circumstances, thermal runaway. As set forth previously, the Fourier number and the Damkohler number can be used to identify these characteristics. The Fourier number can determine the onset of the cure reaction. As in Equation 29 Fo is estimated as $\frac{\Delta T}{T_i + T_o - 2T}$ when there is no reaction occurring.

Therefore, by taking the difference between Fo at the current time step and the previous time step, the onset of reaction can be identified as the point at which this difference becomes nonzero; or accounting for thermocouple noise, some number slightly larger than zero. The point of accelerated reaction occurs when the rate of heat generated exceeds the rate of heat dissipated by conduction, or in Equation 22 when Da exceeds unity. The property estimation according to Fo combined with on-line measurement of heat flux using the dual heat flux sensor is used to calculate the Damkohler number and identify the accelerated reaction point. Finally, thermal runaway has been defined by several researchers (5,6) as the point when the temperature gradient is positive (i.e. $\frac{dT}{dt} > 0$) and the second derivative of temperature indicates an

inflection point, (i.e. $\frac{d^2T}{dt^2} > 0$). This can be related to the profiles of ΔQ and Da . The inflection point of the temperature profile while temperature is increasing occurs at the peak of the ΔQ and Da profiles. Thus, thermal runaway occurs when the Damkohler number is larger than one (i.e. reaction is accelerating), plus the Damkohler number at a previous time step is larger than Da for the current time step.

C. Experimental

Application of the Fourier and Damkohler numbers was made to characterize the progress of curing a graphite/epoxy composite. The pre-preg tape donated by Ciba-Geigy was R922 modified epoxy resin on unidirectional graphite fibers. The nominal thickness of the tape was 0.0127 cm (0.005 in). A die cutter of diameter 10.16 cm (4 in) was used to punch out many circles of pre-preg tape. First, a stack of thirty layers was constructed by aligning the unidirectional fibers of adjacent layers at 90 degrees. A thermocouple was placed on top of these thirty layers with the tip in the center of the circle. Next a stack of eight layers of pre-preg circles was built on top of the first thermocouple, continuing to align fibers of adjacent layers at 90 degrees. A second thermocouple was placed on the stack of 38 layers with the tip at the center. Another eight layers were laid up followed by a third thermocouple. The sequence of eight layers and a thermocouple was repeated three more times to give a stack 70 layers high with six thermocouples. Finally, on top of the 70 layers and the sixth thermocouple, 30 more layers were laid up to achieve a 100 layer stack

of approximately 1.27 cm (0.5 in) (i.e. 100 layers of 0.005 in thickness). The thickness of eight layers was chosen to be the uniform spacing between each thermocouple based on the maximum size of the welded thermocouple tip. American Wire Gage 30 thermocouple wires (0.01 in diameter) of type J (iron-constantan) were welded using a DCC Corporation Hot Spot Welder. Thermocouple tips were measured with a micrometer and determined to be less than 0.1016 cm (0.04 in) in diameter or less than the thickness of an eight layer stack of pre-preg tape. It was assumed that at a spacing (δx) of 0.1016 cm (0.04 in), the temperature profiles were linear so that the change in flux (δq) could be estimated as in Equation 16. The thermocouples were connected to a PC Acquisitor data acquisition board made by DianaChart. The data acquisition board is capable of accepting 14 channels of input and sampling at 500 Hz using an IBM AT computer.

To prevent the pre-preg stack from slipping when heated and pressurized, several paper rings were placed around the 100 layer pre-preg stack. The paper rings were punched out of large index cards with a die cutter having nominal inner diameter of 10.16 cm (4 in) and outer diameter of 12.7 cm (5 in). Then a layer of duct tape was wrapped around the index card rings to hold the entire assembly in place. The wrapped stack was placed in between pre-heated platens of a lab scale hydraulic press. The platens were maintained at 177°C (350°F) using Omega on-off controllers. The press was closed to provide good contact with the surfaces of the pre-preg stack and data collection was initiated.

D. Results and Discussion

The temperature profile for curing a stack of graphite/epoxy composite material is shown in Figure 11. The temperature at the stack surface was measured by a thermocouple and is also shown in Figure 11. The time for the surface to reach its setpoint of 177°C (350°F) was approximately 450 seconds. Three thermocouples located 30 layers, 38 layers, and 46 layers from the surface are T1, T2, and T3, respectively. Figure 11 indicates that the temperature difference between individual thermocouples was noticeable prior to 450 seconds. After the heat up period for the stack surface, the measured temperature inside the composite indicated a crossover of the composite temperature above the surface setpoint temperature. This occurred at approximately 525 seconds. After this crossover point, the heat generated by the reaction exotherm caused the temperature inside the stack to exceed the boundary temperature. The peak of the temperature profile was not very sharp, and occurred near 900 seconds. From Figure 11 it seems that no accelerated reaction occurred because no inflection point can be found, and consequently, thermal runaway would not occur. The explanation for the lack of thermal runaway in this case is the stack was thin enough that in the competing effects of heat generation versus heat dissipation by conduction, the rate of dissipation was greater.

The Damkohler number was calculated using the online properties determined from the Fourier number during the heat up period as in Equation 29. The Da profile is shown in Figure 12. This illustration bears out the conclusions drawn from the temperature profiles. The

point at which the Damkohler number exceeded the zero line was when the heat of reaction became nonzero, (i.e. $\Delta Q > 0$). This occurred around 450 seconds, prior to the crossover point in Figure 11 when the inner thermocouples indicated a higher temperature than the boundary temperature. Furthermore, the estimated Damkohler number in Figure 12 was always less than one, which implies there was no accelerated reaction and thus no thermal runaway. Figure 12 indicates the reaction ended around 2100 seconds when Da became zero (i.e. $\Delta Q = 0$).

A major complication encountered with the Fo and Da analysis was that the thermophysical properties changed as the reaction progressed. The dual heat flux sensor relies on a linear temperature profile between thermocouples and on constant thermophysical properties. One solution to this problem, despite the cost disadvantage, is the use of commercial heat flux sensors which do not rely on the properties of the composite being cured.

E. Verification by DSC

The experimental temperature profile, T_2 , from curing a 100 layer graphite/epoxy composite was approximated on a Perkin-Elmer Model DSC-2C differential scanning calorimeter (DSC). Initially, a sample of the graphite/epoxy pre-preg was scanned from 33°C (91.4°F) to 337°C (638.6°F) at a rate of 20°C/min (68°F/min) to simulate the heat up period in the curing experiment (i.e. T_2). Following this, the cured sample was scanned to determine the baseline in which no reaction heat was generated. From these two scans, the onset of reaction was found to

occur around 350 seconds. This point is shown in Figure 13 as point "A". The Damkohler number prediction seems to have overpredicted the cure onset by approximately 100 seconds.

In order to more closely simulate the temperature profile T2 via DSC, three separate reaction regions for another DSC experiment were chosen. The first region was a scan from 33°C (91.4°F) to 133°C (271.4°F) at a rate of 20°C/min (68°F/min) for a total of 5 minutes. Then the scanning rate was switched to 10°C/min. This second region lasted 4.5 minutes accounting for the scan from 133°C (271.4°F) to 178°C (352.4°F). Finally, the sample was held at 178°C (352.4°F) for 30 minutes in the isothermal mode of the DSC. These three regions are shown in Figure 13 as a dotted line. The square block symbol represents the actual temperature profile of T2. The end of the reaction determined from this DSC experiment occurred at approximately 36 minutes. This corresponds to point B in Figure 13. The Damkohler number prediction shows good agreement with this point by indicating zero Da (i.e. $\Delta Q=0$) near 2100 seconds, or 35 minutes.

IV. RECOMMENDATIONS

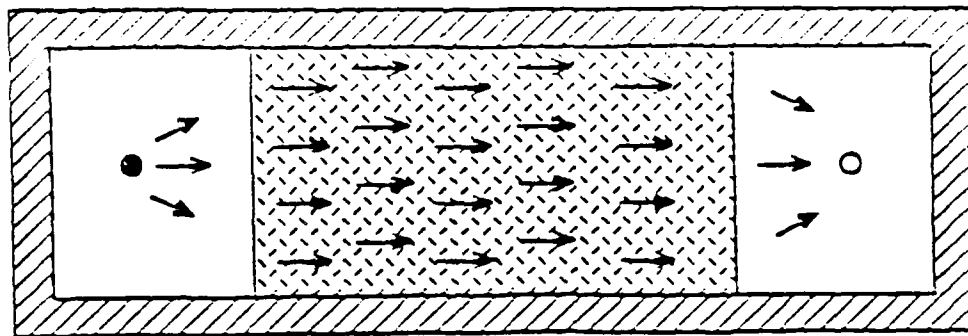
- a. Resin transfer molding (RTM) is a manufacturing technology capable of producing large composites with high strength and complicated geometry. The processing cost is much lower and the cycle time can be much shorter than the autoclave method. The presence of fiber mats in a closed mold, however, makes mold filling and curing more complicated than other processes such as resin injection molding.

Our work presented a systematic approach to characterize various fiber mats. The effort should be extended to characterize resins and to establish the relationship among processing variables, material variables and product properties.

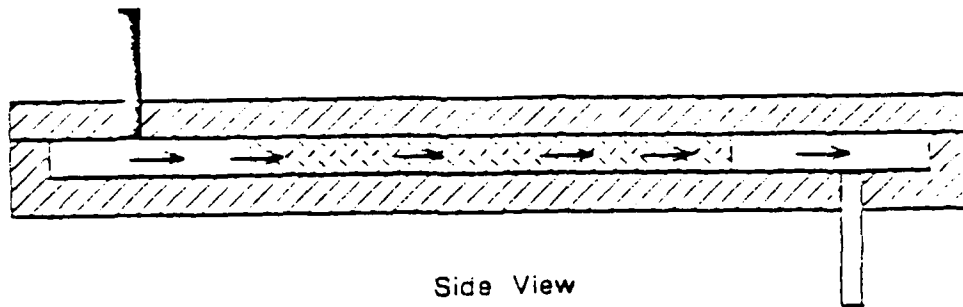
- b. Our experimental results showed that a dual heat flux sensor consisting of three closely placed thermocouples was able to detect the on-set of reaction and the end of reaction. The accuracy of this detection should be evaluated by model simulation. We also suggest that, if it is affordable, heat flux sensors, instead of thermocouples, should be used for cure monitoring because of their better accuracy in determining the local heat flux.

V. REFERENCES

1. Lee, W.I., Loos, A.C. and Springer, G.S., "Heat of Reaction, Degree of Cure, and Viscosity of Hercules 3501-6 Resin," J. Composite Materials, Vol. 16, 1982, pp. 510-520.
2. Abrams, F., Garrett, P., Lagnese, T., LeClair, S., Lee, C.W. and Park, J., "Qualitative Process Automation for Autoclave Curing of Composites," AFWAL-TR-87-4083, November 1987.
3. Miller, B. and Clark, D.B., "Liquid Transport Through Fabrics; Wetting and Steady-State Flow, Part I: A New Experimental Approach," Textile Research Journal, March 1978, pp. 150-155.
4. Ortolano, D.J. and Hines, F.F., "A Simplified Approach to Heat Flow Measurement," Advances in Instrumentation, Vol. 38, Part 2, 1983, pp. 1449-1456.
5. Osinski, J.S., Manzione, L.T. and Chan, C., "Thermal Runaway in Fast Polymerization Reactions," Polymer Process Engineering, Vol. 3, Nos. 1 & 2, 1985, pp. 97-112.
6. Biesenberger, J.A. and Sebastian, D.H., Principles of Polymerization Engineering, Wiley-Interscience Publication, 1983, pp. 403-472.



Top View



Side View

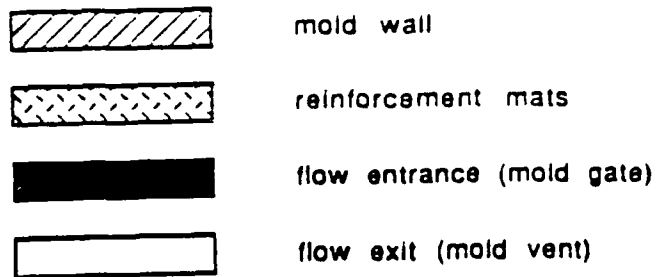


Figure 1

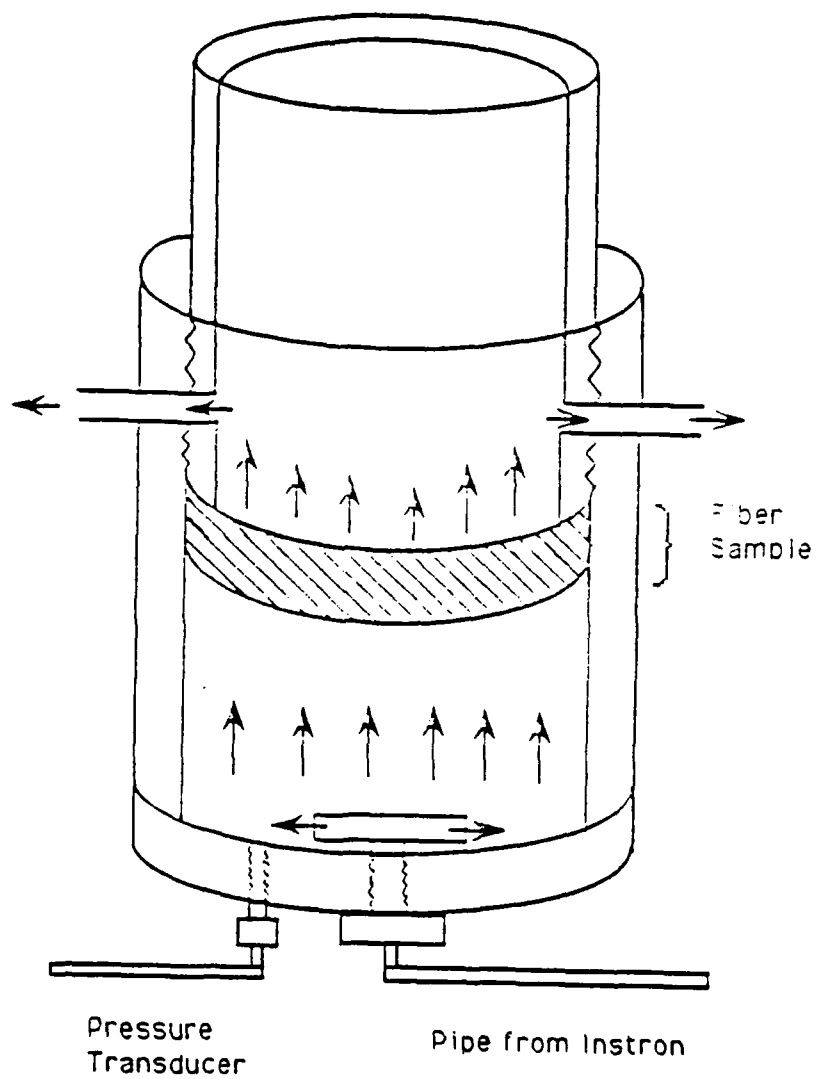


Figure 2

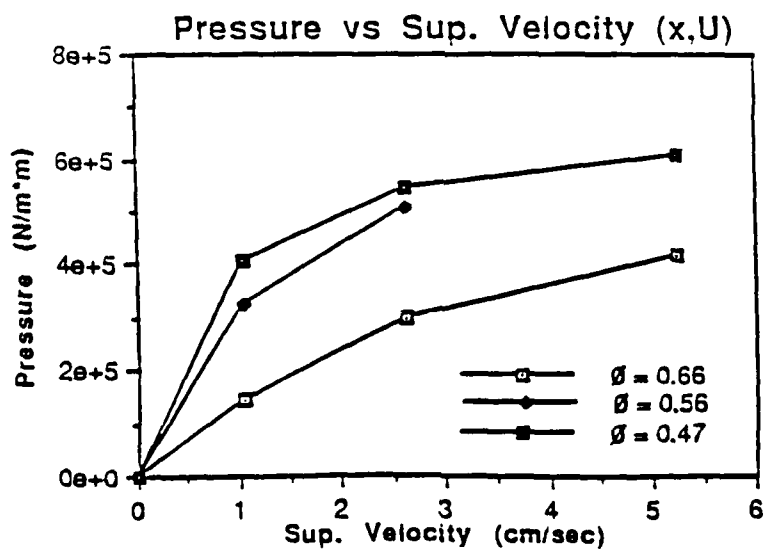
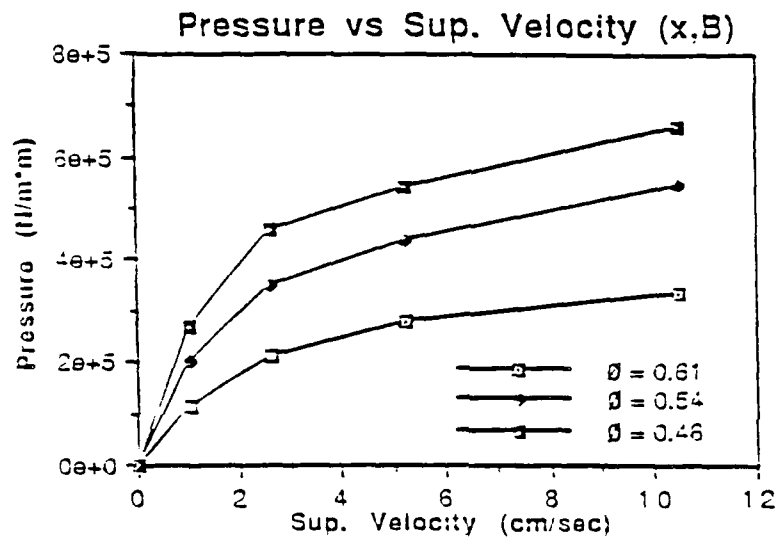
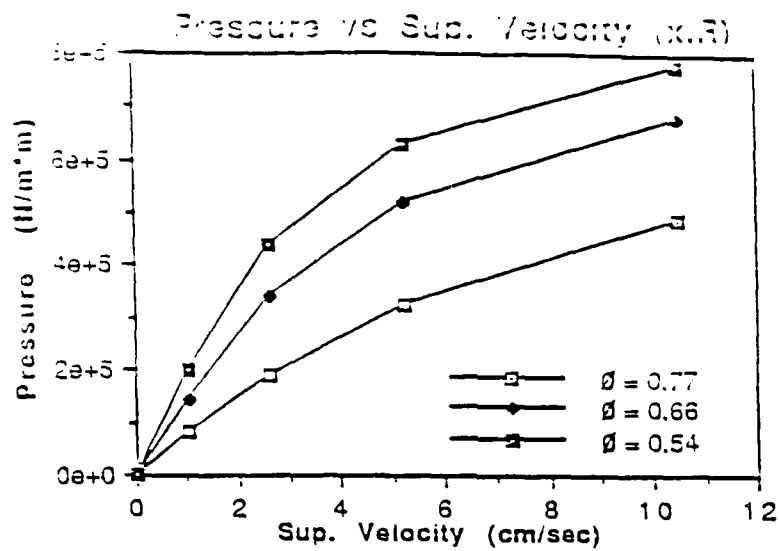


Figure 3

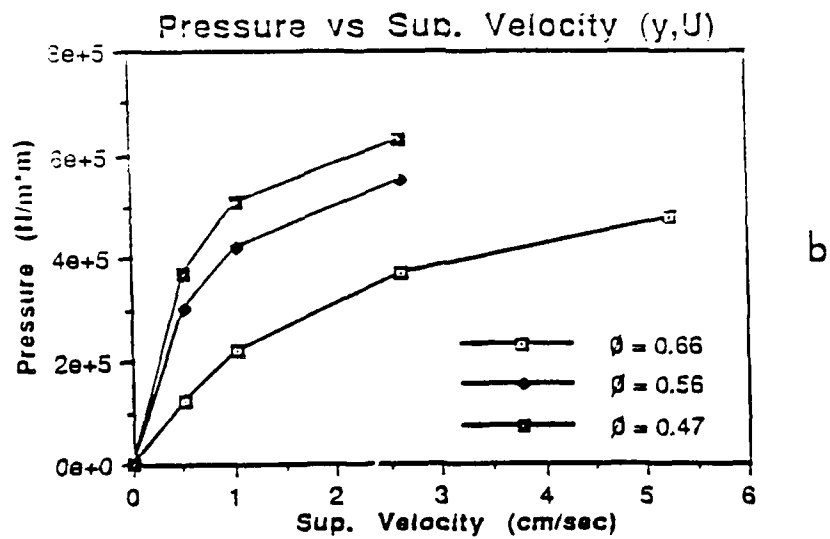
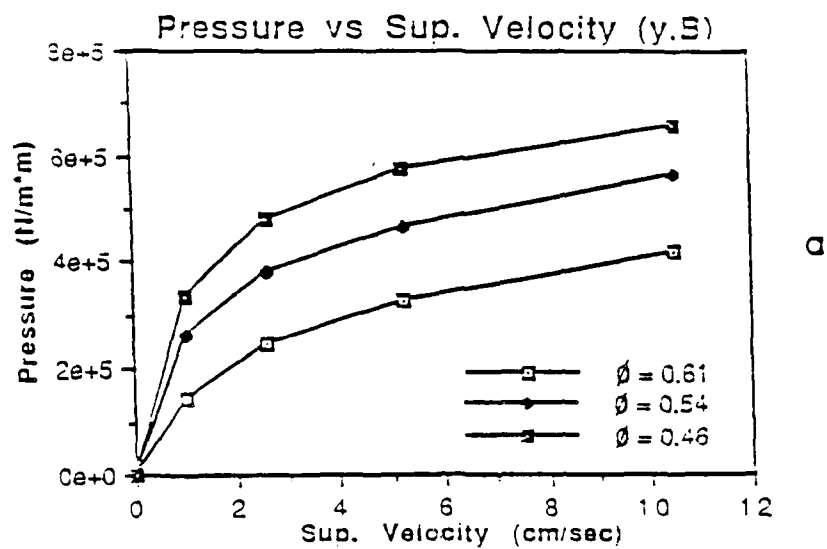


Figure 4

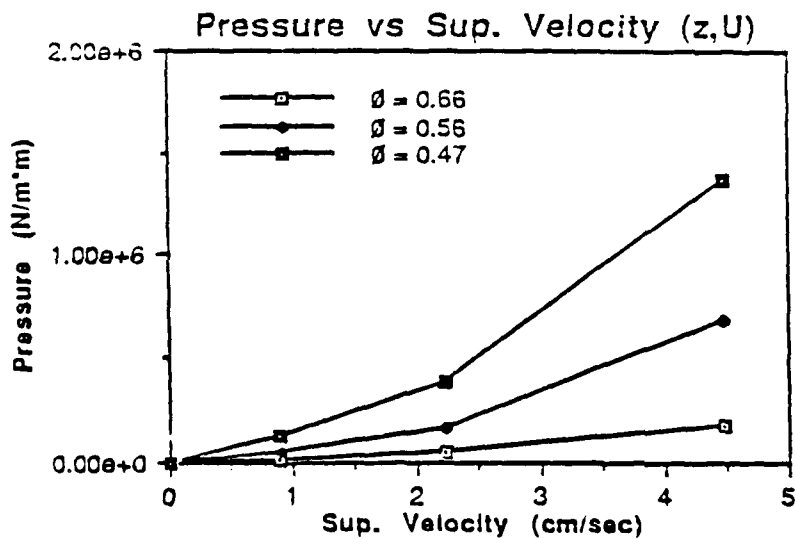
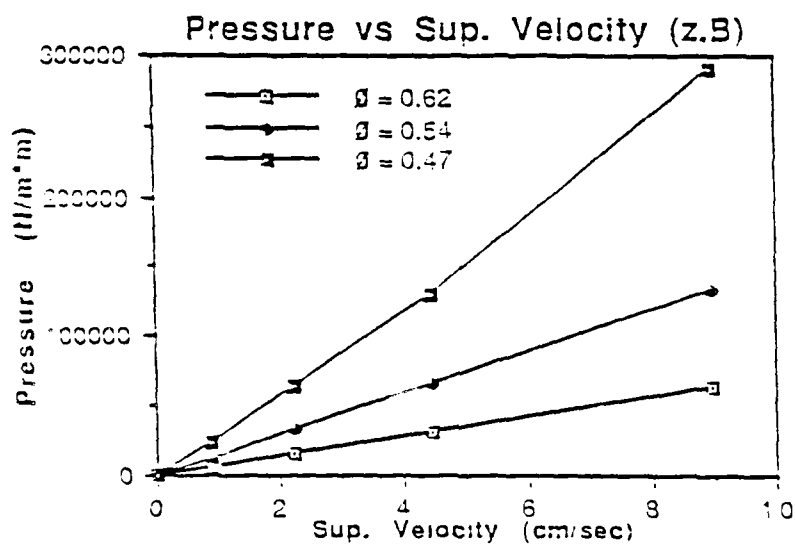
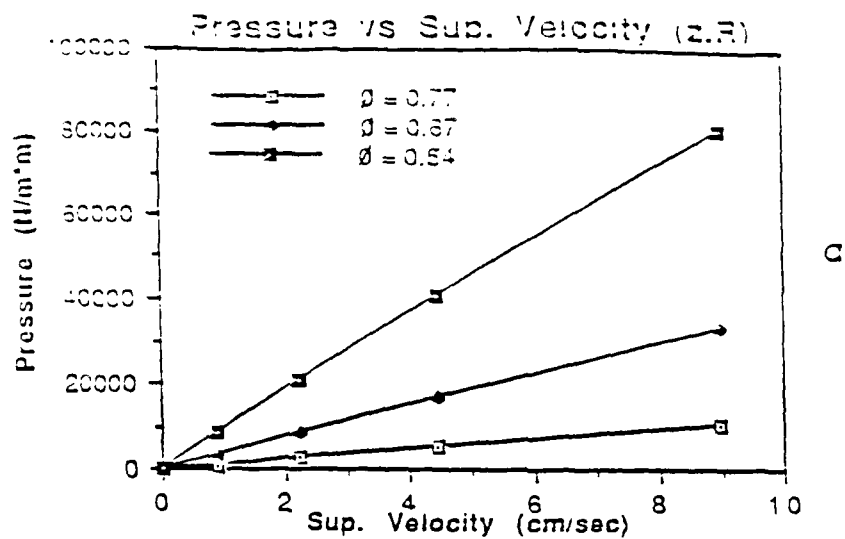


Figure 5

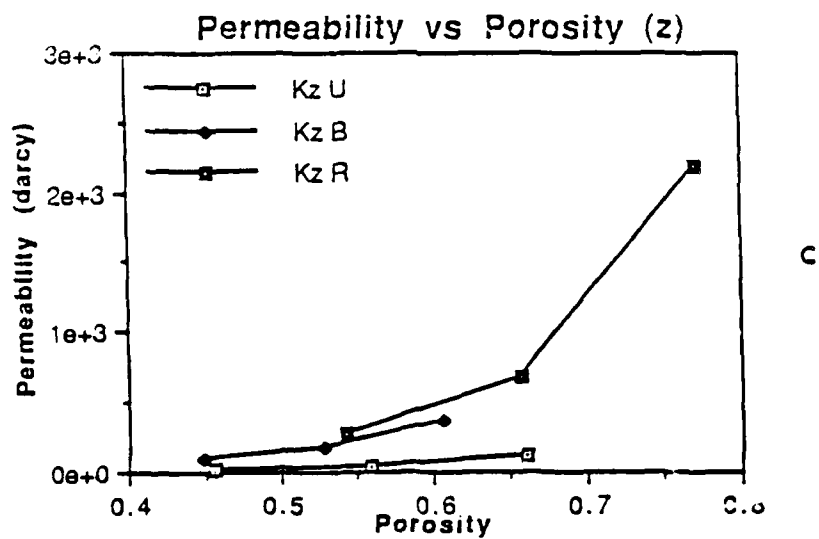
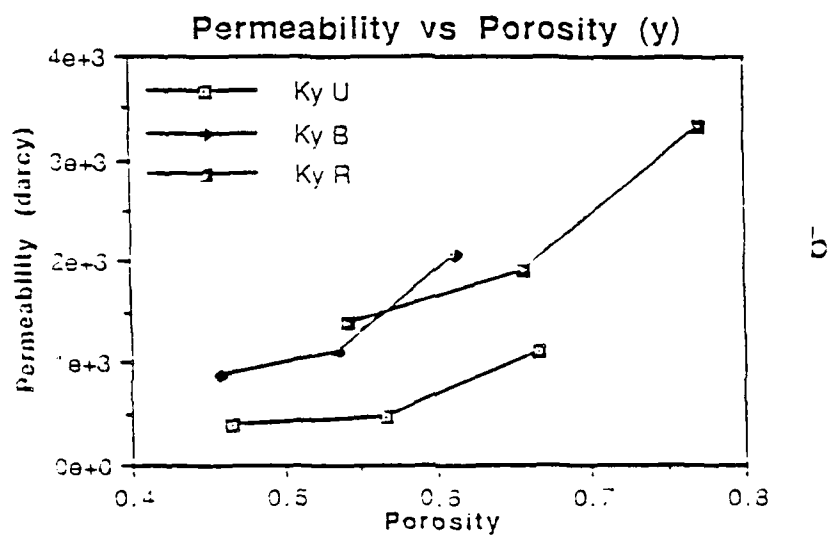
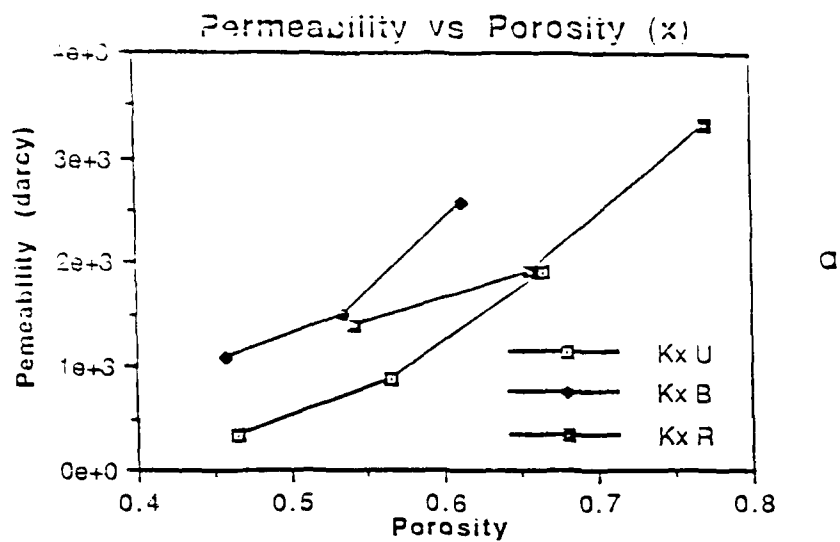


Figure 6

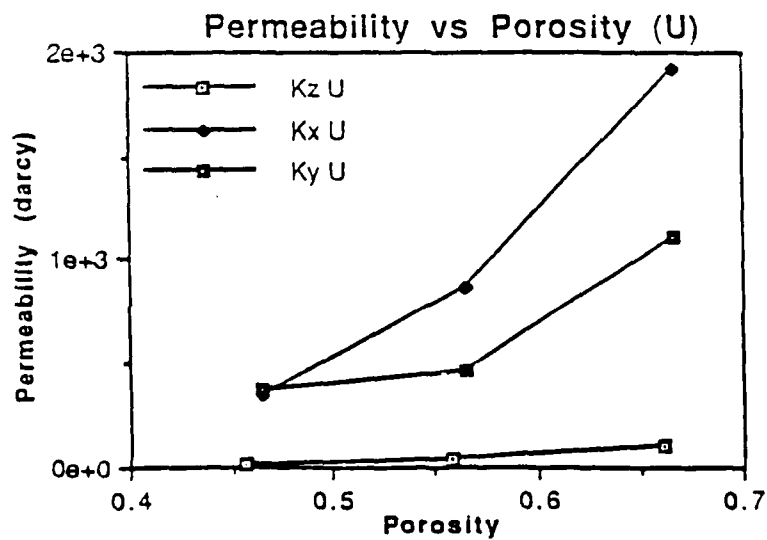
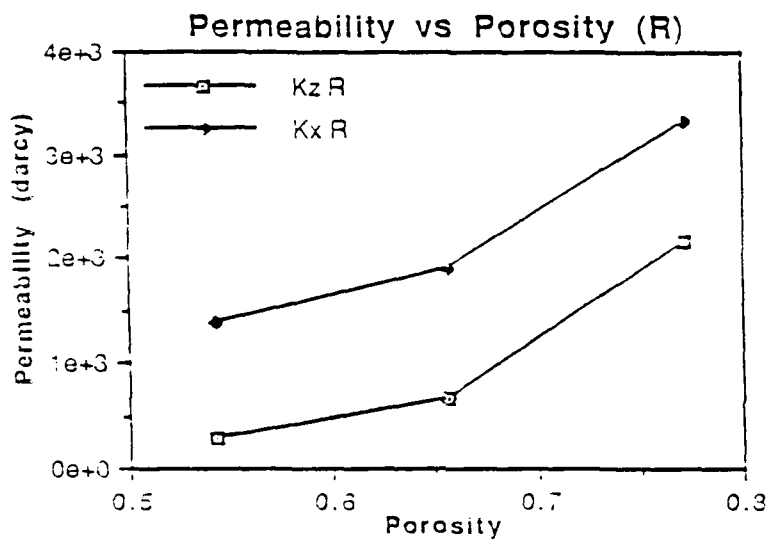
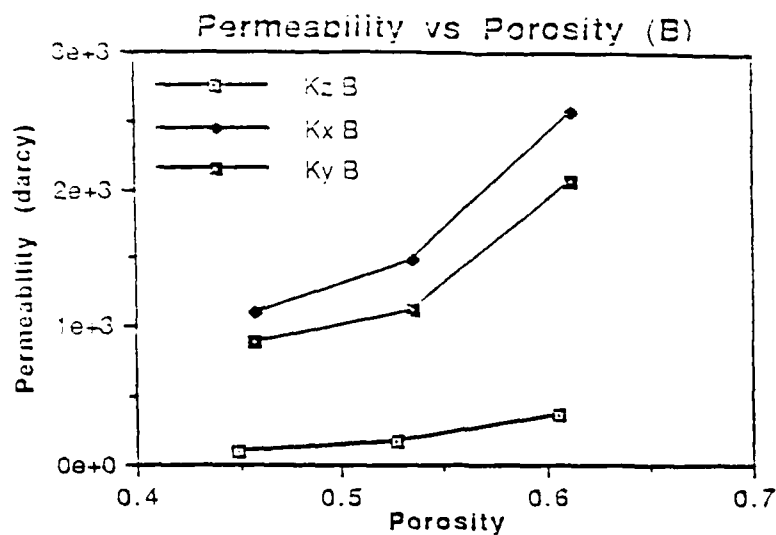


Figure 7

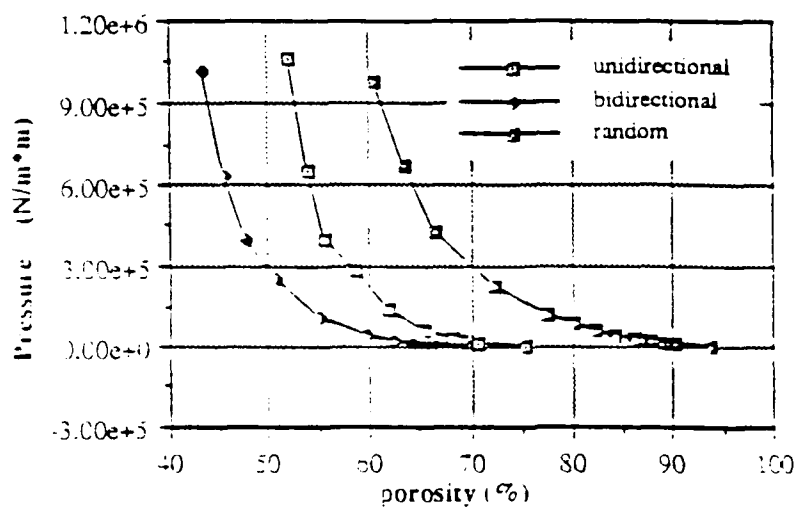


Figure 8

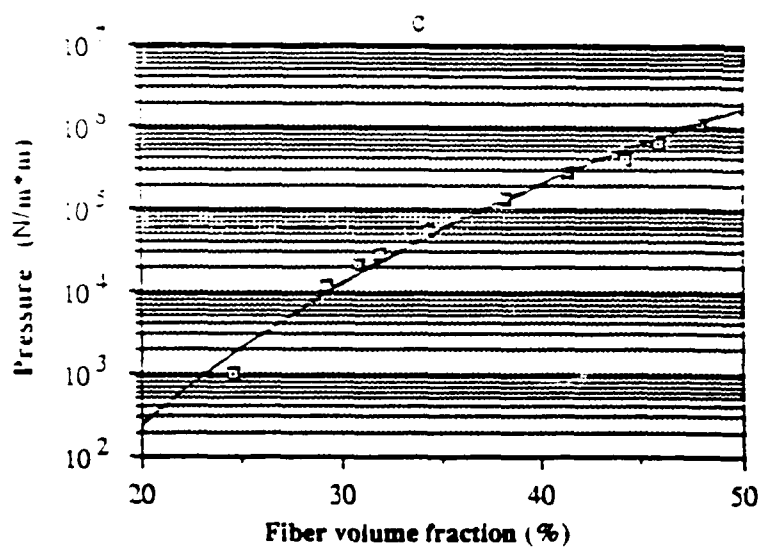
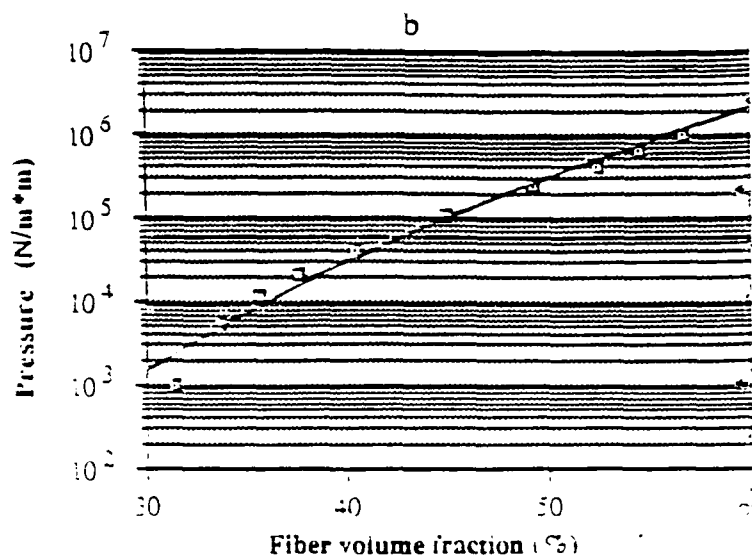
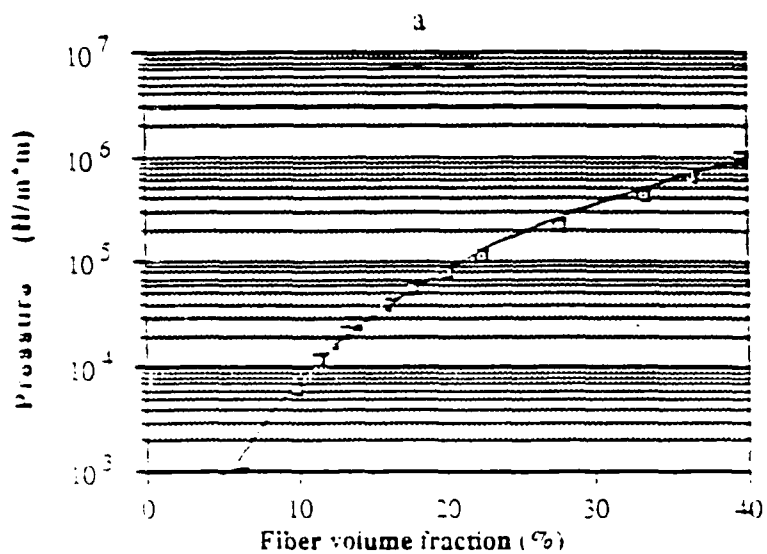


Figure 9

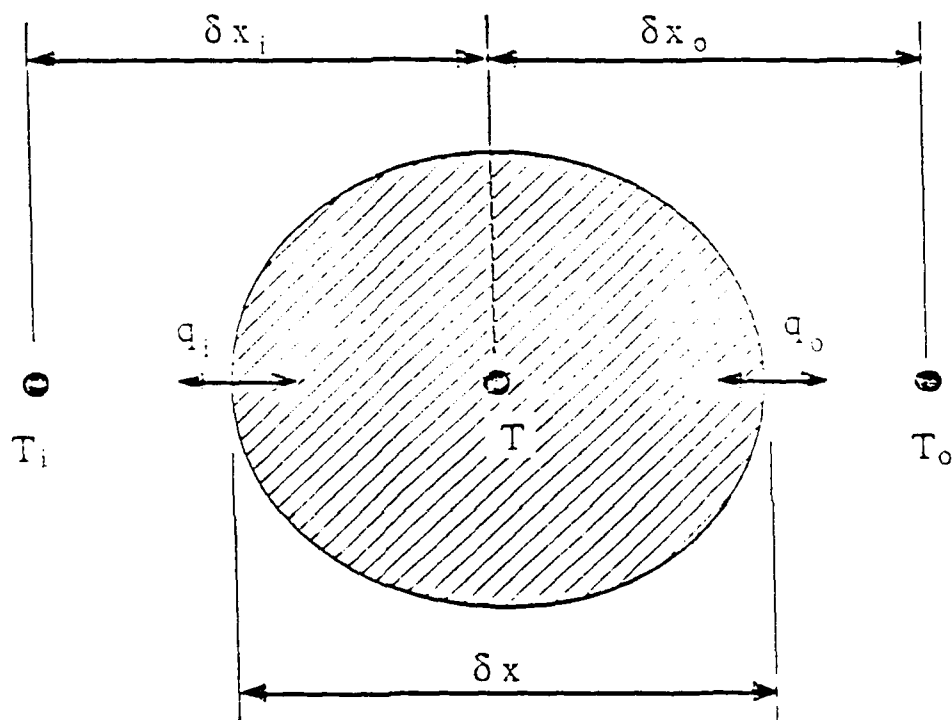


FIGURE 10 : The dual heat flux sensor using three thermocouples

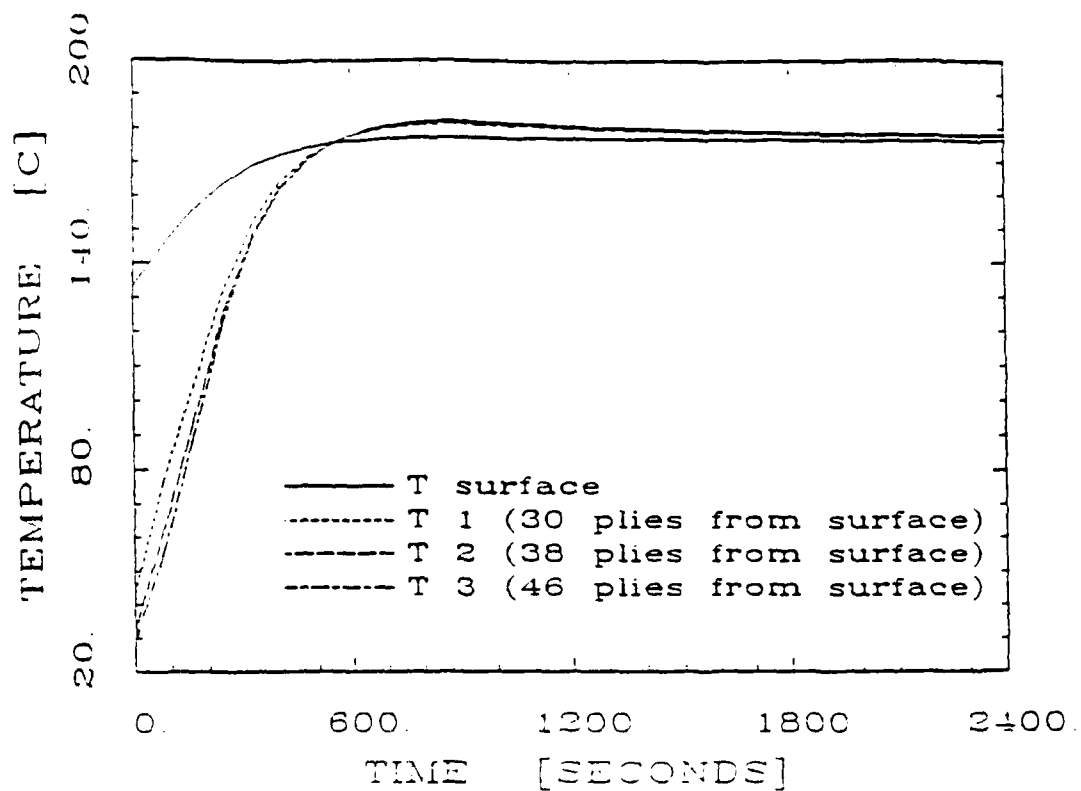


FIGURE 11: Temperature profile for a 100 layer graphite epoxy composite

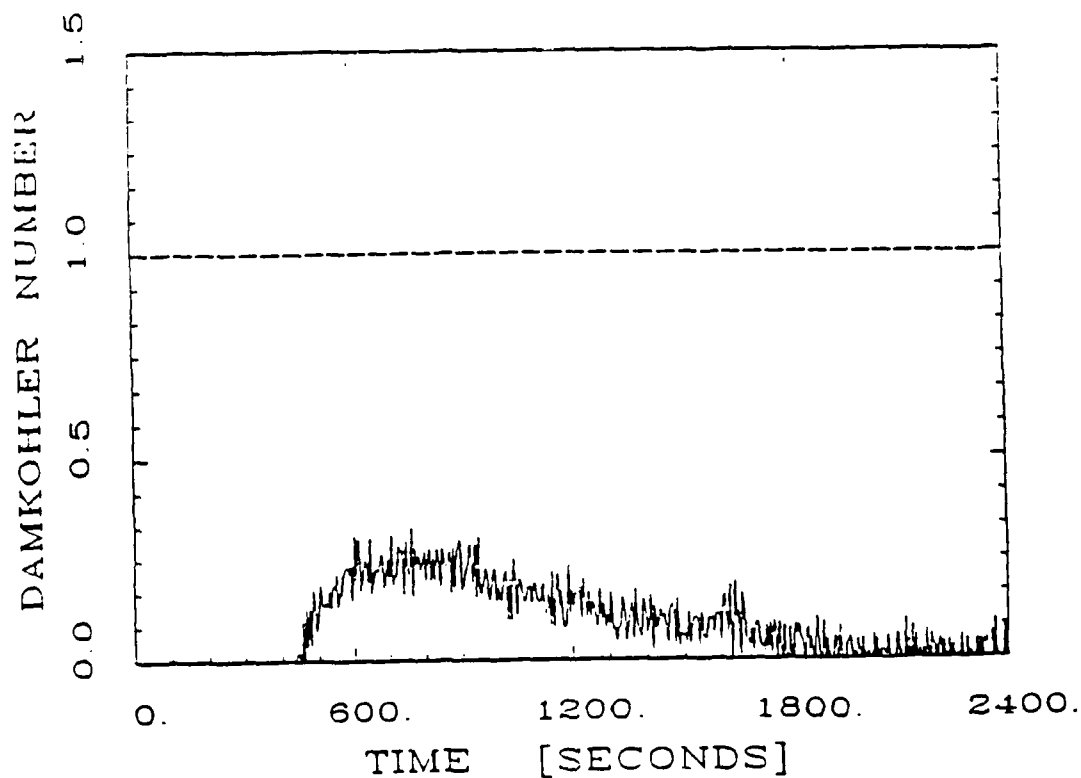


FIGURE 12: Damkohler number estimated during the cure of a 100 layer graphite epoxy composite

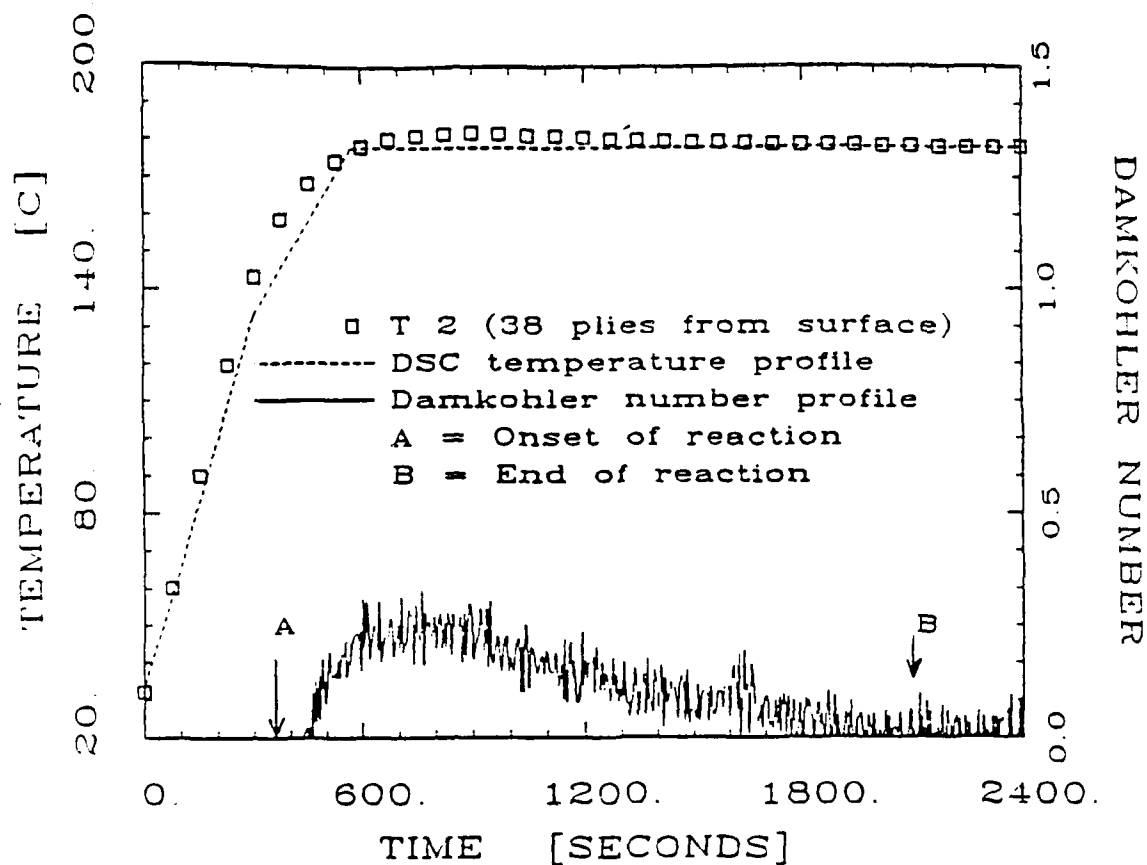


FIGURE 13: Reaction points determined by DSC and superimposed on temperature and Damkohler number profiles

1988-89 USAF-UES RESEARCH INITIATION PROGRAM

Sponsored by the
AIR FORCE OFFICE OF SCIENTIFIC RESEARCH

Conducted by the
Universal Energy Systems, Inc.

FINAL REPORT

PHOTOREFLECTANCE MEASUREMENTS OF THE QUALITY
OF UNDOPED GaAs

Prepared by:	Michael Sydor
Academic Rank:	Prof. of Physics
Department:	Physics
University:	Univ of Minnesota, Duluth
USAF Researcher:	W. C. Mitchel
Contract No:	F49620-88-C-0053
Date:	24 Oct. 1989

PHOTOREFLECTANCE MEASUREMENTS OF THE QUALITY
OF UNDOPED GaAs

by
Michael Sydor

ABSTRACT

Modulated photorefectance is used to measure the unintentional impurity concentrations in undoped epitaxial GaAs. Photorefectance signal above the band gap spreads with the unintentional impurity concentrations and shows well defined Franz-Keldysh peaks whose separation provide a good measure of the current carrier concentrations. In samples less than $3\mu\text{m}$ thick, photorefectance signal at the band edge contains a substrate-epilayer interface effect which precludes the analysis of the data by using the customary third derivative functional fits for low electric fields.

ACKNOWLEDGEMENTS

Research sponsored by the Air Force Office of Scientific Research/AFSC, United States Air Force, under contract F49620-88-C-0053. The United States Government is authorized to reproduce and distribute reprints for governmental purposes notwithstanding any copyright notation hereon.

We would like to thank Dr. D.K. Gaskill and Dr. W.M. Theis, for their help and many fruitful discussions. We would also like to thank B. Lampert, N. McDevitt, Dr. M. Donley, and D. Tomich for their technical assistance in MBE.

I. INTRODUCTION

Photoreflectance (PR) has been established as a quick and an accurate method for measurement of band gap energies, alloy composition, and doping levels in GaAs and AlGaAs¹⁻⁵. As a result the technique could be used in a quick optical assessment of sample quality from Molecular Beam Epitaxy (MBE) and Chemical Vapor Phase Epitaxy. We investigate here the properties of PR due to the unintentional impurities in GaAs, hoping that the technique may serve as a means for selecting the quality of undoped MBE material.

Shay⁴ has first pointed out the physical behavior of PR with carrier concentrations. Peters et al.² use the shift in PR's critical point energy at the band edge, to determine the doping concentrations in the 3×10^{15} - 8×10^{17} cm⁻³ range. Their results are quite good in the 1×10^{16} - 8×10^{17} cm⁻³ range, for samples doped by ion implantation. However their method has limitations below these concentrations, especially for the MBE samples. Furthermore their method relies on very accurate determinations of small shifts in the critical point energy, through the use of Third Derivative Functional Fits (TDFF), from the low field theory⁶. This may not be possible in the case of undoped MBE material.

On the other hand Bottka et al.¹ utilize the energy period of Franz-Keldysh Oscillations (FKO), prominent in doped GaAs, to measure similar carrier concentrations in samples grown by Chemical Vapor Deposition (CVD). Their method also appears excellent above the 1×10^{16} cm⁻³ carrier concentrations, once a determination is made for a quasi-equilibrium photovoltage V_p due to the laser modulation beam. V_p is usually small in doped samples. However, below the

$1 \times 10^{16} \text{cm}^{-3}$ carrier concentrations V_p may vary appreciably, and Bottka's method may need to be modified.

We discuss here the properties of PR in undoped samples and in lightly doped samples at the concentration limits below those treated by Peters et al.² and Bottka et al.¹. We examine the possibility of extending both of these methods to the lower concentrations and present data which show that PR may be used in the determination of the unintentional impurity concentrations in undoped GaAs.

II OBJECTIVES:

A variety of undoped and lightly doped MBE GaAs samples will be examined by Photorefectance to establish optical signatures and criteria for non-destructive estimates of the unintentional impurity concentrations, and thereby the quality of MBE material.

III RESEARCH:

Theoretical Background

The PR signals for GaAs samples can be classified into two categories according to the magnitude of the surface electric field, E_s . The first category is the high field condition, where the surface field is large. This is usually the case for doped samples. The second category is called the low field condition. This usually occurs for undoped samples. Aspnes⁶ showed that the PR signal is in the low field limit when:

$$\hbar\Omega < \Gamma/3 \quad (1)$$

$\hbar\Omega$ is a characteristic energy associated with the critical point. It is related to E_s by:

$$\hbar\Omega = (e^2 E_s^2 \hbar^2 / 8\mu)^{1/3} \quad (2)$$

where μ is the interband reduced mass. Γ is a broadening parameter for the critical point energy, E_{cp} . Aspnes⁶ derived a quick rule of thumb, that if the PR signal is such that:

$$\Delta R/R < 10^{-4} \quad (3)$$

then the signal is in the low field limit.

In the low field limit, the line shape for PR is given by⁶:

$$\Delta R/R = \text{Re}\{C e^{i\theta} (\hbar\omega - E_{cp} + i\Gamma)^{-n}\} \quad (4)$$

where $\hbar\omega$ is the energy of the probe beam, C and θ are an amplitude and phase factor that vary slowly with $\hbar\omega$. n refers to the type of critical point in question. n=2, 2.5, 3 for an exciton, a three dimensional band to band, and a two dimensional band to band transition respectively. Eqn.(4) is often used in theoretical fits of PR data.

In the high field limit, the PR signal is proportional to the product of Airy functions and their derivatives. These take the asymptotic form⁷:

$$\Delta R/R \cong \cos\{(2/3)[(\hbar\omega - E_{cp})/\hbar\Omega]^{3/2} + \pi(d-1)/4\} \quad (5)$$

where d is the dimensionality of the critical point. For GaAs, with a direct transition, d=3. This line shape has an oscillatory nature where the oscillations are termed Franz-Keldysh Oscillations (FKO). Neglecting an amplitude factor⁸ in Eqn. (5), the position of the FKO peaks is approximated by:

$$[\hbar\omega]_j = \hbar\Omega (F_j) + E_g \quad j=1,2,... \quad (6A)$$

$$F_j = [3\pi(j-1/2)/2]^{2/3} \quad (6B)$$

As indicated by Eqn. (6), a plot of $[\hbar\omega]_j$ vs. F_j is a straight line with slope $\hbar\Omega$, and intercept E_g . The labeling of the FKO extrema marked 1,2,... is shown in Fig.1, and a plot of Eqn. (6), for several samples is displayed in Fig. 2. Higher order FKO peaks appear prominently in the lightly doped samples and fall along the same straight lines. The slopes of the lines in Fig. 2 appeared to depend only on the carrier concentrations, independent of temperature fluctuations, the laser energy, its intensity, and the

sample preparation. As can be seen from Fig. 2, CVD samples fell along the same straight lines as the MBE samples for any given carrier concentration.

Experimental

We set up a standard arrangement of modulated photorefectance apparatus^{1,3,4}. We used a 5 mW HeNe laser mounted behind a neutral density filter which allowed us to vary the laser intensity from 10-100 mW/cm². The laser beam was chopped at 400 Hertz. A probe beam from a 100 W Tungsten-Halogen lamp coupled to a .25 m monochromator was used to scan the samples for photorefectance $\Delta R/R$ and the reflectance R over the 700-1000 nm range. We used narrow band pass filters in front of the probe beam detector to check for room temperature photoluminescence⁹, and to examine in detail the behavior of PR at the band edge as a function of the laser intensity. Subsequently the samples were reexamined on a comparable apparatus using a HeCd laser. The reproducibility of the carrier concentration measurements using the PR spectra was excellent. A standard sample provided by Dr. Gaskill¹ of N.R.L., Washington D.C. gave the same results for impurity concentrations in three different PR experiments.

Results and Discussion

At the outset, in our attempt to extend the method of Peters et al.² to the measurements of unintentional impurities in GaAs, we ran into difficulty with the interpretation of PR signal at the band edge. We noticed that the PR at the band edge had a thickness dependent structure. This can be seen in Fig. 1 which shows typical PR traces for undoped MBE samples of GaAs. The thin sample in Fig. 1 shows a distinct broadening and an inflection at the leading edge of the PR just below the band gap

energy at 1.424 eV. This structure was detected only in samples less than 3 μm thick and appeared to originate at the substrate-epilayer interface. Its behavior with laser intensity differed from the PR just above the band edge. Because the exact nature of this structure is unknown, we were unable to determine accurately the critical point energy in many of our samples by using the customary third derivative functional fits⁶ in the manner suggested by Peters et al.². Furthermore, it appeared questionable whether the low field conditions assumed in such fits, were really valid for our samples since the undoped GaAs showed PR indicative of Eqn. (5). We thus abandoned the critical point energy method² at first, but returned to it later by considering an alternate method for the location of the critical point energy near the band edge.

Fortunately the interface effects mentioned above appeared to be confined to the energies at and below the band gap, well away from the first and the second FKO peak. Thus the FKO method¹ appeared quite feasible for our purposes. We found for instance that the first two FKO peaks were always discernable in the undoped MBE samples and that their location was related to the Hall concentration measurements.

A. The FKO Energy Method:

We consider the relationship between the slopes in Fig. 2 and N , according to the generalized Schottky equation used by Bottka et al.¹ $\tau\Omega$ is related to E_s by Eqn.(1). By assuming a reduced mass⁸ $\mu=.057m_0$, the surface electric field can be determined. Bottka et al.¹⁰ have shown that the field so determined is related to the carrier concentration, N , and the built-in potential, V_b , by the generalized Schottky equation:

$$E_s = [2eN(V_b - V_p - kT/e)/\kappa\epsilon]^{1/2} \quad (7)$$

V_p is the quasi-equilibrium photovoltage of the laser, kT/e is a thermal term, and $\kappa\epsilon$ is the dielectric constant times the permittivity of free space. Because of pinning at the surface $V_b = .73$ volts¹¹. $\kappa = 13.18$ for GaAs¹⁰ and V_p was determined from Eqn.(7) by using calibrated samples where N was known. Taking $\Delta V = (V_b - V_p - kT/e)$, we obtain :

$$(\Delta V)N = (E_2 - E_1)^3 (3.46 \times 10^{20}) \text{ cm}^{-3} \quad (8)$$

where $(E_2 - E_1)$ is in eV and E_2 and E_1 refer to the energies of the second and the first FKO, respectively. Treating ΔV as a constant evaluated at $N = 10^{16} \text{ cm}^{-3}$, we were unable to fit Eqn.(8) accurately at the concentrations characteristic of the undoped GaAs. The solid line in Fig. 4 shows the relationship given by Eqn. (8), with $\Delta V = .55$ eV. The experimental points fall in a line below this curve and appear to yield a slowly varying ΔV , with a value of .47 eV at the 10^{15} cm^{-3} concentration. It should be noted, however, that ΔV taken at .55 eV gave us good estimates of doping levels for samples with $N \sim 10^{16} \text{ cm}^{-3}$, at the lower limit of the values considered by Bottka et al.¹

One of the reasons for the departure of Eqn. (8) from the experimental values could come from the damping factor which was ignored in Eqn.(5). The location of the FKO peaks depends on the damping factor. To avoid this problem we consider calibration of PR by using the zero cross-over points between the FKO peaks. We obtain from Eqn. (5):

$$[\pi\omega]_m = E_0 + \pi\Omega (3m\pi/2)^{2/3} \quad m=0,1,2,\dots \quad (9)$$

where E_0 corresponds to $m=0$, the first zero PR cross-over point beyond the band edge. Using Eqns. (2), (7), and (9), we obtain a relationship for the cross-over points equivalent to Eqn. (8):

$$N = C_0 (\Delta E)^3 \quad (10)$$

Where, C_0 is an experimentally determined constant and ΔE is the energy difference between the two zero cross-over points $m = 0$, and $m = 1$. A plot of ΔE vs. N is shown in Fig. 4. The solid line in Fig. 4 fits closely $N = 5.0 \times 10^{20} (\Delta E)^3 \text{ cm}^{-3}$, where ΔE is in eV. Fig. 4 provides an easier calibration curve than Fig. 3 since the cross-over points can be determined more precisely than E_1 and E_2 . The curve provides a convenient graph for a quick estimation of the sample purity for undoped GaAs.

B. The Critical Point Energy Method:

To utilize the shift in the critical point energy with carrier concentrations, we considered the behavior of the intercept E_g in place of the critical point energy used by Peters et al.² The intercept E_g occurs at the nominal band gap energy for the sample. Like the critical point energy obtained with TDFF², the intercept E_g varies slightly with doping. Using the band gap energy located in this fashion, we show in Fig. 5 a plot of E_g vs. the carrier concentration N . This plot is similar to the plot given by Peters et al.². It shows a trend between E_g and N , for the lightly doped samples, but the scatter of the experimental points is too large to provide a reliable measure of the unintentional impurity concentrations in undoped GaAs samples. In general Fig. 5 confirms the results of Peters et al.² and shows, as the authors state, that the critical point energy method is limited to the measurements of carrier concentrations

above 10^{16} cm^{-3} . In our case, the relative shift in E_g for the MBE samples with $N \sim 9 \times 10^{15} \text{ cm}^{-3}$, was in good agreement with the tabulated data shown by Peters et al². The error in finding the intercept E_g was less than 3 meV, and was largely due to the inaccuracy of locating the FKO extrema. Errors due to temperature fluctuations were small, but under some experimental conditions, temperature fluctuation could affect appreciably the critical point energy method. Fig. 6 shows the intercepts E_o and E_g as a function of temperature. Except for a slight departure above 500 K, the experimental points for E_g follow the relationship due to Thurmond¹²:

$$E_g = 1.519 - 5.405 \times 10^{-4} (T^2 / (T + 204))$$

Unlike E_g , the slope of the lines used in the FKO method, are insensitive to the temperature fluctuations. Fig. 7 shows that the slope of $\hbar\omega$ vs. F_j remains nearly constant with a moderate change in temperature. The FKO method is thus inherently more accurate once V_p is determined experimentally.

Summary:

Having examined a large number of undoped and lightly doped MBE samples and a variety of undoped bulk GaAs samples, we found that PR provides some consistent information on the quality of MBE material. Besides providing a nondestructive measure of the unintentional impurity concentrations, we can make the following general observations on PR for undoped and lightly doped GaAs.

1. At room temperature, bulk semi-insulating material produced a weak PR at the band edge but showed no accompanying FKO, as might be expected for flat band conditions. The undoped MBE samples appear to fall in an intermediate category between the semi-insulating bulk and the lightly doped MBE samples, and appear to exhibit the intermediate condition between the low and the high field case.

2. Lightly doped samples with Si $\sim 5 \times 10^{15} \text{ cm}^{-3}$ produced greatly enhanced FKO peaks. Generally the first four peaks could be readily measured, and fell along the straight line plots in Fig. 2.

3. At fixed Si doping concentrations of about $8 \times 10^{15} \text{ cm}^{-3}$, the entire PR signal increased with the increase in Hall mobility. However, its shape and the location of the FKO peaks remained unaltered.

4. Good quality undoped MBE material appeared to give relatively large PR amplitude, narrow well defined second FKO peak, an intercept E_g near 1.423 eV, and energy $\Delta E < 13 \text{ meV}$.

5. A display of experimental points for a variety of samples and measurements in Fig. 2 and Fig. 3 shows that PR provides a reasonable method for the measurement of N independent of the sample origin and PR instrumentation.

6. In measurements of PR for undoped GaAs, the zero base line can be readily established at energies above E_2 . Appreciable fluctuation in PR at energies below 1.415 eV generally signify presence of impurities, many of which appear traceable to the substrate. This is often evident in the thin samples.

IV RECOMMENDATIONS:

Photoreflectance can be used in estimating the unintentional impurity concentrations in MBE grow material in the 10^{14} - 10^{15} cm^{-3} range..

High quality material has typical unintentional impurity concentrations less than 2×10^{14} cm^{-3} .

Precaution should be taken in analyzing samples less than $3\mu\text{m}$ thick, when interface effects distort the band edge PR signal.

REFERENCES

1. Bottka, N., D.K. Gaskill, R.S. Sillmon, R. Henry, R. Glosser, J. Electron. Materials 17, 161 (1988).
2. Peters, L., L. Phaneuf, L.W. Kapitan, and W.M. Theis, J. Appl. Phys. 62(11), 4558 (1987).
3. Glembocki, O.J., B.V. Shanabrook, N. Bottka, W.T. Beard, and J. Comas, Appl. Phys. Letters 46, 970 (1985).
4. Shay, J.L. , Phys. Rev. B 2, 803 (1970).
5. Pollak, Fred.H., C.E. Okeke, P.E. Vanier, and P.M. Raccach, J. App. Phys.50, 5375 (1979).
6. Aspnes, D.E., Surf. Sci. 37, 418 (1973).
7. Aspnes, D.E. and A.A. Studna , Phys. Rev. B7, 4605 (1973).
8. Bottka, N.,D.K. Gaskill, R.J.M. Griffiths, R.R. Bradley, T.B. Joyce, C. Ito, and D. McIntyre. To be published in J. of Crystal Growth.
9. Theis, W.M., G.D. Sanders, C.E. Leak, K.K. Bajaj, and H. Markoc , Phys. Rev. B 37, 3042 (1987).
10. R. Glosser, and N. Bottka SPIE 794, 88 (1987).
11. Spicer, W.E., I. Lindau, P. Skeath, C.Y. Su, and P Chye Phys Rev. Lett. 44, 420, (1980).
12. Thurmond, C.D, J. Electrochem. Soc. 122, 1133 (1975).

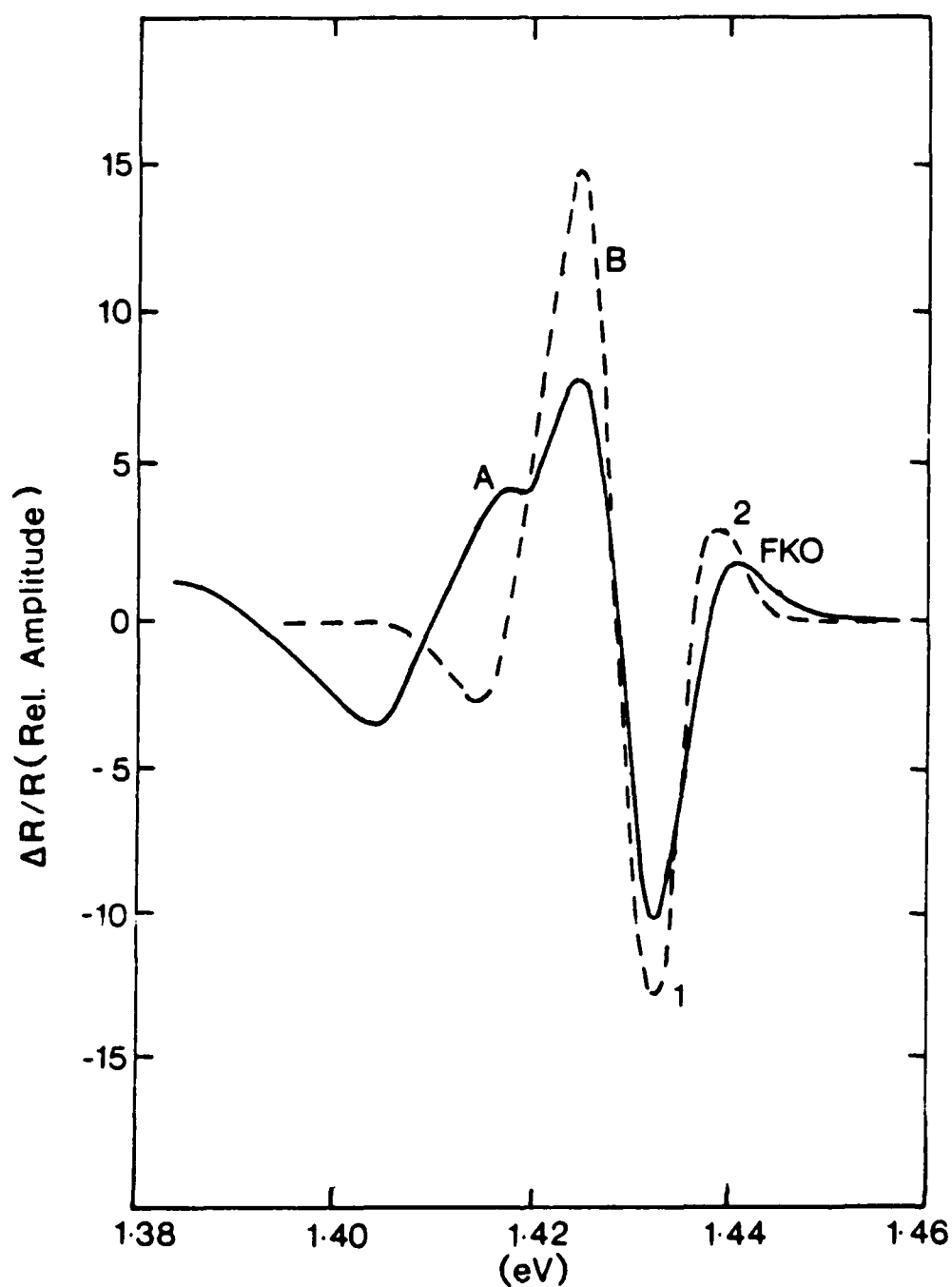


Figure 1. Curve A shows the photoreflectance $\Delta R/R$ for a $2.3 \mu\text{m}$ sample with low unintentional impurity concentration. The structure at A is due to the epilayer-substrate interface. Curve B shows the PR for a typical $4 \mu\text{m}$ undoped sample. 1,2 refer to the labels used in the text for the first two FKO peaks.

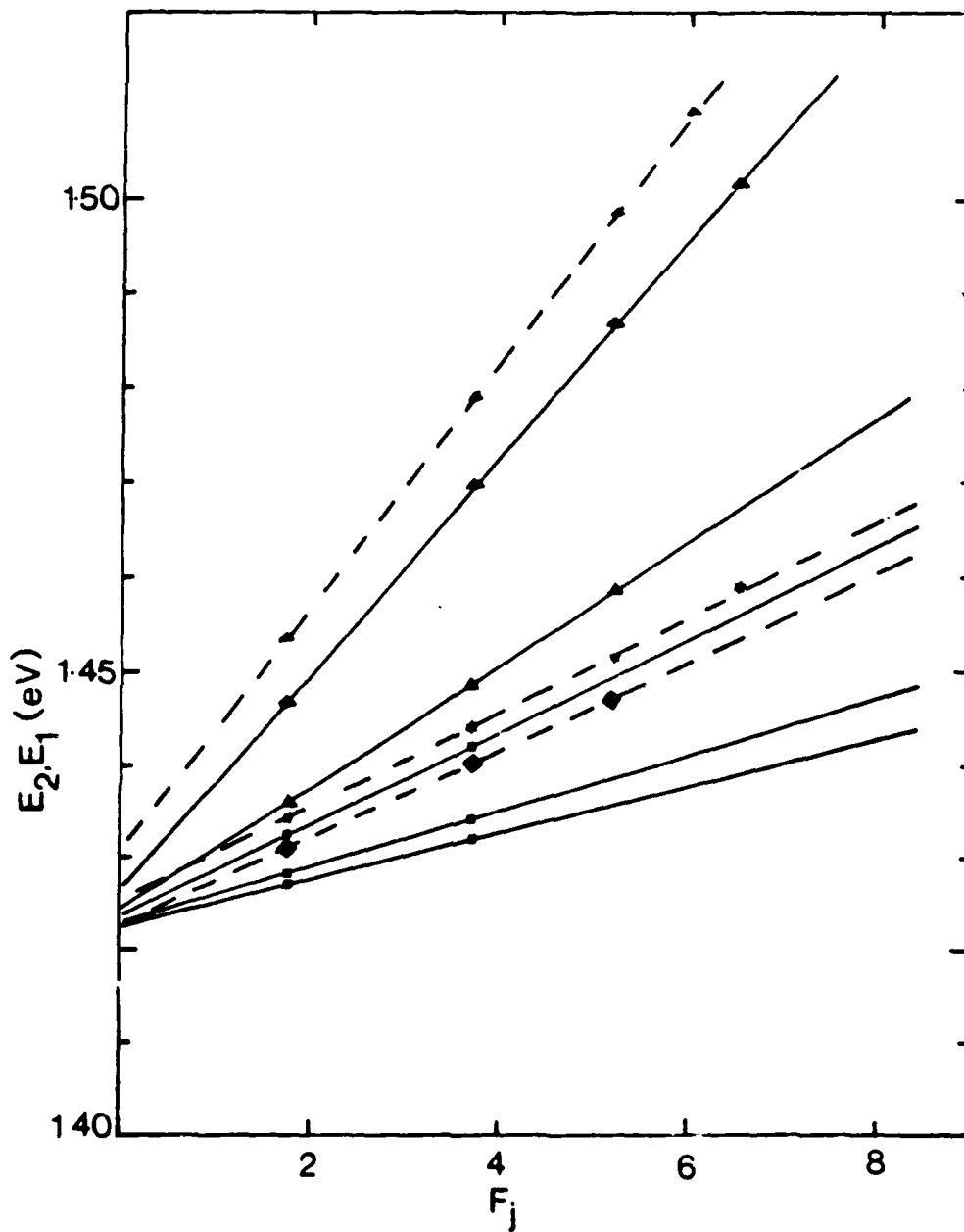


Figure 2. A plot of $[m\omega]_j$ vs. F_j , where j denotes the FKO peak number produces straight line plots whose slopes are determined by the carrier concentration N . (◆) Chemical Vapor Deposition samples. (■) undoped MBE samples. (⌘) NRL calibration sample (CVD). (▲) lightly Si doped MBE samples.

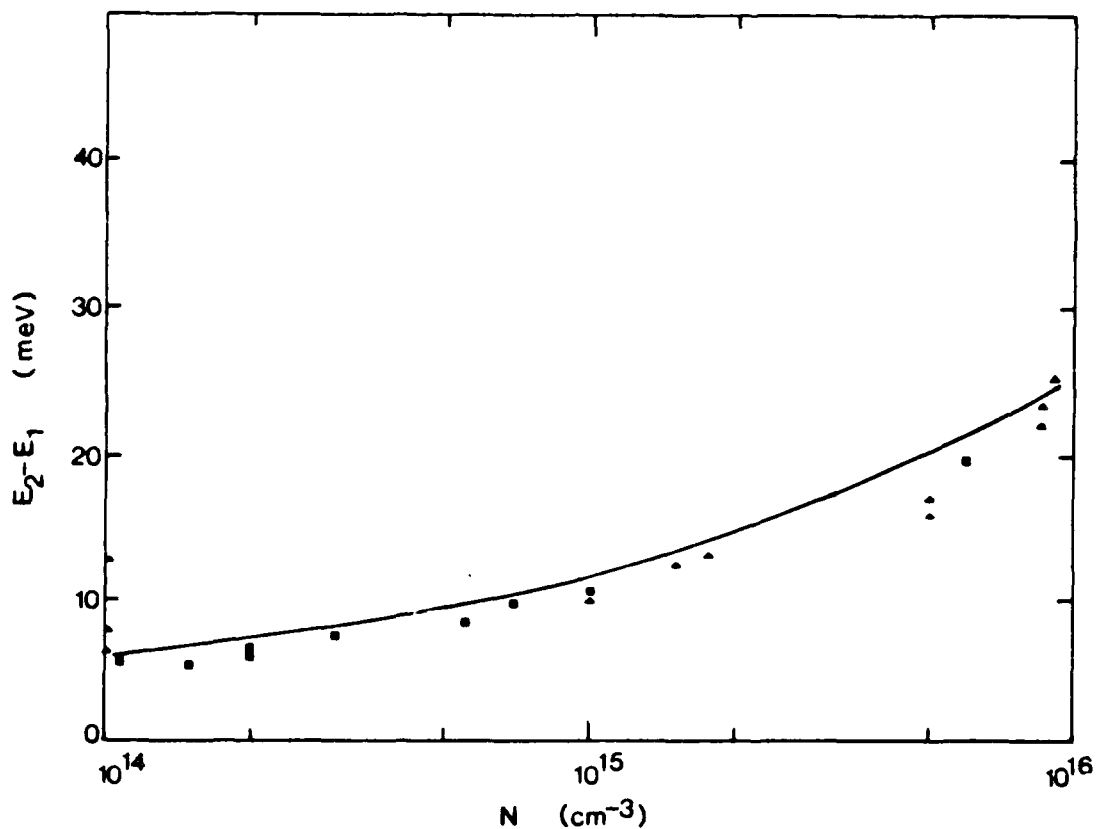


Figure 3. Plot of Energy difference between the first two FKO peaks ($E_2 - E_1$) vs. Hall concentration N , for undoped and lightly (Si) doped GaAs. The solid line represents the theoretical curve given by Eqn. (8) with $\Delta V = .55$ eV.

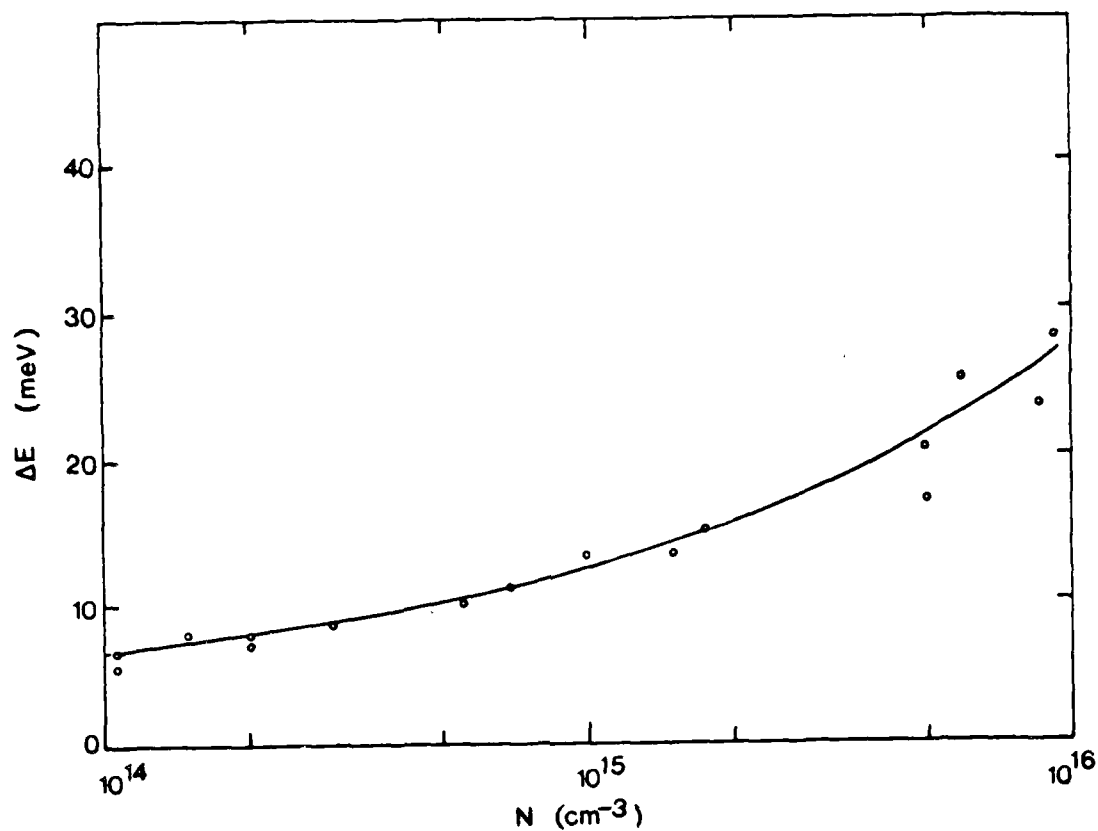


Figure 4. Plot of the separation ΔE vs. carrier concentration N . ΔE is the difference in energy between the first two zero PR cross-over points, following the main PR peak at the band edge. The solid line follows closely a cubic relationship $N = 5.0 \times 10^{20} (\Delta E)^3 \text{ cm}^{-3}$, where ΔE is in eV. The curve provides a convenient graph for estimating the purity of undoped GaAs.

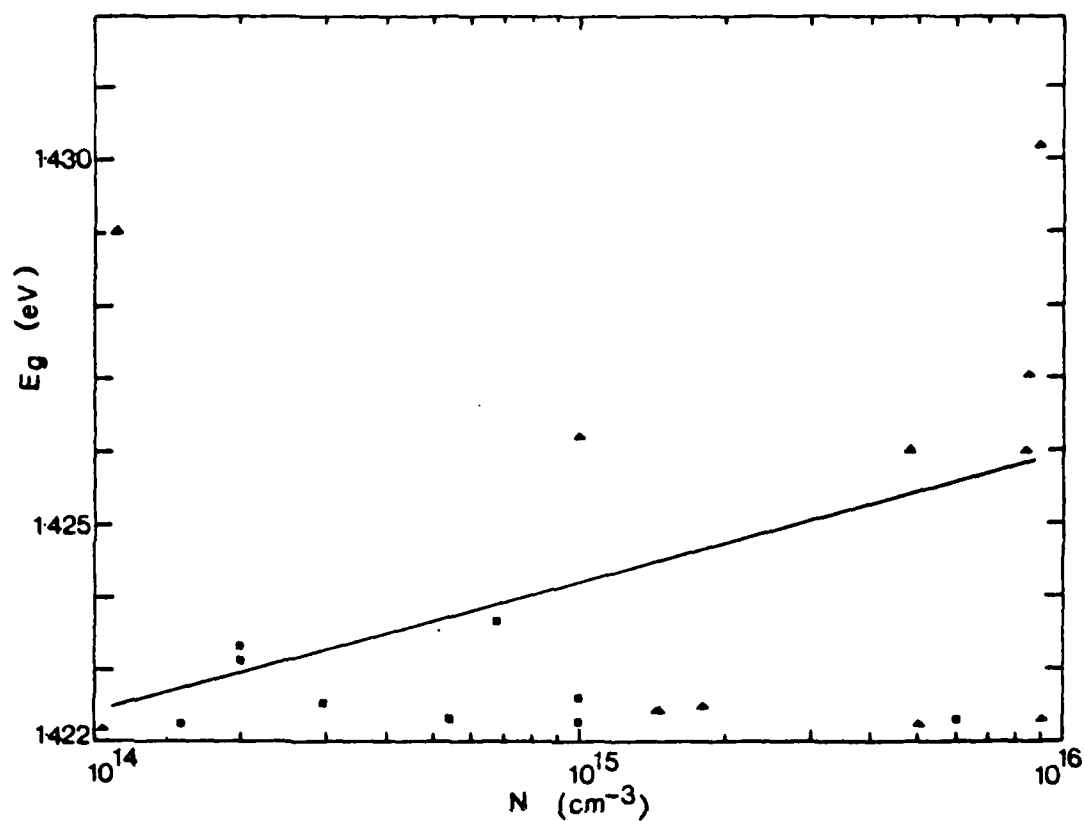


Figure 5. Plot of E_g vs. N shows that the intercept E_g can not be used effectively to determine the carrier concentrations below $1 \times 10^{16} \text{ cm}^{-3}$.

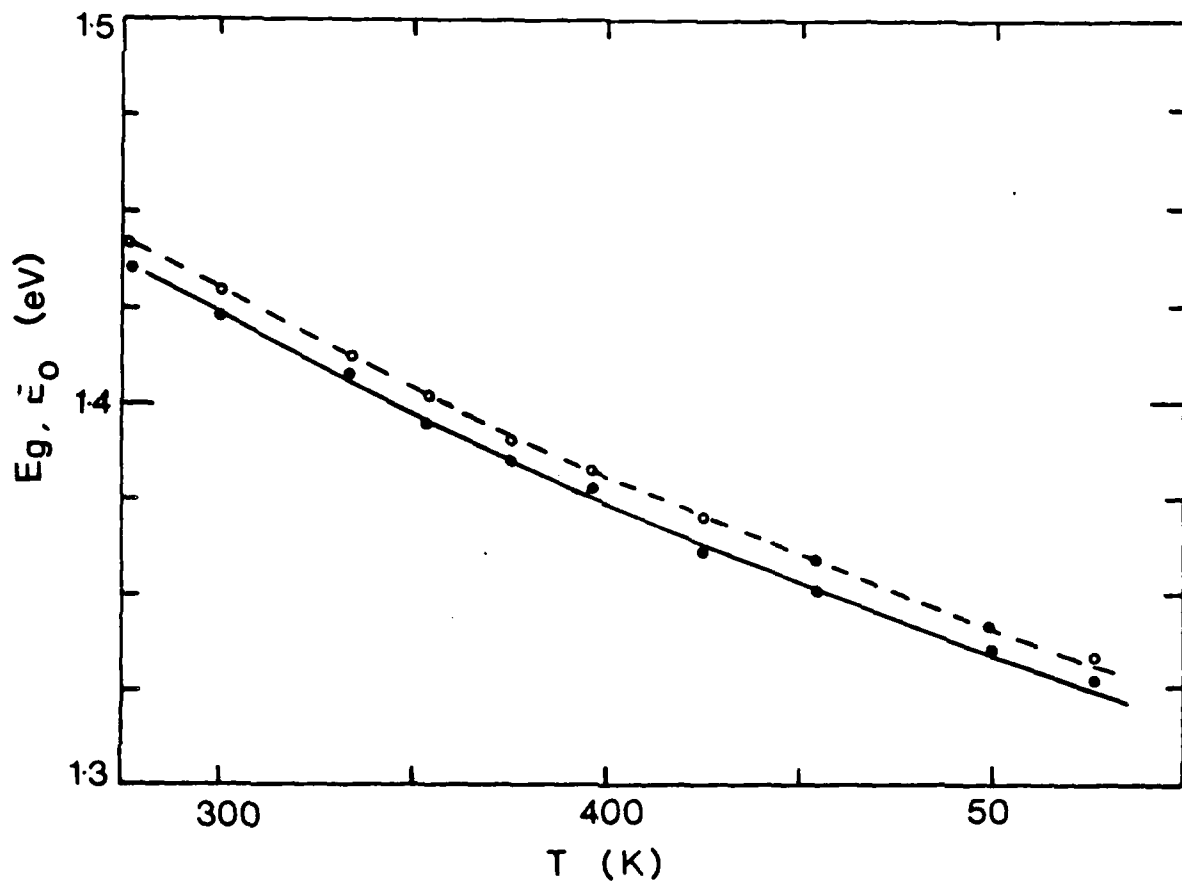


Figure 6. (●) Band gap energy, E_g , determined from FKO intercept method, vs. the Kelvin temperature T . The solid line follows the relationship given by Thurmond¹²: $E_g = 1.519 - 5.405 \times 10^{-4}(T^2/(T+204))$. (○) E_0 , the first zero PR cross-over point beyond the band gap energy. This point is easily located in the PR for undoped GaAs, and serves as a good reference point for comparison of the shifts in PR with temperature, doping, and sample thickness. E_0 is insensitive to the distortion of PR with sample thickness.

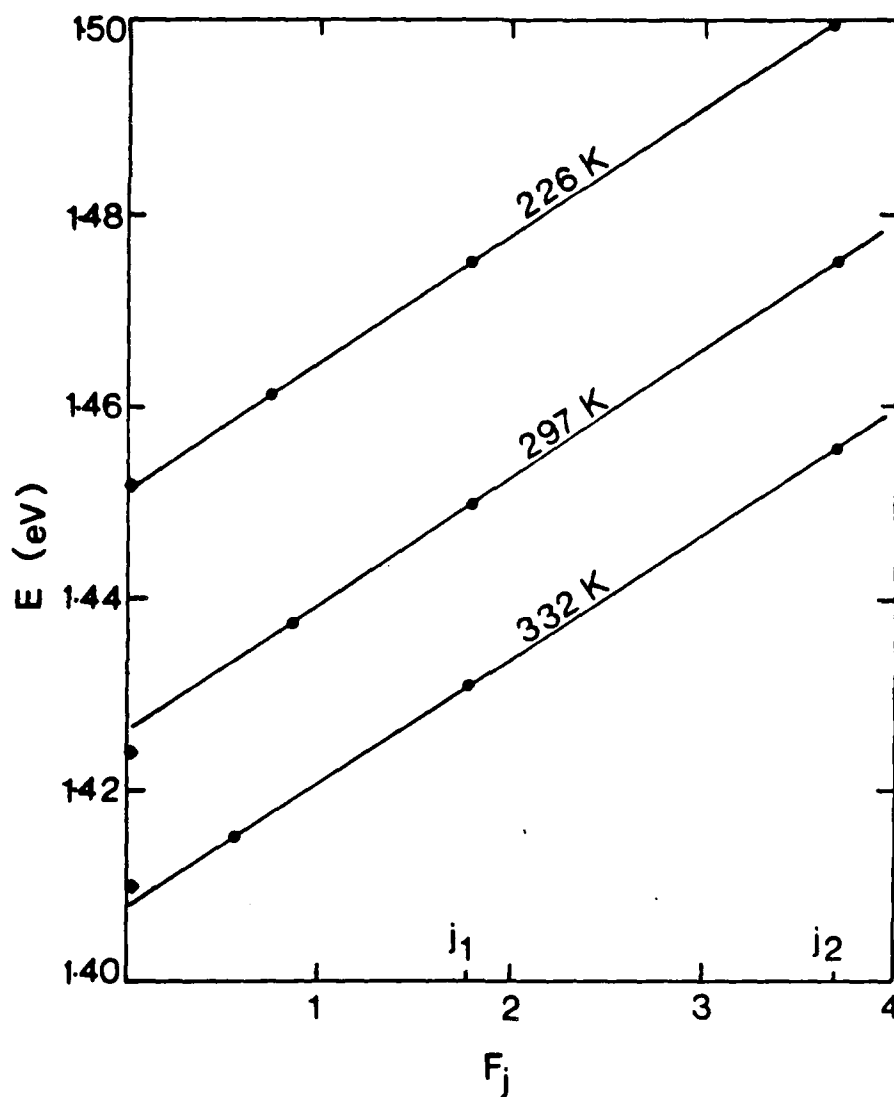


Figure 7. Temperature dependence of the slope $\pi\Omega$, given by Eqn.(6). The slopes, used in the FKO determination of carrier concentrations, are largely independent of temperature fluctuations. (\blacklozenge) Band gap energy, (\bullet) The first cross-over point energies E_0 , (\cdot) The FKO energies E_1 and E_2 . Temperatures are indicated on the graph in each case.

1989 USAF-UES Research Initiation Program Mini-Grant

Sponsored by the
AIR FORCE OFFICE OF SCIENTIFIC RESEARCH

Conducted by
UNIVERSAL ENERGY SYSTEMS, INC.

FINAL REPORT

SYNTHESIS OF 2,6-DIFORMYL PYRIDOBISIMIDAZOLES

Prepared by:	Delbert R. Buffinger
Academic Rank:	Instructor of Chemistry
Department and	Natural Science Department
University:	Wilberforce University
Research Location:	Wilberforce University
Date:	February 15, 1990
Contract No.:	0102-00-320260

SYNTHESIS OF 2,6-DIFORMYL PYRIDOBISIMIDAZOLES

by

Delbert R. Buffinger

ABSTRACT

The synthesis of heterocyclic monomers for use in developing rigid-rod polymers with non-linear optical properties have been investigated. Using as a model system the synthesis of 2-formyl-1-phenyl pyridoimidazole, the synthesis of 2,6-diformyl-1,7-diphenyl pyridobisimidazole was studied and proved to yield poor results following the model's methodology.

ACKNOWLEDGEMENTS

First and foremost, I wish to thank the Air Force Systems Command, the Air Force Office of Scientific Research and Universal Energy Systems, Inc. for their sponsorship of this project.

I would also like to thank my research assistants Calvin and Kelvin Wiley for their work on the project. Their devotion was extremely beneficial to it. A special acknowledgement goes to Dr. Richard Valpey III for his belief in trusting me to carry on his research. His help and technical assistance proved invaluable.

Finally, I would like to recognize Jamie, Sheila, and Teddy for their unending patience with me.

I. INTRODUCTION

The Department of Defense has been carrying out research on new materials for aircraft structural components. One area under investigation is the replacement of metallic based components with those made of high strength polymers. The Materials Laboratory, a branch of the Air Force Aeronautical Systems Division, AFWAL/MLBP at Wright Patterson AFB has spearheaded the research and development of polymers to serve this end. Particular attention is currently focused on rigid-rod aromatic heterocyclic polymers. When processed properly, these materials possess extraordinarily high tensile strength-to-weight ratios. In addition, these polymers whose properties can be altered through the manipulation of their molecular structures have the added capabilities of being able to be spun into fibers, plated into films, molded into shapes and incorporated into molecular composites.

At the focal point of attention is the optical nonlinearity of aromatic rigid-rod polymers. The task to which the project described in this report pertains is ultimately aimed at investigating the atomic structural requirements of nonlinearity. The rationale behind the experiments described herein is that the incorporation of additional heteroatoms with nonbonding electrons in the backbone of the polymer will increase the $n-\pi^*$ transitions

leading to enhanced nonlinear optical coefficients. Specifically, the incorporation of nitrogen atoms in the backbone is to be examined by the synthesis of high molecular weight polymers possessing 2,2'-imidazole linkages (as in figure 1 below).

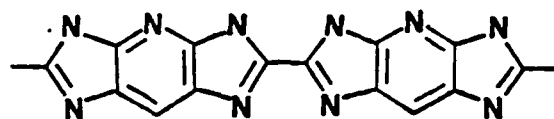


Figure 1: Un-named Polymer

To date, polymers possessing 2,2'-imidazole linkages have yet to be prepared. Using familiar approaches, the polycondensation of tetramines with the diacid of an acylbisimidazole has been attempted.¹ However, these materials decarboxylate during the process. The research described in this report addresses this problem by focusing attention to the synthesis of the corresponding dialdehydes (See figure 2 on the following page).

II. OBJECTIVES

R. Valpey has synthesized a model compound for eluding the experiment conditions for the synthesis of the dialdehyde. This

1. R. Valpey Final Report: Synthesis of 2-Formyl Pyrido-imidazoles, USAF-UES Summer Faculty Research Program, 1988.

compound is comprised of only one imidazole ring and forms only one aldehyde (See figure 3). Using the data from the synthesis of this model compound, the identical conditions were used to attempt to synthesize the dialdehyde.

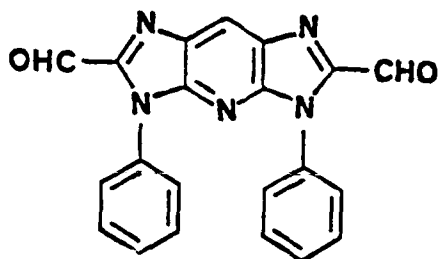


Figure 2: Dialdehyde

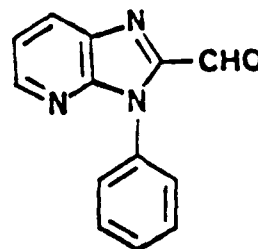


Figure 3: Model Aldehyde

III. RESULTS AND DISCUSSION

The intermediate in the synthesis of the desired dialdehyde, 2,6-dimethyl-1,7-diphenyl pyridobisimidazole was prepared using 2,6-dianilino-3,5-dinitropyridine² with zinc and triethylamine in refluxing acetic anhydride. The final step in the synthesis of the dialdehyde, 2,6-diformyl-1,7-diphenyl pyridobisimidazole, is the oxidation of the aromatic methyl groups of the intermediate. To accomplish this the data from the synthesis of the model compound was crucial. The aromatic methyl group in the model's intermediate, 2-methyl-1-phenyl pyridoimidazole, failed to be oxidized by selenium dioxide,³ benzeneselenic anhydride,⁴ chromium trioxide in acetic anhydride,⁵ ceric ammonium nitrate,⁶ lead tetra-acetate,⁷ and the Etard reaction⁸. Thus none of these methodologies were tried on the dialdehyde's intermediate.

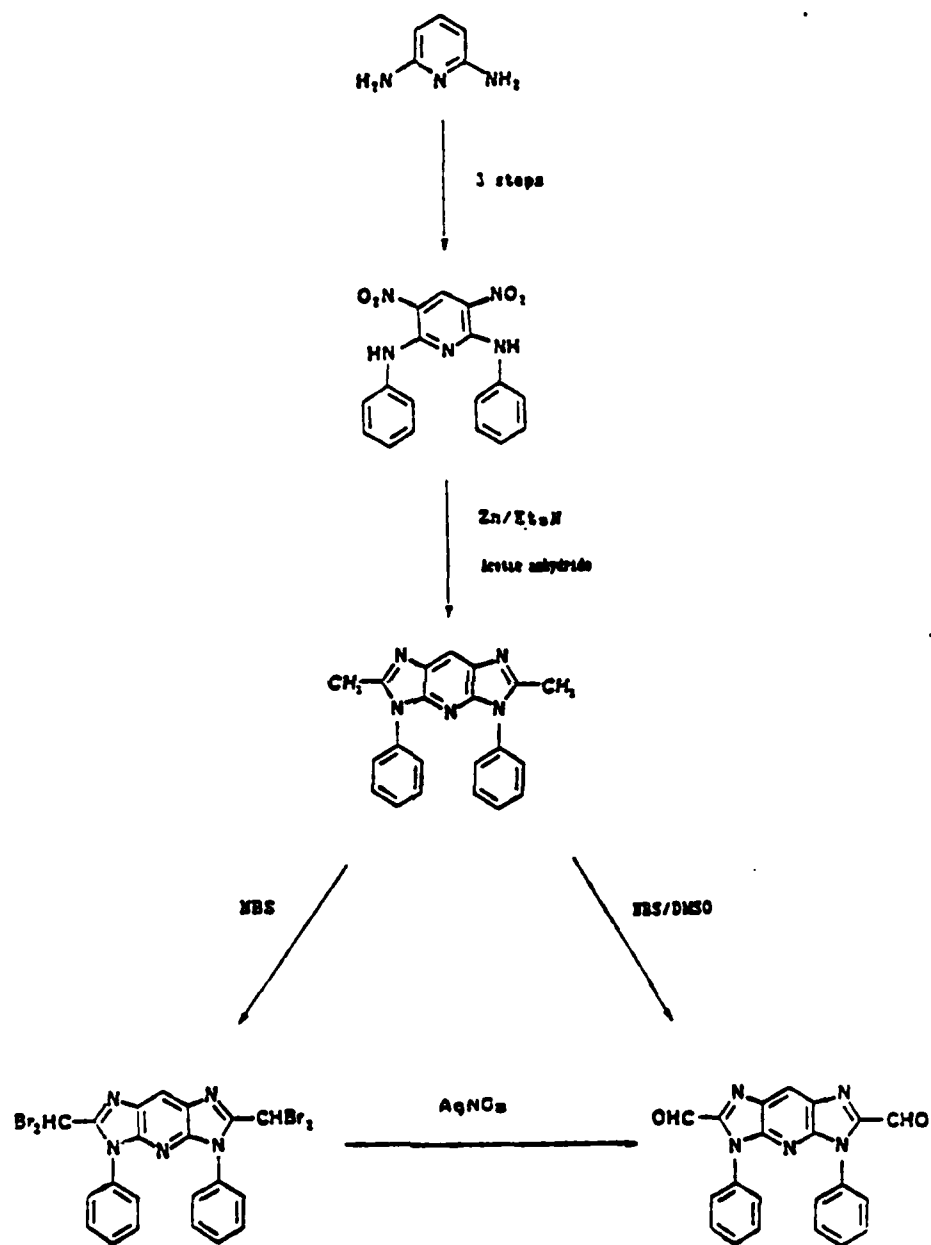
The synthesis of the model compound was achieved by using two similar procedures. The one step route involved the direct

-
2. This known compound was prepared starting with 2,6-diaminopyridine; U.S. patent no. 3,943,125.
 3. D.Liotta Acc. Chem. Res. 1984 17, 28.
 4. D.H. Barton et al. Tetrahedron Lett. 1979 3331.
 5. See S. M. Tsang, E.H. Wood and J.R. Johnson Organic Synthesis Col. Vol III p.641 and references therein.
 6. W.S. Trahanovsky and L.B. Young J. Org. Chem. 1966 31, 2033.
 7. G.W.K. Cavill and D.H. Solomon J. Chem. Soc. 1954, 3943.
 8. W.H. Hartford and M. Darrin Chem. Rev. 1958 58, 1 and references therein.

oxidation of 2-methyl-1-phenyl pyridoimidazole with two molar equivalents of N-bromosuccinimide in DMSO at 110°C. The two step route involved the formation of a bromo or dibromo adduct. The dibromo adduct was formed by using three molar equivalents of N-bromosuccinimide in a solution of 20% acetic acid in ethyl acetate. The model compound was achieved by oxidizing the dibromo adduct with silver nitrate in refluxing 2-methoxyethanol. An alternative method used bromine in place of the N-bromosuccinimide.

The two step route was attempted for the synthesis of the dialdehyde (See scheme 1). Bromination of the dialdehyde's intermediate was achieved by using six molar equivalents of N-bromosuccinimide in a solution of 20% acetic acid in ethyl acetate. This afforded yields of 5-25% for the tetrabromo adduct. Bromination using three molar equivalents of bromine in 40% acetic acid in ethyl acetate was also successful but with lower yields (5-10%). The oxidation of the tetrabromo adduct involving silver nitrate in refluxing 2-methoxyethanol occurred as was noted using TLC. However, attempts at isolation and purification yielded no products.

The one step method seems to be the method of choice since the two step route did not yield the desired dialdehyde. This route was not attempted in this lab, however.



Scheme 1: Dialdehyde Synthesis

IV. EXPERIMENTAL SECTION

Preparation of 2,6-dimethyl-1,7-diphenyl pyridobisimidazole⁹

A mixture of 2,6-dimethyl-3,5-dinitropyridine (5.10 g, 14.5 m.moles), triethyl amine (the triethyl amine does not require distillation but it should be colorless and stored over sodium hydroxide; 4.0 ml, 20 m.moles), and acetic anhydride (40 ml) was mechanically stirred very vigorously while purified zinc dust¹⁰ (110 g) was added slowly in small portions. After 10 g of zinc had been added (approximately fifteen minutes) an exothermic reaction commenced. The remaining Zinc dust was then added at such a rate as to maintain a gentle reflux. The resulting heterogeneous reaction was refluxed for sixteen hours during which time the color changed from black to yellow. After cooling to room temperature glacial acetic acid (8 ml) was added and the yellow slurry was heated at reflux for thirteen hours. The slurry was again cooled to room temperature and excess acetic anhydride

9. R. Valpey Final Report: Synthesis of 2-Formyl Pyrido-imidazoles, USAF-UES Summer Faculty Research Program, 1988.

10. The following procedure was used to purify the zinc dust used in this experiment: Zinc dust (120 g) was slurried for one minute with 2% aqueous HCl (300 ml) two times, deionized water (200 ml) three times, absolute ethanol (200 ml) two times, and finally with anhydrous ether (200 ml) two times. The filtered solid was dried at 100°C in an evacuated drying pistol.

was quenched with 8 ml of water. This addition created an exotherm and resulted in an increase in viscosity. The yellow solution was heated at reflux for four hours then hot filtered to remove the unreacted zinc. The filtrate was added to a liter of 10% ammonium hydroxide. Precipitation was allowed to take place over 30 minutes. The yellow product was collected by filtration. Its color changed to light green during this process. The material was purified by recrystallization from supersaturated absolute ethanol solutions. 3.31 g of the crystals were isolated (67% yield). The product melted at 312°C. The analytical data were as follows:

H-NMR (CDCl₃): δ 8.3(s, 1H), δ 7.2-7.8(m, 10H), δ 2.6(s, 3H)

Preparation of 2,6-(dibromomethyl)-1,7-diphenyl pyridobisimidazole

A mixture of 2,6-dimethyl-1,7-diphenyl pyridobisimidazole (1.0 g, 3.0 m.moles) and N-bromosuccinimide (3.12 g, 18 m.moles) in a solution of 20 % acetic acid in ethyl acetate (20 ml) was heated at reflux for 72 hours during which time the color of the solution changed from yellow to brown and TLC showed loss of the starting material. The reaction was cooled to room temperature and added to a solution of 10% ammonium hydroxide (50 ml). The slurry was filtered. The yellow material was purified by recrystallization from absolute ethanol (0.38 g, 25% yield).

The solid turned black at 174-175°C but did not melt below 340°C.

The analytical data is as follows:

¹H-NMR (CDCl₃): δ8.6(s, 1H), δ7.3-7.6(m, 10H), δ4.6(s, 4H)

Preparation of 2,6-(dibromomethyl)-1,7-diphenyl pyridobisimidazole

A mixture of 2,6-dimethyl-1,7-diphenyl pyridobisimidazole (0.50 g, 1.5 m.moles) and bromine (0.72 g, 4.5 m.moles) in a solution of 20% acetic acid in ethyl acetate (5 ml) was refluxed for 48 hours during which time TLC showed a loss of starting material. The reaction was cooled and added to 10% ammonium hydroxide solution (10ml). The solution was filtered and the yellow solid was recrystallized from absolute ethanol (0.077 g, 10% yield). The solid turned black at 173°C but did not melt below 340°C. The analytical data was the identical to that described in the preceeding paragraph.

Preparation of 2,6-diformyl-1,7-diphenyl pyridobisimidazole

To a refluxing mixture of 2,6-(dibromomethyl)-1,7-diphenyl pyridobisimidazole (0.50 g, 1.5 m.mole) in 20 ml of 2-methoxy-ethanol was added dropwise a solution of silver nitrate (1.35 g,

8 m.mole) in 10 ml of water. The solution turned brown and TLC showed the loss of starting material. The resulting slurry was heated at reflux for an additional hour to insure completion of the reaction. The slurry was cooled and filtered. The TLC of the solid showed a mixture of products and starting material. Purification of the solid in absolute ethanol did not yield any pure products.

V. RECOMMENDATIONS

- A. The synthesis of 2,6-diformyl-1,7-diphenyl pyridobisimidazole through a two step route did not succeed. The use of the one step method seems to be the choice for the synthesis and needs to be addressed.
- B. The ultimate task of using 2,6-diformyl-1,7-diphenyl pyridobisimidazole in a polymerization reaction and subsequent evaluation of the product's properties will then be addressed.

VI. REFERENCES

1. Barton, D.H., et. al., "Preparation of Aldehydes and Ketones by Oxidation of Benzylic Hydrocarbons with Benzeneselenenic Anhydride," Tetrahedron Letters, 1979, pp. 3331-3335.
2. Cavill, G.W.K. and Solomon, D.H., "The Reaction of Lead Tetraacetate with Toluene and Related Compounds," Journal of the Chemical Society, 1954, pp. 3943-3946.
3. Ganem, B., and Boeckman, R.K., "Silver Assisted Dimethylsulfoxide Oxidations; An Improved Synthesis of Aldehydes and Ketones," Tetrahedron Letters, 1974, pp. 917-920.
4. Gilman, H., editor-in-chief, Organic Synthesis, Collective Volumes I-V, New York, John Wiley and Sons Publishers, 1951.
5. Hartford, W.H. and Darrin, M., "The Chemistry of Chromyl Compounds," Chemical Reviews, 1958, pp. 1-72.
6. Liotta, D., "New OrganoSelenium Methodology," Accounts of Chemical Research, 1984, pp. 28-34.
7. Preston, P.N., Benimidazoles and Congeneric Tricyclic Compounds, New York, John Wiley and Sons Publishers, Volume I, pp. 321-331.
8. Trahanovsky, W.S. and Young, B., "Controlled Oxidation of Organic Compounds with Cerium(IV)," Journal of Organic Chemistry, 1966, Volume 31, pp. 2033-2035.
9. Valpey, R., Final Report: The Synthesis of 2-Formyl Pyridoimidazoles, USAF-UES Summer Faculty Research Program, 1988.